— Project Review —

Consortium Project on
Seismic Inverse Methods for Complex Structures

Golden, Colorado, May 17-20, 2010

2009-10 CWP Students and Research Leaders

Norm Bleistein	Dave Hale	Derek Parks	Mamoru Takanashi
Filippo Broggini	Myoung Jae Kwon	Francesco Perrone	Ilya Tsvankin
Tom Cullison	Ken Larner	Paul Sava	Xiaoxiang Wang
Chris Engelsma	Luming Liang	Bharath Shekar	Ran Xuan
Yuanzhong Fan	Yongxia Liu	Steve Smith	Jia Yan
Clement Fleury	Simon Luo	Roel Snieder	Tongning Yang
Jeff Godwin	Yong Ma	John Stockwell	

Visiting Scholar
Lorenzo Casasanta, Politecnico di Milano

Visiting Scientist
Ioan Vlad, Statoil

CWP Staff
Pam Kraus, Program Assistant
Barbara McLenon, Publications Specialist

Center for Wave Phenomena
Colorado School of Mines, Golden, Colorado 80401
(303) 384-2178 fax: (303) 273-3478
email: cwpcsm@dix.mines.edu http://www.cwp.mines.edu

Contents

Acknowledgments

This project review book is prepared for the sponsors of the Consortium Project at the Center for Wave Phenomena. The Consortium Project provides substantial funding for the overall research and educational program at the Center. The Center has also received funds from the following agencies:

- Abu Dhabi National Oil Company
- U.S. Department of Energy
- National Science Foundation
- Petroleum Research Fund of the American Chemical Society
- Research Partnership to Secure Energy for America (RPSEA)

We are extremely grateful for the support of these agencies during the past year and for that of the Consortium sponsors who are listed here.

Aramco Service Company
BHP Billiton Petroleum
BP America Production Co.
Bureau of Geophysical Prospecting
CGGVeritas Services (U.S.) Inc.
Chevron Energy Technology Co.
China Petroleum & Chemical Corp.
ConocoPhillips
ENI S.p.A. E & P Division
ExxonMobil Upstream Research Co.
Halliburton Landmark
Hess Corporation
ION Geophysical Corp.
Japan Oil, Gas and Metals Nat'l Corp.
Marathon Oil Co.
Nexen Petroleum USA Inc.
Paradigm Geophysical Corp.
Petrobras America Corp.
PGS Inc.
Shell International E & P
Statoil
Talisman Energy Inc.
TGS-Nopec Geophysical Co.
Total E & P Services
WesternGeco L.L.C.

In addition to consortium sponsorship, the following companies have supported collaborative projects:

- ConocoPhillips
- ENI S.p.A. E & P Division
- ExxonMobil Upstream Research
- Hess Corporation
- Landmark Graphics Corporation
- Shell Gamechanger Program
- Statoil

CWP Policy on Proprietary Printed Material

New printed material that is produced at the Center for Wave Phenomena under Consortium support is presented to Sponsors before it is released to the general public. We delay general publication by at least 60 days so that Sponsors may benefit directly from their support of the Center for Wave Phenomena.

During this delay, Sponsors may make whatever use of the material inside their organization that they deem proper. However, we expect that all Sponsors will respect the rights of other Sponsors, and of CWP, by not publishing these results externally and independently, in advance of this 60-day delay (even with attribution to CWP). Please refer to your Consortium Membership Agreement under the paragraph entitled "Sponsor Confidentiality Obligation."

Those reports in this book that were produced primarily under consortium support and have not been previously distributed or submitted for publication, will be available for general distribution by October 1, 2009.

If you have independently generated results that duplicate or overlap these, and plan to submit them for publication under your own name before this date, please notify us immediately, so that misunderstandings do not arise.

1 Welcome Words from the Director

The Center for Wave Phenomena (CWP) is an international group with students and faculty from China, France, Japan, Korea, India, Italy, the Netherlands, Nigeria, Romania, Russia, and the United States. The international character of our center reflects not only the rapid globalization that is happening, but also the increasing diversity of the U.S. population. As in any situation where people from different cultures meet, there is sometimes linguistic and cultural confusion.[1] This confusion, however, is compensated by the enrichment inherent to a cultural mix. At CWP we put much emphasis on effective communication as part of the education of our students, through writing, training, and intensive coaching for oral communication. We also provide workshops that address cross-cultural issues that students may encounter. As a result, our students learn to work effectively in the international environment in which geophysicists operate. We cherish the mix of nationalities in CWP and discover daily on the work-floor that apparent differences are only a thin veneer that covers the humanity that we share.

CWP has a double mission of carrying out research and education. In our research we focus on cutting-edge techniques that enhance our capabilities for imaging, modeling, monitoring, visualizing, and interpreting seismic data. In our teaching we aim to deliver the technical skills needed for a career in industry or academia. We also aim to create a nurturing environment for students, a research and learning environment that helps students realize their potential and that fosters a balanced growth in intellectual and human skills needed for effective and compassionate leadership in science and technology. The students, staff, and faculty at CWP constitute a wonderful group of people. What a joy it is to work with this group!

With great pleasure, we welcome representatives of our sponsor companies to the 26th Annual Project Review Meeting and look forward to the opportunity to exchange ideas and thoughts about this past year's projects and our plans for the future. Dialogue with sponsor representatives helps us focus on the scientific problems that are important to your organizations. We look forward to using the Project Review Meeting as a platform for such discussions. It is fitting that we will celebrate the 70th birthday of Norm Bleistein with a dinner at the end of the meeting. Norm is not only one of the founders of CWP, he also has played an important role in educating students over more than 26 years.

This edition of the report on the Consortium Project at the Center for Wave Phenomena summarizes much of the research conducted within CWP since the 2009 Project Review Meeting. Note that the papers in this report and those presented orally during the Annual Project Review Meeting, May 17–20, 2010, only partially overlap.

Roel Snieder, Director
Center for Wave Phenomena
May 2010

[1] I am surprised how often Dutch jokes do not resonate with colleagues of other nationalities.

2 Papers in this Report

The papers in this volume are grouped into the following categories: imaging, velocity estimation, image processing & interpretation, seismic interferometry, electromagnetic fields, and anisotropy. These categories show both similarities to and differences from those of the past few years, indicative of both the continuity and expanding breadth of our research program.

Imaging has traditionally been a major focus at CWP. This book contains five contributions on this topic. *Sava and Vasconcelos* discuss the imaging condition for wave-equation migration which is critical for the development of wide-azimuth wavefield-based velocity analysis required by depth imaging in complex geologic environments. They concentrate in particular on the high computational cost required by the extended images and propose to use extended common-image-point (CIP) gathers constructed at sparse points distributed throughout the image at locations consistent with the geologic structure. *Godwin and Sava* discuss wave-equation imaging with simultaneous sources using a matrix representation of the migration process. They show that the problem of optimal encoding that enhances structure and reduces cross-talk can be cast as the problem of decomposing an approximation of the identity matrix using singular value decomposition. They conclude that by using their amplitude modulation scheme it is possible to achieve migration speed-up factors of an order of magnitude. *Perrone and Sava* discuss a complementary shot encoding scheme that is based on phase delays applied to the recorded data. They compare and contrast conventional encoding schemes and conclude that an optimal combination of high spatial resolution and low cross-talk between unrelated experiments can be achieved at a minimal computational cost increase using dithered-plane encoding. *Vasconcelos, Sava, and Douma* discuss the connections between the extended images constructed by wave-equation imaging and the theory of seismic interferometry. They characterize extended images as locally scattered fields reconstructed by image-domain interferometry and conclude that such images can in principle account for nonlinear effects in the imaging process with application to migration of multiples, and for amplitude corrections. *Bleistein and Gray* close this section with a contribution on true-amplitude 3-D Gaussian beam migration.

The section of **velocity estimation** contains four contributions. *Yang and Sava* discuss the applicability of extended common-image-point gathers to model building using wave-equation migration velocity analysis. They concentrate on the efficient implementation of migration and migration velocity analysis with extended images in the general framework of downward continuation. They also explore the use of differential semblance to velocity analysis with extended images and formulate several alternative penalty operators leading to smooth and convex objective functions. *Yan and Sava* discuss model building for multicomponent data. They suggest the use of a process in which the P and S velocities are estimated sequentially using extended common-image-point gathers. Their proposed method avoids the need for complicated image registration and it is suitable for model building using wave-equation migration velocity analysis adapted for converted waves. *Ma, Hale, Meng and Gong* describe a method for improving the computational efficiency of gradient descent in full waveform inversion; they propose the use of image-guided interpolation and its ad-

joint to compute an image-guided gradient. *Luo and Hale* describe the use of weighted semblance, a simple and inexpensive modification to the conventional semblance calculation, to increase the resolution of NMO-velocity spectra.

The section on **image processing and interpretation** describes algorithms that might typically be applied after seismic imaging to facilitate seismic interpretation and subsurface modeling. *Liang, Hale and Maučec* propose a new method for processing seismic images that simultaneously detects faults and estimates relative displacements of geologic layers on both sides of those faults. *Engelsma and Hale* describe a new method for interactive 3D painting of geologic features in seismic images. Their method uses 3D metric tensor fields to automatically warp a 3D digital paintbrush so that it conforms to imaged features. In a separate paper, they describe a method for visualizing such tensor fields, which are useful in a variety of image-processing algorithms, including image-guided interpolation. *Hale* demonstrates the use of image-guided interpolation to construct 3D images of borehole data that conform to features in a 3D seismic image. *Liang and Hale* describe a new efficient and robust implementation of natural neighbor interpolation, and compare it with other implementations.

The section on **interferometry** starts with a two-part tutorial by *Wapenaar, Snieder, et al.* This tutorial was written on invitation for the 75th anniversary issue of GEOPHYSICS. Part 1 of the tutorial covers the basic principles of seismic interferometry using idealized simple models, and part 2 covers the mathematical background and sketches recent developments in this field of research. The principle of equi-partitioning is often invoked to justify the extraction of the impulse response of a system from field fluctuations. Equipartitioning refers to distribution of energy in a system that is homogeneously distributed in some sense. *Snieder, Slob and Wapenaar* present several examples of equi-partitioning and its relation to seismic interferometry, pointing out that the meaning of equi-partitioninig in these different examples is not necessarily the same. They show that while equi-partitioning may be a necessary condition for Green's function extraction, it is not a sufficient condition. When dense networks of seismometers are available, one can retreive the full wavefield that propagates across the network by cross-correlating the field recorded at each sensor with the field recorded at a master station. *Lin, Ritzwoller, and Snieder* use this to extract the full wavefield that propagates through US-Array in the western part of the USA. Since different stations can be used as a master station, one can retrieve the surface waves propagating in different directions at each point in space. From the surface waves traveling in different directions one can determine the azimuthal anisotropy at every point. They show that the obtained azimuthal anisotropy agrees well with tectonic features, in particular estimates of the strain. One might think that in order to extract scattered waves in seismic interferometry, one just needs to correlate scattered waves with scattered waves. *Fleury, Snieder, and Larner* show that this is not the case. They show, in fact, that the cross-correlation of the scattered waves with the direct wave and the cross-correlation of scattered waves with scattered waves are both needed to extract scattered waves. They show this for a large class of linear systems that include waves that reflect off layers in the subsurface. *Snieder and Fleury* illustrate this principle for the case of isolated scatterers in an acoustic medium. They show that the generalized optical theorem applied to each scatterer is

essential for the correct retrieval of the impulse response from field fluctuations.

The research of the past year on applications of interferometry to electromagnetic fields has led to three papers in **electromagnetic methods**. *Fan, Snieder, et al.* study the application of synthetic aperture methods to Controlled Source Electromagnetics (CSEM). They show that by making suitable combinations of the fields excited by a small antenna, one can synthesize the response of the system to a large antenna. In this process one can direct the antenna in specific directions. They show that this increases the sensitivity of CSEM measurements to hydrocarbons and illustrate this with an example with field data. The inversion of CSEM data is in practice based computationally-intensive data fitting methods. *Kwon and Snieder* investigate the use of the inverse scattering series in CSEM as an alternative. The application of the inverse scattering series has been studied extensively for seismic problems by Art Weglein at the University of Houston. It is the long wavelength of the fields used in CSEM that makes the inverse scattering series an interesting alternative to brute-force data fitting methods. Last year we presented the new formalism for Lagrangian Green's function extraction, and showed that it is possible to extract the impulse response of potential fields from quasi-static field fluctuations. *Snieder, Slob, and Wapenaar* present numerical examples that show that electrostatic potential for a monopole can be extracted from field fluctuations that are generated by random dipoles.

The section on **seismic anisotropy** includes five papers. *Tsvankin et al.* present a comprehensive review of seismic modeling, processing, and inversion for anisotropic media. They discuss the foundations of methods operating with both P-waves and multi-component data, demonstrate the improvements achieved by anisotropic imaging algorithms and outline the possibilities of applying anisotropy parameters in reservoir characterization. *Wang and Tsvankin* develop a 3D inversion algorithm for layered TTI (transversely isotropic with a tilted symmetry axis) media that operates with P-wave NMO ellipses, zero-offset traveltimes, and reflection slopes supplemented by borehole data. They show that if the symmetry axis is perpendicular to the bottom of each layer, it is possible to estimate the interval symmetry-direction velocity V_{P0}, the anisotropy parameter δ, and the reflector orientation using only one borehole constraint – the reflector depth. When the tilt of the symmetry axis represents a free parameter, the input data also must include wide-azimuth VSP traveltimes with the offset reaching at least 1/4 of the maximum reflector depth. *Takanashi and Tsvankin* discuss P-wave nonhyperbolic moveout inversion for horizontally layered VTI (TI with a vertical symmetry axis) models that include a low-velocity isotropic lens (e.g., channel or reef). Finite-difference modeling shows that even a thin lens can cause substantial laterally varying errors in the normal-moveout velocity and the anellipticity parameter η. They propose several criteria to delineate the area influenced by the lens and devise an efficient algorithm for removing lens-induced traveltime shifts from prestack data. *Shekar and Tsvankin* extend the attenuation layer-stripping method, previously developed for pure-mode reflections, to mode-converted (PS) waves with the goal of estimating the interval S-wave attenuation coefficient. Their technique involves application of the PP+PS=SS method and velocity-independent layer stripping (VILS) to PP and PS reflections from the top and bottom of the target layer. A synthetic test on multi-component synthetic data from VTI media confirms that the algorithm can accurately evaluate the interval shear-wave

quality factor in the target without knowledge of the velocity and attenuation in the overburden. *Smith and Tsvankin* study the influence of reservoir compaction on time-lapse P-, PS-, and S-wave reflection data by combining 2D geomechanical and finite-difference seismic modeling. Application to a rectangular compacting reservoir embedded in a homogeneous, isotropic unstressed medium reveals both similarities and differences between the traveltime shifts of compressional and shear waves. The developed methodology helps analyze kinematic and dynamic time-lapse attributes for multi-component data and can be used in the inversion for the compaction-induced stress field.

3 Overview of Developments in CWP

CWP Faculty and Staff

There has been no change in the CWP faculty group since the 2009 Project Review Meeting. The full-time CWP academic faculty includes Dave Hale, Paul Sava, Roel Snieder (director), and Ilya Tsvankin. In accordance with the rotation plan approved by the CWP faculty in 2004, Roel Snieder assumed the position of CWP director in June 2008. Ken Larner and Norm Bleistein remain part of the team in their "retirement," and are actively involved in many aspects of our research and educational program. Program assistant, Pam Beckman, has married and is now Pam Kraus. She manages the CWP office in a most professional and cheerful way. Publication specialist Barbara McLenon provides essential assistance in preparing our scientific manuscripts, public relations material, our website, and the newsletters of CWP and the Geophysics department. John Stockwell not only manages the computer systems of CWP, his insight and expertise in the mathematical aspects of geophysics are invaluable. John is principal investigator of Seismic Unix and is instrumental in maintaining and promoting this software for seismic data processing.

Students and long-term visitors

During the 2009-2010 academic year, 15 graduate students were doing research in CWP. Five new CWP students (Thomas Cullison, Chris Engelsma, Clement Fleury, Jeff Godwin, and Simon Luo) started their graduate studies in the Fall of 2009. In the past year, two students completed their degree work: Derek Parks, MSc., and Jyoti Behura, PhD. In August-December 2009, Lorenzo Casasanta from the Politecnico di Milano visited CWP and worked with Ilya Tsvankin. Ioan Vlad from Statoil is a visiting scientist at CWP from January through December 2010 working with Paul Sava.

Center Support

Currently the Consortium is supported by 25 companies including our newest sponsors, Nexen Petroleum and Paradigm Geophysical. We thank the representatives of our sponsors for their continued support. A full list of sponsor companies over the term of the past year appears on the acknowledgment page at the beginning of this volume.

We have received approximately $860K of additional support since June, 2009, from the National Science Foundation, Petroleum Research Fund of the American Chemical Society, the Research Partnership to Secure Energy for America, ENI, ExxonMobil, Shell, ConocoPhillips, Hess, Statoil, and the Abu Dhabi National Oil Company through its educational partnership with the Colorado School of Mines. Our industrial and government support for research and education complement one another; each gains from, and strengthens, the other. As a net result, for the annual 2009-2010 fee of $52.8K, a company participates in a research project whose total funding level is close to $2.21M, which means that the contribution of every sponsor is leveraged with a factor of 42.

Joint Projects with Industry and Non-Profit Corporations

Roel Snieder and his students continue their work with Shell within the framework of the company's Gamechanger program. Shell has provided funding for the three-year project "Stripping the overburden from the seismic and electromagnetic earth response" started by Roel in collaboration with Kees Wapenaar and Evert Slob of Delft University. Roel started a collaborative program with ConocoPhillips and Boise State University that is focused on various aspects of multiple scattering in imaging and monitoring. Roel also receives funding from the National Science Foundation and the US Department of Energy.

Paul Sava is supported by a grant from ENI dedicated to the development of migration velocity analysis using reverse-time migration techniques. This four-year project will provide full support for one graduate student (Francesco Perrone). In addition, Paul continues a three-year project supported by Statoil on wave-equation velocity analysis and imaging for wide-azimuth data. This research provides 50% support for graduate student Tongning Yang.

Ilya Tsvankin and his student Bharath Shekar continue their work on the two-year project "Azimuthal AVO and attenuation analysis for fracture characterization" funded by the Research Partnership to Secure Energy for America (RPSEA). RPSEA is a non-profit corporation formed by a consortium of premier U.S. energy research universities, industry, and independent research organizations.

Dave Hale and CWP graduate student Luming Liang worked last year with Marco Maučec of Landmark on a new method to estimate fault locations and displacements. Dave also worked with Joe Meng to launch a new multi-year project funded by ConocoPhillips on applications of image-guided interpolation and related technologies to full-waveform inversion. CWP graduate student Yong Ma is supported by this research.

Joint research by CWP students and faculty with geophysicists in sponsoring companies has proven to be extremely valuable for connecting CWP research with the scientific activities of our sponsors. The complementary nature of academic and industrial research has significantly enhanced the value of a number of projects. For this reason, CWP encourages directly sponsored research with companies and non-profit corporations that could lead to sharing of results with the Consortium.

SmartGeo

SmartGeo is an interdisciplinary engineering and science graduate program designed to prepare a new generation of leaders in the development of intelligent geosystems - enabling engineered and natural earth structures and environments that sense their environment and adapt to improve performance. Research efforts focus on advancing intelligent geoconstruction, distributed sensor networks, and real-time monitoring. The research is applied to intelligent earth dams and levees, and remediation of contaminated soil and water. This interdisciplinary graduate program is led by faculty members in civil engineering, geophysics, and computer science. Dave Hale is a principal investigator in the SmartGeo program partly because of his background in both geophysics and computer science.

Educating our students

The Department of Geophysics and other departments at the Colorado School of Mines offer numerous graduate courses from which CWP benefits. In addition to these courses, we have taken the following initiatives to educate CWP students.

- *English Writing & Speaking.* For many students, writing scientific papers is an onerous activity, especially for international students. Over the past several semesters, Diane Witters, a writing consultant whose expertise is English as a Second Language (ESL), has worked with CWP students to improve their writing and speaking skills through one-on-one tutoring sessions and writing workshops. Diane closely coordinates her efforts with CWP faculty. In addition to helping students advance their writing skills, she has assisted foreign students to make the transition from the work culture in their home country to the professional style common in the United States.
- *Mathematics.* In order to ensure that CWP students master the mathematics needed for wave propagation and imaging, John Stockwell teaches a Math Clinic, a graduate course covering the mathematics used in CWP research. The course is attended by a record number of 15 students from both CWP and other research groups in the Geophysics Department. The feedback from students has been extremely positive.
- *The Art of Science and Introduction to Research Ethics.* Roel Snieder offers the interdepartmental course "The Art of Science", which is aimed at helping graduate students develop effective research habits. He also offers this material as a short course. With colleague Carl Mitcham, Roel developed the new graduate course "Introduction to Research Ethics." This course fulfills the requirement for all-important ethics training for students and postdoctoral fellows who are funded by the National Science Foundation.

Short courses and workshops

The CWP faculty has been active in sharing their professional expertise by offering short courses to groups in academia and industry. Please contact CWP if you are interested in hosting one of

these short courses.

- Ilya Tsvankin, with his long-time collaborator Vladimir Grechka of Shell, continued to offer the short course *Seismic anisotropy: Basic theory and applications in exploration and reservoir characterization* as part of the SEG Continuing Education Program. The course provides the necessary background information about anisotropic wave propagation and discusses modeling, inversion, and processing of seismic reflection and VSP data in the presence of anisotropy. The main emphasis of the course is on practical parameter-estimation methods for transversely isotropic and orthorhombic subsurface models.

- Paul Sava traveled extensively giving his course *Wavefield Seismic Imaging.* This course provides a survey of current seismic imaging methods designed for acoustic wavefield data. Wavefield seismic imaging, also known as wave-equation migration, is presented in a unified theoretical framework in connection with related topics, including migration velocity analysis (MVA) and amplitude-versus-angle analysis (AVA). The main target audiences for this course are graduate students engaged in seismic imaging research and practicing geophysicists with a basic understanding of seismic data processing and imaging who wish to become familiar with modern imaging techniques available to the industry. Geologists and reservoir engineers can also benefit from a short version of this course by familiarizing themselves with the concepts that underly practical imaging techniques, their applicability, and limitations.

- Norm Bleistein continued to enjoy his "retirement" by giving his short course *Mathematics of Modeling, Migration and Inversion with Gaussian Beams*, most recently at the 2009 SEG Annual Meeting in Houston. This course is designed for data processing developers with some knowledge of ray theory, migration, and inversion methods, and a desire to learn the fundamentals of modeling, migration and inversion using Gaussian beams. As such, it is a course based on the mathematics that underlies the theory and implementation of Gaussian beams in seismic modeling.

- Roel Snieder developed a short version of the course *The Art of Science.* In this short course he offers elements of his full course that help young researchers develop effective research habits. Because of the wide scope of the material that he uses for his graduate course there is much freedom in the selection of topics for the short course. He has taught this short course at Stanford University, Tohoku University, Utrecht University, and Australian National University. This course is well-suited for industrial research environments as well.

- CWP played a major role in organizing the 13th International Workshop on Seismic Anisotropy in Winter Park on August 10-15, 2008. The Workshop Proceedings were published in September-October 2009 as a special section of the journal GEOPHYSICS, with Ilya Tsvankin, Ken Larner, and James Gaiser of Geokinetics serving as guest editors.

Interaction with Other Research Projects at CSM and Elsewhere

During this past year, as in previous years, faculty and students of CWP have interacted closely with those in other industry-funded research projects in the CSM Department of Geophysics. These include the Reservoir Characterization Project (RCP), led by Tom Davis; the Center for Rock Abuse, led by Mike Batzle; and the Gravity/Magnetics Project, led by Yaoguo Li.

In addition, the CWP faculty have engaged in collaborative efforts with researchers elsewhere. Ilya Tsvankin spent the Spring and Summer of 2009 on sabbatical leave. He was writing a new book and traveled for two months in Europe where he worked with Serge Shapiro at the Free University of Berlin and Walter Söllner at the PGS office in Oslo. He also taught a course on anisotropy at the Free University and gave a number of presentations in several European cities (see more details below). Other collaborations of the CWP faculty include:

- Norm Bleistein
  - Sam Gray (CGGVeritas)
- Dave Hale
  - Marco Maučec, Bill Harlan and Bob Howard (Landmark)
  - Joe Meng (ConocoPhillips)
  - Joe Stefani (Chevron)
- Paul Sava
  - Uwe Albertin (BP)
  - Tariq Alkhalifah (KAUST)
  - Clara Andreoletti and Nicola Bienati (ENI)
  - Andre Bulcao (Petrobras)
  - Sergey Fomel (UT Austin)
  - Paul Fowler (WesternGeco)
  - Marianne Houbiers and Ioan Vlad (Statoil)
  - Panos Kelamis, Yi Luo, and Tong Fei (Aramco)
  - Scott Morton (Hess)
  - Michael Payne, Jie Zhang, Anupama Venkataraman, Rongrong Lu, Alex Martinez (ExxonMobil)
  - Bill Symes (Rice University)
  - Ivan Vasconcelos (ION Geophysical)
  - Stuart Wright (Dawson Geophysical)
  - Yu Zhang and Sam Gray (CGGVeritas)
  - Peter Traynin and Lorie Bear (ExxonMobil)
- Roel Snieder
  - Andrew Curtis and David Halliday (Edinburgh University)

- Malcolm Sambridge (Australian National University)
- Johannes Singer, Jon Sheiman, Mark Rosenquist and David Ramirez Mejia (Shell)
- Grant Gist and Rebecca Saltzer (ExxonMobil)
- Ivan Vasconcelos and Huub Douma (ION Geophysical)
- Kees Wapenaar and Evert Slob (Delft Institute of Technology)
- Kasper van Wijk (Boise State University)
- Phil Anno and Mark Willis (ConocoPhillips)
- Haruo Sato (Tohoku University)

- Ilya Tsvankin
  - Andrey Bakulin and Jörg Herwanger (WesternGeco)
  - James Gaiser (Geokinetics)
  - Vladimir Grechka (Shell Exploration & Production)
  - Subhashis Mallick (University of Wyoming)
  - Ivan Pšenčík (Czech Academy of Sciences)
  - Serge Shapiro (Free University of Berlin)
  - Walter Söllner (PGS)

Travels and Activities of CWP People

Interactions and collaborations that have taken place away from Golden include the following:

- Norm Bleistein
  - Traveled to Israel to visit Zvi Koren at Paradigm in March 2010.

- Dave Hale
  - Presented research on image-guided interpolation to Landmark in Highlands Ranch, Colorado (July 2009).
  - Traveled to Northwestern University to help teach an NSF/Earthscope one-week workshop on industrial-strength processing of seismograms currently being recorded in the USArray experiment (August, 2009).
  - Presented a paper on image-guided interpolation at the SEG Annual Meeting in Houston (October 2009), recognized as one of the top thirty presented at that meeting.
  - Traveled to Rice University to give an invited presentation on the question, "Who will write the software?", as part of the 2010 Oil and Gas High Performance Computing Workshop (March 2010).
  - Continued to develop the open-source Mines Java Toolkit with various collaborators.

- Ken Larner
  - In cooperation with Roel Snieder wrote the book "The Art of Being a Scientist" that was published by Cambridge University Press in August, 2009.

- Served as Chair of the Board of Directors of the SEG Advanced Modeling Project (SEAM).
- Invited speaker for the Geophysical Society of Houston/SEG 2010 Spring Symposium honoring Enders Robinson and Sven Treitel.
- Participated on a team to evaluate the Earth Sciences Institutes in Berlin and Potsdam, Germany.

- Paul Sava
  - Presented a paper at the EAGE Annual Meeting in Amsterdam (June 2009).
  - Traveled to Trondheim to collaborate with colleagues from Statoil (June 2009).
  - Traveled to Milan, Italy, to collaborate with colleagues from ENI (June 2009).
  - Presented the Wavefield Seismic Imaging (WSI) course in Houston for ExxonMobil, in Trondheim for Statoil, and in Milan for Eni.
  - Presented a course on Reverse-Time Migration at the bi-annual Congress of the Brazilian Geophysical Society SBGf (August 2009).
  - Presented a paper at the SEG Annual Meeting, Houston (October 2008), and co-authored nine other presented papers.
  - Delivered a keynote address at the Subsalt Imaging Workshop organized by EAGE in Cairo, Egypt (November 2009) and co-authored another presented paper.
  - Served on the EAGE research committee.

- Roel Snieder
  - Served on the Earth Science Council of the US Department of Energy (DOE).
  - Associate editor of the Journal of the Acoustical Society of America.
  - Presented his outreach lecture "The Global Energy Challenge" 20 times at universities, community colleges, high school and elementary schools, service clubs, and churches. More information is at `http://www.mines.edu/~rsnieder/Global_Energy.html`
  - Visiting Fellow at the Australian National University where he lectured on CO_2 sequestration, taught his short course *The Art of Science*, and presented the annual Totoya Lecture *The Global Energy Challenge.*
  - Invited speaker at the Summer Research Workshop on Carbon Capture and Sequestration, Banff, Canada.
  - Invited speaker, Joint Assembly of the American Geophysical Union, Toronto.
  - Visiting professor of the Center of Excellence Program of Tohoku University, Sendai, Japan.
  - Visited JAPEX in Tokyo.
  - Co-organizer of a research workshop at Shell Research (Houston).
  - Member of the Diversity Committee at the Colorado School of Mines.
  - Chair of the Committee for Ethics Across the Curriculum of the Colorado School of Mines.

- In addition to the activities above he presented 15 presentations and seminars at universities, industry, and international conferences

- Ilya Tsvankin

  - Served as editor of the Proceedings of the 13th International Workshop on Seismic Anisotropy (13IWSA) published as a special section of *Geophysics* (September-October 2009).
  - Worked on the new book "Seismology of azimuthally anisotropic media and seismic fracture characterization" in cooperation with Vladimir Grechka of Shell. The book is scheduled for publication by SEG in 2011.
  - Taught the two-day SEG Continuing Education Course "Seismic anisotropy: Basic theory and applications in exploration and reservoir characterization" at the Free University of Berlin, Germany (June 2009) and as part of the Continuing Education Week of the Denver Geophysical Society (August 2009).
  - Presented a paper at the Annual EAGE Conference in Amsterdam (June 2009).
  - Presented the invited lecture "Characterization of fractured reservoirs using wide-azimuth seismic data" at the Free University of Berlin (June 2009).
  - Visited the PGS office in Oslo, Norway to collaborate with Walter Söllner and give a presentation on anisotropic velocity analysis (June 2009).
  - Presented the lecture "Fracture characterization using surface and borehole seismic data: Advances and challenges" as part of the Distinguished Lecturer Series at the University of Wyoming (October 2009).
  - Coauthored four papers at the SEG Annual International Meeting in Houston (October 2009).
  - Invited speaker at the Spring Symposium of the Geophysical Society of Houston in honor of Enders Robinson and Sven Treitel (March 2010).
  - Gave the presentation "Role of anisotropic methods in characterization of tight gas sandstones" at the National Meeting of the Research Partnership to Secure Energy for America (RPSEA; April 2010).
  - Co-authored a presentation at the 14th International Workshop on Seismic Anisotropy in Perth, Australia (April 2010).

Our students traveled considerably this past year as well. In addition to attending meetings, many of the students held internships during summer 2009. These experiences enrich their education and help foster valuable contacts with potential employers.

Visitors to CWP

CWP has benefited again this year from visits by a number of scientists and friends from other universities and industry. We strongly encourage visits from our sponsor representatives, whether it be for a single day, or for an extended period.

- Evert Slob from Delft University of Technology worked at CWP from January-August 2009 as part of his sabbatical leave. He worked with Roel Snieder and his students on the application of interferometric concepts to electromagnetic fields.
- Paul Fowler (WesternGeco), James Gaiser (Geokinetics), and Edward Jenner (ION/GXT) have regularly participated in the A(nisotropy)-Team seminar and collaborated with CWP faculty and students. Paul has also attented seminars of the I(maging)-Team.
- Alexandre Araman from Total S.A. in Pau (France) came to CSM as an M.S. student in 2008 and collaborated with Ilya Tsvankin on a project involving processing and inversion of multi-component offshore data. Alexandre was primarily affiliated with the Reservoir Characterization Project and defended his M.S. thesis in the Fall of 2009.
- Seiichiro Kuroda from Japan worked at CWP from March-October 2009 on the application of interferometry to ground penetrating radar. He worked with Roel Snieder and Evert Slob and focused on the use of multi-dimensional deconvolution.
- Chenghong Zhu from Sinopec was at CWP from March-August 2009 to get better acquainted with the research carried out at CWP and to establish a common ground for future collaboration.
- Ioan Vlad from Statoil is spending a year (January-December 2010) at CWP to work with Paul SAVA and other members of his team. Ioan continues the collaboration with Tonging Yang that started during his internship with Statoil in the summer of 2009.
- Nicola Bienati and Clara Andreoletti (Eni) visited for a week in January 2009 to participate in joint research with Paul Sava and Francesco Perrone.
- Tariq Alkhalifah (KAUST) visited for a week in July 2009 to work with Paul Sava on anisotropic extended images.
- Uwe Albertin (BP) visited in December 2009 to work with Paul Sava and Paul Fowler (WesternGeco) on wavefield-based migration velocity analysis.

We also had a number of short-term visitors:

- Monica Kohler, Center for Embedded Networked Sensing, University of California
- Leonard Srnka, ExxonMobil
- Diana Sava, The University of Texas at Austin
- Craig Beasley, WesternGeco
- Richard C. Aster, New Mexico Institute of Technology
- Kees Wapenaar, Delft University of Technology
- Andrey Bakulin, WesternGeoco
- Tariq Alkhalifah, King Abdullah University of Science and Technology
- Jeff Shragge, University of Western Australia
- Ben Kadlec, TerraSpark Geosciences

- Christof Stork, Tierra Geophysical
- Chuck Diggins, Fusion Petroleum Technologies, Inc.
- Heloise Lynn, Lynn Inc.
- Scott Morton, Hess Corporation
- Andre Bulcao, Petrobras
- Uwe Albertin, BP
- Marco Maučec, Stew Levin, and Bob Howard, Landmark
- Vladimir Grechka, Shell
- Peter Leary, University of Auckland
- Anatoly Levshin, University of Colorado
- Subhashis Mallick, University of Wyoming

Papers at SEG and EAGE

CWP students an faculty presented a total of nineteen oral presentations, poster papers, and workshop contributions at the 2009 SEG Annual Meeting in Houston. A number of these presentations result from collaborations with sponsor companies and other academic groups. In addition, the CWP faculty and students contributed four presentations at the 2009 EAGE meeting in Amsterdam.

Publications

Student Theses

During recent months, the following theses of CWP students Jyoti Behura (PhD), Ran Xuan (MSc) and Derek Parks (MSc) have been distributed to sponsors.

- Behura, J., 2009, Estimation and analysis of annenuation anisotropy: Ph.D. thesis, Colorado School of Mines. Defended May 1, 2009 [CWP-639].
- Xuan, R., 2009, Probabilistic micro-earthquake location for reservoir monitoring: M.Sc. thesis, Colorado School of Mines. Defended September 18, 2009 [CWP-640].
- Parks, D., 2010, Seismic image flattening as a linear inverse problem: M.Sc. thesis, Colorado School of Mines. Defended January 19, 2010 [CWP-643].

If you would like to receive a copy of these, or any other CWP publications, contact Barbara McLenon: barbara@dix.mines.edu.

The MSc thesis defense of Yongxia Liu is upcoming, her thesis will also be distributed to sponsors.

Book published

The book *The Art of Being a Scientist* by Roel Snieder and Ken Larner was published in August, 2009, by Cambridge University Press (ISBN: 9780521743525). This book, which grew out of a graduate course that Roel has been teaching for the past eight years, is a hands-on guide aimed at helping graduate students and other young researchers acquire the skills needed for a career in research. Though some aspects of the philosophy of science are covered in the book, most of the material is of a practical nature–applicable to all fields of science, engineering, and humanities. More information can be found on `http:/www.mines.edu/~rsnieder/Art_of_Science.html`

Research Reports

As in past years, a significant number of papers authored or co-authored by CWP faculty and students have been published in leading journals. The complete list of CWP papers from 1984 onward is on our web site at `http://www.cwp.mines.edu/bookshelf.html`. Most papers are available there for downloading as PDF files.

Publications in 2009 from CWP faculty and students

[1] Ayzenberg, M., Tsvankin, I., Aizenberg, A., & Ursin, B. 2009. Effective reflection coefficients for curved interfaces in transversely isotropic media. *Geophysics*, **74**, WB33–WB53.

[2] Behera, L., & Tsvankin, I. 2009. Migration velocity analysis for tilted transversely isotropic media. *Geophysical Prospecting*, **57**, 13–26.

[3] Behura, J., & Tsvankin, I. 2009. Role of the inhomogeneity angle in anisotropic attenuation analysis. *Geophysics*, **74**, WB177–WB191.

[4] Behura, J., & Tsvankin, I. 2009. Reflection coefficients in attenuative anisotropic media. *Geophysics*, **74**, WB193–WB202.

[5] Behura, J., & Tsvankin, I. 2009. Estimation of interval anisotropic attenuation from reflection data. *Geophysics*, **74**, A69–A74.

[6] Fan, Y., & Snieder, R. 2009. Required source distribution for interferometry of waves and diffusive fields. *Geophys. J. Int.*, **179**, 1232–1244.

[7] Fuck, R. F., Bakulin, A., & Tsvankin, I. 2009. Theory of traveltime shifts around compacting reservoirs: 3D solutions for heterogeneous anisotropic media. *Geophysics*, **74**, D25–D36.

[8] Fuck, R. F., & Tsvankin, I. 2009. Analysis of the symmetry of a stressed medium using nonlinear elasticity. *Geophysics*, **74**, WB79–WB87.

[9] Hale, D. 2009. A method for estimating apparent displacement vector from time-lapse seismic images. *Geophysics*, **74**, V99–V107.

[10] Lin, F.C., Ritzwoller, M.H., & Snieder, R. 2009. Eikonal tomography: surface wave tomography by phase front tracking across a regional broad-band seismic array. *Geophys. J. Int.*, **177**, 1091-1110.

[11] Ma, Y., & Sava, P. 2009. The effects of multi-scale heterogeneities on wave-equation migration. *Journal of Seismic Exploration*, **18**, 357–383.

[12] Sava, P., & Hill, S. 2009. Overview and classification of wave-equation depth imaging methods. *The Leading Edge*, **28**, 170–183.

[13] Silva, E., & Sava, P. 2009. Modeling and migration with orthogonal isochron rays. *Geophysical Prospecting*, **57**, 773–784.

[14] Snieder, R. 2009. Book review of "Seismic Interferometry" by G.T. Schuster. *J. Acoust. Soc. Am.*, **126**, 3375.

[15] Snieder, R. 2009. Extracting the time-domain building response from random vibrations. *Pages 283–292 of:* Schanz, T., & Iankov, R. (eds), *Coupled site and soil-structure interaction effects with application to seismic risk mitigation.* NATO science for peace and security series - C: Environmental Security. Springer.

[16] Snieder, R., & Larner, K. 2009. *The Art of Being a Scientist, A Guide for Graduate Students and their Mentors.* Cambridge, UK: Cambridge University Press.

[17] Snieder, R., & Young, T. 2009. Facing major challenges in carbon capture and sequestration. *GSA Today*, **19**(11), 36–37.

[18] Snieder, R., Miyazawa, M., Slob, E., Vasconcelos, I., & Wapenaar, K. 2009. A comparison of strategies for seismic interferometry. *Surveys in Geophysics*, **30**, 503–523.

[19] Snieder, R., Sánchez-Sesma, F.J., & Wapenaar, K. 2009. Field fluctuations, imaging with backscattered waves, a generalized energy theorem, and the optical theorem. *SIAM J. Imaging Sci.*, **2**, 763–776.

[20] Vasconcelos, I., R., Snieder, & Douma, H. 2009. Reciprocity theorems and Green's function retrieval in perturbed acoustic media. *Phys. Rev. E*, **80**, 036605.

[21] Wang, X., & Tsvankin, I. 2009. Estimation of interval anisotropy parameters using velocity-independent layer stripping. *Geophysics*, **74**, WB117–WB127.

[22] Yan, J. & Sava, P. 2009. Elastic wavefield separation for VTI media. *Geophysics*, **74**, WB19–WB32.

Computing Environment

In the past year, CWP purchased four desktop PC systems, each consisting of dual-core quad-processor 64 bit, each with 8GB of RAM, and 1 Terabyte of diskspace for each system. In addition, we purchased several eight core Apple Macintosh systems. We now have in excess of 92 new nodes that are available to our students for inhouse parallel applications. Our operating system of choice is Linux (Fedora 9 on most platforms, moving to Fedora 11). The CWP research computing environment also includes an aging 32 processor Linux cluster system that was purchased in 2003. The total amount of disk space available on the CWP Net exceeds 40 Terabytes, roughly double of that available last year. For data transport, our preferred medium consists of USB hard drives, formatted with the ext3 filesystem. CWP faculty and students make regular use of the following commercial packages: Mathematica, Matlab, the Intel C and Fortran compilers, as well as the NAG95 (Fortran 90/95 compiler). In addition to the CWP internal computing facilities, the CSM campus facilities now include a 2144 node high-performance cluster system. CWP has access to this cluster and we aim to expand this cluster with nodes that are dedicated to CWP research.

Software Releases

CWP releases open-source software as well as software that is confidential to the Consortium. Most confidential codes depend heavily on the free software environment, so both are relevant to the Consortium. The period of confidentiality is three years. Some of the codes developed at CWP are part of government-funded research projects and have to be released as open source. Software developed using in-house resources of sponsor companies generally is not available to us for release.

A widely used vehicle of open software distribution is the Seismic Un*x (SU) package. This package has been installed at more than 3900 sites at locations, defined by 69 internet country codes as determined by voluntary direct emails. Another measure of the user base is the active membership in the "seisunix" listserver group (1010+ members up from about 800 in the previous year) and general interest via downloads of more than 15 per day, though these may be more reflecting of internet bots, rather than real users. Release 42 of SU, originally scheduled for release on 20 April 2009, was delayed until 15 February 2010, with nine incremental intermediate releases. This release contains 47 new programs derived from contributions written by Balazs Nemeth while he was at the Potash Corporation of Saskatoon, Saskatchewan, by Chris Liner of the University of Houston, and other users in the worldwide SU users community. For details, please download the release notes from `http://www.cwp.mines.edu/cwpcodes`.

The open-source Mines Java Toolkit is available online from Dave Hale's home page at `http://www.mines.edu/~dhale/jtk/`. This software is the foundation for most of Dave's teaching and research and is also being used by commercial software companies. Anyone with a web browser can view and download the always up-to-date source code repository. Important recent additions are implementations of structure-oriented smoothing and semblance, and an entirely new package for interpolation of scattered data, including image-guided (blended neighbor) interpolation.

Paul Sava and his students continue to work with and develop software for Madagascar, an open-

source software package for geophysical data processing and reproducible numerical experiments. Its mission is to provide a convenient and powerful environment and a technology transfer tool for researchers working with digital image and data processing. The technology developed using the Madagascar project management system is transferred in the form of recorded processing histories that become "computational recipes" to be verified, exchanged, and modified by users of the system. This open-source package is available from `http://www.reproducibility.org`

Annual Project Review Meeting

This year's Annual Project Review Meeting will be held on May 17-20, 2010, on the campus of the Colorado School of Mines in Golden, Colorado. A tradition of recent years is that, prior to the meeting, we hold a short course for sponsors on a topic of particular interest within CWP. This year, in the afternoon of May 17, Gerhard Pratt of the University of Western Ontario will give a short course entitled "What else can the seismic wavefield tell us?" During the following three days, CWP students and faculty will present more than 20 research papers. In addition, the program will include two guest speakers: Sven Treitel (Tridekon Inc.), Zvi Koren (Paradigm Geophysical), and Yu Zhang (CGGVeritas). The evening of May 20 we will celebrate the 70th birthday of Norm Bleistein at a dinner held in his honor. Thank you for joining us!

Extended imaging conditions for wave-equation migration

Paul Sava[1] & Ivan Vasconcelos[2]
[1]*Center for Wave Phenomena, Colorado School of Mines*
[2]*ION Geophysical and School of Geosciences, University of Edinburgh*

ABSTRACT
Wavefield-based migration velocity analysis using the semblance principle requires computation of images in an extended space in which we can evaluate the imaging consistency as a function of overlapping experiments. Usual industry practice is to assemble those seismic images in common-image-gathers (CIG) which represent reflectivity as a function depth and extensions, e.g. reflection angles. We introduce extended common-image-point (CIP) gathers constructed only as a function of the space- and time-lag extensions at sparse and irregularly distributed points in the image. Semblance analysis using CIPs constructed by this procedure is advantageous because we do not need to compute gathers at regular surface locations and we do not need to compute extensions at all depth levels. The CIPs also give us the flexibility to distribute them in the image at irregular locations aligned with the geologic structure. Furthermore, the CIPs remove the depth bias of CIGs constructed as a function of the depth axis. An interpretation of the CIPs using scattering theory shows that they are scattered wavefields associated with sources and receivers inside the subsurface. Thus, when the surface wavefields are correctly reconstructed, the extended CIPs are characterized by focused energy at the origin of the space- and time-lag axes. Otherwise, the energy defocuses from the origin of the lag axes proportionally with the cumulative velocity error in the overburden. This information can be used for wavefield-based tomographic updates of the velocity model, and if the velocity used for imaging is correct, the coordinate-independent CIPs can be decomposed function of the angles of incidence.

Key words: wave-equation, migration, velocity analysis

1 INTRODUCTION

In regions characterized by complex subsurface structure, wave-equation depth migration is a powerful tool for accurately imaging the earth's interior. The quality of the final image greatly depends on the quality of the velocity model. Thus, constructing accurate velocity is essential for imaging (Gray et al., 2001). In particular, it is important to construct subsurface velocity models using techniques that are consistent with the methods used for imaging.

Generally speaking, there are two possible strategies for velocity estimation from surface seismic data in the context of wavefield depth migration which differ by the implementation domain. One possibility is to formulate an objective function in the *data space*, prior to migration, by evaluating the match between recorded and simulated data using an approximate (background) velocity model. Techniques in this category are known by the name of tomography (or inversion). Another possibility is to formulate an objective function in the *image space*, after migration, by measuring and correcting image features that indicate model inaccuracies. Techniques in this category are known as migration velocity analysis (MVA), since they involve migrated images and not the recorded data directly. In both cases, velocity estimation can be done either using rays or waves as the carrier of information, leading to techniques known by the names of *traveltime tomography* (Bishop et al., 1985; Stork, 1992; Al-Yahya, 1987; Fowler, 1988; Etgen, 1990; Chavent & Jacewitz, 1995; Clement et al., 2001; Chauris et al., 2002a,b; Billette et al., 2003; Lambare et al., 2004; Clapp et al., 2004), or *wave-equation tomography* (Gauthier et al., 1986; Tarantola, 1987; Mora, 1989; Woodward, 1992; Pratt, 1999; Sirgue & Pratt, 2004; Biondi & Sava, 1999; Sava & Biondi, 2004a,b; Shen et al., 2003; Albertin et al., 2006).

The key component for an MVA technique implemented in the image space is the analysis of image attributes which

indicate inaccurate imaging. These attributes are often represented by image extensions, e.g. reflectivity as functions of angle or offset which exploit the **semblance principle** stating that images constructed for different seismic experiments are kinematically similar if the correct velocity is used. This property can be exploited for velocity model building by minimizing objective functions to optimize certain image attributes. For example, we can consider flatness or focusing measured on image gathers, which can be quantified using the generic annihilators as discussed by Symes (2009).

In this paper, we discuss an imaging condition for wavefield-based imaging which can be exploited for velocity model building. This imaging condition is best understood in the context of reverse-time migration since it does not require assumptions about the spatial distribution of reflectors in the subsurface. We construct common-image-point gathers at sparse locations in the image, thus reducing computational cost while preserving velocity model building information. We mainly concentrate on exploring the meaning and features of this imaging condition, on the computational aspects which make implementation of this imaging condition efficient and on measurements that can be made on migrated images to establish the accuracy of the velocity model. How such measurements can be used for migration velocity analysis is a vast subject and we leave it outside the scope of this paper.

2 IMAGING CONDITIONS

Conventional seismic imaging methods share the assumption of single scattering at discontinuities in the subsurface. Under this assumption, waves propagate from seismic sources, interact with discontinuities and return to the surface as reflected seismic waves. We commonly speak about a "source" wavefield, originating at the seismic source and propagating in the medium prior to any interaction with discontinuities, and a "receiver" wavefield, originating at discontinuities and propagating in the medium to the receivers (Berkhout, 1982; Claerbout, 1985). The two wavefields kinematically coincide at discontinuities. Any mismatch between the wavefields indicates inaccurate wavefield reconstruction typically assumed to be due to inaccurate velocity. In this context, we do not need to make geometrical assumptions about up- or down-going propagation, since waves can move in any direction as long as they scatter only once. We also do not need to make any assumption about how we reconstruct those two wavefields as long as the wave-equation used accurately describes wave propagation in the medium under consideration.

We can formulate imaging as a process involving two steps: the wavefield reconstruction and the imaging condition. The key elements in this imaging procedure are the source and receiver wavefields, W_s and W_r. We can represent those wavefields as 4-dimensional objects, either in the time domain (for wavefield reconstruction using the two-way acoustic wave-equation) as a function of space $\mathbf{x} = \{x, y, z\}$ and time t, or in the frequency domain (for wavefield reconstruction using the one-way acoustic wave-equation) as a function of space and frequency ω. For imaging, we need to analyze if the wavefields match kinematically in time and then extract the reflectivity information using an imaging condition operating along the space and time axes.

A conventional cross-correlation imaging condition (cIC) based on the reconstructed wavefields can be formulated in the time or frequency domain as the zero lag of the cross-correlation between the source and receiver wavefields (Claerbout, 1985):

$$R(\mathbf{x}) = \sum_{shots} \sum_{t} W_s(\mathbf{x}, t)\, W_r(\mathbf{x}, t) \tag{1}$$

$$= \sum_{shots} \sum_{\omega} \overline{W_s(\mathbf{x}, \omega)} W_r(\mathbf{x}, \omega)\,, \tag{2}$$

where R represents the migrated image and the over-line represents complex conjugation. This operation exploits the fact that portions of the wavefields match kinematically at subsurface positions where discontinuities occur. Alternative imaging conditions use deconvolution of the source and receiver wavefields, but we do not elaborate further on this subject in this paper since the differences between cross-correlation and deconvolution are not central for our discussion in this paper.

An extended imaging condition preserves in the output image certain acquisition (e.g. source or receiver coordinates) or illumination (e.g. reflection angle) parameters (Clayton & Stolt, 1981; Claerbout, 1985; Stolt & Weglein, 1985; Weglein & Stolt, 1999). In shot-record migration, the source and receiver wavefields are reconstructed on the same computational grid at all locations in space and all times or frequencies, therefore there is no a-priori separation that can be transferred to the output image. In this situation, the separation can be constructed by correlation of the wavefields from symmetric locations relative to the image point, measured either in space (Rickett & Sava, 2002; Sava & Fomel, 2005) or in time (Sava & Fomel, 2006). This separation essentially represents local cross-correlation lags between the source and receiver wavefields. Thus, an extended cross-correlation imaging condition (eIC) defines the image as a function of space and cross-correlation lags in space and time. This imaging condition can also be formulated in the time and frequency domains:

$$R(\mathbf{x}, \boldsymbol{\lambda}, \tau) = \sum_{shots} \sum_{t} W_s(\mathbf{x}-\boldsymbol{\lambda}, t-\tau)\, W_r(\mathbf{x}+\boldsymbol{\lambda}, t+\tau) \tag{3}$$

$$= \sum_{shots} \sum_{\omega} e^{2i\omega\tau} \overline{W_s(\mathbf{x}-\boldsymbol{\lambda}, \omega)} W_r(\mathbf{x}+\boldsymbol{\lambda}, \omega) \tag{4}$$

Equations 1-2 represent a special case of equations 3-4 for $\boldsymbol{\lambda} = 0$ and $\tau = 0$. The eIC defined by equations 3-4 can be used to analyze the accuracy of wavefield reconstruction. Assuming that all errors accumulated in the incorrectly-reconstructed wavefields are due to the velocity model, the extended images could be used for velocity model building by exploiting semblance properties emphasized by the space-lags (Biondi & Sava, 1999; Shen et al., 2003; Sava & Biondi, 2004a,b) and focusing properties emphasized by the time-lag (Faye & Jeannot, 1986; MacKay & Abma, 1992, 1993; Nemeth, 1995, 1996). Furthermore, these extensions can be converted to reflection angles (Weglein & Stolt, 1999; Sava & Fomel, 2003, 2006), thus enabling analysis of amplitude varia-

tion with angle for images constructed in complex areas using wavefield-based imaging.

3 COMPUTATIONAL COST ANALYSIS

The main drawback of the extended imaging conditions 3-4 is that they require a large number of computations corresponding to the size of the image given by the space variable $\mathbf{x}$ and by the number of space and time lags given by variables $\boldsymbol{\lambda}$ and τ. In practice, computing and saving the non-zero cross-correlation lags at all image coordinates for large datasets is infeasible. The complete extended image space has 7 dimensions, although due to cost consideration this space is usually analyzed using subsets. We argue later in this paper that calculation of the full extended image may actually not be necessary. In order to analyze the cost of computing wave-equation images with extensions, we can rewrite the expression of the image obtained by eIC using the notation

$$R(x, y, z, \lambda_x, \lambda_y, \lambda_z, \tau) \ , \tag{5}$$

where x, y, z represent the space coordinates, $\lambda_x, \lambda_y, \lambda_z$ represent space-lag extensions and τ represents the time-lag extension. Our discussion is limited to the computational cost of the imaging condition and does not refer to the computational cost of wavefield reconstruction. We distinguish the following 4 special cases:

3.1 1: imaging with no extensions

If we do not use any space and time extensions, the extended image is:

$$R(x, y, z, \lambda_x = 0, \lambda_y = 0, \lambda_z = 0, \tau = 0) \ . \tag{6}$$

As indicated earlier, this subset of the extended image corresponds to the conventional imaging condition. Figures 1(a)-1(b) show conventional images for the Sigsbee 2A dataset (Paffenholz et al., 2002) for correct and low velocities, respectively. The zero lag images indicate velocity inaccuracy by defocusing of point-like events (diffractors or reflector truncations against faults) and by the existence of crossing events in regions of high reflector curvature. This information can be used for velocity model updates (de Vries & Berkhout, 1984; Harlan et al., 1984; Sava et al., 2005; Fomel et al., 2007).

The computational cost C of cIC is proportional to the product $N_x N_y N_z N_t$, where N_x, N_y, N_z represent the number of samples along the space axes, and N_t represents the number time samples used for imaging using reverse-time migration. A similar argument applies for migration by one-way wavefield extrapolation, in which case we replace the number of time samples N_t with the number of frequencies N_ω used for imaging. In both cases, the product of space grid points and time or frequency grid points coincides to the size of the reconstructed seismic wavefields which control the total cost of migration. We use this cost reference when we analyze other cases.

3.2 2: imaging with space-lag extensions

A common special case of wave-equation imaging with extensions is represented by images obtained with horizontal space-lag extensions only:

$$R(x = x_0, y = y_0, z, \lambda_x, \lambda_y, \lambda_z = 0, \tau = 0) \ , \tag{7}$$

where x_0 and y_0 indicate fixed coordinates on the surface. This subset of the extended image corresponds to the so-called space-lag common image gathers (Rickett & Sava, 2002; Sava & Fomel, 2005). Figures 2(a)-2(b) show space-lag gathers for the Sigsbee 2A dataset for correct and low velocities, respectively. The gathers are constructed as a function of depth at fixed surface coordinate $x = 9.25$ km. The space-lag CIGs indicate velocity inaccuracy by defocusing from zero space-lag. In this case, since the Sigsbee 2A data are simulated with off-end acquisition, only the positive side of the defocused events is present in the gather. This information can be used for velocity model updates (Sava & Biondi, 2004a,b; Shen et al., 2003).

Assuming that we are computing the extensions at sparse surface coordinates, we construct CIGs at $N = (\alpha_x N_x)(\alpha_y N_y)$ points, where α_x and α_y represent decimation coefficients along coordinates x and y. The computational cost of this type of imaging condition relative to the cost of the cIC is

$$\frac{C_\lambda}{C} \sim (\alpha_x N_{\lambda_x})(\alpha_y N_{\lambda_y}) \ . \tag{8}$$

If $N_{\lambda_i} = 40$ and $\alpha_i = 10^{-1}$ $(i = \{x, y\})$, then $\frac{C_\lambda}{C} \sim 16$.

3.3 3: imaging with time-lag extension

Another common special case of wave-equation imaging with extensions is represented by images obtained with time-lag extensions only:

$$R(x = x_0, y = y_0, z, \lambda_x = 0, \lambda_y = 0, \lambda_z = 0, \tau) \ , \tag{9}$$

where x_0 and y_0 indicate fixed coordinates on the surface. This subset of the extended image corresponds to the so-called time-lag common image gathers (Sava & Fomel, 2006). Figures 3(a)-3(b) show time-lag gathers for the Sigsbee 2A dataset for correct and low velocities, respectively. The gathers are constructed as a function of depth at fixed surface coordinate $x = 9.25$ km. The time-lag CIGs indicate velocity inaccuracy by departure of the maximum focusing from zero time-lag. This information can be used for velocity model updates, for example by the techniques of (Brown et al., 2008; Yang & Sava, 2009b).

Assuming that we are computing the extensions at sparse space coordinates as in the preceding case, then the computational cost of this type of imaging condition relative to the cost of cIC is

$$\frac{C_\tau}{C} \sim \alpha_x \alpha_y N_\tau \ . \tag{10}$$

If $N_\tau = 10^2$ and $\alpha_i = 10^{-1}$ $(i = \{x, y\})$, then $\frac{C_\tau}{C} \sim 1$, i.e. a

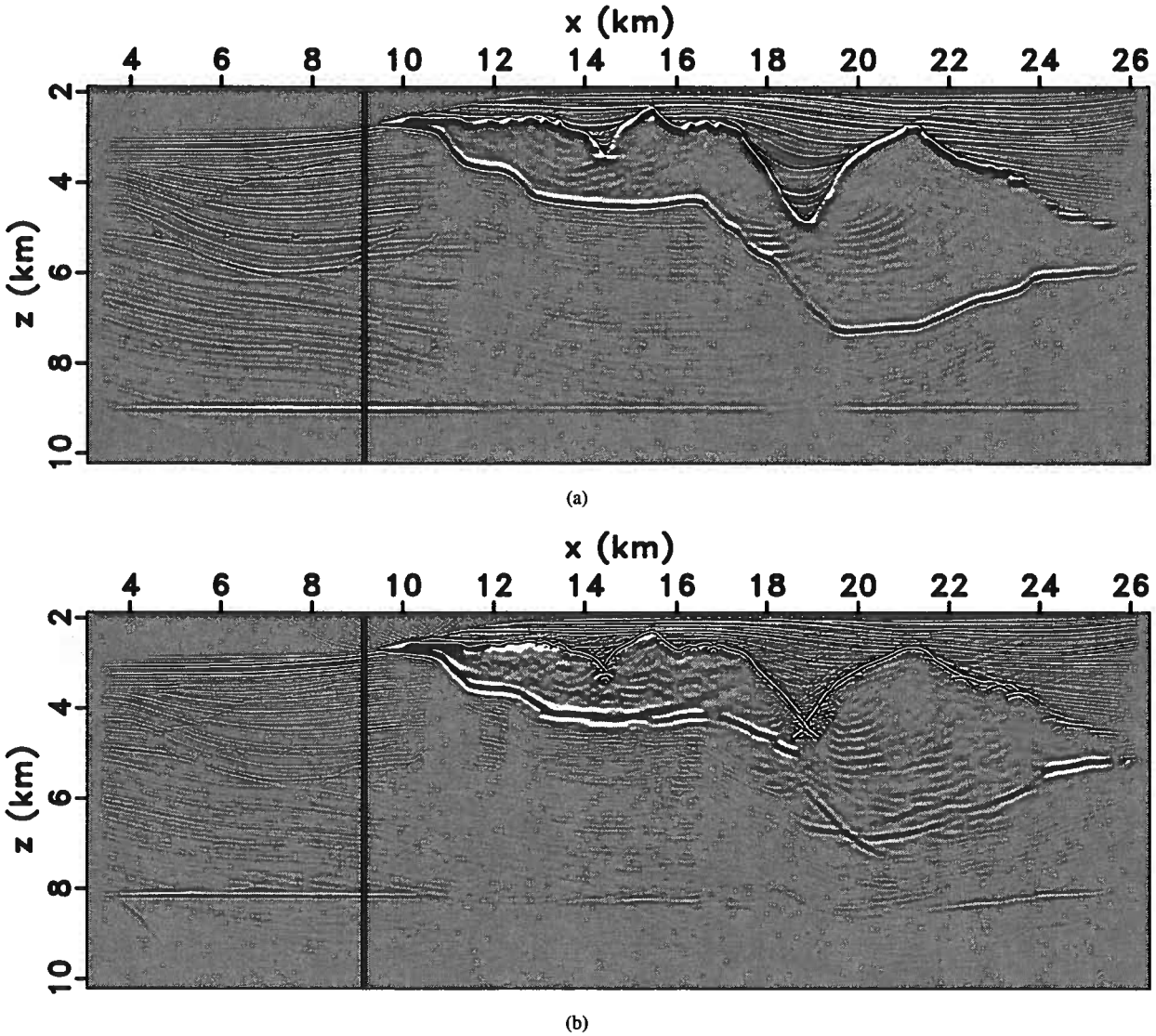

Figure 1. Sigsbee 2A image constructed using (a) correct and (b) low velocities. For the low velocity model, the sediment velocity is 90% of the original.

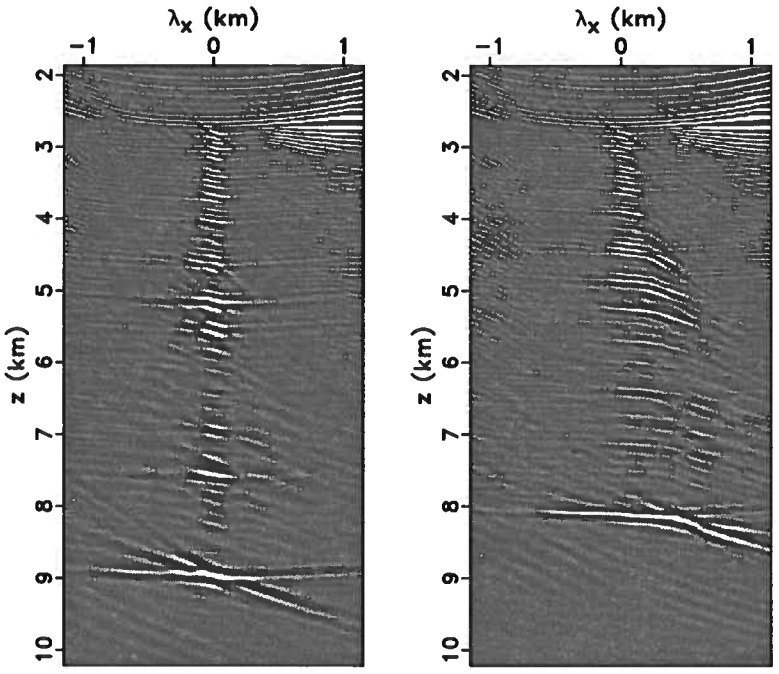

Figure 2. Sigsbee 2A space-lag common-image-gather constructed at $x = 9.25$ km using (a) correct and (b) low velocities. The depth and horizontal space-lag axes are represented to scale.

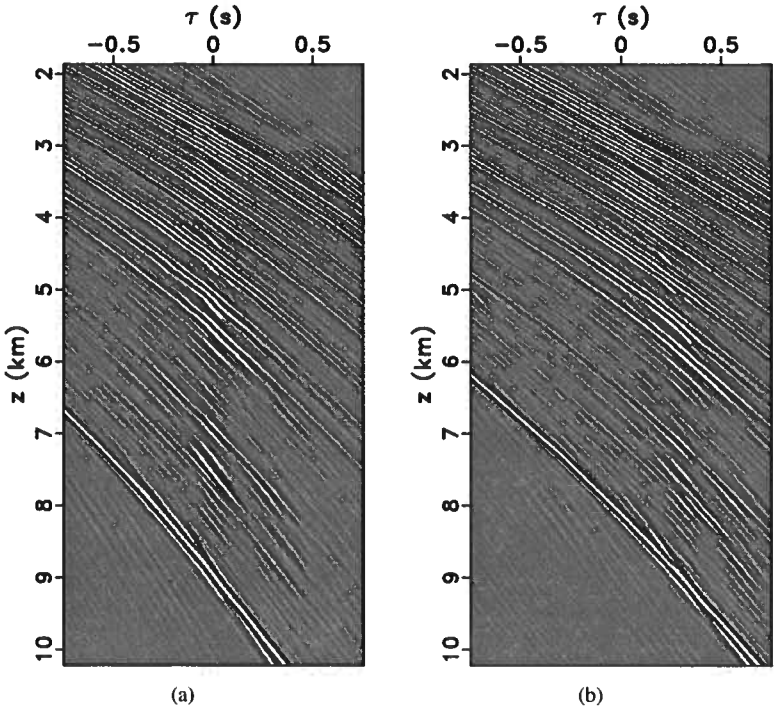

Figure 3. Sigsbee 2A time-lag common-image-gather constructed at $x = 9.25$ km using (a) correct and (b) low velocities.

significantly lower computational cost than the one of imaging with space-lag extensions.

For completeness, we note that a hybrid type of common-image-gather as a function of both space-lags and time-lags can also be computed. Such gathers exploit at the same time the semblance and focusing properties provided by the space-lags and time-lags, respectively (Yang & Sava, 2009a). We can represent such gathers using multidimensional cubes at every location where they are constructed. In this paper, we represent such cube using slices taken at fixed coordinates inside the cube, as indicated in Figures 4(a)-4(b). Figures 5(a)-5(b) show space-lag/time-lag gathers for the Sigsbee 2A dataset for correct and low velocities, respectively. The gathers are constructed as a function of depth at fixed surface coordinate $x = 9.25$ km. The mixed space-lag/time-lag CIGs indicate velocity inaccuracy by defocusing as a function of space-lags and departure of the maximum focusing from zero time-lag. The space-lag and time-lag CIGs discussed earlier represent special cases of this type of gather at $\tau = 0$ or $\boldsymbol{\lambda} = 0$, respectively. The discussion of the relative advantages of using mixed space-lag/time-lag CIGs over the more conventional space-lag or time-lag CIGs falls outside the scope of this paper.

3.4 4: imaging with space- and time-lag extensions

Another special case of imaging with extensions, which is the main focus of our paper, is at the exact opposite end of the spectrum relative to cIC. Instead of computing images as a function of space coordinates, we can compute images as a function of extensions at fixed locations in the image (only one, in the extreme):

$$R\left(x = x_0, y = y_0, z = z_0, \lambda_x, \lambda_y, \lambda_z, \tau\right) \ , \qquad (11)$$

where x_0, y_0, z_0 indicate fixed coordinates in the image space. Such gathers really correspond to unique image points, thus for the rest of this paper, we use the terminology **common-image-point** (CIP) gathers to emphasize the fact that they refer to single image points.

We assume that we compute extensions at a finite number N of locations in the image. In this case, the total computational cost of this type of imaging condition is

$$\frac{C_{\lambda\tau}}{C} \sim N \frac{N_{\lambda_x} N_{\lambda_y} N_{\lambda_z} N_\tau}{N_x N_y N_z} \ . \qquad (12)$$

As discussed later in the paper, assuming that we can exploit the dip information measured on the image constructed with the conventional imaging condition, we can drop one of the space-lag axes from the computation. For example, if we do not use the vertical space-lag axis (a choice appropriate for nearly-horizontal reflectors), then the computational cost drops one order of magnitude

$$\frac{C_{\lambda\tau}}{C} \sim N \frac{N_{\lambda_x} N_{\lambda_y} N_\tau}{N_x N_y N_z} \ . \qquad (13)$$

We can, in principle, make other choices of space-lag parameters to account for different reflector dips in the image. If $N_i = 10^3$, $N_{\lambda_i} = 40$ $(i = \{x, y\})$, $N_\tau = 10^2$, and $N = 10^3$, then $\frac{C_{\lambda\tau}}{C} \sim 0.2$, i.e. a cost smaller than the one of space-lag imaging, and comparable to the cost of time-lag imaging. We achieve smaller computational cost mainly because we can compute the image as a function of space-lag and time-lag extensions at a relatively small number of points distributed (non-uniformly) in the image, for example along the main reflectors identified in the image by a prior imaging with a cheaper imaging condition, e.g. cIC. This smaller computational cost is attractive for imaging if and only if the space- and time-lag extensions characterize properly the migrated images and, in particular, if they provide information about the velocity model accuracy. We discuss this topic in detail in the following sections.

Finally, we note that the strategy of selecting CIP locations could be used for selecting locations at which to construct CIG's. However, as noted earlier, if using CIGs we would then still be suffering from a bias towards horizontal reflectors in the velocity analysis process.

4 COMMON-IMAGE-POINT GATHERS

As indicated earlier, conventional migration velocity analysis is based on the general principle of semblance between images of the interior of the Earth constructed from different seismic experiments. Typically, those experiments represent shots as acquired in the field, but a similar argument applies to other types of experiments synthesized from field data, e.g. plane encoding (Whitmore, 1995) or random encoding (Romero et al., 2000). The collections of images constructed from different experiments are usually organized as a function of surface coordinates at discrete locations. These gathers are refered to as common-image gathers (CIGs), with the understanding that the word "common" refers to the surface position. There are several drawbacks to this type of analysis.

First, due to the typically large computational cost associated with the CIG construction, such gathers are not constructed at all surface positions, but only at a sparse set of coordinates. It is not uncommon that CIGs are constructed, for example, at every 500 m or so in in-line and cross-line directions, which may be **too sparse** for correct evaluation of the image accuracy.

Second, CIGs are usually constructed for fixed surface coordinates, at all depth coordinates. The depth coordinate is finely sampled to describe the seismic wavelet and to capture the rapid variations due to stratigraphic changes. It is not uncommon that the image is sampled every 10 m in depth, which amounts to several (maybe 10 or 20) samples per wavelet. If we are trying to analyze the accuracy of imaging a specific event in the image, this representation may be **too dense** without adding much value for velocity analysis.

Third, the sparse CIG calculation is **independent of the geologic structure**. We see this as a drawback, since it adds no value to compute image extensions at locations that are not useful for velocity analysis, e.g. inside salt bodies. It would make more sense to compute extensions at locations that are

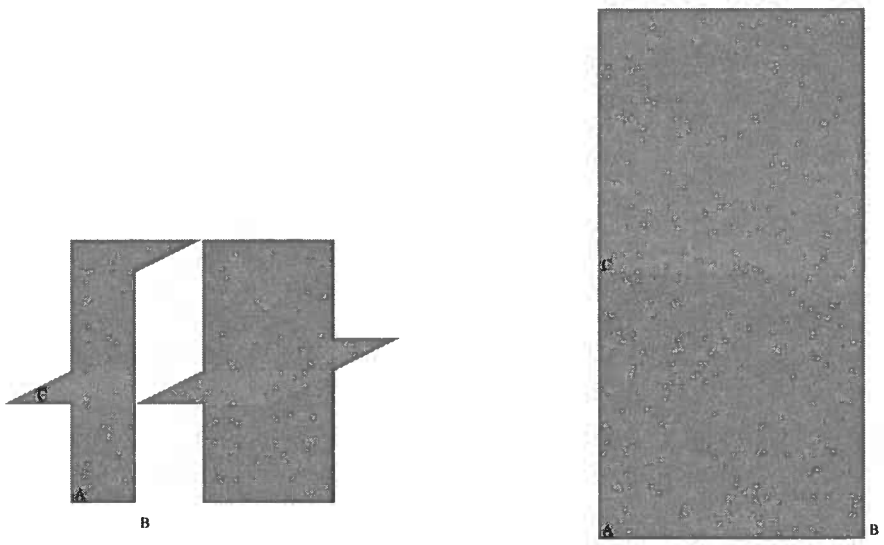

(a) (b)

Figure 4. Orthogonal slices in a 3D cube represented (a) at their true position and (b) at the edges of the cube. The unfolded edge representation allows for unobstructed visualization of the slices. For the cubes used in this paper, panel A represents $z - h_x$ or $h_z - h_x$, panel B represents $z - \tau$ or $h_z - \tau$ and panel C represents $\tau - h_x$.

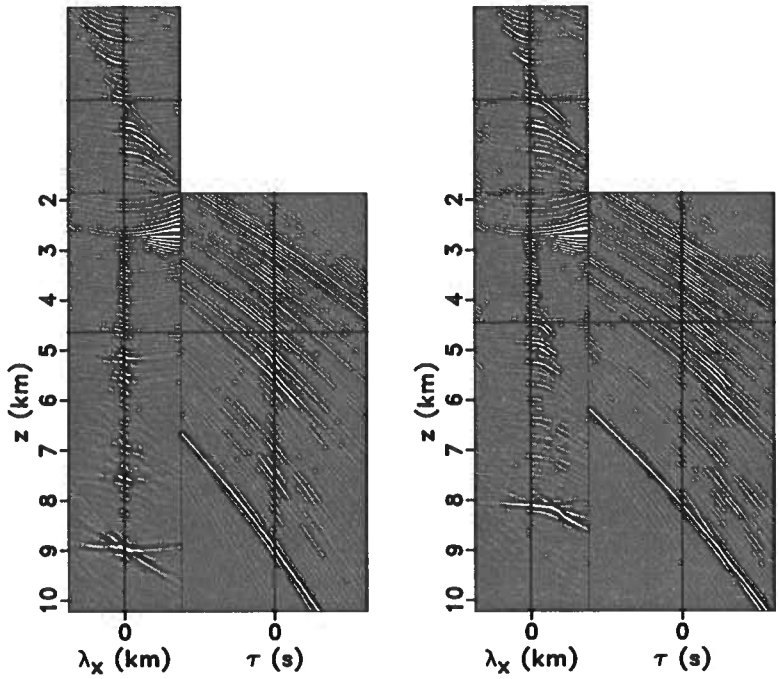

(a) (b)

Figure 5. Sigsbee 2A space-lag/time-lag common-image-gather constructed at $x = 9.25$ km using (a) correct and (b) low velocities.

driven by the structure itself, rather than at locations chosen by a-priori cost considerations.

Fourth, computing CIGs as a function of the depth axis introduces a **depth bias** which makes those gathers most appropriate for nearly-horizontal structures. For steeply-dipping structures, it makes more sense to compute CIGs as a function of another space axis, e.g. the in-line coordinate (Biondi & Symes, 2004), although even this option preserves an azimuthal ambiguity between the in-line and cross-line directions.

In addressing all those issues, we argue for the construction of common-image-point gathers (CIPs) that are constructed as a function of cross-correlation lags at fixed positions in space. Such CIPs can be computed at image coordinates that are as dense or sparse as the image itself dictates. Furthermore, since no space axis is used in the gather construction, it does not matter whether we analyze nearly-horizontal or nearly-vertical reflectors. All reflectors are equally well resolved, aside from aperture limitations which decrease the velocity discrimination power for steep reflectors when data are acquired on a horizontal datum. The selection of parameters characterizing the extended CIPs, i.e. the $\boldsymbol{\lambda}$ and τ range, depends on the frequency band of the reflection data, as well as on the complexity of the analyzed structure. For lower frequency, we can sample sparsely in the extended domain, but for a wider range of parameters; otherwise, we need to sample more densely but for a lower range of parameters. For simple structures, we can distribute the points where we compute the extensions with low density, while for complex structures we need to distribute such points with higher density. The distribution of CIPs can be irregular and consistent with the geologic structure, thus minimizing the computational cost required to characterize the accuracy for a given image.

We also argue that CIPs constructed at individual points in the image represent a natural choice for reverse-time migration. In this case, waves are extrapolated equally well in all space directions and have no bias toward the depth axis as is the case for conventional downward continuation methods. Likewise, CIPs constructed at fixed image positions do not have a bias toward the depth axis, and can handle waves incident at any angles on reflectors with arbitrary dips and azimuths. The key element used to eliminate the depth bias is the use of the time-lag variable τ.

5 MOVEOUT ANALYSIS

In this section, we discuss the general properties of the common-image-point gathers introduced in the preceding section. We describe the moveout functions for different types of reflectors and for diffractors imaged with correct and incorrect velocities. We formulate analytic moveout functions which give insight into the expected behavior of such CIPs in areas of complex velocity variation.

5.1 Reflection moveout

Consider the reflection geometry depicted in Figure 6. In the immediate vicinity of the reflection points, we can assume that the source wavefield, the receiver wavefield and the reflector itself can be approximated by planes and we can also assume that the local velocity in this region is constant. The source, receiver and reflector planes are characterized by unit vectors $\mathbf{n}_s$, $\mathbf{n}_r$, and $\mathbf{n}$, respectively. The vectors are linked according to Snell's law by the relations:

$$|\mathbf{n}_s \cdot \mathbf{n}| = |\mathbf{n}_r \cdot \mathbf{n}| = \cos\theta \;, \tag{14}$$

where θ represents the reflection angle measured relative to the reflector normal $\mathbf{n}$.

For a specific reflection event, without loss of generality, we can set the origin of the time axis at the moment when the two planes characterizing the source and receiver wavefields planes intersect at the reflector. Then, we can write the expressions for the source and receiver wavefield planes as

$$\mathbf{n}_s \cdot \mathbf{x} = 0 \;, \tag{15}$$

$$\mathbf{n}_r \cdot \mathbf{x} = 0 \;, \tag{16}$$

where $\mathbf{x}$ is a variable spanning the planes.

By construction, the extended imaging condition separates the source and receiver wavefield by shifts in space and time using quantities $\boldsymbol{\lambda}$ and τ, respectively. The expressions for the shifted planes in space and time are

$$\mathbf{n}_s \cdot (\mathbf{x} - \boldsymbol{\lambda}) = -v\tau \;, \tag{17}$$

$$\mathbf{n}_r \cdot (\mathbf{x} + \boldsymbol{\lambda}) = +v\tau \;, \tag{18}$$

where v represents the local velocity at the reflection point, assumed to be constant in the region in which the planar assumptions on the source and receiver wavefields holds. Subtracting the expressions 17-18, we obtain

$$(\mathbf{n}_r + \mathbf{n}_s) \cdot \boldsymbol{\lambda} = 2v\tau \;. \tag{19}$$

If we define unit vector $\mathbf{q}$ in the reflection plane, tangent to the reflector (i.e., by construction $\mathbf{q} \cdot \mathbf{n} = 0$), then we can write

$$(\mathbf{q} \cdot \boldsymbol{\lambda}) \sin\theta = v\tau \;. \tag{20}$$

Equation 20 describes the moveout function characterizing a reflection from a single shot-receiver pair in the $\{\boldsymbol{\lambda}, \tau\}$ space, i.e. the space-lags and the time-lag are linearly related by a function which depends on the reflection angle θ, the local velocity v, and by a vector which depends on the reflector dip and reflection azimuth $\mathbf{q}$ (Figure 7(a)). When $\tau = 0$, the moveout function has the form $q_x\lambda_x + q_y\lambda_y + q_z\lambda_z = 0$, i.e. a plane oriented orthogonal to the vector $\mathbf{q}$. When $q_z = 0$, i.e. for a horizontal reflector, the moveout function is $(q_x\lambda_x + q_y\lambda_y)\sin\theta = v\tau$, i.e. the moveout function depends on the local angle of incidence at the reflector and the local reflector slope, Figure 7(a).

We can also express moveout function $s(\boldsymbol{\lambda}, \tau)$ for a single shot-receiver pair using the multidimensional Dirac delta function as (Bracewell, 2006):

$$s(\boldsymbol{\lambda}, \tau) = \delta\left((\mathbf{q} \cdot \boldsymbol{\lambda})\sin\theta - v\tau\right) \;. \tag{21}$$

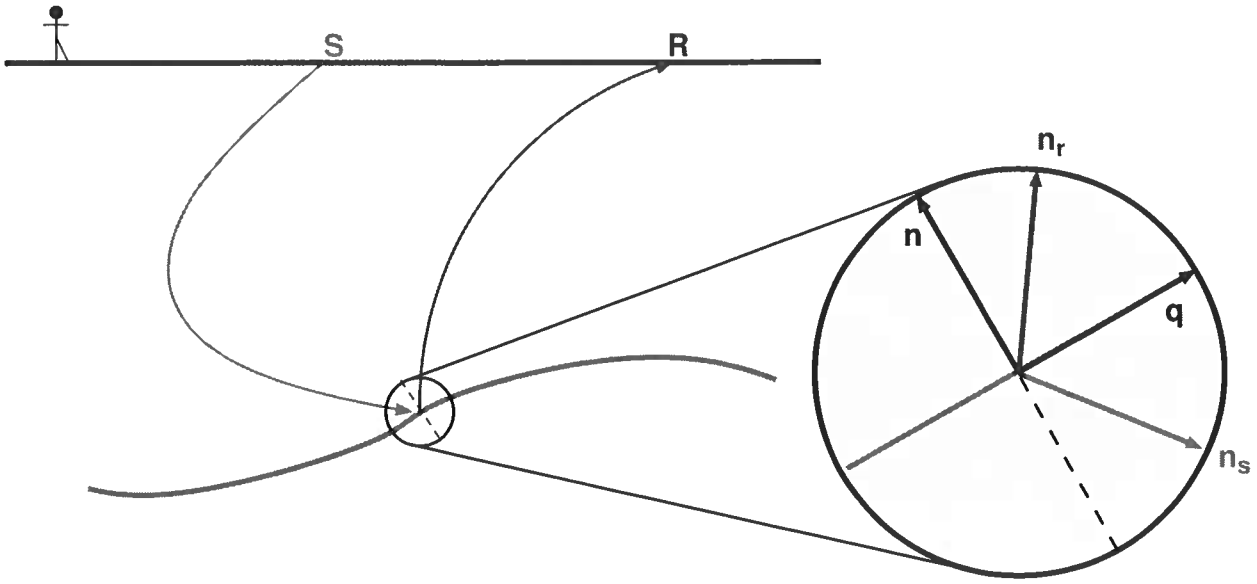

Figure 6. Cartoon illustrating the assumptions made in deriving the moveout functions based on space-lag and time-lag extensions.

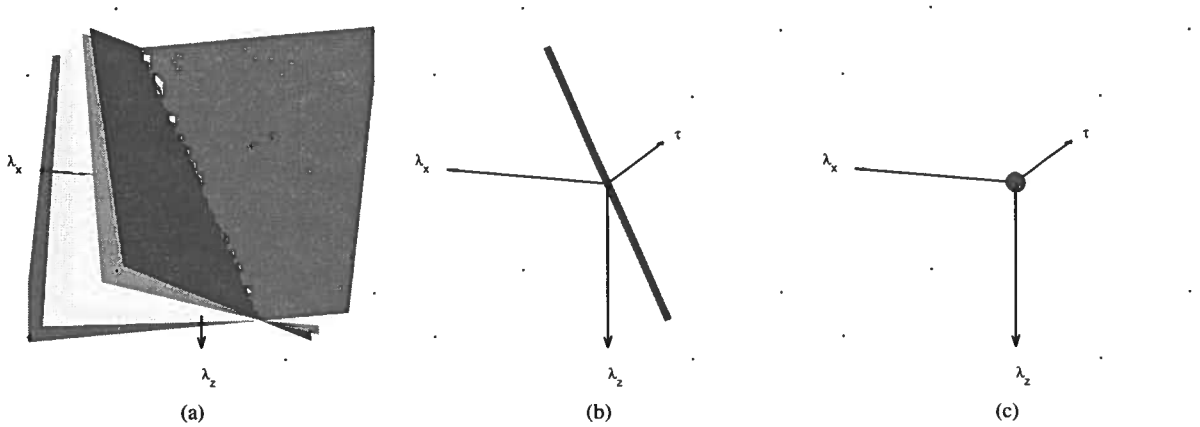

Figure 7. Illustration of (a) the reflection moveout function for individual shots, (b) the reflection moveout function for all shots, and (c) the diffraction moveout function for all shots. Panels (a) and (b) correspond to a reflector dipping at 15°. Panel (a) assumes angles of incidence from $-60°$ to $+60°$.

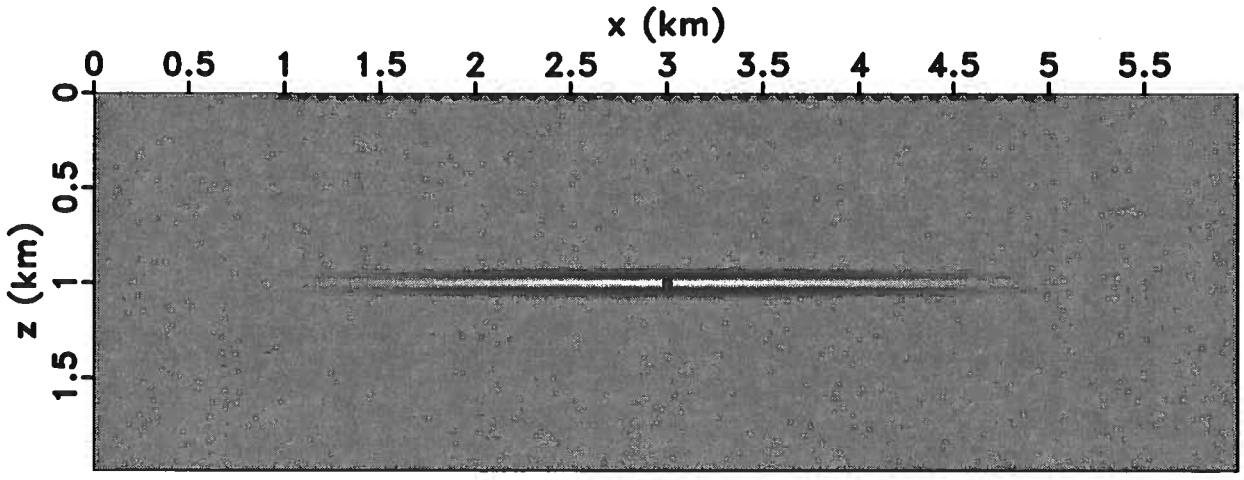

Figure 8. Image of a horizontal reflector in constant velocity media. Sources are distributed along the surface at $z = 0.0$ km between $x = 1.0 - 5.0$ km.

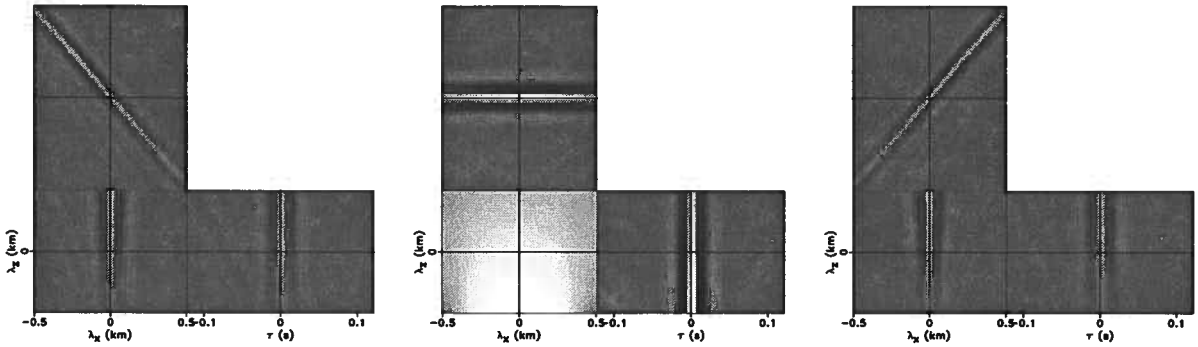

Figure 9. Common-image-point gathers for a horizontal reflector constructed at $\{x, z\} = \{3.0, 1.0\}$ km from shots located at (a) $\{x = 2.0, z = 0.0\}$ km, (b) $\{x = 3.0, z = 0.0\}$ km, and (c) $\{x = 4.0, z = 0.0\}$ km.

This expression simply indicates that $s(\boldsymbol{\lambda}, \tau) = 1$ when $(\mathbf{q} \cdot \boldsymbol{\lambda}) \sin\theta = v\tau$ and $s(\boldsymbol{\lambda}, \tau) = 0$ otherwise.

For illustration, consider the example shown in Figure 8 corresponding to a horizontal reflector imaged with a constant velocity model. Figures 9(a)-9(c) show CIPs for shots located at coordinates $x = 2.0, 3.0, 4.0$ km, respectively. In all cases, the moveout function for an individual shot is a plane in the $\{\boldsymbol{\lambda}, \tau\}$ space depending on the angle of incidence and local velocity. As predicted by the theory, the normal incidence CIP is represented by a plane at $\tau = 0$ and independent of $\boldsymbol{\lambda}$.

In contrast, consider the example shown in Figure 10 corresponding to a dipping reflector imaged with a constant velocity model. Figures 11(a)-11(c) show CIPs for shots located at coordinates $x = 2.0, 3.0, 4.0$ km, respectively. Compared with the CIPs shown in Figures 9(a)-9(c), the moveout depends not only on the angle of incidence and local velocity, but also on the reflector slope.

The moveout characterizing in the $\{\boldsymbol{\lambda}, \tau\}$ space a reflection from many shots located on the surface is given by the superposition of events from different sources, i.e. we construct the moveout function $r(\boldsymbol{\lambda}, \tau)$ by

$$r(\boldsymbol{\lambda}, \tau) = \int d\theta \, \delta\left((\mathbf{q} \cdot \boldsymbol{\lambda}) \sin\theta - v\tau\right) , \qquad (22)$$

therefore

$$r(\boldsymbol{\lambda}, \tau) = \delta(\mathbf{q} \cdot \boldsymbol{\lambda}) \, \delta(v\tau) . \qquad (23)$$

Equation 23 indicates that, aside from a scaling factor, the moveout function characterizing a reflector illuminated from many shots is a line at $\tau = 0$ oriented at an angle parallel to the reflector normal (Figure 7(b)). Such events can be seen in Figure 12(b) for the case of the horizontal reflector shown in Figure 8, and in Figure 13(b) for the case of the dipping reflector shown in Figure 10.

5. 2 Diffraction moveout

We can analyze the moveout function characterizing a diffractor in the $\{\boldsymbol{\lambda}, \tau\}$ space by noting that we can form point diffractors as a superposition of planar reflectors overlapping at the diffractor position. In this case, we can find the moveout function $d(\boldsymbol{\lambda}, \tau)$ by

$$d(\boldsymbol{\lambda}, \tau) = \int d\mathbf{q} \, \delta(\mathbf{q} \cdot \boldsymbol{\lambda}) \, \delta(v\tau) , \qquad (24)$$

therefore

$$d(\boldsymbol{\lambda}, \tau) = \delta(\boldsymbol{\lambda}) \; \delta(v\tau) . \qquad (25)$$

Equation 25 indicates that, aside from a scaling factor, the moveout function characterizing a diffraction illuminated from many shots is a point at $\tau = 0$ and $\boldsymbol{\lambda} = 0$ (Figure 7(c)). Such an event can be seen in Figure 14(b) for a diffractor located at coordinates $\{x, z\} = \{3.0, 1.0\}$ km, which contrasts with the events evaluated at the same position in the cases of horizontal and dipping reflectors, Figures 12(b) and 13(b), respectively. The apparent vertical stretch is related to the fact that we illuminate this diffractor only from the surface, thus the vertical resolution is poorer than the horizontal resolution.

We note here that the temporal resolution of the extended CIPs is high, both for the case of reflection and for the case of diffractions. This is in contrast with the low temporal resolution of more conventional time-lag gathers (Sava & Fomel, 2006). This observation is important for migration velocity analysis where time picking controls the both resolution and inversion accuracy.

5. 3 Velocity error

An important question to address is what is the impact of imaging with incorrect velocity on the CIPs constructed in the $\{\boldsymbol{\lambda}, \tau\}$ domain. We have indicated earlier that the computational cost of constructing such gathers is relatively low since it is simply proportional to the number of points at which lags are evaluated. This is a user-defined parameter and it should reflect the appropriate CIP density necessary to constrain the velocity model. The question is, are those CIPs sensitive to the velocity error?

We address this question with numeric examples. We do not derive moveout functions for incorrect velocity since any such expression would only be valid in simple media, e.g. constant velocity, and not in more complex environments. For velocity analysis we can define a penalty function based on the ideal layout of the CIPs indicated by equations 23 or 25.

Figures 12(a)-14(c) show a comparison of imaging reflectors and diffractors with 3 different velocities, low, correct and high, respectively. In all cases, we track a particular reflection point function of space. This means that the zero lag point of the CIP always characterizes the same seismic event, regardless of its movement due to velocity error. In this experiment, we seek to illustrate that the extended CIPs show velocity inaccuracy even for the case of a complex velocity model imaged with limited-aperture data.

We notice that the shape of the CIPs changes as a function of the velocity model indicating not only that the velocity is erroneous, but also what is the sign of the velocity error. This is true for all types of events, i.e. reflections and diffractions. Since the velocity error is uniform and the velocity model is constant, the moveout function is also uniform indicating similar error from all illumination angles.

The expressions derived in this section are applicable under the assumptions made up-front, i.e. that we operate in the immediate vicinity of the reflection point. In this region, we can approximate the source and receiver wavefields by planes, we can approximate the reflector by a plane and we can assume that the velocity is locally constant. When these assumptions are violated, then the moveout functions discussed here are only accurate for a small range of lag parameters. Otherwise, the discussion made here remains true regardless of the complexity of the velocity model which influences wavefield reconstruction at the considered image point.

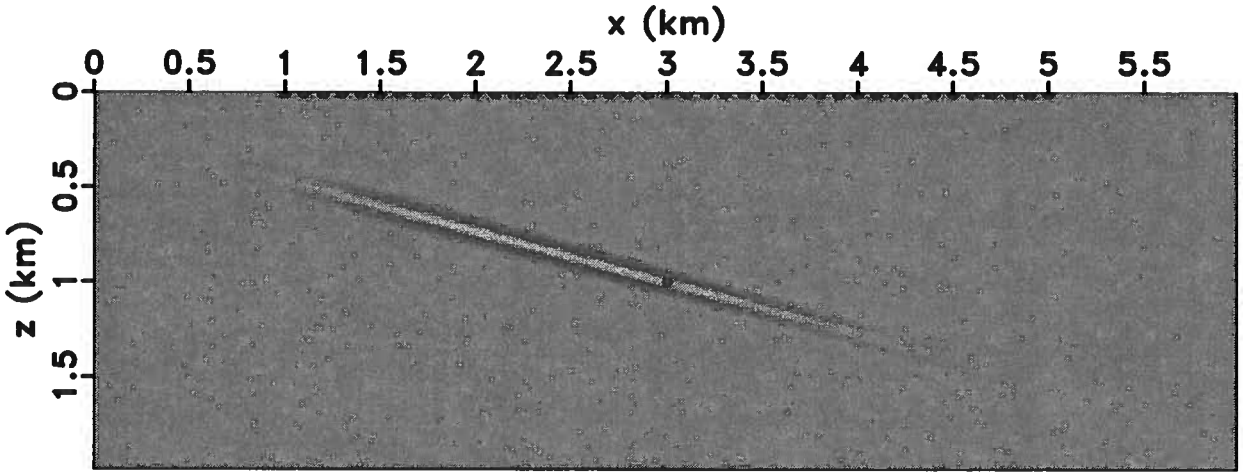

Figure 10. Image of a dipping reflector in constant velocity media. Sources are distributed along the surface at $z = 0.0$ km between $x = 1.0 - 5.0$ km.

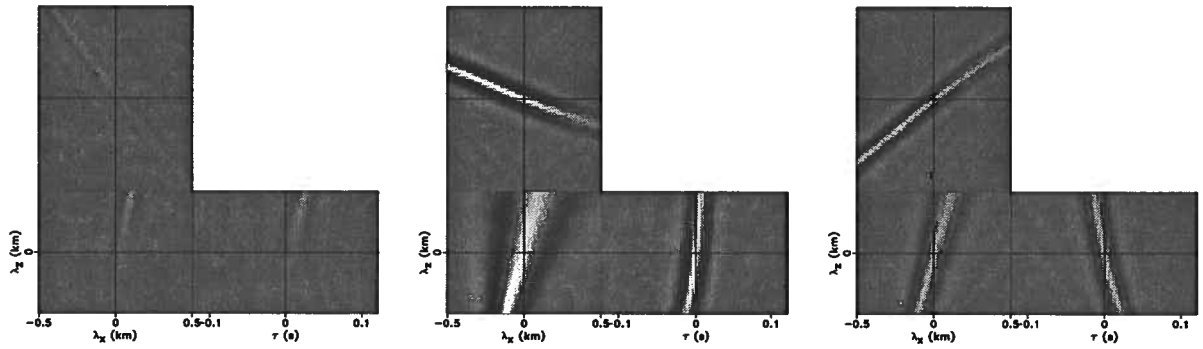

Figure 11. Common-image-point gathers for a dipping reflector constructed at $\{x, z\} = \{3.0, 1.0\}$ km from shots located at (a) $\{x = 2.0, z = 0.0\}$ km, (b) $\{x = 3.0, z = 0.0\}$ km, and (c) $\{x = 4.0, z = 0.0\}$ km.

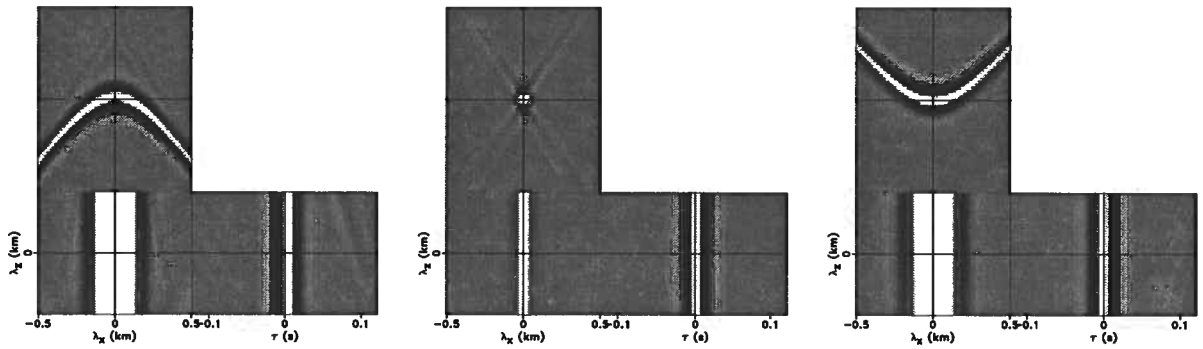

Figure 12. Common-image-point gathers for a horizontal reflector constructed at $\{x, z\} = \{3.0, 1.0\}$ km from all shots located along the surface at $z = 0.0$ km between $x = 1.0 - 5.0$ km for (a) low velocity, (b) correct velocity, and (c) high velocity.

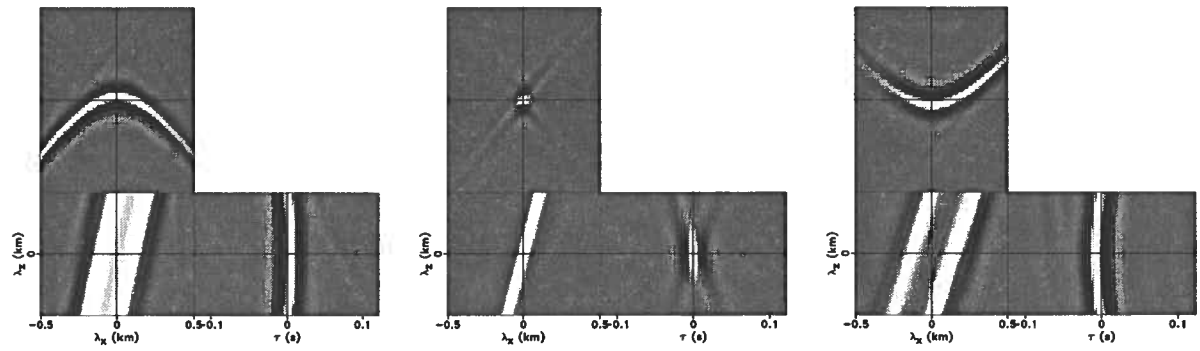

(a) (b) (c)

Figure 13. Common-image-point gathers for a dipping reflector constructed at $\{x, z\} = \{3.0, 1.0\}$ km from all shots located along the surface at $z = 0.0$ km between $x = 1.0 - 5.0$ km for (a) low velocity, (b) correct velocity, and (c) high velocity.

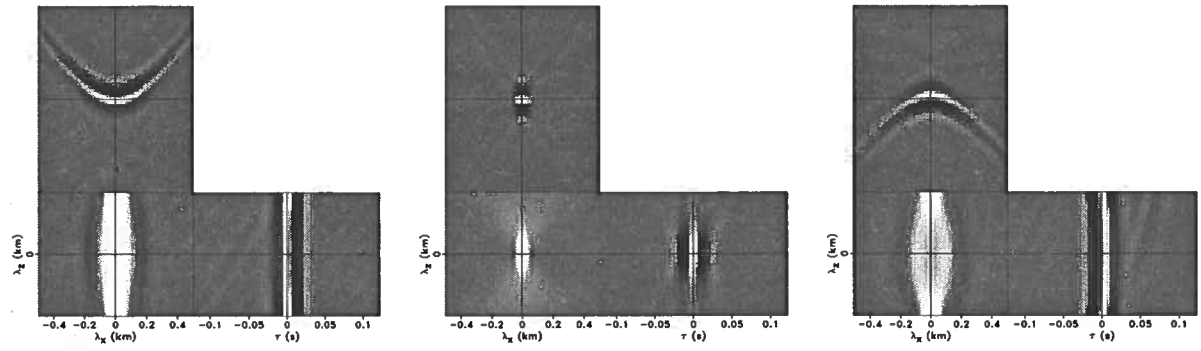

(a) (b) (c)

Figure 14. Common-image-point gathers for a point diffractor constructed at $\{x, z\} = \{3.0, 1.0\}$ km from all shots located along the surface at $z = 0.0$ km between $x = 1.0 - 5.0$ km for (a) low velocity, (b) correct velocity, and (c) high velocity.

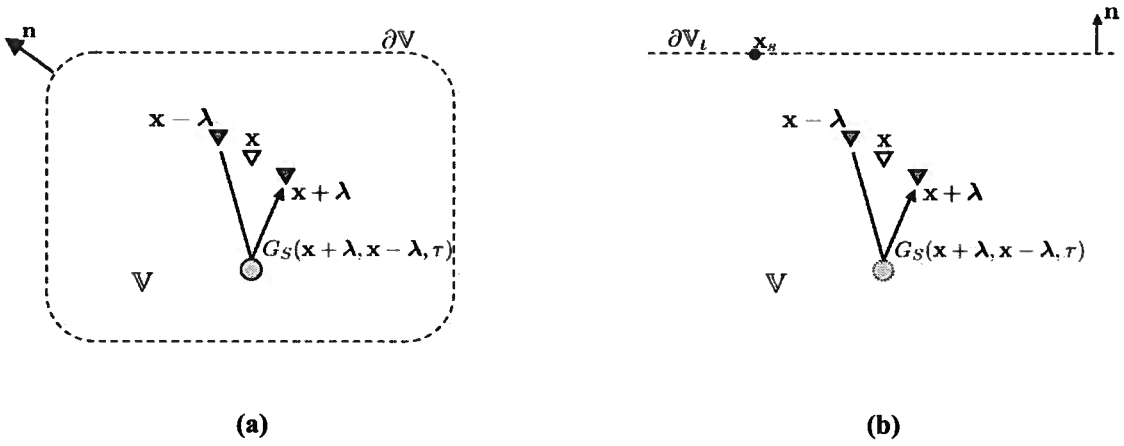

Figure 15. Extended images can be described explicitly in terms of scattered wavefields. As such, an extended image at x correspond to the scattering response $G_S(\mathbf{x}+\boldsymbol{\lambda}, \mathbf{x}-\boldsymbol{\lambda}, \tau)$ due to a pseudo-source at $\mathbf{x}-\boldsymbol{\lambda}$ recorded by a pseudo-receiver at $\mathbf{x}+\boldsymbol{\lambda}$. These cartoons illustrate the differences in evaluating an extended image at x according (a) equation 28 and (b) to equation 30. The grey circle in both cartoons denotes a finite-size scatterer, where in (a) the scatterer is contoured with a solid line to indicate the presence of model singularities (i.e., sharp boundaries), while in (b) the dotted-line contour represents the use of a smooth background model.

6 DESCRIPTION OF THE EXTENDED IMAGES USING SCATTERING THEORY

The extended imaged described in the earlier sections can be interpreted in a more general sense using scattering theory. An imaging condition for migration by wavefield extrapolation can be physically defined in terms of a scattered field G_S, as

$$R(\mathbf{x}) = G_S(\mathbf{x}, \mathbf{x}, \tau = 0) \; . \tag{26}$$

According to this definition, the conventional image $R(\mathbf{x})$ can be thought of a zero-offset scattered field for source and receiver coinciding at the image point $\mathbf{x}$, evaluated at zero time. Here, we use standard notation for the Green's functions, i.e., $G_S(\mathbf{x}, \mathbf{y}, \tau)$ corresponds to a scattered-wave response recorded at $\mathbf{x}$ due to a source at $\mathbf{y}$. Since waves in the subsurface travel with finite wave speeds, the zero-offset scattered-wave response in equation 26 is zero when $\mathbf{x}$ is away from scatterers or interfaces, and it is finite when the image point is at a scatterer or interface. This definition is analogous to the "exploding reflector" concept (Loewenthal et al., 1976; Claerbout, 1985). Based on the definition in equation 26, an extended image can be readily defined by evaluating the scattered field G_S for finite source-receiver offsets and at nonzero times, that is

$$R(\mathbf{x}, \boldsymbol{\lambda}, \tau) = G_S(\mathbf{x}+\boldsymbol{\lambda}, \mathbf{x}-\boldsymbol{\lambda}, \tau) \; . \tag{27}$$

An exact correlation-type representation of Green's functions characterizing the scattered wavefield for a source located at coordinates $\mathbf{x}-\boldsymbol{\lambda}$, a receiver located at coordinates $\mathbf{x}+\boldsymbol{\lambda}$ and scatterers distributed at coordinates $\mathbf{x}$ in a medium of volume $\mathbb{V}$ surrounded by surface $\partial\mathbb{V}$, Figure 15, is given by the expression (Vasconcelos, 2008; Vasconcelos et al., 2009a):

$$\begin{aligned} G_S(\mathbf{x}+\boldsymbol{\lambda}, \mathbf{x}-\boldsymbol{\lambda}, \tau) \;\; = \;\; & \oint_{\mathbf{x}_s \in \partial\mathbb{V}} d^2\mathbf{x}_s \sum_{\omega} e^{2i\omega\tau} \frac{1}{i\omega\rho} \left[\overline{G_0(\mathbf{x}-\boldsymbol{\lambda}, \mathbf{x}_s, \omega)} \nabla G_S(\mathbf{x}+\boldsymbol{\lambda}, \mathbf{x}_s, \omega) \right] \cdot \mathbf{n} \\ - \;\; & \oint_{\mathbf{x}_s \in \partial\mathbb{V}} d^2\mathbf{x}_s \sum_{\omega} e^{2i\omega\tau} \frac{1}{i\omega\rho} \left[G_S(\mathbf{x}+\boldsymbol{\lambda}, \mathbf{x}_s, \omega) \overline{\nabla G_0(\mathbf{x}-\boldsymbol{\lambda}, \mathbf{x}_s, \omega)} \right] \cdot \mathbf{n} \\ + \;\; & \int_{\mathbf{x}_s \in \mathbb{V}} d^3\mathbf{x}_s \sum_{\omega} e^{2i\omega\tau} \frac{1}{i\omega\rho} G(\mathbf{x}+\boldsymbol{\lambda}, \mathbf{x}_s, \omega) \mathcal{V}(\mathbf{x}_s) \overline{G_0(\mathbf{x}-\boldsymbol{\lambda}, \mathbf{x}_s, \omega)} \; . \end{aligned} \tag{28}$$

In equation 28, $\mathbf{x}_s$ represents source positions distributed along the surface $\partial\mathbb{V}$, $\mathcal{V}(\mathbf{x}_s) = \omega^2(v^{-2}(\mathbf{x}_s) - v_0^{-2}(\mathbf{x}))$ is the *scattering potential* (v is the migration velocity model, v_0 is a reference velocity model), G_S is the scattered wavefield due to $\mathcal{V}(\mathbf{x}_s)$, G_0 is the reference wavefield, and $G = G_0 + G_S$ is the total wavefield. Within the context of migration/inversion, the scattering potential $\mathcal{V}$ is typically said to contain the singular part, i.e., the sharp boundaries, of the desired Earth model while the background wavespeed v_0 is assumed to be smooth (Symes, 2009). While this is simply one conventional for the meaning of $\mathcal{V}$, we note that equation 28 is valid for whichever definition or interpretation is chosen for the scattering potential. For the sake of argument, however, in this manuscript we restrict ourselves to the interpretation that $\mathcal{V}$ represents the sharp contrasts in the Earth model. Equation 28 requires the evaluation

of an integral over the whole subsurface volume $\mathbb{V}$, as well as an integral over its bounding surface $\partial\mathbb{V}$. In this expression, $\mathbf{n}$ denotes the unit normal vector on $\partial\mathbb{V}$. The gradients in the integrands of equation 28 are taken at surface coordinates $\mathbf{x}_s$, and physically represent dipole source (i.e., particle-velocity), in addition to monopole sources (i.e., pressure) along the entire surface $\partial\mathbb{V}$. In order for equation 28 to be written in terms of integrals over source positions $\mathbf{x}_s$, we rely on source-receiver reciprocity (Fokkema & Van Den Berg, 1993) to modify the original version of the correlation-type scattering representations (Vasconcelos et al., 2009a). In migration and imaging, implicit within the integrals on the right-hand side of equation 28 is the concept of "double focussing", since apart from the explicit integration over sources $\mathbf{x}_s$ there is an implicit summation over receivers as the extrapolated fields $G_{0,S}(\mathbf{x} \pm \boldsymbol{\lambda}, \mathbf{x}_s, \omega)$ in the integrands consist of the superposition of extrapolating the signals of all receivers for a given source at $\mathbf{x}_s$ (Halliday et al., 2009).

Computing the scattered wavefield in a medium using the integrals in equation 28 is not practical in exploration seismic experiments for three main reasons. First, the number of sources is limited, and typically available only on the surface of the Earth, i.e. the sources $\mathbf{x}_s$ are available on a subset $\partial\mathbb{V}_t$ of $\partial\mathbb{V}$. Second, receivers are also only available at the Earth's surface or have limited subsurface coverage (e.g., in VSP experiments) and therefore responses for receivers at $\mathbf{x} \in \mathbb{V}$ required by the integrands are not readily available. Third, the quantity $\mathcal{V}(\mathbf{x})$ in the integrand of the volume term assumes perfect knowledge of the velocity model, which is also not available in practice.

For conventional implementation of reverse-time migration, the following assumptions are being made:

$$\begin{cases} i)\text{the singularities in the model are ignored in migration,} & \text{sing supp}(\mathcal{V}(\mathbf{x}_s)) = 0; \\ ii)\text{sources are distributed on a finite surface,} & \mathbf{x}_s \in \partial\mathbb{V}_t; \\ iii)\text{sources are located in the far field;} & \\ iv)\text{the reference field is given by the source wavefield,} & G_0(\mathbf{x}-\boldsymbol{\lambda}, \mathbf{x}_s, \omega) \approx W_s(\mathbf{x}-\boldsymbol{\lambda}, \omega); \\ v)\text{the scattered field is given by the receiver wavefield,} & G_S(\mathbf{x}+\boldsymbol{\lambda}, \mathbf{x}_s, \omega) \approx W_r(\mathbf{x}+\boldsymbol{\lambda}, \omega);. \end{cases} \tag{29}$$

Condition $i)$ states that the true Earth model is unknown, therefore migration uses a smooth migration velocity model, from which we obtain $\mathcal{V}(\mathbf{x}_s)$. Condition $ii)$ states that the integral over closed surface $\partial\mathbb{V}$ is replaced by an integral over an open surface $\partial\mathbb{V}_t$, e.g. sources are located only along the surface. Condition $iii)$ states that because dipole sources are not available in conventional exploration seismic surveys, they are replaces by monopole sources. This assumption is only valid in the far field (Wapenaar & Fokkema, 2006). Finally, conditions $iv)$ and $v)$ state that we approximate the Green's functions G_0 and G_S in the subsurface by wavefields reconstructed from the recorded data based on the smooth background velocity model. These wavefields are evaluated numerically by solving a wave-equation whose coefficients are given by the migration velocity model $v_0(\mathbf{x})$. Therefore, under the assumptions listed in equation 29, wavefield imaging using reverse-time migration approximates the scattered wavefield G_S in equation 28 by evaluating only the surface integral

$$\begin{aligned} \mathcal{I}_{\text{surf}}(\mathbf{x}+\boldsymbol{\lambda}, \mathbf{x}-\boldsymbol{\lambda}, \tau) &\approx \oint_{\mathbf{x}_s \in \partial\mathbb{V}_t} d^2\mathbf{x}_s \sum_{\omega} e^{2i\omega\tau} \frac{2}{c\rho} \left[\overline{G_0(\mathbf{x}-\boldsymbol{\lambda}, \mathbf{x}_s, \omega)} G_S(\mathbf{x}+\boldsymbol{\lambda}, \mathbf{x}_s, \omega)\right] \\ &\approx \oint_{\mathbf{x}_s \in \partial\mathbb{V}_t} d^2\mathbf{x}_s \sum_{\omega} e^{2i\omega\tau} \overline{W_s(\mathbf{x}-\boldsymbol{\lambda}, \omega)} W_r(\mathbf{x}+\boldsymbol{\lambda}, \omega)\ . \end{aligned} \tag{30}$$

The surface integral in Equation 30 represents exactly the extended image in equation 4, if we replace the integral of the open surface $\partial\mathbb{V}_s$ with a simple summation over shots:

$$R(\mathbf{x}, \boldsymbol{\lambda}, \tau) \approx \mathcal{I}_{\text{surf}}(\mathbf{x}+\boldsymbol{\lambda}, \mathbf{x}-\boldsymbol{\lambda}, \tau)\ . \tag{31}$$

We can conclude that Equation 30 is adequate if the imaging objective is to map correctly the reflectors in the subsurface using a smooth background velocity model. The comparison between the two expressions also shows that the images $R(\mathbf{x}, \boldsymbol{\lambda}, \tau)$ simply represent scattered wavefields in the extended space of $\boldsymbol{\lambda}$ and τ. We note that using only the surface term to estimate the extended image implicitly corresponds to the single-scattering assumption. To properly migrate multiply-scattered energy (i.e., multiples) the velocity model must contain singularities (i.e., hard interfaces) for the wavefields W_s and W_r to properly position multiple reflections, therefore using only the surface integral may not be sufficient (Vasconcelos et al., 2009b).

The key insight gained by analyzing the extended images via scattering representations is that extended images are, in fact, estimates of scattered wavefields associated to sources and receivers inside the subsurface. Therefore, we can think of fully extended seismic images as dynamic objects whose behavior is described by wave-equations based on the known velocity model. This idea can be exploited in practice using stationary-phase analysis of equation 30 (Vasconcelos et al., 2009b), as discussed in this paper.

As presented here, our formulation of extended images establishes a formal, explicit connection between the fields of seismic imaging and seismic interferometry. In seismic interferometry the cross-correlation of wavefields received at two receivers allows the extraction of the response between these receivers as if one of them acts as a source (Wapenaar & Fokkema, 2006; Vasconcelos et al., 2009b). While most interferometry applications rely on reciprocity formulations for full wavefields (Wapenaar & Fokkema, 2006), a similar response for only the scattered field traveling from one point inside the medium to another can be found using

scattering reciprocity relations (Vasconcelos et al., 2009b). Since an image of a scatterer can be obtained by collapsing the recorded scattered wavefield onto the scatterer location, this formulation based on scattering representations can be used to interpret the imaging condition in the context of seismic interferometry (Vasconcelos, 2008): the image is the zero-time scattered-wave response generated by zero-offset pseudo-experiments in the image domain. Here we expand on this notion of "image-domain interferometry" and show that the representation theorems for the scattered field allow the extended images to be described as scattered wavefields which are "excited" and "recorded" in the image domain, as illustrated by Figure 15.

Finally, while in this manuscript we only briefly discuss the role of the volume term in equation 28, we must also point out that a more complete understanding on how to deal with this volume integral is subject of ongoing research. We know at the moment that the volume integrals play a crucial role in describing behavior of the extended images that is nonlinear on the unknown Earth model i.e., in describing proper amplitude behavior or in migrating multiples. In fact, we hypothesize that the previously reported "reverse-time migration artifacts" (Fletcher et al., 2006; Guitton et al., 2006) that appear when using rough velocity models (i.e., models with singularities) are likely to be intrinsically related to ignoring the volume terms discussed above.

7 SIGSBEE 2A EXAMPLE

In this section, we illustrate the CIP construction described in the preceding sections with the Sigsbee 2A model. For the CIPs shown here, we consider a fixed reflector in the image and track it at different positions as a function of the velocity model used for imaging. This is legitimate since the only way we can identify a reflector is by observing it in the conventional image at zero lags in space and time. We refer to the images shown in Figures 1(a) and 1(b) to identify CIP locations.

Figures 16(a)-16(c)-16(e) show one CIP for the reflector located at $\{x,z\} = \{9.7,4.6\}$ km in the image constructed with the correct velocity, Figure 1(a). The various panels correspond to different shots located on the surface at coordinates $x = \{5.16,6.99,8.82\}$ km. Similarly, Figures 16(b)-16(d)-16(f) show one CIP for the reflector located at $\{x,z\} = \{9.6,4.4\}$ km in the image constructed with the low velocity, Figure 1(b). In both situations, we observe that the CIPs for different shots change as a function of the shot position, i.e. they change as a function of the angle of incidence. This observation enables us to speculate that we can use these CIPs to decompose the reflectivity function of the angle of incidence at various positions in the image using slant-stacks similar to the technique used by Sava & Fomel (2003) for more conventional space-lag gathers.

We can also observe that in the case of CIPs constructed with correct velocity, the events corresponding to different shots intersect at zero lag in space and time, indicating correct imaging. In contrast, in the case of CIPs constructed with incorrect velocity, the events corresponding to different shots do not intersect at zero lag in space and time, indicating incorrect imaging. This observation can be further analyzed in the CIPs obtained by stacking of contributions from different shots, as shown in Figure 17(a) for correct velocity and in Figure 17(b) for incorrect velocity. The CIPs constructed with correct velocity are focused around zero in the $\lambda - \tau$ space, while the CIPs constructed with low velocity show events with moveout in the $\lambda - \tau$ space. The complicated, wavefield-like behavior of the extended images as a function of space and time lags can be described by the physics of scattered fields, as discussed in the preceding sections. The fact that the extended CIPs here only show nonzero scattered-wave responses on positive times for positive space lags or negative times for negative space lags is due to the physical aperture limitations of the towed marine acquisition used in the modeling of Sigsbee 2A data.

In general, for arbitrary distribution of velocity anomalies in the overburden, there is no analytic function characterizing those CIPs. For the case we consider here, i.e. uniform scaling of the sediment velocity in the overburden, the events show nearly hyperbolic moveout. The curvature of the events passing through the zero lag point is indicative of velocity error, but it characterizes the cumulative contributions of all velocity anomalies in the overburden relative to this image point. Unraveling this effective contribution requires a tomographic procedure minimizing a global objective function, as indicated earlier in the paper.

Finally, we note that the gather in Figure 17(a) represents a reflector and not a diffractor and that imaging was performed with correct velocity. Furthermore, we can also identify the dip of the reflector without additional measurements in the image space. In contrast, the gather shown in Figure 18(a) corresponds to the superposition between a diffractor and a reflector, as indicated by the apparent focus in the space-lag panel. The focus is not perfect due to the limited aperture of the surface acquisition array. For imaging with incorrect velocity, Figure 18(b), the CIP is not focused.

8 CONCLUSIONS

Extended common-image-point gathers are effective tools for analyzing velocity accuracy for wave-equation imaging. The extended CIPs can be analyzed at sparse locations in the image volume, thus reducing the computational cost of this imaging condition. One possibility is to construct extended CIPs along the main reflectors which are the most indicative velocity model building components of migrated images. The sparse CIP allows for easier visualization and interpretation of extended images. The CIP construction can be further accelerated if we avoid constructing extensions in the direction orthogonal to the reflector dip. Such CIPs are also not biased toward reflectors with specific dips (e.g. nearly-horizontal), thus making them a natural choice for reverse-time migration.

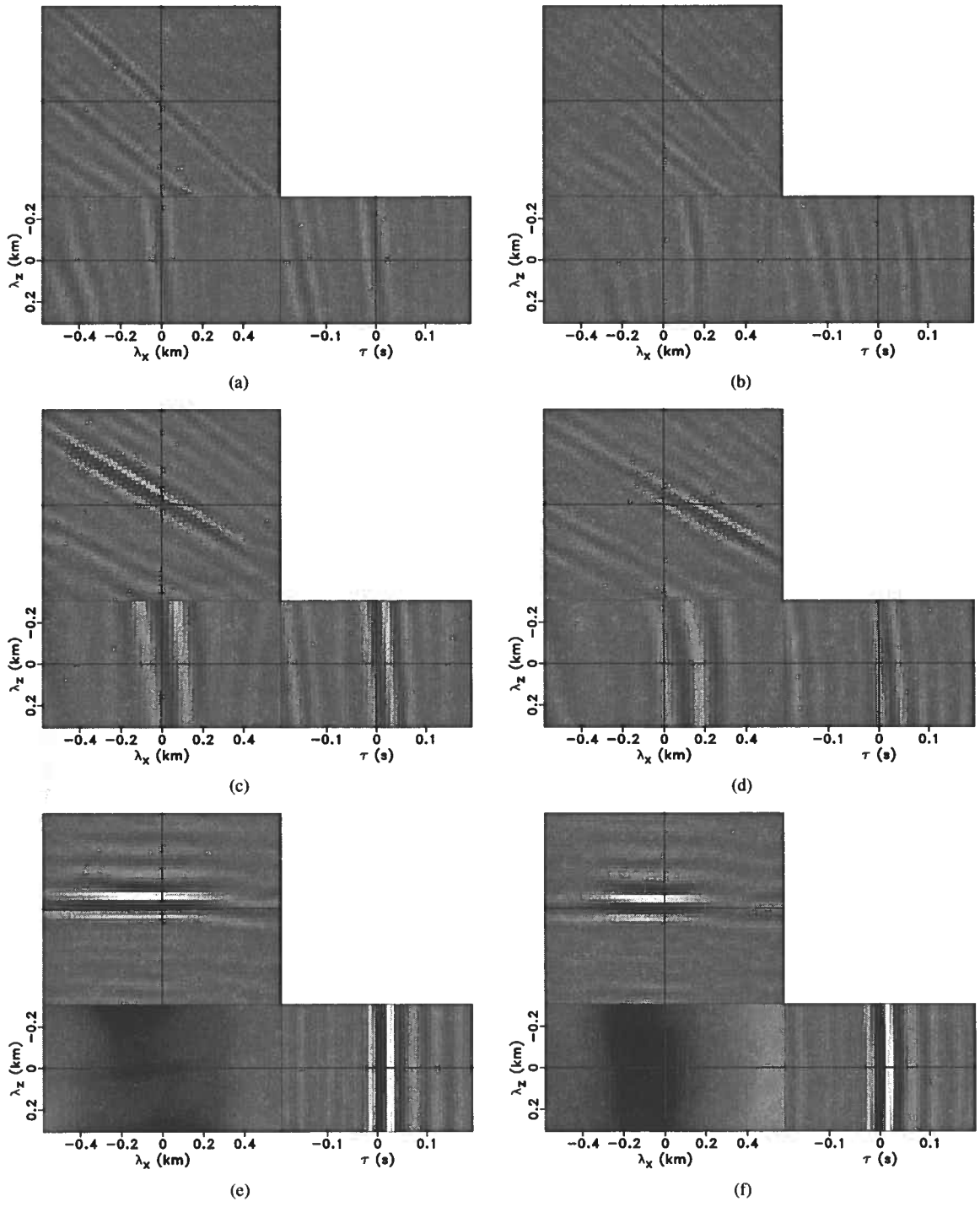

Figure 16. Sigsbee 2A common-image-point gathers constructed for different shots at coordinates $x = \{5.16, 6.99, 8.82\}$ km. Panels (a)-(c)-(e) correspond to coordinates $\{x, z\} = \{9.7, 4.6\}$ km in the image constructed with the correct velocity, Figure 1(a), and panels (b)-(d)-(f) correspond to coordinates $\{x, z\} = \{9.6, 4.4\}$ km in the image constructed with the low velocity, Figure 1(b).

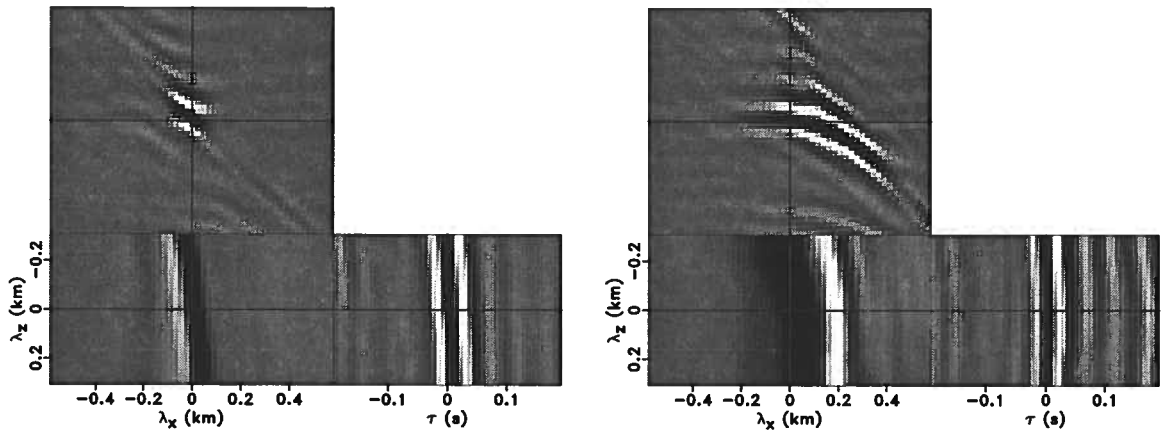

Figure 17. Sigsbee 2A common-image-point gathers constructed for all shots. Panel (a) corresponds to coordinates $\{x, z\} = \{9.7, 4.6\}$ km in the image constructed with the correct velocity, Figure 1(a), and panel (b) correspond to coordinates $\{x, z\} = \{9.6, 4.4\}$ km in the image constructed with the low velocity, Figure 1(b). The image at this locations corresponds to a slanted reflector.

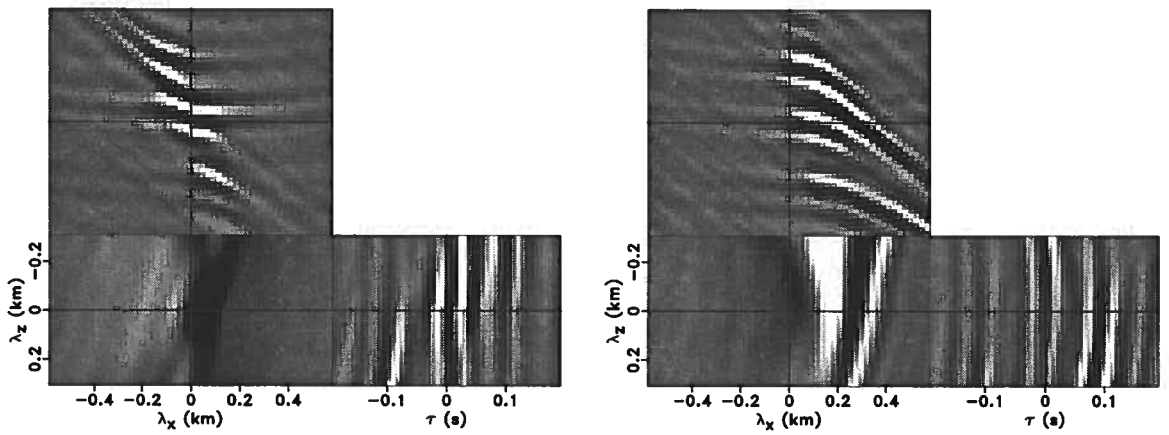

Figure 18. Sigsbee 2A common-image-point gathers constructed for all shots. Panel (a) corresponds to coordinates $\{x, z\} = \{7.65, 5.15\}$ km in the image constructed with the correct velocity, Figure 1(a), and panel (b) correspond to coordinates $\{x, z\} = \{7.65, 4.87\}$ km in the image constructed with the low velocity, Figure 1(b). The image at this location corresponds to the superposition between a reflector and a diffractor embedded in the model.

A key requirement for the effectiveness of this technique is that space-lags and time-lag extensions be analyzed simultaneously. This is particularly the case when defining objective functions which penalize CIPs for departure from their ideal geometry. In this situation, we can use scattering theory to interpret the CIPs as scattered wavefields corresponding to sources inside the model. These scattered wavefields have special properties which depend on the the quality of the velocity model used for reconstruction of the source and receiver wavefields from the surface. In addition to velocity analysis, potential applications the CIPs described in this paper include wide-azimuth angle-domain amplitude analysis, as well as slope estimation and separation of reflections and diffractions.

9 ACKNOWLEDGMENTS

Ivan Vasconcelos acknowledges ION Geophysical for support of this research.

REFERENCES

Al-Yahya, K., 1987, Velocity analysis by iterative profile migration: , PhD thesis, Stanford University.

Albertin, U., Sava, P., Etgen, J., and Maharramov, M., 2006, Image differencing and focusing in wave-equation velocity analysis: 68th Mtg., Eur. Assoc. Expl. Geophys., Abstracts.

Berkhout, A. J., 1982, Imaging of acoustic energy by wave field extrapolation: , Elsevier.

Billette, F., Begat, S. L., Podvin, P., and Lambare, G., 2003, Practical aspects and applications of 2D sterotomography: Geophysics, **68**, no. 3, 1008–1021.

Biondi, B., and Sava, P., 1999, Wave-equation migration velocity analysis: 69th Annual International Meeting, SEG, Expanded Abstracts, 1723–1726.

Biondi, B., and Symes, W., 2004, Angle-domain common-image gathers for migration velocity analysis by wavefield-continuation imaging: Geophysics, **69**, no. 5, 1283–1298.

Bishop, T. N., Bube, K. P., Cutler, R. T., Langan, R. T., Love, P. L., Resnick, J. R., Shuey, R. T., Spindler, D. A., and Wyld, H. W., 1985, Tomographic determination of velocity and depth in laterally varying media: Geophysics, **50**, no. 06, 903–923.

Bracewell, R., 2006, Fourier analysis and imaging: , Springer.

Brown, M., Higginbotham, J., and Clapp, R., 2008, Velocity model building with wave equation migration velocity focusing analysis: 77th Annual International Meeting, SEG, Expanded Abstracts, 3083–3087.

Chauris, H., Noble, M. S., Lambare, G., and Podvin, P., 2002a, Migration velocity analysis from locally coherent events in 2-D laterally heterogeneous media, Part I: Theoretical aspects: Geophysics, **67**, no. 04, 1202–1212.

——— 2002b, Migration velocity analysis from locally coherent events in 2-D laterally heterogeneous media, Part Ii: Applications on synthetic and real data: Geophysics, **67**, no. 04, 1213–1224.

Chavent, G., and Jacewitz, C. A., 1995, Determination of background velocities by multiple migration fitting: Geophysics, **60**, no. 02, 476–490.

Claerbout, J. F., 1985, Imaging the Earth's interior: , Blackwell Scientific Publications.

Clapp, R. G., Biondi, B., and Claerbout, J. F., 2004, Incorporating geologic information into reflection tomography: Geophysics, **69**, no. 2, 533–546.

Clayton, R. W., and Stolt, R. H., 1981, A born-WkBj inversion method for acoustic reflection data: Geophysics, **46**, no. 11, 1559–1567.

Clement, F., Chavent, G., and Gomez, S., 2001, Migration-based traveltime waveform inversion of 2-D simple structures: A synthetic example: Geophysics, **66**, no. 3, 845–860.

de Vries, D., and Berkhout, A. J., 1984, Velocity analysis based on minimum entropy: Geophysics, **49**, no. 12, 2132–2142.

Etgen, J., 1990, Residual prestack migration and interval-velocity estimation: , PhD thesis, Stanford University.

Faye, J. P., and Jeannot, J. P., 1986, Prestack migration velocities from focusing depth analysis: Prestack migration velocities from focusing depth analysis:, Soc. of Expl. Geophys., 56th Ann. Internat. Mtg., Session:S7.6.

Fletcher, R., Fowler, P., Kitchenside, P., and Albertin, U., 2006, Suppressing unwanted internal reflections in prestack reverse-time migration: Geophysics, **71**, E79–E82.

Fokkema, J., and Van Den Berg, P., 1993, Seismic applications of acoustic reciprocity: , Elsevier.

Fomel, S., Landa, E., and Turner, M., 2007, Poststack velocity analysis by separation and imaging of seismic diffractions: Geophysics, **72**, no. 6, U89–U94.

Fowler, P., 1988, Seismic velocity estimation using prestack time migration: , PhD thesis, Stanford University.

Gauthier, O., Virieux, J., and Tarantola, A., 1986, Two-dimensional nonlinear inversion of seismic waveforms - Numerical results: Geophysics, **51**, no. 07, 1387–1403.

Gray, S. H., Etgen, J., Dellinger, J., and Whitmore, D., 2001, Seismic migration problems and solutions: Geophysics, **66**, no. 5, 1622–1640.

Guitton, A., Kaelin, B., and Biondi, B., 2006, Least-square attenuation of reverse time migration artifacts: 75th Annual International Meeting, SEG, Expanded Abstracts, 2348–2352.

Halliday, D., Curtis, A., Vermeer, P., Strobbia, C., and Cluschenko, A., 2009, Source-receiver seismic interferometry: 78th Annual International Meeting, SEG, Expanded Abstracts, 4207–4210.

Harlan, W. S., Claerbout, J. F., and Rocca, F., 1984, Signal/noise separation and velocity estimation: Geophysics, **49**, no. 11, 1869–1880.

Lambare, G., Alerini, M., Baina, R., and Podvin, P., 2004, Stereotomography: a semi-automatic approach for velocity macromodel estimation: Geophys. Prosp., **52**, no. 6, 671–681.

Loewenthal, D., Lu, L., Robertson, R., and Sherwood, J., 1976, The Wave Equation applied to migration: Geophysical Prospecting, **24**, 380–399.

MacKay, S., and Abma, R., 1992, Imaging and velocity estimation with depth-focusing analysis: Geophysics, **57**, no. 12, 1608–1622.

MacKay, S., and Abma, R., 1993, Depth-focusing analysis using a wavefront-curvature criterion: Geophysics, **58**, no. 08, 1148–1156.

Mora, P., 1989, Inversion = migration + tomography: Geophysics, **54**, no. 12, 1575–1586.

Nemeth, T., 1995, Velocity estimation using tomographic depth-focusing analysis: Velocity estimation using tomographic depth-focusing analysis:, Soc. of Expl. Geophys., 65th Ann. Internat. Mtg, 465–468.

Nemeth, T., 1996, Relating depth-focusing analysis to migration velocity analysis: Relating depth-focusing analysis to migration velocity analysis:, Soc. of Expl. Geophys., 66th Ann. Internat. Mtg, 463–466.

Paffenholz, J., Stefani, J., McLain, B., and Bishop, K., 2002, SIgSbEe_2A Synthetic Subsalt Dataset - Image Quality as Function of Migration Algorithm and Velocity Model Error: SIgSbEe_2A Synthetic Subsalt Dataset - Image Quality as Function of Migration Algorithm and Velocity Model Error:, Eur. Assn. Geosci. Eng., 64th Mtg., B019.

Pratt, R. G., 1999, Seismic waveform inversion in the frequency domain, Part 1: Theory and verification in a physical scale model: Geophysics, **64**, no. 3, 888–901.

Rickett, J., and Sava, P., 2002, Offset and angle-domain common image-point gathers for shot-profile migration: Geophysics, **67**, no. 3, 883–889.

Romero, L. A., Ghiglia, D. C., Ober, C. C., and Morton, S. A., 2000, Phase encoding of shot records in prestack migration: Geophysics, **65**, no. 02, 426–436.

Sava, P., and Biondi, B., 2004a, Wave-equation migration velocity analysis - I: Theory: Geophysical Prospecting, **52**, 593–606.

——— 2004b, Wave-equation migration velocity analysis - II: Subsalt imaging examples: Geophysical Prospecting, **52**, 607–623.

Sava, P., and Fomel, S., 2003, Angle-domain common image gathers by wavefield continuation methods: Geophysics, **68**, no. 3, 1065–1074.

Sava, P., and Fomel, S., 2005, Coordinate-independent angle-gathers for wave equation migration: 75th Annual International Meeting, SEG, Expanded Abstracts, 2052–2055.

Sava, P., and Fomel, S., 2006, Time-shift imaging condition in seismic migration: Geophysics, **71**, no. 6, S209–S217.

Sava, P., Biondi, B., and Etgen, J., 2005, Wave-equation migration velocity analysis by focusing diffractions and reflections: Geophysics, **70**, U19–U27.

Shen, P., Symes, W., and Stolk, C. C., 2003, Differential semblance velocity analysis by wave-equation migration: Differential semblance velocity analysis by wave-equation migration:, Soc. of Expl. Geophys., 73rd Ann. Internat. Mtg., 2132–2135.

Sirgue, L., and Pratt, R., 2004, Efficient waveform inversion and imaging: A strategy for selecting temporal frequencies: Geophysics, **69**, no. 1, 231–248.

Stolt, R. H., and Weglein, A. B., 1985, Migration and inversion of seismic data: Geophysics, **50**, no. 12, 2458–2472.

Stork, C., 1992, Reflection tomography in the postmigrated domain: Geophysics, **57**, no. 05, 680–692.

Symes, W., 2009, Migration velocity analysis and waveform inversion: Geophysical Prospecting, **56**, 765–790.

Tarantola, A., 1987, Inverse Problem Theory: methods for data fitting and model parameter estimation: , Elsevier.

Vasconcelos, I., Snieder, R., and Douma, H., 2009a, Representation theorems and green's function retrieval for scattering in acoustic media: Phys. Rev. E, **80**, 036605.

——— 2009b, Wave-equation extended images via image-domain interferometry: 79th Annual International Meeting, SEG, Expanded abstracts.

Vasconcelos, I., 2008, Generalized representations of perturbed fields - applications in seismic interferometry and migration: 77th Annual International Meeting, SEG, Expanded Abstracts, 2927–2931.

Wapenaar, K., and Fokkema, J., 2006, Greens function representations for seismic interferometry: Geophysics, **71**, SI133–SI146.

Weglein, A. B., and Stolt, R. H., 1999, Migration-inversion revisited (1999): The Leading Edge, **18**, no. 8, 950–952.

Whitmore, N. D., 1995, An imaging hierarchy for common angle plane wave seismograms: , PhD thesis, University of Tulsa.

Woodward, M. J., 1992, Wave-equation tomography: Geophysics, **57**, no. 01, 15–26.

Yang, T., and Sava, P., 2009a, Moveout analysis of wave-equation extended images: Geophysics, submitted for publication.

——— 2009b, Wave-equation migration velocity analysis using extended images: 79th Annual International Meeting, SEG, Expanded abstracts.

Simultaneous source imaging by amplitude encoding

Jeff Godwin & Paul Sava
Center for Wave Phenomena, Colorado School of Mines

ABSTRACT

The computational cost of conventional shot-record imaging is large for today's wide-azimuth seismic surveys. One strategy to reduce the overall cost of seismic imaging is to migrate with multiple shot-gathers at once, a technique which is known as blended source imaging. Blended source imaging trades the reduced cost of imaging with the presence of artifacts (cross-talk) in the image. A special case of blended source imaging is that of zero phase-delay, or simultaneous sources. We show that a theoretical framework using a matrix representation of the imaging process adequately describes both conventional and simultaneous source imaging. Furthermore, the matrix representation predicts both the quantity and strength of cross-talk artifacts prior to imaging, thus allowing us to decide a priori the trade off between cross-talk and speed. By exploiting our theoretical framework, we are able to design a simultaneous source encoding scheme, referred to as Truncated Singular Vector encoding (TSV), that trades a significantly reduced cost of imaging with spatial resolution. The TSV encoding allows us to reduce the cost of imaging by at least an order of magnitude relative to conventional shot-record migration. Overall, we provide a framework for finding simultaneous source encoding schemes, that produce good quality images at lower computational cost.

Key words: seismic imaging, migration, blended sources, simultaneous sources, singular value decomposition, shot-encoding, wave-equation, matrix representation.

1 INTRODUCTION

Today's seismic imaging challenges include imaging areas with increasingly complex geology, such as salt domes and overthrust regions. The major issues for imaging these areas are poor data quality and lack of seismic illumination, as the complex geology severely deforms seismic wavefields. One approach to resolving these issues is to obtain large amounts of redundant information from various acquisition directions via wide-azimuth or full-azimuth seismic surveys (Ting & Zhao, 2009). However, wide-azimuth surveys require significantly more time to acquire and even greater amounts to process. Subsequently, the cost of acquiring and processing a wide-azimuth survey is significantly more expensive than the cost of a conventional survey. Additionally, the cost of imaging in complex geology is much greater, because advanced wave-equation imaging algorithms such as reverse-time migration must be used. Therefore, both the financial and computational cost of today's large surveys is increasing at a rapid pace.

However, recent technological advances may reduce the cost of data acquisition and imaging for large seismic surveys. One of these technologies is acquisition using simultaneous or delayed sources (Womack, 1990; Beasley, 2008; Berkhout et al., 2008; Hampson et al., 2008; Blacquiere et al., 2009). As the name implies, simultaneous sources are multiple sources triggered at the same time but at different spatial locations. By acquiring multiple sources in a shot-gather, it is hoped that the amount of time that a survey requires reduces thus decreasing the acquisition costs. The downside to simultaneous source acquisition, is that simultaneous source data creates additional noise in the final seismic image. Presently, this issue is circumvented by deblending the simultaneous source shot-gathers to create separate shot-gathers for each source prior to imaging (Akerberg et al., 2008; Hampson et al., 2008; Spitz et al., 2008; Huo et al., 2009; Kim et al., 2009). The separated shot-gathers are then imaged using a conventional shot-record migration. The drawback to separating the shots is twofold. First, the sources must be separable, which typically implies that they are relatively isolated from one another in space which limits the maximum amount of shots that can be used at once during acquisition. Second, the imaging process is not sped up by separating the shots.

An alternative approach, is to reduce the cost of imaging by using multiple sources at once during imaging. This process, known as blended imaging, combines multiple shot-gathers together prior to migration, which reduces the number of migrations that are needed to produce a final image (Liu, 1999; Morton, 1999; Romero et al., 2000; Soubaras, 2006; Zhang et al., 2007; Berkhout et al., 2009; Perrone & Sava, 2009). Certain forms of blended imaging, such as plane-wave migration, are used in industry today, but many forms of blending (i.e. random phase) are not used today because they introduce a significant amount of noise to the image. However, the presence of the noise may be justified if the cost advantage over conventional shot-record migration is sufficiently high.

In conventional seismic imaging (shot-record migration), seismic data corresponding to individual shots are backpropagated independently to construct the receiver-wavefields. Concurrently, the source-wavefield for each shot is constructed by forward propagating the source using a known velocity model. An imaging condition is then applied to the individual reconstructed source and receiver wavefields to produce an image of the subsurface. Because this process is repeated for each shot, the cost of shot-record migration (SRM) is expressed as

$$C_s^t = N_s C_s, \tag{1}$$

where C_s^t is the total cost in computation time, N_s is the number of shot records, and C_s is the computational cost for each shot (Zhang et al., 2007). Since modern seismic surveys often consist of many tens of thousands of shots, and each shot may image a large area (a few km^2), the overall computational cost for seismic imaging is tremendous.

However, equation 1 hints at two possibilities to reduce the overall cost of imaging:

- reduce the cost of migrating each shot (i.e. reduce C_s), or
- reduce the number of shot-records used for migration (i.e. reduce N_s).

In most scenarios, reducing the cost of migrating each shot C_s is the most practical approach to reducing the cost of imaging because one can choose the algorithm that is used for wavefield reconstruction (i.e. wavefield extrapolation or reverse-time migration). However, much of today's imaging is done in areas with complex geology, so computationally expensive algorithms like reverse-time migration have to be used to produce accurate images. Therefore, most reductions in computational cost typically come from advances in computer hardware. In most cases however, our ability to create more demanding algorithms i.e. full anisotropic reverse-time migration, and acquire more data greatly exceeds the rate of hardware advances.

Furthermore, reducing the number of shots N_s that are used to image is not typically considered because both the signal-to-noise ratio and the illumination of the seismic image are negatively impacted by removing sources. An alternative to reducing the number of sources is to linearly combine multiple independent shot-records together into blended shot-records prior to migration (Romero et al., 2000). By doing so, we effectively reduce the number of migrations that are necessary from N_s to N_e, where N_e is the number of blended experiments. The ultimate goal of blended imaging is to image using all shots in a single migration. Therefore, the total cost of imaging using a blended migration scheme becomes:

$$C_e^t = N_e C_e. \tag{2}$$

Here, C_e^t is the total cost for a blended source migration, C_e is the cost of an individual blended record migration, which we assume to be the same as the SRM cost C_s. In practice, $C_e > C_s$ as blended shots must be migrated over larger aperture ranges (Romero et al., 2000). In general, as the number of blended experiments N_e decreases the overall cost of imaging decreases. In most instances, the reduction in cost by blending greatly outweighs the additional cost of extending the migration aperture as $N_e \ll N_s$, whereas C_e is only *somewhat* greater than C_s.

The blending process usually applies a phase delay to each shot-record and then linearly combines *all* of the shot records together into a series of blended experiments prior to migration (Morton, 1999; Liu, 1999; Romero et al., 2000; Soubaras, 2006; Zhang et al., 2007; Berkhout et al., 2009; Perrone & Sava, 2009). A single blended experiment may also be referred to as a realization. A combination of experiments or realizations, where the combination method may change from experiment to experiment, is referred to as a shot-encoding scheme. During the imaging process, both the encoded source- and receiver-wavefields are reconstructed. The conventional cross-correlation imaging condition is applied to the blended wavefields as follows,

$$R(\mathbf{x}) = \sum_e \sum_t \left(\sum_i W_s^i(\mathbf{x},t) \right) \left(\sum_j W_r^j(\mathbf{x},t) \right), \tag{3}$$

where i and j are the shot-record indices, $W_s{}^i(\mathbf{x},t)$ is the i^{th} reconstructed source wavefield, $W_r{}^j(\mathbf{x},t)$ is the j^{th} reconstructed receiver wavefield, e represents the blended shot-gathers index, t represents time and $\mathbf{x}$ is a vector of locations in space. When $i = j$, equation 3 computes the correlation of wavefields related to a single shot gather. Conversely, when $i \neq j$, equation 3 computes the value of the source and receiver wavefields that are not physically related to one another, hence these terms are referred to as cross-talk. In blended imaging, the cross-talk exists between each source and every other receiver wavefields and vice versa which means that the blended images are contaminated by a significant amount of cross-talk noise. Additionally, cross-talk is unlike most other noise in that it is: coherent, strong (amplitude), and virtually indistinguishable from geology (Romero et al., 2000). Therefore, cross-talk must be removed before an image is usable for interpretation.

Previous attempts to remove cross-talk from blended-images focused on modifying the phase-encoding scheme to introduce inconsistency between unrelated wavefields in order to decrease the contribution of the cross-talk terms (Morton, 1999; Liu, 1999; Romero et al., 2000; Zhang et al., 2007; Berkhout et al., 2009; Perrone & Sava, 2009). In these encoding schemes, multiple realizations of all or some of the shot-gathers are used to create images. Some common phase-encoding schemes include: planar (Liu, 1999), random

(Romero et al., 2000), harmonic (Zhang et al., 2007), and planar with dithering (Perrone & Sava, 2009) . Another shot-encoding option is to modulate the amplitude of the wavefields to reduce the contribution of cross-talk terms to the image (Soubaras, 2006). Regardless of encoding choice, the standard method to attenuate cross-talk in images from separate realizations of blended shots is conventional stacking.

A special case of blended source imaging is simultaneous source imaging, i.e. linearly combining shot-gathers with zero phase- and time-delay. The major advantage of simultaneous source imaging compared to blended imaging is that simultaneous source data can be acquired using the same recording time length, whereas blended source acquisition requires long recording times due to time-delays between sources. Thus, simultaneous source imaging reduces both the cost of conventional acquisition and the data volume (Beasley, 2008; Hampson et al., 2008). However, the same problems with cross-talk in blended source imaging plague simultaneous source imaging as well. To some extent, the cross-talk problem is worse in simultaneous source imaging as it is more difficult to create incoherency in the wavefields during imaging (Romero et al., 2000). Ultimately though, we want to image using simultaneous source data because this saves time in imaging and in acquisition.

This paper focuses on the intersection of using simultaneous sources for data acquisition as well as for imaging. We examine simultaneous source shot-encoding schemes that can be used to reduce the amount of cross-talk present in simultaneous source images. To reduce the cross-talk, we develop a theoretical framework that allows us to evaluate the relative amount of cross-talk produced by an encoding scheme. By exploiting the framework, we are able to design an encoding scheme that minimizes the cross-talk in the image. We illustrate our method on both a simple synthetic model and the Sigsbee salt-model. Overall, the primary goal of this paper is to reduce the cost of imaging by an *order of magnitude* by using simultaneous sources in the imaging process. The long-term goal (beyond this research) is to design a simultaneous source acquisition scheme so that both the cost of data acquisition and the cost of imaging are reduced by an order of magnitude.

2 SIMULTANEOUS SOURCE ENCODINGS

An optimal shot-encoding scheme minimizes the amount of cross-talk present in the migrated images after stacking together images from multiple simultaneous source experiments (Romero et al., 2000). There are two issues that must be addressed when using simultaneous encodings. First, spatially close simultaneous sources form partial plane-waves during the migration process, which reduces the spatial resolution of the migration. Second, the wavefields from sources that are spatially distant from one another may interfere during the imaging condition, producing cross-talk noise which reduces the signal-to-noise ratio of the final image. Therefore, simultaneous source encoding schemes must be carefully designed to minimize the negative effects of both of these issues.

2.1 Matrix representation of wave-equation migration

To design simultaneous source encoding schemes, we could start by randomly selecting possible encodings schemes. However, this search spans a space that is infinitely large, and there is no guarantee that one would ever find an optimal encoding. Rather, we find that conventional seismic imaging can be described by a series of matrix operations, which can be expanded to include simultaneous source imaging. The matrix representation allows us to determine the overall suitability of a simultaneous shot-encoding scheme by determining the amount of cross-talk in the migrated image in advance.

Conventional shot-record migration is composed of two steps: wavefield reconstruction and the application of an imaging condition:

$$R(\mathbf{x}) = \sum_t \sum_e W_s^e(\mathbf{x},t) W_r^e(\mathbf{x},t). \tag{4}$$

For each shot gather, the source-and receiver-wavefields are reconstructed separately. Then, the two wavefields are cross-correlated together and summed over time or frequency, depending on the domain, to form a partial image. All of the partial images are then stacked together to form the final image. Mathematically, each source and receiver-wavefield can be thought to be an element in a vector that holds all source- or receiver-wavefields respectively,

$$\mathbf{W}_S = \left[W_S^1, W_S^2, ..., W_S^i, ..., W_S^{N_s}\right], \tag{5}$$

$$\mathbf{W}_R = \left[W_R^1, W_R^2, ..., W_R^i, ..., W_R^{N_s}\right], \tag{6}$$

where W_S and W_R are row vectors, N_s is the number of shot-gathers, composed of the back projected wavefields, W_S^i and W_R^i, respectively. The i^{th} elements of both W_S and W_R correspond to the same physical shot-gather. Thus, conventional seismic imaging is equivalent to the inner product of the two vectors,

$$R = W_S W_R^T, \tag{7}$$

where R is the constructed image, and the multiplication of two elements of the matrix is actually the application of the imaging condition between those wavefields. As indicated earlier, the application of the imaging condition implies a summation over either time or frequency depending on which domain we use for wavefield reconstruction. The summation over elements implies stacking the partial images together, Figure 1(a).

In order to expand this notation to simultaneous source imaging, we introduce an additional matrix, which we call the encoding matrix E. The encoding matrix is an $N_s \times N_e$ matrix, where N_e is the number of experiments and N_s is the number of shots in the survey. Each column in the encoding matrix corresponds to a single simultaneous source experiment, while each row acts as a weight for a particular wavefield. Thus, each column in the encoding matrix weighs all wavefields to determine how to combine them together prior to imaging. The weights may be fractional, positive or negative numbers, or may be binary numbers to indicate which wavefields to use or not use in an experiment. Figure 2(a) depicts a sample encoding matrix

(a) (b)

Figure 1. Conventional seismic imaging comprises wavefield reconstruction and the application of an imaging condition to produce an image for each shot-gather. If each wavefield is considered to be a component of a vector of source $\mathbf{W}_S$ or receiver $\mathbf{W}_R$ wavefields, then the imaging process is equivalent to the dot product of the W_S and W_R vectors (a). In the vector notation, an identity matrix (b) indicates that each source-wavefield is paired only with its corresponding receiver wavefield.

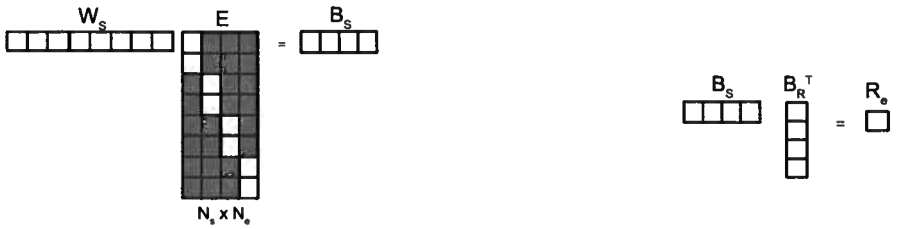

(a) (b)

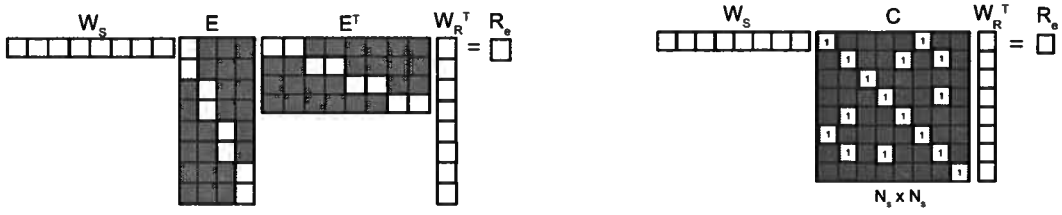

(c) (d)

Figure 2. In contrast to conventional imaging, a simultaneous source encoding (a) uses an encoding matrix E to determine how to combine the source-wavefields together into a smaller vector $\mathbf{B_S}$ of blended wavefields. By analog, simultaneous source imaging (b) is the dot product of the $\mathbf{B_S}$ and $\mathbf{B_R}^T$ vectors. An overview of simultaneous source imaging (c) finds that the process is similar to conventional shot imaging, but with the presence of the encoding matrices. The R_e image is the original image plus additional artifacts from the cross-talk. By multiplying EE^T the cross-talk matrix C (d) is formed. The off-diagonal terms are the cross-talk artifacts that contaminate R_e.

where the weights are binary which selects only some wavefields per experiment.

The encoding matrix reduces the effective number of reconstructed wavefields that are used for imaging as follows:

$$B = WE, then \begin{cases} B_S &= W_S E \\ B_R &= W_R E \end{cases} \tag{8}$$

where WE is the projection of the wavefield vector (i.e W_S or W_R) onto the encoding matrix E, and B is the blended wavefield vector for the source- or receiver-wavefields (i.e. $B_S$or B_R). Therefore, B_S is the $1 \times N_e$ row vector of combined source-wavefields and B_R is an $N_e \times 1$ column vector of combined receiver-wavefields. Because the migration operator is linear, we can perform the combination of the source- and receiver-data, the product of WE, prior to wavefield reconstruction, thus reducing the necessary number of migrations from N_s to N_e. The final simultaneous source image R_e is represented by

$$R_e = B_S B_R^T, \tag{9}$$

and is shown in Figure 2(b). By substituting the expressions for B_S and B_R from equation 8 into equation 9, we obtain

$$R_e = W_S E E^T W_R^T, \tag{10}$$

which is similar to equation 7 and is illustrated in Figure 2(c). We refer to the product EE^T as the cross-talk matrix C, which is square and has dimensions of $N_s \times N_s$. Thus, equation 10 can be written as

$$R_e = W_S C W_R^T. \tag{11}$$

The cross-talk matrix C is similar to the identity I, but with additional off-diagonal terms as shown in Figure 2(d). This is a convenient description because equation 7 can be rewritten to include the identity matrix I to represent the pairing of each source wavefield with its corresponding receiver wavefield as

$$R = W_S I W_R^T. \tag{12}$$

Thus, the C matrix represents the formation of the conventional seismic image (i.e the diagonal terms) plus additional terms in the off-diagonals representing the pairing of wavefields that are not physically related to one another. Subsequently, the off-diagonal components of the C matrix are the cross-talk terms that we generate by using a certain encoding matrix E.

By examining equations 11 and 12, we find that the problem of designing optimal simultaneous source encodings becomes the problem of finding a cross-talk matrix C that is as close to the identity matrix I as possible in order to minimize the cross-talk in the image R_e. Consequently, the process of choosing a simultaneous source encoding becomes one of determining an encoding matrix E such that EE^T has the fewest off-diagonal components, or $EE^T \approx I$. In fact, if an encoding exists such that $EE^T = I$, then we can produce the same image as shot-record migration, at a cost proportional to the number of simultaneous source experiments N_e, instead of N_s. We note that the matrix representation in equation 11 is a more generic expression of the amplitude encoding scheme that Soubaras (2006) previously discussed.

2. 2 Identity matrix decompositions

The question of how to create an optimal simultaneous source encoding then becomes a question of how to decompose the identity matrix into a set of *rectangular* matrices E such that $EE^T \approx I$. In mathematics, a well-known decomposition of the identity matrix into two matrices is through the construction of an orthonormal basis.

For reference, a matrix Q is defined to be an orthonormal basis if $Q^T Q = I$ and $QQ^T = I$. Thus, we can reconstruct the identity matrix I from EE^T, if we use an orthonormal basis for our encoding matrix E. Unfortunately, orthonormal bases are represented by square matrices of the same size as that of the parent matrix or the same size as C which is $N_s \times N_s$ in our case. Therefore, an orthonormal basis encoding matrix provides no cost advantage compared to standard shot-record imaging.

While it may not be possible to directly use an orthonormal basis for an encoding matrix, one option is to truncate the columns of the orthonormal basis to form an encoding matrix that provides a substantial cost reduction. The truncated matrix's rows are no longer linearly independent, and hence no longer completely orthogonal to one another but, they still retain some of their original orthogonality. Soubaras (2006) arrived at a similar idea using a discrete Fourier basis for his experiments. The key in this scheme is to truncate the encoding matrix (orthonormal basis) such that the missing information degrades the image quality only slightly.

A logical choice for an orthonormal basis to use for an encoding matrix is to use the identity matrix itself. To do so, we would truncate columns starting from the end of the identity matrix I to form the encoding matrix E such that it is $N_s \times N_e$. However, truncating the identity matrix to form the encoding matrix removes entire shot-gathers from the reconstructed EE^T matrix which is not optimal because all of the shots should be used for imaging. Therefore only encoding matrices (truncated orthonormal bases) that use all of the shots are viable for consideration as encoding matrices.

2. 3 Data compression

The question then becomes which orthonormal basis should be used for the encoding matrix, and how best to truncate this matrix. This problem is well studied in other fields such as data compression (Rabbani, 1991; Salomon, 2007). In particular, the concept of projecting the wavefields onto an orthonormal basis and truncating the resulting matrix is directly similar to a class of *lossy* data compression algorithms referred to as transform algorithms (Rabbani, 1991; Salomon, 2007). Some common orthonormal bases used in transform compression include: Fourier, wavelet, and the discrete cosine. The key difference between the bases is the level of compression at a certain level of truncation and the quality of the recovered data at a specific level of compression. Along the same lines, Singular Value Decomposition (SVD) can be used to form orthonormal bases to compress data (Eckart & Young, 1936). In all cases, data are *irreversibly* lost once the orthonormal basis is truncated. In the context of the imaging problem, the loss of data

due to compression corresponds to a loss of information in the image, but the compression of the imaging process results in a decrease in the computational cost.

2. 4 Singular value decomposition

Due to data loss, it is impossible to reconstruct the identity matrix from the product of EE^T. An alternate way of approaching the problem is to design the cross-talk matrix C in advance so that it is close to the I matrix, and then decompose the C matrix into two matrices E and E^T. The benefit is that we control how close the approximation C is to the I matrix. In this way, the problem can be reformulated as an inverse problem. The problem of approximating a matrix by decomposition has been extensively studied in mathematics, and the optimal solution is given by the Singular Value Decomposition (SVD) (Eckart & Young, 1936).

In SVD, the matrix A is approximated by,

$$A = U\sigma V^T, \tag{13}$$

where A is an $M \times N$ matrix, U is $M \times N$, σ is an $N \times N$ diagonal matrix corresponding to the singular values, and V^T is $N \times N$. Both the columns of U and V^T form separate orthonormal bases, referred to as the left-singular and right-singular vectors respectively. In the special case where A is a real-valued, square, and symmetric matrix, which is the case for all cross-talk matrices C, then $U = V$ and equation 13 becomes

$$C = U\sigma U^T. \tag{14}$$

This expression is similar to $C = EE^T$ except that in equation 14 U is a square matrix and that σ is present. Thus, we are able to conclude that $E \approx U_{tc}$, where U_{tc} is the truncated matrix U. In order to formalize the relationship between the encoding matrix E and the singular vectors U, we truncate the columns of U (singular vectors) according to SVD theory, which indicates that we should keep the first N_e columns corresponding to the largest singular values. Additionally, we split the singular value matrix σ by taking the square root of the matrix and multiplying it to U_{tc}. Therefore, E and E^T are respectively:

$$E = U_{tc}\sqrt{\sigma_{tc}}, \tag{15}$$

$$E^T = \sqrt{\sigma^{tc}}U_{tc}^T. \tag{16}$$

We refer to the constructed encoding matrix E as the Truncated Singular Vector (TSV) encoding. For SVD, there exists an optimal truncation level for which most of the information in the decomposed matrix is preserved. This point can be identified using the singular values. Large singular values indicate which singular vectors contribute most to the reconstruction of the matrix C. Conversely, small singular values (close to zero) indicate that a singular vector does not have a significant contribution to the reconstruction of C. We note, that the product of EE^T is an *approximation* to C, as a result of truncating U, which in turn is an *approximation* of the identity matrix I, by design. Also, it should be noted that the E matrix from the SVD uses *all* sources, for each simultaneous source experiment.

2. 5 Constructing the cross-talk matrix

The construction of the C matrix to approximate I using SVD is of paramount importance to the quality of the final image R_e. Since the C matrix should be as close to the identity matrix as possible, there are at least a few clear choices. The first is to band the diagonal in the C matrix, such that there are upper and lower diagonals. This is equivalent to applying a boxcar filter to the I matrix, as in Figure 3(a). For the boxcar filter, the full window width is defined as $a = 2\sqrt{3}\sigma$, where a is the window width and σ is the standard deviation. Another option is to use a Gaussian filter, to gradually taper the values away from the diagonal in the approximating matrix as in Figure 3(b). The Gaussian filter is defined as the normal distribution with a mean μ and a standard deviation σ. In both cases, the additional components along the diagonal represent the construction of small plane-waves because this is equivalent to combining the images for spatially closest sources into the output image, which results in loss of spatial resolution. If the product of EE^T is close to the I matrix though, the loss in spatial resolution can be negligible.

There are many other options for possible C matrices, and this is by no means a comprehensive discussion. Our examples demonstrate how SVD can be used to approximate the Gaussian and boxcar diagonal matrices, and to reconstruct images that are very close to the image obtained by shot-record migration. We leave for future research the problem of determining the optimal approximation to the identity matrix.

3 EXAMPLES

We conduct a series of examples to illustrate the ability of the SVD to construct encodings for simultaneous source imaging on two models. The first model consists of point diffractors, which illustrates that our encoding schemes do not suffer from a significant loss of spatial resolution. The second model is the Sigsbee2A salt model which demonstrates the ability of the SVD to handle complex velocity models while maintaining spatial resolution. For each model, the SVD is performed for both the boxcar and Gaussian approximations to the identity matrix, Figures 3(a) and 3(b). The orthonormal matrix U is truncated to form the encoding matrix E based on the chosen number of experiments to perform N_e. The shot-gathers and source-wavelets are combined and weighted linearly according to the encoding matrix E prior to wavefield reconstruction. The combined data are then reconstructed using downward continuation, and the imaging condition is applied, which creates a partial image for an experiment. All of the partial images are stacked to form the final image. For each experiment, the theoretical speed up is given by the ratio:

$$K = \frac{N_s}{N_e} \tag{17}$$

where N_s is the number of sources available, and N_e is the number of experiments using for imaging. The ratio K represents how many times faster the encoded migration is compared to conventional shot record migration.

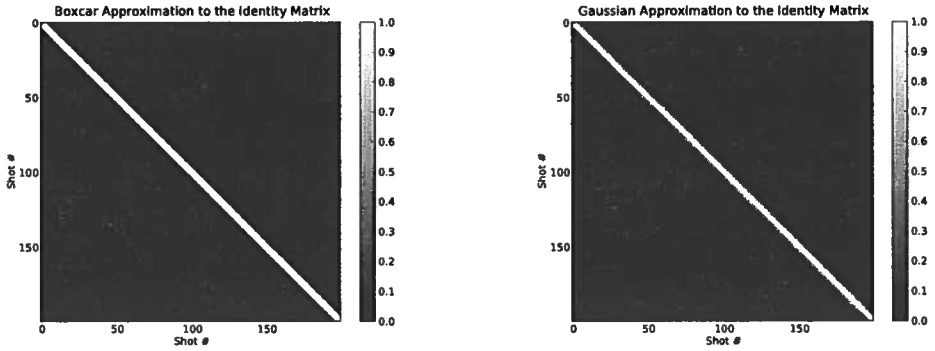

(a) (b)

Figure 3. The boxcar approximation of the identity matrix (b) with a boxcar window width a of 7, corresponding to a standard deviation σ of 2. The Gaussian approximation of the identity matrix (c) with $\mu = 0, \sigma = 2$. The only difference between (a) and (b) is the distribution (i.e. boxcar or Gaussian) used to band the identity matrix.

For each example, we show the encoding matrix E^T, the cross-talk matrix C, and a measure of relative amplitude. The measure of relative amplitude is given by

$$A_s = \sum_c |E_{s,c}|, \tag{18}$$

where A_s is the relative amplitude, c is the column index in the encoding matrix, s is the shot index in the encoding matrix, and E is the encoding matrix. The relative amplitude A_s is then normalized by the maximum value and measures the total effective contribution from each shot based on the weights in the encoding matrix. Ideally, this measure would be 1.0 for each shot, indicating that each shot's total contribution across all encodings is the same as its contribution for conventional shot-record migration. A less ideal condition is that all of the shots have contributions that are approximately 1.0. The relative contribution for each shot can exceed 1.0 because the singular values weight these terms. In this case, the amplitude of the conventional image can be reconstructed by performing a global rescaling. If the amplitude A_s varies as a function of shot, then the simultaneous source image contains spatial amplitude variability, which is a result of the simultaneous source encoding. The spatial variability in the amplitude causes certain portions of the image to be washed out and amplifies other portions of the image.

All the images are compared against one another and are clipped to the same relative range. This allows a direct comparison of amplitudes in the images, even though the amplitudes are not the same for the simultaneous experiments and for the conventional images. By doing so, we assume that the amplitudes in the simultaneous source experiments are erroneous by a constant scaling factor.

3. 1 Model with uniformly distributed point scatterers

The simple model is composed of a constant velocity, isotropic medium with 20 evenly spaced point diffractors arranged in a grid. We simulate 200 shots with receivers distributed over the full aperture of the model. Thus, there is no computational gain by decomposing the migration domain to represent limited aperture for each individual shot. For each simultaneous source experiment, the source wavelets and data are combined together into synthetic source and receiver datasets. The combined source- and receiver-wavefields are reconstructed using downward continuation. The standard cross-correlation imaging condition is applied to the reconstructed wavefields for each experiment to produce a partial image. The simultaneous source partial images are stacked together to form the final image. A conventional shot-record migration using downward continuation for all 200 shots is presented independently in Figure 4. This image serves as the benchmark for the simultaneous source images.

3. 1.1 Boxcar Approximation

The boxcar approximation to the identity matrix uses a window width a of 7, which corresponds to a standard deviation σ of 2. The first boxcar experiment involves 10 simultaneous source experiments which provides a speed-up K of 20. The singular values for the decomposition are shown in Figure 5. For reference, an interesting number of singular values to truncate is 50, where there is an abrupt change in the singular values. We truncate below this point because we are primarily interested in reducing the cost of imaging. Figures 6(a) and 6(b) shows the construction of the encoding matrix and the reconstruction of the C matrix using SVD for the boxcar approximation matrix for 10 simultaneous source experiments respectively. Figure 6(c) shows the amplitudes as a function of shot, which are spatially variable for 10 experiments. The encoding matrix, cross-talk matrix and amplitude variation for 20 experiments is shown in Figures 7(a), 7(b) and 7(c). Additionally, Figures 8(a), 8(b), and 8(c) show the encoding matrix E, the cross-talk matrix C and the amplitudes for 50 experiments.

The final image for 10 encodings using the boxcar approximation is shown in Figure 9(a). Figure 9(b) shows the

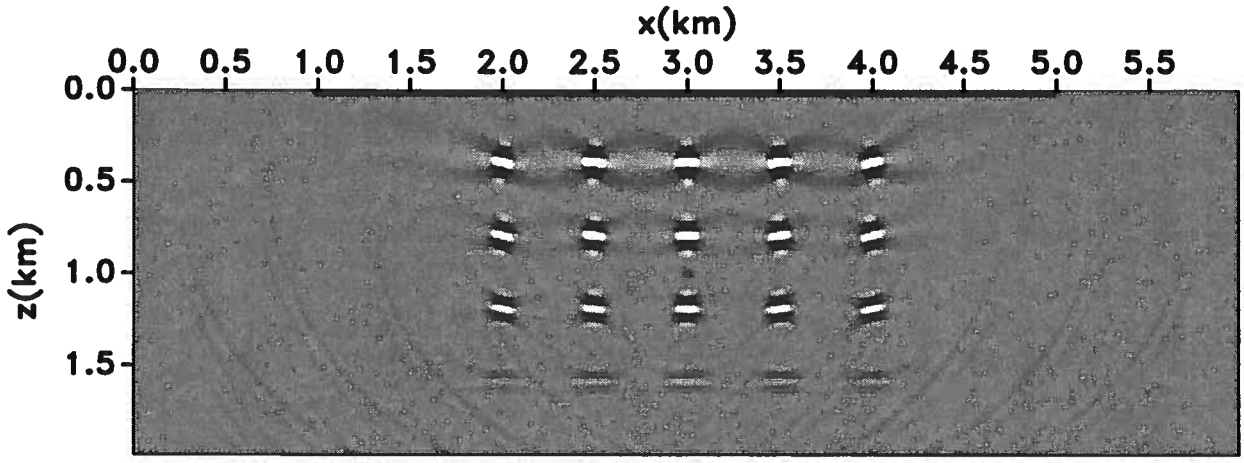

Figure 4. The stacked image for the point scatterer model using conventional shot-record migration for 200 shots.

image for 20 experiments, which results in a ratio K of 10. Figure 9(c) shows the final image for 50 experiments, which has a speed-up K of 4. Clearly, as the number of simultaneous experiments increases, the quality of the image increases. In the limit, the imaging would approximate the image for shot-record-migration, since the reconstructed cross-talk matrix approaches C which is close to the identity matrix.

3. 1.2 Gaussian Approximation

Another set of experiments demonstrates how the Gaussian approximation to the identity matrix I affects the final image. For the Gaussian approximation, the distribution is created with a mean $\mu = 0$ and standard deviation of $\sigma = 2$. The singular values in Figure 10 have smoother variation when compared to the boxcar approximation as in Figure 5 because the Gaussian approximation tapers off slowly instead of having an abrupt change in the cross-talk matrix. This implies that there are not abrupt changes in the simultaneous source image quality by including certain singular values or excluding some. Also, the singular values taper to zero rather quickly, indicating that the encodings corresponding to the zero singular values do not contribute to the image. Thus, the best possible image for the Gaussian approximation can be obtained by using all the singular values that are not zero or approximately the first 70 singular values. Figures 11(a), 11(b) and 11(c) show the encoding matrix, the cross-talk matrix and the amplitudes as a function of space for 10 experiments. The encoding matrix, cross-talk matrix and amplitude variation for 20 experiments are shown in Figures 12(a), 12(b) and 12(c). For the Gaussian approximation, we use truncate at 60 singular values because this seems to correspond to most of the information. Figures 13(a), 13(b) and 13(c) show the encoding matrix, cross-talk matrix and the amplitudes for 60 experiments ($K \approx 3$). The amplitudes are uniform across all shots, which indicates that the relative amplitude is not as spatially variable as for the other examples. Figure 14(a) shows the final image for 10 experiments, which has a speed-up factor K of 20. The image for 20 experiments has a K of 10, Figure 14(b). Figure 14(c) shows the final image for 60 experiments. This image is significantly closer to the target image than the images obtained from the other experiments.

3. 2 Sigsbee2A model

A similar group of experiments is conducted for the Sigsbee2A salt model. In this case, we create a new Sigsbee2A survey using 3200 shots to represent a shot at every possible shot location. Each shot is forward modelled using a finite-difference acoustic algorithm for the *full* aperture available in the Sigsbee model. In other words, the receivers are at every possible grid location on the surface. As in the simple model, there is no computational gain by decomposing the migration domain based on migration aperture, because the shots are simulated with receivers everywhere on the surface. For reference, the migration of all 3200 shots via conventional shot-record migration is shown in Figure 15. We construct the singular values for both the boxcar and Gaussian approximations, Figure 16(a) and 16(b). We evaluate only the Gaussian approximation to the identity matrix for the Sigsbee model because the singular values for the Gaussian approximation quickly taper to zero.

Figure 17(a) shows the image for 10 experiments using the Gaussian approximation. Theoretically, the image in Figure 17(a) is created *320 times* faster than the conventional image, but there is additional overhead in terms of disk usage that slows down the process. For comparison, Figure 17(b) shows the result from the Gaussian approximation for 30 experiments. The image quality is substantially improved for the 30 experiment image, compared to the 10 experiment image. For example, the 30 experiment image is less noisy in the salt body than the 10 experiment image. Additionally, the 30 experiment image is substantially clearer underneath the salt body ($x = 15.0km$, $4.5km < z < 8.0km$). Figure 17(c) shows the result from a Gaussian approximation using 100 experiments.

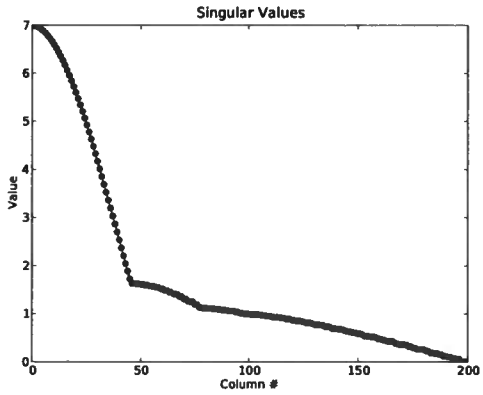

Figure 5. The singular values for the boxcar approximation to the identity matrix for the model with point scatterers. There is an abrupt change in slope of the singular values near $N_e = 50$, which seems to be an optimal point to truncate the singular values at. The singular values gradually taper to zero, indicating that all singular values contribute to the image, although the smaller singular values contribute less than large ones.

This image is created 32× faster than that of the conventional migration. Figure 17(c) is of much better quality than both of the other experiments, and is visually close to Figure 15.

4 DISCUSSION

Our theoretical model has allowed the creation of an optimal simultaneous source encoding scheme that we refer to as the Truncated Singular Vector encoding (TSV). Our experiments confirm that the TSV encoding scheme produces nearly optimal migrated images, as the images are close to the conventionally migrated images with $C_e^t \ll C_s^t$. The main difference between the conventional image and the encoded image is that the amplitude of the encoded image changes spatially depending on the number of encodings used for imaging. Furthermore, the TSV encoding is able to reduce the cost of seismic imaging, by at least an order of magnitude. For the Sigsbee data set, the cost of seismic imaging is reduced by up to *100 times* for 3200 shots. We note that 3200 shots is excessive sampling for imaging Sigsbee and that a good quality image can be obtained using only 500 shots. Regardless, the TSV encoding is equally valid for 3200 shots or 500 shots, although the actual speed-up factor might be different.

In practice, some of the relative speed advantage K gained by using the TSV encoding is offset by the requirement of additional data input and output to produce the encoded experiments. If the combination procedure is efficiently spread over multiple machines with many disks, then this additional cost is negligible. However, the reduced cost comes at the expense of cross-talk noise and a spatial variation of the amplitudes in the image. The spatial amplitude variation is the result of an uneven weighting of shot-gathers by the encoding matrix. A possible way to remove the amplitude variation is to design a cross-talk matrix C that weighs the wavefields to even-out the amplitude effects of the encoding scheme. Presently, both the noise and amplitude variation can be addressed by increasing the number of experiments used in the production of the final image. If all possible experiments are used, then the TSV scheme approximates conventional shot-record migration. The difference between the best possible image for TSV and conventional migration is determined by the choice of the cross-talk matrix C.

One of the outstanding questions is whether or not our approximations to the identity matrix produce the best images via TSV. We chose to examine only the Gaussian and a boxcar taper approximations because they seem to be two obvious candidates. Other interesting candidates include other tapered functions such as a sinc or double-sided, decaying exponential. Further, we have not yet explored how the parameters, such as standard deviation, that control the size or length of the window affect the results. We suspect that overall these parameters control how much spatial resolution is lost during the encoding process because they control how many near wavefields are combined together to form an image. Consequently, these parameters probably influence the singular values and thus are related to the image quality at certain levels of truncation.

More research is needed on how to quantify the amount of noise that is added to the image, and on a way to quantify how much of the image is lost based on the number of experiments. By examining the quality of the image as a function of the number of experiments, one may be able to find an optimum number of simultaneous source experiments to conduct. Right now, we base the number of experiments to use on the singular values.

Additionally, we conjecture that the simultaneous source encoding framework that we have developed is independent of dimensionality, i.e. 2-D or 3-D, because the matrix representation deals solely with reconstructed wavefields based on the physical relation of shots in a large array. Therefore, the simultaneous source encoding scheme is likely applicable to three-dimensional data, as long as the spatial relationship between the sources and the encoding matrix E is maintained.

Lastly, TSV encoding is not dependent on any of the following: survey parameters, geologic structure, the velocity

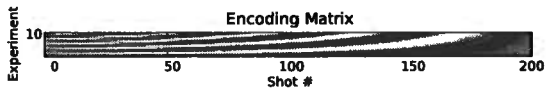

(a)

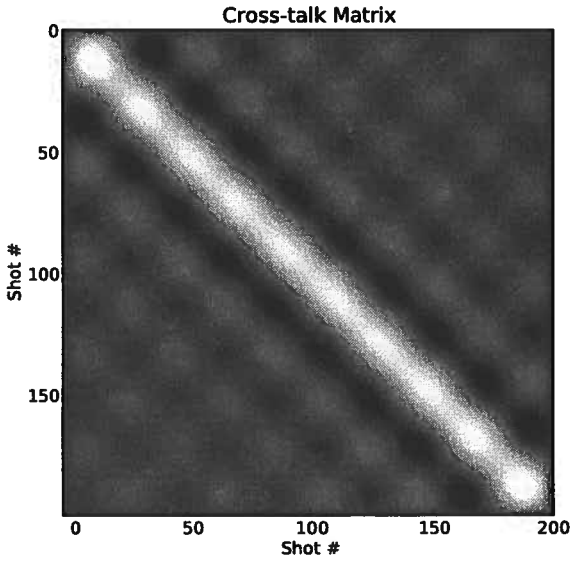

(b)

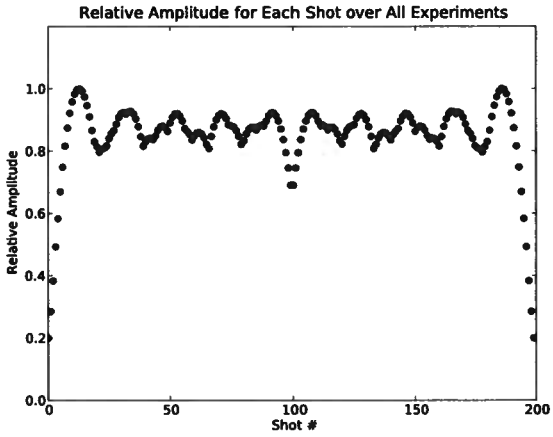

(c)

Figure 6. The transpose of the encoding matrix (a) constructed by truncating the singular vectors for a boxcar approximation for 10 simultaneous source experiments. Note the oscillatory nature of the weights in the encoding matrix. The reconstructed C matrix (b) obtained from EE^T. For both (a) and (b), white values are (1) and black values are (-1). The relative amplitudes (c) across all 10 experiments for each shot-gather. Not all shots contribute to the image equally, which means there is a spatial variation in the amplitude caused by the encoding.

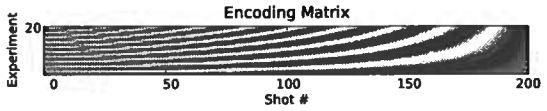

(a)

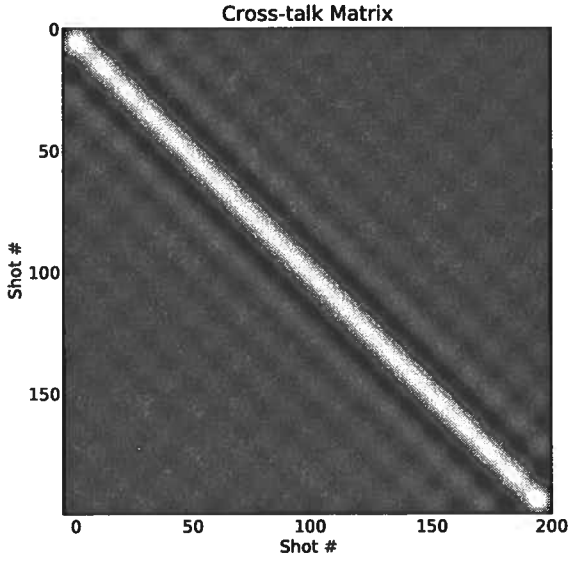

(b)

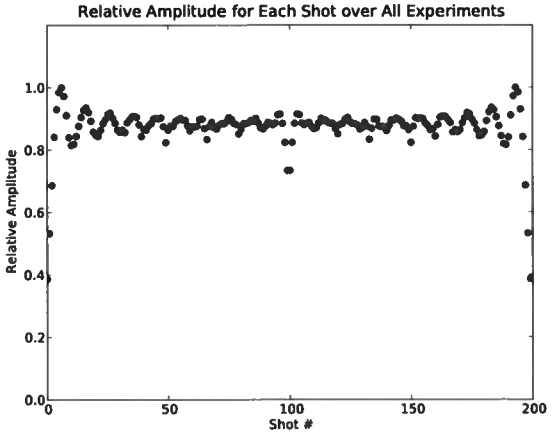

(c)

Figure 7. The transpose of the encoding matrix (a) constructed by truncating the singular vectors for a boxcar approximation. The additional experiments are more oscillatory than those in Figure 6(a). For both (a) and (b), white values are (1) and black values are (-1). There are 20 simultaneous source experiments. The reconstructed C matrix (b), obtained by multiplying EE^T. The overall amplitudes (c) across all 20 experiments for each shot-gather show less variation as a function of shot-gather than those in Figure 6(c).

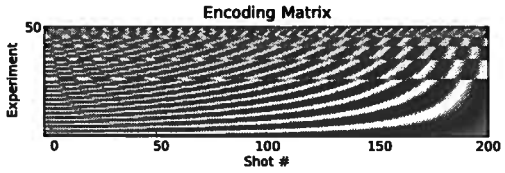

(a)

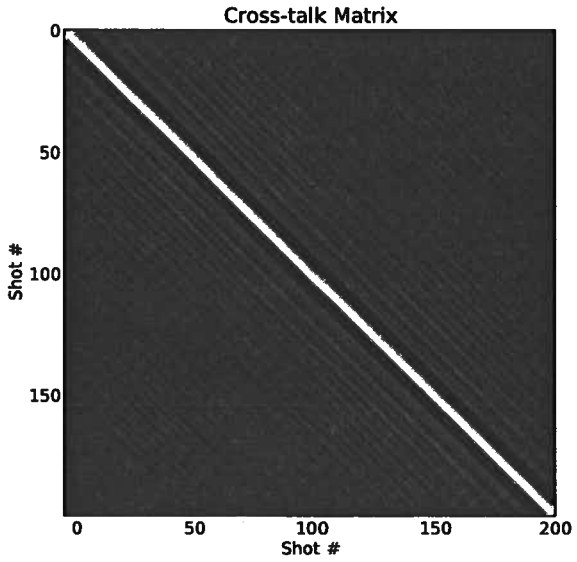

(b)

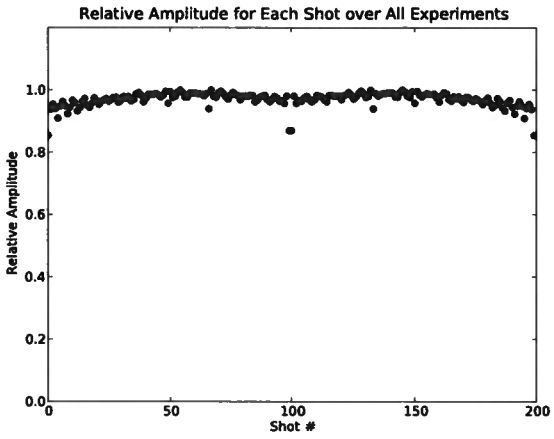

(c)

Figure 8. The transpose of the encoding matrix (a) constructed by truncating the singular vectors for a boxcar approximation. There are 50 simultaneous source experiments. The reconstructed C matrix (b), obtained by multiplying EE^T. For both (a) and (b), white values are (1) and black values are (-1). The overall amplitudes (c) across all 50 experiments for each shot-gather show that the average value of the amplitude is more closely grouped than in Figure 6(c) or Figure 7(c) which indicates that the amplitudes can be globally rescaled.

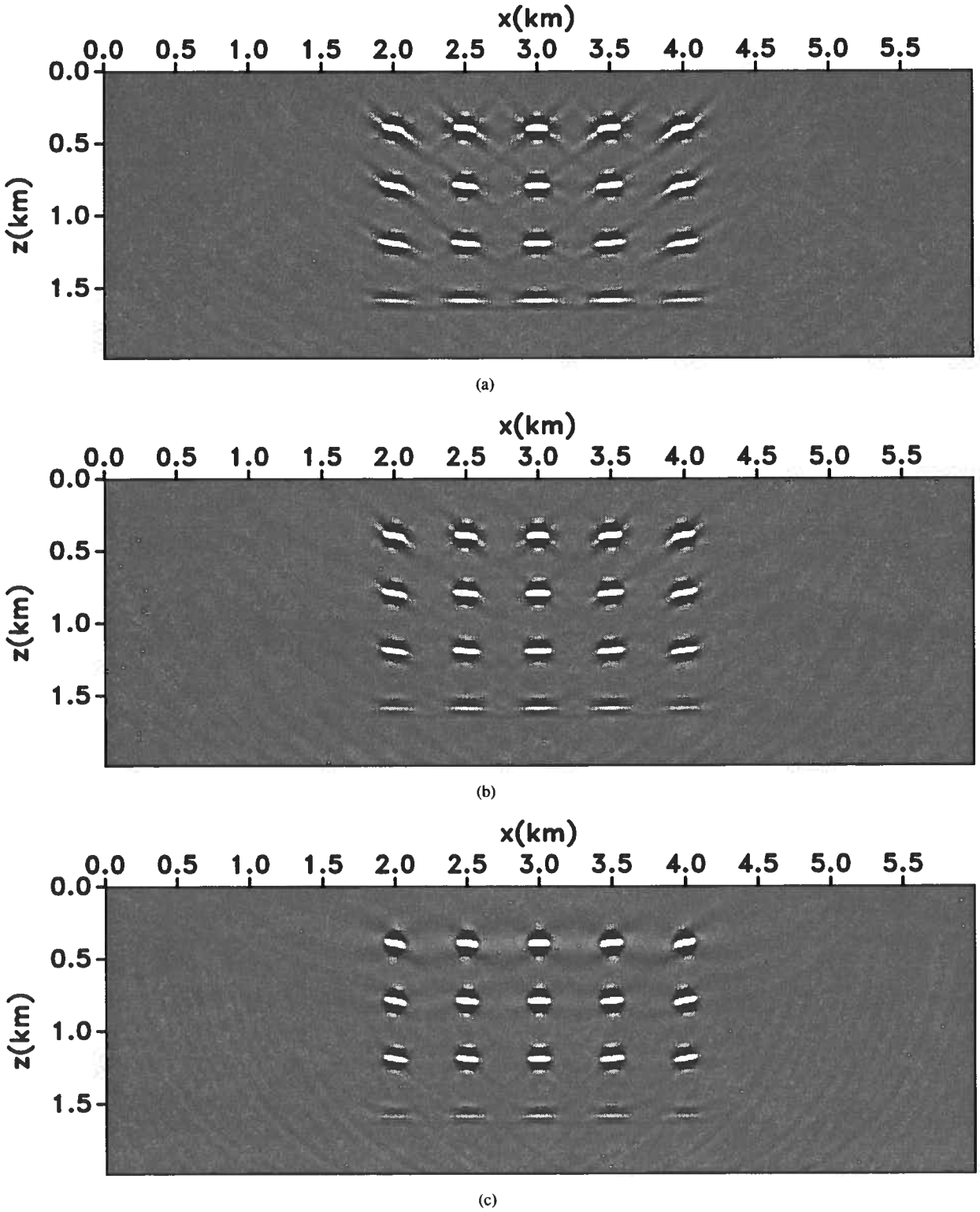

Figure 9. The final stacked images for 10 (a), 20 (b) and 50 (c) experiments using the boxcar approximation. The image quality increases as the number of experiments increases.

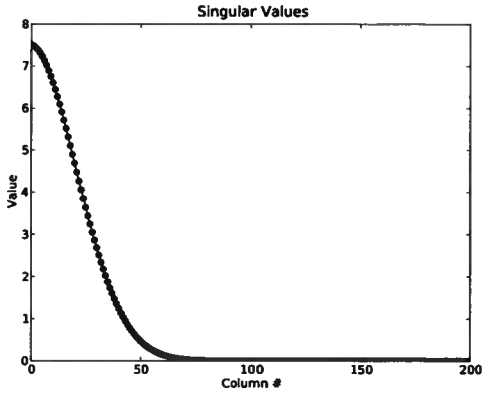

Figure 10. The singular values for the Gaussian approximation to the identity matrix for the model with point scatterers. The Gaussian distribution has a mean $\mu = 0$ and a standard deviation $\sigma = 2$.

model or migration type. The encoding scheme only depends on the number of experiments used to construct the final image, and the approximation to the identity matrix to be decomposed. Therefore, if an optimal combination of the two parameters can be found, then the cost of seismic imaging may be reduced even further.

5 CONCLUSIONS

We develop a theoretical framework that adequately explains both conventional seismic imaging and simultaneous source imaging. The framework allows us to reformulate the problem of simultaneous source imaging in the context of matrix operations and leads to the use of singular value decomposition to construct optimal encoding matrices. This allows us to identify simultaneous source encoding schemes, such as Truncated Singular Vector (TSV), that produce migrated images at much lower cost than conventional shot-record migration. The encoded migrations trade reduced computational cost with increased noise in the image, spatial amplitude variation, and loss of spatial resolution. We demonstrate the validity of these encodings through numerical experiments on both a simple model and on the geologically complex Sigsbee2A salt model. In both cases, the Truncated Singular Vector encoding scheme reduces the cost of imaging by at least an order of magnitude while restricting cross-talk noise and maintaining spatial resolution.

6 ACKNOWLEDGMENTS

We would like to thank Francesco Perrone for many enlightening conversations on this subject, as well as technical support. The reproducible numeric examples in this paper use the Madagascar open-source software package freely available from http://www.reproducibility.org. This research was supported in part by the Golden Energy Computing Organization at the Colorado School of Mines using resources acquired with financial assistance from the National Science Foundation and the National Renewable Energy Laboratory.

REFERENCES

Akerberg, P., Hampson, G., Rickett, J., Martin, H., and Cole, J., 2008, Simultaneous source separation by sparse radon transform: SEG Technical Program Expanded Abstracts, **27**, no. 1, 2801.

Beasley, C. J., 2008, A new look at marine simultaneous sources: The Leading Edge, **27**, no. 7, 914.

Berkhout, A. J. G., Blacquiere, G., and Verschuur, E., 2008, From simultaneous shooting to blended acquisition: SEG Technical Program Expanded Abstracts, **27**, no. 1, 2831.

Berkhout, A., Verschuur, D., and Blacquiere, G., 2009, Seismic imaging with incoherent wavefields: Seismic imaging with incoherent wavefields:, SEG Technical Program Expanded Abstracts, 2894–2898.

Blacquiere, G., Berkhout, G., and Verschuur, E., 2009, Survey design for blended acquisition: Survey design for blended acquisition:, SEG Technical Program Expanded Abstracts, 56–60.

Eckart, C., and Young, G., 1936, The approximation of one matrix by another of lower rank: Psychometrika, **1**, no. 3, 211–218.

Hampson, G., Stefani, J., and Herkenhoff, F., 2008, Acquisition using simultaneous sources: The Leading Edge, **27**, no. 7, 918.

Huo, S., Luo, Y., and Kelamis, P., 2009, Simultaneous sources separation via multi-directional vector-median filter: Simultaneous sources separation via multi-directional vector-median filter:, SEG Technical Program Expanded Abstracts, 31–35.

Kim, Y., Gruzinov, I., Guo, M., and Sen, S., 2009, Source separation of simultaneous source OBC data: Source separation of simultaneous source OBC data:, SEG Technical Program Expanded Abstracts, 51–55.

Liu, F., 1999, Plane wave source composition: An accurate

(a)

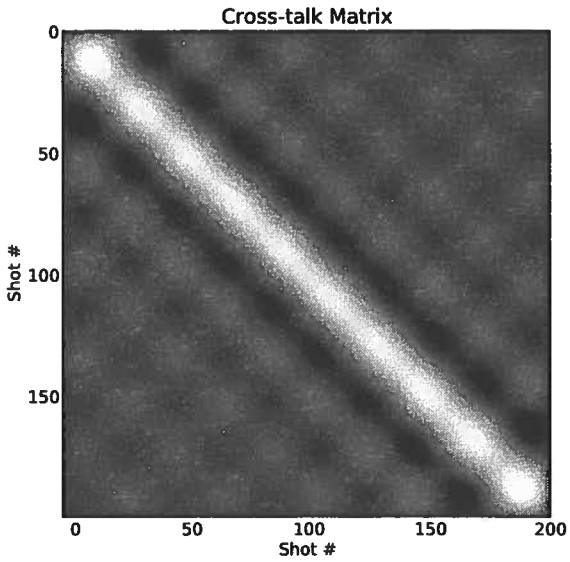

(b)

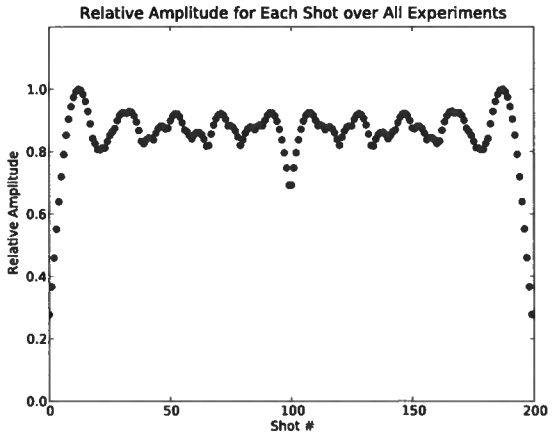

(c)

Figure 11. The transpose of the encoding matrix (a) constructed by truncating the singular vectors for a Gaussian approximation. There are 10 simultaneous source experiments, which means the K is 20. The reconstructed C matrix (b), obtained by multiplying EE^T. In (a) and (b), white values are (+1) and black values are (-1). The overall amplitudes (c) across all 10 experiments for each shot-gather. There is an amplitude variation as a function of shot, so the amplitudes in the final image are spatially variable due to the encoding.

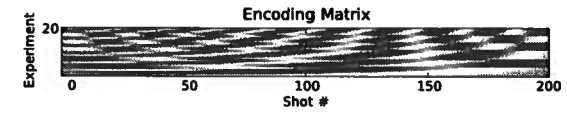

(a)

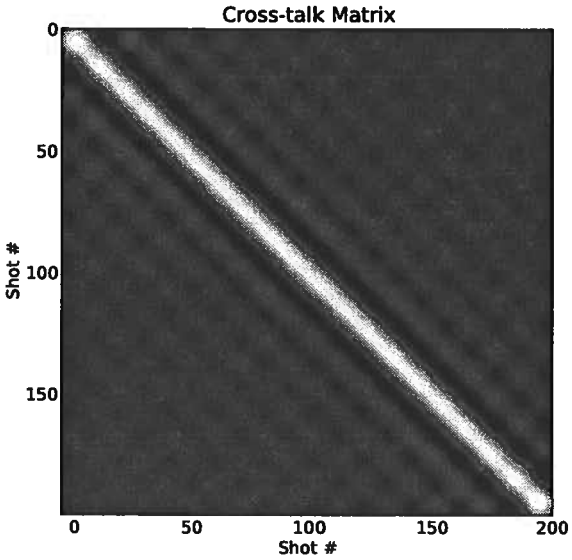

(b)

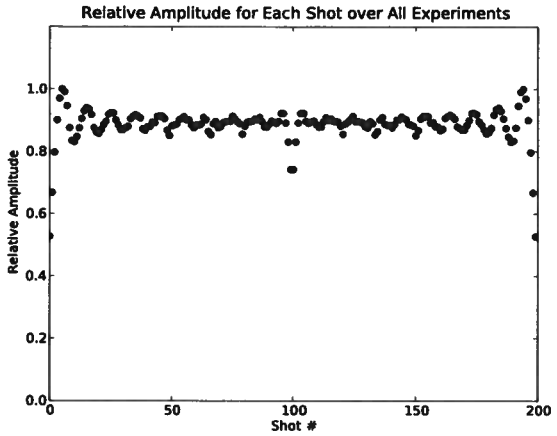

(c)

Figure 12. The transpose of the encoding matrix (a) constructed by truncating the singular vectors for a Gaussian approximation. There are 20 simultaneous source experiments or $K = 10$. The reconstructed C matrix (b), obtained by multiplying EE^T. In (a) and (b), white values are (+1) and black values are (-1). The overall amplitudes (c) across all 20 experiments for each shot-gather. The amplitude variation as a function of shot is identical to the variation for the boxcar, Figure 7(c).

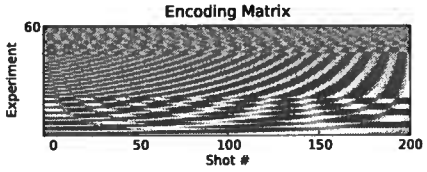

(a)

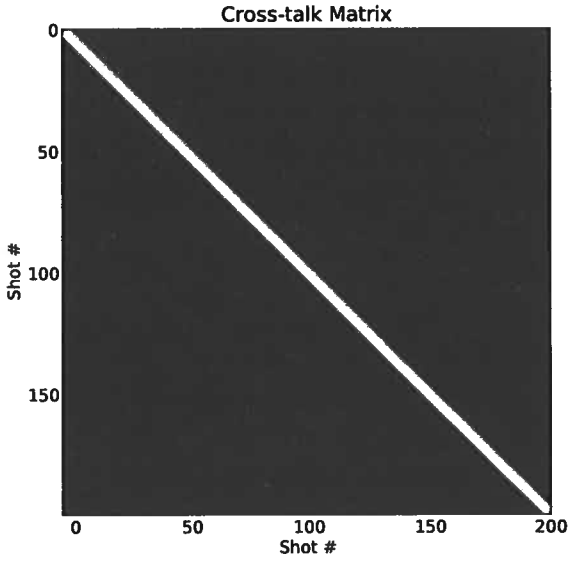

(b)

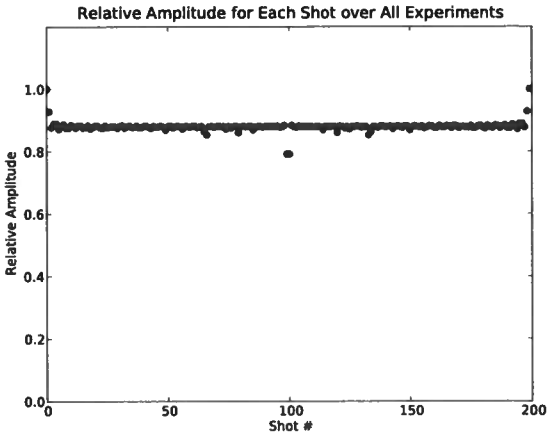

(c)

Figure 13. The transpose of the encoding matrix (a) constructed by truncating the singular vectors for a Gaussian approximation. There are 60 simultaneous source experiments. The reconstructed C matrix, obtained by multiplying EE^T (b). In (a) and (b), white values are (+1) and black values are (-1). The overall amplitudes (c) across all 60 experiments for each shot-gather. The spatial amplitude variation is more consistent in this case, which indicates that the amplitudes can be globally rescaled to match the conventional image's amplitudes.

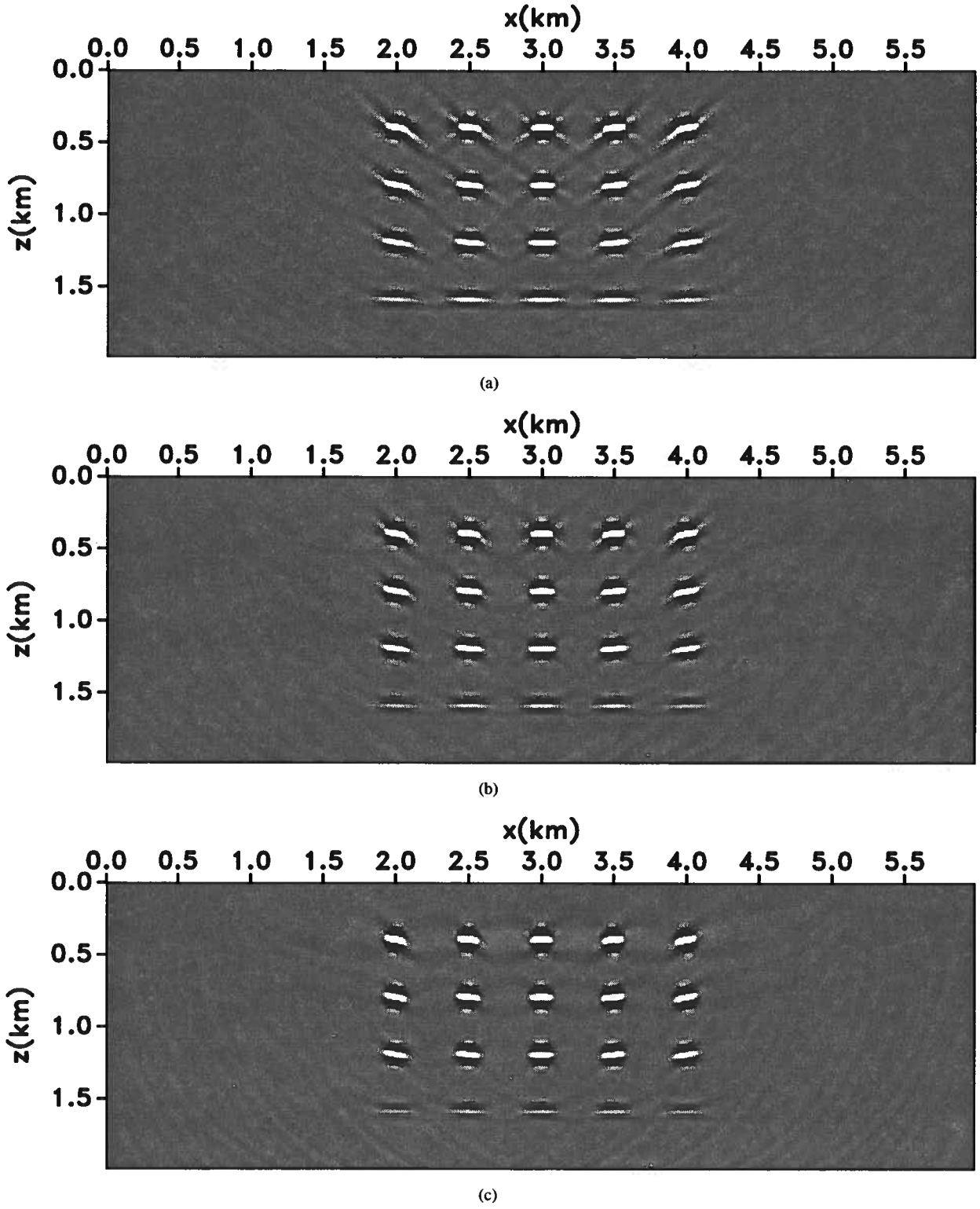

Figure 14. The final stacked image (a) for 10 experiments. The stacked image (b) for 20 experiments and the stacked image (c) for 60 experiments. All experiments used the Gaussian filter as the cross-talk C matrix. The image quality increases as the number of experiments increases.

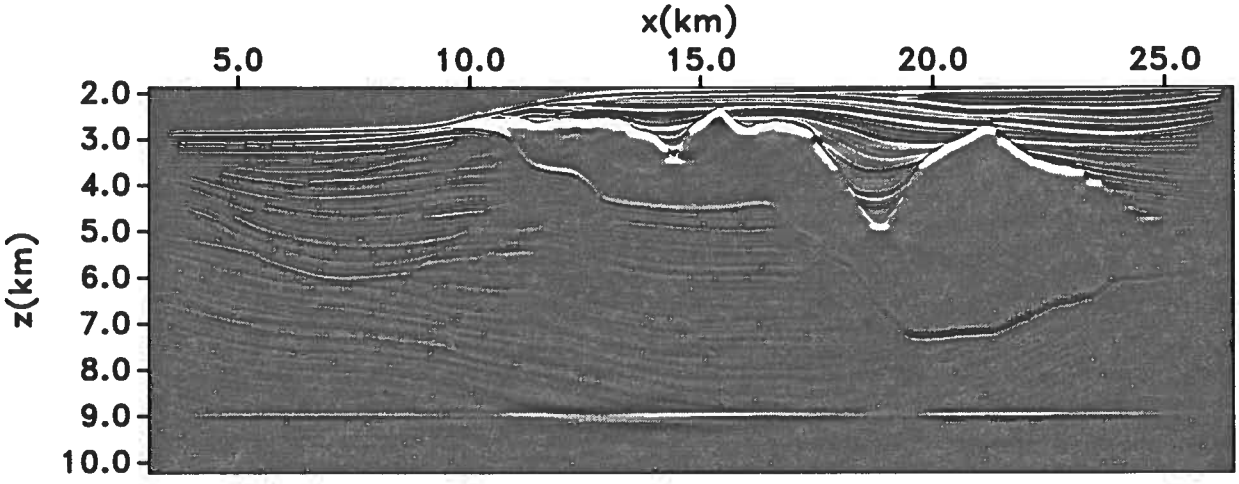

Figure 15. The stacked image of Sigsbee using conventional shot-record migration for all 3200 shots.

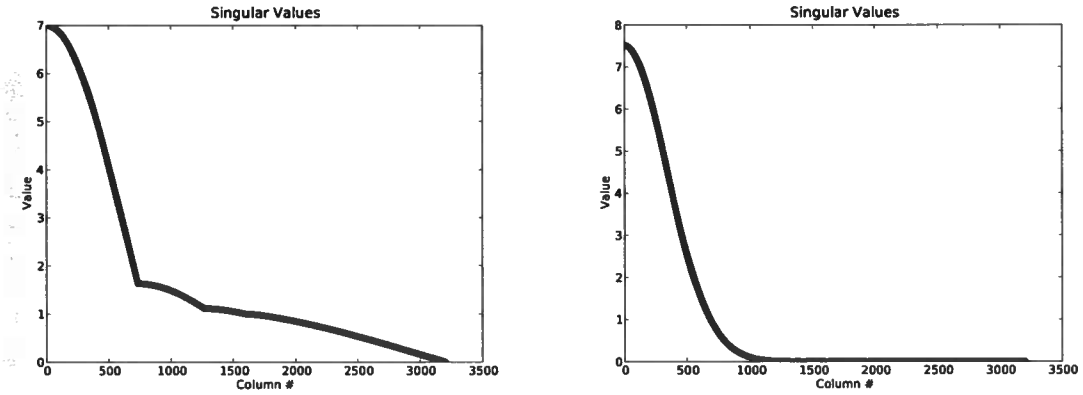

(a) (b)

Figure 16. The singular values for the Sigsbee survey using the boxcar approximation (a) and the Gaussian approximation (b).

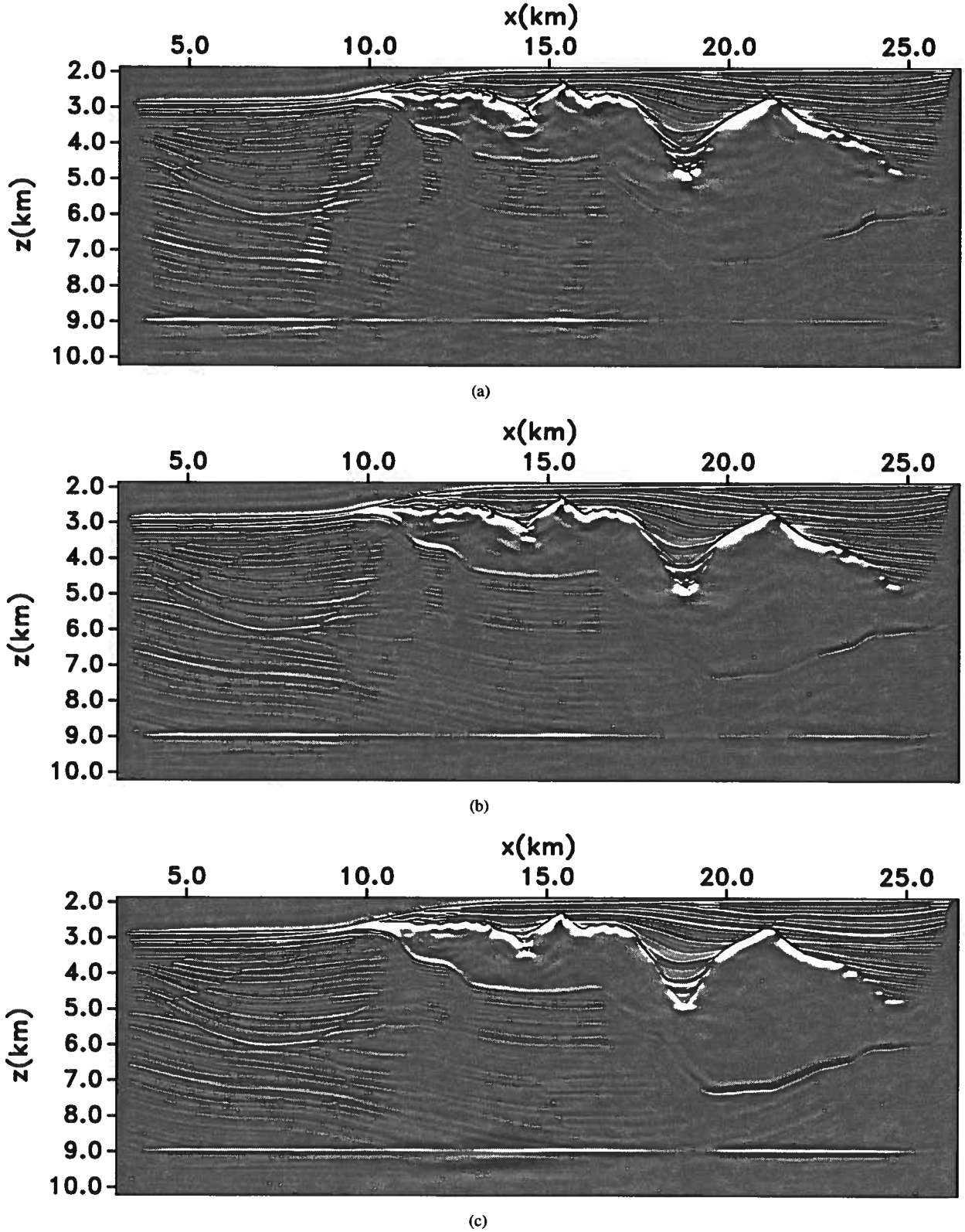

Figure 17. The image of Sigsbee using the Gaussian approximation for 10 experiments (a), 30 experiments (b), and 100 experiments (c). While (a) and (b) cost significantly less than (c), the image quality in (c) is much better than that of the images shown in (a) and (b) when compared against Figure 15.

phase encoding scheme for prestack migration: SEG Technical Program Expanded Abstracts, **21**, no. 1, 1156.

Morton, S. A., 1999, Fastershot-record depth migrations using phase encoding: SEG Technical Program Expanded Abstracts, **17**, no. 1, 1131.

Perrone, F., and Sava, P., 2009, Comparison of shot encoding functions for reverse-time migration: Comparison of shot encoding functions for reverse-time migration:, SEG Technical Program Expanded Abstracts, 2980–2984.

Rabbani, M., 1991, Digital image compression techniques: , Spie Optical Engineering Press, Bellingham Wash. USA.

Romero, L. A., Ghiglia, D. C., Ober, C. C., and Morton, S. A., 2000, Phase encoding of shot records in prestack migration: Geophysics, **65**, no. 2, 426.

Salomon, D., 2007, Data compression : the complete reference: , Springer, London, 4th ed. edition.

Soubaras, R., 2006, Modulated-shot migration: SEG Technical Program Expanded Abstracts, **25**, no. 1, 2430.

Spitz, S., Hampson, G., and Pica, A., 2008, Simultaneous source separation: A prediction-subtraction approach: SEG Technical Program Expanded Abstracts, **27**, no. 1, 2811.

Ting, C., and Zhao, W., 2009, A simulated wide azimuth simultaneous shooting experiment: A simulated wide azimuth simultaneous shooting experiment:, SEG Technical Program Expanded Abstracts, 76–80.

Womack, J. E., 1990, Encoding techniques for multiple source point seismic data acquisition: Geophysics, **55**, no. 10, 1389.

Zhang, Y., Sun, J., and Gray, S., 2007, Reverse-time migration: Amplitude and implementation issues: SEG Technical Program Expanded Abstracts, **26**, no. 1, 2145.

Wave-equation migration with dithered plane waves

Francesco Perrone & Paul Sava
Center for Wave Phenmena, Colorado School of Mines

ABSTRACT
Wave-equation based shot-record migration provides accurate images but is computationally expensive because every shot must be migrated separately. Shot-encoding migration, such as random shot-encoding or plane-wave migration, aims to reduce the computational cost of the imaging process by combining the original data into synthetic experiments. Random shot-encoding migration and plane-wave migration have different and complementary features: the first recovers the full spatial bandwidth of the image but introduces strong artifacts, which are due to the interference between different shot wavefields; the second provides an image with limited spatial detail but free of crosstalk noise. We design a hybrid scheme that combines linear and random shot-encoding in order to counterbalance the drawbacks and merge the advantages of these two techniques. We advocate mixed shot-encoding migration through dithering of plane waves, which increases the spatial bandwidth relative to conventional plane-wave migration and reduces crosstalk noise relative to random shot-encoding migration. Migration with dithered plane waves operates as a hybrid encoding scheme in-between the end members represented by plane-wave migration and random shot-encoding. The combination of complementary encodings is effective in reducing the trade-off between spatial resolution and crosstalk noise; nonetheless, the noise cannot be completely removed. We test two denoising algorithms for eliminating the residual noise in the encoded image. We conclude that because crosstalk noise has spectral properties similar to the signal, denoising techniques in the image domain are less effective than our mixed encoding scheme. In particular in poorly illuminated areas, better encoding is a more effective solution for controlling crosstalk and recovering a correct image. Migration with dithered plane waves has several advantages: every synthetic experiment images in a larger aperture with respect to shot-record migration; crosstalk noise is controlled relative to random shot-encoding; and higher spatial resolution is achievable with regard to linear shot-encoding. Computational cost is also reduced relative to both random and linear shot-encoding migration since fewer synthetic experiments are necessary for obtaining high signal-to-noise ratio and high spatial resolution in the final image.

Key words: imaging, migration, shot-encoding

1 INTRODUCTION

In conventional seismic depth-imaging, data are acquired by means of independent experiments that are then separately imaged. In wave-equation migration, the imaging procedure consists of two steps: wavefield extrapolation, from data recorded on the surface to all locations in the subsurface, and the application of an imaging condition (Claerbout, 1985). The extrapolation step is linear but computationally intensive; the imaging step is relatively cheap from the computational point of view but nonlinear. The imaging condition extracts an image where the data, extrapolated backward in time, match the source wavefield, extrapolated forward in time. A conventional imaging condition evaluates the matching between the source and receiver wavefields through their crosscorrelation (Claerbout, 1985).

In shot-record (shot-profile) migration, every experiment is imaged separately and the total cost is therefore a linear function of the number of experiments. Moreover, the more accurate the wavefield extrapolation scheme, the higher its com-

putational cost. In the case of reverse-time migration (RTM) (Baysal et al., 1983), the computational cost is high, thus posing a challenge for industrial applications. Simultaneous shot migration has several benefits: first, we can reduce the overall time of the migration procedure, thus reducing the cost; second, we can exploit the possibility of imaging in a fixed time and in a bigger aperture with respect to shot-profile migration in the migration velocity analysis loop, which is a crucial step in the seismic inversion process.

Random shot-encoding migration (Morton & Ober, 1998; Romero et al., 2000) is used to image data by simultaneously migrating a number of shots, which are linearly combined after the application of random delays. The main goal is to reduce the computational cost of wave-equation migration. The drawback is that unrelated shots interfere with one another, thus leading to artifacts commonly referred to as crosstalk. For random shot-encoding, the power of the artifacts in the image decreases as $1/M$ with M being the number of encodings considered, i.e., the number of stacked encoded images.

An intrinsic problem in shot-profile migration is that the natural pre-stack gather (the shot indexed gather) cannot be directly or easily related to the incidence angle or other illumination-related quantities (Soubaras, 2006). To overcome this difficulty, several authors propose synthesizing composite shots by applying delays that are linear functions in the original shot positions (Whitmore, 1995; Zhang et al., 2005; Liu et al., 2006). These new synthetic shots are synthetic plane-waves and the new data are, therefore, the response of the subsurface to an incident plane-wave. The natural pre-stack index for these experiments is the ray parameter $p = sin(\alpha)/v$, where α is the take-off angle of the synthetic plane-wave. This index is a surface-related parameter and does not remove the complexity of the overburden at the image point, i.e., it does not represent the illumination of the image point as a function of the angle of incidence.

The angle of incidence represents a preferential domain for indexing seismic images. Stolk & de Hoop (2001) show that wave-equation common-angle image gathers are not affected by multipathing artifacts that characterize kirchhoff migration (Stolk & Symes, 2004); hence, they represent a powerful tool for performing velocity analysis via semblance principle. The plane-wave take-off angle is directly related to the angle of incidence in depth only if the velocity model is layered and laterally homogeneous; in complex velocity models, the angle of incidence can be computed by considering extended images and transforming them into the angle domain (Rickett & Sava, 2002; Sava & Fomel, 2003).

Plane-wave migration, or linear-shot encoding migration (L-SEM), is equivalent to shot-profile migration when one considers all plane waves that describe the data. Zhang et al. (2005) present an equation for the minimum number of plane-wave components necessary for correctly representing the data in a certain range of take-off angles. Soubaras (2006) presents a different strategy that exploits a unitary transformation for combining the original shots. Modulated-shot encoding produces an image equivalent to shot-profile migration as well as image-gathers indexed by ray parameter p, but it is less costly than plane-wave migration. Modulated shot-encoding and plane-wave migration are closely related: both combine the shots through a unitary transformation, but while modulated shot-encoding uses a frequency *independent* unitary transformation, plane-wave migration uses a frequency *dependent* basis. They span the same space frequency-wavenumber $(\omega, \mathbf{p})$, but in different ways. The modulated-shot encoding algorithm represents an improvement over both plane-wave migration and shot-record migration, and the computational gain is preserved in the time-domain implementation (Zhang et al., 2007). In this work, we present an alternative algorithm, suitable for reverse-time migration, which allows straightforward implementation, quality control of the final image, and computational cost reduction.

The artifacts produced in simultaneous migration of different shots originate in the migration operator. The migration operator (wavefield extrapolation followed by the application of an imaging condition) is simply the adjoint of the forward Born operator used for modeling the data (Lailly, 1983) which is "almost" a unitary operator for a single shot-profile experiment. For simultaneous shot migration, the migration operator is no longer unitary and this is evidenced by the artifacts that contaminate the image. An alternative approach to this problem is least-squares migration; in this way we can compensate for the non-unitary nature of the migration operator and eliminate the artifacts in the image (Tang & Biondi, 2009). Least-squares migration is effective but computationally expensive: shot-encoding is intended to reduce the computational cost but a least-squares inversion of such a large linear problem makes the process less cost-effective. It is interesting to observe the similarities between the least-squares approach to simultaneous shot migration and processing of blended data (Berkhout, 2008), where datasets with overlapping shots are processed and imaged in a least-square sense (Verschuur & Berkhout, 2009; Berkhout et al., 2009).

In this paper, we analyze shot-encoding schemes, namely random-shot encoding (R-SEM) (Romero et al., 2000) and plane-wave migration (Zhang et al., 2005), that are suitable for reverse-time migration. We look at the behavior of the two methods with respect to crosstalk artifacts and spatial resolution in the final image. Our goal is to develop an improvement over random shot-encoding that converges faster to the shot-record migration (SRM) result and that controls the artifacts introduced in the image by the interference of different experiments. At the same time, we want to achieve higher spatial resolution with respect to plane-wave migration, which trades speed for spatial resolution by using only certain plane-wave components for reconstructing the image of the subsurface. Moreover, imaging plane-wave components with a high take-off angle (or ray parameter $\mathbf{p}$), when a time-domain finite difference scheme is used (like in RTM), requires an increase in the computational time and cost since long delays have to be taken into account. From this analysis, we design a hybrid encoding scheme that combines L-SEM and R-SEM. First, we construct the linear delay function that produces the synthetic plane-wave response from the original data; then, we dither the planar wavefront with random delays in order to increase the

spatial resolution without migrating additional plane waves. We test it on the synthetic Sigsbee model and show that it is more effective than both L-SEM and R-SEM. In areas with poor or uneven illumination, the hybrid approach recovers the full spatial bandwidth of the image, in contrast to L-SEM, and is less prone to crosstalk noise than R-SEM.

2 SHOT-ENCODING METHODS

The imaging condition is a nonlinear operation; it is not able to distinguish between wavefields from different shots and produces artifacts when several experiments are simultaneously migrated. Let us consider the source wavefields $s_i(\mathbf{x},t)$ and the receiver wavefields $r_i(\mathbf{x},t)$, where the index i indicates the shot number. We can combine wavefields of different shots and extrapolate them all at once because the wave equation we use is linear in the wavefield; however, problems arise in the extraction of the image. Conventional imaging condition involves computing the time crosscorrelation at every location $\mathbf{x}$ in space of the source and receiver wavefields $S(\mathbf{x},t)$ and $R(\mathbf{x},t)$ and stacking over time:

$$I(\mathbf{x}) = \sum_t S(\mathbf{x},t)R(\mathbf{x},t). \tag{1}$$

If the wavefields $S(\mathbf{x},t)$ and $R(\mathbf{x},t)$ are, respectively, the combination of all shot source and receiver wavefields with different delays, then we obtain:

$$\begin{aligned} I(\mathbf{x}) &= \sum_t \sum_i \sum_k s_i(\mathbf{x},t-\tau_i)r_k(\mathbf{x},t-\tau_k) \\ &= \sum_i I_i(\mathbf{x}) + \sum_t \sum_{l\neq k} s_l(\mathbf{x},t-\tau_l)r_k(\mathbf{x},t-\tau_k), \end{aligned}$$

where $I_i(\mathbf{x})$ is the image obtained from the ith shot, and the term $\sum_t \sum_{l\neq k} s_l(\mathbf{x},t-\tau_l)r_k(\mathbf{x},t-\tau_k)$ represents the crosstalk artifacts produced by the imaging condition as result of the simultaneous migration of different experiments. Shot-encoding migration deals with the design of an optimal combination of the original data that allows one to simultaneously migrate several shots at once, control the crosstalk noise, and recover the correct image of the structure that generated the recorded data.

Different encoding schemes have been discussed in the literature. Random shot-encoding (R-SEM) (Romero et al., 2000) and linear shot-encoding (L-SEM) (Zhang et al., 2005) apply simple delays to the source and receiver wavefields of every shot. In random shot-encoding, a random delay is applied to each one of the shot wavefields prior to the composition of the synthetic experiments. The uncorrelation of the delays is reflected in uncorrelated artifacts that can be stacked out by summing up the images obtained from different realizations of random delays.

On the other hand, linear shot-encoding aims to construct the response of the Earth to synthetic plane waves by applying delays that are linear functions of the shot positions. Linear shot-encoding migration has been proven to be equivalent to shot-record migration if a sufficient number of plane-waves is considered. Random shot-encoding is equivalent to shot-record migration when considering an infinite number of realizations of random delays. For both methods, because of the model-dependence of the problem, the question of how many encodings we *really* need for obtaining a correct image is still open (Stork & Kapoor, 2004; Etgen, 2005) . For example, for imaging a single horizontal reflector, we need a single plane wave; on the other hand, for highly heterogeneous media and complex structures, a more complete illumination of the spatial wavenumber domain is required. In the latter case, random shot-encoding can represent a more economic solution, given the acceptable level of crosstalk.

A third encoding scheme that involves more than just simple delays is modulated-shot encoding (Soubaras, 2006) or, in the time-domain implementation, harmonic-source encoding (Zhang et al., 2007). These strategies are effective but not straightforward to implement, especially the time-domain implementation. Harmonic-source encoding involves the convolution of the original data with a filter that decays like $1/t$, and particular care is needed in the choice of the encoding parameters. Nonetheless, both methods halve the computational cost of a typical production project (Soubaras, 2006; Zhang et al., 2007).

Our work aims to find a simple and economic way to image a survey using RTM. We focus on random and linear shot-encoding migration, and all considerations are drawn from these two references and their features with respect to the standard shot-profile migration.

Both random and linear shot-encoding can be described using a general formulation of the encoding procedure. In fact, we can express the synthetic wavefields as a weighted sum of the actual shot wavefields appropriately delayed:

$$S(\mathbf{x},t,\theta) = \sum_k s_k(\mathbf{x},t) * \delta(t - f(\mathbf{x}_k,\theta)) \tag{2}$$

and

$$R(\mathbf{x},t,\theta) = \sum_l r_l(\mathbf{x},t) * \delta(t - f(\mathbf{x}_l,\theta)), \tag{3}$$

where $f(\mathbf{x}_k,\theta)$ represents the delay applied to the kth shot wavefields as a function of the shot position $\mathbf{x}_k$ and the parameter θ. The parameter θ spans the encoding axis. For example, in the case of plane-wave migration in a 2D model (Whitmore, 1995; Zhang et al., 2005), $f(x_k,\theta) = \frac{\sin(\alpha\theta)}{v}(x_k - x_0)$, where x_0 is a reference point and $\alpha\theta$ represents the take-off angle of a single plane wave; for random shot-encoding, $f(\mathbf{x}_k,\theta)$ is a random process with different values for every shot position $\mathbf{x}_k$, where the parameter θ indexes the random delay realizations.

If N represents the total number of shots and M the number of different encodings (plane-waves or random delay realizations), the strategy is effective if $M \ll N$, i.e., if we can obtain an image which is comparable in quality to shot-record migration with a smaller number of migrations.

The wave-equation used in seismic imaging is linear in the wavefield; hence, we can linearly combine wavefields of

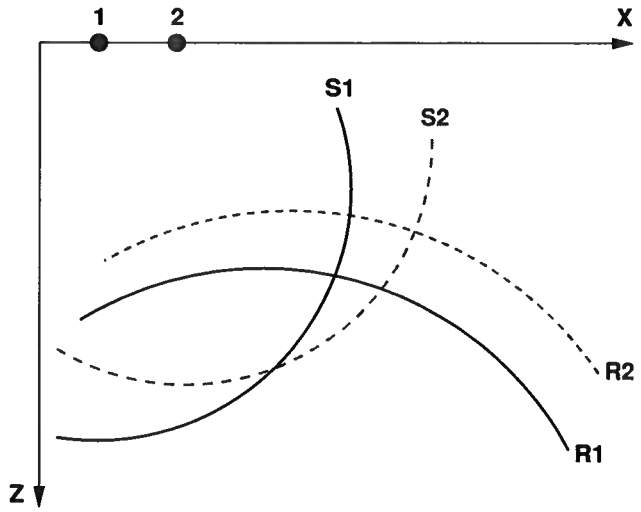

Figure 1. Artifacts generated by the imaging condition: the wavefields corresponding to different shots are represented with different colors ad different lines and indicated with numbers 1 and 2. The source wavefields are S1 and S2, the receiver wavefields R1 and R2. The correct image is produced where the wavefields of the same shots coincide, i.e., where the two solid lines, S1 and R1, and the two dashed lines, S2 and R2, intersect. Shot-encoding migration generates artifacts where S1 intersects R2 and S2 intersects R1.

different shots and numerically propagate their superposition in the subsurface model. However, the imaging condition is a nonlinear operation and introduces crosstalk between different experiments. The cartoon in Figure 1 describes the mechanism that produces crosstalk when two shots are simultaneously migrated. When the source and receiver wavefields belonging to different experiments match in time, the imaging condition extracts an image which does not correspond with a reflection.

If we substitute the expressions for the synthetic wavefields, equation 2 and equation 3, into the imaging condition in equation 1 and then transform in the frequency domain, we obtain

$$I(\mathbf{x}) = \sum_{\omega} \sum_{k} \sum_{l} s_k(\mathbf{x},\omega) r_l^*(\mathbf{x},\omega) W_{kl}, \qquad (4)$$

where

$$W_{kl} = \sum_{\theta} e^{i\omega[f(\mathbf{x}_l,\theta) - f(\mathbf{x}_k,\theta)]}. \qquad (5)$$

The matrix W_{kl}, which has the shot positions $\mathbf{x}_l$ and $\mathbf{x}_k$ as rows and columns, represents the coupling between different shots in equation 4 and it is fully determined by the encoding function $f(\cdot,\cdot)$.

An encoding scheme is considered equivalent to shot-record migration if the crosstalk term in equation 4 approximates the identity matrix, i.e., if the following condition is satisfied:

$$W_{kl} = \sum_{\theta} e^{i\omega[f(\mathbf{x}_l,\theta) - f(\mathbf{x}_k,\theta)]} \approx \delta_{kl}, \qquad (6)$$

where δ_{kl} is the Kronecker symbol.

In the following sections, we study the crosstalk term for linear shot-encoding and random shot-encoding. We highlight the main features in terms of spatial bandwidth achievable in the final image and crosstalk noise, and then we design a strategy for combining the advantages and controlling the drawbacks of these two schemes. We recognize linear shot-encoding and random shot-encoding as end members of a more general family of encodings, which we can span by controlling the correlation of the delays of neighboring shots. Figure 2 describes our idea; fixing the computational cost, we can move from plane-wave migration to random shot-encoding, i.e., from low crosstalk and low spatial bandwidth to high crosstalk and high spatial resolution in the final image. The correlation of the delays of neighboring shots involves a tuning parameter that controls the dithering of an initial plane-wave. In Figures 3(a)-3(c), we respectively show the source wavefield for linear shot-encoding, random shot-encoding and a combination of the two, in which the initial plane wave is dithered by a random perturbation. In the following, we analyze L-SEM and R-SEM and introduce mixed shot-encoding migration (M-SEM) as their combination.

2. 1 Linear shot-encoding migration

In linear shot-encoding, the recorded wavefields of different experiments are combined in order to obtain the response to a synthetic plane wave. The encoding function is linear in the shot position and depends on one parameter, which represents the ray parameter $\mathbf{p}_\theta$ associated with a particular plane wave:

$$f(\mathbf{x}_k,\theta) = \mathbf{p}_\theta \cdot (\mathbf{x}_k - \mathbf{x}_0), \qquad (7)$$

where $\mathbf{x}_0$ represents an arbitrary reference point.

Let us assume that $\mathbf{p}_\theta$ is a continuous parameter; if the expression in equation 7 is substituted into the expression de-

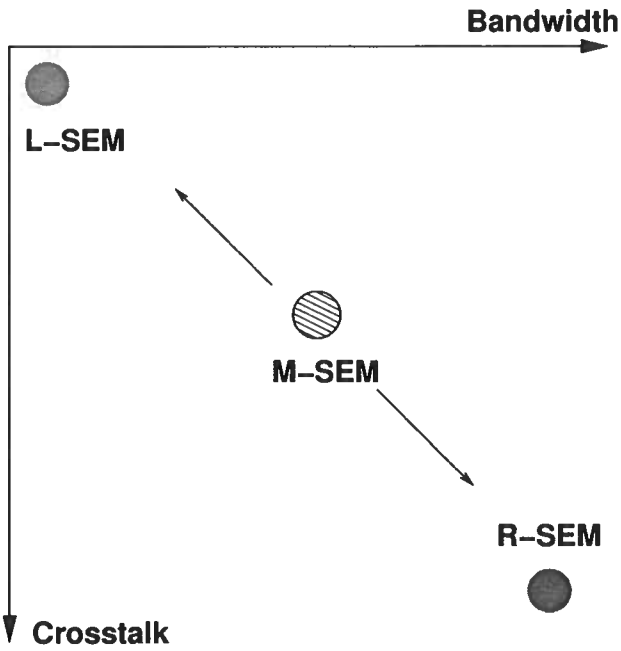

Figure 2. Trade-off between bandwidth and crosstalk for different shot-encoding schemes. L-SEM achieves a clean image with low spatial resolution, while R-SEM obtains a full bandwidth image highly contaminated by crosstalk noise. For drawing the cartoon, we assume fixed computational cost.

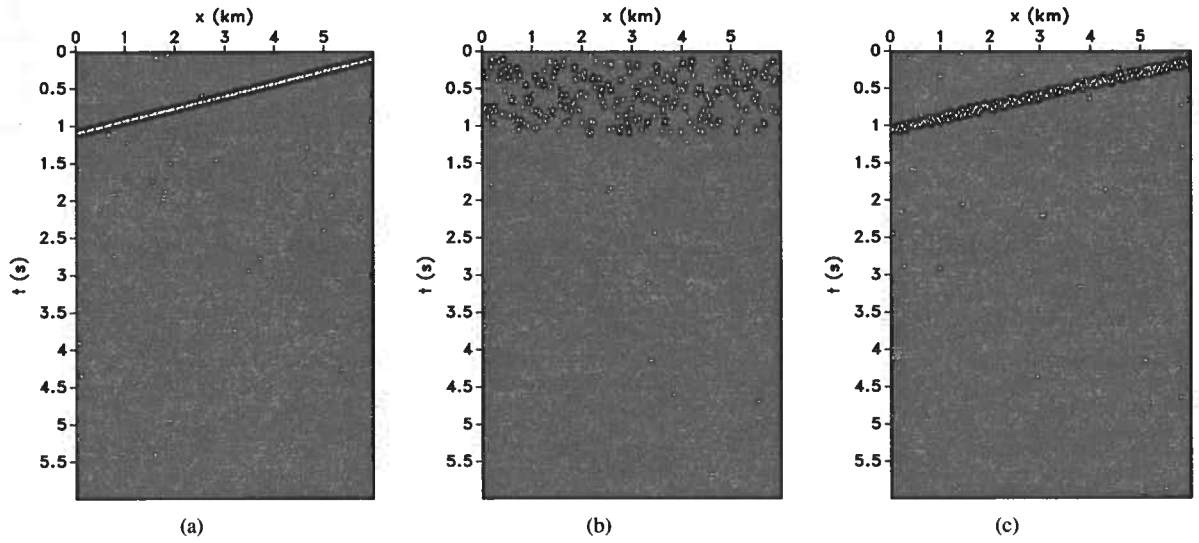

Figure 3. Examples of source wavefield for (a) L-SEM, (b) R-SEM, and (c) M-SEM. Mixed shot-encoding consists in dithering the wavefront we synthesize for L-SEM.

scribing the crosstalk, we obtain

$$W_{kl} = \int e^{i\omega \mathbf{p}_\theta \cdot (\mathbf{x}_k - \mathbf{x}_l)} d\mathbf{p}_\theta. \quad (8)$$

The expression in equation 8 is actually proportional to the Dirac delta $\delta(\mathbf{x}_k - \mathbf{x}_l)$; this means that plane-wave migration is equivalent to shot-record migration if we consider all ray parameters that reconstruct the data. In the real world, we sample the $\mathbf{p}$-space and then we have only a discretized version of the integral in equation 8:

$$W_{kl} = \sum_\theta e^{i\omega \mathbf{p}_\theta \cdot (\mathbf{x}_k - \mathbf{x}_l)}. \quad (9)$$

Several papers discuss the sampling requirements for the $\mathbf{p}$-space (Zhang et al., 2005; Stork & Kapoor, 2004; Etgen, 2005); the take-off angle range constrains the minimum number of plane waves necessary for correctly reconstructing the data in that range. At the same time, the angle range defines the computational cost for RTM and the accuracy of the image reconstruction; reducing the angle range decreases not only the computational cost but also the quality of the final image. If we assume that the ray parameter space is properly sampled and the synthesized plane waves are not aliased, then equation 9 represents a *sinc* function (the DFT of a discrete boxcar function) and tends to a delta function if we increase the take-off angle range.

We can display the crosstalk matrix for a given number of plane waves and analyze the behavior as a function of the number of $\mathbf{p}$ components considered. In Figures 4, we observe how the crosstalk term becomes spikier by imaging more plane-wave components. This is because, for linear shot-encoding, the crosstalk term is actually an approximate representation of the identity operator (equations 8-9).

2. 2 Random shot-encoding migration

In random shot-encoding, the delay of every shot is drawn from a random process and the parameter θ is the realization index. We use the following notation:

$$f(\mathbf{x}_k, \theta) \sim t_{max} \mathcal{U}; \quad (10)$$

at every shot location $\mathbf{x}_k$, the delay $f(\mathbf{x}_k, \theta)$ is a random variable uniformly distributed between 0 and t_{max}; $\mathcal{U}$ represents the uniform distribution between 0 and 1. If we indicate with t_k^θ the delay for the kth shot in the θth synthetic experiment, we can write the crosstalk matrix as

$$W_{kl} = \sum_\theta e^{i\omega[t_l^\theta - t_k^\theta]} = M\delta_{kl} + (1 - \delta_{kl}) \sum_\theta e^{i\omega[t_l^\theta - t_k^\theta]}. \quad (11)$$

Equation 11 shows that the crosstalk depends on the relative delay difference between different shots. The delay difference changes the spatial location of the artifacts in the image for different realizations of random delays. On the other hand, the correct structural image is always obtained at the correct location. Since the delays are random independent variables, the location of the artifacts will be an independent variable as well. The random superposition of the artifacts in space and the null DC component of the wavelet of the recorded signal partially stack out the crosstalk noise; the subsequent stack over different random delay realizations further improves the signal-to-noise ratio, since the positions of the reflectors do not depend on the encoding delays and their contribution will always stack constructively (Romero et al., 2000).

Figure 5 shows the evolution of the crosstalk matrix in equation 11 as more synthetic experiments are imaged and stacked, and highlights the increasing signal-to-noise ratio described above. The main diagonal is a perfect spike and indicates that we are not constraining the range of spatial components in the image. Stacking the images obtained with different realizations of random delays, we decrease the energy of the out-of-diagonal terms and, consequently, the signal-to-noise ratio increases linearly with the number of random delay realizations (Romero et al., 2000). The image obtained by random shot-encoding approaches the shot-profile migration result as $M \to \infty$.

2. 3 Mixed shot-encoding migration

The observations in the previous sections lead to the cartoon in Figure 2. In the space defined by crosstalk and spatial bandwidth, we can recognize plane-wave migration as one extremum (low crosstalk and low bandwidth) and random shot-encoding as the other extremum (high crosstalk as well as high spatial bandwidth). The cartoon corresponds to a slice at constant computational cost, which is the third axis in this abstract space. We assume a constant computational cost in order to consistently compare the different approaches. We can imagine moving in the space described by crosstalk and spatial bandwidth by combining the previously presented encodings. Our new approach aims to simultaneously reduce the crosstalk and increase spatial bandwidth as we move toward the center of the crosstalk-bandwidth plane. Of course, the ideal goal is to move towards the upper-right corner (high bandwidth and low crosstalk), and the combination of linear and random shot-encoding is a proxy for this result. Indeed, if we are able to control the artifacts in the image and reduce the crosstalk power, we can filter them out in post processing, thus preserving the structural information in the image and moving toward the shot-record migration result at a lower cost.

The combination of linear and random shot-encoding involves dithering the plane waves with a random perturbation (Figure 3(c)). The expected result is the reduction of crosstalk (because of the side lobes that characterize the crosstalk term for L-SEM) and an increase in spatial bandwidth (given the spikiness of the crosstalk term for R-SEM). In Figure 6, we show the crosstalk matrix for the new mixed shot-encoding scheme:

$$\begin{aligned} W_{kl} &= \sum_\theta e^{i\omega[\mathbf{p}_\theta(\mathbf{x}_l - \mathbf{x}_k) + (t_l^\theta - t_k^\theta)]} \\ &= M\delta_{kl} + (1 - \delta_{kl}) \sum_\theta e^{i\omega[\mathbf{p}_\theta \Delta\mathbf{x}_{kl} + \Delta t_{kl}^\theta]}; \end{aligned} \quad (12)$$

we can observe the behavior in-between linear and random shot-encoding. The crosstalk term partially preserves the char-

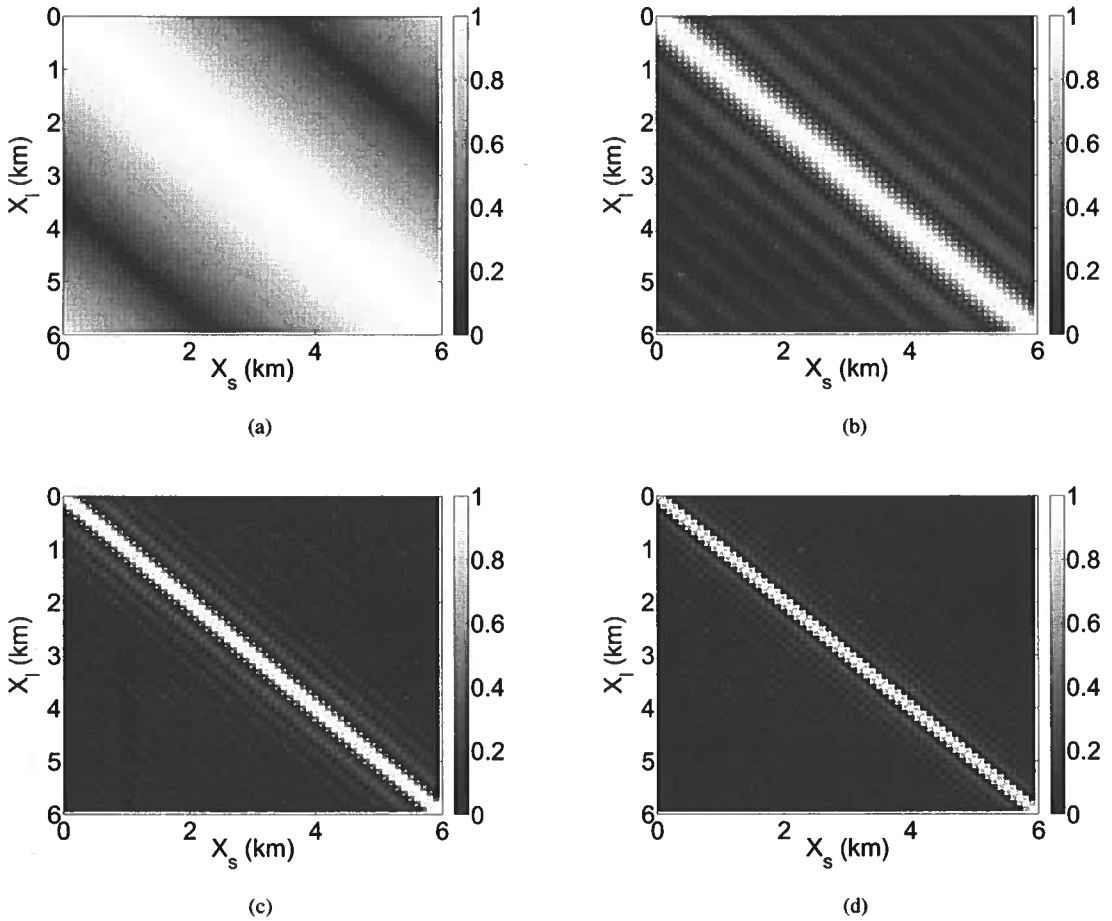

Figure 4. L-SEM crosstalk matrix VS number of plane waves for a single temporal frequency ω: (a) 2, (b) 10, (c) 20, and (d) 30. Increasing the number of plane waves, we sharpen the main diagonal of the crosstalk matrix and better approximate the identity, i.e., we tend toward the shot-record migration result.

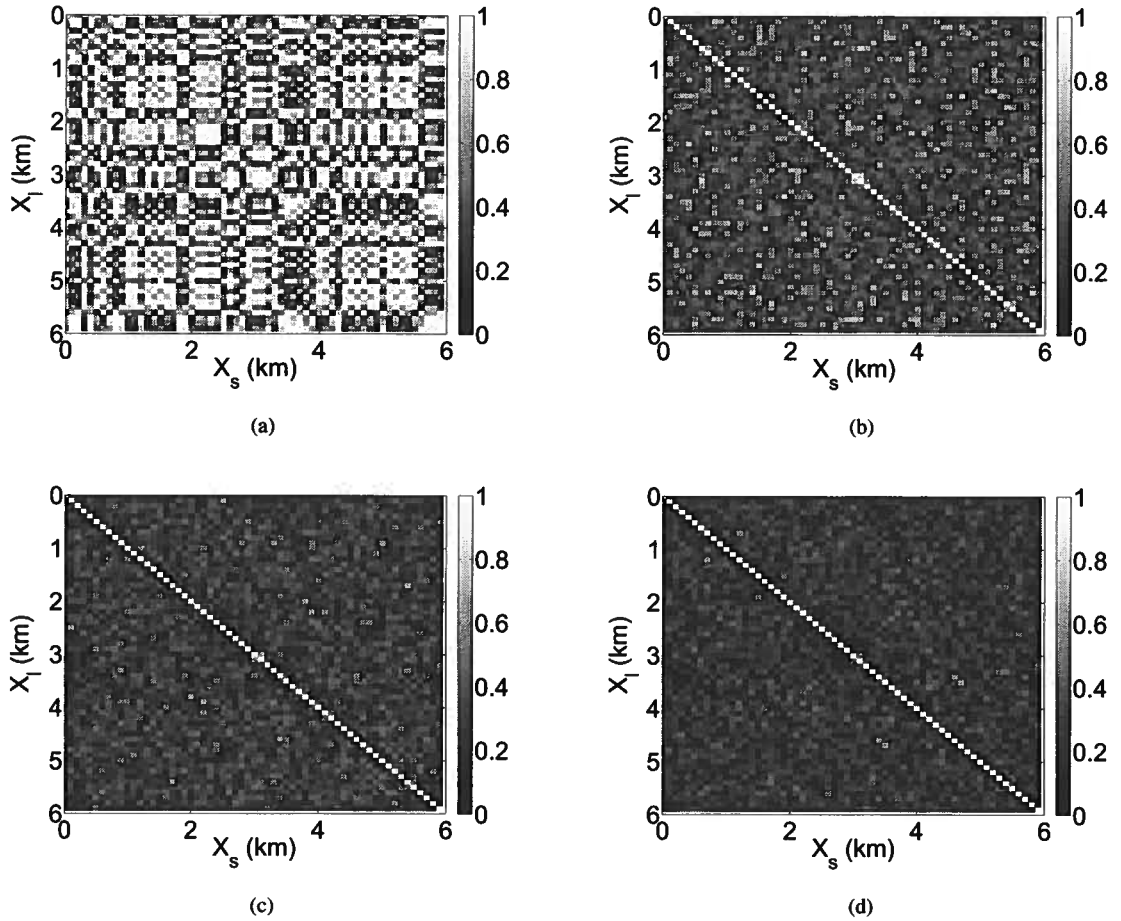

Figure 5. R-SEM crosstalk matrix VS number of synthetic experiments: (a) 2, (b) 10, (c) 20, and (d) 30. The more random-delay realization we consider, the better we approximate the artifact random process. Since the artifacts are zero mean and the stack of a number of experiments is an estimate of the expected value of the process, we are able to remove the crosstalk noise by stacking the images obtained from different random-delay encodings.

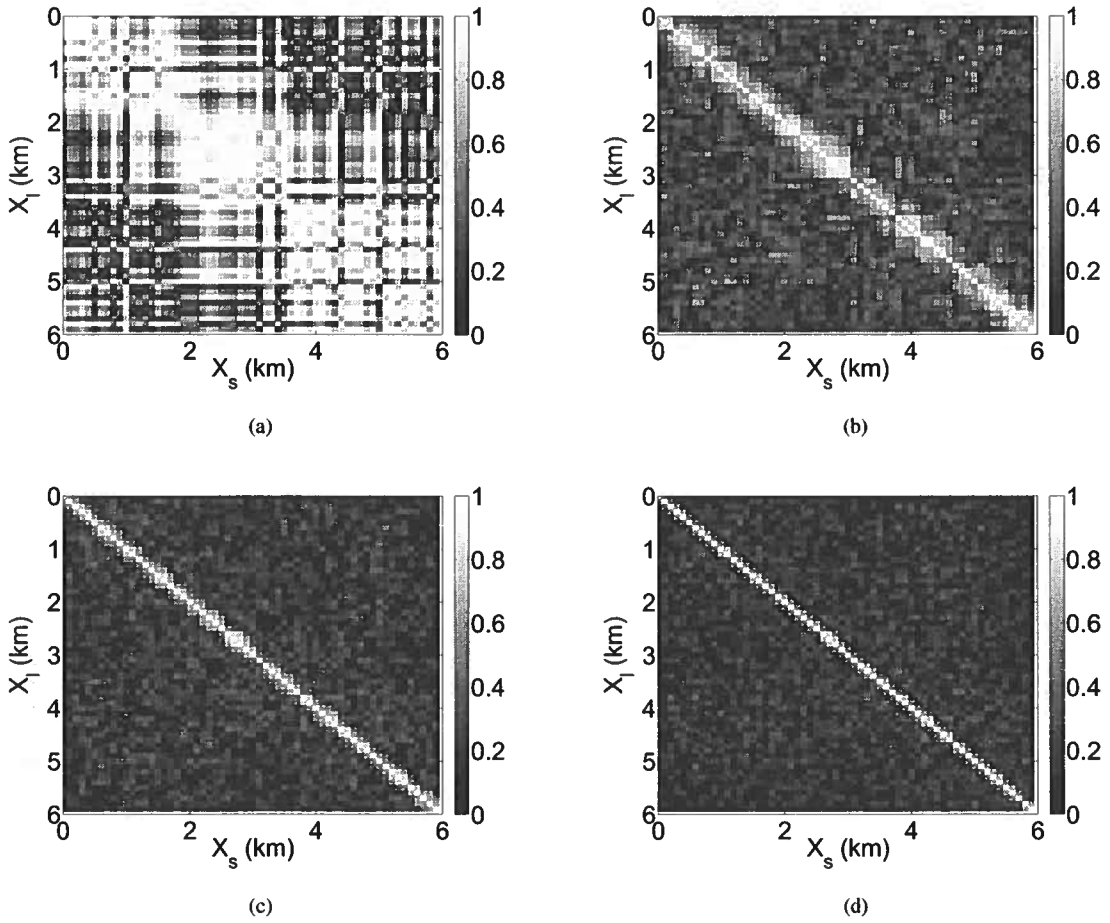

Figure 6. M-SEM crosstalk matrix VS number of experiments: (a) 2, (b) 10, (c) 20, and (d) 30. Combining L-SEM and R-SEM, we obtain a crosstalk matrix characterized by a hybrid behavior. In the panels, we observe the L-SEM convergence footprint and the random fluctuations due to the wavefront dithering. The dithering is particularly effective in sharpening the main diagonal of the crosstalk matrix.

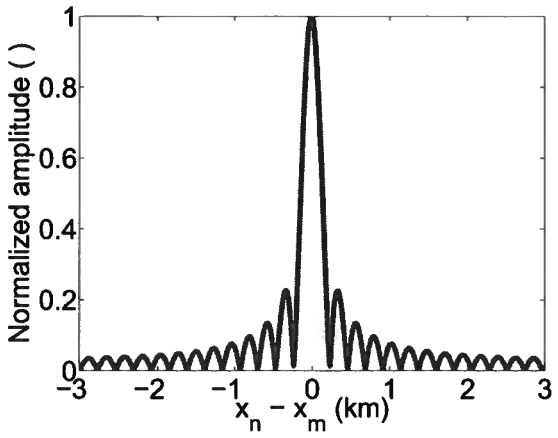

(a)

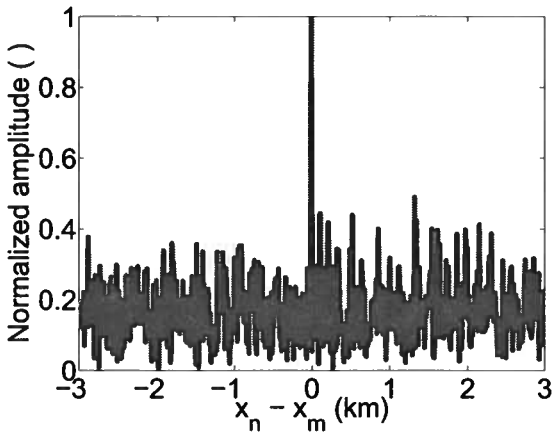

(b)

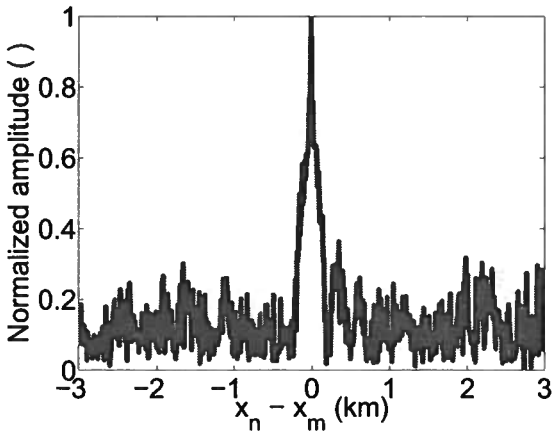

(c)

Figure 7. Slices of the crosstalk panel for 50 synthetic experiments: (a) L-SEM, (b) R-SEM, and (c) M-SEM. They represent the coupling of the wavefields of different shots as a function of the distance between the shots.

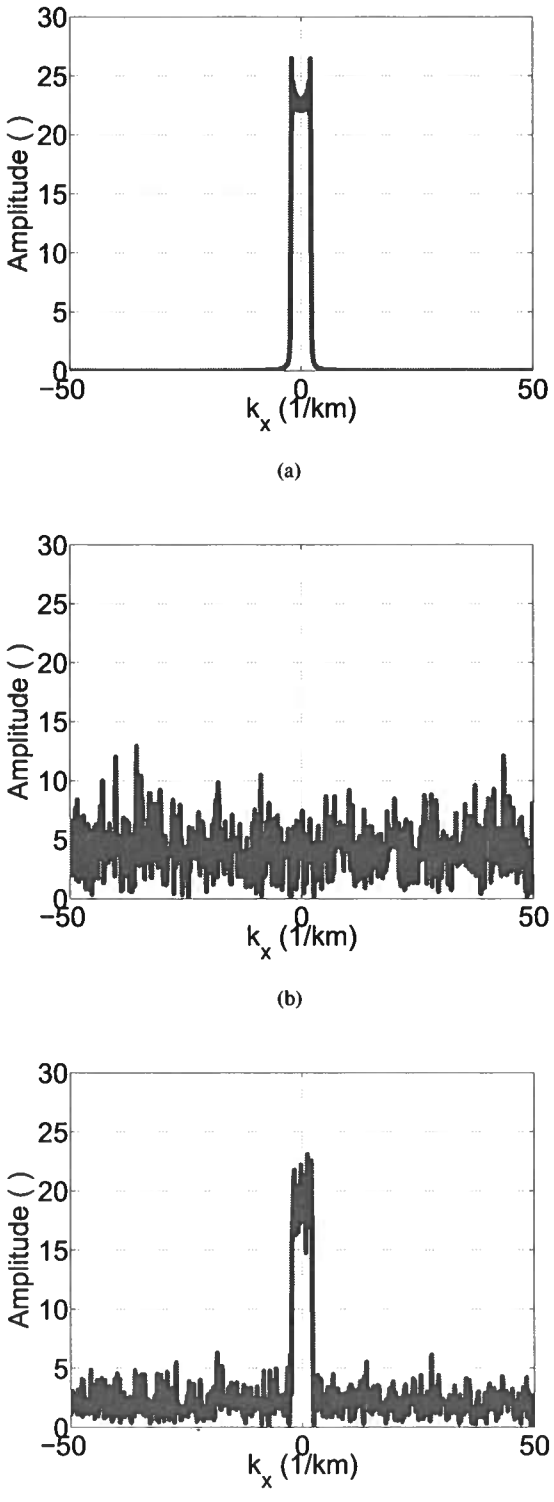

Figure 8. Plane-wave components considered in the imaging procedure for: (a) L-SEM, (b) R-SEM and (c) M-SEM. L-SEM migrates all the plane-wave components in a limited range with the same weight; R-SEM images all the plane-wave components with uneven amplitudes; M-SEM gives more weight to the dithered plane waves but images all components.

acteristic trend of linear shot-encoding with respect to the side lobes while the dithering destroys the coherency of the side lobes and allows for a spikier main lobe.

Restricting our attention to a single column (row) of the panels in Figures 4-6 , we can better appreciate the behavior with respect to spatial bandwidth and artifacts of L-SEM, R-SEM and M-SEM, respectively. Figure 7(a) shows the absolute value of a column (row) of the crosstalk term in the case of L-SEM and 50 plane waves. Note the main lobe and decaying side lobes. Intuitively, we can think of the width of the main lobe as an indicator of the achieved spatial bandwidth, since it describes the coupling between neighboring shots. The amplitude of the side lobes determines the strength of the artifacts in the image. In this case, we expect a loss in spatial resolution but small artifacts in the final image. We verify these considerations in the result section. For R-SEM (Figures 7(b)) we observe a spike at $\mathbf{x}_n - \mathbf{x}_m = 0$, i.e., when the source and receiver wavefields belong to the same shot, over a random noise floor, which represents the interference between different shots. The spike indicates that we are not trading off the bandwidth of the image; the nonzero terms for $\mathbf{x}_n \neq \mathbf{x}_m$ determines the artifacts. M-SEM (Figure 7(c)) presents a behavior in between L-SEM and R-SEM. The spike for the crosscorrelation of wavefields belonging to the same shots ($\mathbf{x}_n - \mathbf{x}_m = 0$) is produced by the dithering, while the linear trend reduces the out-of-diagonal term of the crosstalk matrices.

Figure 8 shows us how the different encodings take into account the plane-wave components. In Figure 8(a), we see that plane-wave migration is constrained by the range of synthesized ray parameters. At the other extremum, R-SEM images all the components but the equalization among them is missing. In Figure 8(b), the "non-flatness" of the spectrum is the counterpart of the artifacts due to crosstalk in the image. Finally, in Figure 8(c), we observe how M-SEM images all the spatial components giving greater weight to those related to the ray parameters of the plane-waves that have been dithered. Again the "non-flatness" reflects the presence of artifacts in the image. Nonetheless, the distortion is less pronounced than for R-SEM.

2. 4 Example of a point scatterer in constant background

We illustrate the features highlighted in the previous sections with a simple exercise that images a point scatterer in a constant velocity background. We compare the results obtained by stacking 50 images constructed with linear, random and mixed shot-encoding (Figure 9). In all three cases, the maximum delay applied to wave-fields is the same and is equal to 1 s. For imaging algorithms implemented in the time domain, like reverse-time migration, the fixed maximum delay ensures that all migrations have same cost, regardless of the encoding type.

Notice the lower focus of the image obtained by L-SEM (Figure 9(a)). The point is spread in the horizontal direction because we have not considered plane waves with high values of θ in the imaging process, i.e., with high ray parameter $\mathbf{p}$. On the other hand, the image is clean because the crosstalk decreases quickly with the distance $(\mathbf{x}_k - \mathbf{x}_l)$. The data synthesized for plane-wave migration contain the minimum number of events: the response to an incident plane-wave contains the same number of reflection events in the shot-profile data. Because of this, the undesired crosscorrelations between wavefields from different experiments, and then the crosstalk, are minimized. R-SEM (Figure 9(b)) represents the other extremum in the trade-off between crosstalk and spatial bandwidth. In this case, a wider range of the spatial components is imaged but crosstalk noise is present in the image, as well. The synthetic experiments contain more events than the single shot-profile data, and then for a encoded image the crosstalk is maximized. The stack of the different experiments is effective for this simple model but the result rapidly worsens with increasing complexity of the subsurface. Figure 9(c) shows the image obtained by M-SEM. We can observe a spatial resolution that is closer to R-SEM but has fewer artifacts. The amplitude spectra of the stacked images in Figure 10 highlight the smaller spatial bandwidth of L-SEM with respect to both R-SEM and M-SEM. Nonetheless, they show the distortion of the spectrum, i.e., the artifacts in the image. Notice the smaller distortion in the case of M-SEM compared to R-SEM (Figure 10(c) and 10(b), respectively).

2. 5 Denoising and image enhancing

Because M-SEM preserves the full-bandwidth information but the image is contaminated with noise, we can consider removing that noise in post-processing by applying a suitable denoising algorithm. The criterion for choosing among different denoising procedures is the preservation of the geologic features in the image. We test two denoising schemes: the first is based on seislet transform (Fomel, 2006), the second is a nonlinear structure-enhancing algorithm (Liu et al., 2009) based on plane-wave destruction filters (Fomel, 2002).

2. 5.1 Denoising using the seislet transform

The seislet transform (Fomel, 2006) is a wavelet-like transform that decomposes the signal into its components at different scales according to the local dip. This transform is very effective in removing uncorrelated noise from a seismic image and preserving the structures that characterize the image itself. After the seislet decomposition, we reconstruct the image using all but the smallest scale coefficients in order to eliminate the incoherent part of the signal. This approach is based on the assumption that the crosstalk is both incoherent and weaker than the desired signal. Unfortunately, this is not always the case.

2. 5.2 Denoising using nonlinear structure-enhancing filters

As an alternative denoising procedure, we test the structure-enhancing algorithm proposed by Liu et al. (2009). The non-

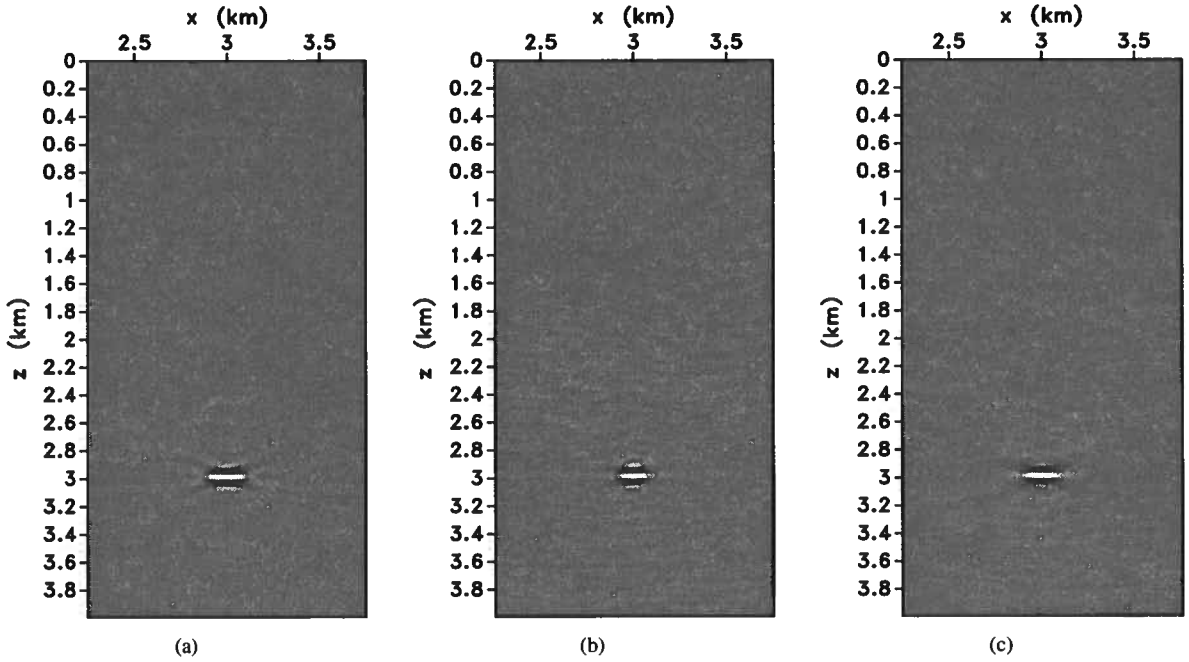

Figure 9. Point scatterer in a constant medium: (a) L-SEM, (b) R-SEM, and (c) M-SEM. Observe the horizontal spreading in L-SEM; the limitation in spatial components reduces the spatial bandwidth of the image. R-SEM produces a sharper image but creates artifacts; M-SEM provides an full-bandwidth image and controls the crosstalk with respect to R-SEM.

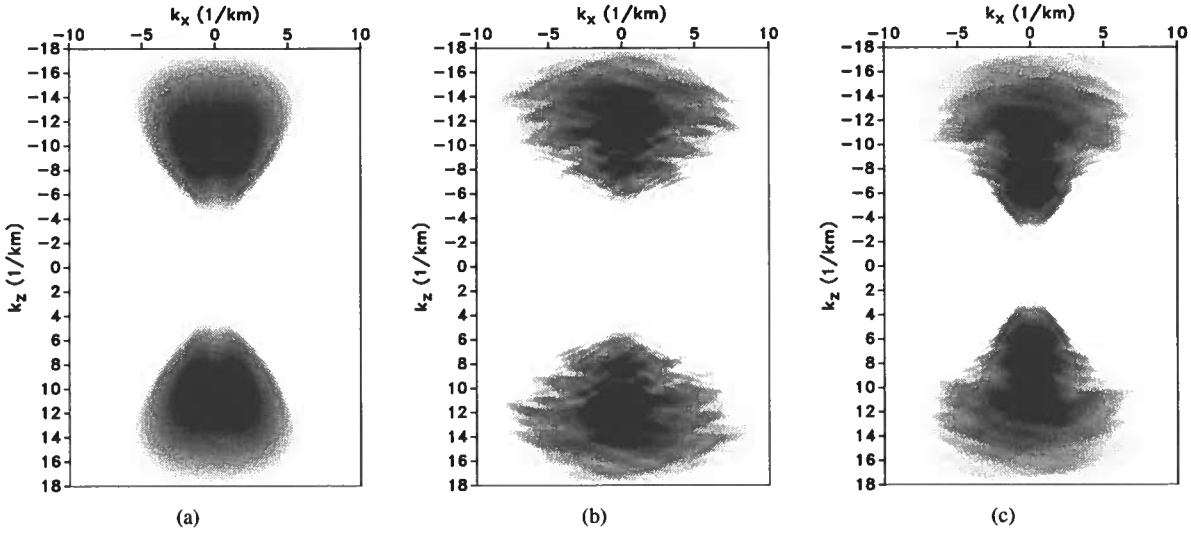

Figure 10. Spatial spectra of the images obtained by (a) L-SEM, (b) R-SEM, and (c) M-SEM. R-SEM distorts the spectrum of the image but recovers all the spatial components; on the contrary, L-SEM is constrained by the plane waves synthesized. M-SEM reduces the distortion of the spectrum and images a wider range of spatial components.

linear structure-enhancing algorithm operates on a extended cube, which is created by plane-wave prediction from a starting image; then, filtering acts across the prediction axis by selecting point-wise the median value of the predicted images. In our case, the starting image is the stack of the mixed shot-encoding synthetic experiments.

3 SIGSBEE EXAMPLE

In this section, we illustrate the technique in a more realistic case by imaging the Sigsbee dataset. In the previous section, we have analyzed the mixed shot-encoding algorithm in the case of a point scatterer in a homogeneous velocity model. We point out the reduction in crosstalk, with respect to random shot-encoding, and the increase in spatial bandwidth with regard to linear shot-encoding migration. Here, we verify those results in a general case.

From the simple example of a point scatterer, we know that the crosstalk is attenuated but not completely suppressed. Nonetheless, if we are able to control the noise during the imaging step, we can apply any denoising algorithm for cleaning up the image from residual artifacts. Results are discussed at the end of the section.

The crosstalk in the final image is heavily dependent on the complexity of the model. In a complex, heterogeneous velocity model, plane waves are distorted and the phase relations that define W_{kl} break down as soon as inhomogeneities are encountered. On the other hand, R-SEM is more robust against this problem since there is no phase coherency to be preserved.

Let us now consider the complex Sigsbee model. Fixed the computational cost, we consider 50 shots for SRM and 50 different experiments that combine all 500 shots of the survey for the three encoding strategies. The migration algorithm used is downward continuation and the maximum delay applied to a single shot is ± 2 s.

Figure 11 shows the image obtained by migrating 50 shots separately (standard shot-record migration). The shot-record migration image represents our benchmark with respect to cost and image quality.

In order to compare the different encoding strategies, we look at the two parts of the image indicated by the boxes in Figure 11. The areas of particular interest are above the salt body, where we want to clearly resolve the stratigraphic sequence, and below the salt body, where the poor illumination and the complexity of the overburden make imaging challenging. In both areas, the signal-to-crosstalk ratio have to be high and the reflectors have to be interpretable despite the interference produced by the simultaneous migration of several shots; furthermore, the spatial spectrum of the image must be accurately recovered in order not to have artifacts in the final result. Indeed, the lack of illumination (mainly due to the salt body) weakens the signal-to-noise ratio for every encoding scheme, and in particular for R-SEM (see Figure 12(b) below the salt body at $z = 5.5$ km). Moreover, because of the heterogeneity of the velocity model in the overburden, synthetic plane-waves are severely distorted and L-SEM becomes inaccurate (see Figure 12(a); at $x = 10$ km the faults are not imaged).

In Figure 12(a) the illumination footprint of L-SEM is easily observable. By imaging only a limited range of plane-wave components, we obtain an illumination pattern which differs from the correct one that would have resulted from shot-record migration. Moreover, not all faults are imaged because of the constraints on the range of migrated plane-wave components ($x = 10$ km). Nonetheless, note the absence of residual diffractions below the salt body ($z = 5$ km) due to the undersampling of the shot domain, previously observed in the shot-record migration image.

The illumination pattern for R-SEM (Figure 12(b)) and M-SEM (Figure 12(c)) is consistent with SRM, but artifacts are introduced by the encoding procedure. In both cases, we are able to image the full spatial bandwidth information of the image but strong crosstalk contaminates the R-SEM result, especially in poorly illuminated areas and near the salt boundaries. M-SEM produces weaker crosstalk both above and below the salt bodies; especially in poorly illuminated areas, M-SEM supplies an interpretable image (compare Figure 12(c) and Figure 12(b) at $z = 5.5$ km).

The close-ups on the selected areas confirm the above considerations. Figure 13(b) is has poor spatial resolution with respect to 13(a): note the spread point diffractor at $z = 5$ km. The number of plane-wave components used is clearly insufficient for the complexity of the Sigsbee model; thus, the information about the faults in the image is largely lost ($x = 10$). R-SEM (Figure 13(c)) recovers a more complete image where the illumination is high but loses coherency under the salt body because of the overwhelming level of crosstalk. In areas of poor illumination, the image is uninterpretable. On the other hand, Figure 13(d) shows that M-SEM recovers most of the image spatial bandwidth (in contrast to L-SEM) and increases the signal-to-crosstalk (in contrast to R-SEM) below the salt body.

The image above the salt body warrants a separate discussion. Looking at the SRM image (Figure 14(a)), we note that L-SEM (Figure 14(b)) produces a clearer image (no residual diffractions) but the amplitudes in the image are also lower. This is likely related to the limitation imposed on the range of plane-wave components that have been imaged. Figure 14(c) shows the image obtained by R-SEM. All the information about the reflectors is preserved and the incoherence of the encoding delays, together with the strong illumination of the area, enable a better control of the artifacts, which appear to be incoherent and uncorrelated with the signal. M-SEM slightly improves the amplitudes of the reflection but also introduces a certain amount of correlated noise in the image (Figure 14(d)). Nonetheless, no information is lost with respect to the SRM (Figure 14(a)).

3. 0.3 Effects of dithering on crosstalk

The previous examples of imaging with mixed shot-encoding involve a 0.5% dithering of the initial plane-wave. It is of interest to look at the effects of the amount of dithering on the quality of the final image.

Intuitively, we obtain the L-SEM image by reducing the

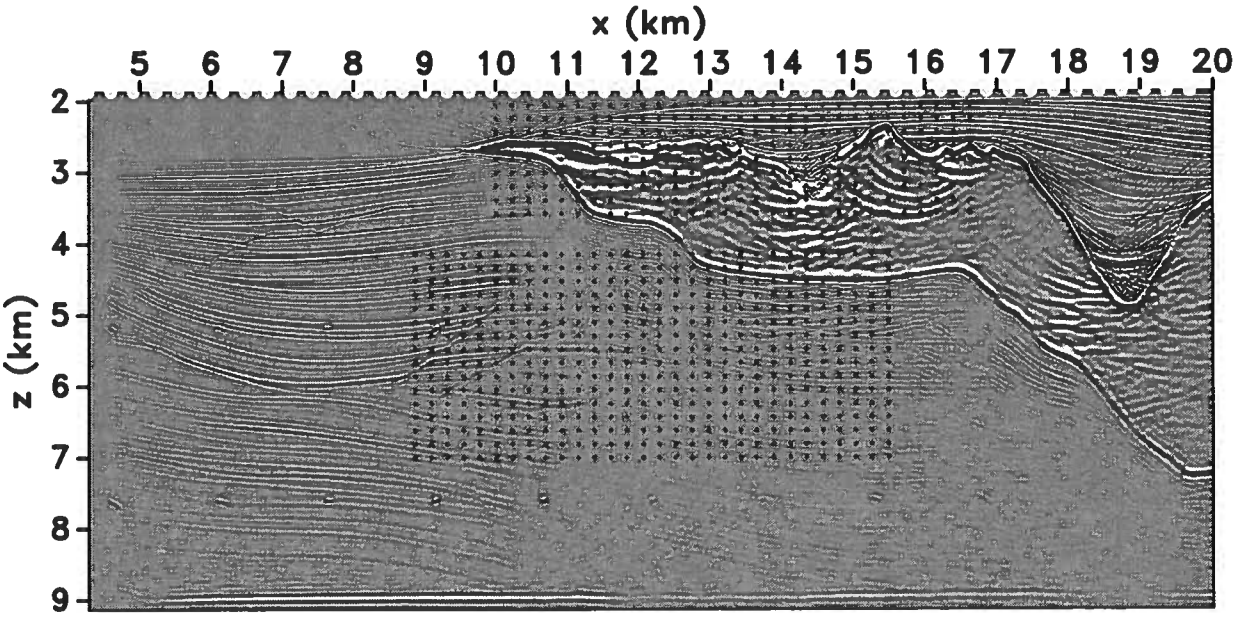

Figure 11. SRM of the Sigsbee dataset; the image is the stack of 50 shot-record migrations. The boxes highlight the areas we analyze in detail in Figures 13-14.

dithering, but relation between the amount of perturbation and the increase in the spatial bandwidth of the image cannot be easily evaluated. In Figure 15(a), we show the standard plane-wave migration image. Figure 15(b) is the result previously discussed (Figure 13(d)); note the considerable increase in spatial detail achieved with respect to plane-wave migration. The faults in the image are now interpretable and the point scatterers are better reconstructed. The illumination pattern is controlled by the main plane-wave components and closely resembles the illumination pattern in Figure 15(a). Increasing the dithering (1% and 10% in Figures 15(c)-15(d), respectively), we equalize the illumination of the image and recover greater spatial detail but, at the same time, we introduce stronger distortion, especially in the subsalt area. We conclude that a relatively small amount of dithering is necessary for sensibly increasing the spatial bandwidth of the final result. Nonetheless, it is difficult to quantify the optimum dithering, again because of the model-dependence of the problem. Given a dataset, we could estimate it *a posteriori*, crossing different image-quality indicators (spatial spectrum, image entropy, etc.) but this strategy would reduce the cost-effectiveness of M-SEM.

3. 0.4 Denoising and image enhancing

Mixed shot-encoding is more robust against crosstalk than R-SEM and it supplies a full spatial bandwidth image; nonetheless, the final image is not completely free from crosstalk. Let us now discuss the effectiveness of the postprocessing denoising algorithm against this kind of noise. Denoising is applied to an image constructed by dithering the planar wavefront with a random perturbation ranging within 0.5% of the maximum delay.

For M-SEM, the seislet denoising is effective above the salt (Figure 16(b)), but it does not improve the image quality below the salt (Figure 17(b)) because of the relatively good quality of the starting image and poor illumination of the area. The latter impacts the signal-to-crosstalk ratio and makes signal and artifacts not easily separable in the seislet domain. Overall, seislet transform is not effective in increasing the quality of the M-SEM result.

In Figure 16(c) we observe that, above the salt, the structure-enhancing algorithm is actually effective in cleaning the image and preserving the reflectors. Below the salt the situation is different; M-SEM already produces weaker artifacts and the nonlinear filtering is able to partially enhance the sediments and reflectors in this poorly illuminated area (Figure 17(c)). Moreover, the procedure is highly sensitive to amplitudes and tends to sharpen amplitude contrasts. This is a positive feature for highlighting faults but it can also lead to misleading amplitude behavior in poorly illuminated areas. In conclusion, the denoising procedure contributes marginal improvements to the initial M-SEM image.

4 DISCUSSION

The examples presented in the previous sections show the robustness of M-SEM against artifacts produced by crosstalk between different shots. A single point scatterer in a homogeneous velocity medium is imaged with more spatial components with respect to L-SEM and, at the same time, the distortion of its spatial spectrum is less significant with respect

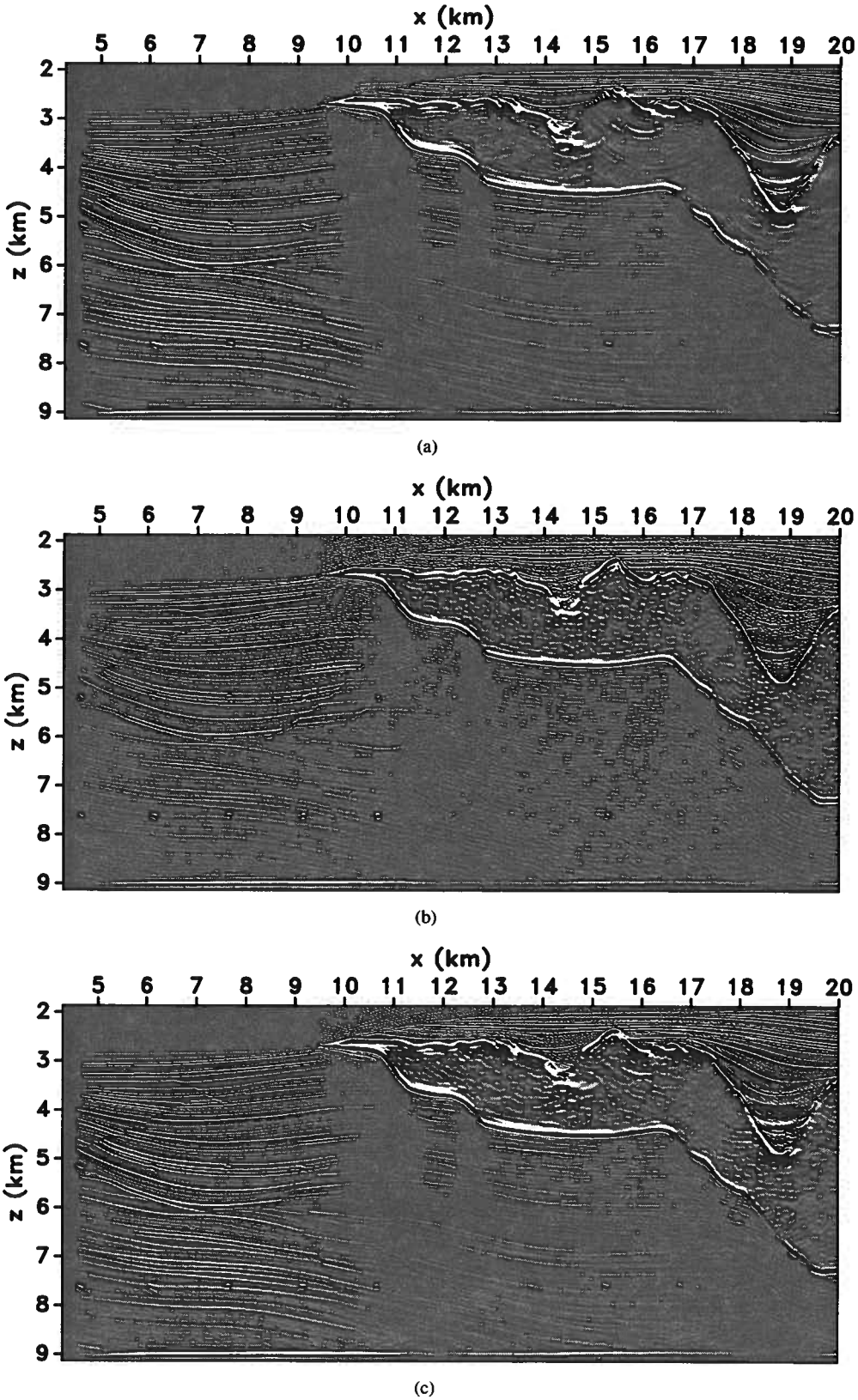

Figure 12. Sigsbee dataset migrated using different encoding schemes: (a) L-SEM, (b) R-SEM, and (c) M-SEM. 50 synthetic experiments have been used for each encoding method.

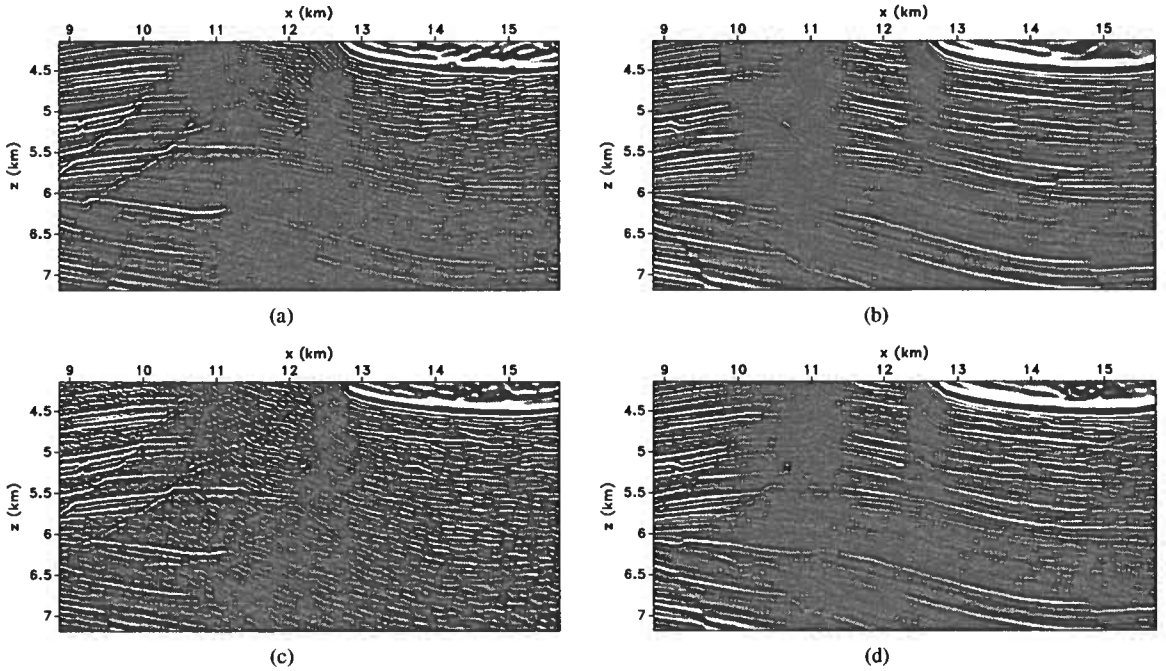

Figure 13. Image detail below the salt body: (a) SRM, (b) L-SEM, (c) R-SEM, and (d) M-SEM. The undersampling of the shot dimension is particularly important below the salt bodies and results in residual diffraction events that distort the image. L-SEM images correctly flat events but loses the fault information and the point diffractors. R-SEM reconstructs the complete spatial information but introduces crosstalk noise below the salt, where illumination is poor. M-SEM obtains a clearer image, with respect to R-SEM, better images the faults and the point diffractors, compared with L-SEM, and achieves an interpretable image below the salt, differently from the undersampled SRM.

to R-SEM. Hence, with M-SEM we span the domain in between the two extremal strategies represented by L-SEM and R-SEM.

This result gives us confidence about the success of M-SEM when applied to imaging in complex velocity models. Indeed, in a heterogeneous velocity field, L-SEM also produces important artifacts caused by the distortion of the planar wavefront and triplications of the wavefield. The delay incoherence, typical for R-SEM, is useful in recovering full bandwidth and effective in destroying the coherence of the artifacts in the migrated image.

The effectiveness of the encoding is directly related to the behavior of the crosstalk matrix. In order to be completely free from artifacts, the sequence of crosstalk matrices must tend to the identity. The encoding problem can then be rephrased in terms of approximation to the identity. In this section, we analyze in greater detail why M-SEM is more effective in imaging in complex velocity models.

The crosstalk term W_{kl} for the three encodings presented in the previous sections is

$$W_{kl}^{L} = \sum_{\theta} e^{i\omega \mathbf{p}_\theta (\mathbf{x}_l - \mathbf{x}_k)}, \tag{13}$$

$$W_{kl}^{R} = \sum_{\theta} e^{i\omega [t_l^\theta - t_k^\theta]}, \tag{14}$$

$$W_{kl}^{M} = \sum_{\theta} e^{i\omega [\mathbf{p}_\theta (\mathbf{x}_l - \mathbf{x}_k) + (t_l^\theta - t_k^\theta)]}, \tag{15}$$

for L-SEM, R-SEM and M-SEM, respectively. In the case of L-SEM and R-SEM, equations 13 and 14 actually approximate the identity but from very different points of view. In the first case, the completeness of the Fourier basis functions is invoked; in the second case, the uncorrelation of delays and artifacts, in the data and the final image, respectively, yields the result. W_{kl}^{L} converges slowly and smoothly toward the identity operator but does not introduce strong artifacts; on the other hand, W_{kl}^{R} converges toward the identity matrix by attenuating the random out-of-diagonal terms. The out-of-diagonal terms contribute strong crosstalk, which is iteratively reduced by stacking different synthetic experiments obtained from different random delay realizations.

The crosstalk matrix for M-SEM in equation 15 can be rewritten as follows:

$$W_{kl}^{M} = \sum_{\theta} e^{i\omega [\mathbf{p}_\theta \Delta \mathbf{x}_{kl} + \Delta t_{kl}^\theta]}; \tag{16}$$

separating the terms for $k = l$ and collecting $\Delta \mathbf{x}_{kl}$ in the exponent, yields

$$W_{kl}^{M} = M\delta_{kl} + (1 - \delta_{kl}) \sum_{\theta} e^{i\omega \left[\left(\mathbf{p}_\theta + \frac{\Delta t_{kl}^\theta}{\Delta \mathbf{x}_{kl}} \right) \Delta \mathbf{x}_{kl} \right]}. \tag{17}$$

The ratio $\frac{\Delta t_{kl}^\theta}{\Delta \mathbf{x}_{kl}}$ has the dimensions of a ray parameter

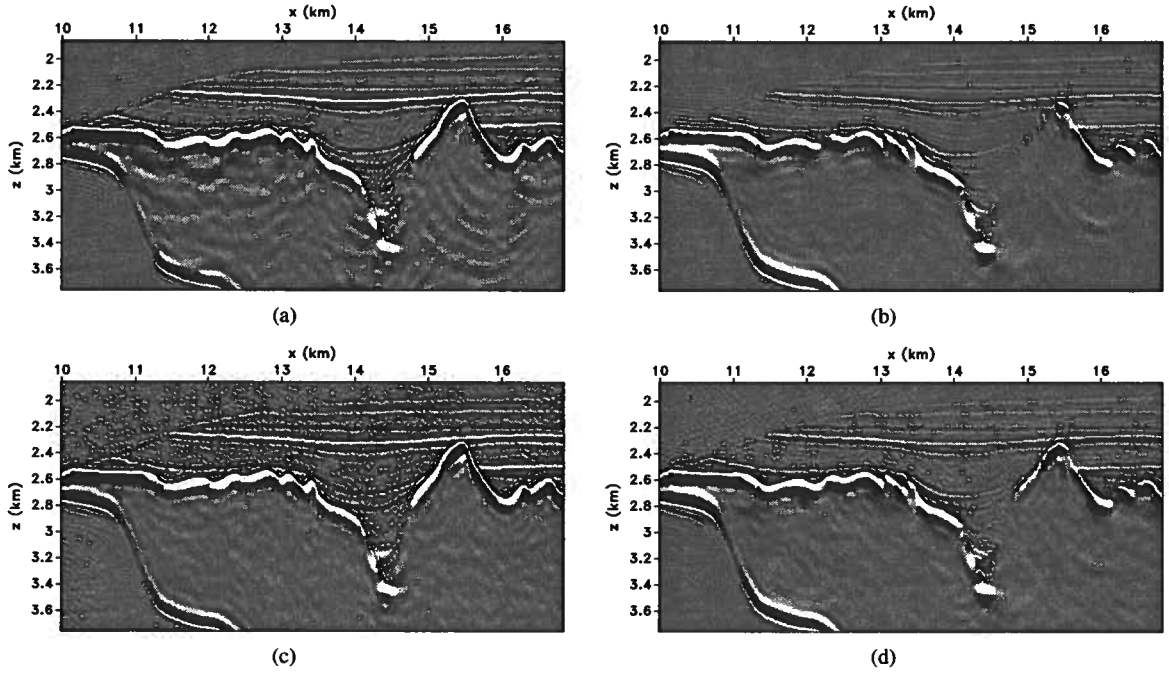

Figure 14. Image detail above the salt body: (a) SRM, (b) L-SEM, (c) R-SEM, and (d) M-SEM. The SRM presents correlated noise due to the undersampling of the shot dimension. L-SEM is able to very well recover nearly horizontal events, but the top of salt is smoothed out and the steep flank of salt canyon are not well imaged. R-SEM introduces random-like noise but images correctly the structures and the rugose top of the salt. M-SEM reduces the crosstalk, images correctly the almost horizontal events and obtains a better image of the top of the salt.

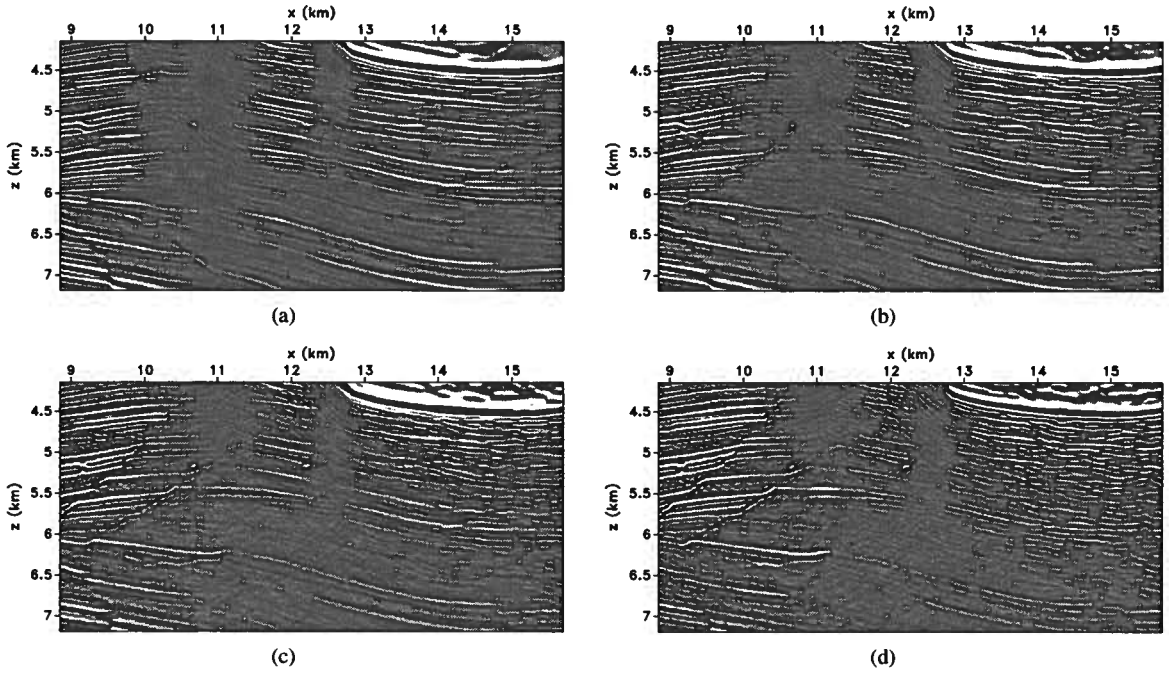

Figure 15. Effects of the amount of dithering on the image: (a) L-SEM, (b) 0.5%, (c) 1% and (d) 10% of the maximum delay. We observe the smooth increase of both spatial detail and crosstalk noise, especially subsalt.

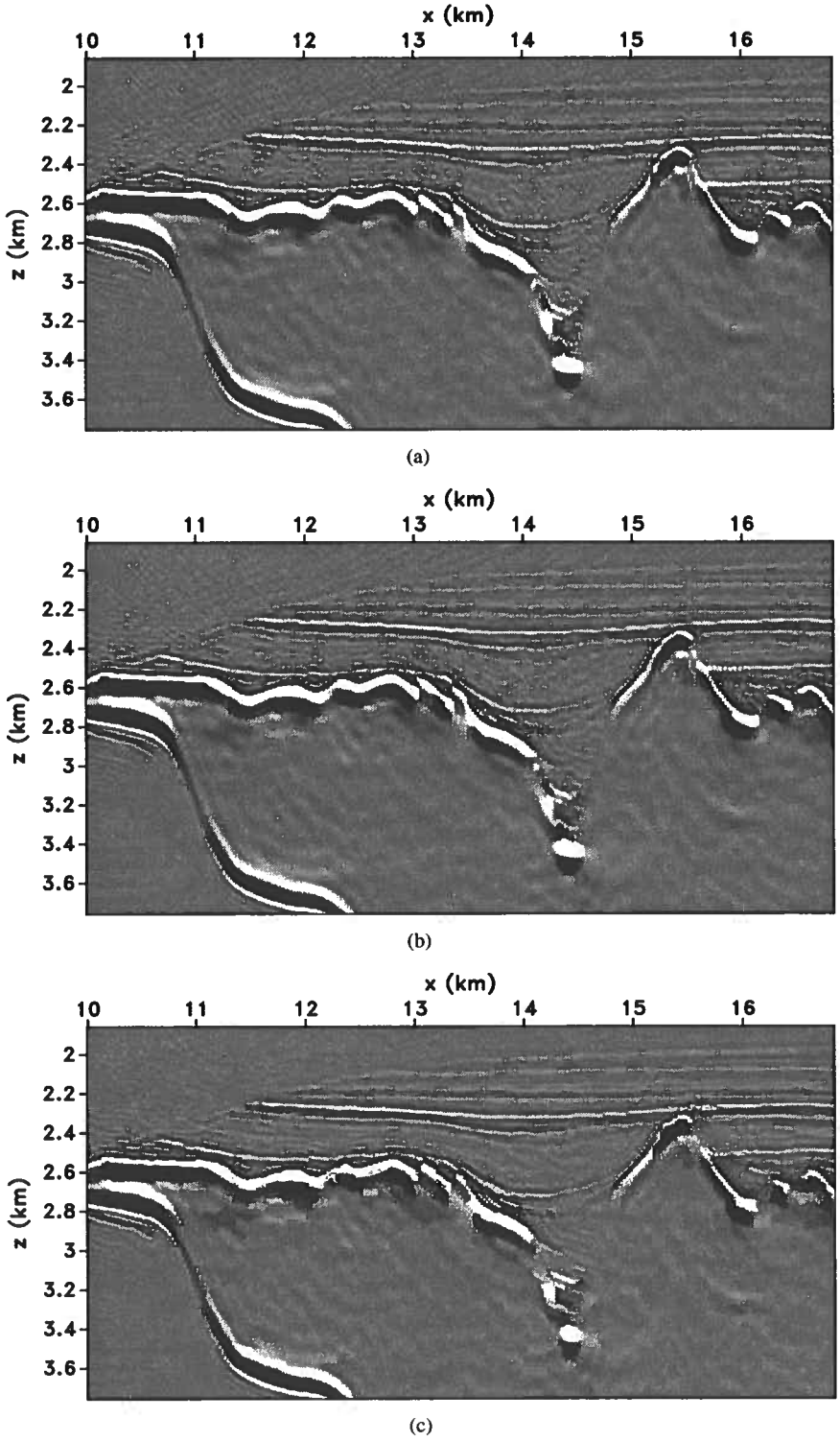

Figure 16. Results after denoising. (a) M-SEM image detail above the salt body. Both (b) seislet transform denoising and (c) nonlinear structure enhancing algorithm are effective in removing incoherent noise where the dip field of the image is slowly varying. If conflicting dips are present, the image is distorted; observe the flank of the salt canyon.

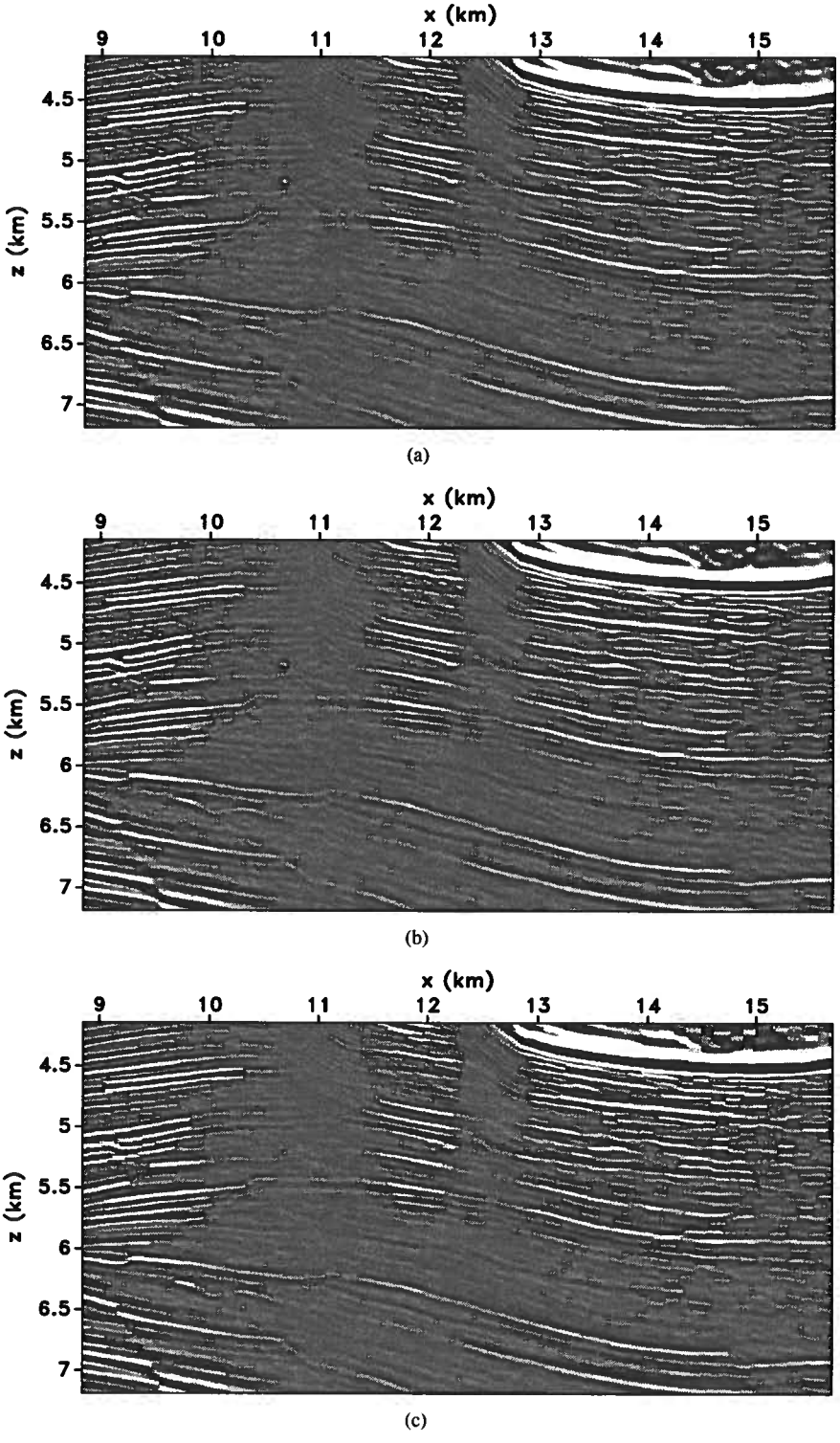

Figure 17. Results after denoising. (a) M-SEM image detail below the salt body. In poorly illuminated areas, crosstalk is hardly distinguishable from the signal. (b) seislet transform denoising removes high scale noise but does not affect the image below the salt body; (c) nonlinear structure enhancing algorithm boosts amplitude differences, sharpening faults, but cancels the point diffractors.

and can be viewed as a perturbation of the the plane-wave ray parameter $\mathbf{p}_\theta$. Note that the perturbation varies spatially since it depends on $\Delta\mathbf{x}_{kl}$; the non-stationary nature of the ratio $\frac{\Delta t^\theta_{kl}}{\Delta \mathbf{x}_{kl}}$ allows us to gain spatial resolution with respect to standard plane-wave migration, since a greater number of "equivalent" spatial components $p^{eq}_\theta = \mathbf{p}_\theta + \frac{\Delta t^\theta_{kl}}{\Delta \mathbf{x}_{kl}}$ is imaged; however, it also introduces a disturbance in the convergence of the crosstalk matrix toward the identity operator, i.e., random-like artifacts in the final image.

Let us consider two limit cases. If $\Delta\mathbf{x}_{kl}$ is "small", i.e., if we are close to one particular shot location, we have

$$p^{eq}_\theta = \mathbf{p}_\theta + \frac{\Delta t^\theta_{kl}}{\Delta \mathbf{x}_{kl}} \longrightarrow \frac{\Delta t^\theta_{kl}}{\Delta \mathbf{x}_{kl}}; \tag{18}$$

on the other hand, if $\Delta\mathbf{x}_{kl}$ is "large", i.e., if we are considering the mutual influence of two distant shots, we have

$$p^{eq}_\theta = \mathbf{p}_\theta + \frac{\Delta t^\theta_{kl}}{\Delta \mathbf{x}_{kl}} \longrightarrow \frac{\sin(\alpha\theta)}{v}. \tag{19}$$

Mixed shot-encoding behaves like R-SEM (see equation 18) when we consider neighboring shots, and resembles L-SEM when we look at the effects on a particular shot from more distant ones (see equation 19). This different behavior explains the increase in the spatial resolution (with respect to L-SEM) and the decrease in crosstalk (with respect to R-SEM) that M-SEM is able to achieve.

The analysis of the distribution of the resulting random variable $\frac{\Delta t^\theta_{kl}}{\Delta \mathbf{x}_{kl}}$ is not straightforward; even though we can intuitively understand $\frac{\Delta t^\theta_{kl}}{\Delta \mathbf{x}_{kl}}$ as a random perturbation of a fixed ray parameter p_θ, this perturbation is now spatially-varying along the shot positions because of the term $\Delta\mathbf{x}_{kl}$. This is counterintuitive since we usually associate a ray parameter with a planar wavefront rather than with one that is dithered and not well-defined.

An alternative way of looking at this is to imagine simultaneously migrating a bundle of plane-waves which are randomly taken in the neighborhood of a given p_θ. Actually, M-SEM images more plane-wave components than L-SEM; indeed, it images all the plane-wave components but with uneven relative amplitudes. This conclusion emerges from Figure 8(c): at the surface, M-SEM constructs not only the basis plane waves synthesized in L-SEM, but also plane-wave components outside the limited range of plane-wave migration. The amplitudes are lower and uneven because the additional plane-wave components are obtained in a statistical, rather than deterministic way. Nonetheless, by constraining the random fluctuations of these components, we can reduce the artifacts in the image without limiting the spatial bandwidth. Moreover, if we are able to shape the profile of plane-wave components synthesized at the surface, we can aim to further decrease the crosstalk noise. Considering the L-SEM result as a benchmark for spatial bandwidth and crosstalk, we can evaluate the effects of the amount of dithering on the crosstalk in the final image. We experimentally found that a dithering of 0.5% of the maximum delay is sufficient for spatial details to emerge (compare Figure 15(b) and 15(a)) in areas with poor illumination.

The illumination pattern varies smoothly with the perturbation of the planar wavefront; the amplitudes in the image are distorted with respect to shot-record migration but most of the geometrical and structural information is reliably recovered, although point scatterers and highly corrugated salt boundaries may be smoothed off. In areas with good illumination, if we increase the dithering, we obtain amplitudes that are closer to shot-record migration. On the other hand, in areas with poor illumination, the signal-to-crosstalk ratio is low and reflectors cannot be interpreted (see Figure 15(c) and 15(d) below the salt body).

Fixing the maximum delay, we analyze the different encodings at equal computational cost. M-SEM recovers more spatial components than L-SEM and controls the crosstalk that R-SEM alone would produce. The results on the Sigsbee dataset prove that M-SEM converges faster than both R-SEM and L-SEM toward an image of comparable quality to the one obtained by shot-record migration; 50 synthetic experiments are sufficient for recovering the structural information of the image, and the overall cost of the imaging step is 10% of standard shot-record migration. For the Sigsbee dataset, we consider take-off angles from -14 to 14 degrees, a central frequency $f = 15$ Hz, and a source spacing of 45 m; if the expression in Zhang et al. (2005) for the minimum number of $\mathbf{p}$ components had been used, at least 109 $\mathbf{p}$ components would have been necessary for correctly reconstructing the data. However, we used only 50 dithered plane waves. The dithering allows one to overcome both the limitation in the recoverable spatial bandwidth of the image and the $\mathbf{p}$ component sampling requirements for correctly representing the data. Moreover, since all the shots are encoded in every synthetic experiment, the shot dimension is not undersampled, and no residual diffraction (caused by the aperture limitation of the single shot) is imaged.

5 CONCLUSIONS

We design a hybrid encoding scheme, which we refer to as mixed shot-encoding, that combines the characteristics of linear and random shot-encoding in order to move across the space defined by spatial bandwidth and crosstalk at fixed computational cost. We analyze the behavior of the shot coupling term and test mixed shot-encoding migration on the Sigsbee dataset, verifying the effectiveness of the algorithm. Dithering a planar wavefront, we increase the spatial bandwidth of a single image with respect to linear shot-encoding, and we introduce weaker crosstalk noise with regard to random-shot encoding. We investigate the effects of the amount of dithering on the final image and verify that one can move smoothly for one extremum, L-SEM, to the other extremum, R-SEM. The migrated image results highly sensitive to dithering. Very little perturbation of the wavefront has significant impact on the final image; in particular, the spatial bandwidth increases faster than crosstalk and a relatively small dithering allows one to recover spatial bandwidth without introducing strong artifacts.

We test the effectiveness of postprocessing denoising for enhancing the structural information in the encoded image and for removing the residual crosstalk noise. In general, denoising performs well in areas with good illumination. In areas with poor illumination, the crosstalk is not distinguishable from the signal and denoising becomes ineffective.

There are several possibilities for further research: 1) an accurate analysis of the convergence rate toward shot-record migration will help in estimating the computational cost gain we can achieve through mixed shot-encoding migration; 2) a statistical analysis of the artifacts can provide indications for designing more sophisticated encoding schemes; 3) shaping of the amplitude spectrum of the migrated plane-wave components can further reduce the crosstalk noise in the image; 4) a parallel research direction is the design of denoising strategies based on adaptive subtraction of the artifacts after remodeling of the data. Finally, if the crosstalk is sufficiently under control, i.e., the signal-to-crosstalk ratio is high, mixed shot-encoding migration produces image gathers that can be used for migration velocity analysis.

6 ACKNOWLEDGMENTS

We would like to acknowledge the financial support provided by a research grant from Eni E&P and stimulating technical discussions with Clara Andreoletti and Nicola Bienati. The reproducible numeric examples in this paper use the Madagascar open-source software package freely available from http://www.reproducibility.org.

REFERENCES

Baysal, E., Kosloff, D. D., and Sherwood, J. W. C., 1983, Reverse time migration: Geophysics, **48**, no. 11, 1514–1524.

Berkhout, A. J., Verschuur, D. J., and Blacquière, G., 2009, Seismic imaging with incoherent wavefields: Seismic imaging with incoherent wavefields:, Soc. of Expl. Geophys., 79th Ann. Internat. Mtg., 2894–2898.

Berkhout, A. J., 2008, Changing the mindset in seismic acquisition: The Leading Edge, , no. 27, 924–938.

Claerbout, J. F., 1985, Imaging the earth's interior: , Blackwell Publishing.

Etgen, J., 2005, How many angles do we *really* need for delayed-shot migration?: How many angles do we *really* need for delayed-shot migration?:, Soc. of Expl. Geophys., 75th Ann. Internat. Mtg., 1985–1988.

Fomel, S., 2002, Applications of plane-wave destruction filters: Geophysics, **67**, no. 6, 1946–1960.

Fomel, S., 2006, Towards the seislet transform: Towards the seislet transform:, Soc. of Expl. Geophys., 76th Ann. Internat. Mtg., 2847–2850.

Lailly, P., 1983, The seismic inverse problem as a sequence of before stack migrations *in* Bednar, J. B., Redner, R., Robinson, E., and Weglein, A., Eds., Conference on inverse scattering: Theory and Applications:: SIAM, 206–220.

Liu, F., Hanson, D. W., Whitmore, N. D., Day, R. S., and Stolt, R. H., 2006, Toward a unified analysis for source plane wave migration: Geophysics, **71**, no. 4, S129–S139.

Liu, Y., Fomel, S., and Liu, G., 2009, Nonlinear structure-enhancing filtering using plane-wave prediction: Nonlinear structure-enhancing filtering using plane-wave prediction:, EAGE, Conference and Exhibition.

Morton, S. A., and Ober, C. C., 1998, Faster shot-record migrations using phase encoding: Faster shot-record migrations using phase encoding:, Soc. of Expl. Geophys., 68th Ann. Internat. Mtg, 1131–1134.

Rickett, J., and Sava, P., 2002, Offset and angle-domain common image-point gathers for shot-profile migration: Geophysics, **67**, 883–889.

Romero, L. A., Ghiglia, D. C., Ober, C. C., and Morton, S. A., 2000, Phase encoding of shot records in prestack migration: Geophysics, **65**, no. 02, 426–436.

Sava, P. C., and Fomel, S., 2003, Angle-domain common-image gathers by wavefield continuation methods: Geophysics, **68**, 1065–1074.

Soubaras, R., 2006, Modulated-shot migration: Modulated-shot migration:, Soc. of Expl. Geophys., 76th Ann. Internat. Mtg., 2430–2433.

Stolk, C. C., and de Hoop, M. V., Seismic inverse scattering in the "wave-equation" approach:, Technical Report CWP-417, Center for Wave Phenomena, Colorado School of Mines, 2001.

Stolk, C. C., and Symes, W. W., 2004, Kinematic artifacts in prestack depth migration: Geophysics, **69**, no. 2, 562–575.

Stork, C., and Kapoor, J., 2004, How many P values do you want to migrate for delayed shot wave equation migration?: How many P values do you want to migrate for delayed shot wave equation migration?:, Soc. of Expl. Geophys., 74th Ann. Internat. Mtg., 1041–1044.

Tang, Y., and Biondi, B., 2009, Least-squares migration/inversion of blended data: Least-squares migration/inversion of blended data:, Soc. of Expl. Geophys., 79th Ann. Internat. Mtg., 2859–2863.

Verschuur, D. J., and Berkhout, A. J., 2009, Target-oriented, least-squares imaging of blended data: Target-oriented, least-squares imaging of blended data:, Soc. of Expl. Geophys., 79th Ann. Internat. Mtg., 2889–2893.

Whitmore, N., 1995, An imaging hierarchy for common-angle plane wave seismograms: , PhD thesis, University of Tulsa.

Zhang, Y., Sun, J., C.Notfors, Gray, S. H., Chernis, L., and Young, J., 2005, Delayed-shot 3d depth migration: Geophysics, **70**, no. 5, E21–E28.

Zhang, Y., Sun, J., and Gray, S., 2007, Reverse-time migration: amplitude and implementation issues: Reverse-time migration: amplitude and implementation issues:, Soc. of Expl. Geophys., 77th Ann. Internat. Mtg., 2145–2148.

Nonlinear extended wave-equation imaging by image-domain seismic interferometry

Ivan Vasconcelos[1], Paul Sava[2] & Huub Douma[1]
[1] *ION Geophysical, GXT Imaging Solutions.*
[2] *Center for Wave Phenomena, Colorado School of Mines*

ABSTRACT
Wave-equation, finite-frequency imaging and inversion still faces considerable challenges in addressing the inversion of highly complex velocity models as well as in dealing with nonlinear imaging (e.g., migration of multiples, amplitude-preserving migration). Extended images (EI's), as we present here, are particularly important for designing image-domain objective functions aimed at addressing standing issues in seismic imaging such as two-way migration velocity inversion or imaging/inversion using multiples. Using general two- and one-way representations for scattered wavefields, we describe and analyze EI's obtained in wave-equation imaging. The presented formulation explicitly connects the wavefield correlations done in seismic imaging with the theory and practice of seismic interferometry. We define extended images as locally scattered fields reconstructed by model-dependent, image-domain interferometry. Because we use the same two- and one-way scattering representations that are used for seismic interferometry, the reciprocity-based EI's can in principle account for all possible nonlinear effects in the imaging process, i.e., migration of multiples, amplitude corrections, etc. In that case, the practice of two-way imaging departs considerably from that of the one-way approach. Here we elaborate on the differences between these approaches in the context of nonlinear imaging, describing these differences both in the wavefield extrapolation steps as well as in imposing the extended imaging conditions. When invoking single-scattering and ignoring amplitude effects in generating EI's, the one- and two-way approaches become essentially the same as those employed in today's migration practice, with the straightforward addition of space- and time-lags in the correlation-based imaging condition. Our formal description of the EI's and the insight that they are scattered fields in the image-domain may be useful in further development of imaging and inversion methods: either in the context of linear, migration-based velocity inversion, or in more sophisticated image-domain nonlinear inverse scattering approaches.

Key words: Inverse scattering, wave equation, imaging, interferometry.

1 INTRODUCTION

Seismic imaging and model estimation still present daunting challenges to the geophysical community when it comes to dealing with areas of high structural complexity or in making use of nonlinear scattering present in the data (in the form of e.g., multiples or amplitude effects). One avenue to address these challenges are the so-called full-waveform inversion methods (e.g., Tarantola, 1984; Pratt, 1999; Sirgue and Pratt, 2004; Plessix, 2006; Tape et al., 2009; Zhu et al., 2009). These methods operate by finding models that best fit the recorded data, and although in principle they are well suited to handle nonlinear scattering effects in the data, waveform inversion methods are notoriously ill-posed in terms of their sensitivity to the choice of starting models. An al-

ternative to deal with the ill-posedness of data-domain nonlinear inversions such as waveform inversion or inverse scattering approaches (e.g., Rose et al., 1985; Budreck and Rose, 1990; Weglein et al., 2003) is to set up the inverse problem in the subsurface image domain (e.g., de Hoop et al., 2006; Symes 2008, 2009). These approaches have demonstrated their potential for linear, wave-equation migration-based velocity inversion (e.g., Chauris, 2000; Mulder and Ten Kroode, 2002; Sava and Biondi, 2004). A key element that is necessary for image-domain finite-frequency inversion methods is the analysis of subsurface image gathers. Extended images (EI's; see Sava and Vasconcelos, 2010), as we describe in this paper, are an extension of traditional subsurface-domain image gathers. As such, our objective with this paper is to provide formalism and insight regarding one- and two-way EI's that will serve as the basis for the development of image-domain inversion approaches.

Most wave-equation-based imaging methods rely on the cross-correlation of source and receiver wavefields to invoke the zero time-lag and zero space-lag imaging condition (e.g., Claerbout, 1971,1985). This imaging condition has recently been extended by correlating wavefields with non-zero lags in the spatial coordinates also (Sava and Fomel, 2003). This allows, for example, studying the dependence of the image gathers on the velocity used in wave-equation-based imaging. Besides allowing for lags in the spatial coordinates when calculating the cross correlations, one can also allow for non-zero lags in the time variable (Rickett and Sava, 2002; Sava and Fomel, 2006; Sava and Vasconcelos, 2009). We refer to the images obtained using non-zero lags in both the spatial and time variables as extended images.

In seismic interferometry the cross-correlation of wavefields received at two receivers allows the extraction of the response between these receivers as if one of them acts as a source (e.g., Claerbout, 1968; Fink, 1997; Rickett and Claerbout, 1999; Weaver and Lobkis, 2001; Campillo and Paul, 2003; Wapenaar, 2004; Schuster et al., 2004; Curtis et al., 2006; Wapenaar et al., 2006, and references therein; Wapenaar et al., 2010). Representation theorems for the scattered field traveling from one point inside the medium to another can be found using scattering reciprocity relations (Wapenaar, 2007; Wapenaar et al., 2008; Vasconcelos et al., 2009). These theorems contain surface integrals like those used in seismic interferometry. Since an image of a scatterer can be obtained by collapsing the recorded scattered wavefield onto the scatterer location, this formulation based on scattering representations can be used to interpret the imaging condition in the context of seismic interferometry (Vasconcelos, 2008): the image is the zero-time scattered-wave response generated by zero-offset pseudo-experiments in the image domain. Here we expand on this notion of "image-domain interferometry" and show that the representation theorems for the scattered field allow the extended images to be described as scattered wavefields which are "excited" and recorded in the image domain. We show this for both the one-way and two-way wave equation formulations.

While explicitly defining EI's from exact two- and one-way scattering reciprocity theorems is the essence of our work in this manuscript, the integral representations as used for seismic interferometry are not entirely new to seismic imaging. Esmersoy and Oristaglio (1988) and Oristaglio (1989) used reciprocity integrals to formulate the wavefield extrapolation step in reverse-time double-focussing migration algorithms, while de Hoop and de Hoop (1995) also used general reciprocity relations to describe the data redatuming for imaging of general acoustic, elastic and electromagnetic fields. In the context of linear, Born-based migration/inversion reciprocity relations have also been used to describe wavefield extrapolation both for two-way (e.g., Clayton and Stolt, 1981; Stolt and Weglein, 1985) and one-way (e.g., Wapenaar et al., 1989; Thorbecke and Berkhout, 2006) imaging. Furthermore, van Manen et al. (2006) were the first to point out the relationship between seismic interferometry and the migration resolution function, which was then developed in detail by Thorbecke and Wapenaar (2007). Vasconcelos (2008) then followed with an explicit general representation of Claerbout's imaging condition (e.g., Claerbout, 1971, 1985) using scattering-based integral relations originally derived for seismic interferometry (Vasconcelos and Snieder, 2008; Vasconcelos et al., 2009a). More recently, Halliday and Curtis (2010) derived the formal link between imaging by double-focussing (Oristaglio, 1989) in terms of the scattering-based version of the source-receiver interferometry method by Curtis and Halliday (2010).

In this manuscript, we further explore the connection first established by Vasconcelos et al. (2009b) between wave-equation imaging and seismic interferometry for general scattering experiments for two-way as well as one-way propagation. We begin our discussion by defining EI's for both two- and one-way imaging explicitly as time- and space-dependent subsurface scattering experiments. Next, we use reciprocity theorems for two- (Vasconcelos et al., 2009a) and one-way scattering (Wapenaar et al., 2008) to provide formal description for the extended imaging conditions. We describe how to generate two- and one-way EI's both in terms of wavefield extrapolation step as well as in terms of evaluating the imaging conditions. Finally, we address the computation of EI's in the context of the single-scattering assumption and connect our reciprocity-based formulation to current practice in two- and one-way migrations.

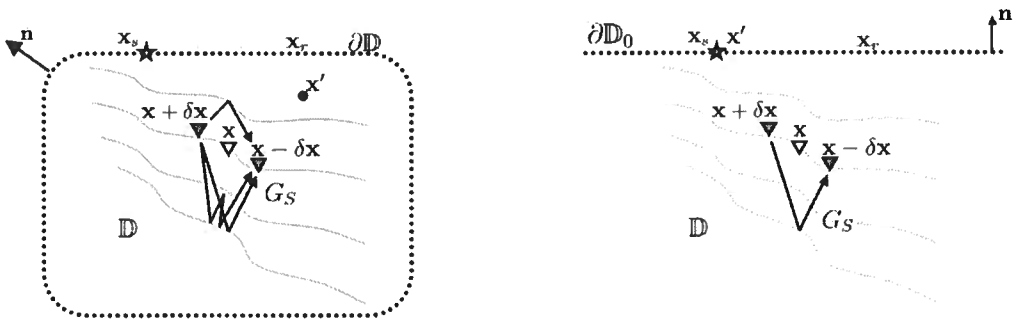

Figure 1. Cartoons illustrating geometries for two-way extended imaging using scattering reciprocity. The point $\mathbf{x}$ (white triangle) is an image point in the subsurface/model domain $\mathbb{D}$. The points $\mathbf{x}+\delta\mathbf{x}$ and $\mathbf{x}-\delta\mathbf{x}$ (grey triangles) are respectively the locations of pseudo-sources and pseudo-receivers in $\mathbb{D}$, that are displaced from $\mathbf{x}$ by a space lag $\delta\mathbf{x}$. $\mathbf{x}_s$ and $\mathbf{x}_r$ represent, respectively, the locations of the physical sources (stars) and receivers (black dots) used in the data acquisition. For each shot in $\mathbf{x}_s$, there are receivers $\mathbf{x}_r$ everywhere on $\partial\mathbb{D}$ or $\partial\mathbb{D}_0$; and the sources themselves also cover the same surfaces. The arrows represent the scattered-wave response G_S. The curved grey lines represent heterogeneity in the subsurface model (e.g., layering). Panel (a) depicts the most general case where the surface $\partial\mathbb{D}$ encloses the subsurface domain and the imaging-condition integration is conducted over $\mathbf{x}'$ in the volume $\mathbb{D}$ as well as on the surface. In panel (a), the subsurface model may contain sharp boundaries which are indicated by the solid grey lines. Panel (b) depicts the more conventional configuration for single-scattering, Born-based imaging where integration is typically conducted over $\mathbf{x}'$ on the open surface $\partial\mathbb{D}_0$, and where sharp model discontinuities are absent (indicated by the dashed grey lines).

2 DEFINING A WAVEFIELD-BASED IMAGE

2.1 Two-way extended images

An imaging condition for migration by wavefield extrapolation can be defined in terms of a scattered field G_S, as (Claerbout, 1971)

$$\mathcal{I}(\mathbf{x}) = G_S(\mathbf{x},\mathbf{x},\tau=0)\,. \tag{1}$$

According to this definition, the conventional image $\mathcal{I}(\mathbf{x})$ can be physically thought of a zero-offset scattered field for source and receiver coinciding at the image point $\mathbf{x}$, evaluated at zero time. Since waves in the subsurface travel with finite wavespeeds, the zero-offset scattered-wave response in equation 1 is zero when $\mathbf{x}$ is away from scatterers or interfaces, and it is finite when the image point is at a scatterer or interface. Thus, it is the principle of causality that makes the image in equation 1 physically suitable for the mapping of discontinuities in the subsurface.

Based on the definition in equation 1, an extended image (EI) can be readily defined by evaluating the scattered field G_S for finite source-receiver offsets and at nonzero times, that is

$$\mathcal{I}_e(\mathbf{x},\delta\mathbf{x},\tau) = G_S(\mathbf{x}+\delta\mathbf{x},\mathbf{x},\tau)\,, \tag{2}$$

where $\delta\mathbf{x}$ and τ can be thought of as space and time lags, respectively. Note that equation 2 states that the extended image $\mathcal{I}_e$ corresponds to the scattered-wave response excited by a source at the image point $\mathbf{x}$ and recorded by receivers at $\mathbf{x}+\delta\mathbf{x}$ at time τ. Since there are no real physical excitations or observations inside the subsurface, we shall from now on refer to them as "pseudo-sources" and "pseudo-receivers". In addition, it is possible to define other types of extended images with "pseudo-acquisition" geometries that are different than that in equation 2. While $\mathcal{I}_e$ in equation 2 represents a common-source-type geometry, defining $\mathcal{I}_e(\mathbf{x},\delta\mathbf{x},\tau) = G_S(\mathbf{x}+\delta\mathbf{x},\mathbf{x}-\delta\mathbf{x},\tau)$ generates a common-mid-point type of geometry, where the conventional image point $\mathbf{x}$ lies at the midpoint between pseudo-sources at $\mathbf{x}-\delta\mathbf{x}$ and pseudo-receivers at $\mathbf{x}+\delta\mathbf{x}$. An illustration of the latter can be found in figure 1. Equations 1 and 2 identify an image as a scattered wavefield, i.e., as a space- and time-dependent object that satisfies the partial differential equation (PDE)

$$\hat{\mathcal{L}}\,\hat{\mathcal{I}}_e = -\mathcal{V}\,\hat{G}_0\,, \tag{3}$$

where $\hat{G}_0$ are frequency-domain Green's functions, $\hat{\mathcal{L}}(\mathbf{x})$ is a wave-equation operator, e.g., $\hat{\mathcal{L}}(\mathbf{x}) = \nabla^2 + c^{-2}(\mathbf{x})\,\omega^2$, and $\mathcal{V}(\mathbf{x})$ is a scattering operator, e.g., given $\hat{\mathcal{L}}_0(\mathbf{x}) = \nabla^2 + c_0^{-2}(\mathbf{x})\,\omega^2$, $\mathcal{V} = \hat{\mathcal{L}}(\mathbf{x}) - \hat{\mathcal{L}}_0(\mathbf{x}) = \omega^2\left[c^{-2}(\mathbf{x}) - c_0^{-2}(\mathbf{x})\right]$. Here, $c(\mathbf{x})$ and $c_0(\mathbf{x})$ pertain to the perturbed and reference subsurface wavespeed models, respectively. Since it follows from the definition of $\mathcal{V}$ that $\mathcal{L} = \mathcal{L}_0 + \mathcal{V}$, we point out that $\hat{\mathcal{I}}_e$ in equation 3 is nonlinear on $\mathcal{V}$. This means that the extended images

based on the definitions in equations 1 through 3 properly take the effects of multiple scattering into account.

It is important to note that the scattering potential $\mathcal{V}$ can be defined arbitrarily. The most common definition in migration/imaging literature (e.g., Oristaglio, 1989; Weglein, 2003; Symes, 2009) is that $c = c_0 + \delta c$ is comprised of a smooth background c_0 and of sharp discontinuities δc (i.e., the singular part of the model). Under this definition, $\mathcal{V}$ thus becomes an operator that accounts for the singularities in the scattered wavefields G_S. We will also use this definition in the context of this manuscript, but we point out that $\mathcal{V}$ can also be defined in other ways, e.g., as a smooth time-lapse change, or by incorporating attenuation (e.g., Vasconcelos et al., 2009).

2.2 One-way extended images

In the context of one-way wave propagation (e.g., Claerbout, 1971; Fishman and McCoy, 1984; Wapenaar et al., 2001; de Hoop et al., 2003), an extended image can be defined as

$$I_e(\mathbf{x}, \delta\mathbf{x}, \tau) = R_0^+(\mathbf{x} + \delta\mathbf{x}, \mathbf{x}, \tau)\,. \tag{4}$$

where $R_0^+(\mathbf{x}+\delta\mathbf{x}, \mathbf{x}, \tau)$ is the finite-time up-going reflectivity response to a downgoing field p^+ (Wapenaar et al., 2004; Wapenaar et al. 2008), for pseudo-sources at the image point $\mathbf{x}$ and pseudo-receivers at $\mathbf{x} + \delta\mathbf{x}$ within the subsurface (see figure 2). Similar to the definition of two-way extended images in terms of G_S in equation 2, the image I_e is also a space- and time-dependent, wavefield-like object. As with the two-way case, equation 4 is a straightforward extension of the classical definition of a subsurface image as a zero-offset and zero-time reflectivity response (e.g., Claerbout, 1971), i.e. $I(\mathbf{x}) = R_0^+(\mathbf{x}, \mathbf{x}, \tau = 0)$.

Despite the similarities in their definitions, the one-way extended image defined via equation 4 is fundamentally different from the two-way image defined in equation 2. The first and most important difference lies in the meaning of these definitions. While it follows from the definition of the two-way EI in equation 2 that $\mathcal{I}_e$ satisfies the PDE in equation 3, the one-way I_e in equation 4 is the kernel operator of the integral equation (e.g., Wapenaar et al., 2004; Wapenaar et al. 2008)

$$\hat{p}^-(\mathbf{x}_d, \mathbf{x}_s, \omega) = \int_{\mathbf{x}_z \in \partial\mathbb{D}_d} \hat{R}_0^+(\mathbf{x}_d, \mathbf{x}_z, \omega)\hat{p}^+(\mathbf{x}_z, \mathbf{x}_s, \omega) d^2\mathbf{x}_z; \tag{5}$$

where $\{\mathbf{x}_d, \mathbf{x}_z\}$ are points in the subsurface plane $\partial\mathbb{D}_d$, and $\hat{p}^-(\mathbf{x}_d, \mathbf{x}_s, \omega)$ and $\hat{p}^+(\mathbf{x}_z, \mathbf{x}_s, \omega)$ are respectively up- and down-going fields recorded at depth due to sources at $\mathbf{x}_s$ on the surface plane $\partial\mathbb{D}_0$. This is illustrated in figure 2. The EI in equation 4 is obtained from $\hat{R}_0^+(\mathbf{x}_d, \mathbf{x}_z, \omega)$ by choosing $\mathbf{x}_z = \mathbf{x}$ and $\mathbf{x}_d = \mathbf{x} + \delta\mathbf{x}$ and after an inverse Fourier transform $\omega \mapsto \tau$. Therefore, while the two-way EI $\mathcal{I}_e$ in equation 2 is a scattered wavefield with physical dimensions (e.g., dimensions of pressure), its one-way counterpart I_e in equation 4 is a dimensionless operator. Furthermore, the decomposition that yields the up/down-separated fields $p^{+,-}$ imposes limitations on spatial aperture (e.g., leading to a decrease in accuracy toward horizontal directions) and ignores the effects of laterally-propagating or evanescent wave modes (e.g., Fishman and McCoy, 1984; Wapenaar et al., 2001); these restrictions do not apply to the two-way extended images described by equation 3. Finally, we note that the one-way EI describes only up-going, back-scattered responses between subsurface points, whereas the two-way EI defined in terms of G_S ideally retrieves both forward- and back-scattered waves with no directional restrictions. Therefore, while one-way EI's retrieve only upward propagating reflection responses, two-way EI's ideally can reconstruct both transmission and reflection responses between subsurface points.

3 EXTENDED IMAGES FROM SCATTERING RECIPROCITY

3.1 Two-way imaging conditions

After defining the two-way EI's according to equations 1 and 2, the next step is to formally define imaging conditions that retrieve images that comply to those definitions. Since our definitions rely on the retrieval of the scattered fields G_S, we can use integral scattering representations to obtain the desired images (e.g., Thorbecke and Wapenaar, 2007; Wapenaar, 2007; Vasconcelos, 2008; Vasconcelos et al., 2009b; Halliday and Curtis, 2010). These scattering representations are similar to those employed in seismic interferometry applications (e.g., Bakulin and Calvert, 2006; Wapenaar, 2007; Vasconcelos and Snieder, 2008).

The extended images $\mathcal{I}_e$ that follow from equation 2 can be obtained reconstructing the scattered field G_S for finite times and by allowing the source and receiver locations to be arbitrarily different (see discussion about equation 2 above). Assuming a common image point $\mathbf{x}$, we write the pseudo-source and receiver locations as $\mathbf{x} + \delta\mathbf{x}$ and $\mathbf{x} - \delta\mathbf{x}$ respectively (figure 1). Using the correlation-type scattering representation for G_S from Vasconcelos et al. (2009a) in equation 2 then gives (Vasconcelos et al., 2009b)

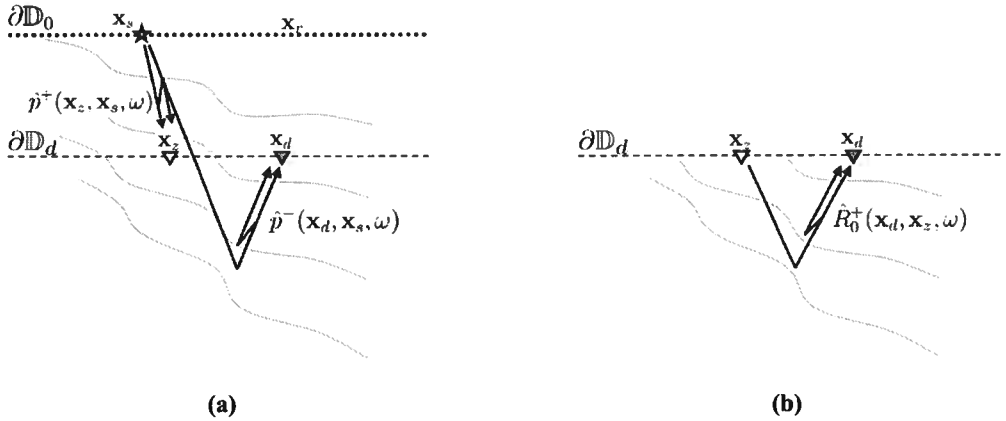

Figure 2. Cartoons illustrating geometries for one-way extended imaging using scattering reciprocity. As in Figure 1, $\mathbf{x}_s$ and $\mathbf{x}_r$ represent sources and receivers that cover the top acquisition surface $\partial\mathbb{D}_0$. $\mathbf{x}_z$ and $\mathbf{x}_d$ (depicted by triangles) are two arbitrary subsurface points that lie on the depth-domain surface $\partial\mathbb{D}_d$. In panel (a), $\hat{p}^{\pm}$ represent up- and down-going fields due to a source at $\mathbf{x}_s$ on $\partial\mathbb{D}_0$, and depth-extrapolated to $\partial\mathbb{D}_d$ from the data recorded by the receivers at all $\mathbf{x}_r \in \partial\mathbb{D}_0$ (black dots). $\hat{p}^{\pm}$ are the full up- or down-going wavefields that include all multiple arrival types. Panel (b) illustrates the up-going reflection impulse response $\hat{R}_0^+$ (equations 4 and 5) for a pseudo-source and a pseudo-receiver both on the depth-domain surface $\partial\mathbb{D}_d$, that contains all up-going primaries and multiples. Note that the response $\hat{R}_0^+$ corresponds to that of a medium that is heterogeneous below $\partial\mathbb{D}_d$ but is homogeneous above it.

$$
\begin{aligned}
\mathcal{I}_e(\mathbf{x},\delta\mathbf{x},\tau) \;&=\; G_S(\mathbf{x}-\delta\mathbf{x},\mathbf{x}+\delta\mathbf{x},t=\tau)\\
&=\int\Big(\oint_{\partial\mathbb{D}}\frac{F(\omega)}{i\omega\rho}\,\left[\nabla p_S(\mathbf{x}-\delta\mathbf{x},\mathbf{x}',\omega)\,p_0^*(\mathbf{x}+\delta\mathbf{x},\mathbf{x}',\omega)\right]\\
&\qquad\qquad\cdot\mathbf{n}\,d^2\mathbf{x}'\Big)\,e^{i\omega\tau}\,d\omega\\
&-\int\Big(\oint_{\partial\mathbb{D}}\frac{F(\omega)}{i\omega\rho}\,\left[p_S(\mathbf{x}-\delta\mathbf{x},\mathbf{x}',\omega)\,\nabla p_0^*(\mathbf{x}+\delta\mathbf{x},\mathbf{x}',\omega)\right]\\
&\qquad\qquad\cdot\mathbf{n}\,d^2\mathbf{x}'\Big)\,e^{i\omega\tau}\,d\omega\\
&+\int\Big(\int_{\mathbb{D}}\frac{F(\omega)}{i\omega\rho}\,p(\mathbf{x}-\delta\mathbf{x},\mathbf{x}',\omega)\,\mathcal{V}(\mathbf{x}')\,p_0^*(\mathbf{x}+\delta\mathbf{x},\mathbf{x}',\omega)\\
&\qquad\qquad d^3\mathbf{x}'\Big)e^{i\omega\tau}\,d\omega\,; \qquad (6)
\end{aligned}
$$

where ρ is density, p_0 is a reference pressure field, p_S are scattered pressure waves and $p = p_0 + p_S$. $F(\omega)$ is a deconvolution-type filter that turns the pressure fields p into impulse responses G. The pressure fields in the integrand require "sources" at $\mathbf{x}'$ to be everywhere on the surface $\partial\mathbb{D}$ as well as in the volume $\mathbb{D}$ (figure 1a). Also, the "observation" points $\mathbf{x}$ and $\mathbf{x} \pm \delta\mathbf{x}$ are also inside the model and do not correspond to physical recording locations. Since in practice we physically excite waves at $\mathbf{x}_s$ and record them at $\mathbf{x}_r$ on the boundary (figure 1), the wavefields in the integrands of equation 6 are obtained after wavefield extrapolation. We address the role of wavefield extrapolation in the next section. Halliday and Curtis (2010) also use equation 6 to arrive at a generalized formula for the scattered field for imaging where the p_S fields in the integrand are themselves replaced by another set of integrals in the context of the source-receiver interferometry formulation (Curtis and Halliday, 2010).

Once $\mathcal{I}_e$ is defined by equation 6, it is straightforward to obtain the conventional image $\mathcal{I}$ (equation 1) by setting constant $\delta\mathbf{x} = \mathbf{0}$ and $\tau = 0$, which thus yields

$$
\begin{aligned}
\mathcal{I}(\mathbf{x}) \;&=\; G_S(\mathbf{x},\mathbf{x},\tau=0)\\
&=\int\Big(\oint_{\partial\mathbb{D}}\frac{F(\omega)}{i\omega\rho}\,\left[\nabla p_S(\mathbf{x},\mathbf{x}',\omega)\,p_0^*(\mathbf{x},\mathbf{x}',\omega)\right]\cdot\mathbf{n}\,d^2\mathbf{x}'\Big)\,d\omega\\
&-\int\Big(\oint_{\partial\mathbb{D}}\frac{F(\omega)}{i\omega\rho}\,\left[p_S(\mathbf{x},\mathbf{x}',\omega)\,\nabla p_0^*(\mathbf{x},\mathbf{x}',\omega)\right]\cdot\mathbf{n}\,d^2\mathbf{x}'\Big)\,d\omega\\
&+\int\Big(\int_{\mathbb{D}}\frac{F(\omega)}{i\omega\rho}\,p(\mathbf{x},\mathbf{x}',\omega)\,\mathcal{V}(\mathbf{x}')\,p_0^*(\mathbf{x},\mathbf{x}',\omega)\,d^3\mathbf{x}'\Big)\,d\omega\,. \qquad (7)
\end{aligned}
$$

Although here we refer to this equation as a "conventional" image, we note that typical implementations of two-way imaging by, e.g. reverse-time migration, do not use the formulation above. We elaborate further on the differences between current migration/imaging practices and the equations above later in this manuscript.

The gradients terms in the integrands of equation 6 imply an implicit requirement for acquiring data with sources and receivers of both monopole and dipole type (e.g., Fokkema and van den Berg, 1993; Wapenaar and Fokkema, 2006). Since dipole (i.e., particle velocity) sources and receivers are seldom available in real-life seismic surveys, it is convenient to use the far-field approximation $\nabla p \cdot \mathbf{n} = i\omega c^{-1} p$ (e.g., Wapenaar and

$$\hat{R}_0^+(\mathbf{x}_d, \mathbf{x}_z, \omega) =$$

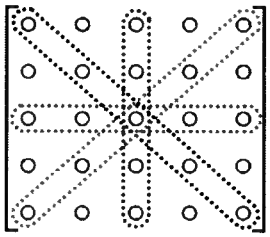

Figure 3. An illustration of the discrete operator $\hat{\mathbf{R}}_0^+ = \hat{R}_0^+(\mathbf{x}_d, \mathbf{x}_z, \omega)$ in matrix form, at a chosen $\partial\mathbb{D}_d$ (figure 2b) and for a fixed frequency ω. Each column of the matrix corresponds to a discrete pseudo-receiver location $\mathbf{x}_d$ and variable $\mathbf{x}_z$, whereas rows represent a fixed pseudo-source coordinate $\mathbf{x}_z$ and variable $\mathbf{x}_d$. The dotted contours highlight different choices of geometries of one-way extended images.

Fokkema, 2006) to recast equation 6 as

$$\begin{aligned}\mathcal{I}_e(\mathbf{x}, \delta\mathbf{x}, \tau) \;=\; & \\ \int\Big(\oint_{\partial\mathbb{D}} \frac{2F(\omega)}{\rho c}\, p_S(\mathbf{x}-\delta\mathbf{x}, \mathbf{x}', \omega) & \\ p_0^*(\mathbf{x}+\delta\mathbf{x}, \mathbf{x}', \omega)\Big) d^2\mathbf{x}'\, e^{i\omega\tau}\, d\omega & \\ + \int\Big(\int_{\mathbb{D}} \frac{F(\omega)}{i\omega\rho}\, p(\mathbf{x}-\delta\mathbf{x}, \mathbf{x}', \omega)\, \mathcal{V}(\mathbf{x}') & \\ p_0^*(\mathbf{x}+\delta\mathbf{x}, \mathbf{x}', \omega)\, d^3\mathbf{x}'\Big) e^{i\omega\tau}\, d\omega\,. & \end{aligned} \tag{8}$$

In the context of imaging conditions, as we point out above, the pressure fields in the integrands of equations 6 and 8 are obtained from wavefield extrapolation and not from direct physical experiments. When the fields in question are in fact direct measurements, then equations 6 and 8 above are the same as used for seismic interferometry applications (e.g., Bakulin and Calvert, 2006; Vasconcelos et al., 2009). It is important to note that in many of the interferometry applications (e.g., Bakulin and Calvert, 2006), the volume terms of equations 6 and 8 can be ignored (Vasconcelos et al., 2009a). For general imaging applications, however, the volume integrals cannot be ignored (Vasconcelos, 2008; Vasconcelos et al., 2009b; Halliday and Curtis, 2010). The connection between the calculation of extended images and seismic interferometry arises directly from the image definitions in equations 1 and 2 together with the use of scattering reciprocity integrals (e.g., Wapenaar, 2007; Vasconcelos, 2008; Vasconcelos et al., 2009b; Halliday and Curtis, 2010). A similar analogy exists for the one-way formulation as well (see below).

Given that the depth-domain fields $\hat{p}^-(\mathbf{x}_d, \mathbf{x}_s, \omega)$ and $\hat{p}^+(\mathbf{x}_z, \mathbf{x}_s, \omega)$ (equation 5 and figure 2) can be generated from the acquired data via wavefield extrapolation, extended images as defined in equation 4 can obtained by solving equation 5 for $\hat{R}_0^+$. The integral representation in equation 5 can also be expressed in discrete matrix-operator form, i.e., $\hat{\mathbf{P}}^- = \hat{\mathbf{R}}_0^+\, \hat{\mathbf{P}}^+$. Here the columns of the fixed-frequency matrices $\hat{\mathbf{P}}^\pm = \hat{\mathrm{P}}^\pm_{ij}$ contain $\hat{p}^\pm(\mathbf{x}, \mathbf{x}_i, \omega)$ for fixed source location $\mathbf{x}_i$ and variable receiver location $\mathbf{x}$, whereas the rows contain $\hat{p}^-(\mathbf{x}_j, \mathbf{x}, \omega)$ for fixed receiver location $\mathbf{x}_j$ and variable source location $\mathbf{x}$ at a particular fixed depth level. Figure 3 illustrates the operator $\hat{\mathbf{R}}_0^+ = \hat{R}_0^+(\mathbf{x}_d, \mathbf{x}_z, \omega)$ as a matrix for a chosen frequency.

A pseudo-inverse reflectivity operator $\bar{\mathbf{R}}_0^+$ can then be obtained from e.g. a regularized least-squares inversion as (e.g., Hansen, 1997; Wapenaar et al., 2008)

$$\bar{R}_0^+(\mathbf{x}_d, \mathbf{x}_z, \omega) = \bar{\mathbf{R}}_0^+ = \mathbf{P}^-(\mathbf{P}^+)^\dagger \left[\mathbf{P}^+(\mathbf{P}^+)^\dagger + \epsilon^2 \mathbf{\Lambda}\right]^{-1} \tag{9}$$

where † stands for the conjugate-transpose, $\mathbf{\Lambda}$ is a shaping/regularization operator and ϵ is a weighting factor. With appropriate choices for ϵ and $\mathbf{\Lambda}$, equation 9 can yield an acceptable estimate of the reflectivity operator, i.e., $\bar{\mathbf{R}}_0^+ \approx \hat{\mathbf{R}}_0^+$. To then obtain an extended image I_e (e.g., equation 4) from the reflectivity operator, one can simply select an appropriate subset of $\hat{\mathbf{R}}_0^+$. For example, selecting a row of the $\hat{\mathbf{R}}_0^+$ (green highlight in Figure 3) operator (figure 3) and choosing a fixed $\mathbf{x}_z = \mathbf{x}$ for variable $\mathbf{x}_d = \mathbf{x} + \delta\mathbf{x}$ yields precisely the extended image as defined by equation 4. This choice leads to an extended image of a common-source type of geometry, similarly to that discussed for the two-way case of equation 2. Conversely, extracting the columns of $\hat{\mathbf{R}}_0^+$ (blue highlight in Figure 3) would yield extended images with a pseudo-acquisition geometry of the common-receiver type. Another choice would be to extract the off-diagonal elements of $\hat{\mathbf{R}}_0^+$ (red highlight in Figure 3) by setting $\mathbf{x}_d = \mathbf{x} - \delta\mathbf{x}$ and $\mathbf{x}_z = \mathbf{x} + \delta\mathbf{x}$ for a fixed image point $\mathbf{x}$: this would then yield $I_e(\mathbf{x}, \delta\mathbf{x}, \tau) = R_0^+(\mathbf{x} - \delta\mathbf{x}, \mathbf{x} + \delta\mathbf{x}, \tau)$, i.e., an extended image with a common-midpoint type of geometry. This geometry would be the same as that of the two-way $\mathcal{I}_e$ described by equations 6 and 8 and illustrated in figure 1.

As with the two-way imaging conditions presented above, extended imaging based on the one-way reciprocity theorem in equation 5 is also directly related to the practice of seismic interferometry. Wapenaar et al. (2008) presented the method of interferometry by multidimensional deconvolution (MDD) that relies on equations 5 and 9 to estimate $\hat{\mathbf{R}}_0^+$ from observed up- and down-going fields.

The approach presented here is the same as that in Wapenaar et al. (2008) except that the fields used in the estimation of the reflectivity operator are depth extrapolated fields, as opposed to physically observed data as used in interferometry (figure 2).

4 WAVEFIELD EXTRAPOLATION FOR NONLINEAR EXTENDED IMAGES

4.1 Two-way extrapolation

While interferometry relies on observed fields p_0 and p_S (e.g., Bakulin and Calvert, 2006; Vasconcelos, 2008), in two-way wave-equation imaging (equation 8) these fields result from extrapolating (i.e., re-datuming) the fields recorded at the acquisition surface to the image point $\mathbf{x}$ (e.g., Claerbout, 1985; Sava and Vasconcelos, 2009). In imaging, $p_0(\mathbf{x},\mathbf{x}',\omega)$ (e.g. equation 8) are depth-extrapolated source wavefields, which translates to numerically solving the following initial value problem

$$\begin{cases} \hat{\mathcal{L}}_0\,\hat{p}_0 = 0, & \hat{p}_0 = \hat{p}_0(\mathbf{x},\mathbf{x}',\omega),\ \mathbf{x}\in\mathbb{D} \text{ and } \mathbf{x}'\in\mathbb{D}\cup\partial\mathbb{D}, \text{with} \\ p_0(\mathbf{x}_r,\mathbf{x}_s,t) = s(t)*\delta(\mathbf{x}_r-\mathbf{x}_s,\mathbf{x}_s,t) & \text{as I.C., for all } \mathbf{x}_{s,r}\in\partial\mathbb{D}; \end{cases} \tag{10}$$

where I.C. stands for "initial conditions", $\mathbf{x}_s$ and $\mathbf{x}_r$ are the acquisition source and receiver coordinates (figure 1a), δ is the Dirac delta, $s(t)$ is the time-domain source signature and $*$ stands for convolution. The problem in equation 10 is translated as forward modeling of each shot at $\mathbf{x}'=\mathbf{x}_s\in\partial\mathbb{D}$ to every point $\mathbf{x}$ inside $\mathbb{D}$ (figure 1a). In addition, based on the fields from surface sources recorded at every $\mathbf{x}\in\mathbb{D}$, the response from each $\mathbf{x}'$ *inside* $\mathbb{D}$ to every $\mathbf{x}\in\mathbb{D}$ must also be calculated. This latter step can be performed, for example, with the method by van Manen et al. (2005). Solving the initial value problem described by equation 10 results in the $\hat{p}_0(\mathbf{x},\mathbf{x}',\omega)$ fields required by the extended imaging condition in equation 8. This reference field p_0 is traditionally named "the source wavefield" in migration practice. The source wavefield calculation in equation 10 is analogous to that performed in current migration practice, with the additional step of modeling the response of sources that are also inside the subsurface. This additional step is necessary for the evaluation of the volume integral in equation 8.

The next step is to compute the scattered fields $\hat{p}_S(\mathbf{x},\mathbf{x}',\omega)$, or "the receiver wavefields", necessary for evaluating the integrands in equation 8. These are obtained by solving the boundary value problem

$$\begin{cases} \hat{\mathcal{L}}\,\hat{p}_S = -\mathcal{V}\,\hat{p}_0, & \hat{p}_S = \hat{p}_S(\mathbf{x},\mathbf{x}',\omega),\ \mathbf{x}\in\mathbb{D} \text{ and } \mathbf{x}'\in\mathbb{D}\cup\partial\mathbb{D}, \text{with} \\ \hat{p}_S(\mathbf{x}_r,\mathbf{x}_s,\omega) = \hat{d}^*_S(\mathbf{x}_r,\mathbf{x}_s,\omega) & \text{as B.C., for all } \mathbf{x}_{s,r}\in\partial\mathbb{D}. \end{cases} \tag{11}$$

where B.C. stands for "Boundary Conditions", which consist of $\hat{d}^*_S(\mathbf{x}_r,\mathbf{x}_s,\omega)$: the full, time-reversed scattered wavefield from the acquired common-shot data. It is important to note here that the receiver extrapolation approach in equation 11 differs from usual migration practice in three points. First, here the boundary value problem described in equation 11 solves the inhomogeneous PDE for scattered fields (e.g., equation 3) as opposed to a homogeneous wave equation (e.g. similar to that in equation 10). As a consequence, the source wavefield p_0 that resulted from solving the problem in equation 10 must in fact be used for extrapolating for the receiver or scattered wavefield p_S as described by the problem in equation 11. Second, receiver wavefield extrapolation according to equation 11 uses the operators $\mathcal{L}$ and $\mathcal{V}$ which differ from the smooth operator $\mathcal{L}_0$ used for the source wavefield (equation 10). In other words, the models used for source and receiver extrapolation are different. This allows for the modeling of multiples in the extrapolation of the receiver wavefields as the wavefields $\hat{p}_0$ and $\hat{p}_S$ are allowed to interact with the singularities in $\mathcal{L}$ and $\mathcal{V}$ (equation 11). Third, as with the source wavefield calculation above, the field $\hat{p}_S(\mathbf{x},\mathbf{x}',\omega)$ must be computed for $\mathbf{x}'\in\mathbb{D}$ in additional to surface sources only (i.e. $\mathbf{x}'=\mathbf{x}_s\in\partial\mathbb{D}$). In the formulation by Halliday and Curtis (2010), the extrapolation for the receiver wavefield p_S is analitically expressed in terms of scattering representation integrals (Vasconcelos et al., 2009a) and inserted into equation 6, as opposed to the boundary value problem approach we present here.

4.2 One-way extrapolation

Wavefield extrapolation for the generation of one-way extended images as discussed above is in fact similar to current practice in one-way migration. The depth-domain source wavefield $\mathbf{P}^+=\hat{p}^+(\mathbf{x}_z,\mathbf{x}_s,\omega)$ (equations 5 and 9) is generated via

$$\begin{cases} \mathbf{P}^+ = \mathbf{T}^+\,\mathbf{S}^+_0, & \text{with} \\ \mathbf{S}^+_0 = \hat{s}^+_0(\mathbf{x}_r,\mathbf{x}_s,\omega) = \delta(\mathbf{x}_r-\mathbf{x}_s,\mathbf{x}_s)\,s(\omega), & \text{for all } \{\mathbf{x}_s,\mathbf{x}_r\}\in\partial\mathbb{D}_0, \end{cases} \tag{12}$$

where $\mathbf{S}_0^+ = \hat{s}_0^+(\mathbf{x}_r, \mathbf{x}_s, \omega)$ are the source data at the acquisition surface (figure 2), $s(\omega)$ is the frequency-domain source excitation function and $\mathbf{T}^+$ is a modeling operator for down-going transmission that maps surface data at $\mathbf{x}_r \in \partial\mathbb{D}_0$ to subsurface-domain wavefields at $\mathbf{x}_z \in \partial\mathbb{D}_d$ (figure 2). In parallel with the source wavefield calculation in equation 12, the one-way receiver fields $\mathbf{P}^- = \hat{p}^-(\mathbf{x}_d, \mathbf{x}_s, \omega)$ (equations 5 and 9; figure 2) are obtained from

$$\begin{cases} \mathbf{P}^- = \left(\mathbf{T}^-\right)^{-1} \mathbf{D}_0^-, & \text{with} \\ \mathbf{D}_0^- = \hat{d}_0^-(\mathbf{x}_r, \mathbf{x}_s, \omega), & \text{for all } \{\mathbf{x}_s, \mathbf{x}_r\} \in \partial\mathbb{D}_0, \end{cases} \tag{13}$$

where $\mathbf{D}_0^- = \hat{d}_0^-(\mathbf{x}_r, \mathbf{x}_s, \omega)$ are the full, up-going reflection data acquired for all shots and receivers on the acquisition surface. $\mathbf{T}^-$ is the modeling operator for up-going transmission that datums depth-domain fields at all $\mathbf{x}_d \in \partial\mathbb{D}_d$ to surface data at $\mathbf{x}_r \in \partial\mathbb{D}_0$ (figure 2). The inverse of $\mathbf{T}^-$ thus maps the reflection data at the surface to the receiver wavefield in the subsurface.

There are three main distinctions between the wavefield extrapolation steps described by equations 12 and 13 and those employed in current one-way migration approaches. First, the up-going surface data $\mathbf{D}_0^- = \hat{d}_0^-(\mathbf{x}_r, \mathbf{x}_s, \omega)$ contains the full recorded reflection response (i.e., with all up-going multiples), as opposed to only primary reflection data. Second, the modeling operators $\mathbf{T}^\pm$ are meant to be full transmission response operators (e.g., Thorbecke, 1997; Wapenaar et al., 2004), i.e., they model amplitude-preserving transmitted fields that contain direct arrivals as well as transmission multiples. Malcolm et al. (2009) offers a scattering-series-based approach that can be used for practical implementation of the nonlinear $\mathbf{T}^\pm$ operators. Finally, we note that the inverse operator $\left(\mathbf{T}^-\right)^{-1}$ is used for the back-propagation of the receiver data $\mathbf{D}_0^-$, whereas common practice does not rely on inverse transmission operators (see next section). In principle, these three differences combined allow for the proper modeling of multiples in the depth-extrapolated fields, which is a key element necessary for the inversion of the full nonlinear reflectivity operator in equations 5 and 9. In the next section we address differences between the steps above and the computation of extended images in current migration practice.

5 EXTENDED IMAGES IN CURRENT MIGRATION PRACTICE

Unlike the discussion above on the nonlinear imaging conditions and on wavefield extrapolation that models multiples in the depth-extrapolated fields, most current migration practices generally rely on the Born approximation (e.g., Claerbout, 1971; Stolt and Weglein, 1985) for both one- and two-way imaging. Furthermore, since the objective behind most migration schemes is structural characterization, it is not uncommon that additional approximations are made that ignore amplitude-related effects in extrapolation and imaging. As a consequence, these approximations bring two major simplifications for practically implementing EI's, namely, *i*) that all of the wavefield extrapolation can be carried out with a single smooth wave-speed model and *ii*) that the evaluation of the imaging conditions is substantially simpler and becomes effectively the same for both two- and one-way imaging.

Two-way imaging in current migration practice is typically achieved first by adapting the receiver wavefield extrapolation in equation 11 to

$$\begin{cases} \hat{\mathcal{L}}_0\, \hat{p}_S = 0 & \text{for } \hat{p}_S(\mathbf{x}, \mathbf{x}', \omega) \text{ with } \mathbf{x} \in \mathbb{D}, \mathbf{x}' = \mathbf{x}_s \in \partial\mathbb{D}_0 \\ \hat{p}_S(\mathbf{x}_r, \mathbf{x}_s, \omega) = \hat{d}_P^*(\mathbf{x}_r, \mathbf{x}_s, \omega) & \text{for all } \mathbf{x}_{s,r} \in \partial\mathbb{D}_0; \end{cases} \tag{14}$$

where the primary-only data $\hat{d}_P(\mathbf{x}_r, \mathbf{x}_s, \omega)$ replaces the full recorded scattered waves $\hat{d}_S(\mathbf{x}_r, \mathbf{x}_s, \omega)$ in equation 11, and these are now backward-extrapolated with the smooth Helmholtz operator $\mathcal{L}_0$, same as used for the source wavefield extrapolation described by equation 10. We point out the homogeneous PDE $\hat{\mathcal{L}}_0\, \hat{p}_S = 0$ is not equivalent to the Born approximation of the inhomogeneous PDE in equation 11. Proper Born modeling would require the inclusion of the forcing term $-\mathcal{V}\hat{p}_0$, i.e., solving for $\hat{\mathcal{L}}_0\, \hat{p}_S = -\mathcal{V}\, \hat{p}_0$ instead. Sources and receivers are no longer assumed to enclose the medium, and are instead available only over a finite surface $\partial\mathbb{D}_0$ (figure 1b). While this assumption mimics realistic geophysical data where physical sources and receivers are only available at the Earth's surface, it also typically introduces artifacts in the wavefield reconstruction and interferometry processes (e.g., Wapenaar, 2006, Wapenaar and Fokkema, 2006). Note that here the responses of both source and receiver wavefields, i.e, $\hat{p}_{0,S}(\mathbf{x}, \mathbf{x}', \omega)$, are computed only for points $\mathbf{x}' = \mathbf{x}_s$ on the surface, while the fields extrapolated in equations 10 and 11 need additional extrapolated sources at the points $\mathbf{x}'$ inside the subsurface volume.

By extrapolating the receiver wavefield according to equation 14 as opposed to equation 11, the nonlinear interactions between the back-propagating receiver wavefield and the model discontinuities present in the operators $\mathcal{L}$ and $\mathcal{V}$ are ignored. Also, when ignoring the contributions of model discontinuities in the extrapolation step (i.e. by ignoring the Born forcing term $\mathcal{V}\, \hat{p}_0$), current two-way migration algorithms thus also ignore the volume integral in

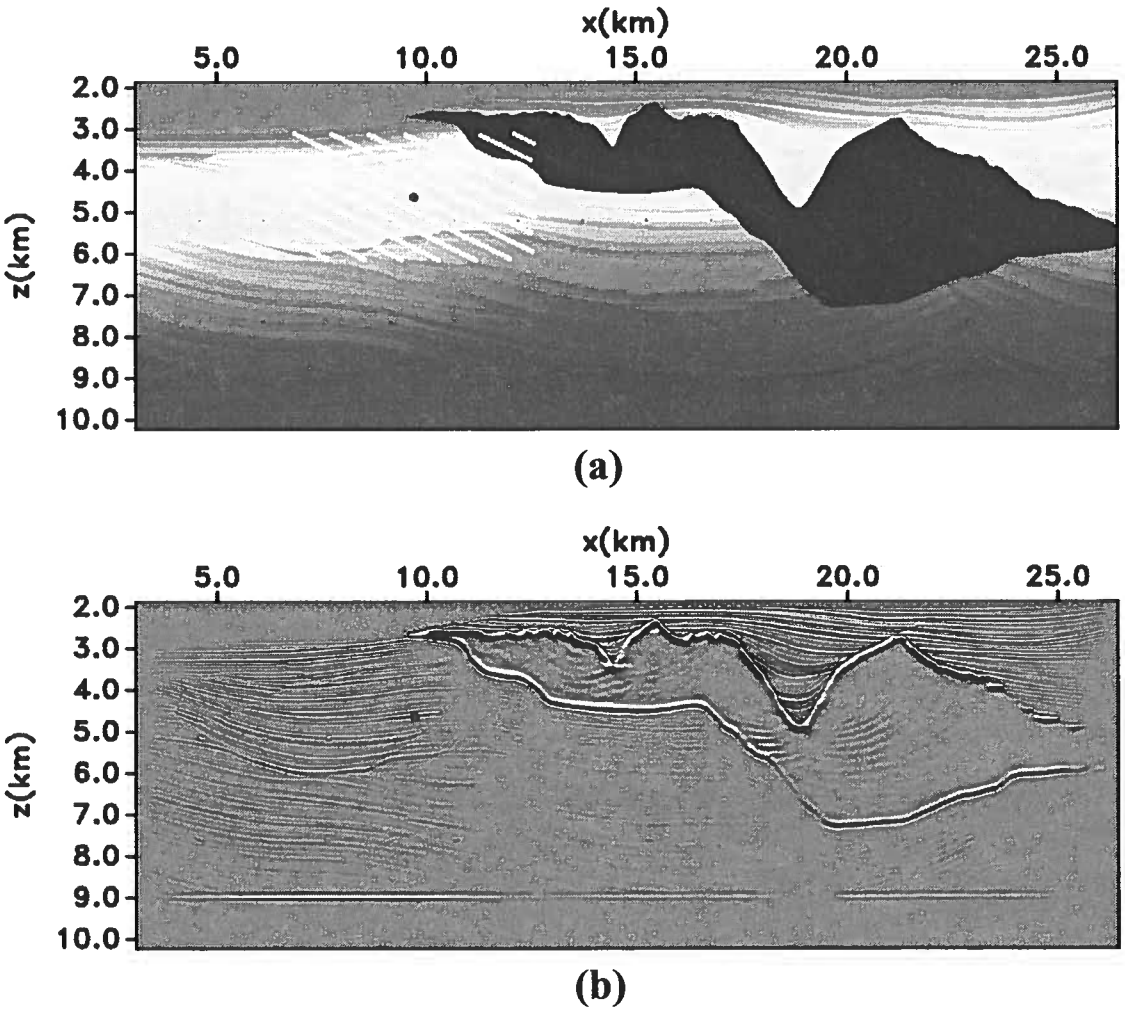

Figure 4. Sigsbee numerical example. Panel (a) shows the true wavespeed model, while panel (b) shows a conventional one-way migrated image. The blue dot in both panels shows the location $\mathbf{x}$ of the extended image portrayed in figure 5. The red dots show the location of the surface acquisition shots $\mathbf{x}_s \in \partial\mathbb{D}_0$. The area highlighted by white lines in panel (a) indicates the spatial coverage of space-lags $\delta\mathbf{x}$ in the extended image (figure 5). The EI in figure 5 is an approximate reconstruction of the scattered waves excited at $\mathbf{x}+\delta\mathbf{x}$ somewhere inside the white-highlighted area and recorded at $\mathbf{x}-\delta\mathbf{x}$. The original acquired data is laid out in a towed-streamer-type geometry whereby the recording receivers lie only on the right-hand side of the shots.

the imaging condition in equation 8. Thus, an EI can be approximated from equation 8 as the surface integral

$$\mathcal{I}_e(\mathbf{x},\delta\mathbf{x},\tau) \approx \int\left(\int_{\partial\mathbb{D}_0} \frac{2F(\omega)}{\rho c}\, p_S(\mathbf{x}-\delta\mathbf{x},\mathbf{x}_s,\omega)\, p_0^*(\mathbf{x}+\delta\mathbf{x},\mathbf{x}_s,\omega) d^2\mathbf{x}_s\right) e^{i\omega\tau}\, d\omega\,;$$

where $\partial\mathbb{D}_0$ is a subset of $\partial\mathbb{D}$ (figure 1), and $\mathbf{x}' = \mathbf{x}_s$ as shown in equation 14. This result yields an estimate for an EI that is a straightforward extension of the conventional correlation-based imaging condition, obtained by adding space lags $\delta\mathbf{x}$ and time lags τ to the cross-correlation of source wavefields p_0 and receiver wavefields p_S (Sava and Vasconcelos, 2009; Sava and Vasconcelos, 2010).

An analogous approach is taken to generate one-way EI's under the single-scattering approximation and using a smooth wavespeed model. For one-way imaging, source wavefield extrapolation is done according to equation 12 with the full transmission operator $\mathbf{T}^+$ replaced by $\mathbf{T}_0^+$, the transmission operator in a smooth medium (e.g., Thorbecke, 1997; Wapenaar et al., 2004). A similar replacement takes place in the receiver wavefield extrapolation, $\mathbf{T}^-$ is replaced by its smooth medium counterpart $\mathbf{T}_0^-$. Additionally, given the computational challenges involved with computing the inverse of the transmission operator (equation 13), $\left(\mathbf{T}_0^-\right)^{-1}$ is typically replaced by the conjugate-transpose $\left(\mathbf{T}_0^-\right)^\dagger$.

Once one-way source and receiver wavefields are extrapolated using the smooth transmission operators $\mathbf{T}_0^+$ and $(\mathbf{T}_0^-)^\dagger$, the image is estimated by cross-correlating the resulting source and receiver fields, i.e.,

$$\tilde{\mathbf{R}}_0^+ \approx \mathbf{P}^-(\mathbf{P}^+)^\dagger; \tag{15}$$

which is an approximation to the inverse in equation 9 (e.g., Claerbout, 1971; Wapenaar et al., 2008). The standard one-way migrated image is then extracted from the diagonal elements of $\tilde{\mathbf{R}}_0^+$ (black highlight in figure 3). From the $\tilde{\mathbf{R}}_0^+$ matrix (equation 15), EI's can be obtained by selecting other specific combinations of its elements, as discussed above discussion regarding figure 3. For example, the off-diagonal elements of $\tilde{\mathbf{R}}_0^+$ (highlighted in red in figure 3) yield the extended image $I_e(\mathbf{x},\delta\mathbf{x},\tau) = \tilde{R}_0^+(\mathbf{x}-\delta\mathbf{x},\mathbf{x}+\delta\mathbf{x},t=\tau)$, which based on equation 15 can be directly evaluated via the integral

$$\begin{aligned} I_e(\mathbf{x},\delta\mathbf{x},\tau) &= \tilde{R}_0^+(\mathbf{x}-\delta\mathbf{x},\mathbf{x}+\delta\mathbf{x},\tau) \\ &= \int\left(\int_{\partial\mathbb{D}_0} p^-(\mathbf{x}-\delta\mathbf{x},\mathbf{x}_s,\omega)\right. \\ &\quad \left.\{p^+(\mathbf{x}+\delta\mathbf{x},\mathbf{x}_s,\omega)\}^*\, d^2\mathbf{x}_s\right) e^{i\omega\tau} d\omega\,. \end{aligned} \tag{16}$$

Thus, in current one-way migration practice, we can readily generate an EI by adding space and time lags to the conventional cross-correlation of receiver and source wavefields (p^- and p^-, respectively, in equation 16), followed by a summation over sources $\mathbf{x}_s$ on the acquisition plane $\partial\mathbb{D}_0$.

Figures 4 and 5 provide a numerical example from the Sigsbee model of a one-way EI that is generated using equation 16. The standard image, displayed in figure 4b, corresponds to the diagonal elements of the estimated $\tilde{\mathbf{R}}_0^+$ matrix (equation 15), evaluated at $\tau = 0$. Because it is an approximate estimate of $\tilde{R}_0^+(\mathbf{x},\mathbf{x},\tau=0)$, the conventional image in figure 4b is commonly interpreted as a representation of the structure of the true model in figure 4a.

The EI in figure 5, however, shows that extended images display an appearance which is similar to that of recorded data, i.e., that of time- and space-dependent band-limited signals with characteristic moveout signatures. This is consistent with the reciprocity-based definitions of the EI as given by equations 4, 9, or 16, that show that an EI are reconstructed reflectivity data acquired by pseudo sources and receivers in the subsurface model. This "reconstruction" is analogous to data reconstruction by seismic interferometry (e.g., Wapenaar and Fokkema, 2006; Bakulin and Calvert, 2006), with the distinction that the computation of extended imaging conditions is done with extrapolated image-domain fields as opposed to actual recordings. While the reflectivity response reconstructed in the EI in figure 5 is predominantly causal as expected from the definition in equation 4, arrivals are also present for $\tau < 0$ due to the approximation made in using only the adjoint of $\mathbf{P}^+$ and not its inverse (see equations 9 and 15). Furthermore, the proper reflectivity moveout signatures are reconstructed only for $\tau > 0$ and $\lambda_x < 0$ because the towed-streamer acquisition of the Sigsbee synthetic data only allows for receivers to be placed on one side of the source locations.

6 DISCUSSION

In this paper, we define extended images (EI's) for both two- and one-way explicitly as scattered fields or, respectively, reflectivity operators that are both excited and recorded within the subsurface and for finite times. These definitions for "an image" (e.g., according to equations 2 and 4), while consistent with the concepts originally offered by Claerbout (e.g., 1971, 1985), differ from the majority of formal definitions for an image which target the direct reconstruction of discontinuities in the Earth parameters, e.g. the scattering potential $\mathcal{V}$ (e.g., Prosser, 1968; Beylkin, 1984; Stolt and Weglein, 1985; Esmersoy and Oristaglio, 1988; Weglein et al., 2003; Symes, 2008). Instead, by defining EI's in terms of space- and time-dynamic objects such as the two-way wavefield G_S, or the one-way reflectivity operator R_0^+ we use wavefield reciprocity (e.g., Fokkema and van den Berg, 1993; Wapenaar et al., 2008; Vasconcelos et al., 2009) to derive formal expression for the nonlinear extended imaging conditions as presented in this manuscript.

By invoking integral reciprocity relations and defining EI's as subsurface-domain scattering experiments, we draw an explicit connection between the computation of extended images via migration-type imaging by wavefield extrapolation and current practices in seismic interferometry. In fact, the integral representations we propose here for generating EI's are precisely the same as those employed in seismic interferometry. The scattering representation we use for our two-way extended imaging condition is directly analogous to that employed in scattered-wave seismic interferometry as discussed by, e.g., Bakulin and Calvert (2006); Vasconcelos et al. (2009a) and Wapenaar et al. (2010). Likewise, our one-way EI formulation is based on the one-way approach by Wapenaar et al. (2008).

When the imaging objective is structural characterization, it is common for current migration practice to rely on the single-scattering approximation and to ignore amplitude effects. In that case, we show here that the two- and one-way extended imaging conditions are essentially the same calculation (described by equations 15 and 16): a straightforward cross-correlation of receiver and source depth-domain wavefields followed by summing over all shots on the acquisition surface. The only difference being that the source and receiver wavefields are generated via two- or one-way extrapolation. This explicitly connects our formulation to common practice in migration-type imaging widely employed today. We point out, however, that this similarity be-

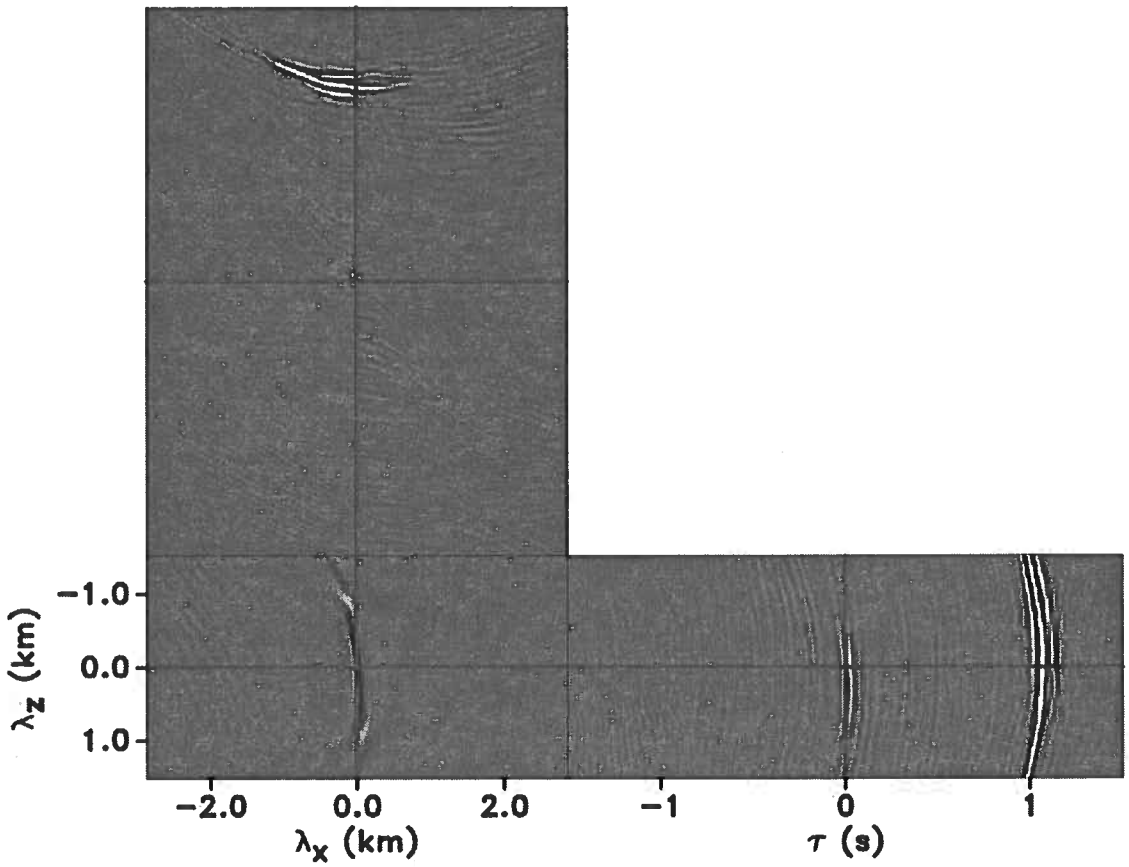

Figure 5. Example of a one-way, fully extended image (EI) of common-mid-point type of geometry, i.e., $I_e(\mathbf{x}, \delta\mathbf{x}, \tau) = \tilde{R}_0^+(\mathbf{x} - \delta\mathbf{x}, \mathbf{x} + \delta\mathbf{x}, t = \tau)$. The EI is shown here for a fixed x-location (indicated by the blue dot in figure 4), and for varying $\delta\mathbf{x}$ and τ. The space-lag $\delta\mathbf{x}$ has components $\{\lambda_x, \lambda_z\}$ which are shown in the figure axes. τ-axis is the time-lag variable.

tween two- and one-way EI's exhibited by equations 15 and 16 is only due to the approximations involved. In their more general form, reciprocity-based two-way EI's are substantially different from their one-way counterparts both in terms of their meaning as well as in terms of the required computations. These differences, however, should only necessarily be addressed in imaging practice if the objective is to deal with nonlinear effects in the imaging process such as e.g. the migration of multiples or amplitude corrections due to transmission effects. Consistently with our findings, Halliday and Curtis (2010) show that Oristaglio's (1989) two-way inversion formula, which is a Born-inversion extension to Claerbout's imaging condition (1971), explicitly follows from interferometry-based integral relations.

Since the reciprocity-based integrals used for interferometry make no single-scattering assumptions and in principle reconstruct full nonlinear scattering responses, our imaging conditions based on image-domain interferometry are suitable for dealing with nonlinear imaging such as multiple-scattered arrivals and associated amplitude effects. To properly account for nonlinear effects in both the two- and one-way case, current extrapolation practices must be modified such that nonlinearity is accounted for at the modeling stage. We show here that while nonlinear transmission operators must be used for both source and receiver wavefields in one-way imaging, in the two-way approach only the receiver wavefields include nonlinear effects and their modeling becomes dependent on previously computed source wavefields.

Apart from the necessary modifications in the wavefield extrapolation step, we show that the imaging conditions that generate nonlinear EI's also differ from standard migration practice. In the two-way case, apart from the evaluation of a surface integral of cross-correlated source and receiver wavefields (akin to the source stacking typically conducted in shot-profile migration) there is an extra volume integral term that must be evaluated. Concurrent with our analysis, Halliday and Curtis (2010) show that the volume terms are necessary both for nonlinear imaging as well as for imaging based on Born inversion (Oristaglio, 1989). While there is no volume integral term to be computed in generating one-way EI's, these in turn require the in-

version of the full source-wavefield data matrix. At this point, computing the two-way volume integral or one-way data matrix inverse both present unsolved computational challenges in practically computing nonlinear EI's. These issues are currently the subject of further investigation.

It is important to emphasize that the greatest challenge in practically computing nonlinear EI's is, at the same time, the main justification for why we should generate them in the first place. As shown in the approach we provide in this manuscript, the computation of both two- and one-way EI's requires knowledge not only of the smooth migration velocity model, but also of the discontinuities (i.e., the singularities) in the subsurface model. That information is obviously not available at the outset of a seismic imaging experiment. It is precisely for the determination of velocity models, e.g., via wave-equation image-domain inversion approaches, that the concept of image extensions was originally developed. Symes (2008, and references therein) provides a comprehensive description of the role of extended images in the velocity inversion problem within the context of differential semblance optimization.

Sava and Vasconcelos (2010) show that EI's can bring additional sensitivity to the wavespeed models used in current migration practice, and can help in advancing migration-based methods for the inversion of background wavespeed models. While using EI's in current migration schemes is in itself potentially beneficial for increasing sensitivity to background migration wavespeed models, our nonlinear EI formulation presented here can be used to devise nonlinear finite-frequency inversions whose objective functions act in the subsurface image domain. Such approaches would bring the advantages of using image extensions and differential semblance as advocated by Symes (2008) to designing practical numerical solutions to the nonlinear seismic inverse scattering problem (e.g., Tarantola, 1984; Rose et al., 1985; Weglein et al., 2003; Symes, 2009). We note also that Halliday and Curtis (2010) show that the scattering-based EI's as presented here are formally connected to exact Born inverse scattering formulations and are thus also suitable for extensions to more sophisticated nonlinear problems.

On a more practical note, we point out that the EI formulation we present here can immediately contribute to current migration routines. For instance, recent examples of two-way reverse-time migration applications that utilize sharp boundaries in the migration velocity model to migrate multiply-scattered arrivals (e.g., Fletcher et al., 2006; Guitton et al., 2006; Jones et al., 2007) rely on a conventional migration practices and do not evaluate the volume integral term in the two-way imaging condition. Our approach for generating two-way reciprocity-based images can be implemented for the imaging of multiple-scattered arrivals using interpretation-based wavespeed models containing sharp discontinuities, i.e., by using sharp horizons picked from pre-existing images and using our two-way formulation to adapt a reverse-time migration scheme. Likewise, our one-way nonlinear EI formulation based on multi-dimensional deconvolution is readily applicable to one-way migrations that rely on amplitude-preserving one-way extrapolators (e.g., Zhang et al., 2007) or to recursive one-way migrations that target the imaging of multiples (e.g., Berkhout and Verschuur, 2006; Malcolm et al., 2009).

7 CONCLUSIONS

Extended images (EI's) in wavefield seismic imaging can be explicitly defined as space- and time-dependent objects in the subsurface domain. In our particular case, we define EI's as time-varying scattered wavefields that are excited and acquired by virtual sources and receivers that surround a particular image point in the subsurface domain. This definition of an EI departs from the typical concept of migrated image as a static representation of the discontinuities in the Earth's subsurface. Two-way EI's are defined as scattered fields that satisfy the partial differential equation for scattering in the subsurface domain, whereas we define one-way EI's as a dimensionless reflectivity operator that relates down-going excitations with the up-going subsurface waves recorded in the data.

Together with exact integral reciprocity relations, our definitions of two- and one-way EI's reveal an immediate connection between wave-equation imaging and the practice of seismic interferometry. Our extended images are, in fact, interferometric reconstructions of two- or one-way scattering experiments that use model-dependent, depth-extrapolated data as opposed to physically observed recordings typically employed in seismic interferometry. Because we use the same general scattering reciprocity integrals used in interferometry to define EI's, we expect that both our two- and one-way formulations for the extended imaging conditions account for nonlinear amplitude and multiple scattering effects.

To migrate multiples or to account for other nonlinear imaging effects, the computation of EI's departs significantly from today's practices in wave-equation migration. First, the depth-extrapolation step must be appropriately modified to model scattering interactions with model discontinuities: only for the receiver wavefields in two-way imaging, and for both source and receiver wavefields in the one-way case. Next, we show that the imaging condition for two-way reciprocity-based EI's requires the inclusion of an additional scattering volume integral term that is not present in typical migration routines. In the one-way case, the extended imaging condition requires the inversion of the full down-going source-wavefield data matrix, which departs from current approaches that use either cross-correlation or single-channel deconvolution.

Our explicit reciprocity-based descriptions of two- and one-way EI's can be used to address, both analytically as well as numerically, the velocity-dependent signatures of these fully extended image gathers. Consequently, these wavefield-based EI's can help in devising general formulations of image-domain objective functions for finite-frequency velocity inversion. In addition, one- and two-way EI's as we describe here can be of immediate use in current reverse-time migration applications, as well as in refining amplitude-preserving one-way wave-equation migration routines.

8 ACKNOWLEDGEMENTS

We thank ION/GXT for supporting this work and granting the permission to publish it. P. Sava thanks the sponsors of the CWP consortium for financial support. I. Vasconcelos is thankful to Andrew Curtis (Edinburgh University) and David Halliday (Schlumberger) for sharing their material on source-receiver interferometry and imaging.

REFERENCES

A. Bakulin and R. Calvert, 2006, The virtual source method: Theory and case study: Geophysics, **71**, SI139–SI150.

G. Beylkin, 1985, Imaging of discontinuities in the inverse scattering problem by inversion of a causal generalized radon transform. J. Math. Phys., **26**, 99–108.

A.J. Berkhout and D.J. Verschuur, 2006, Imaging of multiple reflections: Geophysics, **71**, SI209–SI220.

D.E. Budreck and J.H. Rose, 1990, Three-dimensional inverse scattering in anisotropic elastic media, *Inverse Problems*, **6**, 331–348.

M. Campillo and A. Paul, 1997, Long-range correlations in the diffuse seismic coda, *Science*, **299**, 547–549.

H. Chauris , 2000, *Analyse de vitesse par migration pour l' imagerie des structures complexes en sismique réflexion.* PhD Thesis, École des Mines de Paris.

J.F. Claerbout ,1968, Synthesis of a layered medium from its acoustic transmission response. *Geophysics*, **33**, 264–269.

J.F. Claerbout, 1971, Toward a unified theory of reflector mapping. Geophysics, **36**, 741–768.

J.F. Claerbout, 1985, Imaging the Earth's Interior. Blackwell Scientific Publishers, Oxford.

R.W. Clayton and R.H. Stolt, 1981, A Born-WKBJ inversion method for acoustic reflection data, *Geophysics*, **46**, 1559–1567.

A. Curtis, P. Gerstoft, H. Sato, R. Snieder and K. Wapenaar, 2006, Seismic interferometry – turning noise into signal: The Leading Edge, **25**, 1082–1092.

A. Curtis and D. Halliday, 2010, Source-receiver wavefield interferometry. *submitted.*

M.V. de Hoop and A.T. de Hoop, 1999, Wave-field reciprocity and optimization in remote sensing, *Proc. R. Soc. Lond.*, **456**, 641–682.

M. de Hoop, R. van der Hilst and P. Shen, 2006, Wave-equation reflection tomography: annihilators and sensitivity kernels, *Geophys. J. Intl.*, **167**, 1332–1352.

C. Esmersoy and M. Oristaglio, 1988, Reverse-time wavefield extrapolation, imaging and inversion, *Geophysics*, **53**, 920–931.

M. Fink, 1997, Time-reversed acoustics, *Physics Today*, **50**, 34–40.

L. Fishman and J.J. McCoy, 1984, Derivation and extension of parabolic wave theories. I. The factorized Helmholtz equation, *J. Math. Phys.*, **25**, 285–296.

L. Fishman, J.J. McCoy and S.C. Wales, 1987, Factorization and path integration of the Helmholtz equation: Numerical algorithms, *J. Acoust. Soc. Am.*, **81**, 1355–1376.

R.P. Fletcher, P.J. Fowler, P. Kitchenside and U. Albertin, 2006, Suppressing unwanted internal reflections in prestack reverse-time migration, *Geophysics*, **71**, E79–E82.

J.T. Fokkema and P.M. van den Berg. Seismic applications of acoustic reciprocity. *Elsevier Service Publishing Co.*, 1993.

D. Halliday and A. Curtis, 2010, An interferometric theory of source-receiver scattering and imaging. *submitted.*

P.C. Hansen, 1997, Rank-deficient and discrete ill-posed problems: numerical aspects of linear inversion, *SIAM.*

A. Guitton, B. Kaelin and B. Biondi, 2006, Least-square Attenuation of Reverse Time Migration Artifacts, *SEG Exp. Abs.*, 2348–2352.

I. Jones, M.C. Goodwin, I.D. Berranger, H. Zhou and P. Farmer, 2007, Application of anisotropic 3D reverse time migration to complex North Sea imaging, *SEG Exp. Abs.*, 2140–2144.

A.E. Malcolm, B. Ursin and M.V. de Hoop, 2009, Seismic imaging and illumination using multiples *Geophys. J. Intl.*, **176**, 847–864.

D.-J. van Manen, J.O.A. Robertsson and A. Curtis, 2005, Modeling of wave propagation in inhomogeneous media, *Phys. Rev. Lett.*, **94**, 164301.

D.-J. van Manen, A. Curtis and J.O.A. Robertsson, 2006, Interferometric modelling of wave propagation in inhomogeneous elastic media using time-reversal and reciprocity, *Geophysics*, **71**, SI47–SI60.

W. Mulder and A. Ten Kroode, 2002, Automatic velocity analysis by differential semblance optimization *Geophysics*, **67**, 1184–1191.

M. Oristaglio, 1989, An inverse scattering formula that uses all the data *Inverse Problems*, **5**, 1097–1105.

R.-E. Plessix, 2006, A review of the adjoint-state method for computing the gradient of a functional with geophysical applications *Geophys. J. Intl.*, **167**, 495–503.

R.G. Pratt, 1999, Seismic waveform inversion in the frequency domain, part 1: Theory, and verification in a physical scale model *Geophysics*, **64**, 888–901.

R.T. Prosser, 1968, Formal solutions to inverse scattering problems, *J. Math. Phys.*, **10**, 1819–1822.

J.E. Rickett and J.F. Claerbout, 1999, Acoustic daylight imaging via spectral factorization; helioseismology and reservoir monitoring, The Leading Edge, **19**, 957–960.

J.E. Rickett and P.C. Sava, 1999, Offset and angle-domain common image-point gathers for shot-profile migration, *Geophysics*, **67**, 883-889.

J.H. Rose, M. Cheney and B. DeFacio, 1985, Three dimensional inverse scattering: plasma and variable velocity wave equations, *J. Math. Phys.*, **26**, 2803–2813.

P. Sava and B. Biondi, 2004, Wave-equation migration velocity analysis – I: Theory. *Geophys. Prosp.*, **52**,593–606.

P. Sava and I. Vasconcelos, 2010, Extended imaging conditions for wave-equation migration, *Geophys. Prosp.*, *accepted.*

G.T. Schuster, J. Yu, J. Sheng and J. Rickett, 2004, Interferometric/daylight seismic imaging, *Geophys. J. Intl.*, **157**, 838–852.

L. Sirgue and R.G. Pratt, 2004, Efficient waveform inversion and imaging: a strategy for selecting temporal frequencies *Geophysics*, **69**, 231–248.

R.H. Stolt and A.B. Weglein, 1985, Migration and inversion of seismic data, *Geophysics*, **50**, 2458–2472.

W.W. Symes, 2008, Migration velocity analysis and waveform inversion, *Geophys. Prosp.*, **56**, 765–790.

W.W. Symes, 2009, The seismic reflection inverse problem, *Inverse Problems*, **25**, 123008.

C. Tape, Q. Liu, A. Maggi and J. Tromp, 2009, Adjoint tomography of the Southern California crust, *Science*, **325**, 988–992.

A. Tarantola, 1984, Inversion of seismic reflection data in the acoustic approximation, *Geophysics*, **49**, 1259–1256.

J. Thorbecke, 1997, *Common Focus Point Technology*, PhD Thesis, Delft University of Technology.

J. Thorbecke and A.J. Berkhout, 2006, Recursive prestack depth migration using CFP gathers, *Geophysics*, **71**, S273–S283.

J. Thorbecke and K. Wapenaar, 2007, On the relation between seismic interferometry and the migration resolution function, *Geophysics*, **72**, T61–T66.

I. Vasconcelos, 2008, Generalized representations of perturbed fields – applications in seismic interferometry and migration, *SEG Exp. Abs.*, 2927–2941.

I. Vasconcelos and R. Snieder, 2008, Interferometry by deconvolution, Part 1 – Theory for acoustic waves and numerical examples , *Geophysics*, **73**, S115–S128.

I. Vasconcelos, R. Snieder and H. Douma, 2009a, Representation theorems and Greens function retrieval for scattering in acoustic media, *Phys. Rev. E*, **80**, 036605.

I. Vasconcelos, P. Sava and H. Douma, 2009b, Wave-equation extended images via image-domain interferometry, *SEG Exp. Abs.*, 2839–2843.

C.P.A. Wapenaar, G.L. Peels, V. Budejicky and A.J. Berkhout, 1989, Inverse extrapolation of primary seismic waves, Geophysics, **54**, 853–863.

C.P.A. Wapenaar, M.W.P. Dillen and J.T. Fokkema, 2001, Reciprocity theorems for electromagnetic or acoustic one-way wave fields in dissipative inhomogeneous media, Radio Science, **36**, 851–863.

K. Wapenaar, 2004, Retrieving the elastodynamic Green's function of an arbitrary inhomogeneous medium by cross-correlation. *Phys. Rev. Lett.*, **93**, 254301.

K. Wapenaar, J. Thorbecke, and D. Draganov, 2004, Relations between reflection and transmission responses of three-dimensional inhomogeneous media: Geophysical Journal International, **156**, 179–194.

K. Wapenaar, 2006, Green's function retrieval by cross-correlation in case of one-sided illumination: Geophysical Research Letters, **33**, L19304.

K. Wapenaar and J. Fokkema, 2006, Green's function representations for seismic interferometry: Geophysics, **71**, SI33–SI46.

K. Wapenaar, D. Draganov and J. Robertsson, 2006, Introduction to the supplement on seismic interferometry, *Geophysics*, **71**, SI1–SI4.

K. Wapenaar, E. Slob and R. Snieder, 2008, Seismic and electromagnetic controlled-source interferometry in dissipative media, Geophys. Prosp., **56**, 419–434.

K. Wapenaar, 2007, General representations for wavefield modeling and inversion in geophysics: Geophysics, **72**, SM5–SM17.

R.L. Weaver and O.I. Lobkis, 2001, Ultrasonics without a source: Thermal fluctuation correlations and MHz frequencies: Physical Review Letters, **87**, 134301.

A.B. Weglein, F.V. Araújo, P.M. Carvalho, R.H. Stolt, K.H. Matson, R.T. Coates, D. Corrigan, D.J. Foster, S.A. Shaw, and H. Zhang, 2003, Inverse scattering series and seismic exploration: Inverse Problems, **19**, R27–R83

Y. Zhang, S. Xu, N. Bleistein and G. Zhang, 2007, True-amplitude, angle-domain, common-image gathers from one-way wave-equation migrations, *Geophysics*, **72**, S49–S58.

Amplitude calculations for 3-D Gaussian beam migration using complex-valued traveltimes

Norman Bleistein[1] & S. H. Gray[2]
[1]*Center for Wave Phenomena, Dept. of Geophysics, Colo. Sch. of Mines, Golden, CO 80401-1887, USA*
[2]*CGGVeritas Inc., 715 5th Avenue SW, Calgary, AB T2P 5A2 Canada*

ABSTRACT
Gaussian beams are often used to represent Green's functions in three-dimensional Kirchhoff-type true-amplitude migrations because such migrations made using Gaussian beams yield superior images to similar migrations using classical ray-theoretic Green's functions. Typically, the integrand of a migration formula consists of two Green's functions, each describing propagation to the image point —one from the source and the other from the receiver position.
The use of Gaussian beams to represent each of these Green's functions in 3D introduces two additional double integrals when compared to a Kirchhoff migration using ray-theoretic Green's functions, thereby adding a significant computational burden. Hill proposed a method for reducing those four integrals to two, compromising slightly on the full potential quality of the Gaussian beam representations for the sake of more efficient computation. That approach requires a two-dimensional steepest descent analysis for the asymptotic evaluation of a double integral. The method requires evaluation of the complex traveltimes of the Gaussian beams as well as the amplitudes of the integrands at the determined saddle points. In addition, it is necessary to evaluate the determinant of a certain (Hessian) matrix of second derivatives. Hill did not report on this last part; thus, his proposed migration formula is kinematically correct but lacks correct amplitude behavior. In this paper, we derive a formula for that Hessian matrix in terms of dynamic ray tracing quantities. We also show in a simple example how the integral that we analyze here arises in a true amplitude migration formula.

CONTENTS

1 INTRODUCTION

In oil and gas exploration, a seismic reflection experiment consists of an exploding or vibrating source of energy near the Earth's surface sending elastic waves into the Earth. The seismic waves propagate inside the Earth, and waves reflected from interfaces where material properties change return to the Earth's surface to be recorded by an array of receivers. A seismic survey consists of hundreds or thousands of such experiments in close proximity to one another, each producing a seismic record that gives a distorted picture of the Earth's subsurface. Although reflectors are visible on the records, they tend to be misplaced laterally and obscured by diffracted energy. Further, the records are recorded in time, so they do not provide an image of the Earth's subsurface in depth.

The goal of seismic migration is to undistort the data recorded by the seismic survey, producing accurate maps of reflector locations. The basis for migration is wave propagation theory: given a reasonably accurate profile of seismic wave velocities inside the Earth, the physical waves are simulated by numerical wavefields propagating from the source and receiver locations, and the occurrence of reflection at locations inside the Earth is simulated by an imaging condition involving the wavefields at those locations. There is a vast geophysical literature on migration and associated problems, including problems of analyzing migrated amplitudes and estimating the wave velocities. Some of these problems are treated by Claerbout [1985]. The problem of interest in this paper is true-amplitude migration, which aims to preserve reflection amplitudes to the point where amplitudes of migration data provide accurate estimates of reflection coefficients as a function of source-receiver offset or incidence angle at reflector locations.

1.1 Kirchhoff migration

As with all migration methods, true-amplitude Kirchhoff migration requires downward propagation of the source wavefield and downward propagation of the observed data to image points in the subsurface. The downward propagations are accomplished using Green's identity, operating on data evaluated along one surface to obtain data at a deeper surface via a convolution-type integral of the data with a Green's function. When the sources are something other than the point sources we assume in this paper, we would also downward propagate the sources as such a convolution-type integral. This is Kirchhoff migration [Schneider, 1978]. Each of these propagation processes requires generation of Green's functions at the image point, one from a source, one from a receiver. When Gaussian beam representations of these Green's functions are used, it is necessary to generate the Gaussian beams themselves in neighborhoods of the image points. Then, to obtain the Gaussian beam representation of each Greens function in 3D, it is necessary to carry out a 2D integration of Gaussian beams over all takeoff angles where rays are in the vicinity of the image point. By contrast, the Greens functions for standard Kirchhoff migration, derived from classical asymptotic ray theory, require only a complex function evaluation with no additional integrations.

1.2 Gaussian beam migration

Multiplying the Green's functions together, as required by migration theory, results in the need to evaluate four nested integrals for Gaussian beam migration, as opposed to the multiplication of two complex numbers for Kirchhoff migration. Hill [2001] suggested a method for reducing those four additional integrals to two. Hill's method first replaces integrals over source and receiver ray parameters with integrals over midpoint and offset ray parameters. He then applies the method of steepest descent for integrals with complex exponents to the (innermost) integrals over offset parameters, leaving the (outermost) integrals over midpoint parameters to be computed numerically. He provides a technique for determining the critical (saddle) points and evaluating the complex traveltime and amplitude in the Kirchhoff integral formula. However, for true amplitude integrity, the steepest descent approximation of the integral also requires including the determinant of the Hessian matrix of second derivatives of the complex traveltime with respect to the two offset ray parameters as an additional adjustment factor in the amplitude of the asymptotic approximation. Hill did not evaluate that determinant; thus his method is not a true amplitude Kirchhoff migration. That is, its peak amplitude on reflectors cannot be shown to be proportional to a specular reflection coefficient when the image is produced by a single specular ray pair.

1.3 The Hessian and the method of steepest descent for integrals

The Hessian we seek is a sum of two other Hessians, one with respect to initial transverse ray parameters for the rays from the source to the image point, the other, the same for the rays from the receiver. Those matrices are needed to compute the sum of matrices before evaluating the needed determinant. Červený and Pšenčik [1983] and Červený [2001], Section 5.8, provide the tools for determining those matrices as well as other details of Gaussian beams which come from the dynamic equations using ray tracing, complex-valued traveltime and complex-valued ray amplitude.

The steepest descent method needs the evaluation of the Hessians in offset ray parameters for each choice of the midpoint point ray parameters over which the numerical integration is yet to be done. It is important to note that at those saddle points for which one and/or the other of the central rays from source and receiver misses the image point, the imaginary part of the complex traveltime is positive, and the integrand has exponential decay. Only when both rays from source and

receiver pass through the saddle point is the imaginary part of the traveltime equal to zero. Thus, the remaining outermost integrations are dominated by the region of midpoint ray parameters for which central rays pass nearby the image point.

1.4 Two Hessians

We can exploit this observation to simplify the evaluation of the two Hessians at the saddle points in offset ray parameters. Those Hessians contain terms linear in the offset variables—the q's of ray-centered coordinates. When central rays from both source and receiver pass through the image point, those q's are all zero, producing the zero of the imaginary traveltime. Directly evaluating the coefficients of the terms linear in the q's would require finite difference approximations to derivative operators. This evaluation would be compromised by numerical artifacts arising from differencing quantities that are only moderately well behaved. As an alternative, we propose an approximate evaluation of the two Hessian matrices. In our approximation, we neglect those contributions that are linear in the q's. Near the regions of dominant contribution to the integral, this causes insignificant error because the q's are small; elsewhere the error is limited by the exponential decay of the integrand. The resulting approximation of the Hessians can then be evaluated in terms of dynamic ray quantities. Our approximation has been empirically shown to be adequate for estimating reflection coefficients in 2D [Gray and Bleistein, 2009].

1.5 The 2D problem

The problem in 2D requires the reduction of two single integrals of Gaussian beams over takeoff angles representing the two Green's functions, one from the source, one from the receiver. In 2D the there is only one orthogonal variable, say q, and the dynamic variables are also scalars, Q and P. The second derivative we need is a scalar given by the sum of two other known scalars. That case is discussed by Gray and Bleistein [2009] who present a true amplitude Gaussian beam migration in 2D. They derived the second derivative indirectly by a method that did not expose the approximation we introduce here, although the same approximation is implicit in the final formula. Numerical examples confirm the claim of true amplitude migration. We show one of those examples in the final section of this paper.

The second derivatives we need are the derivatives of the complex traveltimes with respect to the initial transverse ray parameters—for rays from source and receiver—of rays in a *Cartesian* coordinate system. On the other hand, we know about the second derivatives of complex traveltime with respect to the orthogonal coordinate q for rays from source and receiver; these derivatives are expressible in terms of Q and P. Thus, we need to connect the two second derivatives—one for rays from the source, the other for rays from the receiver—through changes of variables and the derivatives of those

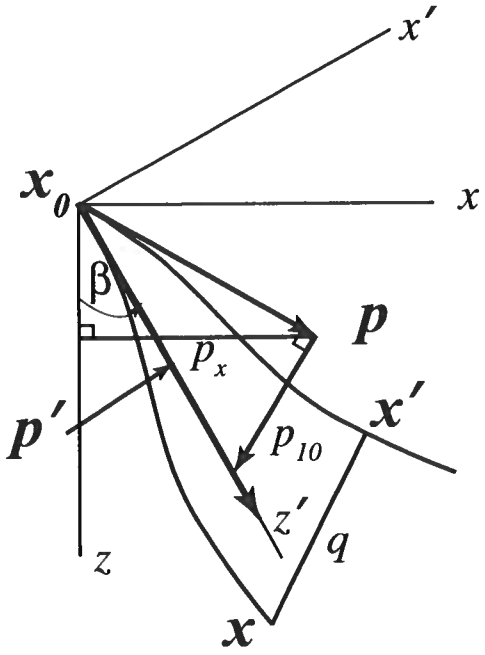

Figure 1. Rotation of Cartesian coordinates in 2D to the direction of the central ray. β is the angle with respect to the z-axis of the initial slowness vector $\boldsymbol{p}'$ to a central ray. In the ray-centered coordinate system the initial transverse slowness on the central ray is p_{10}. Propagating that ray, we find the point $\boldsymbol{x}'$ from which a perpendicular line of length q hits the image point.

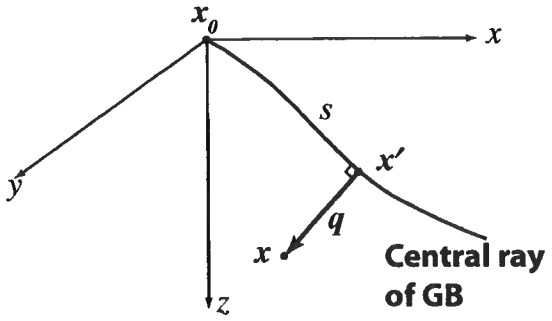

Figure 2. Ray from $\boldsymbol{x}_0$ through $\boldsymbol{x}'$, connectioned along an orthogonal vector $\boldsymbol{q}$ to the point $\boldsymbol{x}$. The vector $\boldsymbol{p}'$ of equation (13) is the initial slowness along the ray from $\boldsymbol{x}_0$ to $\boldsymbol{x}'$.

transformations. This is the key to determining the desired second derivatives of complex traveltime in terms of computed quantities of dynamic ray tracing.

As a first step, we need a transformation of the underlying Cartesian coordinate system to a Cartesian system defined by the initial direction of the ray from a source or receiver to the image point; eventually, we will not need to know that ray which might not be one of the central rays of the Gaussian beams. In Figure 1, that initial point is denoted by $\boldsymbol{x}_0$, which can be the source

point $\boldsymbol{x}_s$ or the receiver point $\boldsymbol{x}_r$. The angle of the initial direction of this ray is denoted by β and the initial direction along the ray from $\boldsymbol{x}_0$ through $\boldsymbol{x}$ is denoted by the initial slowness vector $\boldsymbol{p}'$ in the figure. This transformation is completely geometric, defined by a matrix of rotation of coordinates.

The vector $\boldsymbol{p}$ depicts the initial direction of the ray from $\boldsymbol{x}_0$ through $\boldsymbol{x}'$ along a central ray of a Gaussian beam. The integration variable in Hill's method in 2D is the initial ray parameter p_x, the x-component of $\boldsymbol{p}$ in the Cartesian coordinate system (x, z). The method of steepest descent of a single integral, such as the integral over directions of the rays of the Gaussian beams, requires the second derivative with respect to this integration variable p_x. The 3D depiction is more complicated because there are two transverse slowness coordinates to deal with.

The ray equations in ray-centered coordinates describe the propagation of the orthogonal displacement q between the point $\boldsymbol{x}'$ and $\boldsymbol{x}$. The traveltime at the image point $\boldsymbol{x}$ is approximated to quadratic order in q, as differential equations in the arc length s along the central ray through $\boldsymbol{x}'$. The differential equation for q is coupled with a differential equation for the propagation of $p_1 = \partial\tau/\partial q$. The initial value of p_1 is the projection of $\boldsymbol{p}$ on to the initial direction defined by $\boldsymbol{p}'$ (rather than on the vertical z-axis as is the case for p_x.

The dynamic quantities in 2D, scalars Q and P, are described by differential equations in s along the ray through $\boldsymbol{x}'$. The second derivatives of traveltimes with respect to q are given by the quotient PQ^{-1} for appropriate initial conditions on these dynamic variables. For classical asymptotic ray theory with real traveltimes, the initial conditions for Q and P are real; for Gaussian beams with complex traveltimes, the initial conditions for Q and P are complex. Thus, once the second derivative of traveltime with respect to p_x is transformed to a second derivative with respect to q, we can write that second derivative with respect to p_x in terms of the dynamic quantities Q and P. This latter second derivative is exactly the one that we need to complete the amplitude formula in the method of steepest descent; this was done in Gray and Bleistein [2009], although we used an indirect method to compute that scalar second derivative—simpler to determine than the determinant of second derivatives that we need in 3D.

1.6 Returning to the 3D problem

The next step after the rotation of coordinates is to transform from initial slownesses in the ray-centered coordinate system to the q's mentioned above. This is a standard matrix of propagation of a local ray tube in ray-centered coordinates. It is given by a matrix solution $\mathbf{Q}$ of the dynamic ray tracing equations with appropriate initial data for the pair, $\mathbf{Q}$, $\mathbf{P}$. After these steps, the original Hessian of the complex traveltime in Cartesian slownesses can be written in terms of the Hessian of the same complex traveltime with respect to $\boldsymbol{q} = (q_1, q_2)$.

One other subtlety occurs in the derivation of the Hessian in $\boldsymbol{q}$. In ray-centered coordinates, the arc length along a ray is an independent third parameter with the given location determined by marching out to a specific value of the arc length s and then moving orthogonally to the ray along a vector $\boldsymbol{q}$. However, the image point $\boldsymbol{x}$ is the same for the entire family of Gaussian beams in the integral representing a Green's function. As a result of that, the arc length can be different for each ray that "carries" a Gaussian beam, so that $s = s(\boldsymbol{q})$, as we show below by examining the case of constant velocity in the discussion beginning on page 92; on the other hand, when there are no caustics in the ray family, we can also write down $\boldsymbol{q} = \boldsymbol{q}(s, , p_{10}, p_{20})$; the latter pair on the right here are the two initial slownesses that generalize p_{10} shown in Figure 1 to 3D.

With an explanation of the approximation we make along the way, we arrive at an approximate expression for the desired Hessian of the complex traveltime in Cartesian slownesses that we want in terms of the Hessian of the same complex traveltime with respect to $\boldsymbol{q}$. The latter Hessian is surrounded by the Jacobians of the two transformations of coordinates and their transposes. The formula for the Hessian of one set of Cartesian slownesses—sources or receivers—is stated in equation (50). The final formula for the sum of Hessians needed in this analysis is stated in equation (51).

All quantities in (51) are determined on the discrete set of central rays that are computed. Thus, after a difficult theory, once we have the answer the original rotation to the ray through the image point $\boldsymbol{x}$ is not needed. This is explained in context.

1.7 Content of the sections

Section 2 contains background information necessary for this analysis and establishes a baseline of notation. The asymptotic formula we need to evaluate is stated in equation (19), with I in that equation related to the product of Green's functions as defined by equation (15). The Hessian matrix that we need to determine at a saddle point is defined by equation (18). It is written in terms of the Hessians of transverse slownesses for source and receiver in equation (21).

Section 3 is devoted to the analysis of either of these last two slownesses; they both require the same analysis, one for source coordinates, one for receiver coordinates. Hence, a single analysis suffices for both. Section 4 provides the final formula for the Hessian matrix that we seek.

In Section 5, we present a true amplitude common-shot Kirchhoff migration formula and show that exactly the sort of integral we analyze in this paper appears in that formula. The methodology we present is driven by the fact that the exponent that appears in the migration operator is the complex conjugate of the sum of complex traveltimes of the separate Green's functions.

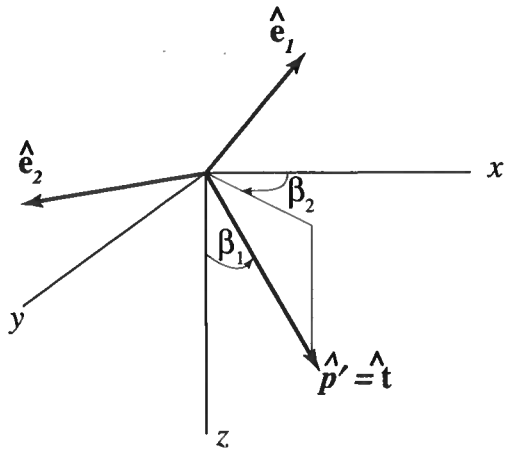

Figure 3. The polar angles define the initial slowness in the Cartesian system. The ray through $\boldsymbol{x}$ has initial direction $\hat{\boldsymbol{p}}'$. $\hat{\mathbf{e}}_1$, $\hat{\mathbf{e}}_2$ are the other initial orthogonal coordinates in this system. Furthermore, the rotation angles β_1 and β_2 are depicted. Each of the central rays of Gaussian beams has its own such triple of initial directions.

That structure is generic and not specific to our example; hence, our derivation applies to the kernel of the integral migration operator for *any* integration operator using Gaussian beams.

Finally, in Section 6, we provide the 2D example that appeared in Gray and Bleistein [2009]. This example supports our claimed accuracy of the method presented here.

The two major results derived in this paper are as follows.

(i) The asymptotically-approximate determinant of a sum of two Hessian matrices that are required to complete the 2D steepest descent formula that provides "true amplitude" of the Gaussian beam migration formula in 3D.

(ii) Strictly speaking, the steepest descent evaluation of integrals is not available in more than once complex variable, but iteration under reasonable assumptions provides us with a formula that is almost to be expected in a double integral with a complex exponent. This analysis is presented in Appendix A.

2 PRELIMINARIES

We need various pieces of background information and notation in order to explain our analysis. That will be done in this preliminary section. Here is a list of what will be discussed.

(i) The kinematic and dynamic equations governing propagation of paraxial rays in ray-centered coordinates.

(ii) The dynamic quantities of the propagator matrix—Červený [2001], Section 4.3.1—and the relationship to the dynamic quantities of Gaussian beams.

(iii) The complex traveltimes from source and receiver to an image point; their dependencies on the original slownesses as well as their dependencies on the transformed slownesses proposed by Hill [2001].

(iv) The Hessian we need to evaluate and its relation to the Hessians in the original slowness variables from source and receiver to image point.

2.1 The kinematic and dynamic equations governing propagation on paraxial rays in ray-centered coordinates

This is item (i) in the list above. We begin by considering a ray defined by Cartesian ray theory with initial point $\boldsymbol{x}_0$ and passing through $\boldsymbol{x}'$ as in Figure 2, the 3D version of Figure 1, omitting the slowness vectors. The point $\boldsymbol{x}_0$ might be the initial point for a ray from a source location, $\boldsymbol{x}_0 = \boldsymbol{x}_s$, or a receiver location, $\boldsymbol{x}_0 = \boldsymbol{x}_r$.

The initial direction of the ray from $\boldsymbol{x}_0$ through $\boldsymbol{x}$ defines the rotation direction in 3D of the new coordinate system in 3D. Associated with that ray is an orthogonal ray-centered coordinate system, (s, q_1, q_2). Figure 3 on page 83 shows the initial orientation of the unit vectors $(\hat{\mathbf{t}}, \hat{\mathbf{e}}_1, \hat{\mathbf{e}}_2)$ in an (s, q_1, q_2) coordinate system. In these coordinates s is arc length along the central ray, as depicted in Figure 2 and q_1 and q_2 are the orthogonal coordinates to the central ray, also orthogonal to one another.

In Figure 2, we depict the coordinates of the point $\boldsymbol{x}$ in terms of the ray-centered coordinates (s, q_1, q_2) on the central ray through $\boldsymbol{x}'$.

In these coordinates, $q_1 = q_2 = 0$ on the central ray through $\boldsymbol{x}'$. Nearby central rays of Gaussian beams from the same point $\boldsymbol{x}_0$ are defined by initial directions that are different from the initial direction of this central ray.

We need a notation for the velocity and its derivatives along the central ray through $\boldsymbol{x}'$:

$$\begin{gathered} \mathrm{v}_0(s) = \mathrm{v}(s,0,0), \quad \mathrm{v}_{0,s} = \left.\frac{\partial \mathrm{v}(s,0,0)}{\partial s}\right|_{q_1 = q_2 = 0}, \\ \mathrm{v}_{0,I} = \left.\frac{\partial \mathrm{v}}{\partial q_I}\right|_{q_1 = q_2 = 0}, \quad \mathrm{v}_{0,IJ} = \left.\frac{\partial^2 \mathrm{v}}{\partial q_I \partial q_J}\right|_{q_1 = q_2 = 0}, \quad I,J = 1,2, \quad \mathbf{V} = \left[\mathrm{v}_{0,IJ}\right]. \end{gathered} \tag{1}$$

The central rays are determined by describing the propagation of the coordinates (q_1, q_2) for each s along the central ray and the slownesses of the real traveltime τ of asymptotic ray theory, defined by

$$p_1 = \frac{\partial \tau}{\partial q_1}, \quad p_2 = \frac{\partial \tau}{\partial q_2}. \tag{2}$$

In our application, we need to move from initial slownesses (p_x, p_y) in the Cartesian coordinate system of the defined integral of interest to the initial ray-centered slownesses (p_{10}, p_{20}) that generalize p_{10} of Figure 1 on page 81 to three dimensions.

The kinematic equations are then given by

$$\begin{aligned} &\frac{dq_I}{ds} = \mathrm{v}_0 p_I, \qquad q_I(0) = 0, \\ &\frac{dp_I}{ds} = -\frac{\mathrm{v}_{0,IJ}}{\mathrm{v}_0^2} q_J, \quad p_I(0) = p_{I0}, \quad I,J = 1,2. \end{aligned} \tag{3}$$

Summation on capital indices on repeated indices from 1 to 2 is understood. The propagation of the transverse slownesses (p_1, p_2). is determined. We determine the q's of interest through the connection of the central ray to the image point.

These equations can also be written in vector form as

$$\begin{aligned} &\frac{d\boldsymbol{q}}{ds} = \mathrm{v}_0 \boldsymbol{p}, \qquad \boldsymbol{q}(0) = \mathbf{0}, \\ &\frac{d\boldsymbol{p}}{ds} = -\frac{1}{\mathrm{v}_0^2} \mathbf{V}\boldsymbol{q}, \quad \boldsymbol{p}(0) = \boldsymbol{p}_0. \end{aligned} \tag{4}$$

In the last equation, $\mathbf{V}$ is the matrix defined in equation (1) and the vectors are vertical arrays of the q's and p's, respectively.

We turn now to the dynamic equations of ray centered coordinates. These are equations for two 2×2 matrices, $\mathbf{Q}$ and $\mathbf{P}$. This is item (ii) of our list in the introduction to this section. These matrices are, in turn, related to the Hessian matrix of second derivatives of the traveltime with respect to $\boldsymbol{q}$ as follows.

$$\mathbf{M} = \left[\frac{\partial^2 \tau}{\partial q_I \partial q_J}\right]_{\boldsymbol{q}=\mathbf{0}}, \quad I,J = 1,2 \quad \mathbf{M} = \mathbf{P}\mathbf{Q}^{-1}, \tag{5}$$

with $\mathbf{Q}$ and $\mathbf{P}$ satisfying the equations

$$\begin{aligned} &\frac{d\mathbf{Q}}{ds} = \mathrm{v}_0 \mathbf{P}, \\ &\frac{d\mathbf{P}}{ds} = -\frac{1}{\mathrm{v}_0^2} \mathbf{V}\mathbf{Q}. \end{aligned} \tag{6}$$

These are the same equations as the kinematic equations (4), except now for 2×2 matrices. We refrain from stating initial conditions since we will define different solutions to these equations below by imposing different initial conditions. Furthermore, when we introduce Gaussian beams through complex-valued initial conditions for $\mathbf{Q}$ and $\mathbf{P}$, we will use T instead of τ for the resulting complex traveltime. Then, τ remains the real traveltime of classical asymptotic ray theory. However, the relation between the Hessian of T with respect to $\boldsymbol{q}$ and the matrices $\mathbf{M}$, $\mathbf{Q}$ and $\mathbf{P}$ stated in equation (5) will remain the same.

2.2 The dynamic quantities of the propagator matrix.

Červený [2001], Section 4.3.1, introduces the propagator matrix $\mathbf{\Pi}(\boldsymbol{x}', \boldsymbol{x}_0)$. This is a matrix of four columns and four rows made up of two different solutions of the dynamic ray equations (6) with different initial conditions as follows.

$$\mathbf{\Pi}(\boldsymbol{x}_0, \boldsymbol{x}_r) = \begin{bmatrix} \mathbf{Q}_1(\boldsymbol{x}', \boldsymbol{x}_0) & \mathbf{Q}_2(\boldsymbol{x}', \boldsymbol{x}_0) \\ \mathbf{P}_1(\boldsymbol{x}', \boldsymbol{x}_0) & \mathbf{P}_2(\boldsymbol{x}', \boldsymbol{x}_0) \end{bmatrix}. \tag{7}$$

The initial conditions for these two pairs of solutions are

$$\begin{array}{ll} \mathbf{Q}_1(\boldsymbol{x}_0, \boldsymbol{x}_0) = \mathbf{I}, & \mathbf{Q}_2(\boldsymbol{x}_0, \boldsymbol{x}_0) = \mathbf{0}, \\ \mathbf{P}_1(\boldsymbol{x}_0, \boldsymbol{x}_0) = \mathbf{0}, & \mathbf{P}_2(\boldsymbol{x}_0, \boldsymbol{x}_0) = \mathbf{I}. \end{array} \tag{8}$$

The solution pair $\mathbf{Q}_1(\boldsymbol{x}', \boldsymbol{x}_0)$ and $\mathbf{P}_1(\boldsymbol{x}', \boldsymbol{x}_0)$ arise naturally when describing propagation of plane waves in (real) asymptotic ray theory. The solution pair $\mathbf{Q}_2(\boldsymbol{x}', \boldsymbol{x}_0)$ and $\mathbf{P}_2(\boldsymbol{x}', \boldsymbol{x}_0)$ arise naturally when describing the propagation from a point, as for the Green's function. The initial data for $\mathbf{\Pi}$ is a 4×4 identity matrix. Furthermore, when the columns are viewed as solutions of the system of differential equations (6), it can be shown that they are *linearly independent* in the sense that the Wronskian—the determinant of the matrix $\mathbf{\Pi}$—is nonzero for all values of s.

Remark

It is useful to understand the dimensions of the two solutions comprising the propagator matrix. Note that the elements of $\mathbf{Q}_1$ are dimensionless quantities, given initially by a matrix of ones and zeroes. Similarly, the elements of $\mathbf{P}_2$ are dimensionless. With $\mathbf{Q}_1$ dimensionless, the second differential equation in (6) reveals that the dimensions of the elements of $\mathbf{P}_1$ are T/L^2—TIME/LENGTH-SQUARED. Similarly, with $\mathbf{P}_2$ dimensionless, the dimensions of $\mathbf{Q}_2$ are L^2/T—LENGTH-SQUARED/TIME. For our physical applications, we will choose the dimension of the elements of $\mathbf{Q}$ to be LENGTH and the dimensions of the elements of $\mathbf{P}$ to be slowness, inverse velocity—TIME/LENGTH. Thus, when adding together linear combinations of the two sets of fundamental solutions, the dimensionality of the coefficients of these solutions will have corresponding dimensionality to yield the desired dimensionality of the sum.

Now let us consider a complex-valued traveltime, T, instead of τ used above in equation (5). Thus, instead of equation (5), we write

$$\mathbf{M}_{GB} = \left[\frac{\partial^2 T}{\partial q_I \partial q_J} \right]_{\boldsymbol{q}=\mathbf{0}}, \quad I, J = 1, 2 \quad \mathbf{M}_{GB} = \mathbf{P}_{GB} \mathbf{Q}_{GB}^{-1}. \tag{9}$$

The pair of functions $\mathbf{Q}(\boldsymbol{x}', \boldsymbol{x}_0) = \mathbf{Q}_{GB}(\boldsymbol{x}', \boldsymbol{x}_0)$ and $\mathbf{P}(\boldsymbol{x}', \boldsymbol{x}_0) = \mathbf{P}_{GB}(\boldsymbol{x}', \boldsymbol{x}_0)$ are solutions of the dynamic equations (6) subject to the initial conditions

$$\begin{aligned} \mathbf{Q}_{GB}(\boldsymbol{x}_0, \boldsymbol{x}_0) &= \frac{\omega_r w_0^2}{\mathrm{v}_0(0)} \mathbf{I}, \\ \mathbf{P}_{GB}(\boldsymbol{x}_0, \boldsymbol{x}_0) &= \frac{i}{\mathrm{v}_0(0)} \mathbf{I}, \end{aligned} \tag{10}$$

In the first equation, ω_r is a reference frequency and w_0 is a length scale. At the reference frequency ω_r, w_0 is the initial "standard deviation" of the Gaussian exponential that arises in the description of the Gaussian beam. For example, in a homogeneous medium with initial arc length zero and initial traveltime zero, the exponential part of the Gaussian beam is

$$\exp\{i\omega T\} = \exp\left\{ i\omega \frac{|\boldsymbol{x}' - \boldsymbol{x}_0|}{\mathrm{V}_0} - \frac{\omega |\boldsymbol{q}|^2}{2\left[\omega_r w_0^2 + i \mathrm{V}_0 |\boldsymbol{x}' - \boldsymbol{x}_0|\right]} \right\}. \tag{11}$$

It is easy to check our claim about w_0 by setting $\boldsymbol{x} = \boldsymbol{x}_0$ in this equation and $\omega = \omega_r$.

As a result of the linearity in the differential equations, we can write the two matrices $\mathbf{Q}_{GB}$ and $\mathbf{P}_{GB}$ in terms of the elemental matrices of equation (8) as follows:

$$\begin{aligned} \mathbf{Q}_{GB}(\boldsymbol{x}', \boldsymbol{x}_0) &= \frac{\omega_r w_0^2}{\mathrm{v}_0(0)} \mathbf{Q}_1(\boldsymbol{x}', \boldsymbol{x}_0) + \frac{i}{\mathrm{v}_0(0)} \mathbf{Q}_2(\boldsymbol{x}', \boldsymbol{x}_0), \\ \mathbf{P}_{GB}(\boldsymbol{x}', \boldsymbol{x}_0) &= \frac{\omega_r w_0^2}{\mathrm{v}_0(0)} \mathbf{P}_1(\boldsymbol{x}', \boldsymbol{x}_0) + \frac{i}{\mathrm{v}_0(0)} \mathbf{P}_2(\boldsymbol{x}', \boldsymbol{x}_0). \end{aligned} \tag{12}$$

2.3 Gaussian beams and the complex traveltimes T

Here we proceed to item (iii) in our list at the beginning of this section. The Gaussian beam representation of a Green's function $G(\boldsymbol{x},\boldsymbol{x}_0,\omega)$ is given by Hill [2001] as*

$$
\begin{aligned}
G(\boldsymbol{x},\boldsymbol{x}_0,\omega) &= \frac{i\omega\omega_r w_0^2}{2\pi \mathrm{v}^{3/2}(\boldsymbol{x}_0)}\int_{D_x} A_{GB}(\boldsymbol{x}',\boldsymbol{x}_0)\exp\{i\omega T(\boldsymbol{x}',\boldsymbol{x}_0)\}\frac{dp_1'dp_2'}{p_3'}.\\
A_{GB}(\boldsymbol{x}',\boldsymbol{x}_0) &= \sqrt{\frac{\mathrm{v}_0(\boldsymbol{x}'(s))}{\det[\mathbf{Q}_{GB}(\boldsymbol{x}'(s))]}},\quad T(\boldsymbol{x}',\boldsymbol{x}_0)=\tau(s)+\frac{1}{2}\boldsymbol{q}^{\mathrm{T}}\mathbf{P}_{GB}\mathbf{Q}_{GB}^{-1}\boldsymbol{q},\\
&\qquad \tau(s)=\int_0^s \frac{ds'}{\mathrm{v}_0(s')}.
\end{aligned}
\tag{13}
$$

In these equations, the superscript T denotes "transpose." The vector $\boldsymbol{p}'=(p_1',p_2',p_3')$ is the initial Cartesian slowness vector of the ray that propagates from $\boldsymbol{x}_0$ to $\boldsymbol{x}'$. The ensemble of central rays in this integral covers a region around the image point $\boldsymbol{x}$. (We do not need to know which ray goes through $\boldsymbol{x}$. This claim will be explained near the end of Section 4.) For each ray, a vector $\boldsymbol{q}$ connects point $\boldsymbol{x}'$ to the image point $\boldsymbol{x}$ and is perpendicular to the ray at $\boldsymbol{x}'$; s is the arc length along that ray to the point $\boldsymbol{x}'$. Thus, the complex traveltime T is implicitly a function of the transverse slownesses, p_1', p_2', and $\tau(s)$ is the traveltime of the classical asymptotic ray theory as noted above. In the application where $\boldsymbol{x}$ is fixed and the initial direction of the ray changes, the arc length s at the upper limit of the integral defining T is also a function of the initial slownesses on the ray from $\boldsymbol{x}_0$ through $\boldsymbol{x}'$ and the image point $\boldsymbol{x}$.

Any correlation-type migration imaging condition involves a product of such Green's functions from source and receiver to image point:

$$
\mathfrak{G}(\boldsymbol{x},\boldsymbol{x}_s,\boldsymbol{x}_r,\omega)=G^*(\boldsymbol{x},\boldsymbol{x}_s,\omega)G^*(\boldsymbol{x},\boldsymbol{x}_r,\omega),
\tag{14}
$$

with $(^*)$ denoting complex conjugate here and below. When we use equation (13) for each Green's function, we obtain

$$
\begin{aligned}
\mathfrak{G}(\boldsymbol{x},\boldsymbol{x}_s,\boldsymbol{x}_r,\omega) &= -\frac{\omega^2\omega_r^2 w_0^4}{4\pi^2 \mathrm{v}^{3/2}(\boldsymbol{x}_s)\mathrm{v}^{3/2}(\boldsymbol{x}_r)} I(\boldsymbol{x},\boldsymbol{x}_s,\boldsymbol{x}_r,\omega),\\
I(\boldsymbol{x},\boldsymbol{x}_s,\boldsymbol{x}_r,\omega) &= \int_{D_{xs}}\frac{dp_{s1}'dp_{s2}'}{p_{s3}'}\int_{D_{xr}}\frac{dp_{r1}'dp_{r2}'}{p_{r3}'}\\
&\qquad \cdot A_{GB}^*(\boldsymbol{x}_s',\boldsymbol{x}_s)A_{GB}^*(\boldsymbol{x}_r',\boldsymbol{x}_r)\exp\{-\omega\Psi(\boldsymbol{x}_s',\boldsymbol{x}_s,\boldsymbol{x}_r',\boldsymbol{x}_r)\},
\end{aligned}
\tag{15}
$$

$$
\Psi(\boldsymbol{x}_s',\boldsymbol{x}_s,\boldsymbol{x}_r',\boldsymbol{x}_r) = -i[T(\boldsymbol{x}_s',\boldsymbol{x}_s)+T(\boldsymbol{x}_r',\boldsymbol{x}_r)]^*.
$$

Hill [2001] proposes the change of variables

$$
\begin{aligned}
&p_{h1}'=p_{r1}'-p_{s1}',\quad p_{h2}'=p_{r2}'-p_{s2}', && p_{r1}'=\frac{p_{m1}'+p_{h1}'}{2},\quad p_{s1}'=\frac{p_{m2}'-p_{h2}'}{2},\\
&\qquad\qquad\qquad\Leftrightarrow\\
&p_{m1}'=p_{r1}'+p_{s1}',\quad p_{m2}'=p_{r2}'+p_{s2}', && p_{r2}'=\frac{p_{m1}'+p_{h1}'}{2},\quad p_{s2}'=\frac{p_{m2}'-p_{h2}'}{2}.
\end{aligned}
\tag{16}
$$

The variables in $\boldsymbol{p}_h$ may be viewed as *offset slowness vectors* and the variables in $\boldsymbol{p}_m$ may be viewed as *midpoint slownesses*.

This change of variables produces an expressions for I with the (p_{m1}',p_{m2}') integrals outermost. He then proposes that the method of steepest descent be applied to the two integrals in the variables p_{h1}' and p_{h2}'. He carries this out as a kinematic process. Therefore, he needs only to determine the saddle points in these two variables for any given choice of the other pair, p_{m1}' and p_{m2}'. He then proposes to compute the integrals over p_{m1}' and p_{m2}' numerically.

In Appendix A we show how to calculate the leading order asymptotic expansion of an integral such as I in equation (15) by the method of steepest descent. This method calculates that expansion by applying the method of steepest descent in one dimension iteravely. The method properly accounts for amplitude as well as complex exponent in that expansion. We assume that for each value of

$\boldsymbol{p}_m'=(p_{m1}',p_{m2}')$ there exists a " simple saddle point"

*Hill [1990, 2001] uses subscripts x, y and z. We use numerical subscripts because we need them for index notation in the matrices to follow.

$$\boldsymbol{p}_h^{'\mathrm{sad}}(\boldsymbol{p}'_m) = (p_{h1}^{'\mathrm{sad}}(\boldsymbol{p}'_m), p_{h2}^{'\mathrm{sad}}(\boldsymbol{p}'_m)), \tag{17}$$

for which

$$\begin{aligned} &\frac{\partial \Psi}{\partial p'_{h1}} = \frac{\partial \Psi}{\partial p'_{h2}} = 0, \qquad && \boldsymbol{p}_h = \boldsymbol{p}_h^{'\mathrm{sad}}(\boldsymbol{p}'_m), \\ &\det[\boldsymbol{\Psi}] \neq 0, \quad \boldsymbol{\Psi} = \left[\frac{\partial^2 \Psi}{\partial p_{hI} \partial p_{hJ}}\right], \quad I, J = 1, 2, && \boldsymbol{p}_h = \boldsymbol{p}_h^{'\mathrm{sad}}(\boldsymbol{p}'_m). \end{aligned} \tag{18}$$

The last constraint here, $\det[\boldsymbol{\Psi}] \neq 0$, makes this saddle point "simple." This is a standard assumption on the Hessian matrix $\boldsymbol{\Psi}$ in two-dimensional integrals.

Remark The condition, $\det[\boldsymbol{\Psi}] \neq 0$

In one dimension, a stationary point is "simple" if the second derivative of the exponent is nonzero at that point. In this case, the difference,

$$\Psi(p) - \Psi(p^{'\mathrm{sad}}) \approx \Psi''(p^{'\mathrm{sad}})(p - p^{'\mathrm{sad}})^2/2,$$

is quadratic. The stationary phase formula relies on this quadratic approximation. The stationary point is called "higher order" if the second derivative at the stationary or saddle point is zero as well; the local approximation is at least cubic and the leading order asymptotic approximation is changed accordingly. See, for example, Bleistein and Handelsman [1986]. For higher dimensional integrals with a real traveltime, (imaginary exponent), this idea is extended by using properties of Hessian matrixies. In particular, these matrices are symmetric, their eigenvalues are real and their eigenvectors are orthogonal. Bleistein and Handelsman [1975, 1986] show how these properties allow a rotation of coordinates to the directions of the eigenvectors, called the "principal directions" of the Hessian. In this case, the function Ψ is locally a sum of signed squares, with the signs of the separate terms depending on the signs of the individual eigenvalues. The same is possible for purely real exponents, such as occur in Laplace-type integrals (op. cit.), except that now all of the eigenvalues have to be of one sign. This leads to the asymptotic expansion derived by the one-dimensional stationary phase or Laplace method formula applied to the integrations in each of the principal directions.
For a complex valued traveltime Ψ, we do not have the same theory for its complex valued Hessian matrix. However, we show in Appendix A that the same condition naturally arises in order to solve for the second derivative of the second variable of integration after having determined the first integral by the formula for the leading order asymptotic approximation by the method of steepest descent. See equation (A.18).

Under these assumptions, the iterated method of steepest descent leads to the following asymptotic formula for I_r in equation (4).

$$\begin{aligned} I(\boldsymbol{x}, \boldsymbol{x}_s, \boldsymbol{x}_r, \omega) \quad \sim \quad & \frac{\pi}{2\omega} \int_{D_m} \frac{dp'_{m1} dp'_{m2}}{\sqrt{\det[\boldsymbol{\Psi}]}} A^*_{GB}(\boldsymbol{x}'_s, \boldsymbol{x}_s) A^*_{GB}(\boldsymbol{x}'_r, \boldsymbol{x}_r) \\ & \cdot \exp\{i\omega[T(\boldsymbol{x}'_s, \boldsymbol{x}_s) + T(\boldsymbol{x}'_r, \boldsymbol{x}_r)]^*\}, \quad \boldsymbol{p}_h = \boldsymbol{p}_h^{'\mathrm{sad}}(\boldsymbol{p}'_m). \end{aligned} \tag{19}$$

The objective of this paper is evaluate $\det[\boldsymbol{\Psi}]$ appearing in this formula. For that purpose, let us first rewrite the matrix $\boldsymbol{\Psi}$ in terms of the separate Hessian matrices for $T(\boldsymbol{x}'_s, \boldsymbol{x}_s)$ and $T(\boldsymbol{x}'_r, \boldsymbol{x}_r)$ appearing in the definition of Ψ in equation (14).

To begin this process, we observe first that

$$\begin{aligned} \frac{\partial \Psi}{\partial p'_{hj}} &= \frac{\partial p'_{rj}}{\partial p'_{hj}} \frac{\partial \Psi}{\partial p'_{rj}} + \frac{\partial p'_{sj}}{\partial p'_{hj}} \frac{\partial \Psi}{\partial p'_{sj}}, \\ &= \frac{\partial \Psi}{\partial p'_{rj}} - \frac{\partial \Psi}{\partial p'_{sj}} \\ &= -i \left[\frac{\partial T(\boldsymbol{x}'_r, \boldsymbol{x}_r)}{\partial p'_{rj}} - \frac{\partial T(\boldsymbol{x}'_s, \boldsymbol{x}_s)}{\partial p'_{sj}}\right]^*, \quad j \doteq 1, 2. \end{aligned} \tag{20}$$

In the second line in this equation, we used equation (16) to evaluate the derivatives of the elements of $\boldsymbol{p}_h$ with respect to the elements of $\boldsymbol{p}_r$ and $\boldsymbol{p}_s$. In the third line, we replaced Ψ by the separate complex traveltimes, the T's, using the definition of Ψ in equation (15).

Differentiating one more time leads to the following representation of the elements of the Hessian matrix of second derivatives of Ψ:

$$\frac{\partial^2 \Psi}{\partial p'_{hj} \partial p'_{hk}} = -i \left[\frac{\partial^2 T(\boldsymbol{x}'_r, \boldsymbol{x}_r)}{\partial p'_{rj} \partial p'_{rk}} + \frac{\partial^2 T(\boldsymbol{x}'_s, \boldsymbol{x}_s)}{\partial p'_{sj} \partial p'_{sk}}\right]^*, \quad j.k = 1, 2. \tag{21}$$

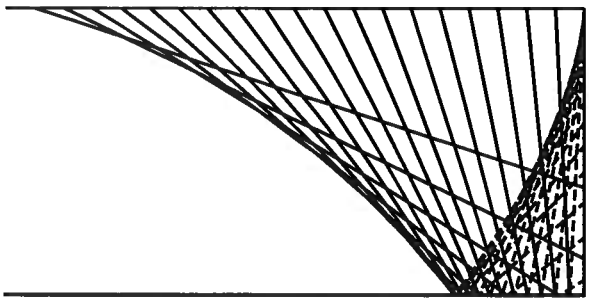

Figure 4. Rays with a caustic point incident on a reflector, shown as solid lines. Reflected rays shown as dashed lines. For a flat reflector, the reflected rays are simple "image rays" from corresponding source points in the lower space. The image rays have the same caustic as the incident rays.

This is item (iv) of the list at the beginning of this section. In the next section we analyze the two matrices on the right hand side of this equation.

We remark that each of the matrices on the right hand side of equation (21) will be singular at a caustic of the central rays {a} from the receiver (first matrix), or {b} from the source (second matrix), respectively. This would undo the original purpose of using Gaussian beams to represent the Green's functions. However, the occurrence of both matrices being singular simultaneously in such a manner as to create a singular sum of matrices is expected to be relatively rarer than singular behavior of one or the other. The sum of the singular matrices being zero requires an alignment of the eigenvectors attached to the pair of zero eigenvalues. In fact, one situation where we know this will occur is when the image point is on a caustic of the incident rays. In that case, the incident rays and the reflected rays lie in a plane, and the eigenvectors of the zero eigenvalues *are* colinear. In Figure 4, we show a 2D example of a family of rays (solid black) incident on a line. The reflected rays (dashed black) continue the caustic of t he incident rays. In fact, those rays emanate from the "image points" of the sources points at 0 km depth. This example is a cartoon of the more general 3D case. Incident and reflected rays start out in the same plane, so that the slice might be thought of as arising from the normal to the local tangent to the reflector surface at the caustic point. Further, if the reflector were curved, that curvature would only slightly distort the directions of the reflected (black) rays. However, those new rays would still exhibit the same caustic as the incident rays.

The true amplitude Kirchhoff migration theory is not valid at caustics in any case. We would not use a caustic reflection point as a place to estimate a reflection coefficient. We only need to regularize the sum of matrices in equation (21) so that the zero determinant of the sum of those two matrices does not cause the running sum producing the true amplitude migration to blow up. So the question of inversion as we define it is moot. Thus, we would content ourselves with some appropriate regularization of the matrix sum.

3 THE HESSIAN MATRIX T

The right hand side of equation (21) contains two Hessian matrices of identical structure. In this section, we show how they can be written in terms of the matrix elements of the propagator matrix $\mathbf{\Pi}$ of equation (6). There is no need to distinguish between source and receiver here through the subscripts s and r and so we speak of a generic Hessian with respect to initial transverse slownesses. Thus, we write

$$\mathbf{T} = [T_{jk}], \quad T_{jk} = \frac{\partial^2 T(\boldsymbol{x}', \boldsymbol{x})}{\partial p'_j \partial p'_k}, \quad j,k = 1,2. \tag{22}$$

As discussed in the Introduction, we proposed to determine this Hessian by transforming from Cartesian coordinates to ray-centered coordinates and relating this Hessian to the Hessian of T with respect to the offset coordinates (q_1, q_2) from a central ray, .

We propose to do this in two steps.

(i) Transform the Hessian from the variables $\boldsymbol{p}'$ of the integral in Cartesian coordinates to the initial ray-centered slownesses orthogonal to the central ray (p_{10}, p_{20}). Implicit in this transformation is a transformation also of the Cartesian coordinates, $\boldsymbol{x}'$ to the ray-centered coordinates (s, q_1, q_2). This transformation is described below.

(ii) Transform the Hessian in (p_{10}, p_{20}) into a Hessian in (q_1, q_2). The Jacobian of this transformation arises from the mapping by rays from a point source.

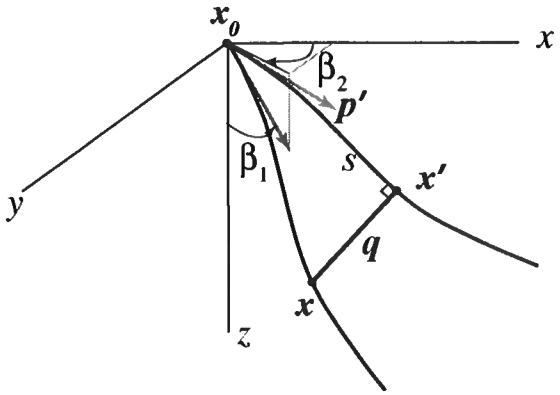

Figure 5. The reference ray from $\boldsymbol{x}_0$ to $\boldsymbol{x}$ and the ray from $\boldsymbol{x}_0$ to $\boldsymbol{x}'$. The initial ray direction of the first ray is defined by the polar angles (β_1, β_2). The initial direction of this ray is defined by the values of $\boldsymbol{p}'$. The initial vector $\boldsymbol{p}_0$ is the vector $\boldsymbol{p}'$ in the coordinate system of the central ray through vx'

A subtlety in Step 1 of this analysis needs discussion. Each (p_1', p_2') of the Cartesian integration variables defines a new central ray. Each central ray has its own ray-centered coordinate system. In each individual coordinate system, the initial slownesses (p_{10}, p_{20}) orthogonal to the central ray are zero on the central ray. By changing coordinate systems with each central ray, we cannot transform derivatives with respect to the variables (p_1', p_2') into derivatives with respect to (p_{10}, p_{20}) because the coordinate system of the latter slownesses keeps changing. That is, there is only one Cartesian coordinate system, but each ray has its own ray-centered coordinate system.

Instead, we introduce the central ray from $\boldsymbol{x}_0$ to $\boldsymbol{x}$ as a reference. We then evaluate the initial values $\boldsymbol{p}_0$ of the vector $\boldsymbol{p}$ on each paraxial ray in a fixed ray-centered coordinate system measured from the initial direction of this reference ray. In this rotated coordinate system $\boldsymbol{p}_0$ is just the new representation of the vector $\boldsymbol{p}'$. In Figure 5, we depict the ray from $\boldsymbol{x}_0$ to $\boldsymbol{x}$ as well the ray $\boldsymbol{x}_0$ to $\boldsymbol{x}'$. We also show the polar angles (β_1, β_2) of the initial direction of the ray to $\boldsymbol{x}$.

Once we have this first transformation from $\boldsymbol{p}'$ to the initial values $\boldsymbol{p}_0$ in place, the second transformation from the initial values of (p_{10}, p_{20}) to (q_1, q_2) is simply a mapping by rays that can be expressed in terms of the appropriate dynamic matrix $\mathbf{Q}_2$.

Gaussian beams were used for a similar purpose in the asymptotic analysis of the integral over Gaussian beams in Hill [2001], Appendix B. He used such transformations in homogeneous media to compare his beam representation to the known leading order ray-theoretic asymptotic approximation of Green's functions. In that appendix, the integral over beams is calculated as an integral in polar angles measured from the distinguished central ray through $\boldsymbol{x}$ as opposed to an integration of slownesses $\boldsymbol{p}_s'$ or $\boldsymbol{p}_r'$ through the points $\boldsymbol{x}_s'$ or $\boldsymbol{x}_r'$, respectively, as in the representations of the Green's functions imbedded in the right hand side in equation (15). The use of polar coordinates as in Hill's appendix was not really necessary; in fact, Hill's [2001] Gaussian beam migration integrates initially over the slownesses $\boldsymbol{p}_s'$ or $\boldsymbol{p}_r'$ as we are doing here. However, in his appendix Hill carried out the asymptotic analysis in homogeneous media; that is all he needed for the purpose of comparison of leading order asymptotic representations of Green's functions; the calculation in homogeneous media is particularly simple in polar coordinates. Here, however, for the Hessian matrices $\mathbf{T}$ of equation (22) for sources and receivers and eventually for the matrix Ψ of equation (18), we need to do a similar analysis in heterogeneous media. Implicit in our analysis is the methodology for calculating the asymptotic expansion that Hill [2001] did, but in heterogeneous media. This is not new: Červený[2001] describes asymptotic expansions for more arbitrary changes of coordinates in heterogeneous media. His method relies on a theorem in Korn & Korn [1968] where the authors show how to simultaneously diagonalize a symmetric complex-valued matrix such as our Hessian matrix $\mathbf{T}$ in equation (22). It is not straightforward to use Červený's method to go from the general discussion of the asymptotic expansion of the double integral to the specific example we have here. Hence, we proceed with the transformations and then they will be applied to facilitate the evaluation of the $\det[\Psi]$. Thereafter we apply the method of Appendix A of this paper to determine the asymptotic expansion in p_h' in equation (19).

We now proceed to the outlined analysis.

3.1 Transformation to a Hessian with respect to p_0.

Figure 3 on page 83 shows the initial directions of a ray in Cartesian and ray-centered coordinates. The vector $\hat{\boldsymbol{p}}'$ is the initial direction of the ray through $\boldsymbol{x}$. In the original Cartesian coordinate system the representation of the vector $\hat{\boldsymbol{p}}' = (\hat{p}'_1, \hat{p}'_2, \hat{p}'_3)$. As a first step, we rotate the Cartesian coordinate system through the angles β_1 and β_2 of the figure, with $\hat{\boldsymbol{p}}'$ being the initial direction of the new z-axis.

The rotation to the new Cartesian coordinates from the old is accomplished by first carrying out a rotation around the z-axis through the angle β_2 and then by a rotation through the angle β_1 about the new y-axis with unit vector $\hat{\mathbf{e}}_2$. We therefore write the transformation of coordinates as a product of two matrix multiplications on the elements of an arbitrary slowness vector $\boldsymbol{p}'$ as follows:

$$\boldsymbol{p}_0 = \begin{bmatrix} p_{10} \\ p_{20} \\ p_{30} \end{bmatrix} = \boldsymbol{\Gamma}_1(\beta_1)\boldsymbol{\Gamma}_2(\beta_2) \begin{bmatrix} p'_1 \\ p'_2 \\ p'_3 \end{bmatrix} = \boldsymbol{\Gamma}_1(\beta_1)\boldsymbol{\Gamma}_2(\beta_2)\boldsymbol{p}'. \tag{23}$$

Here

$$\boldsymbol{\Gamma}_1(\beta_1) = \begin{bmatrix} \cos\beta_1 & 0 & \sin\beta_1 \\ 0 & 1 & 0 \\ -\sin\beta_1 & 0 & \cos\beta_1 \end{bmatrix}, \quad \boldsymbol{\Gamma}_2(\beta_2) = \begin{bmatrix} \cos\beta_2 & \sin\beta_2 & 0 \\ -\sin\beta_2 & +\cos\beta_2 & 0 \\ 0 & 0 & 1 \end{bmatrix},$$

$$\boldsymbol{\Gamma}_1(\beta_1)\boldsymbol{\Gamma}_2(\beta_2) = \begin{bmatrix} \cos\beta_1\cos\beta_2 & \cos\beta_1\sin\beta_2 & \sin\beta_1 \\ -\sin\beta_2 & \cos\beta_2 & 0 \\ -\sin\beta_1 - \cos\beta_2 & \sin\beta_1\sin\beta_2 & \cos\beta_1 \end{bmatrix}. \tag{24}$$

Now in equation (22), we can apply the chain rule to rewrite the Hessian with respect to p'_1, p'_2 as

$$\mathbf{T} = [T_{jk}], \quad T_{jk} = \frac{\partial^2 T(\boldsymbol{x}', \boldsymbol{x})}{\partial p'_j \partial p'_k} = \frac{\partial^2 T(\boldsymbol{x}', \boldsymbol{x})}{\partial p_{\lambda 0} \partial p_{\kappa 0}} \frac{\partial p_{\lambda 0}}{\partial p'_j} \frac{\partial p_{\kappa 0}}{\partial p'_k}, \quad j,k = 1,2, \quad \lambda,\kappa = 1,2. \tag{25}$$

Summation from 1 to 2 over the repeated indices λ and κ is understood in this equation.

This rotation of the representation of the initial slownesses is also the rotation of the initial directions of the coordinate system. It makes the direction of the post rotation z-axis be along the initial tangent of the ray from $\boldsymbol{x}_0$ through $\boldsymbol{x}$.

We can calculate the matrix of derivatives among the slownesses in equation (25) from equation (23) relating these variables. We simply differentiate both sides of equation (25) with respect to p'_1 and p'_2. In doing so, we must take care to note that p'_3 is a function of p'_1 and p'_2 through the eikonal equation in Cartesian coordinates, namely,

$$p'^2_1 + p'^2_2 + p'^2_3 = 1/\mathrm{v}^2. \tag{26}$$

When we carry out these calculations, we find that

$$\left[\frac{\partial p_{\lambda 0}}{\partial p'_j}\right] = \begin{bmatrix} \dfrac{\cos\beta_2}{\cos\beta_1} & \dfrac{\sin\beta_2}{\cos\beta_1} \\ -\sin\beta_2 & \cos\beta_2 \end{bmatrix} = [\Gamma_{\lambda j}] = \boldsymbol{\Gamma}, \quad \lambda, j = 1,2. \tag{27}$$

In analogy with equation (25), let us now introduce the notation

$$\mathbf{T}_0 = [T_{\lambda\kappa 0}], \quad T_{\lambda\kappa 0} = \frac{\partial^2 T(\boldsymbol{x}', \boldsymbol{x})}{\partial p_{\lambda 0} \partial p_{\kappa 0}}, \quad \lambda,\kappa = 1,2. \tag{28}$$

Then we can rewrite $\mathbf{T}$ in equation (25) as

$$T_{jk} = T_{\lambda\kappa 0}\Gamma_{\lambda j}\Gamma_{\kappa k}, \quad j,k = 1,2; \qquad \mathbf{T} = \boldsymbol{\Gamma}^{\mathrm{T}}\mathbf{T}_0\boldsymbol{\Gamma}. \tag{29}$$

We sum over the repeated indices λ, κ in the elements form of equation (28) for T_{jk}. Again, the superscript T denotes transpose in the matrix form of this same equation for $\mathbf{T}$.

Equation (29) completes the transformation of the Hessian of the complex traveltime in the initial slownesses $\boldsymbol{p}'$ to a Hessian in the initial slownesses $\boldsymbol{p}_0$.

3.2 Transformation to a Hessian with respect to q

Varying $\boldsymbol{p}_0$ leads to different rays, $\boldsymbol{q} = \boldsymbol{q}(\boldsymbol{p}_0, s)$. Furthermore, the arc length s along the central ray also changes with $\boldsymbol{p}_0$ because the image point $\boldsymbol{x}$ is fixed: $s = s(\boldsymbol{q})$. As an example, consider the configuration of Figure 5 on page 89

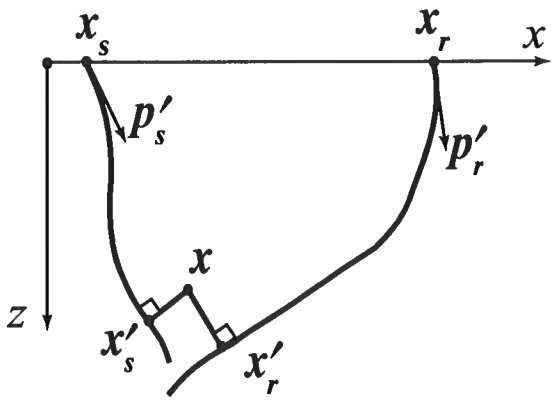

Figure 6. Central rays from the source and receiver propagating to points $\boldsymbol{x}'_s$ and $\boldsymbol{x}'_r$. Those points connect to the image point $\boldsymbol{x}$ by straight lines that are orthogonal to the respective rays at $\boldsymbol{x}'_s$ and $\boldsymbol{x}'_r$, respectively. The exponential decay of the respective complex traveltimes from source and receiver arise from quadratic forms in the respective q's defining the vectors $\boldsymbol{x} - \boldsymbol{x}'_s$ and $\boldsymbol{x} - \boldsymbol{x}'_r$. This configuration might be typical for a choice of $\boldsymbol{p}'_m$ different from $\boldsymbol{p}'^0_m$, for which both rays pass through $\boldsymbol{x}$ and the q's are all equal to zero. The difference of the transverse parts of the vector difference $\boldsymbol{p}'_r - \boldsymbol{p}'_s$ is the 2D vector $\boldsymbol{p}_h$ in the acquisition plane, while the transverse part of the sum $\boldsymbol{p}'_r + \boldsymbol{p}'_s$ is the 2D vector $\boldsymbol{p}'_m$ in the acquisition plane.

for homogeneous media where the rays from $\boldsymbol{x}_0$ to $\boldsymbol{x}'$ are straight lines. Similar to the complex exponent in equation (11) we find that the complex traveltime in equation (13) is

$$T = \frac{s}{\mathrm{V}_0} + \frac{i|\boldsymbol{q}|^2}{2\left[\omega_r w_0^2 + i\mathrm{V}_0 s\right]}, \quad s = \sqrt{|\boldsymbol{x}' - \boldsymbol{x}_0|^2 - \boldsymbol{q}^2}. \tag{30}$$

As claimed, $s = s(\boldsymbol{q})$. We could equally have confirmed that s was a function of $\boldsymbol{p}'$ or $\boldsymbol{p}_0$, but the confirmation at this stage is much easier.

Therefore, we consider a change of variables from $\boldsymbol{p}_0$ to $\boldsymbol{q}$. In that case, we write

$$\frac{\partial T}{\partial p_{\lambda 0}} = \frac{\partial T}{\partial q_\mu}\frac{\partial q_\mu}{\partial p_{\lambda 0}}, \tag{31}$$

and

$$\frac{\partial^2 T}{\partial p_{\lambda 0}\partial p_{\kappa 0}} = \frac{\partial^2 T}{\partial q_\mu \partial q_\nu}\frac{\partial q_\mu}{\partial p_{\lambda 0}}\frac{\partial q_\nu}{\partial p_{\kappa 0}} + \frac{\partial T}{\partial q_\mu}\frac{\partial^2 q_\mu}{\partial p_{\lambda 0}\partial p_{\kappa 0}}, \quad \lambda, \kappa = 1, 2. \tag{32}$$

As previously, summation over the repeated indices μ and ν from 1 to 2 is to be understood.

Viewing this Hessian in $\boldsymbol{q}$ helps us to understand a difficulty in the evaluation process: in general, the saddle points $\boldsymbol{p}'^{\mathrm{sad}}_h(\boldsymbol{p}'_m)$ do not place the central rays through $\boldsymbol{x}$, but rather through some $\boldsymbol{x}'_s$ or $\boldsymbol{x}'_r$ as in Figure 6. In this case, $Im[T] \neq 0$ for one and/or the other central ray from source and receiver. Hence the total traveltime will have some exponential decay. For a certain $\boldsymbol{p}'_m$, say, $\boldsymbol{p}'^0_m$, both rays for the saddle point in $\boldsymbol{p}_h$ will pass through $\boldsymbol{x}$; that is, $\boldsymbol{q}_s = \boldsymbol{q}_r = \boldsymbol{0}$ and $Im[T] = 0$, as well. This is the choice of $\boldsymbol{p}'_m$ that would be the saddle point in $\boldsymbol{p}'_m$ if we were to estimate the integral in $\boldsymbol{p}'_m$ by the method of steepest descent. For this choice of $\boldsymbol{p}'_m = \boldsymbol{p}'^0_m$, *all* of the first derivatives with respect to slownesses are zero, since the first derivatives with respect to the elements of $\boldsymbol{p}_h = \boldsymbol{p}'^{\mathrm{sad}}_h(\boldsymbol{p}'_m)$ are already equal to zero. With all of these derivatives equal to zero, the first derivatives with respect to the elements of $\boldsymbol{q}$ must also be zero here, as well, when $\boldsymbol{p}_h = \boldsymbol{p}'^{\mathrm{sad}}_h(\boldsymbol{p}'_m)$ and $\boldsymbol{p}'_m = \boldsymbol{p}'^0_m$. Furthermore, from the equation for equation (13), we can see that the first derivatives of the traveltime T are linear in the q's.

From the point of view of leading order asymptotic analysis, the smooth variations of the amplitude of the integrand away from $\boldsymbol{p}'^0_m$ matter little as long as that amplitude is correct at $\boldsymbol{p}'^0_m$. The Hessian that we are trying to evaluate is a piece of the amplitude in the integral over $\boldsymbol{p}'_m$, so this observation applies to the evaluation of the Hessian. This is true whether we evaluate the integral numerically or with some asymptotic formula. We avoid using an asymptotic formula because we cannot *a priori* guarantee the nature of the saddle point—whether it is a simple or higher order saddle point of the complex traveltime as a function of $\boldsymbol{p}'_m$. The numerical evaluation will be correct in either case, but it only depends on the amplitude near $\boldsymbol{p}'^0_m$; $Im[T] \neq 0$ away from this value of $\boldsymbol{p}'_m$ and the error in amplitude of the integrand in equation (19) for I is exponentially damped by the value of $Im[T]$. As noted in the introduction, the approximation we propose here has been empirically shown to be adequate for estimating the reflection coefficient in 2D as demonstrated in the numerical example in the last section of this paper.

Thus, we can evaluate the formula for the Hessian in $\boldsymbol{p}_0$ on the right hand side of equation (25)—admittedly incorrect for $\boldsymbol{p}'_m \neq \boldsymbol{p}'^0_m$—by setting all first derivatives of T equal to zero and also setting $\boldsymbol{q} = \mathbf{0}$. Now, in equation (32), we simplify the right hand side to write

$$\frac{\partial^2 T}{\partial p_{\lambda 0} \partial p_{\kappa 0}} = \frac{\partial^2 T}{\partial q_\mu \partial q_\nu} \frac{\partial q_\mu}{\partial p_{\lambda 0}} \frac{\partial q_\nu}{\partial p_{\kappa 0}}, \quad \lambda, \kappa = 1, 2. \tag{33}$$

Furthermore, we will evaluate all derivatives at $\boldsymbol{q} = \mathbf{0}$.

As an aside, let us examine the exponent T for constant velocity, equation (30). The first and second derivatives of that traveltime with respect to $\boldsymbol{q}$ are as follows

$$\begin{aligned} \frac{\partial T}{\partial q_\mu} &= -\frac{1}{\mathrm{V}_0} \frac{q_\mu}{s} + \frac{i q_\mu}{\left[\omega_r w_0^2 + i \mathrm{V}_0 s\right]} - \frac{i|\boldsymbol{q}|^2}{\left[\omega_r w_0^2 + i \mathrm{V}_0 s\right]^2} \frac{q_\mu}{s}, \quad \mu = 1, 2, \\ \frac{\partial^2 T}{\partial q_\mu \partial q_\nu} &= -\frac{1}{\mathrm{V}_0} \left[\frac{\delta_{\mu\nu}}{s} + \frac{q_\mu q_\nu}{s^3}\right] + \frac{i \delta_{\mu\nu}}{\left[\omega_r w_0^2 + i \mathrm{V}_0 s\right]} + \mathrm{O}(|\boldsymbol{q}|^2), \quad \mu, \nu = 1, 2, \\ s &= \sqrt{|\boldsymbol{x}' - \boldsymbol{x}_0|^2 - \boldsymbol{q}^2}. \end{aligned} \tag{34}$$

In the equation for the Hessian $\partial^2 T / \partial q_\mu \partial q_\nu$ above, $\delta_{\mu\nu}$ is the Kronecker delta function, equal to one for $\mu = \nu$ and equal to zero otherwise.

Recall the discussion below equation (32) where we argued that quadratic corrections amplitude functions would affect the integration over slownesses negligibly. The most dominant part of the integrand was the neighborhood of the image point. For rays nearby that point, the quadratic correction is small. For rays further away the quadratic decay arising from T again makes the error negligible. Thus, there is no reason to write down those last terms in the second line in equation (34) to make the point that this Hessian is a complicated function of $\boldsymbol{q}$, even for constant velocity. Neglecting the quadratic terms in the second derivative of T in equation (34) we obtain the approximation

$$\begin{aligned} \frac{\partial^2 T}{\partial q_\mu \partial q_\nu} &= -\frac{\delta_{\mu\nu}}{\mathrm{V}_0 |\boldsymbol{x}' - \boldsymbol{x}_0|} + \frac{i \delta_{\mu\nu}}{\left[\omega_r w_0^2 + i \mathrm{V}_0 |\boldsymbol{x}' - \boldsymbol{x}_0|\right]} \\ &= \frac{i \delta_{\mu\nu} \omega_r w_0^2}{\left[\omega_r w_0^2 + i \mathrm{V}_0 |\boldsymbol{x}' - \boldsymbol{x}_0|\right]}, \quad \boldsymbol{q} = \mathbf{0}. \end{aligned} \tag{35}$$

In the first form here we can identify the two quotients with the matrix solutions of the dynamic ray equations (6). In matrix form

$$\begin{aligned} \mathbf{T}_q &= \left[\frac{\partial^2 T}{\partial q_\mu \partial q_\nu}\right]_{\boldsymbol{q}=\mathbf{0}} = -\mathbf{P}_2 \mathbf{Q}_2^{-1} + \mathbf{P}_{GB} \mathbf{Q}_{GB}^{-1} = \mathbf{P}_{GB} \mathbf{Q}_{GB}^{-1} - \mathbf{P}_2 \mathbf{Q}_2^{-1} \\ &= \mathbf{Q}_{GB}^{-1\mathrm{T}} \mathbf{P}_{GB}^{\mathrm{T}} - \mathbf{P}_2 \mathbf{Q}_2^{-1} = \mathbf{Q}_{GB}^{-1\mathrm{T}} \left[\mathbf{P}_{GB}^{\mathrm{T}} \mathbf{Q}_2 - \mathbf{Q}_{GB}^{\mathrm{T}} \mathbf{P}_2\right] \mathbf{Q}_2^{-1}. \end{aligned} \tag{36}$$

In the first line, we have simply reordered terms. In the second line, we used the fact that each term is a matrix of second derivatives and hence symmetric. Therefore, we replaced one product by its transpose. Then we factored out the two inverse matrices to obtain a difference of products of matrices inside the braces [ ].

Let us now examine the term in square brackets in the last part of the equality in this last equation, (36). To begin, set

$$\Delta = \mathbf{P}_{GB}^{\mathrm{T}} \mathbf{Q}_2 - \mathbf{Q}_{GB}^{\mathrm{T}} \mathbf{P}_2 \tag{37}$$

and differentiate with respect to s:

$$\begin{aligned} \frac{d\Delta}{ds} &= \frac{d\mathbf{P}_{GB}^{\mathrm{T}}}{ds} \mathbf{Q}_2 + \mathbf{P}_{GB}^{\mathrm{T}} \frac{d\mathbf{Q}_2}{ds} - \frac{\mathbf{Q}_{GB}^{\mathrm{T}}}{ds} \mathbf{P}_2 - \mathbf{Q}_{GB}^{\mathrm{T}} \frac{\mathbf{P}_2}{ds} \\ &= -\frac{1}{\mathrm{V}_0^2} \mathbf{Q}_{GB}^{\mathrm{T}} \mathbf{V} \mathbf{Q}_2 + \mathbf{P}_{GB}^{\mathrm{T}} \mathrm{V}_0 \mathbf{P}_2 - \mathbf{P}_{GB}^{\mathrm{T}} \mathrm{V}_0 \mathbf{P}_2 + \frac{1}{\mathrm{V}_0^2} \mathbf{Q}_{GB}^{\mathrm{T}} \mathbf{V} \mathbf{Q}_2 = \mathbf{0}. \end{aligned} \tag{38}$$

In the second line, we have used the dynamic differential equations (6) and the fact that the matrix $\mathbf{V}$ defined in equation (1) is symmetric. Thus we conclude that Δ is constant on rays, given by its initial value. The initial values for $\mathbf{Q}_{GB}$ and $\mathbf{P}_{GB}$ are stated in equation (10) and the initial values of $\mathbf{Q}_2$ and $\mathbf{P}_2$ are stated in equation (8). Using these values we find that

$$\Delta = \mathbf{P}_{GB}^{\mathrm{T}} \mathbf{Q}_2 - \mathbf{Q}_{GB}^{\mathrm{T}} \mathbf{P}_2 = -\frac{\omega_r w_0^2}{\mathrm{V}_0} \mathbf{I} = -\frac{\omega_r w_0^2}{\mathrm{v}_0(0)} \mathbf{I}. \tag{39}$$

This is an identity that arises from the simplectic properties of the propagator matrix as discussed by Červený [2001] in section

4.3.2, starting on page 281 and introduced earlier in Červený and Pšenčik [1983] without resorting to the simplectic method. Note that the derivation of differential equation (38) did not rely on the fact that the velocity is constant in the specific example. Hence, even for heterogeneous media, Δ is given by its initial value on the ray.
Furthermore, the mechanics of the derivation were not peculiar to the particular choices of $\mathbf{Q}$'s and $\mathbf{P}$'s. It relied solely on the differential equations for $\mathbf{Q}$'s and $\mathbf{P}$. Thus, if we redefined Δ for any pairs of $\mathbf{Q}$'s and $\mathbf{P}$'s satisfying the dynamic differential equations (10), it would still be true that Δ is constant on the rays, given by its initial value or by its value at any point on the ray, for that matter.
To complete this discussion, we now use the identity for Δ in the last equation (39) to rewrite $\mathbf{T}_q$ in equation (36) as

$$\mathbf{T}_q = -\frac{\omega_r w_0^2}{v_0(0)} \mathbf{Q}_2^{-1\mathrm{T}} \mathbf{Q}_{GB}^{-1} = -\frac{\omega_r w_0^2}{v_0(0)} \mathbf{Q}_{GB}^{-1} \mathbf{Q}_2^{-1} \tag{40}$$

In the second form here, we have exploited the fact that each of the matrices is symmetric. We took a transpose of the product and then removed the transpose of the matrix $\mathbf{Q}_{GB}^{-1\mathrm{T}}$.

We return now to the heterogeneous case, continuing the analysis of the Hessian on the right hand side of equation (33). Let us begin by considering the first derivatives in that equation. We now show that the matrix of derivatives of (q_1, q_2) with respect to (p_{10}, p_{20}) is just $\mathbf{Q}_2$ by following Červený [2001], Section 4.1.7. To do so, let us set

$$\tilde{\mathbf{Q}} = \left[\frac{\partial q_\mu}{\partial p_{\lambda 0}}\right], \qquad \tilde{\mathbf{P}} = \left[\frac{\partial p_\mu}{\partial p_{\lambda 0}}\right]. \tag{41}$$

This pair of vectors $\boldsymbol{q}_\mu, \boldsymbol{p}_\mu$ satisfies the kinematic ray equations and initial conditions stated in equation (4). When we differentiate those equations with respect to the components of $\boldsymbol{p}_0$ we obtain exactly the dynamic ray equations (6) for the matrices $\tilde{\mathbf{Q}}, \tilde{\mathbf{P}}$. Then, differentiation of the initial conditions of equation (4) yields exactly the initial conditions of the functions $\mathbf{Q}_2, \mathbf{P}_2$ given in equation (8). That is,

$$\tilde{\mathbf{Q}} = \left[\frac{\partial q_\mu}{\partial p_{\lambda 0}}\right] = \mathbf{Q}_2. \tag{42}$$

We use this identity and equation (33) to obtain

$$\mathbf{T}_0 = \mathbf{Q}_2 \mathbf{T}_q \mathbf{Q}_2, \quad \mathbf{T}_q = \left[\frac{\partial^2 T}{\partial q_\mu \partial q_\nu}\right] \quad \mu, \nu = 1, 2. \tag{43}$$

3.2.1 Analysis of $\mathbf{T}_q$

Here, we follow the discussion of Červený [2001], Section 5.8.3. Figure 5 on page 89 shows the central ray of a Gaussian beam. The Gaussian beam is to be evaluated at the point $\boldsymbol{x}$, thus defining the vector $\boldsymbol{q}$ connecting a point on the ray $\boldsymbol{x}'$ to the point $\boldsymbol{x}$. In equation (13) we see that T is a sum of two traveltimes, the first being the central ray real traveltime $\tau(s)$ of asymptotic ray theory connecting $\boldsymbol{x}_0$ to $\boldsymbol{x}'$. The second term is the complex part of the traveltime given by the standard quadratic form in $\boldsymbol{q}$.

It is straightforward to evaluate the Hessian of the second term here with respect to $\boldsymbol{q}$ at $\boldsymbol{q} = \mathbf{0}$. The first term requires a little more effort.

With a slight abuse of notation, let us consider the real ray-theoretic traveltime $\tau(\boldsymbol{x}, \boldsymbol{x}_0)$ from $\boldsymbol{x}_0$ to $\boldsymbol{x}$. We can write a quadratic approximation of that traveltime in terms of the traveltime on the central ray through $\boldsymbol{x}'$ as

$$\tau(\boldsymbol{x}, \boldsymbol{x}_0) = \tau(\boldsymbol{x}', \boldsymbol{x}_0) + \frac{1}{2} \boldsymbol{q} \mathbf{P}_2 \mathbf{Q}_2^{-1} \boldsymbol{q}. \tag{44}$$

This equality allows us to write the traveltime $\tau(\boldsymbol{x}', \boldsymbol{x}_0)$ in terms of the fixed traveltime $\tau(\boldsymbol{x}, \boldsymbol{x}_0)$ minus a quadratic form in the vector $\boldsymbol{q}$; that is,

$$\tau(\boldsymbol{x}', \boldsymbol{x}_0) = \tau(\boldsymbol{x}, \boldsymbol{x}_0) - \frac{1}{2} \boldsymbol{q} \mathbf{P}_2 \mathbf{Q}_2^{-1} \boldsymbol{q}. \tag{45}$$

We use this equation in equation (13) to rewrite the complex traveltime $T(\boldsymbol{x}', \boldsymbol{x}_0)$ as

$$T(\boldsymbol{x}', \boldsymbol{x}_0) = T(\boldsymbol{x}, \boldsymbol{x}_0) + \frac{1}{2} \boldsymbol{q}^{\mathrm{T}} \left[\mathbf{P}_{GB} \mathbf{Q}_{GB}^{-1} - \mathbf{P}_2 \mathbf{Q}_2^{-1}\right] \boldsymbol{q}. \tag{46}$$

Now, when we calculate the second derivative here at $\boldsymbol{q} = \mathbf{0}$, we find that $\mathbf{T}_q$ defined in equation (43) is given by

$$\mathbf{T}_q = \mathbf{P}_{GB} \mathbf{Q}_{GB}^{-1} - \mathbf{P}_2 \mathbf{Q}_2^{-1}, \quad \boldsymbol{q} = \mathbf{0}, \tag{47}$$

in heterogeneous media. This is exactly the same as equation (36) for $\mathbf{T}_q$ in homogeneous media. As noted in the discussion below that equation, the simplification of $\mathbf{T}_q$ did not rely on the fact that the velocity was constant. Thus, the final form of $\mathbf{T}_q$ in equation (40) is valid here as well and we write for the heterogeneous case.

$$\mathbf{T}_q = -\frac{\omega_r w_0^2}{v_0(0)}\mathbf{Q}_2^{-1}\mathbf{Q}_{GB}^{-1}, \quad \boldsymbol{q} = \mathbf{0}. \tag{48}$$

We now have all of the pieces needed to express the Hessian matrix $\boldsymbol{\Psi}$ in equation (21).

4 THE APPROXIMATION OF $\boldsymbol{\Psi}$

We now move back through the sequence of formulas for the various Hessians that we introduced in the previous section. Then we will take the formula for the Hessian with respect to $\boldsymbol{p}'$ and apply it to both the source and receiver traveltimes to obtain a formula for $\boldsymbol{\Psi}$ in equation (21).

To begin, we use $\mathbf{T}_q$ as defined in equation (48) to rewrite $\mathbf{T}_0$ in equation (43) as

$$\mathbf{T}_0 = -\frac{\omega_r w_0^2}{v_0(0)}\mathbf{Q}_2\mathbf{Q}_2^{-1}\mathbf{Q}_{GB}^{-1}\mathbf{Q}_2 = -\frac{\omega_r w_0^2}{v_0(0)}\mathbf{Q}_{GB}^{-1}\mathbf{Q}_2 \tag{49}$$

Now that we have $\mathbf{T}_0$, we can go back a further step by substituting this representation into equation (29) to express the Hessian with respect to $\boldsymbol{p}'$ in terms of $\mathbf{T}_0$ as follows.

$$\mathbf{T} = -\frac{\omega_r w_0^2}{v_0(0)}\boldsymbol{\Gamma}^{\mathrm{T}}\mathbf{Q}_{GB}^{-1}\mathbf{Q}_2\boldsymbol{\Gamma}. \tag{50}$$

The matrix $\boldsymbol{\Gamma}$ appearing on the right side of this equation is defined in terms of the angles β_1 and β_2 in equation (27). It is the matrix of transformation from Cartesian slownesses to ray-centered slownesses; the slowness vector defines the initial direction of the tangent of the ray from the initial point $\boldsymbol{x}_0$ to the image point $\boldsymbol{x}$. Further, recall that the various $\mathbf{Q}$'s and $\mathbf{P}$'s here are solutions of the dynamic ray equations (6) with initial conditions for $\mathbf{Q}_{GB}$ and $\mathbf{P}_{GB}$ given in equation (10) and the initial conditions for $\mathbf{Q}_2$ and $\mathbf{P}_2$ given in equation (8).

Equation (21) tells us that we must add two Hessians of the form defined by the last equation, (50), in order to obtain the Hessian $\boldsymbol{\Psi}$ for Ψ which is related to the two complex traveltimes from source and receiver by equation (15). The only difference in the two components is that one is for sources and the other is for receivers. We can accomplish that distinction by introducing subscripts s and r in the right hand side of equation (50). Thus we find that

$$\boldsymbol{\Psi} = i\omega_r w_0^2\left\{\frac{1}{v_{0r}(0)}\boldsymbol{\Gamma}_r^{\mathrm{T}}\mathbf{Q}_{GBr}^{-1}\mathbf{Q}_{2r}\boldsymbol{\Gamma}_r + \frac{1}{v_{0s}(0)}\boldsymbol{\Gamma}_s^{\mathrm{T}}\mathbf{Q}_{GBs}^{-1}\mathbf{Q}_{2s}\boldsymbol{\Gamma}_s\right\}^*. \tag{51}$$

Note here that the subscript r in ω_r denotes "reference frequency" and is the same for Hessians associated with the traveltimes from source and receiver.

The matrices $\mathbf{Q}_{2r}$ and $\mathbf{Q}_{2s}$ are each singular if $\boldsymbol{x}_r'$ or $\boldsymbol{x}_s'$, respectively, is located at a caustic of the ensemble of central rays from their respective initial points. In order for this sum of matrices to be singular, the singularities of the two matrix products would have to "line up;" that is, their eigenvectors associated with the zero eigenvalue would have to be colinear. We would expect such an occurrence to be relatively rarer than for one and/or the other of the matrix products to be singular. Nonetheless, some regularization of this matrix may be required in numerical computations.

As noted earlier, we can expect the Hessian matrix $\boldsymbol{\Psi}$ to be singular when the image point is located at a caustic of incident rays. However, the underlying inversion theory is not applicable at such a point for estimation of a reflection coefficient, so this anomaly is moot as regards that theory.

In the Introduction and in Section 2.3 we claimed that we did not need to know the actual initial slownesses of the ray from the initial point $\boldsymbol{x}_0 = \boldsymbol{x}_s$ *or* $\boldsymbol{x}_r$ to the image point $\boldsymbol{x}$.

We explain now why we do not need to know those rotation angles on the ray from the source or receiver through the image point explicitly. It is necessary to assume that the actual rays that we do compute are close enough to one another so that the discrete sum over rays is a sufficiently accurate approximation of the continuous integral over rays to satisfy whatever numerical accuracy criterion we impose. That means we can think of the discrete sum as having the properties of the integral.

We will use the matrices Γ_r and Γ_s on the rays that we actually compute. This again is justified by the discussion below equation (32). This is in error except for the distinguished ray pair from source and receiver through the image point. Those errors for other rays are linearly small for small values of the $\boldsymbol{q}$'s nearby and exponentially small for $\boldsymbol{q}$'s further away. This suffices for our leading order approximation of the the integral I in equation (19). Then, all quantities in equation (15) are determined on the central rays of the computed Gaussian beams. As we will see in the common shot example of Section 5 —in particular in equation (60)—the reflectivity in that example needs to be computed on the actual central rays of Gaussian beams that we compute. Hence, we can use Hill's original variables $\boldsymbol{p}_m$ and $\boldsymbol{p}_h$ or even in the variables $\boldsymbol{p}_r'$ and $\boldsymbol{p}_s'$ of equation (15).

4.1 Special case: $\mathbf{V} = \mathbf{0}$

In many applications, the matrix of second derivatives $\mathbf{V}$ defined by equation (1) is set equal to zero. This is equivalent to assuming a piecewise constant or piecewise linear velocity model. As a consequence, in equation (6) we see that the dynamic quantity $\mathbf{P}$ is a constant given by its initial value. Furthermore, the dynamic equations now separate into scalar equations for the pairs Q_{ij} and P_{ij} for fixed ij and there is no interaction with other elements of the matrix; that is, the matrix equations reduce to scalar equations for each of these pairs. Further, for the case of piecewise constant velocity, the matrices $\mathbf{Q}$ and $\mathbf{P}$ become diagonal with the same functions propagating along each diagonal because the initial data are diagonal.† Since the initial data are the same for each diagonal element of $\mathbf{Q}$ and $\mathbf{P}$ in this case, each matrix is a scalar times the identity matrix; We call such a matrix a scalar matrix. Thus, the propagation is reduced to determining the scalar Q's and P's of 2D propagation.

With all of this simplifications,we can replace the matrix of $\mathbf{\Psi}$ by

$$\mathbf{\Psi} = i\omega_r w_0^2 \left\{ \frac{1}{v_{0r}(0)} Q_{2r} Q_{GBr}^{-1} \mathbf{\Gamma}_r^{\mathrm{T}} \mathbf{\Gamma}_r + \frac{1}{v_{0s}(0)} Q_{2s} Q_{GBs}^{-1} \mathbf{\Gamma}_s^{\mathrm{T}} \mathbf{\Gamma}_s \right\}^* . \tag{52}$$

From equation (27), it is straightforward to calculate the products of $\mathbf{\Gamma}$'s appearing here. They are

$$\begin{aligned} \mathbf{\Gamma}_r^{\mathrm{T}} \mathbf{\Gamma}_r &= \begin{bmatrix} \dfrac{1}{\cos^2 \beta_{1r}} & 0 \\ 0 & 1 \end{bmatrix} = \begin{bmatrix} \dfrac{1}{[v_{0r}(0) p'_{3r}]^2} & 0 \\ 0 & 1 \end{bmatrix}, \\ \mathbf{\Gamma}_s^{\mathrm{T}} \mathbf{\Gamma}_s &= \begin{bmatrix} \dfrac{1}{\cos^2 \beta_{1s}} & 0 \\ 0 & 1 \end{bmatrix} = \begin{bmatrix} \dfrac{1}{[v_{0s}(0) p'_{3s}]^2} & 0 \\ 0 & 1 \end{bmatrix}. \end{aligned} \tag{53}$$

Because these rotation matrices are not scalar matrices, $\mathbf{\Psi}$ is not a scalar matrix; that is, they are not scalar multiples of the identity matrix.

5 COMMON-SHOT INVERSION WITH GAUSSION BEAMS; AN EXAMPLE

We will show a particular example of a common-shot inversion formula for which the product of Green's functions leads to an integral of the form of I in equation (15).

We start from the classic imaging condition for common-shot data [Claerbout, 1971],

$$\mathcal{R}(\boldsymbol{x}, \boldsymbol{x}_s, \theta) = \frac{1}{2\pi} \int \frac{U(\boldsymbol{x}, \boldsymbol{x}_s, \omega)}{D(\boldsymbol{x}, \boldsymbol{x}_s, \omega)} d\omega. \tag{54}$$

This formula for the reflectivity $\mathcal{R}$ is asymptotically equivalent to the Kirchhoff inversion formula when U and D are replaced by their ray-theoretic asymptotic expansions; see Keho and Beydoun [1988], Hanitzsch [1997], Zhang et al [2003] and Bleistein et al [2005]. The function $U(\boldsymbol{x}, \boldsymbol{x}_s, \omega)$ is generated by downward propagating $U(\boldsymbol{x}_r, \boldsymbol{x}_s, \omega)$, the observed response to a point source at $\boldsymbol{x}_s$ at the receivers denoted by $\boldsymbol{x}_r$. The function $D(\boldsymbol{x}, \boldsymbol{x}_s, \omega)$ is the full-bandwidth downward propagating wave from a point source, that is, it is the downward part of the Green's function denoted by $G(\boldsymbol{x}, \boldsymbol{x}_s, \omega)$. Both wave fields are propagated into the Earth in some background model of the wavespeed.

Let us replace D by G in the integrand of equation (54) for $\mathcal{R}$ and then multiply numerator and denominator by G^*, the complex conjugate of the downward propagating wave from the source. This leads to

$$\mathcal{R}(\boldsymbol{x}, \boldsymbol{x}_s) = \frac{1}{2\pi} \int \frac{U(\boldsymbol{x}, \boldsymbol{x}_s, \omega) G^*(\boldsymbol{x}, \boldsymbol{x}_s, \omega)}{G(\boldsymbol{x}, \boldsymbol{x}_s, \omega) G^*(\boldsymbol{x}, \boldsymbol{x}_s, \omega)} d\omega. \tag{55}$$

Next, we propose to replace the Green's functions in the denominator here by their leading order ray-theoretic asymptotic expansions and observe that only a product of amplitudes A, independent of ω survive, the multiplication:

$$\mathcal{R}(\boldsymbol{x}, \boldsymbol{x}_s) = \frac{1}{2\pi A^2(\boldsymbol{x}, \boldsymbol{x}_s)} \int U(\boldsymbol{x}, \boldsymbol{x}_s, \omega) G^*(\boldsymbol{x}, \boldsymbol{x}_s, \omega) d\omega. \tag{56}$$

In ray-centered coordinates

†If the velocity is linear in some direction, then that direction and the initial direction of each ray form a plane. The initial values of $\mathbf{Q}$ and $\mathbf{P}$ will be different in the in-plane and out-of-plane directions.

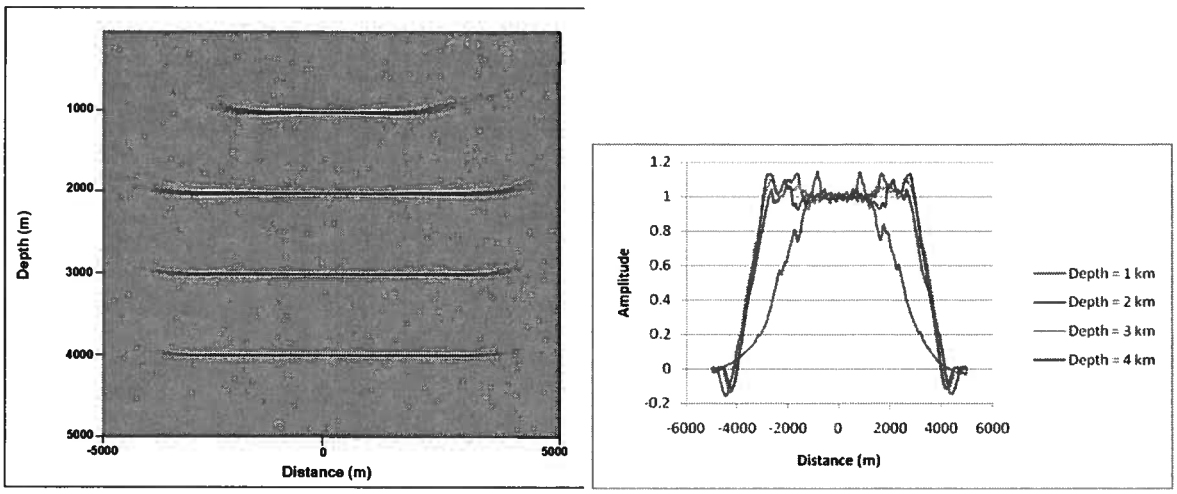

Figure 7. Left: Migrated image (deconvolution imaging condition) from a single shot record in a constant-velocity medium with horizontal reflectors caused by identical density contrasts. Migrated amplitudes are similar for all reflectors. Amplitude artifacts near the maximum offsets are migration aperture truncation effects. Right: Peak amplitude as a function of offset for all reflectors. Amplitude fall-off corresponds to the peak amplitudes along the migration aperture artifacts of the left figure.

$$\frac{1}{A^2(\boldsymbol{x},\boldsymbol{x}_s)} = (4\pi)^2 \frac{\mathrm{v}_0(\boldsymbol{x}_s)\det[\mathbf{Q}_2(\boldsymbol{x},\boldsymbol{x}_s)]}{\mathrm{v}_0(\boldsymbol{x})}. \tag{57}$$

The determinant $\det[\mathbf{Q}_2(\boldsymbol{x},\boldsymbol{x}_s)]$ will be equal to zero at caustics of the rays from the source to the output point; some regularization is required to avoid the zeroes there. That is not important to the discussion here.

When we use this formulas for A in equation (56) for the reflectivity, we find that

$$\mathcal{R}(\boldsymbol{x},\boldsymbol{x}_s) = \frac{8\pi\mathrm{v}_0(\boldsymbol{x}_s)\det[\mathbf{Q}(\boldsymbol{x},\boldsymbol{x}_s)]}{\mathrm{v}_0(\boldsymbol{x})} \int U(\boldsymbol{x},\boldsymbol{x}_s,\omega)G^*(\boldsymbol{x},\boldsymbol{x}_s,\omega)d\omega. \tag{58}$$

The downward propagated field $U(\boldsymbol{x},\boldsymbol{x}_s,\omega)$ can be written in terms of the surface data as

$$U(\boldsymbol{x},\boldsymbol{x}_s,\omega) = 2i\omega \int_{z_r=0} p'_{3r}G^*(\boldsymbol{x},\boldsymbol{x}_r,\omega)U(\boldsymbol{x}_r,\boldsymbol{x}_s,\omega)dx_r dy_r \tag{59}$$

in a standard manner by using Green's theorem. Here, p'_{3r} is the third component of $\boldsymbol{p}'_r$.

Substitution of this representation of $U(\boldsymbol{x},\boldsymbol{x}_s,\omega)$ into equation (58) for the reflectivity leads to

$$\mathcal{R}(\boldsymbol{x},\boldsymbol{x}_s) = \frac{8\pi\mathrm{v}_0(\boldsymbol{x}_s)\det[\mathbf{Q}(\boldsymbol{x},\boldsymbol{x}_s)]}{\mathrm{v}_0(\boldsymbol{x})} \int 2i\omega \int p'_{3r}U(\boldsymbol{x}_r,\boldsymbol{x}_s,\omega)dx_r dy_r \mathfrak{G}(\boldsymbol{x},\boldsymbol{x}_s,\boldsymbol{x}_r,\omega)\,. \tag{60}$$

In this equation, $\mathfrak{G}(\boldsymbol{x},\boldsymbol{x}_s,\boldsymbol{x}_r,\omega)$ is defined in equation (14) and was the starting point for the analysis of this paper. It is not our intention to continue with the discussion of this true amplitude migration formula or any other. We only wanted to show that the integral I that we analyzed asymptotically here does arise in true-amplitude migration formulas as claimed.

6 A NUMERICAL EXAMPLE IN 2D

In Gray and Bleistein [2009], we presented numerical examples in 2D for a common-shot data set. The asymptotic technique derived and implemented there is the 2D analog of what we have presented here. Both a deconvolution imaging condition with a structure similar to the reflectivity formula of equation (54) and a correlation imaging formula similar to the reflectivity formula of equation (60) were tested. See Gray and Bleistein [2009] for details.

The best results were obtained for the deconvolution imaging condition and we present those here. This example models reflections from density contrasts in a medium of constant velocity 2000 m/s. Four horizontal reflectors with identical reflection coefficients are placed at depths of 1000, 2000, 3000, and 4000 m. A single shot record, with a recording aperture of 7000 m on either side of the shot point, is migrated. Half-opening angles were limited to 60 in the migration.

Within the reflection aperture for each reflector the output confirms the "true-amplitude" claim but for numerical noise from the computation and from the peak search.

7 SUMMARY AND CONCLUSIONS

We have obtain a formula for the Hessian matrix of complex traveltimes with respect to transverse Cartesian slowness variables [equation (50)]. We believe that this formula is new. That allows us to add two Hessian matrices of this form to obtain yet another Hessian matrix for the sum of complex traveltimes with respect to Cartesian "offset slownesses," equation (51). The determinant of this Hessian is needed for the asymptotic reduction of four integrals in source and receiver transverse slownesses to two integrals. The formula we evaluate in the first step [equation (50)] requires approximating an earlier representation of that Hessian at the saddle point of the traveltime with respect to the "midpoint slowness."

In two dimensions, the steepest descent analysis is much simpler. There, two integrals in transverse slownesses were reduced to a single integral by the method of steepest descent. The example of Gray and Bleistein [2009], provides a confirmation of "true-amplitude" claim for this method.

REFERENCES

Bleistein, N., 1984, Mathematical Methods for Wave Phenomena: Academic Press, Orlando.

Bleistein, N., 2008, Mathematics of modeling, migration and inversion with Gaussian beams, Course notes: cwp.mines.edu/~norm/ShrtCrse/GBNotes.pdf.

Bleistein, N. and R. A. Handelsman, 1975, Multidimensional stationary phase, an alternative derivation: SIAM J. Math. Anal., 6, 3 480-487.

Bleistein, N. and R. A. Handelsman, Bleistein, 1986, Asymptotic Expansions of Integrals, Dover Publications, Inc., New York.

Bleistein, N., Y. Zhang, S. Xu, G.Zhang and S. H. Gray, 2005, Migration/inversion: think image point coordinates, process in acquisition surface coordinates: Inverse Problems, **21**, 17151744.

Červený, V., 1982, Expansion of a plane wave into Gaussian beams: Studia geoph. et geod., **26**, 120-131.

Červený, V., 2001, *Seismic Ray Theory*. Cambridge University Press, Cambridge.

Červený, V., and I. Pšenčik, 1983, Gaussian beams and paraxial ray approximation in three-dimensional elastic inhomogeneous media: J Geophysics, **53**, 1-15.

Claerbout, J. F., 1971. Toward a unified theory of reflector mapping: Geophysics. v. **36**, p. 467-481

Claerbout, J. F., 1985, Imaging the Earths Interior: Blackwell Scientific Publications, Inc, Oxford.

George, Th, J. Virieux, and R. Madariaga, 1987, Seismic wave synthesis by Gaussian beam summation: A comparison with finite differences: Geophysics, **52**. 8, 1065 .1073.

Gray, S. H., and N. Bleistein, 2009, True-amplitude Gaussian beam migration: Geophysics, **74**, S11-S23.

Hanitzsch, C. 1997, Comparision of weights in prestack amplitude-preserving Kirchhoff depth migration: Geophysics **62**, 1812-1816.

Hill, N. R., 1990, Gaussian beam migration: Geophysics, **55**, 11, 1416-1428.

Hill, N. R., 2001, Prestack Gaussian-beam depth migration: Geophysics, **66**, 4, 1240-1250.

Keho, T. H. and Beydoun, W. B., 1988, Paraxial ray Kirchhoff migration, Geophysics, **53**, 1540-1546.

Korn, G. A., and T. M. Korn, 1968, Mathematical Handbook for Scientists and Engineers: McGraw-Hill, New York.

Schneider, W. A., 1978, Integral formulation for migration in two and three dimensions: Geophysics, v. **43**, p. 49-76.

Zhang, Y., Zhang, G., and Bleistein, N., 2003, True amplitude wave equation migration arising from true-amplitude one-way wave equations: Inverse Problems, **19**, 1113-1138.

Acknowledgements

The authors wish to express extreme gratitude to John Stockwell of the Center for Wave Phenomena at the Colorado School of Mines for a critical reading of the paper. It is much improved by his input. The first author would also like to thank the attendees of a short course on Gaussian beam migration in December, 2008 at Petrobras University. Many stimulating discussion in that course led to the ideas that appear in the method used here. The germ of this approach was formulated by the author on the plane ride home from Brazil, undoubtedly in response to discussions of what had not worked previously. Finally, many thanks to Professor Vastislav Červený, Charles University, Prague,whose ideas underly much of the discussion appearing here and also for his mentoring of and friendship with the first author and to Ivan Pšenčik, Czech Academy of Sciences, for many helpful and stimulating discussions.

APPENDIX A: ITERATED METHOD OF STEEPEST DESCENT IN TWO VARIABLES

In Section 2.3, we claimed a result for the asymptotic expansion of a pair of iterated integrals obtained by the method of steepest descent—specifically for the asymptotic expansion of the integral $I(\boldsymbol{x}, \boldsymbol{x}_s, \boldsymbol{x}_r, \omega)$ of equation (15). To the best of the authors' knowledge, the derivation of the explicit asymptotic formula leading to the asymptotic expansion of this integral presented in equation (19) has not appeared in the open literature. In that equation, $\boldsymbol{\Psi}$ is given by equation (51). We derive the claimed leading order asymptotic expansion of equation (19) here. The derivation of the matrix form of $\boldsymbol{\Psi}$ in equation (51) is the major discussion of Section 2.3.

The classical method of steepest descent for a one-dimensional integral does not generalize to higher dimensions. It would require the analog of the Cauchy integral theorem in two complex variables—essentially four variables. The difficulty is that in higher dimensions

a closed curve does not contain an interior domain as it does in one complex variable; that is, in two dimensions. On the other hand, we show here that the iterated application of the one-complex variable method of steepest descent really behaves much like the corresponding application of the multidimensional method of stationary phase, with the complex determinant of the Hessian matrix of the complex traveltime appearing in the amplitude of the asymptotic expansion. This is an alternative to the method used by Červený [1982] and repeated in Červený [2001]. His method rests on a theorem in linear algebra that gives conditions under which the sum of two complex-valued symmetric matrices can be simultaneous diagonalized. His reference for that result is a paper in the Russian literature, not easily accessible in the western literature. To date, we have not found the counterpart of this theorem in the western literature.

A1 Steepest descent in one dimension

Before beginning the analysis of the double integral, we remind the reader of the corresponding asymptotic expansion in one variable. We introduce the integral

$$I(\omega) = \int f(z) \exp\{-\omega \Psi(z)\} dz. \tag{A.1}$$

Here, the interval of integration is real[3] and positively oriented, but both functions in the integrand are complex-valued. We assume that the exponent has a real saddle point that we can characterize by the equation

$$\frac{d\Psi}{dz} = 0, \quad z = z_{sad}. \tag{A.2}$$

Furthermore, we assume that the second derivative is nonzero at the saddle point,

$$\Psi_{zz} = \left.\frac{d^2\Psi}{dz^2}\right|_{z=z_{sad}} \neq 0; \tag{A.3}$$

Ψ_{zz} may be complex. We seek the leading order asymptotic expansion of this integral for "large" values of the parameter ω.

The Taylor expansion of Ψ near the saddle point has the form

$$\Psi(z) - \Psi(z_{sad}) = \frac{1}{2}\Psi_{zz}(z - z_{sad})^2 + \dots . \tag{A.4}$$

The direction of steepest descent in $z - z_{sad}$ at the saddle point is the direction in which this second order approximation is real and positive, which provides the direction of maximal exponential decay of the integrand. In terms of the phases (denoted by arg in the complex variable literature) of the factors in the complex product appearing on the right side of the last equation, this condition becomes,

$$\arg(\Psi_{zz}) + 2\arg(z - z_{sad}) = 0,\ 2\pi,\ \dots . \tag{A.5}$$

We expect that the direction of choice will be a rotation of the contour of integration—the real line, positively oriented—through an acute angle. Thus from the two unique choices of direction here we choose

$$\arg(z - z_{sad}) = -\arg(\Psi_{zz})/2, \tag{A.6}$$

such that the oriented direction with this angle makes an acute angle with the direction of the (real) path of integration. Application of the formula for evaluation of the integral of equation (A.1) by the method of steepest descent[4] [Bleistein, 1984, equation (7.3.11)] with positive ω leads to the following.

$$\begin{aligned} I(\omega) &\sim \sqrt{\frac{2\pi}{\omega|\Psi_{zz}|}} f(z_{sad}) \exp\{-\omega\Psi(z_{sad}) - i\arg(\Psi_{zz})/2\} \\ &= \sqrt{\frac{2\pi}{\omega\Psi_{zz}}} f(z_{sad}) \exp\{-\omega\Psi(z_{sad})\}. \end{aligned} \tag{A.7}$$

Notice that by defining the integrand on the right hand side of equation for $I(\omega)$ with a minus sign in the exponent, the phase adjustment in the first line here provides exactly the right factor so that the denominator can be expressed

[3]The constraint of the path of integration to the real axis is not necessary. This can be generalized, but the generalization is not needed for our application

[4]There we use $\lambda = -\omega$ as the large parameter. The minus sign modifies the argument of the directions of steepest descent in equation (A.6).

as the (principal value) square root of the second derivative. If we had defined the exponent without that minus sign, then we would have need an additional phase shift of $\pm\pi/2$ in the right hand exponents of this last equation.

The method of steepest descent relies on deforming the path of integration onto a path where the exponential difference $\Psi(z) - \Psi(z_{sad})$ remains real and increasing and then applying the more basic Laplace method [Bleistein, 1984] to the integral on that steepest descent contour.

A2 Iterated steepest descent in two dimensions

This is an extension not found in texts on the method of steepest descent. We consider the iterated integral of equation (15). For this purpose, we introduce indexed variables and consider the integral

$$I(\omega) = \int f(\boldsymbol{z}) \exp\{-\omega\Psi(\boldsymbol{z})\} dz_1 dz_2, \quad \boldsymbol{z} = (z_1, z_2). \tag{A.8}$$

Here, the domain of integration is real, although when considered as iterated integrals, we will allow for deformations into the complex z_1-plane to obtain the asymptotic expansion of the integral with respect to z_1 and similarly for z_2. Both functions in the integrand are complex-valued.

We assume that the exponent has a real saddle point in both variables that we can characterize by the equation

$$\nabla_z \Psi(\boldsymbol{z}) = \boldsymbol{0}, \quad \boldsymbol{z} = \boldsymbol{z}_{sad} = (z_{1sad}, z_{2sad}). \tag{A.9}$$

Furthermore, we assume that the Hessian matrix—the matrix of second derivatives—of Ψ is non-singular at this saddle point; that is

$$\det[\boldsymbol{\Psi}] \neq 0. \quad \boldsymbol{\Psi} = \left[\frac{\partial^2 \Psi}{\partial z_i \partial z_j}\right], i, j = 1, 2. \tag{A.10}$$

We will also assume that

$$\left.\frac{\partial^2 \Psi}{\partial z_1^2}\right|_{\boldsymbol{z}=\boldsymbol{z}_{sad}} \neq 0. \tag{A.11}$$

If this were not the case, we could rotate the coordinate system to make this so; such rotations use matrices with determinant equal to one, so that they do not affect the final formula for the asymptotic expansion of $I(\omega)$ in equation (19).

Let us consider the integration in z_1 alone in equation (A.8). From equation (A.10), that integral has a saddle point when

$$\frac{\partial \Psi(z_1, z_2)}{\partial z_1} = 0. \tag{A.12}$$

By the assumption of the existence of the saddle point in equation (A.10), we know that this equation has a solution for $z_2 = z_{2sad}$, at which point, $z_1 = z_{1sad}$. By the implicit function theorem, equation (A.12) has a unique solution in the neighborhood of $z = z_{sad}$ by virtue of the assumption of equation (A.11) that the second derivative with respect to z_1 is nonzero at the saddle point. Therefore we can write

$$z_1 = Z(z_2), \quad \frac{\partial \Psi(Z(z_2), z_2)}{\partial z_1} \equiv 0 \tag{A.13}$$

in some neighborhood of $\boldsymbol{z} = \boldsymbol{z}_{sad}$.

We can now write down the asymptotic expansion with respect to z_1 of the iterated integral $I(\omega)$ in equation (A.8) by using the formula of equation (A.7) for that asymptotic expansion in one variable:

$$I(\omega) = \sqrt{\frac{2\pi}{\omega}} \int \frac{f(Z(z_2), z_2)}{\sqrt{\Psi_{z_1 z_1}(Z(z_2), z_2)}} \exp\{-\omega\Psi(Z(z_2), z_2)\} dz_2. \tag{A.14}$$

We write down the first derivative with respect to z_2 of this redefined exponent Ψ by applying the chain rule to deal with the dependence of the first variable of Ψ on z_2.

$$\frac{d\Psi(Z(z_2), z_2)}{dz_2} = \frac{\partial \Psi}{\partial z_1}\frac{dZ}{dz_2} + \frac{\partial \Psi}{\partial z_2}. \tag{A.15}$$

The first term here is identically equal to zero as a result of the stationarity condition in equation (A.13). Therefore, let us rewrite the first derivative here accordingly and then write down the second derivative, as well.

$$\frac{d\Psi(Z(z_2),z_2)}{dz_2} = \frac{\partial\Psi}{\partial z_2},$$
$$\frac{d^2\Psi(Z(z_2),z_2)}{dz_2^2} = \frac{\partial^2\Psi}{\partial z_2^2} + \frac{\partial^2\Psi}{\partial z_2\partial z_1}\frac{dZ}{dz_2} \tag{A.16}$$

From the first line here, we see that the condition that the total derivative with respect to z_2 of this new exponent be equal to zero is exactly the condition that the partial derivative with respect to z_2 be equal to zero. This is just the requirement that the second component of the gradient of Ψ be equal to zero in equation (A.9). We then conclude that the saddle point occurs at $z_2 = z_{2sad}$ for which point we also have $z_1 = z_{1sad}$. In summary, the dual saddle point obtained by setting the gradient of the original exponent equal to zero is the same as the simultaneous saddle point in two separate variables determined by iterated application of the method of steepest descent.

Now we must evaluate the second derivative of Ψ in equation (A.15) at the saddle point. To this end, we must first express the derivative of $Z(z_2)$ in terms of derivatives of Ψ. The function $Z(z_2)$ is defined implicitly in equation (A.13). We differentiate that equation with respect to z_2:

$$\frac{\partial^2\Psi(Z(z_2),z_2)}{\partial z_1^2}\frac{dZ(z_2)}{dz_2} + \frac{\partial^2\Psi(Z(z_2),z_2)}{\partial z_1\partial z_2} \equiv 0. \tag{A.17}$$

The coefficient of the derivative of Z is nonzero at the saddle point—equation (A.11)—so we can divide by it and conclude that

$$\frac{dZ(z_2)}{dz_2} = -\frac{\partial^2\Psi(Z(z_2),z_2)}{\partial z_1\partial dz_2}\left[\frac{\partial^2\Psi(Z(z_2),z_2)}{\partial z_1^2}\right]^{-1}. \tag{A.18}$$

We substitute this value of the first derivative into the second line of equation (A.15) to obtain the representation we seek for the second derivative of Ψ with respect to z_2.

$$\begin{aligned}\frac{d^2\Psi(Z(z_2),z_2)}{dz_2^2} &= \left[\frac{\partial^2\Psi}{\partial z_1^2}\frac{\partial^2\Psi}{\partial z_2^2} - \left(\frac{\partial^2\Psi}{\partial z_1\partial z_2}\right)^2\right]\left[\frac{\partial^2\Psi(Z(z_2),z_2)}{\partial z_1^2}\right]^{-1} \\ &= \det[\boldsymbol{\Psi}]\left[\frac{\partial\Psi(Z(z_2),z_2)}{\partial z_1^2}\right]^{-1}.\end{aligned} \tag{A.19}$$

We again apply the asymptotic expansion formula of equation (A.7) to the integral of equation (A.14) and find that

$$I(\omega) \sim \frac{2\pi}{\omega}\frac{f(z_{sad})}{\sqrt{\det[\boldsymbol{\Psi}(z_{sad})]}}\exp\{-\omega\Psi(z_{sad})\}. \tag{A.20}$$

This is the formula that we applied to obtain the asymptotic expansion of the Gaussian beam representation of I in equation (15) to obtain the asymptotic expansion of I in equation (19).

We have presented this general formula heere because it has application to other multidimensional integrals in the analysis of Gaussian beams. In particular, it is applicable to the asymptotic expansion of the basic Green's function itself in heterogeneous media. Hill's [2001] derivation is in homogeneous media. This derivation is an alternative to one presented by Červený [1982] and Červený [2001].

Wave-equation migration velocity analysis with extended common-image-point gathers

Tongning Yang & Paul Sava
Center for Wave Phenomena, Colorado School of Mines

ABSTRACT

Wave-equation migration velocity analysis (WEMVA) is an image-domain velocity model building technique based on band-limited wave propagation and designed especially for complex subsurface environments. It exploits the coherency of reflection events measured in extended images produced by a cross-correlation imaging condition with non-zero lags. Conventional approaches use either space-lags or time-lag common image gathers, in which only partial information of the extended images is used for velocity updates.

We propose an WEMVA approach using the complete information from both space-lags and time-lags of extended images. With this approach, the velocity model building benefits both from the robustness of using the time-lag information and from the high resolution of using the space-lags information. Such an implementation is facilitated by using extended common-image-point gathers (CIPs) constructed sparsely along reflections and defined jointly for space- and time-lags. These CIPs avoid the bias towards nearly-horizontal reflectors so that steeply dipping events are well preserved in the gathers and the corresponding information related to velocity can be used. Also, the computation of the extended images can be avoided in areas where the velocity is known, e.g., inside salt bodies, or areas where the signal-to-noise ratio is too low, e.g., in shadow zones. This significantly reduces the cost of constructing extended images.

A velocity estimation process based on these images requires an objective function based on an operator penalizing the distortion of the images caused by velocity errors. Such an objective function can be designed using the differential semblance principle. The objective function built in this way is uni-modal with respect to the model, thus preventing the inversion from being trapped in local minima. The smoothness of the function around the global minima facilitates the use of gradient-type solvers for achieving convergence towards the true model. The velocity estimation process requires computing the gradient of the objective function which links image errors to velocity model updates. One key component for the construction of the gradient is the adjoint scattering operator which we construct in the framework of frequency-domain downward continuation. Such an operator is formulated by applying the Born linearization to the single square-root equation, and it serves as the foundation for image-domain wavefield tomography algorithms.

Key words: wavefield-extrapolation, velocity analysis, extended images, objective function

1 INTRODUCTION

The focus of seismic exploration is in regions characterized by complex subsurface structure. In such regions, wavefield-based migration is a powerful tool for accurately imaging the earth's interior that has become a commercial routine. However, since wavefield-based migration is sensitive to velocity error, the quality of the final image greatly depends on the accuracy of the velocity model. Thus, a key challenge for imag-

ing in complex geology is an accurate determination of the velocity model in the area under investigation.

In practice, all velocity model building techniques require an information carrier to connect the input (the quantity we can measure from the data), to the output (the unknown quantity we want to resolve). Ray-based methods are techniques which use high-frequency asymptotic rays as the information carrier (Bishop et al., 1985; Zhou, 2003; Stork, 1992; Liu, 1997); while wavefield-based methods are techniques which use band-limited wavefields as the information carrier (Tarantola, 1984; Pratt, 1999; Sava & Biondi, 2004a; Operto et al., 2007; Shen & Symes, 2008; Xie & Yang, 2008).

In complex geology, ray-based methods often fail to produce a good velocity model for several reasons. First, ray-based methods cannot handle complicated wave propagation phenomena such as multi-pathing caused by the complexity of the subsurface. Second, sharp velocity contrasts cause instability for ray-based methods. In addition, the high-frequency assumption embedded in ray-based methods is inconsistent with the finite-frequency characteristic of wavefield-based migration. A wavefield-based velocity analysis technique is expected to provide a more accurate, robust and consistent solution because of its accurate description of wave propagation in a complex subsurface, capability of handling strong velocity variation, and a frequency band that is consistent with wavefield-based migration. Although ray-based methods have the advantage of computational efficiency, wavefield-based methods are more appropriate than ray-based methods for building a velocity model in complex geologic areas. However, the expensive computational cost, reliance on the starting model, and convergence of the results at local minimum are all issues that need to be solved for practical application of wavefield-based methods (Etgen et al., 2009; Virieux & Operto, 2009).

Wavefield-based velocity analysis techniques can be classified by the domain in which the optimization problem is formulated. In the data domain, wavefield-based velocity estimation techniques are described as full- waveform inversion (FWI) (Tarantola, 1987; Mora, 1988; Song et al., 1995), while they are referred to as wavefield-based MVA when implemented in the image domain (Biondi & Sava, 1999; Shen et al., 2003; Albertin et al., 2006; Shen & Symes, 2008; Symes, 2008). The essential difference between these two categories is that FWI defines residuals by directly measuring the misfit between observed and predicted data, while WEMVA defines residuals by measuring the coherency and focusing of extended images. Then, the energy of the residual in either domain is backprojected via band-limited wave propagation into velocity updates.

WEMVA requires residuals defined in the image domain as the input. Thus, one needs first to measure the deficiency of migrated images using focusing or semblance properties. Biondi & Sava (1999) and Sava & Biondi (2004a,b) develop the framework of WEMVA and illustrate the construction of a linearized migration operator and its adjoint. Shen et al. (2003) illustrate the WEMVA method using the differential semblance optimization (DSO). Shen & Calandra (2005) and Shen & Symes (2008) implement a similar DSO scheme for survey-sinking and for shot-profile migration, respectively, and analyze properties of the differential semblance for offset and angle gathers.

Earlier research on image-domain wavefield tomography uses space-lag common-image-gathers (CIGs), which include only partial information of migrated images (Sava & Biondi, 2004a; Shen & Symes, 2008). The additional information embedded in time-lag CIGs, however, has yet to be fully exploited (Yang & Sava, 2009). An approach that simultaneously uses all lags information from the images can benefit from the high resolution of space-lag gathers and the robustness of time-lag gathers, thus having the potential to render an accurate and high-resolution velocity model in areas of complex geology.

Here, we first present the algorithms for migration with conventional and extended images, as well as their adjoint algorithms. We then explain the key steps of the procedures and analyze the required computational cost. Also, we present algorithms of linearized migration with conventional and extended images, as well as their adjoint algorithms. Linearized migration and its adjoint are critical components for image-domain wavefield tomography. We also formulate objective functions of image-domain tomography designed particularly for CIPs. Using the semblance principle, we can construct different objective functions to penalize the residual moveout of events in CIPs. Finally, we demonstrate the characteristics of the objective function by synthetic examples.

2 MIGRATION WITH EXTENDED IMAGES

Under the assumption of single scattering at discontinuities in the subsurface, we can describe seismic migration as a two-steps imaging process: wavefield reconstruction followed by the application of an imaging condition.

Seismic waves generated from the source, represented by the source wavefield, propagate in the medium and interact with discontinuities. The reflected seismic waves, represented by the receiver wavefield, propagate back to the surface and are recorded by geophones. These two wavefields kinematically coincide at discontinuities. Therefore, after we reconstruct the wavefields by solving a wave equation numerically, we can extract the reflectivity information from the reconstructed wavefields using a conventional imaging condition (Claerbout, 1985),

$$R(\mathbf{x}) = \sum_{\omega} \overline{W_s(\mathbf{x},\omega)} W_r(\mathbf{x},\omega) \ , \tag{1}$$

or an extended imaging condition,

$$R(\mathbf{x},\boldsymbol{\lambda},\tau) = \sum_{\omega} \overline{W_s(\mathbf{x}-\boldsymbol{\lambda},\omega)} W_r(\mathbf{x}+\boldsymbol{\lambda},\omega)\, e^{2i\omega\tau} \ . \tag{2}$$

The image R is a function of space coordinates $\mathbf{x}$, of the space-lag $\boldsymbol{\lambda}$ and time-lag extensions τ (Rickett & Sava, 2002; Sava & Fomel, 2006; Sava & Vasconcelos, 2009). The complete set of extended images is a multi-dimensional hypercube, which

allows us to simultaneously access the semblance and focusing information about the images.

Seismic modeling process which maps the reflectivity of the subsurface into data **D** recorded on the surface can be formulated using a linear operator **L** applied to the reflectivity model represented by the image R:

$$\mathbf{D} = \mathbf{L}R\,. \tag{3}$$

Since the modeling is a linear process, the adjoint process can be directly obtained. Such an adjoint process is referred to as migration, and can be conceptually formulated as applying the operator $\mathbf{L}^*$ to data **D** and to obtain the image R. If we use matrix notation, we have

$$R = \mathbf{L}^*\mathbf{D}\,. \tag{4}$$

The pseudo-codes of the algorithm for migration and modeling with both conventional and extended images are detailed in boxes 1 and 2, respectively. The algorithms of modeling and migration are formulated in this work as adjoint pairs. Such algorithm pairs ensure stability if we use the operators in solving a linear inverse problem by conjugate-gradient methods. The particular implementation we illustrate is based on one-way wavefield-extrapolation shot-record migration, but one can generalize the algorithm to other imaging setups such as two-way wave-equation shot-record migration. The algorithms presented here perform computations for each frequency independently, which leads to a straightforward parallelization.

Box 1

MIGRATION WITH CONVENTIONAL IMAGES

```
set     R(x) = 0
        ω = ω_min ... ω_max {
read      W_s(x)
set       W_r(x) = 0
read      T(x,y)
          z = z_min ... z_max {
store       W_r(x,y,z) = T(x,y)
W.E.        T(x,y) = E^-[T(x,y)]
          }
I.C.      R(x) += conj(W_s(x)) W_r(x)
        }
write   R(x)
```

MODELING WITH CONVENTIONAL IMAGES

```
read    R(x)
        ω = ω_min ... ω_max {
read      W_s(x)
set       W_r(x) = 0
I.C.      W_r(x) += W_s(x) R(x)
set       T(x,y) = 0
          z = z_max ... z_min {
W.E.        T(x,y) = E^+[T(x,y)]
inject      T(x,y) += W_r(x,y,z)
          }
write     T(x,y)
        }
```

In the algorithms detailed in boxes 1 and 2, W.E. denotes wavefield extrapolation, I.C. denotes imaging condition, $\mathcal{E}^+$ represents a casual wavefield extrapolator, while $\mathcal{E}^-$ represents an anti-casual wavefield extrapolator. The source wavefield W_s is precomputed before migration and stored in the disk, but it can also be computed inside the algorithms. In the migration algorithm, we first recursively downward continue the receiver wavefield by applying the extrapolator $\mathcal{E}^-$ and store the extrapolated wavefield at every depth level. We only need to store the wavefield for one frequency, which makes the calculation manageable. After the wavefield reconstruction is accomplished, we extract the conventional image by equation 1, or the extended images by equation 2. The final image is the stack of images over all frequencies.

In the modeling algorithm, the reflectivity is injected into the receiver wavefield using the adjoint of the imaging condition in equations 1 or 2. Next, we recursively upward continue the full receiver wavefield from bottom to top by applying the adjoint extrapolator $\mathcal{E}^+$ and inject the wavefield constructed from the model at every depth level. After the wavefield reconstruction is finished, we output the wavefield at the surface.

Box 2

MIGRATION WITH EXTENDED IMAGES

set $R(\mathbf{c},\boldsymbol{\lambda},\tau)=0$
$\omega=\omega_{min}\dots\omega_{max}\{$
read $W_s(\mathbf{x})$
set $W_r(\mathbf{x})=0$
read $T(x,y)$
$z=z_{min}\dots z_{max}\{$
store $W_r(x,y,z)=T(x,y)$
W.E. $T(x,y)=\mathcal{E}^-[T(x,y)]$
$\}$
loop $\lambda,\tau\{$
I.C. $R(\mathbf{c},\boldsymbol{\lambda},\tau)\mathrel{+}=e^{-2i\omega\tau}\overline{W_s(\mathbf{c}-\boldsymbol{\lambda})}W_r(\mathbf{c}+\boldsymbol{\lambda})$
$\}$
$\}$
write $R(\mathbf{c},\boldsymbol{\lambda},\tau)$

MODELING WITH EXTENDED IMAGES

read $R(\mathbf{c},\boldsymbol{\lambda},\tau)$
$\omega=\omega_{min}\dots\omega_{max}\{$
read $W_s(\mathbf{x})$
set $W_r(\mathbf{x})=0$
loop $\lambda,\tau\{$
I.C. $W_r(\mathbf{c}+\boldsymbol{\lambda})\mathrel{+}=W_s(\mathbf{c}-\boldsymbol{\lambda})\,e^{+2i\omega\tau}R(\mathbf{c},\boldsymbol{\lambda},\tau)$
$\}$
set $T(x,y)=0$
$z=z_{max}\dots z_{min}\{$
W.E. $T(x,y)=\mathcal{E}^+[T(x,y)]$
inject $T(x,y)\mathrel{+}=W_r(x,y,z)$
$\}$
write $T(x,y)$
$\}$

The computational cost for such implementations can also be split between the wavefield reconstruction and the imaging condition. Since we use a frequency-domain recursive extrapolator to reconstruct the wavefields, the cost is proportional to the size of the model and the number of frequencies. Thus, it can be estimated as:

$$N_{\text{W.R.}} \sim N_\omega N_{\mathbf{x}} \;, \tag{5}$$

where N_ω represents the number of frequencies and $N_{\mathbf{x}}$ represents the number of samples along the space axes.

The cost for the imaging condition is controlled by several factors: the frequency band, the number of locations we choose to construct the extended images, and the number of lags involved. Thus, it can be estimated as:

$$N_{\text{I.C.}} \sim N_\omega N_{\mathbf{c}} N_{\boldsymbol{\lambda}} N_\tau \;, \tag{6}$$

where $N_{\mathbf{c}}$ represents the number of CIPs and $N_{\boldsymbol{\lambda}}$, N_τ represent the number of space- and time-lags. If we take the conventional space-lags CIGs and extended CIPs as examples, the computational cost for the imaging condition is

$$N_{\text{I.C.}} \sim N_\omega N_z N_{h_x} N_{h_y} N_{\lambda_x} N_{\lambda_y} \;, \tag{7}$$

where N_{h_x} and N_{h_y} represent the number of horizontal locations at which we construct the gathers along in-line and cross-line directions. If we denote the cost of constructing space-lags common-image gathers as $C_{\boldsymbol{\lambda}}$ and the cost of constructing space- and time-lags common-image-point gathers as $C_{\boldsymbol{\lambda}\tau}$, from the equation 6 and 7, we obtain the ratio:

$$\frac{C_{\boldsymbol{\lambda}}}{C_{\boldsymbol{\lambda}\tau}} \sim \frac{N_z N_{h_x} N_{h_y}}{N_{\mathbf{c}} N_{\lambda_z} N_\tau} \;. \tag{8}$$

Suppose $N_z = N_x = N_y = 500$, $N_{h_x} = N_{h_y} = 50$, $N_{\mathbf{c}} = 500$, $N_{\lambda_z} = 20$, $N_\tau = 100$, then $\frac{C_{\boldsymbol{\lambda}}}{C_{\boldsymbol{\lambda}\tau}} \sim 1.2$, which means the cost of computing CIPs is about the same as the cost of computing CIGs. However, we can drop the vertical space-lag axis if we are imaging nearly-horizontal reflectors, or we can eliminate one of the lag axes if we have information about the reflector dip. Then, $\frac{C_{\boldsymbol{\lambda}}}{C_{\boldsymbol{\lambda}\tau}} \sim 25$, thus we achieve a significant reduction in the computational cost of the imaging condition. Therefore, using CIPs for velocity analysis is particularly attractive, as they provide information about the velocity model at smaller cost. Furthermore, as discussed by Sava & Vasconcelos (2009), CIPs have other advantages over CIGs, mainly related to image sampling that is more consistent with the underlying geologic structure.

We migrate the Sigsbee 2A dataset (Paffenholz et al., 2002) as an example. Figure 1(a) shows the background velocity model, constructed by subtracting the perturbation shown in Figure 1(b) from the true velocity model. The image obtained is shown in Figure 1(c), overlain with the dots indicating the locations where CIPs are constructed. The $*$ indicate the positions of CIPs shown in Figure 2(a)-2(d). Since we use the background model for migration, we see that events in all CIPs are not well focused and exhibit residual moveout in λ_x-τ panels. In addition, in Figures 2(c) and 2(d), the CIPs are constructed in subsalt area with an uneven illumination, we see that the CIPs contain significant artifacts. In general, the salt creates uneven illumination and shadow zones, which generate artifacts and distort the images. The distortion is similar to the imperfections caused by the velocity error. If we use such gathers for velocity analysis, we may obtain an incorrect result. Thus, in complex area, illumination compensation is necessary for velocity model building. This important research direction falls outside the scope of this paper.

3 LINEARIZED WAVEFIELD-BASED MIGRATION VELOCITY ANALYSIS WITH EXTENDED IMAGES

To formulate the velocity analysis in the image-domain, we first need to construct an objective function for the optimization problem. In general, there are two approaches we can use to seek the solution. The first approach uses a linearized image perturbation. The second approach, based on differential semblance optimization, is discussed in the next section. To obtain

an image perturbation, one starts by applying the Taylor expansion to an image as follows:

$$R(\mathbf{x}, s_c) = R(\mathbf{x}, s_b) + \Delta R(\mathbf{x}) \ , \tag{9}$$

where

$$s_c = s_b + \Delta s \ . \tag{10}$$

Here, s_c denotes the correct slowness and s_b and Δs denote background slowness and slowness perturbation, respectively. The image perturbation is related to the slowness perturbation by a linearized scattering operator **A**:

$$\Delta R(\mathbf{x}) = \mathbf{A}\Delta s \equiv \frac{\partial R(\mathbf{x}, s)}{\partial s}|_{s=s_b} \Delta s \ . \tag{11}$$

Since the image perturbation is proportional to the slowness perturbation, the velocity analysis can be performed by minimizing the image perturbation. Thus, the corresponding objective function, which defines a linearized optimization problem, is formulated as:

$$J(\Delta s) = \frac{1}{2}\|\Delta R - \mathbf{A}\Delta s\|_2^2 \ . \tag{12}$$

The operator **A** in equations 11 and 12 is used to obtain an image perturbation from a slowness perturbation:

$$\Delta R = \mathbf{A}\Delta s \ . \tag{13}$$

We can directly construct the adjoint MVA process similarly to migration. In this way, we obtain the adjoint pair of operators. The adjoint process describes the backprojection from image perturbation to slowness perturbation:

$$\Delta s = \mathbf{A}^* \Delta R \ , \tag{14}$$

where $\mathbf{A}^*$ represents the adjoint operator.

The pseudo-codes of the algorithm for forward and adjoint linearized MVA with both conventional and extended images are detailed in boxes 3 and 4, respectively. The algorithms are constructed based on the one-way wave-equation shot-record migration, and implemented in the frequency domain.

Box 3

FORWARD SCATTERING WITH CONVENTIONAL IMAGES

```
set     ΔR(x) = 0
read    Δs(x)
        ω = ω_min ... ω_max {
read      W_s(x)
read      W_r(x)
set       T̄_s(x,y) = 0
set       T_r(x,y) = 0
          z = z_min ... z_max {
W.S.        T̄_s(x,y) += S⁻[W̄_s(x,y,z), Δs(x,y,z)]
W.S.        T_r(x,y) += S⁻[W_r(x,y,z), Δs(x,y,z)]
W.E.        T̄_s(x,y) = E⁺[T̄_s(x,y)]
W.E.        T_r(x,y) = E⁻[T_r(x,y)]
store       ΔW̄_s(x,y,z) = T̄_s(x,y)
store       ΔW_r(x,y,z) = T_r(x,y)
          }
I.C.      ΔR(x) += W_r(x) ΔW̄_s(x)
I.C.      ΔR(x) += W̄_s(x) ΔW_r(x)
        }
write   ΔR(x)
```

ADJOINT SCATTERING WITH CONVENTIONAL IMAGES

```
read    ΔR(x)
set     Δs(x) = 0
        ω = ω_min ... ω_max {
read      W_s(x)
read      W_r(x)
I.C.      ΔW̄_s(x) = W̄_r(x) ΔR(x)
I.C.      ΔW_r(x) = W_s(x) ΔR(x)
set       T̄_s(x,y) = 0
set       T_r(x,y) = 0
          z = z_max ... z_min {
inject      T̄_s(x,y) += ΔW̄_s(x,y,z)
inject      T_r(x,y) += ΔW_r(x,y,z)
W.E.        T̄_s(x,y) = E⁻[T̄_s(x,y)]
W.E.        T_r(x,y) = E⁺[T_r(x,y)]
W.S.        Δs(x,y,z) += S⁺[W_s(x,y,z), T̄_s(x,y)]
W.S.        Δs(x,y,z) += S⁺[W̄_r(x,y,z), T_r(x,y)]
          }
        }
write   Δs(x)
```

Box 4

FORWARD SCATTERING WITH EXTENDED IMAGES

set $\Delta R(\mathbf{c},\boldsymbol{\lambda},\tau)=0$
read $\Delta s(\mathbf{x})$
$\omega=\omega_{min}\dots\omega_{max}\{$
read $W_s(\mathbf{x})$
read $W_r(\mathbf{x})$
set $\overline{T_s(x,y)}=0$
set $T_r(x,y)=0$
$z=z_{min}\dots z_{max}\{$
W.S. $\overline{T_s(x,y)}+=\mathcal{S}^-\left[\overline{W_s(x,y,z)},\Delta s(x,y,z)\right]$
W.S. $T_r(x,y)+=\mathcal{S}^-\left[W_r(x,y,z),\Delta s(x,y,z)\right]$
W.E. $\overline{T_s(x,y)}=\mathcal{E}^+\left[\overline{T_s(x,y)}\right]$
W.E. $T_r(x,y)=\mathcal{E}^-\left[T_r(x,y)\right]$
store $\overline{\Delta W_s(x,y,z)}=\overline{T_s(x,y)}$
store $\Delta W_r(x,y,z)=T_r(x,y)$
$\}$
loop $\boldsymbol{\lambda},\tau\{$
I.C. $\Delta R(\mathbf{c},\boldsymbol{\lambda},\tau)+=e^{+2i\omega\tau}W_r(\mathbf{c}+\boldsymbol{\lambda})\,\overline{\Delta W_s(\mathbf{c}-\boldsymbol{\lambda})}$
I.C. $\Delta R(\mathbf{c},\boldsymbol{\lambda},\tau)+=e^{-2i\omega\tau}\overline{W_s(\mathbf{c}-\boldsymbol{\lambda})}\Delta W_r(\mathbf{c}+\boldsymbol{\lambda})$
$\}$
$\}$
write $\Delta R(\mathbf{c},\boldsymbol{\lambda},\tau)$

ADJOINT SCATTERING WITH EXTENDED IMAGES

read $\Delta R(\mathbf{x})$
set $\Delta s(\mathbf{x})=0$
$\omega=\omega_{min}\dots\omega_{max}\{$
read $W_s(\mathbf{x})$
read $W_r(\mathbf{x})$
loop $\boldsymbol{\lambda},\tau\{$
I.C. $\overline{\Delta W_s(\mathbf{c}-\boldsymbol{\lambda})}+=e^{-2i\omega\tau}\overline{W_r(\mathbf{c}+\boldsymbol{\lambda})}\Delta R(\mathbf{c},\boldsymbol{\lambda},\tau)$
I.C. $\Delta W_r(\mathbf{c}+\boldsymbol{\lambda})+=e^{+2i\omega\tau}W_s(\mathbf{c}-\boldsymbol{\lambda})\,\Delta R(\mathbf{c},\boldsymbol{\lambda},\tau)$
$\}$
set $\overline{T_s(x,y)}=0$
set $T_r(x,y)=0$
$z=z_{max}\dots z_{min}\{$
inject $\overline{T_s(x,y)}+=\overline{\Delta W_s(x,y,z)}$
inject $T_r(x,y)+=\Delta W_r(x,y,z)$
W.E. $\overline{T_s(x,y)}=\mathcal{E}^-\left[\overline{T_s(x,y)}\right]$
W.E. $T_r(x,y)=\mathcal{E}^+\left[T_r(x,y)\right]$
W.S. $\Delta s(x,y,z)+=\mathcal{S}^+\left[W_s(x,y,z),\overline{T_s(x,y)}\right]$
W.S. $\Delta s(x,y,z)+=\mathcal{S}^+\left[\overline{W_r(x,y,z)},T_r(x,y)\right]$
$\}$
$\}$
write $\Delta s(\mathbf{x})$

In the algorithms detailed in boxes 3 and 4, W.S. denotes wavefield scattering, $\mathcal{S}^+$ represents a casual wavefield scattering operator, and $\mathcal{S}^-$ represent an anti-casual wavefield scattering operator. These scattering operators characterize the wavefield scattered from the slowness perturbation via the background wavefield (Sava & Vlad, 2008). The background wavefields must be precomputed beforehand.

In the forward MVA algorithm, the total scattered wavefield consists of the scattered wavefield extrapolated from the previous depth level above added to the scattered wavefield generated from the slowness perturbation at the current depth level. At a certain depth level, we first apply the scattering operator $\mathcal{S}$ to obtain the scattered wavefields for the source and receiver, respectively. The imaging conditions cross-correlate the complex conjugate of the source wavefield and receiver wavefield. Taking the complex conjugate is not a linear operation in the complex domain. We can directly compute the complex conjugate of the scattered source wavefield and then downward continue the scattered wavefields by the wavefield extrapolator. After the computation for scattered wavefields is done, we use the conventional or extended imaging conditions to extract the image perturbation. In both cases, we apply the imaging conditions twice, to different combinations of the scattered and background wavefields, respectively, then sum the results from these two computations.

In the adjoint MVA algorithm, we first construct the perturbed wavefields from the image perturbations by the adjoint of the imaging conditions. Notice that we also directly compute the complex conjugate of the perturbed source wavefield to avoid taking the complex conjugate of the wavefield. Next, we inject the perturbed wavefield into the total scattered wavefield extrapolated from the previous depth level below, and upward continue the new scattered wavefield. The slowness perturbation at the current depth level is obtained from the total scattered wavefield by the adjoint of the scattering operator.

The computational cost for the MVA process consists of three parts: wavefield reconstruction (W.R.), wavefield scattering (W.S.), and imaging condition (I.C.). The cost for both wavefield reconstruction and scattering can be estimated by equation 5, scaled by 2 since we need to compute them twice, for the source and receiver sides. The cost for imaging condition can be estimated by equation 6, scaled by 2 for the same reason.

We use the Sigsbee 2A dataset as an example again with the background model in Figure 1(a) and with the slowness perturbation in Figure 1(b) to create the image perturbation. We construct the image perturbation for CIPs located at the same positions denoted by the $*$ in Figure 1(c), as shown in Figures 3(a)- 3(d). Comparing the image perturbation of CIPs to those from background velocity model in Figure2(a)-(d), we notice that the events in Figure 3(a)-3(d) are more oscillatory because we use less frequencies in constructing the image perturbation to save cost. Also, the image perturbation has a phase difference because of the linearization of the wavenumber with respect to slowness in the scattering operator. Next, we apply the adjoint operator to the image perturbation to obtain the backprojection, which is equivalent to the gradient of the corresponding objective function given by equation 12. The backprojection provides a straightforward way to study the forward and adjoint scattering operators. The main fac-

tors that control the shape of the backprojection are (1) the frequency content of the background wavefields, (2) the type of source (e.g., point or plane-wave) from which we generate the background wavefields, and (3) the type of perturbation constructed in the image space. Figure 4(a)-4(c) show the backprojection from a single shot at $x = 12.3$ km using different frequency bands. We can see that with increasing frequency band used, the magnitude of the backprojection become stronger. Figure 5(a)-5(c) show the backprojection from all shots using different frequency bands. Similarly, the magnitude of the backprojection is increasing with more frequencies used. In Figure 5(c), we see that backprojection has a complicated shape due to the complexity of the background model.

In practice, the true slowness perturbation is never known, so the image perturbation is also unknown. However, one can construct a linearized image perturbation to approximate the true one. Thus, the key element for this approach is the construction of the linearized image perturbation. Sava (2003) proposes using Stolt residual migration as the solution, while Yang & Sava (2009) use focusing of the time-lag extended images to address the problem. Generally, the linearized-image perturbation approach can effectively avoid the common cycle-skipping problem for wavefield tomography. The construction of the linearized image perturbation, however, requires a quantity that can be measured directly from the image. Such a quantity is difficult to measure for all types of extended images. An alternative to this approach is to construct penalties of the migrated images itself, as discussed in the following section.

4 DIFFERENTIAL SEMBLANCE OPTIMIZATION WITH EXTENDED IMAGES

An alternative approach to formulate image-domain wavefield tomography relies on applying a penalty function to extended images. The penalty function measures the coherency of images and highlights and penalizes the image imperfections caused by velocity errors. In general, we can formulate an objective function for optimization by first identifying characteristics of the images corresponding to correct velocity. Such features define an ideal shape for the images relative to which we can measure image imperfections. Since the velocity error distorts the wavefields reconstructed in the subsurface, the images constructed with an incorrect velocity does not conform with the ideal shape. This part of the energy in the images is the residual. Therefore, we require the penalty function to annihilate the energy of images corresponding to the ideal shape, and to preserve and highlight the energy of images departing from the ideal shape. As a result, a penalized image is equivalent to the data misfit defined in the image domain. Therefore, the velocity optimization problem is formulated by minimizing the image residual, and the corresponding objective function

$$J(s) \equiv \frac{1}{2}\|\mathbf{P}[R(\mathbf{x},\boldsymbol{\lambda},\tau)]\|_2^2 . \tag{15}$$

In general, $R(\mathbf{x},\boldsymbol{\lambda},\tau)$ are extended images with different extensions and $\mathbf{P}$ is the penalty function.

According to the semblance principle, if data are migrated with the correct velocity model, the subsurface reflectors are imaged at a fixed location for different seismic experiments regardless of the geological structure (Al-Yahya, 1989). Therefore, we can use the image semblance to quantify these imperfections and to update the velocity model. This process is referred to as semblance analysis. Symes & Carazzone (1991) introduce differential semblance as a particular implementation of semblance analysis, and the corresponding velocity analysis process, often referred to as differential semblance optimization (DSO). The underlying idea is to analyze the difference of semblance between neighboring traces within a CIGs or a CIPs. The main advantage of DSO is the convexity of the corresponding objective function, which greatly reduces the difficulty of handling the local minima in common wavefield-tomography methods in the context of wave-equation migration velocity analysis. The DSO approach has been applied to conventional CIGs (Shen et al., 2003; Shen & Calandra, 2005; Shen & Symes, 2008).

4.1 Objective function for extended images

For CIGs constructed in the space-lag domain, Shen et al. (2003) and Shen & Symes (2008) derive the formula to describe the kinematics of a reflector at depth z_0 using extended images by

$$R(z,\boldsymbol{\lambda}) = \delta(\boldsymbol{\lambda})\,\delta(z - z_0) , \tag{16}$$

where z_0 is the depth of the reflector. The reflections should be focused at zero space-lag because the reflectors are imaged at the same subsurface location for different shots when the velocity is correct. Hence, we measure the focusing of events in CIGs, and penalize the residual moveout, which is the energy not concentrated at zero space-lag. The penalty function is formulated as

$$\mathbf{P}_{\boldsymbol{\lambda}}[R] = |\boldsymbol{\lambda}|R . \tag{17}$$

For CIPs constructed in the space- and time-lags domain, Sava & Vasconcelos (2009) describe the kinematics of the extended images by

$$R(\boldsymbol{\lambda},\tau) = \delta(\mathbf{q}\cdot\boldsymbol{\lambda})\,\delta(v\tau) , \tag{18}$$

where $\mathbf{q}$ denotes a unit vector parallel to the reflector and at the intersection of the reflection and reflector planes. When correct velocity v is used for imaging, an event in a CIPs is illuminated by multiple shots and is represented by a line at $\tau = 0$ oriented at an angle parallel to the reflector normal. Thus, we also measure the focusing along the trajectory oriented at an angle parallel to the reflector normal. Similar to the conventional DSO approach, we penalize the residual moveout spread from the tilted line at $\tau = 0$. The penalty function formulated in this way is

$$\mathbf{P}_{(\boldsymbol{\lambda},\tau)}[R] = |\tau|R . \tag{19}$$

Such a penalty function has the advantages that it is straightforward and requires no information about the slope of the reflection.

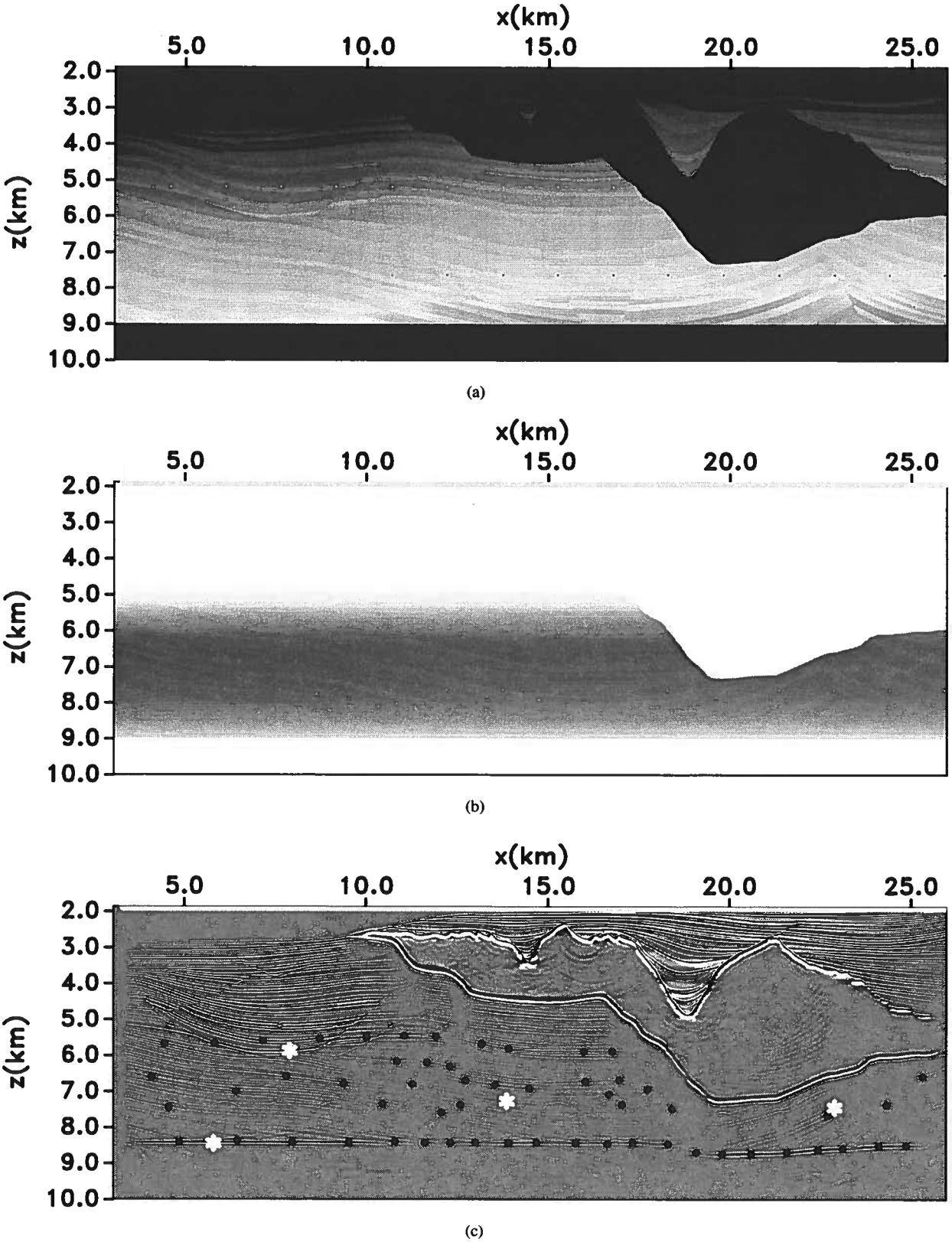

Figure 1. (a) Sigsbee 2A synthetic model, (b) slowness perturbation and (c) migrated image with background velocity model. The dots indicate the positions where CIPs are constructed. The * indicate the positions of the CIPs shown in Figures 2 and 3.

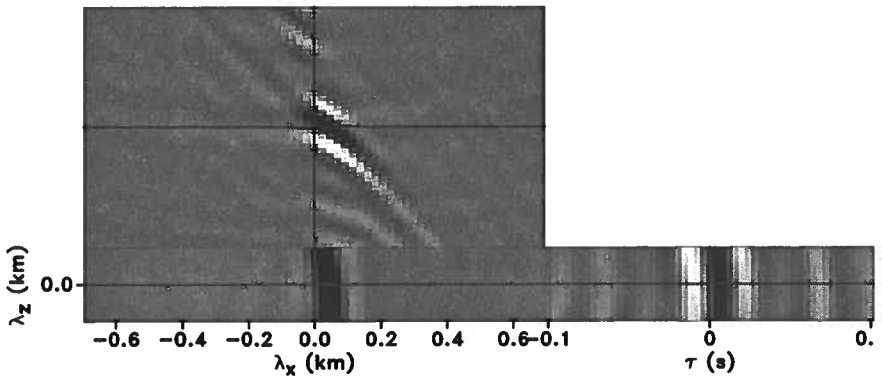

(a)

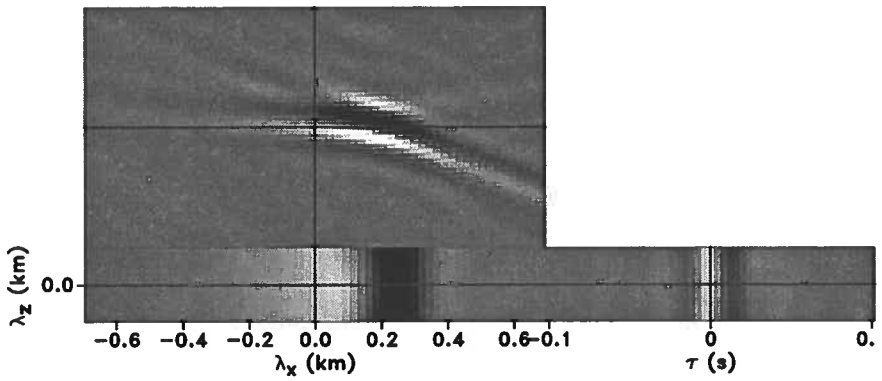

(b)

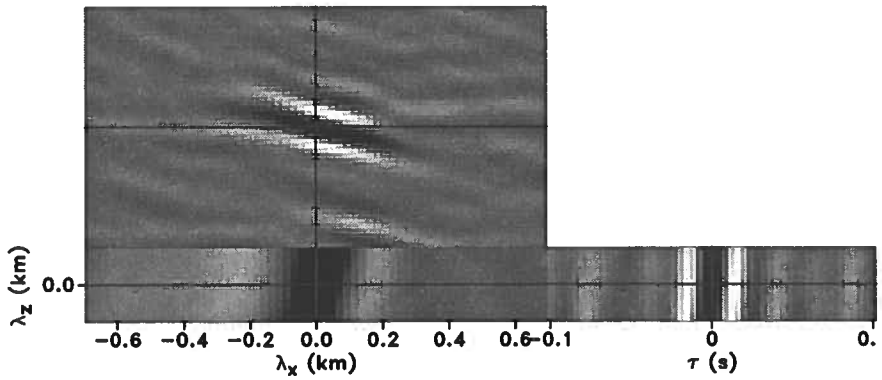

(c)

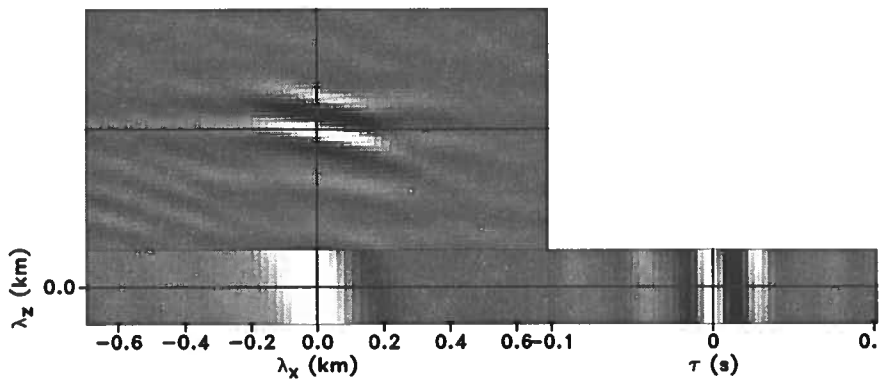

(d)

Figure 2. CIPs chosen from subsurface at (a) $x = 5.81$ km, $z = 8.44$ km (b) $x = 7.92$ km, $z = 5.87$ km, (c) $x = 22.89$ km, $z = 7.44$ km, and (d) $x = 14$ km, $z = 6.62$ km.

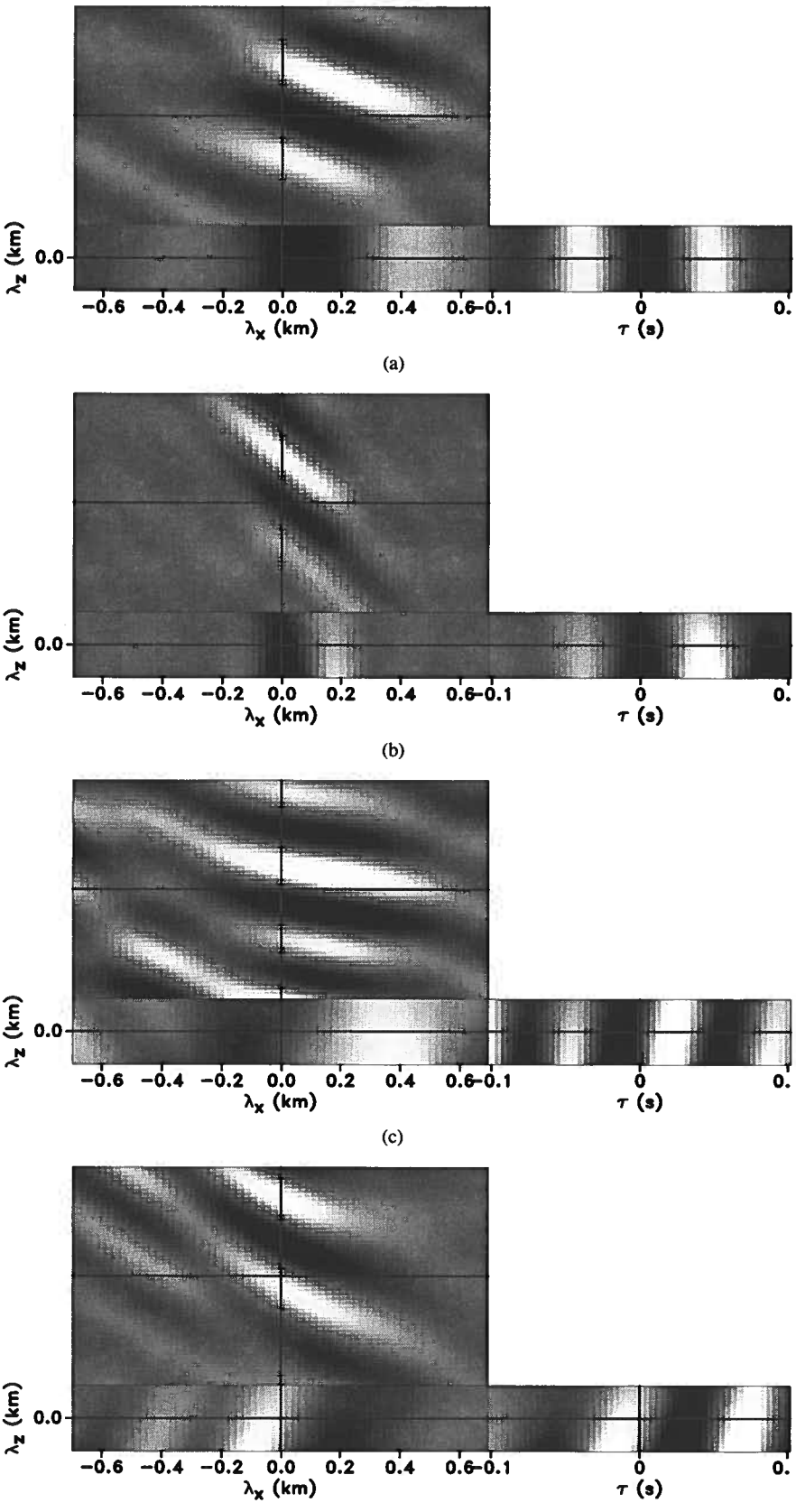

Figure 3. Image perturbation of CIPs chosen from subsurface at (a) $x = 5.81$ km, $z = 8.44$ km (b) $x = 7.92$ km, $z = 5.87$ km, (c) $x = 22.89$ km, $z = 7.44$ km, and (d) $x = 14$ km, $z = 6.62$ km.

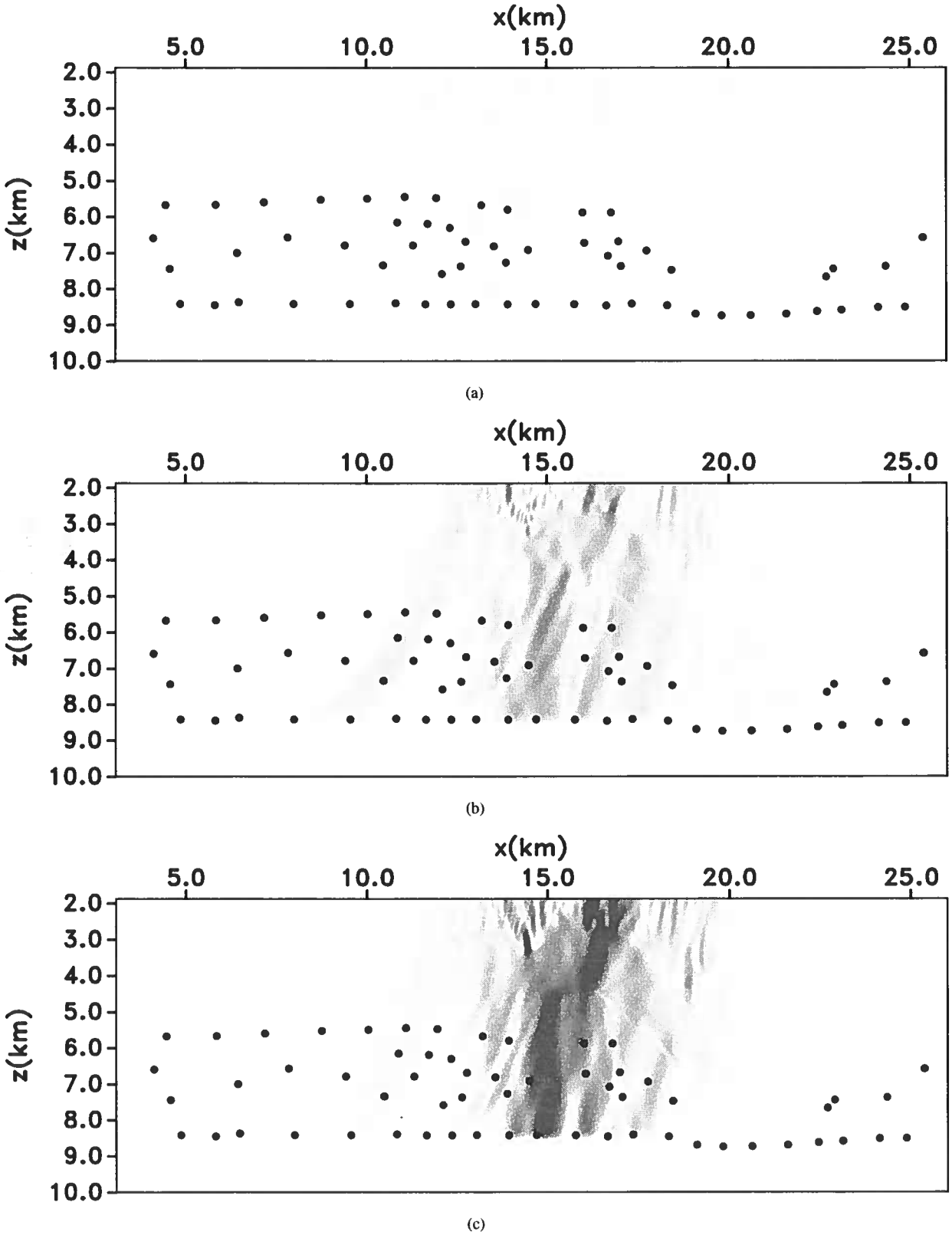

Figure 4. Backprojection from the image perturbation of all CIPs (a) using a single frequency of 3.5 Hz and a single shot at $x = 12.3$ km, (b) using a frequency band from 3-4.5 Hz and a single shot at $x = 12.3$ km, (c) using a frequency band from 3-8.5 Hz and a single shot at $x = 12.3$ km.

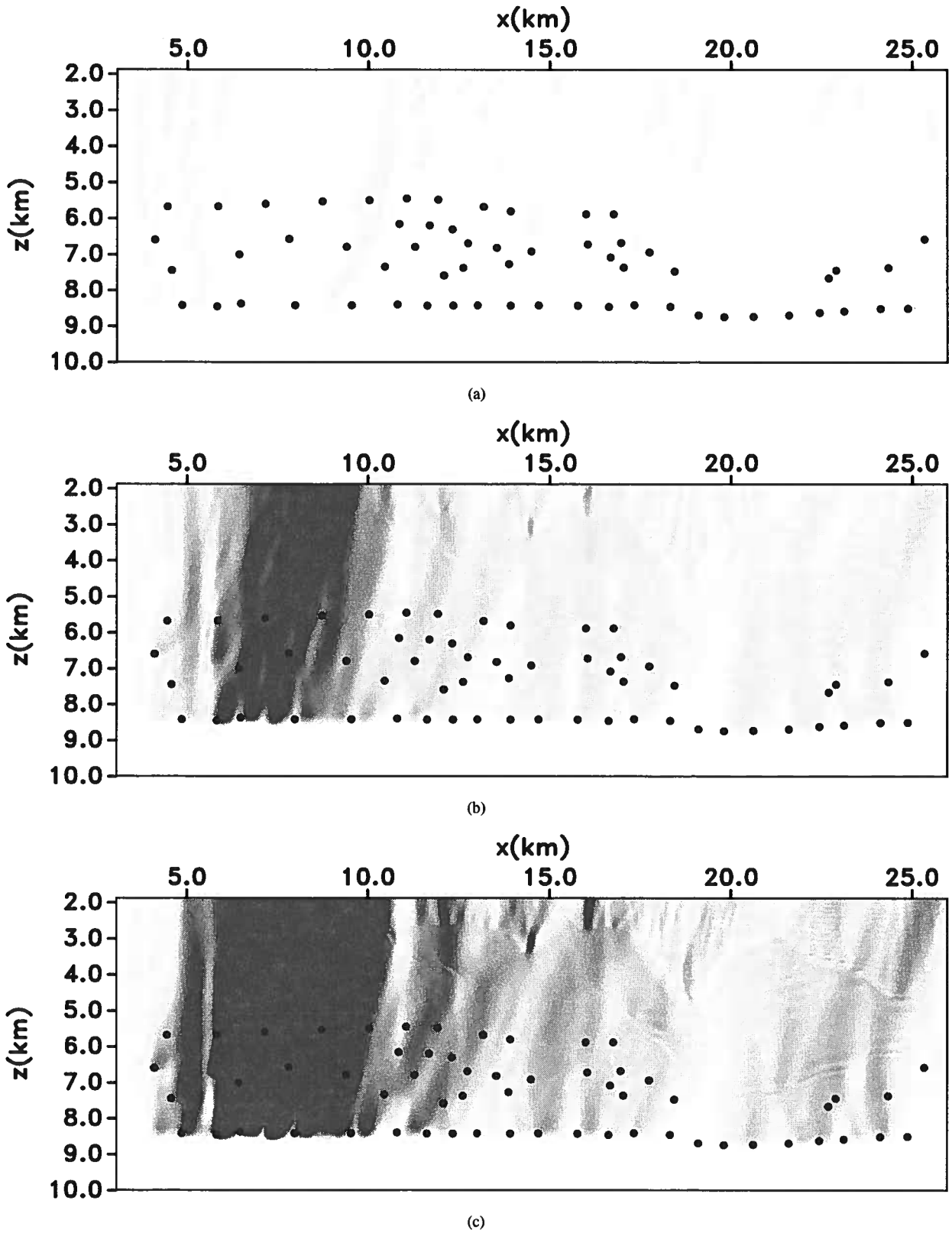

Figure 5. Backprojection from the image perturbation of all CIPs (a) using a single frequency of 3.5 Hz and all shots, (b) using a frequency band from 3-4.5 Hz and all shots, (c) using a frequency band from 3-8.5 Hz and all shots.

Since the residual moveout extends in both the space- and time-lags direction, we can also penalize the energy not concentrated at $\tau = 0$ and spread in the space-lag direction. Thus, we can formulate another penalty function as:

$$\mathbf{P}_{(\boldsymbol{\lambda},\tau)}[R] = |\mathbf{q} \cdot \boldsymbol{\lambda}| R \,, \tag{20}$$

The information about the unit vector $\mathbf{q}$ can be extracted from CIPs by measuring the slope of the event in the $\lambda_x - \lambda_z$ panel, or just by measuring the reflector slope in conventional images.

Furthermore, we can combine the penalty functions above so that we simultaneously penalize the residual moveout in both the space- and time-lags direction. The penalty function is thus

$$\mathbf{P}_{(\boldsymbol{\lambda},\tau)}[R] = R\sqrt{(v\tau)^2 + (\mathbf{q} \cdot \boldsymbol{\lambda})^2} \,. \tag{21}$$

4.2 Event isolation for DSO

When we design the various penalty functions, we implicitly assume that there is only one event in the CIPs. As the τ axis of CIPs represents a time-shift applied to the reconstructed wavefields, however, it is possible that nearby reflections can also be imaged in a given CIPs, although these nearby events do not go through the origin of the lag space. Consider an example shown in Figure 6, which consists of three reflectors embedded in a constant medium. Figures 7(a) and 7(b) shows the CIPs constructed in the middle reflector for correct and incorrect velocity models, respectively. For the CIPs corresponding to correct velocity, Figure 7(a), the event crossing $\tau = 0$ is focused at $\boldsymbol{\lambda} = 0$. For the CIPs corresponding to incorrect velocity, Figure 7(b), the event crossing $\tau = 0$ is characterized residual moveout. Ideally, we expect a CIPs constructed with correct velocity to be focused at $\tau = 0$ and $\mathbf{q} \cdot \boldsymbol{\lambda} = 0$, which is how we have defined the penalty functions shown in Figure 8(a), 9(a) and 10(a). However, when multiple reflectors are presented in the image, multiple reflections will also be part of the CIPs. Of all these events, the only event we need to penalize is the one on which we have picked the CIPs, i.e. the event that goes through $\tau = 0$ and $\boldsymbol{\lambda} = 0$. All other events should not be penalized. Therefore, it is necessary to isolate just the event on which we have constructed the CIP for the application of the penalty function.

To isolate the irrelevant events, we simply apply a mask to CIPs and mute the events that do not contain the origin of the lag space. The key step is to construct the mask whose shape matches the trajectory of the event we want to preserve. we determine the trajectory by finding the similarity of the selected between neighboring traces using cross-correlation method. The maximum cross-correlation value corresponds to the shift between the signals at which they reach the maximum similarity. An example of the application of this procedure is shown in Figure 7(c).

For the illustration of penalty functions, we use the example shown in Figure 6. The CIPs corresponding to correct and erroneous velocities are shown in Figures 7(a) and 7(b), respectively. Figures 8(a) and 8(c) show the penalty function given by equation 19 and the CIPs in Figure 7(c) after the application of the penalty. The energy focused at $\tau = 0$ is annihilated, while the energy at nonzero τ is enhanced, thus defining the image residual. Figures 9(a) and 9(c) show the penalty function given by equation 20 and the CIPs in Figure 7(c) after the application of the penalty. In this case, we remove the energy focused at $\mathbf{q} \cdot \boldsymbol{\lambda} = 0$, and enhance the energy outside the trajectory of $\mathbf{q} \cdot \boldsymbol{\lambda} = 0$. Figures 8(a) and 8(c) show the penalty function given by equation 21 and the CIPs in Figure 7(c) after the application of the penalty. The penalized image is similar to the one shown in 9(c) in that the residual moveout spread in $\boldsymbol{\lambda}$ direction is emphasized. However, the residual moveout spread in τ direction is also enhanced.

Next, to demonstrate the characteristics of the objective functions corresponding to different penalties, we migrate data with models obtained by scaling the correct model with a constant factor ranging from 0.75 to 1.25. For each situation, we construct the CIPs then apply the penalty functions and compute the values of the corresponding objective functions. To emphasize the importance of event isolation,we apply the penalty functions to the un-masked CIPs and obtain the result as shown in Figure 11(a). The thick solid, thin solid and dashed curves correspond to penalty functions given by equation 19, 20 and 21, respectively. We see that without the event isolation, none of the objective functions reach the minimum at the correct velocity. This observation demonstrates that the objective function incorrectly penalize the image imperfections and thus fails to measure the coherency of the events in CIPs. As a result, the objective function implemented in this way cannot produce correct velocity updates. Next, we apply the penalty functions to CIPs with event isolation and obtain the result shown in Figure 11(b). Similarly, the thick solid, thin solid and dashed lines correspond to penalty functions given by equation 19, 20 and 21, respectively. We see that the objective functions for different penalties share similar characteristics. First, for all objective functions, there is only one minimum and it occurs at the correct velocity model. The uni-modal character of the curves ensures the existence of a unique global minimum for the inversion. Second, the objective function is also monotonically increasing with the velocity error except for the objective function with penalty given by equation 21. One possible reason might be that the uneven illumination of the dipping reflectors causes uneven energy in the CIPs. The monotonically increasing objective functions facilitate the use of gradient-type methods in the inversion.

5 CONCLUSIONS

We discuss image-domain wavefield-based migration velocity analysis using extended images analyzed in common-image-point gathers constructed at sparse locations in the image. We present the algorithms of migration and modeling using extended images, as well as the forward and adjoint linearized scattering using extended images. These algorithms are necessary components for the velocity updating procedure. To formulate the velocity optimization problem, a penalty function is required to measure the coherency of the images and to penalize imperfections caused by velocity errors. The penalty func-

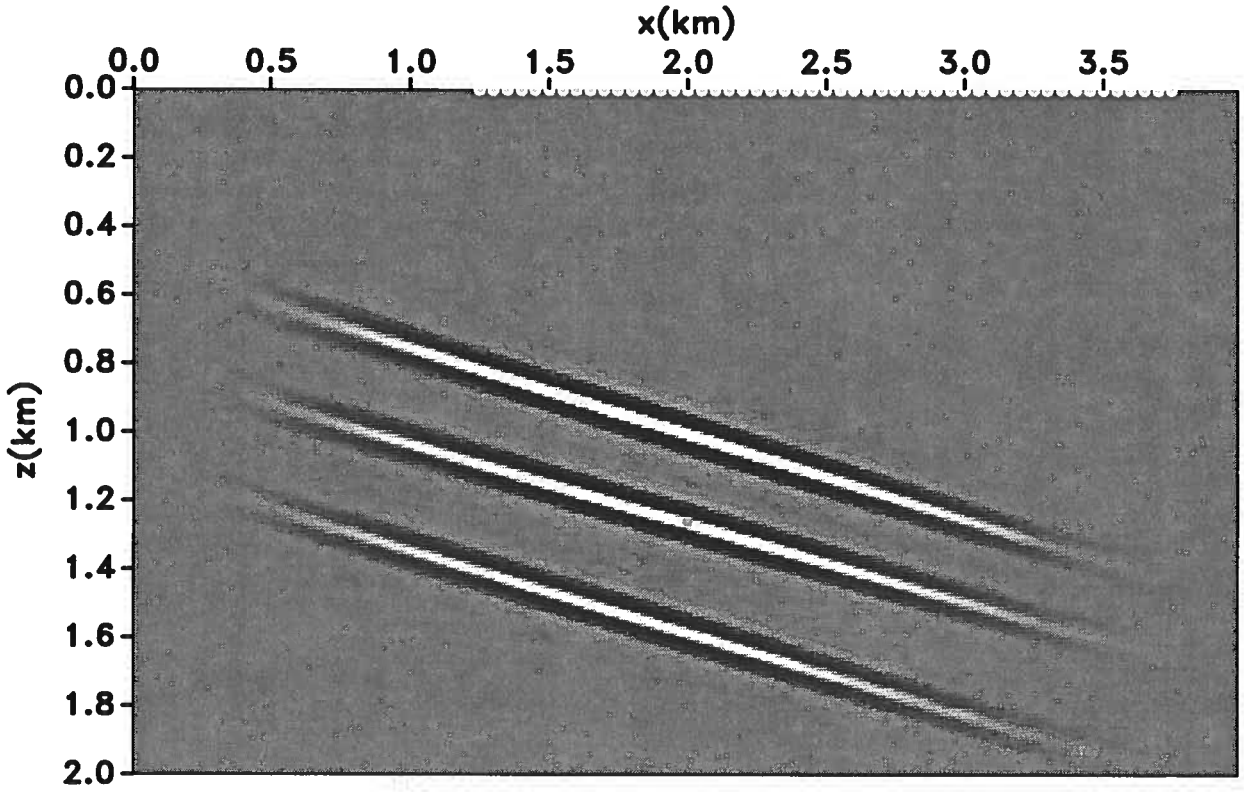

Figure 6. Synthetic example of a dipping reflector in a constant velocity model. The dot indicates the location where we construct CIPs.

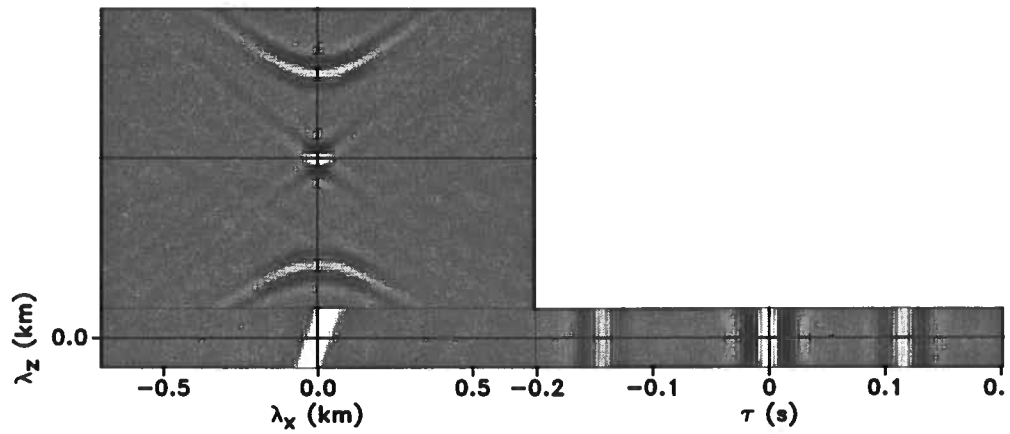

(a)

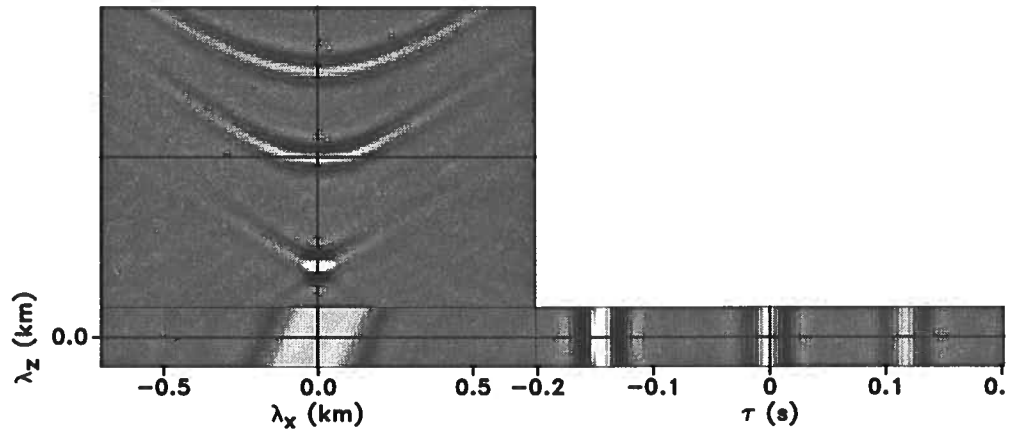

(b)

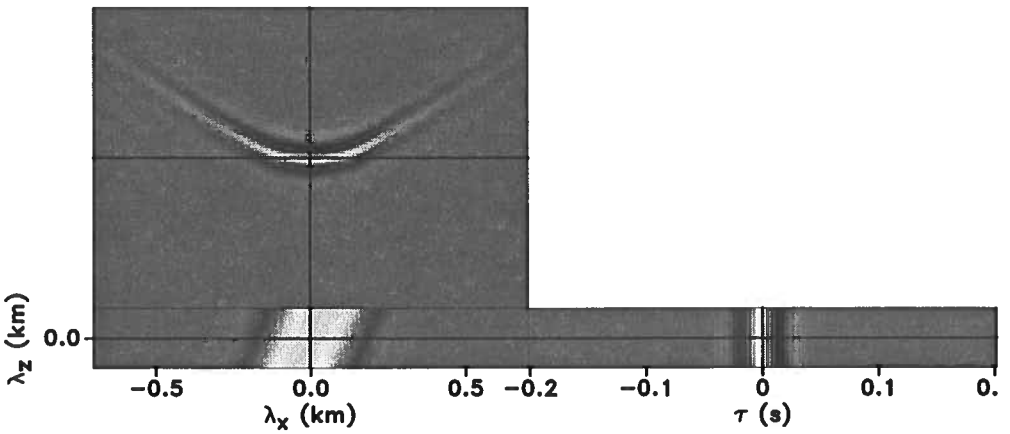

(c)

Figure 7. CIPs chosen from the middle reflector (a) for the correct velocity model. (b) for 90% of the correct velocity model. (c) after the event isolation. Notice that all the events not crossing $\tau = 0$ are eliminated.

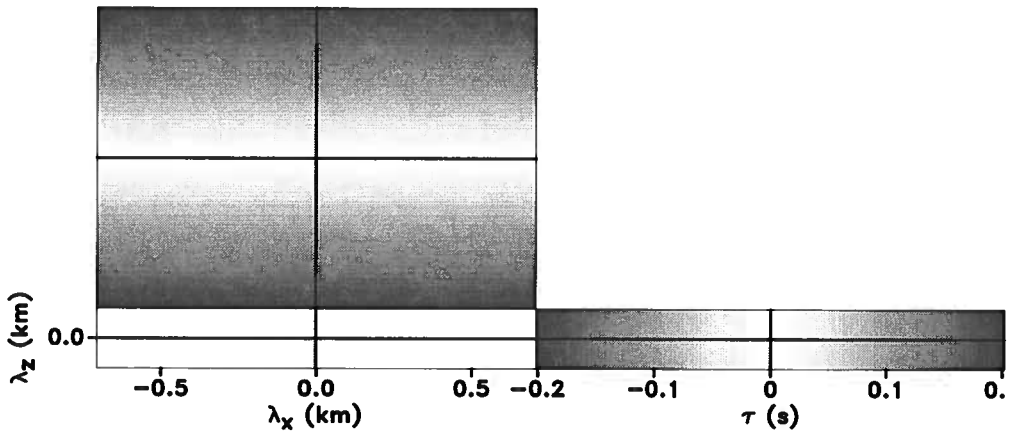

(a)

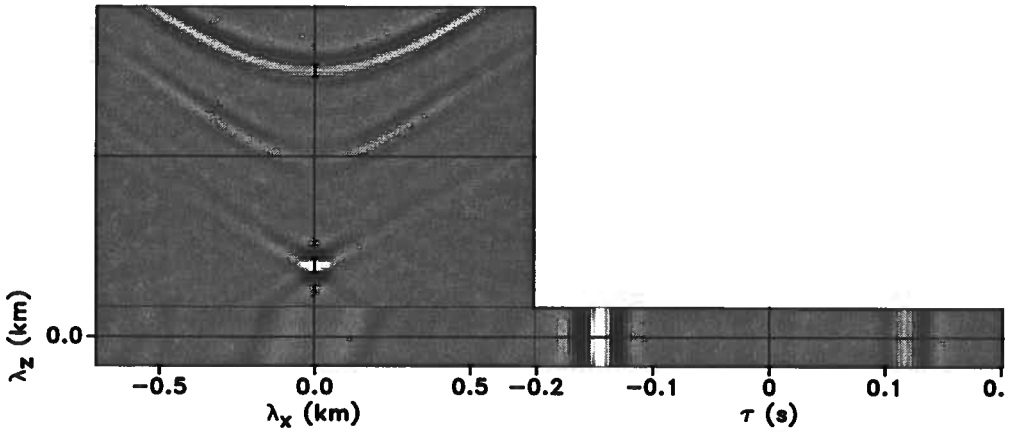

(b)

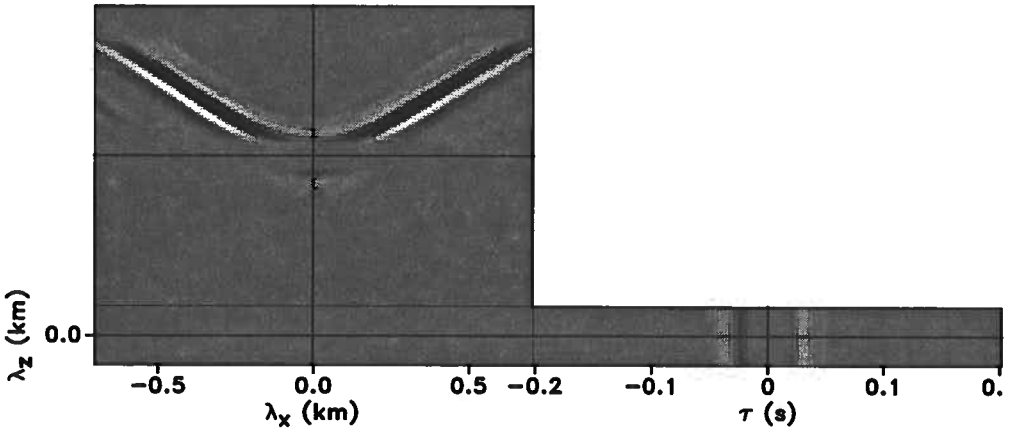

(c)

Figure 8. (a) The penalty function constructed by equation 19. (b) Penalty applied to CIPs shown in Figure 7(b) without event isolation. (c) Penalty applied to CIPs shown in Figure 7(c) with event isolation.

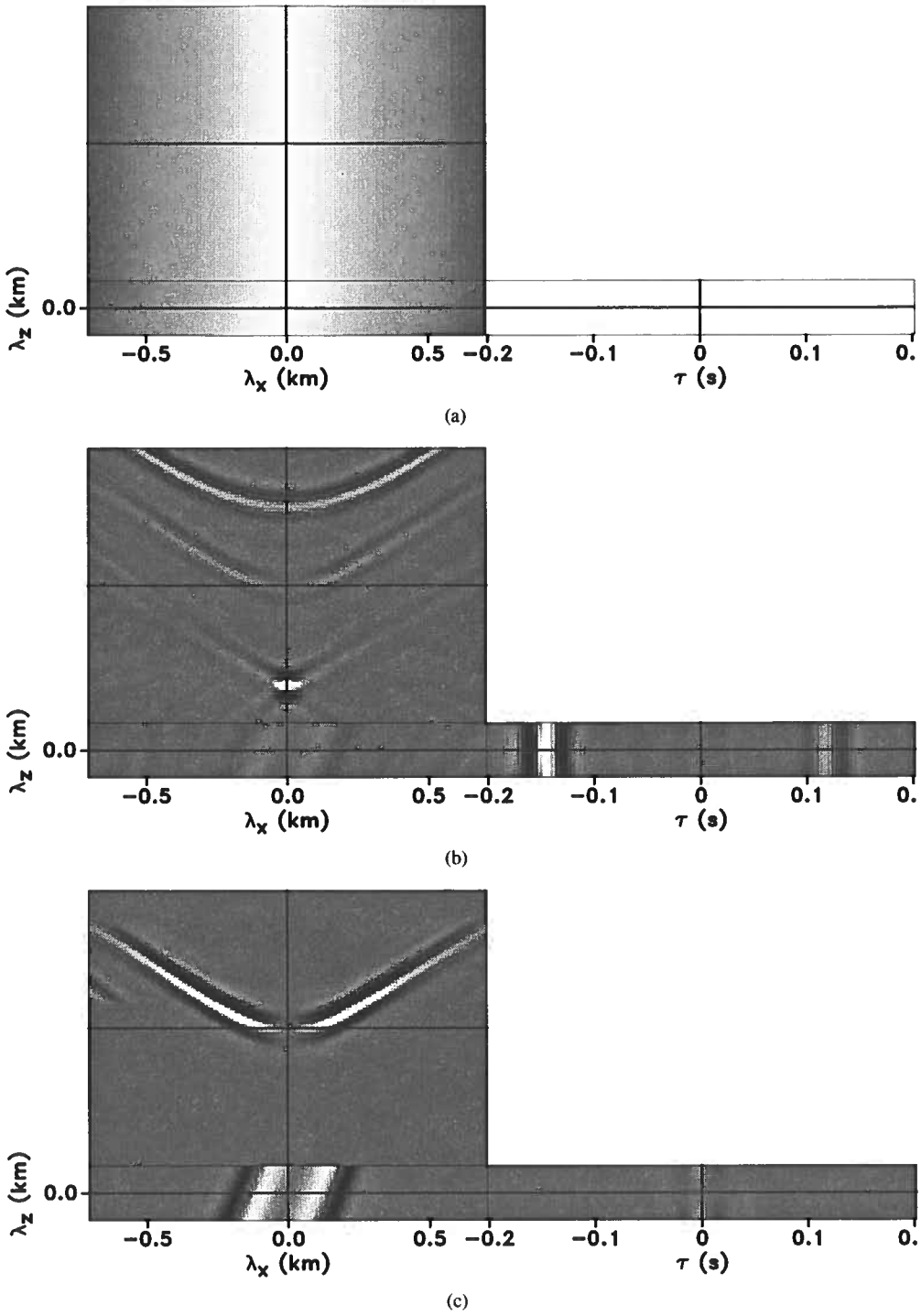

Figure 9. (a) The penalty function constructed by equation 20. (b) Penalty applied to CIPs shown in Figure 7(b) without event isolation. (c) Penalty applied to CIPs shown in Figure 7(c) with event isolation.

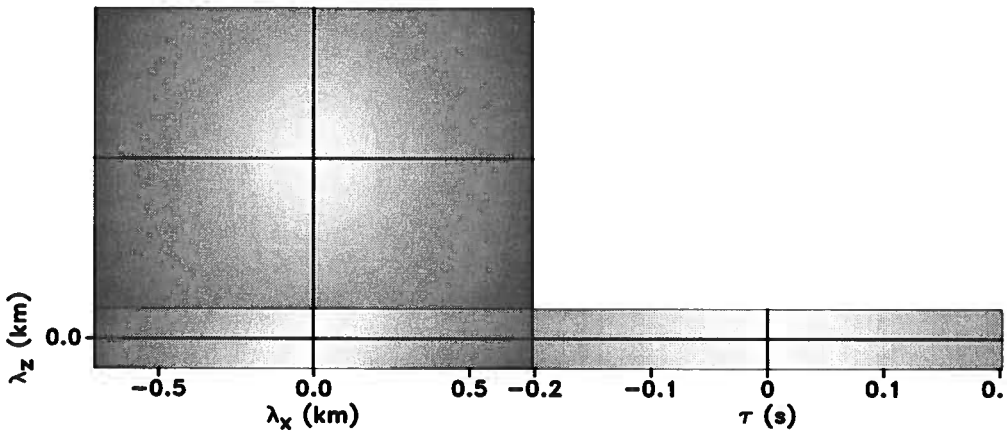

(a)

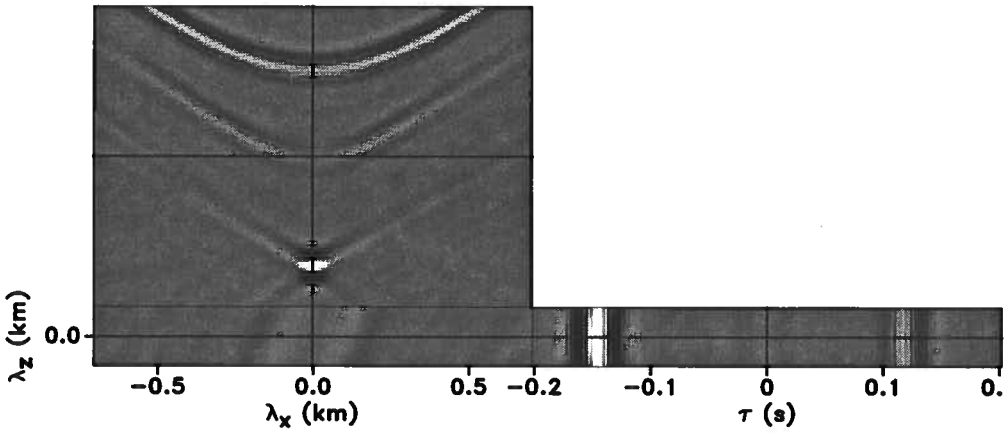

(b)

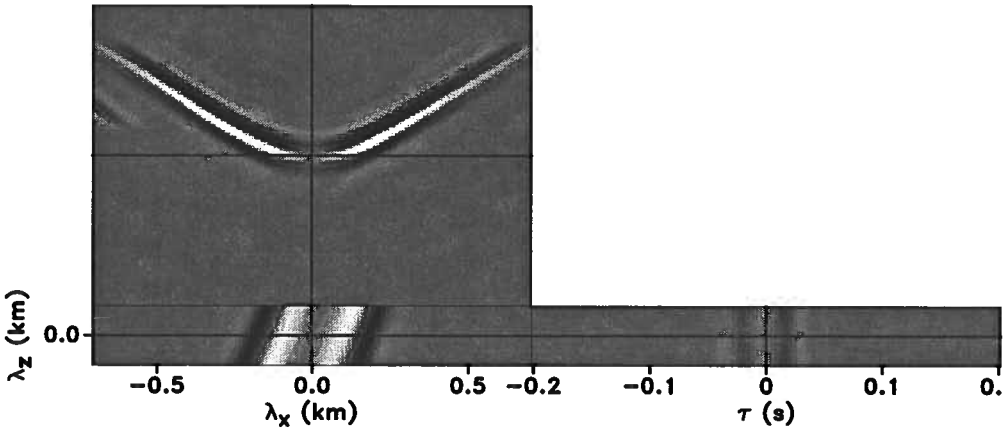

(c)

Figure 10. (a) The penalty function constructed by equation 21. (b) Penalty applied to CIPs shown in Figure 7(b) without event isolation. (c) Penalty applied to CIPs shown in Figure 7(c) with event isolation.

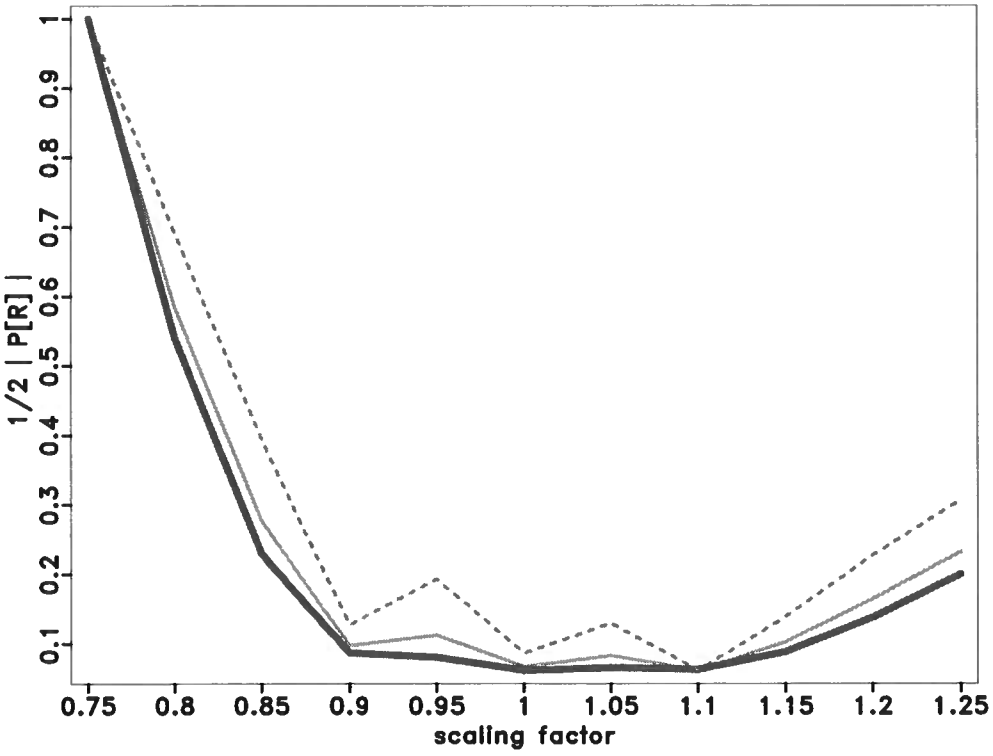

(a)

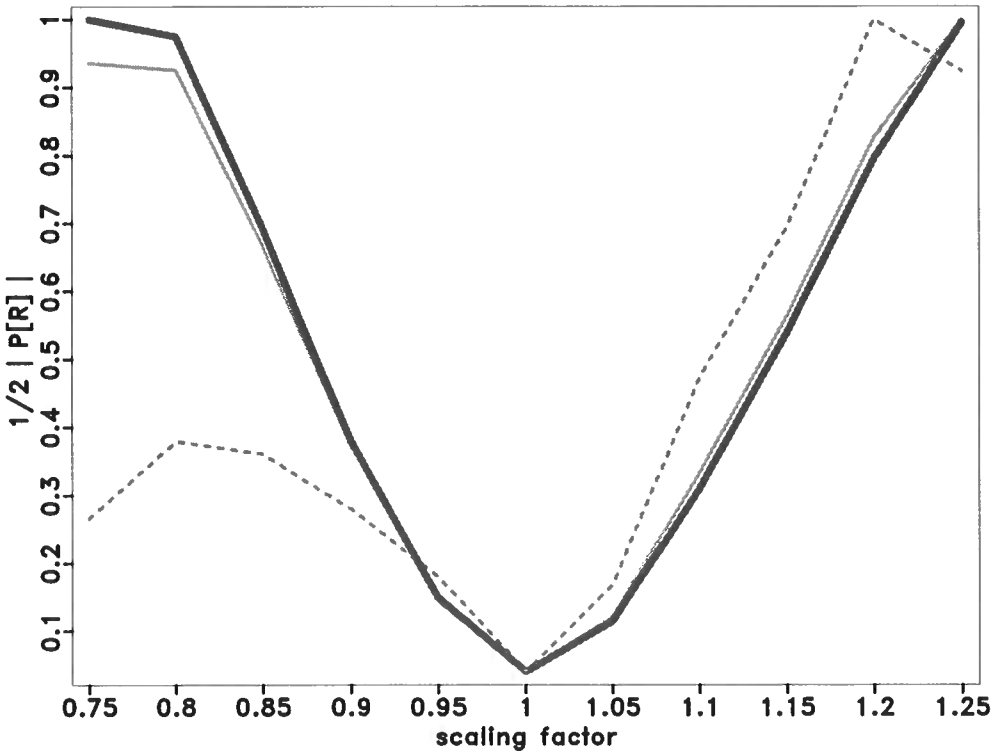

(b)

Figure 11. The plot of the objective functions. The dashed line corresponds to penalty given by equation 19, the thick solid line corresponds to penalty given by equation 20, the thin solid line corresponds to penalty given by equation 21. (a) The objective functions applied to CIPs without event isolation. The curves do not reach the unique minimum at the correct velocity. (b) The objective functions applied to CIPs with event isolation. All the curves reach the unique minimum at the correct velocity.

tion is designed using the semblance principle, and we present here three among the many possibilities. Synthetic examples demonstrate the uni-modal character of the objective function, which guarantees the convergence of inversion to a global minimum, and the smooth variation of the objective function around the minimum, which facilitate the use of gradient-type methods. The events from nearby reflections, however, must be isolated before the objective function is constructed since the penalty functions are designed only for the reflections at the location where the CIPs are constructed.

6 ACKNOWLEDGMENTS

The reproducible numeric examples in this paper use the Madagascar open-source software package freely available from http://www.reproducibility.org. We thank Thomas Cullison for support with CIPs location used in the examples.

REFERENCES

Al-Yahya, K. M., 1989, Velocity analysis by iterative profile migration: Geophysics, **54**, no. 06, 718–729.

Albertin, U., Sava, P., Etgen, J., and Maharramov, M., 2006, Adjoint wave-equation velocity analysis: 74th Annual International Meeting, SEG, Expanded Abstracts, 3009–3013.

Biondi, B., and Sava, P., 1999, Wave-equation migration velocity analysis: 69th Annual International Meeting, SEG, Expanded Abstracts, 1723–1726.

Bishop, T. N., Bube, K. P., Cutler, R. T., Langan, R. T., Love, P. L., Resnick, J. R., Shuey, R. T., Spindler, D. A., and Wyld, H. W., 1985, Tomographic determination of velocity and depth in laterally varying media: Geophysics, **50**, no. 06, 903–923.

Claerbout, J. F., 1985, Imaging the Earth's interior: , Blackwell Scientific Publications.

Etgen, J., Gray, S. H., and Zhang, Y., 2009, An overview of depth imaging in exploration geophysics: Geophysics, **74**, WCA5–WCA17.

Liu, Z., 1997, An analytical approach to migration velocity analysis: Geophysics, **62**, no. 04, 1238–1249.

Mora, P., 1988, Elastic wave-field inversion of reflection and transmission data: Geophysics, **53**, no. 06, 750–759.

Operto, S., Virieux, J., Amestoy, P., Giraud, J. I. L., and Ali, H., 2007, 3d finite-difference frequency-domain modeling of viscoacoustic wave propagation using a massively parallel direct solver: A feasibility study: Geophysics, **72**, no. 05, SM195–SM211.

Paffenholz, J., McLain, B., Zaske, J., and Keliher, P., 2002, Subsalt multiple attenuation and imaging: Observations from the sigsbee 2b synthetic dataset: 72nd Annual International Meeting, SEG, Expanded Abstracts, 2122–2125.

Pratt, R. G., 1999, Seismic waveform inversion in the frequency domain, Part 1: Theory and verification in a physical scale model: Geophysics, **64**, no. 3, 888–901.

Rickett, J., and Sava, P., 2002, Offset and angle-domain common image-point gathers for shot-profile migration: Geophysics, **67**, no. 3, 883–889.

Sava, P., and Biondi, B., 2004a, Wave-equation migration velocity analysis - I: Theory: Geophysical Prospecting, **52**, 593–606.

——— 2004b, Wave-equation migration velocity analysis - II: Subsalt imaging examples: Geophysical Prospecting, **52**, 607–623.

Sava, P., and Fomel, S., 2006, Time-shift imaging condition in seismic migration: Geophysics, **71**, no. 6, S209–S217.

Sava, P., and Vasconcelos, I., 2009, Extended common-image-point gathers for wave-equation migration: 71st Mtg., Eur. Assoc. Expl. Geophys., Abstracts.

Sava, P., and Vlad, I., 2008, Numeric implementation of wave-equation migration velocity analysis operators: Geophysics, **73**, VE145–VE159.

Sava, P., 2003, Prestack residual migration in the frequency domain: Geophysics, **67**, no. 2, 634–640.

Shen, P., and Calandra, H., 2005, One-way waveform inversion within the framework of adjoint state differential migration: 75th Annual International Meeting, SEG, Expanded Abstracts, 1709–1712.

Shen, P., and Symes, W. W., 2008, Automatic velocity analysis via shot profile migration: Geophysics, **73**, no. 05, VE49–VE59.

Shen, P., Stolk, C., and Symes, W., 2003, Automatic velocity analysis by differential semblance optimization: 73th Annual International Meeting, SEG, Expanded Abstracts, 2132–2135.

Song, Z. M., Williamson, P. R., and Pratt, R. G., 1995, Frequency-domain acoustic-wave modeling and inversion of crosshole data: Part Ii: Inversion method, synthetic experiments and real-data results: Geophysics, **60**, no. 03, 796–809.

Stork, C., 1992, Reflection tomography in the postmigrated domain: Geophysics, **57**, no. 05, 680–692.

Symes, W. W., and Carazzone, J. J., 1991, Velocity inversion by differential semblance optimization: Geophysics, **56**, no. 05, 654–663.

Symes, W. W., 2008, Migration velocity analysis and waveform inversion: Geophysical Prospecting, **56**, 765–790.

Tarantola, A., 1984, Inversion of seismic reflection data in the acoustic approximation: Geophysics, **49**, no. 08, 1259–1266.

Tarantola, A., 1987, Inverse Problem Theory: methods for data fitting and model parameter estimation: , Elsevier.

Virieux, J., and Operto, S., 2009, An overview of full-waveform inversion in exploration geophysics: Geophysics, **74**, WCC1–WCC26.

Xie, X. B., and Yang, H., 2008, The finite-frequency sensitivity kernel for migration residual moveout and its applications in migration velocity analysis: Geophysics, **73**, no. 06, S241–S249.

Yang, T., and Sava, P., 2009, Wave-equation migration velocity analysis using extended images: 79th Annual International Meeting, SEG, Expanded abstracts.

Zhou, H., 2003, Multiscale traveltime tomography: Geophysics, **68**, no. 5, 1639–1649.

Analysis of converted-wave extended images for migration velocity analysis

Jia Yan & Paul Sava

ABSTRACT

Converted-wave data have been recognized to have potential in complementing conventional compressional data. However, imaging for converted-waves is more difficult mainly due to the need for estimating shear-wave velocities, in addition to compressional-wave velocities. The common practice is to obtain the shear-wave velocity by registering PS and PP images. Despite its low cost, this procedure is prone to error due to the assumption of imaging simple structure and due to the high potential for cycle skipping. On the other hand, we could obtain S velocities by adapting wave-equation migration velocity analysis (MVA) tools for shear waves. Our assumption is that we can update the S velocities while keeping the known P velocity fixed. We assume that the P-wave velocity is known from MVA of the PP component of the data, then we estimate the S-wave velocity from MVA on the PS component of the data. If P- and S-wave velocities are all correctly estimated, corresponding PP and PS events match in the migrated depth sections. This velocity analysis can make use of both common image gathers (CIGs) and common image point gathers (CIPs). We derive the moveout function for CIPs of converted-wave images and find that they present more complicated moveout than their pure-mode counterparts. We explore the applicability of differential semblance optimization (DSO) to the PP and PS gathers (CIPs and CIGs) to obtain objective functions, based which we can construct optimal velocity models. We find that the objective functions for both PP and PS data are convex, which warrants their use for migration velocity analysis using efficient gradient-descent numerical optimization schemes.

Key words: velocity analysis, common image point gathers, coverted-waves

1 INTRODUCTION

Multicomponent data are acquired both on land and at ocean bottom because converted-waves have been recognized to have potential advantages in several aspects. Converted waves can produce better images of the Earth structure where P-waves have small reflectivity and S-waves have larger reflectivity. Converted waves also complement P-waves in imaging through zones where P-waves are highly attenuated and S-waves are less affected, e.g., gas-concentrated area. Converted-waves also provide invaluable information for lithology estimations, anisotropy parameter estimations, and reservoir characterization (Stewart et al., 2002, 2003).

Despite its usefulness, imaging with converted-waves has not gained the same popularity as imaging with acoustic waves for the following reasons. First, it is much more expensive to acquire multicomponent data than single-component data. Second, it is more difficult to pre-process converted-wave data. For example, gathering, mapping, and binning for converted-wave data are more complicated than pure-mode data due to the asymmetry of PS wave raypaths (Stewart et al., 2002; Thomsen, 1998). Third, it is more difficult to image with converted-wave data because both P- and S-wave velocities are needed. Furthermore, because of the strong influence of anisotropy on shear-waves, the isotropy assumption which cause less problems to acoustic-wave imaging is often insufficient for converted-wave data. This makes it necessary to estimate for additional model parameters, which is theoretically and computationally challenging.

Many authors, including Nicoletis et al. (1998); Kendall et al. (1998); Dai et al. (2000), investigate methods for time or depth migration using converted-wave data. The migration procedures for PP and PS data do not differ in nature, and both include two basic steps: the reconstruction of source

and receiver wavefields at all locations in the subsurface and the application of an imaging condition to extract reflectivity from the reconstructed wavefields. The main difference is that for PP data, both source and receiver wavefields are reconstructed using P-wave velocity; for PS data, source and receiver wavefields are reconstructed with P- and S-wave velocities, respectively. Herrenschmidt et al. (2001) compare various approaches for obtaining migration velocities for converted-wave imaging. They find that time migration is acceptable only when the model has little lateral velocity variation, otherwise only positive or negative offsets get flattened. They conclude that imaging PS data with a prestack depth migration approach most naturally handles complexities in the model.

One of the most difficult problems for imaging with converted-waves is to obtain correct migration models. Although it is common knowledge that prestack depth migration generates better images than time migration, the PS migration velocity is still usually obtained in the time domain, mainly due to a lower cost. The velocity estimation for shear-waves is mostly carried out by the so-called "registration" process: shear-wave velocities are estimated or tuned by correlating corresponding PP and PS reflections in the time-migrated seismic sections and stretching in time the PS section to match with the PP section using the estimated V_P/V_S ratio. Initially, the registration process involves manual picking to correlate PP and PS events (Gaiser, 1996). Later, many authors, including Ogiesoba & Stewart (2003), Fomel & Backus (2003), Nickel & Sonneland (2004), Fomel et al. (2005), and Yuan et al. (2008), develop methods to improve the automation and efficiency of the registration process. Since PP and PS data do not have the same frequency contents, usually a spectral-whitening to both components is necessary to match the PP and PS events. The registration technique has the benefit of fast performance because the operation is usually carried out in the time domain and is relatively not time-consuming. However, velocity analysis using image registration has some inherent problems. First, P- and S-waves are assumed to have similar reflectivity in a long-wavelength scale. This assumption is sometimes violated, since PP and PS waves do not necessarily respond equally to all reflectors. Second, the registration process is prone to cycle-skipping without the aid of well logs. Third, the registration process makes the assumption that there is no lateral mispositioning of the PS image (Fomel & Backus, 2003), and therefore all adjustments of shear-wave velocity are local and vertical.

An alternative for obtaining the S-wave velocities is to carry out a joint PP and PS inversion (Veire & Landrø, 2006; Margrave et al., 2001). The joint inversion technique starts with a rough estimate of V_P/V_S ratio to register corresponding PP and PS events and then inverts for the elastic parameters using approximate PP and PS reflection coefficients (amplitude versus offset (AVO) response). The main benefit of the joint inversion is that it not only estimates V_P and V_S, but also the density ρ, which is an important elastic parameter for lithology analysis. The joint inversion technique, however, also requires registering PP and PS events. Moreover, a key problem, as pointed out by Veire & Landrø (2006), is the difficulty in converting PP and PS seismic amplitudes into true reflection coefficients, especially for complex geology. In these situations, a more sophisticated analysis that converts data to true incidence/reflection angles and inverts with AVA (amplitude versus angle) is necessary (Veire & Landrø, 2006).

Most existing shear-wave velocity analysis tools require registration of PP and PS events in order to estimate the V_P/V_S ratio. This is usually difficult when pure- and converted-waves have different frequency contents, are subject to different reflection coefficients, and the wavelets of the two wave modes are inconsistent with each other. In this paper, we explore the possibility of wave-equation MVA in the depth domain for the shear-mode using converted-wave data only, i.e., we update the S velocity after P velocity analysis, while keeping the P velocity fixed. We assume that the velocity of the P-wave is known from MVA of the PP component of the data, and then we perform MVA on the PS component only. This approach is analog to the layer-stripping approach used for velocity model building for simple structures. In the layer-stripping technique, velocity estimates for the deeper layers rely on the velocity estimates for the shallow layers. This procedure, if not done correctly, introduces velocity errors to the deeper layers from errors accumulated in the shallow layers. The MVA procedure which estimates P- and S-wave velocities independently is subject to a similar problem. Although errors in the *a priori* P-wave velocity might be translated into S-wave velocity, this procedure has the benefit that we do not need to register the PS and PP events. If P- and S-wave velocities are all correctly estimated, corresponding PP and PS events should match in the depth migrated sections.

Wavefield tomography iteratively updates the model by minimizing an objective function. The objective function characterizes the data misfit and reaches its minimum when the velocity model is correct. For seismic data, one can invert for the model in the data domain using a technique commonly known as full waveform inversion (FWI) (Tarantola, 1987; Mora, 1988; Song et al., 1995; Pratt & Worthington, 1990; Pratt, 1999), or in the image domain using a technique commonly known as wave-equation migration velocity analysis (WEMVA) (Biondi & Sava, 1999; Shen et al., 2003; Albertin et al., 2006; Yang & Sava, 2009).

The objective function for WEMVA exploits the errors from extended images due to the incorrect migration velocity. Subsets of extended images can be organized as common-image gathers (CIGs) or common-image point gathers (CIPs) (Sava & Vasconcelos, 2010). The CIGs can be computed in different domains, for example, space-lag domain (Rickett & Sava, 2001), time-lag domain (Sava & Fomel, 2006), space- and time-lag domain(Yang & Sava, 2008), and angle domain (Sava & Fomel, 2003; Yan & Sava, 2008). Velocity errors are characterized by the features of the events, for example misfocusing of the events in the space-lag domain, deviation from zero time-lag in the time-lag domain, or non-flatness of the events in the angle-domain.

Sava & Vasconcelos (2010) develop the concept of CIPs and argue that computational cost for construction of CIPs decreases compared to the cost of constructing regular CIGs.

They derive the moveout function of CIP events for pure-mode and suggest their use for migration velocity analysis. In this paper, we derive the moveout of CIPs for converted-waves, discuss their features, and compare the CIPs for pure-mode and converted-mode waves. We find that compared to PP CIPs, the PS CIPs are characterized by more complicated moveout, which increases the difficulty of using them for migration velocity analysis.

We begin this paper with a review of PP and PS CIGs in the space-lag and angle domains and analyze the differences between the gathers obtained with both correct and incorrect migration velocities. We discuss the influence of the polarity reversal, which exist in both the PS data and the corresponding CIGs. Then we formulate DSO type penalty functions (Shen & Symes, 2008) for pure- and converted-mode data and show that the corresponding objective functions are convex functions suitable for numerical optimization with gradient based techniques.

2 COMMON IMAGE GATHERS

In wave-equation migration, images are obtained through two successive steps: the reconstruction of the source and receiver wavefields and the application of an imaging condition. A conventional imaging condition takes the zero-lag cross correlation of the source and receiver wavefields in both space and time to form an image. This imaging condition, however, does not carry velocity error information. An extended imaging condition is formulated as taking non-zero lags in space and time to retrieve the velocity error:

$$R(\mathbf{x},\boldsymbol{\lambda},\tau)=\sum_{\omega}\overline{W_s(\mathbf{x}+\boldsymbol{\lambda},\omega)}\,W_r(\mathbf{x}-\boldsymbol{\lambda},\omega)e^{2i\omega\tau}\,. \quad (1)$$

Here, $\mathbf{x}=\{x,y,z\}$ denotes the image point coordinates, ω is the angular frequency used to extrapolate the the source and receiver wavefield, W_s and W_r. The variables $\boldsymbol{\lambda}$ and τ are the space- and time-lags, respectively. The over-line indicates complex conjugate. The extended imaging condition provides access to information usable for migration velocity analysis.

Since using both space- and time-lags is computationally expensive, it is desirable to work on subsets of the extended images, e.g., space-lag common image gathers, time-lag common image gathers, or space-time-lag common image point gathers. These subsets of the extended images are cheaper to construct because either some of the lags are set to zero or the full lags are computed at a limited number of points distributed throughout the image.

2. 1 Space-lag-domain common image gathers

To construct common image gathers at certain desired image locations, a special case of the extended imaging condition which uses only space-lags $\boldsymbol{\lambda}=\{\lambda_x,\lambda_y,\lambda_z\}$ is often adopted:

$$R(\mathbf{x},\boldsymbol{\lambda})=\sum_{\omega}\overline{W_s(\mathbf{x}+\boldsymbol{\lambda},\omega)}\,W_r(\mathbf{x}-\boldsymbol{\lambda},\omega)\,. \quad (2)$$

This special case of extended images is often used to construct space-lag common image gathers (Rickett & Sava, 2001; Sava & Fomel, 2005a). The space-lag gathers are used for velocity analysis and indicate velocity errors by misfocusing from zero space lags.

2. 2 Angle-domain common image gathers

Angle-domain common image gathers are often constructed for migration velocity analysis (MVA) or amplitude versus angle (AVA) analysis. They can also be used for velocity analysis and indicate velocity errors by unflatness of the events. To obtain an angle-domain CIG, one needs to map the lag-domain CIG constructed by equation 2 to the angle domain. A general equation for the angle decomposition is formulated by Sava & Fomel (2005b):

$$\tan^2\theta=\frac{(1+\gamma)^2\left|\mathbf{k}_{\boldsymbol{\lambda}}\right|^2-(1-\gamma)^2\left|\mathbf{k}_{\mathbf{x}}\right|^2}{(1+\gamma)^2\left|\mathbf{k}_{\mathbf{x}}\right|^2-(1-\gamma)^2\left|\mathbf{k}_{\boldsymbol{\lambda}}\right|^2} \quad (3)$$

where γ is the velocity ratio of the source and receiver wavefields at the CIG location. The variables $\mathbf{k}_{\mathbf{x}}$ and $\mathbf{k}_{\boldsymbol{\lambda}}$ are the wave vectors for the image point coordinates $\mathbf{x}$ and space-lag vector $\boldsymbol{\lambda}$, respectively. The angle θ is half of the opening angle between the source and receiver rays. Angle gathers can be used for MVA by exploiting the fact that reflections are not flat when data are imaged with incorrect velocity.

3 COMMON IMAGE POINT GATHERS

The space-lag common image gathers use only the space lags and set the time lag to zero, thus discarding valuable information which could be used to characterize velocity errors. Therefore, it is desirable to utilize all types of lags to characterize velocity errors. A major implementation problem is that the extended images using all space- and time-lags are seven-dimensional objects, which are too computationally demanding and require large storage. To reduce the storage and computational cost, Sava & Vasconcelos (2010) introduce the concept of common-image-point gathers (CIPs), which are simply subsets of the extended images constructed at sparse locations in the subsurface. The construction of the CIPs allows us to extend the images to all space and time lags, while reducing the overall computation cost compared to regular CIGs.

In this section, we derive the moveout equation for common image point (CIP) gathers for converted-waves, assuming imaging with both a single shot and multiple shots. The moveout functions offer insight into the expected behavior of such CIPs in areas of complex velocity variations (Sava & Vasconcelos, 2010) and form the basis for the definition of an objective function used for migration velocity analysis.

3. 1 CIP moveout for imaging with a single shot

We use Figure 1 to illustrate the notations adopted in our derivation. In this schematic, the vector $\mathbf{q}$ denotes the direction along which the reflector and the reflection plane inter-

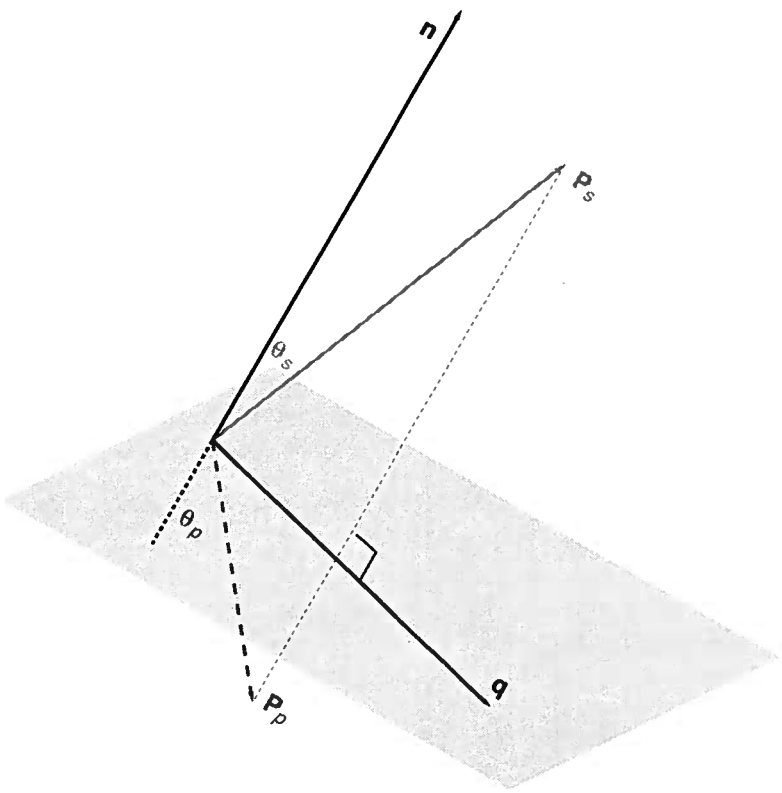

Figure 1. Schematic illustrating a P to S reflection upon a reflector. The reflection plane and the reflector intersect a line defined by the vector $\mathbf{q}$. The reflector has a normal defined by the vector $\mathbf{n}$. The source and receiver rays are characterized by the vectors $\mathbf{p}_p$ and $\mathbf{p}_s$, respectively. The incidence and reflection angles are denoted by θ_p and θ_s, respectively.

sect, and the vector $\mathbf{n}$ denotes the reflector normal. For a P-wave ray vector $\mathbf{p}_p$ incident upon the reflector at an angle θ_p, the S-wave ray $\mathbf{p}_s$ is reflected at an angle θ_s. The incidence and reflection angles are related by the Snell's law:

$$\frac{\sin\theta_p}{v_p} = \frac{\sin\theta_s}{v_s}\,, \tag{4}$$

where v_p and v_s are the P- and S-wave velocities, respectively. The Snell's law simply states that the slowness along the reflector is preserved regardless of the reflector dip. We can express the source and receiver ray vectors as:

$$\mathbf{p}_p = \frac{\mathbf{n}_p}{v_p}\,, \tag{5}$$

$$\mathbf{p}_s = \frac{\mathbf{n}_s}{v_s}\,, \tag{6}$$

where $\mathbf{n}_p$ and $\mathbf{n}_s$ are unit vectors along the source and receiver rays, respectively.

We begin with the conventional imaging condition for P to S reflection. For a subsurface image point $\mathbf{x}$, the conventional imaging condition can be expressed as the intersection of two planes given by the expressions

$$\mathbf{p}_p \cdot \mathbf{x} = 0\,, \tag{7}$$

$$\mathbf{p}_s \cdot \mathbf{x} = 0\,. \tag{8}$$

These relations assume that we take the origin of the space-time coordinate system at the image point $\mathbf{x}$. Equations 7 and 8 represent P and S plane wave-fronts and they intersect at the image point $\mathbf{x}$. This is not a restrictive assumption, but simply indicates that we use relative space-time coordinates. The extended imaging condition shifts the source and receiver planes in space by the space-lag $\boldsymbol{\lambda}$ in the positive and negative directions, respectively, and in time by τ_p and τ_s, respectively:

$$\mathbf{p}_p \cdot (\mathbf{x} - \boldsymbol{\lambda}) = -\tau_p\,, \tag{9}$$

$$\mathbf{p}_s \cdot (\mathbf{x} + \boldsymbol{\lambda}) = +\tau_s\,. \tag{10}$$

Combining equations 7 to 10 leads to the equations:

$$\mathbf{p}_p \cdot \boldsymbol{\lambda} = \tau_p\,, \tag{11}$$

$$\mathbf{p}_s \cdot \boldsymbol{\lambda} = \tau_s\,. \tag{12}$$

Since the source and receiver wavefields have a time separation 2τ (the total time shift in equation 1), we have $\tau_p + \tau_s =$

2τ. Summing the expressions 11 and 12, we obtain:

$$(\mathbf{p}_p + \mathbf{p}_s) \cdot \boldsymbol{\lambda} = 2\tau\,. \tag{13}$$

We can also express the vectors $\mathbf{p}_p$ and $\mathbf{p}_s$ using the geometric relations between the vectors $\mathbf{n}$ and $\mathbf{q}$ and angles θ_p and θ_s as:

$$\mathbf{p}_p = \frac{\sin\theta_p}{v_p}\mathbf{q} - \frac{\cos\theta_p}{v_p}\mathbf{n}\,, \tag{14}$$

$$\mathbf{p}_s = \frac{\sin\theta_s}{v_s}\mathbf{q} + \frac{\cos\theta_s}{v_s}\mathbf{n}\,. \tag{15}$$

These two equations relate the source and receiver ray vectors with the reflector orientation and incidence/reflection angles. Substitution of $v_p = v$ and $v_s = v/\gamma$, together with the Snell's law from equation 4, into equations 14 and 15 yields

$$\mathbf{p}_p + \mathbf{p}_s = 2\frac{\sin\theta}{v}\mathbf{q} + \frac{\left[\sqrt{\gamma^2 - \sin^2\theta} - \cos\theta\right]}{v}\mathbf{n}\,, \tag{16}$$

where the angle θ denotes the incidence angle θ_p, and the variable γ is the ratio between the P- and S-wave velocities. Substituting expression 16 into equation 13, we obtain the moveout equation for PS reflections at an incidence angle θ:

$$\sin\theta\,(\mathbf{q}\cdot\boldsymbol{\lambda}) + \frac{1}{2}\left[\sqrt{\gamma^2 - \sin^2\theta} - \cos\theta\right](\mathbf{n}\cdot\boldsymbol{\lambda}) = v\tau\,, \tag{17}$$

where v and θ are the P-wave velocity and incidence angle, respectively.

For the special case of PP reflections, where $\gamma = 1$, equation 17 reduces to

$$\sin\theta\,(\mathbf{q}\cdot\boldsymbol{\lambda}) = v\tau\,, \tag{18}$$

which is the relation described by Sava & Vasconcelos (2010). Equation 17 describes the moveout function characterizing a reflection from a single shot-receiver pair. The function represents a plane in the $\{\boldsymbol{\lambda}, \tau\}$ space which depends on the incidence angle, the P-wave velocity, the V_P/V_S ratio, and the reflector defined by the vectors $\mathbf{q}$ and $\mathbf{n}$.

To confirm the validity of equation 17, we overlay this function on a CIP reflection shown in Figure 3 for a horizontal reflector (Figure 2) and in Figure 5 for a dipping reflector (Figure 4). In Figures 2 and 4, the dots on the surface at $x = 3.1$ km represent the sources and the lines on the surface represent the receivers. The dots on the reflectors indicate the CIP locations. For both experiments, panels (a) and (b) show the PP and PS reflections as a function of $\boldsymbol{\lambda}$ and τ, respectively. The lines overlaid on top of these subplots indicate that equation 17 accurately predicts the CIP moveout.

3.2 CIP moveout for imaging with multiple shots

The CIP moveout for multiple shots can be analyzed as the stack of single-shot CIPs constructed for different angles of incidence. In the following, we define a new variable $\lambda_\tau = v\tau$ to ensure that all axes have the same dimensionality, i.e. space. Thus, the moveout function for a single shot can also be written as

$$\sin\theta\,(\mathbf{q}\cdot\boldsymbol{\lambda}) + \frac{1}{2}\left[\sqrt{\gamma^2 - \sin^2\theta} - \cos\theta\right](\mathbf{n}\cdot\boldsymbol{\lambda}) = \lambda_\tau\,. \tag{19}$$

In the following, we consider the reflection geometries in the reflection plane, thus setting the y component of all vectors to zero. Since the vector $\mathbf{q}$ at the intersection of the reflection plane and the reflector and the reflector normal vector $\mathbf{n}$ are orthogonal, we can write $\mathbf{q} = \{q_x, q_z\}$ and $\mathbf{n} = \{-q_z, q_x\}$. With the substitution of the $\mathbf{q}$ and $\mathbf{n}$ components into equation 19, we can write

$$(Aq_x - Bq_z)\,\lambda_x + (Aq_z + Bq_x)\,\lambda_z - \lambda_\tau = 0\,, \tag{20}$$

where

$$A = \sin\theta \tag{21}$$

and

$$B = \frac{1}{2}\left[\sqrt{\gamma^2 - \sin^2\theta} - \cos\theta\right]. \tag{22}$$

Equation 20 states that the CIP moveout for a single shot is represented by a plane that passes through the origin of the lag space $\{\boldsymbol{\lambda}, \tau\}$ and is characterized by the vector normal $\mathbf{v} = \{Aq_x - Bq_z, Aq_z + Bq_x, -1\}$. When we consider multiple shots, the CIP moveout can be measured on the superposition of all single-shot CIP reflection planes for various angles of incidence θ. Let us consider reflections from two nearby shots whose vector normals are $\mathbf{v}_1$ and $\mathbf{v}_2$, respectively. When the incidence angle changes from θ to $\theta + d\theta$, the two CIP reflection planes from neighbouring shots intersect along a line. The cross product of the two vector normals $\mathbf{v}_1$ and $\mathbf{v}_2$ gives a vector $\mathbf{V}$, which is parallel to the intersection line. Since both planes pass through the origin, the intersection line also passes through the origin. Thus, we can simply use the vector $\mathbf{V}$ originating at the origin to represent the intersection line of two neighbouring CIP reflection planes. The moveout surface for a CIP gather is the ensemble of the intersection lines for all possible incidence angles.

To derive the intersection line formula for two adjacent CIP reflection planes, we begin by explicitly writing the vector normals of the planes from two neighbouring shots:

$$\mathbf{v}_1 = \begin{pmatrix} A_1 q_x - B_1 q_z \\ A_1 q_z + B_1 q_x \\ -1 \end{pmatrix}, \tag{23}$$

$$\mathbf{v}_2 = \begin{pmatrix} A_2 q_x - B_2 q_z \\ A_2 q_z + B_2 q_x \\ -1 \end{pmatrix}, \tag{24}$$

where

$$A_1 = \sin(\theta)\,, \tag{25}$$

$$A_2 = \sin(\theta + d\theta)\,, \tag{26}$$

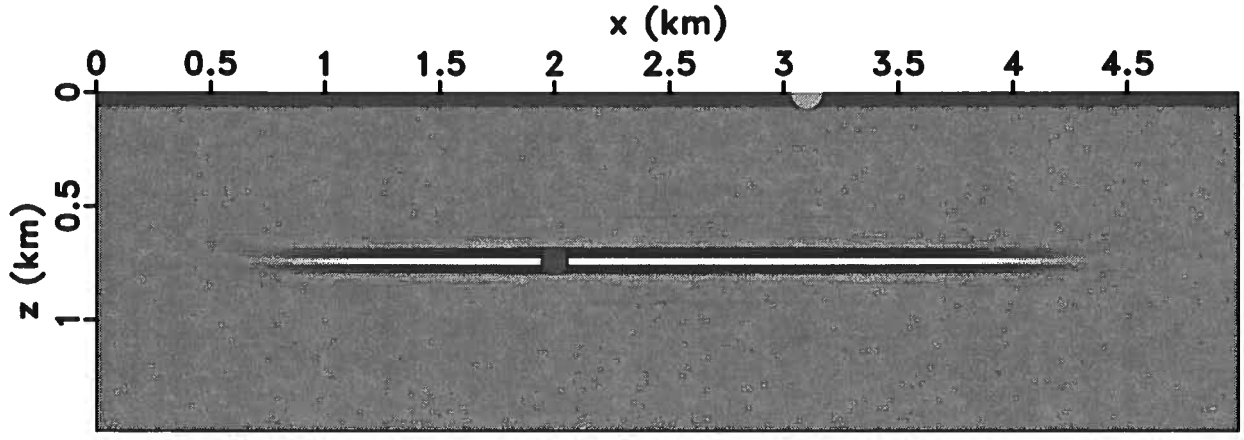

Figure 2. The experiment geometry used to construct the CIP gathers in Figure 3. The dot on the surface represents the shot location, the line on the surface represents the receivers, and the dot on the reflector represents the CIP location.

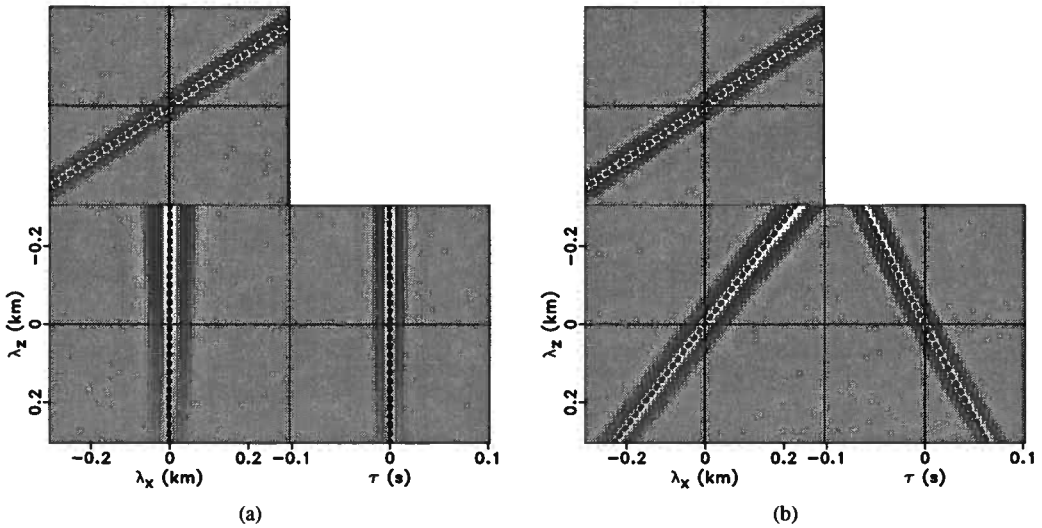

Figure 3. A common image point reflection for (a) PP data and (b) PS data for the experiment shown in Figure 2. The overlain dashed line is given by equation 17 and matches exactly with the CIP reflection moveout.

and

$$B_1 = \frac{1}{2}\left[\sqrt{\gamma^2 - \sin^2\theta} - \cos\theta\right], \quad (27)$$

$$B_2 = \frac{1}{2}\left[\sqrt{\gamma^2 - \sin^2(\theta + d\theta)} - \cos(\theta + d\theta)\right] \quad (28)$$

For a reflector with a dip angle α, the reflector vector $\mathbf{q}$ has components $q_x = \cos\alpha$ and $q_z = -\sin\alpha$. The intersection line, i.e. the cross product of $\mathbf{v}_1$ and $\mathbf{v}_2$, is

$$\mathbf{V} = \begin{pmatrix} \lambda_x \\ \lambda_z \\ \lambda_\tau \end{pmatrix} = d\theta \cos\theta \begin{pmatrix} \frac{1}{2}\tan\theta\left(1 - \frac{\cos\theta}{\sqrt{\gamma^2 - \sin^2\theta}}\right)\cos\alpha + \sin\alpha \\ \frac{1}{2}\tan\theta\left(1 - \frac{\cos\theta}{\sqrt{\gamma^2 - \sin^2\theta}}\right)\sin\alpha - \cos\alpha \\ \frac{1}{2\cos\theta}\left(1 - \frac{\gamma^2\cos\theta}{\sqrt{\gamma^2 - \sin^2\theta}}\right) \end{pmatrix}. \quad (29)$$

By neglecting the quadratic terms $(d\theta)^2$ in the cross product of $\mathbf{v}_1$ and $\mathbf{v}_2$, we assume that the increment of the incidence angle for two nearby shots is small.

By scaling the vector $\mathbf{V}$ by an arbitrary quantity r, we

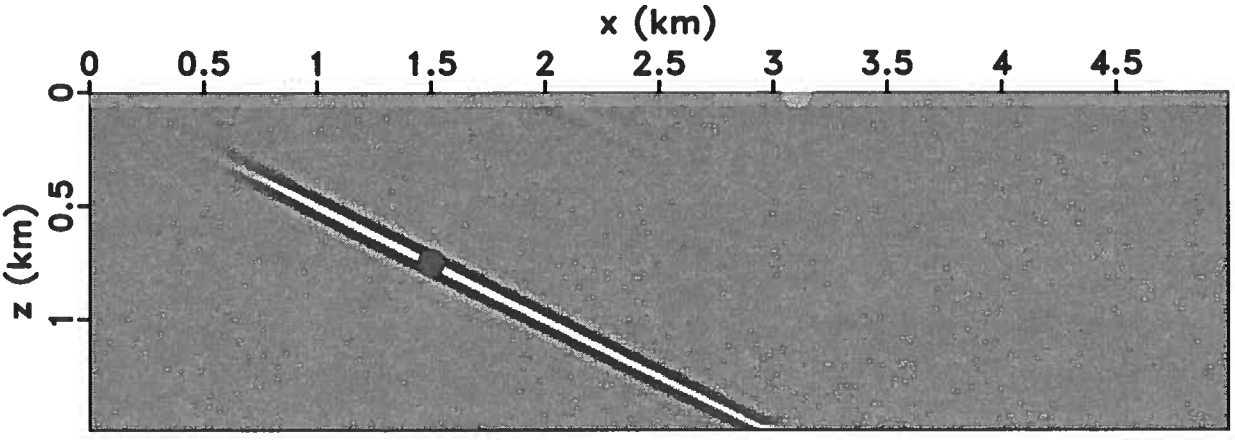

Figure 4. The experiment geometry used to construct the CIP gathers in Figure 5. The dot on the surface represents the shot location, the line on the surface represents the receivers, and the dot on the reflector represents the CIP location.

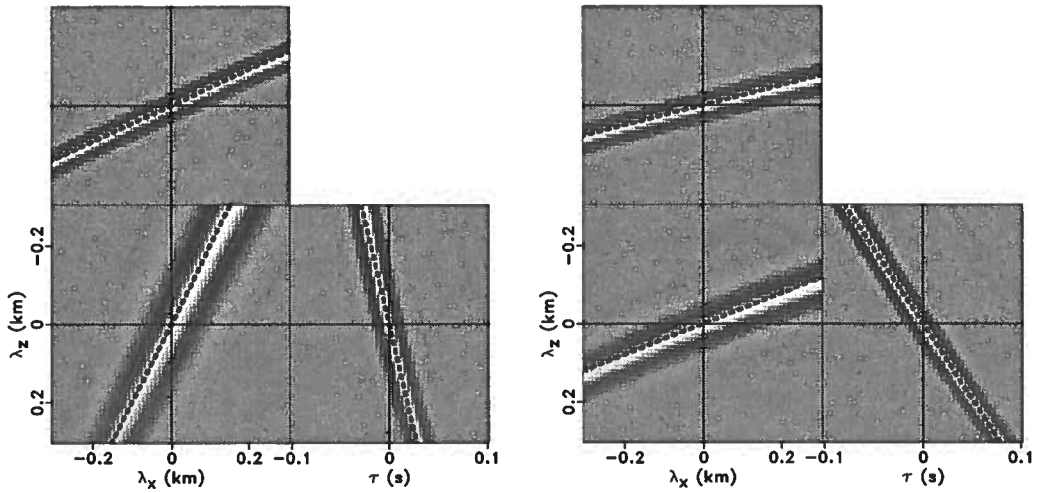

Figure 5. A common image point reflection for (a) PP data and (b) PS data for the experiment shown in Figure 4. The overlain dashed line is given by equation 17 and matches exactly with the CIP reflection moveout.

obtain the parametric form of the PS CIP surface

$$\begin{aligned} & CIP_{PS}(r,\theta,\alpha,\gamma) \\ = \; & r \begin{pmatrix} \frac{1}{2}\tan\theta\left(1-\frac{\cos\theta}{\sqrt{\gamma^2-\sin^2\theta}}\right)\cos\alpha+\sin\alpha \\ \frac{1}{2}\tan\theta\left(1-\frac{\cos\theta}{\sqrt{\gamma^2-\sin^2\theta}}\right)\sin\alpha-\cos\alpha \\ \frac{1}{2\cos\theta}\left(1-\frac{\gamma^2\cos\theta}{\sqrt{\gamma^2-\sin^2\theta}}\right) \end{pmatrix} \end{aligned} \tag{30}$$

where r can take positive and negative values. The surface reduces to the simple form

$$CIP_{PP}(r,\theta,\alpha,\gamma=1) = r\begin{pmatrix} \sin\alpha \\ -\cos\alpha \\ 0 \end{pmatrix} \tag{31}$$

for pure-mode waves.

For a horizontal reflector, the CIP surface simplifies to

$$\begin{aligned} & CIP_{PS}(R,\theta,\alpha=0,\gamma) \\ = \; & r \begin{pmatrix} \frac{1}{2}\tan\theta\left(1-\frac{\cos\theta}{\sqrt{\gamma^2-\sin^2\theta}}\right) \\ -1 \\ \frac{1}{2\cos\theta}\left(1-\frac{\gamma^2\cos\theta}{\sqrt{\gamma^2-\sin^2\theta}}\right) \end{pmatrix}, \end{aligned} \tag{32}$$

by setting the reflector dip α to zero. The surface reduces to the simple form

$$CIP_{PP}(r,\theta,\alpha=0,\gamma=1) = r\begin{pmatrix} 0 \\ -1 \\ 0 \end{pmatrix} \tag{33}$$

for pure-mode waves.

We see that the CIP surfaces for a non-zero dip reflector

and for a zero-dip reflector are related by a rotation with angle α:

$$CIP_{PS}(r,\theta,\alpha,\gamma) = \begin{pmatrix} \cos\alpha & -\sin\alpha & 0 \\ \sin\alpha & \cos\alpha & 0 \\ 0 & 0 & 1 \end{pmatrix} CIP_{PS}(r,\theta,\alpha=0,\gamma). \tag{34}$$

Therefore, the CIP surface for a dipping reflector is simply a rotation about the τ axis from CIP surface for a horizontal reflector. This conclusion is valid for both PP and PS reflections. As will be discussed later, the CIP moveout equations for correct migration velocities allow us to formulate penalty functions for migration velocity analysis.

Figure 6 shows PP and PS reflections CIPs for a horizontal reflector. We plot the CIP reflection planes for all possible incidence angles and construct the intersections of these planes. In Figures 6(c) and (d), we plot the CIP line and surface for PP and PS reflections given by equations 33 and 32, respectively. The PS CIP is a smooth surface symmetric about the $\lambda_x = 0$ plane and reduces to a line along the λ_z axis for pure-mode reflections.

4 CIG AND CIP EXAMPLES

We demonstrate the CIGs and CIPs using two models: one with a horizontal reflector and the other with a dipping reflector. The moveout of the common image gathers and common image point gathers, and especially the difference of the gathers obtained with correct and incorrect velocities, give us clues about how to formulate penalty functions for migration velocity analysis. We discuss this topic in a following section.

4.1 Horizontal reflector

In this example, we use a model with a single horizontal reflector to show the migrated images (Figure 7), space-lag domain CIGs (Figure 8), angle-domain CIGs (Figure 9), and common-image-point gathers (Figure 10), for PP and PS waves. All the images and CIGs are migrated with low, correct, and high velocities. The PS images and gathers are obtained using correct P-wave velocities, but correct or incorrect S-wave velocities. The correct P- and S-wave velocities are 3 km/s and 1.5 km/s, respectively. The low and high P-wave velocities are 2.7 km/s and 3.3 km/s, respectively, and the low and high S-wave velocities are 1.1 km/s and 1.9 km/s, respectively.

The space-lag CIGs displayed in Figure 8 are located at horizontal position $x = 2.5$ km of the model. The gathers for PP waves are all symmetric because of the lateral homogeneity of the P-wave velocity and the symmetric illumination from both sides of the CIG. The gathers for PS waves are anti-symmetric because of the polarity flip in the PS data. Compared to their PP gather counterparts, PS gathers migrated with incorrect velocities have larger curvature, i.e., they cover a smaller range of space lag λ_x in the CIGs. The radius of the CIG moveout can be predicted by the equation $R = \frac{(1-\rho^2)d}{\rho\cos\alpha}$ for homogeneous models (Yang & Sava, 2008), where d is the reflector depth, α is the reflector dip, and ρ is the ratio between the migration velocity and the real velocity. Given the same migration velocity ratio ρ for PP and PS migrations, since only the S velocity is incorrect, the effective ρ for PS data takes a smaller absolute value than that for PP data. Thus, the moveout radius R for PS data is smaller than PP data and covers a the smaller range of λ_x in the CIGs.

The angle-domain CIGs migrated with correct velocities for PP data (Figure 9(b)) and PS data (Figure 9(e)) are flat and positioned at the correct depth of the reflector. When migrated with incorrect velocity, the CIGs are non-flat and at incorrect depth. The PP gathers have continuous polarity, while the PS gathers have reversed polarity at normal incidence. The PS angle-domain CIGs show less moveout than their PP counterparts, resulted from the larger curvature in the lag-domain PS CIGs. This fact indicates that the velocity error observed on the PS image is smaller than that observed on the PP image, due to the fact that we have assumed correct P imaging velocity. In this experiment, although the shear-wave velocity errors reach $(1.5-1.1)/1.1 \approx 36\%$ (Figure 9(d)) or $(1.9-1.5)/1.5 \approx 23\%$ (Figure 9(f)), the shear-wave legs take a small fraction of the entire raypaths because the S-legs have small reflection angles. As expected, the CIGs are less sensitive to the shear-wave velocity error, because the P-wave velocity is assumed correct.

Figure 10 presents the common image point gathers for PP (panels (a), (b), and (c)) and PS data (panels (d), (e), and (f)). The CIP location is indicated by the dot on the reflector, shown in Figure 2. A total number of 61 shots from $x = 1$ km to $x = 4$ km are used for this experiment. For the correct migration velocities, the CIPs for both PP and PS data are correctly predicted by equation 32 in the previous section: the PP CIP is characterized by a line along the λ_z axis, and the PS CIP is characterized by a surface symmetric about the τ axis. For incorrect migration velocities, the CIPs deviate from this shape, which warrants their use for migration velocity analysis.

4.2 Dipping reflector

In this second example, we use a model with a single dipping reflector. Figures 11, 12, 13 and 14 show PP and PS migrated images, space-lag CIGs, angle-domain CIGs, CIPs, respectively. The P- and S-velocity models are the same as for the preceding example, and all the images and CIGs are imaged with the same range of velocities as in the preceding example.

The space-lag CIGs at lateral position $x = 1.6$ km, shown in Figure 12, present similar features as the CIGs for horizontal reflector in the previous example. A major difference for the PS CIGs is that when incorrect S-wave migration velocity is used, the polarity flip does not occur at zero-lag. Instead, the location of the polarity flip is related to the dip of the model. This is because when incorrect migration velocities are used, the back propagated wavefields are not located at the correct reflector positions.

The angle-domain CIGs also show similar features as the

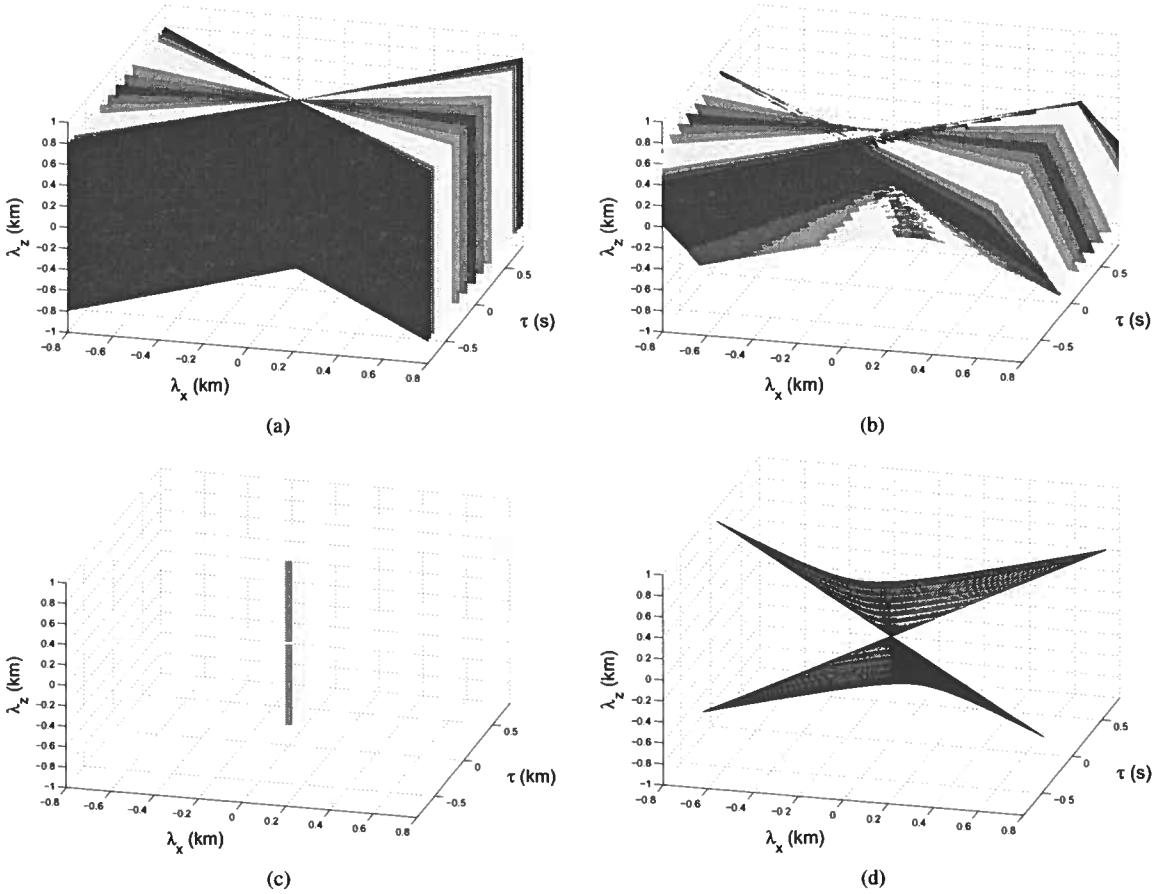

Figure 6. Common image point gather moveout for (a) PP reflection and (b) PS reflection ($\gamma = 2$). The planes in panels (a) and (b) represent reflections from individual shots. The PP reflections insect a line along λ_z axis; the PS reflections intersect a surface. Panels (c) and (d) represent the CIP line and surface predicted by the moveout equations 33 and 32, respectively.

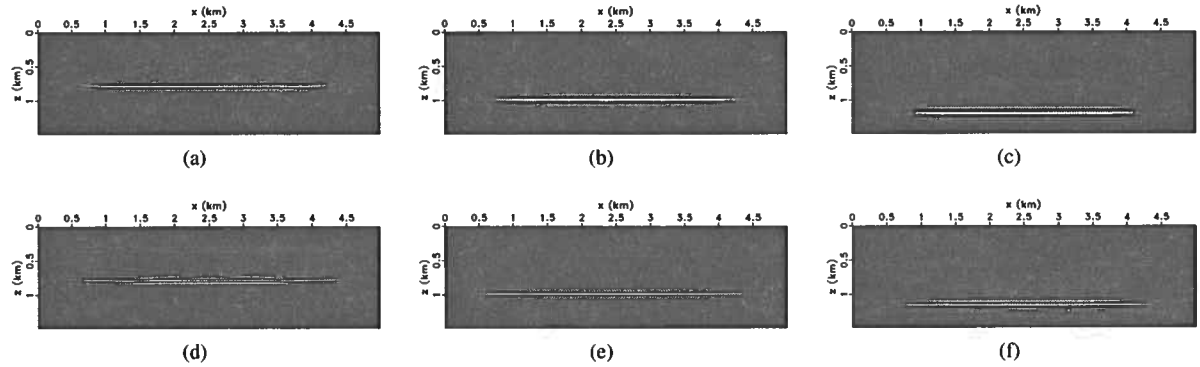

Figure 7. Migrated images for PP (upper row) and PS (lower row) data for a model with a horizontal reflector at depth $z = 1.0$ km (the same model shown in Figure 2). The images are migrated using low (left column), correct (middle column), and high (right column) velocities.

ones for horizontal reflector. When correct migration velocities are used, the gathers are flat and located at the correct reflector depth; the PP CIG has continuous polarity, and PS CIG has a polarity flip at zero incidence angle. When incorrect velocities are used for migration, the polarity flip does not occur at zero incidence angle, but at an angle related to the dip of the model. Nevertheless, the main features for the CIGs persist when correct migration velocities are used.

Figure 14 shows the CIPs for a dipping reflector. the CIP location is indicated by the dot on the reflector, shown in Fig-

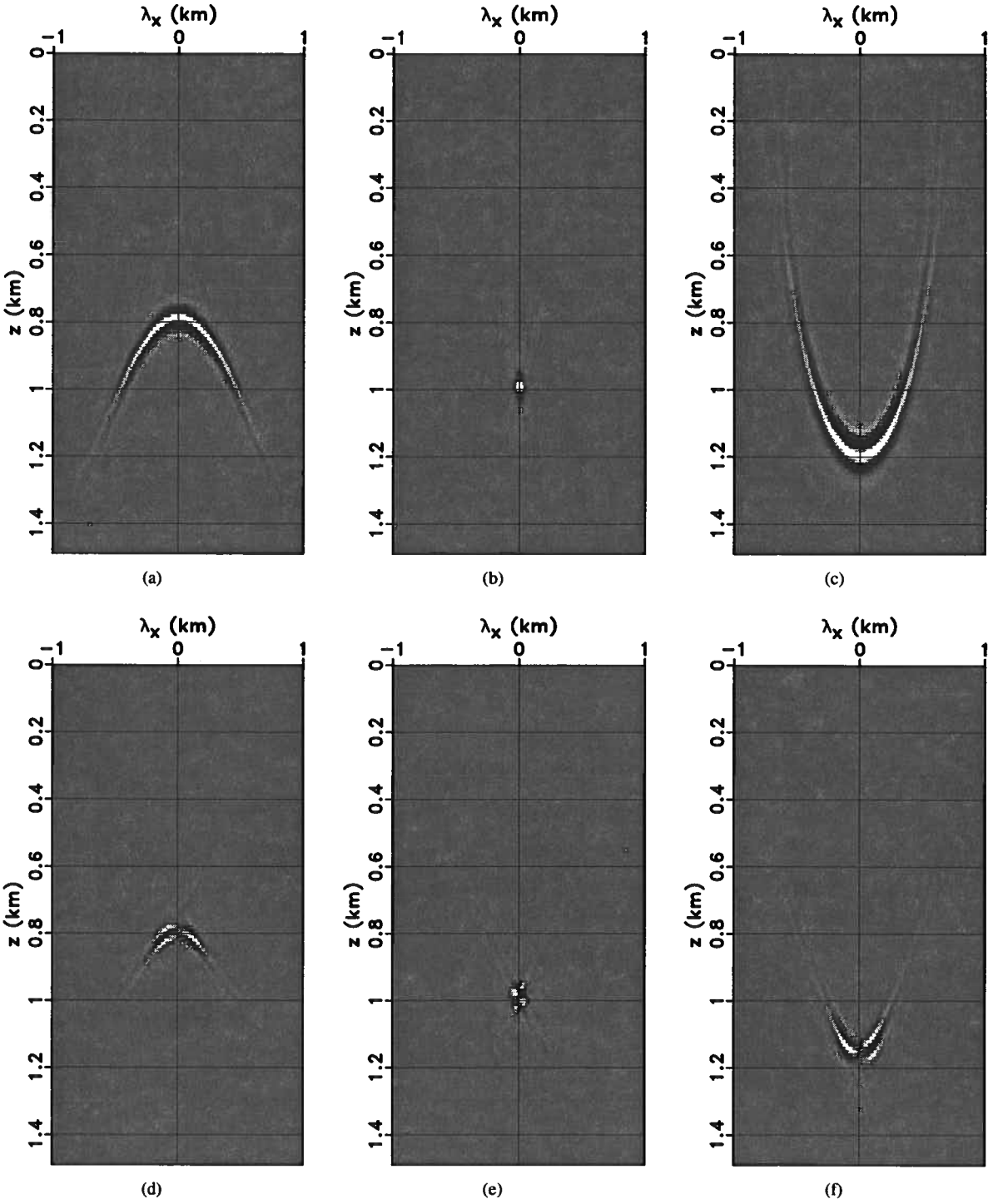

Figure 8. Space-lag CIGs for PP (upper row) and PS (lower row) data. The gathers are constructed using the extended imaging condition given by equation 2. From left to right, the gathers are constructed using low, correct, and high velocities.

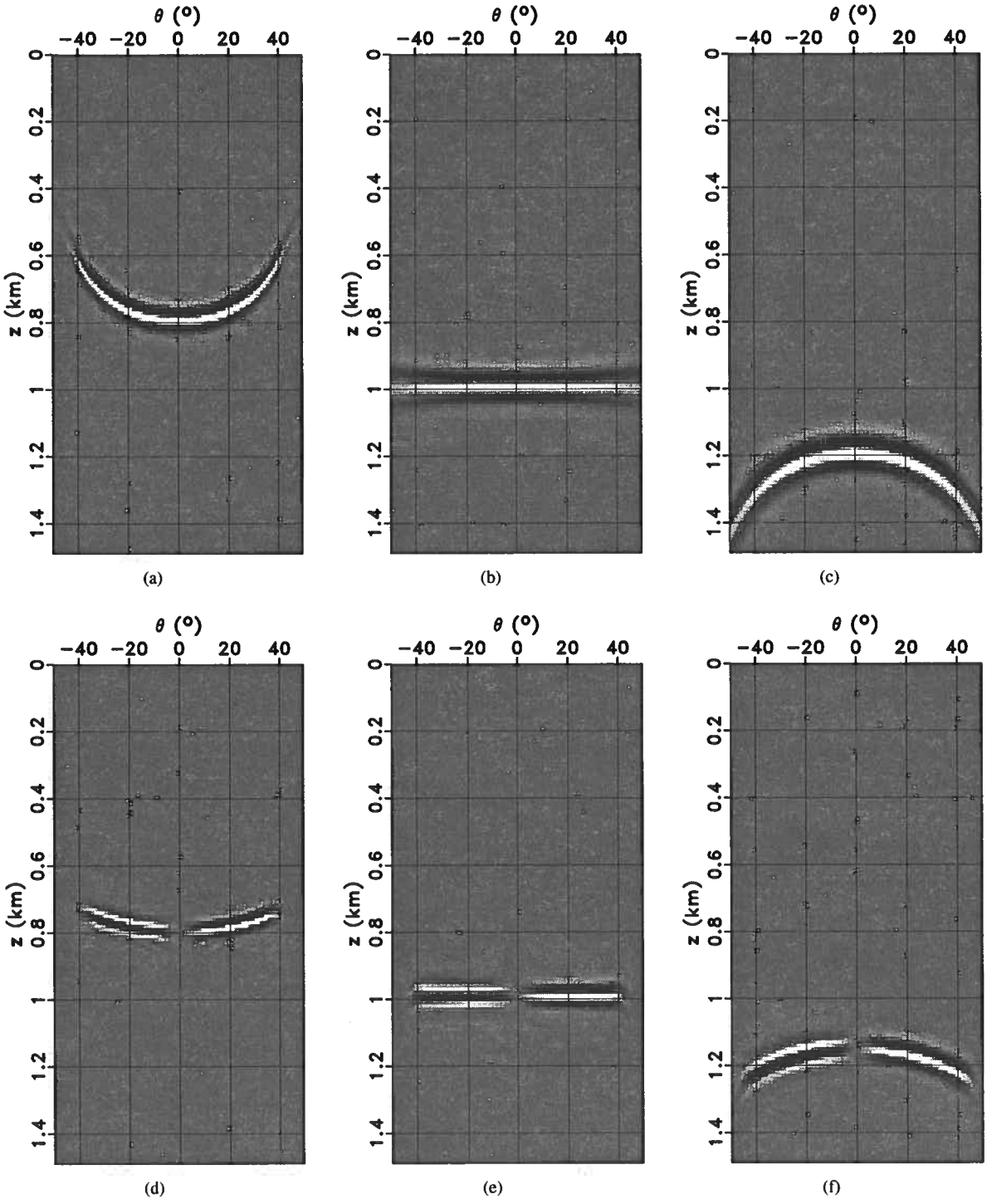

Figure 9. Angle-domain CIGs for PP (upper row) and PS (lower row) data. The gathers are mapped from the corresponding panels in Figure 8 using equation 3.

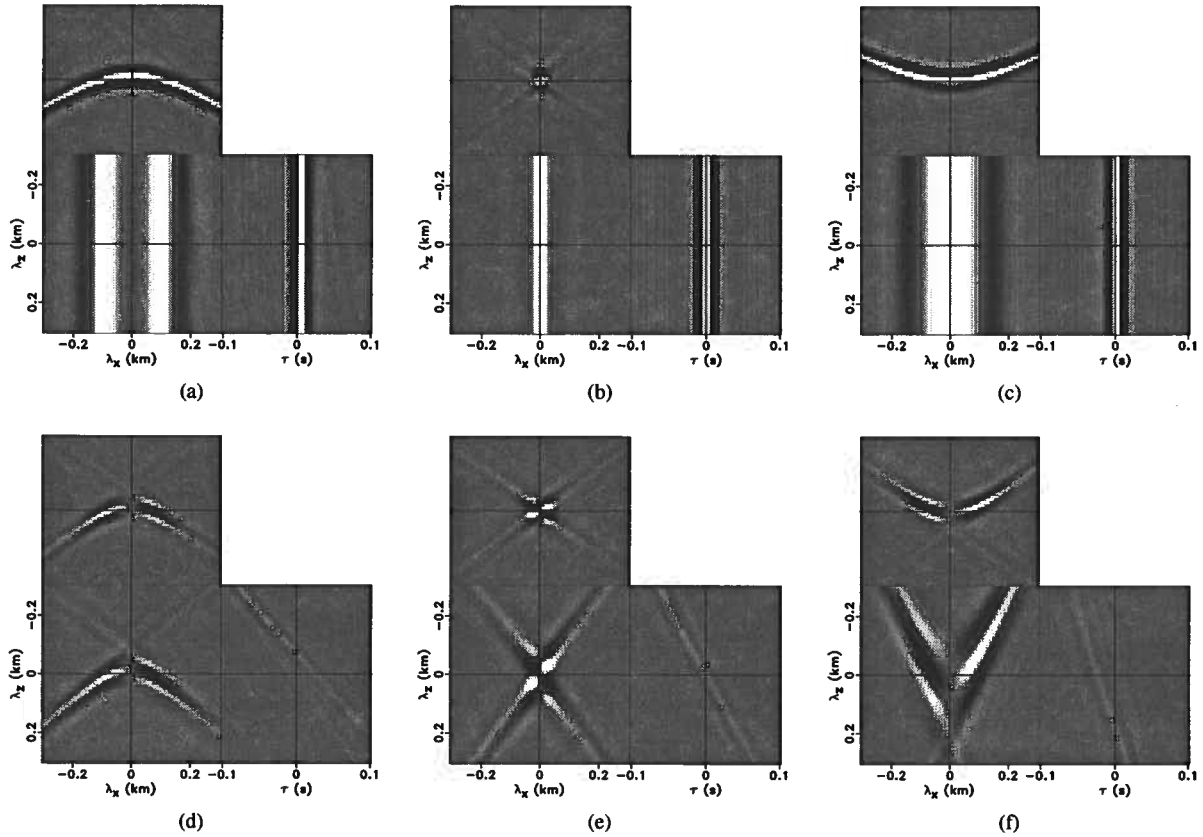

Figure 10. Common image point gathers for PP (upper row) and PS (lower row) data.The CIP location is indicated by the dot on the reflector in Figure 2. A total number of 61 shots from $x = 1$ km to $x = 4$ km are used.

ure 4. A total number of 61 shots from $x = 1$ km to $x = 4$ km are used. The PP CIP obtained with the correct migration velocity is characterized by a line oriented in a direction orthogonal to the reflector. The PS CIP obtained with the correct migration velocity is rotated from the horizontal PS CIP shown in Figure 10 by the dip angle of the reflector. This rotation indicates that the CIPs can be successfully predicted by equation 30.

5 OBJECTIVE FUNCTION FOR MIGRATION VELOCITY ANALYSIS

In order to obtain an optimized migration velocity model, an objective function that reaches its minimum at correct velocity is needed. Shen et al. (2003), Shen (2004), and Shen & Symes (2008) propose the use of differential semblance criteria to formulate the objective function. A differential semblance optimization (DSO) operator P defines a residual by penalizing the departure of image gathers from an ideal shape corresponding to the image constructed with correct velocity. The application of an operator P to the gathers $R(\mathbf{x}, \boldsymbol{\lambda})$ or $R(\mathbf{x}, \theta)$ at incorrect velocity gives an image residual. Thus, the optimization problem can be formulated by minimizing the objective function:

$$J = \frac{1}{2}\|P[R]\|\,. \tag{35}$$

The objective function for wave-equation migration velocity analysis can be defined using images constructed as a function of cross-correlation lags (Rickett & Sava, 2001) or reflection angles (Sava & Fomel, 2003). In particular, we can select subsets of extended images CIGs or CIPs to perform migration velocity analysis.

5.1 PP and PS penalty function for common image gathers

The DSO operators for CIGs in the space-lag domain is give by (Shen, 2004):

$$P_{\boldsymbol{\lambda}}[R] = |\boldsymbol{\lambda}|\, R\,. \tag{36}$$

Based on the fact that the lag- and angle-domain gathers are related by a Radon transform, Shen (2004) shows the equivalence of using the DSO operator in equation 36 for space-lag gathers with a more conventional derivative applied to angle-domain CIGs.

For CIGs at correct migration velocities, the difference

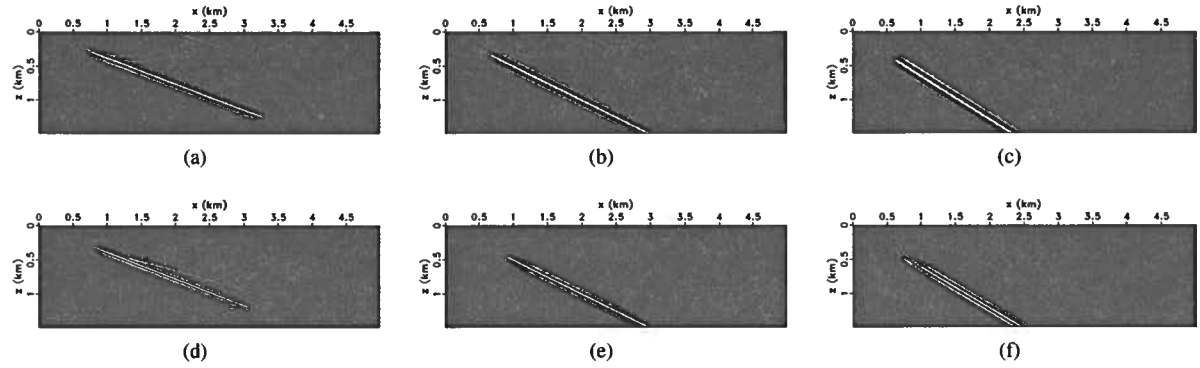

Figure 11. Migrated images for PP (upper row) and PS (lower row) data for a model with a 22° dipping reflector (the same model shown in Figure 4). The images are migrated using low (left column), correct (middle column), and high (right column) velocities.

between PP and PS angle domain CIG is that $R_{PP} = R(\mathbf{x}, \theta)$ is an even function of θ, while $R_{PS} = R(\mathbf{x}, \theta)$ is an odd function of θ. Since, the PP and PS angle-domain CIGs are both flat when migration velocities are correct, we conjecture that it is valid to use the same penalty operator for PP and PS gathers. This penalty function only kinematically penalizes the moveout, and therefore amplitude variation versus angles of the events in the angle gathers does not influence our choice of penalty functions.

It can be expected that because the PS gathers (in both lag- and angle-domains) are constructed with velocity errors only in the receiver wavefield, the objective functions for PS gathers are flatter than those for the PP gathers. This is illustrated in Figure 15, which shows the objective function $J = \frac{1}{2}\|P_{\boldsymbol{\lambda}}[R]\|$ for the PP and PS images constructed for the model shown in Figure 7, migrated with velocities scaled by constant values with respect to the correct velocity. For PS migration, the P velocity is assumed to be correct, and only the S-wave velocity has errors.

5. 2 PP and PS penalty function for common image point gathers

The simple form of the CIP for PP images allows for an easy formulation of a penalty function. For a horizontal reflector, the PP CIP is a line along the λ_z axis, which makes it natural to penalize the events in a CIP by the radial distance from this axis:

$$P_{(\lambda_x,\lambda_z,\lambda_\tau)}[R] = R\sqrt{\lambda_x^2 + \lambda_\tau^2}\,. \tag{37}$$

For a dipping reflector, the PP CIP is oriented at a direction perpendicular to the reflector in the $\{\boldsymbol{\lambda}, \tau\}$ space. We can formulate a penalty function by the distance from this tilted line:

$$P_{(\lambda_x,\lambda_z,\lambda_\tau)}[R] = R\sqrt{(\lambda_x \cos\alpha + \lambda_z \sin\alpha)^2 + \lambda_\tau^2}\,, \tag{38}$$

where α is the dip of the reflector at the CIP location. In a more compact form, the above equation can be written as

$$P_{(\boldsymbol{\lambda},\lambda_\tau)}[R] = R\sqrt{(\mathbf{q}\cdot\boldsymbol{\lambda})^2 + \lambda_\tau^2}\,. \tag{39}$$

Similarly, for PS gathers we can define a penalty function which increases with distance from the surface defined by equation 30 and shown in Figure 6(b). Since the PS CIP for a dipping reflector is a rotation of that for a horizontal reflector, we start our analysis from the CIP for a horizontal reflector, which has a simpler form. Figure 16 shows the geometry used for construction of penalty function for PS images. The surface characterizes the moveout in a the CIP gather for a horizontal reflector and is based on equation 32. The PS CIP surface for a horizontal reflector is symmetric about the plane $\lambda_x = 0$ and this plane intersects the CIP surface along a line L, whose form can be obtained by setting the incidence angle θ to zero in equation 32:

$$L(\gamma, \alpha = 0) = r \begin{pmatrix} 0 \\ -1 \\ \frac{1-\gamma}{2} \end{pmatrix}. \tag{40}$$

This line is a symmetry axis of the CIP surface. In the symmetry plane $\lambda_x = 0$, we can find a vector $\mathbf{A}$ perpendicular to this intersection line L:

$$\mathbf{A}(\gamma, \alpha = 0) = \begin{pmatrix} 0 \\ \frac{\gamma-1}{2} \\ -1 \end{pmatrix}, \tag{41}$$

The vector $\mathbf{A}$ is an axis used for measuring the distance from the CIP surface.

For a dipping reflector, the entire CIP surface is rotated from that of a horizontal reflector by the dip angle α. The shape of the CIP surface remains the same, which enables us to find the symmetry plane of the CIP surface by setting $\theta = 0$ in equation 30:

$$L(\gamma, \alpha) = r \begin{pmatrix} -\sin\alpha \\ -\cos\alpha \\ \frac{1-\gamma}{2} \end{pmatrix}, \tag{42}$$

Note that this line is rotated from the one defined by equation 40 by the dip angle α about the λ_τ axis. A vector perpendicular to this intersection line in the symmetry plane can also be obtained by rotating equation 41 by an angle α about the

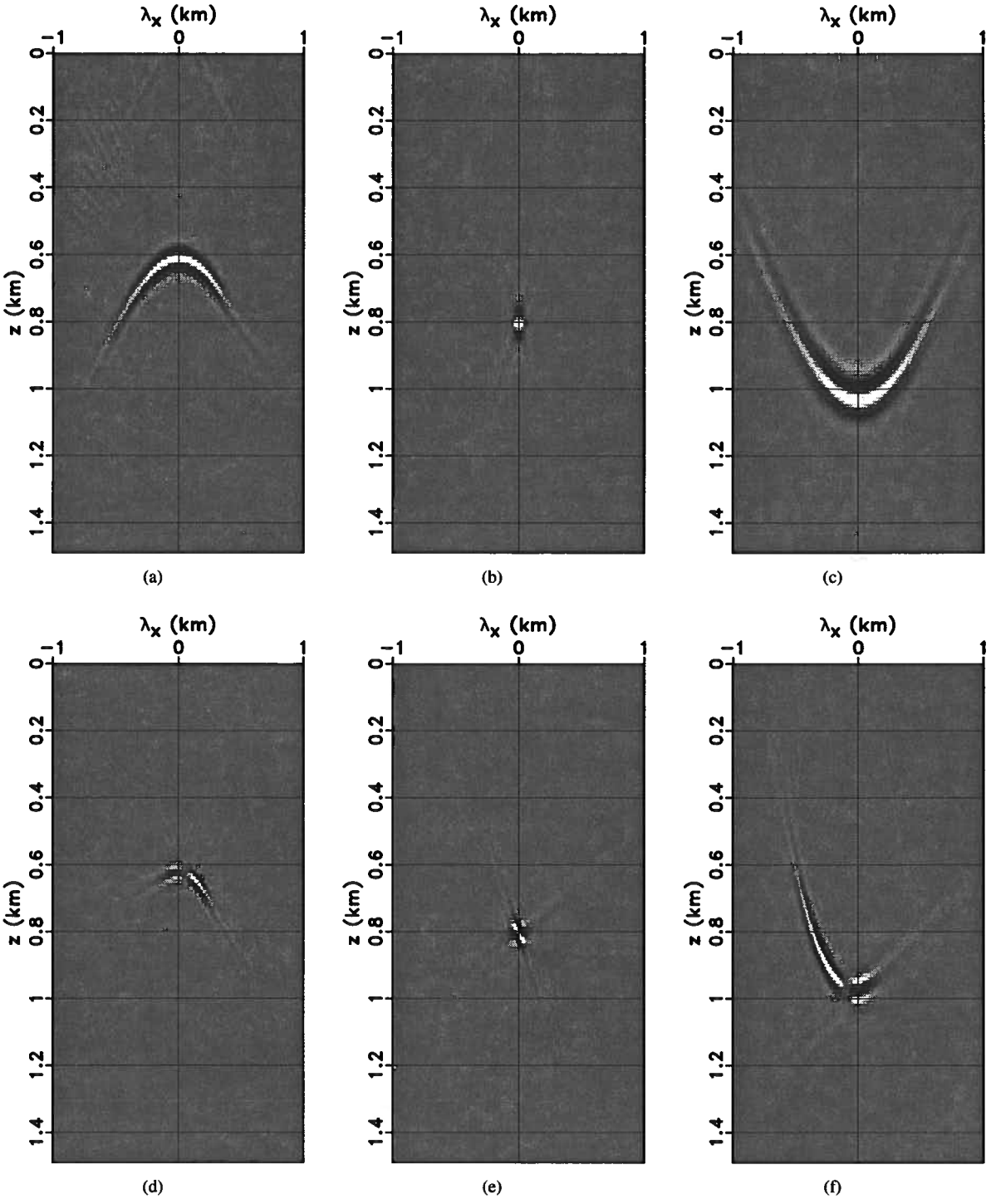

Figure 12. Space-lag CIGs for PP (upper row) and PS (lower row) data. The gathers are constructed using the extended imaging condition given by equation 2. From left to right, the gathers are constructed using low, correct, and high velocities.

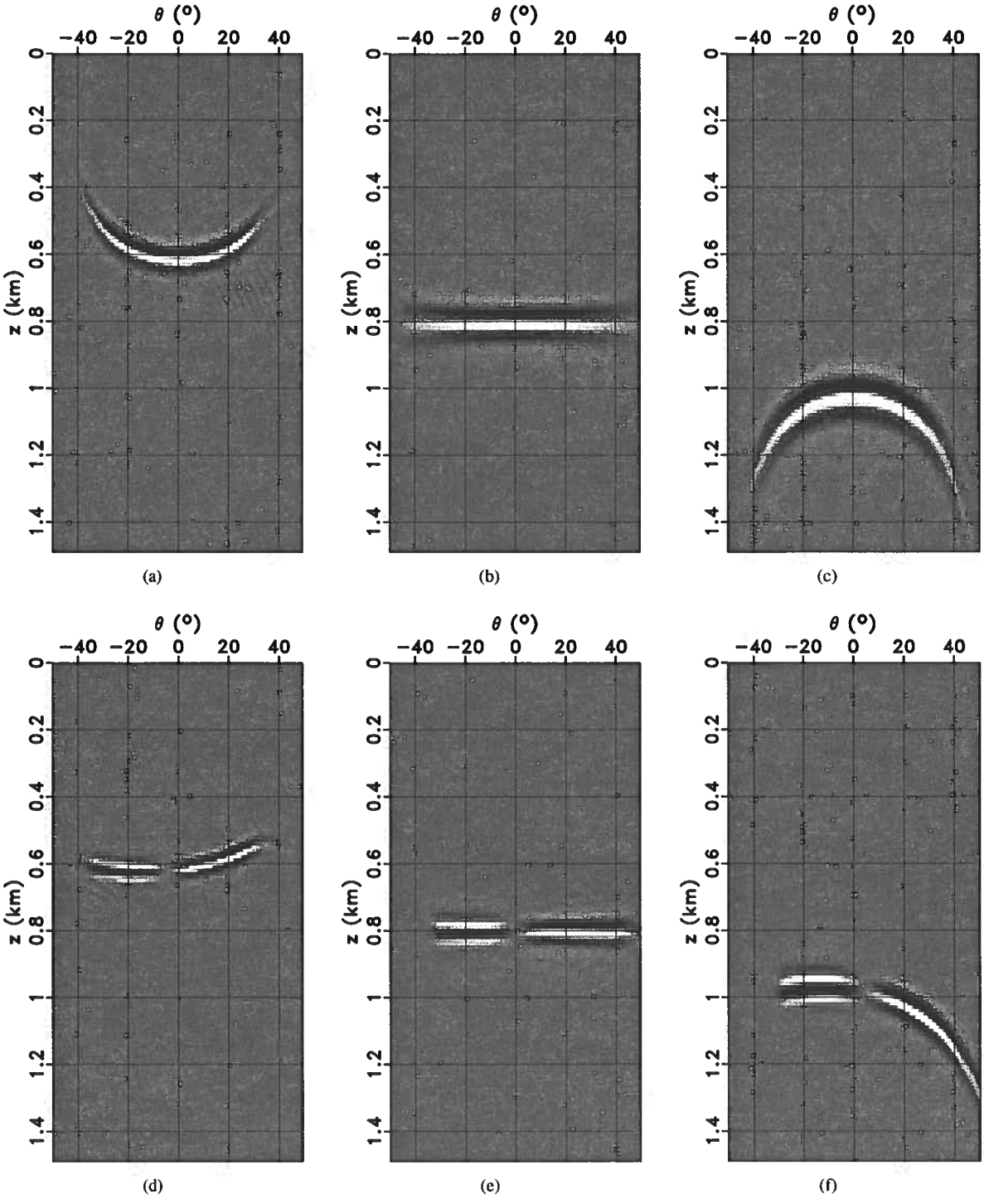

Figure 13. Angle-domain CIGs for PP (upper row) and PS (lower row) data. The gathers are mapped from corresponding panels in Figure 8 using equation 3. The dip used for the angle decomposition is obtained from the migrated images in Figure 11.

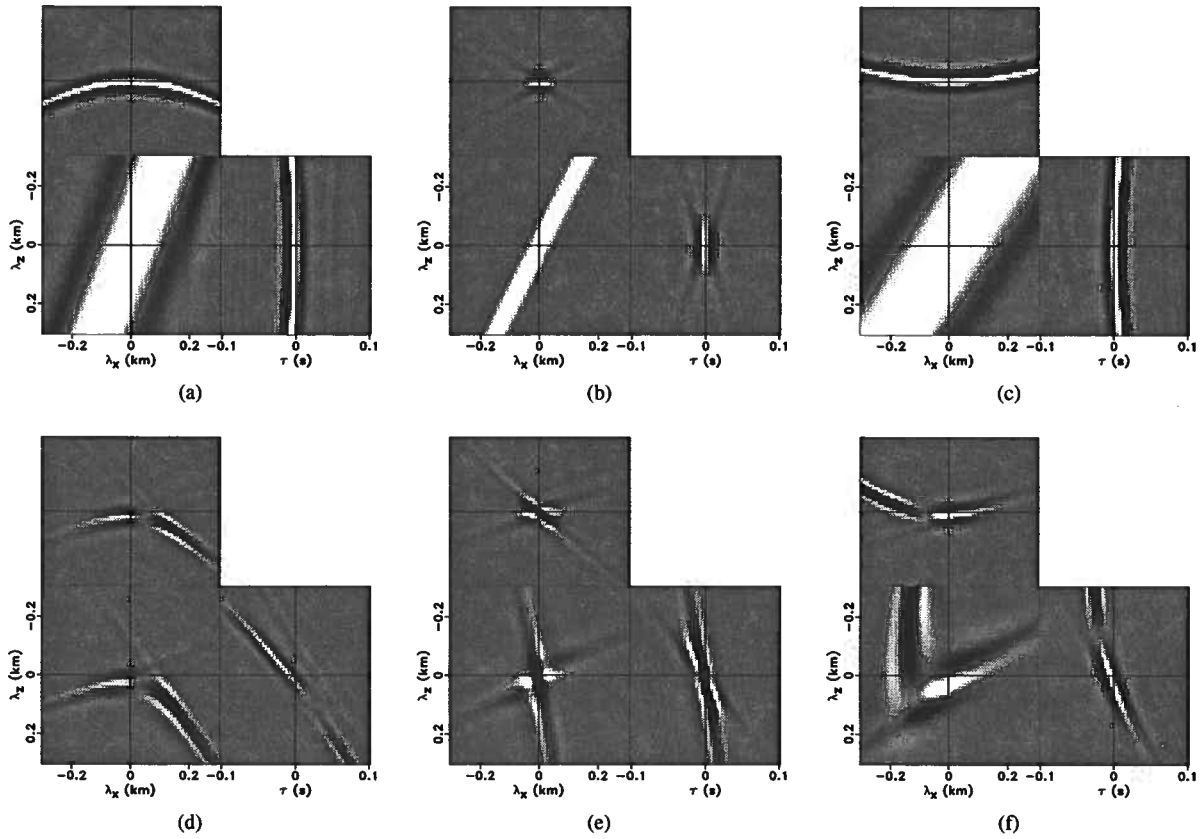

Figure 14. Common image point gathers for PP (upper row) and PS (lower row) data.The CIP location is indicated by the dot on the reflector in Figure 4. A total number of 61 shots from $x = 1$ km to $x = 4$ km are used.

λ_τ axis:

$$\mathbf{A}(\gamma,\alpha) = \begin{pmatrix} \frac{\gamma-1}{2}\sin\alpha \\ \frac{\gamma-1}{2}\cos\alpha \\ -1 \end{pmatrix} . \qquad (43)$$

The line defined by this vector reduces to the line given by equation 41 for $\alpha = 0$.

Based on the geometry shown in Figure 16, we construct a penalty function as the superposition of shifted CIP surfaces corresponding to various distances from the surface defined by equation 30. These surfaces in the $\{\boldsymbol{\lambda}, \tau\}$ space are both shifted by a distance d along the axis vector $\mathbf{A}(\gamma,\alpha)$ and also scaled by a factor d. A possible CIP penalty function is thus given by the parametric form

$$\begin{aligned} & P_{(\lambda_x,\lambda_z,\lambda_\tau,\alpha,\gamma)}[R] \\ = \; & P_{(\lambda_x(r,\theta),\lambda_z(r,\theta),\lambda_\tau(r,\theta),\alpha,\gamma)}[R] \\ = \; & R\sum_d |d| \cdot \left[CIP_{PS}(r,\theta,\alpha,\gamma) - d\frac{\mathbf{A}(\alpha)}{|\mathbf{A}(\alpha)|} \right] \end{aligned} \qquad (44)$$

Here, d ranges from negative to positive values along the axis defined by vector $\mathbf{A}(\gamma,\alpha)$.

We plot the PP (equation 37) and PS (equation 44) penalty functions in Figure 17 for both horizontal (panels (c) and (d)) and dipping (panels (c) and (d)) reflectors. The penalty function is zero at the CIP line/surface (shown in Figures 10(b) and (e) for horizontal reflectors, and in Figures 14(b) and (e) for dipping reflectors), and increases away from the line/surface. Figure 18 shows the objective function $J = \frac{1}{2}\|P_{(\boldsymbol{\lambda},\lambda_\tau)}[R]\|$ for both PP and PS data. The well behaved convex functions indicate that the formulated penalty functions can be used for migration velocity analysis.

6 CONCLUSIONS

We study the features of common image gathers and common image point gathers. For correct migration velocities, the CIGs are characterized by focused points in the lag domain and by flat events in the angle domain. For incorrect migration velocities, the CIGs are misfocusing in the lag domain and are non-flat in the angle domain. The PP CIGs show continuous polarity, while the PS CIGs have polarity reversals at zero space-lags or zero incidence angles for correct velocity, or away from these points for incorrect velocity.

For correct migration velocities, the CIPs for pure wave-modes are characterized by a line in the space- and time-lag space oriented orthogonal to the reflector; the CIPs for converted-waves are characterized by surfaces which contain

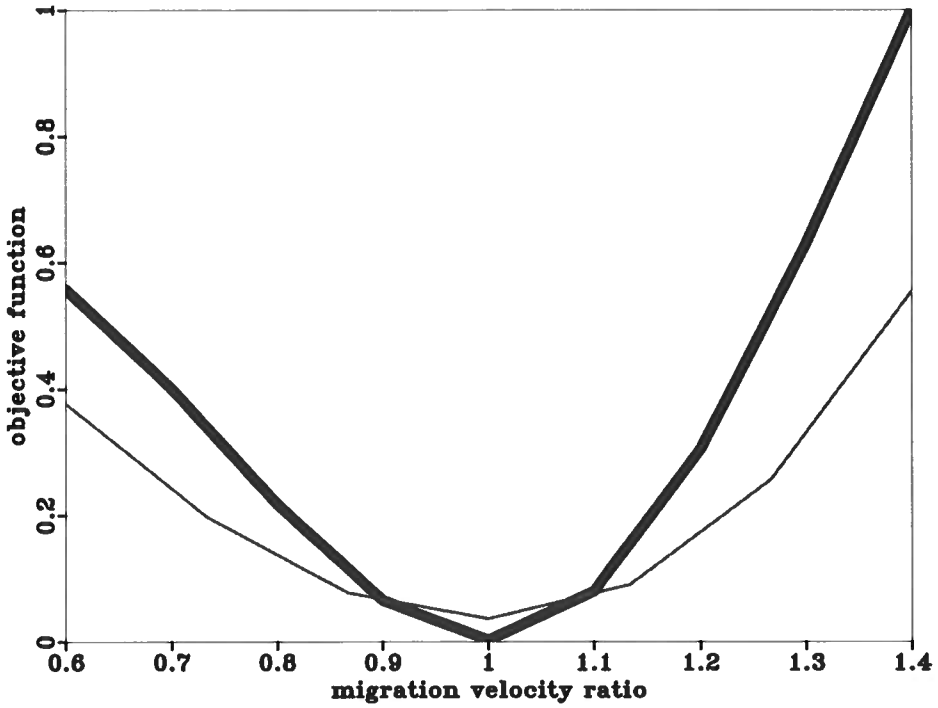

Figure 15. Objective function for PP and PS CIPs by applying the penalty functions $P_\lambda = |\lambda|$ to PP and PS CIGs, respectively. The thick line is the curve for PP data, and the thin line is the curve for PS data. The horizontal axis is the ratio of migration velocity and true model velocity. The PS CIP gathers are obtained using correct P-wave velocity.

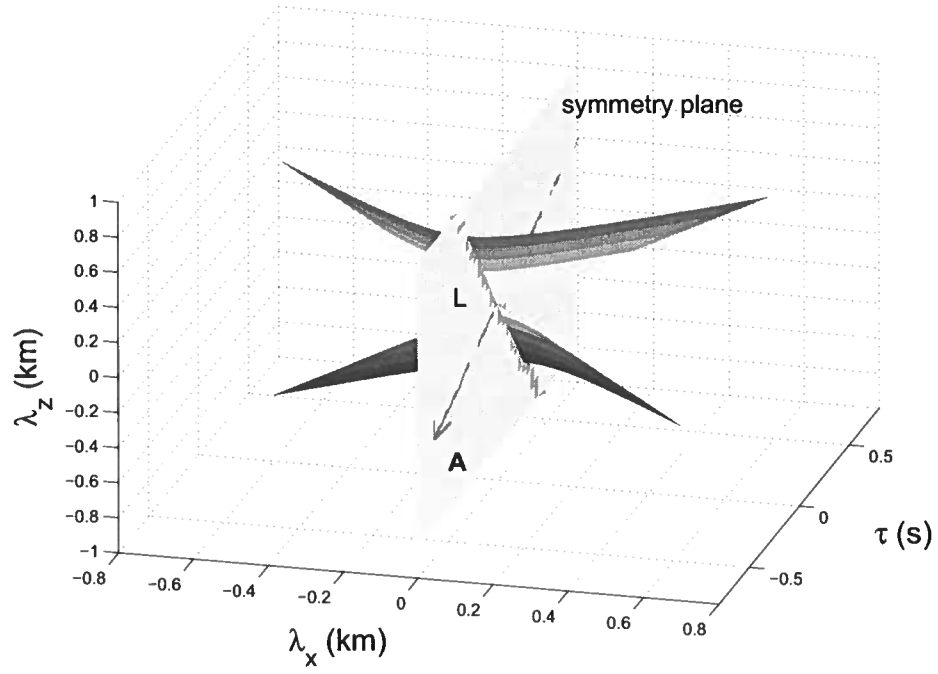

Figure 16. A cartoon showing the penalty function construction for PS CIPs. For simplicity, we use a horizontal reflector in this cartoon. The curved surface is the CIP surface for PS data, and the plane $\lambda_x = 0$ is the symmetry axis of the surface. The CIP surface and its symmetry axis intersect along the line L. In the symmetry plane, we can find a vector $\mathbf{A}$ perpendicular to the line L.

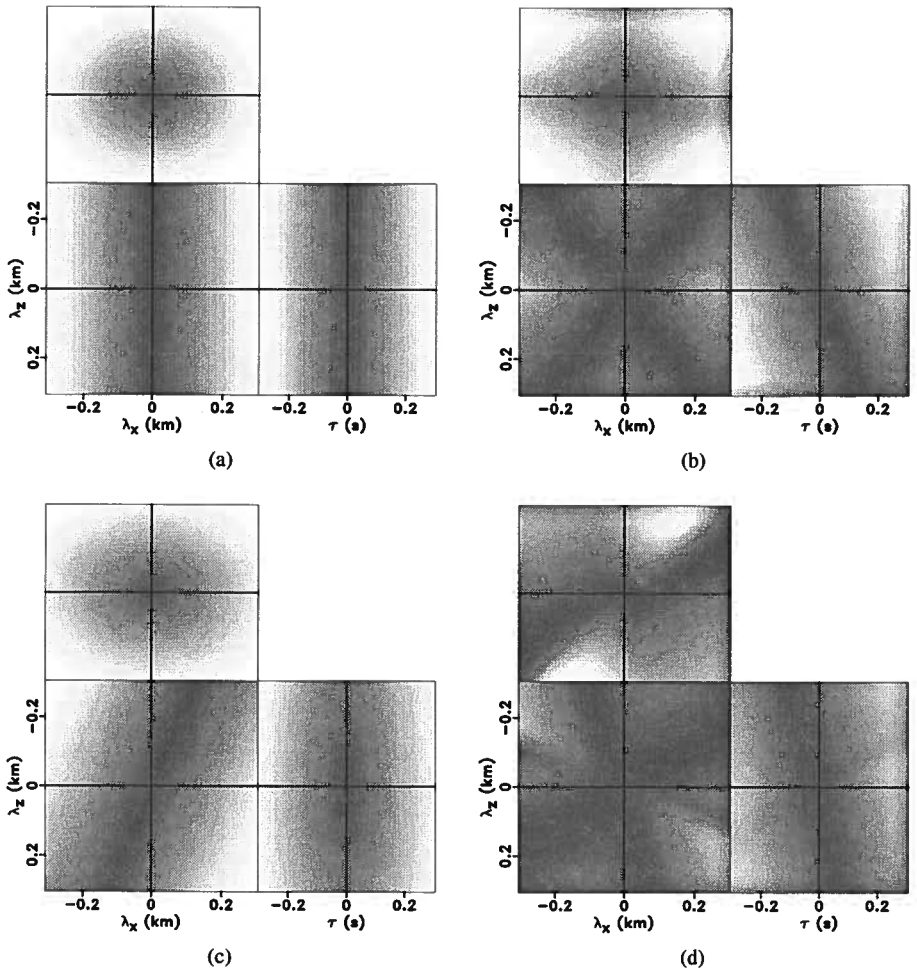

Figure 17. Panels (a) to (d) show penalty functions for PP horizontal, PS horizontal, PP dipping, PS dipping CIPs, respectively. The PP and PS penalty functions are given byequations 39 and 44, respectively. The dips used for panels (c) and (d) are both 22 °.

the origin of the space- and time-lag space. For incorrect migration velocities, the PP CIPs are not characterized by focused lines but by surfaces which depend on the migration velocities; the PS CIPs are also characterized by surfaces deviating from their ideal shape corresponding to correct velocity.

The deviation of CIGs and CIPs gathers obtained with incorrect migration velocities from the ones obtained with correct migration velocities warrants their use for migration velocity analysis. We use differential semblance optimization (DSO) to define penalty functions for CIGs and CIPs and for PP and PS waves. We formulate objective functions by penalizing the departure of the gathers from the ideal shape obtained with correct migration velocities. The objective functions for both CIGs and CIPs and for both PP and PS data are convex, which allows their use in velocity optimization using gradient-descent methods.

7 ACKNOWLEDGMENTS

The reproducible numeric examples in this paper use the Madagascar open-source software package freely available from http://www.reproducibility.org.

REFERENCES

Albertin, U., Sava, P., Etgen, J., and Maharramov, M., 2006, Adjoint wave-equation velocity analysis: 74th Annual International Meeting, SEG, Expanded Abstracts, 3009–3013.

Biondi, B., and Sava, P., 1999, Wave-equation migration velocity analysis: SEG Technical Program Expanded Abstracts, **18**, no. 1, 1723–1726.

Dai, H., Li, X. Y., and Mueller, M., 2000, Compensating for the effects of gas clouds by prestack migration: A case study from Valhall: Compensating for the effects of gas clouds by prestack migration: A case study from Valhall:, Soc. of Expl. Geophys., 70th Ann. Internat. Mtg, 1047–1050.

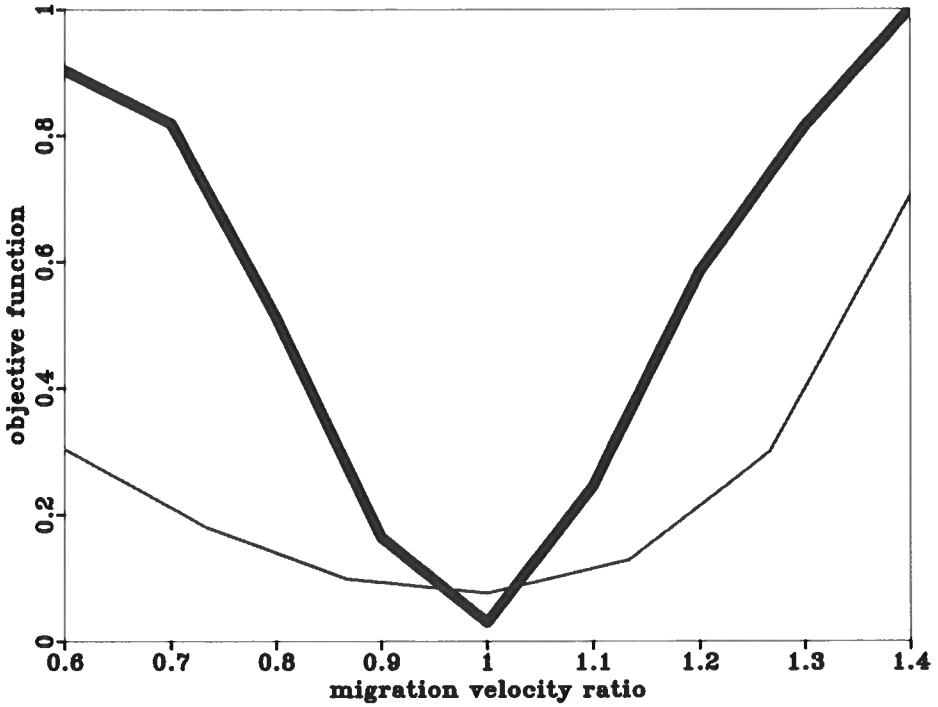

Figure 18. Objective function for PP and PS CIPs by applying the penalty functions, Figure 17(a) and (b), to PP and PS CIP gathers respectively. The thick line is the curve for PP data, and the thin line is the curve for PS data. The horizontal axis is the ratio of migration velocity and true model velocity. The PS CIP gathers are obtained using correct P-wave velocity.

Fomel, S., and Backus, M. M., 2003, Multicomponent seismic data registration by least squares: SEG Technical Program Expanded Abstracts, **22**, no. 1, 781–784.

Fomel, S., Backus, M., Fouad, K., Hardage, B., and Winters, G., 2005, A multistep approach to multicomponent seismic image registration with application to a West Texas carbonate reservoir study: SEG Technical Program Expanded Abstracts, **24**, no. 1, 1018–1021.

Gaiser, J. E., 1996, Multicomponent Vp/Vs correlation analysis: Geophysics, **61**, no. 04, 1137–1149.

Herrenschmidt, A., Granger, P.-Y., Audebert, F., Gerea, C., Etienne, G., Stopin, A., Alerini, M., Lebegat, S., Lambaré, G., Berthet, P., Nebieridze, S., and Boelle, J.-L., 2001, Comparison of different strategies for velocity model building and imaging of PP and PS real data: The Leading Edge, **20**, no. 9, 984–995.

Kendall, R. R., Gray, S. H., and Murphy, G. E., 1998, Subsalt imaging using prestack depth migration of converted waves: Mahogany Field, Gulf of Mexico: Subsalt imaging using prestack depth migration of converted waves: Mahogany Field, Gulf of Mexico:, Soc. of Expl. Geophys., 68th Ann. Internat. Mtg, 2052–2055.

Margrave, G. F., Stewart, R. R., and Larsen, J. A., 2001, Joint PP and PS seismic inversion: The Leading Edge, **20**, no. 9, 1048–1052.

Mora, P., 1988, Elastic wave-field inversion of reflection and transmission data: Geophysics, **53**, no. 06, 750–759.

Nickel, M., and Sonneland, L., 2004, Automated PS to PP event registration and estimation of a high-resolution Vp-Vs ratio volume: Automated PS to PP event registration and estimation of a high-resolution Vp-Vs ratio volume:, Soc. of Expl. Geophys., 74th Ann. Internat. Mtg., 869–872.

Nicoletis, L. M., Svay-Lucas, J., and Prigent, H., 1998, True amplitude pre-stack imaging of converted waves: True amplitude pre-stack imaging of converted waves:, Soc. of Expl. Geophys., 68th Ann. Internat. Mtg, 734–737.

Ogiesoba, O. C., and Stewart, R. R., 2003, Vp/Vs from multicomponent seismic data and automatic PS to PP time mapping: SEG Technical Program Expanded Abstracts, **22**, no. 1, 789–792.

Pratt, R. G., and Worthington, M. H., 1990, Inverse theory applied to multi-source cross-hole tomography. part 1: Acoustic wave-equation method: Geophys. Prosp., **38**, no. 03, 287–310.

Pratt, R. G., 1999, Seismic waveform inversion in the frequency domain, Part 1: Theory and verification in a physical scale model: Geophysics, **64**, no. 3, 888–901.

Rickett, J., and Sava, P., 2001, Offset and angle domain common-image gathers for shot-profile migration: Offset and angle domain common-image gathers for shot-profile migration:, Soc. of Expl. Geophys., 71st Ann. Internat. Mtg, 1115–1118.

Sava, P. C., and Fomel, S., 2003, Angle-domain common-image gathers by wavefield continuation methods: Geo-

physics, **68**, no. 3, 1065–1074.

Sava, P., and Fomel, S., 2005a, Coordinate-independent angle-gathers for wave equation migration: SEG Technical Program Expanded Abstracts, **24**, no. 1, 2052–2055.

——— 2005b, Wave-equation common-angle gathers for converted waves: SEG Technical Program Expanded Abstracts, **24**, no. 1, 947–950.

Sava, P., and Fomel, S., 2006, Time-shift imaging condition in seismic migration: Geophysics, **71**, no. 6, S209–S217.

Sava, P., and Vasconcelos, I., 2010, Extended imaging condition for wave-equation migration: Geophysical Prospecting, in press.

Shen, P., and Symes, W. W., 2008, Automatic velocity analysis via shot profile migration: Geophysics, **73**, no. 5, VE49–VE59.

Shen, P., Stolk, C., and Symes, W., 2003, Automatic velocity analysis by differential semblance optimization: 73th Annual International Meeting, SEG, Expanded Abstracts, 2132–2135.

Shen, P., 2004, Wave-equation migration velocity analysis by differential semblance optimization: Ph.D. thesis, Rice Univeristy.

Song, Z. M., Williamson, P. R., and Pratt, R. G., 1995, Frequency-domain acoustic-wave modeling and inversion of crosshole data: Part II: Inversion method, synthetic experiments and real-data results: Geophysics, **60**, no. 03, 796–809.

Stewart, R. R., Gaiser, J., Brown, R. J., and Lawton, D. C., 2002, Converted-wave seismic exploration: Methods: Geophysics, **67**, no. 05, 1348–1363.

Stewart, R. R., Gaiser, J., Brown, R. J., and Lawton, D. C., 2003, Converted-wave seismic exploration: Applications: Geophysics, **68**, no. 1, 40–57.

Tarantola, A., 1987, Inverse Problem Theory: methods for data fitting and model parameter estimation: , Elsevier Science Publ. Co., Inc.

Thomsen, L., 1998, Converted-wave reflection seismology over anisotropic, inhomogenous media: Converted-wave reflection seismology over anisotropic, inhomogenous media:, Soc. of Expl. Geophys., 68th Ann. Internat. Mtg, 2048–2051.

Veire, H. H., and Landrø, M., 2006, Simultaneous inversion of PP and PS seismic data: Geophysics, **71**, no. 3, R1–R10.

Yan, J., and Sava, P., 2008, Isotropic angle-domain elastic reverse-time migration: Geophysics, **73**, no. 6, S229–S239.

Yang, T., and Sava, P., 2008, Wave-equation extended images for semblance and depth focusing velocity analysis: SEG Technical Program Expanded Abstracts, **27**, no. 1, 2351–2355.

Yang, T., and Sava, P., 2009, Wave-equation migration velocity analysis using extended images: SEG Technical Program Expanded Abstracts, **28**, no. 1, 3715–3719.

Yuan, J. J., Nathan, G., Calvert, A., and Bloor, R., 2008, Automated C-wave registration by simulated annealing: SEG Technical Program Expanded Abstracts, **27**, no. 1, 1043–1047.

Full waveform inversion with image-guided gradient

Yong Ma[1], Dave Hale[1], Zhaobo (Joe) Meng[2] & Bin Gong[2]
[1]*Center for Wave Phenomena, Colorado School of Mines, Golden, CO 80401, USA*
[2]*Seismic Technology, ConocoPhillips Company, Houston, TX 77252, USA*

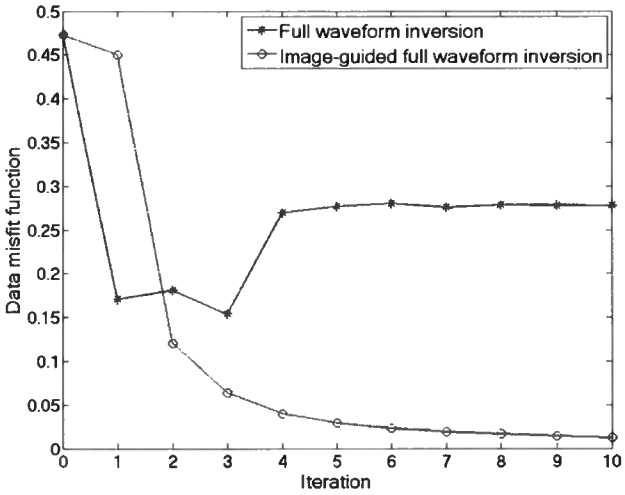

Figure 1. Change of data misfit functions vs. iterations in full waveform inversion and image-guided full waveform inversion.

ABSTRACT

The objective of seismic full waveform inversion (FWI) is to estimate a model of the subsurface that minimizes the difference between recorded seismic data and synthetic data simulated in that model. Although FWI can yield accurate and high-resolution models, multiple problems have prevented widespread application of this technique in practice. First, FWI is computationally intensive, in part because it typically requires many iterations of costly gradient-descent calculations to converge to a solution model. Second, FWI often converges to spurious local minima in the data misfit function of the difference between recorded and synthetic data. Third, FWI is an underdetermined inverse problem with many solutions, most of which may make no geological sense. These problems are related to a typically large number of model parameters and to the absence of low frequencies in recorded data.

FWI with an image-guided gradient mitigates these problems by reducing the number of parameters in the subsurface model. We represent the subsurface model with a sparse set of values, and from these values, we use image-guided interpolation (IGI) to compute finely- and uniformly-sampled gradients of the data misfit function in FWI. Because the interpolation is guided by seismic images, gradients computed in this way conform to geologic structures and subsequently yield models that also agree with subsurface structures. Because of sparse parametrization in the model space, IGI creates models that are more blocky than finely-sampled models, and this blockiness from the model space mitigates the absence of low frequencies in recorded data. A smaller number of parameters to invert also reduces the number of iterations required to converge to a solution model. Tests with a synthetic model and data demonstrate these improvements.

Key words: waveform inversion, image-guided

1 INTRODUCTION

With greater computing power, seismic full waveform inversion (FWI) (Tarantola, 1984; Pratt *et al.*, 1998; Pratt, 1999; Symes, 2008) has become an increasingly practical tool for estimating subsurface parameters, which is the ultimate goal in exploration seismology. FWI iteratively updates an estimated subsurface model and computes corresponding synthetic data to reduce the difference (the data misfit) between the synthetic and recorded data. The FWI technique is attractive in its capability to estimate a subsurface model with generally higher resolution (Operto *et al.*, 2004) than traveltime tomography (Stork, 1992; Woodward, 1992; Vasco & Majer, 1993; Zelt & Barton, 1998) and migration velocity analysis (MVA) (Yilmaz & Chambers, 1984; Sava & Biondi, 2004a,b). In practice, a macromodel generated by traveltime tomography or MVA may serve as a starting model for FWI.

Although FWI has a long history and definite benefits, two obstacles have prevented its widespread application in exploration seismology. One obstacle is computational cost. FWI requires a huge amount of simulations and reconstructions of seismic wavefields, and its computational cost is proportional to the number of sources or the number of shots. For large 3D models and seismic data sets, these computations may be prohibitive. Therefore, various efforts from different perspectives have been expended to reduce the computational cost. One such method is to apply phase-encoding techniques (Krebs *et al.*, 2009) that combine all shots together to form a simultaneous source. The computational cost of FWI using encoding techniques is thereby reduced by a factor roughly equal to the number of shots.

FWI also requires multiple iterations of gradient descent to minimize the data misfit (see Figure 1), and the computational cost is therefore proportional to the number of required iterations. To reduce this number, one may reduce the number of model parameters of the subsurface. To reduce the number of parameters, one can represent a finely-sampled model using a sparse set of parameters and some basis functions. Many different compression methods employed for this purpose, such as Fourier transform, wavelet transform, curvelet transform, etc., share the same principle of projecting a model into another sparse domain. Through this sparse representation, one discards unwanted or unresolvable details that could be present in a more complete model. The wavelet transform is a representative technique used in inverse problems (Meng & Scales, 1996). However, such methods do not account for geological structures of the subsurface that may be apparent in seismic images and so may yield models that are geologically unreasonable.

A second obstacle is that the inverse problem posed by FWI has no unique solution. Many different models may yield synthetic data that match recorded data within a reasonable tolerance that accounts for uncertainties and inadequacies in both recorded data and the theory underlying computed synthetic data. In particular, low-wavenumber components of models are often poorly recovered by FWI because corresponding low-frequency content in data is rarely recorded. In practice, it can be difficult to obtain an adequate initial model that is consistent with unrecorded low frequencies. This fact and the nonlinear relationship between model and data in FWI lead to cycle-skipping and local minima, which correspond to models that poorly approximate the subsurface.

To mitigate such problems, multiscale approaches (Bunks, 1995; Sirgue & Pratt, 2004; Boonyasiriwat *et al.*, 2009) have been proposed. These methods recursively add higher-frequency details to models first computed from lower-frequency data. The fidelity of multiscale techniques depends fundamentally on the fidelity of low-frequency content in recorded data. In practice, the low frequencies required to bootstrap a multiscale FWI technique may be unavailable. Other methods for addressing the problems of cycle-skipping and local minima have been proposed as well. These include minimizing data misfit functions in logarithmic and Laplace domains (Shin & Min, 2006; Shin & Ha, 2008).

To obtain better subsurface models, *a priori* information may be useful. The *a priori* knowledge can take different forms. For example, both geological and geophysical data, such as those obtained from boreholes, may provide useful *a priori* constraints. Other useful constraints may be specified shapes and orientations of geologic structures in the subsurface.

Inspired by image-guided interpolation (IGI) (Hale, 2009a), we have proposed the use of structure-orientated metric tensor fields to constrain FWI gradients (Meng, 2009). We have first presented this idea at the 2009 SEG post-convention workshop (Meng *et al.*, 2009). In this paper, we show how IGI and its adjoint may be used to calculate and guide gradients, with structural information derived from seismic images as the *a priori* constraints. We first review basic concepts of FWI and illustrate some practical problems with a synthetic example. We then construct *image-guided FWI* by incorporating the image-guided interpolation and its adjoint to constrain the calculations of *image-guided gradients*. Subsurface models computed from these image-guided gradients conform to geologic structures apparent in the seismic images. Synthetic results further demonstrate the effectiveness of image-guided FWI in reducing the number of iterations required for convergence of FWI (see Figure 1).

2 FULL WAVEFORM INVERSION

Full waveform inversion (Tarantola, 2005) uses recorded seismic data $\mathbf{d}$ to estimate parameters of a subsurface model $\mathbf{m}$, given a forward operator $\mathbf{F}$ that syn-

thesizes data. In FWI, we seek a model $\mathbf{m}$ that minimizes the difference $\mathbf{d} - \mathbf{F}(\mathbf{m})$. In seismic inversion, as for most geophysical inversion problems, the forward data-synthesizing operator $\mathbf{F}$ is a non-linear function of model parameters, such as seismic wave velocities.

2.1 FWI as an optimization problem

Unfortunately, the forward operator $\mathbf{F}$ has no inverse $\mathbf{F}^{-1}$ for almost any geophysical inverse problem, so we cannot simply invert the model from the data using $\mathbf{m} = \mathbf{F}^{-1}(\mathbf{d})$. Therefore, FWI is usually formulated as a least-squares optimization problem, in which we compute a model $\mathbf{m}$ that minimizes the data misfit function

$$E(\mathbf{m}) = \frac{1}{2}\|\mathbf{d} - \mathbf{F}(\mathbf{m})\|^2 , \tag{1}$$

where $\|.\|$ denotes an L2 norm. All information in recorded seismic waveforms should, in principle, be taken into account in the data misfit function. Therefore, FWI comprehensively minimizes the difference in traveltimes, amplitudes, converted waves, multiples, etc. between recorded and synthetic data. This all-or-nothing approach distinguishes FWI from other methods, such as traveltime tomography, which only focuses on traveltime differences. Monte Carlo (random) methods (Nocedal & Wright, 2000; Tarantola, 2005) test randomly generated models to find one that minimizes the data misfit function $E(\mathbf{m})$. However, the typically large number of model parameters makes such Monte Carlo methods impractical.

The gradient descent method is a more practical alternative to a random search. We begin with an initial model $\mathbf{m}_0$, which can be found using other inversion methods (e.g., traveltime tomography or migration velocity analysis); then we use the gradient of the data misfit function $\mathbf{g} \equiv \nabla_{\mathbf{m}} E = \frac{\partial E}{\partial \mathbf{m}}$ evaluated at $\mathbf{m}_0$ to search locally for a model $\mathbf{m} = \mathbf{m}_0 + \delta\mathbf{m}$ that reduces the data misfit $E(\mathbf{m})$.

The Taylor series expansion of equation 1 about the initial model is

$$E(\mathbf{m}_0 + \delta\mathbf{m}) = E(\mathbf{m}_0) + \delta\mathbf{m}^T\mathbf{g}_0 + \frac{1}{2}\delta\mathbf{m}^T\mathbf{H}_0\delta\mathbf{m} + \dots , \tag{2}$$

where $E(\mathbf{m}_0)$ denotes the data misfit evaluated at $\mathbf{m}_0$, $\mathbf{g}_0 = \mathbf{g}(\mathbf{m}_0)$, and $\mathbf{H}_0$ denotes the Hessian matrix comprised of the 2nd partial derivatives of $E(\mathbf{m})$, again evaluated at $\mathbf{m}_0$. If we ignore any term higher than the 2nd order in equation 2, this Taylor approximation is quadratic in the model perturbation $\delta\mathbf{m}$, and we can minimize the data misfit $E(\mathbf{m})$ by solving a set of linear equations:

$$\mathbf{H}_0\delta\mathbf{m} = -\mathbf{g}_0 \tag{3}$$

with a solution

$$\delta\mathbf{m} = -\mathbf{H}_0^{-1}\mathbf{g}_0 . \tag{4}$$

In Newton's method for minimization of the data misfit $E(\mathbf{m})$, we begin with the initial model $\mathbf{m}_0$ and solve iteratively for

$$\delta\mathbf{m}_i = -\mathbf{H}_i^{-1}\mathbf{g}_i , \tag{5}$$

and

$$\mathbf{m}_{i+1} = \mathbf{m}_i - \mathbf{H}_i^{-1}\mathbf{g}_i , \tag{6}$$

where $\mathbf{g}_i \equiv \mathbf{g}(\mathbf{m}_i)$, and $\mathbf{H}_i$ is the Hessian matrix for the model $\mathbf{m}_i$. If we neglect nonlinearity (e.g., multiple scattering) in the forward operator $\mathbf{F}$, we obtain a Gauss-Newton method (Pratt *et al.*, 1998). However, in practice, the large size of the Hessian matrix $\mathbf{H}_i$, which depends on the number of parameters in the model, prevents the application of Newton-like methods.

Alternatively, the model update in equation 6 can be iteratively approximated by replacing the inverse of the Hessian matrix with a scalar step length α_i:

$$\mathbf{m}_{i+1} = \mathbf{m}_i - \alpha_i\mathbf{h}_i , \tag{7}$$

where the search direction $\mathbf{h}_i$ is determined by conjugate gradients (Vigh & Starr, 2008; Gong *et al.*, 2008):

$$\begin{aligned} \mathbf{h}_0 &= \mathbf{g}_0 , \\ \beta_i &= \frac{\mathbf{g}_i^T(\mathbf{g}_i - \mathbf{g}_{i-1})}{\mathbf{g}_{i-1}^T\mathbf{g}_{i-1}} , \\ \mathbf{h}_i &= \mathbf{g}_i + \beta_i\mathbf{h}_{i-1} . \end{aligned} \tag{8}$$

In each iteration, we compute the step length α_i using a quadratic line search algorithm (Nocedal & Wright, 2000)

2.2 Implementation of FWI

A gradient-descent implementation of FWI consists of four steps performed iteratively, beginning with an initial model $\mathbf{m}_0$:

(i) Compute $\mathbf{d} - \mathbf{F}(\mathbf{m}_i)$, the difference between recorded data $\mathbf{d}$ and synthetic data $\mathbf{F}(\mathbf{m}_i)$ computed for the current model $\mathbf{m}_i$;

(ii) Compute the gradient $\mathbf{g}_i = \nabla_{\mathbf{m}} E_i$;

(iii) Search for a step length α_i in the conjugate direction $\mathbf{h}_i$;

(iv) Compute the updated model $\mathbf{m}_{i+1}$ using equation 7.

Most of the computational cost in this implementation lies in steps (ii) and (iii).

This version of FWI can be implemented both in the time domain (Tarantola, 1984, 1986; Mora, 1989) and in the frequency domain (Pratt, 1999). Perhaps, the greatest benefit of using frequency domain FWI is that we can select only a few frequencies for inversion (Sirgue & Pratt, 2004). Unfortunately, this advantage does not extend to inversion for deep subsurface models that require more frequencies. Because the gradient calculation for full waveform inversion is similar to the process

of reverse time migration (RTM)(Tarantola & Valette, 1982; Pratt, 1999), a straightforward approach is to perform FWI using an RTM engine. Vigh & Starr (2008) note that the advantages of implementing FWI in the time domain include increased parallelism and reduced memory requirements, thereby making FWI more applicable to large 3D models and data sets. In the examples shown in this report, we used RTM and implemented FWI in the time domain.

2.3 Synthetic example

Figure 2a depicts a subsurface velocity model with two anomalies. One is a low-velocity zone and the other is a high-velocity bar, as shown separately in Figure 2c. We refer to the model in Figure 2a as the true model $\mathbf{m}$. Figure 2b displays the initial model $\mathbf{m}_0$ that we used in FWI; it is simply the true model $\mathbf{m}$ without the two anomalies.

To test FWI, we first create data $\mathbf{d} = \mathbf{F}(\mathbf{m})$ using the true model $\mathbf{m}$. Henceforth, for consistency with the discussion above, we refer to these data as the "recorded" data, even though we compute these noise-free data using the forward operator $\mathbf{F}$, a finite-difference constant-density solution to the 2D acoustic wave equation. A total of 25 shots are evenly distributed on the top surface with an interval of 120 m; the receiver interval is 10 m. The source is a Ricker wavelet with a peak frequency of 15 Hz. For example, Figure 3a shows a common-shot gather for shot number 13 of the recorded data $\mathbf{d}$. Figure 3b shows the corresponding synthetic data $\mathbf{F}(\mathbf{m}_0)$ computed for the initial model $\mathbf{m}_0$ displayed in Figure 2b. Figure 3c displays the difference $\mathbf{d} - \mathbf{F}(\mathbf{m}_0)$, which is also known as the data residual, that part of the recorded data that cannot be explained by the current model. In the four steps of FWI, computation of this data residual is step (i).

In step (ii), we compute the gradient of the data misfit. As discussed by (Tarantola & Valette, 1982; Pratt, 1999), this gradient is equal to the output of RTM applied to the data residual shown in Figure 3c, using the current model $\mathbf{m}_0$ shown in Figure 2b. This method for the calculation of gradient is also referred to as the adjoint-state method (Tromp *et al.*, 2005). Figure 4a shows the gradient $\mathbf{g}_0$ computed in this way for the first iteration of FWI.

In step (iii), we then compute a step length α_0 that determines how much to change our velocity model in this first iteration. We compute the step length using a quadratic line search algorithm and search in a direction defined by conjugate gradients (Vigh & Starr, 2008; Gong *et al.*, 2008). This line search requires computation of at least 2 synthetic data sets.

Finally, in step (iv), we update the current velocity model according to equation 7. Figure 5a is the change $\delta\mathbf{m}$ in velocity computed in the 1st iteration; in this 1st iteration, this change is simply a scaled version of

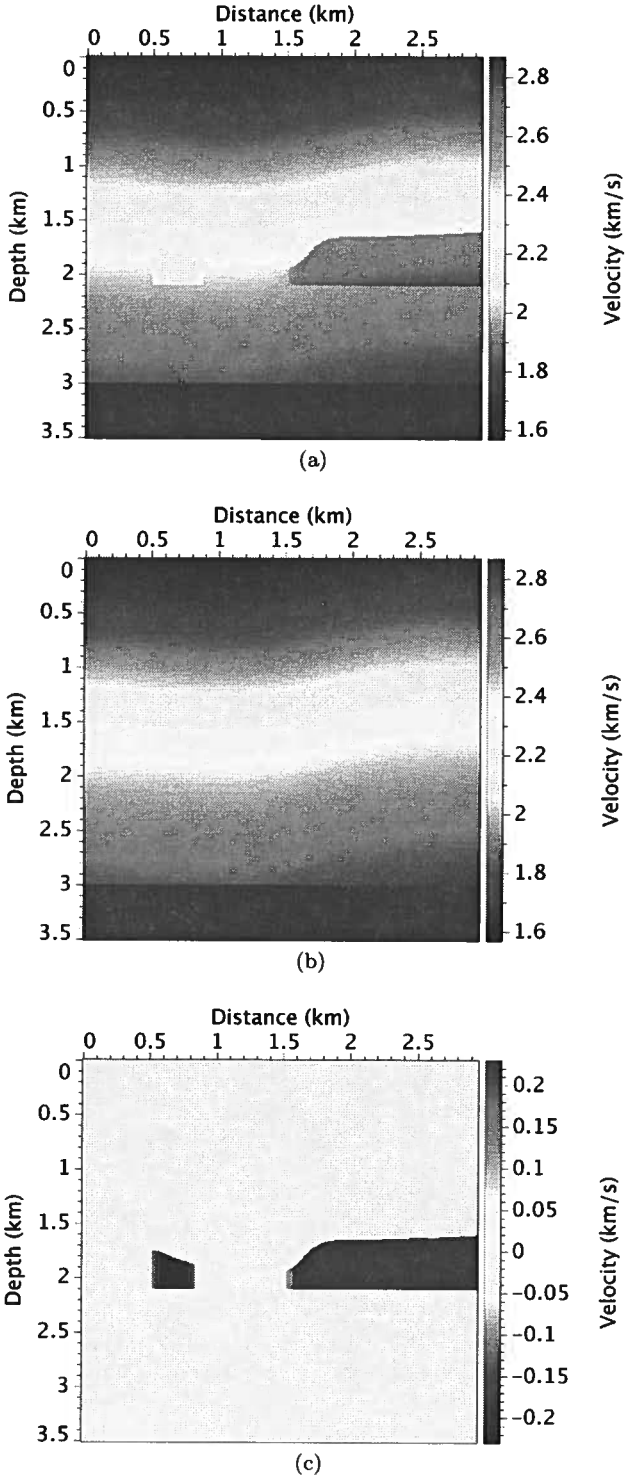

Figure 2. (a) The LVZ model courtesy of ConocoPhillips, (b) the initial velocity model, and (c) velocity anomalies (one low velocity zone and one high velocity bar) created by subtracting the initial model in (b) from the true model in (a).

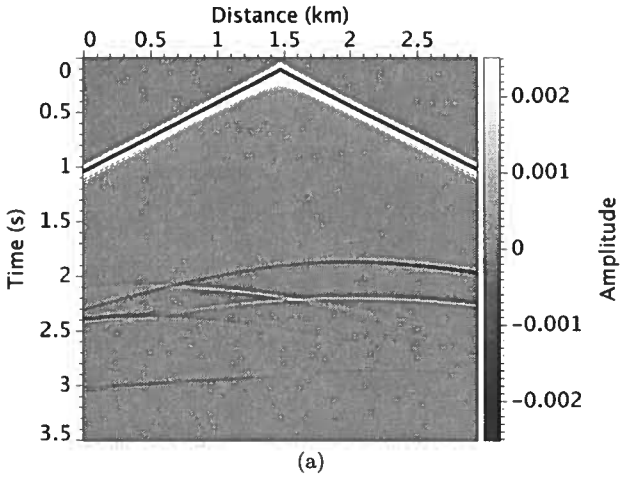

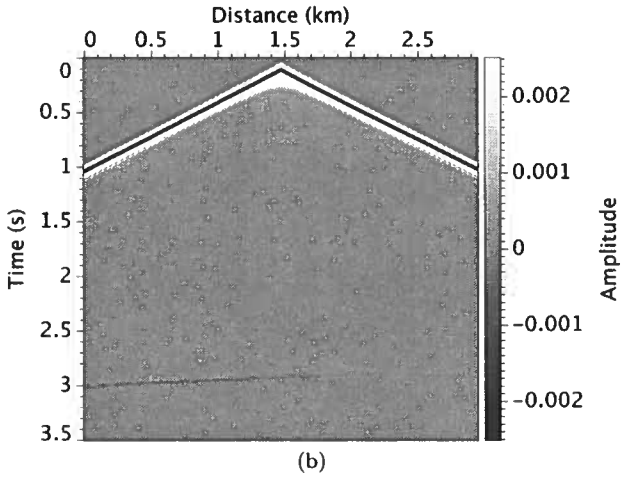

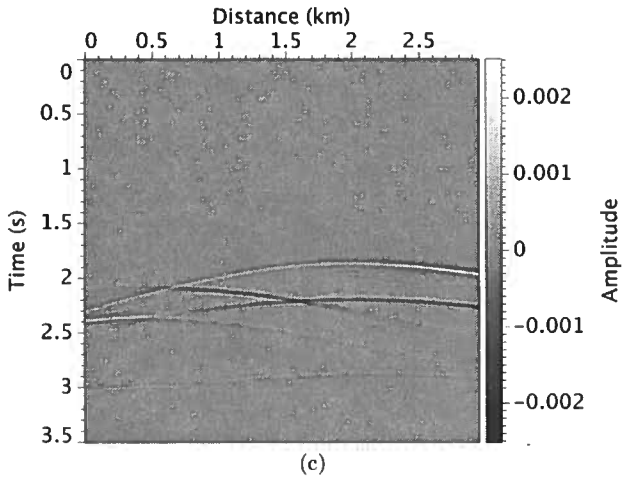

Figure 3. (a) The common-shot gather of shot number 13 in the recorded data set, (b) the corresponding synthetic common-shot gather simulated in the initial velocity model (Figure 2b), and (c) the data residual for this shot.

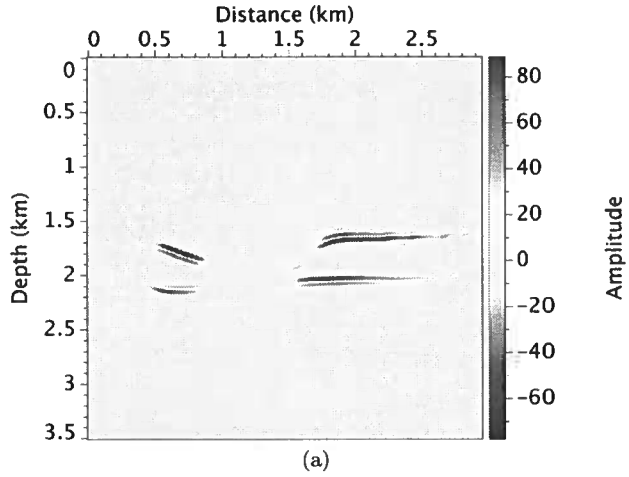

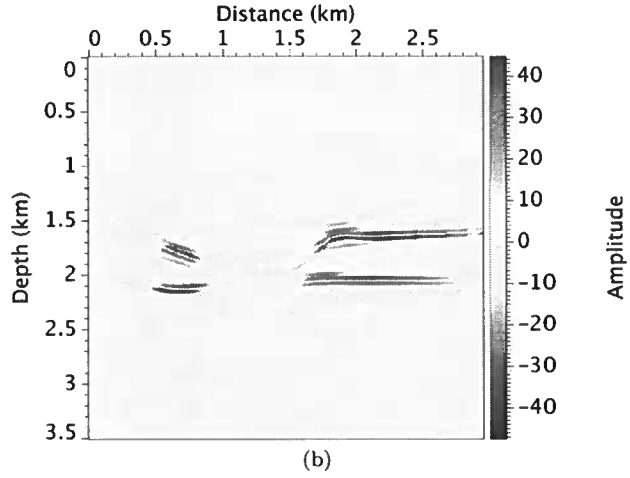

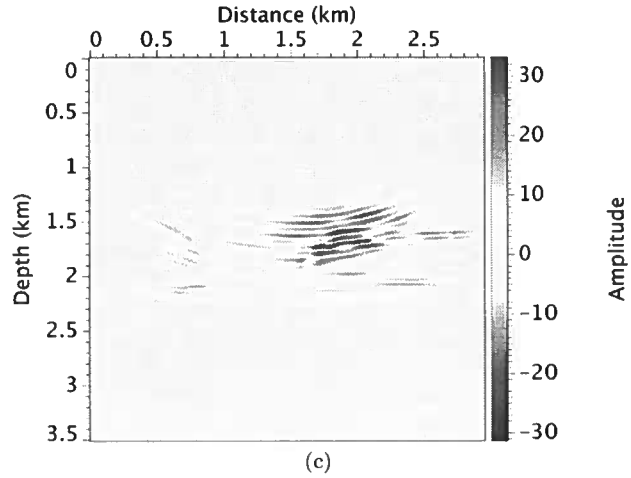

Figure 4. Gradient of the data misfit function in (a) the 1st iteration, (b) the 2nd iteration and (c) the 5th iteration.

the gradient computed in step (ii). In subsequent iterations, the iterative four-step FWI process introduces additional details, as indicated by the gradients displayed in Figure 4b and c, which correspond to the 2nd and 5th iterations, respectively. Figure 5b and c show the corresponding accumulated velocity updates, the difference between the current and initial velocity models.

After the 1st iteration, the data residual corresponding to shot number 13, as shown in Figure 6a, becomes significantly smaller than that in Figure 3c. However, in subsequent iterations, the data residuals shown in Figure 6b and c increase.

In principle, each iteration of FWI should reduce the data misfit $E(\mathbf{m})$, but in the search for a step length α_i, FWI risks producing unsatisfactory models with larger data residuals. Figure 1 plots the data misfit function $E(\mathbf{m})$ as a function of the number of iteration. For example, the data residual after the 2nd iteration of FWI is even larger than the residual of the 1st iteration; a similar case occurs in the 4th iteration. This up-and-down relationship between $E(\mathbf{m})$ and the iteration number has two main causes. First, FWI sometimes fails to find a step length α_i that decreases the data misfit function $E(\mathbf{m})$, within a limited number (e.g., 5 in this paper) of gradient descent trials. We cannot simply stop FWI, and to continue FWI, we must provide a step length and hope FWI can reduce the data misfit function in subsequent iterations. FWI, in fact, reduces the data residual in the 3rd iteration, but we encounter another increase of the data residual in the 4th iteration. Second, we use the conjugate direction $\mathbf{h}_i$ instead of the gradient direction $\mathbf{g}_i$, which guarantees the descent of the data misfit function. In contrast, the conjugate direction may temporally increase the data residual.

Another problem noted in FWI is that, as shown in Figure 5, the accumulated velocity updates produced by FWI contain the imprint of the seismic wavelet; these updates look more like migrated images rather than any reasonable perturbations to our initial velocity model. Because we use a Ricker wavelet with a peak frequency of 15 Hz, which lacks low frequencies, local-minima and cycle-skipping problems may take place in the above conventional FWI example.

3 IMAGE-GUIDED FWI

Conjugate-gradient methods are guaranteed to minimize positive-definite quadratic misfit functions within M iterations, where M is the number of model parameters in the solution vector $\mathbf{m}$ (Nocedal & Wright, 2000). More precisely, the convergence rate of a conjugate-gradient method depends on the condition number of the Hessian matrix $\mathbf{H}$ (Cohen, 1972; Wheeler & Wilton, 1988). The condition number is the ratio of the largest eigenvalue of the Hessian matrix $\mathbf{H}$ to the smallest eigenvalue, and in practice, FWI is usually ill-posed due

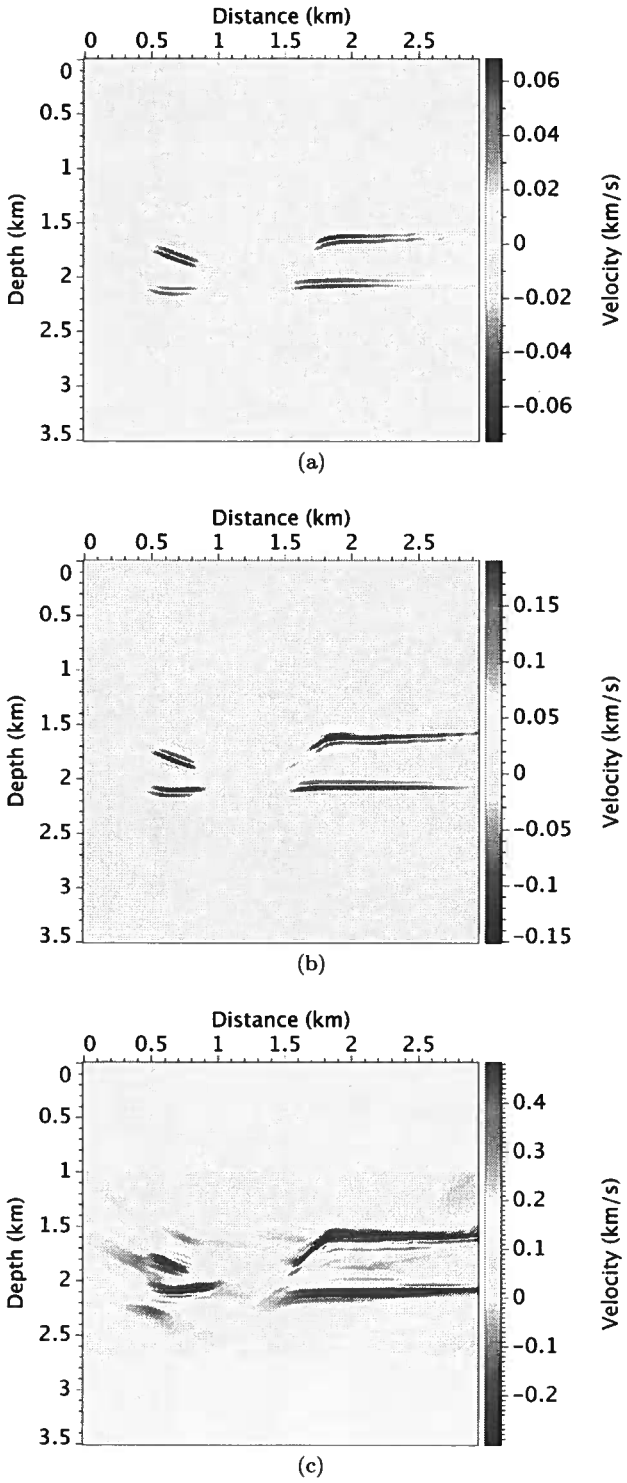

Figure 5. Accumulated velocity updates after (a) 1 iteration, (b) 2 iterations and (c) 5 iterations.

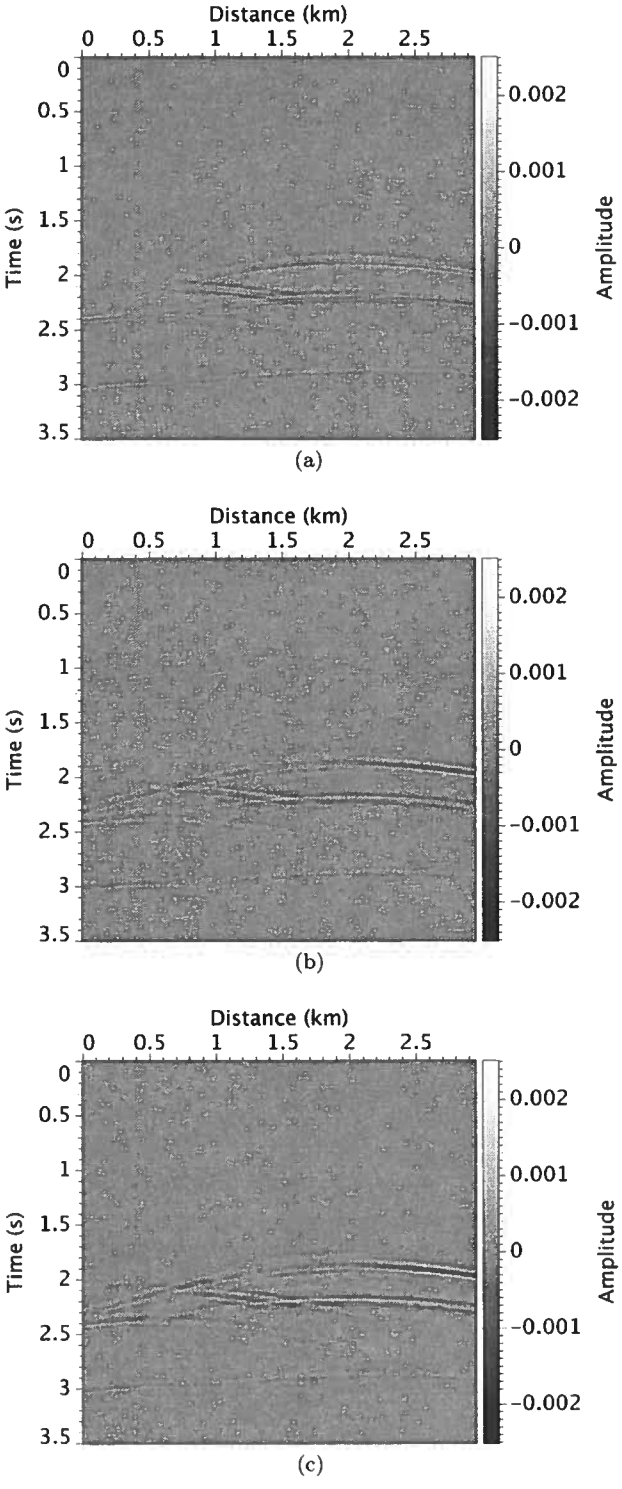

Figure 6. Data residual after (a) 1 iteration, (b) 2 iterations and (c) 5 iterations.

to a typically large condition number of the Hessian matrix. A large condition number often tends to appear, especially when an inverse problem has a large number of model parameters in $\mathbf{m}$, some of which do not cause the data misfit function $E(\mathbf{m})$ to change significantly. If the data misfit function $E(\mathbf{m})$ is insensitive to the change of a model parameter in the solution vector $\mathbf{m}$, the eigenvalue corresponding to this parameter is small and may be nearly zero, thereby yielding a large condition number. In this case, the gradient descent method converges slowly.

Conversely, if FWI only needs to invert a few model parameters, to which the data misfit function is sensitive, we can reduce the condition number of the Hessian matrix and thereby the number of required iterations. Pratt et al. (1998, Appendix A) discuss a point collocation scheme to reparameterize the model space $\mathbf{m}$ for this purpose. In this section, our scheme is to use image-guided interpolation (Hale, 2009a) to reduce the number of model parameters in the calculation of the gradient of the data misfit function. We then use this *image-guided gradient* in FWI.

3.1 Fewer model parameters

Similar to the point collocation scheme, subspace methods (Kennett *et al.*, 1988; Oldenburg *et al.*, 1993) reconstruct the finely- and uniformly-sampled (dense) model $\mathbf{m}$ from a sparse model $\mathbf{s}$ that contains a much smaller number of model parameters than the dense model $\mathbf{m}$:

$$\mathbf{m} = \mathbf{R}\mathbf{s} \,, \tag{9}$$

where $\mathbf{R}$ denotes a linear operator that projects model parameters from the sparse model to the dense model.

Differentiating both sides of equation 9, we have

$$\delta\mathbf{m} = \mathbf{R}\delta\mathbf{s} \,. \tag{10}$$

Then, substituting equation 10 into equation 5, we can reformulate the inverse problem posed in equation 5, with respect to a smaller number of model parameters in the sparse model $\mathbf{s}$, as

$$\mathbf{H}_i\mathbf{R}\delta\mathbf{s}_i = -\mathbf{g}_i \,. \tag{11}$$

However, we cannot solve equation 11 with a solution like $\delta\mathbf{s}_i = -\left(\mathbf{H}_i\mathbf{R}\right)^{-1}\mathbf{g}_i$ in the sparse domain $\mathbf{s}$ because equation 11 is overdetermined, i.e., there are more equations than parameters. Alternatively, we obtain a solution for equation 11 in the sparse domain $\mathbf{s}$:

$$\delta\mathbf{s}_i = -\left(\mathbf{R}^T\mathbf{H}_i\mathbf{R}\right)^{-1}\mathbf{R}^T\mathbf{g}_i \,, \tag{12}$$

where $\mathbf{R}^T$ is the adjoint operator of $\mathbf{R}$. This adjoint operator projects model parameters from the dense model $\mathbf{m}$ to the sparse model $\mathbf{s}$.

Like equation 7, the model update $\delta\mathbf{s}_i$ can be iteratively approximated by replacing the inverse of the

projected Hessian matrix $(\mathbf{R}^T\mathbf{H}_i\mathbf{R})$ with a scalar step length α_i:

$$\mathbf{s}_{i+1} = \mathbf{s}_i - \alpha_i \mathbf{h}_i^{\mathbf{s}} , \tag{13}$$

where the conjugate direction $\mathbf{h}_i^{\mathbf{s}}$ is determined by

$$\begin{aligned}
\mathbf{h}_0^{\mathbf{s}} &= \mathbf{R}^T\mathbf{g}_0 , \\
\beta_i &= \frac{\left(\mathbf{R}^T\mathbf{g}_i\right)^T\left(\mathbf{R}^T\mathbf{g}_i - \mathbf{R}^T\mathbf{g}_{i-1}\right)}{\left(\mathbf{R}^T\mathbf{g}_{i-1}\right)^T\mathbf{R}^T\mathbf{g}_{i-1}} \\
&= \frac{\mathbf{g}_i^T\mathbf{R}\mathbf{R}^T\left(\mathbf{g}_i - \mathbf{g}_{i-1}\right)}{\mathbf{g}_{i-1}^T\mathbf{R}\mathbf{R}^T\mathbf{g}_{i-1}} , \\
\mathbf{h}_i^{\mathbf{s}} &= \mathbf{R}^T\mathbf{g}_i + \beta_i \mathbf{h}_{i-1}^{\mathbf{s}} .
\end{aligned} \tag{14}$$

In equation 13, the step length can again be achieved with a quadratic line-search method. Equation 14 differs from equation 8 in that the gradient $\mathbf{g}_i$ is replaced by $\mathbf{R}^T\mathbf{g}_i$, which implies that equation 13 provides a solution for the FWI problem in the sparse domain $\mathbf{s}$. Because of fewer model parameters involved, the projected Hessian matrix $(\mathbf{R}^T\mathbf{H}_i\mathbf{R})$ can become better-conditioned and thus equation 13 requires fewer iterations than equation 7 to converge to a solution model $\mathbf{s}$.

As noted in equation 9, we can apply the linear operator $\mathbf{R}$ to both sides of equation 13 and thereby project the sparse model update $\delta\mathbf{s}_i$ to obtain the dense model update $\delta\mathbf{m}_i$:

$$\mathbf{m}_{i+1} = \mathbf{m}_i - \alpha_i \mathbf{h}_i^{\mathbf{m}} , \tag{15}$$

where we compute the search direction $\mathbf{h}_i^{\mathbf{m}}$ by projecting the sparse conjugate direction $\mathbf{h}_i^{\mathbf{s}}$ to the dense domain:

$$\begin{aligned}
\mathbf{h}_0^{\mathbf{m}} &= \mathbf{R}\mathbf{h}_0^{\mathbf{s}} = \mathbf{R}\mathbf{R}^T\mathbf{g}_0 , \\
\beta_i &= \frac{\left(\mathbf{R}^T\mathbf{g}_i\right)^T\left(\mathbf{R}^T\mathbf{g}_i - \mathbf{R}^T\mathbf{g}_{i-1}\right)}{\left(\mathbf{R}^T\mathbf{g}_{i-1}\right)^T\mathbf{R}^T\mathbf{g}_{i-1}} \\
&= \frac{\mathbf{g}_i^T\mathbf{R}\mathbf{R}^T\left(\mathbf{g}_i - \mathbf{g}_{i-1}\right)}{\mathbf{g}_{i-1}^T\mathbf{R}\mathbf{R}^T\mathbf{g}_{i-1}} , \\
\mathbf{h}_i^{\mathbf{m}} &= \mathbf{R}\mathbf{R}^T\mathbf{g}_i + \beta_i \mathbf{h}_{i-1}^{\mathbf{m}} .
\end{aligned} \tag{16}$$

Equations 15 and 16 provide a solution for FWI in the dense space $\mathbf{m}$ while taking the advantage of fewer model parameters.

3.2 Choice of R

The projection operator $\mathbf{R}$ can take different forms, including Fourier transform, wavelet transform, cubic splines, etc. Unfortunately, none of these forms accounts for the geological information of the subsurface. In this paper, we implement $\mathbf{R}$ with image-guided interpolation (IGI) (Hale, 2009a), which uses metric tensor fields to guide interpolation of a few sparsely scattered data points, making the interpolant conform to structural features in the gradient image.

3.2.1 Image-guided interpolation

The input of IGI is a set of scattered data, a set

$$\mathcal{F} = \{f_1, f_2, ..., f_K\}$$

of K known sample values $f_k \in \mathbb{R}$ that correspond to a set

$$\chi = \{\mathbf{x}_1, \mathbf{x}_2, ..., \mathbf{x}_K\}$$

of K known sample points $\mathbf{x}_k \in \mathbb{R}^n$. Combining these two sets forms a space (e.g., the sparse model $\mathbf{s}$), in which $\mathcal{F}$ and χ denote sample values and coordinates, respectively. The result of the interpolation is a function $q(\mathbf{x}) : \mathbb{R}^n \rightarrow \mathbb{R}$, such that $q(\mathbf{x}_k) = f_k$. Here, the dense model $\mathbf{m}$ consists of all interpolation points $\mathbf{x}$ and values $q(\mathbf{x})$.

Image-guided interpolation is a two-step process:

$$\mathbf{R} = \mathbf{Q}\mathbf{P} , \tag{17}$$

where $\mathbf{P}$ and $\mathbf{Q}$ denote nearest neighbor interpolation and blended neighbor interpolation, respectively. We follow the steps in Hale (2009a) to describe the details of $\mathbf{P}$ and $\mathbf{Q}$:

(i) $\mathbf{P}$: solve

$$\begin{aligned}
\nabla t(\mathbf{x}) \cdot \mathbf{D}(\mathbf{x}) \nabla t(\mathbf{x}) = 1, \mathbf{x} \notin \chi ; \\
t(\mathbf{x}) = 0, \mathbf{x} \in \chi
\end{aligned} \tag{18}$$

for
$t(\mathbf{x})$: the minimum time from $\mathbf{x}$ to the nearest known sample point $\mathbf{x}_k$, and
$p(\mathbf{x})$: the nearest neighbor interpolant corresponding to f_k, the value of the sample point $\mathbf{x}_k$ nearest to the point $\mathbf{x}$.

(ii) $\mathbf{Q}$: for a specified constant $e \geq 2$ (e.g., $e = 4$ in this paper), solve

$$q(\mathbf{x}) - \frac{1}{e}\nabla \cdot t^2(\mathbf{x})\mathbf{D}(\mathbf{x})\nabla q(\mathbf{x}) = p(\mathbf{x}) \tag{19}$$

for the blended neighbor interpolant $q(\mathbf{x})$.

In equation 18, the metric tensor field $\mathbf{D}(\mathbf{x})$ (van Vliet & Verbeek, 1995; Fehmers & Höcker, 2003) represents structural features of the subsurface, such as structural orientation, coherence, and dimensionality, and therefore the image-guided interpolation result makes geological sense. In n dimensions, each metric tensor field $\mathbf{D}$ is a symmetric positive-definite $n \times n$ matrix (Hale, 2009a). Here, the minimum time $t(\mathbf{x})$ measures a non-Euclidean distance between a sample point $\mathbf{x}_k$ and a interpolation point $\mathbf{x}$. By this measurement, we can determine that a sample point $\mathbf{x}_k$ is nearest to a point $\mathbf{x}$ if the time $t(\mathbf{x})$ to $\mathbf{x}_k$ is less than that to any other sample point.

Letting $\mathbf{p}$ and $\mathbf{q}$ denote vectors that contain all elements in $p(\mathbf{x})$ and $q(\mathbf{x})$, respectively, we can rewrite

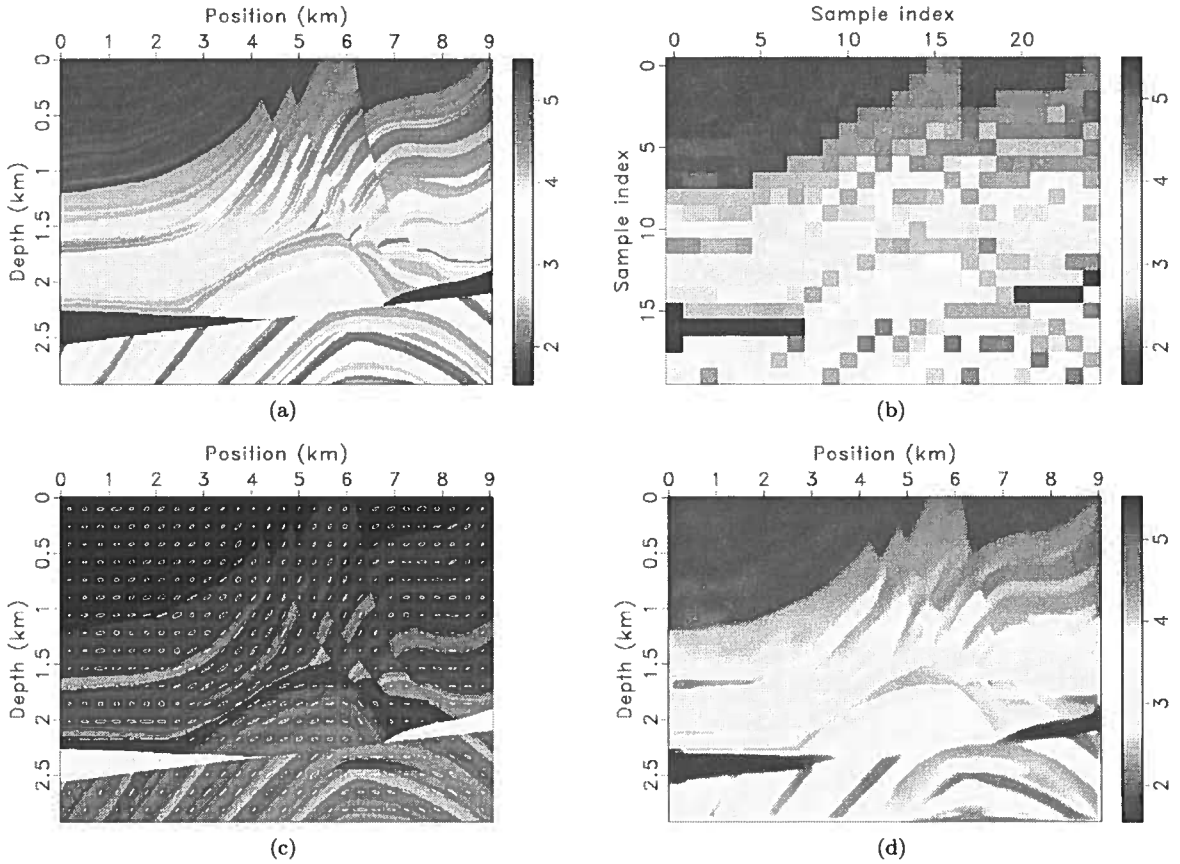

Figure 7. (a) The original Marmousi model, (b) a decimated Marmousi model, with only 0.2% samples remaining, (c) the metric tensor fields illustrated by ellipses, and (d) a Marmousi model produced by image-guided interpolation.

equation 19 in a matrix-vector form:

$$\left(\mathbf{I}+\mathbf{B}^T\mathbf{D}\mathbf{B}\right)\mathbf{q}=\mathbf{p}\,, \tag{20}$$

where $\mathbf{B}$ corresponds to a finite-difference approximation of the gradient operator (Hale, 2009b). Therefore, $\mathbf{q}=\mathbf{Q}\mathbf{p}$, where

$$\mathbf{Q}=\left(\mathbf{I}+\mathbf{B}^T\mathbf{D}\mathbf{B}\right)^{-1}\,, \tag{21}$$

and this inverse can be efficiently approximated by conjugate-gradient iterations because $\mathbf{I}+\mathbf{B}^T\mathbf{D}\mathbf{B}$ is symmetric and positive-definite (SPD). Intuitively, the nearest neighbor interpolation operator $\mathbf{P}$ *scatters* values f_k from sample points $\mathbf{x}_k$ to the interpolation ponits $\mathbf{x}$, and $\mathbf{Q}$ *smooths* the nearest neighbor interpolant $\mathbf{p}$.

Figure 7 illustrates an example of image-guided interpolation with a Marmousi velocity model. This example demonstrates the power of IGI for reducing the number of model parameters. Figure 7a shows the original Marmousi model with 400×500 samples; Figure 7b represents an undersampled Marmousi model, with only 20×25 (0.2%) samples remaining; ellipses in Figure 7c indicate the metric tensor field $\mathbf{D}(\mathbf{x})$ of the Marmousi model; Figure 7d displays the image-guided interpolation result. With IGI, we can reconstruct the Marmousi model in great detail from only a sparsely-sampled model. It is more practical to compute the metric tensor field from migrated images.

3.2.2 Adjoint image-guided interpolation

Note that $\mathbf{Q}^T=\mathbf{Q}$, so we can configure the adjoint image-guided interpolation as

$$\mathbf{R}^T=\mathbf{P}^T\mathbf{Q}^T=\mathbf{P}^T\mathbf{Q}\,. \tag{22}$$

The adjoint operator $\mathbf{R}^T$ is again a two-step process:

(i) $\mathbf{Q}^T$ or $\mathbf{Q}$: solve equation 19 again to *smooth* the input image;

(ii) $\mathbf{P}^T$: solve equation 18 for $t(\mathbf{x})$ and *gather* information from the interpolation points $\mathbf{x}$ to the sample points $\mathbf{x}_k$.

3.3 Synthetic example of image-guided FWI

Because we choose image-guided interpolation as the operator to link the dense model $\mathbf{m}$ and the sparse model $\mathbf{s}$, we refer to the gradient $\mathbf{R}\mathbf{R}^T\mathbf{g}_i$ in equation 16 as the image-guided gradient. We also refer to implementation of FWI using the image-guided gradient as image-guided FWI, which again consists of four steps performed iteratively, beginning with an initial model $\mathbf{m}_0$:

(i) Compute the data difference $\mathbf{d} - \mathbf{F}(\mathbf{m}_i)$;
(ii) Compute the gradient $\mathbf{g}_i$ and the image-guided gradient $\mathbf{R}\mathbf{R}^T\mathbf{g}_i$;
(iii) Search for a step length α_i in the conjugate direction $\mathbf{h}_i^{\mathbf{m}}$;
(iv) Compute the updated model $\mathbf{m}_{i+1}$ using equation 15.

Compared with the four steps of conventional FWI, the only significant difference is the calculation of an image-guided gradient in step (ii). To illustrate the feasibility of image-guided FWI, we test this technique using the previous model with the same experimental settings and compare the image-guided FWI results with conventional FWI results.

In step (i), we start with the same initial model $\mathbf{m}_0$ displayed in Figure 2b, and so we obtain the same data residual $\mathbf{d} - \mathbf{F}(\mathbf{m}_0)$ displayed in Figure 3c.

In step (ii), we first compute the gradient of the data misfit function just like step (ii) in the conventional FWI, and thereby obtain a gradient displayed in Figure 4a that corresponds to the data residual shown in Figure 3c and the current model $\mathbf{m}_0$ shown in Figure 2b, respectively. We then compute the image-guided gradient. To obtain this gradient, one must compute the metric tensor field $\mathbf{D}(\mathbf{x})$ that corresponds to the original gradient $\mathbf{g}_0$ of the data misfit function $E(\mathbf{m})$. Because of the structural coincidence between the migrated image and the gradient, we can obtain the metric tensor field $\mathbf{D}(\mathbf{x})$ from the migrated image. Figure 8a displays ellipses which correspond to the structural orientation of the subsurface over the migrated image. One also needs to choose several sample points, as depicted by red dots in Figure 8b. In this example, we only select 6 samples, two of which are located in the middle of the reflectivities. Figure 8c shows the image-guided gradient $\mathbf{R}\mathbf{R}^T\mathbf{g}_0$ computed in this way for the 1st iteration of image-guided FWI.

In step (iii), we use the same quadratic line-search algorithm to compute a step length α_0. The search direction is determined by conjugate gradients in equation 16.

Finally, in step (iv), we update the current velocity model according to equation 15. Figure 9a is the change $\delta\mathbf{m}$ in the velocity model computed in the 1st iteration of image-guided FWI; this change is simply a scaled version of the image-guided gradient in step (ii). Figure 10a depicts the data residual of shot number 13 after the 1st

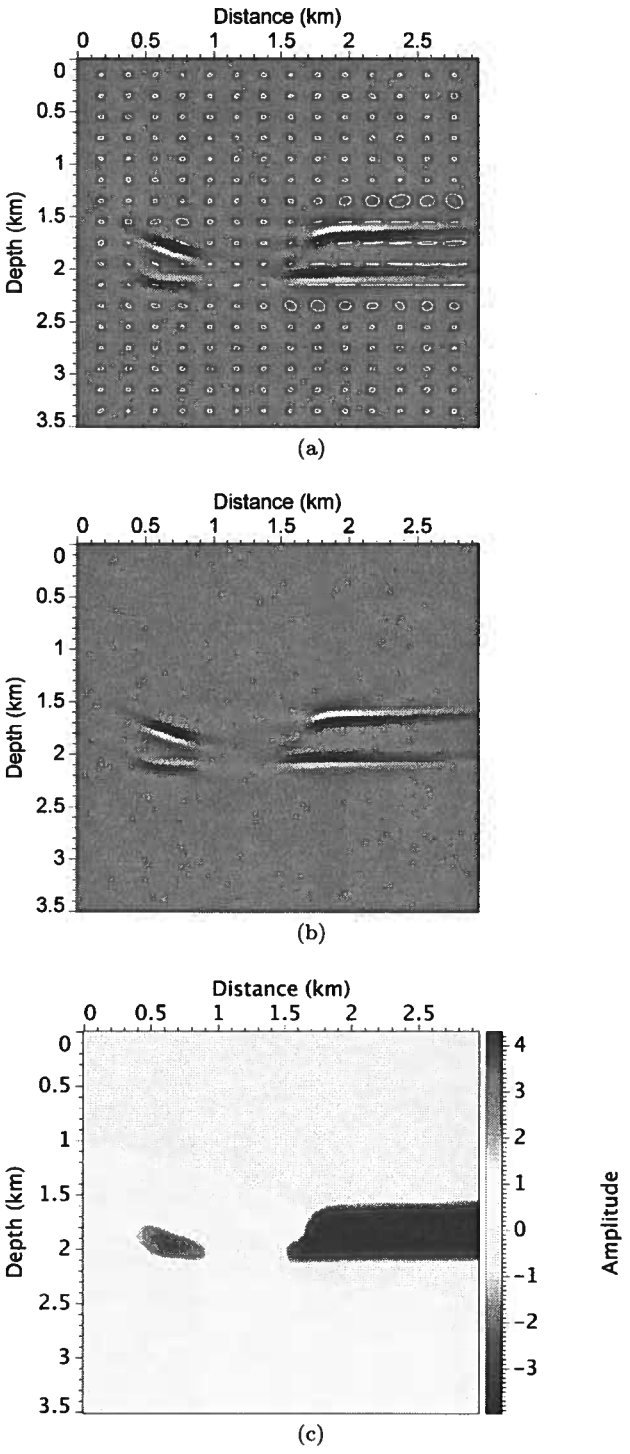

Figure 8. (a) The metric tensor field and (b) selected sample locations overlaid on the migrated image. (c) Image-guided gradient $\mathbf{R}\mathbf{R}^T\mathbf{g}_0$.

iteration; this data residual starts next iteration in step (i).

On the one hand, image-guided FWI with the image-guided gradient (shown in Figure 8c), can recover, even in the 1st iteration, most velocity anomalies, as indicated by Figure 9a. On the other hand, a comparison between the data residual shown in Figure 10a and the data residual shown in Figure 6a indicates that the 1st iteration of image-guided FWI does not reduce the data misfit as significantly as the conventional FWI does. This is because the image-guided gradient $\mathbf{R}\mathbf{R}^T\mathbf{g}_0$ employed in image-guided FWI cannot clearly depict the boundaries of the velocity anomalies due to the smoothing process $\mathbf{Q}$ embedded in the second step of the image-guided interpolation $\mathbf{R}$.

We solve this problem that is apparent in the 1st iteration of image-guided FWI by running several iterations of conventional FWI to enhance the boundaries of velocity anomalies. Figure 9b and c are accumulated velocity updates after the 2nd and 5th iterations, respectively. With enhanced boundaries, the data misfit corresponding to shot number 13 significantly decreases, as shown in Figure 10b and c.

4 DISCUSSION

The synthetic example demonstrates the process of image-guided FWI, which only changes one step in the four-step implementation of conventional FWI. Using an image-guided gradient, image-guided FWI speeds up the convergence of FWI.

4.1 Limitation of line search

We used a quadratic line-search method in this paper to seek a scalar step length that determines how much the velocity model can update. An ideal situation for this quadratic line search would be that it only requires 2 attempts of gradient descent to calculate a step length that decreases the data misfit function. Unfortunately, in many cases, even after many attempts of gradient descent, FWI cannot find a step length to decrease the data misfit function. Because each gradient descent requires a simulation of seismic wavefields of all sources in a full model space, the line-search approach is quite expensive. Figure 1 clearly indicates the failure of the conventional FWI in searching for a proper step length in the 2nd and 4th iterations, within 5 trials of gradient descent.

Although more sophisticated line-search methods may help mitigate the limitations of the quadratic line search, we offer the option of image-guided FWI to avoid the same limitations, as indicated by the change of the data misfit function in Figure 1. Image-guided FWI successfully finds a step length to decrease the data misfit

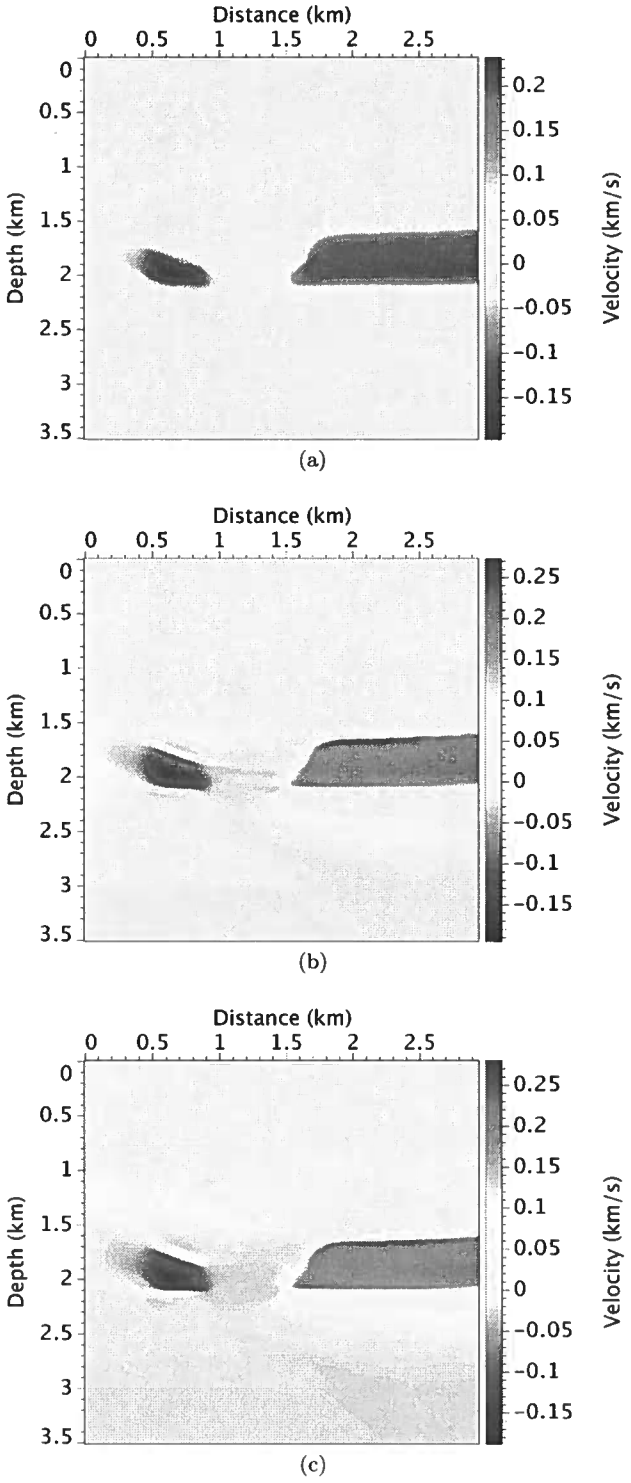

Figure 9. Accumulated velocity updates after (a) 1 iteration, (b) 2 iterations and (c) 5 iterations. In (a)-(c), the image-guided gradient is only used in the first iteration.

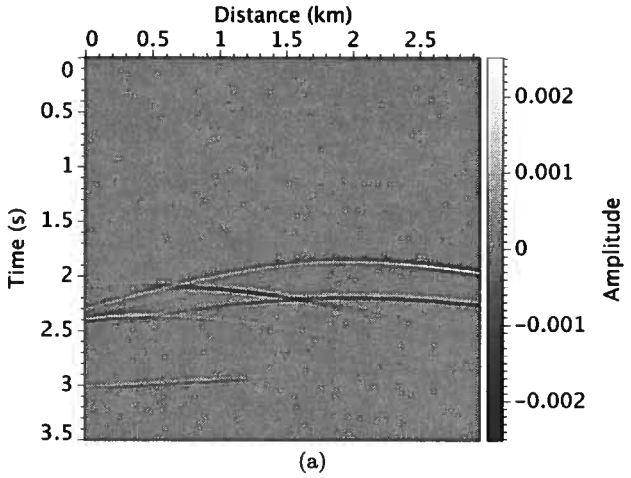

Figure 10. Data residual after (a) 1 iteration, (b) 2 iterations and (c) 5 iterations. In (a)-(c), the image-guided gradient is only used in the first iteration.

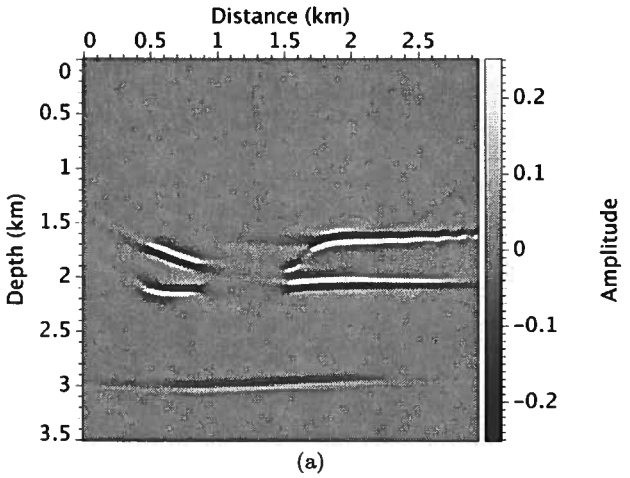

Figure 11. Migrated images with (a) the initial model, (b) the FWI model after 5 iterations, and (c) the image-guided FWI model after 5 iterations. Two red lines in each figures indicate the correct depth of reflectors.

function in the first 10 iterations, with 5 attempts of gradient descent.

4.2 Low frequencies

As mentioned before, the absence of low frequencies in data is one of the major reasons that causes local minima and cycle-skipping, and thereby prevents FWI from converging to a correct model. Multiscale approaches are proposed to solve the problem by gradually adding high-frequency details to inversion results obtained from low-frequency data. Although those multiscale approaches often start from impractically low frequencies, a question remains. Do low frequencies in data really help? As noted earlier, the velocity updated by FWI maintains imprints of the seismic wavelet. For this reason, even though one can take advantage of low frequencies in data, wavelet imprints remain and counteract the velocity updates. Migrated images can explain this counteraction.

Figure 11 compares migrated images with the initial model shown in Figure 2b, the updated model with changes shown in Figure 5c, and the updated model with changes shown in Figure 9c, respectively. Because of velocity anomalies, deeper reflectors in Figure 11a do not locate at the correct depth; these deeper reflectors in Figure 11b appear at almost the same position as in Figure 11a. This implies that the velocity updated by conventional FWI cannot correct the traveltime mismatch in the data set. One reason for this is the wavelet imprint that appears in the velocity updates shown in Figure 5. Only the migrated image, with the image-guided FWI model, places these deeper reflectors at the correct depth, as indicated by Figure 11c.

5 CONCLUSIONS

We have proposed image-guided FWI for speeding up the convergence and mitigating the absence of low frequencies. In contrast to multiscale approaches that take advantage of unliable low frequencies in the data space, our method reduces the number of model parameters and yields low frequencies in the model space by computing the image-guided gradient with image-guided interpolation and its adjoint. The synthetic example shown in this paper illustrates that image-guided FWI improves both inversion speed and quality without appending significant additional cost. Because the structural features of the subsurface are taken into consideration, models updated by image-guided FWI make good geological sense. Further investigation on criteria of selecting sample points is needed for image-guided interpolation.

6 ACKNOWLEDGMENT

This work was done in part during Yong Ma's 2009 summer internship with ConocoPhillips; Yong Ma wants to thank Leming Qu from Boise State University for many thoughtful discussions during the internship. This work is partially sponsored by the research agreement between ConocoPhillips Company and Colorado School of Mines (SST-20090254-SRA). Special thanks to Diane Witters for polishing this manuscript.

REFERENCES

Boonyasiriwat, C., Valasek, P., Routh, P., Cao, W., Schuster, G. T., and Macy, B., 2009, An efficient multiscale method for time-domain waveform tomography: Geophysics, **74**, no. 6, WCC59–WCC68.

Bunks, C., 1995, Multiscale seismic waveform inversion: Geophysics, **60**, no. 5, 1457.

Cohen, A. I., 1972, Rate of convergence of several conjugate gradient algorithms: SIAM Journal on Numerical Analysis, **9**, no. 2, 248–259.

Fehmers, G. C., and Höcker, C. F. W., 2003, Fast structural interpretation with structure-oriented filtering: Geophysics, **68**, no. 4, 1286–1293.

Gong, B., Chen, G., Yingst, D., and Bloor, R., 2008, 3D waveform inversion based on reverse time migration engine: SEG Technical Program Expanded Abstracts, **27**, no. 1, 1900–1903.

Hale, D., 2009a, Image-guided blended neighbor interpolation of scattered data: SEG Technical Program Expanded Abstracts, **28**, no. 1, 1127–1131.

——— 2009b, Structure-oriented smoothing and semblance: CWP Report, **635**, no. 635.

Kennett, B., Sambridge, M., and Williamson, P., 1988, Subspace methods for large inverse problems with multiple parameter classes: Geophysical Journal, **94**, no. 2, 237–247.

Krebs, J. R., Anderson, J. E., Hinkley, D., Neelamani, R., Lee, S., Baumstein, A., and Lacasse, M.-D., 2009, Fast full-wavefield seismic inversion using encoded sources: Geophysics, **74**, no. 6, WCC177–WCC188.

Meng, Z., and Scales, J. A., 1996, 2D tomography in multi-resolution analysis model space: SEG Technical Program Expanded Abstracts, **15**, no. 1, 1126–1129.

Meng, Z., Qu, L., Ma, Y., and Hale, D., 2009, Dip guided full waveform inversion for high resolution velocity:, pages 2009 SEG Post–convention Workshop in W8: Full wave–equation methods for complex imaging challenges.

Meng, Z., 2009, Dip guided full waveform inversion: US Patent pending, pages 41279–USPRO, ConocoPhillips.

Mora, P., 1989, Inversion = migration + tomography: Geophysics, **54**, no. 12, 1575.

Nocedal, J., and Wright, S. J., 2000, Numerical optimization: , Springer.

Oldenburg, D., McGillvray, P., and Ellis, R., 1993, Generalized subspace methods for large-scale inverse problems: Geophysical journal international, **114**, no. 1, 12–20.

Operto, S., Ravaut, C., Improta, L., Virieux, J., Herrero, A., and Dell'Aversana, P., 2004, Quantitative imaging of complex structures from dense wide-aperture seismic data by multiscale traveltime and waveform inversions: a case study: Geophysical Prospecting, **52**, no. 6, 625–651.

Pratt, R., Shin, C., and Hicks, G., 1998, Gauss-Newton and full newton methods in frequency-space seismic waveform inversion: Geophysical Journal International, **133**, no. 2, 341–362.

Pratt, R. G., 1999, Seismic waveform inversion in the frequency domain, part 1: Theory and verification in a physical scale model: Geophysics, **64**, no. 3, 888.

Sava, P., and Biondi, B., 2004a, Wave-equation migration velocity analysis. i. theory: Geophysical Prospecting, **52**, no. 6, 593–606.

——— 2004b, Wave-equation migration velocity analysis. II. subsalt imaging examples: Geophysical Prospecting, **52**, no. 6, 607–623.

Shin, C., and Ha, W., 2008, A comparison between the behavior of objective functions for waveform inversion in the frequency and laplace domains: Geophysics, **73**, no. 5, VE119–VE133.

Shin, C., and Min, D., 2006, Waveform inversion using a logarithmic wavefield: Geophysics, **71**, no. 3, R31–R42.

Sirgue, L., and Pratt, R. G., 2004, Efficient waveform inversion and imaging: A strategy for selecting temporal frequencies: Geophysics, **69**, no. 1, 231.

Stork, C., 1992, Reflection tomography in the postmigrated domain: Geophysics, **57**, no. 5, 680–692.

Symes, W. W., 2008, Migration velocity analysis and waveform inversion: Geophysical Prospecting, **56**, no. 6, 765–790.

Tarantola, A., and Valette, B., 1982, Generalized nonlinear inverse problems solved using the least-squares criterion: Reviews of Geophysics, **20**, no. 2, 219–232.

Tarantola, A., 1984, Inversion of seismic-reflection data in the acoustic approximation: Geophysics, **49**, no. 8, 1259–1266.

Tarantola, A., 1986, A strategy for nonlinear elastic inversion of seismic reflection data: Geophysics, **51**, no. 10, 1893—1903.

Tarantola, A., 2005, Inverse problem theory and methods for model parameter estimation: , Society for Industrial and Applied Mathematics.

Tromp, J., Tape, C., and Liu, Q., 2005, Seismic tomography, adjoint methods, time reversal and banana-doughnut kernels: Geophysical Journal International, **160**, no. 1, 195–216.

van Vliet, L. J., and Verbeek, P. W., 1995, Estimators for orientation and anisotropy in digitized images: Proceeding of the First Annual Conference of the Advanced School for Computing and Imaging, pages 442–450.

Vasco, D., and Majer, E., 1993, Wavepath travel-time tomography: Geophysical Journal International, **115**, no. 3, 1055–1069.

Vigh, D., and Starr, E., 2008, 3D prestack plane-wave, full-waveform inversion: Geophysics, **73**, no. 5, VE135–VE144.

Wheeler, J., and Wilton, D., 1988, Comparison of convergence rates of the conjugate gradient method applied to various integral equation formulations: Comparison of convergence rates of the conjugate gradient method applied to various integral equation formulations:, Antennas and Propagation Society International Symposium, 229–232.

Woodward, M. J., 1992, Wave-equation tomography: Geophysics, **57**, no. 1, 15–26.

Yilmaz, O., and Chambers, R., 1984, Migration velocity analysis by wave-field extrapolation: Geophysics, **49**, no. 10, 1664–1674.

Zelt, C. A., and Barton, P. J., 1998, Three-dimensional seismic refraction tomography: A comparison of two methods applied to data from the faeroe basin: J. Geophys. Res., **103**, no. B4, 7187–7210.

Velocity analysis using weighted semblance

Simon Luo & Dave Hale
Center for Wave Phenomena, Colorado School of Mines, Golden, CO 80401, USA

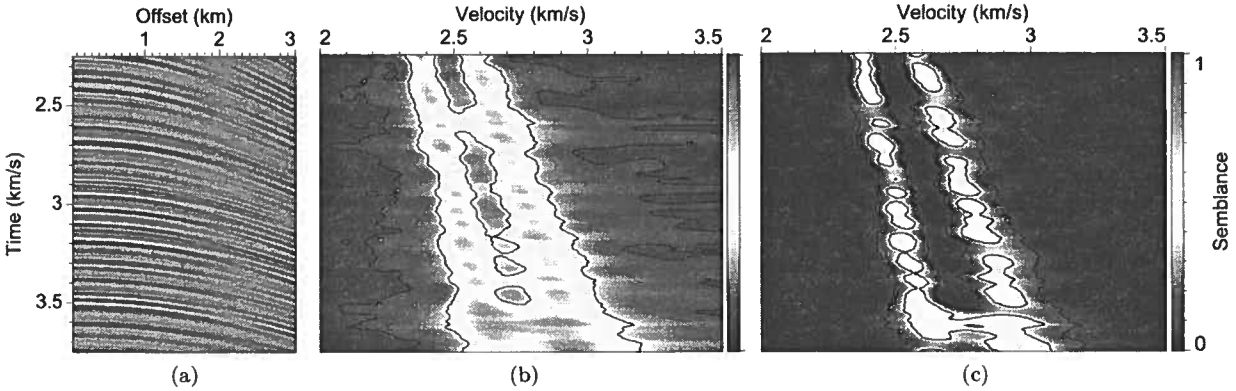

Figure 1. A synthetic common midpoint gather (a), conventional semblance (b) and weighted semblance (c) velocity spectrum.

ABSTRACT

Increasing the resolution of semblance-based velocity spectra, or semblance spectra, can improve the accuracy of normal moveout velocity estimates. The resolution of semblance spectra depends on the sensitivity of semblance to changes in velocity. By weighting terms in the semblance calculation that are more sensitive to changes in velocity, we can increase resolution.

Our implementation of weighted semblance is a straightforward extension of conventional semblance. Somewhat surprisingly, we increase resolution by choosing a weighting function that *minimizes* semblance. Compared to conventional semblance, weighted semblance better distinguishes semblance peaks for interfering events.

Key words: semblance resolution velocity analysis

1 INTRODUCTION

Normal moveout (NMO) velocity analysis using semblance spectra (Taner & Koehler, 1969) is an important first step toward building a velocity model. The accuracy of the velocity model depends on one's ability to pick the correct velocity, which in turn depends on the accuracy and resolution of the semblance spectrum. In cases involving interfering events such as those shown in the common midpoint (CMP) gather in Figure 1a, it may be difficult to distinguish two sets of semblance peaks in the conventional semblance spectrum shown in Figure 1b. In comparison, it is easier to differentiate semblance peaks and pick the correct NMO velocity in the higher-resolution weighted semblance spectrum shown in Figure 1c.

Semblance is a normalized coherency coefficient. It has been shown that emphasizing terms in a coherency coefficient calculation that are sensitive to changes in velocity can increase the resolution of the corresponding velocity spectra. For example, Celis & Larner (2002) introduce a selective-correlation sum that improves the resolution of velocity spectra by discarding crosscorrelations between traces with relatively small differential moveout of events. Selective-correlation is effectively a weighted crosscorrelation sum with weights of either zero or unity, depending on the differential moveout between traces.

We can likewise increase the resolution of semblance spectra by weighting terms in the conventional semblance calculation. Unlike Celis and Larner, however, we do not discard terms in the semblance calculation but instead weight all terms on the basis of their sensitivity to changes in velocity. Our implementation of *weighted semblance* is based on work presented in Hale (2009). Hale uses a weighted semblance coefficient to prevent smoothing of seismic images across faults. We do something different, i.e. increase resolution, by using a different weighting scheme.

In this paper we describe a method for computing weighted semblance for the purpose of increasing resolution of semblance spectra. The method is easy to implement, and its computational cost is comparable to that of conventional semblance.

2 SEMBLANCE METHODS

Weighted semblance is a straightforward extension of conventional semblance. In this section, we will first discuss conventional semblance, and we will introduce our implementation of weighted semblance. We will then derive the weighting function and show how it is used to increase resolution.

2.1 Conventional semblance

Conventional semblance is a normalized coherency measure that was first defined by Taner & Koehler (1969). A comparison of semblance and other coherency measures can be found in Neidell & Taner (1971). Semblance is routinely used to estimate NMO velocity as a function of zero-offset time. Following normal moveout correction of a CMP gather, semblance as defined by Neidell and Taner is computed as

$$s_{NT}[i] = \frac{\sum_{j=i-M}^{i+M}\left(\sum_{k=0}^{N-1} q[j,k]\right)^2}{N\sum_{j=i-M}^{i+M}\sum_{k=0}^{N-1} q[j,k]^2}, \qquad (1)$$

where i and j are time sample indices, k is a trace number, and $q[j,k]$ is the trace amplitude at time index j and trace number k of the NMO-corrected gather. The inner sums over k correspond to N NMO-corrected traces in a CMP gather, while the outer sums correspond to a time-smoothing window with length $2M+1$ centered at time index i. Here, the time-smoothing is performed by a boxcar filter.

In general, we are free to use any time-smoothing filter, but in practice, it is often a good idea to replace a boxcar filter with one that decays more smoothly. For the examples shown in this paper, the boxcar filter is replaced with a two-sided decaying exponential filter. We can represent the time-smoothing filter using an additional weighting function $h[j]$. The derivations are independent of the choice of $h[j]$, so its exact form is not important. We rewrite Neidell and Taner's conventional semblance as

$$s_c[i] = \frac{\sum_j h[i-j]\left(\sum_k q[j,k]\right)^2}{N\sum_j h[i-j]\sum_k q[j,k]^2}, \qquad (2)$$

where it is assumed that the unspecified summation limits include all indices for which the summation terms are defined.

The semblance value reflects how well the moveout path corresponding to the trial NMO velocity fits the moveout of signal in the data. A good fit produces a peak in the semblance spectrum, whereas a poor fit produces semblance values closer to zero. Assuming there is no noise and no signal amplitude variation with offset, semblance is maximized when the values of $q[j,k]$ do not vary with index k. That is, $s[i] = 1$ when the NMO-corrected events are aligned across traces at time index i.

The resolution of semblance spectra depends on the sensitivity of NMO times to changes in velocity. If a small change in trial velocity results in a relatively large change in NMO time, the semblance value will change rapidly with the mismatch between the NMO times corresponding to the trial velocity and the correct velocity. The greater the change in NMO time for a change in trial velocity, the higher the resolution of the semblance spectrum.

2.2 Conventional semblance rewritten

Before we consider weighted semblance, let us introduce an alternative expression for conventional semblance. We express conventional semblance as a normalized correlation coefficient by first defining a reference trace $r[j]$ as a summation over trace number (equivalently, a stack over offset) of the NMO-corrected traces in the CMP gather:

$$r[j] \equiv \sum_k q[j,k]. \qquad (3)$$

To simplify notation, we also define

$$\begin{aligned} C_{rq}[i] &\equiv \sum_j h[i-j]\sum_k r[j]q[j,k], \\ C_{rr}[i] &\equiv \sum_j h[i-j]\sum_k r[j]^2, \\ C_{qq}[i] &\equiv \sum_j h[i-j]\sum_k q[j,k]^2. \end{aligned} \qquad (4)$$

Conventional semblance $s_c[i]$ can then be written as

$$s_c[i] = \frac{C_{rq}[i]^2}{C_{rr}[i]C_{qq}[i]}. \quad (5)$$

Equation 5 and equation 2 are equivalent expressions for conventional semblance.

2.3 Weighted semblance

To obtain weighted semblance, we modify conventional semblance by introducing weights $w[j,k]$ into equations 4:

$$\begin{aligned} W_{rq}[i] &\equiv \sum_j h[i-j] \sum_k w[j,k] r[j] q[j,k], \\ W_{rr}[i] &\equiv \sum_j h[i-j] \sum_k w[j,k] r[j]^2, \\ W_{qq}[i] &\equiv \sum_j h[i-j] \sum_k w[j,k] q[j,k]^2. \end{aligned} \quad (6)$$

Then, weighted semblance $s_w[i]$ is given by

$$s_w[i] = \frac{W_{rq}[i]^2}{W_{rr}[i]W_{qq}[i]}. \quad (7)$$

Weighted semblance is clearly equal to conventional semblance for $w[j,k] = 1$. Moreover, it can be shown using the Cauchy-Schwarz inequality that weighted semblance is bounded between zero and one if the weights $w[j,k]$ and $h[j]$ are non-negative.

2.4 Weighting function

We use a weighting function $w[j,k]$ to emphasize terms in the semblance calculation that are most sensitive to changes in velocity.

The form of the weighting function should reflect the change in NMO time for a given change in velocity; i.e., the weights should vary with both offset and time. Consider the first-order Taylor series expansion of the hyperbolic moveout equation about the unknown correct velocity $\tilde{v}$:

$$t[j,k] = \sqrt{\tau[j]^2 + \tilde{\gamma} x[k]^2} + \frac{x[k]^2}{2\sqrt{\tau[j]^2 + \tilde{\gamma} x!k]2}} (\gamma - \tilde{\gamma}), \quad (8)$$

where $\tau[j]$ is the zero-offset time at time index j, $x[k]$ is the offset at trace number k, $\gamma \equiv 1/v^2$, and $\tilde{\gamma} \equiv 1/\tilde{v}^2$. The correct time is given by $\tilde{t}[j,k] = \sqrt{\tau[j]^2 + \tilde{\gamma} x[k]^2}$, so we can rewrite equation 8 as

$$t[j,k] - \tilde{t}[j,k] = \frac{x[k]^2}{2\tilde{t}[j,k]} (\gamma - \tilde{\gamma}). \quad (9)$$

Thus, the change in NMO time that results from a small change in velocity is proportional to offset squared and inversely proportional to time.

To reflect this proportionality, we choose a weighting function $w[j,k]$ that has a similar dependency on offset and time:

$$w[j,k] = a + b\frac{c[j]x[k]^2}{t[j,k]}, \quad (10)$$

where a and b are parameters to be determined, and $c[j]$ is calculated as the ratio of the zero-offset time to the average offset squared:

$$c[j] = \frac{\tau[j]N}{\sum_k x[k]^2}. \quad (11)$$

Multiplying by $c[j]$ ensures that b is unitless.

The relative values of the parameters a and b in equation 10 effectively determine how the far offsets are weighted. In cases where we expect large weights for the farthest offsets, the ratio of b to a must approach infinity. To satisfy this condition more easily, we choose

$$a = 1 - b, \quad (12)$$

so that

$$w[j,k] = 1 - b + b\frac{c[j]x[k]^2}{t[j,k]}. \quad (13)$$

In addition, we allow b values only between zero and one. Bounding b ensures that the weighting function is non-negative, which is sufficient for weighted semblance to remain normalized between zero and one.

After substituting equation 13 for $w[j,k]$ in equations 6, we have for weighted semblance

$$s_w[i] = \frac{W_{rq}[i]^2}{W_{rr}[i]W_{qq}[i]}, \quad (14)$$

where

$$\begin{aligned} W_{rq}[i] &= (1-b)C_{rq}[i] + bB_{rq}[i], \\ W_{rr}[i] &= (1-b)C_{rr}[i] + bB_{rr}[i], \\ W_{qq}[i] &= (1-b)C_{qq}[i] + bB_{qq}[i], \end{aligned} \quad (15)$$

where $C_{rq}[i]$, $C_{rr}[i]$, and $C_{qq}[i]$ are defined in equations 4, and $B_{rq}[i]$, $B_{rr}[i]$, and $B_{qq}[i]$ are defined as

$$\begin{aligned} B_{rq}[i] &\equiv \sum_j h[i-j] \sum_k \frac{c[j]x[k]^2}{t[j,k]} r[j] q[j,k], \\ B_{rr}[i] &\equiv \sum_j h[i-j] \sum_k \frac{c[j]x[k]^2}{t[j,k]} r[j]^2, \\ B_{qq}[i] &\equiv \sum_j h[i-j] \sum_k \frac{c[j]x[k]^2}{t[j,k]} q[j,k]^2. \end{aligned} \quad (16)$$

Weighted semblance is now a function of the parameter b.

Note that although the weighting function is derived from the hyperbolic moveout equation, we do not make any assumptions about how the seismic data are NMO-corrected. Because semblance is calculated after NMO correction, we are free to use any moveout equa-

tion, hyperbolic or non-hyperbolic, to correct the data. Our method for increasing resolution works in either case.

2.5 Increasing resolution

To increase the resolution of semblance spectra, we minimize semblance with respect to b. Recall that in the case where the trial velocity equals the correct velocity, semblance is calculated along what are assumed to be constant trace amplitudes, i.e., amplitude is independent of trace number.

If amplitude $q[j,k]$ is independent of trace index k, then $q[j,k] = r[j]/N$ can be pulled out of the summation over k in equations 4 and equations 16. Then, semblance is unity, regardless of the weighting function. Because semblance peaks where $s_c[i] = 1$ are not influenced by the weighting function, we can increase the resolution of semblance spectra by minimizing semblance away from the peaks.

To minimize semblance $s_w[i]$ for any time index i, we set the first derivative with respect to b equal to zero:

$$\frac{ds_w(b)}{db} = 0. \tag{17}$$

Solving this equation, we find that semblance as a function of b has two stationary points:

$$b_1 = \frac{C_{rq}[i]}{C_{rq}[i] - B_{rq}[i]}, \tag{18}$$

$$b_2 = \left(1 + \frac{2C_{rq}[i]B_{rr}[i]B_{qq}[i] - B_{rq}[i]A[i]}{2B_{rq}[i]C_{rr}[i]C_{qq}[i] - C_{rq}[i]A[i]}\right)^{-1}, \tag{19}$$

where

$$A[i] = C_{rr}[i]B_{qq}[i] + C_{qq}[i]B_{rr}[i]. \tag{20}$$

A typical plot of $s_w(b)$ is shown in Figure 2. Note that one stationary point is a local minimum while the other is a local maximum. Also, note that stationary point b_1 always gives a semblance of zero. Although Figure 2 shows b_1 as a local minimum and b_2 as a local maximum, this is not always the case. Depending on the values of equations 4 and equations 16, in some cases b_1 may be a local maximum and b_2 a local minimum.

When calculating weighted semblance, we choose the stationary point that corresponds to the local minimum. Let us define

$$R_{rq}[i] \equiv \frac{C_{rq}[i]}{C_{rq}[i] - B_{rq}[i]},$$

$$R_{rr}[i] \equiv \frac{C_{rr}[i]}{C_{rr}[i] - B_{rr}[i]},$$

$$R_{qq}[i] \equiv \frac{C_{qq}[i]}{C_{qq}[i] - B_{qq}[i]}. \tag{21}$$

These ratios give the b values of the zero and the two discontinuities in the plot of semblance as a function of b. Moreover, their relative values determine which of the two stationary points is a local minimum. It can be shown that b_2 corresponds to a local minimum if either

$$R_{rr}[i] < R_{rq}[i] < R_{qq}[i], \tag{22}$$

or

$$R_{qq}[i] < R_{rq}[i] < R_{rr}[i]. \tag{23}$$

Thus, if b is between zero and one, we minimize semblance by choosing stationary point b_2 in cases where either inequality 22 or inequality 23 holds, and by choosing stationary point b_1 in all other cases.

If b is not between zero and one, we simply choose the minimum value of $s_w(0)$ and $s_w(1)$. We choose the minimum because we are increasing resolution by minimizing semblance.

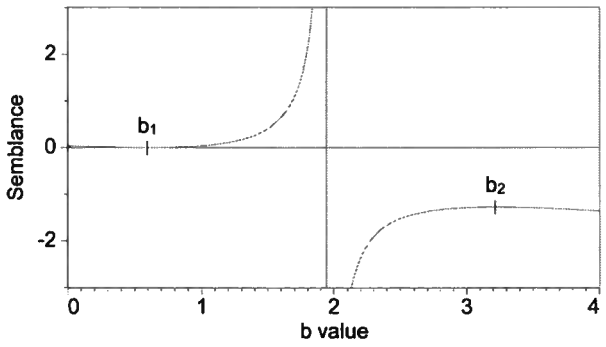

Figure 2. Plot of semblance as a function of b.

3 RESULTS

To illustrate the action of the weighting function $w[j,k]$ on the resolution of semblance spectra, we compare weighted semblance to conventional semblance for synthetic CMP gathers and for a field CMP gather from the North Viking Graben.

3.1 Synthetic gather

For all synthetic data examples, the CMP gathers have cable length 3 km, receiver group interval 50 m, and a Ricker wavelet peak frequency of 25 Hz.

The first CMP gather consists of a series of synthetic primary reflections with linearly increasing NMO velocities. The velocity increases from 2 km/s at zero-offset time $\tau = 0$ s to 3 km/s at $\tau = 4$ s. Figure 3a depicts the CMP gather, and Figure 3b depicts the b values used in the weighting function $w[j,k]$. In the conventional and weighted semblance spectrum shown in Figures 3c and 3d, respectively, the contour lines mark $s = 0.1$ and $s = 0.4$. Note the spread in spectral amplitude across a range of velocities in the conventional semblance spectra. In comparison, in the weighted semblance spectrum, both the spread in amplitude and the area enclosed by the contour lines have decreased.

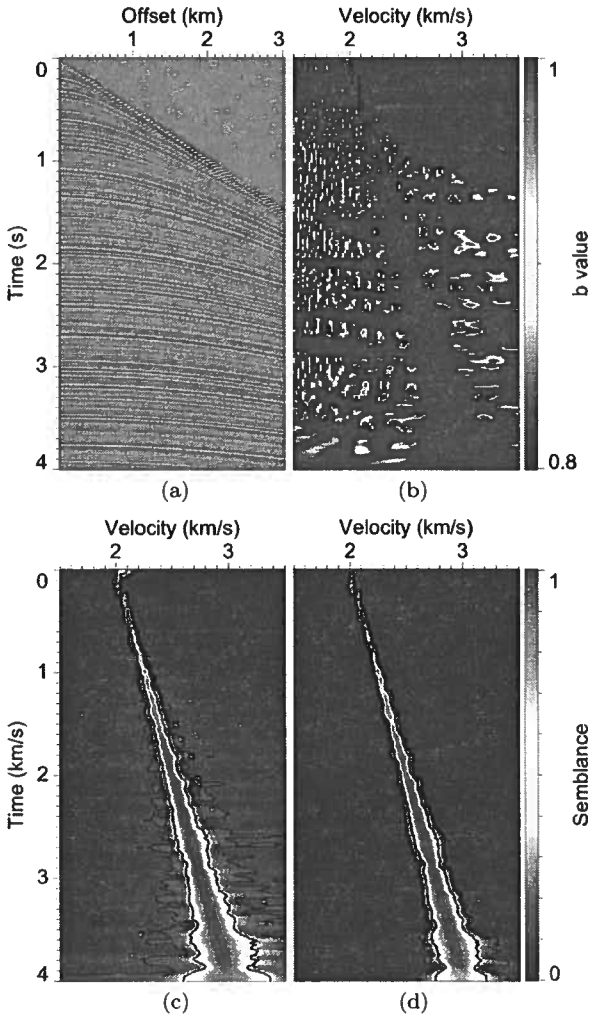

Figure 3. Synthetic CMP gather (a), plot of b values (b), conventional (c) and weighted (d) semblance spectrum.

We can directly compare semblance peaks by plotting semblance as a function of trial velocity for a chosen zero-offset time. Figure 4 depicts this plot for the first synthetic CMP gather at zero-offset time $\tau = 3.2$ s. In the figure, we see that minimizing semblance has reduced the semblance values at velocities away from the peak. As a result, the weighted semblance peak is sharper than the conventional semblance peak.

3.2 Synthetic gather with multiples

We add a second set of reflections to the synthetic CMP gather shown in Figure 3a to simulate interfering multiples. The second set of reflections have NMO velocities that increase linearly from 1.98 km/s at zero-offset time $\tau = 0$ s to 2.70 km/s at $\tau = 4$ s.

Figure 5a depicts the CMP gather, and Figure 5b depicts a plot of the b values used in the weighting function $w[j,k]$. Figures 5c and 5d depict the conventional and weighted semblance spectrum, respectively. As confirmed by the semblance curve in Figure 6, the weighted semblance spectrum affords higher resolution as it better distinguishes the two sets of semblance peaks. Again, minimizing semblance has reduced the semblance values at velocities away from the peaks.

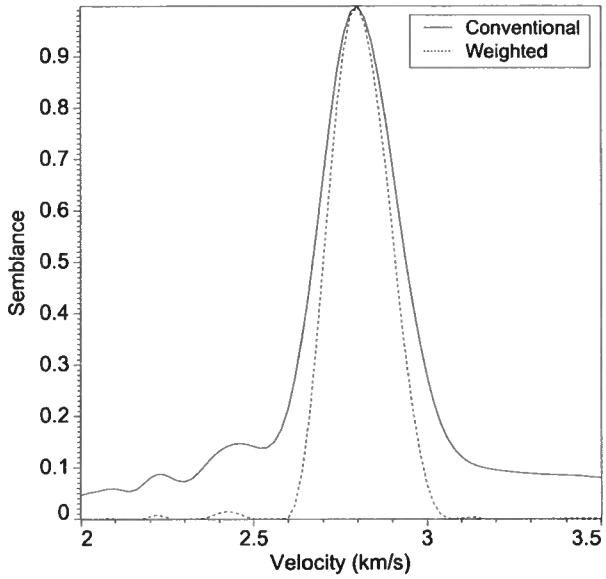

Figure 4. Plot of semblance as a function of trial velocity at $\tau = 3.2$ s.

Note that the weighted semblance peaks have smaller amplitude compared to the conventional semblance peaks. This is a result of minimizing semblance. A necessary assumption for this minimization was that the NMO-corrected trace amplitudes are constant for the correct trial velocity. For our synthetic data, and for field data especially, this assumption is incorrect. Thus, in minimizing semblance, we actually expect the peak amplitudes to decrease in most cases.

3.3 Synthetic gather with multiples and noise

Next we consider a synthetic gather contaminated by additive noise. For this example, we added bandlimited random noise to the CMP gather shown in Figure 5a with a signal-to-noise ratio of 1. Here, the signal-to-noise ratio is computed as the ratio of the root-mean-square (rms) amplitude of the signal to the rms amplitude of the noise.

Figure 7a depicts the noise-contaminated synthetic CMP gather, and Figure 7b plots the b values used in the weighting function. Figure 7c depicts the conventional semblance spectrum, and Figure 7d depicts the weighted semblance spectrum.

Again, we see an increase in resolution and a decrease in overall amplitude going from weighted to con-

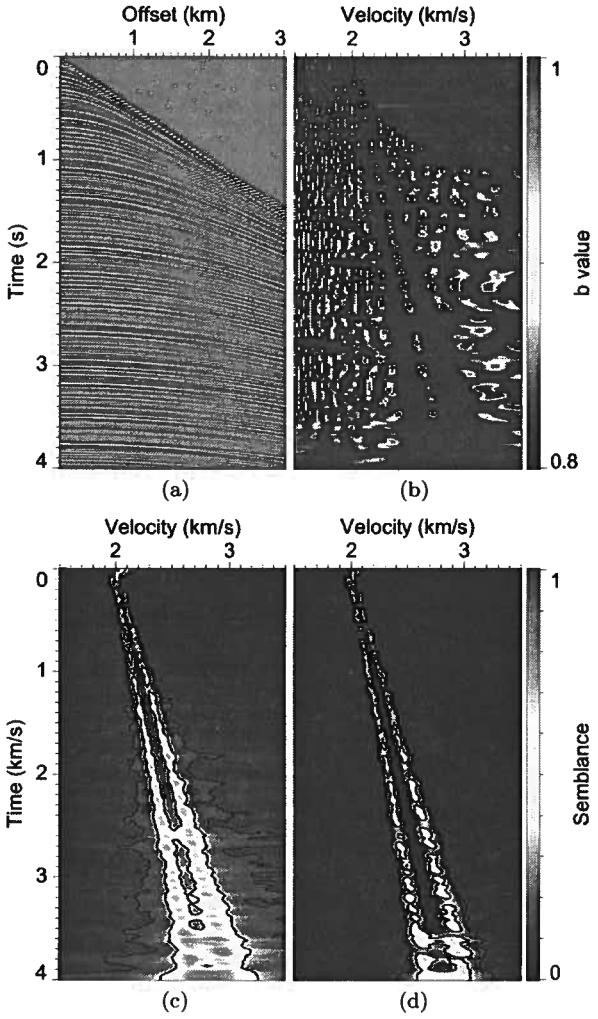

Figure 5. Synthetic CMP gather (a), plot of b values (b), conventional (c) and weighted (d) semblance spectrum.

ventional semblance. However, because the conventional semblance peaks have relatively low amplitudes to begin with, the reduction in amplitude of the weighted semblance peaks has almost completely eliminated the $s = 0.4$ contour line in Figure 7d.

3.4 Viking Graben example

Our final example compares conventional and weighted semblance for a CMP gather taken from a 2D seismic dataset from the North Viking Graben. The cable length is 3 km, and the offset sampling interval is 50 m. The multiples in the data have been suppressed in order to make the semblance peaks easier to identify.

Figure 8a depicts the CMP gather, while Figure 8b depicts a plot of the b values used in the semblance weighting function. Figure 8c shows the conventional

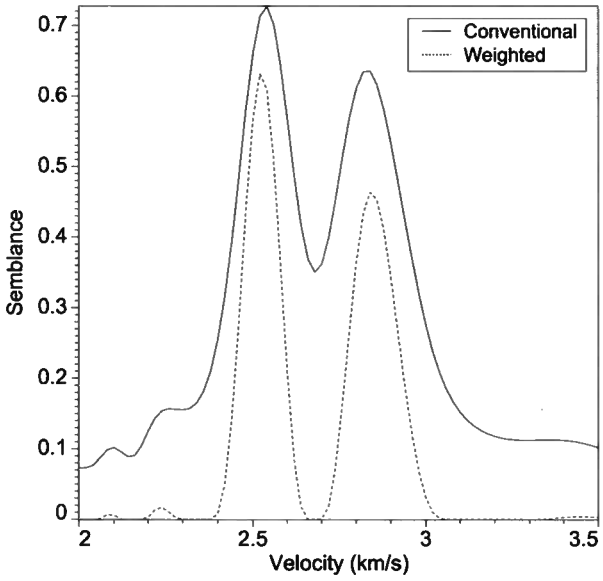

Figure 6. Plot of semblance as a function of trial velocity at $\tau = 3.2$ s.

semblance spectrum, and Figure 8d shows the weighted semblance spectrum.

In the weighted semblance spectrum, the spread in semblance associated with the near offsets has been reduced, and the decrease in the area enclosed by the contours indicates that the semblance peaks are sharper as well.

4 CONCLUSION

Weighting terms in the semblance calculation that are sensitive to changes in velocity increases the resolution of semblance spectra. Our implementation of weighted semblance increases resolution by using a weighting function to minimize semblance while maintaining a normalized semblance value bounded between zero and one.

Implementing the weighted semblance calculation requires a small change to the conventional semblance implementation. This change increases the cost of calculating semblance. However, the cost is still comparable to that of conventional semblance because the computational complexity of calculating weighted semblance remains on the order of $N_x \times N_t \times N_v$, where N_x, N_t, and N_v are the number of offset, time, and velocity samples, respectively.

Weighted semblance increases the resolution of semblance spectra for synthetic data consisting of isolated and interfering events and for field seismic data as well. Using weighted semblance to obtain a higher resolution semblance spectra can improve the accuracy of NMO velocity estimates and velocity models, which

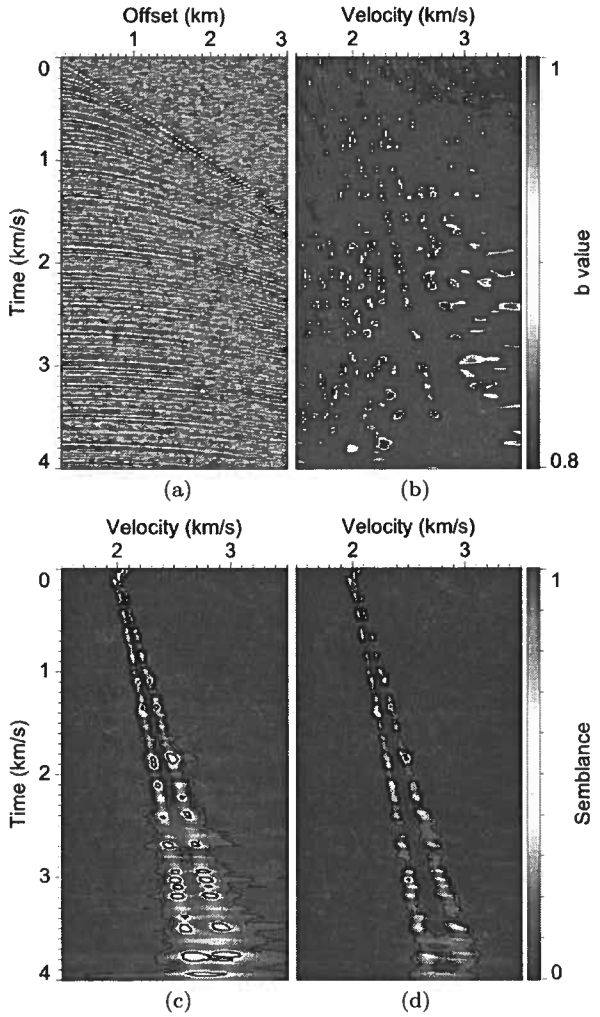

Figure 7. Synthetic CMP gather (a), plot of b values (b), conventional (c) and weighted (d) semblance spectrum.

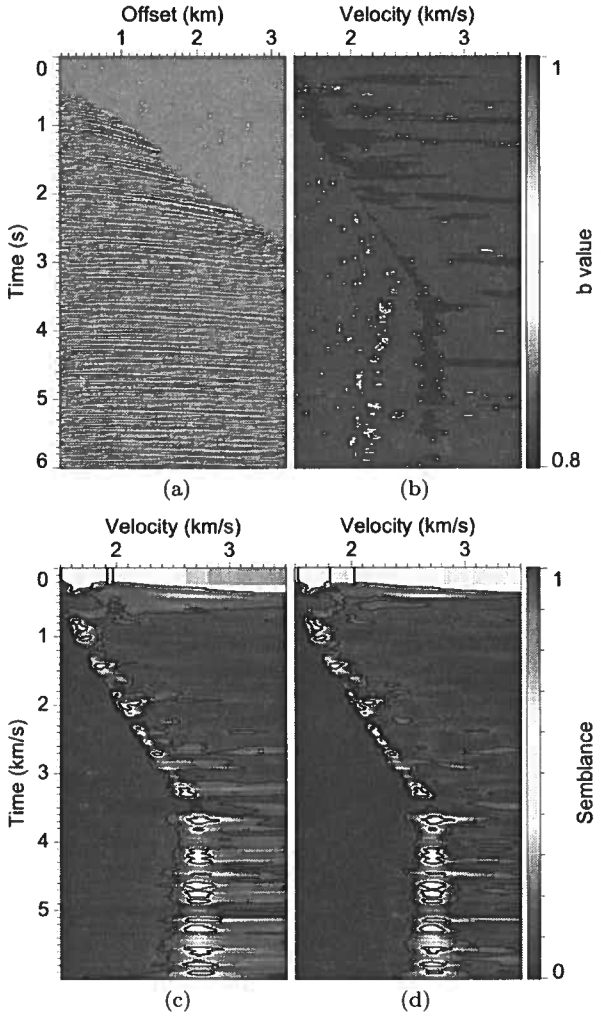

Figure 8. Viking Graben CMP gather (a), plot of b values (b), conventional (c) and weighted (d) semblance spectrum.

in turn can improve the quality of seismic images of the subsurface.

ACKNOWLEDGEMENTS

Thanks to Mobil for providing the Viking Graben seismic data. Thanks also to our sponsors and colleagues at the Center for Wave Phenomena at the Colorado School of Mines. Thanks especially to Ken Larner, Jeff Godwin, and Diane Witters for helping review and revise this paper.

REFERENCES

Celis, V., and Larner, K., Selective-correlation velocity analysis:, M.Sc. thesis, CWP-434, Center for Wave Phenomena, Colorado School of Mines, 2002.

Hale, D., Structure-oriented smoothing and semblance:, Technical Report CWP-635, Center for Wave Phenomena, Colorado School of Mines, 2009.

Neidell, N. S., and Taner, M. T., 1971, Semblance and other coherency measures for multichannel data: Geophysics, **36**, 482–297.

Taner, M. T., and Koehler, F., 1969, Velocity spectra – digital computer derivation and applications of velocity functions: Geophysics, **34**, 859–881.

Estimating fault displacements in seismic images

Luming Liang[1], Dave Hale[1] & Marko Maučec[2]

[1] *Center for Wave Phenomena, Colorado School of Mines, Golden, CO 80401, USA*

[2] *Landmark Graphics Corporation, Halliburton, Highlands Ranch, CO 80129, USA*

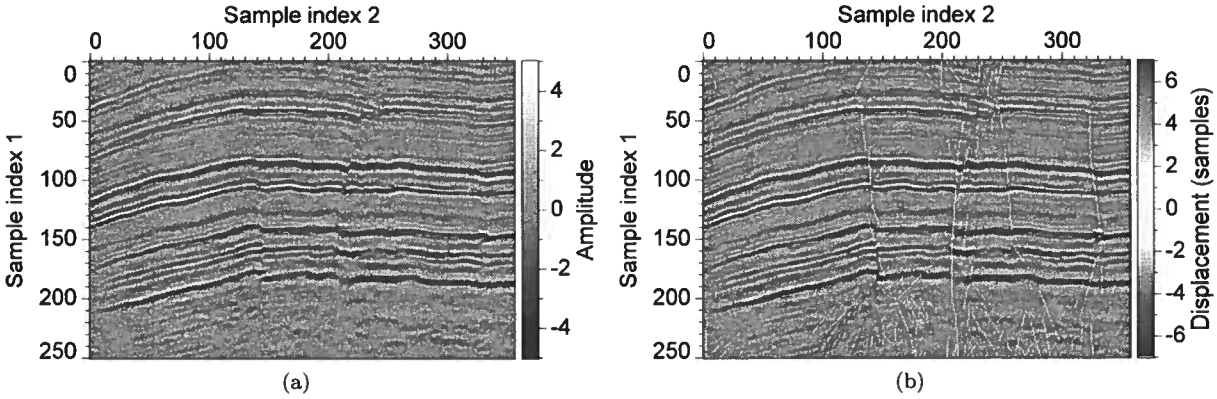

Figure 1. A 2D seismic section (a) showing extensional faulting and the same section with vertical displacements of faults highlighted (b). Signs of displacements indicate that geological layers have been displaced either downward (positive) or upward (negative) from left to right.

ABSTRACT

Geologic faults complicate the mapping of depositional layers. Most existing seismic image processing techniques highlight *fault locations* but fail to estimate *fault displacements.*

We model faults as a displacement vector field. Unlike traditional attributes (e.g., semblance or coherence), our estimated fault displacement vector field provides information about fault displacements, as well as fault locations. This vector field can be used to automatically determine relative displacements of faulted layers, and thereby simplify the mapping of such layers.

Key words: fault displacements, crosscorrelation, seismic interpretation

1 INTRODUCTION

In seismic images of the earth's subsurface, such as the one shown in Figure 1a, we typically see interfaces between geologic layers, because rocks or fluids within these layers vary from one layer to the next, causing changes in acoustic impedance. It is these changes that we image with seismic waves.

Discontinuities are often apparent in these images. In Figure 1a, the two most obvious discontinuities appear in the central part of the image. Discontinuities of this kind correspond to geologic faults, which are fractures in rocks. Faults tend to be more vertical than layers, as rocks on one side of a fault tend to be displaced downward or upward relative to rocks on the other side. In seismic images, faults appear as discontinuities in otherwise nearly continuous layers. Geoscientists quickly learn to estimate the amount of displacement along a fault as they attempt to unravel the geologic history of the subsurface that has been imaged.

In an ideal 2D seismic image, without any random

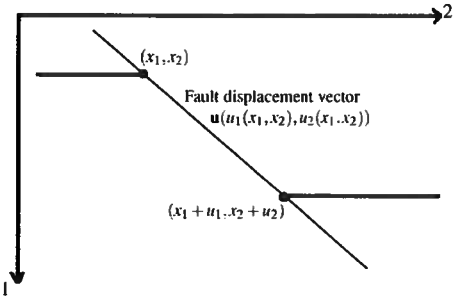

Figure 2. The fault displacement vector $u(x)$.

or coherent noise, faults appear as curves of discontinuities. These discontinuities are easily detected by human interpreters. Because faults never consist of a single fracture the term "fault zone" is sometimes used (Kadlec et al., 2008). However, in this paper, we consider a fault to be a single curve.

Seismic image processing today routinely includes steps to highlight the locations of faults (Bahorich and Farmer, 1995; Cohen and Coifman, 2002; Gibson et al., 2005; Al-Dossary and Marfurt, 2006; Kadlec et al., 2008; Hale, 2009b). That processing cannot yet reliably estimate the displacements along the faults. Fault displacements are today estimated manually using a tedious process of viewing seismic images and interactively picking corresponding points on both sides of a fault.

We seek to replace this manual picking with a process that produces an image of fault displacements. This process extracts fault curves from 2D seismic images and estimates fault displacements along these curves.

1.1 Fault model

Many mathematical models for faults have been proposed by geologists and geophysicists (Watterson, 1986; Barnett et al., 1987) based on their investigations and conclusions about seismic images and well logs. Barnett et al. (1987) claim that fault displacements consist of two components which can be considered separately: near-field and far-field. The near-field components are displacements that occur in the rock volume closely surrounding a fault. The far-field components are related to the bulk deformation of a larger region. Our model considers only near-field displacements.

In this paper, we consider only 2D slices of 3D seismic images, so that faults appear as curves of discontinuities in a 2D seismic image. Ideally, faults we detect are exactly one pixel wide, see Figure 1b.

Fault displacement vectors, which have both vertical and horizontal components, vary continuously along these curves. We represent the seismic image with a 2D scalar array: $f(x_1,x_2)$, where x_1 and x_2 denote uniformly sampled vertical and horizontal coordinates, respectively. An estimated fault displacement is a 2D vector: $\mathbf{u} = \mathbf{u}(u_1,u_2)$ (as in Figure 2), where $u_1 = u_1(x_1,x_2)$ and $u_2 = u_2(x_1,x_2)$ are vertical and horizontal components of the displacement, respectively. In Figure 1b, colored pixels represent the vertical component u_1 of the vectors $\mathbf{u}$. Those vectors should be zero (or nearly zero) at locations where no faults are present.

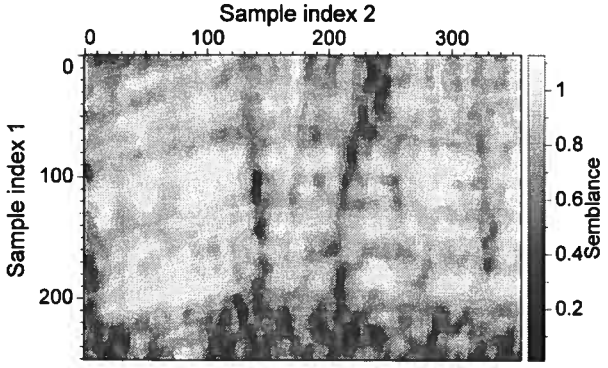

Figure 3. Semblance for the seismic image in Figure 1a, computed using the method described by Hale (2009b).

A nearly horizontal fault cannot be easily detected, even by human interpreters. Consequently, faults considered here are more vertical than horizontal; we assume that the angle between a fault curve and a vertical line is less than 45 degrees.

1.2 Estimating fault location

A feature shared by most fault detection techniques is the computation of attributes that highlight discontinuities in seismic images. Examples of such attributes include coherence (Bahorich and Farmer, 1995), entropy (Cohen and Coifman, 2002), curvature (Al-Dossary and Marfurt, 2006) and semblance (Hale, 2009b). Depending on which attribute is chosen, discontinuities in seismic images cause attribute values to be anomalously low or high.

Figure 3 illustrates structure-oriented semblance computed using the method by Hale (2009b). Potential fault locations are indicated by dark pixels. However, the information we obtain from this attribute is limited. Darker areas indicate fault zones but fail to locate fault curves. Fault locations are poorly resolved. This defect is common in this sort of algorithm.

This resolution problem is often due to the use of overlapping windows of samples when computing seismic attributes. Windows containing imaged faults smear information from both sides of the faults, over a distance proportional to the effective window width. Smaller windows cause less smearing, but yield less accurate measurements of discontinuity.

To overcome this problem, methods that involve more heuristics or human interactions have been proposed. Kadlec et al. (2007) present an interactive method for computing a fault surface. Rather than us-

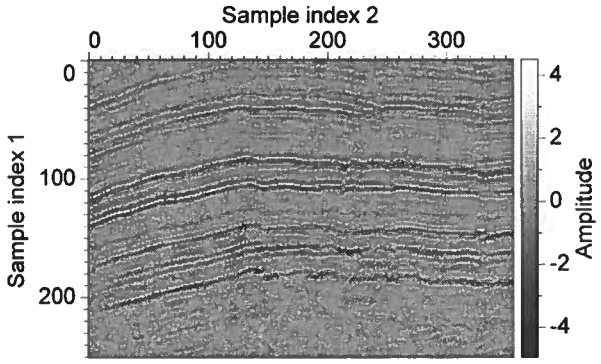

Figure 4. Automatic horizon picking using ridges and valleys detection as described by Patel et al. (2008). No significant differences exist between a fault area (red box) and an unfaulted area (blue box).

ing the attributes mentioned above, they manually pick seed points in the image and then let the points evolve to surfaces using a level set method.

Gibson et al. (2005) present a similar method. They also model faults in 3D as growing surfaces, but require no human interaction, because the seed points are generated from semblance. Then, these points are grouped into small fault patches using a highest-confidence-first merging strategy.

These methods compare automatic fault detection with human picking. The authors claim advantages in automatic fault detection over human picking in that the methods save time and are more accurate.

1.3 Research on fault displacement

Compared to automatic fault picking, automatic estimation of fault displacements is potentially more useful but less well developed. As mentioned above, fault displacements are today usually estimated manually by experienced interpreters.

Methods for automatically picking horizons in seismic images are most closely related to our work. Techniques of this kind appear also in the fields of computer vision and machine intelligence, although the problem of how to automatically pick horizons stems from geophysical applications.

In the method described by Farakloioti and Petrou (2004), horizons can be automatically identified as median surfaces of layers. The key part of this process is connected-component analysis, which is designed to join fragments that have consistent orientation and proximity. However, this method does not attempt to find correspondences between horizons on each side of a fault and leaves fault zones blank.

New approaches that use genetic algorithms (Aurnhammer and Tönnies 2005) and a multi-scale Bayesian model (Admasu and Tönnies, 2006) have been proposed to solve this problem. The former algorithm works for only 2D seismic images; the latter works for both 2D and 3D images. In addition to seismic images, these algorithms require horizon curves or surfaces in unfaulted regions as additional information; e.g., median surfaces extracted by Farakloioti and Petrou (2004) or valleys and ridges traced out by Patel et al. (2009). These two approaches match layers on both sides of faults, but neither yields displacements along fault curves or surfaces. Moreover, both approaches are sensitive to errors in the input horizons. This sensitivity is illustrated in Figure 4. In the case shown in Figure 4, two layers on each side of a fault join coincidentally in the red box. The method mistakenly picked one horizon across the fault in the red box. Because the method cannot distinguish the faulted and unfaulted areas highlighted there, layers would be mistakenly matched.

For these reasons, newer algorithms are based on interactive horizon picking. Patel et al. (2008; 2009) propose a framework for computer-assisted seismic analysis, designed for a small group of interpreters. Their first step is automatic horizon picking in unfaulted areas, which is similar to Farakloioti and Petrou's (2004) method. By considering the amplitude of a 2D seismic image as height values in a terrain, Patel et al. trace out the valleys and ridges, which are texture primitives defined by Tüceryan and Jain (1990). Then, they create curves from these valleys and ridges as horizons. The difference is in their second step. Rather than relying on an entirely automatic method, they employ a semi-automatic method that uses human intervention when the auto-picking result is incorrect, as in the red square in Figure 4.

In this paper, we describe a method for automatically and simultaneously estimating both fault locations and fault displacements. We require only a seismic image as the input. Faults are simply located where our estimated fault displacements are nonzero.

2 PROBLEMS

A simple way to estimate vertical displacements across faults is to crosscorrelate each pair of adjacent traces in a seismic image. We search for peaks of normalized local crosscorrelations to estimate displacements between traces. Local correlations enable us to estimate displacements that may vary vertically. Normalization makes our estimates insensitive to vertical variations in seismic amplitudes.

Normalized local crosscorrelations are often used in geophysical applications; e.g., to estimate relative displacements from two time-lapse seismic images (Hale, 2009a) and to enhance stacking (Liu et al., 2009).

Normalized local crosscorrelations are defined for

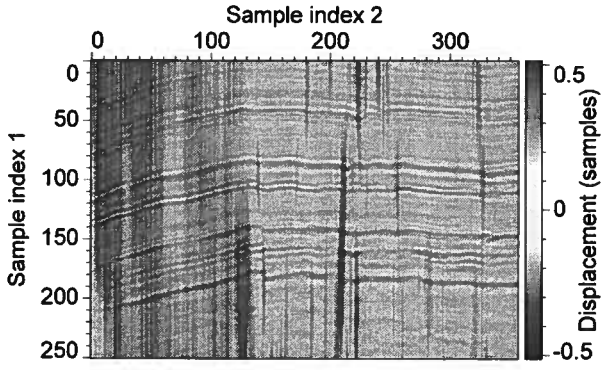

Figure 5. The estimated vertical displacements using the simple method.

two traces f and g by

$$c[k;l] \equiv \frac{c_{fg}[k;l]}{\sqrt{c_{ff}[k;0]}\sqrt{c_{gg}[k+l;0]}}, \quad (1)$$

where

$$c_{fg}[k;l] \equiv \sum_j f[j]g[j+l] \times w[k-j] \quad (2)$$

and $w[k]$ is a Gaussian window

$$w[k] \equiv e^{\frac{-k^2}{2\sigma^2}} \quad (3)$$

that, for some specified radius σ, makes crosscorrelations local.

Crosscorrelations are normalized by the factors

$$c_{ff}[k;0] \equiv \sum_j f^2[j] \times w[k-j] \quad (4)$$

and

$$c_{gg}[k;0] \equiv \sum_j g^2[j] \times w[k-j]. \quad (5)$$

For each integer lag l, equation 1 gives a normalized local crosscorrelation coefficient for every sample indexed by k. We use a fast implementation of equation 1 (Hale, 2006). When estimating displacements, we must store for each sample only those correlation coefficients required to locate correlation peaks. For example, if the maximum correlation coefficient appears at lag l, we need only store values for lags $l-1$, l, and $l+1$. We then fit a quadratic function to those values to locate the correlation peak with sub-pixel precision. Details are described by Hale (2009a), and source code is available in the Mines Java Toolkit (http://mines.edu/dhale/jtk/). Figure 5 shows vertical displacements estimated by finding the peaks of local crosscorrelations of consecutive pairs of traces in the seismic section shown in Figure 1a.

Although these trace-to-trace vertical displacements roughly conform to the orientations of the geological layers in the seismic image, they do not properly describe fault displacements. Estimated displacements are apparently incorrect at some locations, such as the point near a fault with sample indices (160,143). Near this point, vertical displacements across the fault should be positive (about 5 or 6 samples), which means that the relative displacement of layers is downward from left to right. However, the estimated displacement value at that point is negative. Furthermore, faults appear as zones of displacement, not as curves, and displacements are not zero where layers are dipping but not faulted. In the remainder of this section, we describe in detail the shortcomings of this simple trace-to-trace correlation method for estimating fault displacements.

2.1 Inadequacy of using two traces

In Figure 6 are three subsets of pixels centered on the pixel with sample indices (160, 143) in Figure 1a. At this location, two layers on each side of a fault join coincidentally. Human interpreters can estimate the correct relative displacement of layers on each side; however, the simple method fails to do so. One problem with the simple method is that it is near sighted, as illustrated in Figure 6.

Using our eyes, we can easily identify the location of the fault and roughly estimate the displacement between layers on each side of the fault shown in Figure 6a. From left to right across the fault, layers are clearly displaced downward.

However, if we zoom in the image, and only look at Figure 6b, we may misinterpret the fault displacements. In this case, we can still see the location of the fault, but may unfortunately pick a wrong correspondence between layers on each side of the fault. If we continue to magnify the image until we can see only the 5×5 region shown in Figure 6c, we may even be unaware of any faulting. Note that the window size used in many such image processing applications is often kept small because computational cost is higher if larger windows are used.

When computing local crosscorrelations for pairs of traces, our window height is controlled by the Gaussian half-width σ in equation 3, but the window width is only 2 samples. Correlating local windows of only two traces near a fault is insufficient and quite different from what human interpreters do. Human interpreters use traces farther away from a fault to both locate the fault and estimate displacements.

Of course, correlating a single pair of traces that are farther apart will introduce another source of error, as displacements estimated from traces away from a fault may poorly approximate those apparent at a fault. What human interpreters correlate visually are not single pairs of traces, but many traces on both sides of faults.

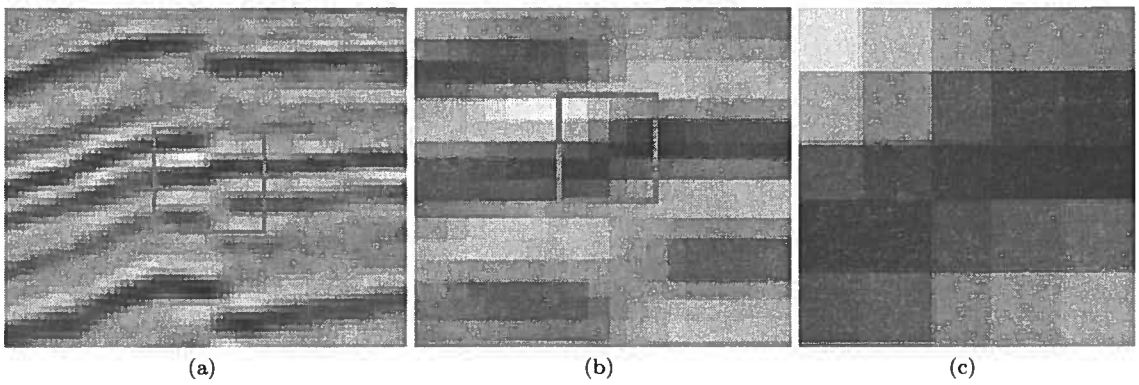

Figure 6. Zoomed views of the fault located around (160, 143) in Figure 1a.

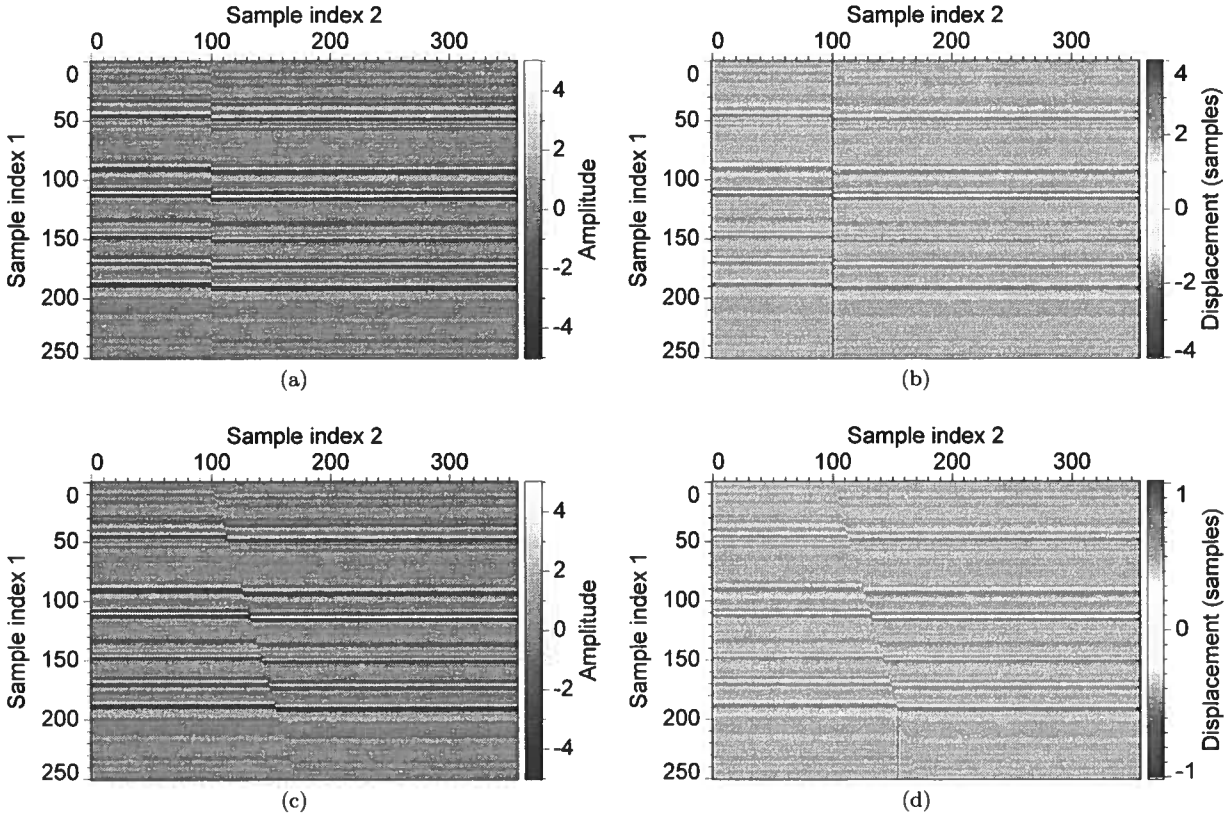

Figure 7. Crosscorrelation of adjacent pairs of traces in two seismic images with vertical (a) and non-vertical (c) faults yields corresponding estimates of the vertical components of displacements (b) and (d).

2.2 Faults are not vertical

Another problem with the simple trace-to-trace correlation method is that it performs poorly for faults that are not vertical. Each trace in a seismic image is a vertical sequence of pixels. To estimate displacements for non-vertical faults, we should crosscorrelate sequences of pixels that are parallel to the fault.

Figure 7 shows for a synthetic example the use of crosscorrelation of traces to estimate displacements. In this example, displacement is constant along the faults. As expected, displacements estimated from an image with a vertical fault are accurate. However, displacements estimated from image with the a non-vertical fault are inaccurate and inconsistent.

Figure 8 illustrates the source of this problem. Crosscorrelation of adjacent traces, vertical sequences

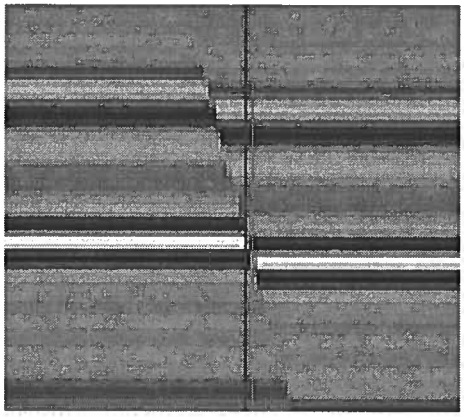

Figure 8. For a non-vertical fault, most samples in two adjacent traces (marked with red and blue lines) are similar, so that local trace-to-trace crosscorrelation fails to yield accurate estimates of even the vertical component of displacement.

of pixels, is inadequate, because so many of those pixels are identical for a fault that is not vertical.

2.3 Dipping layers are not faults

Faults need not be vertical and geologic layers also need not be horizontal. Displacements are nonzero for dipping structures. In Figure 5, vertical displacements vary slowly along both dipping layers and faulted areas. Which displacements correspond to faults?

Our goal is to determine the fault displacement vector field, which should be zero where faults do not exist. Locating faults in Figure 5 is even harder than locating faults in the original seismic image shown in Figure 1a.

Aimed to the three inadequacies mentioned above, we propose three improvements in following three sections in addition to the simple estimation.

3 FILTERING

Many papers describe filtering techniques for seismic images to aid interpretation (Luo et al., 2002; Fehmers and Höcker, 2003; Lu, 2006; AlBinHassan et al., 2006; Lu and Lu, 2009; Hale, 2009b). Most of these techniques enhance features, like structural layers, while suppressing noise. The Van Gogh filter (Fehmers and Höcker, 2003) is an application of a coherence-enhancing diffusion (Weickert, 1999) in geophysics. The key to this method is to solve a partial differential equation guided by a diffusion tensor field. Another seismic image filter is the edge-preserving filter, which was first proposed by Luo (2002), and then extended to 3D (AlBinHassan et al., 2006) by himself and his colleagues. The most significant advantages of the edge-preserving filter are that it is efficient and it is easy to implement.

However, none of these filters assist the correlations we require. We design a filter to assist the crosscorrelations between two sides of a fault. This filter gathers information from nearby traces, but does not gather information across the fault. Our filter generates two traces on each side of a fault by weighted averaging traces. The filter is designed as follows.

Left-to-right and right-to-left smoothing
Inputs:
seismic image $q(x_1, x_2)$ with $n_1 \times n_2$ samples
filter coefficient α
Outputs:
seismic image $q^-(x_1, x_2)$, filtered from left to right
seismic image $q^+(x_1, x_2)$, filtered from right to left
for all x_1
$q^-(x_1, 0) = q(x_1, 0)$
for $x_2 = 1, 2, ..., n_2 - 1$
for all x_1
find shifts $u(x_1)$ and
peak correlation coefficients $c_{max}(x_1)$,
for all x_1
use sinc interpolation to compute a shifted trace
$\tilde{q}(x_1) = q^-(x_1 + u(x_1), x_2 - 1)$
for all x_1
$a = \alpha \times c_{max}(x_1)$
$q^-(x_1, x_2) = a \times \tilde{q}(x_1) + (1 - a) \times q(x_1, x_2)$
By simply reversing the filtering direction, we get the right-to-left smoothing $q^+(x_1, x_2)$.

The **left-to-right and right-to-left smoothing** filter is an adaptive one-sided exponential filter (Oppenheim et al., 1999). The input of the filter is a 2D image, which is regarded as a set of 1D vertical traces. The image is processed trace-by-trace from left to right and right to left. The change made to the traditional one-sided exponential filter is to preserve the fault as much as possible during the smoothing. Normalized local crosscorrelation is used to find vertical shifts between consecutive traces. Traces are then warped with these shifts before they are used in the smoothing process. This operation is the key to avoid gathering information across faults before locating them. Coefficient α in this filter controls the effective length of the one-sided exponential filter (Oppenheim et al., 1999).

This filter is efficient because the one-sided exponential filter is the cheapest smoothing technique. In addition, the smoothing is confined by discontinuities between traces. By comparing the images in Figure 9 with the input image in Figure 1a, one sees that discontinuities are clearer and layers do not extend across the fault.

In practice, we compute displacement fields by picking one trace from the left-to-right smoothed image shown in Figure 9a and another trace from the right-to-left smoothed image shown in Figure 9b. This conforms to the process that a pair of eyes uses to find a fault: first scanning the image from left to right and then from

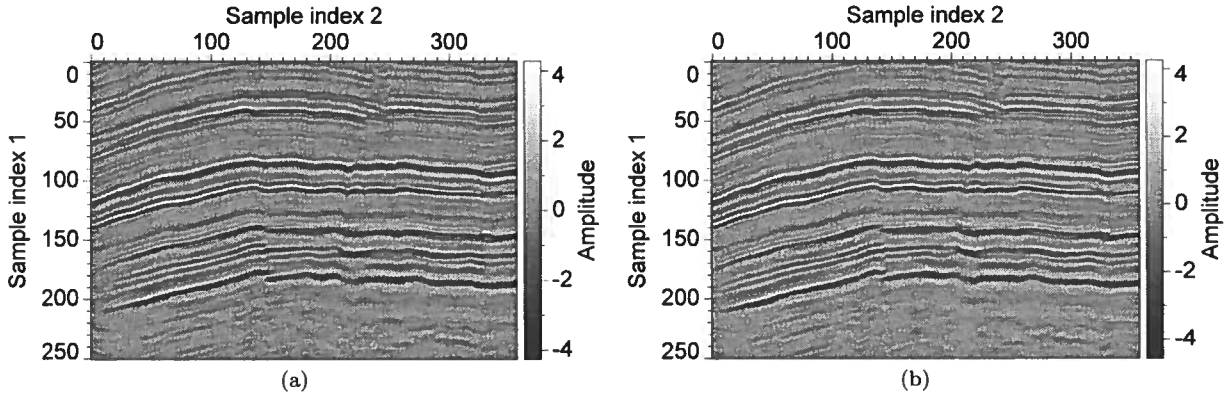

Figure 9. Filtering the image shown in Figure 1a from left to right (a) and from right to left (b).

right to left, and locating the fault curves as observed differences.

4 SHEARING

When faults are not vertical, we should correlate non-vertical sequences of pixels, as shown in Figure 10. Unfortunately, we do not yet know the locations and orientations of faults. One possible way to solve this problem is to search for all orientations on each pixel of the image. Therefore, a filter that hence rotates the window locally is a plausible way. However, the computation of rotation around one pixel does not contribute to computing rotations in other places. This fact makes the orientation search time-consuming.

Although the rotation-based search method is expensive, it gives us a clue to reduce the cost. Paeth (1990) implements the rotation of an image by consecutively shearing the image three times. The shear transformation is an affine transformation where one coordinate of each point is changed in proportion to its another coordinate. In 2D, we have two kinds of shear transform: horizontal shear (x coordinates change in proportion to y coordinates) and vertical shear (y coordinates change in proportion to x coordinates), see Figure 11.

As shown in Figure 12, we shear the seismic image horizontally to make the faults vertical. We define an integer l_1 as the maximum vertical displacement of a fault and a float s as the shear amount of the image that controls the number of samples will be moved. Mathematically, shearing a 2D scalar field $f(x_1, x_2)$ is to create a new 2D scalar field $f'(x_1, x_2)$ and

$$f'(x_1, x_2) = f(x_1, x_2 - sx_1), \tag{6}$$

where $s > 0$ indicates the rows will be moved to the right, $s < 0$ indicates the rows will be moved to the left. $s \in (-1, 1)$ because we stipulate that a fault in our model must form less than a 45 degree angle from the vertical line. To sample the range of shear amount

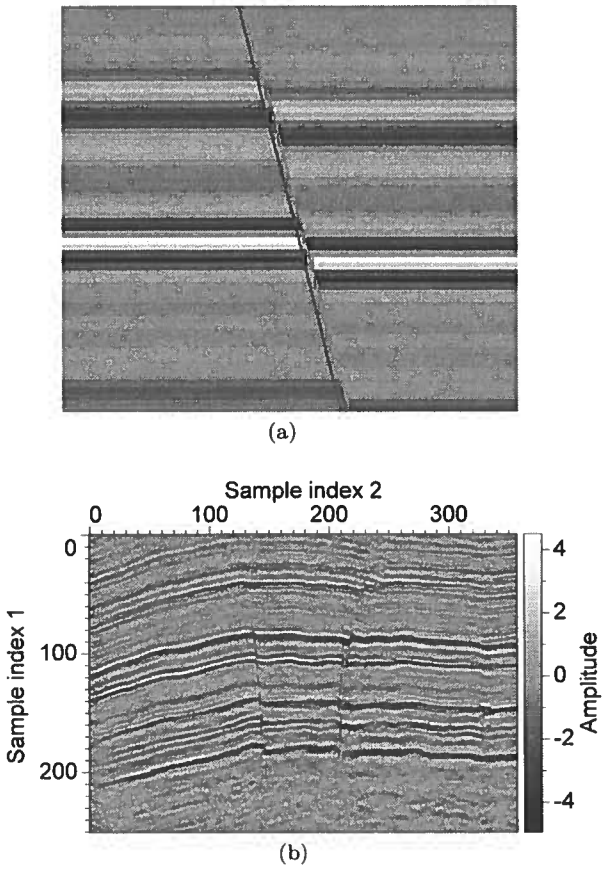

Figure 10. Ideal trace-picking in a non-vertical fault zone: (a) the magnification of a part of 7c; (b) the ideal trace picking for the image in Figure 1a.

$(-1, 1)$, we define another integer $l_2 \in (-l_1, l_1)$ and $s = \frac{l_2}{l_1}$. Since s is not an integer, we should translate the sequence (row) by a float amount. We use sinc interpolation to perform this sub-pixel translation.

The shear transform may move out and truncate

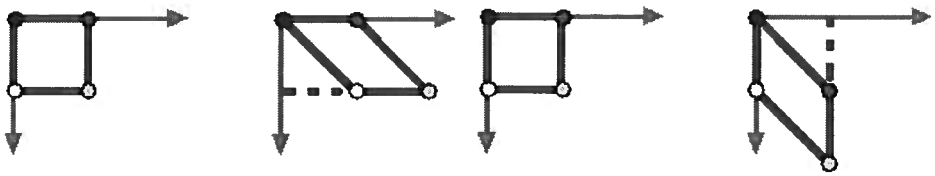

Figure 11. Shear transform: (a)horizontal shear; (b) vertical shear.

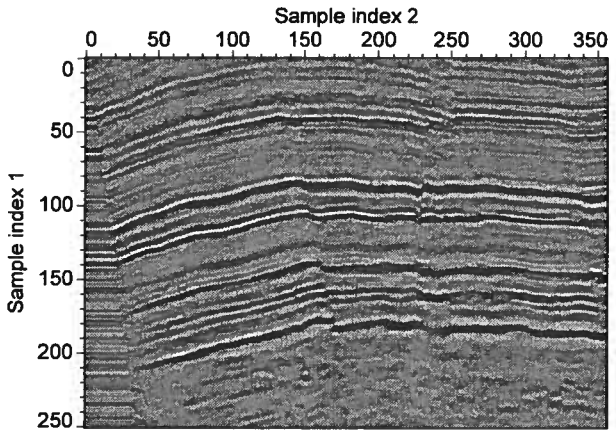

Figure 12. By shearing the image shown in Figure 1a with shear amount $s = \frac{2}{15}$, we make faults at some places vertical.

a part of the input image. To avoid losing data after shearing, we extrapolate the image before shearing it.

5 LOCATING

We assess fault locations through a two-stage pattern analysis. In the first stage of analysis, we estimate the location of a rough fault zone; in the second stage, we pick out the precise one-pixel-wide fault out from the fault zone.

In a seismic image which contains only horizontal geologic layers, vertical displacements between traces are zeros before and after shearing. However, the shearing may change the displacement between traces when the layers are dipping. As shown in Figure 13, f and f' are images before and after shearing.

We model a dipping geologic layer at a certain point as a line segment. Therefore, f becomes a univariate function g:

$$f(x_1, x_2) = g(x_1 - px_2), \tag{7}$$

where p is the slope. As shown in equation 6, $f'(x_1, x_2) = f(x_1, x_2 - sx_1)$, therefore

$$\begin{aligned} f'(x_1, x_2) &= g[x_1 - p(x_2 - sx_1)] \\ &= g[(1 + sp)x_1 - px_2]. \end{aligned} \tag{8}$$

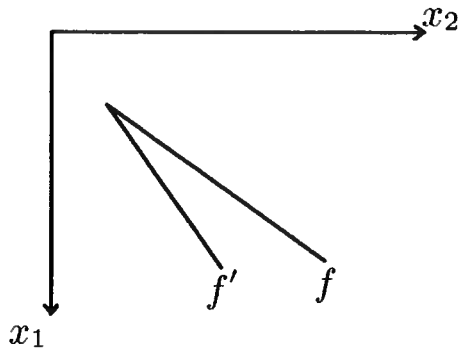

Figure 13. Shearing a dipping layer.

Since f represents a line segment, we have

$$\triangle f = \frac{\partial f}{\partial x_1}\triangle x_1 + \frac{\partial f}{\partial x_2}\triangle x_2 = 0. \tag{9}$$

Thus,

$$p = \frac{\triangle x_1}{\triangle x_2} = -\frac{\frac{\partial f}{\partial x_2}}{\frac{\partial f}{\partial x_1}}. \tag{10}$$

Similarly, we have

$$p' = -\frac{\frac{\partial f'}{\partial x_2}}{\frac{\partial f'}{\partial x_1}}, \tag{11}$$

where p' is the slope of the layer after shearing. Substituting f' in equation 11 by equation 8, we obtain

$$\begin{aligned} p' &= -\frac{\frac{\partial g[(1+sp)x_1 - px_2]}{\partial x_2}}{\frac{\partial g[(1+sp)x_1 - px_2]}{\partial x_1}} \\ &= -\frac{-p\frac{\partial g}{\partial x_2}}{(1+sp)\frac{\partial g}{\partial x_1}} \\ &= \frac{p}{1+sp}. \end{aligned} \tag{12}$$

Here, p' is a function of the shear amount s. Note that slopes p and p' are also vertical displacements right at the selected point before and after shearing, respectively. When $p = 0$, $p'(s) = p = 0$, which indicate that the shearing does not affect the horizontal layer.

The above analysis reveals the effect of shearing on a dipping layer where no fault exists. However, in a

zone where a fault exists, the function $p'(s)$ does not follow the function shown in equation 12. Because $s = \frac{l_2}{l_1}$ and l_1 is a constant, $p'(s)$ is sampled according to l_2. Figure 14 illustrates different patterns of function relationships. One can see a peak in the black curve in Figure 14b, which corresponds to the black pixel in Figure 14a. This pixel is right on a fault. In Figure 14b, the horizontal coordinate l_2 of the peak indicates that shearing the image by amount $\frac{l_2}{l_1}$ makes the fault vertical. Curves in Figure 14c approximately conform to the relationship shown in equation 12. Figure 15 illustrates such relationship in real data. We can still distinguish the blue curve from others.

In the first stage, we distinguish samples around a fault with samples far away from a fault according to the following criterion: if shifts vary slowly according to different shearings, there is no fault. In other words, if there is an outstanding point in the displacement-shear curve, as the black curve shown in Figure 14, there is a fault.

In practice, we set a fault threshold η and compute the average value $ave(p'(s))$ as well as the maximum value $\max(p'(s))$ of vertical displacements with different shearings at a particular point. If $\max(p'(s)) > \eta$ and $\max(p'(s)) > c|ave(p'(s))|$, there exists a fault. The coefficient c must be chosen carefully to distinguish the curves which are not slowly varying. We name c as the fault coefficient. The first-stage pattern analysis yields fault displacement zones shown in Figure 16a.

A second-stage pattern analysis is required to pick one-pixel-wide fault curves from the fault zones. We plot the displacement-to-shearing function for five consecutive points along a horizontal line around fault location $(105, 140)$. Five curves share a same pattern. However, only one of these five samples has fault. We choose the yellow point because its corresponding curve has the largest maximum displacement value. By scanning horizontally across every fault zones, we get the fault displacement field as shown in Figure 16b.

5.1 Compute displacement vector

After we obtain the vertical shift v_1 and the shear amount s, we can compute the displacement vector

$$u_1(x_1, x_2) = v_1(x_1, x_2 - sx_1),$$
$$u_2(x_1, x_2) = -su_1(x_1, x_2).$$

The horizontal components of the fault displacement vector field is shown in Figure 18a. Signs of horizontal displacements indicate that geologic layers have been displaced either rightward (positive) or leftward (negative). By combining the horizontal components with the vertical components (shown in Figure 18b), we finally get the fault displacement vector field.

6 PARAMETERS

Because several changeable parameters exist in our algorithm (c, η and l_1), we illustrate the effect of changing these coefficients in this section. The standard choices of these coefficients are $c = 0.25$, $\eta = 0.4$ and $l_1 = 15$ for the image shown in Figure 1a. When illustrating the effect of changing one of these coefficients, we keep two others unchanged.

6.1 The fault coefficient c

The fault coefficient c largely controls the identification of a fault. From Figure 14, one can easily tell the difference between the pattern of fault place and the pattern of non-fault place. Consequently, c can be chosen in a large range in this synthetic image. However, in the real data, as shown in Figure 15, the pattern corresponding to the fault place is less distinguish. In this case, the possible range of c is largely confined. One can see some incorrect identifications of faults in the left half of the image in Figure 19a due to a relatively small value for c. When c increases, these inaccurate picks disappear, as shown in Figure 19b and c. However, the fault located at $(105, 140)$ is not identified in Figure 19b and c.

Because (1) seismic images are often contaminated by random noise and (2) dips are varying along geologic layers, an adaptive c or a more sophisticated pattern analysis is required for processing seismic images with lower illumination qualities.

6.2 The fault threshold η

Choosing different fault thresholds η shows us different levels of detail for fault displacement fields. (Note Figure 20a, b, c and d.) A reasonable fault threshold is related to the sampling interval of the image. Interpreters can change the fault threshold interactively to get the most satisfactory result.

6.3 The maximum vertical displacement l_1

The continuity of fault curves is related to the maximum vertical displacement l_1. As mentioned above, we must investigate the problem in a relatively large area. l_1 controls the vertical window size, thus cannot be set too small. Figure 21a, b and c illustrate this effect on the displacement field by changing l_1.

As Figure 21 demonstrates, a larger l_1 value yields more continuous fault curves. However, shorter faults with rapidly changing orientation can be well detected using a smaller l_1. The reason is that using a larger l_1 tends to catch longer faults. Detailed differences between $l_1 = 12$ and $l_1 = 18$ can be found in Figure 22.

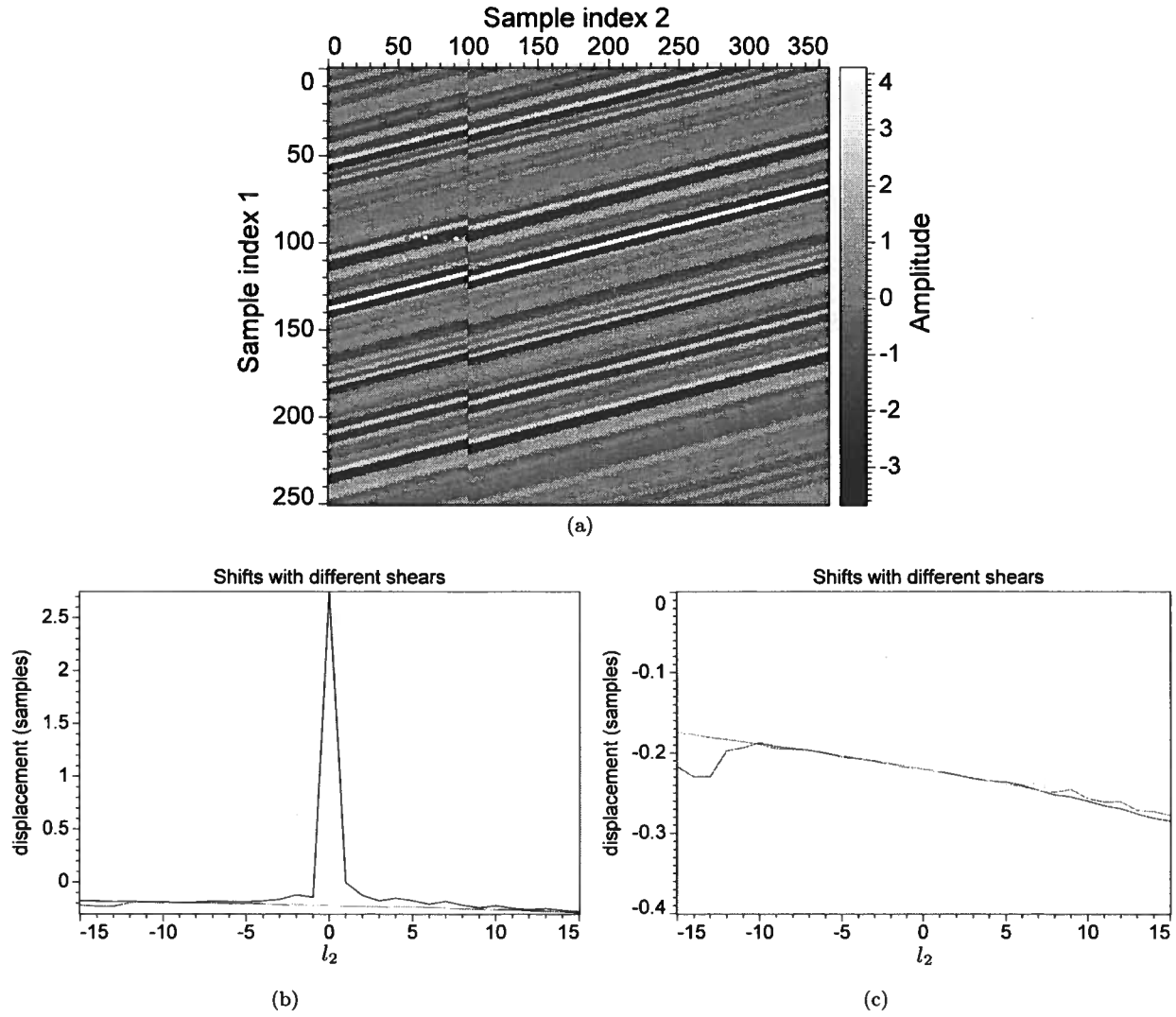

Figure 14. Investigating the function relationship between the vertical displacement and l_2. Five curves in (b) correspond to five points selected from the synthetic image (a) with the same colors. Leaving the black curve (b) out, we get similar patterns (c).

7 CONCLUSION

Our estimation of fault displacement vector fields in seismic images consists of four primary steps:

- filter the seismic image;
- shear the image to make faults vertical;
- estimate fault displacements from the sheared images using normalized local crosscorrelation;
- apply two-stage pattern analysis to exactly locate faults.

By following these steps sequentially, one obtains fault curves as well as the displacement vector field defined in section 1.1. If one omits the second-stage pattern analysis, one can get a fault displacement zone which is similar to the fault zone model estimated by Kadlec et al. (2008).

The fault displacement vector field estimated by our method has a sub-pixel precision in the vertical and horizontal components but does not have sub-pixel precision fault locations. Exact faults are usually located between two pixels.

This fault displacement vector field can be used to improve estimating the structure tensors (Hale, 2009b) at places around a fault. These tensors can be further used to adaptively smooth the seismic image or guide interpolation. Another potential usage is to place streamlines on seismic images, which is similar to the auto-

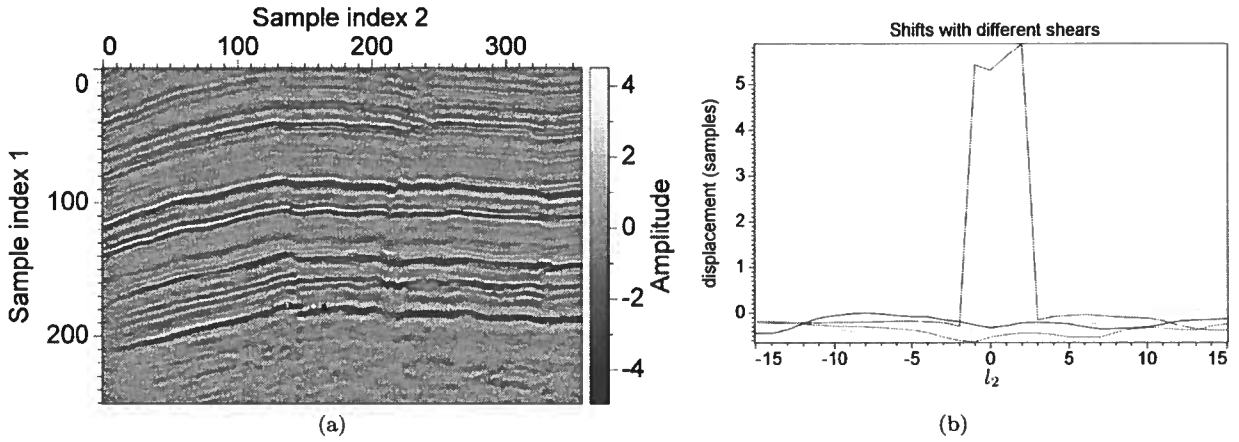

Figure 15. Investigating the function relationship between the vertical displacement and l_2. Five curves (b) correspond to five points selected from the synthetic image (a) with the same colors.

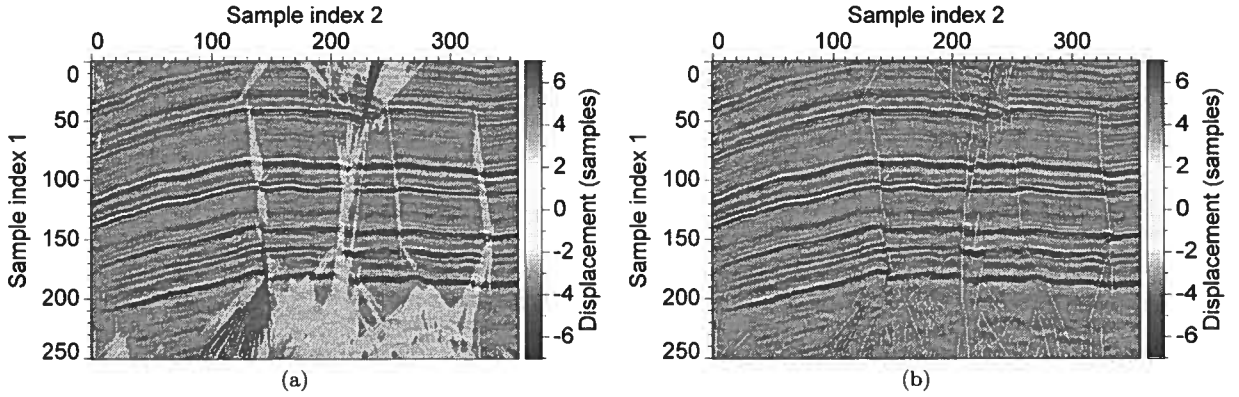

Figure 16. Applying the second stage pattern analysis on the fault displacement zone (a), we obtain the fault displacement field (b).

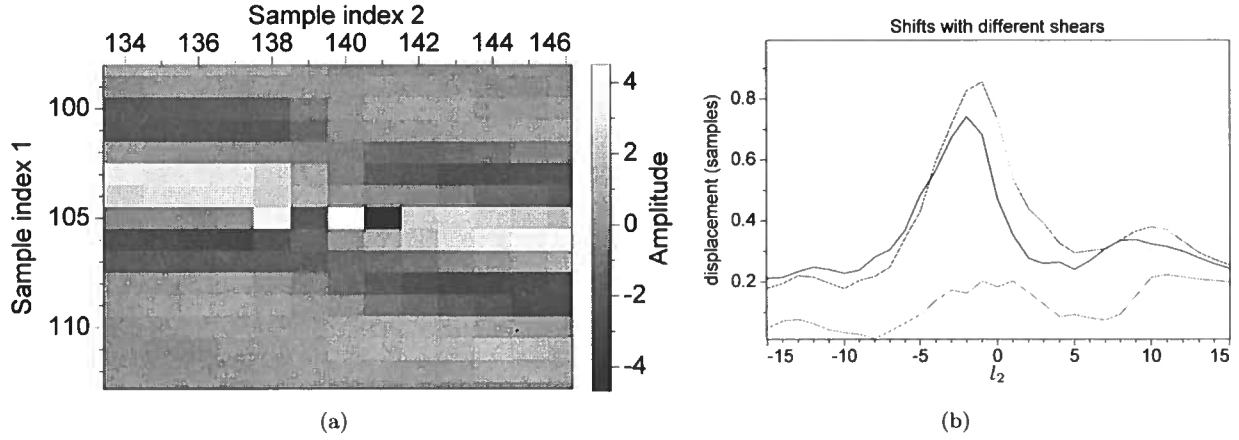

Figure 17. Investigating the function relationship between the vertical displacement and l_2 in the fault zone around (105, 140). Five curves (b) correspond to five points selected from the image (a) with same colors.

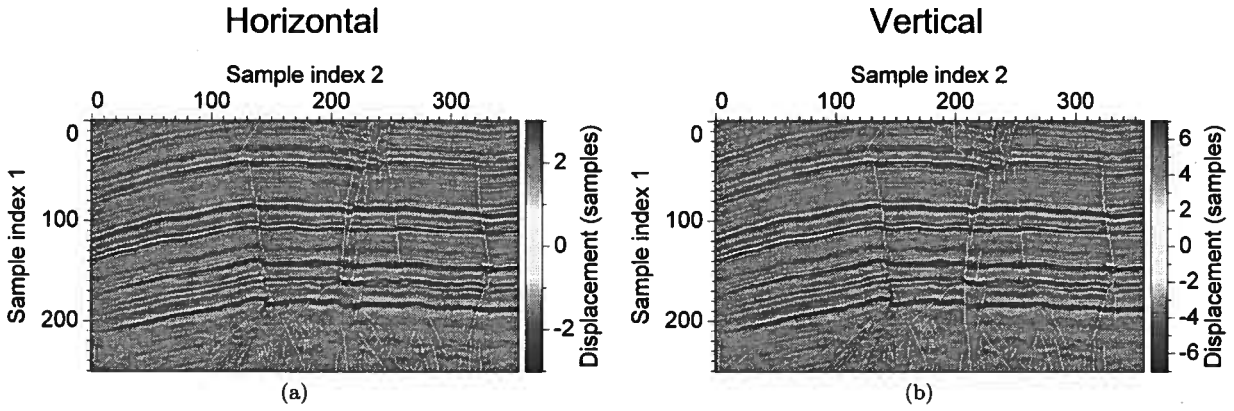

Figure 18. Fault displacement vector field: (a) horizontal components; (b) vertical components;

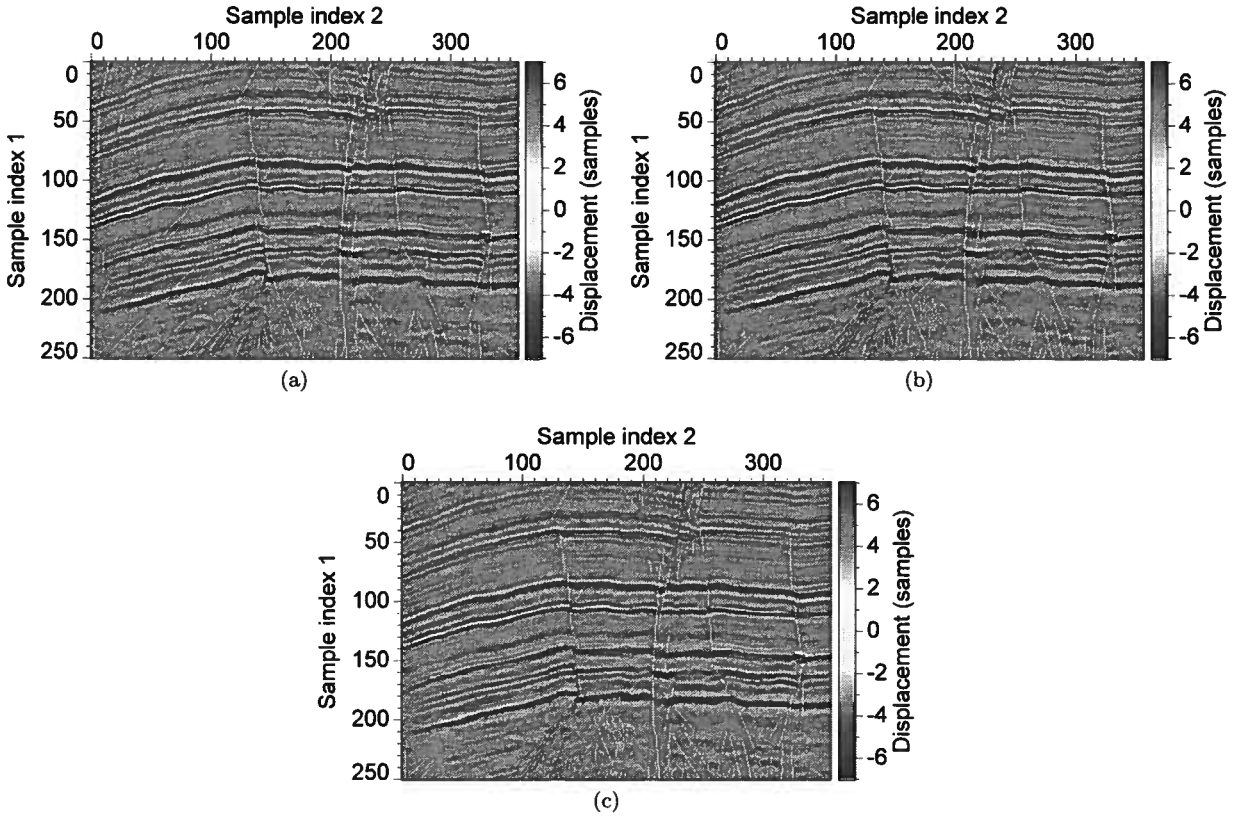

Figure 19. Vertical components of displacement vector fields estimated by using different fault coefficient c: (a) 0.2; (b) 0.25; (c) 0.3.

matic horizon picking. Furthermore, the fault displacement vectors can also used in flattening seismic images.

ACKNOWLEDGMENTS

Thanks to the Rocky Mountain Oilfield Test Center, a facility of the U.S. Department of Energy, for providing the seismic image used here. We would like to thank our colleagues for their discussions and feedback on this

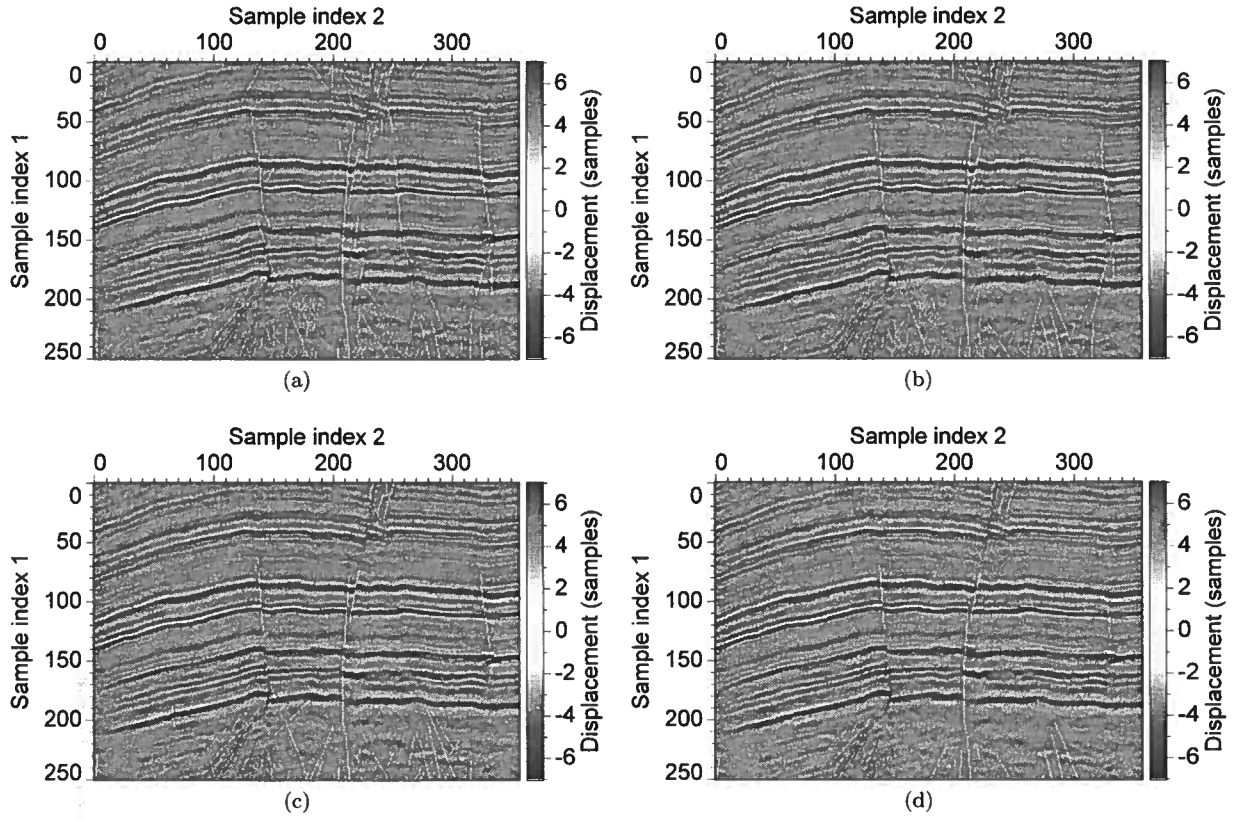

Figure 20. Vertical components of displacement vector fields estimated by using different fault threshold η: (a) 0.4; (b) 0.5; (c) 0.6; (d) 0.7.

research. We especially thank Diane Witters for her help with writing.

REFERENCES

Admasu, F., and K. Tönnies, 2006. Multi-scale bayesian based horizon matchings across faults in 3d seismic data *Proc. Deutsche Arbeitsgemeinschaft für Mustererkennung DAGM2006, Lecture Notes in Computer Science*, **4174**, 384–393.

AlBinHassan, N. M., Y., Luo, and M. N. Al-Faraj, 2006. 3D edge-preserving smoothing and applications. *Geophysics*, **71**(4), 5–11.

Al-Dossary, S., and K. J. Marfurt, 2006. 3D volumetric multispectral estimates of reflector curvature and rotation. *Geophysics*, **71**(5), 41–51.

Aurnhammer, M., and K. Tönnies, 2005. A genetic algorithm for automated horizon correlation across faults in seismic images. *IEEE Transactions on evolutionary computation*, **8**(5), 201–210.

Bahorich, M., and S. Farmer, 1995. 3-D seismic discontinuity for faults and stratigraphic features: The coherence cube. *The Leading Edge*, **14**(10), 1053–1058.

Barnett, J. A. M., J. Mortimer, J. H. Rippon, J.J. Walsh and J. Watterson, 1987. Displacement geometry in the volume containing a single normal fault. *The American Association of Petroleum Geologists Bulletin*, **71**(8), 925–937.

Cohen, I. and R. R. Coifman 2002. Local discontinuity measures for 3-D seismic data. *Geophysics*, **67**(6), 1933–1945.

Gibson, D., M. Spann, J. Turner, and T. Wright, 2005. Fault surface detection in 3-D seismic data. *IEEE Transactions on Geoscience and Remote Sensing*, **43**(9), 2094–2102.

Faraklioti, M., and M. Petrou 2004. Horizon picking in 3D seismic data volumes. *Machine Vision and Applications*, **15**, 216–219.

Fehmers, G. C. and C. F. Höcker, 2003. Fast structural interpretation with structure-oriented filtering. *Geophysics*, **68**(4), 1286–1293.

Hale, D., 2006, Fast local cross-correlations of images. *SEG Expanded Abstracts*, **25**, 3160–3164

Hale, D., 2009a. A method for estimating apparent displacement vectors from time-lapse seismic images. *Geophysics*, **74**(5), 99–107.

Hale, D., 2009b, Structure-oriented smoothing and semblance: CWP Report 635, 261–270

Kadlec, B. J., G. A. Dorn, H.M. Tufo, and D.A. Yuen 2008, Interactive 3-D computation of fault surfaces using level sets, *Visual Geoscience*, **13**, 133–138.

Liu, G., S. Fomel, L. Jin, and X. Chen, 2009, Stacking seismic data using local correlation, *Geophysics*, **43**(3), 43–48.

Lu, W., 2006, Adaptive noise attenuation of seimic images

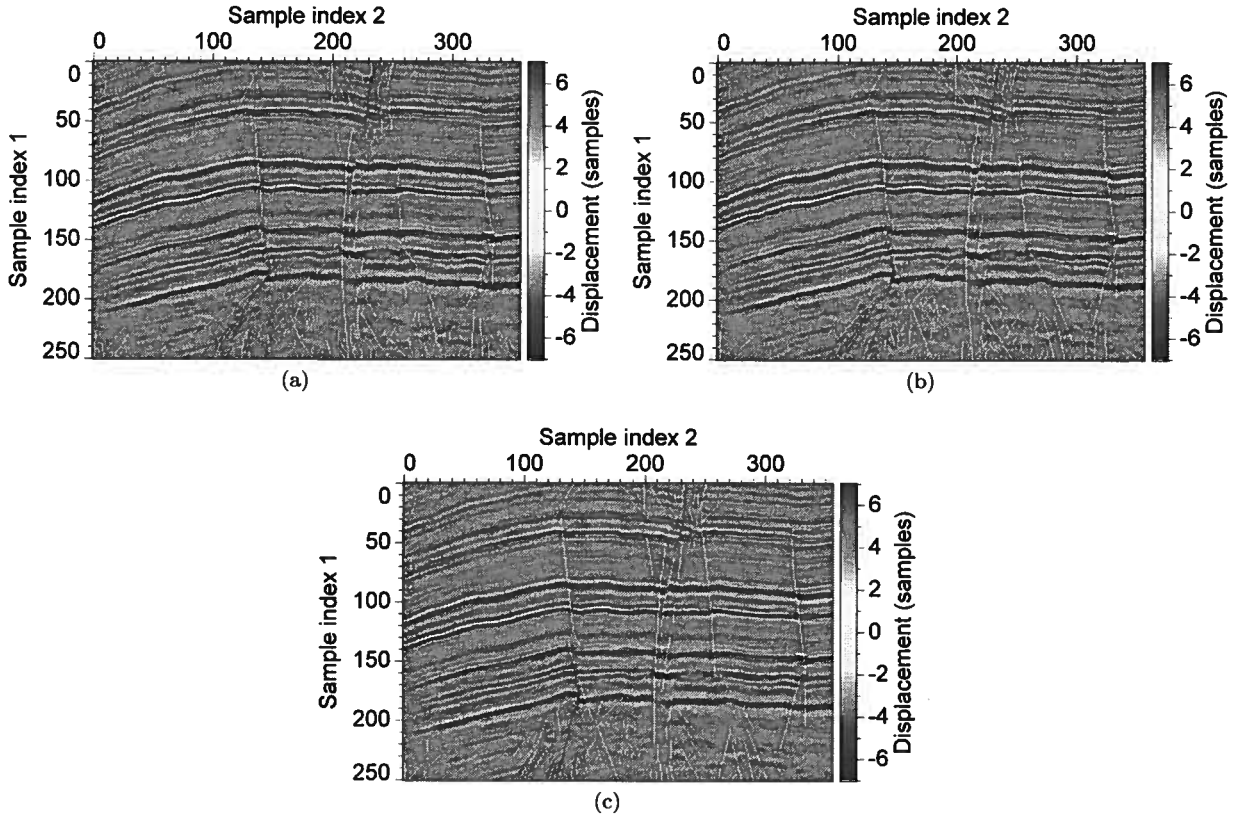

Figure 21. Vertical components of displacement vector fields estimated by using different maximum vertical displacement l_1: (a) 12; (b) 15; (c) 18.

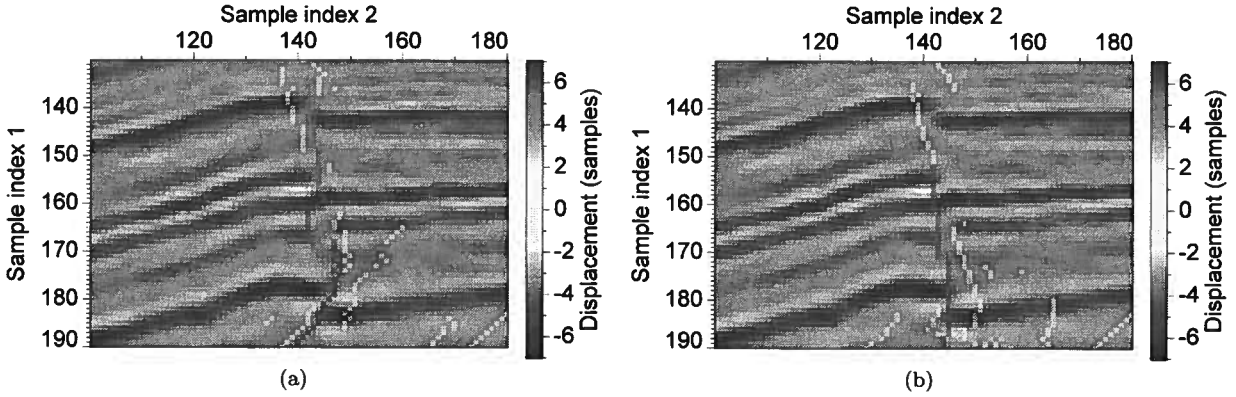

Figure 22. Subsets of vertical displacement fields estimated by using different maximum vertical displacement l_1: (a) 12; (b) 18.

based on singular value decomposition and texture direction detection, *Journal of Geophysics and Engineering*, **3**, 28–34.

Lu, Y. and W. Lu, 2009, Edge-preserving polynomial fitting method to suppress random seismic noise, *Geophysics*, **74**(4), 69–73.

Luo, Y., M. Marhoon, S. Al-Dossary, and M. Alfaraj, 2002, Acquistion ProcessingEdge-preserving smoothing and applications, *The Leading Edge*, **21**(136), 136–141.

Oppenheim, A. V., R. W. Schafer, and J. R. Buck, 1999. Discrete-Time Signal Processing (2nd Edition). *Prentice Hall*

Patel, D., C. Giertsen, J. Thurmond, and M.E. Gröller, 2009. The seismic analyzer: Interpreting and illustrating 2D

Seismic Data. *IEEE Transactions on Visualization and Computer Graphics*, **14**(6), 1571–1578.

Patel, D., Ø. Sture, H. Hauser, C. Giertsen and M.E. Gröller, 2009. Knowledge-assisted visualization of seismic data. *Computer & Graphics*, **33**, 585–596.

Parth, A. W., 1990. A fast algorithm for general raster rotation. *Graphics Gems*, 179–195, Academic Press.

Tüceryan, M. and A. K. Jain, 1990. Texture segmentation using voronoi polygons. *IEEE Transactions on Pattern Analysis and Machine Intelligence*, **12**, 211–216.

Weickert, J., 1999. Coherence-Enhancing Diffusion Filtering. *International Journal of Computer Vision*, **31**(2/3), 111–127.

Watterson, J., 1986. Fault dimensions, displacements and growth. *Pure and Applied Geophysics*, **124**, 365–373.

Fault_(geology). http://en.wikipedia.org/wiki/Fault_(geology).

Painting seismic images in 3D

Chris Engelsma & Dave Hale

Center for Wave Phenomena, Colorado School of Mines, Golden, CO 80401, USA

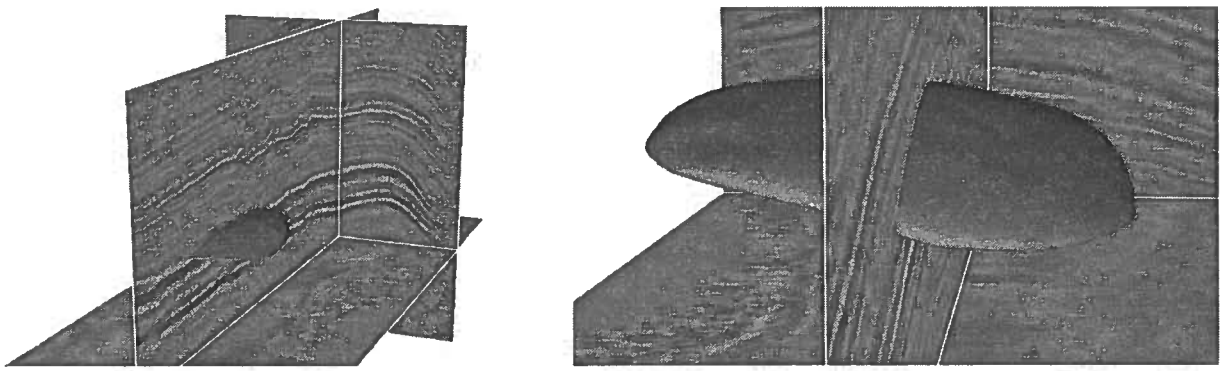

(a) (b)

Figure 1. A seismic image painted using a 3D digital paintbrush that conforms to features in the image

ABSTRACT

Seismic interpretation today includes picking seismic horizon surfaces or, more generally, the boundary between geologic bodies. A more efficient and useful approach may be to directly interpret those geologic bodies as 3D volumes. We do this by painting voxels in 3D seismic images of subsurface geology. In our painting method, a human interpreter controls the maximum size of a digital 3D paintbrush, and as the interpreter interactively moves the brush, features in the 3D seismic image automatically control its shape, orientation and size.

Key words: 3D painting seismic interpretation

1 INTRODUCTION

For decades, geophysicists and geologists have interpreted seismic sections using colored pencils and paper, where different colors were used for different geologic layers. When painting software became widely available on personal computers in the 1980s, one could use such software to perform seismic interpretation. Digital painting has a couple of advantages over drawing on paper: it can be applied in multiple overlays that can be toggled on and off and mistakes in digital painting are easy to undo. Whether with colored pencils or computer software, it is more direct and intuitive to color geologic bodies than to pick the seismic horizons that bounds these bodies.

However, we live in a 3D world, and today we interpret 3D seismic images. For 3D images, 2D painting techniques would be slow and tedious. For example, imagine interactively painting every 2D slice of a 3D image using 2D painting software. Typically, we instead pick horizon surfaces.

1.1 What is 3D Painting?

Many painting software packages offer a variety of tools for creating and editing images. Most of these tools assign color values to pixels of a 2D image displayed on a 2D computer screen. Painting in 3D requires painting voxels (3D pixels) of a 3D image displayed on a 2D computer screen. Painting in 3D is inherently more difficult, in part because of the projection from 3D to 2D, but also because 3D space-filling images can seldom be

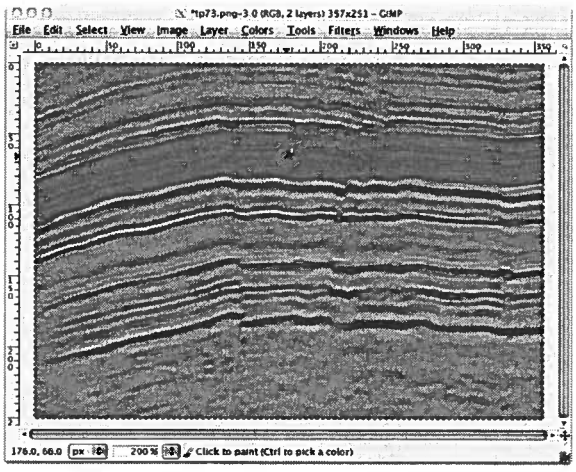

Figure 2. A seismic section being painted using GIMP, an open source 2D paint program. Repeating this process for a 3D image would become cumbersome and tedious.

displayed in their entirety. Usually we can only visualize 2D slices of 3D images and paintings.

However, recently introduced techniques enable painting on a 2D screen with a simulated 3D environment. For example, an artist's brush stroke may be realistically reproduced by constructing virtual brushes, and thereby transforming the user's cursor into a convincing paintbrush (Baxter et al, 2001; Baxter and Lin, 2004). Another simulated 3D painting method involves interactively painting texture directly onto a triangulated surface with perspective projection on a 2D screen. This method enables an artist to paint textures directly onto scanned surfaces in real-time (Hanrahan and Haeberli, 1990; Agrawala et al, 1995).

The techniques mentioned above use virtual brushes and surfaces to paint. While the painting environment is almost 3D, the user is unable to paint anything that does not lie within the surface on which the paintbrush is confined. Confinement of the paintbrush to a single surface inhibits efficient painting of 3D volumes, such as those filled by 3D seismic images. As Figure 1 suggests, when painting 3D geologic structures, we should paint volumes directly. In this paper, we refer to such direct painting of volumes as *painting in 3D* or simply *3D painting*.

Methods for 3D painting of subsurface geology have been proposed by others. Like our method, these other painting methods employ image processing algorithms to guide the painting of imaged geologic structures.

1.2 Predictive painting from plane-wave destruction

Fomel (2008) proposed a method for 3D painting using local estimates of slopes of reflections in seismic images. The method he uses is called *predictive painting* because it estimates the reflection slopes using lateral (trace-to-trace) prediction-error filters. This method uses reflection slopes to guide extrapolation of painted values from any reference trace to other traces in the seismic image. Fomel's (2008) method is interactive in that a user specifies one or more reference traces. Paint then flows automatically from those traces to other traces along imaged geologic layers. When multiple reference traces are specified, this method averages painting values extrapolated from different reference traces. In effect, paint flows laterally in directions that minimize lateral prediction errors.

Therefore, this painting method works best when traces in a seismic image can be well predicted by adjacent traces. However, this method works less well when painting across faults, or across unconformities and folds, within stratigraphic features such as channels, or within steeply dipping layers and salt diapirs. The reason this method works poorly in these cases is because these geologic features are not well described by lateral trace-to-trace prediction of seismic reflections.

1.3 GPU-accelerated "visulation"

A different visualization and simulation ("visulation") method developed by Kadlec (2009) uses structure tensors (van Vliet and Verbeek, 1995) computed from 3D images to guide the painting of those images. For example, an interpreter might first pick seed points on 2D slices of 3D seismic images. These seed points then serve as sources of paint in a simulation of an anisotropic fluid flow that is governed by the structure tensors. At each time step of the flow simulation, paint diffuses from the source voxels to other voxels in the 3D image, and a human interpreter can interactively stop the simulation, say, when paint has flowed far enough or when new seed points must be specified to fill in unpainted regions.

1.4 Our painting method

Like the two methods summarized above, our 3D painting algorithm has three features: an ability to interactively select and paint a 3D voxel, a mechanism for automatically painting other voxels, and a user-friendly interface. Of these two methods, our method is most similar to that of Kadlec (2009), in that our painting is guided by structure tensors computed from a 3D seismic image.

Relative to these other methods, our method works more like typical 2D painting software, in which an interpreter drags a digital paintbrush across an image. All voxels inside the digital 3D paintbrush are painted, while those outside remain unchanged. The key difference is that the size, shape, and orientation of our 3D paintbrush conforms to features in a 3D seismic image. In this way, our paintbrush facilitates efficient painting within, but not across, geologic features.

2 CONSTRUCTING THE BRUSH

Suppose that one wants to paint an object displayed on the computer screen. In traditional painting software, the user is given a digital canvas (a 2D image) and a set of painting tools. These tools may for example include circles (or other simple brush shapes) in various sizes, like the one shown in Figure 2.

With any of these tools, painting is interactive, because the user selects pixels with a cursor, but software paints the selected pixels and other pixels nearby automatically. This automatic painting of nearby pixels is essential because users rarely want to paint every pixel one at a time.

Our 3D painting algorithm is an expansion on the paintbrush concept. Our 3D paintbrush has a maximum size that the user controls, much like the radius of a circular brush in a 2D painting program. However, its actual size, shape, and orientation in 3D depend on features in the seismic image. More precisely, the aspects of our 3D paintbrush depend on structure tensors that we compute from a 3D seismic image.

2.1 Structure tensors S(x)

Before painting a 3D seismic image, we first compute a structure tensor field from that image. As described by van Vliet and Verbeek (1995) and Fehmers and Hocker (2003), each structure tensor in our 3D tensor field is a smoothed outer product of image gradients.

Let $\mathbf{g}(\mathbf{x}) = \nabla f(\mathbf{x})$ denote the gradient vector field computed for an image $f(\mathbf{x})$. Both the gradient $\mathbf{g}(\mathbf{x})$ and image $f(\mathbf{x})$ are uniformly sampled functions of $\mathbf{x}$, which represents the spatial coordinates of image voxels. Then, the structure tensor field is defined by

$$\mathbf{S}(\mathbf{x}) = \langle \mathbf{g}(\mathbf{x})\ \mathbf{g}^T(\mathbf{x}) \rangle, \tag{1}$$

where $\langle\ \cdot\ \rangle$ denotes Gaussian smoothing along all spatial coordinate axes.

Intuitively, the gradient vector field $\mathbf{g}(\mathbf{x})$ represents estimates of both the magnitudes and directions of greatest change in the image $f(\mathbf{x})$. The structure tensor field $\mathbf{S}(\mathbf{x})$ represents much the same information, only it is averaged within a Gaussian window around each sample. This spatial averaging improves the fidelity of orientations and other attributes that we may extract from structure tensors, but it also decreases our ability to detect abrupt changes in those attributes.

The eigen-decomposition of a 3D structure tensor $\mathbf{S}$ is

$$\mathbf{S} = \lambda_u \mathbf{u}\mathbf{u}^T + \lambda_v \mathbf{v}\mathbf{v}^T + \lambda_w \mathbf{w}\mathbf{w}^T, \tag{2}$$

where the eigenvalues of λ_u, λ_v, and λ_w are sorted so that

$$\lambda_u \geq \lambda_v \geq \lambda_w \geq 0. \tag{3}$$

From the definition in equation 1 above, it is easy to show that each structure tensor $\mathbf{S}$ is positive semi-definite, so that all of the eigenvalues are non-negative.

For any image voxel, the eigenvector $\mathbf{u}$, which corresponds to the largest eigenvalues λ_u, indicates the direction in which the image changes most. In a seismic image, the eigenvector $\mathbf{u}$ is generally orthogonal to imaged geologic layers. The eigenvector $\mathbf{w}$, which corresponds to the smallest eigenvalue λ_w, indicates the direction in which the image changes least; it may be aligned with images of buried channels. Both eigenvectors $\mathbf{v}$ and $\mathbf{w}$ tend to lie in planes of locally planar features in 3D seismic images.

2.2 Our 3D paintbrush

We compute our 3D paintbrush from a metric tensor field $\mathbf{D}(\mathbf{x})$ that we derive from the structure tensor field $\mathbf{S}(\mathbf{x})$. A metric tensor field defines a measure of distance between two points. For a constant metric tensor $\mathbf{D}$, we may analytically compute the distance $t(\mathbf{x})$ from a voxel to any point $\mathbf{x}$ as

$$t(\mathbf{x}) = \sqrt{\mathbf{x}^T \mathbf{D}^{-1} \mathbf{x}}. \tag{4}$$

When $\mathbf{D}$ equals the identity matrix, $t(\mathbf{x})$ is simply Euclidean distance.

More generally, if $\mathbf{D} = \mathbf{D}(\mathbf{x})$ is a non-constant metric tensor field, we must compute distances numerically by solving an eikonal equation:

$$\nabla t(\mathbf{x}) \cdot \mathbf{D}(\mathbf{x}) \nabla t(\mathbf{x}) = 1, \tag{5}$$

with the boundary condition $\mathrm{t}(\mathbf{0}) = 0$. In this case, $t(\mathbf{x})$ denotes non-Euclidean distance from the voxel to any point $\mathbf{x}$.

The surface outline of the 3D paintbrush shown in Figure 1 is simply a contour of constant distance $t(\mathbf{x}) = t_{max}$, where t_{max} denotes a user-specified maximum brush size in voxels. In this example, that maximum brush size is $t_{max} = 58$ voxels.

To compute distance $t(\mathbf{x})$, we first interactively select one voxel in the 3D seismic image. This voxel becomes the origin at which the distance $\mathrm{t}(\mathbf{0}) = 0$. Beginning with this point, we then numerically solve the eikonal equation 5 for distances $t(\mathbf{x})$. Voxels for which $t(\mathbf{x}) < t_{max}$ lie inside our 3D paintbrush, and voxels for which $t(\mathbf{x}) > t_{max}$ lie outside.

In geophysics, eikonal equations are often used to compute traveltimes. The eikonal equation 5 above, with anisotropic and spatially varying coefficients $\mathbf{D}(\mathbf{x})$, is the same used by Hale (2009a) for image-guided interpolation. In that application, as in our 3D painting

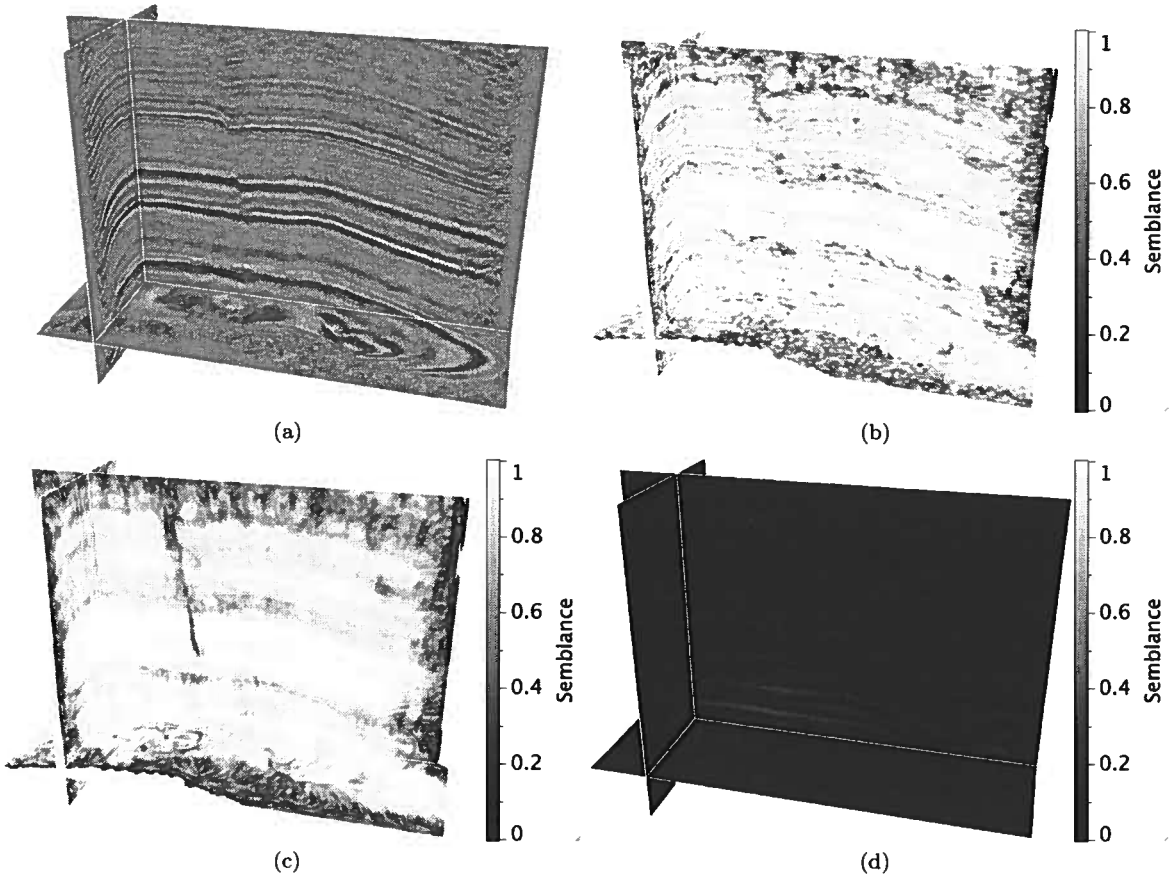

Figure 3. A 3D seismic image (a), from which we computed eigenvalues s_1 (b), s_2 (c), and s_3 (d). Note the apparent existence of geologic bedding in s_1 and s_2. Note also the near-zero values for s_3.

algorithm, "time" is a synonym for "non-Euclidean distance" as computed in a metric tensor field.

2.3 Metric tensors D(x)

When the Euclidean metric tensor $\mathbf{D} = \mathbf{I}$, the maximum brush size t_{max} is the radius, measured in voxels, of a simple spherical paintbrush. In common 2D image painting software, t_{max} would denote the radius, measured in pixels, of a circular paintbrush. Such a spherical (or, in 2D, circular) paintbrush might be appropriate in a region of a 3D seismic image with no significant features, say, within a large salt diapir. In this case, paint should flow isotropically from the user-specified voxel (the origin $\mathbf{x} = \mathbf{0}$) to all points $\mathbf{x}$ for which $t(\mathbf{x}) \leq t_{max}$.

In contrast, when painting imaged geologic bodies, such as depositional layers, fault blocks, and channels, paint should flow anisotropically within, but not across, the boundaries of these bodies. In other words, distances between points in different geologic bodies should be much greater than distances between points within a single geologic body.

We construct an anisotropic paintbrush, like that

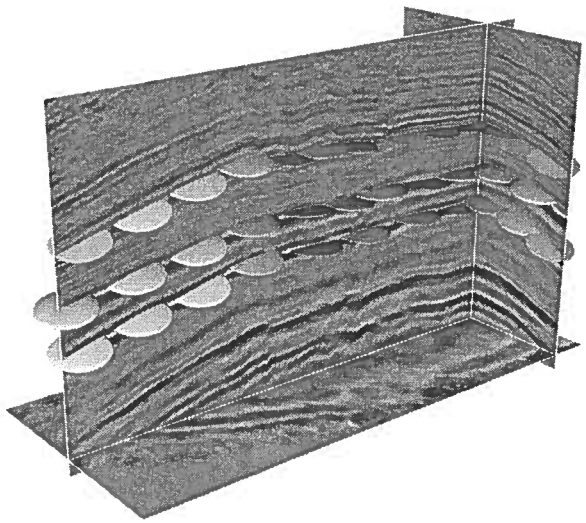

Figure 4. Tensors derived from a seismic image are overlain on that image. Each tensor is represented as an ellipsoid glyph. These tensors guide the eikonal equation which gives the paintbrush its shape.

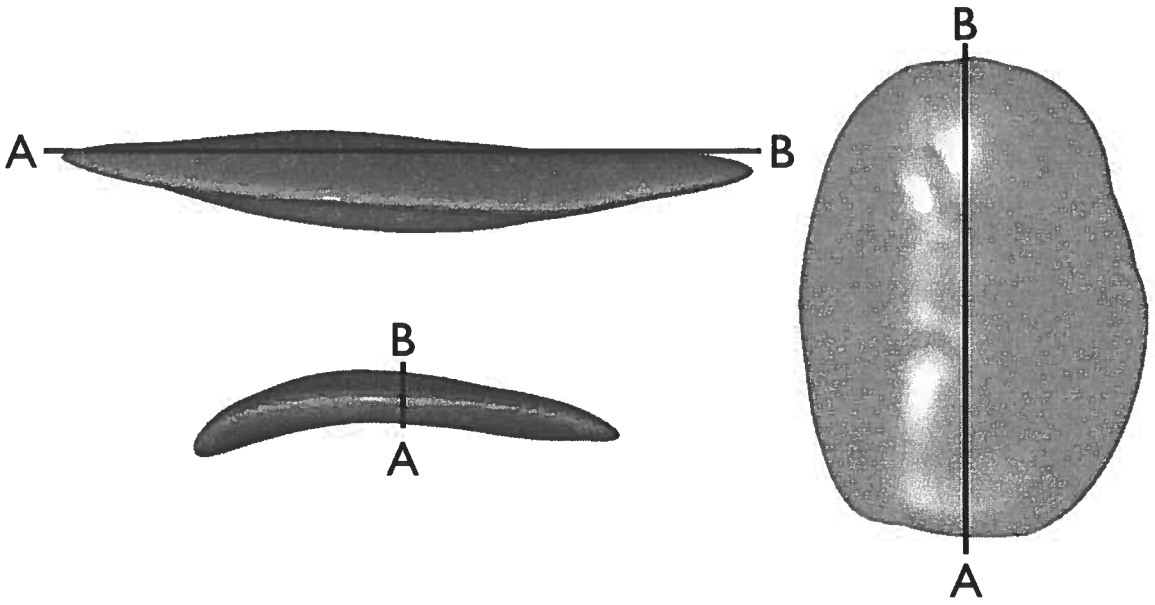

Figure 5. Three different views of a 3D paintbrush. Reference markers A and B show relative orientation. The shape and orientation of this brush depends on the metric tensor field $\mathbf{D}(\mathbf{x})$ in the vicinity of the voxel (inside the brush) that was selected interactively by the painter.

shown in Figure 1, by computing an anisotropic metric tensor field $\mathbf{D}(\mathbf{x})$. We choose the eigenvectors of each metric tensor $\mathbf{D}$ to be the same as those for the corresponding structure tensor $\mathbf{S}$. The difference between $\mathbf{D}$ and $\mathbf{S}$ lies only in their eigenvalues.

Specifically, in the eigen-decomposition of $\mathbf{D}$,

$$\mathbf{D} = s_3\mathbf{u}\mathbf{u}^T + s_2\mathbf{v}\mathbf{v}^T + s_1\mathbf{w}\mathbf{w}^T, \tag{6}$$

we construct eigenvalues s_1, s_2, and s_3 such that

$$0 \leq s_3 \leq s_2 \leq s_1 \leq 1, \tag{7}$$

where s_1, s_2, and s_3 are computed using semblance.

Figure 3 shows slices of semblances s_1, s_2, and s_3 computed using data provided from the US Department of Energy. When representing these tensors $\mathbf{D}(\mathbf{x})$ as ellipsoids (Engelsma and Hale, 2010) in a typical 3D seismic image, we expect these ellipsoids to be relatively flat and oblate. Figure 4 shows a set of ellipsoids which represents metric tensors in a 3D seismic image. Note that each ellipsoid is relatively oblate indicating that the local feature is more coherent along geologic boundaries and less so across each boundary.

Semblances are useful, in part, because they are an amplitude-independent measure of the coherence of features in seismic images. Semblances and, hence, the eigenvalues of $\mathbf{D}$, are normalized in the range [0,1].

The largest eigenvalue s_1, corresponding to the eigenvector $\mathbf{w}$, is semblance computed within a locally linear (1D) set of voxels aligned with $\mathbf{w}$. Each eigenvalue s_2, corresponding to the eigenvector $\mathbf{v}$, is semblance computed within a locally planar (2D) set of voxels orthogonal to the corresponding eigenvector $\mathbf{u}$. (The plane orthogonal to $\mathbf{u}$ contains the eigenvectors $\mathbf{v}$ and $\mathbf{w}$). Finally, each eigenvalue s_3 represents semblance computed for a locally spherical (3D) set of voxels. We compute these three measures of semblance using the structure-oriented method proposed by Hale (2009b).

Because the eigenvalues of $\mathbf{D}$ are bounded between [0,1], $t(\mathbf{x})$ computed using equation 5 will never exceed those computed for a constant identity tensor $\mathbf{D} = \mathbf{I}$. In other words, our non-Euclidean distances $t(\mathbf{x})$ will always be less than or equal to Euclidean distances. Therefore, when specifying the maximum distance t_{max}, one may think intuitively of Euclidean distance, and know that the 3D paintbrush, like that shown in Figure 1, lies inside a sphere with radius t_{max}. In noisy incoherent regions of a 3D seismic image, where all three semblances are low, the brush will be much smaller than that sphere.

The upper bound t_{max} also simplifies computation of the distances $t(\mathbf{x})$. When a user selects a voxel in the 3D seismic image, that point becomes the origin for the eikonal equation 5. In solving that equation, we need only consider voxels at locations $\mathbf{x}$ that lie inside a sphere centered at the origin with radius t_{max}. For any voxels outside of that sphere, distances $t(\mathbf{x})$ must exceed t_{max}.

For typical 3D seismic images with zero mean, 3D (volume) semblance s_3 tends to be much smaller than 1D (linear) semblance s_1 or 2D (planar) semblance s_2.

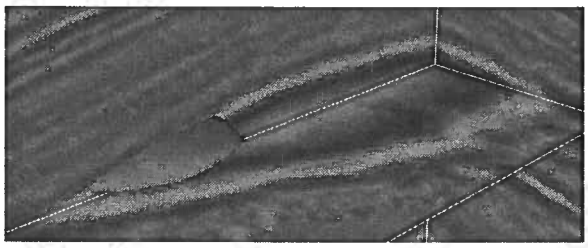

Figure 6. A painter has dragged the cursor along one panel in a 3D seismic image. Because the paintbrush paints voxels, points in the formation which extend beyond the plane of the paintbrush are painted, honoring the geologic structure.

That is, the sum of image voxels within any 3D window with radius greater than a seismic wavelength will be nearly zero. Any locally planar feature in a seismic image will yield a large semblance s_2, which is computed from a locally planar set of voxels. However, for the same feature, semblance s_2 should be no greater than semblance s_1, computed for a linear subset of those voxels. In other words, when the values of a locally planar set of image voxels are nearly constant, both s_1 and s_2 will be nearly one. In such cases, distances $t(\mathbf{x})$ are relatively small within the plane of the eigenvectors $\mathbf{v}$ and $\mathbf{w}$, and are much larger in the orthogonal direction of the eigenvector $\mathbf{u}$. Figure 4 demonstrates the relative geometric relationship between all eigenvectors in the form of oblate ellipsoids.

3 THE PAINTER'S INTERFACE

We designed our 3D painting to work similar to computer programs for 2D painting. As illustrated in Figure 1, we display our 3D paintbrush as a surface. We construct that surface by applying the marching cubes algorithm (Lorenson and Cline, 1987) to our numerically computed distance field $t(\mathbf{x})$. This algorithm requires only a simple scan of the voxels within the bounding sphere of our paintbrush. It produces a set of triangle vertices and normal vectors that when rendered appear as the continuous red surface shown in Figure 1.

Figure 5 displays multiple views of a 3D paintbrush with a different size, shape, and orientation. These attributes of the paintbrush vary, as they depend on both the tensor field $\mathbf{D}(\mathbf{x})$ and the location of the origin voxel selected by the painter.

In Figure 6, a painter has dragged a mouse cursor along a set of voxels in one vertical slice of a 3D seismic image. As the painter's cursor moves, the shape of the brush changes to conform to features in the image.

4 DISCUSSION

Painting geologic structures in 3D is a natural extension of classical interpretation techniques. It is also an improvement on triangulating flat horizons by allowing the user to fill entire geologic structures rather than trace the horizons between layers. This added dimensionality of the structure allows for extensive and interactive reservoir estimation. It is important to note that our painting algorithm does not alter the seismic image. Instead, the painted voxels are painted on a separate canvas. This enables the painter to separate the painted areas from the image, allowing for further interpretation and extraction.

4.1 Extracting geologic layers

The same algorithm used to render the brush can be implemented to extract painted voxels in 3D. This allows for a macroscopic investigation of geologic structure. Because painting is tensor-driven (not amplitude-driven), structures such as salt diapirs can be highlighted. Visualization of 3D volumes is analogous to visualizing triangulated horizon surfaces. The difference between extracting horizons and extracting surfaces is that volumes provide further insight into the structure of the subsurface. From an interpretation standpoint, this technique provides insight to the structural characteristics of geologic entities.

4.2 Production estimation

Aside from being a useful visual tool, the combination of a painted area with measured data from well logs permits us to estimate volumetric information. This method can be useful for hydrocarbon and mineral extraction. Well logs give an idea of locations of areas of interest because they consist of measured material properties. Therefore, we may use them as a guide to paint. For example, using gamma ray logs as a guide to paint sandstone may be done quickly using the interactive 3D brush. By changing the blending properties of paint, the painter can choose to overwrite previously painted voxels or to mix them together. For instance, by choosing to overwrite previously painted voxels, a painter may want to specify whether a geologic layer is strictly sand or shale. By blending painted voxel values together, however, allows for more realistic mixtures of rock layers (e.g. dirty sandstone). In either case, the painter is guided by the log information. Painting a target body and integrating over all voxels produces an accurate volume measurement. Approximation of geologic volume could provide a different way to estimate the barrels of oil within a reservoir.

5 CONCLUSIONS

Painting images in 3D is an important topic in seismic interpretation. However, painting is typically restricted to a 2D canvas. Instead of painting images, interpreters

draw boundaries between layers for simplicity. We show that by constructing a paintbrush using metric tensors that are derived from structure tensors and from the semblances of the image, we are able to paint with a brush that conforms to the image. This enables one to more accurately paint voxels of data in a manner that is consistent with geologic structure of the subsurface. Our painting algorithm is much like 2D painting software, however, our paintbrush extends beyond the canvas by painting volumes instead of surfaces. Moreover, our algorithm allows for both a level of interactivity and automation.

We also keep the painted voxels separate from the original image, permitting further interpretation and visualization of the subsurface. By extracting geologic bodies, we can visualize the thickness and overall shape of a geologic entity such as a salt diapir or gas pockets. We suggest an alternative method for estimating original oil in place by integrating over painted voxels from a geologic area of interest. This involves coupling the seismic image with data measured from well logs.

6 ACKNOWLEDGEMENTS

Thanks to the Rocky Mountain Oilfield Testing Center, a facility of the U.S. Department of Energy, for the dataset producing the seismic images in this paper. We thank our colleagues for their discussion and input on this topic. We also thank Diane for her editing of this paper.

REFERENCES

Agrawala, M., A.C. Beers and M. Levoy, 1995, 3D painting on scanned surfaces: Proceedings of the Symposium on Interactive 3D Graphics SI3D '95, 145–150.

Baxter, W.V., V. Scheib, M.C. Lin, and D. Manocha, 2001, DAB: Interactive haptic painting with 3D virtual brushes: Proceedings of the 28th Annual Conference on Computer Graphics and Interactive Techniques, SIGGRAPH 2001, 461–468.

Baxter, W.V., and M.C. Lin, 2004, A versatile interactive 3D brush model: Proceedings of Pacific Graphics '04, 319–328.

Engelsma, C. and D.Hale, 2010, Visualization of 3D tensor fields derived from seismic images: CWP Report, To appear.

Fehmers, G.C. and C.F.W. Höcker, 2003, Fast structural interpretations with structure-oriented filtering: Geophysics, **63**, 1286–1293.

Fomel, S., 2008. Predictive painting of 3-D seismic volumes: SEG Expanded Abstracts 27, 864.

Hale, D., 2009a. Image-guided blended neighbor interpolation: CWP Report 634, 247–260

Hale, D., 2009b. Structure-oriented smoothing and semblance: CWP Report 635, 261–270.

Hanrahan, P., and P. Haeberli, 1990, Direct WYSIWYG painting and texturing on 3D shapes: Computer Graphics, **24**, 215–223.

Jeong, W.K., P.T. Fletcher, R. Tao, and R.T. Whitaker, 2007, Interactive visualization of volumetric white matter connectivity in DT-MRI using a parallel-hardware Hamilton-Jacobi solver: IEEE Transactions on Visualization and Computer Graphics, **13**, 1480–1487.

Kadlec, B., 2009. Interactive GPU-based "visulation" and structure analysis of 3-D implicit surfaces for seismic interpretation: Ph.D. dissertation. University of Colorado at Boulder.

Lorenson, W.E. and H.E. Cline, 1987, Marching cubes: a high resolution 3D surface construction algorithm: Computer Graphics, **21**, 163–169.

van Vliet, L.J. and P.W. Verbeek, 1995, Estimators for orientation and anisotropy in digitized images: Proceedings of the first annual conference of the Advanced School for Computing and Imaging ASCI '95, 442–450.

Visualization of 3D tensor fields derived from seismic images

Chris Engelsma & Dave Hale

Center for Wave Phenomena, Colorado School of Mines, Golden, CO 80401, USA

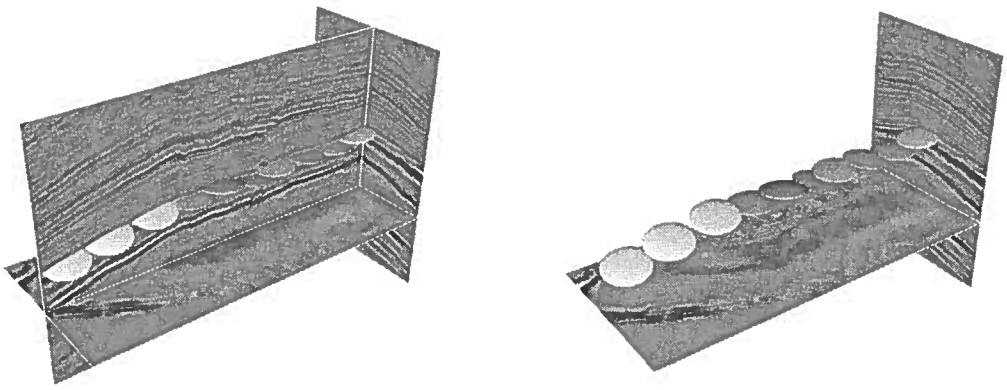

(a) (b)

Figure 1. A 3D seismic image with a traced layer displaying the tensors as ellipsoids (a), and removing that slice shows the 3-dimensional structure of the tensors from that layer (b).

ABSTRACT

In image processing, tensors derived from seismic images are used as parameters in procedures such as structure-oriented smoothing. Visualizing these tensors allows us to qualitatively assess their computation and construction. We describe a computationally effective technique to render these tensors as ellipsoid glyphs.

Key words: seismic visualization ellipsoid tensor

1 INTRODUCTION

Visualizing tensor fields has always been a complicated task. While there are many ways in which scientists can visualize scalar or vector fields, displaying tensor fields in an intuitive manner remains a challenge. In recent years, a number of techniques have been proposed discussing methods for displaying 3D tensors. In the medical industry, the continuity of tensor fields is emphasized by constructing hyperstreamlines or streamtubes for diffusion MRI tensors (Delmarcelle and Hesselink, 1993; Jianu et al, 2009). In stress evaluation, the effects of a tensor field on a given media have been visualized through bending mesh volumes, simulating the effects of a stress tensor to demonstrate anisotropic deformation (Zheng and Pang, 2002). In geophysics, tensors are being used to help guide seismic horizon tracing (Höllt et al, 2009). Recently, a number of methods have been proposed for displaying 3D tensors.

For the purposes of image processing in exploration geophysics, tensors are often derived directly from the images. While a method such as hyperstreamlining would give insight into the continuity of the tensor field, it is also advantageous to render each tensor individually by depicting them in an intuitive manner as Figure 1 demonstrates. These discrete representations of tensors in 3D are called "glyphs". Glyph representation can take many forms, and the benefits of choosing differ-

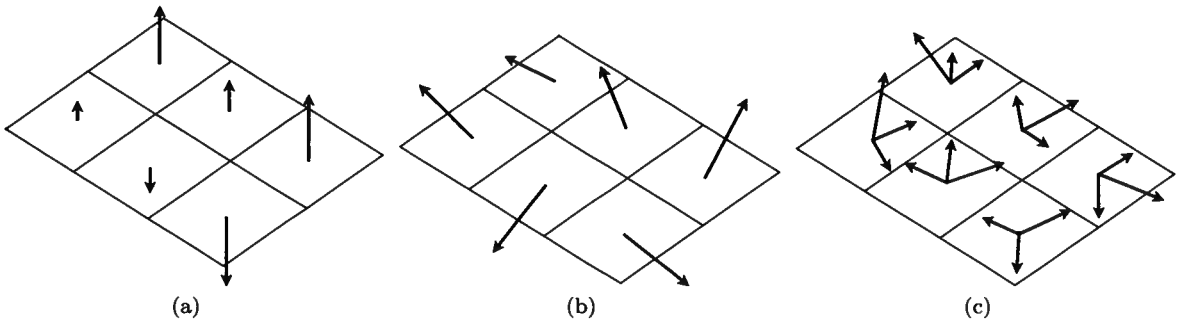

Figure 2. A scalar field (a), a vector field (b), and a tensor field (c). The visualization complexity increases dramatically with the number of quantities represented at each node.

ent shapes have been explored (Kindlmann, 2004). However, for the purpose of this paper, each tensor glyph is represented as an ellipsoid.

Tensors help increase the efficacy of image processing by guiding the orientation of the operation. This is the principle behind structure-oriented smoothing (Hale, 2009). Because these tensors are used as parameters in different processing techniques, we must determine their accuracy. We therefore wish to explore a method of visualizing these parameters in a discretized manner, allowing us to evaluate any arbitrary tensor. We describe an algorithm to visualize tensors derived from seismic images, and demonstrate methods for evaluating the tensor's authenticity. By displaying tensors as ellipsoid glyphs, this visualization method provides an intuitive and interactive method for relating the tensors directly back to the image. We also expedite the rendering process by making our method computationally fast and efficient.

2 TENSOR GEOMETRY

The challenge with visualizing tensors stems from their multivariate nature. With scalar fields, each sample is a representative of one number. Vector fields follow the same concept, but each point is now represented by three numbers in 3D. Tensor fields introduce another step in intricacy because we are now representing six unique numbers at every point in space. A visual representation of this increasing complexity is shown in Figure 2. Simultaneous visualization of six numbers extends beyond conventional visualization techniques unless we understand the geometry of the tensors.

2.1 Metric tensor field D(x)

An ideal structure-oriented procedure which honors the dominant structural features of our image (e.g. rock bedding layers and faults), requires a tensor field that accurately represents these features. This is accomplished by first computing the structure tensors $\mathbf{S}(\mathbf{x})$ (van Vliet and Verbeek, 1995; Fehmers and Höcker, 2003), which are smooth outer-products of image gradients. The eigen-decomposition of a 3D structure tensor $\mathbf{S}(\mathbf{x})$ yields:

$$\mathbf{S} = \lambda_u \mathbf{u}\mathbf{u}^T + \lambda_v \mathbf{v}\mathbf{v}^T + \lambda_w \mathbf{w}\mathbf{w}^T, \tag{1}$$

where the eigenvalues of λ_u, λ_v, and λ_w are sorted so that

$$\lambda_u \geq \lambda_v \geq \lambda_w \geq 0. \tag{2}$$

By convention, $\mathbf{u}$ is defined as the eigenvector that traverses the direction of the largest gradient. In a 3D seismic image, this typically refers to the direction perpendicular to geologic layering. Both eigenvectors $\mathbf{v}$ and $\mathbf{w}$ tend to lie in the plane of locally planar features in the image.

We then compute anisotropic metric tensors $\mathbf{D}(\mathbf{x})$, using a process outlined by Hale (2009), whereby we compute image semblances. We choose the eigenvectors of each metric tensor $\mathbf{D}$ to be the same as those for the corresponding structure tensor $\mathbf{S}$. The difference between $\mathbf{D}$ and $\mathbf{S}$ lie only in their eigenvalues. Specifically, the eigen-decomposition on $\mathbf{D}(\mathbf{x})$ is

$$\mathbf{D} = s_3 \mathbf{u}\mathbf{u}^T + s_2 \mathbf{v}\mathbf{v}^T + s_1 \mathbf{w}\mathbf{w}^T, \tag{3}$$

where we construct eigenvalues s_1, s_2, and s_3 such that

$$0 \leq s_3 \leq s_2 \leq s_1 \leq 1. \tag{4}$$

Our metric tensor $\mathbf{D}(\mathbf{x})$ is a 3×3 symmetric, positive-definite matrix. The largest eigenvalue s_1, corresponding to the eigenvector $\mathbf{w}$, is semblance computed within a locally linear (1D) set of voxels aligned with $\mathbf{w}$. Each eigenvalue s_2, corresponding to the eigenvector $\mathbf{v}$, is semblance computed within a locally planar (2D) set of voxels orthogonal to the corresponding eigenvector $\mathbf{u}$. (The plane orthogonal to $\mathbf{u}$ contains the eigenvectors $\mathbf{v}$ and $\mathbf{w}$). Finally, each eigenvalue s_3 represents

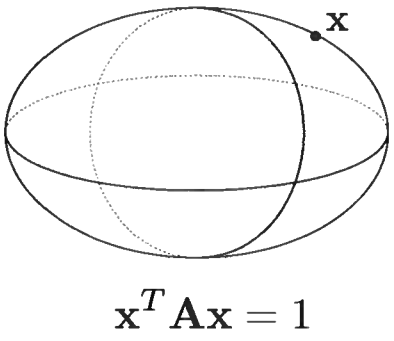

Figure 3. A non-axis-aligned ellipsoid.

semblance computed for a locally spherical (3D) set of voxels.

2.2 Ellipsoid glyphs

We consider the definition of an ellipsoid to be

$$\mathbf{x}^T\mathbf{A}\mathbf{x} = 1, \tag{5}$$

where $\mathbf{A}$ is a square symmetric positive-definite matrix, and $\mathbf{x}$ is any point along the surface of the ellipsoid which satisfies this equation (note Figure 3). We can likewise define a unit sphere in the same manner by replacing matrix $\mathbf{A}$ with the identity matrix $\mathbf{I}$.

Equation 2 provides a useful definition because it describes an ellipsoid that is not axis-aligned; the eigenvectors of $\mathbf{A}$ are arbitrarily aligned in space. Considering the definition of eigenvector orthonormality, we define the eigenvectors as the three principle axis radii, and the inverse of the square root of the eigenvalues as their respective sizes (see Figure 4) (Strang, 2003). This geometric relationship enables us to construct the tensors as ellipsoids; in a computer, these are illustrated as glyphs.

2.3 Geologic analogy

Ellipsoid glyph representations of metric tensors demonstrate the local orientation of the image. In particular, for a perfectly horizontal layer, we expect the ellipsoid to be oblate, because $\lambda_u > \lambda_v \approx \lambda_w$. Likewise, for complete isotropy within an image, we expect our ellipsoid to be a sphere ($\lambda_u = \lambda_v = \lambda_w$). The local geologic orientation of the formation is also reflected, so ellipsoids incorporate the same strike and dip qualities as their corresponding locations in the seismic image. Because the intention of displaying these ellipsoids is to qualitatively assess the how accurately the tensors have been constructed, we expect that they follow the bedding layers in the image. This allows us to judge the veracity of image processing techniques guided by these tensors.

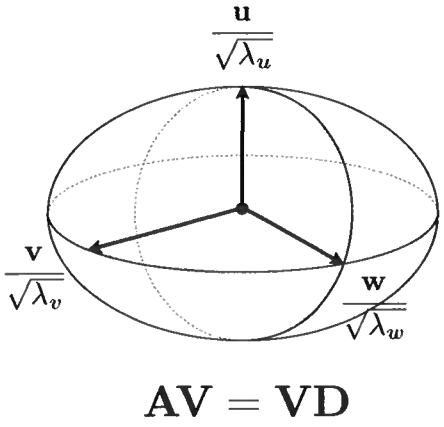

Figure 4. Eigenvalue and eigenvector relationship to the three principle radii of an ellipsoid. Each axis within the ellipsoid is equal to the eigenvector divided by the square root of their eigenvalues.

3 ACCELERATED RENDERING

Constructing each glyph requires computing the location of roughly one thousand vertices to be used in a triangle mesh (see Figure 5). This computation becomes costly when one begins to display a large set of ellipsoids throughout a 3D survey. We therefore expedite the rendering process. If we first compute the vertex locations for a unit circle, we then obtain the desired ellipsoid by applying the appropriate matrix transformations. This greatly reduces the computational cost.

We compare the equations of a unit circle,

$$\mathbf{x}^T\mathbf{x} = 1, \tag{6}$$

to our desired transformed ellipsoid coordinates,

$$\mathbf{y}^T\mathbf{A}\mathbf{y} = 1. \tag{7}$$

We also define the eigen-decomposition of $\mathbf{A}$ to be

$$\mathbf{A} = \mathbf{V}\mathbf{D}\mathbf{V}^T, \tag{8}$$

where $\mathbf{V}$ is a 3×3 orthogonal matrix containing the eigenvectors of $\mathbf{A}$ stored as column vectors, and $\mathbf{D}$ is a diagonal matrix storing eigenvalues $\lambda_u \geq \lambda_v \geq \lambda_w$. We now replace $\mathbf{A}$ in equation 8 with equation 7, and we get

$$\mathbf{y}^T\mathbf{V}\mathbf{D}\mathbf{V}^T\mathbf{y} = 1. \tag{9}$$

Given the property of a diagonal matrix that $\mathbf{D} = \mathbf{D}^{\frac{1}{2}}\mathbf{D}^{\frac{1}{2}}$, we expand equation 9 to get

$$\mathbf{y}^T\mathbf{V}\mathbf{D}^{\frac{1}{2}}\mathbf{D}^{\frac{1}{2}}\mathbf{V}^T\mathbf{y} = 1. \tag{10}$$

Equation 10 is the equation of an ellipsoid in terms of

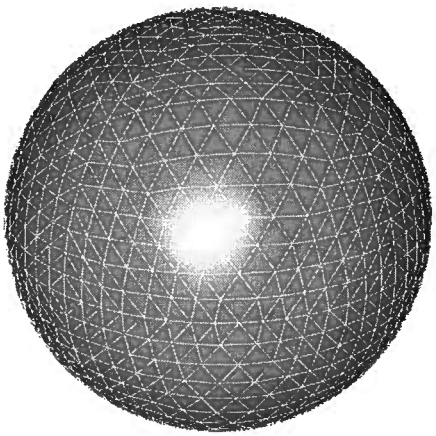

(a)

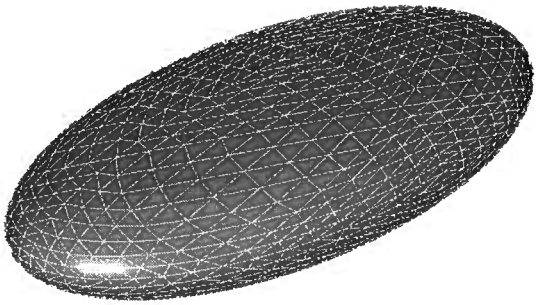

(b)

Figure 5. Two glyphs: a unit sphere (a) and an ellipsoid (b). The ellipsoid was computed using matrix transformations on the sphere's mesh.

the eigenvectors and eigenvalues of $\mathbf{A}$. From equation 6, we observe that the variable $\mathbf{x}$ represents the coordinates of a unit sphere. To transform the sphere into an ellipsoid, we derive our desired coordinates $\mathbf{y}$ in terms of our computed coordinates $\mathbf{x}$:

$$\mathbf{y} = \mathbf{V}\mathbf{D}^{-\frac{1}{2}}\mathbf{x}. \tag{11}$$

$\mathbf{V}$ represents a rotation matrix which realigns the principle axes of the unit sphere. The matrix $\mathbf{D}^{-\frac{1}{2}}$ is a nonuniform scaling matrix containing the inverse of the square root of the eigenvalues. Performing equation 11 is more computationally efficient than explicitly computing each vertex because this process passes 12 numbers to the graphics card instead of recalculating one thousand coordinates for each ellipsoid. The vertex coordinates for a unit sphere are only computed once and stored.

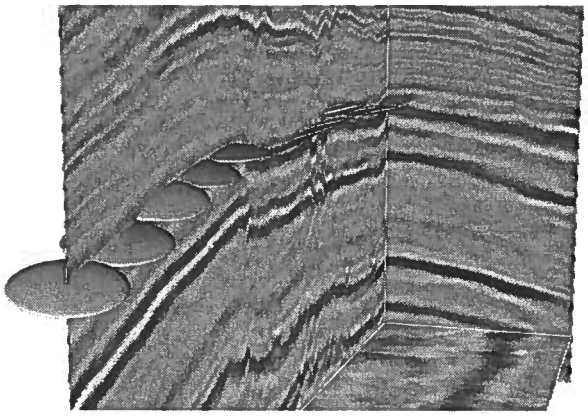

Figure 6. Ellipsoids selected to follow a single layer by "point-and-click" method. The strike and dip of the local formation is apparent.

4 IMPLEMENTATION METHODS

Here we discuss two methods for overlaying ellipsoid glyphs on 3D seismic data. Both methods offer different techniques to visualize tensors, and both may be used for different investigative purposes. We show two approaches to displaying tensor fields: a point-and-click and an axis-aligned panel method.

4.1 Point-and-click method

Figure 6 shows ellipsoids that are selected along a given layer. This is performed by a succession of mouse clicks which place an ellipsoid's center on the sample nearest to the cursor. Note that every ellipsoid appears oblate with varying thicknesses, and that each ellipsoid has a dip that reflects the local orientation. Focusing on the shape of the ellipsoids is important for determining whether or not the tensor field has been correctly computed. Note also that the ellipsoids appear in 3D relative to the image slice. This allows the user to rotate freely, preserving the location and visibility of the tensor.

In a similar way, the user can drag the cursor along the image and observe the changes in the ellipsoids at each point in space. By not sticking the ellipsoids as in Figure 6, the user can watch the tensor mold to the layers and identify discrepancies this way.

4.2 Axis-aligned panels

Placement of ellipsoids along an axis-aligned panel (see Figure 7) shows an overall distribution of tensor clusters. This process involves discretizing tensors along a

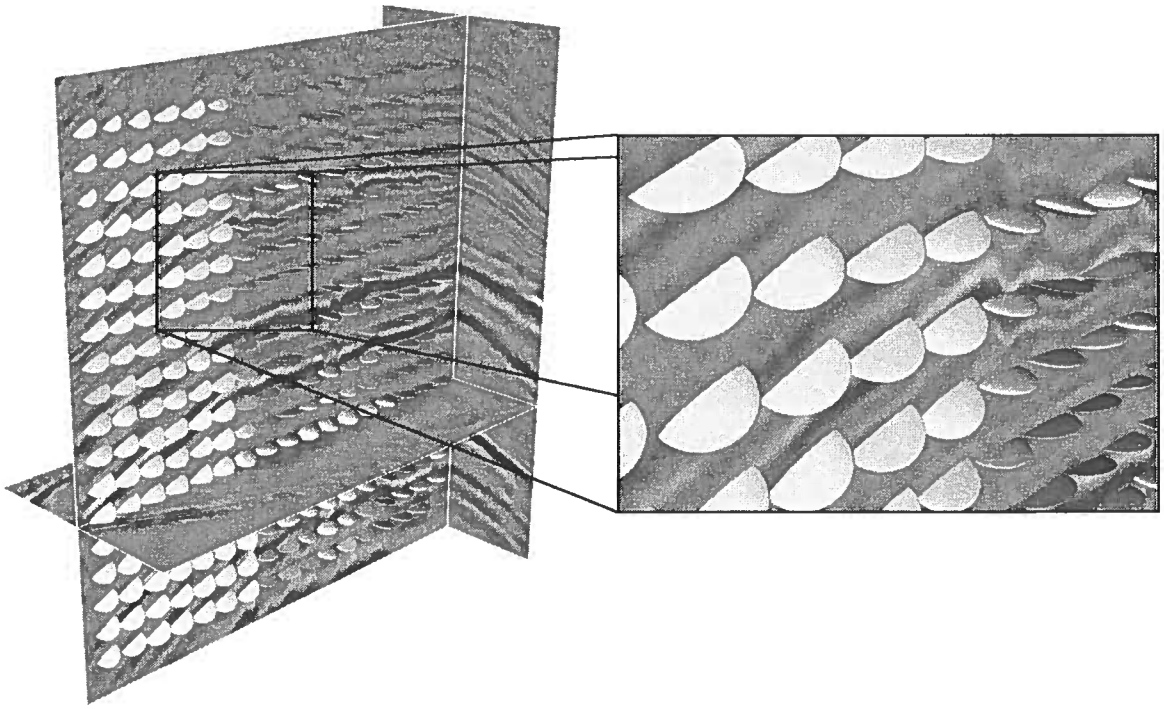

Figure 7. A panel of tensor ellipsoids. Each ellipsoid represents a metric tensor, and is equally sampled along the x-axis panel. The closeup emphasizes the variation in shape as well as angle of each ellipsoid at each point in space.

3D seismic panel, allowing the user to qualitatively assess many tensors simultaneously. From a macroscopic viewpoint, this will enable the user to grab a broad perspective of the underlying structure. While Figure 7 shows ellipsoids attached to a single panel, displaying ellipsoids on all three axis-aligned panels is a reasonable interpretation method as well.

The caveat of this approach is that ellipsoids will not necessarily fall directly on a point of interest. Because the ellipsoids are evenly sampled along the panel, the user is only permitted to see tensors that lie on that sampling interval. For a more detailed survey of tensor ellipsoids, the point-and-click approach is more effective.

5 CONCLUSIONS

Displaying tensor fields is an ongoing topic of research in the field of visualization. The inherent problem with displaying tensors is due to the amount of information contained in each sample. In geophysical applications of image processing, tensors are derived from the seismic images in order to design structure-oriented operations. For the purpose of quality assessment, we choose to display these tensors as glyphs shaped as ellipsoids.

Constructing ellipsoids from tensors works in our favor, as our metric tensors fit this geometric relationship. By performing an eigen-decomposition of the tensor matrix, we obtain three orthonormal eigenvectors and their corresponding eigenvalues, which can be represented as the three principle axis directions and their corresponding radii. Expediting the process involves precomputing the vertices of a unit sphere, and performing both a rotation and scaling matrix.

Because our tensors are derived from the seismic image, we show that the shape of the ellipsoid relates to the local orientation of the image. Flat layers yield disc-shaped, oblate ellipsoids, and isotropic environments are more spherical. Ellipsoids must have the same strike and dip of the surrounding area.

We demonstrate two methods of displaying tensor fields: the first dynamically selects ellipsoids at a clicked voxel; the second involves discretizing ellipsoids along an axis-aligned panel. Both techniques provide intuitive visualization of the geologic substructure, with point-and-click placement allowing for detailed investigation of a specific point.

6 ACKNOWLEDGEMENTS

We thank the Rocky Mountain Oilfield Testing Center, a facility of the U.S. Department of Energy, for providing us with the data used for Figures 1, 6, and 7. We also thank our colleagues for their continual discussion and feedback on this topic. We also thank Diane for her very helpful editing of this paper.

REFERENCES

Delmarcelle, T. and L. Hesselink, 1993, Visualizing second-order tensor fields with hyperstreamlines: IEEE Computer Graphics and Applications, **13**, 25–33.

Fehmers, G.C. and C.F.W. Höcker, 2003, Fast structural interpretations with structure-oriented filtering: Geophysics, **63**, 1286–1293.

Hale, D., 2009. Structure-oriented smoothing and semblance: CWP Report 635, 261–270.

Höllt, T. et al, 2009, Seismic horizon tracing with diffusion tensors: Presented at IEEE VisWeek 2009.

Jianu, R., Ç. Demiralp, and D.H. Laidlaw, 2009, Exploring 3D DTI fiber tracts with linked 2D representations: IEEE Transactions on Visualization and Computer Graphics, **15**, 1449–1456.

Kindlmann, G., 2004, Superquadric tensor glyphs: In Proceedings of the Joint Eurographics - IEEE TCVG/EG Symposium on Visualization '04, 147–154.

Strang, G., 2003, Introduction to linear algebra: Wellesley-Cambridge Press, 553.

van Vliet, L.J. and P.W. Verbeek, 1995, Estimators for orientation and anisotropy in digitized images: Proceedings of the first annual conference of the Advanced School for Computing and Imaging ASCI '95, 442–450.

Zheng, X. and A. Pang, 2002, Volume deformation for tensor visualization: Proceedings of the conference on Visualization '02, 379–386.

Image-guided 3D interpolation of borehole data

Dave Hale
Center for Wave Phenomena, Colorado School of Mines, Golden CO 80401, USA

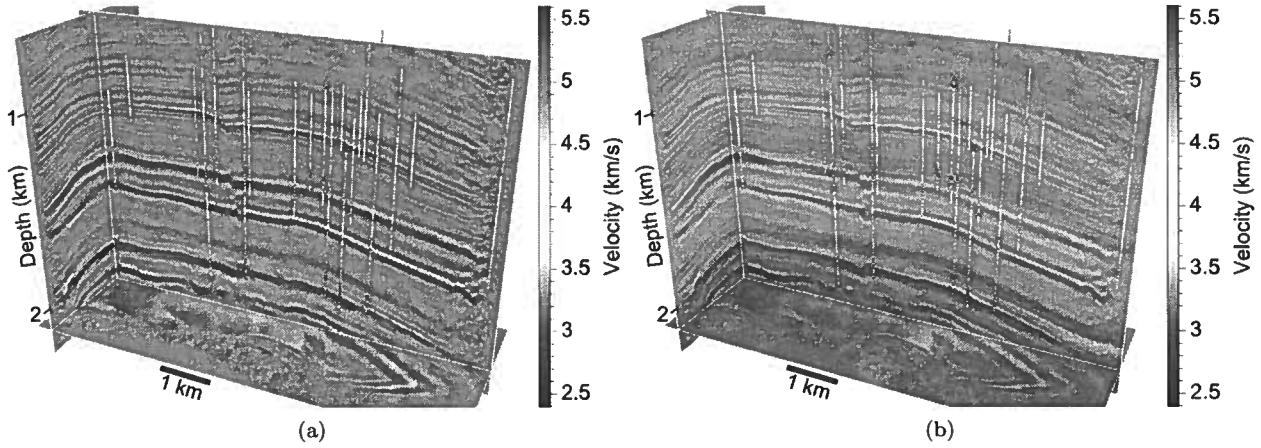

Figure 1. Slices of a 3D seismic image (a) with P-wave velocities measured in boreholes and an image-guided 3D interpolation (b) of those measured velocities.

ABSTRACT

A blended neighbor method for image-guided interpolation enables resampling of borehole data onto a uniform 3D sampling grid, without picking horizons and without flattening seismic images. Borehole measurements gridded in this way become new 3D images of subsurface properties. Property values conform to geologic layers and faults apparent in the seismic image that guided the interpolation.

The freely available Teapot Dome data set, which includes a 3D seismic image, horizons picked from that image, and numerous well logs, provides an ideal demonstration of image-guided interpolation of borehole data. In this example, seismic horizons picked by others coincide with thin layers apparent in the new 3D images of interpolated borehole data, even though the horizons were not used in the interpolation process.

Key words: seismic image well logs interpolation interpretation

1 INTRODUCTION

Seismic images are often used to guide the interpolation of subsurface properties that are measured more directly and (usually) more precisely in boreholes. Figure 1 provides an example for a 3D seismic image and sonic (P-wave velocity) logs from the Teapot Dome oilfield in Wyoming. These data are provided by the Rocky Mountain Oilfield Test Center, a facility of the U.S. Department of Energy (Anderson, 2009). Figure 1b shows interpolated velocities, displayed with translucent color so that the corresponding three slices of the 3D seismic image are visible as well. At depths where sonic logs are available, the interpolation of velocities is guided by the seismic image.

In a more conventional seismic interpretation, we might first pick horizons corresponding to coherent re-

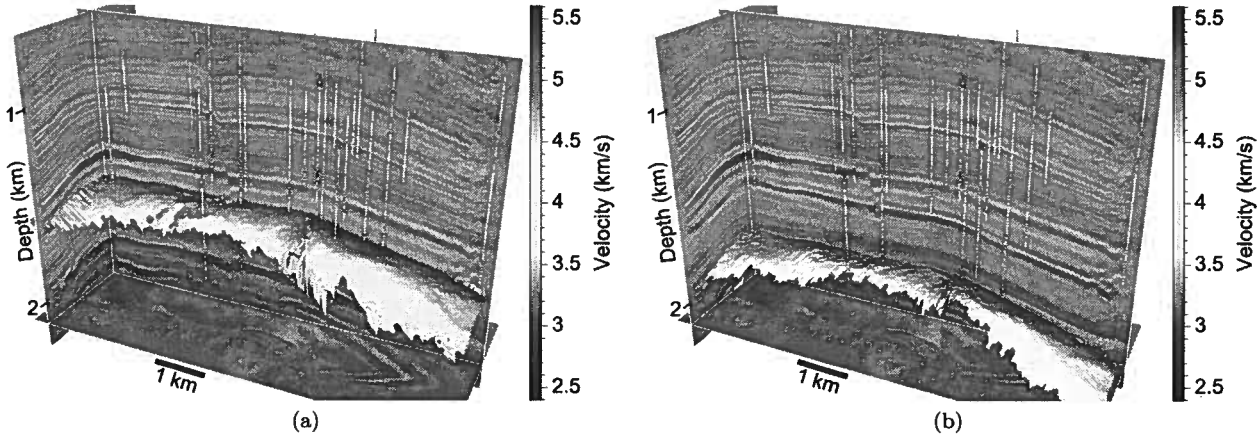

Figure 2. Two low-velocity layers in the 3D interpolated velocity image conform to the Crow Mountain (a) and Tensleep (b) horizons that were picked interactively (by others) from the 3D seismic image. Only the seismic image, not the horizons, was used to guide the 3D interpolation of the velocity logs.

flections in the seismic image. Two examples are shown in Figure 2. These two horizons correspond to the Crow Mountain and Tensleep formations, and are provided as part of the Teapot Dome data set. Typically, we would pick horizons like these interactively, with or without help from automatic event-tracking software. One reason we might construct horizon surfaces like these is to facilitate interpolation of properties measured in boreholes.

I interpolated the velocities shown in Figure 2 (and in Figure 1b) without using horizons. Instead, I used the seismic image to automatically and more directly guide 3D interpolation of the velocity logs. Although the horizons in Figure 2 were not used, they coincide with low-velocity layers apparent in the 3D interpolation shown in Figure 1b.

An obvious advantage of image-guided interpolation without horizons is that we save the time and effort of picking horizons. The savings may be significant, as seismic processing and interpretation have become interwoven parts of an iterative seismic imaging and inversion process. Another advantage in using a 3D seismic image directly is that we simultaneously interpolate at all locations between and on horizons that we might have picked. A third advantage is that our interpolation may be guided by images of geologic features, including unconformities and diapirs, that may be difficult to represent accurately and efficiently with picked surfaces.

Some of these advantages may be obtained by first flattening a seismic image (Stark, 2004; Lomask *et al.*, 2006). By removing *structure* from a 3D image, flattening creates a stack of simpler 2D interpolation problems, like those we today solve routinely for 2D maps corresponding to picked horizons. However, automatic flattening as described by Stark (2004) and Lomask *et al.* (2006) is perfomed using vertical shifts that may distort distances measured within horizontal slices of a flattened image (Lee, 2001). Moreover, vertical shifts often cannot account for intrusions, such as overhanging salt diapirs; and flattened images are at best ambiguous in the presence of unconformities caused by erosion. Finally, flattening highlights *stratigraphic* features, such as channels, in 3D seismic images; and we may wish to use those features to guide the sequence of 2D interpolations. In other words, image-guided interpolation may be desirable even after flattening.

The purpose of this paper is to demonstrate image-guided interpolation of borehole data, without flattening and without picking horizons. I first review the blended neighbor interpolation method described by Hale (2009) using a 2D seismic image. I then describe the application of this method to the 3D seismic image and well logs from the Teapot Dome data set, and illustrate the method with several examples. Finally, I discuss current limitations and potential extensions of image-guided interpolation.

2 IMAGE-GUIDED INTERPOLATION

Let us assume that spatially scattered data to be interpolated are a set

$$\mathcal{F} = \{f_1, f_2, \ldots, f_K\} \tag{1}$$

of K known sample values $f_k \in \mathbb{R}$ that correspond to a set

$$\mathcal{X} = \{\mathbf{x}_1, \mathbf{x}_2, \ldots, \mathbf{x}_K\} \tag{2}$$

of K known sample points $\mathbf{x}_k \in \mathbb{R}^n$. Together these two sets comprise a set

$$\mathcal{K} = \{(f_1, \mathbf{x}_1), (f_2, \mathbf{x}_2), \ldots, (f_K, \mathbf{x}_K)\} \tag{3}$$

of K known samples. These samples may be scattered such that the n-dimensional sample points in the set

$\mathcal{X}$ may have no regular geometric structure. The classic interpolation problem is to use the known samples in $\mathcal{K}$ to construct a function $q(\mathbf{x}) : \mathbb{R}^n \rightarrow \mathbb{R}$, such that $q(\mathbf{x}_k) = f_k$.

As stated, this problem has no unique solution; there exist an infinite number of functions $q(\mathbf{x})$ that satisfy the interpolation conditions $q(\mathbf{x}_k) = f_k$. Additional criteria may include measures of smoothness, robustness, and efficiency. Because tradeoffs exist among such criteria, a variety of methods for interpolating scattered data are commonly used today.

In this paper I add the requirement that the interpolation should conform to features in a uniformly sampled image, as in Figures 1 and 2. That is, the interpolation must be *image-guided.*

2.1 Blended neighbor interpolation

The blended neighbor method (Hale, 2009) was developed specifically to facilitate image-guided interpolation. This process consists of two steps:

Step 1: solve the eikonal equation

$$\nabla t(\mathbf{x}) \cdot \mathbf{D}(\mathbf{x}) \nabla t(\mathbf{x}) = 1, \quad \mathbf{x} \notin \mathcal{X};$$
$$t(\mathbf{x}_k) = 0, \quad \mathbf{x}_k \in \mathcal{X} \qquad (4)$$

for

$t(\mathbf{x})$: the minimal time from $\mathbf{x}$ to the nearest known sample point $\mathbf{x}_k$, and

$p(\mathbf{x})$: the value f_k corresponding to the sample point $\mathbf{x}_k$ nearest to the point $\mathbf{x}$.

Step 2: solve the blending equation

$$q(\mathbf{x}) - \frac{1}{2} \nabla \cdot t^2(\mathbf{x}) \mathbf{D}(\mathbf{x}) \nabla q(\mathbf{x}) = p(\mathbf{x}), \qquad (5)$$

for the blended neighbor interpolant $q(\mathbf{x})$.

Here, *time* is simply a short word for *non-Euclidean distance.* By this measure of distance, a sample point $\mathbf{x}_k$ is *nearest* to a point $\mathbf{x}$ if the time $t(\mathbf{x})$ along some path to $\mathbf{x}_k$ is less than that for any other sample point. In step (1), I compute this minimal-time map $t(\mathbf{x})$ by solving the eikonal equation 4.

The metric tensor field $\mathbf{D}(\mathbf{x})$ provides the anisotropic and spatially varying coefficients of that eikonal equation. Intuitively, we must choose the tensor field $\mathbf{D}(\mathbf{x})$ so that, by our time measure of non-Euclidean distance, two points within the same geologic formation are near, while two points in different formations are much farther away. In this way, known sample values f_k for sample points x_k that are geologically nearby are given the most weight in any interpolated value $q(\mathbf{x})$.

In step (1), as I compute the time $t(\mathbf{x})$ from each point $\mathbf{x}$ to the location $\mathbf{x}_k$ of the nearest known sample, I also record the value $p(\mathbf{x}) = f_k$ of that nearest known sample. The function $p(\mathbf{x})$ is therefore a *nearest neighbor* interpolant.

In step (2), I compute the *blended neighbor* interpolant $q(\mathbf{x})$ by smoothing the nearest neighbor interpolant $p(\mathbf{x})$, and the extent of smoothing is controlled by the time map $t(\mathbf{x})$. At any known sample point $\mathbf{x}_k$, equation 4 states that $t(\mathbf{x}_k) = 0$, so that no smoothing is performed, and equation 5 becomes simply $q(\mathbf{x}_k) = p(\mathbf{x}_k) = f_k$. In other words, the function $q(\mathbf{x})$ interpolates exactly the known sample values.

Figure 3 illustrates the process of blended neighbor interpolation guided by a 2D seismic image. In this example I specified the 21 known samples illustated in Figure 3a. (For clarity, each sample is plotted with an opaque disk larger than the image pixel that represents the sample value.) The values $f_k \in [0, 1]$ in this example are arbitrary; I chose them to alternate vertically, while generally decreasing from left to right.

Figure 3b shows the time map $t(\mathbf{x})$ computed in step (1) for these known samples. The time map is displayed with translucent color on top of the seismic image displayed with shades of gray. Times are smallest near the known sample points $\mathbf{x}_k$ and largest in the corners that are farthest from any of those points. Contours of constant-time are not circular, because they are warped by the metric tensor field $\mathbf{D}(\mathbf{x})$. As described below, I computed this tensor field so that times would increase slowly in directions in which the seismic image is most coherent, while increasing rapidly near strong reflections and faults.

While computing the times $t(\mathbf{x})$ in step (1), I also computed the nearest neighbor interpolant $p(\mathbf{x})$ shown in Figure 3c. As expected, this interpolant conforms to structure in the seismic image, but it is discontinuous at locations $\mathbf{x}$ for which times $t(\mathbf{x})$ to two or more nearest known sample points $\mathbf{x}_k$ are equal.

These discontinuities are removed by solving the blending equation in step (2), which yields the continuous blended neighbor interpolant $q(\mathbf{x})$ shown in Figure 3d. Contours of constant color are well aligned with structures and faults in the seismic image, and interpolated values (colors) match the known sample values f_k at the known sample points $\mathbf{x}_k$.

As in the eikonal equation 4, the coefficients $\mathbf{D}(\mathbf{x})$ in the blending equation 5 are anisotropic and spatially varying. Therefore, the direction and extent of blending of the nearest neighbor values in step (2) depend on the metric tensor field $\mathbf{D}(\mathbf{x})$, in addition to the time map $t(\mathbf{x})$ computed in step (1).

2.2 Computing the metric tensor field

As discussed above, both steps (1) and (2) of blended neighbor interpolation are guided by a metric tensor field $\mathbf{D}(\mathbf{x})$. Blended neighbor interpolation becomes *image-guided* when we compute this tensor field from an image.

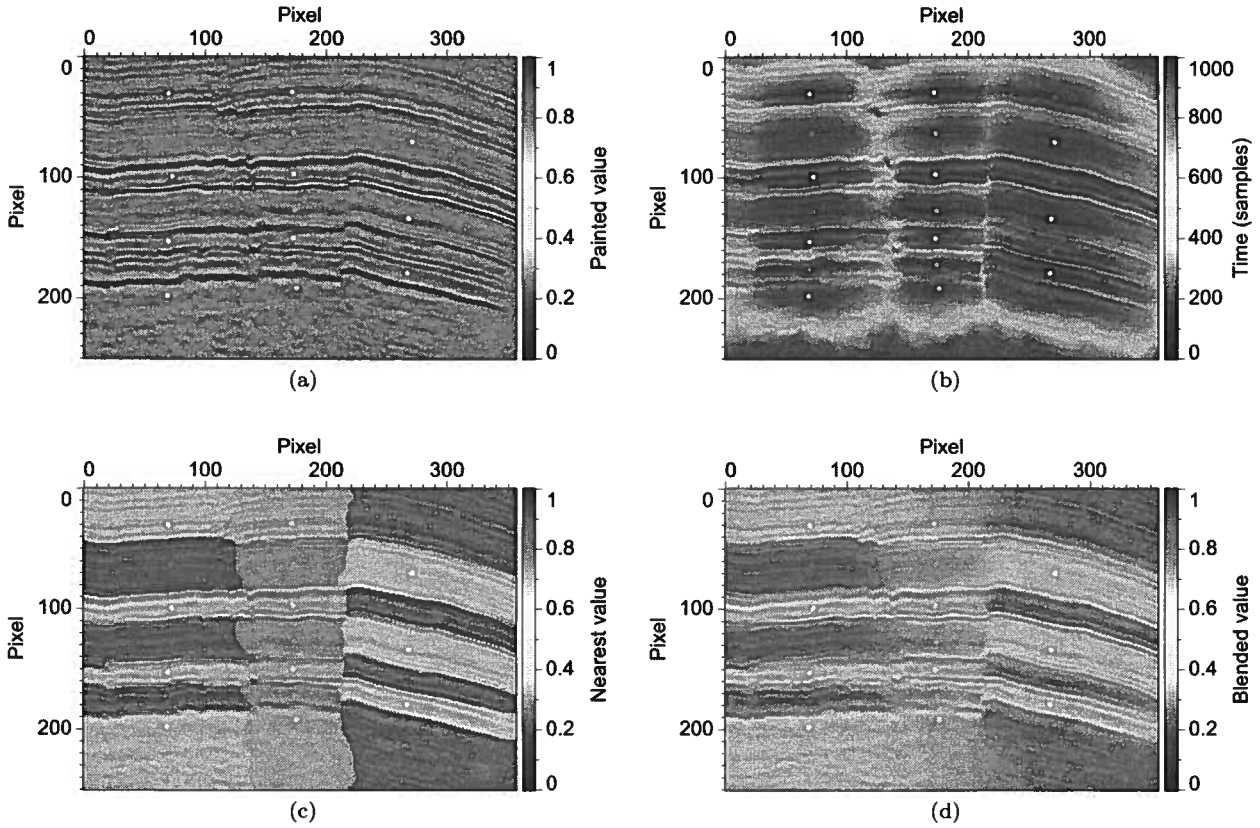

Figure 3. A simple example of image-guided 2D interpolation. For a set $\mathcal{K}$ of known (here, painted) samples (a), we first use equation 4 to compute the time map (b) and nearest neighbor interpolant (c), and then solve equation 5 for the blended neighbor interpolant (d).

I compute the metric tensor field $\mathbf{D}(\mathbf{x})$ from a seismic image by first computing structure tensors $\mathbf{S}(\mathbf{x})$. As described by van Vliet & Verbeek (1995) and Fehmers & Höcker (2003), these structure tensors are spatially smoothed outer products of image gradient vectors. In n dimensions, each structure tensor $\mathbf{S}$ is a symmetric positive-definite (SPD) $n \times n$ matrix, e.g., 2×2 for 2D images, and 3×3 for 3D images. I compute the eigenvectors of the metric tensors $\mathbf{D}(\mathbf{x})$ to be the same as those in the structure tensors $\mathbf{S}(\mathbf{x})$, but I modify the eigenvalues.

Equations 4 and 5 imply that the eigenvalues of $\mathbf{D}(\mathbf{x})$ have units of velocity squared. I scale the tensor field $\mathbf{D}(\mathbf{x})$ so that the maximum eigenvalue (maximum velocity squared) for any of these tensors is one. Eigenvalues less than one therefore imply slower velocities and larger times in directions of the corresponding eigenvectors. Times will be smaller in directions for which velocities (eigenvalues) are faster (larger).

In the 2D example of Figure 3, I computed the metric tensor field $\mathbf{D}(\mathbf{x})$ from a structure tensor field $\mathbf{S}(\mathbf{x})$ by

$$\mathbf{D}(\mathbf{x}) = s\frac{\mathbf{S}^{-1}(\mathbf{x})}{1-c(\mathbf{x})}. \tag{6}$$

I computed the constant scale factor s so that the maximum eigenvalue in the metric tensor field $\mathbf{D}(\mathbf{x})$ is one. The function $c(\mathbf{x})$ is a measure of coherence or semblance (e.g., Bahorich & Farmer, 1995), computed for each image pixel along the slope of the most linear feature at that pixel. Any such measure in the range $0 \le c(\mathbf{x}) < 1$ could be used. The effect of the divisor $1 - c(\mathbf{x})$ is to increase the eigenvalues of $\mathbf{D}(\mathbf{x})$, thereby decreasing times $t(\mathbf{x})$, between locations where features in images are most coherent.

Note that each matrix $\mathbf{D}$ in the metric tensor field $\mathbf{D}(\mathbf{x})$ is SPD, because the eigenvalues of each inverse matrix $\mathbf{S}^{-1}$ in equation 6 are reciprocals of the corresponding positive eigenvalues of an SPD matrix $\mathbf{S}$.

I chose the values and colors in Figure 3 to highlight the ability of image-guided interpolation to conform to structures and faults apparent in a seismic image. In practice we might interactively paint values that are

more realistic. Alternatively, the known samples might correspond to geophysical data, such as well logs.

3 TEAPOT DOME EXAMPLE

The freely available Teapot Dome data set, which includes a time-migrated 3D seismic image and hundreds of well logs (Anderson, 2009), enables a realistic demonstration of image-guided 3D interpolation of borehole data.

3.1 Seismic image

To reduce the large number of zero traces in the 3D seismic image, I rotated and trimmed the seismic survey coordinate rectangle, as shown in Figure 4. As illustrated by the constant-time slice shown there, roughly half of the traces in the original 3D seismic image are zero. After resampling to a spatial grid aligned with the solid (red) coordinate rectangle, a smaller fraction of traces are zero, and the spatial coordinate axes are more nearly aligned with the anticlinal structure apparent in the image. The original spatial sampling intervals are 110 ft in both inline and crossline directions. I used 2D sinc interpolation to interpolate traces on the resampled grid with spatial sampling intervals of 25 m in both directions.

In the original seismic survey coordinate system, the (east-west) axis is the inline direction, and the longer (north-south) axis is the crossline direction. Although the original and resampled coordinate grids are not aligned (because of the rotation in the coordinate transformation), I hereafter refer to the shorter (northeast-southwest) resampled coordinate axis as the *inline* direction and the longer (northwest-southeast) one as the *crossline* direction.

Figure 5 shows two sets of three orthogonal slices of the resampled seismic image, after conversion of the vertical axis from time to depth. (I discuss the time-to-depth conversion process in the next section.) In a typical 3D seismic image, many such slices are possible. I chose these slices for their intersections with structural features apparent in the image and with wells.

3.2 Well logs

Well logs in the Teapot Dome data set are provided in two groups. The numerous so-called "shallow" wells do not penetrate to the depths displayed in Figure 5. None of the "deeper" wells extends to the bottom depth (2.2 km) shown there, and less than twenty of them extend to the depth of the 1.5 km slice shown in Figure 5b. In the examples shown in this paper, I ignored all borehole data provided with the shallow wells. The velocity logs displayed in Figure 1 are those available for the deeper wells.

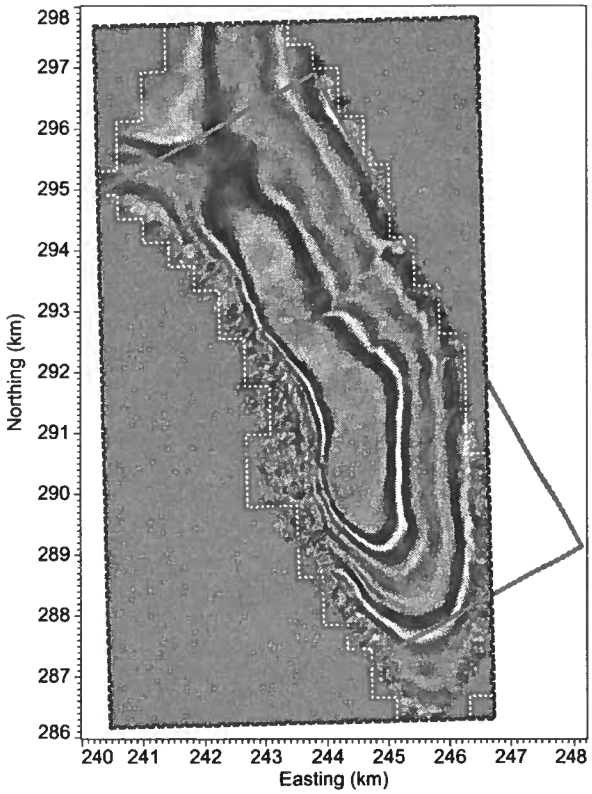

Figure 4. Original (dashed blue) and resampled (solid red) coordinate rectangles for the Teapot Dome data set. The (dotted green) polygon is the boundary of the Teapot Dome oilfield. The constant-time (0.95 s) slice shown here illustrates the anticlinal structure apparent in the 3D seismic image.

For the purpose of demonstrating image-guided interpolation, I selected four types of well logs: P-wave velocity, density, porosity and gamma ray.

Well logs are provided in LAS (Log ASCII Standard) format, and directional surveys are provided for boreholes that are not vertical. I performed only minimal pre-processing of the well logs. Specifically, I used elevations (of the kelly bushing, derrick floor, etc.) and directional survey data to convert distances measured along boreholes to inline, crossline and depth coordinates in the resampled seismic coordinate system. I discarded all logs with missing or clearly invalid elevation data, and all logs not entirely contained within the spatial boundaries of the resampled seismic image volume shown in Figure 5.

I also discarded entirely any well logs that contain clearly erroneous values: velocities outside the range $[0.2, 20]$ km/s, densities outside the range $[0.5, 10.0]$ gm/cc, porosities outside the range $[0, 0.8]$, and gamma ray radioactivies outside the range $[0, 300]$ API units. These bounds are broad and were chosen to exclude only those logs that contained data that are obviously

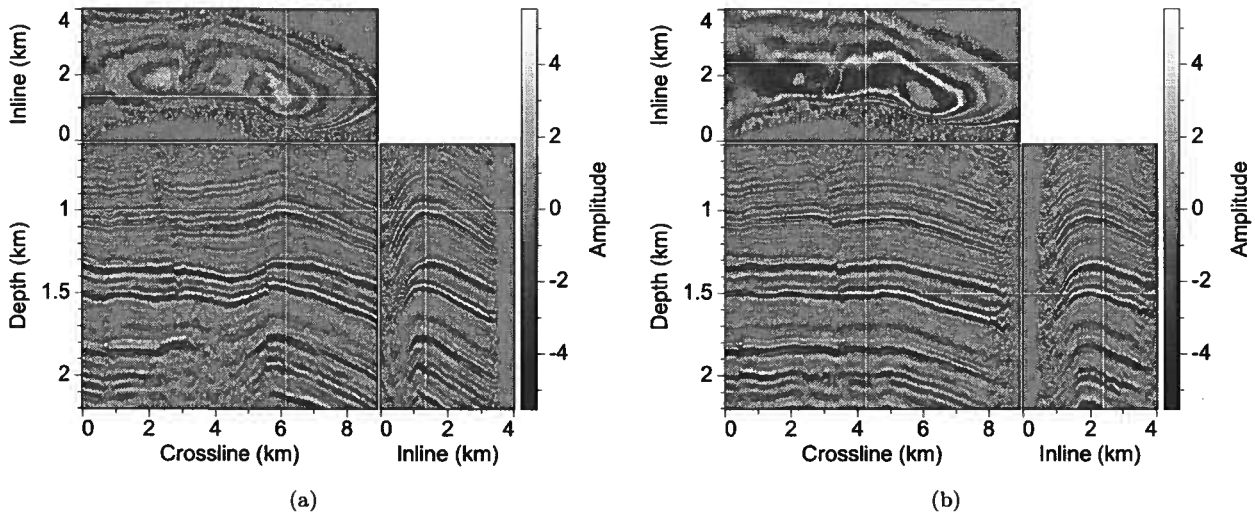

Figure 5. Two sets (a) and (b) of three orthogonal slices of the 3D seismic image used to guide interpolation of Teapot Dome borehole data. The horizontal constant-depth slice at 1 km (a) is intersected by many more wells than is the deeper slice at 1.5 km (b).

invalid. As shown below, the remaining well logs certainly contain measurements with significant errors, and those errors are especially apparent after image-guided 3D interpolation.

Whereas well logs are sampled every six inches along the boreholes, the depth sampling interval for the seismic image is 4 m. This difference in spatial sampling intervals (roughly a factor of 25) raises an important question. How finely should we sample the interpolated borehole data?

3.3 Initial gridding of well logs

Interpolation on a fine grid that would preserve all detail in the well logs would be about 25 times more costly than interpolation on the vertically coarser seismic grid. This high cost might be reduced by interpolating for only a subset of the seismic image and well data. For computational efficiency and convenience in this demonstration, I sampled interpolated values using the sampling intervals of the seismic image: 25 m in both inline and crossline directions, and 4 m in depth. Here *the interpolation grid* is that of the 3D seismic image.

For each type of log — velocity, density, porosity and gamma ray — I obtained the set of known samples defined by equation 3 with a simple binning and averaging procedure. First, I rounded the spatial coordinates of each well log sample to the coordinates of the nearest bin in the interpolation grid. Each known sample location $\mathbf{x}_k$ therefore corresponds to one such bin, and each known sample value f_k is the average of all well log samples for which $\mathbf{x}_k$ is the nearest bin. After this binning and averaging procedure, only those bins in the interpolation grid that are intersected by well logs of the appropriate type have values. Values for other bins in the grid are unknown and will be interpolated using the two-step process of equations 4 and 5.

3.4 Computing the tensor field

Before solving equations 4 and 5, we must first specify a metric tensor field $\mathbf{D}(\mathbf{x})$. As in the 2D example of Figure 3, I derived $\mathbf{D}(\mathbf{x})$ from structure tensors $\mathbf{S}(\mathbf{x})$ computed from the seismic image. For the 3D seismic image displayed in Figure 5, each structure tensor $\mathbf{S}$ is a 3×3 SPD matrix with eigen-decomposition

$$\mathbf{S} = \lambda_u \mathbf{u}\mathbf{u}^T + \lambda_v \mathbf{v}\mathbf{v}^T + \lambda_w \mathbf{w}\mathbf{w}^T, \tag{7}$$

where λ_u, λ_v and λ_w are the eigenvalues and $\mathbf{u}$, $\mathbf{v}$ and $\mathbf{w}$ the corresponding eigenvectors of $\mathbf{S}$.

Let us label the eigenvalues and eigenvectors of $\mathbf{S}$ so that $\lambda_u \geq \lambda_v \geq \lambda_w \geq 0$. Then, eigenvectors $\mathbf{u}$, corresponding to the largest eigenvalues λ_u, indicate directions in which image gradients are highest, orthogonal to features that are locally linear or planar. The eigenvectors $\mathbf{w}$, corresponding to the smallest eigenvalues λ_w, will be aligned with locally linear features, such as channels and the intersections of geologic faults and layers, in seismic images. Both eigenvectors $\mathbf{v}$ and $\mathbf{w}$ lie within the planes of any locally planar features.

In other words, for each image sample, the orthonormal eigenvectors $\mathbf{u}$, $\mathbf{v}$ and $\mathbf{w}$ specify the local orientation of the predominant image feature. The corresponding eigenvalues λ_u, λ_v and λ_w contain information about the shape of that feature. For example, locally linear features correspond to eigenvalues $\lambda_u \approx \lambda_v \gg \lambda_w$. For locally planar features, $\lambda_u \gg \lambda_v \approx \lambda_w$.

The eigenvalues λ_u, λ_v and λ_w of structure tensors

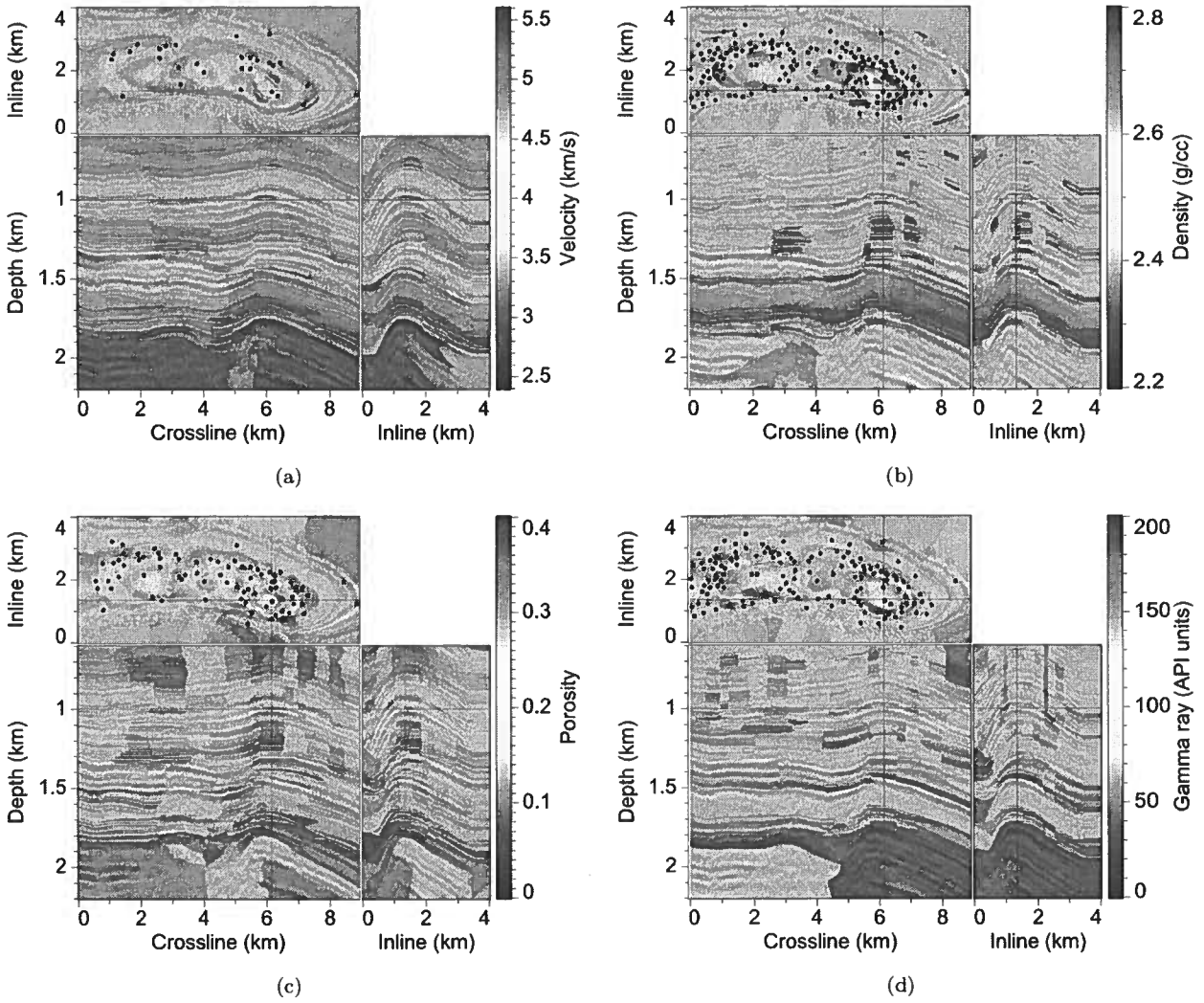

Figure 6. Image-guided nearest neighbor interpolation of velocity (a), density (b), porosity (c) and gamma ray (d) logs. Slices here correspond to those displayed for the seismic image in Figure 5a.

S are proportional to the magnitudes of image gradients squared, and therefore depend on the amplitudes of events in seismic images. Geologically, weak events may be as significant as strong ones; important geologic interfaces may or may not correspond to large contrasts in acoustic impedance.

Therefore, in image-guided interpolation, I discard the eigenvalues λ_u, λ_v and λ_w of the structure tensors **S** and use normalized local measures of semblance (coherence) to compute metric tensors

$$\mathbf{D} = \lambda_3 \mathbf{u}\mathbf{u}^T + \lambda_2 \mathbf{v}\mathbf{v}^T + \lambda_1 \mathbf{w}\mathbf{w}^T, \qquad (8)$$

such that $0 \leq \lambda_3 \leq \lambda_2 \leq \lambda_1 \leq 1$.

Each eigenvalue λ_1 corresponds to a semblance of image samples measured along a 1D curvi-linear trajectory defined by eigenvectors **w**. Likewise, each eigenvalue λ_2 corresponds to a semblance of image samples along a 2D curvi-planar surface defined by the eigenvectors **v** and **w**. Finally, each eigenvalue λ_3 corresponds to a semblance of image samples within a local isotropic 3D window.

Recall that the eigenvalues of **D** have units of velocity squared. (See equation 4.) In equation 8 these eigenvalues are semblances, normalized measures of coherence in the range [0,1]. Therefore, at locations and in directions where semblance equals one, time in the map $t(\mathbf{x})$ is equivalent to Euclidean distance. Time exceeds Euclidean distance at locations and in directions where semblance is less than one, where image samples are less coherent.

In regions with no seismic image, the dead traces in Figure 5, I specified eigenvalues $\lambda_1 = \lambda_2 = 1$, $\lambda_3 = 0.01$, and eigenvectors **u**, **v** and **w** aligned with depth, crossline and inline coordinate axes, respectively.

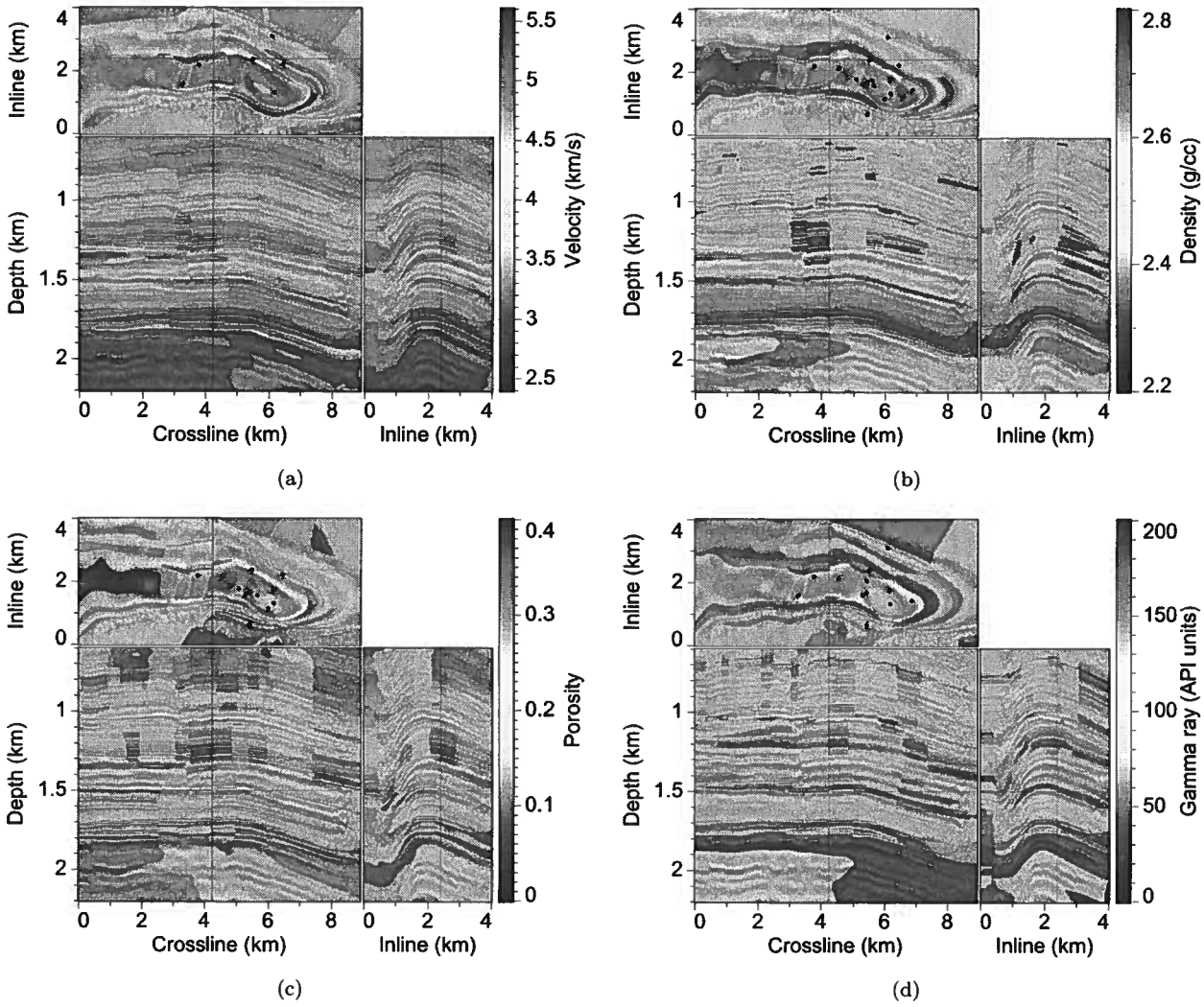

Figure 7. Image-guided nearest neighbor interpolation of velocity (a), density (b), porosity (c) and gamma ray (d) logs. Slices here correspond to those displayed for the seismic image in Figure 5b.

These default metric tensors $\mathbf{D}$ correspond to planar horizontal layering.

3.5 Nearest neighbor interpolation

The known samples $(f_k, \mathbf{x}_k)$ obtained by initial gridding of well log data and the tensor field $\mathbf{D}(\mathbf{x})$ computed from the image are the parameters required for step (1) of image-guided interpolation. In this step I simultaneously compute both the time map $t(\mathbf{x})$ and the nearest neighbor interpolant $p(\mathbf{x})$ by solving a finite-difference approximation of the eikonal equation 4.

Recall that "nearest" here implies *nearest in time*, based on a non-Euclidean distance that is defined by the metric tensor field $\mathbf{D}(\mathbf{x})$. Because the eigenvalues of $\mathbf{D}(\mathbf{x})$ are computed from semblances measured in local $(\mathbf{u}, \mathbf{v}, \mathbf{w})$ coordinate systems, times along paths of high image semblance (within imaged layers) are relatively small, while those along paths of low semblance (across imaged faults or layers) are relatively large.

Figures 6 and 7 display the nearest neighbor interpolants $p(\mathbf{x})$ for four different borehole measurements. Again, interpolated values are displayed with translucent color on top of the seismic image used to guide the interpolation.

For each log type, black dots in the horizontal constant-depth slices indicate the intersections of well logs with those slices. These dots represent only a tiny subset of the well log samples used to perform the 3D interpolation.

Figure 6 shows that a relatively small number of wells have velocity logs at a depth of 1 km, while a much larger number of wells have density, porosity and gamma ray logs at that depth. Well intersections plotted

at a depth of 1.5 km in Figure 7 indicate, for all four log types, that a much smaller number of well logs extend to this depth.

For example, Figure 7a indicates that only six velocity logs extend to a depth of 1.5 km. However, the velocity variation seen in the constant-depth slice at 1.5 km is not the result of interpolating only six logged velocities. The interpolation is three-dimensional, so that many logged velocities above and below this slice contribute to the interpolated velocities shown there.

As in the 2D example of Figure 3c, all of the nearest neighbor interpolants shown in Figures 6 and 7 exhibit discontinuities. I chose the slices displayed in Figure 6 specifically to highlight some of those discontinuities. Most of those discontinuities do not coincide with geologic faults. Rather, they reflect inconsistencies among properties measured within wells and those measured within their nearest neighbor wells.

For example, anomalously low (light blue) porosities are apparent in the upper middle part of the vertical crossline slice in Figure 6c. These low porosities are suspect because they are inconsistent with those measured in wells that are nearby with respect to the non-Euclidean metric tensor field $\mathbf{D}(\mathbf{x})$ computed from the seismic image. Image-guided nearest neighbor interpolation may lead us to look more closely at the porosity logs of nearby wells, to look for possible sources of error.

In the same way, we may use consistency with nearest neighbors as a measure of the fidelity of each well log sample. For example, the three slices of interpolated velocities shown in Figure 6 intersect an apparent high-velocity anomaly. These high velocities are likely caused by erroneous samples in the nearest velocity log. This hypothesis is supported by the fact that the anomaly coincides with the shallowest samples, which were acquired last, for that log. In the well logs provided with the Teapot Dome data set, the deepest (first recorded) and shallowest (last recorded) samples often exhibit anomalous values.

At depths greater than 1.9 km, large areas of constant interpolated values are apparent in Figures 6 and 7. Because no wells extend to these depths, all of the well log samples that lie in shallower geologic layers appear to be relatively far away, so that the nearest neighbor sample value is a poor interpolant.

3.6 Blended neighbor interpolation

Step (2) of image-guided interpolation is the solution of a finite-difference approximation of the blending equation 5. Parameters in this equation include the metric tensor field $\mathbf{D}(\mathbf{x})$, as well as the time map $t(\mathbf{x})$ and nearest neighbor interpolant $p(\mathbf{x})$. Figures 8 and 9 show slices of blended neighbor interpolants $q(\mathbf{x})$ corresponding to the nearest neighbor interpolants $p(\mathbf{x})$ shown in Figures 6 and 7.

As illustrated by these examples, the blending equation 5 smooths the nearest neighbor interpolants, and the extent of smoothing is controlled by the time map $t(\mathbf{x})$. Little smoothing is performed at locations $\mathbf{x}$ near the known well log samples, where times $t(\mathbf{x})$ are small; more smoothing is performed where those times are larger. In step (2) the metric tensor field $\mathbf{D}(\mathbf{x})$ causes this smoothing to be performed along seismically imaged geologic layers, but not across those layers or across faults. In this sense, the blending step (2) is an averaging of values from neighbors that are geologically nearby.

When solving the blending equation 5, I clipped all times in the time map $t(\mathbf{x})$ to be less than 10. Recall that, at locations and in directions where semblances are highest (that is, where eigenvalues of $\mathbf{D}$ equal one), one unit of time is equivalent to one spatial sample.

This time constraint limits the amount of smoothing performed. Where well log samples are dense, times are small anyway, and this limit has no effect on blended neighbor interpolants. In regions more sparsely sampled by well logs, this limit causes the blended neighbor interpolant to appear more like the nearest neighbor interpolant.

Setting an upper bound on times in the map $t(\mathbf{x})$ is analogous to setting an upper bound on the distance at which subsurface properties are correlated, as in kriging (e.g., Cressie, 1993). The difference here is that distance is defined by the metric tensor field $\mathbf{D}(\mathbf{x})$.

This upper bound also reduces the computational cost of solving the finite-difference approximation of the blended equation 5. For the conjugate-gradient solver that I use, that cost grows linearly with times in the map $t(\mathbf{x})$. For this example, the computation time required to solve the blending equation 5 is a few minutes on a modern workstation, roughly one tenth of the time required to solve the eikonal equation 4. If times had not been clipped, this cost would have been much higher.

Finally, by limiting the times in the map $t(\mathbf{x})$, we limit the range of influence of anomalous well-log values. After such values have been found and, if erroneous, corrected or discarded, we might increase the upper bound on times in $t(\mathbf{x})$, and thereby permit smoothing over greater non-Euclidean distances.

4 DISCUSSION

The Teapot Dome example demonstrates the process of image-guided 3D interpolation of borehole data. Instead of first picking horizons or flattening a seismic image, we may use the image to define a non-Euclidean metric tensor field that directly guides interpolation.

4.1 Two interpolants

In practice both the nearest neighbor and blended neighbor interpolants may be useful. The nearest neigh-

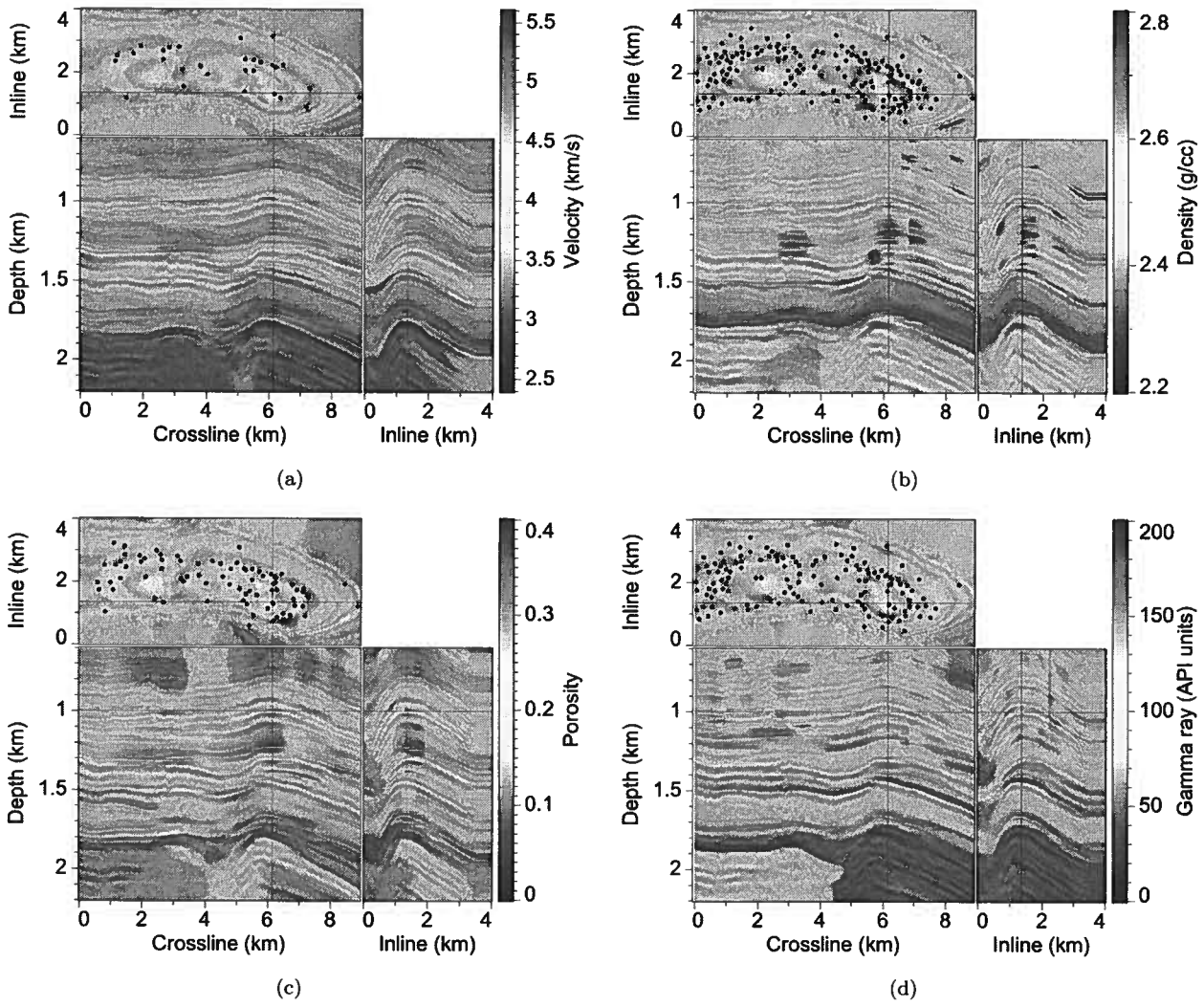

Figure 8. Image-guided blended-neighbor interpolation of velocity (a), density (b), porosity (c) and gamma ray (d) logs. Slices here correspond to those displayed for the seismic image in Figure 5a.

bor interpolant may be used to detect inconsistencies in borehole data acquired within the same seismically imaged geologic layers. Well log sample values that are inconsistent with those of geologically nearby log samples may be erroneous and perhaps should be discarded.

For example, we might compute, for each well log sample, the difference between the sample value and the mean of its nearest neighbor values. We might then discard log samples for which that difference exceeds some multiple of the standard deviation of the nearest neighbor values. We could also use more robust statistical measures in similar ways.

The nearest neighbor interpolant is also a useful first step toward computing the blended neighbor interpolant. Within seismically imaged layers, the blended neighbor interpolant is continuous and therefore geologically more reasonable than the discontinuous nearest neighbor interpolant.

The blended neighbor interpolants shown in Figures 8 and 9 are consistent with the borehole data and structures apparent in the corresponding seismic image. These interpolants are also consistent with expected trends. Velocities tend to increase with depth and porosities tend to decrease with depth. Also evident are some significant deviations from those trends.

For example, the strong reflector at a depth of about 1.5 km coincides with a significant change in both velocity and density, the factors of acoustic impedance. A thin layer at that depth with relatively low velocity, low density, high porosity, and low gamma ray radioactivity corresponds to the Crow Mountain sandstone formation marked by the light-blue horizon displayed in

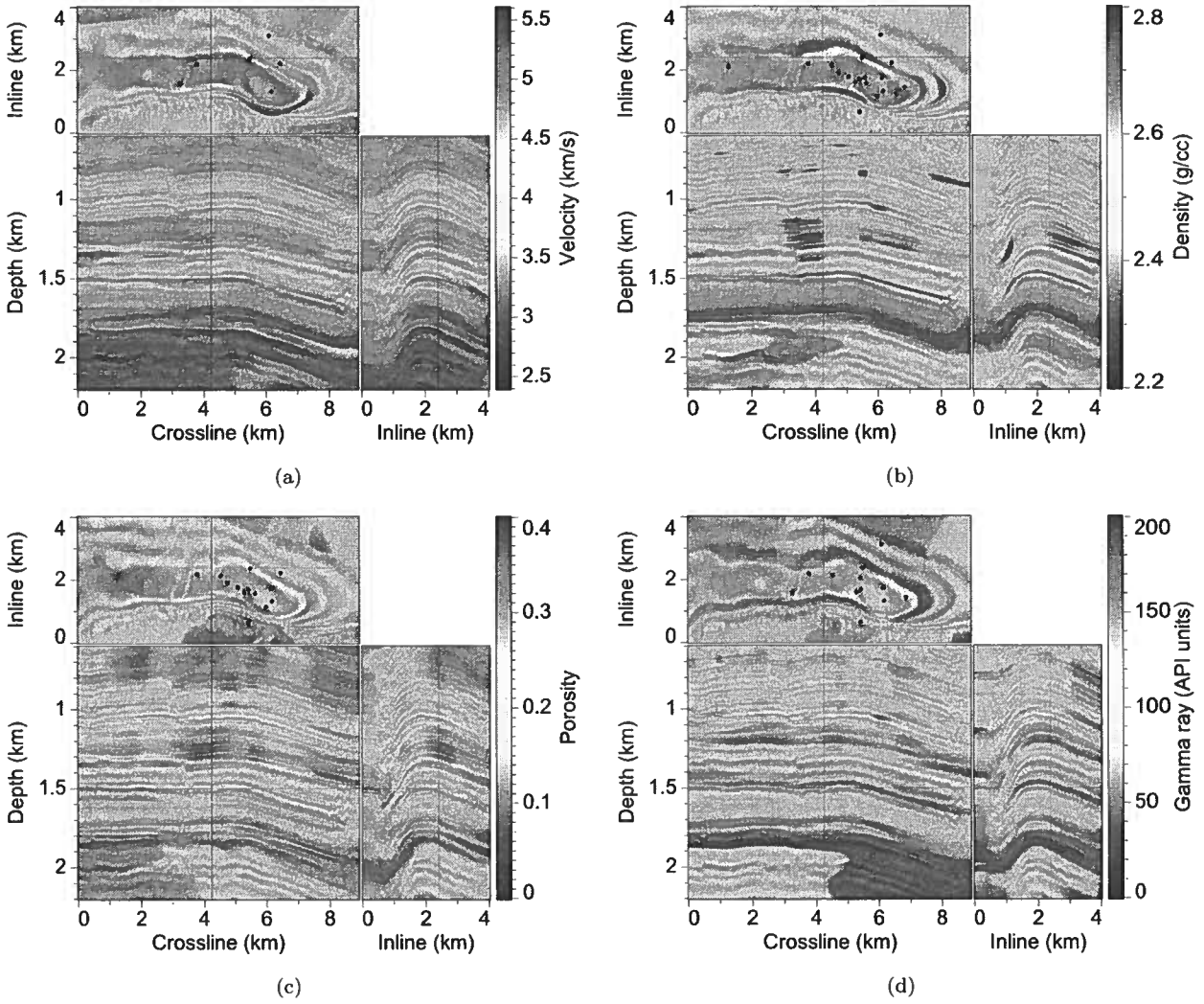

Figure 9. Image-guided blended-neighbor interpolation of velocity (a), density (b), porosity (c) and gamma ray (d) logs. Slices here correspond to those displayed for the seismic image in Figure 5b.

Figure 2a. The low (dark blue) density of this formation is especially visible in the slices of interpolated densities.

As another example, the Tensleep sandstone formation marked by the light-yellow horizon in Figure 2b corresponds to the low-velocity (light yellow) layer apparent at a depth of about 1.8 km/s in Figures 8 and 9. At the depths of both the Tensleep and Crow Mountain formations, the interpolated velocities shown here depend on velocities logged in only six wells.

After interpolating relevant borehole data onto a shared uniform 3D sampling grid, thereby creating 3D images of subsurface properties, we can easily combine them to create other images. For example, we might use the velocity and density images to compute a 3D image of acoustic impedance.

4.2 Time-to-depth conversion

Before seismic images can be used to guide interpolation of borehole data, the vertical axis of those images must be converted from vertical two-way time to depth. This conversion requires a uniformly sampled function $\tau(\mathbf{x}) = \tau(x, y, z)$ that specifies, for each point with horizontal coordinates x and y and depth coordinate z, the corresponding vertical two-way time τ. Given the uniformly sampled function $\tau(x, y, z)$, it is easy to convert a time-migrated seismic image $s_\tau(x, y, \tau)$ from time to depth using the mapping

$$s_z(x, y, z) = s_\tau[x, y, \tau(x, y, z)], \tag{9}$$

where $s_z(x, y, z)$ is the seismic image after time-to-depth conversion. The more difficult task is to construct the uniformly sampled function $\tau(x, y, z)$.

In the Teapot Dome example, that function was constructed in a typical manner, by correlating seismic horizons picked on time-migrated images with corresponding features in well logs (D. Witte, personnel communication, 2009). Specifically, for all well logs intersecting a seismic horizon, points with horizontal coordinates x and y and times τ were chosen from the horizon, and corresponding points with approximately the same x and y coordinates and depths z were chosen from the log. Depths z where then interpolated, first within each horizon for all x and y, using a minimum-curvature algorithm (Briggs, 1974), and then vertically between horizons for all times, using a simple linear interpolation, to obtain a uniformly sampled function $z(x,y,\tau)$. A simple inverse linear interpolation was then used to obtain the required function $\tau(x,y,z)$.

Image-guided interpolation suggests an alternative to this procedure that does not require picking seismic horizons. As in the typical procedure, we may first choose points (x,y,τ) from the seismic image and corresponding points (x,y,z) from the well logs. These points comprise scattered known samples of $z(x,y,\tau)$ that we may interpolate, using the time-migrated 3D seismic image $s_\tau(x,y,\tau)$ to guide our interpolation. Again, inverse linear interpolation would yield the required uniformly sampled function $\tau(x,y,z)$.

Other alternatives include direct interpolation of vertical traveltimes τ measured in checkshot surveys or vertical seismic profiles. In all of these alternatives, we replace three steps — (1) horizon picking, (2) interpolation within horizons, and (3) interpolation between horizons — with image-guided 3D interpolation.

4.3 Other interpolation methods

I developed the two-step blended neighbor method for image-guided interpolation to be both intuitive and computationally efficient. The method is intuitive because the blended neighbor interpolant is a smoothed version of the simplest nearest neighbor interpolant. The method is efficient primarily because it does not require the computation of times (non-Euclidean distances) from every interpolation grid point $\mathbf{x}$ to every known sample point $\mathbf{x}_k$.

Blended neighbor interpolation requires only the time $t(\mathbf{x})$ to the *nearest* (smallest in time) known sample point $\mathbf{x}_k$. Computation of the time map $t(\mathbf{x})$ displayed in Figure 3b does not require times from every interpolation grid point $\mathbf{x}$ to every known sample point $\mathbf{x}_k$.

Some well-known alternative methods, such as interpolation using Green's functions or radial basis functions (e.g., Wessel & Bercovici, 1998) or kriging (e.g., Cressie, 1993), require many more distance computations. For a constant metric tensor field $\mathbf{D}(\mathbf{x}) = \mathbf{D}$, the cost of computing these many distances is insignificant. However, the cost of computing non-Euclidean distances in a spatially varying metric tensor field $\mathbf{D}(\mathbf{x})$ is much higher, requiring numerical solution of the eikonal equation 4. This high cost makes many well-known alternative methods impractical for image-guided 3D interpolation of borehole data.

4.4 Limitations

When interpolating velocities and densities, properties that determine acoustic impedance, we should use seismic amplitudes to help estimate these properties between boreholes. However, as described here, image-guided 3D interpolation uses only estimates of image structure and semblance to guide interpolation of borehole data. It does not directly use the amplitudes of seismic reflections.

Seismic reflection amplitudes are especially useful in quantifying rapid vertical variations in velocities and densities. Those amplitudes are often less useful in quantifying long-wavelength vertical variations, because low frequencies are typically absent in recorded seismograms. One possible use of image-guided 3D interpolation would be to provide an a priori long-wavelength model for a more sophisticated joint inversion of seismic amplitudes and borehole data.

Another current limitation of image-guided interpolation is its reliance entirely on structure tensors $\mathbf{S}(\mathbf{x})$ computed from seismic images. While such automatic estimates of the orientations and shapes of subsurface structures are typically more reliable than reflection amplitudes, seismic interpreters routinely pick reflectors in noisy 3D seismic images for which automatic methods would fail. Moreover, not all subsurface properties conform to reflectors in seismic images. In practice a semi-automatic interpolation process, one guided by both seismic images and human interpreters, is likely to be optimal.

5 CONCLUSION

Notwithstanding its current limitations, image-guided interpolation provides an attractive new method for using a 3D seismic image to interpolate subsurface properties measured in boreholes. The method requires only a metric tensor field, which I compute automatically from the image, and the borehole data to be interpolated. In contrast to methods widely used today, image-guided interpolation does not require picking seismic horizons or faults; nor does it require image flattening.

The examples for the Teapot Dome data shown in this paper illustrate that the method produces interpolants consistent with seismic horizons picked by others. For depths where borehole data have been acquired, the most significant errors in the interpolants likely correspond to errors in well logs. The nearest neighbor interpolant naturally highlights such errors, as they cause

significant lateral discontinuities in interpolated subsurface properties at locations halfway (in time) between well logs. This observation suggests that we might use nearest neighbor interpolants to quantify the spatial consistency and, hence, the fidelity of well log samples.

Unlike nearest neighbor interpolants, blended neighbor interpolants are continuous, the latter being simply smoothed versions of the former. The extent of smoothing depends on times, non-Euclidean distances, to the nearest borehole measurements. By limiting these times to not exceed a specified maximum, we can reduce both the influence of erroneous measurements and the computational cost of image-guided interpolation.

ACKNOWLEDGMENTS

Thanks to the Rocky Mountain Oilfield Test Center, a facility of the U.S. Department of Energy, for providing the 3D seismic image, horizons, and well logs used in this study. Thanks also to Transform Software and Services, especially Amelia Webster, for providing their time-to-depth conversion of the 3D seismic image. I also thank Chris Engelsma for explaining to me the uses and significance of various types of well logs.

REFERENCES

Anderson, T., 2009, History of geologic investigations and oil operations at Teapot Dome, Wyoming: History of geologic investigations and oil operations at Teapot Dome, Wyoming:, 2009 AAPG Annual Convention, Denver, Colorado.

Bahorich, M., and Farmer, S., 1995, The coherence cube: The Leading Edge, **14**, no. 10, 1053–1058.

Briggs, I., 1974, Machine contouring using minimum curvature: Geophysics, **39**, no. 1, 39–48.

Cressie, N., 1993, Statistics for spatial data: , Wiley.

Fehmers, G., and Höcker, C., 2003, Fast structural interpretation with structure-oriented filtering: Geophysics, **68**, no. 4, 1286–1293.

Hale, D., 2009, Image-guided blended neighbor interpolation of scattered data: Image-guided blended neighbor interpolation of scattered data:, SEG, 79th Annual International Meeting, SEG, Expanded Abstracts, 1127–1131.

Lee, R., 2001, Pitfalls in seismic data flattening: The Leading Edge, **20**, no. 2, 160–164.

Lomask, J., Guitton, A., Fomel, S., Claerbout, J., and Valenciano, A., 2006, Flattening without picking: Geophysics, **71**, no. 4, P13–P20.

Stark, T., 2004, Relative geologic time (age) volumes — Relating every seismic sample to a geologically reasonable horizon: The Leading Edge, **23**, no. 9, 928–932.

van Vliet, L., and Verbeek, P., 1995, Estimators for orientation and anisotropy in digitized images: Estimators for orientation and anisotropy in digitized images:, Proceedings of the first annual conference of the Advanced School for Computing and Imaging, 442–450.

Wessel, P., and Bercovici, D., 1998, Interpolation with splines in tension: a Green's function approach: Mathematical Geology, **30**, no. 1, 77–93.

A stable and fast implementation of natural neighbor interpolation

Luming Liang & Dave Hale

Center for Wave Phenomena, Colorado School of Mines,Golden, CO 80401, USA

April 20, 2010

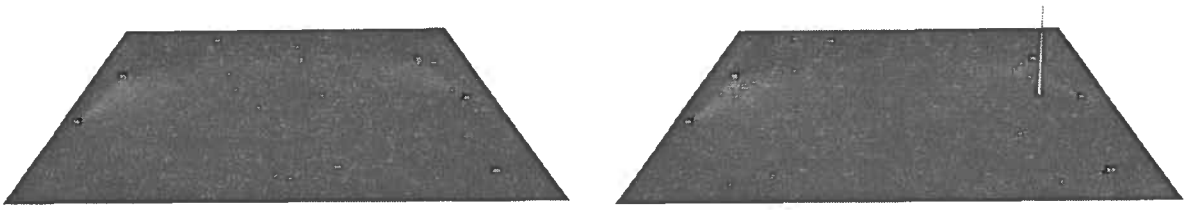

(a) (b)

Figure 1. 3D surfaces generated by two implementations of natural neighbor interpolation: (a) the proposed implementation and (b) compound signed decomposition implementation.

ABSTRACT

Natural neighbor interpolation is a powerful method for data estimation in geoscience applications where measurements are scattered. However, this method is not easy to implement, and some simple implementations are numerically unstable. We describe a stable and fast implementation and make some in-depth comparisons with existing implementations.

Key words: interpolation, natural neighbor, Voronoi diagram, Delaunay triangulation

1 INTRODUCTION

Interpolation of scattered data is fundamental for many applications in geoscience. These applications include numerical modeling of mantle convection, crustal deformation and associated thermal conduction/advection, seismic tomography, and the interpolation of topographic, gravitational, magnetic or other data fields (Sambridge et al., 1995).

For a given set of known samples, using different interpolation methods may yield totally different results. However, if we implement a single method in different ways, we may also get different results. Surfaces in Figure 1 are interpolated using two implementations of a single method called natural neighbor interpolation. The spike in surface (b) shows a numerical instability. This leads us to the principle focus of this paper: implementation is a crucial and often overlooked issue in natural neighbor interpolation.

Generally, the purpose in interpolation of scattered data is to determine values of any point in space, using N pairs $(\mathbf{x}_i, f_i), (i = 1, 2, ..., N)$ as inputs, where $\mathbf{x}_i \in \mathbb{R}^n$ is the coordinate n-tuple of the ith known sample point and $f_i \in \mathbb{R}$ is the corresponding data value.

Numerous interpolation methods exist in the literature. Examples include inverse-distance weighted averaging (IDWA), kriging, adaptive normalized convolution (ANC), radial basis function (RBF) based interpolation, and natural neighbor interpolation. These methods can be divided into two categories, depending on which points are used to determine the interpolated value at a point $\mathbf{x}$. These two categories are global and local interpolations. In global interpolations, all known data are used. The computational cost of global meth-

ods increases with the amount of known data. In contrast, local techniques only use part of the data that fall within a defined neighborhood of $\mathbf{x}$. Therefore, if the number of known samples increases, the cost does not grow so quickly.

IDWA and RBF based interpolations were initially introduced as global methods. However, local versions exist based on some simple definitions of local neighborhoods. For example, one can use a fixed number of nearest data (usually called k-nearest neighbors) to perform the interpolation. Alternatively, one can simply use all data lying inside a circle centered at $\mathbf{x}$ with fixed radius. Since data in geoscience applications are often distributed sparsely and anisotropically, these simple locality definitions may be inadequate. Natural neighbor interpolation, a local method based on the Voronoi diagram (Sibson, 1981; Berg et al., 2008), has an intrinsic advantage in dealing with geoscience interpolation problems (Watson et al., 1987; Watson, 1992; Foster and Evans, 2008). The Voronoi diagram adapts automatically to the spatial distribution of scattered geoscience data.

There have been a number of implementations proposed for natural neighbor interpolation. However, these methods are either computationally costly or difficult to implement. We propose a fast and stable implementation of natural neighbor interpolation. The key idea of this implementation is to reuse intermediate results during computation as much as possible. We will describe our method after introducing some basic definitions and reviewing existing implementations.

2 NATURAL NEIGHBOR INTERPOLATION

Natural neighbor interpolation was first proposed by Sibson (1981). Before we go into further detail about this particular interpolation method, let's consider the definitions of the Voronoi diagram and Delaunay triangulation as well as the relationship between them. These concepts are building blocks of natural neighbor interpolation.

2.1 Voronoi diangram and Delaunay triangulation

The Voronoi diagram of known data sites $\mathbf{x}_i (i = 1, ..., N)$ is a space partition (Berg et al., 2008). Each site $\mathbf{x}_i$ is encompassed by a convex polygon $V(\mathbf{x}_i)$ called the Voronoi cell (see Figure 2), which is defined as a set of points that are closer to $\mathbf{x}_i$ than to any other known data sites $\mathbf{x}_j (j \neq i)$. If two polygons $V(\mathbf{x}_i)$ and $V(\mathbf{x}_j)$ share an edge, we call them adjacent cells. For example in Figure 2, $V(\mathbf{x}_1)$ and $V(\mathbf{x}_2)$ are adjacent, but $V(\mathbf{x}_1)$ is *not* adjacent to $V(\mathbf{x}_3)$.

Simply connecting sites with those in adjacent Voronoi cells yields the Delaunay triangulation of the sites. (See Figure 2.) The Voronoi diagram and its corresponding Delaunay triangulation are dual (Berg et al., 2008) which means that

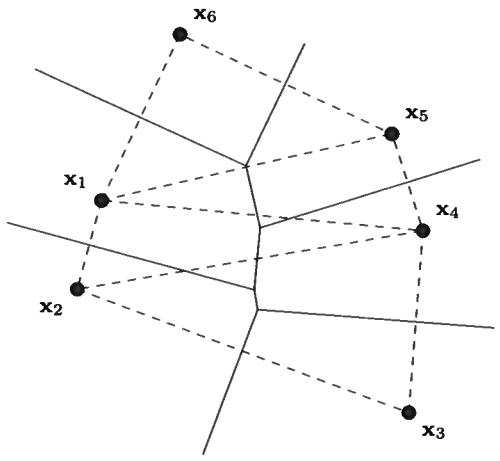

Figure 2. The Voronoi diagram (solid lines) and its dual graph–Delaunay triangulation (dashed lines).

- Edges in the Delaunay triangulations are perpendicular to the corresponding Voronoi edge. For example, the Delaunay edge which connects $\mathbf{x}_i$ and $\mathbf{x}_j$ is perpendicular to the Voronoi edge shared by cells $V(\mathbf{x}_i)$ and $V(\mathbf{x}_j)$. If $\mathbf{x}_i$ and $\mathbf{x}_j$ are not adjacent, there is no edge connecting $\mathbf{x}_i$ and $\mathbf{x}_j$. The Delaunay triangulation is unique because the Voronoi diagram is unique.
- Vertices of Voronoi polygons are circumcenters (centers of circles passing through three vertices) of corresponding Delaunay triangles. The Voronoi vertex shared by cells $V(\mathbf{x}_i), V(\mathbf{x}_j)$ and $V(\mathbf{x}_k)$ is the circumcenter of Delaunay triangle $\triangle \mathbf{x}_i \mathbf{x}_j \mathbf{x}_k$.

Duality plays an important role in the definition and computation of natural neighbor interpolation.

2.2 Definitions

Natural neighbors are defined as two sites whose Voronoi cells share a common edge. To determine the natural neighbors of an interpolation point $\mathbf{x}$, one can imagine this point is virtually inserted into the Voronoi diagram. This virtual insertion modifies the original Voronoi diagram and creates a new Voronoi cell $V(\mathbf{x})$, a set of points that are closer to $\mathbf{x}$ than to any known $\mathbf{x}_i$. Figure 3c shows that $V(\mathbf{x}_1)$, $V(\mathbf{x}_2)$, $V(\mathbf{x}_3)$, $V(\mathbf{x}_4)$ and $V(\mathbf{x}_5)$ share edges with $V(\mathbf{x})$; consequently, sample points $\mathbf{x}_1$, $\mathbf{x}_2$, $\mathbf{x}_3$, $\mathbf{x}_4$ and $\mathbf{x}_5$ are natural neighbors of $\mathbf{x}$. Weighted averaging of the sample values for these natural neighbors gives the interpolated value at $\mathbf{x}$.

Different averaging functions yield a variety of natural neighbor interpolants. Among them, Sibson's interpolant (Sibson, 1981) is the most commonly used one

in natural neighbor interpolation and is defined as

$$f(\mathbf{x}) = \frac{\sum_i a_i \cdot f(\mathbf{x}_i)}{\sum_i a_i}, \tag{1}$$

where a_i is the overlap area corresponding to the known data site $\mathbf{x}_i$. (See Figure 3c.) The term overlap area here refers to the area shared by $V(\mathbf{x}_i)$ and $V(\mathbf{x})$. [The overlap polygon is called the second-order Voronoi cell (Sambridge et al., 1995).] In this paper, we consider only Sibson's interpolant.

If sample point $\mathbf{x}_i$ lies outside of the convex hull of all known sample points, the overlap polygon is unbounded and a_i in equation 1 is infinite. Therefore, only points that lie inside the convex hull of known sample points $\mathbf{x}_i$ can be interpolated using equation 1. This brings about the extrapolation problem.

2.3 Features and developments

A number of advantages of natural neighbor interpolation are discussed in the literature (Sibson, 1981; Watson et al., 1987; Sambridge et al., 1995; Bobach et al., 2006; Bobach et al., 2009). Some of these inherent advantages allow this type of interpolation to conform well to geoscience requirements. Li and Götze (1999) and Foster and Evans (2008) give benchmarks for a number of scattered data interpolation methods with geophysical applications. Comparisons show that natural neighbor interpolation performs best in their test cases.

However, significant disadvantages of natural neighbor interpolation is that its implementation is relatively difficult. Several papers are concerned with the following implementation issues:

- simplicity (Park et al., 2006)
- numerical stability (Hiyoshi, 2008)
- extrapolation (Park et al., 2006; Bobach et al., 2009)
- extension to 3D (Sambridge et al., 1995; Boissonnat and Cazals, 2000)

Except for discrete sibson interpolation (Park et al., 2006), all of the implementations mentioned above rely on the Voronoi diagram or Delaunay triangulation. In this paper, we refer to these methods as geometric implementations. Generally, interpolating a value $f(\mathbf{x})$ at an arbitrary point $\mathbf{x}$ using a geometric implementation requires three steps:

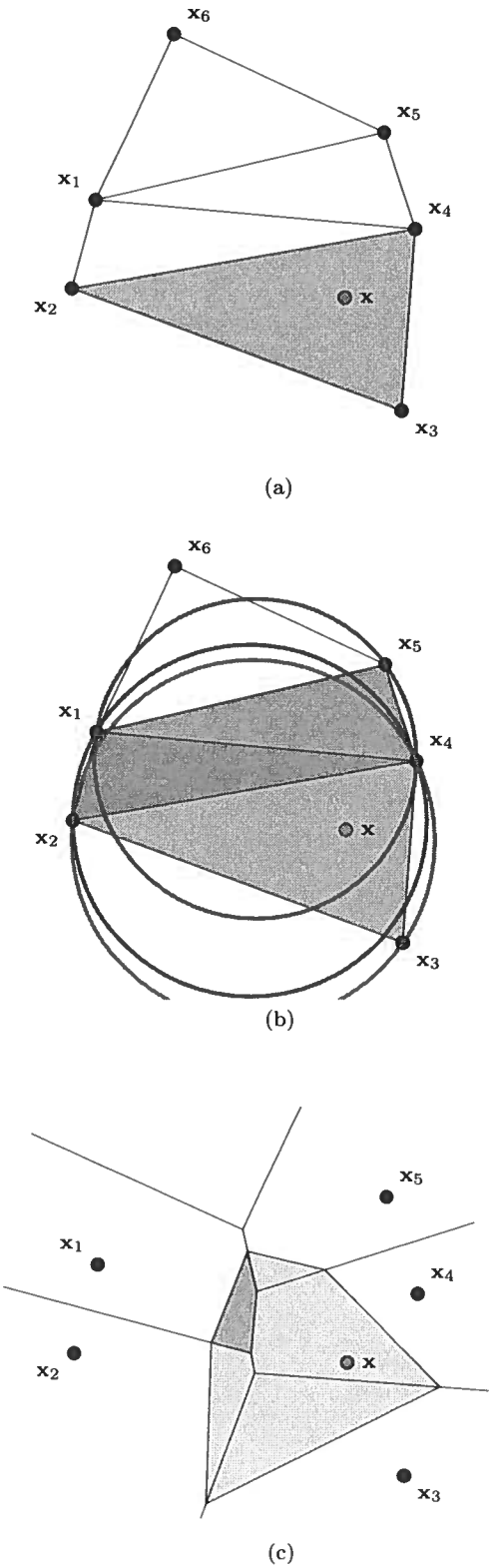

Figure 3. Three steps of the geometric method for computing the value at $\mathbf{x}$. The darker area in (c) is the overlap area corresponding to $\mathbf{x}_1$

Natural Neighbor Interpolation (NNI)

(1) Locate the point **x**. Does **x** lie inside the convex hull of known data sites? Which Delaunay triangle contains **x**? (See Figure 3a.)
(2) Determine which triangles will no longer be Delaunay triangles if **x** is added to the Delaunay triangulation of known data sites. (Which triangles have circumcircles that contain **x**?) For example, shaded triangles in Figure 3b are in this set.
(3) For all vertices of these triangles (the natural neighbors), compute Sibson's weights. (See Figure 3c.)

Henceforth, we will illustrate different geometric implementations by following this three-step process.

2.4 Extension to 3D

Natural neighbor interpolation is defined in $\mathbb{R}^n$. In practice, 2D and 3D natural neighbor interpolations are most widely used. Hence, there is a need for an easy and efficient extension of a 2D implementation to 3D. 3D geometric implementations rely on more complex data structures, for example, 3D Voronoi polyhedra and Delaunay tetrahedra. In 2D, the key to computing Sibson's weights in step (3) is to determine overlap areas. In 3D, one must compute volumes of overlap polyhedra. In addition, computational cost is higher in 3D implementations.

In the next section, we will first discuss implementations in 2D and then investigate their extensions to 3D version.

3 GEOMETRIC IMPLEMENTATIONS

In 2D, different methods for computing the overlap areas in step (3) of NNI lead to different geometric implementations. Since the vertices of overlap polygons are circumcenters of Delaunay triangles, a brute-force method for computing Sibson's weight is to collect the centers, and then determine areas of the overlap polygons. However, this implementation is computationally costly. Below, we introduce more efficient implementations.

3.1 Watson-Sambridge

Watson et al. (1987) and Watson (1992) introduced the natural neighbor interpolation into geoscience with this implementation, which was first extended to 3D by Sambridge et al. (1995). Many applications using natural neighbor interpolation have adopted this implementation (Li ánd Götze, 1999). Watson (2001) used the name *compound signed decomposition* as he extended the implementation to n dimensions and spherical coordinates.

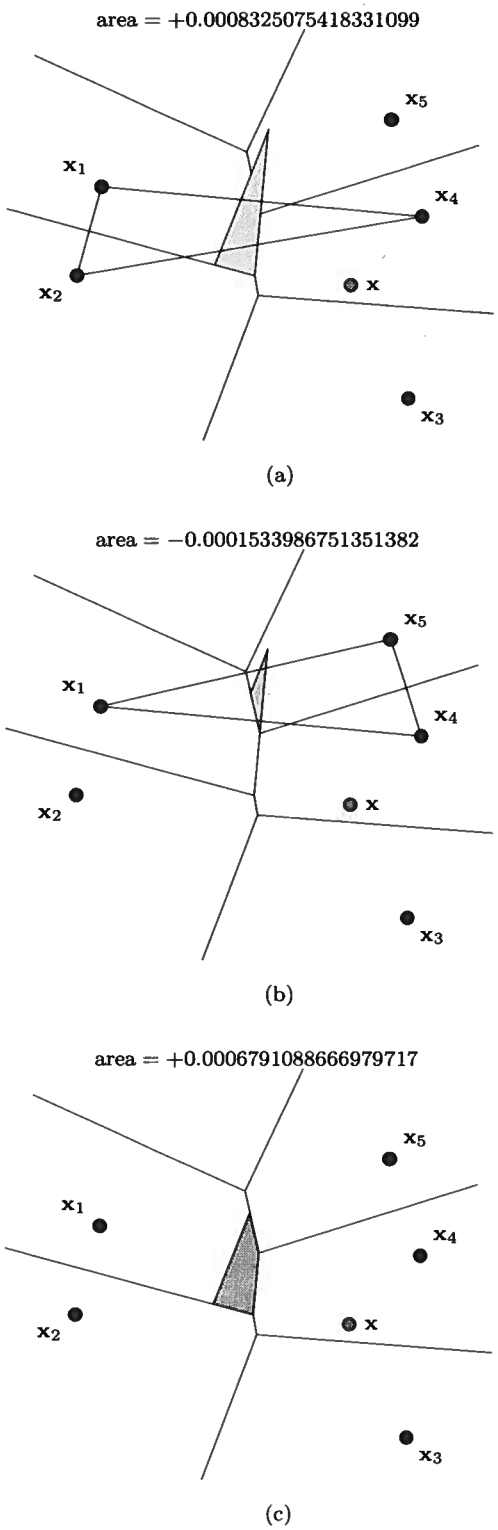

Figure 4. The computation of the overlap area for $\mathbf{x}_1$ with the Watson-Sambridge implementation.

The compound signed decomposition implementation is summarized by the sequence shown in Figure 4. To compute the overlap area corresponding to $\mathbf{x}_1$, the method walks through Delaunay triangles that reference $\mathbf{x}_1$ and other natural neighbors of $\mathbf{x}$. (See Figure 4a and b; $\mathbf{x}_1\mathbf{x}_2\mathbf{x}_4$ and $\mathbf{x}_1\mathbf{x}_4\mathbf{x}_5$ are such triangles.) Vertices of the shaded triangles in Figure 4a and b are circumcenters. The sign of a triangle's area is determined by the order of its vertices. If its vertices lie in counterclockwise order, the area is positive. In contrast, clockwise order yields a negative area. By summing up areas with appropriate signs, one can determine areas of overlap polygons. (See Figure 4c.) This implementation naturally combines steps (2) and (3) in the three-step process for NNI.

Although widely used, this implementation is not ideal, as illustrated by the instability shown in Figure 1b. The spike is caused by rounding errors, numerical instability addressed by Hiyoshi (2008). Sambridge et al. (1995) emphasize that this instability occurs when an interpolation point lies exactly on a Delaunay edge. However, in the case shown in Figure 1, the interpolation point does *not* lie exactly on a Delaunay edge. This singularity is caused by catastrophic cancellation, subtracting one large value from another large value, as shown in Figure 5. Here, $\mathbf{x}$ is close to Delaunay edge $\mathbf{x}_1\mathbf{x}_4$. This fact makes the center of the circle passing through $\mathbf{x}$, $\mathbf{x}_1$ and $\mathbf{x}_4$ distant from $\mathbf{x}$. Note that the circumcenter of triangle $\triangle\mathbf{x}_1\mathbf{x}\mathbf{x}_4$ lies far outside this figure, so that the shaded areas in Figure 5a and b are huge. Even when using double precision, 16 significant digits, one cannot avoid this catastrophic cancellation in this implementation.

3.2 Braun-Sambridge

To avoid catastrophic cancellation, Braun and Sambridge (1995) developed another implementation, which computes areas using Lasserre's method (Lasserre, 1983).

By definition, all points inside the overlap polygons satisfy a system of linear inequality constraints:

$$\mathbf{A}\mathbf{x} \leqslant \mathbf{b}, \tag{2}$$

where $\mathbf{A}$ is a $m \times n$ matrix and $\mathbf{b}$ is a vector with n elements. Here, m is the number of polygon boundaries and n is the dimensionality. In 2D, $n = 2$. For $\mathbf{x}_1$ in Figure 6, the first bounding edge of the shaded overlap polygon is $\mathbf{c}_1\mathbf{c}_2$, the perpendicular bisector of $\mathbf{x}\mathbf{x}_1$. Other bounding edges are perpendicular bisectors of $\mathbf{x}_1\mathbf{x}_2$, $\mathbf{x}_1\mathbf{x}_4$ and $\mathbf{x}_1\mathbf{x}_5$. Note that $\mathbf{x}_2$, $\mathbf{x}_4$ and $\mathbf{x}_5$ are natural neighbors of $\mathbf{x}$ and are also adjacent to $\mathbf{x}_1$ in the Voronoi diagram.

Lasserre (1983) designed a recursive formula to compute volume in n dimensions:

$$V(n, \mathbf{A}, \mathbf{b}) = \frac{1}{n} \sum_{i=0}^{m} \frac{\mathbf{b}_i}{|a_{it}|} V_{it}'(n-1, \bar{\mathbf{A}}_{i,t}, \bar{\mathbf{b}}_t), \tag{3}$$

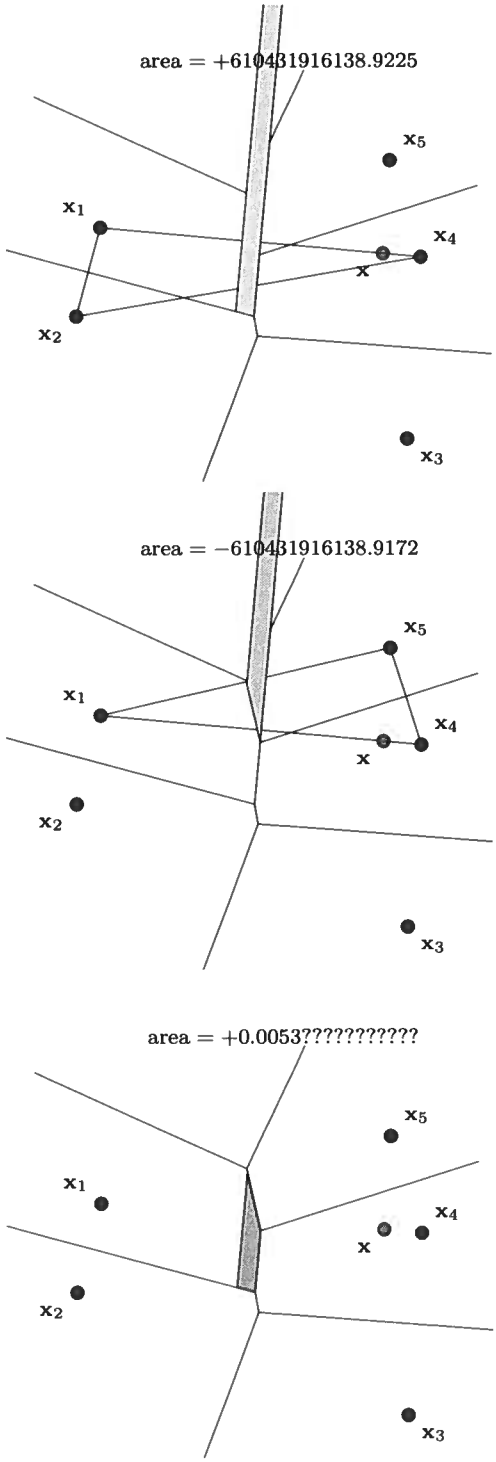

Figure 5. The computation of the overlap area for $\mathbf{x}_1$ in the Watson-Sambridge implementation when $\mathbf{x}$ is close to one Delaunay edge.

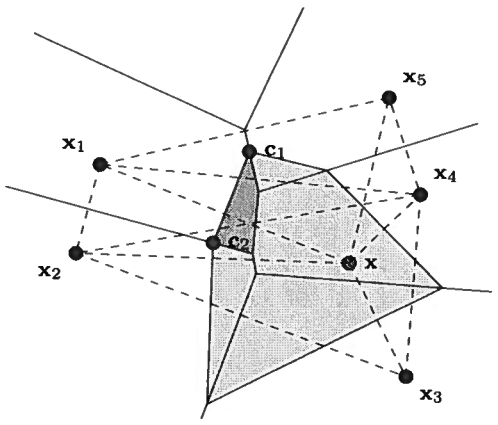

Figure 6. Braun-Sambridge implementation. Perpendicular bisectors of dashed lines are boundaries of overlap polygons.

where $\bar{\mathbf{A}}_{i,t}$ is the reduced matrix obtained from $\mathbf{A}$ by eliminating the tth variable using the equation $\mathbf{a}_i \cdot \mathbf{x} = \mathbf{b}_i$, where $\mathbf{a}_i$ is the ith row by $\mathbf{A}$, $\bar{\mathbf{b}}_t$ is the corresponding reduced vector and a_{it} is the tth element of $\mathbf{a}_i$. More detail can be found in Braun and Sambridge (1995).

This method avoids the catastrophic cancellation in Watson-Sambridge implementation. However, it is computationally more costly.

3.3 Hiyoshi

To overcome the instability in the compound signed decomposition implementation, Hiyoshi (2008) presents another solution.

The following typographical errors in his paper should be corrected as indicated below.

- **Lemma 2.** on page 345 should be

$$2 \cdot \overrightarrow{\mathbf{x_i x}} \cdot \overrightarrow{\mathbf{m_i r_{i,j}}} = \Xi_{t_{i,j}}(\mathbf{x}).$$

- In pages 334-337, all $\Gamma(\mathbf{x})$ should be $\Gamma(\mathbf{x_i})$.

Hiyoshi's idea is to replace subtractions in step (3) with dot products of vectors. In addition, he does not restrict his implementation to Sibson's interpolation, but he gives a general framework for all natural neighbor interpolants (for example, the Laplace interpolant). More detail can be found in Hiyoshi (2008). Unfortunately, this method is much difficult to implement than other methods.

3.4 Boissonnat-Cazals

Again, to avoid instabilities caused by subtractions in computing overlap areas, Boissonnat and Cazals (2000) propose another decomposition method. Instead of using compound signed decomposition, they decompose the polygons into triangles with only positive areas, as shown in Figure 7.

However, the extension to 3D of their decomposition is complicated.

3.5 3D implementations

All implementations mentioned above, with the exception of that by Hiyoshi (2008), have 3D versions. However, same 3D versions are complicated and thus difficult to implement.

Compared to the 2D version, the 3D Watson-Sambridge implementation maintains a large table to store vertex orders, which determine signs of tetrahedra. Numerical instabilities present in the 2D implementation remain in the 3D version.

Extending the 2D Braun-Sambridge implementation to 3D is more straightforward. The only change from 2D to 3D in this method is $n = 3$ rather than $n = 2$, so that in equation 2 matrix $\mathbf{A}$ has 3 columns and $\mathbf{b}$ has 3 elements. The same recursive scheme can be used to compute the volume bounded by the system of inequality constraints.

In Boissonnat-Cazals implementation, some parts need to be modified for computing volumes. Instead of decomposing 2D overlap polygons into triangles, their 3D implementation decomposes overlap polyhedra into tetrahedra. The volumes of overlap polyhedra are thereby reduced to sums of volumes of tetrahedra.

4 OUR IMPLEMENTATION

In this section, we describe an efficient and stable implementation. Our implementation is similar to the Braun-Sambridge implementation and to the Boissonat-Cazals implementation, in that it also decomposes overlap polygons into smaller parts. However, instead of decomposing polygons into triangles, we compute areas by accumulating edge contributions. The key idea of our implementation is to reuse edge contributions as much as possible. Triangles inside a polygon, like the shaded triangles in Figure 7, never appear inside another polygon. However, edges are always shared by more than one overlap polygon, as shown in Figure 8. This fact makes our implementation efficient.

4.1 2D implementation

Our implementation is simply a stable and efficient method for computing the overlap areas a_i for the natural neighbors.

As in other implementations of natural neighbor interpolation, we first find the natural neighbor triangle that contains the point x, and then recursively visit adjacent triangles, taking care to visit no triangle more

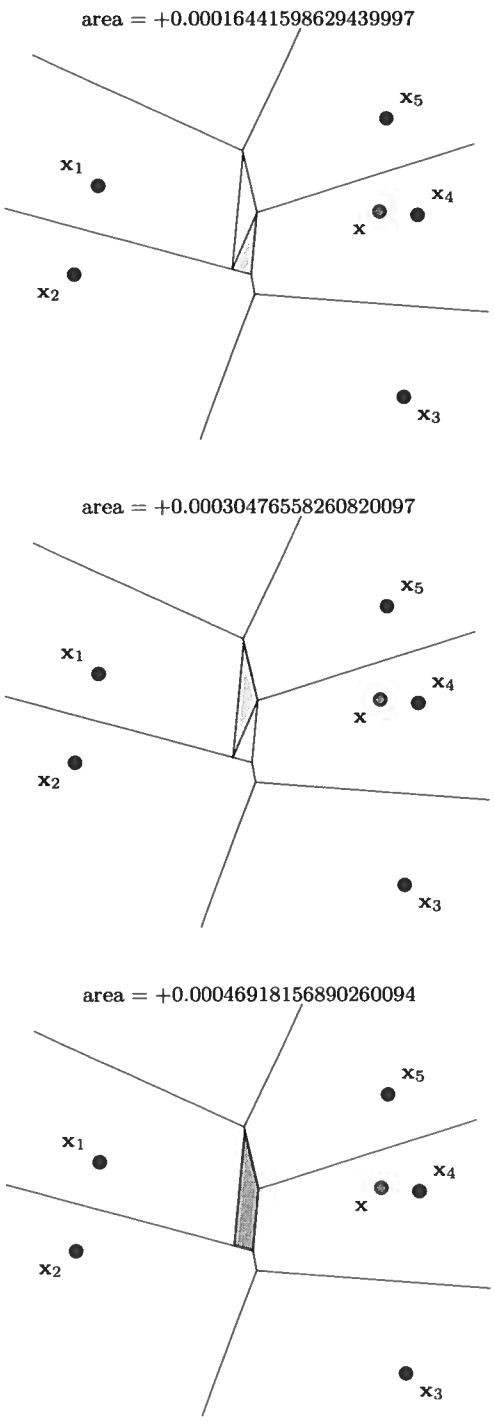

Figure 7. Illustration of the Boissonnat-Cazals implementation for the situation shown in Figure 5.

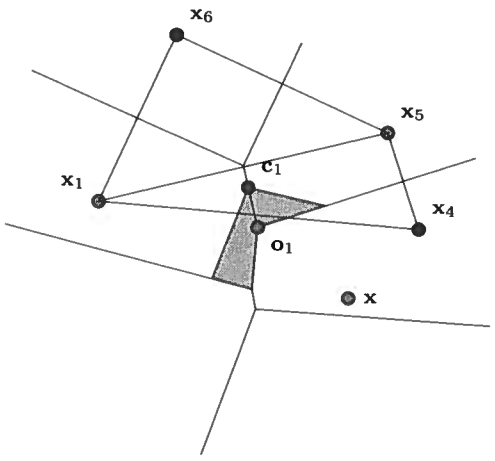

Figure 8. An edge $\mathbf{c}_1\mathbf{o}_1$ shared by two overlap polygons. This edge has one green endpoint $\mathbf{o}_1$ and one blue endpoint $\mathbf{c}_1$. $\mathbf{o}_1$ and $\mathbf{c}_1$ are the circumcenters of $\triangle\mathbf{x}_1\mathbf{x}_4\mathbf{x}_5$ and $\triangle\mathbf{x}_1\mathbf{x}\mathbf{x}_5$, respectively.

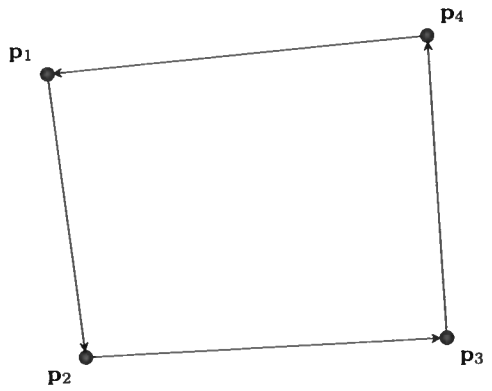

Figure 9. Computing area of a polygon by accumulating edge contributions.

than once, until we have visited all natural neighbor triangles.

As in the Watson-Sambridge method, as we visit each natural neighbor triangle, we accumulate contributions to the overlap areas a_i for the natural neighbors x_i. However, to avoid catastrophic cancellation, we accumulate these overlap areas a_i in a different way.

We use the fact (Gelder, 1995) that the area of any polygon with k vertices $\mathbf{p}_i (i = 1..k)$ is

$$\mathbf{A} = \frac{1}{2}\sum_{i=1}^{k}(\mathbf{p}_i \times \mathbf{p}_{i+1}), \tag{4}$$

where the index $i + 1$ is computed modulo k, so that $\mathbf{p}_{k+1} = \mathbf{p}_1$. This formula for area is valid for any planar polygon in 2D or 3D (see Figure 9). The area of the

polygon is the magnitude of the vector sum $\mathbf{A}$, which is orthogonal to the plane containing all polygon vertices $\mathbf{p}_i$. The out-of-plane component of this vector is positive if the vertices $\mathbf{p}_i$ are indexed in counterclockwise order when viewed from above the plane.

All polygon vertices $\mathbf{p}_i$ in Equation 4 are circumcenters of triangles. Some of those triangles are the so-called natural neighbor triangles. Let the $\mathbf{o}_j$ denote the corresponding circumcenters of these triangles. We accumulate the contributions of cross products $\mathbf{o}_j \times \mathbf{o}_{j+1}$ in the area formula as we visit each natural neighbor triangle (see Figure 10).

Specifically, as we visit each natural neighbor triangle, we accumulate the contributions of up to three cross products in the area formula. Each such pair corresponds to the natural neighbor triangle and one adjacent triangle, if the latter exists and is also a natural neighbor triangle. The circumcenters of these two natural neighbor triangles contribute one cross product to the area formula. Each such cross product contributes to the overlap areas for the two natural neighbors shared by the two natural neighbor triangles.

Because each triangle has three edges, it may have up to three adjacent triangles, and there exist up to three possible contributions of the sort $\mathbf{o}_j \times \mathbf{o}_{j+1}$. Therefore, up to three overlap areas a_i may be updated as we visit each natural neighbor triangle.

For each edge of a natural neighbor triangle that we visit, if we find that an adjacent triangle does not exist or is not a natural neighbor triangle, then we know that the corresponding edge must be one of the natural neighbor edges e_i. (Indeed, this is how we find the natural neighbor edges, as we recursively visit natural neighbor triangles.) We store each such triangle edge e_i that we find in a circular linked list of edges stored in counterclockwise order. We also store the circumcenter $\mathbf{c}_i$ of the triangle formed by the edge e_i and the interpolation point $\mathbf{x}$, along with the circumcenter $\mathbf{o}_j$ of the triangle being visited. We named $\mathbf{c}_i$ new circumcenters, and $\mathbf{o}_j$ old circumcenters.

In Figure 10 and 11, we have 5 natural neighbors $\mathbf{x}_1..\mathbf{x}_5$ and 3 natural neighbor triangles. Thus we have 5 natural neighbor edges $e_1..e_5$, 5 overlap areas $a_1..a_5$, 5 new circumcenters $\mathbf{c}_1..\mathbf{c}_5$ and 3 old circumcenters $\mathbf{o}_1..\mathbf{o}_3$. In this case, $i = 1..5$ and $j = 1..2$.

After we have visited all natural neighbor triangles, we then process the edges in circular linked list of natural neighbor edges e_i. Each such edge e_i contributes three cross products to the overlap areas. Two of these contributions correspond to the cross product $\mathbf{c}_i \times \mathbf{o}_j$, where $\mathbf{c}_i$ and $\mathbf{o}_j$ are the two circumcenters stored with the edge. The third contribution corresponds to the cross product $\mathbf{c}_j \times \mathbf{c}_{j+1}$. For example, in Figure 11c, $\mathbf{x}_1\mathbf{x}_2$ (e_2) contributes $\mathbf{c}_2\mathbf{o}_2$ to a_1, $\mathbf{o}_2\mathbf{c}_2$ to a_2 and $\mathbf{c}_1\mathbf{c}_2$ to a_1.

Our accumulation of all overlap areas a_i is complete after we have

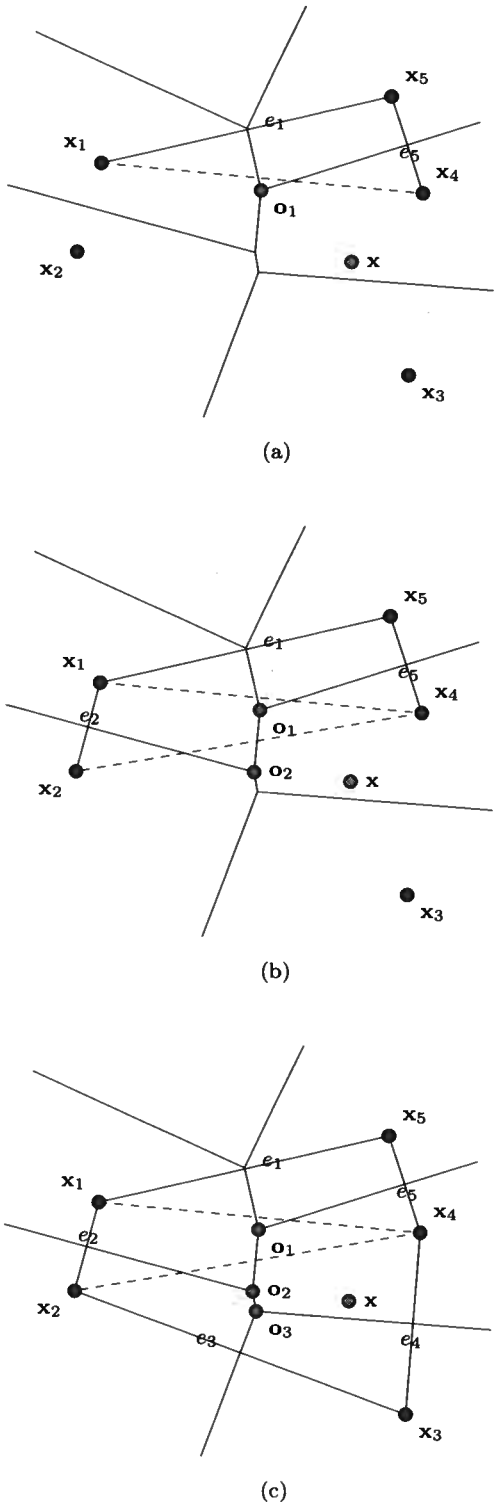

Figure 10. The first step: visiting natural neighbor triangles. During the visit, edge contributions $\mathbf{o}_j \times \mathbf{o}_{j+1}, j = 1..2$ are accumulated into corresponding overlap areas. Moreover, linked list of natural neighbor edges $e_i, i = 1..5$ are stored.

(1) visited all natural neighbor triangles and
(2) processed all natural neighbor edges.

We then compute the sum a of the overlap areas a_i and the Sibson weights $\frac{a_i}{a}$ for each natural neighbor of the interpolation point $\mathbf{x}$.

Our implementation is similar to the Watson-Sambridge implementation. First, when computing the Sibson weights, we visit each natural neighbor triangle only once. Second, as we visit each natural neighbor triangle, we accumulate overlap areas for up to three natural neighbor vertices $\mathbf{x}_i$.

The key difference is that, in our implementation, we never compute circumcenters of triangles formed by the interpolation point $\mathbf{x}$ and triangle edges that shared by two natural neighbor triangles (dashed lines in Figure 10). These shared triangle edges lie inside the polygon formed by the natural neighbor edges, and numerical instabilities in the Watson-Sambridge implementation occur when the point $\mathbf{x}$ lies near these inside edges.

Another difference is that, as we visit natural neighbor triangles, we construct a list of natural neighbor edges for processing later (solid lines in Figure 10). Construction of this edge list makes our implementation only slightly more costly than the Watson-Sambridge implementation.

To further improve numerical stability, we perform all computations in a shifted coordinate system in which the interpolation point $\mathbf{x}$ is the origin. In other words, we subtract the point x from each of its natural neighbor vertices $\mathbf{x}_i$, before computing circumcenters and cross products.

4.2 Extension to 3D

This implementation can be naturally extended to 3D. In Gelder (1995), the volume of a polyhedron R, which has m faces $(F_1, F_2, ..., F_m)$, is given by

$$V = \frac{1}{3}\sum_{i=1}^{m} \mathbf{P}_{F_j} \cdot \mathbf{A}_j, \tag{5}$$

where $\mathbf{A}_j$ is the vector area of F_j ($\mathbf{A}_j$ can be computed as A in equation 4) and $\mathbf{P}_{F_j}$ is an arbitrary vertex of F_j. Substituting equation 4 in equation 5, one can see that the volume computation simply involves computing edge contributions.

Similar to the 2D case, boundaries of the natural neighbor region must be found and stored. In 3D, triangular faces of tetrahedra, rather than Delaunay edges, must be stored. Then, the corresponding green endpoints and blue endpoints are determined by computing circumcenters of tetrahedra.

4.3 Performance

We illustrate Watson-Sambridge, Braun-Sambridge and our implementation for 2D in Figure 12. The nine black dots represent the locations of known samples located uniformly in the space $[0,1] \times [0,1]$. The value of a known sample (x, y) is $f(x, y) = \sin(\pi x)\sin(\pi y)$. We interpolate between these known samples using natural neighbor interpolation and compute differences between the interpolation values and $f(x, y)$ at all samples in $[0,1] \times [0,1]$ with the sampling interval 0.01. Colors represent sample values. We can clearly see some shortcomings in the Watson-Sambridge implementation. As explained earlier, instabilities occur near Delaunay edges.

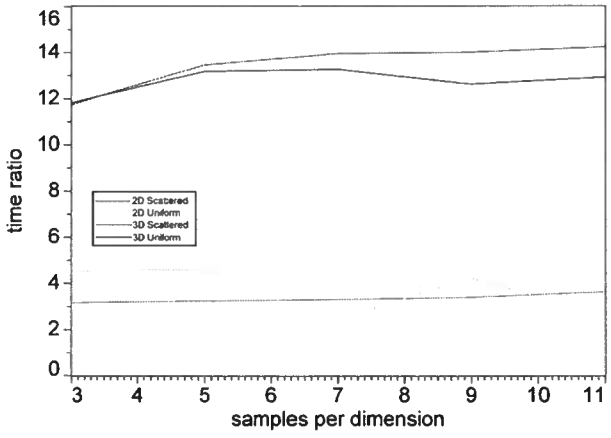

Figure 13. The ratio of CPU time of the Braun-Sambridge implementation and our implementation, with different known samples. Here, the horizontal axis indicates how many samples are known in each dimension, e.g., 3 samples per dimension means we have $3 \times 3 \times 3 = 27$ known samples.

We benchmarked these implementations in 2D and 3D. We selected 3×3, 5×5, 7×7, 9×9 and 11×11 known samples in 2D and $3 \times 3 \times 3$, $5 \times 5 \times 5$, $7 \times 7 \times 7$, $9 \times 9 \times 9 \times 9$ and $11 \times 11 \times 11$ known samples in 3D from the functions $f(x, y) = \sin(\pi x)\sin(\pi y)$ and $f(x, y, z) = \sin(\pi x)\sin(\pi y)\sin(\pi z)$, respectively. Tables 1-4 show the time consumed by different implementations (the unit is second). The terms "scattered" and "uniform" in these tables show the distributions of known samples.

We benchmarked these implementations on an Apple Mac Pro apple workstation with 3 GHz Intel Xeon CPU. Our method is slower than the Watson-Sambridge implementation but faster than the Braun-Sambridge implementation. Figure 13 demonstrates the efficiency of our method compared to the Braun-Sambridge method in different situations.

5 CONCLUSION

An efficient and stable implementation of natural neighbor interpolation is described in this report. The key idea is to reuse terms in the area formula as much as possible, without sacrificing accuracy. In addition, several simple improvements in computational issues are

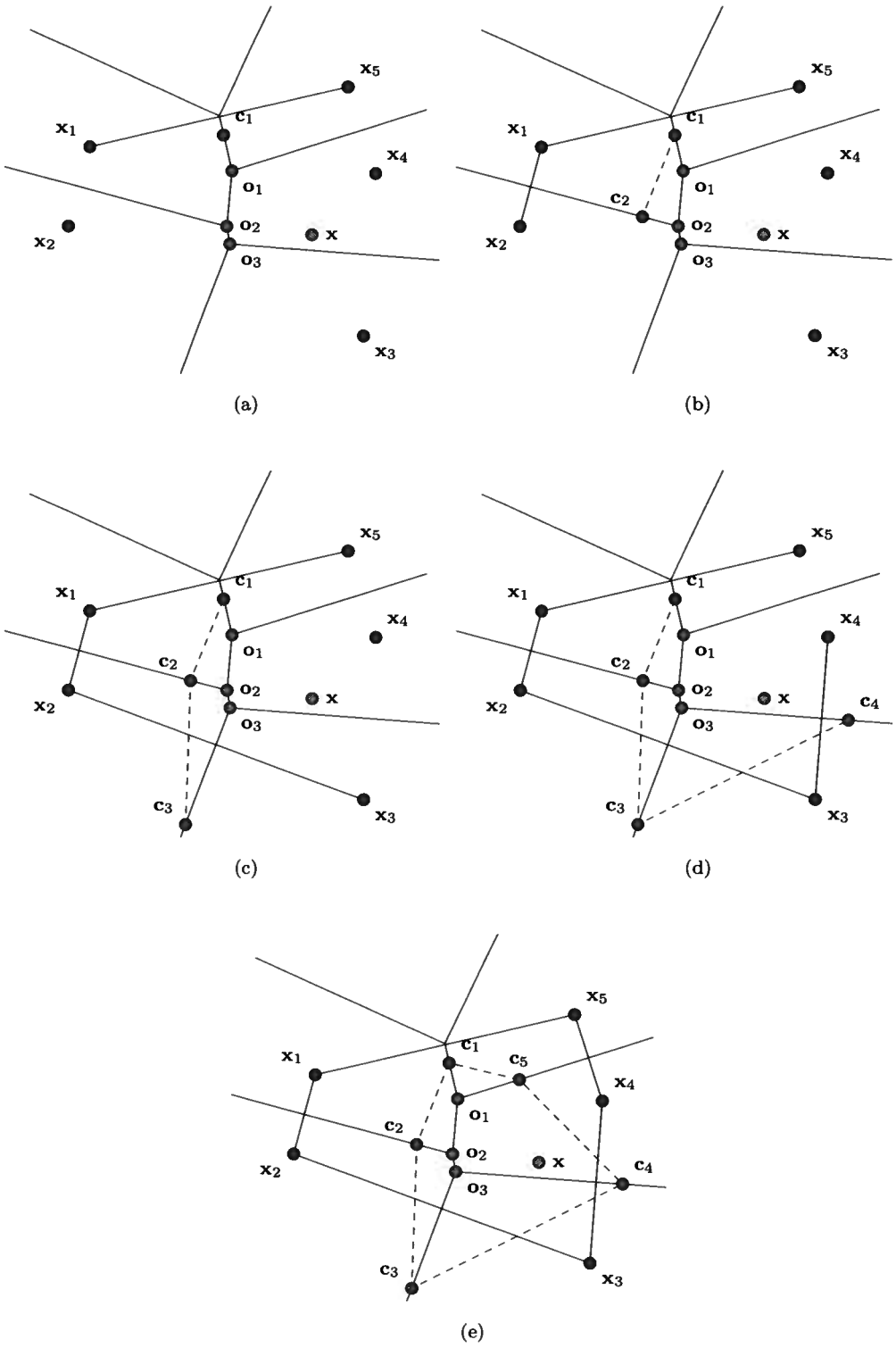

Figure 11. The second step: traversing the linked edge list stored in the first step. Edge contributions are computed and accumulated into corresponding areas when boundaries (dashed lines) are traversed.

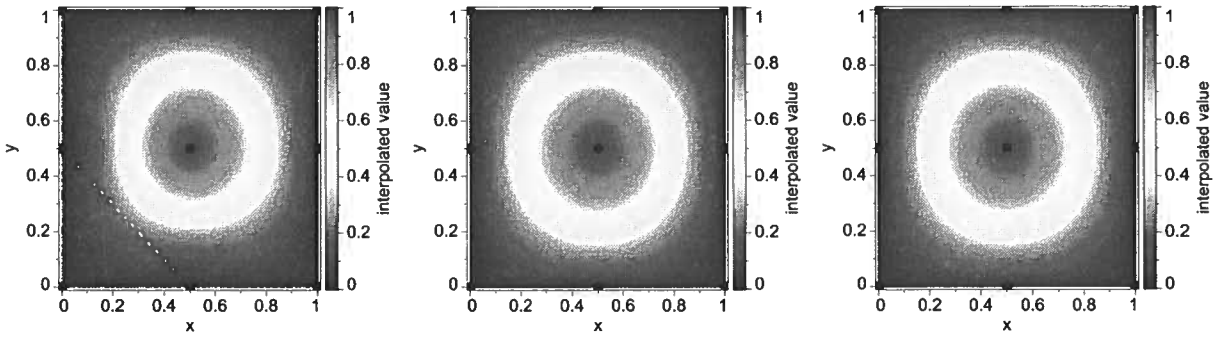

(a) (b) (c)

Figure 12. Comparisons of different implementations: (a)-(c) are interpolation results of the Watson-Sambridge implementation, the Braun-Sambridge implementation and our implementation, respectively.

	Watson-Sambridge	Braun-Sambridge	Our
3×3	1.22	5.02	1.59
5×5	1.23	5.44	1.68
7×7	1.39	6.14	1.86
9×9	1.41	6.42	1.89
11×11	1.55	7.10	1.96

Table 1. The computational time of different implementations of natural neighbor interpolation in 2D for scattered data.

	Watson-Sambridge	Braun-Sambridge	Our
3×3	1.12	6.47	1.43
5×5	1.14	6.70	1.52
7×7	1.21	3.94	1.50
9×9	1.24	4.24	1.62
11×11	1.30	4.13	1.61

Table 2. The computational time of different implementations of natural neighbor interpolation in 2D for uniform data.

	Watson-Sambridge	Braun-Sambridge	Our
$3 \times 3 \times 3$	0.63	8.42	0.75
$5 \times 5 \times 5$	0.98	16.45	1.14
$7 \times 7 \times 7$	1.02	17.02	1.22
$9 \times 9 \times 9$	1.13	19.50	1.36
$11 \times 11 \times 11$	1.22	20.86	1.44

Table 3. The computational time of different implementations of natural neighbor interpolation in 3D for scattered data.

	Watson-Sambridge	Braun-Sambridge	Our
$3 \times 3 \times 3$	0.67	10.90	0.81
$5 \times 5 \times 5$	0.85	13.33	1.01
$7 \times 7 \times 7$	0.91	14.76	1.10
$9 \times 9 \times 9$	0.92	14.27	1.11
$11 \times 11 \times 11$	0.99	15.48	1.21

Table 4. The computational time of different implementations of natural neighbor interpolation in 3D for uniform data.

introduced, such as preventing substantial value subtraction and avoiding the use of formulas which have divisions.

Instead of using geometric implementations, one can also implement natural neighbor interpolation using discrete sibson interpolation (Park et al., 2006). The main advantage of discrete sibson interpolation is that this method is easy to implement because overlap areas need not be explicitly computed. The main disadvantage is that one has to compute values at every sample points in order to determine the value at one particular sample point.

We also restrict the topic to 2D and 3D implementations. In some applications, like the natural-elements method (Braun and Sambridge, 1995) for solving partial differential equations, the extension to higher dimensions may be useful. In the implementations mentioned above, the Braun-Sambridge implementation is the most straightforward one for extending to higher than three dimensions; this is the implementation used in the natural-elements method (Braun and Sambridge, 1995). However, in most cases, solving partial differential equations using the natural-elements method only requires 2D or 3D natural neighbor interpolation. Hence, the proposed method can be a good substitution for the Braun-Sambridge implementation because of its high efficiency.

The code for our implementation can be found in Mines Java Toolkit: http://boole.mines.edu/jtk/trunk/src/edu/mines/jtk/interp/.

ACKNOWLEDGMENTS

We'd like to thank our colleagues for their discussions and feedback on this research. We also want to thank Prof. Hisamoto Hiyoshi for the generous provision of his manuscript. We especially thank Diane Witters for her help with writing.

REFERENCES

Berg, M. D., O. Cheong, M. V. Kreveld, and M. Overmars, 2008. Computational Geometry: Algorithms and Applications (Third Edition).

Bobach, T., M. Hering-Bertram, and G. Umlauf, 2006. Comparison of Voronoi based scattered data interpolation schemes. *Proceeding of 6th International Conference on Visualization, Imaging, and Image Processing.*

Bobach, T., G. Farin, D. Hansford, and G. Umlauf, 2009. Natural neighbor extrapolation using ghost points. *Computer-Aided Design*, **41**(5), 350–365.

Boissonnat, J. D. and F. Cazals, 2000. Smooth surface reconstruction via natural neighbour interpolation of distance functions. *Proceedings of the sixteenth annual symposium on Computational geometry*, 223–232.

Braun, J. and M. Sambridge, 1995. A numerical method for solving partial differential equations on highly irregular evolving grids. *Nature*, **378**, 655–660.

Foster, M. P. and A. N. Evans, 2008. An evaluation of interpolation techniques for reconstructing ionospheric TEC maps. *IEEE Transactions on Geoscience and Remote Sensing.*, **46**, 2153–2164.

Gelder, A. V., 1995. Efficient Computation of Polygon Area and Polyhedron. *Graphics Gem, 4th edition.* Academic Press.

Hiyoshi, H., 2008. Stable Computation of Natural Neighbor Interpolation. *International Journal of Computational Geometry & Applications.*, **18**(4), 321-341.

Hoff, K. E., J. Keyser, M. Lin, D. Manocha, and T. Culver, 1999. Fast Computation of Generalized Voronoi Diagrams Using Graphics Hardware. *Proc. SIGGRAPH 99 Conf.*, 277-286.

Lasserre, J. B., 1983. An analytical expression and an algorithm for the volume of a convex polyhedron in R^n *Journal of optimization theory and applications*, **39**(3), 363–377.

Li, X. and H. J. Götze, 1999. Comparison of Some Gridding Methods. *The Leading Edge*, **18**(8), 898–900.

Park, S. W., L. Linsen, O. Kreylos, J. D. Owens, and B. Hamann, 2006. Discrete Sibson Interpolation. *IEEE Transactions on visualization and computer graphics.*, **12**(2), 243-253.

Sambridge, M., J. Braun, and H. McQueen, 1995. Geophysical parameterization and interpolation of irregular data using natural neighbours. *Geophys. J. Int.*, **122**, 837–857.

Sibson, R., 1981, A brief description of natural neighbor interpolation, *in* V. Barnett, ed., Interpreting Multivariate Data: John Wiley & Sons, 21–36.

Watson, D. F. and G.M. Philip, 1987. Neighborhood-based interpolation. *Geobyte*, **2**(2), 12–16.

Watson, D. F., 1992. Contouring: A Guide to the Analysis

and Display of Spatial Data. Pergamon, Oxford.

Watson, D. F., 2001. Compound signed decomposition, the core of natural neighbor interpolation in n-Dimensional Space. www.iamg.org/images/File/documents/oldftp/Watson/core.ps

Tutorial on seismic interferometry. Part I: Basic principles and applications

K. Wapenaar[1], D. Draganov[1], R. Snieder[2], X. Campman[3] & A. Verdel[3]

[1] *Department of Geotechnology, Delft University of Technology, Delft, The Netherlands*
[2] *Center for Wave Phenomena, Colorado School of Mines, Golden, Colorado 80401, USA*
[3] *Shell International Exploration and Production B.V., Rijswijk, The Netherlands*

ABSTRACT

In part I of this two-part tutorial we explain the basic principles of seismic interferometry (also known as Green's function retrieval) step-by-step and discuss its applications. We start with a 1D example (a plane wave propagating along the x-axis) and show that the crosscorrelation of the responses at two receivers along the x-axis gives the Green's function of the direct wave between these receivers. The 1D analysis continues with the introduction of the different aspects of interferometry with transient sources (as in exploration seismology) and with noise sources (as in passive seismology). Next we discuss 2D and 3D direct wave interferometry and show that the main contributions to the retrieved Green's function come from sources in Fresnel zones around stationary points. The main application of direct wave interferometry is the retrieval of seismic surface wave responses from ambient noise and the subsequent tomographic determination of the surface-wave velocity distribution of the subsurface.

In a classic paper, Claerbout showed that the autocorrelation of the transmission response of a layered medium gives the reflection response of that medium. This is essentially 1D reflected wave interferometry. We discuss this extensively as an introduction to 2D and 3D reflected wave interferometry. One of the main applications of reflected wave interferometry is the retrieval of the seismic reflection response from ambient noise and the subsequent imaging of the reflectors in the subsurface.

A common aspect of direct and reflected wave interferometry is that virtual sources are created at positions where there are only receivers, without requiring knowledge of the subsurface medium parameters nor of the positions of the actual sources.

Key words: seismic interferometry

INTRODUCTION

In this two-part tutorial we give an overview of the basic principles and the underlying theory of seismic interferometry and discuss applications and new advances. The term "seismic interferometry" refers to the principle of generating new seismic responses of virtual sources* by crosscorrelating seismic observations at different receiver locations. One can distinguish between controlled-source and passive seismic interferometry. Controlled-source seismic interferometry, pioneered by Schuster (2001), Bakulin and Calvert (2004) and others, (2004, 2006) which is discussed extensively in Part II. Note, however, that creating a virtual source is the essence of virtually all seismic interferometry methods (see e.g. Schuster (2001), who already used this terminology). In this paper (Parts I and II) we use the term "virtual source" whenever appropriate. When it refers to Bakulin and Calvert's method we will mention this explicitly.

*In the literature on seismic interferometry, the term "virtual source" often refers to the method of Bakulin and Calvert

comprises a new processing methodology for seismic exploration data. Apart from crosscorrelation, controlled-source interferometry also involves summation of correlations over different source positions. Passive seismic interferometry, on the other hand, is a methodology for turning passive seismic measurements (ambient seismic noise or (micro-) earthquake responses) into deterministic seismic responses. Here we further distinguish between retrieving surface-wave transmission responses (Campillo and Paul, 2003; Shapiro and Campillo, 2004; Sabra et al., 2005a) and exploration-type reflection responses (Claerbout, 1968; Scherbaum, 1987b; Draganov et al., 2007, 2009). In passive interferometry of ambient noise, no explicit summation of correlations over different source positions is required, since the correlated responses are a superposition of simultaneously acting uncorrelated sources.

In all cases, the response that is retrieved by crosscorrelating two receiver recordings (and summing over different sources) can be interpreted as the response that would be measured at one of the receiver locations as if there were a source at the other. Because such a point-source response is equal to a Green's function convolved with a wavelet, seismic interferometry is also often called "Green's function retrieval". Both terminologies are used in this paper. The term interferometry is borrowed from radio astronomy, in which it refers to crosscorrelation methods applied to radio signals from distant objects Thompson et al. (2001). The name Green's function honors George Green who, in a privately published essay, introduced the use of impulse responses in field representations Green (1828). Challis and Sheard (2003) give a brief history of Green's life and theorem. Ramírez and Weglein (2009) review applications of Green's theorem in seismic processing.

Early successful results of Green's function retrieval from noise correlations were obtained in the field of ultrasonics Weaver and Lobkis (2001, 2002). The experiments were done with diffuse fields in a closed system. Here "diffuse" means that the amplitudes of the normal modes are uncorrelated but have equal expected energies. Hence, the crosscorrelation of the field at two receiver positions does not contain cross-terms of unequal normal modes. The sum of the remaining terms is proportional to the modal representation of the Green's function of the closed system Lobkis and Weaver (2001). Hence, the crosscorrelation of a diffuse field in a closed system converges to its impulse response. Later it was recognized, e.g. Godin (2007), that this theoretical explanation is akin to the fluctuation-dissipation theorem (Callen and Welton, 1951; Rytov, 1956; Rytov et al., 1989; Le Bellac et al., 2004).

The Earth is a closed system, but at the scale of global seismology the wavefield is far from diffuse. At the scale of exploration seismology, an ambient noise field may have a diffuse character, but the encompassing system is not closed. Hence, for seismic interferometry the normal-mode approach breaks down. Throughout this paper we consider seismic interferometry (or Green's function retrieval) in open systems, including half-spaces below a free surface. Instead of a treatment per field of application or a chronological discussion, we have chosen for a setup in which we explain the principles of seismic interferometry step by step. In Part I we start with the basic principles of 1D direct-wave interferometry and conclude with a discussion of the principles of 3D reflected-wave interferometry. We discuss applications in controlled-source as well as passive interferometry and, where appropriate, we review the historical background. To stay focussed on seismic applications, we refrain from a further discussion of the normal-mode approach, nor do we discuss the many interesting applications of Green's function retrieval in underwater acoustics (e.g. Roux and Fink (2003), Sabra et al. (2005c), Brooks and Gerstoft (2007)).

DIRECT-WAVE INTERFEROMETRY

1D analysis of direct-wave interferometry

We start our explanation of seismic interferometry by considering an illustrative 1D analysis of direct-wave interferometry. Figure 1a shows a plane wave, radiated by an impulsive unit source at $x = x_S$ and $t = 0$, propagating in the rightward direction along the x-axis. We assume that the propagation velocity c is constant and the medium is lossless. There are two receivers along the x-axis, at x_A and x_B, respectively. Figure 1b shows the response observed by the first receiver at x_A. We denote this response as $G(x_A, x_S, t)$, where G stands for Green's function. Throughout this paper we use the common convention that the first two arguments in $G(x_A, x_S, t)$ denote the receiver and source coordinates, respectively (here x_A and x_S), whereas the last argument denotes time (t) or angular frequency (ω). In our example this Green's function consists of an impulse at $t_A = (x_A - x_S)/c$, hence $G(x_A, x_S, t) = \delta(t - t_A)$, where $\delta(t)$ is the Dirac delta function. Similarly, the response at x_B is given by $G(x_B, x_S, t) = \delta(t - t_B)$, with $t_B = (x_B - x_S)/c$ (Figure 1c). Seismic interferometry involves the crosscorrelation of responses at two receivers, in this case at x_A and x_B. Looking at Figure 1a, it appears that the raypaths associated with $G(x_A, x_S, t)$ and $G(x_B, x_S, t)$ have the path from x_S to x_A in common. The traveltime along this common path cancels in the crosscorrelation process, leaving the traveltime along the remaining path from x_A to x_B, i.e., $t_B - t_A = (x_B - x_A)/c$. Hence, the crosscorrelation of the responses in Figures 1b and 1c is an impulse at $t_B - t_A$, see Figure 1d. This impulse can be interpreted as the response of a source at x_A, observed by a receiver at x_B, i.e., the Green's function $G(x_B, x_A, t)$. An interesting observation is that the propagation velocity (c) and the position of the actual source (x_S) need not be

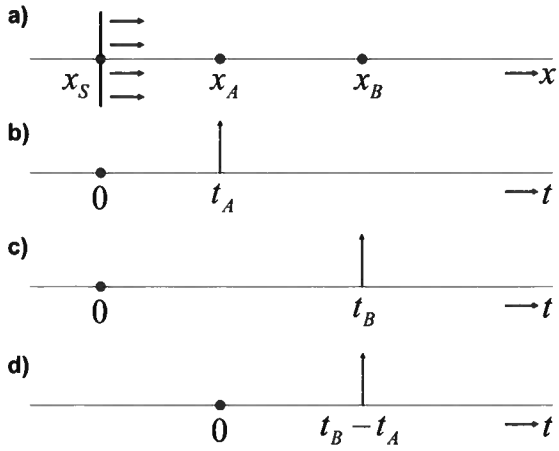

Figure 1. 1D example of direct-wave interferometry. (a) A plane wave traveling rightward along the x-axis, emitted by an impulsive source at $x = x_S$ and $t = 0$. (b). The response observed by a receiver at x_A. This is the Green's function $G(x_A, x_S, t)$. (c) As in (b), but for a receiver at x_B. (d) Crosscorrelation of the responses at x_A and x_B. This is interpreted as the response of a source at x_A, observed at x_B, i.e., $G(x_B, x_A, t)$.

known. The traveltimes along the common path from x_S to x_A compensate each other, independent of the propagation velocity and the length of this path. Similarly, if the source impulse would occur at $t = t_S$ instead of at $t = 0$, the impulses observed at x_A and x_B would be shifted by the same amount of time, t_S, which would be canceled in the crosscorrelation. Hence, also the absolute time t_S at which the source emits its pulse needs not be known.

Let us discuss this example a bit more precisely. We denote the crosscorrelation of the impulse responses at x_A and x_B as $G(x_B, x_S, t) * G(x_A, x_S, -t)$. The asterisk denotes temporal convolution, but the time-reversal of the second Green's function turns the convolution into a correlation, defined as $G(x_B, x_S, t) * G(x_A, x_S, -t) = \int G(x_B, x_S, t+t')G(x_A, x_S, t')\mathrm{d}t'$. Substituting the delta functions into the right-hand side gives $\int \delta(t + t' - t_B)\delta(t' - t_A)\mathrm{d}t' = \delta(t - (t_B - t_A)) = \delta(t - (x_B - x_A)/c)$. This is indeed the Green's function $G(x_B, x_A, t)$, propagating from x_A to x_B. Since we started this derivation with the crosscorrelation of the Green's functions, we have obtained the following 1D Green's function representation

$$G(x_B, x_A, t) = G(x_B, x_S, t) * G(x_A, x_S, -t). \qquad (1)$$

This representation formulates the principle that the crosscorrelation of observations at two receivers (x_A and x_B) gives the response at one of those receivers (x_B) as if there were a source at the other (x_A). It also shows why seismic interferometry is often called Green's function retrieval.

Note that the source is not necessarily an impulse. If the source function is defined by some wavelet $s(t)$, then the responses at x_A and x_B can be written as $u(x_A, x_S, t) = G(x_A, x_S, t) * s(t)$ and $u(x_B, x_S, t) = G(x_B, x_S, t) * s(t)$, respectively. Let $S_s(t)$ be the autocorrelation of the wavelet, i.e., $S_s(t) = s(t) * s(-t)$. Then the crosscorrelation of $u(x_A, x_S, t)$ and $u(x_B, x_S, t)$ gives the right-hand side of equation 1, convolved with $S_s(t)$. This is equal to the left-hand side of equation 1, convolved with $S_s(t)$, hence

$$G(x_B, x_A, t) * S_s(t) = u(x_B, x_S, t) * u(x_A, x_S, -t). \qquad (2)$$

In words: if the source function is a wavelet instead of an impulse, then the crosscorrelation of the responses at two receivers gives the Green's function between these receivers, convolved with the autocorrelation of the source function. This principle holds true for any source function, including noise. Figures 2a and 2b show the responses at x_A and x_B, respectively, of a bandlimited noise source $N(t)$ at x_S (the central frequency of the noise is 30 Hz; the figures show only 4 s of a total of 160 s of noise). In this numerical example the distance between the receivers is 1200 m and the propagation velocity is 2000 m/s, hence, the traveltime between these receivers is 0.6 s. As a consequence, the noise response at x_B in Figure 2b is 0.6 s delayed with respect to the response at x_A in Figure 2a (similar as the impulse in Figure 1c is delayed with respect to the impulse in Figure 1b). Crosscorrelation of these noise responses gives, analogous to equation 2, the impulse response between x_A and x_B, convolved with $S_N(t)$, i.e., the autocorrelation of the noise $N(t)$. The correlation is shown in Figure 2c, which indeed reveals a bandlimited impulse centered at $t = 0.6$ s (the traveltime from x_A to x_B). Note that from registrations at two receivers of a noise field from an unknown source in a medium with unknown propagation velocity, we have obtained a bandlimited version of the Green's function. By dividing the distance between the receivers (1200 m) by the traveltime estimated from the bandlimited Green's function (0.6 s) we obtain an estimate of the propagation velocity between the receivers (2000 m/s). This illustrates that direct-wave interferometry can be used for tomographic inversion.

Until now we considered a single plane wave propagating in the positive x-direction. In Figure 3a we consider the same configuration as in Figure 1a, except that now an impulsive unit source at $x = x'_S$ radiates a leftward-propagating plane wave. Figure 3b is the response at x_A, given by $G(x_A, x'_S, t) = \delta(t - t'_A)$, with $t'_A = (x'_S - x_A)/c$. Similarly, the response at x_B is $G(x_B, x'_S, t) = \delta(t - t'_B)$, with $t'_B = (x'_S - x_B)/c$ (Figure 3c). The crosscorrelation of these responses gives $\delta(t - (t'_B - t'_A)) = \delta(t + (x_B - x_A)/c)$, which is equal to the time-reversed Green's function $G(x_B, x_A, -t)$. Hence, for the configuration of Figure 3a we obtain the following Green's function representation

$$G(x_B, x_A, -t) = G(x_B, x'_S, t) * G(x_A, x'_S, -t). \qquad (3)$$

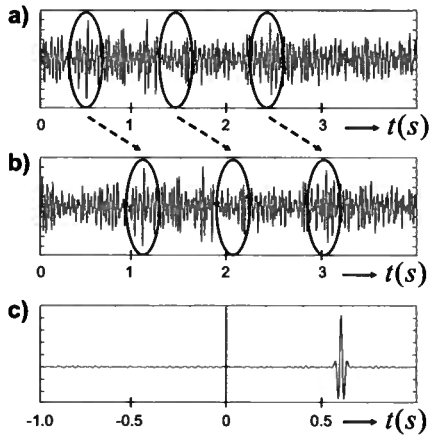

Figure 2. As in Figure 1, but this time for a noise source $N(t)$ at x_S. (a) The response observed at x_A, i.e., $u(x_A, x_S, t) = G(x_A, x_S, t) * N(t)$. (b) As in (a), but for a receiver at x_B. (c) The crosscorrelation, which is equal to $G(x_B, x_A, t) * S_N(t)$, with $S_N(t)$ the autocorrelation of the noise.

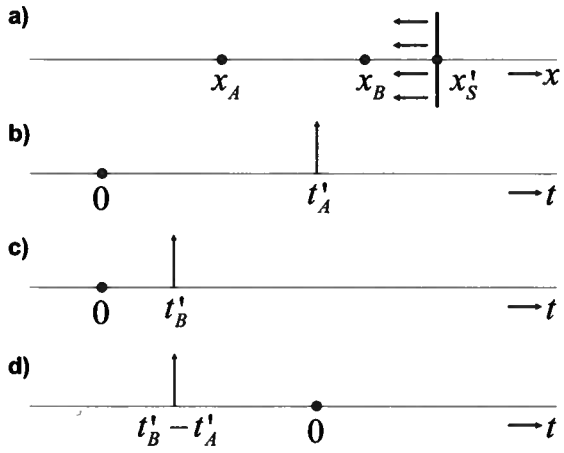

Figure 3. As in Figure 1, but this time for a leftward-traveling impulsive plane wave. The crosscorrelation in (d) is interpreted as the time-reversed Green's function $G(x_B, x_A, -t)$.

We can combine equations 1 and 3 as follows

$$G(x_B, x_A, t) + G(x_B, x_A, -t) = \sum_{i=1}^{2} G(x_B, x_S^{(i)}, t) * G(x_A, x_S^{(i)}, -t), \quad (4)$$

where $x_S^{(i)}$ for $i = 1, 2$ stands for x_S and x_S', respectively. For the 1D situation this combination may not seem very useful. We analyze it here, however, because this representation better resembles the 2D and 3D representations we encounter later. Note that since $G(x_B, x_A, t)$ is the causal response of an impulse at $t = 0$ (meaning it is non-zero only for $t > 0$), it does not overlap with

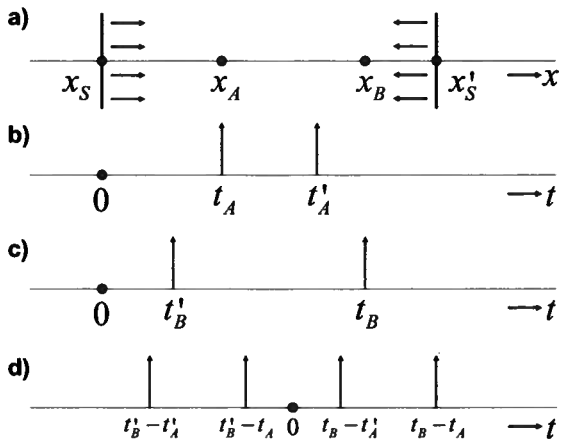

Figure 4. As in Figures 1 and 3, but with simultaneously rightward- and leftward-traveling impulsive plane waves. The crosscorrelation in (d) contains crossterms which have no physical meaning.

$G(x_B, x_A, -t)$ (which is non-zero only for $t < 0$). Hence, $G(x_B, x_A, t)$ can be resolved from the left-hand side of equation 4 simply by extracting the causal part. If the source function is a wavelet $s(t)$ with autocorrelation $S_s(t)$, we obtain, analogous to equation 2,

$$\{G(x_B, x_A, t) + G(x_B, x_A, -t)\} * S_s(t) = \sum_{i=1}^{2} u(x_B, x_S^{(i)}, t) * u(x_A, x_S^{(i)}, -t). \quad (5)$$

Here $G(x_B, x_A, t) * S_s(t)$ may have some overlap with $G(x_B, x_A, -t) * S_s(t)$ for small $|t|$ (depending on the length of the autocorrelation function $S_s(t)$). Hence $G(x_B, x_A, t) * S_s(t)$ can be extracted from the left-hand side of equation 5, except for small distances $|x_B - x_A|$.

The right-hand sides of equations 4 and 5 state that the crosscorrelation is applied to the responses of each source separately, after which the summation over the sources is carried out. For impulsive sources or transient wavelets $s(t)$ these steps should not be interchanged. Let us see why. Suppose the sources at x_S and x_S' would act simultaneously, as illustrated in Figure 4a. Then the response at x_A would be given by $u(x_A, t) = \sum_{i=1}^{2} G(x_A, x_S^{(i)}, t) * s(t)$ and the response at x_B by $u(x_B, t) = \sum_{j=1}^{2} G(x_B, x_S^{(j)}, t) * s(t)$. These responses are shown in Figures 4b and 4c for an impulsive source ($s(t) = \delta(t)$). The crosscorrelation of these responses, shown in Figure 4d, contains two crossterms at $t_B - t_A'$ and $t_B' - t_A$ which have no physical meaning. Hence, for impulsive or transient sources the order of crosscorrelation and summation matters. This is different for noise sources. Consider two simultaneously acting noise sources $N_1(t)$ and $N_2(t)$ at x_S and x_S', respectively. Then the responses at x_A and x_B are given by $u(x_A, t) = \sum_{i=1}^{2} G(x_A, x_S^{(i)}, t) * N_i(t)$ and $u(x_B, t) = \sum_{j=1}^{2} G(x_B, x_S^{(j)}, t) * N_j(t)$, respectively, see Figures 5a

and 5b. Note that, because each of these responses is the superposition of a rightward- and a leftward-propagating wave, the response in Figure 5b is not a shifted version of that in Figure 5a (unlike the responses in Figures 2a and b). We assume that the noise sources are uncorrelated, hence $\langle N_j(t) * N_i(-t)\rangle = \delta_{ij} S_N(t)$, where δ_{ij} is the Kronecker delta function and $\langle\cdot\rangle$ denotes ensemble averaging. In practice the ensemble averaging is replaced by integrating over sufficiently long time. In the numerical example the duration of the noise signals is again 160 s (only 4s of noise is shown in Figures 5a and 5b). For the cross correlation of the responses at x_A and x_B we may now write

$$\begin{aligned}\langle u(x_B,t) * u(x_A,-t)\rangle &= \Big\langle \sum_{j=1}^{2}\sum_{i=1}^{2} G(x_B,x_S^{(j)},t) * N_j(t) \\ &\quad * G(x_A,x_S^{(i)},-t) * N_i(-t)\Big\rangle \\ &= \sum_{i=1}^{2} G(x_B,x_S^{(i)},t) * G(x_A,x_S^{(i)},-t) * S_N(t). \qquad (6)\end{aligned}$$

Combining this with equation 4 we finally obtain

$$\begin{aligned}\{G(x_B,x_A,t) + G(x_B,x_A,-t)\} * S_N(t) = \\ \langle u(x_B,t) * u(x_A,-t)\rangle. \qquad (7)\end{aligned}$$

This expression shows that the crosscorrelation of two observed fields at x_A and x_B, each of which is the superposition of rightward- and leftward-propagating noise fields, gives the Green's function between x_A and x_B plus its time-reversed version, convolved with the autocorrelation of the noise, see Figure 5c. The crossterms, unlike in Figure 4d, do not contribute because the noise sources $N_1(t)$ and $N_2(t)$ are uncorrelated.

Miyazawa et al. (2008) applied equation 7 with x_A and x_B at different depths along a borehole in the presence of industrial noise, at Cold Lake, Alberta, Canada. By choosing for u different components of multicomponent sensors in the borehole, they retrieved separate Green's functions for P- and S-waves, the latter with different polarizations. From the arrival times in the Green's functions they derived the different propagation velocities and were able to accurately quantify shear-wave splitting.

Despite the relative simplicity of our 1D analysis of direct-wave interferometry, we can make a number of observations about seismic interferometry that also hold true for more general situations:

- We can distinguish between interferometry for impulsive or transient sources on the one hand (equations 4 and 5) and interferometry for noise sources on the other hand (equation 7). In the case of impulsive or transient sources, the responses of each of these sources must be crosscorrelated separately, after which a summation over the sources takes place. In the case of uncorrelated noise sources a single crosscorrelation suffices.
- It appears that an isotropic illumination of the receivers is required to obtain a time-symmetric response between the receivers (of which the causal part is the actual response). In 1D, "isotropic illumination" means equal illumination by rightward- and leftward-propagating waves. In 2D and 3D it means equal illumination from all directions (discussed in next subsection).
- Instead of the time-symmetric response $G(x_B,x_A,t) + G(x_B,x_A,-t)$, in the literature we often encounter an anti-symmetric response $G(x_B,x_A,t) - G(x_B,x_A,-t)$. This is merely a result of differently defined Green's functions. Note that a simple time differentiation of the Green's functions would turn the symmetric response into an anti-symmetric one and vice versa (see Wapenaar and Fokkema (2006) for a more detailed discussion on this aspect).

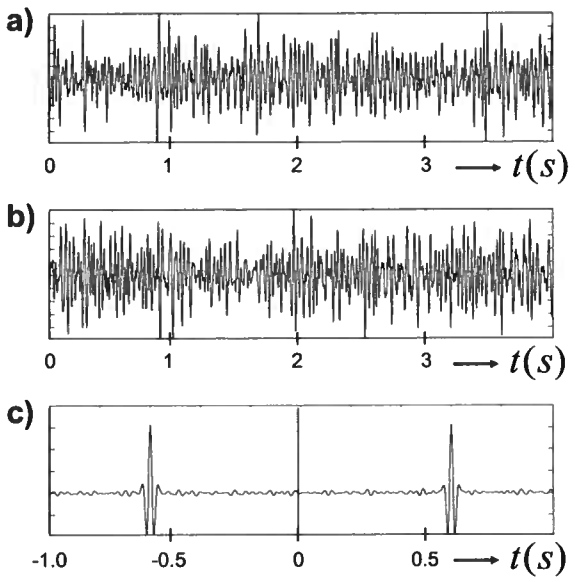

Figure 5. As in Figure 4, but this time with simultaneously rightward- and leftward-traveling uncorrelated noise fields. The crosscorrelation in (c) contains no crossterms.

2D and 3D analysis of direct-wave interferometry

We extend our discussion of direct-wave interferometry to configurations with more dimensions. In the following we mainly use heuristic arguments, illustrated with a numerical example. For a more precise derivation, based on stationary-phase analysis, we refer to Snieder (2004).

Consider the 2D configuration shown in Figure 6a. The horizontal dashed line corresponds to the 1D configuration of Figure 1a, with two receivers at $\mathbf{x}_A$ and $\mathbf{x}_B$, 1200 m apart (the boldface $\mathbf{x}$ denotes a Cartesian coordinate vector). The propagation velocity c is 2000 m/s and the medium is again assumed to be loss-

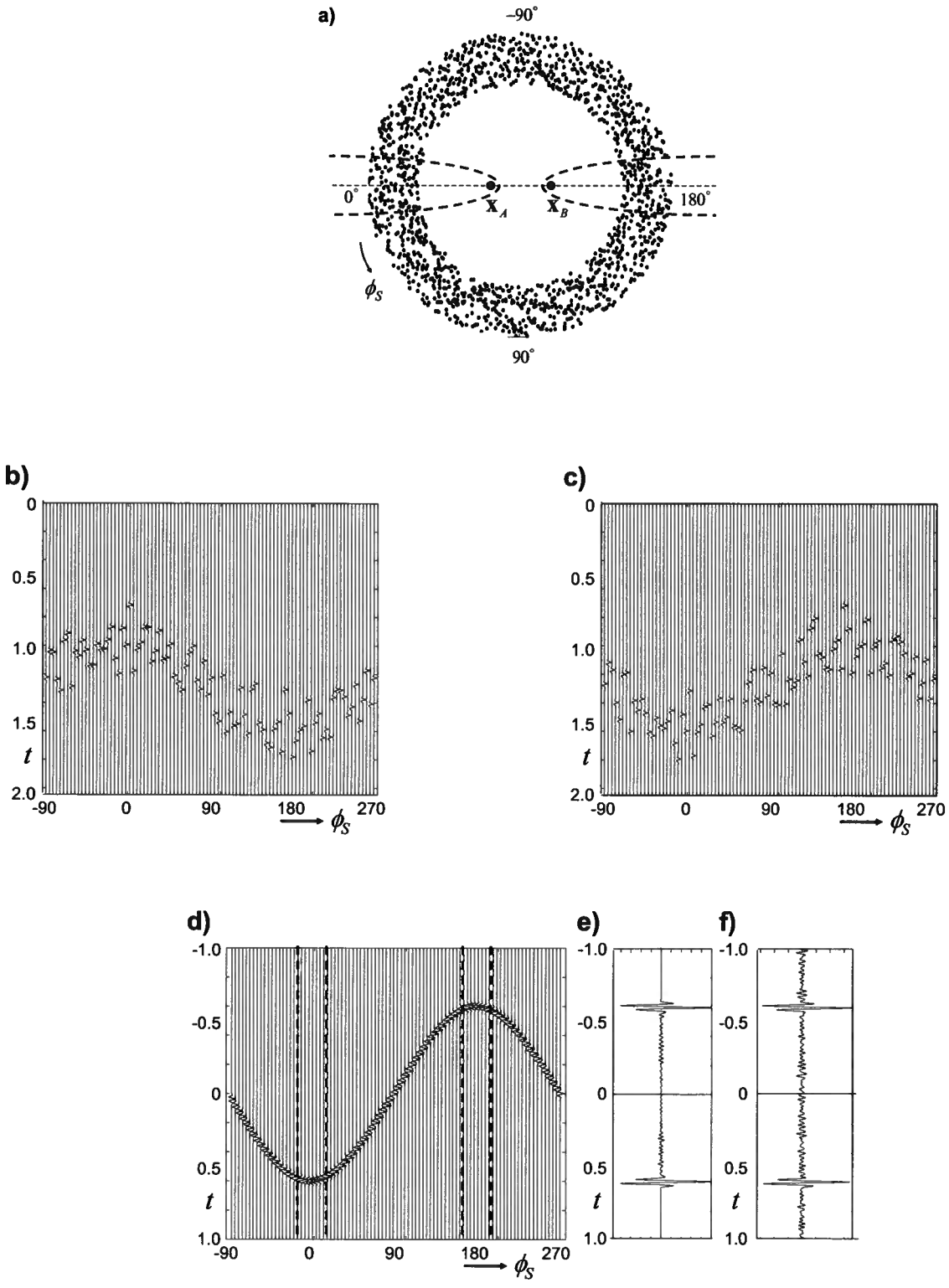

Figure 6. 2D example of direct-wave interferometry. (a) Distribution of point sources, isotropically illuminating the receivers at $\mathbf{x}_A$ and $\mathbf{x}_B$. The thick dashed lines indicate the Fresnel zones. (b) Responses at $\mathbf{x}_A$ as a function of the (polar) source coordinate ϕ_S. (c) Responses at $\mathbf{x}_B$. (d) Crosscorrelation of the responses at $\mathbf{x}_A$ and $\mathbf{x}_B$. The dashed lines indicate again the Fresnel zones. (e) The sum of the correlations in (d). This is interpreted as $\{G(\mathbf{x}_B,\mathbf{x}_A,t)+G(\mathbf{x}_B,\mathbf{x}_A,-t)\} * S_s(t)$. The main contributions come from sources in the Fresnel zones indicated in (a) and (d). (f) Single crosscorrelation of the responses at $\mathbf{x}_A$ and $\mathbf{x}_B$ of simultaneously acting uncorrelated noise sources. The duration of the noise signals was 9600 s.

less. Instead of plane-wave sources, we have many point sources denoted by the small black dots, distributed over a "pineapple slice", emitting transient signals with a central frequency of 30 Hz. In polar coordinates, the positions of the sources are denoted by (r_S, ϕ_S). The angle ϕ_S is equidistantly sampled ($\Delta\phi_S = 0.25^o$), whereas the distance r_S to the center of the slice is chosen randomly between 2000 and 3000 m. The responses at the two receivers at $\mathbf{x}_A$ and $\mathbf{x}_B$ are shown in Figures 6b and 6c, respectively, as a function of the (polar) source coordinate ϕ_S (for display purposes, only every 16th trace is shown). These responses are crosscorrelated (for each source separately) and the crosscorrelations are shown in Figure 6d, again as a function of ϕ_S. Such a gather is often called a "correlation gather". Note that the traveltimes in this correlation gather vary smoothly with ϕ_S, despite the randomness of the traveltimes in Figures 6b and 6c. This is because in the crosscorrelation process only the time *difference* along the paths to $\mathbf{x}_A$ and $\mathbf{x}_B$ matters. Note that the source in Figure 6a with $\phi_S = 0^o$ plays the same role as the plane-wave source at x_S in Figure 1a. For this source the crosscorrelation gives a signal at $|\mathbf{x}_B - \mathbf{x}_A|/c = 0.6$ s, which is seen in the trace at $\phi_S = 0^o$ in Figure 6d. Similarly, the source at $\phi_S = 180^o$ plays the same role as the plane-wave source at x'_S in Figure 3a and leads to the trace at $\phi_S = 180^o$ in Figure 6d with a signal at -0.6 s. Analogous to equation 5 we sum the crosscorrelations of all sources, that is, we sum all traces in Figure 6d, which leads to the time-symmetric response in Figure 6e, with two events at 0.6 and -0.6s. These two events are again interpreted as the response of a source at $\mathbf{x}_A$, observed at $\mathbf{x}_B$, plus its time-reversed version, i.e., $\{G(\mathbf{x}_B, \mathbf{x}_A, t) + G(\mathbf{x}_B, \mathbf{x}_A, -t)\} * S_s(t)$, where $S_s(t)$ is the autocorrelation of the source wavelet. Because the sources have a finite frequency content, not only the sources exactly at $\phi_S = 0^o$ and $\phi_S = 180^o$ contribute to these events, but also the sources in Fresnel zones around these angles. These Fresnel zones are denoted by the thick dashed lines in Figures 6a and 6d. In Figure 6d it can be seen that the centers of these Fresnel zones are the stationary points of the traveltime curve of the crosscorrelations. Note that the events in all traces outside the Fresnel zones in Figure 6d interfere destructively and hence give no coherent contribution in Figure 6e. The noise between the two events in Figure 6e is due to the fact that the traveltime curve in Figure 6d is not 100 % smooth because of the randomness of the source positions in Figure 6a.

The response in Figure 6e has been obtained by summing crosscorrelations of independent transient sources. Using the same arguments as in the previous subsection, we can replace the transient sources by simultaneously acting noise sources. The crossterms disappear when the noise sources are uncorrelated, hence, a single crosscorrelation of noise observations at $\mathbf{x}_A$ and $\mathbf{x}_B$ gives, analogous to equation 7, $\{G(\mathbf{x}_B, \mathbf{x}_A, t) + G(\mathbf{x}_B, \mathbf{x}_A, -t)\} * S_N(t)$, where $S_N(t)$ is the autocorrelation of the noise, see Figure 6f. Note that the symmetry of the responses in Figures 6e and 6f relies again on the isotropic illumination of the receivers, i.e., on the net power-flux of the illuminating wavefield being (close to) zero (van Tiggelen, 2003; Malcolm et al., 2004; Sánchez-Sesma et al., 2006; Snieder et al., 2007; Perton et al., 2009; Weaver et al., 2009; Yao et al., 2009).

Of course what has been demonstrated here for a 2D distribution of sources also holds for a 3D source distribution. In that case all sources in Fresnel volumes rather than Fresnel zones contribute to the retrieval of the direct wave between $\mathbf{x}_A$ and $\mathbf{x}_B$. Furthermore, the sources (in 2D or 3D) are not necessarily primary sources, but can also be secondary sources, i.e., scatterers in a homogeneous embedding. These secondary sources are not independent, but the late coda of the multiply scattered response reasonably resembles a diffuse wave field. Hence, in situations with few primary sources but many secondary sources only the late coda is used for Green's function retrieval Campillo and Paul (2003). It is, however, not clear how well a scattering medium should be illuminated by different sources for the scatterers to act as *independent* secondary sources. Fan and Snieder (2009) show an example where the scattered waves excited by a single source are equipartitioned, in the sense that energy propagates equally in all directions, but where the crosscorrelation of those scattered waves does not resemble the Green's function at all.

One of the most widely used applications of direct-wave interferometry is the retrieval of seismic surface waves between seismometers and the subsequent tomographic determination of the surface-wave velocity distribution of the subsurface. This approach has been pioneered by Campillo and Paul (2003), Shapiro and Campillo (2004), Sabra et al. (2005b,a) and Shapiro et al. (2005). In layered media, surface waves consist of several propagating modes, of which the fundamental mode is usually the strongest. As long as only the fundamental mode is considered, surface waves can be seen as an approximate solution of a 2D wave equation with a frequency-dependent propagation velocity. Hence, by considering the 2D configuration of Figure 6a as a plan view, the analysis above holds for ambient surface-wave noise. The Green's function of the fundamental mode of the direct surface wave can thus be extracted by crosscorrelating ambient noise recordings at two seismometers. When many seismometers are available, this can be repeated for any combination of two seismometers. In other words, each seismometer can be turned into a virtual source, the response of which is observed by all other seismometers.

Figure 7, reproduced with permission from Lin et al. (2009), shows a beautiful example of the Rayleigh-wave response of a virtual source, southeast of Lake Tahoe, California. The white triangles represent over

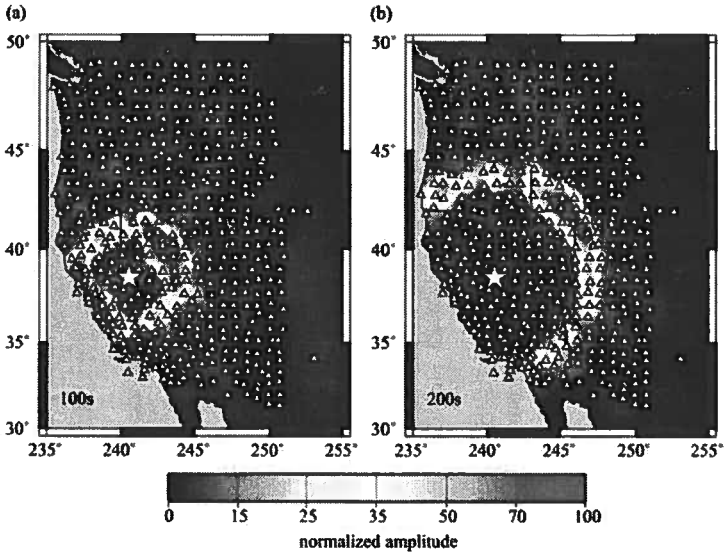

Figure 7. Two snapshots of the Rayleigh-wave response of a virtual source (the white star), southeast of Lake Tahoe, California Lin et al. (2009). The white triangles represent over 400 seismometers (USArray stations). The shown response was obtained by crosscorrelating three years of ambient noise, recorded at the station denoted by the star, with that recorded at all other stations.

400 seismometers (USArray stations). Ocean-generated ambient seismic noise (Longuet-Higgins, 1950; Webb, 1998; Stehly et al., 2006) was recorded between October 2004 and November 2007. Since this noise is coming from the ocean, it is far from isotropic. This means that the crosscorrelation of the noise between any two stations does not yield time-symmetric results like those in Figure 6. However, as long as one of the Fresnel zones is sufficiently covered with sources, it is possible to retrieve either $G(\mathbf{x}_B, \mathbf{x}_A, t)*S_N(t)$ or $G(\mathbf{x}_B, \mathbf{x}_A, -t)*S_N(t)$ (note that the location and shape of the Fresnel zone is different for each combination of stations). The snapshots shown in Figures 7a and 7b were obtained by crosscorrelating the noise recorded at the station denoted by the star with that recorded at all other stations. The amplitudes exhibit azimuthal variation due to the anisotropic illumination. Responses like this are used for tomographic inversion of the Rayleigh-wave velocity of the crust and for the measurement of azimuthal anisotropy in the crust.

Bensen et al. (2007) have shown that it is possible to retrieve the Rayleigh-wave velocity as a function of frequency. Brenguier et al. (2007) have combined these approaches to 3D tomographic inversion. From noise measurements at the Piton de la Fournaise volcano they retrieved the Rayleigh-wave group velocity distribution as a function of frequency and used this to derive a 3D S-wave velocity model of the interior of the volcano. In the past couple of years the applications of direct surface-wave interferometry have expanded spectacularly. Without any claim of completeness, we mention Larose et al. (2005, 2006), Gerstoft et al. (2006), Yao et al. (2006, 2008), Kang and Shin (2006), Bensen et al. (2008), Gouédard et al. (2008a,b), Liang and Langston (2008), Lin et al. (2008), Ma et al. (2008), Li et al. (2009) and Picozzi et al. (2009). The success of these applications is explained by the fact that surface waves are by far the strongest events in ambient seismic noise. In the next section we show that the retrieval of reflected waves from ambient seismic noise is an order more difficult.

Note that direct surface-wave interferometry has an interesting link with early work by Aki (1957, 1965) and Toksöz (1964) on the spatial autocorrelation method (SPAC). The SPAC method employs a circular array of seismometers, plus a seismometer at the center of the circle. Assuming a distribution of uncorrelated fundamental-mode Rayleigh waves, propagating as plane waves in all directions, the spatial autocorrelation function obtained from the circular array reveals the local surface-wave velocity as a function of frequency and, subsequently, the local depth-dependent velocity profile. An important difference with the interferometry approach is that the distances between the receivers in the SPAC method are usually smaller than half a wavelength Henstridge (1979), making it a local method, whereas in direct-wave interferometry the distances are assumed much larger than the wavelength because otherwise the stationary-phase arguments would not hold. More recent discussions on the SPAC method are given by Okada (2003, 2006) and Asten (2006). An interesting discussion on the relation between the SPAC method and seismic interferometry is given by Yokoi and Margaryan (2008).

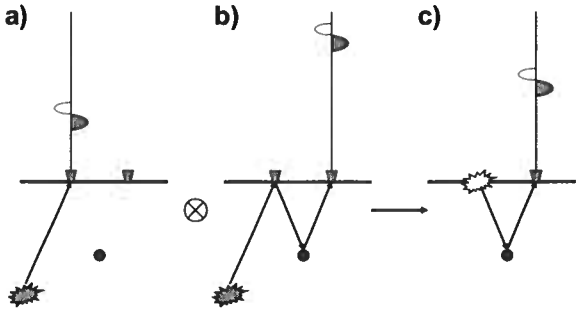

Figure 8. Basic principle of reflected-wave interferometry Schuster (2001, 2009). (a) A subsurface source emits a wave to the surface where it is received by a geophone. (b) A second geophone receives a reflected wave. (c) Crosscorrelation eliminates the propagation along the path from the source to the first geophone. The result is interpreted as the reflection response of a source at the position of the first geophone, observed by the second geophone.

REFLECTED-WAVE INTERFEROMETRY

1D analysis of reflected-wave interferometry

The figure on the cover of Schuster's book on seismic interferometry Schuster (2009), reproduced in Figure 8, explains the basic principle of reflected wave interferometry very well. Figure 8a shows a source in the subsurface which radiates a transient wave to the Earth's surface, where it is received by a geophone. The trace contains the delayed source wavelet. Figure 8b shows how the wave is reflected downward by the surface, reflected upward again by a scatterer in the subsurface, and received by a second geophone at the Earth's surface. The trace contains the wavelet, which is further delayed due to the propagation along the additional path from receiver 1 via the scatterer to receiver 2. The propagation paths in Figures 8a and 8b have the path from the subsurface source to the first receiver in common. By crosscorrelating the two traces (Schuster denotes this by $\otimes$), the propagation along this common path is eliminated, leaving the path from receiver 1 via the scatterer to receiver 2 (Figure 8c). Hence, the result can be interpreted as a reflection experiment with a source at the position of the first geophone, of which the reflection response is received by the second geophone.

Let us see how this method deals with multiple reflections. To this end we consider a configuration consisting of a homogeneous lossless layer, sandwiched between a free surface and a homogeneous lossless half-space, see Figure 9a. An impulsive unit source in the lower half-space emits a vertically upward-propagating plane wave, which reaches the surface after a time t_0. Since it was transmitted by a single interface on its way to the surface, the first arrival is given by $\tau\delta(t - t_0)$,

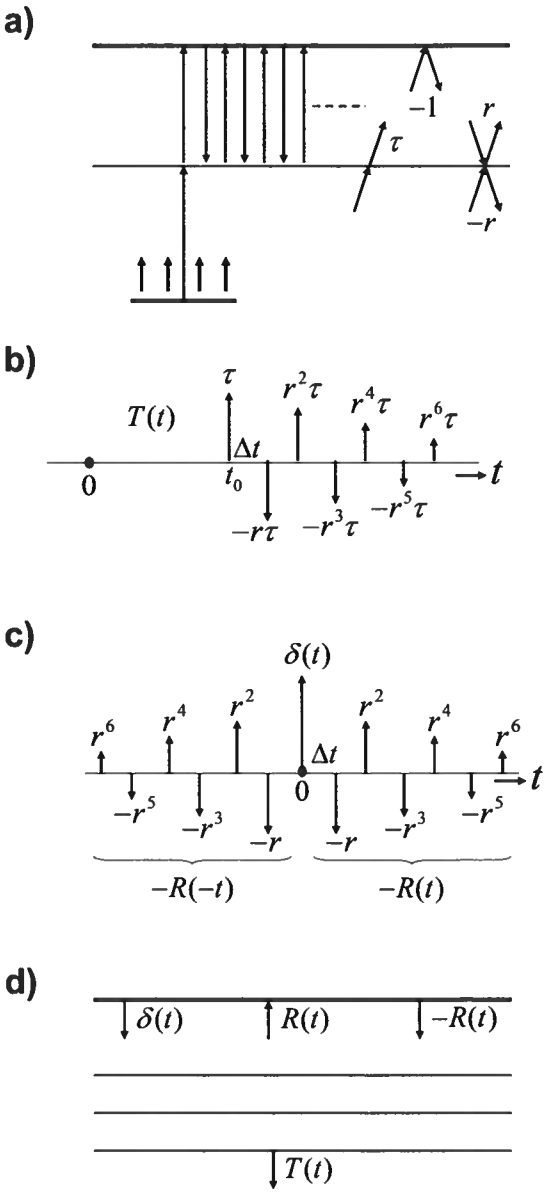

Figure 9. From transmission to reflection response (1D). (a) Simple layered medium with an upgoing plane wave radiated by a source in the lower half-space. (b) The transmission response $T(t)$, observed at the free surface. (c) The autocorrelation $T(t) * T(-t)$. The causal part is, apart from a minus sign, the reflection response $R(t)$. (d) Configuration, used to derive the same relation for an arbitrarily layered medium.

where τ is the transmission coefficient of the interface (we use lower-case symbols for local transmission and reflection coefficients). This arrival is represented by the impulse at $t = t_0$ in Figure 9b. The wave is re-

flected downward by the free surface (reflection coefficient -1) and subsequently reflected upward by the interface (reflection coefficient r). Hence, the next arrival reaching the surface is $-r\tau\delta(t-t_0-\Delta t)$, with $\Delta t = 2\Delta z/c$, where Δz is the thickness of the first layer and c its propagation velocity. Figure 9b shows the total upgoing wavefield reaching the free surface. It is denoted as $T(t)$, where capital T stands for the global transmission response. It consists of an infinite series of impulses with regular intervals Δt (starting at t_0), and amplitudes $a_0 = \tau$, $a_1 = -r\tau$, $a_2 = r^2\tau$, $a_3 = -r^3\tau$, etc. Seismic interferometry for a vertically propagating plane wave reduces to evaluating the autocorrelation of the global transmission response, hence $T(t) * T(-t)$. We obtain the simplest result if we consider so-called "power-flux normalized" up- and downgoing waves (Frasier, 1970; Kennett et al., 1978; Ursin, 1983; Chapman, 1994). This simply means that we define the local transmission coefficient τ as the square-root of the product of the transmission coefficients for acoustic pressure and particle velocity. Hence, for an upgoing wave, $\tau = \sqrt{(1-r)(1+r)} = \sqrt{1-r^2}$ (which is by the way also the transmission coefficient for a downgoing wave). The autocorrelation for zero time-lag is $(a_0^2+a_1^2+a_2^2+a_3^2+\cdots)\delta(t) = \tau^2(1+r^2+r^4+r^6+\cdots)\delta(t) = \tau^2(1-r^2)^{-1}\delta(t) = \delta(t)$. This is represented by the impulse at $t = 0$ in Figure 9c. The autocorrelation for time-lag Δt is $(a_1a_0 + a_2a_1 + a_3a_2 + \cdots)\delta(t-\Delta t) = -r\tau^2(1+r^2+r^4+\cdots)\delta(t-\Delta t) = -r\delta(t-\Delta t)$, which is represented by the impulse at Δt in Figure 9c. For time-lags $2\Delta t$, $3\Delta t$ etc. we obtain $r^2\delta(t-2\Delta t)$, $-r^3\delta(t-3\Delta t)$, etc. Apart from an overall minus-sign, these impulses together (except the one at $t = 0$) represent the global reflection response $R(t)$ of a downgoing plane wave, illuminating the medium from the free surface. Hence, the causal part of the autocorrelation is equal to $-R(t)$. Similarly, the acausal part is $-R(-t)$. Taking everything together, we have $T(t) * T(-t) = \delta(t) - R(t) - R(-t)$, or

$$R(t) + R(-t) = \delta(t) - T(t) * T(-t). \tag{8}$$

This expression shows that the global reflection response can be obtained from the autocorrelation of the global transmission response. This can be understood intuitively if one bears in mind that the reflection response, including all its multiples, is implicitly present in the coda of the transmission response, see Figure 9b. Note the analogy of equation 8 with the expression for direct-wave interferometry, equation 4. In both cases the left-hand side is a superposition of a causal response and its time-reversed version. The main difference is that the right-hand side of equation 4 is a superposition of crosscorrelations of rightward- and leftward-propagating waves, which was necessary to get the time-symmetric response, whereas the right-hand side of equation 8 is a single autocorrelation. Note, however, that the free surface in Figure 9a acts as a mirror, which removes the requirement of having sources at both sides of the receivers to obtain a time-symmetric response.

It can easily be shown that equation 8 holds for arbitrary horizontally layered media. To this end consider the configuration shown in Figure 9d. Here the illuminating wavefield is an impulsive downgoing plane wave at the free surface (denoted by $\delta(t)$ in Figure 9d). The upgoing wave arriving at the free surface is the global reflection response $R(t)$, which is reflected downward by the free surface with reflection coefficient -1. Hence, the total downgoing wavefield just below the surface is $D(t) = \delta(t) - R(t)$, and the total upgoing wavefield is $U(t) = R(t)$. The total downgoing wavefield below the lowest interface is given by the global transmission response $T(t)$. We assume again that the downgoing and upgoing waves are flux-normalized. Hence, the global transmission response of the downgoing plane wave source at the free surface is equal to that of an upgoing plane wave source below the lowest interface Frasier (1970). Because we consider a lossless medium, we can use the principle of power conservation to derive a relation between the wavefields at the top and the bottom of the configuration. The power-flux is most easily defined in the frequency domain. To this end we define the Fourier transform of a time-dependent function as

$$\hat{f}(\omega) = \int_{-\infty}^{\infty} f(t)\exp(-j\omega t)\mathrm{d}t, \tag{9}$$

where ω is the angular frequency and j the imaginary unit. The net power-flux just below the free surface is given by

$$\begin{aligned}\hat{D}\hat{D}^* - \hat{U}\hat{U}^* &= (1-\hat{R})(1-\hat{R}^*) - \hat{R}\hat{R}^* \\ &= 1-\hat{R}-\hat{R}^*,\end{aligned} \tag{10}$$

where the asterisk * denotes complex conjugation. Since the net power-flux is independent of depth, the right-hand side of equation 10 is equal to the net power-flux in the lower half-space, $\hat{T}\hat{T}^*$. Hence, $1-\hat{R}-\hat{R}^* = \hat{T}\hat{T}^*$, or

$$\hat{R} + \hat{R}^* = 1 - \hat{T}\hat{T}^*. \tag{11}$$

Because complex conjugation in the frequency domain corresponds to time-reversal in the time domain, the inverse Fourier transform of this equation gives again equation 8, which has now been proven to hold for arbitrarily layered media.

Note that the central assumption in this derivation is the conservation of acoustic power, which of course only holds in lossless media. We assumed already in our discussions of direct-wave interferometry that the medium was lossless, but in the present derivation the essence of this assumption has become manifest. Most approaches to seismic interferometry rely on the assumption that the medium is lossless. In Part II we also encounter approaches that account for losses, or that

use the essence of this assumption to estimate loss parameters.

We should note here that equation 8 for arbitrarily layered media was derived more than 40 years ago by Jon Claerbout at Stanford University Claerbout (1968). His expression looks slightly different because he did not use flux-normalization. For his derivation he used a recursive method introduced by Thomson (1950), Haskell (1953) and others. Later he proposed the shorter derivation using energy conservation, see the discussion on acoustic daylight imaging on his website http://sepwww.stanford.edu/sep/jon/. Frasier (1970) generalized Claerbout's result for obliquely propagating plane P- and SV-waves in a horizontally layered elastic medium.

Analogous to equations 5 and 7, equation 8 can be modified for transient or noise signals. For example, let $u(t) = T(t) * N(t)$ be the upgoing wavefield at the surface, with $N(t)$ representing the noise signal emitted by the source in the lower half-space. Then, analogous to equation 7, we obtain from equation 8

$$\{R(t) + R(-t)\} * S_N(t) = S_N(t) - \langle u(t) * u(-t) \rangle, \quad (12)$$

where $S_N(t)$ is the autocorrelation of the noise. This equation shows that the autocorrelation of passive noise measurements gives the reflection response of a transient source at the surface. Quite remarkable indeed! Note again that the position of the actual source does not need to be known, but it should lie below the lowest interface. In the next subsection we show that the latter assumption can be relaxed in 2D and 3D configurations.

Early applications of equation 12, some more successful than others, are discussed by Baskir and Weller (1975), Scherbaum (1987a,b), Daneshvar et al. (1995), Cole (1995) and Poletto and Petronio (2003, 2006).

2D and 3D analysis of reflected-wave interferometry

Claerbout conjectured for the 2D and 3D situation that "by crosscorrelating noise traces recorded at two locations on the surface, we can construct the wavefield that would be recorded at one of the locations if there was a source at the other" (this citation is from Rickett and Claerbout (1999), but the conjecture was already mentioned in the PhD thesis by Cole (1995)). Note that this statement could be applied literally to direct-wave interferometry, as discussed in the previous section, but Claerbout's conjecture concerned reflected-wave interferometry. Of course this terminology was not used at that time and the links between direct-wave and reflected-wave interferometry were discovered several years later. Duvall et al. (1993) and Rickett and Claerbout (1999) applied crosscorrelations to noise observations at the surface of the Sun and were able to retrieve helioseismological shot records.

Claerbout's 1D relation (equation 8) and his conjecture for the 3D situation inspired Jerry Schuster at the University of Utah. During a sabbatical in 2000 at Stanford University he analyzed the conjecture by the method of stationary phase. Let us briefly review his line of thought (Schuster, 2001; Schuster et al., 2004; Schuster and Zhou, 2006). First, consider again the configuration shown in Figure 8. It was silently assumed that the first geophone is located precisely at the specular reflection point of the drawn ray in Figure 8b. As a consequence, the ray in Figure 8a coincides with the first branch of the ray in Figure 8b, so in a 1D crosscorrelation process the traveltime along this ray cancels, which leaves the traveltime of the reflection response. In practice the source position and hence the position of the specular reflection point are unknown. However, when there are multiple (unknown) sources in the subsurface,

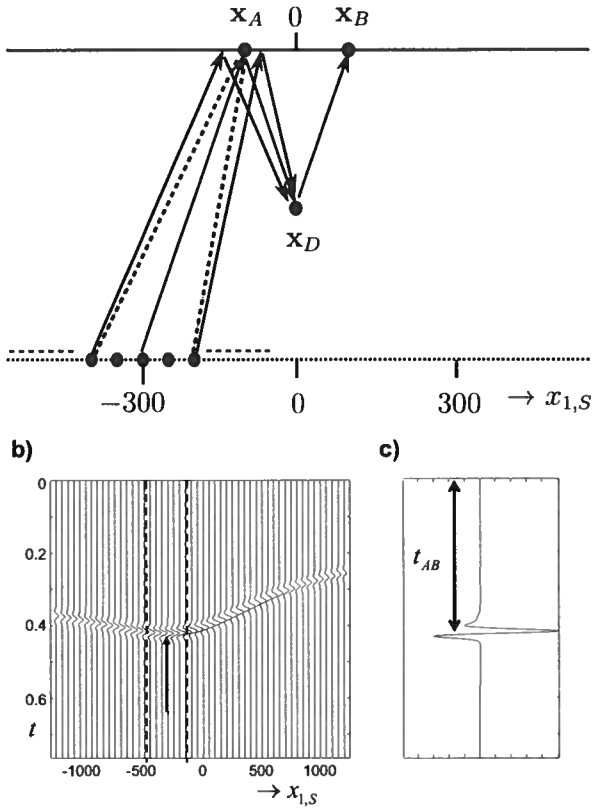

Figure 10. Basic principle of reflected-wave interferometry revisited. (a) Configuration with multiple sources in the subsurface. Only the ray emitted by the source at $x_{1,S} = -300$ m has its specular reflection point at one of the geophone positions. (b) Crosscorrelations of the responses at $\mathbf{x}_A$ and $\mathbf{x}_B$ as a function of the source coordinate $x_{1,S}$. The traveltime curve connecting these events is stationary at $x_{1,S} = -300$ m. The thick dashed lines indicate the Fresnel zone. (c) The sum of the correlations in (b). This is interpreted as the reflection response of a source at $\mathbf{x}_A$, observed by a receiver at $\mathbf{x}_B$.

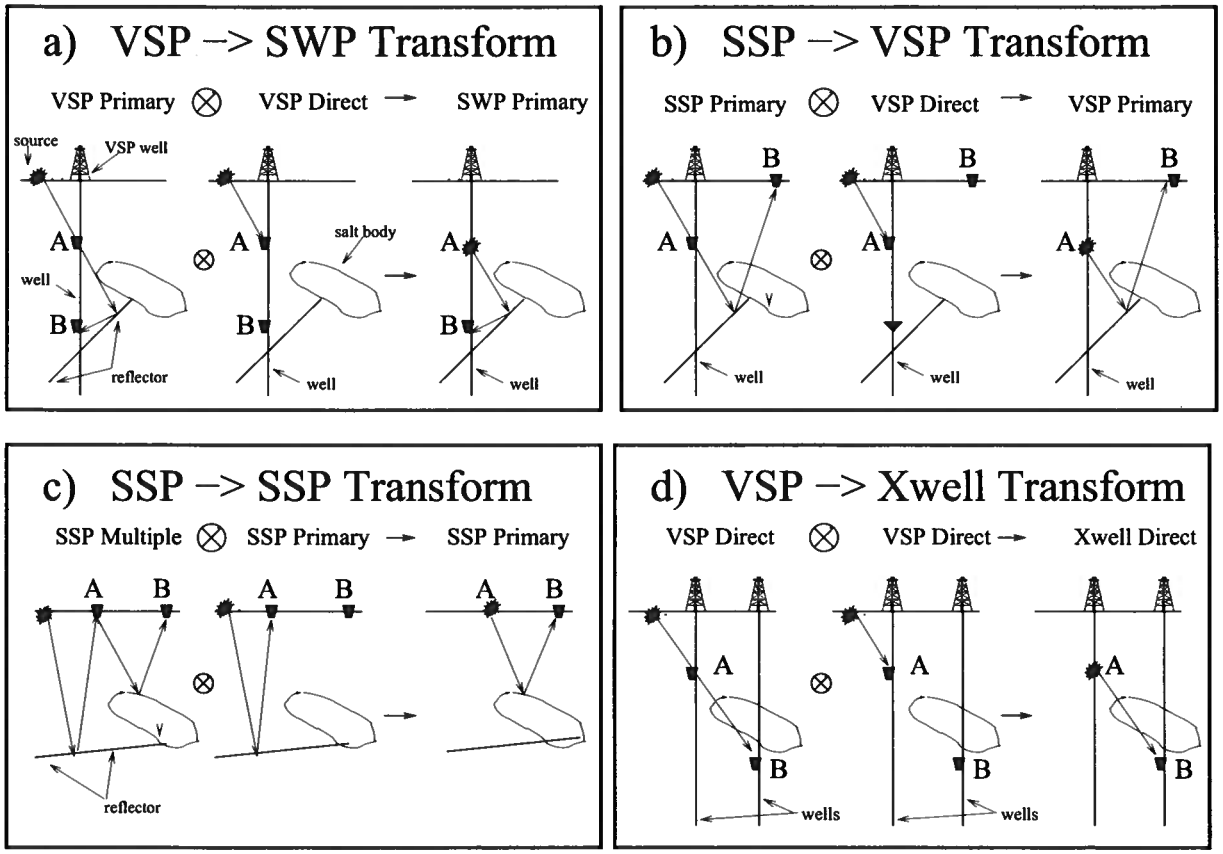

Figure 11. Some examples of interferometric redatuming Schuster (2009). Each diagram shows that crosscorrelation of the trace recorded at A with the one at B, and summing over source locations, leads to the response of a source at A, closer to the target than the original sources.

it is again possible to extract the reflection response. To see this, consider the situation depicted in Figure 10a, in which there are multiple noise sources buried in the subsurface. The ray that leaves the source at $x_{1,S} = -300$ m reflects at $\mathbf{x}_A$ (the position of the first geophone) on its way to the scatterer at $\mathbf{x}_D$ and the second geophone at $\mathbf{x}_B$, hence this is the specular ray. The rays leaving the other sources have their specular reflection points left and right from $\mathbf{x}_A$ (the solid rays in Figure 10a). The direct arrivals at $\mathbf{x}_A$ follow the dashed paths and do not coincide with the solid rays, except for the source at $x_{1,S} = -300$ m. For each of the sources we crosscorrelate the direct arrival at $\mathbf{x}_A$ with the scattered wave recorded at $\mathbf{x}_B$. This gives the correlation gather shown in Figure 10b, in which the horizontal axis denotes the source coordinate $x_{1,S}$. The trace at $x_{1,S} = -300$ m shows an impulse (indicated by the vertical arrow) at t_{AB}, which is the traveltime from $\mathbf{x}_A$ via the scatterer to $\mathbf{x}_B$. The impulses in the surrounding traces arrive before t_{AB}. If we sum the traces for all $x_{1,S}$, the main contribution comes from an area (the Fresnel zone, indicated by the dashed lines) around the point $x_{1,S} = -300$ m where the traveltime curve is stationary (indicated by the vertical arrow); the other contributions cancel. Hence, the sum of the correlations, shown in Figure 10c, contains an impulse at t_{AB} and can be interpreted as the reflection response that would be measured at $\mathbf{x}_B$ if there was a source at $\mathbf{x}_A$. In other words, the source has been repositioned from its unknown position at depth to a known position $\mathbf{x}_A$ at the surface. Note that this procedure works for any $\mathbf{x}_A$ and $\mathbf{x}_B$, as long as the array of sources contains a source that emits a specular ray via $\mathbf{x}_A$ and the scatterer to $\mathbf{x}_B$. In the Appendix we give a simple proof that the stationary point of the traveltime curve in a correlation gather corresponds to the source from which the rays to $\mathbf{x}_A$ and $\mathbf{x}_B$ leave in the same direction.

This example shows that it is possible to reposition (or "redatum") sources without knowing the velocity model and the position of the original sources. In exploration geophysics, redatuming is known as a process that brings sources and/or receivers from the acquisition level to another depth level, using extrapolation operators based on a macro velocity model Berryhill (1979, 1984). In seismic interferometry, as illustrated in Figure

10, the extrapolation operator comes directly from the data (in this example the observed direct wave at $\mathbf{x}_A$).

In the years following his sabbatical, Schuster showed that the interferometric redatuming concept, indicated in Figure 10, can be applied to a wide range of configurations (mostly for controlled-source data). His work inspired many other researchers to develop interferometric methods for exploration geophysics. We mention some examples. VSP data can be transformed into crosswell data Minato et al. (2007) or into single-well reflection profiles to improve salt-flank delineation and imaging (Willis et al., 2006; Xiao et al., 2006; Hornby and Yu, 2007; Lu et al., 2008). Interferometry can be used to turn multiples in VSP data into primaries and in this way enlarge the illuminated area (Yu and Schuster, 2006; Jiang et al., 2007; He et al., 2007). Surface multiples can be turned into primaries at the position of missing traces Wang et al. (2009). Crosscorrelation of refracted waves gives virtual refractions which can be used for improved estimation of the subsurface parameters Dong et al. (2006b); Mikesell et al. (2009). Surface waves can be predicted by interferometry and subsequently subtracted from exploration seismic data Curtis et al. (2006); Dong et al. (2006a); Halliday et al. (2007); Xue et al. (2009); Halliday et al. (2010). In his recent book, Schuster (2009) systematically discusses all possible interferometric transformations between surface data, VSP data, single well profiles and cross-well data. Figure 11 shows some examples. Another approach to interferometric redatuming of controlled-source data, known as the "virtual source method" Bakulin and Calvert (2004, 2006), is discussed in Part II of this paper.

The example discussed in Figure 10 deals only with primary reflections and therefore confirms Claerbout's conjecture only partly. The 1D analysis in the previous subsection showed that not only primary reflections, but also all multiples are recovered from the autocorrelation of the transmission response. Claerbout's conjecture for the 3D situation can be proven along similar lines. Instead of using the principle of power conservation, a so-called power reciprocity theorem is used as the starting point. In general, an acoustic reciprocity theorem formulates a relation between two acoustic states de Hoop (1988); Fokkema and van den Berg (1993). One can distinguish between convolution- and correlation-type theorems. The theorems of the correlation type reduce to power-conservation laws when the two states are chosen identical, which is why they are also called power reciprocity theorems. Because reflection and transmission responses are defined for downgoing and upgoing waves, the derivation makes use of a correlation-type reciprocity theorem for (flux-normalized) one-way wavefields Wapenaar and Grimbergen (1996). Consider the configuration in Figure 12a. An arbitrary inhomogeneous lossless medium is sandwiched between a free surface and a homogeneous lower half-space. Impulsive sources are distributed along a horizontal plane in this lower half-space. For this configuration we derived Wapenaar et al. (2002, 2004)

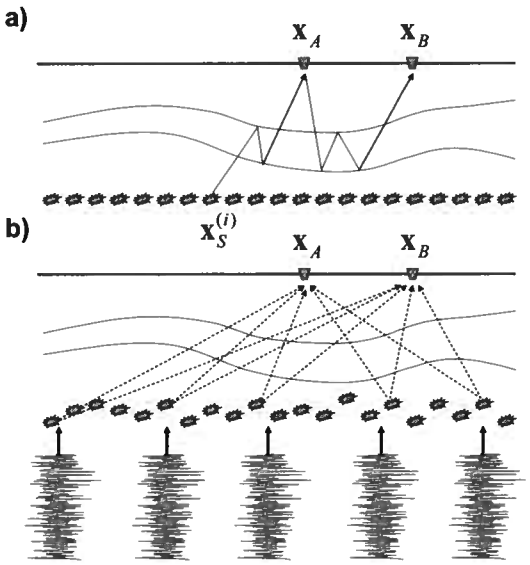

Figure 12. From transmission to reflection response (3D). (a) Arbitrary inhomogeneous lossless medium, with sources in the homogeneous lower half-space and receivers at $\mathbf{x}_A$ and $\mathbf{x}_B$ at the free surface. According to equation 13, the reflection response $R(\mathbf{x}_B, \mathbf{x}_A, t)$, implicitly present in the coda of the transmission response, is retrieved by crosscorrelating transmission responses observed at $\mathbf{x}_A$ and $\mathbf{x}_B$ and summing over the sources. (b) When the sources are simultaneously acting, mutually uncorrelated noise sources, the observed responses at $\mathbf{x}_A$ and $\mathbf{x}_B$ are each a superposition of transmission responses. According to equation 14, the reflection response $R(\mathbf{x}_B, \mathbf{x}_A, t)$ is now retrieved from the direct crosscorrelation of the observations at $\mathbf{x}_A$ and $\mathbf{x}_B$.

$$R(\mathbf{x}_B, \mathbf{x}_A, t) + R(\mathbf{x}_B, \mathbf{x}_A, -t) \approx \delta(\mathbf{x}_{H,B} - \mathbf{x}_{H,A})\delta(t) - \sum_i T(\mathbf{x}_B, \mathbf{x}_S^{(i)}, t) * T(\mathbf{x}_A, \mathbf{x}_S^{(i)}, -t). \quad (13)$$

Here $\mathbf{x}_{H,A}$ and $\mathbf{x}_{H,B}$ denote the horizontal components of $\mathbf{x}_A$ and $\mathbf{x}_B$, respectively. $T(\mathbf{x}_{A(B)}, \mathbf{x}_S^{(i)}, t)$ is the upgoing transmission response of an impulsive point source at $\mathbf{x}_S^{(i)}$ in the subsurface, observed at $\mathbf{x}_{A(B)}$ at the free surface. Its coda includes all surface-related and internal multiple reflections (only a few rays are shown in Figure 12a). The right-hand side of equation 13 involves a crosscorrelation of transmission responses at $\mathbf{x}_A$ and $\mathbf{x}_B$ for each source $\mathbf{x}_S^{(i)}$, followed by a summation for all source positions. The time-symmetric response on the left-hand side is the reflection response that would be recorded at $\mathbf{x}_B$ if there was a source at $\mathbf{x}_A$, plus its time-reversed version. The main approximation is the negligence of evanescent waves. Apart from that,

the retrieved reflection response $R(\mathbf{x}_B, \mathbf{x}_A, t)$ contains all primary, surface-related and internal multiple reflections, which are unraveled by equation 13 from the coda of the transmission responses.

When the impulsive sources are replaced by uncorrelated noise sources, then the responses at $\mathbf{x}_A$ and $\mathbf{x}_B$ are given by $u(\mathbf{x}_A, t) = \sum_i T(\mathbf{x}_A, \mathbf{x}_S^{(i)}, t) * N_i(t)$ and $u(\mathbf{x}_B, t) = \sum_j T(\mathbf{x}_B, \mathbf{x}_S^{(j)}, t) * N_j(t)$, see Figure 12b (each dashed ray represents a complete transmission response). Using a similar derivation as the one that transformed equation 4 into equation 7 we obtain from equation 13

$$\{R(\mathbf{x}_B, \mathbf{x}_A, t) + R(\mathbf{x}_B, \mathbf{x}_A, -t)\} * S_N(t) \approx \delta(\mathbf{x}_{H,B} - \mathbf{x}_{H,A}) S_N(t) - \langle u(\mathbf{x}_B, t) * u(\mathbf{x}_A, -t) \rangle,$$

where $S_N(t)$ is the autocorrelation of the noise. This equation shows that the direct crosscorrelation of passive noise measurements gives the reflection response of a transient source at the free surface. Although equations 13 and 14 have been derived for the situation in which the sources at $\mathbf{x}_S^{(i)}$ lie all at the same depth (Figure 12a), these equations remain approximately valid when the depths are randomly distributed (as in Figure 12b), because in the crosscorrelation process only the time difference matters (we used a similar reasoning for direct-wave interferometry to explain why the traveltime curves in Figure 6d remained smooth). Moreover, despite the initial assumption that the medium is homogeneous below the sources, Draganov et al. (2004) showed with numerical examples that the randomness of the source depths helps to suppress non-physical ghosts related to reflectors below the sources, whereas the physical response of these deeper reflectors shows up correctly in $R(\mathbf{x}_B, \mathbf{x}_A, t)$. Later this has also been explained with theoretical arguments Wapenaar and Fokkema (2006).

Equations 13 and 14 have been used by various authors to turn ambient seismic noise into exploration-like seismic reflection data Draganov et al. (2006); Hohl and Mateeva (2006); Torii et al. (2007); Draganov et al. (2007, 2009). It is interesting to note that in the teleseismic community it has been independently recognized that the coda of transmission responses from distant sources contains reflection information that can be used to image the Earth's crust (Bostock et al., 2001; Shragge et al., 2001, 2006; Rondenay, 2001; Mercier et al., 2006). The link between teleseismic coda imaging and seismic interferometry has been exploited by Kumar and Bostock (2006), Nowack et al. (2006), Chaput and Bostock (2007) and Tonegawa et al. (2009).

We conclude this section with an example of retrieving exploration-like seismic reflection data from ambient noise, recorded by Shell in a desert area near Ajdabeya, Libya. Figure 13a shows 10 s of noise, arbitrarily selected from a total of 11 hours of noise, recorded along a line of 20 km. Each receiver channel represents a group of 48 vertical-component geophones,

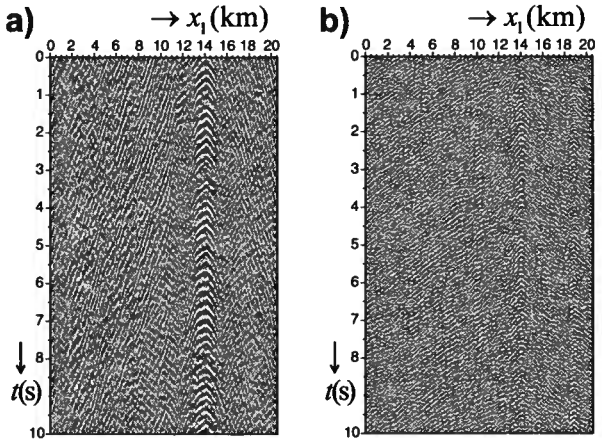

Figure 13. (a) 10 s of ambient noise, arbitrarily selected from a total of 11 hours of noise, recorded in a desert area near Ajdabeya, Libya. The main events are remnants of surface waves caused by traffic at x_1 =14 km. (b) The same noise window, after further suppression of the surface waves.

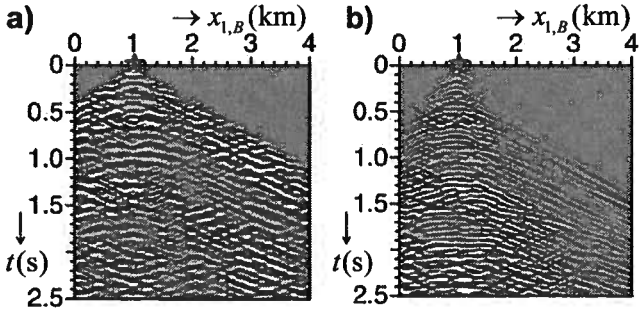

Figure 14. (a) Reflection response (shot record), obtained by crosscorrelating 11 hours of ambient noise Draganov et al. (2009). (b) For comparison, an active shot record measured at the same location.

designed to suppress surface waves. Nevertheless, the main events in Figure 13a are parts of the surface waves that fell outside the suppression band of the geophone groups; these surface waves were caused by traffic on a road intersecting the line at x_1 =14 km. Bandpass and k-f filtering was used to suppress the surface waves further, see Figure 13b.

We use equation 14 to retrieve the reflection response. Strictly speaking, application of equation 14 requires decomposition of the filtered geophone data of Figure 13b into the upgoing transmission response. In the acoustic approximation, decomposition mainly involves the application of an angle-dependent amplitude filter. Since it is very difficult to obtain true amplitude

responses from ambient noise anyway, the decomposition step is skipped. Using equation 14, with $\mathbf{x}_A$ fixed ($x_{1,A} = 1$ km) and $\mathbf{x}_B$ chosen variable ($x_{1,B} = 0 \cdots 4$ km), a seismic shot record $R(\mathbf{x}_B, \mathbf{x}_A, t)$ is retrieved from the noise, of which the first 2.5 s are shown in Figure 14a. The red star at $x_{1,B} = x_{1,A} = 1$ km denotes the position of the virtual source. An active seismic reflection experiment, carried out with the source at the same position, is shown in Figure 14b. Note that, particularly in the red shaded areas, the reflections retrieved from the ambient noise (Figure 14a) correspond quite well with those in the active shot gather (Figure 14b). For more details about this experiment as well as a pseudo 3D reflection image obtained from the ambient noise, see Draganov et al. (2009).

CONCLUSIONS

We have discussed the basic principles of seismic interferometry in a heuristic way. We have shown that, whether we consider controlled-source or passive interferometry, virtual sources are created at positions where there are only receivers. Of course no new information is generated by interferometry, but information hidden in noise or in a complex scattering coda, is reorganized into easy interpretable responses that can be further processed by standard tomographic inversion or reflection imaging methodologies. The main strength is that this "information unraveling" neither requires knowledge of the subsurface medium parameters nor of the positions or timing of the actual sources. Moreover, the processing consists of simple crosscorrelations and is almost entirely data-driven.

In Part II we discuss the relation between interferometry and time-reversed acoustics, review a mathematically sound derivation, and indicate recent and new advances.

ACKNOWLEDGEMENTS

This work is supported by the Netherlands Research Centre for Integrated Solid Earth Science (ISES), the Dutch Technology Foundation STW, applied science division of NWO and the Technology Program of the Ministry of Economic Affairs (grant VENI.08115), and by the NSF through grant EAS-0609595. We thank associate editor Sven Treitel and reviewers Jerry Schuster, Kasper van Wijk and Mark Willis for their valuable comments and suggestions, which helped improve this paper. We are grateful to Fan-Chi Lin, Mike Ritzwoller and Wiley-Blackwell (publisher of Geophysical Journal International) for permission to show the snapshots of the virtual Rayleigh-wave response (Figure 7). Jerry Schuster is acknowledged for providing Figure 11. Last, but not least, we thank the Libyan National Oil Company for permission to publish the Ajdabeya data results (Figures 13 and 14) and Shell in Libya for collecting and making available the passive data.

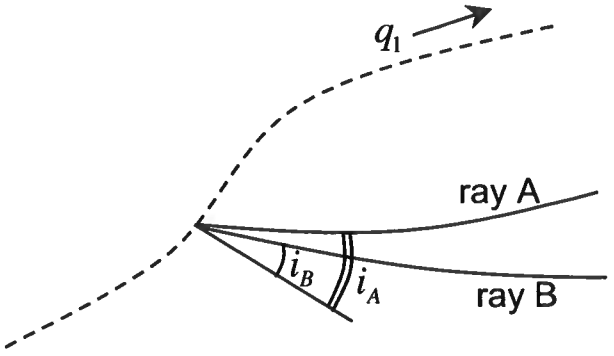

FIG. A-1 Two rays, A and B, that propagate from a common point on the surface with sources (dashed line) and their take-off angles at this source surface.

APPENDIX A: STATIONARY-PHASE ANALYSIS

We give a simple proof that the stationary point of the traveltime curve in a correlation gather corresponds to the source from which the rays to the receivers at $\mathbf{x}_A$ and $\mathbf{x}_B$ leave in the same direction. Consider two rays A and B that propagate from an arbitrary source point to the two receivers, see Figure A-1. This propagation may be direct, or it may involve bounces off reflectors or scatterers; the fate of these rays is irrelevant for the argument presented here. The sources involved in interferometry are located on the surface indicated by the dashed line in Figure A-1. This surface, which need not be planar, is in 3D parameterized by two orthogonal coordinates q_1 and q_2. We first keep q_2 fixed and consider only variations in q_1.

The travel time from a given source to the receiver at $\mathbf{x}_A$ is denoted by t_A, and the travel time from that source to the receiver at $\mathbf{x}_B$ by t_B. These travel times are, in general, functions of the source position q_1. In seismic interferometry, the traveltimes of the signals that are crosscorrelated are subtracted. This means that the traveltime t_{corr} of the crosscorrelation for a given source position is given by

$$t_{\text{corr}}(q_1) = t_B(q_1) - t_A(q_1). \tag{A1}$$

The condition that the traveltime is stationary means that

$$\frac{\partial t_{\text{corr}}(q_1)}{\partial q_1} = \frac{\partial t_B(q_1)}{\partial q_1} - \frac{\partial t_A(q_1)}{\partial q_1} = 0. \tag{A2}$$

A standard derivation Aki and Richards (1980) relates the slowness along the surface to the take-off angle

$$\frac{\partial t_A(q_1)}{\partial q_1} = \frac{\sin i_A}{c}, \tag{A3}$$

with c the propagation velocity. A similar expression holds for t_B. Inserting this in equation (A-2) implies that at the stationary point

$$i_A = i_B. \tag{A4}$$

This means that at the stationary source point the rays take off in the same direction.

The reasoning above was applicable to variations in the source coordinate q_1. The same reasoning applies to variations with the orthogonal source coordinate q_2. This means that the rays take off in the same direction as measured in two orthogonal planes, hence, the rays have the same direction in three dimensions. Therefore, the rays radiating from the stationary source position are parallel.

References

Aki, K. and P. G. Richards, 1980, Quantitative seismology, Vol. I: W.H. Freeman and Company, San Fransisco.

Aki, K., 1957, Space and time spectra of stationary stochastic waves, with special reference to microtremors: Bulletin of the Earthquake Research Institute, **35**, 415–457.

Aki, K., 1965, A note on the use of microseisms in determining the shallow structures of the earth's crust: Geophysics, **30**, 665–666.

Asten, M. W., 2006, On bias and noise in passive seismic data from finite circular array data processed using SPAC methods: Geophysics, **71**, V153–V162.

Bakulin, A. and R. Calvert, 2004, Virtual source: new method for imaging and 4D below complex overburden: 74th Annual International Meeting, SEG, Expanded Abstracts, 2477–2480.

Bakulin, A. and R. Calvert, 2006, The virtual source method: Theory and case study: Geophysics, **71**, SI139–SI150.

Baskir, E. and C. E. Weller, 1975, Sourceless reflection seismic exploration (abstract of paper presented at the 44th Annual International SEG Meeting): Geophysics, **40**, 158–159.

Bensen, G. D., M. H. Ritzwoller, M. P. Barmin, A. L. Levshin, F. Lin, M. P. Moschetti, N. M. Shapiro, and Y. Yang, 2007, Processing seismic ambient noise data to obtain reliable broad-band surface wave dispersion measurements: Geophysical Journal International, **169**, 1239–1260.

Bensen, G. D., M. H. Ritzwoller, and N. M. Shapiro, 2008, Broadband ambient noise surface wave tomography across the United States: Journal of Geophysical Research - Solid Earth, **113**, B05306–1–B05306–21.

Berryhill, J. R., 1979, Wave-equation datuming: Geophysics, **44**, 1329–1344.

Berryhill, J. R., 1984, Wave-equation datuming before stack: Geophysics, **49**, 2064–2066.

Bostock, M. G., S. Rondenay, and J. Shragge, 2001, Multiparameter two-dimensional inversion of scattered teleseismic body waves. 1. Theory for oblique incidence: Journal of Geophysical Research, **106**, 30771–30782.

Brenguier, F., N. M. Shapiro, M. Campillo, A. Nercessian, and V. Ferrazzini, 2007, 3-D surface wave tomography of the Piton de la Fournaise volcano using seismic correlations: Geophysical Research Letters, **34**, L02305–1–L02305–5.

Brooks, L. A. and P. Gerstoft, 2007, Ocean acoustic interferometry: Journal of the Acoustical Society of America, **121**, no. 6, 3377–3385.

Callen, H. B. and T. A. Welton, 1951, Irreversibility and generalized noise: Physical Review, **83**, 34–40.

Campillo, M. and A. Paul, 2003, Long-range correlations in the diffuse seismic coda: Science, **299**, 547–549.

Challis, L. and F. Sheard, 2003, The Green of Green functions: Physics Today, **56**, 41–46.

Chapman, C. H., 1994, Reflection/transmission coefficients reciprocities in anisotropic media: Geophysical Journal International, **116**, 498–501.

Chaput, J. A. and M. G. Bostock, 2007, Seismic interferometry using non-volcanic tremor in Cascadia: Geophysical Research Letters, **34**, L07304–1–L07304–5.

Claerbout, J. F., 1968, Synthesis of a layered medium from its acoustic transmission response: Geophysics, **33**, 264–269.

Cole, S., 1995, Passive seismic and drill-bit experiments using 2-D arrays: Ph.D. thesis, Stanford University.

Curtis, A., P. Gerstoft, H. Sato, R. Snieder, and K. Wapenaar, 2006, Seismic interferometry - turning noise into signal: The Leading Edge, **25**, no. 9, 1082–1092.

Daneshvar, M. R., C. S. Clay, and M. K. Savage, 1995, Passive seismic imaging using microearthquakes: Geophysics, **60**, 1178–1186.

de Hoop, A. T., 1988, Time-domain reciprocity theorems for acoustic wave fields in fluids with relaxation: Journal of the Acoustical Society of America, **84**, 1877–1882.

Dong, S., R. He, and G. T. Schuster, 2006a, Interferometric prediction and least squares subtraction of surface waves: 76th Annual International Meeting, SEG, Expanded Abstracts, 2783–2786.

Dong, S., J. Sheng, and G. T. Schuster, 2006b, Theory and practice of refraction interferometry: 76th Annual International Meeting, SEG, Expanded Ab-

stracts, 3021–3025.
Draganov, D., K. Wapenaar, and J. Thorbecke, 2004, Passive seismic imaging in the presence of white noise sources: The Leading Edge, **23**, no. 9, 889–892.
Draganov, D., K. Wapenaar, W. Mulder, and J. Singer, 2006, Seismic interferometry on background-noise field data: 76th Annual International Meeting, SEG, Expanded Abstracts, 590–593.
Draganov, D., K. Wapenaar, W. Mulder, J. Singer, and A. Verdel, 2007, Retrieval of reflections from seismic background-noise measurements: Geophysical Research Letters, **34**, L04305–1–L04305–4.
Draganov, D., X. Campman, J. Thorbecke, A. Verdel, and K. Wapenaar, 2009, Reflection images from ambient seismic noise: Geophysics, **74**, A63–A67.
Duvall, T. L., S. M. Jefferies, J. W. Harvey, and M. A. Pomerantz, 1993, Time-distance helioseismology: Nature, **362**, 430–432.
Fan, Y. and R. Snieder, 2009, Required source distribution for interferometry of waves and diffusive fields: Geophysical Journal International, **179**, 1232–1244.
Fokkema, J. T. and P. M. van den Berg, 1993, Seismic applications of acoustic reciprocity: Elsevier, Amsterdam.
Frasier, C. W., 1970, Discrete time solution of plane P-SV waves in a plane layered medium: Geophysics, **35**, 197–219.
Gerstoft, P., K. G. Sabra, P. Roux, W. A. Kuperman, and M. C. Fehler, 2006, Green's functions extraction and surface-wave tomography from microseisms in southern California: Geophysics, **71**, SI23–SI31.
Godin, O. A., 2007, Emergence of the acoustic Green's function from thermal noise: Journal of the Acoustical Society of America, **121**, no. 2, EL96–EL102.
Gouédard, P., P. Roux, M. Campillo, and A. Verdel, 2008a, Convergence of the two-point correlation function toward the Green's function in the context of a seismic-prospecting data set: Geophysics, **73**, V47–V53.
Gouédard, P., L. Stehly, F. Brenguier, M. Campillo, Y. Colin de Verdière, E. Larose, L. Margerin, P. Roux, F. J. Sánchez-Sesma, N. M. Shapiro, and R. L. Weaver, 2008b, Cross-correlation of random fields: mathematical approach and applications: Geophysical Prospecting, **56**, 375–393.
Green, G., 1828, An essay on the application of mathematical analysis to the theories of electricity and magnetism: Privately published.
Halliday, D. F., A. Curtis, J. O. A. Robertsson, and D.-J. van Manen, 2007, Interferometric surface-wave isolation and removal: Geophysics, **72**, A69–A73.
Halliday, D., A. Curtis, P. Vermeer, C. L. Strobbia, A. Glushchenko, D.-J. van Manen, and J. Robertsson, 2010, Interferometric ground-roll removal: Attenuation of scattered surface waves in single-sensor data: Geophysics, **75**, (accepted).
Haskell, N. A., 1953, The dispersion of surface waves on multilayered media: Bulletin of the Seismological Society of America, **43**, 17–34.
He, R., B. Hornby, and G. Schuster, 2007, 3D wave-equation interferometric migration of VSP free-surface multiples: Geophysics, **72**, S195–S203.
Henstridge, J. D., 1979, A signal processing method for circular arrays: Geophysics, **44**, 179–184.
Hohl, D. and A. Mateeva, 2006, Passive seismic reflectivity imaging with ocean-bottom cable data: 76th Annual International Meeting, SEG, Expanded Abstracts, 1560–1563.
Hornby, B. E. and J. Yu, 2007, Interferometric imaging of a salt flank using walkaway VSP data: The Leading Edge, **26**, no. 6, 760–763.
Jiang, Z., J. Sheng, J. Yu, G. T. Schuster, and B. E. Hornby, 2007, Migration methods for imaging different-order multiples: Geophysical Prospecting, **55**, 1–19.
Kang, T.-S. and J. S. Shin, 2006, Surface-wave tomography from ambient seismic noise of accelerograph networks in southern Korea: Geophysical Research Letters, **33**, L17303–1–L17303–5.
Kennett, B. L. N., N. J. Kerry, and J. H. Woodhouse, 1978, Symmetries in the reflection and transmission of elastic waves: Geophysical Journal of the Royal Astronomical Society, **52**, 215–230.
Kumar, M. R. and M. G. Bostock, 2006, Transmission to reflection transformation of teleseismic wavefields: Journal of Geophysical Research - Solid Earth, **111**, B08306–1–B08306–9.
Larose, E., A. Khan, Y. Nakamura, and M. Campillo, 2005, Lunar subsurface investigated from correlation of seismic noise: Geophysical Research Letters, **32**, L16201–1–L16201–4.
Larose, E., L. Margerin, A. Derode, B. van Tiggelen, M. Campillo, N. Shapiro, A. Paul, L. Stehly, and M. Tanter, 2006, Correlation of random wave fields: An interdisciplinary review: Geophysics, **71**, SI11–SI21.
Le Bellac, M., F. Mortessagne, and G. G. Batrouni, 2004, Equilibrium and non-equilibrium statistical thermodynamics: Cambridge Univ. Press, Cambridge, UK.
Li, H., W. Su, C.-Y. Wang, and Z. Huang, 2009, Ambient noise Rayleigh wave tomography in western Sichuan and eastern Tibet: Earth and Planetary Science Letters, **282**, 201–211.
Liang, C. and C. A. Langston, 2008, Ambient seismic noise tomography and structure of eastern North America: Journal of Geophysical Research - Solid Earth, **113**, B03309–1–B03309–18.
Lin, F.-C., M. P. Moschetti, and M. H. Ritzwoller, 2008, Surface wave tomography of the western United States from ambient seismic noise: Rayleigh and Love wave phase velocity maps: Geophysical Journal International, **173**, 281–298.
Lin, F.-C., M. H. Ritzwoller, and R. Snieder, 2009,

Eikonal tomography: surface wave tomography by phase front tracking across a regional broad-band seismic array: Geophysical Journal International, **177**, 1091–1110.

Lobkis, O. I. and R. L. Weaver, 2001, On the emergence of the Green's function in the correlations of a diffuse field: Journal of the Acoustical Society of America, **110**, 3011–3017.

Longuet-Higgins, M. S., 1950, A theory for the generation of microseisms: Philosophical Transactions of the Royal Society of London. Series A, **243**, 1–35.

Lu, R., M. Willis, X. Campman, and T. M. N. Ajo-Franklin, J., 2008, Redatuming through a salt canopy and target-oriented salt-flank imaging: Geophysics, **73**, S63–S71.

Ma, S., G. A. Prieto, and G. C. Beroza, 2008, Testing community velocity models for Southern California using the ambient seismic field: Bulletin of the Seismological Society of America, **98**, 2694–2714.

Malcolm, A. E., J. A. Scales, and B. A. van Tiggelen, 2004, Extracting the Green function from diffuse, equipartitioned waves: Physical Review E, **70**, 015601(R)–1–015601(R)–4.

Mercier, J.-P., M. G. Bostock, and A. M. Baig, 2006, Improved green's functions for passive-source structural studies: Geophysics, **71**, SI95–SI102.

Mikesell, D., K. van Wijk, A. Calvert, and M. Haney, 2009, The virtual refraction: Useful spurious energy in seismic interferometry: Geophysics, **74**, A13–A17.

Minato, S., K. Onishi, T. Matsuoka, Y. Okajima, J. Tsuchiyama, D. Nobuoka, H. Azuma, and T. Iwamoto, 2007, Cross-well seismic survey without borehole source: 77th Annual International Meeting, SEG, Expanded Abstracts, 1357–1361.

Miyazawa, M., R. Snieder, and A. Venkataraman, 2008, Application of seismic interferometry to extract P- and S-wave propagation and observation of shear-wave splitting from noise data at Cold Lake, Alberta, Canada: Geophysics, **73**, D35–D40.

Nowack, R. L., S. Dasgupta, G. T. Schuster, and J.-M. Sheng, 2006, Correlation migration using Gaussian beams of scattered teleseismic body waves: Bulletin of the Seismological Society of America, **96**, 1–10.

Okada, H., 2003, The microtremor survey method: Society of Exploration Geophysicists.

Okada, H., 2006, Theory of efficient array observations of microtremors with special reference to the SPAC method: Exploration Geophysics, **37**, 73–85.

Perton, M., F. J. Sánchez-Sesma, A. Rodríguez-Castellanos, M. Campillo, and R. L. Weaver, 2009, Two perspectives on equipartition in diffuse elastic fields in three dimensions: Journal of the Acoustical Society of America, **126**, 1125–1130.

Picozzi, M., S. Parolai, D. Bindi, and A. Strollo, 2009, Characterization of shallow geology by high-frequency seismic noise tomography: Geophysical Journal International, **176**, 164–174.

Poletto, F. and L. Petronio, 2003, Transmitted and reflected waves in tunnel SWD: 73rd Annual International Meeting, SEG, Expanded Abstracts, 1211–1214.

Poletto, F. and L. Petronio, 2006, Seismic interferometry with a TBM source of transmitted and reflected waves: Geophysics, **71**, SI85–SI93.

Ramírez, A. C. and A. B. Weglein, 2009, Green's theorem as a comprehensive framework for data reconstruction, regularization, wavefield separation, seismic interferometry, and wavelet estimation: A tutorial: Geophysics, **74**, W35–W62.

Rickett, J. and J. Claerbout, 1999, Acoustic daylight imaging via spectral factorization: Helioseismology and reservoir monitoring: The Leading Edge, **18**, no. 8, 957–960.

Rondenay, S., M. G. Bostock, and J. Shragge, 2001, Multiparameter two-dimensional inversion of scattered teleseismic body waves. 3. Application to the Cascadia 1993 data set: Journal of Geophysical Research, **106**, 30795–30807.

Roux, P. and M. Fink, 2003, Green's function estimation using secondary sources in a shallow water environment: Journal of the Acoustical Society of America, **113**, no. 3, 1406–1416.

Rytov, S. M., Y. A. Kravtsov, and V. I. Tatarskii, 1989, Principles of statistical radiophysics. 3: Elements of random fields: Springer, Berlin.

Rytov, S. M., 1956, On thermal fluctuations in distributed systems: Doklady Akademii nauk SSSR, **110**, 371.

Sabra, K. G., P. Gerstoft, P. Roux, W. A. Kuperman, and M. C. Fehler, 2005a, Extracting time-domain Green's function estimates from ambient seismic noise: Geophysical Research Letters, **32**, L03310–1–L03310–5.

——— 2005b, Surface wave tomography from microseisms in Southern California: Geophysical Research Letters, **32**, L14311–1–L14311–4.

Sabra, K. G., P. Roux, and W. A. Kuperman, 2005c, Arrival-time structure of the time-averaged ambient noise cross-correlation function in an oceanic waveguide: Journal of the Acoustical Society of America, **117**, no. 1, 164–174.

Sánchez-Sesma, F. J., J. A. Pérez-Ruiz, M. Campillo, and F. Luzón, 2006, Elastodynamic 2D Green function retrieval from cross-correlation: Canonical inclusion problem: Geophysical Research Letters, **33**, L13305–1–L13305–6.

Scherbaum, F., 1987a, Seismic imaging of the site response using microearthquake recordings. Part I. Method: Bulletin of the Seismological Society of America, **77**, 1905–1923.

——— 1987b, Seismic imaging of the site response using microearthquake recordings. Part II. Application to the Swabian Jura, Southwest Germany, seismic network: Bulletin of the Seismological Society of Amer-

ica, **77**, 1924–1944.
Schuster, G. T. and M. Zhou, 2006, A theoretical overview of model-based and correlation-based redatuming methods: Geophysics, **71**, SI103–SI110.
Schuster, G. T., J. Yu, J. Sheng, and J. Rickett, 2004, Interferometric/daylight seismic imaging: Geophysical Journal International, **157**, 838–852.
Schuster, G. T., 2001, Theory of daylight/interferometric imaging: tutorial: 63rd Annual International Meeting, EAGE, Extended Abstracts, Session: A32.
Schuster, G. T., 2009, Seismic interferometry: Cambridge University Press.
Shapiro, N. M. and M. Campillo, 2004, Emergence of broadband Rayleigh waves from correlations of the ambient seismic noise: Geophysical Research Letters, **31**, L07614–1–L07614–4.
Shapiro, N. M., M. Campillo, L. Stehly, and M. H. Ritzwoller, 2005, High-resolution surface-wave tomography from ambient seismic noise: Science, **307**, 1615–1618.
Shragge, J., M. G. Bostock, and S. Rondenay, 2001, Multiparameter two-dimensional inversion of scattered teleseismic body waves. 2. Numerical examples: Journal of Geophysical Research, **106**, 30783–30793.
Shragge, J., B. Artman, and C. Wilson, 2006, Teleseismic shot-profile migration: Geophysics, **71**, SI221–SI229.
Snieder, R., K. Wapenaar, and U. Wegler, 2007, Unified Green's function retrieval by cross-correlation; connection with energy principles: Physical Review E, **75**, 036103–1–036103–14.
Snieder, R., 2004, Extracting the Green's function from the correlation of coda waves: A derivation based on stationary phase: Physical Review E, **69**, 046610–1–046610–8.
Stehly, L., M. Campillo, and N. M. Shapiro, 2006, A study of the seismic noise from its long-range correlation properties: Journal of Geophysical Research, **111**, B10306–1–B10306–12.
Thompson, A. R., J. M. Moran, and G. W. Swenson Jr., 2001, Interferometry and synthesis in radio astronomy: Wiley-Interscience, New York.
Thomson, W. T., 1950, Transmission of elastic waves through a stratified solid medium: Journal of Applied Physics, **21**, 89–93.
Toksöz, M. N., 1964, Microseisms and an attempted application to exploration: Geophysics, **39**, 154–177.
Tonegawa, T., K. Nishida, T. Watanabe, and K. Shiomi, 2009, Seismic interferometry of teleseismic S-wave coda for retrieval of body waves: an application to the Philippine Sea slab underneath the Japanese Islands: Geophysical Journal International, **178**, 1574–1586.
Torii, K., T. Matsuoka, K. Onishi, K. Shirashi, T. Aizawa, Y. Yamanaka, S. Ito, T. Kimura, Y. Asano, and T. Takeda, 2007, Application of seismic interferometry to natural earthquakes measured by small-scale array: 77th Annual International Meeting, SEG, Expanded Abstracts, 1362–1366.
Ursin, B., 1983, Review of elastic and electromagnetic wave propagation in horizontally layered media: Geophysics, **48**, 1063–1081.
van Tiggelen, B. A., 2003, Green function retrieval and time reversal in a disordered world: Physical Review Letters, **91**, 243904–1–243904–4.
Wang, Y., Y. Luo, and G. T. Schuster, 2009, Interferometric interpolation of missing seismic data: Geophysics, **74**, SI37–SI45.
Wapenaar, K. and J. Fokkema, 2006, Green's function representations for seismic interferometry: Geophysics, **71**, SI33–SI46.
Wapenaar, C. P. A. and J. L. T. Grimbergen, 1996, Reciprocity theorems for one-way wave fields: Geophysical Journal International, **127**, 169–177.
Wapenaar, K., D. Draganov, J. Thorbecke, and J. Fokkema, 2002, Theory of acoustic daylight imaging revisited: 72nd Annual International Meeting, SEG, Expanded Abstracts, 2269–2272.
Wapenaar, K., J. Thorbecke, and D. Draganov, 2004, Relations between reflection and transmission responses of three-dimensional inhomogeneous media: Geophysical Journal International, **156**, 179–194.
Weaver, R. L. and O. I. Lobkis, 2001, Ultrasonics without a source: Thermal fluctuation correlations at MHz frequencies: Physical Review Letters, **87**, 134301–1–134301–4.
Weaver, R. L. and O. I. Lobkis, 2002, On the emergence of the Green's function in the correlations of a diffuse field: pulse-echo using thermal phonons: Ultrasonics, **40**, 435–439.
Weaver, R., B. Froment, and M. Campillo, 2009, On the correlation of non-isotropically distributed ballistic scalar diffuse waves: Journal of the Acoustical Society of America, **126**, 1817–1826.
Webb, S. C., 1998, Broadband seismology and noise under the ocean: Reviews of Geophysics, **36**, 105–142.
Willis, M. E., R. Lu, X. Campman, M. N. Toksöz, Y. Zhang, and M. V. de Hoop, 2006, A novel application of time-reversed acoustics: Salt-dome flank imaging using walkaway VSP surveys: Geophysics, **71**, A7–A11.
Xiao, X., M. Zhou, and G. T. Schuster, 2006, Salt-flank delineation by interferometric imaging of transmitted P- and S-waves: Geophysics, **71**, SI197–SI207.
Xue, Y., S. Dong, and G. T. Schuster, 2009, Interferometric prediction and subtraction of surface waves with a nonlinear local filter: Geophysics, **74**, SI1–SI8.
Yao, H., R. D. van der Hilst, and M. V. de Hoop, 2006, Surface-wave array tomography in SE Tibet from ambient seismic noise and two-station analysis - I. Phase velocity maps: Geophysical Journal International, **166**, 732–744.
Yao, H., C. Beghein, and R. D. van der Hilst, 2008,

Surface-wave array tomography in SE Tibet from ambient seismic noise and two-station analysis - II. Crustal and upper-mantle structure: Geophysical Journal International, **173**, 205–219.

Yao, H., X. Campman, M. V. de Hoop, and R. D. van der Hilst, 2009, Estimation of surface wave Green's functions from correlation of direct waves, coda waves, and ambient noise in SE Tibet: Physics of the Earth and Planetary Interiors, **177**, 1–11.

Yokoi, T. and S. Margaryan, 2008, Consistency of the spatial autocorrelation method with seismic interferometry and its consequence: Geophysical Prospecting, **56**, 435–451.

Yu, J. and G. T. Schuster, 2006, Crosscorrelogram migration of inverse vertical seismic profile data: Geophysics, **71**, S1–S11.

Tutorial on seismic interferometry. Part II: Underlying theory and new advances

Kees Wapenaar[1], Evert Slob[1], Roel Snieder[2] and Andrew Curtis[3]

[1] *Department of Geotechnology, Delft University of Technology, Delft, The Netherlands*
[2] *Center for Wave Phenomena, Colorado School of Mines, Golden, Colorado 80401, USA*
[3] *School of GeoSciences, The University of Edinburgh, Edinburgh, EH9 3JW, UK*

ABSTRACT

In part II of this two-part tutorial we review the underlying theory of seismic interferometry and discuss various new advances. In the 1990's the method of time-reversed acoustics was developed. This method employs the fact that the acoustic wave equation for a lossless medium is invariant for time-reversal. When ultrasonic responses recorded by piezoelectric transducers are reversed in time and fed simultaneously as source signals to the transducers, they focus at the position of the original source, even when the medium is very complex. In seismic interferometry the time-reversed responses are not physically sent into the earth, but they are convolved with other measured responses. The effect is essentially the same: the time-reversed signals focus and create a virtual source which radiates waves into the medium that are subsequently recorded by receivers. A mathematical derivation, based on reciprocity theory, formalizes this principle: the crosscorrelation of responses at two receivers, integrated over different sources, gives the Green's function emitted by a virtual source at the position of one of the receivers and observed by the other receiver.

The basic Green's function representations for seismic interferometry assume a lossless non-moving acoustic or elastic medium. We discuss many variants and extensions, including interferometric representations for attenuation and/or moving media, unified representations for waves and diffusion phenomena, bending waves, quantum mechanical scattering, potential fields, elastodynamic, electromagnetic, poroelastic and electroseismic waves. We discuss the relation with the generalized optical theorem, discuss variants for virtual receivers and virtual reflectors and indicate the potential applications of time-lapse interferometry. Finally we discuss the improvements that can be obtained with interferometry by deconvolution. A trace-by-trace deconvolution process compensates for complex source functions and the attenuation of the medium. Interferometry by multidimensional deconvolution compensates in addition for the effects of one-sided and/or irregular illumination.

Key words: seismic interferometry

INTRODUCTION

In Part I we discussed the basic principles of seismic interferometry (also known as Green's function retrieval*), using mainly heuristic arguments. In Part II we continue our discussion, starting with an analysis of the relation between seismic interferometry and the field

*Note that by "Green's function" we mean the response of an impulsive point source in the actual medium rather than in a background medium.

of time-reversed acoustics, pioneered by Fink (1992, 1997). This analysis includes a heuristic discussion of the "virtual source method" of Bakulin and Calvert (2004, 2006) and a review of an elegant physical derivation by Derode et al. (2003b,a) of Green's function retrieval by crosscorrelation. After that, we review exact Green's function representations for seismic interferometry in arbitrary inhomogeneous anisotropic lossless solids Wapenaar (2004) and discuss the approximations that lead to the commonly used expressions. We conclude with an overview of recent and new advances, including approaches that account for attenuating and/or non-reciprocal media, methods for obtaining virtual receivers or virtual reflectors, the relationship with imaging theory, and last but not least, interferometry by deconvolution. The discussion of each of these advances is necessarily brief, but we include many references for further reading.

INTERFEROMETRY AND TIME-REVERSED ACOUSTICS

Review of time-reversed acoustics

In the early 1990's Mathias Fink and coworkers at the University of Paris VII initiated a new field of research, called time-reversed acoustics (Fink, 1992, 1997; Derode et al., 1995; Draeger and Fink, 1999; Fink and Prada, 2001). Here we briefly review this research field and in the next subsections we discuss the links with seismic interferometry. Time-reversed acoustics makes use of the fact that the acoustic wave equation for a lossless acoustic medium is invariant under time-reversal (because it only contains even-order time derivatives, i.e., zeroth and second order). This means that, when $u(\mathbf{x}, t)$ is a solution, then $u(\mathbf{x}, -t)$ is a solution as well. Figure 1 illustrates the principle in the context of an ultrasonic experiment Derode et al. (1995); Fink (2006). A piezoelectric source at A in Figure 1a emits a short pulse (duration 1 μs) which propagates through a highly scattering medium (a set of 2000 randomly distributed steel rods with a diameter of 0.8 mm). The transmitted wavefield is received by an array of piezoelectric transducers at B. The received traces, of which three are shown in Figure 1a, exhibit a long coda (more than 200 μs) because of multiple scattering between the rods. Next the traces are reversed in time and simultaneously fed as source signals to the transducers at B (Figure 1b). This time-reversed wavefield propagates through the scattering medium and focuses at the position of the original source. Figure 1c shows the received signal at the original source position; the duration is of the same order as the original signal ($\sim$1 μs). Figure 1d shows beam profiles around the source position (amplitudes measured along the x-axis denoted in Figure 1b). The narrow beam is the result of this experiment (back-propagation via the scattering medium), whereas the wide beam was obtained when the steel rods were removed. The resolution is impressive and at the time the stability of this experiment amazed many researchers. From a numerical experiment one might expect such a good reconstruction, but when waves have scattered at tens to hundreds of scatterers in a real experiment, the fact that the wavefield refocusses at the original source point is fascinating. Snieder and Scales (1998) have analyzed this phenomenon in detail. In their analysis they compared wave scattering with particle scattering. They showed for their model that, whereas particles behave chaotically after having encountered typically eight scatterers, waves remain stable after thirty or more scatterers. The instability of particle scattering is explained by the fact that particles follow a single trajectory. A small disturbance in initial conditions or scatterer positions causes the particle to follow a completely different trajectory after only a few encounters with the scatterers. Waves, on the other hand, have a finite wavelength and travel along all possible trajectories visiting all the scatterers in all possible combinations. Hence, a small perturbation in initial conditions or scatterer positions has a much less dramatic effect for wave scattering than for particle scattering. Consequently, wave propagation experiments through a strongly scattering medium have a high degree of repeatability. Combined with the invariance of the wave equation for time-reversal this explains the excellent reproduction of the source wavefield after back-propagation through the scattering medium.

As a historical side note we mention that the idea of emitting time-reversed signals into a system was already proposed and implemented in the 1960's Parvulescu (1961, 1995). This was a single channel method, aiming to compress a complicated response at a detector (for example in an ocean waveguide) into a single pulse. The method was proposed as a fast alternative to digital crosscorrelation, which with the computers at that time would cost in the order of ten days computation time per correlation for signal lengths typically considered in underwater acoustics Stewart et al. (1965).

Snieder et al. (2002) and Grêt et al. (2006) employ the repeatability of acoustic experiments in a method they call coda wave interferometry (here the term "interferometry" is used in the classical sense). Because the scattering coda is repeatable when an experiment is carried out twice under the same circumstances, any change in the coda between two experiments can be attributed to changes in the medium. Because of the relatively long duration of the coda, minor time-lapse changes in, for example, the background velocity can be monitored with high accuracy by coda wave interferometry.

Apart from the repeatability, another important aspect of time-reversed acoustics is its potential to image beyond the diffraction limit. Consider again the time-reversal experiment in Figure 1. An important effect of the scattering medium between the source at A and the

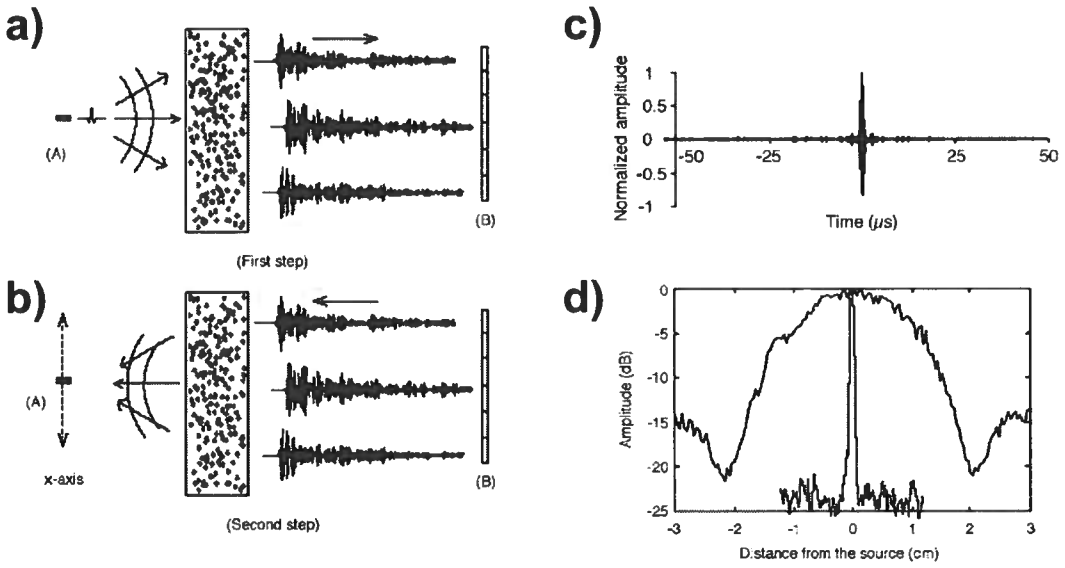

Figure 1. Time-reversed acoustics in a strongly scattering random medium Derode et al. (1995); Fink (2006). (a) The source at A emits a short pulse which propagates through the random medium. The scattered waves are recorded by the array at B. (b) The array at B emits the time-reversed signals, which, after back-propagation through the random medium, focus at A. (c) The back-propagated response at A. (d) Beam profiles around A.

transducer array at B is a widening of the effective aperture angle. That is, waves that arrive at each receiver include energy from a much wider range of take-off angles from the source location than would be the case without scatterers. A consequence is that time-reversal experiments in strongly scattering media have so-called super-resolution properties de Rosny and Fink (2002); Lerosey et al. (2007). Hanafy et al. (2009) and Cao et al. (2010) use this property in a seismic time-reversal method to accurately locate trapped miners after a mine collapse.

An essential condition for the stability and high-resolution aspects of time-reversed acoustics is that the time-reversed waves propagate through the same physical medium as in the forward experiment. Here we see a link between time-reversed acoustics and seismic interferometry. Instead of doing a real reverse-time experiment, in seismic interferometry one convolves forward and time-reversed responses. Since both responses are measured in one-and-the same physical medium, seismic interferometry has the same stability and high-resolution properties as time-reversed acoustics. This link is made more explicit in the next two subsections.

Finally, note that time-reversed acoustics should be distinguished from reverse time migration, such as proposed by McMechan (1982, 1983), Baysal et al. (1983), Whitmore (1983) and Gajewski and Tessmer (2005), in which time-reversed waves are propagated numerically through a macro model. No matter how much detail one puts into a macro model, results like the one illustrated in Figure 1 can only be obtained when the same physical medium is used in the forward as in the reverse-time experiment. Time-reversed acoustics and reverse time migration serve different purposes. The field of reverse time migration has advanced significantly during the last few years and contractors and oil companies are now applying this routinely for depth imaging (Etgen et al., 2009; Zhang and Sun, 2009; Clapp et al., 2010).

"Virtual source method"

The method of time-reversed acoustics inspired Rodney Calvert and Andrey Bakulin at Shell to develop what they call the "virtual source method" Bakulin and Calvert (2004, 2006)†

In essence, their virtual source method is an elegant data-driven alternative for model-driven redatuming, similar as Schuster's methods discussed in Part I (we point out the differences in a moment). For an acquisition configuration with sources at the surface and receivers in the subsurface, for example in a near horizontal borehole (Figure 2), the reflection response is described as $u(\mathbf{x}_B, \mathbf{x}_S^{(i)}, t) = G(\mathbf{x}_B, \mathbf{x}_S^{(i)}, t) * s(t)$, where

†Recall from part I that creating a virtual source is the essence of all seismic interferometry methods, hence, we use the term "virtual source" whenever appropriate. When it refers to Bakulin and Calvert's method we mention this explicitly (except when it is clear from the context).

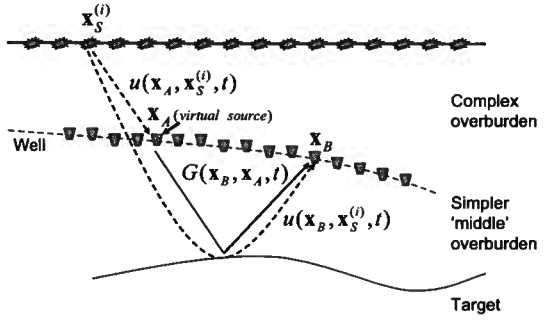

Figure 2. Basic principle of the "virtual source method" of Bakulin and Calvert (2004, 2006). Receivers in a borehole record both the downgoing wavefield through the complex overburden and the reflected signal from the deeper target. Crosscorrelation and summing over source locations gives the reflection response of a virtual source in the borehole, free of overburden distortions.

$s(t)$ is the source wavelet and $G(\mathbf{x}_B, \mathbf{x}_S^{(i)}, t)$ the Green's function, describing propagation from a point source at $\mathbf{x}_S^{(i)}$ via a target below the borehole to a receiver at $\mathbf{x}_B$ in the borehole (we adopted the notation of Part I; the asterisk denotes temporal convolution). The downgoing wavefield observed by a downhole receiver at $\mathbf{x}_A$ is given by $u(\mathbf{x}_A, \mathbf{x}_S^{(i)}, t) = G(\mathbf{x}_A, \mathbf{x}_S^{(i)}, t) * s(t)$. Using source-receiver reciprocity, i.e., $u(\mathbf{x}_A, \mathbf{x}_S^{(i)}, t) = u(\mathbf{x}_S^{(i)}, \mathbf{x}_A, t)$, this can also be interpreted as the response of a downhole source at $\mathbf{x}_A$, observed by an array of receivers $\mathbf{x}_S^{(i)}$ after propagation through the complex overburden. This is comparable with the response of the ultrasonic experiment in Figure 1a. Hence, if all traces $u(\mathbf{x}_S^{(i)}, \mathbf{x}_A, t)$ would be reversed in time and fed simultaneously as source signals to the sources at $\mathbf{x}_S^{(i)}$, similar as in Figure 1b, the back-propagating wavefield would focus at $\mathbf{x}_A$. Instead of doing this physically, the time-reversed signals are convolved with the reflection responses, and subsequently summed over the different source positions at the surface, according to

$$C(\mathbf{x}_B, \mathbf{x}_A, t) = \sum_i u(\mathbf{x}_B, \mathbf{x}_S^{(i)}, t) * u(\mathbf{x}_A, \mathbf{x}_S^{(i)}, -t). \quad (1)$$

The correlation function $C(\mathbf{x}_B, \mathbf{x}_A, t)$ is interpreted as the response of a virtual downhole source at $\mathbf{x}_A$, measured by a downhole receiver at $\mathbf{x}_B$, hence $C(\mathbf{x}_B, \mathbf{x}_A, t) \approx G(\mathbf{x}_B, \mathbf{x}_A, t) * S_s(t)$. The wavelet of the virtual source, $S_s(t)$, is the autocorrelation of the wavelet $s(t)$ of the real sources at the acquisition surface. Similar to Schuster's methods, equation 1 can be seen as a form of source redatuming, using a measured version of the redatuming operator, i.e., $u(\mathbf{x}_A, \mathbf{x}_S^{(i)}, -t) = G(\mathbf{x}_A, \mathbf{x}_S^{(i)}, -t) * s(-t)$. Whereas in Schuster's methods the emphasis is on aspects like transforming multiples into primaries, enlarging the illumination area, interpolating missing traces etc., the emphasis of Bakulin and Calvert's virtual source method is on the elimination of the propagation distortions of the complex inhomogeneous overburden. Similar to Figure 1, where the time-reversed complex signals at B back-propagate through the strongly scattering medium and focus to a short duration pulse at A, in Bakulin and Calvert's method the sources at the surface are focused to a virtual source in the borehole, compensating for a complex overburden. Similar to the time-reversed acoustics method, the focusing occurs with a time-reversed measured response, hence the redatuming takes place in the same physical medium as the one in which the data were measured. This distinguishes the virtual source method from classical redatuming Berryhill (1979, 1984) and the Common Focal Point (CFP) method (Berkhout, 1997; Berkhout and Verschuur, 2001). Each of these methodologies has its own applications and hence its own right of existence. Classical redatuming and the CFP method are applied to data acquired by sources and receivers at the surface, using as operators either model-based Green's functions (redatuming) or dynamic focusing operators that are aimed to converge iteratively to the Green's functions (CFP method). The virtual source method uses sources at the surface and receivers in a borehole that directly measure the operators. The idea of using measured Green's functions as redatuming operators may seem simple with hindsight, but the consequences are far reaching. Bakulin et al. (2007) give an impressive overview of the applications in imaging and reservoir monitoring.

Note that a new method for wavelet estimation has been proposed as an interesting corollary of the virtual source method Behura (2010). When the virtual source coincides with a real source at $\mathbf{x}_A$, the response at $\mathbf{x}_B$ from the real source is given by $G(\mathbf{x}_B, \mathbf{x}_A, t) * s(t)$. The virtual source response, obtained by equation 1, is given by $G(\mathbf{x}_B, \mathbf{x}_A, t) * S_s(t)$, with $S_s(t) = s(t) * s(-t)$. Hence, deconvolution of the virtual source response by the actual response gives the (time-reversed) wavelet.

Last but not least, we remark that an important difference of equation 1 with the previously discussed expressions for seismic interferometry in Part I, is the single-sidedness of the correlation function $C(\mathbf{x}_B, \mathbf{x}_A, t) \approx G(\mathbf{x}_B, \mathbf{x}_A, t) * S_s(t)$ (there is no time-reversed term $G(\mathbf{x}_B, \mathbf{x}_A, -t)$). Moreover, this correlation function is only approximately proportional to the causal Green's function. These are consequences of the anisotropic illumination of the receivers in the borehole, which are primarily illuminated from above. In the subsection "Acoustic representation" we will come back on the approximations of one-sided illumination and indicate various improvements. The most effective improvement is discussed in the subsection "Interferometry by multidimensional deconvolution".

Derivation of seismic interferometry from time-reversed acoustics

The virtual source method discussed in the previous subsection, although very elegant, is an intuitive application of time-reversed acoustics. Derode et al. (2003b,a) show more precisely how the principle of Green's function retrieval by crosscorrelation in open systems can be derived from time-reversed acoustics. Their derivation, which is based entirely on physical arguments, shows that Green's function retrieval (which is equivalent to seismic interferometry), holds for arbitrarily inhomogeneous lossless media, including highly scattering media as shown in Figure 1. Here we briefly review their arguments, but we replace their notation by that used in Part I.

Consider a lossless arbitrary inhomogeneous acoustic medium in a homogeneous embedding. In this configuration we define two points with coordinate vectors $\mathbf{x}_A$ and $\mathbf{x}_B$. Our aim is to show that the acoustic response at $\mathbf{x}_B$ due to an impulsive source at $\mathbf{x}_A$ [i.e., the Green's function $G(\mathbf{x}_B, \mathbf{x}_A, t)$] can be obtained by crosscorrelating observations of wavefields at $\mathbf{x}_A$ and $\mathbf{x}_B$ due to sources on a closed surface $\partial\mathbb{D}$ in the homogeneous embedding. The derivation starts by considering another experiment, namely an impulsive source at $t = 0$ at $\mathbf{x}_A$, and receivers at $\mathbf{x}$ on $\partial\mathbb{D}$ (Figure 3a). The response at any point $\mathbf{x}$ on $\partial\mathbb{D}$ is denoted by $G(\mathbf{x}, \mathbf{x}_A, t)$. Imagine that we record this response for all $\mathbf{x}$ on $\partial\mathbb{D}$, reverse the time axis, and simultaneously feed these time-reversed functions $G(\mathbf{x}, \mathbf{x}_A, -t)$ to sources at all positions $\mathbf{x}$ on $\partial\mathbb{D}$ (Figure 3b). The superposition principle states that the wavefield at any point $\mathbf{x}'$ inside $\partial\mathbb{D}$ due to these sources on $\partial\mathbb{D}$ is given by

$$u(\mathbf{x}', t) \propto \oint_{\partial\mathbb{D}} \underbrace{G(\mathbf{x}', \mathbf{x}, t)}_{\text{"propagator"}} * \underbrace{G(\mathbf{x}, \mathbf{x}_A, -t)}_{\text{"source"}} \mathrm{d}^2\mathbf{x}, \quad (2)$$

where $\propto$ denotes "proportional to". According to this equation, $G(\mathbf{x}', \mathbf{x}, t)$ propagates the source function $G(\mathbf{x}, \mathbf{x}_A, -t)$ from $\mathbf{x}$ to $\mathbf{x}'$ and the result is integrated over all sources on $\partial\mathbb{D}$. Due to the invariance of the acoustic wave equation for time-reversal, we know that the wavefield $u(\mathbf{x}', t)$ must focus at $\mathbf{x}' = \mathbf{x}_A$ and $t = 0$. This property is the basis of time-reversed acoustics and explains why the focusing in Figure 1 occurs. Derode et al. (2003a,b) go one step further in their interpretation of equation (2). Since $u(\mathbf{x}', t)$ focusses for $\mathbf{x}' = \mathbf{x}_A$ at $t = 0$, the wavefield $u(\mathbf{x}', t)$ for arbitrary $\mathbf{x}'$ and t can be seen as the response of a virtual source at $\mathbf{x}_A$ and $t = 0$. This virtual source response, however, consists of a causal and an acausal part, according to

$$u(\mathbf{x}', t) = G(\mathbf{x}', \mathbf{x}_A, t) + G(\mathbf{x}', \mathbf{x}_A, -t). \quad (3)$$

This is explained as follows: the wavefield generated by the acausal sources on $\partial\mathbb{D}$ first propagates to all $\mathbf{x}'$ where it gives an acausal contribution, next it focusses in $\mathbf{x}_A$ at $t = 0$ and finally, since the energy focussed at that point is not extracted from the system, it must propagate outwards again to all $\mathbf{x}'$ giving the causal contribution. The propagation paths from $\mathbf{x}'$ to $\mathbf{x}_A$ are the same as those from $\mathbf{x}_A$ to $\mathbf{x}'$, but are travelled in opposite direction, which explains the time-symmetric form of $u(\mathbf{x}', t)$. Combining equations (2) and (3), applying source-receiver reciprocity to $G(\mathbf{x}, \mathbf{x}_A, -t)$ in equation

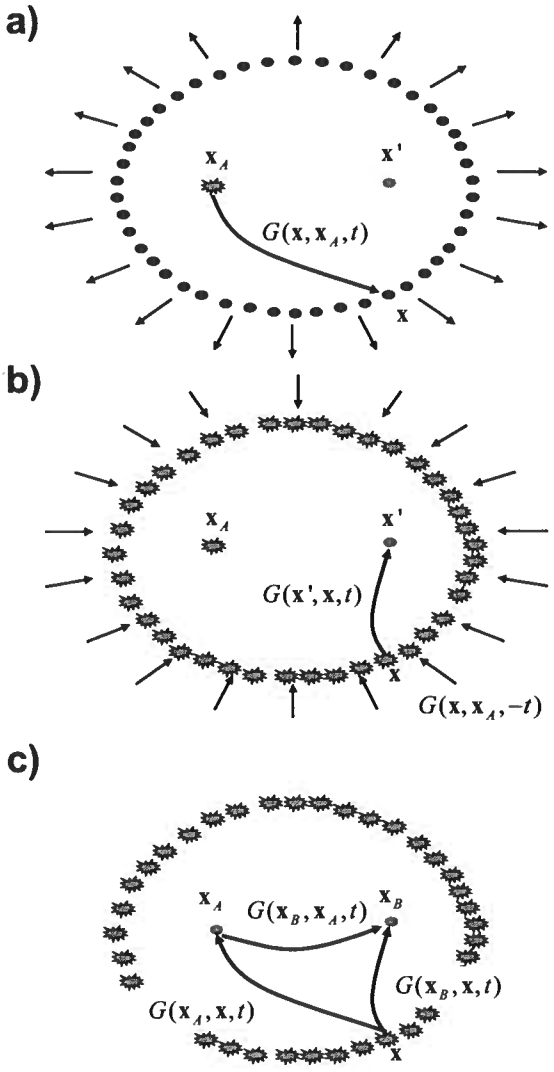

Figure 3. Derivation of Green's function retrieval, using arguments from time-reversed acoustics Derode et al. (2003a,b). (a) Response of a source at $\mathbf{x}_A$, observed at any $\mathbf{x}$ (the ray represents the full response, including primary and multiple scattering due to inhomogeneities). (b) The time-reversed responses are emitted back into the medium. (c) The response of a virtual source at $\mathbf{x}_A$ can be obtained from the crosscorrelation of observations at two receivers and integration along the sources.

(2) and setting $\mathbf{x}' = \mathbf{x}_B$ yields

$$G(\mathbf{x}_B, \mathbf{x}_A, t) + G(\mathbf{x}_B, \mathbf{x}_A, -t) \propto \oint_{\partial \mathbb{D}} G(\mathbf{x}_B, \mathbf{x}, t) * G(\mathbf{x}_A, \mathbf{x}, -t) \mathrm{d}^2\mathbf{x}. \quad (4)$$

We recognize the by now well-known form of an interferometric relation, with on the left-hand side the Green's function between $\mathbf{x}_A$ and $\mathbf{x}_B$ plus its time-reversed version and on the right-hand side crosscorrelations of wavefield observations at $\mathbf{x}_A$ and $\mathbf{x}_B$, integrated along the sources at $\mathbf{x}$ on $\partial\mathbb{D}$ (Figure 3c). The right-hand side can be reduced to a single crosscorrelation of noise observations in a similar way as discussed in Part I (we will briefly review this in the subsection "Acoustic representation").

Note that equation 4 holds for an arbitrarily inhomogeneous medium inside $\partial\mathbb{D}$, hence, the reconstructed Green's function $G(\mathbf{x}_B, \mathbf{x}_A, t)$ contains the ballistic wave (i.e., the direct wave) as well as the coda due to multiple scattering in the inhomogeneous medium. In itself this is not new, since equation 13 in Part I was also derived for inhomogeneous media. However, because equation 4 was derived directly from the principle of time-reversed acoustics, it now follows that seismic interferometry has the same favorable stability and resolution properties as time-reversed acoustics. Sens-Schönfelder and Wegler (2006) and Brenguier et al. (2008b) exploit the stability properties by applying coda wave interferometry Snieder et al. (2002) to Green's functions obtained by crosscorrelating noise observations at different seismometers on a volcano. They show that they can measure velocity variations with an accuracy of 0.1% with a temporal resolution of a single day. Brenguier et al. (2008a) use a similar method to monitor changes in seismic velocity associated with earthquakes near Parkfield, California.

The derivation of Derode et al. (2003b,a) that we have reviewed here is entirely based on elegant physical arguments, but it is not mathematically exact. In the next section we derive exact expressions and show the approximations that need to be made to arrive at equation 4.

GREEN'S FUNCTION REPRESENTATIONS FOR SEISMIC INTERFEROMETRY

Equations 13 and 14 in Part I express the reflection response of a 3D inhomogeneous medium in terms of crosscorrelations of the transmission responses of that medium. We derived these relations in 2002, as a generalization of Claerbout's 1D expressions (equations 8 and 12 in Part I). The derivation was based on a correlation-type reciprocity theorem for one-way wavefields. In order to establish a link with the independently upcoming field of Green's function retrieval, in 2004 we derived the equivalent of these relations in terms of Green's functions for full wavefields Wapenaar (2004). The starting point was the Rayleigh-Betti reciprocity theorem for elastodynamic wavefields. Apart from establishing the mentioned link, this derivation has the additional advantage that the inherent approximations of the one-way reciprocity theorem of the correlation type are circumvented (or at least postponed to a later stage in the derivation).

Elastodynamic representation

Here we briefly review our derivation of the elastodynamic Green's function representation for interferometry and discuss the connection with the methods we have discussed in the previous section and in Part I. Consider an arbitrarily heterogeneous and anisotropic lossless solid medium with stiffness $c_{ijkl}(\mathbf{x})$ and mass density $\rho(\mathbf{x})$. In this medium an external force distribution $f_i(\mathbf{x}, t)$ generates an elastodynamic wavefield, characterized by stress tensor $\tau_{ij}(\mathbf{x}, t)$ and particle velocity $v_i(\mathbf{x}, t)$. The Fourier transforms of these time-dependent quantities are defined via

$$\hat{f}(\omega) = \int_{-\infty}^{\infty} f(t) \exp(-j\omega t) \mathrm{d}t, \quad (5)$$

where ω is the angular frequency and j the imaginary unit. In the space-frequency domain the stress-strain relation reads $j\omega\hat{\tau}_{ij} - c_{ijkl}\partial_l\hat{v}_k = 0$ and the equation of motion $j\omega\rho\hat{v}_i - \partial_j\hat{\tau}_{ij} = \hat{f}_i$. Here ∂_j denotes the partial derivative in the x_j-direction and Einstein's summation convention applies to repeated subscripts. In the following we consider two independent elastodynamic states (i.e., sources and wavefields), which are distinguished by subscripts A and B. For an arbitrary spatial domain $\mathbb{D}$, enclosed by boundary $\partial\mathbb{D}$ with outward pointing normal $\mathbf{n} = (n_1, n_2, n_3)$, the Rayleigh-Betti reciprocity theorem that relates these two states is given by

$$\int_{\mathbb{D}} \{\hat{f}_{i,A}\hat{v}_{i,B} - \hat{v}_{i,A}\hat{f}_{i,B}\} \mathrm{d}^3\mathbf{x} = \oint_{\partial\mathbb{D}} \{\hat{v}_{i,A}\hat{\tau}_{ij,B} - \hat{\tau}_{ij,A}\hat{v}_{i,B}\} n_j \mathrm{d}^2\mathbf{x} \quad (6)$$

(Knopoff and Gangi, 1959; de Hoop, 1966; Aki and Richards, 1980). This theorem is also known as a reciprocity theorem of the convolution type, because all products in the frequency domain, like $\hat{v}_{i,A}\hat{\tau}_{ij,B}$, correspond to convolutions in the time domain.

Similarly to the acoustic situation, we can apply the principle of time-reversal invariance for elastic waves in a lossless medium Bojarski (1983). Time-reversal corresponds to complex conjugation in the frequency domain. Hence, when stress tensor $\hat{\tau}_{ij}$ and particle velocity $\hat{v}_i$ are solutions of the stress-strain relation and the equation of motion with source term $\hat{f}_i$, then $\hat{\tau}_{ij}^*$ and $-\hat{v}_i^*$ obey the same equations with source term $\hat{f}_i^*$ (the minus-sign in $-\hat{v}_i^*$ comes from the replacement $(j\omega)^* = -j\omega$ in the equation of motion). Making these substitutions

for state A, we obtain

$$\int_{\mathbb{D}} \{\hat{f}^*_{i,A}\hat{v}_{i,B} + \hat{v}^*_{i,A}\hat{f}_{i,B}\}\mathrm{d}^3\mathbf{x} = \oint_{\partial\mathbb{D}} \{-\hat{v}^*_{i,A}\hat{\tau}_{ij,B} - \hat{\tau}^*_{ij,A}\hat{v}_{i,B}\}n_j\mathrm{d}^2\mathbf{x}. \quad (7)$$

This is an elastic reciprocity theorem of the correlation type, because products like $\hat{v}^*_{i,A}\hat{\tau}_{ij,B}$, correspond to correlations in the time domain.

Next we replace the wavefields in both states in equation 7 by Green's functions. This means that we replace the force distributions by unidirectional impulsive point forces in both states, according to $f_{i,A}(\mathbf{x},t) = \delta(\mathbf{x}-\mathbf{x}_A)\delta(t)\delta_{ip}$ and $f_{i,B}(\mathbf{x},t) = \delta(\mathbf{x}-\mathbf{x}_B)\delta(t)\delta_{iq}$ in the time domain, or $\hat{f}_{i,A}(\mathbf{x},\omega) = \delta(\mathbf{x}-\mathbf{x}_A)\delta_{ip}$ and $\hat{f}_{i,B}(\mathbf{x},\omega) = \delta(\mathbf{x}-\mathbf{x}_B)\delta_{iq}$ in the frequency domain, with $\mathbf{x}_A$ and $\mathbf{x}_B$ both in $\mathbb{D}$ and where indices p and q denote the directions of the applied forces. Accordingly, for the particle velocities we substitute $\hat{v}_{i,A}(\mathbf{x},\omega) = \hat{G}_{ip}(\mathbf{x},\mathbf{x}_A,\omega)$ and $\hat{v}_{i,B}(\mathbf{x},\omega) = \hat{G}_{iq}(\mathbf{x},\mathbf{x}_B,\omega)$, respectively. Here $\hat{G}_{ip}(\mathbf{x},\mathbf{x}_A,\omega)$ represents the i-component of the particle velocity at $\mathbf{x}$, due to a unit force source in the p-direction at $\mathbf{x}_A$, etc. Substituting these sources and Green's functions into equation 7, using the stress-strain relation and source-receiver reciprocity (i.e., $\hat{G}_{ip}(\mathbf{x},\mathbf{x}_A,\omega) = \hat{G}_{pi}(\mathbf{x}_A,\mathbf{x},\omega)$), gives

$$\hat{G}_{qp}(\mathbf{x}_B,\mathbf{x}_A,\omega) + \hat{G}^*_{qp}(\mathbf{x}_B,\mathbf{x}_A,\omega) = -\oint_{\partial\mathbb{D}} \frac{c_{ijkl}(\mathbf{x})}{j\omega}\Big((\partial_l\hat{G}_{qk}(\mathbf{x}_B,\mathbf{x},\omega))\hat{G}^*_{pi}(\mathbf{x}_A,\mathbf{x},\omega) - \hat{G}_{qi}(\mathbf{x}_B,\mathbf{x},\omega)\partial_l\hat{G}^*_{pk}(\mathbf{x}_A,\mathbf{x},\omega)\Big)n_j\mathrm{d}^2\mathbf{x}, \quad (8)$$

or, in the time domain,

$$\partial_t\{G_{qp}(\mathbf{x}_B,\mathbf{x}_A,t) + G_{qp}(\mathbf{x}_B,\mathbf{x}_A,-t)\} = -\oint_{\partial\mathbb{D}} c_{ijkl}(\mathbf{x})\Big(\partial_l G_{qk}(\mathbf{x}_B,\mathbf{x},t) * G_{pi}(\mathbf{x}_A,\mathbf{x},-t) - G_{qi}(\mathbf{x}_B,\mathbf{x},t) * \partial_l G_{pk}(\mathbf{x}_A,\mathbf{x},-t)\Big)n_j\mathrm{d}^2\mathbf{x}. \quad (9)$$

Note that this representation has a similar form as many of the expressions we have encountered before. It is an exact representation for the Green's function between $\mathbf{x}_A$ and $\mathbf{x}_B$ plus its time-reversed version, expressed in terms of crosscorrelations of wavefield observations at $\mathbf{x}_A$ and $\mathbf{x}_B$, integrated along the sources at $\mathbf{x}$ on $\partial\mathbb{D}$. It holds for an arbitrarily inhomogeneous anisotropic medium (inside as well as outside $\partial\mathbb{D}$), and the closed boundary $\partial\mathbb{D}$ containing the sources of the Green's functions may have any shape. When a part $\partial\mathbb{D}_0$ of the boundary is a stress-free surface, like in Figure 4, then the integrand of the right-hand side of equation 7 is zero on $\partial\mathbb{D}_0$. Consequently, the boundary integral in equation 9 needs only be evaluated over the remaining part $\partial\mathbb{D}_1$ (meaning that sources are only required on that part of the boundary). Note that equation 9 still holds in the limiting case in which $\mathbf{x}_A$ and $\mathbf{x}_B$ lie at the free surface. In that case the Green's functions on the left-hand side have a traction source at $\mathbf{x}_A$ Wapenaar and Fokkema (2006).

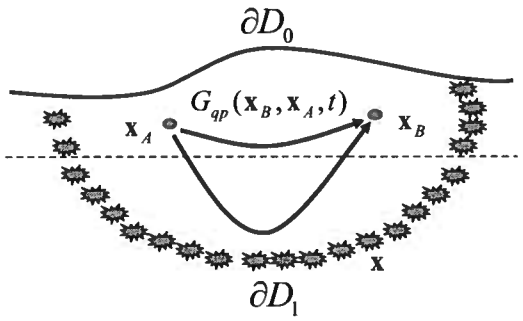

Figure 4. Configuration for elastodynamic Green's function retrieval (the rays represent the full response, including primary and multiple scattering as well as mode conversion due to inhomogeneities). Since in this configuration a part of the closed boundary is a free surface ($\partial\mathbb{D}_0$), sources are only required on the remaining part of the boundary ($\partial\mathbb{D}_1$). The shallow sources (say above the dashed line) are mainly responsible for retrieving the surface waves and the direct and shallowly refracted waves in $G_{qp}(\mathbf{x}_B,\mathbf{x}_A,t)$, whereas the deeper sources mainly contribute to the retrieval of the reflected waves in $G_{qp}(\mathbf{x}_B,\mathbf{x}_A,t)$.

An important difference with earlier expressions is that the right-hand side of representation 9 contains a combination of two terms, where each of the terms is a crosscorrelation of Green's functions with different types of sources at $\mathbf{x}$ (e.g., the operator ∂_l in $\partial_l G_{qk}(\mathbf{x}_B,\mathbf{x},t)$ is a differentiation with respect to x_l, which changes the character of the source at $\mathbf{x}$ of this Green's function). For modeling applications this is not a problem, since in modeling any type of source can be defined. This is exploited by van Manen et al. (2006, 2007), who use equation 9 for what they call interferometric modeling. They model the response of different types of sources on a boundary and save the responses for all possible receiver positions in the volume enclosed by the boundary. Next they apply equation 9 to obtain the responses of all possible source positions in that volume. Hence, for the cost of modeling responses of sources on a boundary (and calculating many crosscorrelations), they obtain responses of sources throughout a volume. This can be very useful for non-linear inversion schemes, where in each iteration Green's functions for sources in a volume are required.

The requirement of correlating responses of different types of sources makes equation 9 in its present form less practicable for application in seismic interferometry. This is particularly true for passive data, where one has to rely on the availability of natural sources. To

accommodate this, equation 9 can be modified Wapenaar and Fokkema (2006). Here we only indicate the main steps. Using a high-frequency approximation, assuming the medium outside $\partial\mathbb{D}$ is homogeneous and isotropic, the sources can be decomposed into P- and S-wave sources and their derivatives in the direction of the normal on $\partial\mathbb{D}$. These derivatives can be approximated, leading to a simplified version of equation 9 in which only crosscorrelations of Green's functions with the same source type occur. This approximation is accurate when $\partial\mathbb{D}$ is a sphere with large radius. It can also be used for arbitrary surfaces $\partial\mathbb{D}$, but at the expense of amplitude errors. Because the approximation does not affect the phase, it is usually considered acceptable for seismic interferometry. Finally, when the sources are mutually uncorrelated noise sources for P- and S-waves on $\partial\mathbb{D}$, equation 9 reduces to

$$\{G_{qp}(\mathbf{x}_B,\mathbf{x}_A,t)+G_{qp}(\mathbf{x}_B,\mathbf{x}_A,-t)\}*S_N(t)\approx \frac{2}{\rho c_P}\langle v_q(\mathbf{x}_B,t)*v_p(\mathbf{x}_A,-t)\rangle, \qquad (10)$$

where $v_p(\mathbf{x}_A,t)$ and $v_q(\mathbf{x}_B,t)$ are the p- and q-components of the particle velocity of the noise responses at $\mathbf{x}_A$ and $\mathbf{x}_B$, respectively, $S_N(t)$ is the autocorrelation of the noise and c_P the P-wave propagation velocity of the homogeneous medium outside $\partial\mathbb{D}$. For the configuration of Figure 4, the Green's function $G_{qp}(\mathbf{x}_B,\mathbf{x}_A,t)$ retrieved by equation 10 contains the surface waves between $\mathbf{x}_A$ and $\mathbf{x}_B$ as well as the reflected and refracted waves, assuming the noise sources are well distributed over the source boundary $\partial\mathbb{D}_1$ in the half-space below the free surface. In practice equation 10 is used either for surface-wave or for reflected-wave interferometry.

For surface-wave interferometry, typically the sources at and close to the surface give the most relevant contributions, say the sources above the dashed line in Figure 4. In our earlier, more intuitive discussions on direct-wave interferometry in Part I, we considered the fundamental surface-wave mode as an approximate solution of a 2D wave equation in the horizontal plane and argued that the Green's function of this fundamental mode can be extracted by crosscorrelating ambient noise. Equation 10 is a corollary of the exact representation 9 and thus accounts not only for the fundamental mode of the direct surface wave, but also for higher order modes as well as for scattered surface waves. Halliday and Curtis (2008) carefully analyze the contributions of the different sources to the retrieval of surface waves. They show that, when only sources at the surface are available, there is strong spurious interference between higher modes and the fundamental mode, whereas the presence of sources at depth (between the free surface and, say, the dashed line in Figure 4) enables the correct recovery of all modes independently. Nevertheless, they show that it is possible to obtain the latter result using only surface sources if modes are separated before crosscorrelation, are correlated separately, and reassembled thereafter. Halliday and Curtis (2009b) analyze the requirements in terms of source distribution for the retrieval of scattered surface waves. Halliday et al. (2010a) use the acquired insights to remove scattered surface waves (ground-roll) from seismic shot records (Figure 5).

For reflected-wave interferometry, the deeper situated sources (typically those below the dashed line in Figure 4) give the main contributions. This is in agreement with our earlier discussion on the retrieval of the 3D reflection response from transmission data, for which we considered a configuration with sources in the lower half-space (Figure 12 in Part I). For this configuration, the Green's function representations 9 and 10 can be seen as alternatives for the reflection representations 13 and 14 in Part I, generalized for an anisotropic solid medium.

Acoustic representation

Starting with Rayleigh's reciprocity theorem (Rayleigh, 1878; de Hoop, 1988; Fokkema and van den Berg, 1993) and the principle of time-reversal invariance Bojarski (1983); Fink (1992), we obtain the acoustic analogue of equation 8, according to

$$\hat{G}(\mathbf{x}_B,\mathbf{x}_A,\omega)+\hat{G}^*(\mathbf{x}_B,\mathbf{x}_A,\omega)= -\oint_{\partial\mathbb{D}}\frac{1}{j\omega\rho(\mathbf{x})}\Big((\partial_i\hat{G}(\mathbf{x}_B,\mathbf{x},\omega))\hat{G}^*(\mathbf{x}_A,\mathbf{x},\omega) -\hat{G}(\mathbf{x}_B,\mathbf{x},\omega)\partial_i\hat{G}^*(\mathbf{x}_A,\mathbf{x},\omega)\Big)n_i\mathrm{d}^2\mathbf{x} \qquad (11)$$

(van Manen et al., 2005; Wapenaar et al., 2005). Here $\hat{G}(\mathbf{x}_A,\mathbf{x},\omega)=\hat{G}(\mathbf{x},\mathbf{x}_A,\omega)$ is a solution of the wave equation

$$\rho\partial_i(\rho^{-1}\partial_i\hat{G})+(\omega^2/c^2)\hat{G}=-j\omega\rho\delta(\mathbf{x}-\mathbf{x}_A), \qquad (12)$$

for an arbitrarily inhomogeneous lossless fluid medium with propagation velocity $c=c(\mathbf{x})$ and mass density $\rho=\rho(\mathbf{x})$.

Before we discuss its use in seismic interferometry, we remark that equation 11 has been used in almost the same form in optical holography Porter (1970), seismic migration Esmersoy and Oristaglio (1988) and acoustic inverse scattering Oristaglio (1989) (except that in those papers the Green's functions are defined without the factor $j\omega\rho$ in the right-hand side of equation 12, leading to a somewhat different form of equation 11). In the imaging and inversion literature, $\hat{G}(\mathbf{x}_B,\mathbf{x}_A,\omega)+\hat{G}^*(\mathbf{x}_B,\mathbf{x}_A,\omega)$ is also called the homogeneous Green's function, because $\hat{G}_h(\mathbf{x},\mathbf{x}_A,\omega)=\hat{G}(\mathbf{x},\mathbf{x}_A,\omega)+\hat{G}^*(\mathbf{x},\mathbf{x}_A,\omega)$ obeys the homogeneous wave equation

$$\rho\partial_i(\rho^{-1}\partial_i\hat{G}_h)+(\omega^2/c^2)\hat{G}_h=0 \qquad (13)$$

("homogeneous" meaning source-free in this context). $\hat{G}_h(\mathbf{x},\mathbf{x}_A,\omega)$ can also be seen as the resolution function

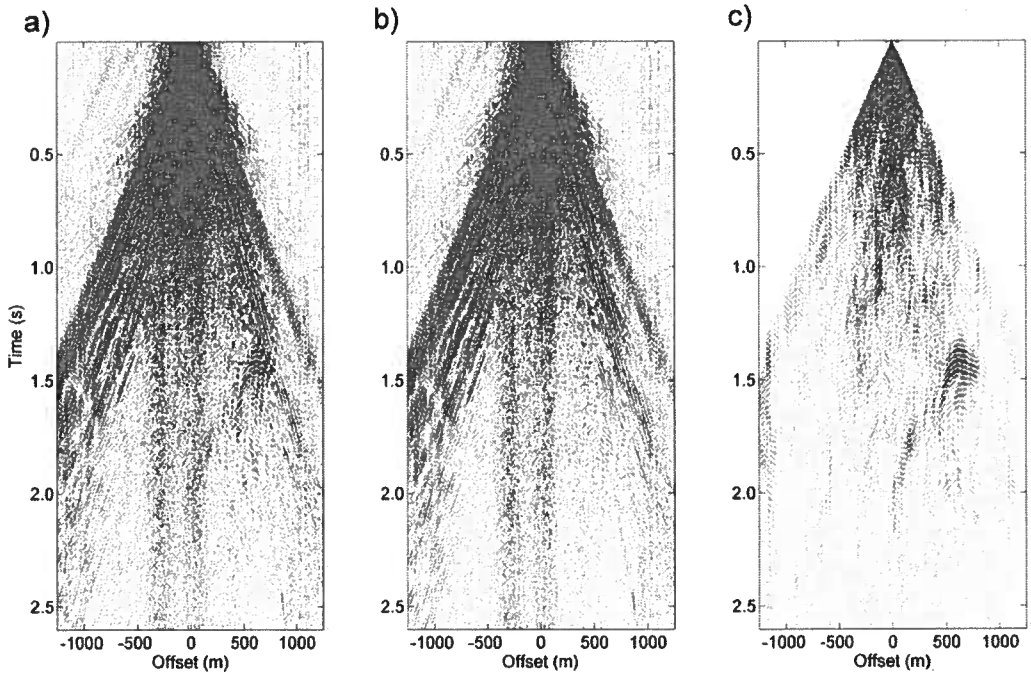

Figure 5. Example of interferometric ground-roll removal applied to shot records, while preserving the direct ground roll Halliday et al. (2010a). (a) Raw data. (b) Results of interferometric scattered ground roll removal. (c) The subtracted scattered ground roll.

of the imaging integral. For a homogeneous medium it is given by

$$\hat{G}_h(\mathbf{x},\mathbf{x}_A,\omega) = j\omega\rho\Big(\frac{\mathrm{e}^{-jkr}}{4\pi r} - \frac{\mathrm{e}^{jkr}}{4\pi r}\Big) = \omega\rho\,\frac{\sin(kr)}{2\pi r}, \quad (14)$$

with $k = \omega/c$ and $r = |\mathbf{x} - \mathbf{x}_A|$. This function has its maximum for $r \to 0$, where the amplitude is equal to $\omega^2\rho/2\pi c$. The width of the main lobe (measured at the zero crossings) is equal to the wavelength $\lambda = 2\pi/k$. For a further discussion on the relation between seismic interferometry and the migration resolution integral, see van Manen et al. (2006), Thorbecke and Wapenaar (2007) and Halliday and Curtis (2010).

Consider again the acoustic Green's function representation for seismic interferometry (equation 11). Note that, in comparison with e.g. equation 4, the right-hand side contains a combination of two terms, where each term is a crosscorrelation of Green's functions with different types of sources (monopoles and dipoles) at $\mathbf{x}$. Here we discuss in more detail how we can combine the two correlation products in equation 11 into a single term. To this end we assume that the medium outside $\partial\mathbb{D}$ is homogeneous, with constant propagation velocity c and mass density ρ. In the high frequency regime, the derivatives of the Green's functions can be approximated by multiplying each constituent (direct wave, scattered wave etc.) by $-jk\,|\cos\alpha|$, where α is the angle between the relevant ray and the normal on $\partial\mathbb{D}$. The main contributions to the integral in equation 11 come from stationary points on $\partial\mathbb{D}$. At those points the ray angles for both Green's functions are identical (see the Appendix of Part I). This implies that the contributions of the two terms under the integral in equation 11 are approximately equal (but opposite in sign), hence

$$\hat{G}(\mathbf{x}_B,\mathbf{x}_A,\omega) + \hat{G}^*(\mathbf{x}_B,\mathbf{x}_A,\omega) \approx -\frac{2}{j\omega\rho}\oint_{\partial\mathbb{D}} (n_i\partial_i\hat{G}(\mathbf{x}_B,\mathbf{x},\omega))\hat{G}^*(\mathbf{x}_A,\mathbf{x},\omega)\mathrm{d}^2\mathbf{x}. \quad (15)$$

The integrand contains a single crosscorrelation product of dipole and monopole source responses. When only monopole responses are available, the operation $n_i\partial_i$ can be replaced by a pseudo-differential operator acting along $\partial\mathbb{D}$, or by multiplications with $-jk\,|\cos\alpha|$ at the stationary points when the ray angles are known. Hence, for controlled-source interferometry, in which case the source positions are known and $\partial\mathbb{D}$ is a smooth surface, equation 15 is a useful expression. In passive interferometry, the positions of the sources are unknown and $\partial\mathbb{D}$ can be very irregular. In that case the best one can do

is to replace the operation $n_i\partial_i$ by a factor $-jk$, which leads to

$$\hat{G}(\mathbf{x}_B,\mathbf{x}_A,\omega)+\hat{G}^*(\mathbf{x}_B,\mathbf{x}_A,\omega)\approx \frac{2}{\rho c}\oint_{\partial\mathbb{D}}\hat{G}(\mathbf{x}_B,\mathbf{x},\omega)\hat{G}^*(\mathbf{x}_A,\mathbf{x},\omega)\mathrm{d}^2\mathbf{x}. \quad (16)$$

This approximation is accurate when $\partial\mathbb{D}$ is a sphere with large radius so that all rays are approximately normal to $\partial\mathbb{D}$ (i.e., $\alpha\approx 0$). For arbitrary surfaces this approximation involves an amplitude error. Moreover, spurious events may occur due to incomplete cancelation of contributions from different stationary points. However, since the approximation does not affect the phase, equation 16 is usually considered acceptable for seismic interferometry. Transforming both sides of equation 16 back to the time domain yields

$$G(\mathbf{x}_B,\mathbf{x}_A,t)+G(\mathbf{x}_B,\mathbf{x}_A,-t)\approx \frac{2}{\rho c}\oint_{\partial\mathbb{D}}G(\mathbf{x}_B,\mathbf{x},t)*G(\mathbf{x}_A,\mathbf{x},-t)\mathrm{d}^2\mathbf{x}, \quad (17)$$

which is equal to equation 4, i.e., the expression obtained by Derode et al. (2003a,b), with proportionality factor $2/\rho c$.

Of course there are situations for which the derivation presented above does not apply. For example, when $\partial\mathbb{D}$ is enclosing the water layer for marine seismology applications, the assumption that the medium is homogeneous outside $\partial\mathbb{D}$ breaks down and hence the derivatives of the Green's functions need to be obtained in another way. Ramírez and Weglein (2009) discuss a correlation-based processing scheme for ocean bottom data, based on a variant of equation 11, in which the time-reversed Green's function and its derivative are taken as analytic direct-wave solutions in the water layer. In the following we restrict the application of equations 15 – 17 to situations for which they were derived.

The practical application of equations 11 and 15 – 17 requires discretization of the integrals. The accuracy depends on the regularity of the distribution of the sources along $\partial\mathbb{D}$ (van Manen et al., 2005; Fan and Snieder, 2009; Yao and van der Hilst, 2009). A bias can be introduced in Green's function estimates when amplitudes of energy have directional variations. Curtis and Halliday (2010a) present an algorithm to remove this bias. In the subsection "Interferometry by multidimensional deconvolution" we present another effective way to compensate for illumination irregularities.

Equations 11 and 15 – 17 have been used for interferometric wavefield modeling van Manen et al. (2005) as well as for the derivation of passive and controlled-source seismic interferometry. For passive interferometry, the configuration is chosen similarly to Figure 4, in which a part of the closed boundary $\partial\mathbb{D}$ is a free surface at which no sources are required, hence, the closed boundary integral reduces to an integral over the remaining part $\partial\mathbb{D}_1$. When the sources on $\partial\mathbb{D}_1$ are noise sources, the responses at $\mathbf{x}_A$ and $\mathbf{x}_B$ are given by $u(\mathbf{x}_A,t)=\int_{\partial\mathbb{D}_1}G(\mathbf{x}_A,\mathbf{x},t)*N(\mathbf{x},t)\mathrm{d}^2\mathbf{x}$ and $u(\mathbf{x}_B,t)=\int_{\partial\mathbb{D}_1}G(\mathbf{x}_B,\mathbf{x}',t)*N(\mathbf{x}',t)\mathrm{d}^2\mathbf{x}'$, respectively. Assuming the noise sources are mutually uncorrelated, according to $\langle N(\mathbf{x}',t)*N(\mathbf{x},-t)\rangle=\delta(\mathbf{x}-\mathbf{x}')S_N(t)$ for $\mathbf{x}$ and $\mathbf{x}'$ on $\partial\mathbb{D}_1$, the crosscorrelation of the responses at $\mathbf{x}_A$ and $\mathbf{x}_B$ gives

$$\langle u(\mathbf{x}_B,t)*u(\mathbf{x}_A,-t)\rangle = \int_{\partial\mathbb{D}_1}G(\mathbf{x}_B,\mathbf{x},t)*G(\mathbf{x}_A,\mathbf{x},-t)*S_N(t)\mathrm{d}^2\mathbf{x}. \quad (18)$$

Combining this with equation 17, we obtain

$$\{G(\mathbf{x}_B,\mathbf{x}_A,t)+G(\mathbf{x}_B,\mathbf{x}_A,-t)\}*S_N(t)\approx \frac{2}{\rho c}\langle u(\mathbf{x}_B,t)*u(\mathbf{x}_A,-t)\rangle. \quad (19)$$

Representations 17 and 19 can be seen as alternatives for equations 13 and 14 in Part I. The main difference is that in the present derivation we did not need to neglect evanescent waves and the receiver positions $\mathbf{x}_A$ and $\mathbf{x}_B$ can be anywhere in $\mathbb{D}$ (instead of at the free surface).

For controlled-source interferometry, equations 11 and 15 – 17 apply to any of the configurations in Figure 11 of Part I Schuster (2009) and Figure 2 in Part II Korneev and Bakulin (2006). However, in none of these configurations the sources form a closed boundary around the receivers at $\mathbf{x}_A$ and $\mathbf{x}_B$, as prescribed by the theory, so the closed boundary integral is by necessity replaced by an open boundary integral. Assuming the medium is sufficiently inhomogeneous such that all energy is scattered back to the receivers, one-sided illumination suffices Wapenaar (2006a). However, in many practical situations this condition is not fulfilled, so the open boundary integral introduces artifacts, often denoted as spurious multiples Snieder et al. (2006b). A partial solution, implemented by Bakulin and Calvert (2006), is the application of a time window to $G(\mathbf{x}_A,\mathbf{x},t)$ in equation 17 (or $u(\mathbf{x}_A,\mathbf{x}_S^{(i)},t)$ in equation 1), with the aim of selecting direct waves only. The artifacts can be further suppressed by applying up/down decomposition to both Green's functions at the right-hand side of equation 17 Mehta et al. (2007a); van der Neut and Wapenaar (2009). Note that in the latter two cases, the direct wave part of $G(\mathbf{x}_A,\mathbf{x},t)$ (or $u(\mathbf{x}_A,\mathbf{x}_S^{(i)},t)$ in equation 1) propagates only through the overburden. This implies that the condition of having a lossless medium only applies to the overburden, hence, the medium below the receivers in Figure 2 may be attenuating. This is shown more rigorously by Slob and Wapenaar (2007a) and Vasconcelos et al. (2009). An even more effective suppression of artifacts related to one-sided illumination is discussed in the subsection "Interferometry by multidimensional deconvolution".

RECENT AND NEW ADVANCES

Most of what has been discussed in the previous sections covers the state-of-the-art of seismic interferometry. Here we briefly indicate some recent and new advances.

Media with losses

Until now we generally assumed that the medium is lossless and non-moving, which is equivalent to assuming that the underlying wave equation is invariant for time-reversal. Moreover, in all cases the Green's functions obey source-receiver reciprocity. In a medium with losses the wave equation is no longer invariant for time-reversal, but, as long as the medium is not moving, source-receiver reciprocity still holds. When the losses are not too high, the methods discussed above yield a Green's function with correct traveltimes and approximate amplitudes Roux et al. (2005); Slob and Wapenaar (2007b). Snieder (2007) shows that when the losses are significant a volume integral $-2\omega \int_{\mathbb{D}} \hat{\kappa}_i(\mathbf{x},\omega)\hat{G}(\mathbf{x}_B,\mathbf{x},\omega)\hat{G}^*(\mathbf{x}_A,\mathbf{x},\omega)\mathrm{d}^3\mathbf{x}$ (where $\hat{\kappa}_i(\mathbf{x},\omega)$ denotes the imaginary part of the compressibility) should be added to the right-hand side of any of equations 11, 15 or 16 (actually the minus sign in front of the integral is absent in Snieder's analysis because he uses another convention for the Fourier transform). This means that, in addition to the requirement of having sources at the boundary $\partial\mathbb{D}$ (as in Figures 3c and 4), sources are required throughout the domain $\mathbb{D}$. When these sources are uncorrelated noise sources, the final expression for Green's function retrieval has again a similar form as equation 19. This volume integral approach to Green's function retrieval is not restricted to acoustic waves in lossy media but also applies to electromagnetic waves in conducting media Slob and Wapenaar (2007a) as well as to pure diffusion phenomena Snieder (2006).

In most practical situations sources are not available throughout a volume. Interferometry by crossconvolution (Slob et al., 2007a; Halliday and Curtis, 2009b) is another approach that accounts for losses. Draganov et al. (2010) compensate for losses with an inverse attenuation filter. By doing this adaptively (aiming to minimize artifacts) they estimate the attenuation parameters. The methodology discussed in the subsection "Interferometry by multidimensional deconvolution" also accounts very effectively for losses.

Non-reciprocal media

In a moving medium (with or without losses), both the time-reversal invariance and source-receiver reciprocity break down. It has previously been shown that with some modifications time-reversed acoustic focusing (as in Figure 1) can still work in a moving medium Dowling (1993); Roux et al. (2004). Using reciprocity theory,

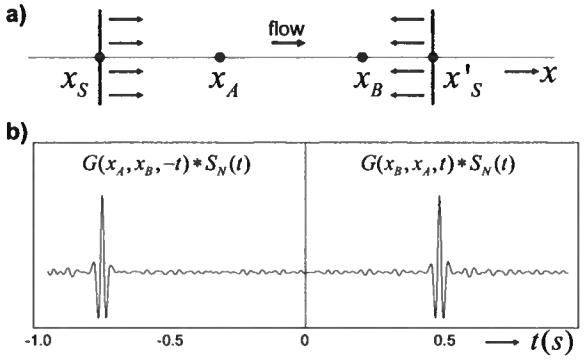

Figure 6. 1D example of direct-wave interferometry in a moving medium. (a) Rightward- and leftward-propagating noise signals in a rightward flowing medium. (b) Crosscorrelation of the responses at x_A and x_B. The causal part stems from the rightward-propagating wave and is interpreted as the Green's function propagating "downwind" from x_A to x_B. The acausal part stems from the leftward-propagating wave and is interpreted as the time-reversed Green's function propagating "upwind" from x_B to x_A.

it has recently been shown that Green's function retrieval by crosscorrelation is also possible in a moving medium (Wapenaar, 2006b; Godin, 2006). The required modification to the Green's function representation is surprisingly simple: the time-reversed Green's function $G(\mathbf{x}_B,\mathbf{x}_A,-t)$ on the left-hand side of equations 17 and 19 should be replaced by $G(\mathbf{x}_A,\mathbf{x}_B,-t)$ (assuming all Green's functions appearing in the representation are defined in the moving medium). Hence, in non-reciprocal media the retrieved function $G(\mathbf{x}_B,\mathbf{x}_A,t) + G(\mathbf{x}_A,\mathbf{x}_B,-t)$ is no longer time-symmetric, see Figure 6 for a 1D illustration. Interferometry in moving media has potential applications in solar seismology and in infrasound Evers and Siegmund (2009); Haney (2009).

It has been shown that with similar simple modifications, global scale interferometry accounts for the Coriolis force of a rotating earth Ruigrok et al. (2008) and electromagnetic interferometry accounts for non-reciprocal effects in bi-anisotropic media Slob and Wapenaar (2009). A moving conductive medium in the presence of a static magnetic field is an example of a bi-anisotropic medium. Electromagnetic interferometry in bi-anisotropic media may find applications in controlled-source electromagnetic (CSEM) acquisition with receivers in the air in areas with strong tidal currents.

Unified formulations

The wave equation for a medium with losses can be seen as a special case of the more general differential equation

$$\left[\sum_{n=1}^{N} a_n(\mathbf{x},t) * \frac{\partial^n}{\partial t^n} - H(\mathbf{x},t)*\right] u(\mathbf{x},t) = s(\mathbf{x},t), \quad (20)$$

where the $a_n(\mathbf{x},t)$ are medium parameters, $H(\mathbf{x},t)$ is a spatial differential operator and $s(\mathbf{x},t)$ is a source function. Snieder et al. (2007) derive unified Green's function representations for fields obeying this differential equation, assuming $H(\mathbf{x},t)$ is either symmetric or antisymmetric. These representations, consisting of a boundary and a volume integral, capture interferometry for acoustic wave propagation (with or without losses), diffusion, advection, bending waves in mechanical structures, and quantum mechanical scattering problems. Weaver (2008) provided an alternative derivation based on Ward identities. A recent extension Snieder et al. (2010) also accounts for potential fields (for which all $a_n = 0$ and H is independent of time in equation 20).

Similarly, for a matrix-vector differential equation of the form

$$\left[\mathbf{A}(\mathbf{x},t) * \frac{D}{Dt} + \mathbf{D}_{\mathbf{x}} + \mathbf{B}(\mathbf{x},t)*\right]\mathbf{u}(\mathbf{x},t) = \mathbf{s}(\mathbf{x},t), \quad (21)$$

where $\mathbf{A}$ and $\mathbf{B}$ are medium parameter matrices, $\frac{D}{Dt}$ the material time derivative and $\mathbf{D}_{\mathbf{x}}$ a spatial differential operator matrix, a unified Green's matrix representation has been derived Wapenaar et al. (2006). This representation, again consisting of a boundary and a volume integral, captures interferometry for acoustic, elastodynamic, electromagnetic, poroelastic, piezoelectric and electroseismic wave propagation as well as for diffusion and flow. For the situation of uncorrelated noise sources distributed along a boundary (for the situation of lossless media) or throughout a volume (for media with losses), the unified Green's matrix representation is given by

$$\{\mathbf{G}(\mathbf{x}_B,\mathbf{x}_A,t) + \mathbf{G}^t(\mathbf{x}_A,\mathbf{x}_B,-t)\} * S_N(t) \approx \langle \mathbf{u}(\mathbf{x}_B,t) * \mathbf{u}^t(\mathbf{x}_A,-t)\rangle, \quad (22)$$

(superscript ^{t} denotes transposition), where $\mathbf{u}(\mathbf{x}_A,t)$ and $\mathbf{u}(\mathbf{x}_B,t)$ are the noise responses at $\mathbf{x}_A$ and $\mathbf{x}_B$, respectively. In subscript notation this becomes

$$\{G_{qp}(\mathbf{x}_B,\mathbf{x}_A,t) + G_{pq}(\mathbf{x}_A,\mathbf{x}_B,-t)\} * S_N(t) \approx \langle u_q(\mathbf{x}_B,t) * u_p(\mathbf{x}_A,-t)\rangle. \quad (23)$$

Note the resemblance to equation 10 for elastodynamic Green's function retrieval. For example, for electroseismic waves, $\mathbf{u}^t = (\mathbf{E}^t, \mathbf{H}^t, \{\mathbf{v}^s\}^t, -\boldsymbol{\tau}_1^t, -\boldsymbol{\tau}_2^t, -\boldsymbol{\tau}_3^t, \mathbf{w}^t, p^f)$, where $\mathbf{E}$ and $\mathbf{H}$ are the electric and magnetic field vectors, $\mathbf{v}^s$ the particle velocity of the solid phase, $\boldsymbol{\tau}_i$ the traction, $\mathbf{w}$ the filtration velocity of the fluid through the pores, and p^f the pressure of the fluid phase. Accordingly, for example the (9,1)-element of $\mathbf{G}(\mathbf{x}_B,\mathbf{x}_A,t)$, i.e., $G_{9,1}(\mathbf{x}_B,\mathbf{x}_A,t)$, is the vertical particle velocity of the solid phase at $\mathbf{x}_B$ due to an impulsive horizontal electric current source at $\mathbf{x}_A$. According to equations 22 and 23 it is retrieved by crosscorrelating the 9th element of $\mathbf{u}(\mathbf{x}_B,t)$, i.e., the vertical velocity noise field at $\mathbf{x}_B$, with the first element of $\mathbf{u}(\mathbf{x}_A,t)$, being the horizontal electric noise field at $\mathbf{x}_A$ (Figure 7). For a further discussion on electroseismic interferometry, including numerical examples, see de Ridder et al. (2009).

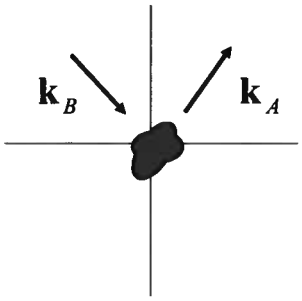

Figure 8. The generalized optical theorem for the angle-dependent scattering amplitude $f(\mathbf{k}_A,\mathbf{k}_B)$ Heisenberg (1943) has a similar form as the Green's function representation for seismic interferometry.

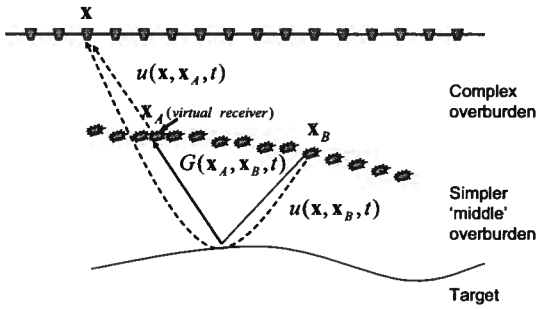

Figure 9. Using reciprocity, Bakulin and Calvert's virtual source method (Figure 2) can be reformulated into a virtual receiver method. Receivers at the surface record both the "direct" and the reflection responses of microseismic sources above a deeper target. Crosscorrelation and summing over receiver locations gives the reflection response at a virtual receiver at the position of a microseismic source, free of overburden distortions.

Relation with the generalized optical theorem

It has recently been recognized (Snieder et al., 2008; Halliday and Curtis, 2009a) that the frequency domain Green's function representation for seismic interferometry resembles the generalized optical theorem (Heisenberg, 1943; Glauber and Schomaker, 1953; Newton, 1976; Marston, 2001), given by

$$\frac{-1}{2j}\{f(\mathbf{k}_A,\mathbf{k}_B) - f^*(\mathbf{k}_B,\mathbf{k}_A)\} = \frac{k}{4\pi}\oint f(\mathbf{k},\mathbf{k}_B)f^*(\mathbf{k},\mathbf{k}_A)\mathrm{d}\Omega, \quad (24)$$

where $f(\mathbf{k}_A,\mathbf{k}_B)$ is the far field angle-dependent scattering amplitude of a finite scatterer (Figure 8), including

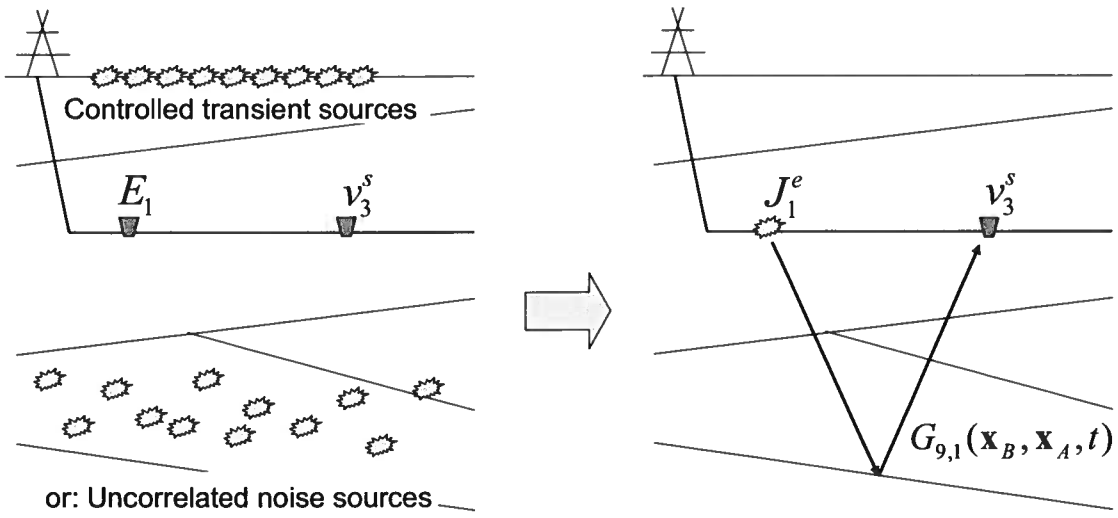

Figure 7. Principle of electroseismic interferometry for controlled transient sources at the surface or uncorrelated noise sources in the subsurface. In this example the vertical component of the particle velocity of the solid phase is crosscorrelated with the horizontal component of the electric field, yielding the electroseismic response of a horizontal electric current source observed by a vertical geophone.

all linear and non-linear interactions of the wavefield with the scatterer. Note that the optical theorem has a form similar to interferometry representation 16 for acoustic waves. The analysis of this resemblance has led to new insights in interferometry as well as in scattering theorems. Snieder et al. (2008) use the generalized optical theorem to explain the cancellation of specific spurious arrivals in Green's function extraction. Halliday and Curtis (2009a) show that the generalized optical theorem can be derived from the interferometric Green's function representation and use this to derive an optical theorem for surface waves in layered elastic media. Snieder et al. (2009b) discuss how the scattering amplitude can be derived from field fluctuations. In other related work, Halliday and Curtis (2009b) and Wapenaar et al. (2010) show that the Born approximation is an insufficient model to explain all aspects of seismic interferometry, even for the situation of a single point scatterer, and use this insight to derive improved models for the scattering amplitude of a point scatterer.

Virtual receivers, reflectors, and imaging

Until now we have discussed seismic interferometry as a method that retrieves the response of a virtual source by crosscorrelating responses at two receivers. Using reciprocity, it is also possible to create a virtual receiver by crosscorrelating the responses of two sources. Curtis et al. (2009) use this principle to turn earthquake sources into virtual seismometers with which real seismograms can be recorded, located non-invasively deep within the Earth's subsurface. They argue that this methodology has the potential to improve the resolution of imaging the earth's interior by earthquake seismology. Since an earthquake source acts like a double couple, by reciprocity the virtual receiver acts like a strainmeter, a device that is not easily implemented by a physical instrument. In a similar way, microseismic sources near a reservoir could be turned into virtual receivers to improve the resolution of reservoir imaging (Figure 9). Note that imaging using virtual receivers requires knowledge of the position of the sources, but simply recording seismograms on the virtual seismometers does not.

Another variant is the virtual reflector method Poletto and Farina (2008); Poletto and Wapenaar (2009). This method creates new seismic signals by processing real seismic responses of impulsive or transient sources. Under proper recording coverage conditions, this technique allows obtaining seismograms as if at the position of the receivers (or sources) there was an ideal reflector. The algorithm consists of convolution of the recorded traces, followed by integration of the cross-convolved signals along the receivers (or sources). Similar to other interferometry methods, the virtual reflector method does not require information on the propagation velocity

of the medium. Poletto and Farina (2010) illustrate the method with synthetic marine and real borehole data.

Curtis (2009), Schuster (2009, Chapter 8) and Curtis and Halliday (2010b) discuss source-receiver interferometry. This method combines the virtual source and the virtual receiver methodologies and thus involves a double integration over sources and receivers. It creates the response of a virtual source observed by a virtual receiver. This method is related to prestack redatuming Berryhill (1984), in which sources and receivers are repositioned from the acquisition surface to a new datum plane in the subsurface, using one-way wavefield extrapolation operators based on a macro model. In source-receiver interferometry, the operators are replaced by measured responses, for example in VSP's, hence source-receiver interferometry can be seen as the data-driven variant of prestack redatuming. Note, however, that in general the measured responses used in source-receiver interferometry are full wavefields rather than one-way operators. Therefore the application of source-receiver interferometry is not restricted to data-driven prestack redatuming, but it can be used for other applications as well. For example, Halliday et al. (2010b) show that the elastodynamic version of source-receiver interferometry can be seen as a generalization of a method that turns PP- and PS-data into SS-data, previously proposed by Grechka and Tsvankin (2002) and Grechka and Dewangan (2003). In a similar fashion, the internal multiple prediction method of Jakubowicz (1998) can be derived as a special case of source-receiver interferometry. Also, the surface wave removal methods of Dong et al. (2006), Curtis et al. (2006) and Halliday et al. (2007, 2010a) require both physically recorded and interferometrically constructed Green's function estimates between the locations of an active source and active receiver. Previously the interferometric estimate was obtained by having to place a receiver beside every source, and turning the former into a virtual source (or vice versa using virtual receiver interferometry). However, by using source-receiver interferometry this becomes unnecessary since the interferometric wavefield estimate can be made between real source and real receiver directly Curtis and Halliday (2010b).

Similar double integrals appear in the acoustic inverse scattering imaging formulation of Oristaglio (1989). Halliday and Curtis (2010) were able to derive explicitly a generalized version of Oristaglio's formulation from a version of source-receiver interferometry for a medium with scattering perturbations. This was possible because this form of interferometry is the first to combine both active sources and receivers, similarly to geometries used for imaging.

Time-lapse seismic interferometry

As a consequence of the stability of time-reversed acoustics, seismic interferometry has large potential for time-lapse methods. We already indicated the use of passive interferometry for monitoring changes in volcanic interiors (Sens-Schönfelder and Wegler, 2006; Brenguier et al., 2008b). Using the same principles, Brenguier et al. (2008a) monitor post-seismic relaxation along the San Andreas Fault at Parkfield, and Ohmi et al. (2008) monitor temporal variations of the crustal structure in the source region of the 2007 Noto Hanto earhquake in central Japan. Kraeva et al. (2009) show a relation between seasonal variations of ambient noise crosscorrelations and remote microseismic activity related to ocean storms, and Haney (2009) reports on time-dependent effects in correlations of infrasound that arise due to time-varying temperature fields and temperature inversion layers in the atmosphere. The interpretation in all these methods is based on measuring the time-shift in either the direct wave or the coda wave of the Green's functions retrieved by interferometry. These time-shifts give information about the average velocity change between the receivers, which can be further "regionalized" by tomographic inversion Brenguier et al. (2008b).

In the field of controlled-source interferometry, Bakulin et al. (2007) and Mehta et al. (2008) discuss the potential of the "virtual source method" for time-lapse reservoir monitoring. They exploit the fact that virtual source data are obtained from permanent down-hole or ocean-bottom cable receivers, and hence have a high degree of repeatability. Because virtual source data represent reflection responses, local time-lapse changes in these data can be reliably attributed to local changes in the reservoir.

In order to better quantify the time-lapse changes in the data obtained by seismic interferometry, the interferometric Green's function representation (equation 11) has been modified to account for time-lapse changes, according to

$$\begin{aligned}\hat{G}(\mathbf{x}_B,\mathbf{x}_A,\omega)+\hat{\bar{G}}^*(\mathbf{x}_B,\mathbf{x}_A,\omega)=\\ -\oint_{\partial\mathbf{D}}\frac{1}{j\omega\rho(\mathbf{x})}\Big((\partial_i\hat{G}(\mathbf{x}_B,\mathbf{x},\omega))\hat{\bar{G}}^*(\mathbf{x}_A,\mathbf{x},\omega)\\ -\hat{G}(\mathbf{x}_B,\mathbf{x},\omega)\partial_i\hat{\bar{G}}^*(\mathbf{x}_A,\mathbf{x},\omega)\Big)n_i\mathrm{d}^2\mathbf{x}\\ +j\omega\int_{\mathbf{D}}\Delta\hat{\kappa}(\mathbf{x},\omega)\hat{G}(\mathbf{x}_B,\mathbf{x},\omega)\hat{\bar{G}}^*(\mathbf{x}_A,\mathbf{x},\omega)\mathrm{d}^3\mathbf{x},\end{aligned}\quad(25)$$

with $\Delta\hat{\kappa}(\mathbf{x},\omega)=\hat{\kappa}(\mathbf{x},\omega)-\hat{\bar{\kappa}}^*(\mathbf{x},\omega)$ (Vasconcelos and Snieder, 2008a; Vasconcelos et al., 2009; Douma, 2009). Here the quantities with/without a bar refer to the reference/monitor state (for simplicity we assumed here that time-lapse changes occur only in the compressibility). The equivalent theory for source-receiver interferometry is given in Halliday and Curtis (2010). Equation 25 and its generalization for other wave types Wapenaar (2007) provides a basis for deriving local time-lapse changes of the medium parameters from interferometric time-lapse data. This is subject of ongoing research.

Interferometry by deconvolution and crosscoherence

In the previous treatment of interferometry we focused on Green's function extraction by crosscorrelation. Since time-reversal corresponds to complex conjugation in the frequency domain, the crosscorrelation is, in the frequency domain, given by

$$\hat{C}(\mathbf{x}_B,\mathbf{x}_A,\omega) = \hat{u}(\mathbf{x}_B,\omega)\hat{u}^*(\mathbf{x}_A,\omega)\ . \qquad (26)$$

According to expression 19 the crosscorrelation does not just give the superposition of the Green's function and it's time-reversed counterpart, because the left-hand side of that expression is convolved with the autocorrelation of the noise that excites the field fluctuations. This means that equation 26 gives the product of the Green's function and the power spectrum $\hat{S}_N(\omega)$ of the noise. The power spectrum thus leaves an imprint on the extracted Green's function, unless it is properly accounted for. This imprint can be eliminated by using deconvolution instead of crosscorrelation. In the frequency domain deconvolution corresponds to spectral division, hence the deconvolution approach consists of replacing expression 26 by

$$\hat{D}(\mathbf{x}_B,\mathbf{x}_A,\omega) = \frac{\hat{u}(\mathbf{x}_B,\omega)}{\hat{u}(\mathbf{x}_A,\omega)}\ . \qquad (27)$$

When $\hat{u}(\mathbf{x}_A,\omega)$ is small, this spectral division is unstable. In practice one needs to regularize the deconvolution. The simplest way to do this is to use the following water-level regularization

$$\hat{D}(\mathbf{x}_B,\mathbf{x}_A,\omega) = \frac{\hat{u}(\mathbf{x}_B,\omega)\hat{u}^*(\mathbf{x}_A,\omega)}{|\hat{u}(\mathbf{x}_A,\omega)|^2+\epsilon^2}\ , \qquad (28)$$

where ϵ^2 is a stabilization parameter. When $\epsilon^2 = 0$ expression 28 reduces to equation 27, while for $\epsilon^2 \gg |\hat{u}(\mathbf{x}_A,\omega)|^2$ equation 28 corresponds to a scaled version of the correlation defined in expression 26.

A significant difference between crosscorrelation and deconvolution is that crosscorrelation gives the Green's function, but that deconvolution does not. This raises the question what wave state is retrieved by deconvolving field measurements recorded at different points? There is a simple proof that the wave states obtained by crosscorrelation, deconvolution, and regularized deconvolution all satisfy the same equation as the real system does Snieder et al. (2006a). Let us denote the field equation of the system by

$$\hat{L}(\mathbf{x},\omega)\hat{u}(\mathbf{x},\omega) = 0\ . \qquad (29)$$

For the acoustic wave equation in a constant density medium, for example, the operator $\hat{L}$ is given by $\hat{L}(\mathbf{x},\omega) = \nabla^2 + \omega^2/c^2(\mathbf{x})$. Since the right-hand side of expression 29 equals zero, this expression holds for source-free regions, which is the case at the receivers. Applying $\hat{L}$ to equation 27 with $\mathbf{x}_B$ replaced by $\mathbf{x}$ gives

$$\begin{aligned}\hat{L}(\mathbf{x},\omega)\hat{D}(\mathbf{x},\mathbf{x}_A,\omega) &= \hat{L}(\mathbf{x},\omega)\left(\frac{\hat{u}(\mathbf{x},\omega)}{\hat{u}(\mathbf{x}_A,\omega)}\right)\\ &= \frac{1}{\hat{u}(\mathbf{x}_A,\omega)}\hat{L}(\mathbf{x},\omega)\hat{u}(\mathbf{x},\omega)\\ &= 0\ , \qquad (30)\end{aligned}$$

where we used in the second identity that $\hat{L}(\mathbf{x},\omega)$ acts on the x-coordinates only, and where the field equation 29 is used in the last identity. Note that the same reasoning applies to the correlation of expression 26 and the regularized deconvolution in expression 28. All these procedures thus produce a wave state that satisfies the same wave equation as the original system does. For the correlation this wave state is the Green's function, but for the deconvolution a different wave state is obtained.

To understand which wave state is extracted by deconvolution, we note that

$$\hat{D}(\mathbf{x}_A,\mathbf{x}_A,\omega) = \frac{\hat{u}(\mathbf{x}_A,\omega)}{\hat{u}(\mathbf{x}_A,\omega)} = 1\ . \qquad (31)$$

This corresponds, in the time, domain to

$$D(\mathbf{x}_A,\mathbf{x}_A,t) = \delta(t)\ . \qquad (32)$$

Deconvolution thus gives a wave state that for $t \neq 0$ vanishes at the virtual source location $\mathbf{x}_A$. This means that the wave field vanishes at that location, and for this reason the phrase "clamped boundary condition" has been used Vasconcelos and Snieder (2008a). Deconvolution thus gives a wave state where the field vanishes at one point in space. This wave state is, in general, not equal to the Green's function.

Despite this strange boundary condition, interferometry by deconvolution has a distinct advantage for attenuating media. Consider the example of Figure 1a of part I of this work where a plane wave propagates along a line from a source at x_S to receivers at x_A and x_B, respectively. For a homogeneous attenuating medium, the field recorded at x_A equals $\hat{u}(x_A,\omega) = \hat{G}(x_A,x_S,\omega)\hat{N}(\omega) = \exp(-\gamma(x_A - x_S))\exp(-ik(x_A - x_S))\hat{N}(\omega)$, where γ is an attenuation coefficient and $\hat{N}(\omega)$ the source spectrum. A similar expression holds for the field at x_B. The correlation of the fields recorded at x_A and x_B is given by

$$\hat{C}(x_B,x_A,\omega) = e^{-\gamma(x_A+x_B-2x_S)}e^{-ik(x_B-x_A)}\hat{S}_N(\omega)\ , \qquad (33)$$

with $\hat{S}_N(\omega) = |\hat{N}(\omega)|^2$. This field has the same phase as the field that propagates from x_A to x_B, but the attenuation is not correct because it depends on the source location x_S, which is, of course, not related to the field that propagates between x_A and x_B. In contrast, the deconvolution of the recorded fields satisfies

$$\begin{aligned}\hat{D}(x_B,x_A,\omega) &= e^{-\gamma(x_B-x_A)}e^{-ik(x_B-x_A)}\\ &= \hat{G}(x_B,x_A,\omega)\ , \qquad (34)\end{aligned}$$

which does correctly account for the phase *and* the am-

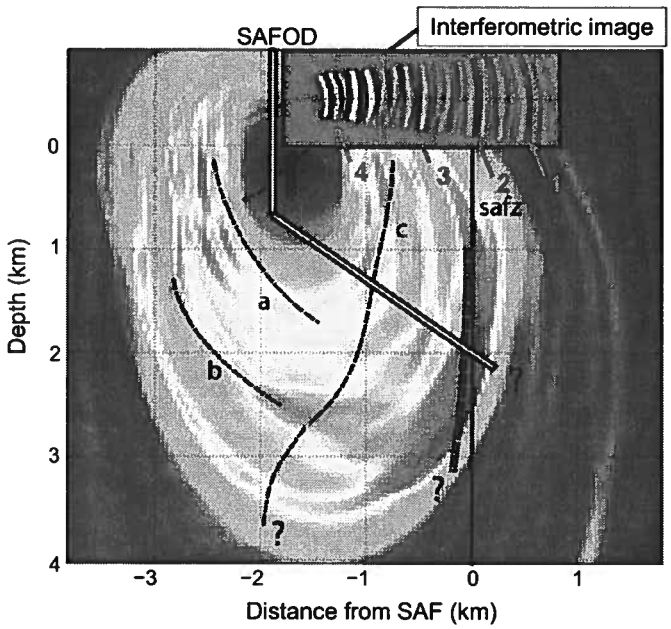

Figure 10. Images of the San Andreas fault (SAF). An image from deconvolution interferometry using drill-bit noise Vasconcelos and Snieder (2008b) is superposed on an image obtained from surface seismic data and microseismic events from the SAF, measured at the surface and in the pilot hole Chavarria et al. (2003). Event 2 (red arrow) is a prominent reflector, consistent with the surface trace of the SAF. Event 3 is interpreted to be a blind fault at Parkfield. Events 1 and 4 are interpreted to be artifacts, possibly because of drillstring multiples and improperly handled converted-wave modes.

plitude, and which does not depend on $\hat{N}(\omega)$. This property of the deconvolution approach for one-dimensional systems has been used to extract the velocity and attenuation in the near-surface (Trampert et al., 1993; Mehta et al., 2007b), and to determine the structural response of buildings from incoherent ground motion (Snieder and Şafak, 2006; Thompson and Snieder, 2006; Kohler et al., 2007). This method has even been used to detect changes in the near-surface shear wave velocity during the shaking caused by an earthquake Sawazaki et al. (2009).

The application of deconvolution interferometry changes when one can separate the wavefield into an unperturbed wave u_0 and a perturbation u_S Vasconcelos and Snieder (2008b). Such a separation can be achieved by time-gating when impulsive shots are used Mehta et al. (2007a); Bakulin et al. (2007), by using array methods, or by using 4-component data. In this case one can define a new deconvolution

$$\hat{D}'(\mathbf{x}_B,\mathbf{x}_A,\omega) = \frac{\hat{u}_S(\mathbf{x}_B,\omega)}{\hat{u}_0(\mathbf{x}_A,\omega)}\,, \qquad (35)$$

which gives an estimate of the perturbed Green's function $\hat{G}_S$. This has been used to illuminate the San Andreas fault from the side using drill-bit noise (Figure 10) and to do subsalt imaging from below using internal multiples Vasconcelos et al. (2008). A comparison of crosscorrelation, deconvolution, and multi-dimensional deconvolution (presented in the next section) is given by Snieder et al. (2009a).

A method related to deconvolution is the crosscoherence, which is defined as

$$\hat{H}(\mathbf{x}_B,\mathbf{x}_A,\omega) = \frac{\hat{u}(\mathbf{x}_B,\omega)}{|\hat{u}(\mathbf{x}_B,\omega)|}\frac{\hat{u}^*(\mathbf{x}_A,\omega)}{|\hat{u}(\mathbf{x}_A,\omega)|}\,. \qquad (36)$$

This can be seen as either a spectrally normalized crosscorrelation, or as a variant of deconvolution that is symmetric in $\hat{u}(\mathbf{x}_A,\omega)$ and $\hat{u}(\mathbf{x}_B,\omega)$. This method of combining data was proposed by Aki in his seminal papers on retrieving surface waves from micro-tremors Aki (1957, 1965). It has been used extensively in engineering Bendat and Piersol (2000) in the extraction of response functions, and is commonly used in the determination of shallow shear velocity from ground vibrations, e.g. Chávez-García and Luzón (2005). Note that the reasoning leading to equation 30 is not applicable to the crosscoherence because of the presence of the normalized spectrum in the denominator of expression 36. This implies that the crosscoherence does not necessarily lead to a wave state that satisfies the same equation as the real system does.

Interferometry by multidimensional deconvolution

Interferometry by multidimensional deconvolution (MDD) is the natural extension of interferometry by deconvolution to two or three dimensions. It has been proposed for controlled source data Schuster and Zhou (2006); Wapenaar et al. (2008a) as well as for passive data Wapenaar et al. (2008b). Here we discuss the principle for controlled source data and briefly indicate the modifications for noise data. Consider again Figure 2, which we initially used to introduce the virtual source method of Bakulin and Calvert (2004). We express the upgoing wavefield at $\mathbf{x}_B$ as follows

$$u^-(\mathbf{x}_B,\mathbf{x}_S^{(i)},t) = \int G(\mathbf{x}_B,\mathbf{x}_A,t) * u^+(\mathbf{x}_A,\mathbf{x}_S^{(i)},t)\mathrm{d}\mathbf{x}_A, \qquad (37)$$

where superscripts $^+$ and $^-$ refer to downgoing and upgoing waves, respectively. Note that the integration takes place along the receivers at $\mathbf{x}_A$ in the borehole. This convolutional data representation is valid in media with or without losses. However, unlike equation 1, which is an explicit, but approximate, expression for the Green's function $G(\mathbf{x}_B,\mathbf{x}_A,t)$ (convolved with the autocorrelation $S_s(t)$ of the source wavelet), equation 37 is an implicit, but exact, expression for $G(\mathbf{x}_B,\mathbf{x}_A,t)$ (with $G(\mathbf{x}_B,\mathbf{x}_A,t)$ being the reflection response of the medium below the receiver level with a homogeneous half-space above it Wapenaar et al. (2008a)). Equation 37 can be solved by MDD, assuming responses are available for

many source positions $\mathbf{x}_S^{(i)}$. In that case equation 37 holds for each source separately. In the frequency domain, the resulting set of simultaneous equations can be represented in matrix notation (Berkhout, 1982), according to

$$\hat{\mathsf{U}}^- = \hat{\mathsf{G}}\hat{\mathsf{U}}^+, \tag{38}$$

where the (j,i)-element of $\hat{\mathsf{U}}^+$ is given by $\hat{u}^+(\mathbf{x}_A^{(j)}, \mathbf{x}_S^{(i)}, \omega)$, etc. This equation can be solved for $\hat{\mathsf{G}}$ for example via weighted least-squares inversion Menke (1989), according to

$$\hat{\mathsf{G}} = \hat{\mathsf{U}}^-\mathsf{W}\{\hat{\mathsf{U}}^+\}^\dagger\left(\hat{\mathsf{U}}^+\mathsf{W}\{\hat{\mathsf{U}}^+\}^\dagger + \epsilon^2\mathsf{I}\right)^{-1}, \tag{39}$$

where the superscript † denotes transposition and complex conjugation, W is a diagonal weighting matrix, I the identity matrix, and ϵ^2 a stabilization parameter. Equation 39 is the multi-dimensional extension of equation 28. Applying this equation for each frequency component and transforming the result to the time domain accomplishes interferometry by MDD.

To get more insight in equation 37 and its solution by MDD, we convolve both sides with the time-reversed downgoing wave field $u^+(\mathbf{x}'_A, \mathbf{x}_S^{(i)}, -t)$ and sum over the source positions $\mathbf{x}_S^{(i)}$ van der Neut et al. (2010). This gives

$$C(\mathbf{x}_B, \mathbf{x}'_A, t) = \int G(\mathbf{x}_B, \mathbf{x}_A, t) * \mathcal{I}(\mathbf{x}_A, \mathbf{x}'_A, t)\mathrm{d}\mathbf{x}_A, \tag{40}$$

with

$$C(\mathbf{x}_B, \mathbf{x}'_A, t) = \sum_i u^-(\mathbf{x}_B, \mathbf{x}_S^{(i)}, t) * u^+(\mathbf{x}'_A, \mathbf{x}_S^{(i)}, -t) \tag{41}$$

and

$$\mathcal{I}(\mathbf{x}_A, \mathbf{x}'_A, t) = \sum_i u^+(\mathbf{x}_A, \mathbf{x}_S^{(i)}, t) * u^+(\mathbf{x}'_A, \mathbf{x}_S^{(i)}, -t). \tag{42}$$

Note that, according to equation 41, $C(\mathbf{x}_B, \mathbf{x}'_A, t)$ is nearly identical to the correlation function of equation 1, hence, equation 41 represents the virtual source method of Bakulin and Calvert (2004, 2006), but applied to decomposed wavefields Mehta et al. (2007a). According to equation 42, $\mathcal{I}(\mathbf{x}_A, \mathbf{x}'_A, t)$ contains the correlation of the incident wave fields. We call this the illumination function. For equidistant sources and a homogeneous overburden, the illumination function will approach $\mathcal{I}(\mathbf{x}_A, \mathbf{x}'_A, t) = \delta(\mathbf{x}_A - \mathbf{x}'_A)S_s(t)$ (with $\mathbf{x}_A$ and $\mathbf{x}'_A$ both in the borehole). Hence, for this situation equation 40 reduces to $C(\mathbf{x}_B, \mathbf{x}'_A, t) = G(\mathbf{x}_B, \mathbf{x}'_A, t) * S_s(t)$ (meaning that for this situation the correlation method gives the correct Green's function, convolved with $S_s(t)$). For the situation of an irregular source distribution and/or a complex overburden, the illumination function can become a complicated function of space and time. Equation 40 shows that the correlation method (i.e., Bakulin and Calvert's virtual source method) gives the Green's function, distorted by the illumination function. These distortions manifest themselves as an irregular radiation pattern of the virtual source, and artifacts (spurious multiples) related to the one-sided illumination. The true Green's function follows by multidimensionally deconvolving the correlation function by the illumination function. Van der Neut and Bakulin (2009) demonstrate that this indeed improves the radiation pattern of the virtual source and suppresses the artifacts.

Note that MDD can be carried out without knowing the source positions and the medium parameters (similar to crosscorrelation interferometry) and without making assumptions about the regularity of the source positions $\mathbf{x}_S^{(i)}$ and the attenuation parameters of the medium (the latter properties are unique for the deconvolution approach). The application of equations 41 and 42 requires decomposition into downgoing and upgoing waves and hence the availability of pressure and particle velocity data. The retrievable source-receiver offset-range by MDD is limited by the highest velocity in the domain between the sources and the receivers. The available spatial bandwidth in the recorded data may not always be sufficient to retrieve full-range offsets. This is likely to occur in alternating velocity zones. This also occurs in areas where velocities decrease with increasing depth, which is the usual situation for electromagnetic waves Slob (2009).

Note that for the situation of uncorrelated noise sources, equations 41 and 42 would need to be replaced by $C(\mathbf{x}_B, \mathbf{x}'_A, t) = \langle u^-(\mathbf{x}_B, t) * u^+(\mathbf{x}'_A, -t)\rangle$ and $\mathcal{I}(\mathbf{x}_A, \mathbf{x}'_A, t) = \langle u^+(\mathbf{x}_A, t) * u^+(\mathbf{x}'_A, -t)\rangle$, analogous to equation 19. For a further discussion of MDD applied to passive data, see Wapenaar et al. (2008b), van Groenestijn and Verschuur (2009) and van der Neut et al. (2010).

The MDD principle is not entirely new. It has been applied for example for multiple elimination of ocean bottom data (Wapenaar and Verschuur, 1996; Amundsen, 1999; Holvik and Amundsen, 2005). Like the 1D deconvolution method of Snieder et al. (2006a) discussed above, this can be seen as a methodology that changes the boundary conditions of the system: it transforms the response of the subsurface including the reflecting ocean bottom and water surface into the response of a subsurface without these reflecting boundaries. In hindsight this methodology appears to be an extension of a 1D deconvolution approach proposed by Riley and Claerbout (1976). Slob et al. (2007b) apply MDD to up/down decomposed CSEM data Amundsen et al. (2006) and demonstrate the insensitivity to dissipation as well as the effect of changing the boundary conditions: the effect of the air wave, a notorious problem in CSEM prospecting, is largely suppressed.

Interferometry by MDD is from a theoretical point of view more accurate than the crosscorrelation approach but the involved processing is less attractive because it is not a trace-by-trace process but involves inversion of large matrices. Moreover, in most cases it re-

quires decomposition into downgoing and upgoing fields. Nevertheless, the fact that interferometry by MDD corrects for an irregular source distribution, suppresses spurious multiples due to one-sided illumination, improves the radiation pattern of the virtual source, and accounts for dissipation, makes it a worthwhile method to be further investigated as an alternative to interferometry by crosscorrelation, both for passive as for controlled-source data applications.

CONCLUSIONS

In part I we discussed the basic principles of seismic interferometry in a heuristic way. In this paper (part II) we discussed interferometry in a more formal way. First we reviewed the methodology of time-reversed acoustics, pioneered by Mathias Fink and coworkers, and used physical arguments due to Arnaud Derode to derive seismic interferometry from the principle of time-reversed acoustics. We continued with a mathematical derivation, based on general reciprocity theory, leading to exact Green's function representations which are the basis for controlled-source as well as passive interferometry. Finally we discussed generalizations and variations of these representations and showed that these form the basis for a rich variety of new applications.

The fact that seismic interferometry leads to new responses directly from measured data has stirred a lot of enthusiasm and cooperation between researchers in seismology, acoustics and electromagnetic prospecting in the past decennium. We believe we have only seen the start and expect to see many new developments and applications in different fields in the years to come.

ACKNOWLEDGEMENTS

This work is supported by the Netherlands Research Centre for Integrated Solid Earth Science (ISES), the Dutch Technology Foundation STW, applied science division of NWO and the Technology Program of the Ministry of Economic Affairs (grant DCB.7913), and by the NSF through grant EAS-0609595. We thank associate editor Sven Treitel and reviewers Dirk-Jan van Manen, Matt Haney and Huub Douma for their valuable comments and suggestions, which helped improve this paper. We are grateful to Matthias Fink, David Halliday and Ivan Vasconcelos for permission to show the time-reversed acoustics experiment (Figure 1), the interferometric ground-roll removal experiment (Figure 5) and the interferometric SAF image (Figure 10), respectively.

References

Aki, K. and P. G. Richards, 1980, Quantitative seismology, Vol. I: W.H. Freeman and Company, San Fransisco.

Aki, K., 1957, Space and time spectra of stationary stochastic waves, with special reference to microtremors: Bulletin of the Earthquake Research Institute, **35**, 415–457.

Aki, K., 1965, A note on the use of microseisms in determining the shallow structures of the earth's crust: Geophysics, **30**, 665–666.

Amundsen, L., L. Løseth, R. Mittet, S. Ellingsrud, and B. Ursin, 2006, Decomposition of electromagnetic fields into upgoing and downgoing components: Geophysics, **71**, G211–G223.

Amundsen, L., 1999, Elimination of free surface-related multiples without need of the source wavelet: 69th Annual International Meeting, SEG, Expanded Abstracts, 1064–1067.

Bakulin, A. and R. Calvert, 2004, Virtual source: new method for imaging and 4D below complex overburden: 74th Annual International Meeting, SEG, Expanded Abstracts, 2477–2480.

Bakulin, A. and R. Calvert, 2006, The virtual source method: Theory and case study: Geophysics, **71**, SI139–SI150.

Bakulin, A., A. Mateeva, K. Mehta, P. Jorgensen, J. Ferrandis, I. Sinha Herhold, and J. Lopez, 2007, Virtual source applications to imaging and reservoir monitoring: The Leading Edge, **26**, no. 6, 732–740.

Baysal, E., D. D. Kosloff, and J. W. C. Sherwood, 1983, Reverse time migration: Geophysics, **48**, 1514–1524.

Behura, J., 2010, Virtual real source: Geophysics, **75**, (submitted).

Bendat, J. S. and A. G. Piersol, 2000, Random data: analysis & measurement procedures: John Wiley & Sons, New York.

Berkhout, A. J. and D. J. Verschuur, 2001, Seismic imaging beyond depth migration: Geophysics, **66**, 1895–1912.

Berkhout, A. J., 1982, Seismic migration. Imaging of acoustic energy by wave field extrapolation: Elsevier.

Berkhout, A. J., 1997, Pushing the limits of seismic imaging, Part I: Prestack migration in terms of double dynamic focusing: Geophysics, **62**, 937–954.

Berryhill, J. R., 1979, Wave-equation datuming: Geophysics, **44**, 1329–1344.

Berryhill, J. R., 1984, Wave-equation datuming before stack: Geophysics, **49**, 2064–2066.

Bojarski, N. N., 1983, Generalized reaction principles and reciprocity theorems for the wave equations, and the relationship between the time-advanced and time-retarded fields: Journal of the Acoustical Society of America, **74**, 281–285.

Brenguier, F., M. Campillo, C. Hadziioannou, N. M. Shapiro, R. M. Nadeau, and E. Larose, 2008a, Postseismic relaxation along the San Andreas Fault at

Parkfield from continuous seismological observations: Science, **321**, 1478–1480.

Brenguier, F., N. M. Shapiro, M. Campillo, V. Ferrazzini, Z. Duputel, O. Coutant, and A. Nercessian, 2008b, Towards forecasting volcanic eruptions using seismic noise: Nature Geoscience, **1**, 126–130.

Cao, W., S. M. Hanafy, G. T. Schuster, G. Zhan, and C. Boonyasiriwat, 2010, Demonstration of super-resolution and super-stacking properties of time reversal mirrors in locating seismic sources: Geophysics, **75**, xxx–xxx.

Chavarria, J. A., P. Malin, R. D. Catchings, and E. Shalev, 2003, A look inside the San Andreas fault at Parkfield through vertical seismic profiling: Science, **302**, 1746–1748.

Chávez-García, F. J. and F. Luzón, 2005, On the correlation of seismic microtremors: Journal of Geophysical Research, **110**, B11313–1–B11313–12.

Clapp, R. G., H. Fu, and O. Lindtjorn, 2010, Selecting the right hardware for reverse time migration: The Leading Edge, **29**, 48–58.

Curtis, A. and D. Halliday, 2010a, Directional balancing for seismic and general wavefield interferometry: Geophysics, **75**, (accepted).

——— 2010b, Source-receiver wavefield interferometry: Physical Review E, (submitted).

Curtis, A., P. Gerstoft, H. Sato, R. Snieder, and K. Wapenaar, 2006, Seismic interferometry - turning noise into signal: The Leading Edge, **25**, no. 9, 1082–1092.

Curtis, A., H. Nicolson, D. Halliday, J. Trampert, and B. Baptie, 2009, Virtual seismometers in the subsurface of the Earth from seismic interferometry: Nature Geoscience, **2**, 700–704.

Curtis, A., 2009, Source-receiver seismic interferometry: 79th Annual International Meeting, SEG, Expanded Abstracts, 3655–3659.

de Hoop, A. T., 1966, An elastodynamic reciprocity theorem for linear, viscoelastic media: Applied Scientific Research, **16**, 39–45.

de Hoop, A. T., 1988, Time-domain reciprocity theorems for acoustic wave fields in fluids with relaxation: Journal of the Acoustical Society of America, **84**, 1877–1882.

de Ridder, S. A. L., E. Slob, and K. Wapenaar, 2009, Interferometric seismoelectric Green's function representations: Geophysical Journal International, **178**, 1289–1304.

de Rosny, J. and M. Fink, 2002, Overcoming the diffraction limit in wave physics using a time-reversal mirror and a novel acoustic sink: Physical Review Letters, **89**, 124301–1–124301–4.

Derode, A., P. Roux, and M. Fink, 1995, Robust acoustic time reversal with high-order multiple scattering: Physical Review Letters, **75**, 4206–4209.

Derode, A., E. Larose, M. Campillo, and M. Fink, 2003a, How to estimate the Green's function of a heterogeneous medium between two passive sensors? Application to acoustic waves: Applied Physics Letters, **83**, no. 15, 3054–3056.

Derode, A., E. Larose, M. Tanter, J. de Rosny, A. Tourin, M. Campillo, and M. Fink, 2003b, Recovering the Green's function from field-field correlations in an open scattering medium (L): Journal of the Acoustical Society of America, **113**, no. 6, 2973–2976.

Dong, S., R. He, and G. T. Schuster, 2006, Interferometric prediction and least squares subtraction of surface waves: 76th Annual International Meeting, SEG, Expanded Abstracts, 2783–2786.

Douma, H., 2009, Generalized representation theorems for acoustic wavefields in perturbed media: Geophysical Journal International, **179**, 319–332.

Dowling, D. R., 1993, Phase-conjugate array focusing in a moving medium: Journal of the Acoustical Society of America, **94**, 1716–1718.

Draeger, C. and M. Fink, 1999, One-channel time-reversal in chaotic cavities: Theoretical limits: Journal of the Acoustical Society of America, **105**, 611–617.

Draganov, D., R. Ghose, E. Ruigrok, J. Thorbecke, and K. Wapenaar, 2010, Seismic interferometry, intrinsic losses, and Q-estimation: Geophysical Prospecting, **57**, (accepted).

Esmersoy, C. and M. Oristaglio, 1988, Reverse-time wave-field extrapolation, imaging, and inversion: Geophysics, **53**, 920–931.

Etgen, J., S. H. Gray, and Y. Zhang, 2009, An overview of depth imaging in exploration geophysics: Geophysics, **74**, WCA5–WCA17.

Evers, L. G. and P. Siegmund, 2009, Infrasonic signature of the 2009 major sudden stratospheric warming: Geophysical Research Letters, **36**, L23808–1–L23808–6.

Fan, Y. and R. Snieder, 2009, Required source distribution for interferometry of waves and diffusive fields: Geophysical Journal International, **179**, 1232–1244.

Fink, M. and C. Prada, 2001, Acoustic time-reversal mirrors: Inverse Problems, **17**, R1–R38.

Fink, M., 1992, Time-reversal of ultrasonic fields: Basic principles: IEEE Transactions on Ultrasonics, Ferroelectrics, and Frequency Control, **39**, 555–566.

Fink, M., 1997, Time reversed acoustics: Physics Today, **50**, 34–40.

Fink, M., 2006, Time-reversal acoustics in complex environments: Geophysics, **71**, SI151–SI164.

Fokkema, J. T. and P. M. van den Berg, 1993, Seismic applications of acoustic reciprocity: Elsevier, Amsterdam.

Gajewski, D. and E. Tessmer, 2005, Reverse modelling for seismic event characterization: Geophysical Journal International, **163**, 276–284.

Glauber, R. and V. Schomaker, 1953, The theory of electron diffraction: Physical Review, **89**, 667–671.

Godin, O. A., 2006, Recovering the acoustic Green's

function from ambient noise cross correlation in an inhomogeneous moving medium: Physical Review Letters, **97**, 054301–1–054301–4.

Grechka, V. and P. Dewangan, 2003, Generation and processing of pseudo-shear-wave data: Theory and case study: Geophysics, **68**, 1807–1816.

Grechka, V. and I. Tsvankin, 2002, PP+PS=SS: Geophysics, **67**, 1961–1971.

Grêt, A., R. Snieder, and J. Scales, 2006, Time-lapse monitoring of rock properties with coda wave interferometry: Journal of Geophysical Research, **111**, B03305–1–B03305–11.

Halliday, D. and A. Curtis, 2008, Seismic interferometry, surface waves and source distribution: Geophysical Journal International, **175**, 1067–1087.

Halliday, D. and A. Curtis, 2009a, Generalized optical theorem for surface waves and layered media: Physical Review E, **79**, 056603.

——— 2009b, Seismic interferometry of scattered surface waves in attenuative media: Geophysical Journal International, **178**, 419–446.

Halliday, D. and A. Curtis, 2010, An interferometric theory of source-receiver scattering and imaging: Geophysics, **75**, (submitted).

Halliday, D. F., A. Curtis, J. O. A. Robertsson, and D.-J. van Manen, 2007, Interferometric surface-wave isolation and removal: Geophysics, **72**, A69–A73.

Halliday, D., A. Curtis, P. Vermeer, C. L. Strobbia, A. Glushchenko, D.-J. van Manen, and J. Robertsson, 2010a, Interferometric ground-roll removal: Attenuation of scattered surface waves in single-sensor data: Geophysics, **75**, (accepted).

Halliday, D., A. Curtis, and K. Wapenaar, 2010b, Generalised PP+PS=SS: Geophysics, **75**, (in preparation).

Hanafy, S. M., W. Cao, K. McCarter, and G. T. Schuster, 2009, Using super-stacking and super-resolution properties of time-reversal mirrors to locate trapped miners: The Leading Edge, **28**, no. 3, 302–307.

Haney, M. M., 2009, Infrasonic ambient noise interferometry from correlations of microbaroms: Geophysical Research Letters, **36**, L19808–1–L19808–5.

Heisenberg, W., 1943, Die „beobachtbaren Größen" in der Theorie der Elementarteilchen: Zeitschrift für Physik, **120**, 513–538.

Holvik, E. and L. Amundsen, 2005, Elimination of the overburden response from multicomponent source and receiver seismic data, with source designature and decomposition into PP-, PS-, SP-, and SS-wave responses: Geophysics, **70**, S43–S59.

Jakubowicz, H., 1998, Wave equation prediction and removal of interbed multiples: 68th Annual International Meeting, SEG, Expanded Abstracts, 1527–1530.

Knopoff, L. and A. F. Gangi, 1959, Seismic reciprocity: Geophysics, **24**, 681–691.

Kohler, M. D., T. H. Heaton, and S. C. Bradford, 2007, Propagating waves in the steel, moment-frame Factor building recorded during earthquakes: Bulletin of the Seismological Society of America, **97**, 1334–1345.

Korneev, V. and A. Bakulin, 2006, On the fundamentals of the virtual source method: Geophysics, **71**, A13–A17.

Kraeva, N., V. Pinsky, and A. Hofstetter, 2009, Seasonal variations of cross correlations of seismic noise in Israel: Journal of Seismology, **13**, 73–87.

Lerosey, G., de Rosny, A. Tourin, and M. Fink, 2007, Focusing beyond the diffraction limit with far-field time reversal: Science, **315**, 1120–1122.

Marston, P. L., 2001, Generalized optical theorem for scatterers having inversion symmetry: Applications to acoustic backscattering: Journal of the Acoustical Society of America, **109**, no. 4, 1291–1295.

McMechan, G. A., 1982, Determination of source parameters by wavefield extrapolation: Geophysical Journal of the Royal Astronomical Society, **71**, 613–628.

McMechan, G. A., 1983, Migration by extrapolation of time-dependent boundary values: Geophysical Prospecting, **31**, 413–420.

Mehta, K., A. Bakulin, J. Sheiman, R. Calvert, and R. Snieder, 2007a, Improving the virtual source method by wavefield separation: Geophysics, **72**, V79–V86.

Mehta, K., R. Snieder, and V. Graizer, 2007b, Extraction of near-surface properties for a lossy layered medium using the propagator matrix: Geophysical Journal International, **169**, 271–280.

Mehta, K., J. L. Sheiman, R. Snieder, and R. Calvert, 2008, Strengthening the virtual-source method for time-lapse monitoring: Geophysics, **73**, S73–S80.

Menke, W., 1989, Geophysical data analysis: Academic Press.

Newton, R. G., 1976, Optical theorem and beyond: American Journal of Physics, **44**, no. 7, 639–642.

Ohmi, S., K. Hirahara, H. Wada, and K. Ito, 2008, Temporal variations of crustal structure in the source region of the 2007 Noto Hanto Earthquake, central Japan, with passive image interferometry: Earth, Planets and Space, **60**, 1069–1074.

Oristaglio, M. L., 1989, An inverse scattering formula that uses all the data: Inverse Problems, **5**, 1097–1105.

Parvulescu, A., 1961, Signal detection in a multipath medium by M.E.S.S. processing: Journal of the Acoustical Society of America, **33**, 1674.

Parvulescu, A., 1995, Matched-signal ("MESS") processing by the ocean: Journal of the Acoustical Society of America, **98**, 943–960.

Poletto, F. and B. Farina, 2008, Seismic virtual reflector - Synthesis and composition of virtual wavefields: 78th Annual International Meeting, SEG, Expanded Abstracts, 1367–1371.

Poletto, F. and B. Farina, 2010, Synthesis and com-

position of virtual reflector (VR) signals: Geophysics, **75**, (submitted).

Poletto, F. and K. Wapenaar, 2009, Virtual reflector representation theorem (acoustic medium): Journal of the Acoustical Society of America, **125**, no. 4, EL111–EL116.

Porter, R. P., 1970, Diffraction-limited, scalar image formation with holograms of arbitrary shape: Journal of the Optical Society of America, **60**, 1051–1059.

Ramírez, A. C. and A. B. Weglein, 2009, Green's theorem as a comprehensive framework for data reconstruction, regularization, wavefield separation, seismic interferometry, and wavelet estimation: A tutorial: Geophysics, **74**, W35–W62.

Rayleigh, J. W. S., 1878, The theory of sound. Volume II: Dover Publications, Inc. (Reprint 1945).

Riley, D. C. and J. F. Claerbout, 1976, 2-D multiple reflections: Geophysics, **41**, 592–620.

Roux, P., W. A. Kuperman, W. S. Hodgkiss, H. C. Song, T. Akal, and M. Stevenson, 2004, A nonreciprocal implementation of time reversal in the ocean: Journal of the Acoustical Society of America, **116**, 1009–1015.

Roux, P., K. G. Sabra, W. A. Kuperman, and A. Roux, 2005, Ambient noise cross correlation in free space: Theoretical approach: Journal of the Acoustical Society of America, **117**, no. 1, 79–84.

Ruigrok, E., D. Draganov, and K. Wapenaar, 2008, Global-scale seismic interferometry: theory and numerical examples: Geophysical Prospecting, **56**, 395–417.

Sawazaki, K., H. Sato, H. Nakahara, and T. Nishimura, 2009, Time-lapse changes of seismic velocity in the shallow ground caused by strong ground motion shock of the 2000 Western-Tottori earthquake, Japan, as revealed from coda deconvolution analysis: Bulletin of the Seismological Society of America, **99**, 352–366.

Schuster, G. T. and M. Zhou, 2006, A theoretical overview of model-based and correlation-based redatuming methods: Geophysics, **71**, SI103–SI110.

Schuster, G. T., 2001, Theory of daylight/interferometric imaging: tutorial: 63rd Annual International Meeting, EAGE, Extended Abstracts, Session: A32.

Schuster, G. T., 2009, Seismic interferometry: Cambridge University Press.

Sens-Schönfelder, C. and U. Wegler, 2006, Passive image interferometry and seasonal variations of seismic velocities at Merapi Volcano, Indonesia: Geophysical Research Letters, **33**, L21302–1–L21302–5.

Slob, E. and K. Wapenaar, 2007a, Electromagnetic Green's functions retrieval by cross-correlation and cross-convolution in media with losses: Geophysical Research Letters, **34**, L05307–1–L05307–5.

——— 2007b, GPR without a source: Cross-correlation and cross-convolution methods: IEEE Transactions on Geoscience and Remote Sensing, **45**, 2501–2510.

Slob, E. and K. Wapenaar, 2009, Retrieving the Green's function from cross correlation in a bianisotropic medium: Progress In Electromagnetics Research, PIER, **93**, 255–274.

Slob, E., D. Draganov, and K. Wapenaar, 2007a, Interferometric electromagnetic Green's functions representations using propagation invariants: Geophysical Journal International, **169**, 60–80.

Slob, E., K. Wapenaar, and R. Snieder, 2007b, Interferometry in dissipative media: Adressing the shallow sea problem for Seabed Logging applications: 77th Annual International Meeting, SEG, Expanded Abstracts, 559–563.

Slob, E., 2009, Interferometry by deconvolution of multicomponent multioffset GPR data: IEEE Transactions on Geoscience and Remote Sensing, **47**, 828–838.

Snieder, R. and E. Şafak, 2006, Extracting the building response using seismic interferometry: Theory and application to the Millikan Library in Pasadena, California: Bulletin of the Seismological Society of America, **96**, 586–598.

Snieder, R. K. and J. A. Scales, 1998, Time-reversed imaging as a diagnostic of wave and particle chaos: Physical Review E, **58**, 5668–5675.

Snieder, R., A. Grêt, H. Douma, and J. Scales, 2002, Coda wave interferometry for estimating nonlinear behavior in seismic velocity: Science, **295**, 2253–2255.

Snieder, R., J. Sheiman, and R. Calvert, 2006a, Equivalence of the virtual-source method and wave-field deconvolution in seismic interferometry: Physical Review E, **73**, 066620–1–066620–9.

Snieder, R., K. Wapenaar, and K. Larner, 2006b, Spurious multiples in seismic interferometry of primaries: Geophysics, **71**, SI111–SI124.

Snieder, R., K. Wapenaar, and U. Wegler, 2007, Unified Green's function retrieval by cross-correlation; connection with energy principles: Physical Review E, **75**, 036103–1–036103–14.

Snieder, R., K. van Wijk, M. Haney, and R. Calvert, 2008, Cancellation of spurious arrivals in Green's function extraction and the generalized optical theorem: Physical Review E, **78**, 036606.

Snieder, R., M. Miyazawa, E. Slob, I. Vasconcelos, and K. Wapenaar, 2009a, A comparison of strategies for seismic interferometry: Surveys in Geophysics, **30**, 503–523.

Snieder, R., F. J. Sánchez-Sesma, and K. Wapenaar, 2009b, Field fluctuations, imaging with backscattered waves, a generalized energy theorem, and the optical theorem: SIAM Journal on Imaging Sciences, **2**, no. 2, 763–776.

Snieder, R., E. Slob, and K. Wapenaar, 2010, Lagrangian Green's function extraction, with applications to potential fields, diffusion, and acoustic waves: New Journal of Physics, in press.

Snieder, R., 2006, Retrieving the Green's function of

the diffusion equation from the response to a random forcing: Physical Review E, **74**, 046620–1–046620–4.

Snieder, R., 2007, Extracting the Green's function of attenuating acoustic media from uncorrelated waves: Journal of the Acoustical Society of America, **121**, no. 5, 2637–2643.

Stewart, J. L., W. B. Allen, R. M. Zarnowitz, and M. K. Brandon, 1965, Pseudorandom signal-correlation methods of underwater acoustic research I: Principles: Journal of the Acoustical Society of America, **37**, 1079–1090.

Thompson, D. and R. Snieder, 2006, Seismic anisotropy of a building: The Leading Edge, **25**, 1093.

Thorbecke, J. and K. Wapenaar, 2007, On the relation between seismic interferometry and the migration resolution function: Geophysics, **72**, T61–T66.

Trampert, J., M. Cara, and M. Frogneux, 1993, *SH* propagator matrix and Q_S estimates from borehole- and surface-recorded earthquake data: Geophysical Journal International, **112**, 290–299.

van der Neut, J. and A. Bakulin, 2009, Estimating and correcting the amplitude radiation pattern of a virtual source: Geophysics, **74**, SI27–SI36.

van der Neut, J. and K. Wapenaar, 2009, Controlled-source elastodynamic interferometry by cross-correlation of decomposed wavefields: 71st Annual International Meeting, EAGE, Extended Abstracts, Session: X044.

van der Neut, J., E. Ruigrok, D. Draganov, and K. Wapenaar, 2010, Retrieving the earth's reflection response by multi-dimensional deconvolution of ambient seismic noise: a post-processing tool for passive interferometry: 72nd Annual International Meeting, EAGE, Extended Abstracts, Session: (submitted).

van Groenestijn, G. J. A. and D. J. Verschuur, 2009, Estimation of primaries by sparse inversion from passive seismic data: 79th Annual International Meeting, SEG, Expanded Abstracts, 1597–1601.

van Manen, D.-J., J. O. A. Robertsson, and A. Curtis, 2005, Modeling of wave propagation in inhomogeneous media: Physical Review Letters, **94**, 164301–1–164301–4.

van Manen, D.-J., A. Curtis, and J. O. A. Robertsson, 2006, Interferometric modeling of wave propagation in inhomogeneous elastic media using time reversal and reciprocity: Geophysics, **71**, SI41–SI60.

van Manen, D.-J., J. O. A. Robertsson, and A. Curtis, 2007, Exact wave field simulation for finite-volume scattering problems: Journal of the Acoustical Society of America, **122**, EL115–EL121.

Vasconcelos, I. and R. Snieder, 2008a, Interferometry by deconvolution: Part 1 - Theory for acoustic waves and numerical examples: Geophysics, **73**, S115–S128.

——— 2008b, Interferometry by deconvolution: Part 2 - Theory for elastic waves and application to drill-bit seismic imaging: Geophysics, **73**, S129–S141.

Vasconcelos, I., R. Snieder, and B. Hornby, 2008, Imaging internal multiples from subsalt VSP data - Examples of target-oriented interferometry: Geophysics, **73**, S157–S168.

Vasconcelos, I., R. Snieder, and H. Douma, 2009, Representation theorems and Green's function retrieval for scattering in acoustic media: Physical Review E, **80**, 036605–1–036605–14.

Wapenaar, K. and J. Fokkema, 2006, Green's function representations for seismic interferometry: Geophysics, **71**, SI33–SI46.

Wapenaar, C. P. A. and D. J. Verschuur, 1996, Processing of ocean bottom data: Processing of ocean bottom data:, Delft University of Technology, The Delphi Acquisition Project, Volume I (available at http:// geodus1.ta.tudelft.nl/ PrivatePages/ C.P.A.Wapenaar/ Daylight2/ DELP_96G.pdf).

Wapenaar, K., J. Fokkema, and R. Snieder, 2005, Retrieving the Green's function in an open system by cross-correlation: a comparison of approaches (L): Journal of the Acoustical Society of America, **118**, 2783–2786.

Wapenaar, K., E. Slob, and R. Snieder, 2006, Unified Green's function retrieval by cross correlation: Physical Review Letters, **97**, 234301–1–234301–4.

Wapenaar, K., E. Slob, and R. Snieder, 2008a, Seismic and electromagnetic controlled-source interferometry in dissipative media: Geophysical Prospecting, **56**, 419–434.

Wapenaar, K., J. van der Neut, and E. Ruigrok, 2008b, Passive seismic interferometry by multi-dimensional deconvolution: Geophysics, **73**, A51–A56.

Wapenaar, K., E. Slob, and R. Snieder, 2010, On seismic interferometry, the generalized optical theorem and the scattering matrix of a point scatterer: Geophysics, **75**, (accepted).

Wapenaar, K., 2004, Retrieving the elastodynamic Green's function of an arbitrary inhomogeneous medium by cross correlation: Physical Review Letters, **93**, 254301–1–254301–4.

Wapenaar, K., 2006a, Green's function retrieval by cross-correlation in case of one-sided illumination: Geophysical Research Letters, **33**, L19304–1–L19304–6.

——— 2006b, Nonreciprocal Green's function retrieval by cross correlation: Journal of the Acoustical Society of America, **120**, EL7–EL13.

Wapenaar, K., 2007, General representations for wavefield modeling and inversion in geophysics: Geophysics, **72**, SM5–SM17.

Weaver, R. L., 2008, Ward identities and the retrieval of Green's functions in the correlations of a diffuse wave field: Wave Motion, **45**, 596–604.

Whitmore, N. D., 1983, Iterative depth migration by backward time propagation: 53rd Annual International Meeting, SEG, Expanded Abstracts, 382–385.

Yao, H. and R. D. van der Hilst, 2009, Analysis of ambient noise energy distribution and phase velocity

bias in ambient noise tomography, with application to SE Tibet: Geophysical Journal International, **179**, 1113–1132.

Zhang, Y. and J. Sun, 2009, Practical issues in reverse time migration: true amplitude gathers, noise removal and harmonic source encoding: First Break, **27**, no. 1, 53–59.

Equipartitioning is not sufficient for Green's function extraction

Roel Snieder[1], Yuanzhong Fan[1], Evert Slob[2], & Kees Wapenaar[2]
[1] *Center for Wave Phenomena, Colorado School of Mines, Golden CO 80401, USA, email rsnieder@mines.edu*
[2] *Faculty of Civil Enineering and Geosciences, Delft University of Technology, Delft, The Netherlands*

ABSTRACT
The extraction of the earth's Green's function from field fluctuations is a rapidly growing area of research. The principle of Green's function extraction is often related to the requirement of equipartitioning, which stipulates that the energy of field fluctuations is distributed evenly in some sense. We show the meaning of equipartitioning for a variety of different formulations for Green's function retrieval. We show that equipartitioning is not a sufficient condition, and provide several examples that illustrate this point. We discuss the implications of lack of equipartitioning for various schemes for the reconstruction of the Green's function in seismology. The theory for Green's function extraction is usually based on a statistical theory that relies on ensemble averages. Since there is only one earth, one usually replaces the ensemble average with a time average. We show that such a replacement only makes sense when attenuation is taken into account, and show how the theory based for Green's function extraction for oscillating systems can be extended to incorporate attenuation.

Key words: seismic interferometry, equipartitioning, field fluctuations

1 INTRODUCTION

The extraction of the elastic earth response from field fluctuations is an area of research that has spectacularly grown over the last decade (Larose *et al.*, 2006; Curtis *et al.*, 2006; Wapenaar *et al.*, 2008; Schuster, 2009). This line of research was spurred to a large extent by the seminal work of Lobkis and Weaver (2001). In seismology, the principle of Green's function retrieval from field fluctuations is known by other names that include *Green's function extraction* and *seismic interferometry*.

The principle of Green's function retrieval relies on various formulations of wave theory that all require in one form or another for field fluctuations to be "evenly" distributed in space. As we show in section 2, the precise meaning of this requirement differs for different formulations, but in all cases the required distribution of sources implies that the energy of the field fluctuations is evenly distributed in space. Using the classical mechanics terminology (Goldstein, 1980), this principle is referred to as *equipartitioning*. Since the energy of strongly scattered waves diffuses through space, the expression *diffuse waves* is also used, e.g. (Campillo & Paul, 2003; Malcolm *et al.*, 2004; Weaver & Lobkis, 2006; Sánchez-Sesma *et al.*, 2008). The concepts of equipartitioning and diffuse waves have received so much attention that one might think that the Green's function can be retrieved whenever the wavefield is equipartitioned, but we show in this work that this not the case.

In section 2 we review different formulations of equipartitioning and discuss what the requirement of equipartitioning means for the distribution of sources of field fluctuations. We provide in section 3 a number of examples of equipartitioned fields that do not allow for Green's function extraction. We discuss in sections 4 and 5 the implications of a lack of adequate sources of field fluctuations for Green's function retrieval in the earth, and argue that attenuation plays an essential role in practical Green's function extraction of the earth response. In appendix A we show how attenuation can be incorporated in Green's function retrieval of damped oscillating systems.

2 VARIOUS REQUIREMENTS FOR EQUIPARTITIONING

The retrieval of the Green's function has been linked to the equipartitioning of waves, e.g. (Lobkis & Weaver, 2001; Campillo & Paul, 2003; Snieder *et al.*, 2007), which sometimes is referred to as the wavefield being *diffuse*. The latter term indicates that the waves are strongly scattered and propagate with equal strength in each direction. In different studies, the equipartitioning requirement is presented in different ways. In the next subsections review the meaning of equipartitioning as presented in different studies.

2.1 An acoustic source

The first explanation of equipartitioning, as given by Snieder *et al.* (2007), is heuristic. Consider an explosive point source in an acoustic medium at location A, as shown in the left panel of figure 1. The medium can be inhomogeneous, but if the medium is locally homogeneous in the vicinity of the source, the waves radiate isotropically as show in the left panel. Because of the isotropic character of the source, the waves propagate towards points B and C with equal amplitude.

Consider next the situation shown in right panel of figure 1 where the source at location A is replaced by a receiver acting as a virtual source. The waves radiated toward points B and C can be retrieved by cross-correlating the waves recorded at A with the waves recorded at locations B and C, respectively. In this situation one can only hope to retrieve the waves propagating to point B if there is a physical wave propagating from A to B, as indicated by the dashed arrow in figure 1, because no amount of data processing can produce a wave that does not propagate through the physical system. Similarly, a wave propagating along the solid arrow must be present to give, after cross-correlation, the wave propagating from A to C. Because in a real medium the waves propagating from an isotropic source at point A towards B and C have equal amplitude, the waves obtained from cross-correlation in the right panel must also propagate from point A in all directions with the same amplitude if the true Green's function is to be retrieved. This means that the wave propagating along the dashed and solid arrows in figure 1 must have the same intensity. This only happens when the energy of the waves propagating through the point A is independent of direction. In other words, the wavefield must be equipartitioned in the sense that the energy propagation is independent of direction.

2.2 Normal modes

The theory and practice of Green's function extraction was spurred by the work of Lobkis and Weaver (2001). Their derivation applies to any closed and undamped

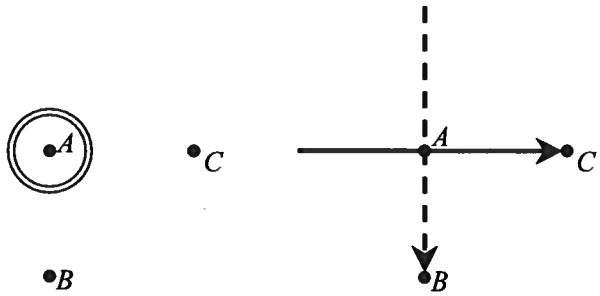

Figure 1. Left panel: a point source in a homogeneous acoustic medium at point A that emits equal amounts of energy toward points B and C. Right panel: equal energy transport along the dashed and solid arrows is needed to retrieve the Green's function for the propagation from the source point A to the points B and C.

scalar system that has normal modes $u_n(\mathbf{r})$. We briefly review their derivation because the role of equipartitioning, which in this case stipulates that different normal modes carry equal energy, is particularly clear. The Green's function can be expressed in the normal modes (Snieder, 2004b) as

$$G(\mathbf{r},\mathbf{r}',t) = \sum_m \frac{u_m(\mathbf{r})u_m(\mathbf{r}')}{\omega_m} \sin(\omega_m t)\, H(t)\ . \qquad (1)$$

where ω_m is the angular frequency of mode m and $H(t)$ is the Heaviside function.

We consider a state of the wavefield where the modal coefficients a_m and b_m are random variables:

$$u(\mathbf{r},t) = \sum_m \frac{1}{\omega_m} (a_m \cos\omega_m t + b_m \sin\omega_m t)\, u_m(\mathbf{r})\ . \qquad (2)$$

The modal coefficients are assumed to have zero mean

$$\langle a_m \rangle = \langle b_m \rangle = 0\ , \qquad (3)$$

and covariance given by

$$\langle a_n a_m \rangle = \langle a_n b_m \rangle = S^2 \delta_{nm}\ \ ,\ \ \langle a_n b_m \rangle = 0\ . \qquad (4)$$

In this work $\langle \cdots \rangle$ denotes the expectation value. The presence of the $1/\omega_m$ term in expression (2) can be understood as follows. The time derivative of equation (2) is given by $\dot{u}(\mathbf{r},t) = \sum_m (-a_m \sin\omega_m t + b_m \cos\omega_m t)\, u_m(\mathbf{r})$. From condition (4) and the fact that the modes are normalized, it follows that the different modes in equation (2) have equal kinetic energy. Because the kinetic energy of a normal mode of a linear system is equal to the potential energy (Goldstein, 1980), condition (4) implies that the normal modes carry equal energy; they are equipartitioned.

We next define the cross-correlation by

$$C_{AB}(\tau) = \langle u(\mathbf{r}_A,t) u(\mathbf{r}_B,t+\tau) \rangle\ . \qquad (5)$$

Inserting the normal mode expansion (2) gives

$$C_{AB}(\tau) = \sum_{n,m} \frac{u_n(\mathbf{r}_A)u_m(\mathbf{r}_B)}{\omega_n\omega_m} \times \{\langle a_n a_m\rangle \cos\omega_n t \cos\omega_m(t+\tau) + \langle a_n b_m\rangle \cos\omega_n t \sin\omega_m(t+\tau) + \langle b_n a_m\rangle \sin\omega_n t \cos\omega_m(t+\tau) + \langle b_n b_m\rangle \sin\omega_n t \sin\omega_m(t+\tau)\} \ . \quad (6)$$

Because of expression (4), the second and third term on the right hand side vanish and the cross-terms between different modes are zero so that

$$C_{AB}(\tau) = S^2 \sum_m \frac{u_m(\mathbf{r}_A)u_m(\mathbf{r}_B)}{\omega_m^2} \times \{\cos\omega_m t \cos\omega_m(t+\tau) + \sin\omega_m t \sin\omega_m(t+\tau)\} \ . \quad (7)$$

The term in curly brackets is equal to $\cos\omega_m\tau$, hence the cross-correlation is given by

$$C_{AB}(\tau) = S^2 \sum_m \frac{u_m(\mathbf{r}_A)u_m(\mathbf{r}_B)}{\omega_m^2} \cos\omega_m\tau \ . \quad (8)$$

Note that this expression does not depend on the absolute time t, but only on the lag-time τ. This may seem gratifying because only the lag time τ has physical meaning. Since t is not present in expression (8) one might think that the ensemble average can be replaced by a time average, but we show in section 4 that this conclusion is not correct.

The cross-correlation in expression (8) is not equal to the Green's function in equation (1), and instead we consider the time-derivative:

$$\frac{dC_{AB}(\tau)}{d\tau} = -S^2 \sum_m \frac{u_m(\mathbf{r}_A)u_m(\mathbf{r}_B)}{\omega_m} \sin\omega_m\tau \ . \quad (9)$$

This result is valid for all τ. For positive τ the right hand side is equal to $-S^2 G(\mathbf{r}_A, \mathbf{r}_B, \tau)$, while for negative τ the right hand side is equal to $S^2 G(\mathbf{r}_A, \mathbf{r}_B, -\tau)$, hence

$$\frac{dC_{AB}(\tau)}{d\tau} = -S^2 \left(G(\mathbf{r}_A, \mathbf{r}_B, \tau) - G(\mathbf{r}_A, \mathbf{r}_B, -\tau)\right) \ . \quad (10)$$

The cross-correlation is thus equal to the superposition of the Green's function and its time-reversed counterpart. Also note that this derivation hinges on equipartitioning as defined in equation (4). Note this definition of equipartitioning is different from the one given in section 2.1, and it is not obvious that these definitions are equivalent.

2.3 Waves generated on a bounding surface

We next treat the case of acoustic waves that are excited on a surface surrounding receivers. Because waves propagate outward through this surface, the system is open and thus does not support discrete normal modes. The following treatment is valid in the frequency domain using the following Fourier convention: $f(t) = \int F(\omega)\exp(i\omega t)d\omega$. Assuming that the surface is a large sphere ∂V, the radiation boundary condition on this sphere is

$$\frac{\partial u}{\partial n} = iku \ , \quad (11)$$

where k is the wavenumber and n the distance orthogonal to ∂V. In this case Green's function retrieval is expressed as the following surface integral (Derode *et al.*, 2003; Wapenaar *et al.*, 2005; Snieder *et al.*, 2007)

$$G(\mathbf{r}_A, \mathbf{r}_B, \omega) - G^*(\mathbf{r}_A, \mathbf{r}_B, \omega) = 2i\omega \oint_{\partial V} \frac{1}{\rho(\mathbf{r})c(\mathbf{r})} G(\mathbf{r}_A, \mathbf{r}, \omega)G(\mathbf{r}_B, \mathbf{r}, \omega)dS \ . \quad (12)$$

(Equation (12) differs slightly from equivalent expressions published elsewhere (Derode *et al.*, 2003; Wapenaar *et al.*, 2005) because of different Fourier conventions.) Time-reversal corresponds, in the frequency domain, to complex conjugation, hence $G - G^*$ in the left hand side of equation (12) accounts for the difference of the causal Green's function and its time-reversed counterpart, as shown in equation (10).

To complete the theory for Green's function retrieval one assumes uncorrelated sources $q(\mathbf{r}, \omega)$ of field fluctuations on the surface ∂V that satisfy

$$\langle q(\mathbf{r}_1, \omega)q^*(\mathbf{r}_2, \omega)\rangle = \frac{1}{\rho(\mathbf{r}_1)c(\mathbf{r}_1)}\delta(\mathbf{r}_1 - \mathbf{r}_2)|S(\omega)|^2 \ , \quad (13)$$

where $|S(\omega)|^2$ is the power spectrum of these sources. The factor $1/\rho c$ can be explained as follows. The power flux in an acoustic medium is given by pv^* (Morse & Ingard, 1968), with p pressure and v velocity. The velocity is related to the pressure through the impedance: $v = p/\rho c$, hence the power flux is given by $|p|^2/\rho c$. The factor $1/\rho c$ in equation (12) and the definition (13) for the sources thus ensures that all sources on the surface radiate the same amount of energy. Any wave that propagates back to the surface radiates outward by virtue of the radiation boundary condition (11). All sources on the surface radiate an equal power flux into the surface, and because of the lack of attenuation, the energy is ultimately radiated out off the surface. This is yet another example of equipartitioning.

Note that the treatment in this section treats each frequency independent from other frequencies. As a result the power spectrum $|S(\omega)|^2$ may vary with frequency, ad thus there is no reason why there should be equipartitioning between different frequencies. This treatment is different from the use of equipartitioning in the normal-mode treatment of the previous section, where expression (4) stipulates that all modes do carry the same energy.

2.4 Attenuating waves

The Green's function can also be extracted for attenuating acoustic media. In the time domain, attenuation can be described by a time-dependent compress-

ibility κ that accounts for the relaxation of the acoustic medium (Dahlen & Tromp, 1998). This corresponds to a frequency-dependent compressibility. Because of the Kramers-Kronig relations (Aki, 2002) the imaginary component of the compressibility is nonzero in the case of attenuation. For the case where the field or its normal derivative vanishes at the bounding surface, Green's function extraction can be expressed, in the frequency domain, as (Snieder, 2007)

$$G(\mathbf{r}_A,\mathbf{r}_B,\omega) - G^*(\mathbf{r}_A,\mathbf{r}_B,\omega) = \\ 2\omega \int_V (Im\ \kappa(\mathbf{r},\omega))\, G(\mathbf{r}_A,\mathbf{r},\omega) G^*(\mathbf{r}_B,\mathbf{r},\omega) dV\ , \quad (14)$$

where Im denotes the imaginary part. The Green's function can be retrieved by cross-correlating field fluctuations that are excited by uncorrelated sources throughout the volume that satisfy (Snieder, 2007)

$$\langle q(\mathbf{r}_1,\omega) q^*(\mathbf{r}_2,\omega)\rangle = (Im\ \kappa(\mathbf{r}_1,\omega))\, \delta(\mathbf{r}_1-\mathbf{r}_2) |S(\omega)|^2\ . \quad (15)$$

The source strength prescribed by expression (15) can be related to the attenuation. The potential energy of an acoustic wave p is equal to $\kappa|p|^2$ (Morse & Ingard, 1968). The time derivative of the potential energy corresponds, in the frequency domain, to

$$-i\omega\kappa|p|^2 = -i\omega\, (Re\ \kappa)\, |p|^2 + \omega\, (Im\ \kappa)\, |p|^2\ , \quad (16)$$

where Re denotes the real part. The first term in the right hand side denotes the transfer between potential and kinetic energy. This transfer is periodic and does not lead to an energy loss. The last term in expression (16) accounts for attenuation. The term $Im\ \kappa$ in the source strength (15) ensures that at every point in the medium the sources supply the same amount of energy that is locally dissipated. The source strength required for Green's function extraction of attenuating acoustic waves thus requires a balance between the injected energy and dissipated energy throughout the volume. This is another formulation of the equipartitioning requirement.

2.5 Potential fields

The principle of Green's function extraction can also be applied to potential fields. When the electrostatic potential V or the normal component of the electric field $-\partial V/\partial n$ vanishes at the boundary, Green's function extraction is expressed as (Snieder *et al.*, 2010)

$$G(\mathbf{r}_A,\mathbf{r}_B) = \int \varepsilon(\mathbf{r})\, (\nabla G(\mathbf{r}_A,\mathbf{r}) \cdot \nabla G(\mathbf{r}_B,\mathbf{r}))\, d^3r\ , \quad (17)$$

where $\varepsilon(\mathbf{r})$ is the electrical permittivity. Since the potential field is static, the Green's function does not depend on frequency. The electrostatic potential is real, which explains the absence of complex conjugates in this expression.

The Green's function for the electrostatic potential follows (Snieder *et al.*, 2010) by averaging over quasi-static field fluctuations excited by random electric dipoles $\mathbf{p}$ that are spatially uncorrelated and satisfy

$$\langle p_i(\mathbf{r}_1) p_j(\mathbf{r}_2)\rangle = |S|^2 \varepsilon(\mathbf{r}_1) \delta(\mathbf{r}_1 - \mathbf{r}_2) \delta_{ij}\ . \quad (18)$$

We next consider the energy of the field excited by such sources. The energy E of an electric field $\mathbf{E}$ is given by (Griffiths, 1999)

$$E = \frac{1}{2}\int \varepsilon\, (\mathbf{E}\cdot\mathbf{E})\, d^3r = \frac{1}{2}\int \varepsilon\, (\nabla V \cdot \nabla V)\, d^3r\ . \quad (19)$$

The last term in this expression has the same form as the right hand side of equation (17). Using field fluctuations excited by dipoles with a strength proportional to ε ensures that the electrostatic energy is constant throughout space. This is yet another expression of the principle of equipartitioning.

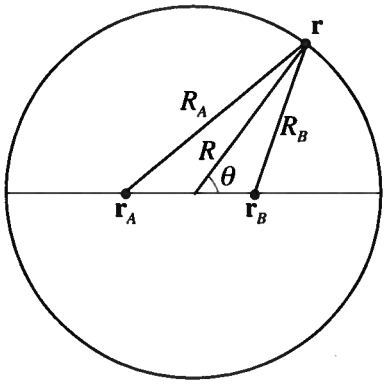

Figure 2. Geometry of the problem where sources distributed on a sphere radiate waves in phase.

3 EQUIPARTITIONING MAY NOT BE SUFFICIENT

The examples of the previous section show that in all cases the sources of the field fluctuations used for Green's function extraction must have a position and strength such that the energy density in the system is constant. This principle is formulated in different ways in various examples. Because equipartitioning is such a unifying underlying principle, one might think that the Green's function can be extracted whenever the field is equipartitioned. In this section we present counterexamples to show that even though equipartitioning may be necessary, it is not a sufficient condition for Green's function extraction.

3.1 An acoustic source

We first treat the case of acoustic waves excited on a spherical surface, as treated in section 2.1. We consider sources on a large sphere with radius R as shown in figure 2 that radiate in phase with a common frequency

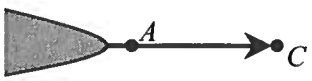

Figure 3. Sources in the stationary phase zone, indicated as the grey shaded area suffice for the extraction of the wave that propagates from A to C.

spectrum $S(\omega)$. The sources radiate inward from all points on the surface with the same intensity, and the associated wave field is certainly equipartitioned. The wavefield recorded at location $\mathbf{r}_B$ is given by

$$u(\mathbf{r}_B) = -\oint \frac{e^{ikR_B}}{4\pi R_B} dS \,, \tag{20}$$

where the distance R_B is defined in figure 2. A similar expression holds for the waves recorded at location $\mathbf{r}_A$. The integral can be evaluated exactly (Martin, 2006), but for simplicity we approximate it assuming that the radius R of the sphere is large compared to r_A and r_B. This approximation is exact in the limit $R \to \infty$. In that case we can use the approximation $R_B = R - r_B \cos\theta$ in the exponent of equation (20), and we replace R_B by R in the denominator. This gives

$$u(\mathbf{r}_B) = -\oint \frac{e^{ik(R - r_B\cos\theta)}}{4\pi R} dS$$

$$= -\frac{e^{ikR}}{4\pi R}\oint e^{-ikr_B\cos\theta} dS = -\frac{e^{ikR}}{R}\mathrm{sinc}(kr_B) \,. \tag{21}$$

A similar expression holds for $u(\mathbf{r}_A)$, hence

$$\langle u(\mathbf{r}_A) u^*(\mathbf{r}_B)\rangle = \frac{|S(\omega)|^2}{R^2}\mathrm{sinc}(kr_A)\mathrm{sinc}(kr_B) \,. \tag{22}$$

According to expression (12), exact Green's function extraction should give

$$G(\mathbf{r}_A, \mathbf{r}_B, \omega) - G^*(\mathbf{r}_A, \mathbf{r}_B, \omega)$$
$$= 2iIm\left(G(\mathbf{r}_A, \mathbf{r}_B, \omega)\right) = \frac{k}{2\pi}\mathrm{sinc}(k|\mathbf{r}_A - \mathbf{r}_B|) \,, \tag{23}$$

where we used that for the employed homogeneous medium $G(\mathbf{r}_A, \mathbf{r}_B, \omega) = -\exp(ik|\mathbf{r}_A - \mathbf{r}_B|)/4\pi(k|\mathbf{r}_A - \mathbf{r}_B|)$. Expressions (22) and (23) have different space dependencies, and thus describe different physical functions. This means that the cross-correlation of fields excited by simultaneous sources on the sphere does not give the Green's function, despite the fact that the wave field is equipartitioned. This should not be surprising, because we violated condition (13) which calls for uncorrelated sources. This example shows that while equipartitioning may be a necessary condition, but it is not a sufficient condition.

In this particular example, one may construct the Green's function for a given pair of receivers without equipartitioning. In order to extract the wave propagating from point A to point C in figure 3 it suffices to have sources in the grey area (Snieder, 2004a). Waves excited in the grey area provide a cross-correlation that is, to first order, independent of the source location. The grey area is called the *stationary phase region.* Sources outside this region do not give a net contribution to the cross-correlation, and hence for the wave that propagates from A to C one only needs sources in the stationary phase region. Equipartitioning is thus not even necessary if one only seeks to retrieve the direct wave that propagates from A to C. In fact, there are several studies that indicate that the surface wave extracted from the cross-correlation of microseismic noise propagate preferentially away from coastlines, e.g. (Stehly *et al.*, 2006). This is an indication that although the surface waves are not equipartitioned, it is still possible to extract surface waves from the cross-correlation of such measurements. Alternatively, one can pre-process data that are not equipartitioned to make the energy flux less dependent on direction (Mulargia & Castellaro, 2008; Curtis & Halliday, 2010).

3.2 Normal modes

Let us next consider a closed undamped system with normal modes as treated in section 2.2. We assume that all the modes carry the same energy, but we drop the condition that the excitation coefficients of the modes are uncorrelated. This means that instead of equation (4) we assume that

$$a_n = b_n = \frac{S}{\omega_n} \,. \tag{24}$$

This state is clearly equipartitioned. Repeating the steps leading to equation (9) gives for these modal coefficients

$$\frac{dC_{AB}(\tau)}{d\tau} = S^2 \sum_{n,m} \frac{u_n(\mathbf{r}_A) u_m(\mathbf{r}_B)}{\omega_n}$$

$$\times \{\sin((\omega_m - \omega_n)t + \omega_m\tau) + \cos((\omega_m + \omega_n)t + \omega_m\tau)\} \,. \tag{25}$$

Note that this expression is different from expression (9) in two ways: first, it contains a double sum over modes rather than a single sum; second, it depends on τ *and* t instead of τ only. Both differences are due to the fact that we used correlated modal coefficients. This example also illustrates that equipartitioning is not a sufficient condition for Green's function retrieval.

3.3 Waves generated on a bounding surface

In the previous examples we violated the requirement for Green's function retrieval in trivial ways. In this section we show a more subtle example of a wave state that is equipartitioned, but that does not give the correct Green's function. We consider an open acoustic system, as discussed in section 2.3, and present a numerical example in two space dimensions (Fan & Snieder, 2009) with the geometry shown in figure 4. In an area of 80

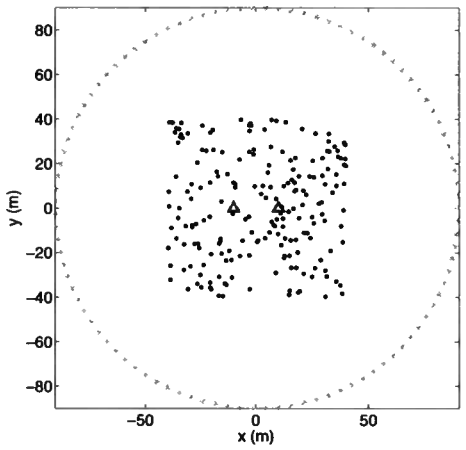

Figure 4. Geometry for the numerical example of 2D scattering by 200 scatterers (dots) of waves excited by sources on a circle. Receivers are indicated by triangles.

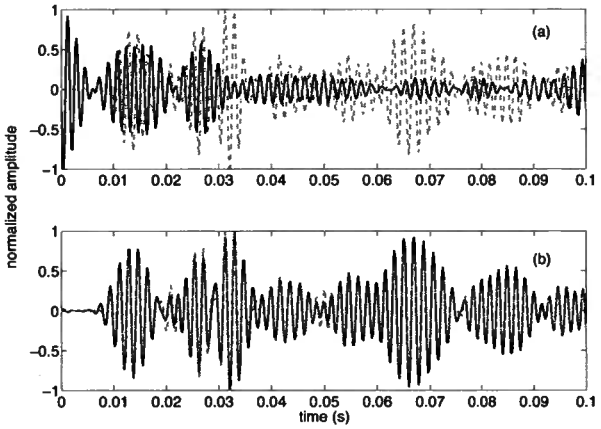

Figure 5. Top panel: the true Green's function (red line) and the Green's function estimated from the cross correlation of waves excited by a single source (black line). Bottom panel: the true Green's function (red line) and the Green's function estimated from the cross correlation of waves excited by 300 sources placed uniformly on a circle (black line).

m by 80 m, 200 strong isotropic point scatterers are located. We computed synthetic seismograms using a variation of Foldy's method (Groenenboom, 1995). Sources are placed on a circle with a radius of 90 m. Two receivers are placed in the center of the scattering region at a distance of 20 m. The distance between both receivers and the edge of the region with scatterers is 30 m. We show the true Green's function within the employed frequency band by the red lines in both panels of figure 5. The Green's function estimated from equation (12) using 300 sources placed uniformly on a circle with a radius of 90 m is indicated by the black lines in the bottom panel of figure 5. In this case the Green's function is retrieved accurately.

In the numerical example, the transport scattering mean free path is given by $l_* = 1/(N\sigma)$ (Sheng, 1995), where σ is the scattering cross section and N is the scatterer density. The transport mean free path is defined as the distance over which the direction of wave propagation is randomized by scattering (Sheng, 1995). For the employed scatterer configuration, $\sigma = 1.6$ m, $N = 200/(80 \text{ m})^2$, hence $l_* = 5$ m. Both receivers are separated by a distance of 30 m from the edge of the scattering domain, which means that any wave recorded at the receivers has propagated over at least six times the transport mean free path. The waves used in this numerical experiment have propagated over at least six times this distance, and thus for all practical purposes are equipartitioned.

We next consider the case where one source is placed at a distance of 90 m from the center of the scattering array. Since this wave field is equipartitioned because of strong scattering, one might think that computing the cross-correlation of the waves generated by this single source would give the Green's function. The cross-correlation of these waves is shown by the black solid line in the upper panel of figure 5. This cross-correlation does not resemble the true Green's function (indicated in red) at all. The cross-correlation of waves excited by a single source does not give the Green's function because equation (12) requires sources everywhere on a closed surface; replacing this by a single source on that surface is not an adequate discretization of the surface integral. Yet the wave state generated by a single source is for all practical purposes equipartitioned after it has propagated over at least six times the transport mean free path to the receivers. This is another example of an equipartitioned wave state that does not suffice to give the Green's function.

4 WHAT DOES THIS MEAN FOR THE EARTH?

One might wonder which of the schemes for Green's function retrieval presented in section 2 is applicable to the earth. The short answer is that none of these methods is applicable for all types of wave propagation at all frequencies in the earth. The different schemes each have different restrictions that we discuss below.

First consider the model of sources that generate waves propagating in all possible directions, as discussed in section 2.1. Conceptually, this model is applicable to surface waves that are excited by uncorrelated noise sources near the earth's surface. The extraction of surface wave from the cross-correlation of noise has been very successful in the microseismic band with periods between 5 s and 10 s (Campillo & Paul, 2003). The path coverage obtained by cross-correlating waves recorded at numerous receivers pairs has fundamentally changed crustal tomography (Shapiro *et al.*, 2005; Sabra *et al.*, 2005). The extraction of the surface waves from

noise has also been applied to longer periods (Shapiro & Campillo, 2004; Nishida *et al.*, 2009). The station density currently offered by US Array makes it possible to even retrieve the full surface wave field propagating from one receiver through the array (Lin *et al.*, 2009). In practice, the microseismic noise is not generated with the same strength at all locations, and the retrieved surface waves are strongest in directions propagating away from oceanic regions with large wave activity (Stehly *et al.*, 2006). When the isotropy in the microseismic noise is a limiting factor in the retrieval of the surface waves, one can cross-correlate the coda of extracted surface waves again in order to utilize surface waves that are better equipartitioned (Stehly *et al.*, 2008). One can retrieve the different elements of the Green's tensor by cross-correlating different pairs of components of the recorded ground motion (Campillo & Paul, 2003; Snieder, 2004a).

The work of Lobkis and Weaver (2001) had a huge impact because the theory is very elegant and the employed formulation in normal modes is natural for global seismologists. Although the derivation is correct, it is strictly speaking not applicable to the earth for a number of reasons. First, the modes of the earth certainly are not equipartitioned. Since most of the noise is generated near the surface of the earth, the modes that are confined to the near-surface carry more energy than modes that penetrate deep into the earth. In practice, the fundamental mode surface wave carries the most energy, and it is for this reason that estimates of the earth's Green's function usually are dominated by the fundamental mode surface wave. The second reason why the method is not applicable to the earth is that the formalism truly calls for an ensemble average. The employed model assumes there is no attenuation, which means that once the modes are excited, they oscillate forever without any change in the modal excitation. This means that a time average is not equivalent to an ensemble average, and one would need an ensemble of earths to implement the theory. We show in appendix A that for a damped oscillator that is periodically kicked for $t > 0$, the cross-correlation $C(\tau) = \langle x(t)x(t+\tau)\rangle$ is given by

$$\frac{dC(\tau)}{d\tau} = -\frac{\langle F^2\rangle}{4m^2T\gamma}\left(G(\tau) - G(-\tau)\right) . \tag{26}$$

In this expression T is the time between kicks, $\langle F^2\rangle$ is the average of the square of the forces during the kicks, and γ is the damping parameter. This equation shows that expression (10) can be generalized to include attenuation. Third, for an *undamped* oscillator that is excited by random forces with zero mean, the cross-correlation grows linearly with time

$$\frac{dC(\tau)}{d\tau} = -\frac{\langle F^2\rangle}{2m^2T}t\left(G(\tau) - G(-\tau)\right) . \tag{27}$$

(In essence the change from expression (26) to (27) follows from taking the limit: $\lim_{\gamma\to 0}\left\{1-\exp(-2\gamma t)\right\}/\gamma = 2t$.) Because of this secular growth, such a system cannot be in equilibrium.

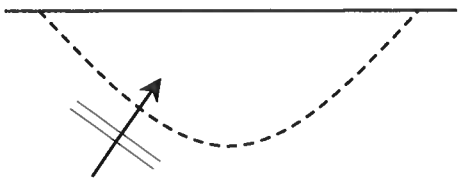

Figure 6. Teleseismic waves propagating through a bounding surface illuminate the crust from below.

This growth is due to the fact that the energy of an undamped kicked oscillator grows linearly with time, even when the average of the forces vanishes (Snieder *et al.*, 2010). These last two points are mostly academic, because in practice there is attenuation, and when the earth is continuously excited, the modal coefficients are effectively "reset" at a time equal to the attenuation time of waves in the earth. For thermal fluctuations this can be described by using time-dependent modal coefficients that satisfy in the notation of this paper $\langle a_n(t)a_m(t')\rangle = \delta_{nm}2k_BT\exp(\gamma|t-t'|)$, where k_BT is the thermal energy (Weaver & Lobkis, 2003). As we show in expression (26), the theory of Lobkis and Weaver (2001) can be extended to include attenuation and an explicit description of the force that excites field fluctuations.

As discussed in section 2.3, the Green's function can be retrieved from the cross-correlation of field fluctuations excited by sources on a bounding surface. This principle can be extended to elastic waves without including sources at the earth's surface (Wapenaar, 2004). In practice, however, there are insufficient sources in the interior of the earth to provide the required excitation for field fluctuations on the closed surface surrounding the receivers. This hurdle has been overcome (Bostock, 2004; Bostock *et al.*, 2002; Kumar & Bostock, 2006) by using teleseismic waves that impinge on the crust from below, as shown in figure 6. In that case the teleseismic waves propagating through the dashed surface in figure 6 replace the sources on that surface. The reflections of these waves by the earth's free surface can be used to image the crust. This principle was theoretically shown earlier by Claerbout (1968) who demonstrated that the reflection response of a layered system can be retrieved from the cross-correlation of the transmission response.

In reality the earth is attenuating, and one may wonder whether the formalism for attenuating waves presented in section 2.4 can be the basis for Green's function extraction. In order to use this theory one must have sources that are proportional to the attenuation. For a damped system in equilibrium, the excitation must balance the attenuation; otherwise the system would not be in equilibrium. This principle was shown originally for voltage fluctuations in a resistor (Nyquist, 1928) and was later generalized as the *fluctuation dissipation theorem* (Greene & Callen, 1951; Callen & Welton, 1951; Weber, 1956). According to this theorem, the

response of a system in thermal equilibrium can be extracted from field fluctuations. The condition of equilibrium implies that thermal fluctuations must balance the dissipation. Unfortunately, thermal fluctuations in the earth are extremely weak. Boltzman's constant is given by $k_B = 1.4 \times 10^{-23}$ J/K, and the thermal energy for a mantle temperature of 600 K is equal to $k_B T = 8.4 \times 10^{-21}$ J. In comparison, a child with a mass of 50 kg jumping from a table 1 m high releases an energy equal to 500 J. It is thus clear that thermal fluctuations and the fluctuation dissipation theorem are irrelevant for observable field fluctuations in the earth. Thermal fluctuations are more for electrical fields where the accuracy of voltmeters is getting close to the voltage generated by thermal fluctuations (Slob *et al.*, 2010).

5 DISCUSSION

The different examples in this work require equipartitioning in some sense for Green's function retrieval, but it it not clear to what extent these different requirements are equivalent. For example, does the condition that the modes of a closed system carry the same energy imply that the energy density is homogeneous in space and that energy propagates equally in all directions? Questions like this require further research. As we show in by several examples in section 3, the requirement of equipartitioning is not sufficient for Green's function retrieval.

As shown in the previous section, none of the sources of field fluctuations in the earth is adequate to provide the full Green's function. In general, the surface waves in the retrieved Green's function are strongest, e.g. (Shapiro & Campillo, 2004; Halliday *et al.*, 2008a). The body waves are usually underrepresented, and, with the exception of studies based on teleseismic body waves (Bostock, 2004; Bostock *et al.*, 2002; Kumar & Bostock, 2006), the number of studies that report extracting body waves is modest (Roux *et al.*, 2005; Gerstoft *et al.*, 2006; Draganov *et al.*, 2007; Draganov *et al.*, 2009). The reason for the under-representation of body waves is that for the retrieval of the direct surface wave it suffices to have sources anywhere on the earth surface in a region that straddles a line through the used receivers, as sketched in figure 3. This is a relatively weak condition that is readily satisfied. Forghani and Snieder (2010) show in more detail why it is more difficult to extract body waves from field fluctuations then it is for surface waves. The dominance of the fundamental mode surface waves in Green's function extraction has led to spectacular advances in surface wave tomography, e.g. (Shapiro *et al.*, 2005; Sabra *et al.*, 2005). The extension of this principle beyond the microseismic band (Shapiro & Campillo, 2004; Nishida *et al.*, 2009) holds promise for the determination of mantle structure as well. In most applications of Green's function extraction the surface wave is very strong. For this reason Draganov *et al.* (2009) process the recorded noise extensively before cross-correlation in order to suppress surface waves. The over-representation of surface waves in Green's function retrieval can be advantageous when using the retrieved surface wave for adaptive ground-roll removal in exploration seismology (Halliday *et al.*, 2008b; Xue *et al.*, 2009).

Green's function extraction has also been successful in quasi one-dimensional problems, because for waves propagating along a line one needs only sources on the line on both sides of the receiver. In fact, in the presence of an open boundary one needs only a source on one side of the receivers. This has successfully been applied to Green's function retrieval for buildings that are shaken at the base (Snieder & Şafak, 2006; Kohler *et al.*, 2007). Another example is Green's function retrieval for the shallow subsurface (Trampert *et al.*, 1993; Mehta *et al.*, 2007; Sawazaki *et al.*, 2009). In this application, the low wave velocity in the near surface results in near-vertical wave propagation. In combination with a locally layered earth structure, this makes the wave propagation quasi one-dimensional. In these quasi 1D applications, deconvolution rather than correlation is used because it removes the spectral variations of the excitation without introducing unwanted artifacts (Vasconcelos & Snieder, 2008).

Much research on Green's function extraction was spurred by the work of Lobkis and Weaver (Lobkis & Weaver, 2001). Their normal mode formulation is only relevant for the long-wavelength motion of the earth that is described well by a superposition of normal modes. Although the theory of Lobkis and Weaver (2001) is correct for the low-frequency motion, it is not directly applicable to the earth because the lack of attenuation used in their theory implies one of two things: either the earth is excited once and the modal coefficient keep their value in time, or the earth is excited continuously and the elastic energy in the earth grows linearly with time. In the former case the ensemble average needed in their theory cannot be taken because we have only one realization. In the latter case, the earth is not in equilibrium. These inconsistencies are resolved by accounting for the (weak) attenuation that is present in the earth. Because of attenuation, the vibrations of the earth damp out over a typical attenuation time. This causes the ambient vibrations of the earth to be in equilibrium, and the modal coefficients are effectively "reset" after the characteristic attenuation time. We have shown that attenuation can be incorporated in Green's function extraction based on normal modes, which explains why the theory the Lobkis and Weaver (2001) not only inspired the seismological community; it also provided a recipe for Green's function extraction (by cross-correlation) that is for practical purposes correct.

Acknowledgements. We appreciate the thoughtful comments of Simon Luo and Francesco Perrone.

REFERENCES

Aki, K.and Richards, P.G. 2002. *Quantitative Seismology.* Second edn. Sausalito: Univ. Science Books.

Bostock, M.G. 2004. Kirchhoff-approximate inversion of teleseismic wavefields. *Geophys. J. Int.*, **149**, 787–795.

Bostock, M.G., Hyndman, R.D., Rondenay, S., & Peacock, S.M. 2002. An inverted continental Moho and serpentinization of the forearc mantle. *Nature*, **417**, 536–538.

Callen, H.B., & Welton, T.A. 1951. Irreversibility and generalized noise. *Phys. Rev.*, **83**, 34–40.

Campillo, M., & Paul, A. 2003. Long-range correlations in the diffuse seismic coda. *Science*, **299**, 547–549.

Claerbout, J.F. 1968. Synthesis of a layered medium from its acoustic transmission response. *Geophysics*, **33**, 264–269.

Curtis, A., & Halliday, D. 2010. Directional balancing for seismic and general wavefield interferometry. *Geophysics*, **75**, SA1–SA14.

Curtis, A., Gerstoft, P., Sato, H., Snieder, R., & Wapenaar, K. 2006. Seismic interferometry – turning noise into signal. *The Leading Edge*, **25**, 1082–1092.

Dahlen, F.A., & Tromp, J. 1998. *Theoretical Global Seismology.* Princeton: Princeton University Press.

Derode, A., Larose, E., Tanter, M., de Rosny, J., Tourin, A., Campillo, M., & Fink, M. 2003. Recovering the Green's function from far-field correlations in an open scattering medium. *J. Acoust. Soc. Am.*, **113**, 2973–2976.

Draganov, D., Wapenaar, K., Mulder, W., Singer, J., & Verdel, A. 2007. Retrieval of reflections from seismic background-noise measurements. *Geophys. Res. Lett.*, **34**, L04305.

Draganov, D., Campman, X., Thorbecke, J., Verdel, A., & Wapenaar, K. 2009. Reflection images from ambient seismic noise. *Geophysics*, **74**, A63–A67.

Fan, Y., & Snieder, R. 2009. Required source distribution for interferometry of waves and diffusive fields. *Geophys. J. Int.*, **179**, 1232–1244.

Forghani, F., & Snieder, R. 2010. Underestimation of body-waves and feasibility of surface-wave reconstruction by seismic interferometry. *The Leading Edge, submitted.*

Gerstoft, P., Fehler, M.C., & Sabra, K.G. 2006. When Katrina hit California. *Geophys. Res. Lett.*, **33**, L17308.

Goldstein, H. 1980. *Classical Mechanics, 2nd Ed.* Reading MA: Addison-Wesley.

Greene, R.F., & Callen, H.B. 1951. On the formulation of thermodynamic fluctuation theory. *Phys. Rev.*, **83**, 1231–1235.

Griffiths, D.J. 1999. *Introduction to Electrodynamics.* 3rd edn. Upper Saddle River, NJ: Prentice Hall.

Groenenboom, J.and Snieder, R. 1995. Attenuation, Dispersion and Anisotropy by Multiple Scattering of Transmitted Waves Through Distributions of Scatterers. *J. Acoust. Soc. Am.*, **98**, 3482–3492.

Halliday, D., Curtis, A., & Kragh, E. 2008a. Seismic surface waves in a suburban enviroment: active and passive interferometric methods. *The Leading Edge*, **27**, 210–218.

Halliday, D.F., Curtis, A., Robertsson, J.O.A., & van Manen, D.-J. 2008b. Interferometric surface-wave isolation and removal. *Geophysics*, **72**, A69–A73.

Kohler, M.D., Heaton, T.H., & Bradford, S.C. 2007. Propagating waves in the steel, moment-frame Factor Building recorded during earthquakes. *Bull. Seismol. Soc Am.*, **97**, 1334–1345.

Kumar, M.R., & Bostock, M.G. 2006. Transmission to reflection transformation of teleseismic wavefields. *J. Geophys. Res.*, **111**, B08306.

Larose, E., Margerin, L., Derode, A., van Tiggelen, B., Campillo, M., Shapiro, N., Paul, A., Stehly, L., & Tanter, M. 2006. Correlation of random wavefields: an interdisciplinary review. *Geophysics*, **71**, SI11–SI21.

Lin, F.C., Ritzwoller, M.H., & Snieder, R. 2009. Eikonal tomography: surface wave tomography by phase front tracking across a regional broad-band seismic array. *Geophys. J. Int.*, **177**, 1091–1110.

Lobkis, O.I., & Weaver, R.L. 2001. On the emergence of the Green's function in the correlations of a diffuse field. *J. Acoust. Soc. Am.*, **110**, 3011–3017.

Malcolm, A., Scales, J., & van Tiggelen, B.A. 2004. Extracting the Green's function from diffuse, equipartitioned waves. *Phys. Rev. E*, **70**, 015601.

Martin, P.A. 2006. *Multiple scattering.* Encyclopedia of mathematics and its applications, vol. 107. Cambridge, UK: Cambridge Univ. Press.

Mehta, K., Snieder, R., & Graizer, V. 2007. Extraction of near-surface properties for lossy layered medium using propagator matrix. *Geophys. J. Int.*, **168**, 271–280.

Morse, P.M., & Ingard, K.U. 1968. *Theorerical Acoustics.* New York: McGraw-Hill.

Mulargia, F., & Castellaro, S. 2008. Passive imaging in nondiffusive acoustic wavefields. *Phys. Rev. Lett.*, **100**, 218501.

Nishida, K., Montagner, J.-P., & Kawakatsu, H. 2009. Global Surface Wave Tomography Using Seismic Hum. *Science*, **326**, 112.

Nyquist, H. 1928. Thermal agitation of electric charge in conductors. *Phys. Rev.*, **32**, 110–113.

Roux, P., Sabra, K.G., Gerstoft, P., & Kuperman, W.A. 2005. P-waves from cross correlation of seismic noise. *Geophys. Res. Lett.*, **32**, L19303, doi: 10.1029/2005GL023803.

Sabra, K.G., Gerstoft, P., Roux, P., Kuperman, W.A., & Fehler, M.C. 2005. Surface wave tomography from microseisms in Southern California. *Geophys. Res. Lett.*, **32**, L14311.

Sánchez-Sesma, F.J., Pérez-Ruiz, J.A., Luzón, F., Campillo, M., & Rodríguez-Castellanos, A. 2008. Diffuse fields in dynamic elasticity. *Wave Motion*, **45**, 641–654.

Sawazaki, K., Sato, H., Nakahara, H., & Nishimura, T. 2009. Time-Lapse Changes of Seismic Velocity in the Shallow Ground Caused by Strong Ground Motion Shock of the 2000 Western-Tottori Earthquake, Japan, as Revealed from Coda Deconvolution Analysis. *Bull. Seismol. Soc. Am.*, **99**, 352–366.

Schuster, G. 2009. *Seismic Interferometry.* Cambridge, UK: Cambridge Univ. Press.

Shapiro, N.M., & Campillo, M. 2004. Emergence of broadband Rayleigh waves from correlations of the ambient seismic noise. *Geophys. Res. Lett.*, **31**, L07614.

Shapiro, N.M., Campillo, M., Stehly, L., & Ritzwoller, M.H. 2005. High-resolution surface-wave tomography from ambient seismic noise. *Science*, **307**, 1615–1618.

Sheng, P. 1995. *Introduction to Wave Scattering, Localiza-*

tion, and Mesoscopic Phenomena. San Diego: Academic Press.

Slob, E., Snieder, R., & Revil, A. 2010. Retrieving electric resistivity data from self-potential measurements by cross-correlation. *Geophys. Res. Lett.*, **37**, L04308.

Snieder, R. 2004a. Extracting the Green's function from the correlation of coda waves: A derivation based on stationary phase. *Phys. Rev. E*, **69**, 046610.

Snieder, R. 2004b. *A Guided Tour of Mathematical Methods for the Physical Sciences.* 2nd edn. Cambridge, UK: Cambridge Univ. Press.

Snieder, R. 2007. Extracting the Green's function of attenuating heterogeneous acoustic media from uncorrelated waves. *J. Acoust. Soc. Am.*, **121**, 2637–2643.

Snieder, R., & Şafak, E. 2006. Extracting the building response using seismic interferometry; theory and application to the Millikan Library in Pasadena, California. *Bull. Seismol. Soc. Am.*, **96**, 586–598.

Snieder, R., Wapenaar, K., & Wegler, U. 2007. Unified Green's function retrieval by cross-correlation; connection with energy principles. *Phys. Rev. E*, **75**, 036103.

Snieder, R., E., Slob., & Wapenaar, K. 2010. Lagrangian Green's function extraction, with applications to potential fields, diffusion, and acoustic waves. *New J. Phys., in press.*

Stehly, L., Campillo, M., & Shapiro, N.M. 2006. A study of seismic noise from long-range correlation properties. *J. Geophys. Res.*, **111**, B10306.

Stehly, L., Campillo, M., Froment, B., & Weaver, R.L. 2008. Reconstructing Green's function by correlation of the coda of the correlation (C3) of ambient seismic noise. *J. Geophys. Res.*, **113**, B11306.

Trampert, J., Cara, M., & Frogneux, M. 1993. *SH* propagator matrix and Q_s estimates from borehole- and surface-recorded earthquake data. *Geophys. J. Int.*, **112**, 290–299.

Vasconcelos, I., & Snieder, R. 2008. Interferometry by deconvolution, Part 1 Theory for acoustic waves and numerical examples. *Geophysics*, **73**, S115–S128.

Wapenaar, K. 2004. Retrieving the elastodynamic Green's function of an arbitrary inhomogeneous medium by cross correlation. *Phys. Rev. Lett.*, **93**, 254301.

Wapenaar, K., Fokkema, J., & Snieder, R. 2005. Retrieving the Green's function by cross-correlation: a comparison of approaches. *J. Acoust. Soc. Am.*, **118**, 2783–2786.

Wapenaar, K., Draganov, D., & Robertsson, J.O.A. (eds). 2008. *Seismic Interferometry: History and Present Status.* SEG Geophysics Reprints Series, vol. 26. Tulsa, OK: Society of Exploration Geophysics.

Weaver, R.L., & Lobkis, O.I. 2003. Elastic wave thermal fluctuations, ultrasonic waveforms by correlation of thermal phonons. *J. Acoust. Soc. Am.*, **113**(5), 2611–2621.

Weaver, R.L., & Lobkis, O.I. 2006. The mean and variance of diffuse field correlations in finite bodies. *J. Acoust. Soc. Am.*, **118**, 3447–3456.

Weber, J. 1956. Fluctuation-dissipation theorem. *Phys. Rev.*, **101**, 1620–1626.

Xue, Y., Dong, S., & Schuster, G.T. 2009. Interferometric prediction and subtraction of surface waves with a nonlinear local filter. *Geophysics*, **74**, SI1.

APPENDIX A: RETRIEVING THE GREEN'S FUNCTION OF A KICKED OSCILLATOR BY CROSS-CORRELATION

As a prototype of the behavior of an excited mode we consider the response of a kicked damped oscillator that satisfies

$$m\ddot{x} + 2\gamma\dot{x} + \omega_0^2 x = F(t) \; , \tag{A1}$$

where $F(t)$ is the excitation and γ the damping. The Green's function of the oscillator is the solution to a force $F(t) = \delta(t)$ and is given by

$$G(t) = \frac{1}{\omega} e^{-\gamma t} \sin(\omega t) H(t) \; , \tag{A2}$$

where $H(t)$ is the Heaviside function and

$$\omega = \sqrt{\omega_0^2 - \gamma^2} \; . \tag{A3}$$

We consider a forcing that for $t > 0$ consists of a sequence of kicks at times $t_n = nT$:

$$F(t) = \sum_{n=0}^{\infty} F_n \delta(t - nT) \; . \tag{A4}$$

The kicks F_n are random with zero mean, while the different kicks are uncorrelated

$$\langle F_n \rangle = 0 \;\; , \;\; \langle F_n F_m \rangle = \langle F^2 \rangle \delta_{nm} \; , \tag{A5}$$

where $\langle \cdots \rangle$ denotes an ensemble average. The response to this forcing is given by

$$x(t) = \frac{1}{m} \sum_{0<nT<t} G(t - nT) F_n \; . \tag{A6}$$

Because of the random nature of the kicks, $x(t)$ is a random function. Since the kicks have zero mean, the expectation value of $x(t)$ vanishes

$$\langle x(t) \rangle = 0 \; . \tag{A7}$$

We define the cross-correlation as

$$C(\tau) = \langle x(t) x(t+\tau) \rangle \; . \tag{A8}$$

Using expression (A6) the covariance is given by

$$\begin{aligned} C(\tau) = \;& \frac{1}{m^2} \textstyle\sum_{0<nT<t} \sum_{0<mT<t+\tau} \\ & \times G(t - nT) G(t + \tau - mT) \langle F_n F_m \rangle \; . \end{aligned} \tag{A9}$$

We consider the case $\tau > 0$ first. Using expression (A5) for the expectation value of the kicks one can reduce the double sum in equation (A9) to a single sum where only the kicks at times $0 < nT < t$ contribute

$$C(\tau) = \frac{\langle F^2 \rangle}{m^2} \sum_{0<nT<t} G(t - nT) G(t + \tau - nT) \; . \tag{A10}$$

We assume that the time interval between kicks is much less than the period ($\omega T \ll 1$). In that case the sum over

kicks in expression (A10) can be replaced by an integral using

$$\begin{aligned}\textstyle\sum_{0<nT<t} f(t-nT) \quad &\rightarrow \frac{1}{T}\int_0^t f(t-t')dt' \\ &= \frac{1}{T}\int_0^t f(t')dt' \,,\end{aligned} \tag{A11}$$

where the change of variable $t' \rightarrow t - t'$ is used in the last identity. Using this in equation (A10) gives

$$C(\tau) = \frac{\langle F^2\rangle}{m^2 T}\int_0^t G(t')G(t'+\tau)dt' \,. \tag{A12}$$

Inserting expression (A2) in the right hand side, evaluating the time integral and using equation (A4) gives

$$\begin{aligned}C(\tau) = &\frac{\langle F^2\rangle}{4m^2\omega_0^2 T\gamma}e^{-\gamma\tau}\left(\cos\omega\tau + \frac{\gamma}{\omega}\sin\omega\tau\right) \\ &-\frac{\langle F^2\rangle}{4m^2\omega^2 T\gamma}e^{-2\gamma t}e^{-\gamma\tau}\times \\ &\left(\cos\omega\tau - \frac{\gamma^2}{\omega_0^2}\cos\omega(2t+\tau) + \frac{\gamma\omega}{\omega_0^2}\sin\omega(2t+\tau)\right) \,.\end{aligned} \tag{A13}$$

Note the different frequencies in the denominator of the two terms in this expression. The second term in this expression decays exponentially with time because of the term $\exp(-2\gamma t)$, this term accounts for the transients associated with starting the kicks. For long times ($\gamma t \rightarrow \infty$) only the first term remains. This term does not depend on t, and hence the average over time t in the long time limit is equal to the expectation value. Taking the derivative of the first term with respect to τ, and using equations (A2) and (A4), gives in the long time limit ($\gamma t \rightarrow \infty$)

$$\frac{dC(\tau)}{d\tau} = -\frac{\langle F^2\rangle}{4m^2 T\gamma}G(\tau) \qquad \text{for } \tau > 0 \,. \tag{A14}$$

For $\tau < 0$ the derivation is analogous, except that now only the kicks at times $0 < nT < t + \tau$ contribute, and that the substitution (A11) should be modified into

$$\begin{aligned}\textstyle\sum_{0<nT<t+\tau} f(t-nT) \quad &\rightarrow \tfrac{1}{T}\int_0^{t+\tau} f(t-t')dt' \\ &= \tfrac{1}{T}\int_{-\tau}^t f(t')dt' \,.\end{aligned} \tag{A15}$$

Using this, and taking the same steps as in the derivation of expression (A13), gives for the long-time behavior of the cross-correlation

$$C(\tau) = \frac{\langle F^2\rangle}{4m^2\omega_0^2 T\gamma}e^{\gamma\tau}\left(\cos\omega\tau - \frac{\gamma}{\omega}\sin\omega\tau\right) + O\left(e^{-2\gamma t}\right) \tag{A16}$$

Taking the derivative and using equations (A2) and (A4) gives in the long-time limit

$$\frac{dC(\tau)}{d\tau} = \frac{\langle F^2\rangle}{4m^2 T\gamma}G(-\tau) \qquad \text{for } \tau < 0 \,. \tag{A17}$$

Expressions (A14) and (A17) can be combined to the expression (26) that is valid for all τ. Note that the factor that multiplies the Green's function does not depend on frequency, this means that the kicked oscillator delivers an equal energy to the system regardless of the frequency, in the multi-mode system analyzed by Lobkis and Weaver (2001) this implies equipartitioning of energy among modes.

Let us next consider what happens when the attenuation is switched off. Mathematically this is achieved by taking the lime $\gamma \rightarrow 0$. We take this limit for the case $\tau > 0$ and apply it to expression (A13). In the limit $\gamma \rightarrow 0$ the transient terms in the last line of equation (A13) do not decay exponentially with time. Expanding all terms in γ and using that according to equation (A4) ω and ω_0 are equal to each other to first order in γ, gives

$$\begin{aligned}C(\tau) = &\frac{\langle F^2\rangle}{4m^2\omega_0^2 T} \\ &\times\left(2t\cos\omega_0 t + \tfrac{1}{\omega_0}\left(\sin\omega_0\tau - \sin\omega_0(\tau+2t)\right)\right) \,.\end{aligned} \tag{A18}$$

Note that the first term grows linearly with time. This means that for the kicked undamped oscillator the correlation does not approach a constant value for long times, and that the ensemble average cannot be replaced by a time average. Physically this is due to the fact that the energy of a kicked undamped oscillator grows linearly with time, even when the mean of the kicks vanishes (Snieder *et al.*, 2010). For long times ($\omega_0 t \gg 1$) the first term in equation (A18) dominates, and a comparison with expression (A2) shows that

$$\frac{dC(\tau)}{d\tau} = -\frac{\langle F^2\rangle}{2m^2 T}tG(\tau) \qquad \text{for } \tau > 0 \,. \tag{A19}$$

Apart from the secular growth term (t), the cross-correlation does produce the correct Green's function. A similar analysis for $\tau < 0$ leads to equation (27).

Eikonal tomography: Surface wave tomography by phase-front tracking across a regional broad-band seismic array

Fan-Chi Lin[1], Michael H. Ritzwoller[1] & Roel Snieder[2]
[1] *Center for Imaging the Earth's Interior, Dept. of Physics, University of Colorado at Boulder*
[2] *Center for Wave Phenomena, Colorado School of Mines, Golden, CO 80401*

ABSTRACT
We present a new method of surface wave tomography based on applying the Eikonal equation to observed phase travel time surfaces computed from seismic ambient noise. The source-receiver reciprocity in the ambient noise method implies that each station can be considered to be an effective source and the phase travel time between that source and all other stations is used to track the phase front and construct the phase travel time surface. Assuming that the amplitude of the waveform varies smoothly, the Eikonal equation states that the gradient of the phase travel time surface can be used to estimate both the local phase speed and the direction of wave propagation. For each location, we statistically summarize the distribution of azimuthally dependent phase speed measurements based on the phase travel time surfaces centered on different effective source locations to estimate both the isotropic and azimuthally anisotropic phase speeds and their uncertainties. Examples are presented for the 12 and 24 sec Rayleigh waves for the EarthScope/USArray Transportable Array stations in the western US. We show that: (i) the major resulting tomographic features are consistent with traditional inversion methods; (ii) reliable uncertainties can be estimated for both the isotropic and anisotropic phase speeds; (iii) "resolution" can be approximated by the coherence length of the phase speed measurements and is about equal to the station spacing; (iv) no explicit regularization is required in the inversion process; and (v) azimuthally dependent phase speed anisotropy can be observed directly without assuming its functional form.

Key words: seismic interferometry, anisotropy, crustal structure

1 INTRODUCTION

The seismic surface wave tomography inverse problem is normally approached in one of two ways that can be thought of as either "single-station" or "array-based" methods. Both methods have proven effective at revealing the spatial variability of surface wave speeds from global to regional scales.

The first (single-station) approach to surface wave tomography is based on travel time measurements between a set of seismic sources (typically earthquakes) and a set of receivers one receiver at a time. The travel times are then interpreted in terms of wave speeds in the medium of propagation using ray theory with straight or potentially bent rays (e.g., Trampert and Woodhouse, 1996; Ekstrom et al., 1997; Ritzwoller and Levshin, 1998; Yoshizawa and Kennett, 2002) or finite frequency kernels (e.g. Dahlen et al., 2000; Ritzwoller et al. 2002; Levshin et al., 2005). This method results in a set of frequency-dependent dispersion maps of either Rayleigh or Love wave group or phase speed. This approach also has been applied to ambient noise data (e.g. Sabra et al., 2005; Shapiro et al., 2005; Yao et al. 2006; Moschetti et al., 2007; Lin et al. 2007; Yang et al., 2007; Bensen et al., 2008), which provides wave travel times between pairs of receivers. In this case, one station can be considered to be an "effective" source, but it is equivalent

to the earthquake tomography problem in which the sources excite the wavefield. A variant of this method involves waveform fitting which in some cases bypasses the dispersion maps to construct the 3-D variation of shear wave speed directly in earths interior (e.g. Woodhouse & Dziewonski 1984; Nolet, 1990; van der Lee and Fredriksen, 2005).

The second approach to surface wave tomography deals with stations as components of an array and interprets the phase difference observed between waves recorded across the array in terms of the dispersion characteristics of the medium. In doing so, this method either applies geometrical constraints on the stations, typically that they lie nearly along a great circle with the earthquake (e.g. Brisbourne & Stuart 1998; Prindle & Tanimoto 2006), or inverts for the characteristics of the incoming wave-front along with the surface wave dispersion characteristics of the medium lying within the array (e.g. Alsina et al. 1993; Friederich 1998; Yang & Forsyth 2006).

In both approaches, the surface wave dispersion maps result from a regularized inverse problem that is typically solved by matrix inversion. Regularization in most cases is ad-hoc, and includes spatial smoothing as well as matrix damping. As in many geophysical inverse problems, a trade-off between the amplitude of the heterogeneity and the resolution emerges that affects confidence in the smaller structural scales when high resolution is desired. This trade-off is most severe for azimuthal anisotropy, as has been well documented by previous studies (e.g. Laske & Master 1998; Levshin et al. 2001; Trampert and Woodhouse 2003; Smith et al. 2004; Deschamps et al. 2008), in which the amplitude of anisotropy is particularly poorly determined. These problems are exacerbated by the fact that uncertainty information that emerges for the maps tends to be unreliable. Theoretical approximations made in the inversion, such as the assumption of straight (great-circle) rays or approximate sensitivity kernels, also affect the quality of the resulting maps. This particularly calls into question the robustness of information about azimuthal anisotropy because the magnitude of the travel time effects of azimuthal anisotropy and ray bending, for example, is similar.

The purpose of this paper is to present a new method of surface wave tomography that complements the traditional methods. The method is based on tracking surface wavefronts across an array of seismometers (Pollitz 2008) and should, therefore, be seen to lie within the tradition of array-based methods, although as will be seen in the discussion below the method degenerates to phase measurements obtained at single stations. The method is applicable, in principle, to surface waves generated both by earthquakes and ambient noise, but applications in this paper will concentrate on ambient noise recordings across the Transportable Array (TA) component of EarthScope/USArray (Fig. 1). Because it is an array-based method, however, an array is needed. The TA provides an ideal setting, but large PASSCAL experiments are suitable for the method and the emergence of large-scale arrays in Europe and China that mimic the station spacing of the TA also provide nearly optimal targets.

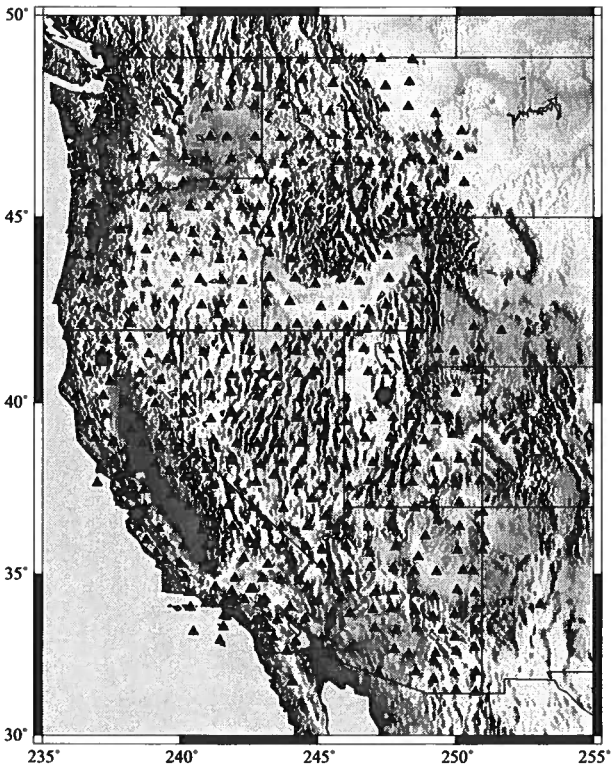

Figure 1. The 499 stations used in this study are identified by black triangles. Waveforms are taken continuously from October, 2004 until November, 2007. Most stations are from the EarthScope/USArray Transportable Array (TA), but a few exceptions exist, such as NARS Array stations in Mexico. The four red symbols identify locations used later in the paper.

The method described in this paper is performed in three steps. We discuss the method here in the context of ambient noise tomography such that each station can be considered to be an effective source as well as a receiver. The relevance of the method to earthquake tomography is discussed later in the paper. In the first step, a phase delay (or travel time) surface is computed across the array centered on each station. We refer to this step as wavefront or phase-front tracking. In the second step, the gradient of each travel time surface is computed at each spatial node. Invoking the Eikonal equation, the magnitude of the gradient approximates local phase slowness and the direction of the gradient is the direction of propagation of the geometrical ray. Steps 1 and 2 are performed with every station in the array as the effective source for the travel time surface.

Finally, in step 3, for each spatial node the local phase speeds and wave path directions are compiled and averaged from the travel time surfaces centered on each individual station in the array. Because step 2 invokes the Eikonal equation, we refer to the method as "Eikonal tomography".

Eikonal tomography complements traditional surface wave tomography in several ways. First, there is no explicit regularization and, hence, the method is largely free from ad-hoc choices. The method as we implement it does, however, involve smoothing in tracking the phase-fronts. Second, the method accounts for bent rays, but ray tracing is not needed. The gradient of the phase front provides information about the local direction of travel of the wave. The use of bent rays in traditional tomography would necessitate iteration with ray tracing performed on each iteration. Third, the method naturally generates error estimates for the resulting phase speed maps. In our opinion, this is more useful than relying on global misfit obtained by traditional inversion methods. Fourth, in the context of estimating azimuthal anisotropy, Eikonal tomography directly measures azimuth dependent phase velocities at each node. Unlike the traditional tomographic method, no ad-hoc assumption about the functional dependence of the phase velocity with azimuth is made. Finally, in the construction of phase speed maps, the ray tracing and matrix construction and inversion of the traditional methods have been replaced by surface fitting, computation of gradients, and averaging. The method, therefore, is computationally very fast and parallelizes trivially.

Although we have applied Eikonal tomography successfully from 8 sec to 40 sec period across the western US, we present results here only for the 12 sec and 24 sec Rayleigh waves. In principle, the same method can be applied to Love waves as well. The results shown in this study are presented to illustrate the method. Interpretation of the results will be the subject of future contributions.

2 THEORETICAL PRELIMINARIES

The traditional approach to seismic tomography begins with a statement of the forward problem that links unknown earth functionals (such as seismic wave speeds, surface wave phase or group speeds, etc.) with observations. In surface wave tomography, when mode coupling and the directionality of scattering are neglected, this involves the computation of travel times from the 2-D distribution of (frequency dependent) surface wave phase speeds, $c(\mathbf{r})$, that can be written in integral form as

$$t(\mathbf{r}_s, \mathbf{r}_r) = \int A(\mathbf{r}, \mathbf{r}_s, \mathbf{r}_r) \frac{dx^m}{c(\mathbf{r})} \qquad (1)$$

where $\mathbf{r}_s$ and $\mathbf{r}_r$ are the source and receiver locations, r is an arbitrary point in the medium, and $m = 1$ or 2 denotes line and area integrals, respectively. For "ray theories", $m = 1$ and the integral kernel, $A(\mathbf{r}, \mathbf{r}_s, \mathbf{r}_r)$, vanishes except along the path, which is typically either a great-circle (straight ray) or a path determined by the spatial distribution of phase speed (geometrical ray theory) which is known only approximately. Ray theories are fully accurate at infinite frequency and approximate at any finite frequency. For $m = 2$, the integral is over area, and the integral kernel represents the finite frequency spatial extent of structural sensitivity. The sensitivity kernel may be ad-hoc (e.g., Gaussian beam) or determined from a scattering theory (e.g, Born/Rytov) given a particular 1D or higher dimensional input model. Spatially extended kernels are referred to as finite frequency kernels, to contrast them with ray theories. Much of recent theoretical work in surface wave seismology has been devoted to developing increasingly sophisticated, and presumably accurate, representations of the integral kernel in equation 1 (e.g. Zhou et al. 2004; Tromp et al. 2005), although debate continues about whether approximate finite frequency kernels are preferable practically to ray theories based on bent rays with ad-hoc cross-sections (e.g., Yoshizawa and Kennett, 2002; van der Hilst & de Hoop 2005; Montelli et al. 2006; Trampert and Spetzler, 2006).

Equation 1 defines travel time as a "global" constraint on structure; that is, it is a variable that depends on the unknown structure over an extended region of model space and is defined to be contrasted with "local" constraints. The traditional primacy of the forward problem in defining the inverse problem necessitates that the inverse problem is similarly global in character. Travel time observations constrain phase speeds non-locally, that is over an extended region of model space.

In contrast, Eikonal tomography places the inverse problem in the primary role once the phase travel time surfaces, $\tau(\mathbf{r}_i, \mathbf{r})$, for positions $\mathbf{r}$ relative to an effective source located at $\mathbf{r}_i$ are known. The Eikonal equation (e.g., Wielandt, 1993; Shearer, 1999) is based on the following

$$\frac{1}{c_i(\mathbf{r})^2} = |\bigtriangledown \tau(\mathbf{r}_i, \mathbf{r})|^2 - \frac{\bigtriangledown^2 A_i(\mathbf{r})}{A_i(\mathbf{r})\omega^2} \qquad (2)$$

which is derived directly from the Helmholtz equation. When the second term on the right is small, then

$$\frac{\hat{\mathbf{k}}_i}{c_i(\mathbf{r})} \cong \bigtriangledown \tau(\mathbf{r}_i, \mathbf{r}) \qquad (3)$$

Here, c_i is the phase speed for travel time surface i at position $\mathbf{r}$, ω is frequency, and A is the amplitude of an elastic wave at position $\mathbf{r}$. The gradient is computed relative to the field vector $\mathbf{r}$ and $\hat{\mathbf{k}}_i$ is the unit wave number vector for travel time surface i at position $\mathbf{r}$. The Eikonal equation, equation 3, derives by ignoring the second term on the right hand side in equation 2. In this case, the magnitude of the gradient of the phase

travel time is simply related to the *local* phase slowness at $\mathbf{r}$ and the direction of the gradient provides the *local* direction of propagation of the wave. Thus, the Eikonal equation places local constraints on the surface wave speed.

Dropping the second term on the right hand side of equation 2 is justified either at high frequencies or if the spatial variation of the amplitude field is small compared with the gradient of the travel time surface. The latter is the less restrictive constraint and will hold if lateral phase speed variations are sufficiently smooth to produce a relatively smooth amplitude field. Moreover, when repeated measurements are performed with phase travel time surfaces from different effective sources, the errors caused by dropping the amplitude term are likely to interfere destructively, but will contribute to the estimated uncertainty especially when the wavelength is shorter than the length-scale of velocity structure (Bodin & Maupin, 2008). We take this interpretation as the basis for the use of the Eikonal equation and use synthetic tests, presented in section 5.1, to confirm that the effect of dropping the amplitude term is not a significant source of error in this study. In addition, in ambient noise tomography, absolute amplitude information is typically lost due to time- and frequency-domain normalization prior to cross-correlation (Bensen et al., 2007). In this circumstance, the computation of the second term on the right hand side of equation 2 is impossible.

The question may arise whether Eikonal tomography should be considered to be a geometrical ray theory or a finite frequency theory. The question is motivated by considering globally constrained inverse problems and is somewhat inapt for a locally constrained inversion. We believe, however, that the answer is that Eikonal tomography has elements of both. Certainly, the Eikonal equation presents information about the local direction of propagation of a wave and is, therefore, not a straight ray method but is "geometrical" in character. But, the phase travel time surfaces that are taken as data in the inversion possess spatially extended sensitivity (finite frequency information) and Lin and Ritzwoller (*On the determination of empirical surface wave sensitivity kernels, manuscript in preparation*, 2009) shows how approximate empirical finite frequency kernels can be determined from them. Thus, ignoring the second term on the right hand side of equation 2 does not equate with rejecting finite frequency information. However, the resulting interpretation of the local gradient of the phase travel time surface in terms of a wave propagating with a single well-defined direction, $\hat{\mathbf{k}}$, is consistent with a single forward scattering approximation. If there were more than one scatterer, i.e., multipathing, then the equation could not be interpreted as defining an unambiguous direction of travel at each point. Thus, we do not see Eikonal tomography as a ray method, but summarize it as an approximate finite frequency, geometrical (i.e., bent ray), single forward scattering method.

3 PHASE-FRONT TRACKING

Eikonal tomography for ambient noise begins by constructing cross-correlations between each station-pair. The ambient noise cross-correlation method to estimate the Rayleigh and Love wave empirical Greens functions (EGFs) is described by Bensen et al. (2007) and Lin et al. (2008). We use the method to produce Rayleigh wave EGFs and phase velocity curves between 8 and 40 sec period and have processed all available vertical component records from the USArray/TA observed between October 2004 and November 2007. These stations are shown in Figure 1. The symmetric component cross-correlation (average of positive and negative lag waveforms) between each station pair is used to construct the EGFs.

Each phase travel time surface is defined relative to a given station location, $\mathbf{r}_i$, which is coincident with the effective source location of the wave field. If $\mathbf{r}$ denotes an arbitrary location, then the travel time surfaces relative to effective sources i is given by $\tau(\mathbf{r}_i, \mathbf{r}) for 1 \leq i \leq n$, where n is the number of stations. The construction of the phase travel time surfaces across the array starts by mapping the phase travel times in space centered on the effective source locations. Figure 2a presents example great-circle ray paths for an effective source at TA station R06C and Figure 2b shows the EGFs to all other TA stations plotted as a record section band-pass filtered from 15 to 30 sec period. The coherence of the information contained in this record section can be seen in wavefield snap-shots such as those in Figure 3, in which the amplitude of the normalized envelope function for each EGF is color coded. Plots such as these illustrate that the entire Rayleigh wavefield can be seen to propagate away from the effective source. The plot also illustrates how the amplitude of the EGF varies with azimuth, with the largest amplitudes pointing directly toward or away from the coast relative to the central station. Nevertheless, reliable phase times are measurable at nearly all azimuths, which is essential in order to map the phase travel time surface.

Phase travel times to all stations from an effective source are measured using the method of Lin et al. (2008) on each EGF between 8 and 40 sec period. For a fixed frequency, the measured phase travel time is assigned to each station whose EGF has a signal-to-noise ratio (SNR) exceeding 15, where SNR is defined by Bensen et al. (2007). To construct a phase travel time surface, these phase travel times must be interpolated onto a finer, regular grid. To do this, we fit a minimum curvature surface onto a $0.2^\circ \times 0.2^\circ$ grid across the western US. The result for central station R06A for the 24 sec Rayleigh wave is shown in Figure 4a. Variations in the method of interpolation have minimal effect on the

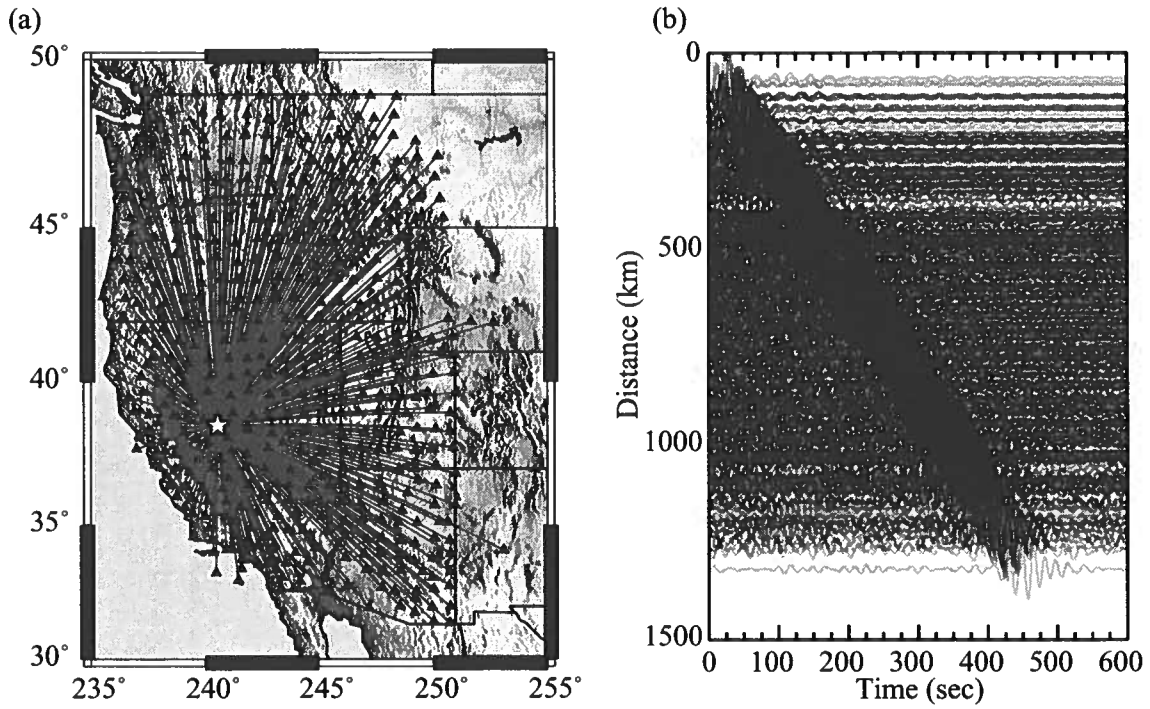

Figure 2. (a) Great circle paths linking station R06C (southeast of Lake Tahoe, identified by the white star) with all TA stations where cross-correlations were obtained. (b) Symmetric component record section for 15-30 sec period band-passed vertical-vertical cross-correlations with station R06C in common. More than 450 cross-correlations are shown. Clear move-out near 3km/s is observed.

resulting surface, averaging less than 0.2 sec except near the central station and on the maps periphery. An example is shown in Figure 4b in which a second interpolation scheme invokes an extra tension term in the surface fitting (Smith and Wesson, 1990). The difference near the center is expected because the real travel time surface will have singular curvature at the effective source. Accurate modeling of the phase time surface near the source, therefore, would require a different method of interpolation than that used here. In addition, travel time measurements obtained between stations separated by less than 1-2 wavelengths are less reliable than those from longer paths. Thus, from each travel time surface we remove the region within two wavelengths of the central station and also any region in which the phase travel time difference between the two interpolation methods is greater than 1.0 sec. Finally, as an added quality control measure, for each location we include measurements from this location only when at least three of the four quadrants of the East-West and North-South axes are occupied by at least one station within 150 km. The resulting truncated phase travel time map centered on station R06A for the 24 sec Rayleigh wave is shown in Figure 5a. Several other examples with either a different central station or a different period are also shown in Figure 5. This method of phase front tracking is not perfect, as several irregularities in the contours of constant travel time in Figure 5c testify. Statistical averaging is needed to reduce the effects of these irregularities, as discussed later in section 4.

The phase-front tracking process introduced here is essentially the only place in the Eikonal tomography method where the inverter has the freedom to make ad-hoc choices. The choice of using a minimum curvature surface fitting method as our interpolation scheme minimizes the variation of the gradient and hence gives the smoothest resulting velocity variation. With this interpolation scheme, however, the phase travel time surface within an area bounded by the three to four closest stations will always have similar gradients. This spatial coherence of the variation of the gradient, as we will discuss later on in section 4.2 and 5.1, limits our ability to resolve velocity anomalies much smaller than the station spacing. If higher resolution is desired, a more sophisticated interpolation scheme will be required.

4 EIKONAL TOMOGRAPHY

For the Eikonal equation, equation 3, the magnitude of the gradient of the phase travel time is simply related to the local phase slowness at position $\mathbf{r}$ and the direction of the gradient provides a measure of the direction of propagation of the wave. Taking the gradient on the

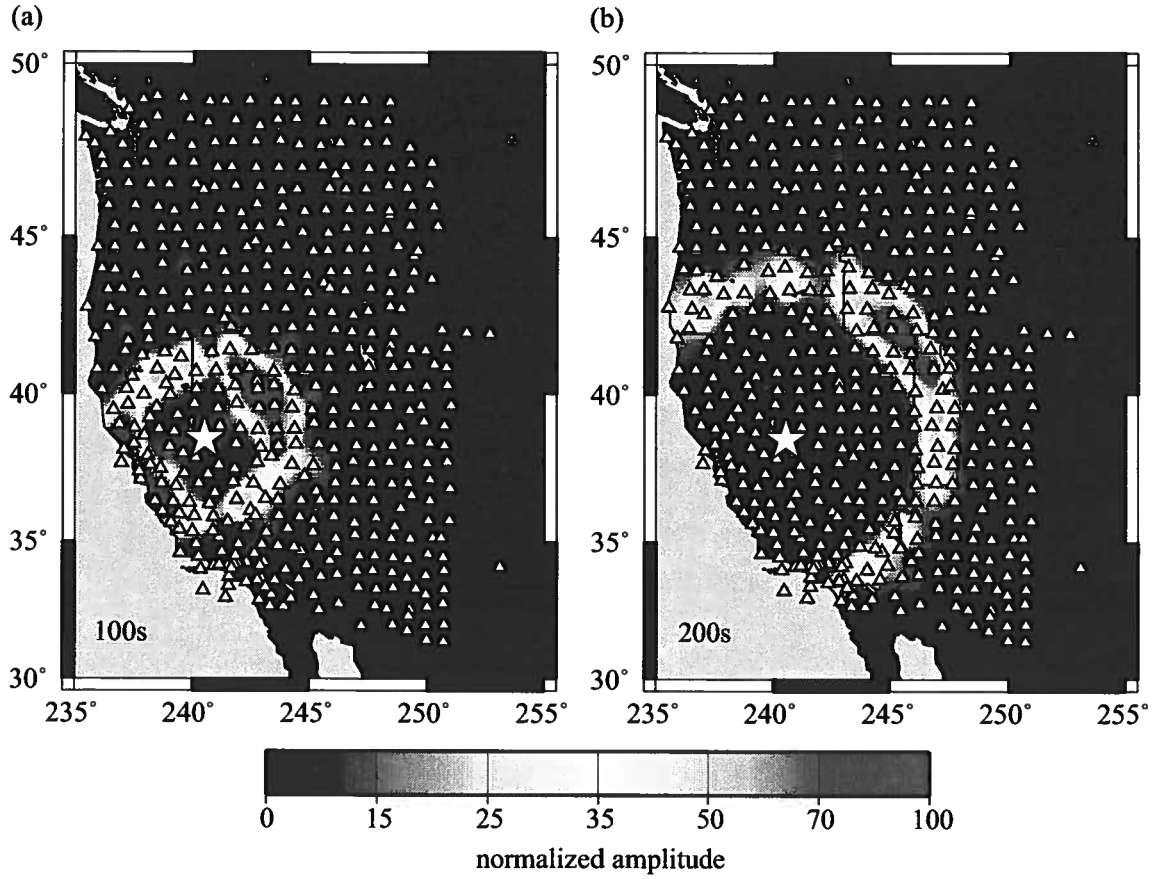

Figure 3. Snapshots of the normalized amplitude of the ambient noise cross-correlation wavefield with TA station R06C (star) in common at the center. Each of the 15-30 sec band-passed cross-correlations is first normalized by the rms of the trailing noise (Lin et al. 2008) and fit with an envelope function in the time domain. The resulting normalized envelope functions amplitudes are then interpolated spatially. Two instants in time are shown, illustrating clear move-out and the unequal azimuthal distribution of amplitude.

phase travel time surface gives the local phase speed as a function of the direction of propagation of the wave. Hence, there is no need for a tomographic inversion. If the Eikonal equation is looked at as an inverse problem, the gradient is seen as the inverse operator that maps travel time observations into model values (phase slownesses) and is applied without the need first to construct the forward operator.

4.1 Isotropic wave speeds

Figure 6 shows the result of applying the Eikonal equation to the phase travel time surface for the 24 sec Rayleigh wave shown in Figure 5a centered on station R06A. For each individual central station i, the resulting phase speed map is noisy (Figure 6a) due to imperfections in the phase travel time map. This is caused by errors in the input phase travel times which, in a similar measurement, Lin et al. (2008) estimated to be about 1 sec, on average. This is a significant error when spacing between stations is small. But, there are n stations, which in the present study for the TA is about 490. This allows the statistics of the phase speed estimates to be determined. For example, Figure 7a shows the 455 Rayleigh wave phase speed measurements at a period of 24 sec as a function of the propagation direction for the point in Nevada identified by the star in Figure 1. To determine the isotropic phase speed and its uncertainty for each point, we first calculate the mean slowness, s_0, and the standard deviation of the mean slowness, σ_{s_0}, from the distribution of slowness measurements, s_i:

$$s_0 = \frac{1}{n}\sum_{i=1}^{n} s_i \tag{4}$$

$$\sigma_{s_0}{}^2 = \frac{1}{n(n-1)}\sum_{i=1}^{n}(s_i - s_0)^2 \tag{5}$$

where n is the number of effective sources. This intermediate step properly accounts for error propagation.

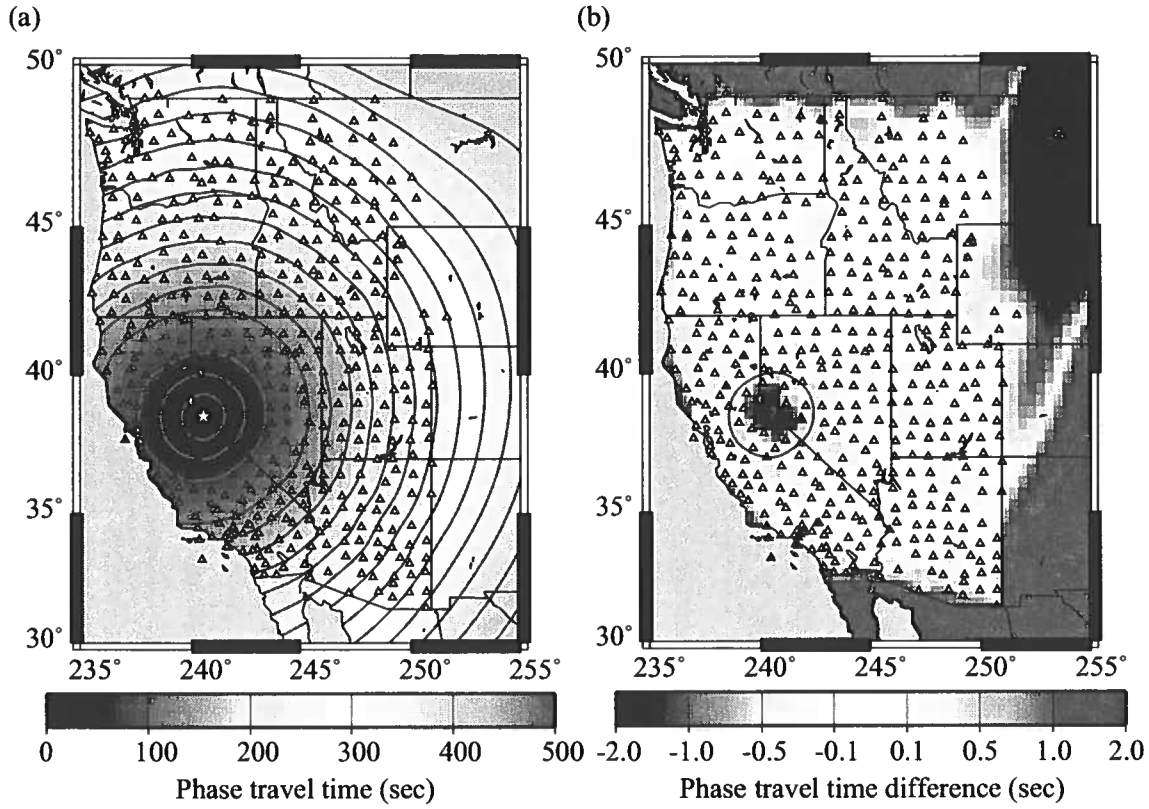

Figure 4. (a) The phase travel time surface for the 24 sec Rayleigh wave centered on TA station R06C (star). Contours are separated by 24 sec intervals. (b) The difference in phase speed travel time using two different phase-front interpolation schemes. The 48 sec contour is identified with a grey circle centered on station R06C.

The isotropic phase speed, c_0, and its uncertainty, σ_{c_0}, are then determined by

$$c_0 = \frac{1}{s_0} \tag{6}$$

$$\sigma_{c_0} = \frac{1}{{s_0}^2}\sigma_{s_0} \tag{7}$$

The local phase speed uncertainty, σ_{c_0}, is mapped for the 24 sec Rayleigh wave in Figure 8a where only the region in which the number of measurements is greater than half the total number of the effective sources is shown. The average uncertainty across the map is about 7 m/sec or about 0.2% of the phase speed. Note that this uncertainty estimate only accounts random errors within travel time measurements. Systematic errors introduced by the tomography method itself will be discussed in Section 5.1.

Example phase speed measurements and the uncertainty map for the 12 sec period Rayleigh wave are displayed in Figures 7b and 8b, respectively. Uncertainty at this period is largest along the western and northern edges of the region which is most likely due to small scale wave-front distortion resulting from large velocity contrasts. The average uncertainty is about 8 m/sec, which is slightly larger than at 24 sec. This is not unexpected because the validity of the Eikonal equation relies on smoothly varying velocity structures and this is a less robust assumption for surface waves at shorter periods.

The isotropic phase speed maps at periods of 24 sec and 12 sec are plotted in Figures 9a and 10a, respectively. For comparison, the phase speed maps determined from the phase speed measurements using a traditional tomographic method based on the straight ray approximation (Barmin et al., 2001) are shown in Figures 9b and 10b. Differences between the methods are illustrated in Figures 9c and 10c.

Agreement between the isotropic maps produced with Eikonal tomography and the traditional straight ray tomography is generally favorable, but there are regions of significant disagreement. At 24 sec period, the differences are greatest near the western boundary of the map where Eikonal tomography seems to recover crisper, more highly resolved features that correlate better with known geological structures. For the 24 sec Rayleigh wave, the phase velocity contrast between the fast and slow anomalies is generally too gentle to make ray paths deviate significantly from great circle paths.

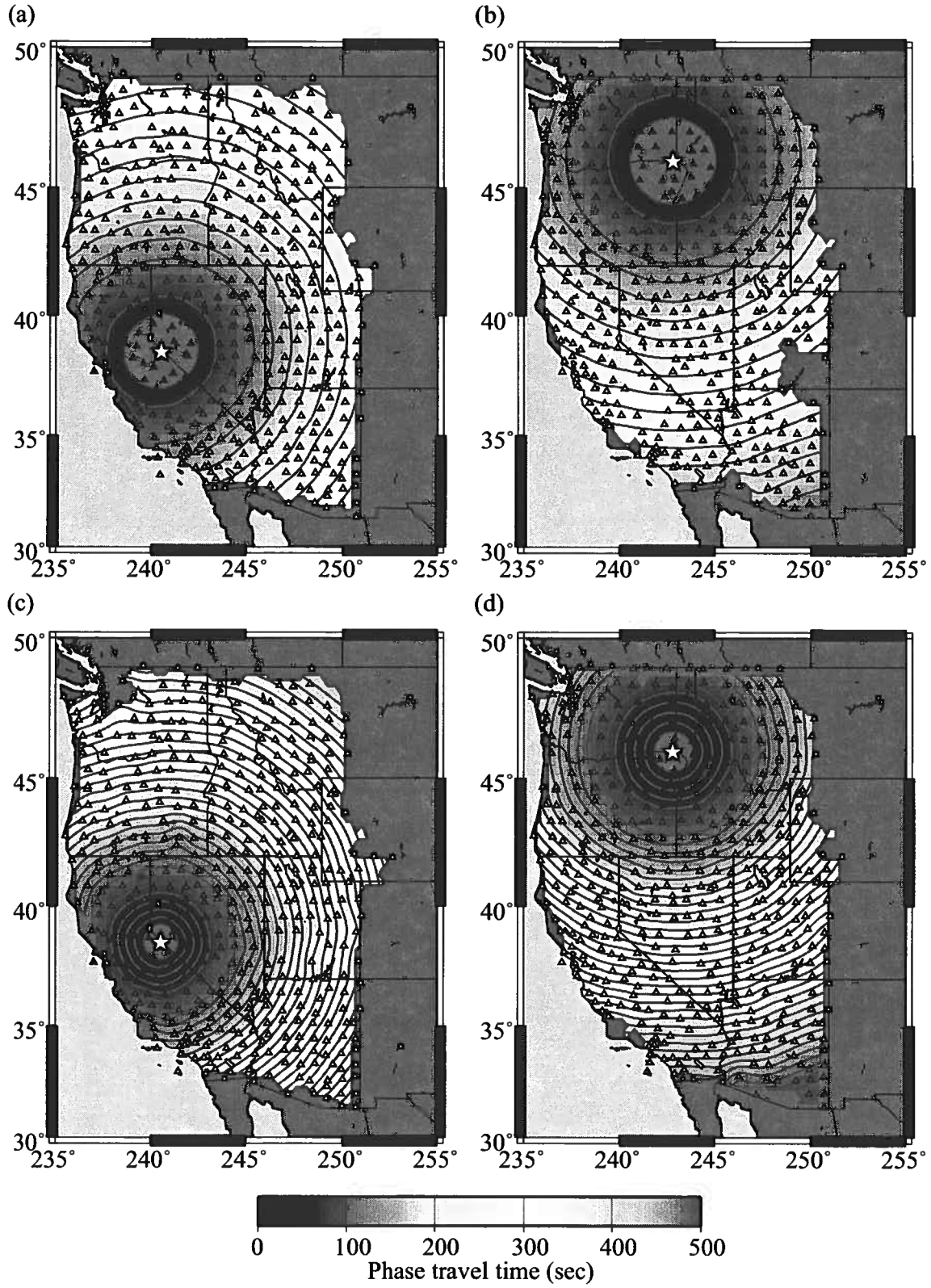

Figure 5. Rayleigh wave phase speed travel time surfaces at periods of (a,b) 24 sec and (c,d) 12 sec centered on two "effective sources": stations R06C (eastern California) and F10A (northeastern Oregon). Travel time level lines are presented in increments of the wave period. The maps are truncated within 2 wavelengths of the central station and where the three out of four quadrant selection criterion is not satisfied. These two criteria usually take effect only near the periphery of the station coverage.

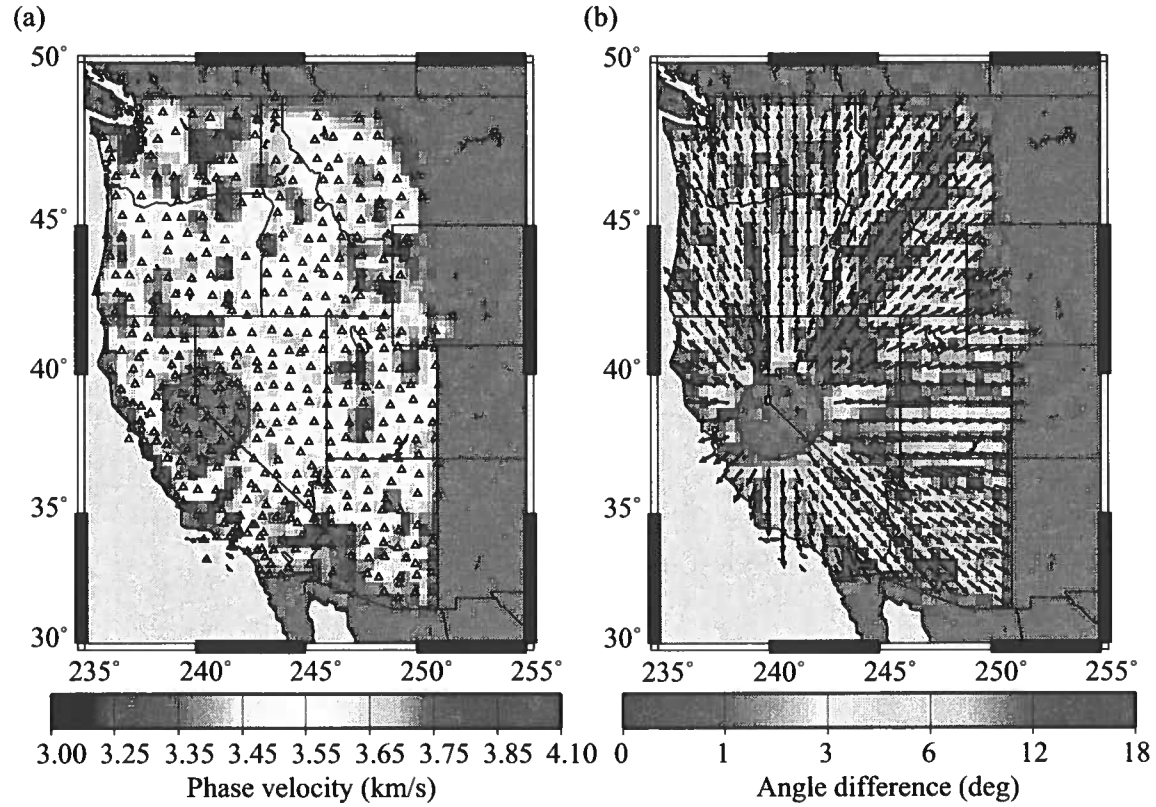

Figure 6. (a) The phase speed inferred from the Eikonal equation for the 24 sec Rayleigh wave travel time surface shown in Fig. 5a centered on station R06A. (b) The propagation direction determined from the gradient of the phase travel time surface at each point is shown with arrows. The difference between the observed propagation direction and the straight ray prediction (radially away from stations R06A) is shown as the background color.

This is also indicated in Figure 6b where the average deviation of propagation direction from great circle path is only about 3°. It is not likely, therefore, that the differences observed between Eikonal and traditional tomography at this period are purely because Eikonal tomography accounts for bent rays. Differences more likely result from the regularization applied in the straight ray inversion, which tends to distort the velocity anomalies near the edges of the map. At 12 sec period, however, velocity contrasts are more significant and the off-great-circle effect is more pronounced. The effect of modeling bent rays in Eikonal tomography can be seen in at least two features of the 12 sec map. First, a lineated anomaly associated with the Cascade Range is better observed with Eikonal tomography. Second, Eikonal tomography also produces wave speeds that are systematically slower than the straight ray inversion (Figure 10c) in most of the region. The bent rays travel faster than the straight rays (Roth et al. 1993) and to fit the data equally well with bent rays requires depression of wave speeds, on average. This can be seen clearly in the histograms of differences presented in Figure 11, where the mean difference between the two 12 sec maps is about 10 m/sec (about 0.3% of the phase speed), whereas the 24 sec maps differ, on average, only by ~5 m/sec.

4.2 Coherence length of the measurements

Traditional estimates of resolution typically are based on applying the inverse operator (relating observations to model variables) to the forward operator (relating model variables to observations) in an inverse problem. With Eikonal tomography, neither an inverse nor a forward operator are constructed explicitly, so resolution is not straightforward to determine. Checkerboard tests are possible, but numerical simulations would need to accurately calculate the phase travel time between each station pair.

We take a different approach and attempt to estimate the resolution based on the coherence length of the measurements. To do so, we first estimate the statistical correlation, ρ, of slowness measurements between locations j and k by

$$\rho_{jk} = \frac{\left[\sum_{i=1}^{n}(s_{ji} - s_{j0})(s_{ki} - s_{k0})\right]^2}{\sum_{i=1}^{n}(s_{ji} - s_{j0})^2 \sum_{i=1}^{n}(s_{ki} - s_{k0})^2} \qquad (8)$$

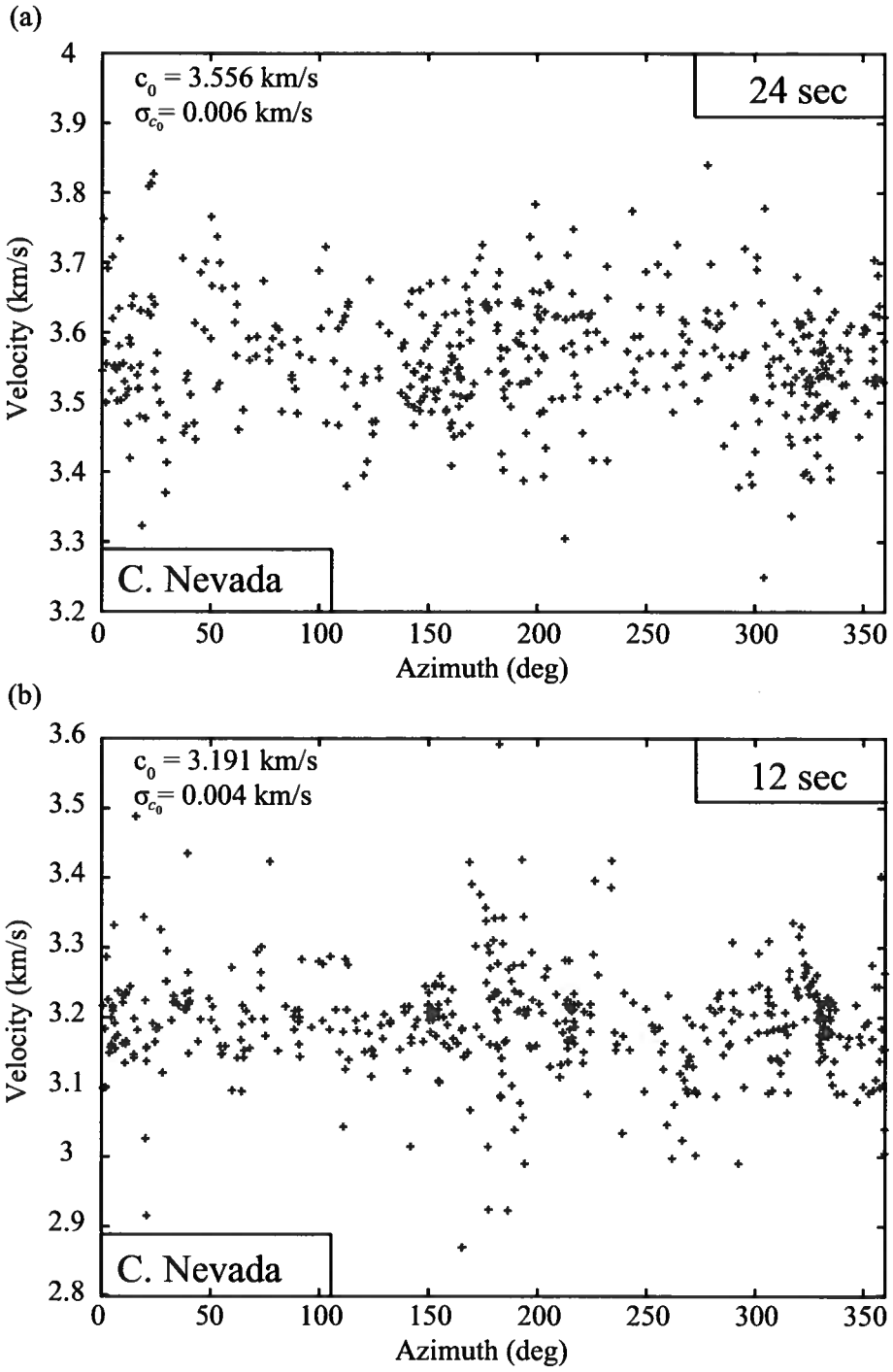

Figure 7. (a) Example of the azimuthal distribution of the Rayleigh wave phase velocity measurements at 24 sec period for the point in central Nevada indicated by the star in Figure 1. (b) Same as (a), but for the 12 sec Rayleigh wave phase speed at the same location. The mean and standard deviation of the mean are identified at upper left in each panel.

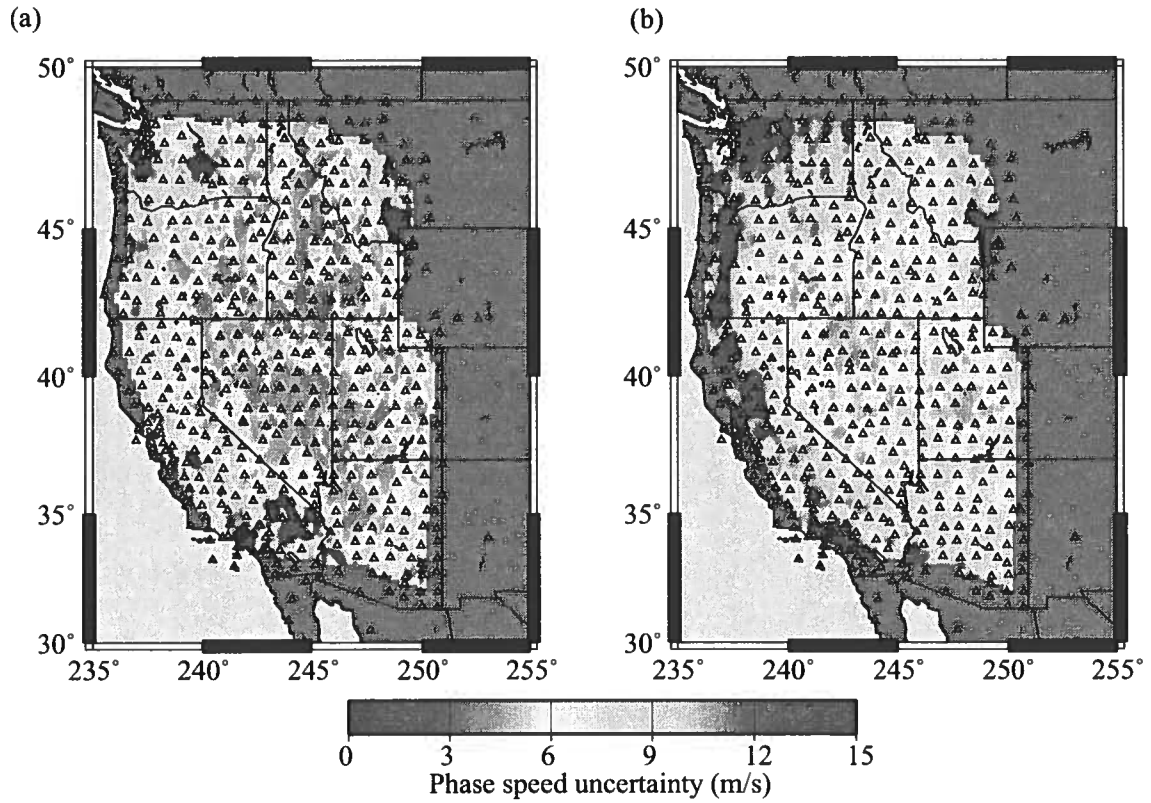

Figure 8. (a) The 24 sec period isotropic Rayleigh wave phase speed uncertainty map, determined from the distribution of phase speed measurements based on applying the Eikonal equation to each of the phase travel time maps at each point. (b) The 12 sec isotropic Rayleigh wave phase speed uncertainty map.

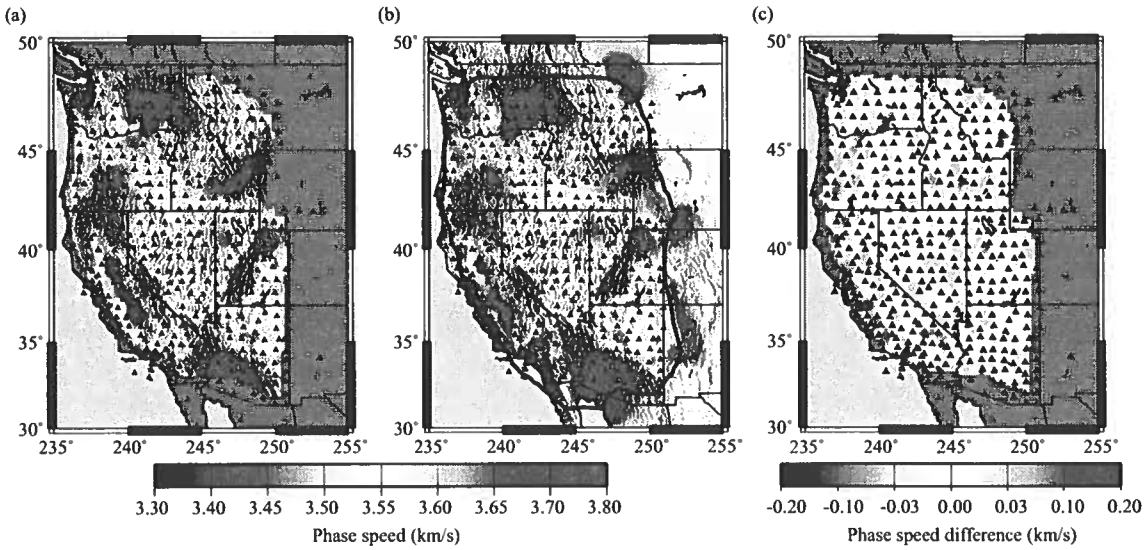

Figure 9. (a) The 24 sec Rayleigh wave isotropic phase speed map derived from Eikonal tomography. The isotropic phase speed at each point is calculated from the distribution of local phase speeds determined from each of the phase travel time maps. (b) Same as (a), but the straight ray inversion of Barmin et al. (2001) is used. The black line is the 100 km resolution contour. (c) The difference between Eikonal and straight ray tomography is shown where positive values indicate that the Eikonal tomography gives a higher local phase speed.

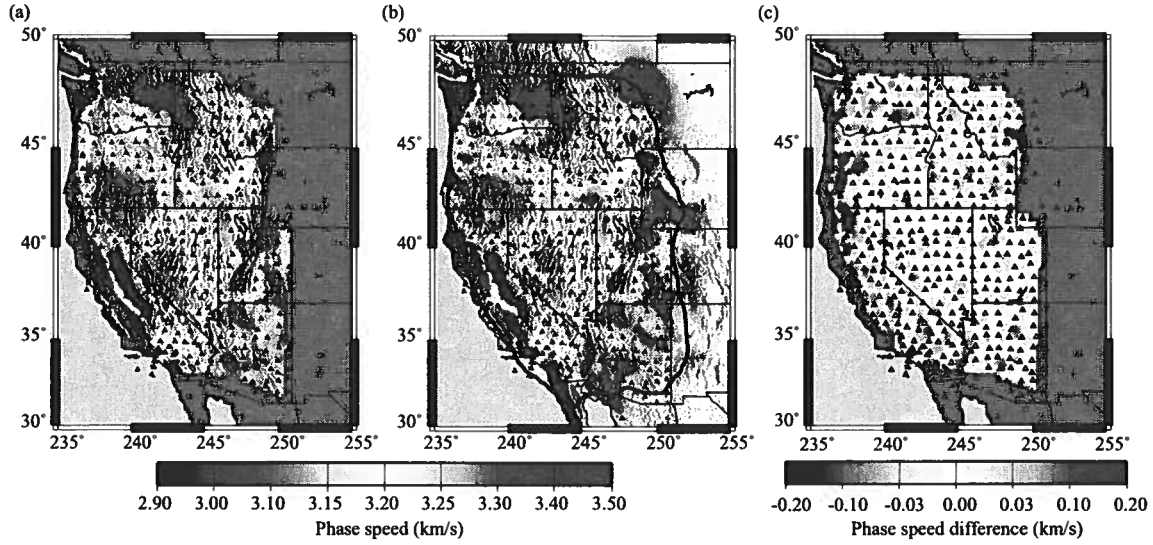

Figure 10. The same as Figure 9, but for the 12 sec Rayleigh wave. The result of Eikonal tomography is slightly slower (yellow-red shades), on average, than the straight ray tomography because it models off-great-circle propagation.

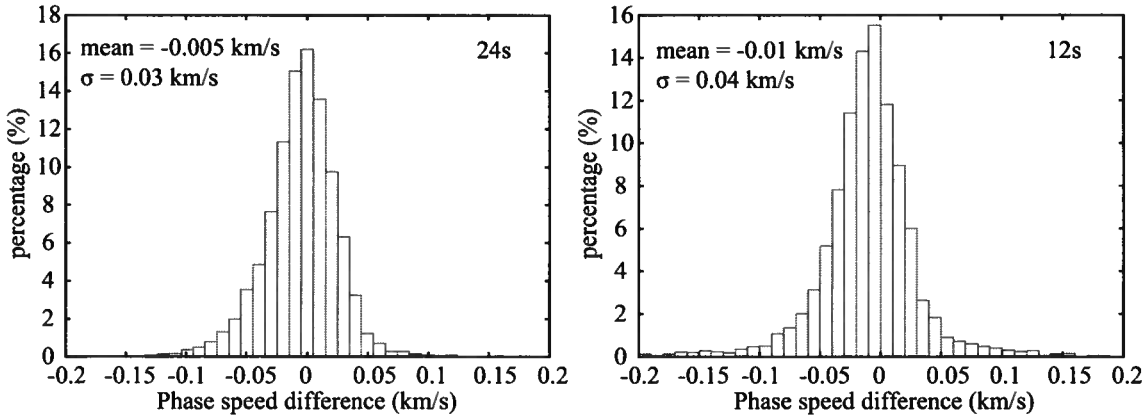

Figure 11. Normalized histograms of the Rayleigh wave phase speed difference across the studied region between Eikonal tomography and straight ray tomography at 12 and 24 sec period. The mean differences result because Eikonal tomography models off-great-circle propagation, which is more significant at 12 sec than 24 sec period.

where i is the index of the effective sources and s_{j0} and s_{k0} are the mean slowness at locations j and k, respectively. The statistical correlation, ρ, varies between 0 and 1 and represents the degree of coherence or independence between the measurements made at the two locations. Using the point in central Nevada (Figure 1) as an example again, the statistical correlation between the phase speed observations at that point and the neighboring points is summarized as a correlation surface shown in Figure 12a. We follow Barmin et al. (2001) and estimate the coherence length of the measurements by fitting the correlation surface with a cone, where the base radius of the cone is taken as the coherence length estimate R.

Although this is different from the traditional definition of resolution, it does provide information about the length scale of features that can be resolved in a region. The coherence length estimated in this way for the 24 sec Rayleigh wave is shown in Figure 12b. In most regions, coherence length is somewhat smaller than the average inter-station spacing of 70 km across the western US. Although this result is comparable to the resolution estimated by the straight ray tomography (Lin et al. 2008), there are fundamental differences between the two. When the observed phase travel times are affected by a velocity structure much smaller than the inter-station distance, without a more sophisticated interpolation scheme, the minimum curvature fitting method we use will smear the travel time anomalies to an area confined by the few closest nearby stations. This smear-

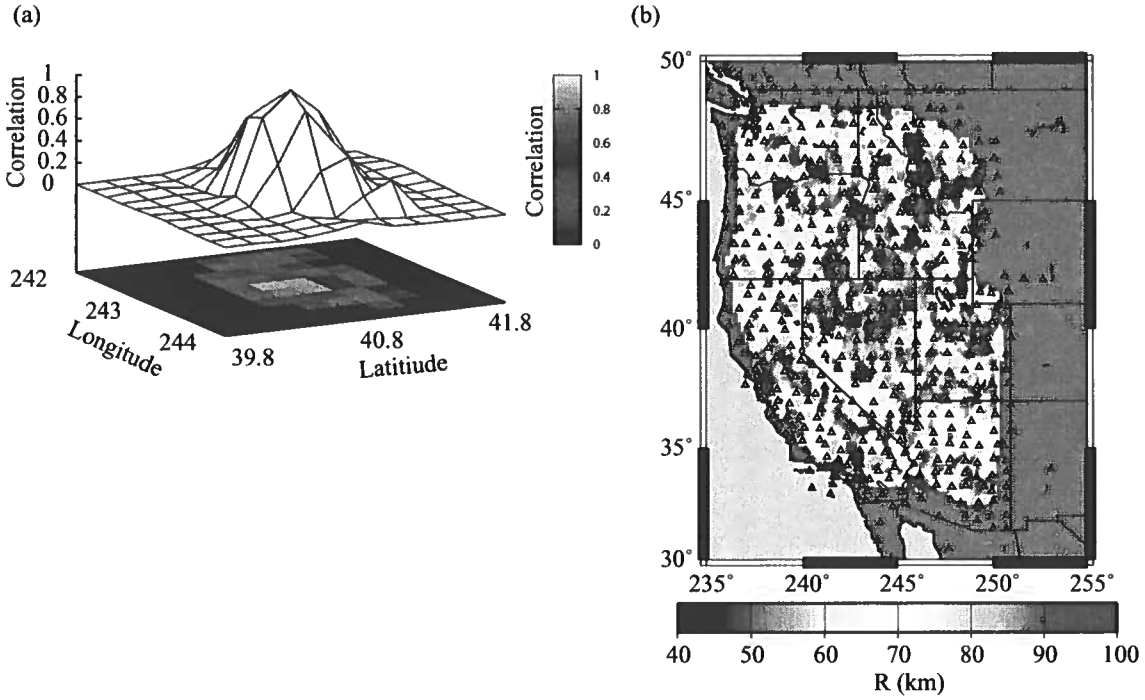

Figure 12. (a) An example of the spatial coherence of the measurements for the 24 sec Rayleigh wave at the point in central Nevada indicated by the star in Figure 1. (b) The radius (R) of the cone fit to the coherence surface at each location, which bears a similarity to resolution.

ing effect is further evidenced in out synthetic tests in section 5.1. Thus, the station spacing constrains the coherence length as well as the smallest scale of structure that can be confidently resolved. Increasing the number of effective sources will tend to reduce the estimated uncertainty, but most likely will have little impact on the coherence length.

4.3 Azimuthal anisotropy

Eikonal tomography also provides an estimate of azimuthal anisotropy. In traditional surface wave inversions, it is commonly assumed that the Rayleigh wave phase speed exhibits the following functional dependence on azimuth, which is derived based on theoretical studies of weakly anisotropic media (Smith & Dahlen, 1973),

$$c(\Psi) = c_0 + A\cos[2(\Psi - \varphi)] + B\cos[4(\Psi - \alpha)] \quad (9)$$

where Ψ is the azimuthal angle measured positive clockwise from north, A and B are the amplitude of anisotropy, and φ and α define the orientation of the anisotropic fast axes for the 2Ψ and 4Ψ components of anisotropy. Although the estimated 2Ψ fast directions may be robust in the traditional inversion, the amplitude of the anisotropy almost inevitably depends on the regularization parameters chosen (e.g., Smith et al., 2004). In Eikonal tomography, the velocity as a function of azimuth of the wave is measured directly and it is then determined if the relationship reflects a simple function of azimuth.

As with the measurement of isotropic phase velocity, the estimation of anisotropy begins with the set of phase speeds estimated at a single spatial location from the set of phase speed travel time maps segregated by azimuth, as in the example shown in Figure 7a for the 24 sec Rayleigh wave for a point in central Nevada. Due to phase travel time errors in the maps, the measured phase speeds are significantly scattered and any azimuthally dependent trend is obscured. Scatter is reduced substantially by stacking and binning in two stages. First, we combine the azimuthally dependent phase speed measurements obtained at the target point with measurements at the eight surrounding spatial points (3×3 grid with the target point at the center). We use a 0.6° grid separation approximately equal to the coherence length estimate described in the last section, which effectively guarantees that measurements are statistically independent from one another. To reduce mapping the lateral variation of isotropic phase speed into azimuthal anisotropy, we remove the isotropic speed difference between each point and the center point of the 3×3 grid for all of the measurements. This stacking process increases the number of measurements for the center point, but does so at the expense of reducing spatial resolution. Second, we com-

bine all of the azimuthally dependent phase speed measurements in each 20° azimuthal bin into a mean speed and its standard deviation of the mean for that bin. Here, again, the mean slowness and the standard deviation of the mean slowness are first calculated and then converted to the mean speed and its uncertainty.

Figure 13 shows examples for four different geographical locations of the stacked azimuthally dependent phase speed measurements with their uncertainties for the 24 sec Rayleigh wave. For the examples in Utah and Nevada, Figures 13a and b, where good azimuthal data coverage exists, a clear 2Ψ variation is observed for the entire 360° of azimuth. On the other hand, Figures 13c and d show two examples near the western boundary of the map where azimuthal coverage is limited. Nevertheless, the 2Ψ velocity signal is still observed robustly because measurements cover at least 180°. Based on these observations, for each period and location, we adopt the assumption of a weakly anisotropic medium, fit the results with the 2Ψ part of the cosinusoid, and use it to estimate the amplitude and fast direction of anisotropy with associated uncertainties. Here, robust statistics are used. Measurements that cannot be fit within 2 standard deviations are removed to minimize the effect of significant outliers, but the difference between the robust statistics and non-robust statistics is small overall. Adding the 4Ψ term does not improve the data fit appreciably which indicates that the 4Ψ variation of Rayleigh waves is weaker and our dataset is not sufficient to constrain it. The observed 2Ψ azimuthal anisotropy exhibits different amplitudes and fast directions in different locations. This minimizes concern about systematic errors in the input phase travel times due to azimuthally inhomogeneous ambient noise sources which could result in a uniform fast direction for the entire region.

Azimuthal anisotropy for the 24 sec Rayleigh wave is summarized in Figure 14a. The peak-to-peak amplitude of anisotropy is presented in Figure 14b. Figure 15a presents the variance reduction after introducing the 2Ψ anisotropy term. Significant improvements ($> 80\%$) are observed over extended regions, which not only indicates the robustness of the measurements but also suggests that azimuthal anisotropy is a general feature of Rayleigh waves in the western US. We note that the regions with poor variance reduction ($< 40\%$) are generally accompanied by weak anisotropy ($< 0.5\%$), which may be a real feature or may be due to a spatially rapid and unresolvable change in fast direction. The estimated uncertainty of the observed azimuthal anisotropy fast directions and amplitudes are summarized in Figure 15b and 15c, respectively. As in traditional anisotropy tomography, the fast directions are generally robust features. We estimate the uncertainties of the fast directions to be less than 6° in most of regions. Again, regions with larger uncertainties in the fast direction generally result from weak anisotropy. Uncertainties in the amplitude of anisotropy are generally smaller (< 3m/s or 0.1% of the isotropic phase speed) in regions with nearly complete azimuthal data coverage than near the periphery of the studied region where only part of entire azimuthal range has measurements.

For comparison, the 2Ψ 24 sec Rayleigh wave phase speed anisotropy determined by traditional straight ray inversion (e.g., Barmin et al., 2001) with two different smoothing strengths is summarized in Figure 16a and 16d with amplitudes plotted in Figure 16b and 16e. The difference in fast directions compared to Eikonal tomography is also summarized as histograms in Figure 16c and 16f, where only regions with anisotropy amplitude larger than 0.5% in the Eikonal tomography are included. Overall, the observed anisotropy fast direction patterns are consistent between the two traditional inversions and the Eikonal tomography inversion. This is not unexpected because the off-great-circle effect is relatively weak at 24 sec period. The anisotropy amplitude is significantly smaller in the second case of the straight ray inversion, which indicates that the smoothing regularization was too strong. Most places with a significant difference in fast directions ($> 30°$) occur near a transition in the fast direction of anisotropy where the results of neither model are robust.

With the traditional inversion method, it is tricky to select the right regularization parameters and methods to do so are typically ad-hoc. Many studies use trade-off curves between misfit and model roughness or the number of degrees of freedom to select the preferred regularization parameters (e.g. Boschi 2006; Zhou et al. 2005). This is, however, difficult for azimuthal anisotropy because by including 2Ψ azimuthal anisotropy, for example, the number of degrees of freedom at each node increases to 3 from 1 for an isotropic wave speed inversion despite the fact that the improvement in misfit is usually modest. For traditional tomography applied to the 24 sec Rayleigh wave phase speed data, the standard deviation of travel time misfit drops from around 3 sec for a homogeneous reference model to 1.57 sec after the straight ray isotropic speed inversion (Figure 9b). However, it then only decreases slightly to 1.53 sec and 1.54 sec for the two 2Ψ azimuthal anisotropy inversions (Figure 16a and 16d). With Eikonal tomography, through the stacking and binning process, we effectively separate the velocity variation due to measurement error from anisotropy and are able to inspect the observed azimuthally dependent phase speed measurements visually. In this way, the observed variance reduction is statistically meaningful and can be used to indicate the confidence level of the result.

The 12 sec Rayleigh wave 2Ψ azimuthal anisotropy results based on Eikonal tomography are presented in Figure 17. Overall, the anisotropy is robustly measured despite the fact that the amplitudes of anisotropy are generally weaker and the fast direction pattern is slightly different than the 24 sec results. Figure 18a

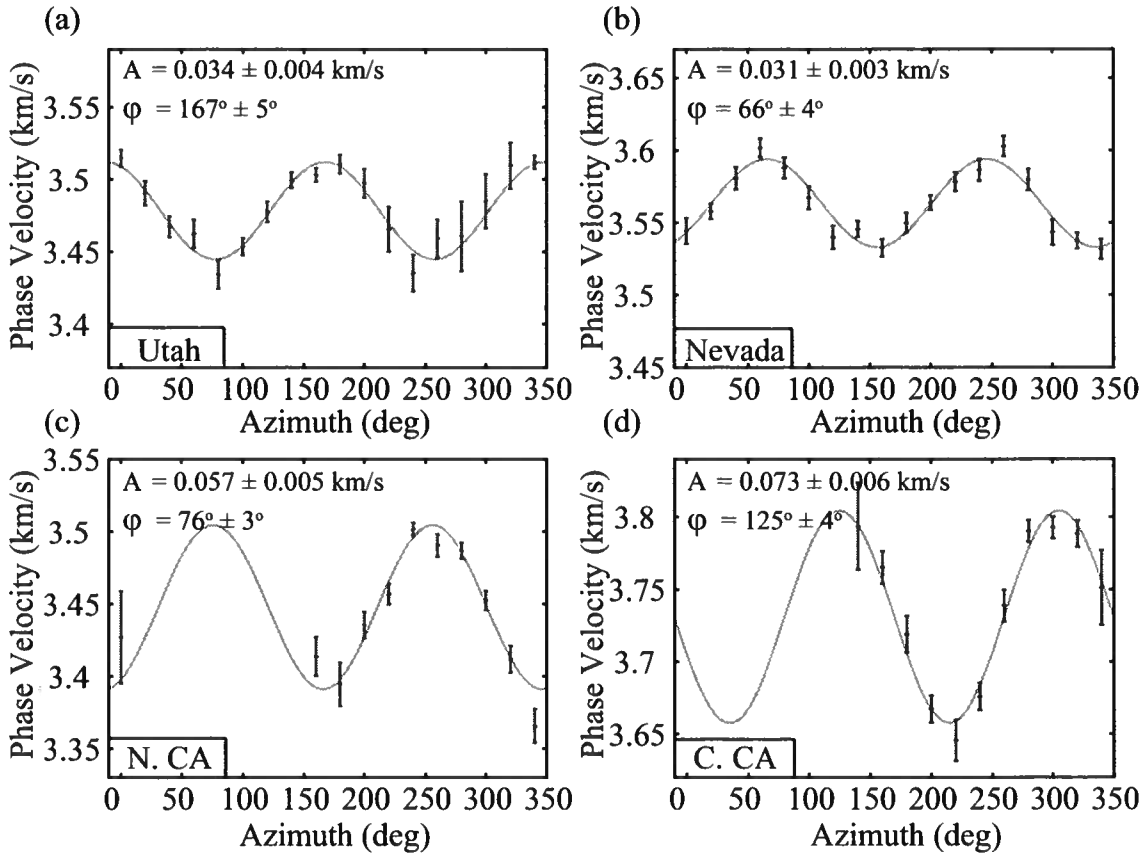

Figure 13. Examples of the azimuthal dependence of phase velocity measurements for the 24 sec Rayleigh wave at four points in the western US where large amplitude 2Ψ azimuthal variation can be observed: (a) Utah, (b) Nevada, (c) northern California, and (d) central California. The locations are indicated by the circle, star, square, and diamond in Figure 1, respectively. Error bars are estimated based on the distribution of phase velocity measurements in each 20° azimuthal bin for the given location and its 8 nearest neighboring grid points. For each case, the solid line is the best fit of the 2Ψ azimuthal variation.

shows an example of the 12 sec 2Ψ azimuthal anisotropy determined by our traditional straight ray inversion with anisotropy amplitude plotted in Figure 18b. The difference in fast directions compared to the Eikonal tomography is summarized in the histogram in Figure 18c. Compared to 24 sec period, more significant differences in both the fast directions and the amplitude patterns are observed, particularly near regions where there are discrepancies between the two isotropic wave speed maps (Figure 10). We believe that the off-great-circle effect, which is more important for 12 sec Rayleigh waves, is responsible for most of the observed differences between the methods at this period.

5 DISCUSSION

5.1 Numerical simulations to test for systematic errors

To assess possible systematic errors due to approximations in the Eikonal tomography method, which include both dropping the amplitude term in equation 2and using a minimum curvature surface fitting method to interpolate the phase travel time surface, we perform a series of 2D finite difference simulations to solve the Helmholtz equation numerically and obtain a synthetic travel time database. We invert this database based on Eikonal tomography and evaluate the difference between the tomography result and the input phase speed model to constrain the systematic errors.

Two cases, 12 and 36 second periods, are studied here which represent periods at the short and long period ends of our study. The isotropic wave speed maps derived from the USArray dataset and Eikonal tomography are used here as the input models (Figure 19a and 20a). In each simulation, a periodic source centered at one station location is used to generate a single frequency out-going wave which propagates in the 2D medium of the input wave speed model. The resulting waveforms observed at all other station locations are used to measure the phase travel times between those stations and the effective source, where the measure-

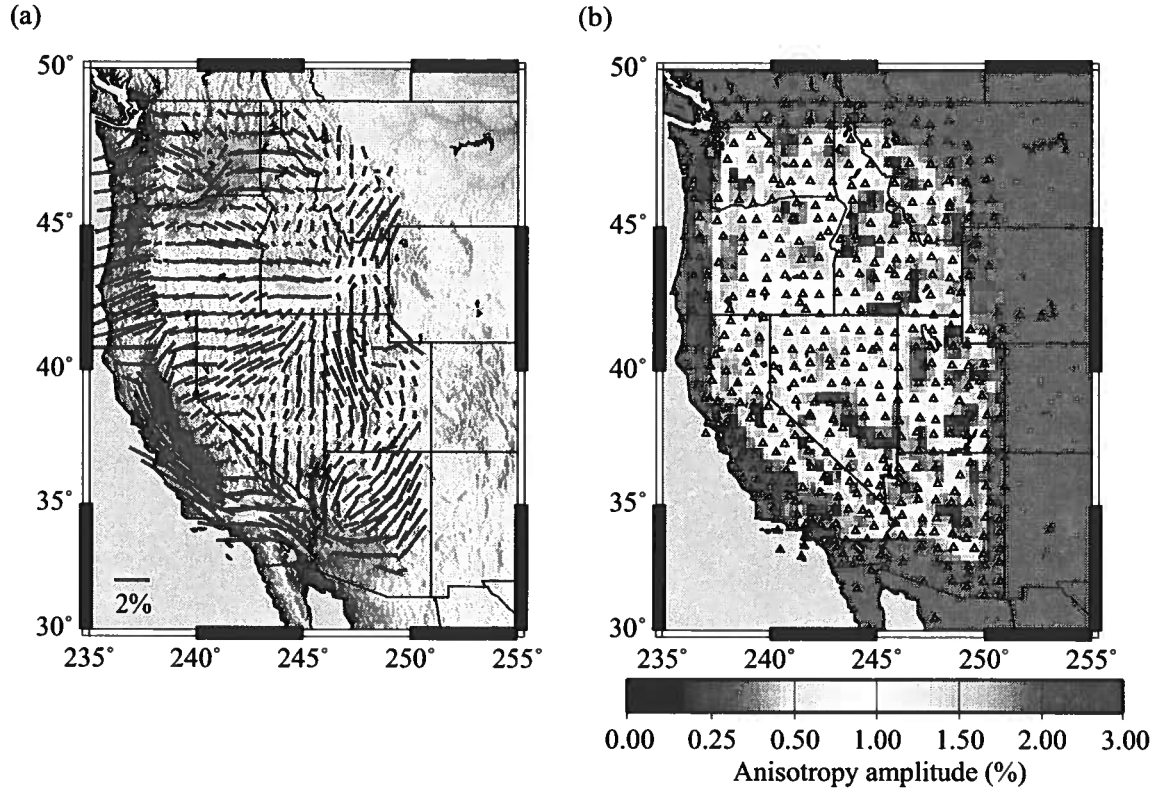

Figure 14. (a) The 24 sec period Rayleigh wave azimuthal anisotropy fast axis directions and peak-to-peak amplitudes, $2A/c_0$, which are proportional to the length of the bars. (b) Peak-to-peak amplitude of anisotropy presented in percent.

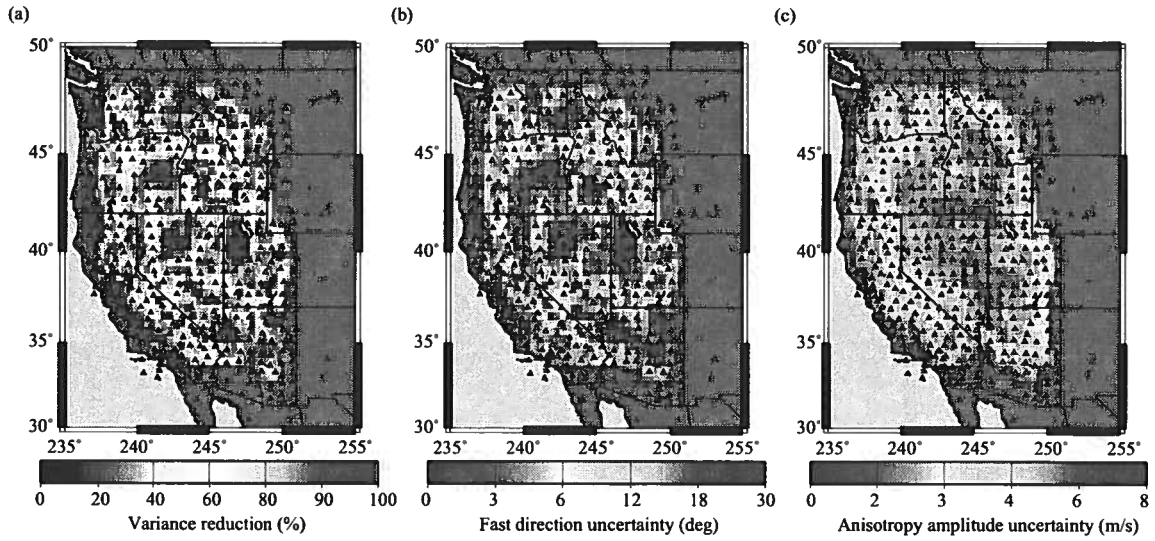

Figure 15. (a) Variance reduction of the 24 sec Rayleigh wave 2Ψ azimuthal anisotropy relative to the isotropic speed at each point. (b) The uncertainty in the angle of the fast direction, φ. (c) The uncertainty of the amplitude of anisotropy.

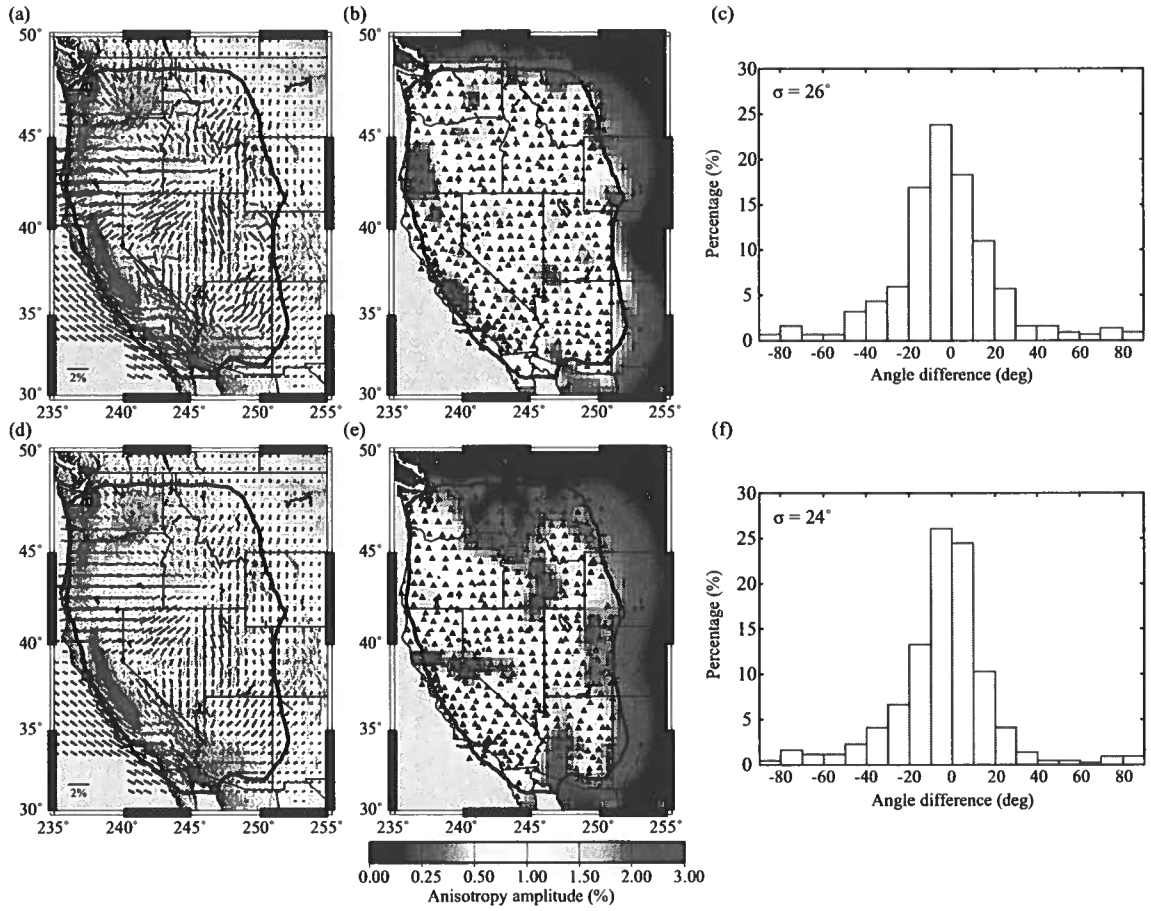

Figure 16. (a)-(b) Same as Figure 14a-b, but here the 24 sec Rayleigh wave azimuthal anisotropy result is determined with the traditional straight ray method of Barmin et al. (2001) with a regularization chosen to approximate the amplitudes in Fig. 14b. The black line is the 100 km resolution contour. (c) The normalized histogram of the difference in fast directions between the Eikonal tomography result (Fig. 14a) and the straight ray tomography result. (d)-(f) same as (a)-(c) but with stronger smoothing regularization. Patterns of anisotropy remain largely unchanged, but amplitudes diminish with greater the damping.

ments are made when the waveform stabilizes after several cycles. Although synthetic travel times are available between all station pairs, to be comparable with the inversion with real data, only those measurements included in the original datasets are included. We follow the same procedure described in Section 3 and 4 to invert these synthetic datasets based on Eikonal tomography and both the isotropic and anisotropy results are shown in Figures 19b, 19c, 20b, and 20c.

Unsurprisingly, the resulting isotropic speed maps, for both 12 and 36 sec, closely replicate the large scale features of the input models, although small scale anomalies in the input models tend to be smoothed out. This smoothing effect is expected, as discussed in section 4.2. To assess other systematic errors, we smooth the input models with a spatial Gaussian filters with a standard deviation of 35 km and summarized the differences between the isotropic inversion results and the smoothed input models in Figure 19d and 20d. Deviations are most significant near the periphery of our station coverage, particularly near regions with large velocity contrasts such as regions near the Central Valley of California and the Sierra Nevada for the 12 second case and the Southern Sierra Nevada for the 36 second case where delamination is inferred by previous studies (e.g. Yang & Forsyth 2006). Similar anisotropic deviations are also observed for both the 12 and 36 sec cases (Figure 19c and 20c), where the amplitude of the anisotropy tends to correlate with the observed isotropic wave speed deviations. This suggests that rapid velocity contrasts near the periphery of the maps tend to distort the wavefront dramatically and the method becomes less robust. The observed isotropic (Figures 19d and 20d) and anisotropic (Figures 19c and 20c) deviations are also summarized as histograms in Figures 19e, 20e, 19f, and 20f, respectively.

We test whether we can reduce these deviations by including amplitude measurements in our synthetic

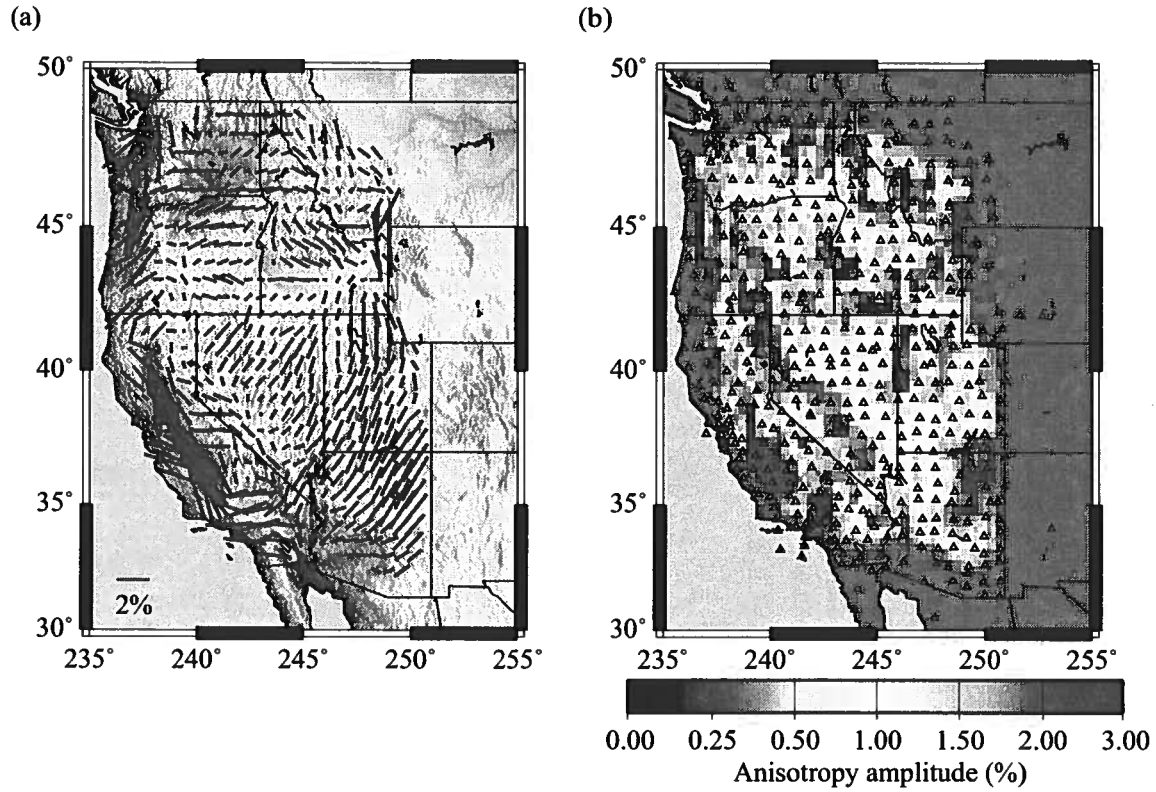

Figure 17. Same as Figure 14, but for the 12 sec Rayleigh wave.

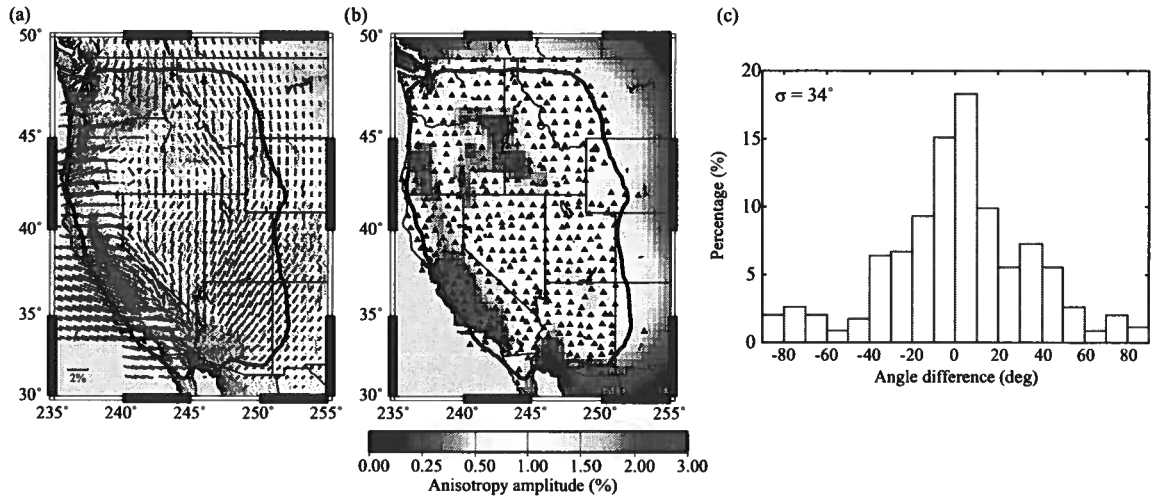

Figure 18. Same as Figure 16, but for the 12 sec Rayleigh wave. Agreement between the Eikonal and straight ray tomography is worse at 12 sec than 24 sec because of the larger effect of off-great-circle propagation.

datasets. Again, minimum curvature surface fitting is used to first interpolate the synthetic amplitudes measured at each station to construct amplitude surfaces before calculating the second term in equation 2 . The effect of including the amplitude term is in general unnoticeable, which is partly because the surface interpolation schemes we use here provides relatively smooth amplitude surfaces which tend to minimize the Laplacian term in the equation 2 . This is inevitable unless a denser station network is available.

The observed isotropic and anisotropic amplitude deviations, with standard deviations approximately

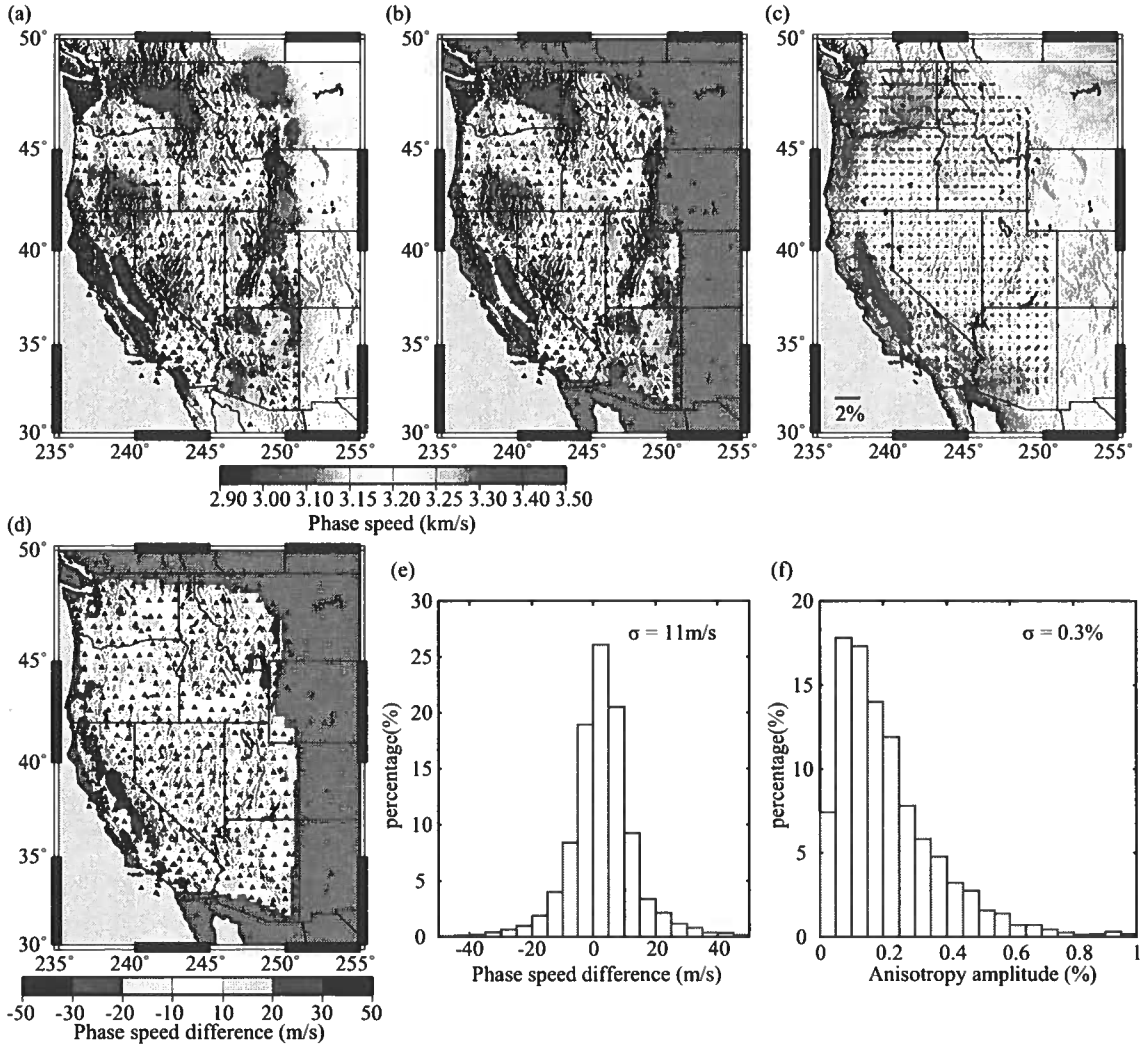

Figure 19. (a) The input wave speed model for the 12 sec simulations. The model is derived based on the isotropic result of Eikonal tomography with real data (Figure 10a) where the model gradually smears into a homogeneous model near the boundary of the station coverage. (b)-(c) The isotropic and anisotropic inversion results from Eikonal tomography with the 12 sec synthetic dataset. (d) The difference between the synthetic inversion and smoothed input model where positive values indicate that the synthetic inversion gives a higher local phase speed. (e) Normalized histogram of the speed difference across the studied region between the synthetic inversion and the smoothed input model. (f) Normalized histogram of the anisotropic peak-to-peak amplitude of the synthetic inversion across the studied region.

equal to 10m/s and 0.3% peak-to-peak (or 6m/s assuming 4km/s isotropic speed) (Figures 19e, 19f, 20e, and 20f), respectively, are generally small relative to the observed isotropic velocity variations (Figure 9a and 10a) and anisotropy amplitudes (Figures 14b and 17b). They are, however, approximately on the same scale as the estimated uncertainties derived from our statistical analysis (Figures 8a, 8b, and 15c). This suggests that the estimated uncertainties described in Section 4, which only accounts the random measurement errors, may underestimate the difference between the tomography results and the real medium properties. When numerical solutions are available, such as here, systematic errors due to the tomography method can be numerically estimated and a better estimation of the uncertainty can be made by summing the effects of the systematic and random measurement errors. However, this may prove impractical due to the heavy computation required. Considering the positive correlation between random (Figures 8a, 8b, and 15c) and systematic errors (Figures 19c, 19d, 20c, 20d), here we propose 1.5 as a rule of thumb scaling factor to multiply the random error uncertainty estimations to provide a more realistic uncertainty estimate.

We would like to emphasis here that the systematic

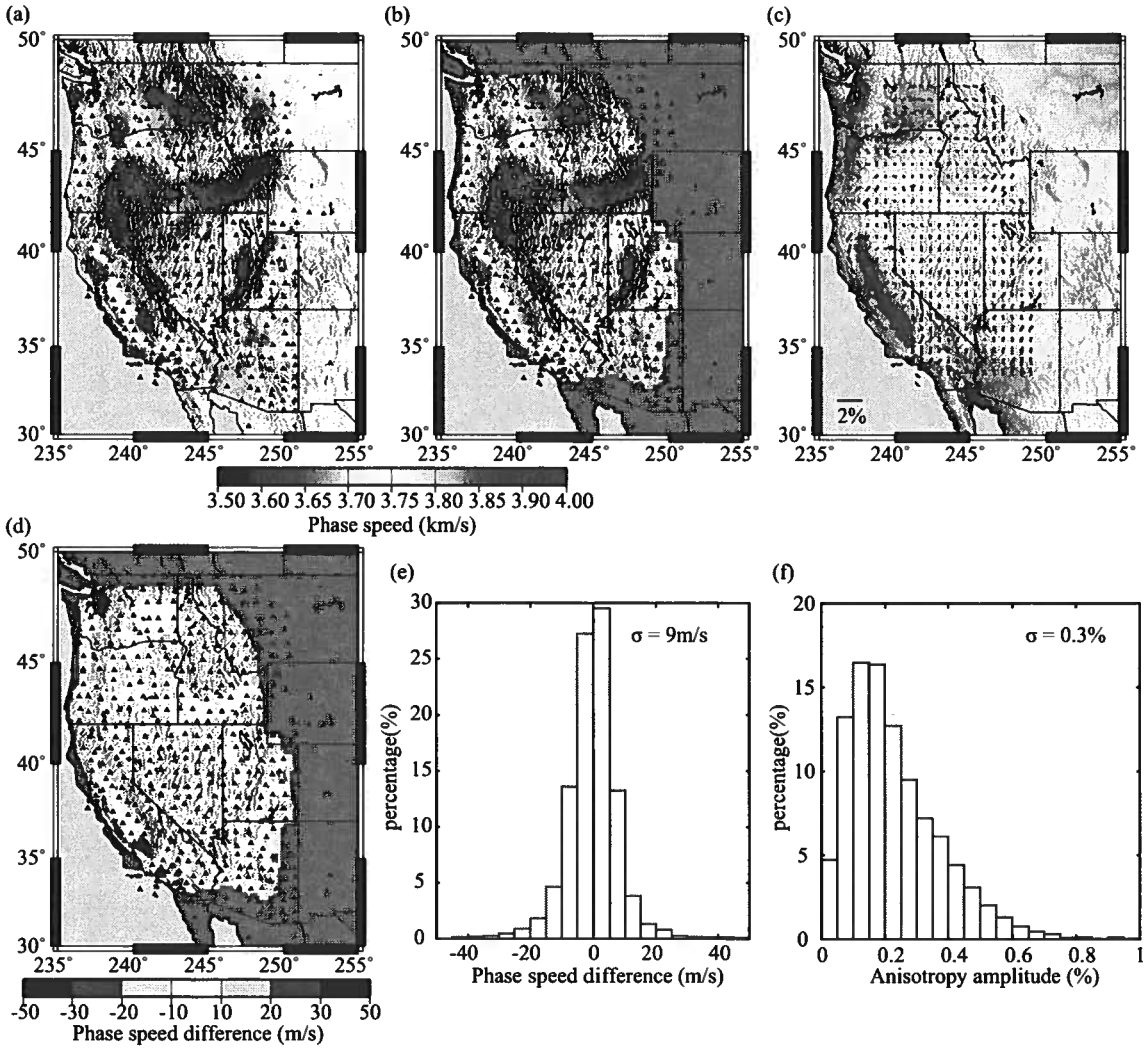

Figure 20. Same as Figure 19, but for the 36 sec simulations.

errors discussed here are solely due to the imperfection in the tomography method and do not account for systematic errors in travel time measurements. Systematic travel time measurement errors can arise, for example, due to timing errors or inhomogeneous noise source distributions for noise cross-correlation measurements. We believe that the effect of inhomogeneous noise source distribution in our results is small, however. Travel time errors due to inhomogeneous source distribution are likely similar between nearby stations. When the gradient is calculated in Eikonal tomography, these errors will cancel.

5.2 Advantages and limitations of Eikonal tomography

There are several significant advantages of Eikonal tomography over traditional surface wave tomography methods.

First, the implementation of the inverse operator for Eikonal tomography depends on operations to the data without explicitly solving the forward problem. For a wave propagating in an inhomogeneous medium, the observed wave properties such as phase travel time are only linearly related to the local velocity structure when structural perturbations are small. In other words, any linearized forward operator, such as the ray or finite frequency sensitivity integrals, and the inverse operator derived from it can only be considered approximate. Errors caused by this linearization are often overlooked or are unknown, and moving beyond them requires itera-

tive simulations which are computationally expensive. Eikonal tomography extracts the information about local velocity structure directly from the data without explicitly constructing the forward operator. It, therefore, finesses the nonlinear nature of the problem and should result in a better estimate of both the local isotropic and anisotropic phase speeds, especially where off-great-circle propagation is important.

Second, uncertainties in local phase speeds can be estimated with Eikonal tomography. Instead of minimizing a penalty functional that usually includes some combination of global misfit and model norm or roughness constraints, Eikonal tomography directly estimates local phase speed from independent measurements based on different phase travel time surfaces. Therefore, the uncertainties of the resulting local phase speeds can be determined statistically in a straightforward way. The uncertainties are important for later 3D inversion and quantitative comparisons between different models.

Third, Eikonal tomography is free from explicit model regularization. The method, therefore, eliminates the need to make ad-hoc choices of the damping and regularization parameters which are sometimes controversial and may result in dubious models. This particularly is a problem for studies of surface wave azimuthal anisotropy because the increased number of degrees of freedom is often not offset by a comparable improvement in misfit. Eikonal tomography with the additional smoothing intrinsically embedded in the phase front tracking process has no explicit regularization and the subjectivity of the inverter to affect the tomographic result is restricted.

Fourth, the azimuthal dependence of phase speeds can be measured directly without assuming its parametric form. Unlike classic studies of Pn azimuthal anisotropy (e.g., Morris et al. 1969) where the wave speed variation with the direction of propagation is observed directly, traditional surface wave tomography typically posits the relationship between phase speed and the direction of wave propagation based on theoretical studies of weakly anisotropic media (e.g. Smith & Dahlen 1973). The ability to measure and observe the azimuthal dependence of phase speeds directly leads to greater confidence in the information about anisotropy.

There are several limitations on Eikonal tomography worthy of note. First, unlike traditional inversion methods where the resolution is controlled by path or kernel densities, Eikonal tomography estimates the coherence length of the measurements which is controlled by station spacing. Without applying a more sophisticated travel time surface interpolation method, this prohibits the use of this technique to resolve structures smaller than the inter-station spacing.

Second, when long period or more complicated surface waves are considered, the second term in equation 2 can have values more similar to the magnitude of the phase speed anomalies that we seek to resolve. Although our simulations shows that the amplitude term is relatively unimportant for our dataset, other theoretical and numerical studies, such as Wielandt (1993) and Friederich et al. (2000), suggest that when either the velocity anomaly is smaller than a wavelength or the incoming wave is complicated by multipathing, neglect of the amplitude term by the Eikonal equation can blur the velocity anomaly and cause systematic errors in the phase speed measurements. It is possible to solve this problem by inverting both phase and amplitude together which amounts to recasting the problem in terms of the Helmholtz equation. Amplitude measurements are, however, less accurate than phase measurements and the second spatial derivative of the amplitude variation tends to be unstable and is underestimated, particularly when the station spacing is sparse. The situation is even worse for measurements based on ambient noise cross-correlations where amplitudes have been separately normalized for different stations so that meaningful amplitude information has been lost. Amplitude anomalies then mainly reflect the distribution of ambient noise sources not structural gradients.

Third, travel time interpolation schemes usually are unreliable near the periphery of the station coverage which results in increasing both random and systematic errors. Hence, the area that can be imaged by the Eikonal tomography method is generally smaller than when a traditional tomography method is applied (Figure 9 and 10). It requires a large scale array, such as the TA, to really take the advantages of the Eikonal tomography method where both applicable area can be extended and measurement uncertainties can be significantly reduced when ambient noise method is applied.

5.3 Applicability to earthquake tomography

To construct the phase travel time surfaces in this study we use measurements of ambient noise. In principle, however, Eikonal tomography can be applied to phase travel time measurements based on earthquake waveforms. There are a few differences, however, considering the nature of earthquake measurements.

First, surface waves emitted by a distant source usually develop a certain amount of multipathing that can potentially invalidate the assumption of smoothly varying amplitudes. In fact, this is the fundamental concept of the two plane wave inversion method (e.g., Yang & Forsyth 2006). Friederich et al. (2000) showed numerically how wave complexity can contribute to uncertainties in the local phase speeds inferred from the Eikonal equation. This problem is relatively minor for measurements based on ambient noise cross-correlations in the western US because the effective sources (i.e., the stations in the ambient noise method) usually are relatively close, with average distances near 700 km. Other than at the short period end of our study and near regions with sharp velocity contrasts, this is usually too short

for multipathing to be well developed. Second, surface wave studies based on teleseismic events usually focus on longer periods (> 25 sec) due to the strong scattering and attenuation of shorter period signals. At longer periods, when a wavelength is larger than the size of a velocity anomaly, the second term in equation 2 can blur and distort the velocity anomaly which we wish to resolve (Friederich et al. 2000).

Considering these factors, the amplitude term may play a bigger role in Eikonal tomography based on earthquake measurements and the second term in equation 2 should probably be properly taken into account. Unlike ambient noise cross-correlation measurements where only the phase information is retained, the amplitude of the surface wave emitted by an earthquake can be used in the inversion as well. By including amplitude information, the Helmholtz equation can be applied instead of the Eikonal equation, and may resolve the local phase velocity structure with greater certainty (Wielandt 1993; Friederich et al. 2000; Pollitz 2008).

6 CONCLUSIONS

We present a new method of surface wave tomography called Eikonal tomography and argue that this method presents an improvement over traditional methods of ambient noise tomography, particularly as the method is applied to data from the Transportable Array component of EarthScope/USArray. The method initiates by tracking phase fronts across the array to produce phase travel time maps centered on each station, considered as an "effective source". The method culminates by interpreting the local gradients of the phase time surfaces in terms of local phase speed and the direction of propagation of the wave. The most significant advantages of Eikonal tomography compared with traditional straight-ray tomography is its more accurate representation of wave propagation, its ability to produce meaningful uncertainty information about the inferred phase speed maps, and its production of more reliable information about azimuthal anisotropy. Improvements in the isotropic dispersion maps result predominantly from the methods ability to track the direction of propagation of waves, which is tantamount to use of off-great-circle geometrical rays but without the need for iteration. Improvements in information about azimuthal anisotropy derive from the methods freedom from ad-hoc choices in regularization. This provides more reliable information about the amplitude of anisotropy, in particular. In addition, the method provides a local visualization of how phase speeds vary with azimuth, which we believe adds considerably to confidence in the results. Eikonal tomography is an approximate method. It accurately tracks the direction of wave propagation but only approximately incorporates what may be traditionally thought of as finite-frequency effects and assumes a single wave propagating at each point in space. To improve the ability to resolve small scale feature and reduce systematic errors, future work will focus on finding more sophisticated interpolation schemes as well as incorporating the amplitude term of equation 2 .

REFERENCES

Alsina, D, Snieder, R, & Maupin, V. 1993. A test of the great circle approximation in the analysis of surface waves. *Geophys. Res. Lett.*, **20**(10), 915–918.

Barmin, M. P., Ritzwoller, M. H., & Levshin, A. L. 2001. A fast and reliable method for surface wave tomography. *Pure Appl. Geophys.*, **158**(8), 1351–1375.

Bensen, G. D., Ritzwoller, M. H., Barmin, M. P., Levshin, A. L., Lin, F., Moschetti, M. P., Shapiro, N. M., & Yang, Y. 2007. Processing seismic ambient noise data to obtain reliable broad-band surface wave dispersion measurements. *Geophys. J. Int.*, **169**(3), 1239–1260.

Bensen, G. D., Ritzwoller, M. H., & Shapiro, N. M. 2008. Broadband ambient noise surface wave tomography across the United States. *J. Geophys. Res.*, **113**(B5).

Bodin, Thomas, & Maupin, Valerie. 2008. Resolution potential of surface wave phase velocity measurements at small arrays. *Geophys. J. Int.*, **172**(2), 698–706.

Boschi, L. 2006. Global multiresolution models of surface wave propagation: comparing equivalently regularized Born and ray theoretical solutions. *Geophys. J. Int.*, **167**(1), 238–252.

Brisbourne, A. M., & Stuart, G. W. 1998. Shear-wave velocity structure beneath North Island, New Zealand, from Rayleigh-wave interstation phase velocities. *Geophys. J. Int.*, **133**(1), 175–184.

Dahlen, FA, Hung, SH, & Nolet, G. 2000. Frechet kernels for finite-frequency traveltimes - I. Theory. *Geophys. J. Int.*, **141**(1), 157–174.

Deschamps, F., Lebedev, S., Meier, T., & Trampert, J. 2008. Azimuthal anisotropy of Rayleigh-wave phase velocities in the east-central United States. *Geophys. J. Int.*, **173**(3), 827–843.

Ekstrom, G., Tromp, J., & Larson, E. W. F. 1997. Measurements and global models of surface wave propagation. *J. Geophys. Res.*, **102**(B4), 8137–8157.

Friederich, W. 1998. Wave-theoretical inversion of teleseismic surface waves in a regional network: phase-velocity maps and a three-dimensional upper-mantle shear-wave-velocity model for southern Germany. *Geophys. J. Int.*, **132**(1), 203–225.

Friederich, W., Hunzinger, S., & Wielandt, E. 2000. A note on the interpretation of seismic surface waves over three-dimensional structures. *Geophys. J. Int.*, **143**(2), 335–339.

Laske, G., & Masters, G. 1998. Surface-wave polarization data and global anisotropic structure. *Geophys. J. Int.*, **132**(3), 508–520.

Levshin, A. L., Barmin, M. P., Ritzwoller, M. H., & Trampert, J. 2005. Minor-arc and major-arc global surface wave diffraction tomography. *Phys. Earth Planet. Int.*, **149**(3-4), 205–223.

Levshin, AL, Ritzwoller, MH, Barmin, MP, Villasenor, A, & Padgett, CA. 2001. New constraints on the arctic crust

and uppermost mantle: surface wave group velocities, P-n, and S-n. *Phys. Earth Planet. Inter.*, **123**(2-4, Sp. Iss. SI), 185–204.

Lin, F. C., Moschetti, M. P., & Ritzwoller, M. H. 2008. Surface wave tomography of the western United States from ambient seismic noise: Rayleigh and Love wave phase velocity maps. *Geophys. J. Int.*, **173**(1), 281–298.

Montelli, R., Nolet, G., & Dahlen, F. A. 2006. Comment on 'Banana-doughnut kernels and mantle tomography' by van der Hilst and de Hoop. *Geophys. J. Int.*, **167**(3), 1204–1210.

Morris, G. B., Raitt, R. W., & Shor, G. G. 1969. Velocity anisotropy and delay-time maps of mantle near Hawaii. *J. Geophys. Res.*, **74**(17), 4300–&.

Moschetti, M. P., Ritzwoller, M. H., & Shapiro, N. M. 2007. Surface wave tomography of the western United States from ambient seismic noise: Rayleigh wave group velocity maps. *Geochem. Geophys. Geosys.*, **8**(AUG 21), Q08010.

Nolet, G. 1990. Paritioned wave-form inversion and 2-dimensional structure in the Network of Autonomously Recording Seismographs. *J. Geophys. Res.*, **95**(B6), 8499–8512.

Pollitz, Fred F. 2008. Observations and interpretation of fundamental mode Rayleigh wavefields recorded by the Transportable Array (USArray). *J. Geophys. Res.*, **113**(B10), B10311.

Prindle, K., & Tanimoto, T. 2006. Teleseismic surface wave study for S-wave velocity structure under an array: Southern California. *Geophys. J. Int.*, **166**(2), 601–621.

Ritzwoller, MH, & Levshin, AL. 1998. Eurasian surface wave tomography: Group velocities. *J. Geophys. Res.*, **103**(B3), 4839–4878.

Roth, M, Muller, G, & Snieder, R. 1993. VELOCITY SHIFT IN RANDOM-MEDIA. *Geophys. J. Int.*, **115**(2), 552–563.

Sabra, K. G., Gerstoft, P., Roux, P., Kuperman, W. A., & Fehler, M. C. 2005b. Surface wave tomography from microseisms in Southern California. *Geophys. Res. Lett.*, **32**(14), L14311.

Shapiro, N. M., Campillo, M., Stehly, L., & Ritzwoller, M. H. 2005. High-resolution surface-wave tomography from ambient seismic noise. *Science*, **307**(5715), 1615–1618.

Shearer, P. 1999. *Introduction to seismology.* Cambridge: Cambridge University Press.

Sherburn, Steven, White, Robert S., & Chadwick, Mark. 2006. Three-dimensional tomographic imaging of the Taranaki volcanoes, New Zealand. *Geophys. J. Int.*, **166**(2), 957–969.

Smith, M. L., & Dahlen, F. A. 1973. Azimuthal Dependence of Love and Rayleigh-Wave Propagation in a Slightly Anisotropic Medium. *J. Geophys. Res.*, **78**(17), 3321–3333.

Trampert, J, & Spetzler, J. 2006. Surface wave tomography: finite-frequency effects lost in the null space. *Geophys. J. Int.*, **164**(2), 394–400.

Trampert, J, & Woodhouse, JH. 1996. High resolution global phase velocity distributions. *Geophys. Res. Lett.*, **23**(1), 21–24.

Trampert, J, & Woodhouse, JH. 2003. Global anisotropic phase velocity maps for fundamental mode surface waves between 40 and 150 s. *Geophys. J. Int.*, **154**(1), 154–165.

Tromp, J., Tape, C., & Liu, Q. Y. 2005. Seismic tomography, adjoint methods, time reversal and banana-doughnut kernels. *Geophys. J. Int.*, **160**(1), 195–216.

van der Hilst, R. D., & de Hoop, M. V. 2005. Banana-doughnut kernels and mantle tomography. *Geophys. J. Int.*, **163**(3), 956–961.

Van Der Lee, S, & Frederiksen, A. 2005. Surface wave tomography applied to the North American upper mantle. *In:* Levander, A., & Nolet, G (eds), *Seismic Earth: Array Analysis of Broadband Seismograms.* American Geophysical Union, Washington, D.C.: American Geophysical Union Monograph.

Wielandt, E. 1993. Propagation and Structural Interpretation of Nonplane Waves. *Geophys. J. Int.*, **113**(1), 45–53.

Woodhouse, J. H., & Dziewonski, A. M. 1984. Mapping the Upper Mantle - 3-Dimensional Modeling of Earth Structure by Inversion of Seismic Waveforms. *J. Geophys. Res.*, **89**(NB7), 5953–&.

Yang, Y., & Forsyth, D. W. 2006. Rayleigh wave phase velocities, small-scale convection, and azimuthal anisotropy beneath southern California. *J. Geophys. Res.*, **111**(B7), B07306.

Yang, Y. J., Ritzwoller, M. H., Levshin, A. L., & Shapiro, N. M. 2007. Ambient noise rayleigh wave tomography across Europe. *Geophys. J. Int.*, **168**(1), 259–274.

Yang, Yingjie, Ritzwoller, Michael H., Lin, F. C, Moschetti, M. P., & Shapiro, Nikolai M. 2008. Structure of the crust and uppermost mantle beneath the western United States revealed by ambient noise and earthquake tomography. *J. Geophys. Res.*, **113**(B12), B12310.

Yao, H. J., van der Hilst, R. D., & de Hoop, M. V. 2006. Surface-wave array tomography in SE Tibet from ambient seismic noise and two-station analysis - I. Phase velocity maps. *Geophys. J. Int.*, **166**(2), 732–744.

Yoshizawa, K, & Kennett, BLN. 2002. Determination of the influence zone for surface wave paths. *Geophys. J. Int.*, **149**(2), 440–453.

Zhou, Y., Dahlen, F. A., & Nolet, G. 2004. Three-dimensional sensitivity kernels for surface wave observables. *Geophys. J. Int.*, **158**(1), 142–168.

Zhou, Y., Dahlen, F. A., Nolet, G., & Laske, G. 2005. Finite-frequency effects in global surface-wave tomography. *Geophys. J. Int.*, **163**(3), 1087–1111.

General representation theorem for perturbed media and application to Green's function retrieval for scattering problems

Clement Fleury, Roel Snieder, & Ken Larner
Center for Wave Phenomena, Colorado School of Mines

ABSTRACT
Green's function reconstruction relies on representation theorems. For acoustic waves, it has been shown theoretically and observationally that a representation theorem of the correlation-type leads to the retrieval of the Green's function by cross-correlating fluctuations recorded at two locations and excited by uncorrelated sources. We extend the theory to any system that satisfies a linear partial differential equation, and define an *interferometric operation* that is more general than cross-correlation for the reconstruction. We analyze Green's function reconstruction for perturbed media and establish a representation theorem specifically for field perturbations. That representation is then applied to the general treatment of scattering problems, enabling interpretation of the contributions to Green's function reconstruction in terms of direct and scattered waves. Perhaps surprising, Green's functions that account for scattered waves cannot be reconstructed from scattered waves alone. For acoustic waves, retrieval of scattered waves also requires cross-correlating direct and scattered waves at receiver locations. The addition of cross-correlated scattered waves with themselves is necessary to cancel the spurious events that contaminate the retrieval of scattered waves from the cross-correlation of direct with scattered waves. We illustrate these concepts with numerical examples for the case of an open scattering medium. The same reasoning holds for the retrieval of any type of perturbations, and can be applied to perturbation problems such as electromagnetic waves in conductive media, and elastic waves in heterogeneous media.

Key words: representation theorem – Green's function retrieval – interferometry – perturbation theory – scattering problem.

1 INTRODUCTION

The extraction of Green's functions from wave field fluctuations has recently received considerable attention. The technique, known in much of the literature as interferometry, is described in tutorials (Curtis *et al.* 2006; Larose *et al.* 2006; Wapenaar *et al.* 2007) and has been applied to a large variety of fields including ultrasonics (Lobkis & Weaver 2001; Malcolm *et al.* 2004; Weaver & Lobkis 2001), global (Campillo & Paul 2003; Sabra *et al.* 2005a; Shapiro *et al.* 2005) and exploration (Bakulin & Calvert 2006; Miyazawa *et al.* 2008) seismology, helioseismology (Rickett & Claerbout 1999), medical imaging (Sabra *et al.* 2007), structural engineering (Kohler *et al.* 2007; Snieder & Safak 2006; Thompson & Snieder 2006), and ocean acoustics (Roux & Kuperman 2004; Sabra *et al.* 2005b). The theory relies on representation theorems (of either the convolution or correlation type) and allows for the retrieval of Green's functions for acoustic (Wapenaar & Fokkema 2006), elastic (Snieder 2002; Van Manen *et al.* 2006; Wapenaar *et al.* 2004), and electromagnetic (Slob *et al.* 2007; Wapenaar *et al.* 2006) waves. For acoustic media, the impulse response between two receivers is retrieved by cross-correlating and summing the signals recorded by the two receivers

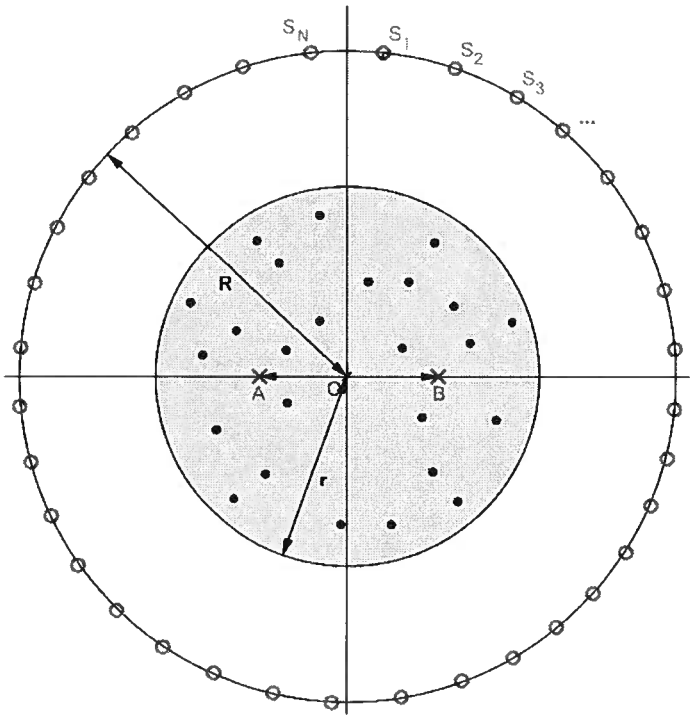

Figure 1. Two receivers, A and B, separated by a distance $d = 1.9$ km, are embedded in a two-dimensional acoustic scattering medium (unperturbed velocity $c_0 = 3.8$ km/s) characterized by n uniformly distributed isotropic point scatterers localized inside a circle of radius $r = 1.0$ km. A dense distribution of $N = 1000$ sources evenly spaced along a circle of radius $R = 4.0$ km surrounds the medium. For $n = 500$, the heterogeneous medium is considered strongly scattering. For $n = 10$, the scattering regime is weak.

for uncorrelated sources enclosing the studied system. This process, sometimes referred to as the *virtual source* method (Bakulin & Calvert 2006), is equivalent to having a source at one of the receiver locations. Further studies have extended the concept to a wide class of linear systems (Gouédard *et al.* 2008; Snieder *et al.* 2007; Wapenaar & Fokkema 2004; Wapenaar *et al.* 2006; Weaver 2008), and our work aims to accomplish the same objective.

We explore a general formulation of representation theorem for any system that satisfies a linear partial differential equation (or, mathematically, for any field in the appropriate Sobolev space). In particular, this formulation involves no assumption of spatial reciprocity or time-reversal invariance. We introduce a bilinear *interferometric operator* as a means of reconstructing the Green's function and study the influence of perturbations on the interferometric operator, and thereby derive a general representation theorem for perturbed media. The perturbed field can be retrieved by using a process characterized by the interferometric operation, which is generally more complex than cross-correlation. For common systems, this interferometric operation can be simplified using the symmetry properties of differential operators. We apply the theory to scattering problems and illustrate the approach with an example involving scattered acoustic waves, obtaining a result that concurs with that published by Vasconcelos *et al.* (2009) on the representation theorem for scattering in acoustic media. In geophysics, applications of perturbation reconstruction exist in the areas of, for example, crustal seismology, seismic imaging, well monitoring, and waveform inversion.

After exposing this general representation theorem for perturbed media, we give an innovative interpretation of Green's function reconstruction. To emphasize the connection between the general formulation and the particular case of scattering problems, we refer to unperturbed field as *direct field*, and field perturbation as *scattered field*. Perturbation retrieval can be understood in terms of interferences between unperturbed fields and field perturbations. One might think that field perturbations can be reconstructed with contributions from just field perturbations alone; the retrieval of field perturbations, however, requires the interferences with unperturbed fields. For acoustic media, this means that the *scattering response* between two receivers cannot be retrieved by cross-correlating only late coda waves. Here, the scattering response is defined as the superposition of the causal and acausal scattering Green's functions between the two points. In the numerical experiments conducted here (see Figure 1), two receivers are embed-

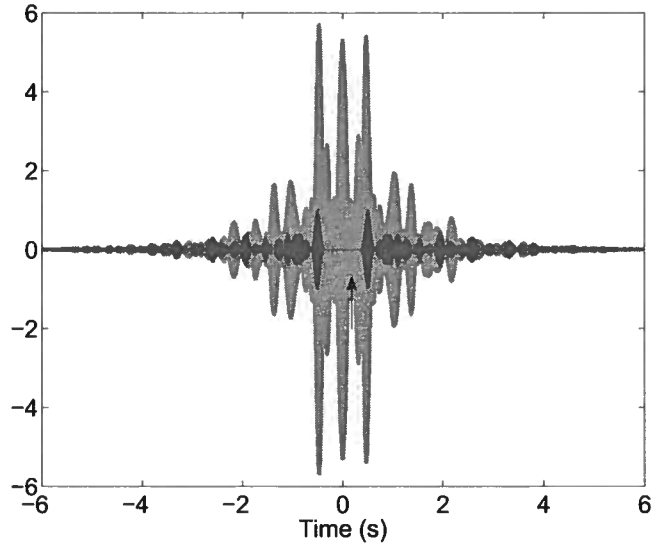

(a)

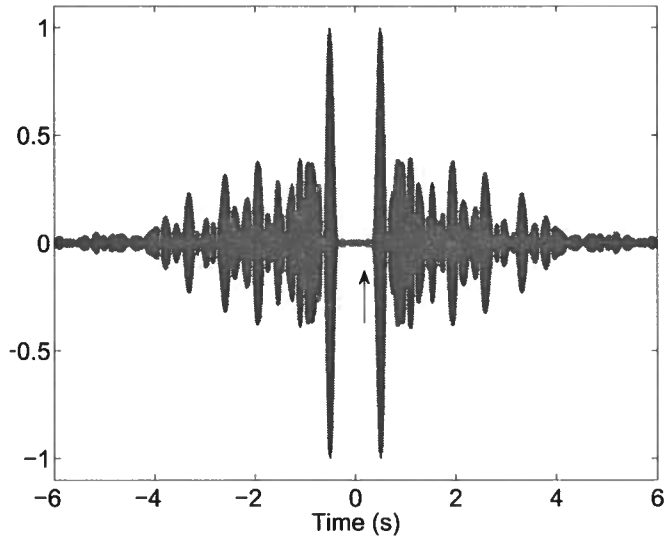

(b)

Figure 2. The blue curves show the actual *scattering response* (superposition of the causal and acausal scattering Green's functions) between two points embedded in a strongly heterogenous medium. The red curves represent the wave reconstructed by cross-correlating the waves recorded by two receivers at the same locations. Note the black arrow, which corresponds to the time of the first expected physical arrival. In panel (a), only scattered waves are cross-correlated. The reconstruction fails no matter how dense is the distribution of sources enclosing the medium. This failure of interferometry is not caused by restrictions of source distribution, aperture, or equipartitioning, but is a consequence of the missing contribution of recorded direct waves. In panel (b), both direct and scattered waves are cross-correlated, yielding a result confirming that the scattering response can be retrieved by interferometry.

ded in a scattering medium and surrounded by sources that are activated seperately, and consequently, generate uncorrelated wavefields. The numerical scheme is based on computation of the analytical solution to the two-dimensional heterogeneous acoustic wave equation for a distribution of isotropic point scatterers (Groenenboom & Snieder 1995). In Figure 2, we compare the actual scattering response for a source at the receiver lo-

cation with the signal reconstructed by cross-correlating and summing the scattered waves recorded at the receiver positions. For a strongly scattering medium (average wavelength larger than several scattering mean free paths (Tourin *et al.* 2000)), Figure 2(a) shows that the reconstruction completely fails to retrieve the scattering response from cross-correlation of only the scattered waves recorded at the receiver locations. The reconstructed wave with only scattered waves is totally innaccurate: the early arrivals are non-physical because they do not respect causality, arriving before the minimum travel-time between the two receivers, while the late arrivals show no resemblance to the actual scattering response. Accurate retrieval of the scattered waves instead requires contributions from both direct and scattered waves, as shown in Figure 2(b).

In this paper, we provide an interpretation of this result; one can find a similar approach by Halliday & Curtis (2009) and Snieder & Fleury (2010), the latter of which describes the case of multiple scattering by discrete scatterers. In Snieder & Fleury (2010), we identify different scattering paths, show their contributions to the retrieval of either physical or nonphysical arrivals, and analyze how cancelations occur to allow the scattering Green's function to emerge. Our interpretation, along with that given by Halliday & Curtis (2009), leads to the same important conclusion: the cross-correlation of purely scattered waves does not allow extraction of the correct scattered waves.

The paper is organized as follows. In section 2, we describe the general systems under consideration and introduce the concept of perturbation. In section 3, we define the interferometric operator and its relation to representation theorems, emphasizing the influence of perturbations on this operator. Section 4 presents the general representation theorems for perturbations that follow this approach. In section 5, we apply this theory to interpret the reconstruction of Green's function perturbations; section 6 offers discussions and conclusions.

2 GREEN'S FUNCTION PERTURBATIONS FOR GENERAL SYSTEMS

Consider a general system governed by a linear partial differential equation in the frequency domain. In order to avoid the complexity of formalism that could obscure the main purpose of this paper, we leave the vector case for Appendix A. Let the complex scalar field $u_0(\mathbf{r},\omega)$ be defined in a volume D_{tot}. One can adapt the result of this work to the time domain using the Fourier convention $u_0(\mathbf{r},t) = \int u_0(\mathbf{r},\omega) exp(-j\omega t) d\omega$. Henceforth, we suppress the frequency dependence of variables and operators. The unperturbed field $u_0(\mathbf{r})$ is a solution of the unperturbed equation

$$H_0(\mathbf{r}) \cdot u_0(\mathbf{r}) = s(\mathbf{r}), \tag{1}$$

where H_0 is the linear differential operator and s is the source term, associated with the unperturbed system. The dot denotes a contraction when vectors and tensors are considered. For acoustic waves, one may define H_0 as the propagator for non-uniform density media: $H_0 = \nabla \cdot (\rho_0^{-1}\nabla) + \rho_0^{-1}\omega^2/c_0^2$, where ρ and c denote density and velocity, respectively.

Assuming a perturbation of the system, the perturbed field $u_1(\mathbf{r})$ follows from

$$H_1(\mathbf{r}) \cdot u_1(\mathbf{r}) = s(\mathbf{r}) \tag{2}$$

$$H_0(\mathbf{r}) \cdot u_1(\mathbf{r}) = V(\mathbf{r}) \cdot u_1(\mathbf{r}) + s(\mathbf{r}), \tag{3}$$

where V is the perturbation operator, and $H_1 = H_0 - V$ is the linear differential operator associated with the perturbed system. For example, for acoustic waves, with a change in velocity for the medium, the perturbation operator is $V = \rho_0^{-1}\omega^2/c_0^2(1 - c_0^2/c_1^2)$. Alternatively, a change in experimental conditions might imply a variation in density; then, a way to account for this perturbation is to consider $V = (\rho_0^{-1} - \rho_1^{-1})\omega^2/c_0^2 + \nabla \cdot ((\rho_0^{-1} - \rho_1^{-1})\nabla)$. One could also neglect attenuation in the medium in the first approximation and correct for it by introducing the perturbation $V = j\omega^2\Im(\kappa_0^{-1} - \kappa_1^{-1})$, where $\Im$ denotes the imaginary part and $\kappa = \rho c^2$ is the bulk modulus. We are free to arbitrarily choose or even interchange the reference 0 and perturbed 1 states for any perturbation problem. Indeed, the perturbation need not necessarily introduce more complexity; its definition depends on the characteristics of the perturbation problem that one tries to solve.

For a problem to be well-defined, one needs to specify boundary conditions. Assume that the boundary conditions are unperturbed, and consider a regular problem with homogeneous boundary conditions:

$$B(\mathbf{r}) \cdot u_{0,1}(\mathbf{r}) = 0 \text{ on the boundary}, \tag{4}$$

where B denotes the linear boundary condition operator for the total volume D_{tot}. One can, for example, apply the Sommerfeld radiation condition for acoustic waves, but the boundary conditions need not be limited to being homogeneous. In Appendix B, we extend our reasoning to any unperturbed boundary conditions.

The Green's functions $G_0(\mathbf{r},\mathbf{r}_S)$ and $G_1(\mathbf{r},\mathbf{r}_S)$ for both unperturbed and perturbed systems are defined as solutions for an impulsive source at location $\mathbf{r}_S$,

$$s(\mathbf{r}) = \delta(\mathbf{r} - \mathbf{r}_S). \tag{5}$$

From the above equations, one obtains the familiar relation between unperturbed and perturbed Green's functions, known as the Lippmann-Schwinger equation (Rodberg & Thaler 1967):

$$G_1(\mathbf{r},\mathbf{r}_S) = G_0(\mathbf{r},\mathbf{r}_S) + \int_D G_0(\mathbf{r},\mathbf{r}_1)\cdot V(\mathbf{r}_1)\cdot G_1(\mathbf{r}_1,\mathbf{r}_S)d^3r_1, \tag{6}$$

where D is a subvolume of the total domain D_{tot}. We introduce the notation,

$$(f|g) \equiv \int_D f(\mathbf{r})\cdot g(\mathbf{r})d^3r, \tag{7}$$

so that the Lippmann-Schwinger equation can be written as

$$G_1(\mathbf{r},\mathbf{r}_S) = G_0(\mathbf{r},\mathbf{r}_S) + \left(G_0(\mathbf{r},\mathbf{r}_1)\,|V(\mathbf{r}_1)|\,G_1(\mathbf{r}_1,\mathbf{r}_S)\right). \tag{8}$$

Finally, we define the Green's function perturbation or *scattering Green's function* that characterizes the field perturbation $u_S(\mathbf{r}) = u_1(\mathbf{r}) - u_0(\mathbf{r})$ as

$$G_S(\mathbf{r},\mathbf{r}_S) = G_1(\mathbf{r},\mathbf{r}_S) - G_0(\mathbf{r},\mathbf{r}_S), \tag{9}$$

or

$$G_S(\mathbf{r},\mathbf{r}_S) = \left(G_0(\mathbf{r},\mathbf{r}_1)\,|V(\mathbf{r}_1)|\,G_1(\mathbf{r}_1,\mathbf{r}_S)\right). \tag{10}$$

To clarify the terminology used throughout this paper, the unperturbed field, perturbed field, and field perturbation are denoted by u_0, u_1, and u_S, respectively.

3 DEFINITION OF THE INTERFEROMETRIC OPERATOR

To establish a representation theorem for perturbations, we first derive a general expression for Green's function retrieval by using a representation theorem of the correlation type (Wapenaar & Fokkema 2006). Consider two states of the field u, labeled A and B, governed by the partial differential equation $\mathcal{L}_{A,B}$,

$$\mathcal{L}_{A,B}: \quad H(\mathbf{r})\cdot u_{A,B}(\mathbf{r}) = s_{A,B}(\mathbf{r}), \tag{11}$$

where the subscript $_{A,B}$ refers to either state A or B. Following Fokkema & Van den Berg (1993) and Fokkema *et al.* (1996), we evaluate $\left(u_A|\overline{\mathcal{L}}_B\right) - (\overline{u}_B|\mathcal{L}_A)$, where $\overline{f}$ denotes the complex conjugate of f; consequently,

$$\left(u_A\,|\overline{H}|\,\overline{u}_B\right) - (\overline{u}_B|H|u_A) = (u_A|\overline{s}_B) - (\overline{u}_B|s_A). \tag{12}$$

For impulsive sources, $s_{A,B}(\mathbf{r}) = \delta(\mathbf{r}-\mathbf{r}_{A,B})$, and the fields $u_{A,B}(\mathbf{r}) = G(\mathbf{r},\mathbf{r}_{A,B})$, the Green's functions in states A and B, so (12) becomes the general representation theorem of correlation-type for interferometry,

$$\begin{aligned} G(\mathbf{r}_B,\mathbf{r}_A) - \overline{G}(\mathbf{r}_A,\mathbf{r}_B) &= \left(G(\mathbf{r},\mathbf{r}_A)\,|\overline{H}(\mathbf{r})|\,\overline{G}(\mathbf{r},\mathbf{r}_B)\right) \\ &- \left(\overline{G}(\mathbf{r},\mathbf{r}_B)\,|H(\mathbf{r})|\,G(\mathbf{r},\mathbf{r}_A)\right). \end{aligned} \tag{13}$$

This result is a general extension of the representation theorem in Snieder *et al.* (2007). In order to interpret and characterize the Green's function reconstruction more conveniently, we define the operator I_H,

$$I_H\{f,g\} \equiv \left(f\,|\overline{H}|\,g\right) - \left(g\,|H|\,f\right), \tag{14}$$

so that the general representation theorem can be written as

$$G(\mathbf{r}_B,\mathbf{r}_A) - \overline{G}(\mathbf{r}_A,\mathbf{r}_B) = I_H\{G(\mathbf{r},\mathbf{r}_A),\overline{G}(\mathbf{r},\mathbf{r}_B)\}. \tag{15}$$

The operation $I_H\{\cdot,\cdot\}$ describes how Green's functions in a subvolume D "interfere" to reconstruct the Green's function between the two points A and B. We consequently refer to I_H as the *interferometric operator*, associated with H, that acts on functions f and g, and call the result of operation (14) an *interference* between f and g. For acoustic waves, the interferometric operation is the following volume integration:

$$I_H\{f,g\} = \int_D [f(\mathbf{r})\nabla\cdot(\rho^{-1}\nabla g)(\mathbf{r}) - g(\mathbf{r})\nabla\cdot(\rho^{-1}\nabla f)(\mathbf{r})]d^3r. \tag{16}$$

Using Green's theorem, this volume integral becomes an integral over the bounding surface δD enclosing volume D:

$$I_H\{f,g\} = \oint_{\delta D} \rho^{-1}(\mathbf{r})[f(\mathbf{r})\nabla g(\mathbf{r}) - g(\mathbf{r})\nabla f(\mathbf{r})]\cdot\hat{\mathbf{n}}d^2r, \tag{17}$$

where $\hat{\mathbf{n}}$ is the outward unit normal vector at $\mathbf{r}$. Then, equation (15) retrieves the familiar representation theorem for acoustic waves (Wapenaar & Fokkema 2006):

$$G(\mathbf{r}_B,\mathbf{r}_A) - \overline{G}(\mathbf{r}_A,\mathbf{r}_B) = \oint_{\delta D} \rho^{-1}(\mathbf{r})[G(\mathbf{r},\mathbf{r}_A)(\mathbf{r})\nabla\overline{G}(\mathbf{r},\mathbf{r}_B) - \overline{G}(\mathbf{r},\mathbf{r}_B)\nabla G(\mathbf{r},\mathbf{r}_A)] \cdot \hat{\mathbf{n}} d^2r. \tag{18}$$

Returning to the general case, just as the unperturbed linear partial differential operator H_0 becomes $H_1 = H_0 - V$ after perturbating the system, the interferometric operators for unperturbed and perturbed systems, I_0 and I_1, relate in the following way:

$$\begin{aligned} I_0 &= I_{H_0} \\ I_1 &= I_0 - I_V. \end{aligned} \tag{19}$$

Note that, in general, I_0 and I_1 differ; that is, the interferometric operator is perturbed for a perturbed system. The exception ($I_1 = I_0$) occurs when $I_V = 0$. Consider, for example, the acoustic case previously described. The unperturbed Green's function is retrieved using expression (18), and, for a perturbation in velocity only,

$$I_V\{f,g\} = \int_D \frac{\omega^2}{\rho_0 {c_0}^2}\left[\left(1 - \left(\frac{c_0}{c_1}\right)^2\right) - \left(1 - \left(\frac{c_0}{c_1}\right)^2\right)\right] f(\mathbf{r})g(\mathbf{r})d^3r = 0, \tag{20}$$

so $I_1 = I_0$. If, instead, density rather than velocity is perturbed,

$$I_V\{f,g\} = \oint_{\delta D} (\rho_0^{-1}(\mathbf{r}) - \rho_1^{-1}(\mathbf{r}))[f(\mathbf{r})\nabla g(\mathbf{r}) - g(\mathbf{r})\nabla f(\mathbf{r})] \cdot \hat{\mathbf{n}} d^2r \neq 0. \tag{21}$$

Therefore, the interferometric operator changes ($I_1 \neq I_0$) with such a perturbation. Similarly, with a perturbation in attenuation,

$$I_V\{f,g\} = j\omega^2 \int_D \Im(\kappa_0^{-1} - \kappa_1^{-1}) g(\mathbf{r})f(\mathbf{r})d^3r \neq 0. \tag{22}$$

These examples illustrate that, in general, the same interferometric operation cannot be used to reconstruct both perturbed and unperturbed Green's functions; we need to estimate the perturbation of the interferometric operator, I_V, itself in order to apply interferometry for perturbed media. As seen in equations (21) and (22), the interferometric operator in general requires knowledge of medium properties for the perturbed system, a limiting factor because usually we know only the unperturbed medium properties. Equation (20), however, is a specific example of an interferometric operator that does remain unperturbed ($I_0 = I_1$) for nonzero perturbation. For benign cases such as this one, we need only know or estimate unperturbed medium properties, and measure or model both perturbed and unperturbed fields, in order to reconstruct the Green's functions.

Let us investigate such systems for which the interferometric operator is unperturbed ($I_V = 0$). Starting by reformulating the general representation theorem for both perturbed and unperturbed media, we retrieve the Green's functions using

$$G_{0,1}(\mathbf{r}_B,\mathbf{r}_A) - \overline{G}_{0,1}(\mathbf{r}_A,\mathbf{r}_B) = I_{0,1}\{G_{0,1}(\mathbf{r},\mathbf{r}_A), \overline{G}_{0,1}(\mathbf{r},\mathbf{r}_B)\}. \tag{23}$$

This expression clearly depends on the properties of the interferometric operator, and, according to definition (14), the reconstruction involves integration over the volume D. Because the integrand is a function of differential operators H_0 or H_1, and of the Green's functions between any point in D and points A or B, we need to know H_0, V, and the Green's functions for all points in the volume D in order to apply the interferometric operator and retrieve the Green's functions between A and B. In particular, estimation of the Green's functions for all points in D requires having sources throughout the entire volume D. To apply interferometry in practice, this requirement for sources or receivers over the entire volume is yet more limiting than the need to estimate perturbations of the medium properties; it would severely restrict the possibility of retrieving even unperturbed Green's functions.

In practice, we are interested in systems for which we can reconstruct Green's functions with a limited number of sources and receivers. Just as for acoustic waves in equation (18), we therefore aim for problems that enable us to transform the integration over volume D in expression (14) into integration over its boundary δD. This transformation allows significant reduction in the number of sources. In Appendix C, we show that this transformation can be done if and only if operators are *self-adjoint*. We also demonstrate that the self-adjoint symmetry of the operators implies spatial reciprocity under specific boundary conditions. In addition, the transformation of volume into surface integrals also constrains to just the surface δD the medium properties that must be known for the reconstruction. For perturbation problems that we are considering, we can always find a boundary of integration δD (for example, δD_{tot}) along which the system is unperturbed (there are no changes of the medium properties along δD). Then, under the assumption that H_0 and V are self-adjoint, the interferometric operation associated with this particular volume D can

be reduced to an integration over δD, and the interferometric operator is then unperturbed under the assumption that the properties of the medium are unchanged along this boundary. Consequently, we can reconstruct the perturbed Green's function independently of the perturbations in the rest of the volume. For example, for a perturbation of densities in an acoustic medium, expression (21) illustrates that the interferometric operator is unperturbed ($I_V = 0$) when the density is unchanged on the boundary δD.

To summarize, interferometry can be interpreted as the application of an interferometric operator. This technique is practical for systems characterized by self-adjoint operators and for perturbation problems in which the interferometric operator is unperturbed.

4 REPRESENTATION FOR GREEN'S FUNCTION PERTURBATIONS

In the previous section, we established a general representation theorem for perturbed systems. Here, we derive a representation for field perturbations. This general representation differs from the traditional representation theorem for the special case of scattered acoustic waves (Vasconcelos *et al.* 2009) because, in general, we must take into account the perturbation of the interferometric operator. The perturbation of Green's function, defined in section 2, can be retrieved by interferometry by taking the difference of the two equations (23) for the perturbed and unperturbed states to give

$$G_S(\mathbf{r}_B,\mathbf{r}_A) - \overline{G}_S(\mathbf{r}_A,\mathbf{r}_B) = I_1\{G_1(\mathbf{r},\mathbf{r}_A),\overline{G}_1(\mathbf{r},\mathbf{r}_B)\} - I_0\{G_0(\mathbf{r},\mathbf{r}_A),\overline{G}_0(\mathbf{r},\mathbf{r}_B)\}. \tag{24}$$

Using relation (19) between unperturbed and perturbed interferometric operators, we have

$$\begin{aligned} G_S(\mathbf{r}_B,\mathbf{r}_A) - \overline{G}_S(\mathbf{r}_A,\mathbf{r}_B) &= I_0\{G_1(\mathbf{r},\mathbf{r}_A),\overline{G}_1(\mathbf{r},\mathbf{r}_B)\} - I_0\{G_0(\mathbf{r},\mathbf{r}_A),\overline{G}_0(\mathbf{r},\mathbf{r}_B)\} \\ &- I_V\{G_1(\mathbf{r},\mathbf{r}_A),\overline{G}_1(\mathbf{r},\mathbf{r}_B)\}. \end{aligned} \tag{25}$$

Equation (25) is a general representation theorem for perturbation. Additionally, the interferometric operator is bilinear, i.e., $I_H\{\alpha f,g\} = I_H\{f,\alpha g\} = \alpha I_H\{f,g\}$, $I_H\{f,g+h\} = I_H\{f,g\} + I_H\{f,h\}$, and $I_H\{f+g,h\} = I_H\{f,h\} + I_H\{g,h\}$. We exploit the bilinearity of I_0 and expand $I_0\{G_1(\mathbf{r},\mathbf{r}_A),\overline{G}_1(\mathbf{r},\mathbf{r}_B)\}$ in terms of unperturbed fields and field perturbations:

$$\begin{aligned} I_0\{G_1(\mathbf{r},\mathbf{r}_A),\overline{G}_1(\mathbf{r},\mathbf{r}_B)\} &= I_0\{G_0(\mathbf{r},\mathbf{r}_A),\overline{G}_0(\mathbf{r},\mathbf{r}_B)\} + I_0\{G_S(\mathbf{r},\mathbf{r}_A),\overline{G}_S(\mathbf{r},\mathbf{r}_B)\} \\ &+ I_0\{G_0(\mathbf{r},\mathbf{r}_A),\overline{G}_S(\mathbf{r},\mathbf{r}_B)\} + I_0\{G_S(\mathbf{r},\mathbf{r}_A),\overline{G}_0(\mathbf{r},\mathbf{r}_B)\}. \end{aligned} \tag{26}$$

This decomposition allows for the identification of different types of interference between unperturbed Green's functions and Green's function perturbations. Then, inserting equation (26) into representation theorem (25), gives

$$\begin{aligned} G_S(\mathbf{r}_B,\mathbf{r}_A) - \overline{G}_S(\mathbf{r}_A,\mathbf{r}_B) &= I_0\{G_S(\mathbf{r},\mathbf{r}_A),\overline{G}_0(\mathbf{r},\mathbf{r}_B)\} + I_0\{G_0(\mathbf{r},\mathbf{r}_A),\overline{G}_S(\mathbf{r},\mathbf{r}_B)\} \\ &+ I_0\{G_S(\mathbf{r},\mathbf{r}_A),\overline{G}_S(\mathbf{r},\mathbf{r}_B)\} - I_V\{G_1(\mathbf{r},\mathbf{r}_A),\overline{G}_1(\mathbf{r},\mathbf{r}_B)\}. \end{aligned} \tag{27}$$

Representation theorem (27) illustrates that the retrieval of Green's function perturbations requires a combination of interferences between both unperturbed Green's functions and Green's function perturbations. In section 5, we analyze the individual contributions of the different terms on the right-hand side of equation (27) to the reconstruction. Notice in particular the term $I_V\{G_1(\mathbf{r},\mathbf{r}_A),\overline{G}_1(\mathbf{r},\mathbf{r}_B)\}$, which represents the interference between perturbed Green's functions associated with the operator V, and accounts for the perturbation of the interferometric operator. Where possible, we prefer to consider situations for which $I_V = 0$ because in such cases,

$$\begin{aligned} G_S(\mathbf{r}_B,\mathbf{r}_A) - \overline{G}_S(\mathbf{r}_A,\mathbf{r}_B) &= I_0\{G_S(\mathbf{r},\mathbf{r}_A),\overline{G}_0(\mathbf{r},\mathbf{r}_B)\} + I_0\{G_0(\mathbf{r},\mathbf{r}_A),\overline{G}_S(\mathbf{r},\mathbf{r}_B)\} \\ &+ I_0\{G_S(\mathbf{r},\mathbf{r}_A),\overline{G}_S(\mathbf{r},\mathbf{r}_B)\}. \end{aligned} \tag{28}$$

Representation theorem (28) is a function of only the unperturbed interferometric operator I_0, and, consequently, depends only on the properties of the unperturbed medium. For these special cases, such as acoustic waves with velocity perturbation, the preturbation retrieval does not require an estimation of the perturbation V.

Now, let us return to the general case, $I_V \neq 0$, and establish another form of representation theorem for perturbations, one that characterizes only the causal Green's function perturbation, $G_S(\mathbf{r}_B,\mathbf{r}_A)$, rather than the superposition of the causal and acausal functions, $G_S(\mathbf{r}_B,\mathbf{r}_A) - \overline{G}_S(\mathbf{r}_A,\mathbf{r}_B)$. This representation will help in analyzing the individual contribution of the interference between direct and scattered fields to the partial retrieval of the scattered field $G_S(\mathbf{r}_B,\mathbf{r}_A)$. Rearranging relation (23) for unperturbed systems and inserting it into equation (10) yields

$$\begin{aligned} G_S(\mathbf{r}_B,\mathbf{r}_A) &= \left(\left|I_0\{G_0(\mathbf{r},\mathbf{r}_1),\overline{G}_0(\mathbf{r},\mathbf{r}_B)\} + \overline{G}_0(\mathbf{r}_1,\mathbf{r}_B)\right| |V(\mathbf{r}_1)|\, G_1(\mathbf{r}_1,\mathbf{r}_A)\right) \\ &= I_0\{\left(G_0(\mathbf{r},\mathbf{r}_1)\,|V(\mathbf{r}_1)|\,G_1(\mathbf{r}_1,\mathbf{r}_A)\right),\overline{G}_0(\mathbf{r},\mathbf{r}_B)\} + \left(\overline{G}_0(\mathbf{r}_1,\mathbf{r}_B)\,|V(\mathbf{r}_1)|\,G_1(\mathbf{r}_1,\mathbf{r}_A)\right). \end{aligned} \tag{29}$$

Using once again expression (10), which defines the Green's function perturbation, we identify the first term on the right-hand side of (29) with $I_0\{G_S(\mathbf{r},\mathbf{r}_A),\overline{G}_0(\mathbf{r},\mathbf{r}_B)\}$ to obtain

$$G_S(\mathbf{r}_B,\mathbf{r}_A) = I_0\{G_S(\mathbf{r},\mathbf{r}_A),\overline{G}_0(\mathbf{r},\mathbf{r}_B)\} + \left(\overline{G}_0(\mathbf{r},\mathbf{r}_B)\,|V(\mathbf{r})|\,G_1(\mathbf{r},\mathbf{r}_A)\right). \tag{30}$$

This representation theorem for perturbations generalizes to any physical system the representation theorem for the special case of acoustic waves (Vasconcelos *et al.* 2009),

$$\begin{aligned} G_S(\mathbf{r}_B,\mathbf{r}_A) &= \oint_{\delta D} \rho_0^{-1}(\mathbf{r})[G_S(\mathbf{r},\mathbf{r}_A)\nabla\overline{G}_0(\mathbf{r},\mathbf{r}_B) - \overline{G}_0(\mathbf{r},\mathbf{r}_B)\nabla G_S(\mathbf{r},\mathbf{r}_A)]\cdot\hat{\mathbf{n}}d^2r \\ &+ \int_D \overline{G}_0(\mathbf{r},\mathbf{r}_B)V(\mathbf{r})G_1(\mathbf{r},\mathbf{r}_A)d^3r. \end{aligned} \tag{31}$$

Representation theorems (25) and (30) offer the possibility of extracting field perturbations (e.g., scattered waves) between points A and B as if one of these points acts as a source. They allow calculation of perturbation propagation between these two points without the need for a physical source at either of the two locations. These representation theorems have potential for estimating not only perturbations in fields but perturbations in medium properties by treating expression (30) as an integral equation for the perturbation V given the field perturbation G_S. They can therefore be used for detecting, locating, monitoring, and modeling medium perturbations. In geoscience, this theory has application to a diversity of techniques including passive imaging using seismic noise, seismic migration, modeling for inversion of electromagnetic data, and remote monitoring of hydrocarbon reservoirs, aquifers, and CO_2 injection for carbon sequestration.

5 ANALYSIS OF THE DIFFERENT CONTRIBUTIONS TO THE RETRIEVAL OF PERTURBATIONS

Here, we analyze the different terms that contribute to representation theorem (27) for perturbations. In particular, we interpret the contribution of the interference between field perturbations, corresponding to the term $I_0\{G_S(\mathbf{r},\mathbf{r}_A),\overline{G}_S(\mathbf{r},\mathbf{r}_B)\}$, and explain why perturbations cannot be reconstructed by using solely the interference between perturbations; that is, the reconstruction of perturbations requires knowledge of the unperturbed fields for the system. We show that the contribution of the interference between unperturbed fields and field perturbations, corresponding to the terms $I_0\{G_S(\mathbf{r},\mathbf{r}_A),\overline{G}_0(\mathbf{r},\mathbf{r}_B)\}$ and $I_0\{G_0(\mathbf{r},\mathbf{r}_A),\overline{G}_S(\mathbf{r},\mathbf{r}_B)\}$, is responsible for retrieving only field perturbations that are contaminated by spurious events. The interference between just the field perturbations is necessary to cancel these contaminants. To a certain extent, the cancelation mechanism involved in the reconstruction process can be connected to the general optical theorem as discussed below.

5.1 Partial retrieval of field perturbations

First, consider the contributions of the interferences between unperturbed fields and field perturbations. Rearranging the terms in representation theorem (30), we have the two following expressions, equation (33) being the negative conjugate of equation (32):

$$I_0\{G_S(\mathbf{r},\mathbf{r}_A),\overline{G}_0(\mathbf{r},\mathbf{r}_B)\} = G_S(\mathbf{r}_B,\mathbf{r}_A) - \left(\overline{G}_0(\mathbf{r},\mathbf{r}_B)\,|V(\mathbf{r})|\,G_1(\mathbf{r},\mathbf{r}_A)\right), \tag{32}$$

$$I_0\{G_0(\mathbf{r},\mathbf{r}_A),\overline{G}_S(\mathbf{r},\mathbf{r}_B)\} = -\overline{G}_S(\mathbf{r}_A,\mathbf{r}_B) + \left(G_0(\mathbf{r},\mathbf{r}_A)\,|\overline{V}(\mathbf{r})|\,\overline{G}_1(\mathbf{r},\mathbf{r}_B)\right). \tag{33}$$

Equations (32) and (33) show that the terms $I_0\{G_S(\mathbf{r},\mathbf{r}_A),\overline{G}_0(\mathbf{r},\mathbf{r}_B)\}$ and $I_0\{G_0(\mathbf{r},\mathbf{r}_A),\overline{G}_S(\mathbf{r},\mathbf{r}_B)\}$ contribute to the causal and acausal Green's function perturbation between A and B, respectively. Note, however, the two additional volume integrals that depend on the perturbation operator:
$\left(\overline{G}_0(\mathbf{r},\mathbf{r}_B)\,|V(\mathbf{r})|\,G_1(\mathbf{r},\mathbf{r}_A)\right)$ and $\left(G_0(\mathbf{r},\mathbf{r}_A)\,|\overline{V}(\mathbf{r})|\,\overline{G}_1(\mathbf{r},\mathbf{r}_B)\right)$. Their presence thus contaminates the estimate of the Green's function perturbation with spurious contributions (called *spurious arrivals* by Snieder *et al.* (2008)). In general, we cannot neglect them because they do not vanish regardless of the subspace D under consideration. Depending on the perturbation V, however, these spurious contributions can be relatively small. The summation of equations (32) and (33) thus gives a retrieval of the field perturbation, $G_S(\mathbf{r}_B,\mathbf{r}_A) - \overline{G}_S(\mathbf{r}_A,\mathbf{r}_B)$, contaminated with spurious arrivals.

To get insight into the physical meaning of this partial reconstuction, let us particularize the general description of equations (32) and (33) to the case of acoustic waves in which direct waves interfere with scattered waves. Figure 3 illustrates the reconstruction obtained by cross-correlating just direct and scattered waves for both weakly and strongly scattering media (Figures 3(a) and 3(b), respectively). Interestingly, for a weakly scattering medium (average

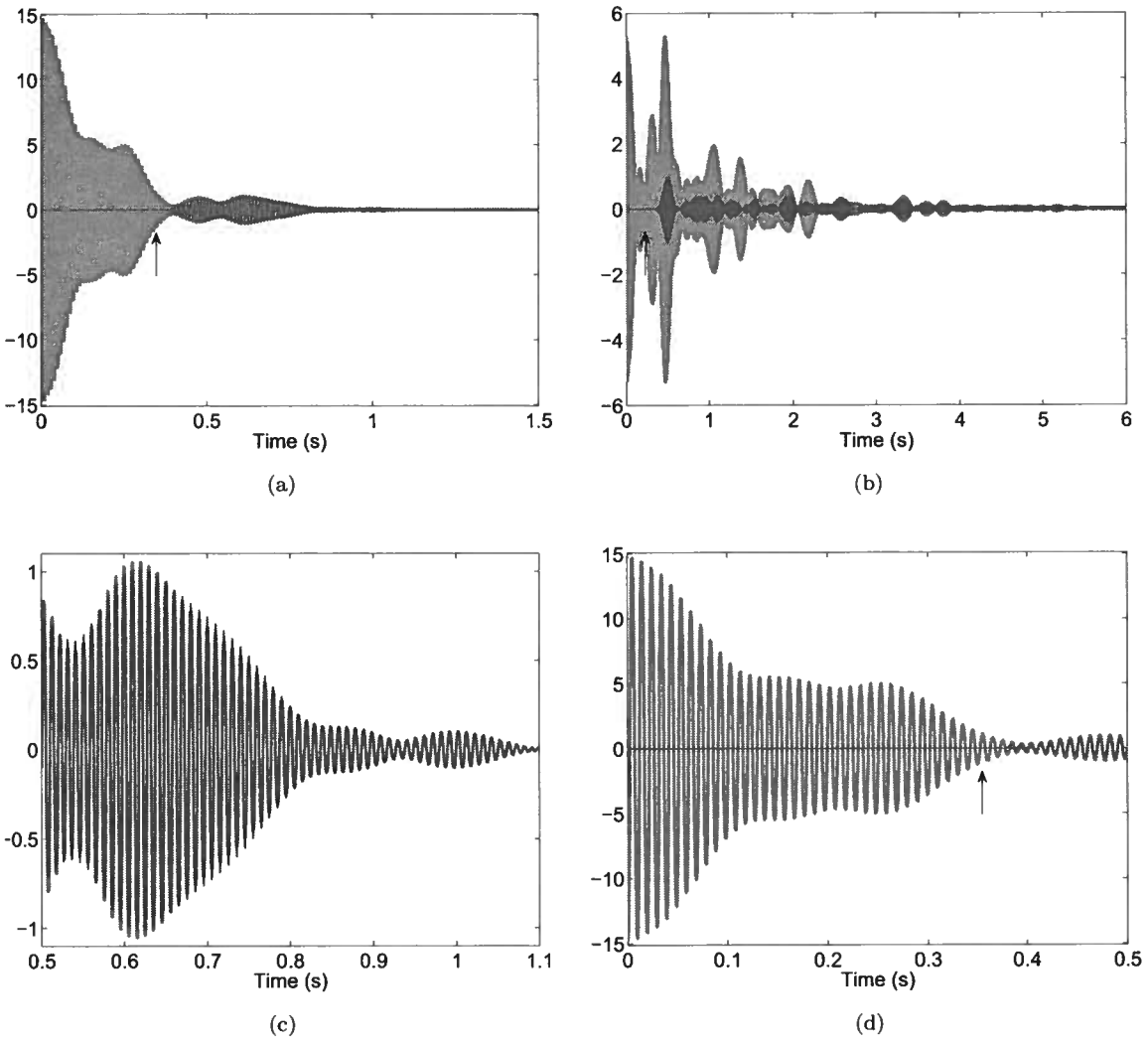

Figure 3. The causal part of the actual *scattering response* (blue curves) between two points embedded in heterogeneous media is compared to the reconstructed wave (red curves) obtained by cross-correlating direct and scattered waves recorded by two receivers at the same locations. Panels (a) and (b) show the signals for a weakly and strongly scattering medium, respectively. Panel (c) and (d) provide zooms on the late and early parts of experiment in weakly scattering regime, respectively. In both scattering regimes, the reconstruction is inaccurate. The weakly scattering case, however, suggests a partial retrieval of the scattering response: the reconstructed and reference signals are similar in their late parts (Panel (c)) while the early part of the reconstructed signal (i.e., the portion before the time of the direct arrival, denoted by the arrow) is purely erroneous (Panel (d)) and contains only the spurious arrivals.

wavelength less or about the scattering mean free path), Figure 3(c) shows a reconstructed signal that fully retrieves the late portion of the scattering response. The early part of the signal, however, contains strong nonphysical arrivals, prior to the true first arrival (arrow), as seen in Figure 3(d). These observations suggest that while the signal reconstructed by cross-correlating direct and scattered waves does contain the scattering response, it is contaminated by spurious arrivals. Figure 3(a) shows that, for a strongly scattering medium, the reconstructed signal is contaminated so severely that no similarities can be found between the reconstructed and reference signals; the contribution of the spurious arrivals dominates the reconstruction. In summary, because the physical nature of the spurious arrival is the same for both weakly and strongly scattering media, cross-correlating direct and scattered waves retrieves the scattered waves but generates unexpected arrivals that can be more intense than the useful signal. These spurious arrivals must cancel in order for the retrieval of scattered waves to be completed.

5.2 Cancelation of the spurious arrivals

The interference between direct and scattered waves, i.e., the first two terms in (27), partially retrieves the scattered waves. We are interested in studying the mechanism for canceling the spurious arrivals described in the previous subsection. According to representation theorem (27), completion of the reconstruction requires the additional contributions from the interferences $I_0\{G_S(\mathbf{r},\mathbf{r}_A),\overline{G}_S(\mathbf{r},\mathbf{r}_B)\}$, and $I_V\{G_1(\mathbf{r},\mathbf{r}_A),\overline{G}_1(\mathbf{r},\mathbf{r}_B)\}$. In the introduction, we showed numerically that the interference between scattered waves alone does not correctly retrieve scattered waves. Taken individually, the interference between unperturbed fields and field perturbations, $I_0\{G_S(\mathbf{r},\mathbf{r}_A),\overline{G}_0(\mathbf{r},\mathbf{r}_B)\}$ and $I_0\{G_S(\mathbf{r},\mathbf{r}_A),\overline{G}_0(\mathbf{r},\mathbf{r}_B)\}$, the interference between just the field perturbations $I_0\{G_S(\mathbf{r},\mathbf{r}_A),\overline{G}_S(\mathbf{r},\mathbf{r}_B)\}$, or the interference $I_V\{G_1(\mathbf{r},\mathbf{r}_A),\overline{G}_1(\mathbf{r},\mathbf{r}_B)\}$ does not reconstruct field perturbations. The summation of all their contributions, however, is expected to accurately retrieve the perturbations and, consequently, cancel the spurious arrivals.

We develop the following relation for the interference between field perturbations by rewriting $I_0\{G_S(\mathbf{r},\mathbf{r}_A),\overline{G}_S(\mathbf{r},\mathbf{r}_B)\}$:

$$\begin{aligned}
I_0\{G_S(\mathbf{r},\mathbf{r}_A),\overline{G}_S(\mathbf{r},\mathbf{r}_B)\} &= I_0\{(G_0(\mathbf{r},\mathbf{r}_1)\,|V(\mathbf{r}_1)|\,G_1(\mathbf{r}_1,\mathbf{r}_A))\,,(\overline{G}_0(\mathbf{r},\mathbf{r}_2)\,|\overline{V}(\mathbf{r}_2)|\,\overline{G}_1(\mathbf{r}_2,\mathbf{r}_B))\}\\
&= \big((I_0\{G_0(\mathbf{r},\mathbf{r}_1),\overline{G}_0(\mathbf{r},\mathbf{r}_2)\}\,|V(\mathbf{r}_1)|\,G_1(\mathbf{r}_1,\mathbf{r}_A))\,|\overline{V}(\mathbf{r}_2)|\,\overline{G}_1(\mathbf{r}_2,\mathbf{r}_B)\big)\\
&= \big(([G_0(\mathbf{r}_2,\mathbf{r}_1)-\overline{G}_0(\mathbf{r}_1,\mathbf{r}_2)]\,|V(\mathbf{r}_1)|\,G_1(\mathbf{r}_1,\mathbf{r}_A))\,|\overline{V}(\mathbf{r}_2)|\,\overline{G}_1(\mathbf{r}_2,\mathbf{r}_B)\big)\\
&= \big((G_0(\mathbf{r}_2,\mathbf{r}_1)\,|V(\mathbf{r}_1)|\,G_1(\mathbf{r}_1,\mathbf{r}_A))\,|\overline{V}(\mathbf{r}_2)|\,\overline{G}_1(\mathbf{r}_2,\mathbf{r}_B)\big)\\
&- \big((\overline{G}_0(\mathbf{r}_1,\mathbf{r}_2)\,|\overline{V}(\mathbf{r}_2)|\,\overline{G}_1(\mathbf{r}_2,\mathbf{r}_B))\,|V(\mathbf{r}_1)|\,G_1(\mathbf{r}_1,\mathbf{r}_A)\big)\,. \qquad (34)
\end{aligned}$$

Here, we used expression (10) for field perturbations in the first identity, the bilinearity of I_0 in the second identity, and representation theorem (23) in the third identity; so that finally,

$$I_0\{G_S(\mathbf{r},\mathbf{r}_A),\overline{G}_S(\mathbf{r},\mathbf{r}_B)\} = \big(G_S(\mathbf{r}_1,\mathbf{r}_A)\,|\overline{V}(\mathbf{r}_1)|\,\overline{G}_1(\mathbf{r}_1,\mathbf{r}_B)\big) - \big(\overline{G}_S(\mathbf{r}_1,\mathbf{r}_B)\,|V(\mathbf{r}_1)|\,G_1(\mathbf{r}_1,\mathbf{r}_A)\big)\,. \qquad (35)$$

We next show that the interaction between Green's function perturbations indirectly retrieves the Green's function perturbation by contributing to the cancelation of the spurious arrivals. The right-hand side of equation (35) is the complement of the spurious contributions $-\big(\overline{G}_0(\mathbf{r},\mathbf{r}_B)\,|V(\mathbf{r})|\,G_1(\mathbf{r},\mathbf{r}_A)\big)$ and $\big(G_0(\mathbf{r},\mathbf{r}_A)\,|\overline{V}(\mathbf{r})|\,\overline{G}_1(\mathbf{r},\mathbf{r}_B)\big)$ in equations (32) and (33); that is, the summation of these integrals retrieves the term $-I_V\{G_1(\mathbf{r},\mathbf{r}_A),\overline{G}_1(\mathbf{r},\mathbf{r}_B)\}$. For cases in which $I_V = 0$, the interaction between perturbations entirely cancels the spurious arrivals,

$$I_0\{G_S(\mathbf{r},\mathbf{r}_A),\overline{G}_S(\mathbf{r},\mathbf{r}_B)\} + \big(G_0(\mathbf{r},\mathbf{r}_A)\,|\overline{V}(\mathbf{r})|\,\overline{G}_1(\mathbf{r},\mathbf{r}_B)\big) - \big(\overline{G}_0(\mathbf{r},\mathbf{r}_B)\,|V(\mathbf{r})|\,G_1(\mathbf{r},\mathbf{r}_A)\big) = 0, \qquad (36)$$

and the reconstruction is then completed by summing the contributions from equations (32), (33) and (35) (the sum reduces to representation theorem (28)). For the general case ($I_V \neq 0$),

$$\begin{aligned}
I_0\{G_S(\mathbf{r},\mathbf{r}_A),\overline{G}_S(\mathbf{r},\mathbf{r}_B)\} + \big(G_0(\mathbf{r},\mathbf{r}_A)\,|\overline{V}(\mathbf{r})|\,\overline{G}_1(\mathbf{r},\mathbf{r}_B)\big) - \big(\overline{G}_0(\mathbf{r},\mathbf{r}_B)\,|V(\mathbf{r})|\,G_1(\mathbf{r},\mathbf{r}_A)\big)&\\
= -I_V\{G_1(\mathbf{r},\mathbf{r}_A),\overline{G}_1(\mathbf{r},\mathbf{r}_B)\}, \qquad (37)&
\end{aligned}$$

and the summation of equations (32), (33) and (35) gives

$$(32)+(33)+(35) = G_S(\mathbf{r}_B,\mathbf{r}_A) - \overline{G}_S(\mathbf{r}_A,\mathbf{r}_B) + I_V\{G_1(\mathbf{r},\mathbf{r}_A),\overline{G}_1(\mathbf{r},\mathbf{r}_B)\}. \qquad (38)$$

The retrieval is incomplete and does not produce the Green's function perturbation because of the term $I_V\{G_1(\mathbf{r},\mathbf{r}_A),\overline{G}_1(\mathbf{r},\mathbf{r}_B)\}$ that still contaminates the right-hand side of equation (38). Accurate reconstruction requires an additional estimate of this interaction between perturbed fields associated with V.

In any case, a direct consequence for scattering problems is that we cannot reconstruct the scattering Green's function by merely using the contribution of scattered waves alone. This explains the failure of interferometry based solely on the interference of scattered waves, as shown in Figure 2. The interference between Green's function perturbations nevertheless plays a fundamental role in the retrieval of the perturbation because they are needed to cancel spurious arrivals. Our numerical experiments illustrate this observation for scattered acoustic waves (Figure 4). For both weakly and strongly scattering media, combining the contributions of both interference between direct and scattered waves and interference between just scattered waves cancels the spurious arrivals and reconstructs the superposition of the causal and acausal scattering Green's functions. Note, additionally, that in order for this experiment to be successful, the distribution of sources must be sufficiently dense on a close surface surrounding the receivers (see numerical set-up description in Figure 1). Considerations of narrow aperture and limited number of sources are independent problems that limit the accuracy of reconstructions (Fan & Snieder 2009; Snieder 2004).

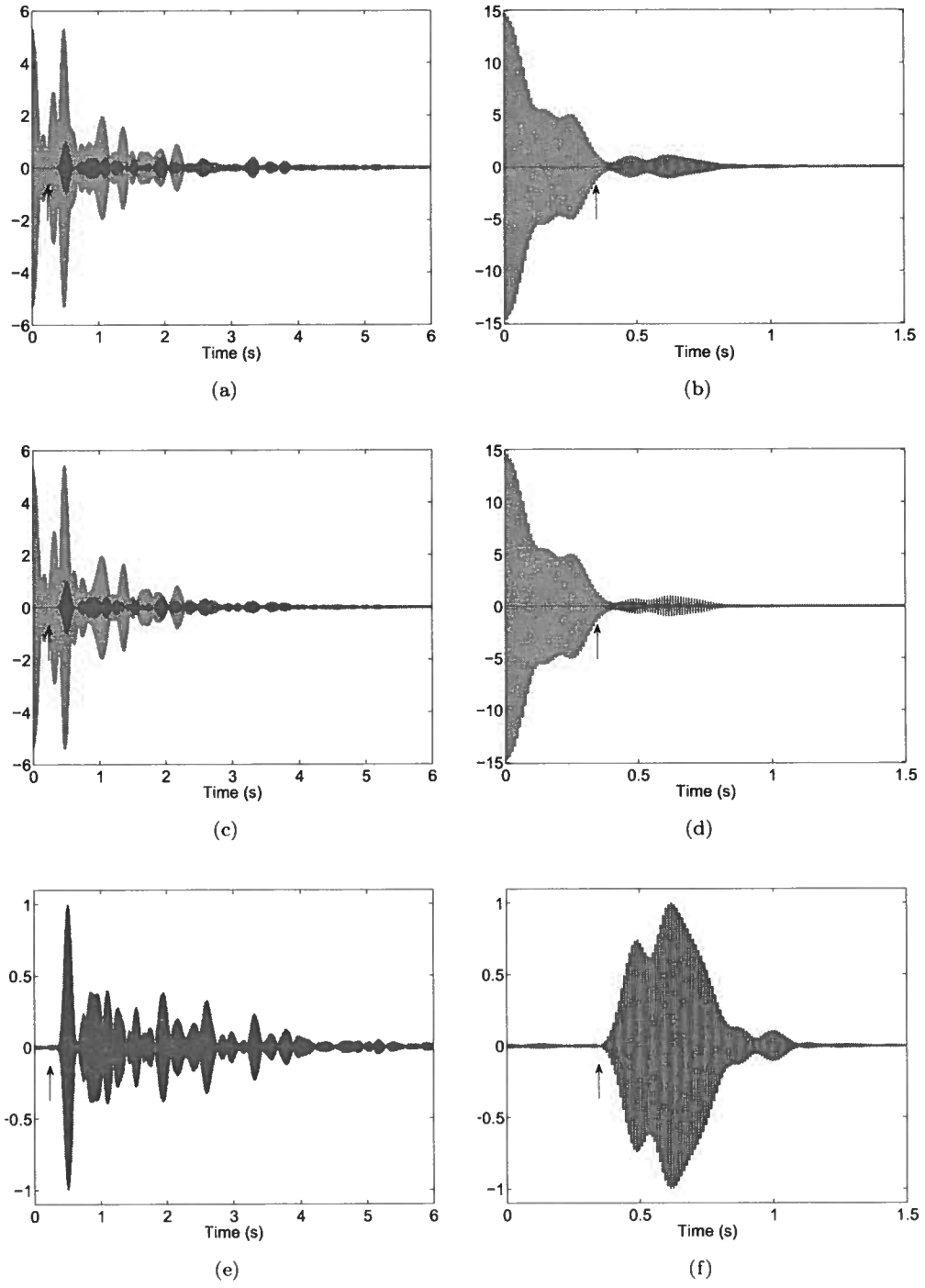

Figure 4. The blue curves show the causal part of the *scattering response* between two points embedded in heterogeneous acoustic media. The red curves correspond to the reconstructed signals for the different individual contributions discussed in section 5. For strongly scattering media (left column), the summation of the reconstructed signal by cross-correlating direct and scattered waves (a) with that obtained by cross-correlating scattered waves (c) leads to the retrieval of the scattering response and cancelation of the spurious arrivals (e). Likewise, (b), (d), and (f) show success of the reconstruction for weakly scattering media(right column).

5.3 Connection with the general optical theorem

Above, we emphasize the process that leads to the reconstruction of perturbations. Interestingly, for problems with unperturbed interferometric operators, the interference between field perturbations alone contributes entirely to the cancelation of the spurious arrivals that arise from the interferences between unperturbed fields and field perturbations in the reconstruction process, and rewriting equation (36) gives

$$\left(\overline{G}_0(\mathbf{r},\mathbf{r}_B)\,|V(\mathbf{r})|\,G_1(\mathbf{r},\mathbf{r}_A)\right) - \left(G_0(\mathbf{r},\mathbf{r}_A)\,|\overline{V}(\mathbf{r})|\,\overline{G}_1(\mathbf{r},\mathbf{r}_B)\right) = I_0\{G_S(\mathbf{r},\mathbf{r}_A),\overline{G}_S(\mathbf{r},\mathbf{r}_B)\}. \tag{39}$$

In a sense, we can interpret this mechanism as an extension of the general optical theorem, as has been suggested for acoustic waves (Snieder *et al.* 2009, 2008). The general optical theorem (Marston 2001; Schiff 1968) concerns the scattering amplitude $f_k(\hat{\mathbf{n}},\hat{\mathbf{n}}')$ of scattered waves with wave number k, and unit vectors $\hat{\mathbf{n}}$ and $\hat{\mathbf{n}}'$ representing the directions of the outgoing and incoming waves, respectively. With a far-field approximation in expression (17), the interferometric operator for the constant-density wave equation ($\rho_0 = 1$) becomes

$$I_0\{f,g\} = 2jk \oint_{\delta D} f(\mathbf{r})g(\mathbf{r})d^2r \tag{40}$$

for a homogenous medium as the unperturbed state ($G_0(\mathbf{r},\mathbf{r}_S) = \dfrac{e^{-jk\|\mathbf{r}-\mathbf{r}_S\|}}{4\pi\|\mathbf{r}-\mathbf{r}_S\|}$). With the medium perturbed by a single scattering object positioned at $\mathbf{r}_x$, the scattering Green's function in the far field is given by

$$G_S(\mathbf{r},\mathbf{r}_S) = 4\pi G_0(\mathbf{r},\mathbf{r}_x)f_k(\hat{\mathbf{n}},\hat{\mathbf{n}}_S)G_0(\mathbf{r}_x,\mathbf{r}_S). \tag{41}$$

If A and B are far from the scatterer and δD is a sphere centered at $\mathbf{r}_x$ with radius R, the interference between scattered Green's functions is

$$I_0\{G_S(\mathbf{r},\mathbf{r}_A),\overline{G}_S(\mathbf{r},\mathbf{r}_B)\} = 2jk \oint_{\delta D} G_0(\mathbf{r}_x,\mathbf{r}_A)\overline{G}_0(\mathbf{r}_x,\mathbf{r}_B)f_k(\hat{\mathbf{n}},\hat{\mathbf{n}}_A)\overline{f}_k(\hat{\mathbf{n}},\hat{\mathbf{n}}_B)(4\pi)^2 G_0(\mathbf{r},\mathbf{r}_x)\overline{G}_0(\mathbf{r},\mathbf{r}_x)d^2r. \tag{42}$$

The integration over the sphere δD is equivalent to an integration over solid angle by $d^2r = R^2 d\hat{n}$, and $(4\pi)^2 G_0(\mathbf{r},\mathbf{r}_x)\overline{G}_0(\mathbf{r},\mathbf{r}_x) = \dfrac{1}{R^2}$ so that

$$I_0\{G_S(\mathbf{r},\mathbf{r}_A),\overline{G}_S(\mathbf{r},\mathbf{r}_B)\} = 2jkG_0(\mathbf{r}_x,\mathbf{r}_A)\overline{G}_0(\mathbf{r}_x,\mathbf{r}_B) \oint f_k(\hat{\mathbf{n}},\hat{\mathbf{n}}_A)\overline{f}_k(\hat{\mathbf{n}},\hat{\mathbf{n}}_B)d\hat{n}. \tag{43}$$

In the far-field approximation for the scattering Green's function, one can modify previously established equations by using expression (41) instead of (10) for the field perturbation. Consequently, the spurious contributions introduced in equations (32) and (33) are

$$\left(\overline{G}_0(\mathbf{r},\mathbf{r}_B)\,|V(\mathbf{r})|\,G_1(\mathbf{r},\mathbf{r}_A)\right) = 4\pi\overline{G}_0(\mathbf{r}_x,\mathbf{r}_B)f_k(\hat{\mathbf{n}}_B,\hat{\mathbf{n}}_A)G_0(\mathbf{r}_x,\mathbf{r}_A), \tag{44}$$

$$\left(G_0(\mathbf{r},\mathbf{r}_A)\,|\overline{V}(\mathbf{r})|\,\overline{G}_1(\mathbf{r},\mathbf{r}_B)\right) = 4\pi G_0(\mathbf{r}_x,\mathbf{r}_A)\overline{f}_k(\hat{\mathbf{n}}_A,\hat{\mathbf{n}}_B)\overline{G}_0(\mathbf{r}_x,\mathbf{r}_B), \tag{45}$$

and we thus retrieve the general optical theorem from equation (39):

$$f_k(\hat{\mathbf{n}}_B,\hat{\mathbf{n}}_A) - \overline{f}_k(\hat{\mathbf{n}}_A,\hat{\mathbf{n}}_B) = \frac{2jk}{4\pi}\oint f_k(\hat{\mathbf{n}},\hat{\mathbf{n}}_A)\overline{f}_k(\hat{\mathbf{n}},\hat{\mathbf{n}}_B)d\hat{n}. \tag{46}$$

This interpretation of the cancelations, however, is limited to problems with unperturbed interferometric operators. For general systems, the spurious arrivals do not cancel by summing the interferences associated with the unperturbed operator H_0. Unless the interferometric operator is unperturbed ($I_V = 0$), the interference associated with V on the right-hand side of equation (38) still contaminates the perturbations we desire to reconstruct by adding the contributions from equations (32), (33) and (35). In general, we have to evaluate the contribution of $I_V\{G_1(\mathbf{r},\mathbf{r}_A),\overline{G}_1(\mathbf{r},\mathbf{r}_B)\}$ in order to cancel the spurious arrivals and reconstruct the exact field perturbations. Thus as stated in section 3, because the perturbation operator is usually unknown, interferometry appears practical for perturbation problems only with an interferometric operator that is unperturbed.

In summary, we have shown that the scattering response cannot be retrieved by cross-correlating scattered waves alone. To reconstruct scattered waves, we need to consider the contribution from cross-correlation of direct and scattered waves. The key to the ability to cancel the spurious arrivals and succeed in the reconstruction for any kind of perturbation problem is that we consider systems for which the interferometric operator is unperturbed, $I_V = 0$.

6 DISCUSSION AND CONCLUSION

We have derived a representation theorem for general systems and in particular for perturbed media. This makes it possible to retrieve Green's functions and their perturbations for a large variety of linear differential systems that include acoustic, elastic, and electromagnetic waves. We show the extension to vector fields in Appendix A. We investigate the reconstruction of Green's functions, applying an interferometric operator to unperturbed fields and field perturbations. This mathematical description of interferometry simplifies the analysis of the reconstruction of perturbations: we interpret this process as summing contributions from different types of interference between perturbations and unperturbed Green's functions. In geophysics, this description can be applied to a range of problems. For example, one can extend conventional interferometry techniques for seismic waves to some possible applications in imaging and inverse problems: the representation theorem can be related to sensitivity kernels used in waveform inversion (Tarantola & Tarantola 1987), in imaging (Colton & Kress 1998), or in tomography (Woodward 1992); the theorem also allows the establishment of formal connections with seismic migration (Clearbout 1985) and with inverse scattering methods (Beylkin 1985; Borcea *et al.* 2002).

Our study of the retrieval of perturbations differs from previous work because we show explicitly that not only fields are perturbed but the operator itself changes when the medium is perturbed. For most general systems, we would need to modify the interferometric process used for the reconstruction after the application of a perturbation. We obtain this fundamental result after deriving the perturbation of the interferometric operator. Our analysis emphasizes the importance of those systems for which the interferometric operator is unperturbed because such systems appear to offer the prospect for practical application of interferometry. In these cases, reconstruction of the Green's function perturbations does not require knowledge or estimation of the perturbations of the medium properties. We also demonstrate that perturbations cannot be retrieved by measuring only field perturbations; knowledge of the unperturbed state of the studied system is essential as well. Perturbations are reconstructed by combining interferences between field perturbations and unperturbed fields. The contribution from interference of field perturbations alone cancels the erroneous arrivals generated by interference of unperturbed fields with field perturbations.

Simulations for scattering acoustic media show the importance of direct arrivals in the extraction of scattering responses and verify the failure to reconstruct scattering Green's function by cross-correlating just scattered waves. This result is intriguing and should be carefully considered when designing applications because our result appears to be in contradiction to many results in seismology. Campillo & Paul (2003), for example, have shown that cross-correlation of just late coda in earthquake data, allows for retrieval of direct surface waves. Also, Stehly *et al.* (2008) have used the coda of the cross-correlation of seismic noise for improving the reconstruction of Green's functions. Indeed, the main components of late coda waves are scattered waves. So, what might be the source of this apparent discrepancy with our results? We base our reasoning on interpretations of representation theorems for perturbed systems, and study the extraction of scattered waves without performing any time averaging as is done in the work published in these papers. Further work needs to be done to explore the hypothesis that it could be the averaging that allows reconstruction from scattered waves alone. Perhaps what is being reconstructed by the time averaging in those papers is just some component of the Green's function, or some average Green's function, not the Green's function itself. In geoscience, Campillo & Paul (2003), Halliday & Curtis (2008), Roux *et al.* (2005), and Shapiro *et al.* (2005) have shown that direct surface waves are beautifully extracted by interferometry; but examples of reconstruction of scattered surface and body waves are lacking. Again, the general formulation of the representation theorem for perturbed media states that we can in principle retrieve any and all perturbations for a given system.

ACKNOWLEDGMENTS

This work was supported by the NSF through grant EAS-0609595.

REFERENCES

Bakulin, A., and Calvert, R., 2006, The virtual source method: Theory and case study: Geophysics, **71**, no. 24, SI139–SI150.

Beylkin, G., 1985, Imaging of discontinuities in the inverse scattering problem by inversion of a causal generalized Radon transform: Journal of Mathematical Physics, **26**, 99.

Borcea, L., Papanicolaou, G., Tsogka, C., and Berryman, J., 2002, Imaging and time reversal in random media: Inverse Problems, **18**, 1247–1279.

Campillo, M., and Paul, A., 2003, Long-range correlations in the diffuse seismic coda: Science, **299**, no. 5606, 547.

Clearbout, J., 1985, Imaging the Earth's interior.: , Blackwell Scientific Publications, Inc.

Colton, D., and Kress, R., 1998, Inverse acoustic and electromagnetic scattering theory: , Springer Verlag.

Curtis, A., Gerstoft, P., Sato, H., Snieder, R., and Wapenaar, K., 2006, Seismic interferometry–turning noise into signal: The Leading Edge, **25**, no. 9, 1082.

Fan, Y., and Snieder, R., 2009, Required source distribution for interferometry of waves and diffusive fields: Geophysical Journal International, **179**, no. 2, 1232–1244.

Fokkema, J., and Van den Berg, P., 1993, Seismic applications of acoustic reciprocity: , Elsevier.

Fokkema, J., Blok, H., and Van den Berg, P., 1996, Wavefields & Reciprocity: Proceedings of a Symposium in Honour of A. T. de Hoop: , Coronet Books.

Gouédard, P., Stehly, L., Brenguier, F., Campillo, M., Colin de Verdiere, Y., Larose, E., Margerin, L., Roux, P., Sanchez-Sesma, F., Shapiro, N., , *et al.*, 2008, Cross-correlation of random fields: mathematical approach and applications: Geophysical prospecting, **56**, no. 3, 375–394.

Groenenboom, J., and Snieder, R., 1995, Attenuation, dispersion, and anisotropy by multiple scattering of transmitted waves through distributions of scatterers: Journal of the Acoustical Society of America, **98**, 3482.

Halliday, D., and Curtis, A., 2008, Seismic interferometry, surface waves and source distribution: Geophys. J. Int, **175**, no. 3, 1067–1087.

Halliday, D., and Curtis, A., 2009, Seismic interferometry of scattered surface waves in attenuative media: Geophysical Journal International, **178**, no. 1, 419–446.

Kohler, M., Heaton, T., and Bradford, S., 2007, Propagating waves in the steel, moment-frame Factor building recorded during earthquakes: Bull. Seismol. Soc Am., **97**, 1334–1345.

Lanczos, C., 1996, Linear differential operators: , Society for Industrial Mathematics.

Larose, E., Margerin, L., Derode, A., van Tiggelen, B., Campillo, M., Shapiro, N., Paul, A., Stehly, L., and Tanter, M., 2006, Correlation of random wavefields: An interdisciplinary review: Geophysics, **71**, no. 4, SI11–SI21.

Lobkis, O., and Weaver, R., 2001, On the emergence of the Green's function in the correlations of a diffuse field: The Journal of the Acoustical Society of America, **110**, 3011.

Malcolm, A., Scales, J., and van Tiggelen, B., 2004, Extracting the Green's function from diffuse, equipartitioned waves: Physical Review E, **70**, no. 1, 15601.

Marston, P., 2001, Generalized optical theorem for scatterers having inversion symmetry: Applications to acoustic backscattering: The Journal of the Acoustical Society of America, **109**, 1291.

Miyazawa, M., Venkataraman, A., Snieder, R., and Payne, M., 2008, Analysis of microearthquake data at Cold Lake and its applications to reservoir monitoring: Geophysics, **73**, O15.

Rickett, J., and Claerbout, J., 1999, Acoustic daylight imaging via spectral factorization: Helioseismology and reservoir monitoring: The leading edge, **18**, no. 8, 957.

Rodberg, L., and Thaler, R., 1967, Introduction to the quantum theory of scattering: , Academic Press New York.

Roux, P., and Kuperman, W., 2004, Extracting coherent wave fronts from acoustic ambient noise in the ocean: The Journal of the Acoustical Society of America, **116**, 1995.

Roux, P., Sabra, K., Gerstoft, P., Kuperman, W., and Fehler, M., 2005, P-waves from cross-correlation of seismic noise: Geophys. Res. Lett, **32**, L19303.

Sabra, K., Gerstoft, P., Roux, P., Kuperman, W., and Fehler, M., 2005a, Surface wave tomography from microseisms in Southern California: Geophys. Res. Lett, **32**, L14311.

——— 2005b, Using ocean ambient noise for array self-localization and self-synchronization: IEEE Journal of Oceanic Engineering, **30**, no. 2, 338–347.

Sabra, K., Conti, S., Roux, P., and Kuperman, W., 2007, Passive in vivo elastography from skeletal muscle noise: Applied Physics Letters, **90**, 194101.

Schiff, L., 1968, Quantum Mechanics: , McGraw-Hill, New York, 3rd edition.

Shapiro, N., Campillo, M., Stehly, L., and Ritzwoller, M., 2005, High-resolution surface-wave tomography from ambient seismic noise: Science, **307**, no. 5715, 1615.

Slob, E., Draganov, D., and Wapenaar, K., 2007, Interferometric electromagnetic Green's functions representations using propagation invariants: Geophysical Journal International, **169**, no. 1, 60–80.

Snieder, R., and Fleury, C., 2010, Cancellation of spurious arrivals in Green's function retrieval of multiply scattered waves: The Journal of the Acoustical Society of America, submitted.

Snieder, R., and Safak, E., 2006, Extracting the building response using seismic interferometry: theory and application to the Millikan Library in Pasadena, California: Bulletin of the Seismological Society of America, **96**, no. 2, 586.

Snieder, R., Wapenaar, K., and Wegler, U., 2007, Unified Green's function retrieval by cross-correlation; connection with energy principles: Physical Review E, **75**, no. 3, 36103.

Snieder, R., VanWijk, K., Haney, M., and Calvert, R., 2008, Cancellation of spurious arrivals in Green's function extraction and the generalized optical theorem: Physical Review E, **78**, 036606.

Snieder, R., Sánchez-Sesma, F., and Wapenaar, K., 2009, Field fluctuations, imaging with backscattered waves, a generalized energy theorem, and the optical theorem: SIAM J. Imaging Sci.

Snieder, R., 2002, Coda wave interferometry and the equilibration of energy in elastic media: Physical review E, **66**, no. 4, 46615.

Snieder, R., 2004, Extracting the Green's function from the correlation of coda waves: A derivation based on stationary phase: Physical Review E, **69**, no. 4,

046610.

Stehly, L., Campillo, M., Froment, B., and Weaver, R., 2008, Reconstructing Green's function by correlation of the coda of the correlation (C 3) of ambient seismic noise: Journal of Geophysical Research, **113**, no. B11, b11306.

Tarantola, A., and Tarantola, A., 1987, Inverse problem theory: , Elsevier Amsterdam etc.

Thompson, D., and Snieder, R., 2006, Seismic anisotropy of a building: The Leading Edge, **25**, no. 9, 1093.

Tourin, A., Derode, A., Peyre, A., and Fink, M., 2000, Transport parameters for an ultrasonic pulsed wave propagating in a multiple scattering medium: The Journal of the Acoustical Society of America, **108**, 503.

Van Manen, D., Curtis, A., and Robertsson, J., 2006, Interferometric modeling of wave propagation in inhomogeneous elastic media using time reversal and reciprocity: Geophysics, **71**, no. 4.

Vasconcelos, I., Snieder, R., and Douma, H., 2009, Representation theorems and Green's function retrieval for scattering in acoustic media: Physical Review E, **80**, no. 3, 36605.

Wapenaar, K., and Fokkema, J., 2004, Reciprocity theorems for diffusion, flow, and waves: Journal of Applied Mechanics, **71**, 145.

Wapenaar, K., and Fokkema, J., 2006, Green's function representations for seismic interferometry: Geophysics, **71**, SI33–SI46.

Wapenaar, K., Thorbecke, J., and Draganov, D., 2004, Relations between reflection and transmission responses of three-dimensional inhomogeneous media: Geophysical Journal International, **156**, no. 2, 179–194.

Wapenaar, K., Slob, E., and Snieder, R., 2006, Unified Green's function retrieval by cross correlation: Physical Review Letters, **97**, no. 23, 234301.

Wapenaar, K., Draganov, D., Robertsson, J., and S.E.G.G.R.S., 2007, Seismic interferometry: History and present status: LEADING EDGE, **25**, 1082–1092.

Weaver, R., and Lobkis, O., 2001, Ultrasonics without a source: Thermal fluctuation correlations at MHz frequencies: Physical Review Letters, **87**, no. 13, 134301.

Weaver, R., 2008, Ward identities and the retrieval of Green's functions in the correlations of a diffuse field: Wave Motion, **45**, 596–604.

Woodward, M., 1992, Wave-equation tomography: Geophysics, **57**, no. 1, 15–26.

APPENDIX A: EXTENSION TO VECTOR SPACES AND $N \times N$ DIFFERENTIAL OPERATORS

Here, we extend our reasoning to vector fields by using the tensor notation previously introduced. Consider the unperturbed field $\boldsymbol{u_0}(\mathbf{r})$, defined in the vector space D_{tot} of dimension n, which is a solution of equation

$$\boldsymbol{H_0}(\mathbf{r}) \cdot \boldsymbol{u_0}(\mathbf{r}) = \boldsymbol{s}(\mathbf{r}), \tag{A1}$$

where $\boldsymbol{H_0}$ and $\boldsymbol{s}$ are the $n \times n$ linear differential operator and the source term, respectively. For elastic waves, the propagator is

$$\boldsymbol{H_0} = \rho\omega^2\boldsymbol{\delta} + \boldsymbol{\nabla} \cdot \boldsymbol{c} \cdot \boldsymbol{\nabla}, \tag{A2}$$

where $\boldsymbol{c}$ is the elasticity tensor and $\boldsymbol{\delta}$ the Kronecker tensor; $\boldsymbol{u_0}$ is the displacement vector. For electromagnetic waves in isotropic media (ϵ, permittivity; σ, conductivity; μ, permeability), the operator is

$$\boldsymbol{H_0} = \begin{bmatrix} \boldsymbol{\nabla}\times & -j\omega\mu\boldsymbol{\delta} \\ (j\omega\epsilon - \sigma)\boldsymbol{\delta} & \boldsymbol{\nabla}\times \end{bmatrix} \text{ with } \boldsymbol{u_0} = \begin{bmatrix} \boldsymbol{e_0} \\ \boldsymbol{h_0} \end{bmatrix}, \tag{A3}$$

where $\boldsymbol{e}$ and $\boldsymbol{h}$ denote the electric and magnetic fields, respectively. We give two examples of systems for which our reasoning applies; futher cases of study can be found in Wapenaar *et al.* (2006). The perturbed field $\boldsymbol{u_1}(\mathbf{r})$ satisfies

$$\boldsymbol{H_0}(\mathbf{r}) \cdot \boldsymbol{u_1}(\mathbf{r}) = \boldsymbol{V}(\mathbf{r}) \cdot \boldsymbol{u_1}(\mathbf{r}) + \boldsymbol{s}(\mathbf{r}), \tag{A4}$$

where $\boldsymbol{V}$ is the perturbation operator. Elastic waves can be perturbed in the presence of viscosity ($\boldsymbol{\eta}$ tensor), in which case we write $\boldsymbol{V}$ as

$$\boldsymbol{V} = -j\omega\boldsymbol{\nabla} \cdot \boldsymbol{\eta} \cdot \boldsymbol{\nabla}. \tag{A5}$$

A change in medium properties ($\delta\epsilon$, $\delta\sigma$, $\delta\mu$) influences electromagnetic waves by a perturbation

$$\boldsymbol{V} = \begin{bmatrix} 0 & j\omega\delta\mu\boldsymbol{\delta} \\ (\delta\sigma - j\omega\delta\epsilon)\boldsymbol{\delta} & 0 \end{bmatrix}. \tag{A6}$$

Assume a regular problem with unperturbed homogeneous boundary conditions. We relate the Green's tensors $\boldsymbol{G_1}(\mathbf{r}, \mathbf{r}_S)$ and $\boldsymbol{G_0}(\mathbf{r}, \mathbf{r}_S)$ by using the Lippmann-Schwinger equation:

$$\boldsymbol{G_1}(\mathbf{r}, \mathbf{r}_S) = \boldsymbol{G_0}(\mathbf{r}, \mathbf{r}_S) + (\boldsymbol{G_0}(\mathbf{r}, \mathbf{r}_1) \,|\boldsymbol{V}(\mathbf{r}_1)|\, \boldsymbol{G_1}(\mathbf{r}_1, \mathbf{r}_S))\,; \tag{A7}$$

let the perturbation of the Green's tensor $\boldsymbol{G_S}(\mathbf{r}, \mathbf{r}_S)$ be given by $\boldsymbol{G_S}(\mathbf{r}, \mathbf{r}_S) = \boldsymbol{G_1}(\mathbf{r}, \mathbf{r}_S) - \boldsymbol{G_0}(\mathbf{r}, \mathbf{r}_S)$.

The new bilinear interferometric operator $I_{\boldsymbol{H}}$ now acts on matrices,

$$I_{\boldsymbol{H}}\{\boldsymbol{F}, \boldsymbol{G}\} = \left(\boldsymbol{F}^T \,|\overline{\boldsymbol{H}}|\, \boldsymbol{G}\right) - \left(\boldsymbol{G}^T \,|\boldsymbol{H}|\, \boldsymbol{F}\right), \tag{A8}$$

where $\boldsymbol{F}^T$ denotes the transpose of the matrix $\boldsymbol{F}$. We introduce the unperturbed and perturbed interferometric operators as

$$\begin{aligned} I_0\{\boldsymbol{F}, \boldsymbol{G}\} &= I_{\boldsymbol{H}_0}\{\boldsymbol{F}, \boldsymbol{G}\} \\ I_1\{\boldsymbol{F}, \boldsymbol{G}\} &= I_{\boldsymbol{H}_0}\{\boldsymbol{F}, \boldsymbol{G}\} - I_{\boldsymbol{V}}\{\boldsymbol{F}, \boldsymbol{G}\}. \end{aligned} \tag{A9}$$

Consequently, the general representation theorem for vector systems becomes

$$\boldsymbol{G}_{0,1}(\mathbf{r}_B, \mathbf{r}_A) - \boldsymbol{G}^H_{0,1}(\mathbf{r}_A, \mathbf{r}_B) = I_{0,1}\{\boldsymbol{G}_{0,1}(\mathbf{r}, \mathbf{r}_A), \overline{\boldsymbol{G}}_{0,1}(\mathbf{r}, \mathbf{r}_B)\}, \tag{A10}$$

where $\boldsymbol{G}^H_{0,1}$ denotes the hermitian conjugate of $\boldsymbol{G}_{0,1}$. For elastic waves,

$$I_0\{\boldsymbol{F}, \boldsymbol{G}\} = \oint_{\delta D} \left(\boldsymbol{F}^T(\mathbf{r}) \cdot \boldsymbol{c}(\mathbf{r}) \cdot \boldsymbol{\nabla} \cdot \boldsymbol{G}(\mathbf{r}) - \boldsymbol{G}^T(\mathbf{r}) \cdot \boldsymbol{c}(\mathbf{r}) \cdot \boldsymbol{\nabla} \cdot \boldsymbol{F}(\mathbf{r})\right) \cdot \hat{\mathbf{n}} d^2r \tag{A11}$$

and

$$I_{\boldsymbol{V}}\{\boldsymbol{F}, \boldsymbol{G}\} = j\omega \int_D \left(\boldsymbol{F}^T(\mathbf{r}) \cdot \boldsymbol{\nabla} \cdot \boldsymbol{\eta}(\mathbf{r}) \cdot \boldsymbol{\nabla} \cdot \boldsymbol{G}(\mathbf{r}) + \boldsymbol{G}^T(\mathbf{r}) \cdot \boldsymbol{\nabla} \cdot \boldsymbol{\eta}(\mathbf{r}) \cdot \boldsymbol{\nabla} \cdot \boldsymbol{F}(\mathbf{r})\right) d^3r. \tag{A12}$$

For electromagnetic waves, we derive

$$\begin{aligned} I_0\{\boldsymbol{F},\boldsymbol{G}) &= \oint_{\delta D} \boldsymbol{G}^T(\mathbf{r}) \cdot \begin{bmatrix} \times & 0 \\ 0 & \times \end{bmatrix} \cdot \boldsymbol{F}(\mathbf{r}) \cdot \hat{\mathbf{n}} d^2 r \\ &+ \int_D \boldsymbol{F}^T(\mathbf{r}) \cdot \begin{bmatrix} 0 & j\omega\mu\boldsymbol{\delta} \\ -(\sigma + j\omega\epsilon)\boldsymbol{\delta} & 0 \end{bmatrix} \cdot \boldsymbol{G}(\mathbf{r}) d^3 r \\ &+ \int_D \boldsymbol{G}^T(\mathbf{r}) \cdot \begin{bmatrix} 0 & j\omega\mu\boldsymbol{\delta} \\ (\sigma - j\omega\epsilon)\boldsymbol{\delta} & 0 \end{bmatrix} \cdot \boldsymbol{F}(\mathbf{r}) d^3 r, \end{aligned} \tag{A13}$$

and

$$\begin{aligned} I_V\{\boldsymbol{F},\boldsymbol{G}\} &= \int_D \boldsymbol{F}^T(\mathbf{r}) \cdot \begin{bmatrix} 0 & -j\omega\delta\mu\boldsymbol{\delta} \\ (\delta\sigma + j\omega\delta\epsilon)\boldsymbol{\delta} & 0 \end{bmatrix} \cdot \boldsymbol{G}(\mathbf{r}) d^3 r \\ &+ \int_D \boldsymbol{G}^T(\mathbf{r}) \cdot \begin{bmatrix} 0 & -j\omega\delta\mu\boldsymbol{\delta} \\ (j\omega\delta\epsilon - \delta\sigma)\boldsymbol{\delta} & 0 \end{bmatrix} \cdot \boldsymbol{F}(\mathbf{r}) d^3 r. \end{aligned} \tag{A14}$$

Following the same reasoning as for scalar fields, the two representation theorems for perturbations are

$$\boldsymbol{G}_S(\mathbf{r}_B,\mathbf{r}_A) - \boldsymbol{G}_S^H(\mathbf{r}_A,\mathbf{r}_B) = I_1\{\boldsymbol{G}_1(\mathbf{r},\mathbf{r}_A), \overline{\boldsymbol{G}}_1(\mathbf{r},\mathbf{r}_B)\} - I_0\{\boldsymbol{G}_0(\mathbf{r},\mathbf{r}_A), \overline{\boldsymbol{G}}_0(\mathbf{r},\mathbf{r}_B)\} \tag{A15}$$

and

$$\boldsymbol{G}_S(\mathbf{r}_B,\mathbf{r}_A) = I_0\{\boldsymbol{G}_S(\mathbf{r},\mathbf{r}_A), \overline{\boldsymbol{G}}_0(\mathbf{r},\mathbf{r}_B)\} + \left(\boldsymbol{G}_0^H(\mathbf{r},\mathbf{r}_B)\,|\boldsymbol{V}(\mathbf{r})|\,\boldsymbol{G}_1(\mathbf{r},\mathbf{r}_A)\right). \tag{A16}$$

This leads to the same analysis of contributions to the Green's function reconstruction as in section 5 by applying the following decomposition:

$$I_0\{\boldsymbol{G}_S(\mathbf{r},\mathbf{r}_A), \overline{\boldsymbol{G}}_0(\mathbf{r},\mathbf{r}_B)\} = \boldsymbol{G}_S(\mathbf{r}_B,\mathbf{r}_A) - \left(\boldsymbol{G}_0^H(\mathbf{r},\mathbf{r}_B)\,|\boldsymbol{V}(\mathbf{r})|\,\boldsymbol{G}_1(\mathbf{r},\mathbf{r}_A)\right) \tag{A17}$$

$$I_0\{\boldsymbol{G}_0(\mathbf{r},\mathbf{r}_A), \overline{\boldsymbol{G}}_S(\mathbf{r},\mathbf{r}_B)\} = -\boldsymbol{G}_S^H(\mathbf{r}_A,\mathbf{r}_B) + \left(\boldsymbol{G}_0^T(\mathbf{r},\mathbf{r}_A)\,|\overline{\boldsymbol{V}}(\mathbf{r})|\,\overline{\boldsymbol{G}}_1(\mathbf{r},\mathbf{r}_B)\right) \tag{A18}$$

$$I_0\{\boldsymbol{G}_S(\mathbf{r},\mathbf{r}_A), \overline{\boldsymbol{G}}_S(\mathbf{r},\mathbf{r}_B)\} = \left(\boldsymbol{G}_S^T(\mathbf{r}_1,\mathbf{r}_A)\,|\overline{\boldsymbol{V}}(\mathbf{r}_1)|\,\overline{\boldsymbol{G}}_1(\mathbf{r}_1,\mathbf{r}_B)\right) - \left(\boldsymbol{G}_S^H(\mathbf{r}_1,\mathbf{r}_B)\,|\boldsymbol{V}(\mathbf{r}_1)|\,\boldsymbol{G}_1(\mathbf{r}_1,\mathbf{r}_A)\right). \tag{A19}$$

APPENDIX B: TREATMENT OF GENERAL UNPERTURBED BOUNDARY CONDITIONS

Here, we generalize the results of this paper to any unperturbed boundary conditions. For boundary conditions that remain unchanged after perturbing the system, both perturbed and unperturbed fields fulfill equation

$$B(\mathbf{r}) \cdot u_{0,1}(\mathbf{r}) = f(\mathbf{r}) \text{ on boundary,} \tag{B1}$$

where B is the boundary condition operator for the total volume considered D_{tot}. In particular, the unperturbed and perturbed Green's functions, $G_0(\mathbf{r},\mathbf{r}_S)$ and $G_1(\mathbf{r},\mathbf{r}_S)$, between points r and $\mathbf{r}_S$ each satisfy equation (B1). To account for this, relation (8) between unperturbed and perturbed Green's functions is modified as follows:

$$G_1(\mathbf{r},\mathbf{r}_S) = G_0(\mathbf{r},\mathbf{r}_S) + (G_0(\mathbf{r},\mathbf{r}_1)\,|V(\mathbf{r}_1)|\,G_1(\mathbf{r}_1,\mathbf{r}_S)) - \mathcal{G}(\mathbf{r}) \cdot (V(\mathbf{r}_1)|G_1(\mathbf{r}_1,\mathbf{r}_S)), \tag{B2}$$

where $\mathcal{G}$ is a solution of the homogeneous unperturbed system with boundary conditions (B1):

$$H_0(\mathbf{r}) \cdot \mathcal{G}(\mathbf{r}) = 0. \tag{B3}$$

One can verify that this new formulation satisfies boundary conditions (B1) by applying operator B to equation (B2). The perturbation of Green's function $G_S(\mathbf{r},\mathbf{r}_S)$ satisfies a different expression:

$$G_S(\mathbf{r},\mathbf{r}_S) = (G_0(\mathbf{r},\mathbf{r}_1)\,|V(\mathbf{r}_1)|\,G_1(\mathbf{r}_1,\mathbf{r}_S)) - \mathcal{G}(\mathbf{r}) \cdot (V(\mathbf{r}_1)|G_1(\mathbf{r}_1,\mathbf{r}_S)). \tag{B4}$$

The main results of this article, however, remain unchanged. We introduce the interferometric operator and derive the same general representation theorem (23) as for homogeneous boundaries. Additional derivations are needed in order to demonstrate expression (30). Consider equation (B4) for $G_S(\mathbf{r}_A,\mathbf{r}_B)$, and insert the general representation

theorem for unperturbed media $G_0(\mathbf{r}_B,\mathbf{r}_1) = I_0\{G_0(\mathbf{r},\mathbf{r}_1),\overline{G}_0(\mathbf{r},\mathbf{r}_B)\} + \overline{G}_0(\mathbf{r}_1,\mathbf{r}_B)$ to obtain

$$\begin{aligned} G_S(\mathbf{r}_B,\mathbf{r}_A) &= \left(I_0\{G_0(\mathbf{r},\mathbf{r}_1),\overline{G}_0(\mathbf{r},\mathbf{r}_B)\}\,|V(\mathbf{r}_1)|\,G_1(\mathbf{r}_1,\mathbf{r}_A)\right) \\ &+ \left(\overline{G}_0(\mathbf{r}_1,\mathbf{r}_B)\,|V(\mathbf{r}_1)|\,G_1(\mathbf{r}_1,\mathbf{r}_A)\right) \\ &- \mathcal{G}(\mathbf{r}_B)\cdot(V(\mathbf{r}_1)|G_1(\mathbf{r}_1,\mathbf{r}_A)) \\ &= I_0\{G_S(\mathbf{r},\mathbf{r}_A),\overline{G}_0(\mathbf{r},\mathbf{r}_B)\} \\ &+ \left(\overline{G}_0(\mathbf{r}_1,\mathbf{r}_B)\,|V(\mathbf{r}_1)|\,G_1(\mathbf{r}_1,\mathbf{r}_A)\right) \\ &+ I_0\{\mathcal{G}(\mathbf{r})\cdot(V(\mathbf{r}_1)|G_1(\mathbf{r}_1,\mathbf{r}_A)),\overline{G}_0(\mathbf{r},\mathbf{r}_B)\} \\ &- \mathcal{G}(\mathbf{r}_B)\cdot(V(\mathbf{r}_1)|G_1(\mathbf{r}_1,\mathbf{r}_A)). \end{aligned} \tag{B5}$$

Additionally,

$$\begin{aligned} I_0\{\mathcal{G}(\mathbf{r})\cdot(V(\mathbf{r}_1)|G_1(\mathbf{r}_1,\mathbf{r}_A)),\overline{G}_0(\mathbf{r},\mathbf{r}_B)\} &= (\mathcal{G}(\mathbf{r})\cdot(V(\mathbf{r}_1)|G_1(\mathbf{r}_1,\mathbf{r}_A))\,|\underbrace{\overline{H}_0(\mathbf{r})|\overline{G}_0(\mathbf{r},\mathbf{r}_B)}_{\delta(\mathbf{r}-\mathbf{r}_B)}) \\ &- (\overline{G}_0(\mathbf{r},\mathbf{r}_B)|\underbrace{H_0(\mathbf{r})|\mathcal{G}(\mathbf{r})}_{=0}\cdot(V(\mathbf{r}_1)|G_1(\mathbf{r}_1,\mathbf{r}_A))) \\ &= \mathcal{G}(\mathbf{r}_B)\cdot(V(\mathbf{r}_1)|G_1(\mathbf{r}_1,\mathbf{r}_A)). \end{aligned} \tag{B6}$$

Summing these two equations yields

$$G_S(\mathbf{r}_B,\mathbf{r}_A) = I_0\{G_S(\mathbf{r},\mathbf{r}_A),\overline{G}_0(\mathbf{r},\mathbf{r}_B)\} + \left(\overline{G}_0(\mathbf{r},\mathbf{r}_B)\,|V(\mathbf{r})|\,G_1(\mathbf{r},\mathbf{r}_A)\right). \tag{B7}$$

Equation (B7) is identical to representation theorem (30), which holds for unperturbed homogeneous boundary conditions. By analogy, one can show that all the results presented in section 5 holds for any type of unperturbed boundary conditions.

APPENDIX C: PROPERTIES OF SELF-ADJOINT DIFFERENTIAL OPERATOR: VOLUME/SURFACE INTEGRALS AND SPATIAL RECIPROCITY

The interferometric operator is defined as

$$\begin{aligned} I_H\{f,g\} &= (f\,|\overline{H}|\,g) - (g\,|H|\,f) \\ &= \int_D (f\cdot\overline{H}\cdot g - g\cdot H\cdot f)\,dV. \end{aligned} \tag{C1}$$

In section 3, we explain why for practical applications it is useful to convert a volume into a surface integral to reduce the integration over the sub-volume D to its bounding surface δD. In this appendix, we show how this relates to the concept of self-adjoint operator. We introduce what is sometimes referred to as *extended* Green's identify in the literature (Lanczos 1996) and define the adjoint $\tilde{H}$ of a linear differential operator H. The adjoint is the unique operator such that for any pair of functions (f,g), an operator P_H exits and

$$\int_D \left(g\cdot H\cdot f - f\cdot\tilde{\overline{H}}\cdot g\right)dV = -\oint_{\delta D} P_H(f,g)\cdot\hat{\mathbf{n}}dS = \text{boundary term}. \tag{C2}$$

A differential operator is self-adjoint if $H = \tilde{H}$. For self-adjoint operators, equation (C1) can be written using the *extended* Green's identify and consequently,

$$I_H\{f,g\} = \oint_{\delta D} P_H(f,g)\cdot\hat{\mathbf{n}}dS, \tag{C3}$$

so the general representation theorem becomes

$$G(\mathbf{r}_B,\mathbf{r}_A) - \overline{G}(\mathbf{r}_A,\mathbf{r}_B) = \oint_{\delta D} P_H(G(\mathbf{r},\mathbf{r}_A),\overline{G}(\mathbf{r},\mathbf{r}_B))\cdot\hat{\mathbf{n}}dS. \tag{C4}$$

For self-adjoint operators, in order to efficiently extract the Green's function between two points A and B, we need to know the operator P_H, which depends on the properties of the system, and the Green's functions on an enclosing surface δD. For more general systems ($H \neq \tilde{H}$), relation (C4) is no longer valid, but we can alway decompose the

interferometric operator into surface and volume integrals and express the representation theorem as

$$\begin{aligned} G(\mathbf{r}_B,\mathbf{r}_A)-\overline{G}(\mathbf{r}_A,\mathbf{r}_B) &= \oint_{\delta D} P_H(G(\mathbf{r},\mathbf{r}_A),\overline{G}(\mathbf{r},\mathbf{r}_B))\cdot\hat{\mathbf{n}}dS \\ &+ \int_D G(\mathbf{r},\mathbf{r}_A)\cdot\left(\overline{H-\tilde{H}}\right)\cdot G(\mathbf{r},\mathbf{r}_B)dV. \end{aligned} \tag{C5}$$

Note that the results of this paper do not require space- and time-reciprocity. This means that the order of spatial coordinates matters in the relations we establish. To facilitate the use and interpretation of representation theorems (25) and (30) in practice, we desire systems that are spatially reciprocal, as holds for particular boundary conditions and symmetry of linear differential operators. For example, consider a representation theorem of the convolution type. By analogy with the representation theorem of the correlation type obtained in section 3, we get

$$G(\mathbf{r}_B,\mathbf{r}_A)-G(\mathbf{r}_A,\mathbf{r}_B)=\int_D \left(G(\mathbf{r},\mathbf{r}_A)\cdot H(\mathbf{r})\cdot G(\mathbf{r},\mathbf{r}_B)-G(\mathbf{r},\mathbf{r}_B)\cdot H(\mathbf{r})\cdot G(\mathbf{r},\mathbf{r}_A)\right)dV. \tag{C6}$$

For operators such that $\overline{H}=\tilde{H}$, which include self-adjoint real operators, e.g., the wave propagator, use of Green's identity (C2) with $D=D_{tot}$ yields

$$G(\mathbf{r}_B,\mathbf{r}_A)-G(\mathbf{r}_A,\mathbf{r}_B)=\oint_{\delta D_{tot}} P_H(G(\mathbf{r},\mathbf{r}_A),G(\mathbf{r},\mathbf{r}_B))\cdot\hat{\mathbf{n}}dS. \tag{C7}$$

Depending on boundary conditions, the right-hand side of equation (C7) vanishes and consequently, we obtain $G(\mathbf{r}_B,\mathbf{r}_A)=G(\mathbf{r}_A,\mathbf{r}_B)$, i.e., spatial reciprocity. Typically, the integral $\oint_{\delta D_{tot}} P_H(G(\mathbf{r},\mathbf{r}_A),G(\mathbf{r},\mathbf{r}_B))\cdot\hat{\mathbf{n}}dS$ will go to zero if the Green's functions $G(\mathbf{r},\mathbf{r}_{A,B})$ or their derivatives vanish on δD_{tot}. For acoustic waves, the Sommerfield radiation and free surface conditions lead to spatial reciprocity. Systems with free boundaries, however, are of limited interest because we cannot practically apply interferometry. Indeed, for such systems, equation (C4) shows that $G(\mathbf{r}_B,\mathbf{r}_A)-\overline{G}(\mathbf{r}_A,\mathbf{r}_B)=0$; that is, for self-adjoint operators, free boundaries always lead to reconstruction of a null signal.

Cancellation of spurious arrivals in Green's function retrieval of multiple scattered waves

Roel Snieder & Clement Fleury
Center for Wave Phenomena, Colorado School of Mines

ABSTRACT
The Green's function for wave propagation can be extracted by cross-correlating field fluctuations excited on a closed surface that surrounds the employed receivers. This study treats an acoustic multiple scattering medium with discrete scatterers and show that for a given source the cross-correlation of waves propagating along most combinations of scattering paths gives unphysical arrivals. Because theory predicts that the true Green's function is retrieved, such unphysical arrivals must cancel after integration over all sources. This cancellation occurs because the scattering amplitude of each scatterer satisfies the generalized optical theorem. The cross-correlation of scattered waves with themselves does not lead to the correct retrieval of scattered waves, because the cross-terms between the direct and scattered waves is essential.

Key words: interferometry, multiple scattering

1 INTRODUCTION

The extraction of the Green's function for wave propagation by correlation of field fluctuations is an active area of research in a variety of different fields that has reached the stage where material is documented in review papers and books (Larose *et al.*, 2006; Curtis *et al.*, 2006; Wapenaar *et al.*, 2008; Schuster, 2009; Snieder *et al.*, 2009; Wapenaar *et al.*, 2010a; Wapenaar *et al.*, 2010b). The central idea is that field fluctations recorded at two points lead after cross-correlation to the superposition of the causal and time-reversed Green's function for wave propagation between those points. This principle has recently been extended to other types of fields (Wapenaar *et al.*, 2006; Snieder *et al.*, 2007; Weaver, 2008; Gouédard *et al.*, 2008), including static fields (Slob *et al.*, 2010; Snieder *et al.*, 2010). Green's function retrieval for the acoustic waves treated here is based on the cross-correlation of field fluctuations that are excited by sources with equal power spectrum that are located on a closed surface surrounding the used receivers (Derode *et al.*, 2003; Wapenaar *et al.*, 2005). When these sources are located on a spherical surface ∂V where the waves satisfy a radiation boundary condition, the principle of Green's function extraction for acoustic waves is, in the frequency domain, formulated as (Snieder *et al.*, 2007)

$$\oint_{\partial V} G(\mathbf{r}_P,\mathbf{r})G^*(\mathbf{r}_Q,\mathbf{r})dS = -\frac{\rho}{2ik}\left(G(\mathbf{r}_P,\mathbf{r}_Q)-G^*(\mathbf{r}_P,\mathbf{r}_Q)\right) , \quad (1)$$

where $\mathbf{r}_P$ and $\mathbf{r}_Q$ denote the locations of receivers. In this expression we assumed that the density ρ and velocity c are constant on the boundary ∂V, and the asterisk denotes complex conjugation. Throughout this paper we use a formulation in the frequency domain using the following Fourier convention: $F(t) = \int f(\omega)\exp(-i\omega t)d\omega$. For brevity we omit the frequency dependence in the remainder of this work.

For media with discrete scatterers or reflectors, the Green's function can be seen as a superposition of the waves that propagate along all possible scattering paths. Both Green's functions in the left hand side of equation (1) contain a sum over all scattering paths from the integration point $\mathbf{r}$ to the locations $\mathbf{r}_P$ and $\mathbf{r}_Q$, respectively. The left hand side of expression (1) therefore consists of a double sum over scattering paths that end at $\mathbf{r}_P$ and $\mathbf{r}_Q$, respectively. An example of two such paths is shown in figure 1. Let us denote the travel time for the path on the left as t_{S1AP} and the path on the right as t_{S2BQ}. In the time domain, the arrival time of the cross-correlation is given by the difference of the arrival times of the waves that are being cross-correlated. The

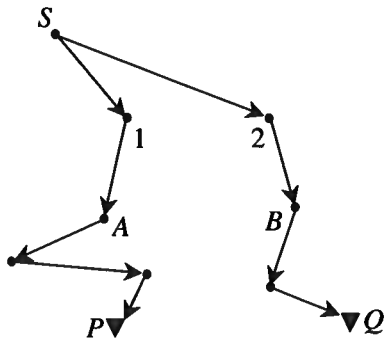

Figure 1. Two scattering paths from a source S to receivers at points P and Q where the first scatterer along each path is different.

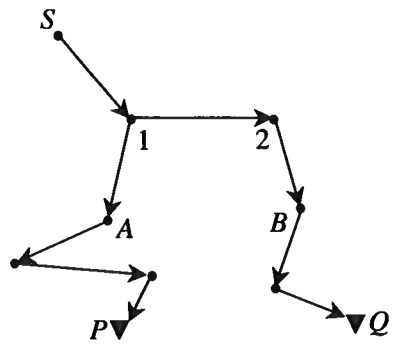

Figure 2. Two scattering paths from a source S to receivers at points P and Q that share the first scatterer along the paths.

cross-correlation of the waves that propagate along the paths of figure 1 thus produces a wave arriving at time $t_{S1AP} - t_{S2BQ}$. This travel time does not correspond to a physical wave that propagates between the points P and Q via the scattering path $A12B$. Such a contribution thus is a *spurious arrival* that does not correspond to a physical wave. These spurious arrivals arise because of the cross-correlation of wave propagating along different scattering paths, we refer to such contributions as *cross terms*. Expression (1) guarantees, though, that the left hand side gives the true Green's function after integration over surrounding sources, hence the spurious arrivals should disappear after integration over all sources. Earlier work treated the cancellation of spurious arrival in the case of one scatterer (Snieder *et al.*, 2008), here we analyze the mechanism by which spurious arrivals cancel upon integration over sources in multiple scattering acoustic media with isolated scatterers.

Let us consider the cross-terms between different scattering paths in more detail. When we consider two different scattering paths that propagate from a source S to receivers P and Q, there are two possibilities; the first scatterer along these paths is the same (figure 2), or the first scatterer on both paths is different (figure 1). Suppose that there are M scatterers in the medium, then there are M ways in which one can choose the first scatterer in figure 2. In contrast, for the cross-terms along the paths shown in figure 1 the are $M(M-1)$ ways to choose the first scatterers along those paths. For a medium with many scatterers, the cross-terms in figure 1 are thus more prevalent than the cross-terms shown in figure 2. We show in this work that despite the fact that that number of scattering paths shown in figure 1 is much larger than those in figure 2, it is the superposition of the scattering paths in both figures that leads to the cancellation of spurious arrivals.

We review the employed scattering theory in section 2. In section 3 we show how the integrals that arise in the cross-correlation can be evaluated in the stationary phase approximation. In section 4 we derive the central result that the sum of these contributions vanishes by virtue of the generalized optical theorem. In section 5 we evaluate the final nonzero contribution of the cross-correlation of waves that propagate from the source to scatterers to a common scattering path, and show that this correctly gives the scattered wave that propagates along that path. An essential element in the cancellation is that one needs cross-terms of the direct wave and scattered waves. In fact, when the Green's function retrieval is based on scattered waves only, the spurious arrivals do not vanish and one does *not* retrieve the scattered waves. Numerical examples of this principle and an alternative derivation for a general linear system are shown in a companion paper (Fleury *et al.*, 2010).

2 THE MULTIPLE SCATTERED WAVES

In this work we consider a homogeneous acoustic medium in which isolated scatterers are embedded. The employed acoustic wave equation is given by

$$\nabla \cdot \left(\frac{1}{\rho} \nabla p \right) + \frac{\omega^2}{\kappa} p = q \,, \tag{2}$$

where ρ is the mass density, κ the bulk modulus, and q the (injection) source. The Green's function $G(\mathbf{r}, \mathbf{r}_0)$ is defined as the solution of expression (2) with $q(\mathbf{r}) = \delta(\mathbf{r} - \mathbf{r}_0)$. The Green's function of the homogeneous reference medium in which the scatterers are embedded is

$$G_0(\mathbf{r}, \mathbf{r}') = -\frac{\rho}{4\pi} \frac{e^{ik|\mathbf{r}-\mathbf{r}'|}}{|\mathbf{r}-\mathbf{r}'|} \,, \tag{3}$$

where $k = \omega\sqrt{\rho/\kappa}$ is the wavenumber. Scatterer j has scattering amplitude $f_j(\hat{\mathbf{n}}, \hat{\mathbf{n}}')$ (Morse & Ingard, 1968; Martin, 2006), where $\hat{\mathbf{n}}'$ is the direction of the incoming wave and $\hat{\mathbf{n}}$ the direction of the outgoing wave. The contribution to the Green's function of the wave propagating from a source at $\mathbf{r}_0$ via scatterers $1 \cdots N$ at locations $\mathbf{r}_1, \cdots, \mathbf{r}_N$ to a receiver at $\mathbf{r}$ is given by

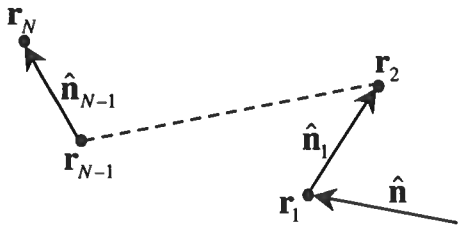

Figure 3. Definition of geometric variables for a scattering path involving N scatterers.

$$G^{path\ 1\cdots N}(\mathbf{r},\mathbf{r}_0) = -\frac{\rho}{4\pi}\frac{e^{ik|\mathbf{r}-\mathbf{r}_N|}}{|\mathbf{r}-\mathbf{r}_N|}f_N(\hat{\mathbf{n}}_N,\hat{\mathbf{n}}_{N-1}) \times \frac{e^{ik|\mathbf{r}_N-\mathbf{r}_{N-1}|}}{|\mathbf{r}_N-\mathbf{r}_{N-1}|}\cdots f_1(\hat{\mathbf{n}}_1,\hat{\mathbf{n}}_0)\frac{e^{ik|\mathbf{r}_1-\mathbf{r}_0|}}{|\mathbf{r}_1-\mathbf{r}_0|}\ , \tag{4}$$

where the unit vector $\hat{\mathbf{n}}_i$ points from $\mathbf{r}_i$ to $\mathbf{r}_{i+1}$. In this expression, the propagation between scatterers i and j is denoted by $\exp(ik|\mathbf{r}_i-\mathbf{r}_j|)/|\mathbf{r}_i-\mathbf{r}_j|$. This description of scattering is valid when the scatterers are in each other's far field. When this condition is not valid one can expand the scattering coefficients in a sum over spherical harmonics and replace the propagators by spherical Hankel functions (Martin, 2006); in that case the analysis presented here is not applicable. The same scatterer can occur twice, or more, along the path, allowing for loops.

In the remainder of this work we focus on one particular scattering path, the treatment presented here is applicable to each scattering path separately. For brevity we introduce the following notation

$$G_{1\cdots N}(\hat{\mathbf{n}}) = \frac{e^{ik|\mathbf{r}_N-\mathbf{r}_{N-1}|}}{|\mathbf{r}_N-\mathbf{r}_{N-1}|}f_{N-1}(\hat{\mathbf{n}}_{N-2},\hat{\mathbf{n}}_{N-1})\cdots \times \frac{e^{ik|\mathbf{r}_2-\mathbf{r}_1|}}{|\mathbf{r}_2-\mathbf{r}_1|}f_1(\hat{\mathbf{n}}_1,\hat{\mathbf{n}})\ , \tag{5}$$

where the corresponding scattering path and variables are defined in figure 3. This quantity describes the wave propagation for a wave incident from direction $\hat{\mathbf{n}}$ on scatterer 1, and then propagates via scatterers $1,2,\cdots,N-1$ to location $\mathbf{r}_N$. A comparison of expressions (4) and (5) shows that

$$G^{path\ 1\cdots N}(\mathbf{r},\mathbf{r}_0) = -\frac{\rho}{4\pi}\frac{e^{ikr_{01}}}{r_{01}}G_{1\cdots N}(\hat{\mathbf{r}}_{01})\ . \tag{6}$$

Throughout this work we use the notations

$$\mathbf{r}_{IJ} = \mathbf{r}_J - \mathbf{r}_I \ \text{ and } \ r_{IJ} = |\mathbf{r}_{IJ}|\ , \tag{7}$$

hence in expression (6), $\mathbf{r}_{01} = \mathbf{r}_1 - \mathbf{r}_0$ is the vector pointing from a source at $\mathbf{r}_0$ to the position $\mathbf{r}_1$ of the first scatterer along the path considered.

3 SPURIOUS ARRIVALS FROM CROSS-TERMS

The waves traveling from the source S to receivers at $\mathbf{r}_P$ and $\mathbf{r}_Q$ either encounter different scatterers as the first scatterer along their paths, as shown in figure 1, or they may encounter the same first scatterer along their paths, see figure 2. In the notation of figure 1 we denote the first scatterers encountered on the two scattering paths by the labels "1" and "2", respectively. The next points along these paths are denoted with the labels "A" and "B". These points can either be scatterers, or the receivers where the wave field is recorded. The scatterers along the path considered are not necessarily spatially adjacent, the figures only show them in spatial order for reasons of clarity. The scattering paths beyond points A and B is independent of the location of the source, and in the following we don't show the continuation of those paths to the receivers P and Q.

We consider the scattering diagrams shown in figure 4. These diagrams show all the waves that propagate from the source and visit the scatterers 1 and 2 one or two times. As mentioned earlier, we do not show the fate of the waves beyond the points A and B because this part of the wave paths does not change during the integration over the sources on ∂V. There are five such diagrams, in the following we compute the contribution of each diagram to the cross-correlation. We evaluate the contribution of each diagram using the stationary phase approximation (Bleistein & Handelsman, 1975; Snieder, 2004) which becomes exact as the surface ∂V goes to infinity (van de Hulst, 1949). Note that the diagrams T_1 and T_2 are topologically identical in the sense that both diagram describe a cross term between scattered waves that travel from the source to consecutive scatterers along the scattering path. Diagram T_2 follows from diagram T_1 by substituting $1 \rightarrow A$ and $2 \rightarrow 1$. In section 5 we take into account that the cross-correlation of scattered waves also contains cross-terms from scattering paths that propagate directly from the source to scatterers A and 1 instead of the scatterers 1 and 2.

We first analyze the term T_1 that corresponds to the diagram in the top left of figure 4. Using expressions (4) and (5), the wave that propagates along the left path of term T_1 in figure 4 from the source S via the scatterer A a receiver P is given by

$$u_{left} = -\frac{\rho}{4\pi}\frac{e^{ikr_{S1}}}{r_{S1}}f_1(\hat{\mathbf{r}}_{1A},\hat{\mathbf{r}}_{S1})\frac{e^{ikr_{1A}}}{r_{1A}}G_{A\cdots P}(\hat{\mathbf{r}}_{1A})\ , \tag{8}$$

where $G_{A\cdots P}(\hat{\mathbf{r}}_{1A})$ accounts for the propagation from scatterer A to receiver P along the scattering path. The subscript S refers to the source location. The unit vector $\hat{\mathbf{r}}_{1A}$ is defined using expression (7). Similarly, the wave propagating along the right path of term T_1 in figure 4 is given by

$$u_{right} = -\frac{\rho}{4\pi}\frac{e^{ikr_{S2}}}{r_{S2}}f_2(\hat{\mathbf{r}}_{2B},\hat{\mathbf{r}}_{S2})\frac{e^{ikr_{2B}}}{r_{2B}}G_{B\cdots Q}(\hat{\mathbf{r}}_{2B})\ . \tag{9}$$

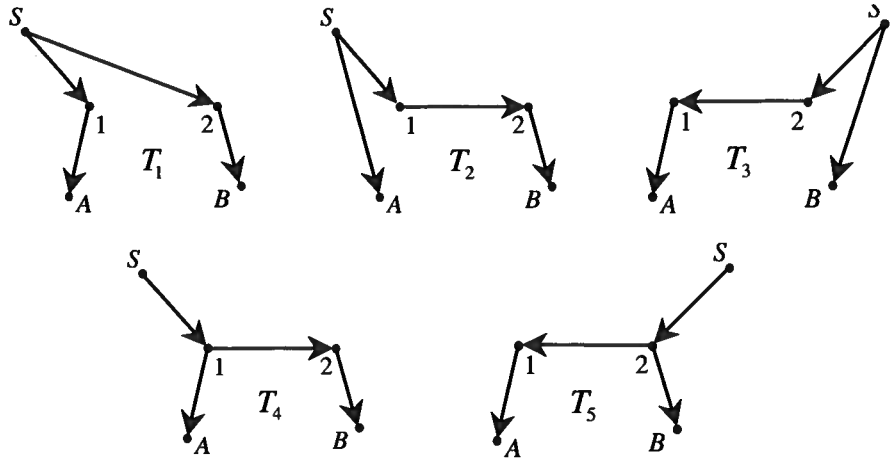

Figure 4. Scattering diagrams for wave propagation from a source S to points A and B that visit the scatterers 1 and 2 one or two times. For simplicity the scattering paths from scatterer A to receiver P and scatterer B to receiver Q are not shown.

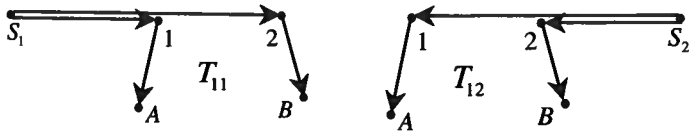

Figure 5. Stationary points for the source integration in expression (11) for term T_1.

The contribution to the cross-correlation of these two paths is given by

$$T_1 = \oint \left(-\frac{\rho}{4\pi}\frac{e^{ikr_{1A}}}{r_{1A}} f_1(\hat{\mathbf{r}}_{1A},\hat{\mathbf{r}}_{S1})\frac{e^{ikr_{S1}}}{r_{S1}} G_{A\cdots P}(\hat{\mathbf{r}}_{1A})\right)\left(-\frac{\rho}{4\pi}\frac{e^{ikr_{2B}}}{r_{2B}} f_2(\hat{\mathbf{r}}_{2B},\hat{\mathbf{r}}_{S2})\frac{e^{ikr_{S2}}}{r_{S2}} G_{B\cdots Q}(\hat{\mathbf{r}}_{2B})\right)^* dS\,, \tag{10}$$

where the integration is over sources on a spherical surface surrounding the scatterers and the receivers. Rearranging terms, T_1 can be written as

$$T_1 = \left(\frac{\rho}{4\pi}\right)^2 \frac{e^{ik(r_{1A}-r_{2B})}}{r_{1A}r_{2B}} G_{A\cdots P}(\hat{\mathbf{r}}_{1A}) G^*_{B\cdots Q}(\hat{\mathbf{r}}_{2B}) \oint \frac{e^{ik(r_{S1}-r_{S2})}}{r_{S1}r_{S2}} f_1(\hat{\mathbf{r}}_{1A},\hat{\mathbf{r}}_{S1}) f_2^*(\hat{\mathbf{r}}_{2B},\hat{\mathbf{r}}_{S2}) dS\,. \tag{11}$$

The surface integral can be evaluated with the stationary phase approximation following the steps taken by Snieder *et al.* (2008). Instead of repeating these steps, we recognize that, apart from the terms containing the scattering amplitude, the surface integral is equal to the superposition of the causal and a-causal unperturbed Green's function of equation (3):

$$\left(\frac{\rho}{4\pi}\right)^2 \oint \frac{e^{ik(r_{S1}-r_{S2})}}{r_{S1}r_{S2}} dS = \oint G_0(\mathbf{r}_1,\mathbf{r}) G_0^*(\mathbf{r}_2,\mathbf{r}) dS = -\frac{\rho}{2ik}\left(G_0(\mathbf{r}_1,\mathbf{r}_2) - G_0^*(\mathbf{r}_1,\mathbf{r}_2)\right) = \frac{\rho^2}{8\pi ik}\left(\frac{e^{ikr_{12}}}{r_{12}} - \frac{e^{-ikr_{12}}}{r_{12}}\right)\,, \tag{12}$$

where the first and last identities follow from equation (3) and the second equality from expression (1). We use this result in the stationary phase approximation of the integral (11), but must insert the stationary phase locations for the source position in the variables that depend on the source position.

Following the analysis of Snieder *et al.* (2008), the surface integral in equation (11) has two stationary phase points that are shown in figure 5. For the stationary phase point in the left panel of figure 5, $\hat{\mathbf{r}}_{S1} = \hat{\mathbf{r}}_{S2} = \hat{\mathbf{r}}_{12}$, and $r_{S1} - r_{S2} = -r_{12}$. For the stationary phase point of the right panel $\hat{\mathbf{r}}_{S1} = \hat{\mathbf{r}}_{S2} = -\hat{\mathbf{r}}_{12}$, and $r_{S1} - r_{S2} = r_{12}$. Using these results, expression (11) is in the stationary phase approximation given by

$$\begin{aligned} T_1 \;&= \frac{\rho^2}{8\pi ik}\frac{e^{ik(r_{1A}-r_{2B})}}{r_{1A}r_{2B}}\left(\frac{e^{ikr_{12}}}{r_{12}} f_1(\hat{\mathbf{r}}_{1A},-\hat{\mathbf{r}}_{12}) f_2^*(\hat{\mathbf{r}}_{2B},-\hat{\mathbf{r}}_{12}) - \frac{e^{-ikr_{12}}}{r_{12}} f_1(\hat{\mathbf{r}}_{1A},\hat{\mathbf{r}}_{12}) f_2^*(\hat{\mathbf{r}}_{2B},\hat{\mathbf{r}}_{12})\right) \\ &\times G_{A\cdots P}(\hat{\mathbf{r}}_{1A}) G^*_{B\cdots Q}(\hat{\mathbf{r}}_{2B})\,. \end{aligned} \tag{13}$$

Note that apart from contributions from the scattering amplitude, the phase of the first term in this expression is given by $k(r_{1A} + r_{12} - r_{2B})$. In the time domain this corresponds to a wave arriving at time $t = (r_{1A} + r_{12} - r_{2B})/c$,

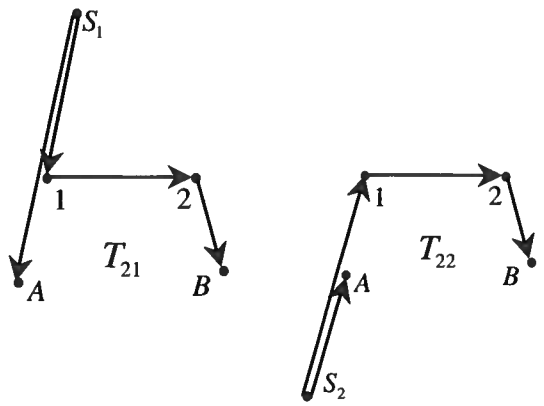

Figure 6. Stationary points for the source integration in expression (14) for term T_2.

where c is the wave velocity of the reference medium. This wave, with an arrival time that depends on the *difference* of the travel times $(r_{A1} + r_{12})/c$ and r_{2B}/c along the scattering path rather than its *sum*, does not correspond to a physical arrival. The same consideration holds for the second term in expression (13), whose phase depends on $k(r_{1A} - r_{12} - r_{2B})$. Hence both terms of T_1 are spurious arrivals that must ultimately be cancelled by other terms.

4 CANCELLATION OF THE SPURIOUS ARRIVALS

In this section we analyze the contributions of the diagrams T_2 through T_5 shown in figure 4. Using expression (4), the term T_2 can be written as

$$\begin{aligned} T_2 &= \oint \left(-\frac{\rho}{4\pi}\frac{e^{ikr_{SA}}}{r_{SA}} G_{A\cdots P}(\hat{\mathbf{r}}_{SA})\right)\left(-\frac{\rho}{4\pi}\frac{e^{ikr_{2B}}}{r_{2B}} f_2(\hat{\mathbf{r}}_{2B},\hat{\mathbf{r}}_{12})\frac{e^{ikr_{12}}}{r_{12}} f_1(\hat{\mathbf{r}}_{12},\hat{\mathbf{r}}_{S1})\frac{e^{ikr_{S1}}}{r_{S1}} G_{B\cdots Q}(\hat{\mathbf{r}}_{2B})\right)^* dS \\ &= \left(\frac{\rho}{4\pi}\right)^2 \frac{e^{-ikr_{2B}}}{r_{2B}}\frac{e^{-ikr_{12}}}{r_{12}} f_2^*(\hat{\mathbf{r}}_{2B},\hat{\mathbf{r}}_{12}) G^*_{B\cdots Q}(\hat{\mathbf{r}}_{2B}) \oint \frac{e^{ik(r_{SA}-r_{S1})}}{r_{2A}r_{S1}} G_{A\cdots P}(\hat{\mathbf{r}}_{SA}) f_1^*(\hat{\mathbf{r}}_{12},\hat{\mathbf{r}}_{S1}) dS\,. \end{aligned} \tag{14}$$

The integral can be evaluated in the stationary phase approximation We consider the contribution of the stationary phase using expression (12) and evaluate the scattering amplitude for incoming waves excited at each stationary source position. The stationary phase points are shown in figure 6, and their contribution is given by $T_2 = T_{21} + T_{22}$ with

$$T_{21} = \frac{\rho^2}{8\pi ik}\frac{e^{ik(r_{1A}-r_{2B})}}{r_{1A}r_{2B}}\frac{e^{-ikr_{12}}}{r_{12}} f_1^*(\hat{\mathbf{r}}_{12},\hat{\mathbf{r}}_{1A}) f_2^*(\hat{\mathbf{r}}_{2B},\hat{\mathbf{r}}_{12}) G_{A\cdots P}(\hat{\mathbf{r}}_{1A}) G^*_{B\cdots Q}(\hat{\mathbf{r}}_{2B})\,, \tag{15}$$

and

$$T_{22} = -\frac{\rho^2}{8\pi ik}\frac{e^{-ik(r_{1A}+r_{2B})}}{r_{1A}r_{2B}}\frac{e^{-ikr_{12}}}{r_{12}} f_1^*(\hat{\mathbf{r}}_{12},\hat{\mathbf{r}}_{A1}) f_2^*(\hat{\mathbf{r}}_{2B},\hat{\mathbf{r}}_{12}) G_{A\cdots P}(\hat{\mathbf{r}}_{A1}) G^*_{B\cdots Q}(\hat{\mathbf{r}}_{2B})\,, \tag{16}$$

where we used $\hat{\mathbf{r}}_{S1} = \hat{\mathbf{r}}_{A1}$ for the stationary phase point in the left panel of figure 6 that, and $\hat{\mathbf{r}}_{S1} = \hat{\mathbf{r}}_{1A}$ for the other stationary point. Note that the directions $1A$ and $A1$ are reversed in expressions (15) and (16) because of the opposite orientation of the stationary phase points in figure 6. In the time domain term T_{21} corresponds to a wave arriving at time $t = (r_{1A} - r_{2B} - r_{12})/c$. Because it contains the difference of arrival times, it does not correspond to any physical wave that propagates between the scatterers.

Term T_3 can be obtained from the analysis for T_2 by interchanging points A and B, points 1 and 2 and taking the complex conjugate. Applying these substitutions to expression (15) gives for the spurious arrival of T_{31} due to one of the stationary phase points

$$T_{31} = -\frac{\rho^2}{8\pi ik}\frac{e^{ik(r_{1A}-r_{2B})}}{r_{1A}r_{2B}}\frac{e^{ikr_{12}}}{r_{12}} f_1(\hat{\mathbf{r}}_{1A},-\hat{\mathbf{r}}_{12}) f_2(-\hat{\mathbf{r}}_{12},\hat{\mathbf{r}}_{2B}) G_{A\cdots P}(\hat{\mathbf{r}}_{1A}) G^*_{B\cdots Q}(\hat{\mathbf{r}}_{2B})\,, \tag{17}$$

where we used that $\hat{\mathbf{r}}_{21} = -\hat{\mathbf{r}}_{12}$. This is, again, a spurious arrival because it corresponds to a wave arriving at a time difference $t = (r_{1A} - r_{2B} + r_{12})/c$. The contribution from the other stationary phase point follows by making the substitutions given above in expression (16) and is given by

$$T_{32} = \frac{\rho^2}{8\pi ik}\frac{e^{ik(r_{1A}+r_{2B})}}{r_{1A}r_{2B}}\frac{e^{ikr_{12}}}{r_{12}} f_1(\hat{\mathbf{r}}_{1A},-\hat{\mathbf{r}}_{12}) f_2(-\hat{\mathbf{r}}_{12},\hat{\mathbf{r}}_{B2}) G_{A\cdots P}(\hat{\mathbf{n}}_{1A}) G^*_{B\cdots Q}(\hat{\mathbf{n}}_{B2}) \,. \tag{18}$$

Using equation (4) the contributions to term T_4 of the paths shown in figure 4 are given by

$$\begin{aligned} T_4 &= \oint \left(-\frac{\rho}{4\pi}\frac{e^{ikr_{1A}}}{r_{1A}} f_1(\hat{\mathbf{r}}_{1A},\hat{\mathbf{r}}_{S1})\frac{e^{ikr_{S1}}}{r_{S1}} G_{A\cdots P}(\hat{\mathbf{r}}_{1A})\right) \\ &\times \left(-\frac{\rho}{4\pi}\frac{e^{ikr_{2B}}}{r_{2B}} f_2(\hat{\mathbf{r}}_{2B},\hat{\mathbf{r}}_{12})\frac{e^{ikr_{12}}}{r_{12}} f_1(\hat{\mathbf{r}}_{12},\hat{\mathbf{r}}_{S1})\frac{e^{ikr_{S1}}}{r_{S1}} G_{B\cdots Q}(\hat{\mathbf{r}}_{2B})\right)^* dS \\ &= \frac{\rho^2}{16\pi^2}\frac{e^{ik(r_{1A}-r_{2B})}}{r_{1A}r_{2B}}\frac{e^{-ikr_{12}}}{r_{12}} f_2^*(\hat{\mathbf{r}}_{2B},\hat{\mathbf{r}}_{12}) \oint \frac{1}{r_{S1}^2} f_1(\hat{\mathbf{r}}_{1A},\hat{\mathbf{r}}_{S1}) f_1^*(\hat{\mathbf{r}}_{12},\hat{\mathbf{r}}_{S1}) dS \\ &\times G_{A\cdots P}(\hat{\mathbf{r}}_{A1}) G^*_{B\cdots Q}(\hat{\mathbf{r}}_{2B}) \,. \end{aligned} \tag{19}$$

The surface element dS is related to the increment $d\Omega$ in solid angle by the relation $(1/r_{S1}^2)dS = d\Omega$. Replacing $\hat{\mathbf{r}}_{S1}$, which depends on the source position over which we integrate, by a new integration variable $\hat{\mathbf{r}}$ gives

$$T_4 = \frac{\rho^2}{16\pi^2}\frac{e^{ik(r_{1A}-r_{2B})}}{r_{1A}r_{2B}}\frac{e^{-ikr_{12}}}{r_{12}} f_2^*(\hat{\mathbf{r}}_{2B},\hat{\mathbf{r}}_{12}) \oint f_1(\hat{\mathbf{r}}_{1A},\hat{\mathbf{r}}) f_1^*(\hat{\mathbf{r}}_{12},\hat{\mathbf{r}}) d\Omega \, G_{A\cdots P}(\hat{\mathbf{r}}_{A1}) G^*_{B\cdots Q}(\hat{\mathbf{r}}_{2B}) \,. \tag{20}$$

Term T_5 of figure 4 follows from this expression by interchanging $A \leftrightarrow B$, $1 \leftrightarrow 2$, and taking the complex conjugate

$$T_5 = \frac{\rho^2}{16\pi^2}\frac{e^{ik(r_{1A}-r_{2B})}}{r_{1A}r_{2B}}\frac{e^{ikr_{12}}}{r_{12}} f_1(\hat{\mathbf{r}}_{1A},-\hat{\mathbf{r}}_{12}) \oint f_2^*(\hat{\mathbf{r}}_{2B},\hat{\mathbf{r}}) f_2(-\hat{\mathbf{r}}_{12},\hat{\mathbf{r}}) d\Omega \, G_{A\cdots P}(\hat{\mathbf{r}}_{A1}) G^*_{B\cdots Q}(\hat{\mathbf{r}}_{2B}) \,. \tag{21}$$

Note that T_4 and T_5 also depend on the difference of path length, and thus are unphysical arrivals.

The sum $T_{spur} = T_1 + T_{21} + T_{31} + T_4 + T_5$ of the spurious terms of equations (13), (15), (17), (20) and (21) gives after a rearrangement of terms

$$\begin{aligned} T_{spur} = \; & \frac{\rho^2 e^{ik(r_{1A}-r_{2B})}}{4\pi k r_{1A}r_{2B}} \left(\frac{e^{ikr_{12}}}{r_{12}} f_1(\hat{\mathbf{r}}_{1A},-\hat{\mathbf{r}}_{12}) F_2^*(\hat{\mathbf{r}}_{2B},-\hat{\mathbf{r}}_{12}) + \frac{e^{-ikr_{12}}}{r_{12}} f_2^*(\hat{\mathbf{r}}_{2B},\hat{\mathbf{r}}_{12}) F_1(\hat{\mathbf{r}}_{1A},\hat{\mathbf{r}}_{12})\right) \\ & \times G_{A\cdots P}(\hat{\mathbf{r}}_{A1}) G^*_{B\cdots Q}(\hat{\mathbf{r}}_{2B}) \end{aligned} \tag{22}$$

with

$$F_1(\hat{\mathbf{r}}_{1A},\hat{\mathbf{r}}_{12}) = -\frac{1}{2i} f_1(\hat{\mathbf{r}}_{1A},\hat{\mathbf{r}}_{12}) + \frac{1}{2i} f_1^*(\hat{\mathbf{r}}_{12},\hat{\mathbf{r}}_{1A}) + \frac{k}{4\pi}\oint f_1(\hat{\mathbf{r}}_{1A},\hat{\mathbf{r}}) f_1^*(\hat{\mathbf{r}}_{12},\hat{\mathbf{r}}) d\Omega \,, \tag{23}$$

and

$$F_2^*(\hat{\mathbf{r}}_{2B},-\hat{\mathbf{r}}_{12}) = \frac{1}{2i} f_2^*(\hat{\mathbf{r}}_{2B},-\hat{\mathbf{r}}_{12}) - \frac{1}{2i} f_2(-\hat{\mathbf{r}}_{12},\hat{\mathbf{r}}_{2B}) + \frac{k}{4\pi}\oint f_2^*(\hat{\mathbf{r}}_{2B},\hat{\mathbf{r}}) f_2(-\hat{\mathbf{r}}_{12},\hat{\mathbf{r}}) d\Omega \,. \tag{24}$$

The scatterers 1 and 2 must both satisfy the generalized optical theorem

$$\frac{1}{2i}\left(f_j(\hat{\mathbf{r}}_A,\hat{\mathbf{r}}_B) - f_j^*(\hat{\mathbf{r}}_B,\hat{\mathbf{r}}_A)\right) = \frac{k}{4\pi}\oint f_j(\hat{\mathbf{r}}_A,\hat{\mathbf{r}}) f_j^*(\hat{\mathbf{r}}_B,\hat{\mathbf{r}}) d\Omega \,. \tag{25}$$

This theorem has been derived for quantum mechanics (Heisenberg, 1943; Glauber & Schomaker, 1953) and acoustics (Marston, 2001). By virtue of this theorem, both F_1 and F_2 in expressions (23) and (24) vanish. Because of equation (22) the sum T_{spur} of the spurious arrivals of the diagrams of figure 4 is thus equal to zero.

Since the sum $T_1 + T_{21} + T_{31} + T_4 + T_5$ vanishes, the only nonzero contribution comes from the terms T_{22} and T_{32}, hence the sum $T = T_1 + T_2 + T_3 + T_4 + T_5$ of all diagrams in figure 4 is given by

$$\begin{aligned} T \; = & \frac{\rho^2}{8\pi ik}\frac{e^{ik(r_{1A}+r_{12}+r_{2B})}}{r_{1A}r_{12}r_{2B}} f_1(\hat{\mathbf{r}}_{1A},-\hat{\mathbf{r}}_{12}) f_2(-\hat{\mathbf{r}}_{12},\hat{\mathbf{r}}_{B2}) G_{A\cdots P}(\hat{\mathbf{r}}_{1A}) G^*_{B\cdots Q}(\hat{\mathbf{r}}_{B2}) \\ & - \frac{\rho^2}{8\pi ik}\frac{e^{-ik(r_{1A}+r_{12}+r_{2B})}}{r_{1A}r_{12}r_{2B}} f_1^*(\hat{\mathbf{r}}_{12},\hat{\mathbf{r}}_{A1}) f_2^*(\hat{\mathbf{r}}_{2B},\hat{\mathbf{r}}_{12}) G_{A\cdots P}(\hat{\mathbf{r}}_{A1}) G^*_{B\cdots Q}(\hat{\mathbf{r}}_{2B}) \,. \end{aligned} \tag{26}$$

In the next section we consider the sum of the diagrams T_1 through T_5 and their contribution to expression (26) for all scatterers along the scattering path, and we treat the sum of all those contributions.

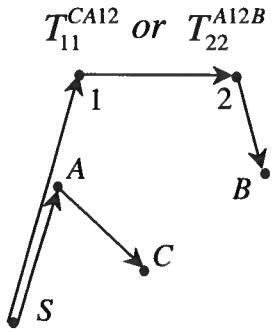

Figure 7. Two different ways of accounting for the cross-terms of two scattering paths.

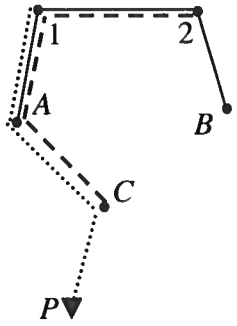

Figure 8. The terms $T_1 + T_2 + T_3 + T_4 + T_5$ cancel for the scatterers connected by the solid lines, for those connected by the dashed lines, and for those connected by the dashed lines. In the end only the path from the receiver P to the first scatterer along the path gives a nonzero contribution (with a similar contribution from receiver Q to the last scatterer along the path).

5 THE ENDPOINT CONTRIBUTIONS FROM A SCATTERING PATH

According to equation (26) the total contribution of the diagrams T_1 through T_5 of figure 4 reduces to the term T_{22} of figure 6 and a corresponding diagram T_{32} that connects to scatterer B. We consider the stationary source position for term T_{22} in figure 7, but now we have added the next scatterer along the path from scatterer A, and call this scatterer C. Comparing diagram T_{22} of figure 6 with diagram T_{11} of figure 5 one recognizes that diagram T_{22} can be interpreted in two ways: first, as illustrated in figure 7 it can be seen either as diagram T_{11} of the scatterers $CA12$, because it follows from diagram T_{11} in figure 5 by replacing $A12B \rightarrow CA12$. Second, it can be seen as diagram T_{22} of the scatterers $A12B$ because it is identical to the diagram shown in the right panel of figure 6. Ultimately, the cross-correlation of all waves excited by the source S that visit scatterers along the scattering path under consideration contains a sum over pairs of scatterers along that path. In the previous section, we called those scatterers 1 and 2, but the cross-correlation also contains a contribution from the scatterers A and 1 as shown in figure 7. We should avoid counting such a contribution twice, because, as shown in figure 7 this scattering diagram corresponds to the cross-correlation of the same waves. Therefore the contribution T_{22} for the scatterers $A12B$ plays the role of contribution T_{11} of the scatterers $CA12$ and contributes to the cancellation of the terms T_2 through T_5 for the scatterers $CA12$. This means that the endpoint contribution for the scatterers $A12B$ (indicated by the solid path in figure 8) contributes to the cancellation of the terms T_1 through T_5 for the scatterers $CA12$ (indicated by the dashed lines in figure 8). The diagrams T_1 through T_5 thus cancel when one sums the contribution of adjacent sets of four scatterers along the scattering path. This cancellation stops when one reaches one of the ends of the scattering path at one of the receivers; in figure 8 the three scatterers and receiver P that give a nonzero endpoint contribution are connected by dotted lines. According to expression (26), the net remaining contribution is given by the cross-term of the direct wave that propagates to the receiver P and a scattered wave that propagates to scatterer C. Because of symmetry, there is a similar contribution from receiver Q.

In the following we evaluate the contribution of equation (26) at the endpoints of the scattering path. As argued above, the contributions of expression (26) that end at the receivers P or Q are the only terms that give a nonzero contribution. For ease of notation, we rename the scatterers along the path with indices $1, 2, \cdots, N$; this index enumarates the scatterers along the path starting at receiver P. We first consider the cross-term that remains at the end of scattering path at receiver P as shown in figure 9. This cross-term consists of the the direct wave G_0 that travels to receiver P with the scattered wave $G_S^{path\ 1\cdots N}$ that propagates along the scatterers $1, \cdots N$ to receiver Q.

The contribution of this cross-term is, in the notation of figure 9, given by

$$\begin{aligned} T_{22} &= \oint \left(-\frac{\rho}{4\pi} \frac{e^{ikr_{SP}}}{r_{SP}} \right) \\ &\times \left(-\frac{\rho}{4\pi} \frac{e^{ikr_{S1}}}{r_{S1}} G_{1\cdots NQ}(\hat{\mathbf{r}}_{S1}) \right)^* dS \qquad (27) \\ &= \left(-\frac{\rho}{4\pi} \right)^2 \oint \frac{e^{ik(r_{SP}-r_{S1})}}{r_{SP} r_{S1}} G^*_{1\cdots NQ}(\hat{\mathbf{r}}_{S1}) dS \, . \end{aligned}$$

Since we only need to account for the equivalent of term T_{22} we consider the contribution of the stationary phase point shown in figure 9, and using equation (12), the contribution of this stationary phase point is given by

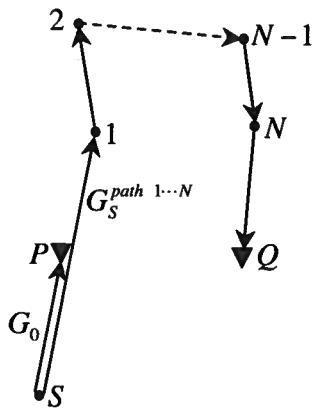

Figure 9. The stationary source position that gives a nonzero contribution the scattering path $P1\cdots NQ$.

$$\begin{aligned} T_{22} &= -\frac{\rho^2}{8\pi ik}\frac{e^{-ikr_{P1}}}{r_{P1}}G^*_{1\cdots NQ}(\hat{\mathbf{r}}_{S1}) \\ &= -\frac{\rho^2}{8\pi ik}\left(-\frac{4\pi}{\rho}\right)\left(G^{path\ 1\cdots N}(\mathbf{r}_P,\mathbf{r}_Q)\right)^* \\ &= \frac{\rho}{2ik}\left(G^{path\ 1\cdots N}(\mathbf{r}_P,\mathbf{r}_Q)\right)^* , \end{aligned} \tag{28}$$

where we used that at the stationary point $\hat{\mathbf{r}}_{S1} = \hat{\mathbf{r}}_{P1}$, and expression (6) in the second identity. As indicated in figure 9, this contribution consists of the correlation of the direct wave $G_0(\mathbf{r}_P,\mathbf{r}_S)$, that propagates from the source to the receiver at $\mathbf{r}_P$ with the scattered wave $G_S^{path\ 1\cdots N}(\mathbf{r}_Q,\mathbf{r}_S)$, that travels from the source via scatterers $1\cdots N$ to the receiver at $\mathbf{r}_Q$. The contribution from the term T_{32} at the other end of the scattering path follows by taking the complex conjugate, replacing P and Q, and reversing the order of the scatterers $(1\cdots N \rightarrow N\cdots 1)$, which gives

$$\begin{aligned} T_{32} &= -\frac{\rho}{2ik}G^{path\ N\cdots 1}(\mathbf{r}_Q,\mathbf{r}_P) \\ &= -\frac{\rho}{2ik}G^{path\ 1\cdots N}(\mathbf{r}_P,\mathbf{r}_Q) , \end{aligned} \tag{29}$$

where we used reciprocity in the last identity. Adding the contributions from equations (28) and (30) finally yields

$$T_{22} + T_{32} = -\frac{\rho}{2ik}\left(G^{path\ 1\cdots N}(\mathbf{r}_P,\mathbf{r}_Q) - \left(G^{path\ 1\cdots N}(\mathbf{r}_P,\mathbf{r}_Q)\right)^*\right) . \tag{30}$$

This is nothing but expression (1) for the wave propagating along the scattering path under consideration.

6 DISCUSSION

We have shown for a multiple scattering system with discrete scatterers that the cross-correlation of different scattering paths vanishes when one integrates over all sources on a surface that bound the region with scatterers and receivers. One might think that the cancellation of spurious arrivals occurs because the phase of each of these arrivals is different for different pairs of scattering paths and that the resulting destructive interference causes the spurious arrivals to cancel, but this is not the reason. The cancellation process involves the sum of the five scattering diagrams shown in figure 4, and the sum of these scattering diagrams vanishes because every scatterer must satisfy the generalized optical theorem. The cancellation of spurious arrivals for multiple scattered waves shown here complements an earlier proof that for an isolated scatterer the spurious arrivals cancel (Snieder *et al.*, 2008). Because of the extremely large number of spurious cross-terms in a multiple scattering medium, the cancellation of spurious arrivals is much more important in a multiple scattering medium than in a medium with just one scatterer. For weakly scattering media where scattering can be treated in the Born approximation, the cross-terms of scattered waves with scattered waves is of higher order and can thus be ignored in Green's function extraction (Sato, 2009; Sato, 2010).

It is essential in the cancellation of the spurious arrivals that the power spectrum of the sources on the boundary ∂V is constant and that sources are present everywhere on this boundary because these requirements ensure that the surface integral in the Green's function extraction is adequately sampled. If these conditions are not met, the angular integrals in the terms T_1 through T_5 are multiplied with variations in the power spectrum and/or spatial density of sources, and as a result the spurious arrivals may not cancel (Snieder *et al.*, 2008; Fan & Snieder, 2009). This is important for practical reasons, since in applications there may be gaps in the source distribution on ∂V, and even if sources are present everywhere on ∂V, the power spectrum of these source may vary. In that case the spurious arrivals may contaminate estimates for the Green's function obtained from cross-correlation of field fluctuations.

As shown in sections 4 and 5, the extraction of the wave propagating along the scattering path considered follows from the cross-correlation of the direct wave propagating to one receiver with the scattered wave propagating along the scattering path to the other receiver, because cross-terms between scattered waves ultimately cancel. Suppose one estimates the Green's function by cross-correlating scattered waves only. In that case the cross-terms of scattered waves with the direct wave is missing and the extracted Green's function contains spurious arrivals. It has been noted earlier that the cross-correlation of scattered waves with scattered waves does *not* give the scattered waves (Snieder *et al.*, 2008; Snieder *et al.*, 2006), and this study confirms that conclusion for multiple scattering media. The failure to extract scattered waves by cross-correlating only scattered waves is ultimately due

to the fact that the scattered waves do not satisfy the wave equation (Vasconcelos *et al.*, 2009). We show in a companion paper (Fleury *et al.*, 2010) a general theory applicable to a large class of linear differential equations that confirms that cross-correlating perturbed fields does not lead to retrieval of field perturbations, and show a numerical example for wave propagation that shows that the scattered waves are only extracted by cross-correlation when the direct wave is included. The cancellation of spurious arrivals can also be shown using a diagrammatic analysis (Margerin & Sato, 2010).

Acknowledgments: We thank Filippo Broggini for his insightful and critical comments. This work was supported by the NSF through grant EAS-0609595.

REFERENCES

Bleistein, N., & Handelsman, R.A. 1975. *Asymptotic expansions of integrals.* New York: Dover.

Curtis, A., Gerstoft, P., Sato, H., Snieder, R., & Wapenaar, K. 2006. Seismic interferometry – turning noise into signal. *The Leading Edge*, **25**, 1082–1092.

Derode, A., Larose, E., Campillo, M., & Fink, M. 2003. How to estimate the Green's function for a heterogeneous medium between two passive sensors? Application to acoustic waves. *Appl. Phys. Lett.*, **83**, 3054–3056.

Fan, Y., & Snieder, R. 2009. Required source distribution for interferometry of waves and diffusive fields. *Geophys. J. Int.*, **179**, 1232–1244.

Fleury, C., Snieder, R., & Larner, K. 2010. General representation theorem for perturbed media and application to Greens function retrieval for scattering problems. *Annual Project Review Book of the Center for Wave Phenomena.*

Glauber, R., & Schomaker, V. 1953. The theory of electron diffraction. *Phys. Rev.*, **89**, 667–671.

Gouédard, P., Stehly, L., Brenguier, F., Campillo, M., Colin de Verdière, Y., Larose, E., Margerin, L., Roux, P., Sánchez-Sesma, F.J., Shapiro, N.M., & Weaver, R.L. 2008. Cross-correlation of random fields: mathematical approach and applications. *Geophys. Prosp.*, **56**, 375–393.

Heisenberg, W. 1943. Die "beobachtbaren Größen" in der Theorie der Elementarteilchen. *Z. Phys.*, **120**, 513–538.

Larose, E., Margerin, L., Derode, A., van Tiggelen, B., Campillo, M., Shapiro, N., Paul, A., Stehly, L., & Tanter, M. 2006. Correlation of random wavefields: an interdisciplinary review. *Geophysics*, **71**, SI11–SI21.

Margerin, L., & Sato, H. 2010. Reconstruction of Green's function from random noise sources in a multiple scattering media. *Wave Motion, submitted.*

Marston, P.L. 2001. Generalized optical theorem for scatterers having inversion symmetry: Applications to acoustic backscattering. *J. Acoust. Soc. Am.*, **109**, 1291–1295.

Martin, P.A. 2006. *Multiple scattering.* Encyclopedia of mathematics and its applications, vol. 107. Cambridge, UK: Cambridge Univ. Press.

Morse, P.M., & Ingard, K.U. 1968. *Theorerical Acoustics.* New York: McGraw-Hill.

Sato, H. 2009. Green's function retrieval from the CCF of coda waves in a scattering medium. *Geophys. J. Int.*, **179**, 1580–1583.

Sato, H. 2010. Retrieval of Green's function having coda waves from the cross-correlation function in a scattering medium illuminated by a randomly homogeneous distribution of noise sources on the basis of the first-order Born approximation. *Geophys. J. Int.*, **180**, 759–764.

Schuster, G. 2009. *Seismic Interferometry.* Cambridge, UK: Cambridge Univ. Press.

Slob, E., Snieder, R., & Revil, A. 2010. Retrieving electric resistivity data from self-potential measurements by cross-correlation. *Geophys. Res. Lett.*, **37**, L04308.

Snieder, R. 2004. *A Guided Tour of Mathematical Methods for the Physical Sciences.* 2nd edn. Cambridge, UK: Cambridge Univ. Press.

Snieder, R., Wapenaar, K., & Larner, K. 2006. Spurious multiples in seismic interferometry of primaries. *Geophysics*, **71**, SI111–SI124.

Snieder, R., Wapenaar, K., & Wegler, U. 2007. Unified Green's function retrieval by cross-correlation; connection with energy principles. *Phys. Rev. E*, **75**, 036103.

Snieder, R., van Wijk, K., Haney, M., & Calvert, R. 2008. The cancellation of spurious arrivals in Green's function extraction and the generalized optical theorem. *Phys. Rev. E*, **78**, 036606.

Snieder, R., Miyazawa, M., Slob, E., Vasconcelos, I., & Wapenaar, K. 2009. A comparison of strategies for seismic interferometry. *Surveys in Geophysics*, **30**, 503–523.

Snieder, R., E., Slob., & Wapenaar, K. 2010. Lagrangian Green's function extraction, with applications to potential fields, diffusion, and acoustic waves. *New J. Phys., in press.*

van de Hulst, H.C. 1949. On the Attenuation of Plane Waves by Obstacles of Arbitrary Size and Form. *Physica*, **15**, 740–746.

Vasconcelos, I., R., Snieder, & Douma, H. 2009. Reciprocity theorems and Green's function retrieval in perturbed acoustic media. *Phys. Rev. E*, **80**, 036605.

Wapenaar, K., Fokkema, J., & Snieder, R. 2005. Retrieving the Green's function by cross-correlation: a comparison of approaches. *J. Acoust. Soc. Am.*, **118**, 2783–2786.

Wapenaar, K., Slob, E., & Snieder, R. 2006. Unified Green's function retrieval by cross-correlation. *Phys. Rev. Lett.*, **97**, 234301.

Wapenaar, K., Draganov, D., & Robertsson, J.O.A. (eds). 2008. *Seismic Interferometry: History and Present Status.* SEG Geophysics Reprints Series, vol. 26. Tulsa, OK: Society of Exploration Geophysics.

Wapenaar, K., Draganov, D., Snieder, R., Campman, X., & Verdel, A. 2010a. Tutorial on seismic interferometry. Part I: Basic principles and applications. *Annual Project Review Book of the Center for Wave Phenomena.*

Wapenaar, K., Slob, E., Snieder, R., & Curtis, A. 2010b. Tutorial on seismic interferometry. Part II: Underlying theory. *Annual Project Review Book of the Center for Wave Phenomena.*

Weaver, R.L. 2008. Ward identities and the retrieval of Green's functions in the correlations of a diffuse field. *Wave Motion*, **45**, 596–604.

Increasing the sensitivity of controlled source electromagnetics by using synthetic aperture

Y. Fan[1], R. Snieder[1], E. Slob[1,2], J. Hunziker[2], J. Singer[3], J. Sheiman[3] & M. Rosenquist[3]

[1] *Center for Wave Phenomena, Colorado School of Mines, Golden, USA*
[2] *Section of Applied Geophysics and Petrophysics, Department of Geotechnology, Delft University of Technology, Delft, The Netherlands*
[3] *Shell International Exploration & Production, Houston, USA*

ABSTRACT

Controlled-source electromagnetics (CSEM) has been used as a de-risking tool in the hydrocarbon exploration industry. Although there have been successful applications of CSEM, this technique is still not widely used in the industry because the limited types of hydrocarbon reservoirs CSEM can detect. In this paper, we apply the concept of synthetic aperture to CSEM data. Synthetic aperture allows us to design sources with specific radiation patterns for different purposes. The ability to detect reservoirs is dramatically increased after forming an appropriate synthetic aperture antenna. Consequently, the types of hydrocarbon reservoirs that CSEM can detect are significantly extended. In this paper, we mainly show one type of synthetic aperture antenna whose field can be steered into a designed angle. Consequently, the field concentrates on the target reservoir and the airwave is reduced. We show a synthetic example and a data example to illustrate the increased sensitivity obtained by applying synthetic aperture CSEM source. Because synthetic apertures are constructed as a data processing step, there is no additional cost for the CSEM acquisition. Aside from the applications to marine CSEM, synthetic aperture can be widely applied to other electromagnetic methods such as on land electromagnetics and bore hole electromagnetics.

Introduction

After the development in academia starting in the late 1970s (Spiess et al. 1980; Cox 1981; Young and Cox 1981) and the early industry experiments (Srnka 1986; Constable et al. 1986; Chave et al. 1991; Hoversten and Unsworth 1994), CSEM was introduced to the industry at the beginning of this century as a method to explore hydrocarbons. Since then the research and commercial surveys on CSEM have boomed (Constable and Srnka 2007; Chopra et al. 2007).

The fundamental concept and the assumption of using CSEM as a detector of hydrocarbons is that porous rocks are resistive when they are saturated with gas or oil (Edwards 2005; Constable and Srnka 2007). In a standard CSEM survey, a horizontal current dipole is used as the source to generate an electromagnetic field and is towed close to the sea floor to avoid energy loss in the conductive sea water. The receivers are located on the sea floor. A resistive hydrocarbon reservoir in the subsurface (a target with a resistivity of approximate 50 to 100 Ωm) embedded in the conductive background (about 1 Ωm), acts as a secondary source that refracts the electromagnetic field back to the receivers. In this way, one can infer the presence of a resistive body in the subsurface from the measured electromagnetic field.

The main challenge of CSEM is the diffusive nature of electromagnetic field in the conductive subsurface. Thus the secondary field that refracts from the target is significantly small at most of the offsets than the field which does not carry any information of the subsurface, such as the direct arrival and the air wave, (Edwards 2005; Constable and Srnka 2007). So it is not surprise that most of the successful CSEM applications are in the deep water environment (deeper than 1km) with the shallow target (less than 3km).

We introduce the concept of synthetic aperture to CSEM data. Synthetic aperture allows us to design

sources with specific radiation patterns for different purposes. Here we construct a synthetic aperture antenna to steer the electromagnetic field into a designed direction (Note that the use of synthetic aperture is not limited to field steering). By doing this, one can concentrate the energy into a direction where the target is located. At the same time, the air wave can be significantly reduced by increasing the propagation path in the sea water. Consequently, the ability to detect the reservoirs is dramatically increased after applying appropriate synthetic apertures without any cost increase. Aside from the applications to CSEM, synthetic aperture can be widely applied to other electromagnetic methods such as CSEM on land and bore hole electromagnetics.

1 SYNTHETIC APERTURE METHOD

Although synthetic aperture is a widely used concept for waves such as radar and sonar (Barber 1985; Ralston et al. 2007; Zhou et al. 2009; Cutrona 1975; Riyait et al. 1995; Bellettini and Pinto 2002), to the best of the authors' knowledge, this is the first time that synthetic aperture is introduced to a diffusive field like CSEM.

A general formula for constructing a synthetic aperture S_A is

$$S_A(x,\omega) = \sum_{n=1}^{N} a_n e^{i\phi_n} s(x, x_n, \omega). \quad (1)$$

At a single angular frequency ω, a synthetic aperture at location x is a superposition of the sequentially distributed sources that are located from x_1 to x_N with an amplitude weighting a_n and a phase shift ϕ_n. The source function for the individual source is represented by $s(x, x_n, \omega)$. For example, a horizontal 100 m dipole source centered at x_n with a current of 100 A and a frequency of 1 Hz can be represented by

$$s(x, x_n, \omega) = \begin{cases} 100\ A & (x_n - 50 < x < x_n + 50), \\ 0 & (otherwise). \end{cases} \quad (2)$$

Using the combination of amplitude weighting and a phase shift for sequential sources, enables us to propagate the field with a specific radiation pattern. For example, with a linear phase shift, the field can be steered into a certain direction as illustrated in figure 1. The larger semicircle represents the field whose source starts earlier (smaller value of ϕ_n in frequency domain); while the smaller one is from the source that starts later (larger value of ϕ_n in frequency domain). In this particular example, the total field is steered from the vertical direction to the right by applying a linear phase shift to individual sources.

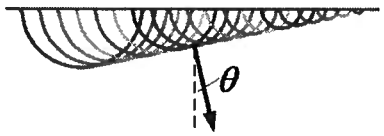

Figure 1. Field steering by applying a linear phase shift

2 SYNTHETIC AND FIELD DATA EXAMPLE

2.1 Synthetic data example

In the numerical model shown we use a hydrocarbon reservoir (5km in the x and y directions with a thickness of 100 m) located 1 km below the sea floor. The sea water is 1km deep with a resistivity of 0.3 Ωm. The subsurface background is a half space with a resistivity of 1 Ωm. The resistivity of the reservoir is set to be 100 Ωm. The receivers are located at the sea floor and a 100 m dipole source with a current of 100 A is continuously towed 100 m above the receivers. Although only the inline electrical field E_x is discussed in this paper, the synthetic aperture principle holds for the other components of the electrical and magnetic fields as well.

In this example, we focus on the construction of a synthetic aperture with the field steered toward the target direction. Figure 2(a) shows the inline electrical fields with the reservoir (dashed line) and without the reservoir (solid line) from a single 100 m dipole whose center is located at x =-6.5 km. There is a slight increase in the field around the position x=0 km when the reservoir is present. This 20% difference is shown by the ratio of the field with the reservoir to the field without the reservoir (black solid curve in figure 2(e)).

Simply superposing the 50 (N=50 in equation 1) employed sequential sources, is equivalent to setting the weighting function a_n=1 and ϕ_n=0 in equation 1. This superposition gives a 5 km long dipole source with a current of 100 A. The total E_x field is given by figure 2(b). The ratio of the fields with and without the reservoir is shown by the red dashed curve in panel (e). Although the overall signal strength increases compared to the single 100 m source (panel (a)), the difference between the models with and without the reservoir does not significantly increase by simply using a longer dipole.

Instead of using a zero phase shift in equation 1, we next apply a linear phase shift to the sequential sources using $\phi_n = c_1 k_r n \Delta s$, where Δs is the distance between the centers of two neighboring sources, k_r is the real part of the complex wave number and c_1 is a coefficient to control how much the field is steered. The steering angle θ (as defined in figure 1) is related to this coefficient by $c_1 = sin\theta$. As shown in figure 1, this phase shift effectively deploys the sources on the left at an earlier time than those on the right. Consequently, the total field propagates toward the right. Figure 2(c) shows the Ex field excited by this new synthetic aperture source.

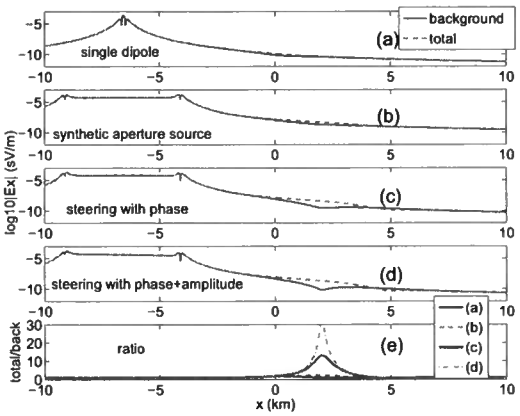

Figure 2. Panels (a) to (d) show the inline electrical fields with the reservoir (dashed lines) and without the reservoir (solid) for four different sources; a 100 m dipole source (panel (a)); a 5 km dipole source (panel (b)); a 5 km synthetic source obtained from field steering toward the target by the phase shift (panel (c)); A 5 km synthetic source obtained from field steering toward the target by the phase shift and the amplitude compensation (panel (d)). Panel (e) shows the ratio between the fields with and without the reservoir. The four curves in panel (e) represent the ratios from each of the panels above.

The ratio of the steered fields is illustrated by the blue solid curve in the bottom panel. This example shows that the detectability significantly increases by steering the field toward the target.

There are two reasons for the improved detectability. First, the total electrical field as well as the z component of the E field increases at the target location when the field propagation is steered from the vertical direction to a tilted angle. The z component of the E field diagnoses changes in the conductivity in the vertical direction (Edwards 2005). The second reason is the reduction of the background field. We will investigate the mechanism of the background field reduction in the future.

Although we already see the improvement of field steering with linear phase shift. The high decay factor makes the steering of the diffusive field not accurate by only using phase shift. The attenuation of a diffusive field, causes the sources on the left side to give a smaller contribution to the synthetic aperture construction because they propagates longer. These sources are indicated by the bigger semicircles in figure 1. In order to have a more effective steered field, we use an energy compensation term $a_n = e^{-c_2 k_i n \Delta s}$, where c_2 is a constant that controls the amplitude weighting. In this particular example, c_2 is chosen to be 0.1 m^{-1} as an empirical value that gives a maximum response.After we include this energy compensation, the difference between the models with and without the target further increases, as shown in figure 2(d). This difference is quantified by the ratio of the fields with and without the target and is illustrated by the magenta dashed line in panel (e).

The examples show that the synthetic aperture technique dramatically increases the difference in electrical field response between the models with and without the reservoir by a factor of 30. Note that this is achieved without altering the data acquisition. If noise is added in the above example, the main observation still holds. But we can not steer the field as effective as the noise free data and therefore the anomaly ratio is not as big as the factor of 30. We also see the effect of noise in the real data example below.

2.2 Real data example

Next, we apply this steering concept to the real data. In the real data, the field 'without' the target is defined as the measured field at a reference site under which there is no reservoir. For a standard single dipole measurement, the inline electrical fields with and without the reservoir are shown by the pink and black solid curves, respectively, in the upper panel of figure 3. The corresponding ratio of the two fields is shown by the solid curve in the lower panel of figure 3. The reservoir is known to be located between x=3 km and x=6 km. A slight difference in the electrical field can be observed between the offset of 6 km and 10 km due to the presence of the reservoir. Beyond the offset of 10 km, the ratio oscillates because the field reaches the noise level. This oscillation makes it difficult to interpret the data.

Next, we construct a 4 km synthetic aperture source with no field steering (zero phase shift). The fields with and without the reservoir are shown by the pink and black dashed curves in the upper panel of figure 3, respectively, and the corresponding ratio is the dashed curve in the lower panel. Because the longer dipole source has a better signal to noise ratio (the signal is stronger), both the Ex field (upper panel) and the ratio (lower panel) are smoother than the field generated by an individual source . The overall difference between the models, however, does not change too much.

As we did in the synthetic example, next we construct a 4km synthetic aperture source with field steering toward the reservoir using a phase shift ($c_1 = 0.8$) and amplitude weighting ($c_2 = 0.7\ \mathrm{m}^{-1}$). Figure 4 shows that the difference between the models has significantly increased after we apply the field steering. One can be more confident to infer the presence of the reservoir from figure 4 than from figure 3. Note that the negative offset does not show any difference in the field both before and after the field steering as we expect. This is because there is no reservoir on the negative offset side. At the same time, the consistency on the negative offset

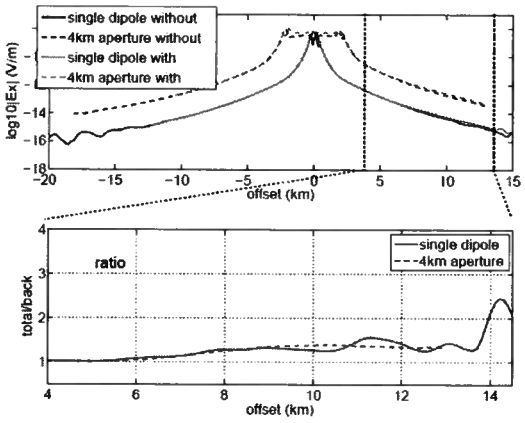

Figure 3. Upper panel: inline electrical field with the reservoir (pink lines) and without the reservoir (black lines) from a single dipole (solid lines) and 4 km synthetic aperture (dashed lines) without the field steering. Lower panel: ratio of the field with the reservoir to the field without the reservoir from the single dipole (solid lines) and the synthetic aperture (dashed lines).

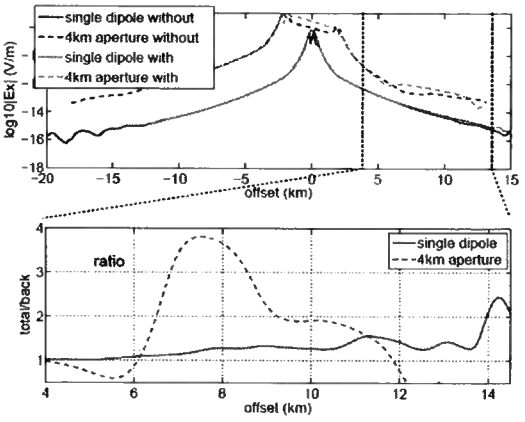

Figure 4. Upper panel: inline electrical field with the reservoir (pink lines) and without the reservoir (black lines) from a single dipole (solid lines) and 4 km synthetic aperture (dashed lines) with the field steering toward the reservoir. Lower panel: ratio of the field with the reservoir to the field without the reservoir from the single dipole (solid lines) and the synthetic aperture (dashed lines).

side, where there is no reservoir, confirms that our field steering is only sensitive to the presence of the reservoir.

3 DISCUSSION AND CONCLUSION

The synthetic aperture technique opens a new line of research in CSEM data processing. Hidden information in CSEM data can be retrieved by using the synthetic aperture technique with little extra cost because there is no need to change the acquisition. The ability to detect the reservoirs is dramatically increased after applying appropriate synthetic apertures. The depth of the reservoir that CSEM detects can also increase with the use of synthetic aperture methods. Consequently, the types of hydrocarbon reservoirs that CSEM can detect are extended. Other types of synthetic aperture, aside field steering, can be designed, e.g. field focusing and the synthetic vertical source. In this paper, we only show examples of constructing synthetic aperture source in a line (2D synthetic aperture). In principle, one can construct 3D synthetic aperture to better detect the 3D structure of the subsurface. For example, when data are collected with antennas along parallel lines, one not only can steer the field in the inline direction, but also in the crossline direction. The synthetic aperture technique is not limited to the source side. It can also be applied to the receiver side by the same principle. Besides the application to the current marine CSEM system, synthetic aperture can also be used in land surveys and bore hole applications.

4 ACKNOWLEDGMENTS

The authors are grateful for the financial support through a Shell Gamechanger Project. The electromagnetic research team in Shell provided technical support in the research and we thank them for the permission for using the real data.

REFERENCES

Barber, B. C., 1985, Theory of digital imaging from orbital synthetic-aperture radar: Int. J. Remote Sens., **6**, 1009–1057.

Bellettini, A. and M. Pinto, 2002, Theretical accuracy of synthetic aperture sonar micronavigation using a displaced phase-center antenna: IEEE J. Oceanic Eng., **27**.

Chave, A. D., S. C. Constable, and R. N. Edwards, 1991, Electrical exploration methods for the seafloor, *in* M. Nabighian ed., Electromagnetic methods in applied geophysics, volume **2**, 931–966, SEG.

Chopra, S., K. Strack, C. Esmersoy, and N. Allegar, 2007, Introduction to this special section: CSEM: The Leading Edge, **26**, 323–325.

Constable, S. and L. J. Srnka, 2007, An introduction to marine controlled-source electromagnetic methods for hydrocarbon exploration: Geophysics, **72**, WA3–WA12.

Constable, S. C., C. S. Cox, and A. D. Chave, 1986, Offshore electromagnetic surveying techniques: SEG Expanded Abstracts, **5**, 81–82.

Cox, C. S., 1981, On the electrical conductivity of the oceanic lithosphere: Physics of The Earth and Planetary Interiors, **25**, 196–201.

Cutrona, L., 1975, Comparison of sonar system performance achievable using synthetic-aperture techniques with the performance achievable by more conventional means: J. Acoust. Soc. Am., **58**, 336–348.

Edwards, N., 2005, Marine controlled source electromagnetics: Principles, methodologies, future commercial applications: Surveys in Geophysics, **26**, 675–700.

Hoversten, G. M. and M. Unsworth, 1994, Subsalt imaging via seaborne electromagnetics: Offshore Technology Conference, **26**, 231–240.

Ralston, T. S., D. L. Marks, C. P. Scott, and S. A. Boppart, 2007, Interferometric synthetic aperture microscopy: Nature Physics, **3**, 129–134.

Riyait, V., M. Lawlor, A. Adams, O. Hinton, and B. Sharif, 1995, Real-time synthetic aperture sonar imaging using a parallel architecture: Image Processing, IEEE Transactions on, **4**, 1010–1019.

Spiess, F. N., K. C. Macdonald, T. Atwater, R. Ballard, A. Carranza, D. Cordoba, C. Cox, V. M. D. Garcia, J. Francheteau, J. Guerrero, J. Hawkins, R. Haymon, R. Hessler, T. Juteau, M. Kastner, R. Larson, B. Luyendyk, J. D. Macdougall, S. Miller, W. Normark, J. Orcutt, and C. Rangin, 1980, East Pacific Rise: Hot springs and geophysical experiments: Science, **207**, 1421–1433.

Srnka, L. J., 1986, Method and apparatus for offshore electromagnetic sounding utilizing wavelength effects to determine optimum source and detector positions: U.S. Patent 4,617,518.

Young, P. D. and C. S. Cox, 1981, Electromagnetic active source sounding near the east pacific rise: Geophys. Res. Lett., **8**, 1043–1046.

Zhou, X., N. Chang, and S. Li, 2009, Applications of SAR interferometry in earth and environmental science research: Sensors, **9**, 1876–1912.

Comparison of scattering series solutions for acoustic wave and electromagnetic diffusion equations

Myoung Jae Kwon & Roel Snieder
Center for Wave Phenomena, Colorado School of Mines

ABSTRACT

Inverse scattering series (ISS) is a tool for the interpretation of geophysical data that theoretically does not require a priori knowledge about the target of an experiment. The ISS method has been applied to seismic exploration, in particular to velocity estimation and multiple suppression. Compared to seismic exploration, electromagnetic methods are characterized by rapid spatial decay of the probing field and strong perturbation of the medium parameters. As a prototype for the convergence of the forward and inverse scattering series, we analyze the 3D Green function for homogeneous media. The analysis suggests that for parameters representing geophysical exploration of hydrocarbon reservoirs, the convergence speed of scattering series solutions for electromagnetic diffusion is faster than that for acoustic wave propagation. The model tests also show that for the diffusion equation, one can improve the convergence of the inverse scattering series by choosing a reference medium that is less conductive than the actual medium is. This research provides insights into the convergence requirements of the ISS method and guidelines for further applications of the ISS method to the interpretation of field data.

Key words: inverse scattering series (ISS), acoustic wave equation, electromagnetic diffusion equation

1 INTRODUCTION TO SCATTERING SERIES

Scattering theory is a form of perturbation analysis, and the goal of the inverse scattering problem is to obtain a quantitative description of an unknown scatterer from knowledge of the scattering data. The theory originates from inverse problems in quantum scattering theory and formal solutions of inverse scattering problems (Gel'fand & Levitan1951; Jost & Kohn1952; Moses1956; Prosser1969). Inverse scattering series (ISS) describes the model perturbation as a series in order of a scattered field. The ISS method was applied to seismic exploration for reconstruction of subsurface velocity (Weglein *et al.*1981) and attenuation of multiples in seismic reflection data (Weglein *et al.*1997; Weglein *et al.*2003). The main advantage of the ISS method is that no a priori knowledge of the subsurface (e.g., velocity) is assumed and all refraction, diffraction, and multiple reflection phenomena are, in principle, taken into account. Recent studies show that the ISS method can be applied to diverse seismic problems that include imaging, direct non-linear inversion, data reconstruction, and wavefield separation (Ramirez & Weglein2009; Weglein *et al.*2009; Zhang & Weglein2009a; Zhang & Weglein2009b).

Scattering theory relates the difference between the actual (perturbed) and reference (unperturbed) fields to the difference between their corresponding medium properties (Figure 1). We consider the following differential equations as governing equations for the actual and reference media:

$$L(\mathbf{r};\omega)\,G(\mathbf{r},\mathbf{r}_s;\omega) = -\delta(\mathbf{r}-\mathbf{r}_s), \tag{1}$$

$$L_0(\mathbf{r};\omega)\,G_0(\mathbf{r},\mathbf{r}_s;\omega) = -\delta(\mathbf{r}-\mathbf{r}_s), \tag{2}$$

where L, L_0 and G, G_0 are the actual and reference differential operators and Green functions, respectively, for a single angular frequency ω, $\delta(\mathbf{r}-\mathbf{r}_s)$ is the Dirac delta function, and $\mathbf{r}$ and $\mathbf{r}_s$ are the receiver and source

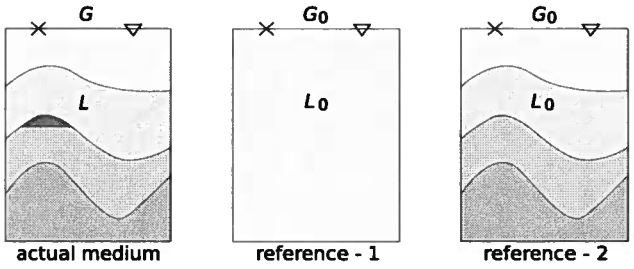

Figure 1. Actual medium versus different choices of reference medium. The symbols × and ▽ indicate the source and receiver, respectively. G and G_0 are the Green functions for the actual and reference media, respectively. Note that given the actual medium, there are several possible choices of the reference medium.

locations, respectively. The information about the actual and reference media properties is encapsulated in L and L_0. The perturbation P is defined as the difference between two differential operators:

$$P(\mathbf{r};\omega) = L(\mathbf{r};\omega) - L_0(\mathbf{r};\omega). \tag{3}$$

The Lippmann-Schwinger equation (Taylor1972; Colton & Kress1998) relates G, G_0 and P:

$$G(\mathbf{r},\mathbf{r}_s;\omega) = G_0(\mathbf{r},\mathbf{r}_s;\omega) + \int G_0(\mathbf{r},\mathbf{r}';\omega)P(\mathbf{r}';\omega)G(\mathbf{r}',\mathbf{r}_s;\omega)\,d\mathbf{r}', \tag{4}$$

or in operator form:

$$G = G_0 + G_0PG. \tag{5}$$

The scattered field is the difference between the two Green functions ($G - G_0$) and can be expanded in an infinite series in order of the perturbation P (in operator form):

$$S = G_0PG_0 + G_0PG_0PG_0 + \cdots. \tag{6}$$

Equation (6) is known as the Born, Neumann, or forward scattering series. This series provides an interpretation of the scattered field S in terms of G_0 and P. The interpretation of the forward scattering series is shown in Figure 2; G_0PG_0 denotes the portion of the scattered field S that experiences a single scattering event from points where the actual medium differs from the reference medium; $G_0PG_0PG_0$ denotes the portion that experiences two scattering events, and so on.

The inverse scattering series describes the perturbation P as a series expansion in order of the scattered field S:

$$P = P_1 + P_2 + P_3 + \cdots, \tag{7}$$

where P_n is the portion of P that is the nth order of the scattered field. Substituting the above equation into equation (6) and equating terms that are equal order of the scattered field S, we derive the following set of

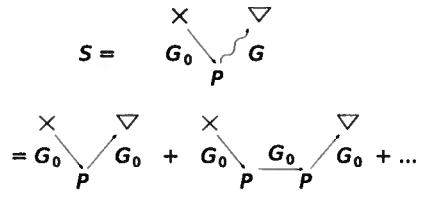

Figure 2. Schematic illustration of the forward scattering series from Weglein et al. (2003). The symbols × and ▽ indicate source and receiver. S, P, G_0, and G are the scattered field, perturbation, and Green functions for the reference and actual media, respectively. The straight and wiggled arrows indicate signals through the reference and perturbed media, respectively.

integral equations represented in operator form:

$$\begin{aligned} S &= G_0P_1G_0, && (8)\\ 0 &= G_0P_2G_0 + G_0P_1G_0P_1G_0, && (9)\\ 0 &= G_0P_3G_0 + G_0P_1G_0P_2G_0 + G_0P_2G_0P_1G_0 \\ &+ G_0P_1G_0P_1G_0P_1G_0, && (10)\\ &\cdots \\ 0 &= G_0P_nG_0 + G_0P_1G_0P_{n-1}G_0 + \cdots \\ &+ G_0P_1G_0P_1\cdots P_1G_0P_1G_0. && (11) \end{aligned}$$

Solving the above set of equations, we determine the perturbation to the nth order of the scattered field. Equation (8) is the linear or Born approximation which allows P_1 to be determined from the scattered field S. P_2 is then computed from P_1 with equation (9). Equation (10) determines P_3 from P_1 and P_2. Continuing in this manner, the entire series for the perturbation P is constructed, starting with the scattered field. To derive the nth order term in the inverse series, we solve the following Fredholm integral equation of the first kind:

$$f_n(G_0,S,P_1,P_2,\cdots,P_{n-1};\omega) = \int G_0(\mathbf{r},\mathbf{r}';\omega)P_n(\mathbf{r}';\omega)G_0(\mathbf{r}',\mathbf{r}_s;\omega)\,d\mathbf{r}'. \tag{12}$$

Solving this equation efficiently for P_n is an essential element of application of the inverse scattering series.

In equation (7), we assume that P_1 is the portion of P that is linear in the scattered field. In fact, only the linear component in the scattered field ultimately contributes to the reconstruction of the model, and the non-linear components are subtracted in the inversion (Snieder1990a; Snieder1990b). Generally, the series solutions in equations (6) and (7) converge within finite range of perturbation and scattered field (radius of convergence), and the series solutions coincide with the exact solutions inside the radius of convergence. When the series converges, we only require the Green function for the reference medium G_0 and the scattered field S for the reconstruction of the perturbation. In other words, we utilize the measured data as it is and do not need a priori knowledge about the actual medium, which

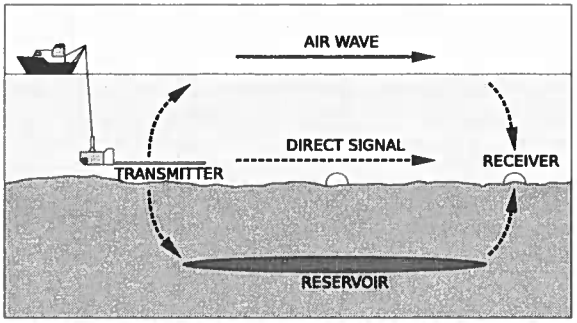

Figure 3. Schematic representation of controlled-source electromagnetic (CSEM) exploration from MacGregor et al. (2006). An electromagnetic transmitter is towed close to the seafloor to maximize the coupling of electric and magnetic fields with seafloor rocks. These fields are recorded by receivers deployed on the seafloor some distance from the transmitter.

most geophysical data processing requires. This property of the ISS method demonstrates the potential of the method for geophysical inversion or model reconstruction.

2 COMPARISON OF WAVE PROPAGATION AND DIFFUSION IN GEOPHYSICAL EXPLORATION

As existing hydrocarbon reservoirs are being depleted, we are forced to explore hydrocarbon in more challenging environments. Seismic exploration, which is based on wave propagation, provides good structural information of the subsurface medium and has been the major exploration method for the discovery of hydrocarbon reservoirs. Recently, the controlled-source electromagnetic (CSEM) exploration method has been considered a useful complementary tool for hydrocarbon discovery because the method can provide more decisive information about the reservoir composition than the seismic method does. The CSEM method is an electromagnetic exploration method designed for marine environments (Figure 3); the theoretical foundation for the CSEM method was laid in the 1980s (Chave & Cox1982; Cox *et al.*1986). Since then, the application of the CSEM method for hydrocarbon exploration has been extensively studied (Hoversten *et al.*2006; Constable & Srnka2007). The electromagnetic field is sensitive to electric conductivity, which is predominantly influenced by water content within the subsurface: increasing water content causes larger conductivity. Hydrocarbons, whether gas or petroleum, are poor electric conductors. The significant difference of electric conductivity in water and hydrocarbon makes the CSEM method an ideal tool for distinguishing a hydrocarbon reservoir from a water saturated reservoir.

Assuming time harmonic dependency ($e^{-i\omega t}$) and a given electric current source $\mathbf{J}^s$, the electric field $\mathbf{E}$ and magnetic field $\mathbf{H}$ responses within an isotropic medium are derived from the following frequency domain expressions of Maxwell's equations (Jackson1999):

$$\nabla \times \mathbf{E}(\mathbf{r}) - i\omega\mu(\mathbf{r})\mathbf{H}(\mathbf{r}) = 0, \tag{13}$$

$$\nabla \times \mathbf{H}(\mathbf{r}) - [\sigma(\mathbf{r}) - i\omega\epsilon(\mathbf{r})]\,\mathbf{E}(\mathbf{r}) = \mathbf{J}^s(\mathbf{r}), \tag{14}$$

where μ, σ and ϵ are magnetic permeability, electric conductivity and dielectric permittivity of the medium, respectively. The electric and magnetic fields can be expressed in terms of vector potential $\mathbf{A}$ as

$$\mathbf{E}(\mathbf{r}) = i\omega\mu\mathbf{A}(\mathbf{r}) + \frac{\nabla(\nabla \cdot \mathbf{A}(\mathbf{r}))}{\sigma - i\omega\epsilon}, \tag{15}$$

$$\mathbf{H}(\mathbf{r}) = \nabla \times \mathbf{A}(\mathbf{r}). \tag{16}$$

Within a homogeneous medium, equations (13) and (14) yield the following Helmholtz equation of vector potential:

$$\nabla^2\mathbf{A}(\mathbf{r}) + \left(\omega^2\mu\epsilon + i\omega\mu\sigma\right)\mathbf{A}(\mathbf{r}) = -\mathbf{J}^s(\mathbf{r}), \tag{17}$$

where the two terms, $\mu\epsilon$ and $\mu\sigma$, are related to the wave velocity c and diffusivity d of the response:

$$\mu\epsilon = \frac{1}{c^2} \quad \text{and} \quad \mu\sigma = \frac{1}{d}. \tag{18}$$

In many geophysical applications, the magnetic permeability can be assumed to be that of free space.

In geophysical applications of electromagnetic methods, wave propagation is significant in the high frequency range (i.e., ground penetrating radar) or in an insulating medium (i.e., air). For most earth materials and frequencies of electromagnetic methods used in hydrocarbon exploration, diffusion is dominant and the contribution of wave propagation is negligible. In contrast, seismic exploration is always governed by wave propagation. Seismic exploration is performed over a scale of many wavelengths, whereas the CSEM signal exhibits strong spatial decay and diffuses over a few skin depths δ that describe the length scale where the amplitude decays to e^{-1}. Furthermore, the strength of the medium perturbation in CSEM exploration is stronger than that in seismic exploration. In other words, the range of electric conductivity in the earth medium is generally wider than the range of seismic wave velocity (Palacky1987; Mavko *et al.*1998).

The application of the ISS method to geophysical exploration has focused on seismic exploration (Weglein *et al.*1981; Weglein *et al.*1997; Weglein *et al.*2003). In this study, we perform a comparative analysis of scattering series methods for acoustic wave and electromagnetic diffusion equations and study the feasibility of applying the ISS method to electromagnetic exploration, which involves a diffusive field within a strongly perturbed medium.

3 FORMULATION OF SCATTERING SERIES SOLUTIONS

For the identification of the differences of the properties of the scattering series method for the acoustic wave and electromagnetic diffusion equations, we consider the simplest case of a homogeneous 3D medium and compare two different states of this infinite homogeneous medium. We analyze the series expression between the perturbation and scattered field at a single point and study the spatial variation of the series expansion.

We consider hydrocarbon exploration and assume that wave propagation of the electromagnetic response is negligible within the medium. We derive the electromagnetic response from equations (15) - (17). Equation (17) is the Helmholtz equation of vector potential $\mathbf{A}$, and each component of the vector potential is proportional to the corresponding component of the electric current source $\mathbf{J}_s$. We can therefore describe the electromagnetic diffusion by the Helmholtz equation of a scalar field. The acoustic wave propagation also involves a scalar field, i.e., pressure field. Given a point source at the origin, both the acoustic wave propagation and electromagnetic diffusion within the homogeneous medium are described by the Helmholtz equation of the scalar Green function G:

$$\nabla^2 G(\mathbf{r}) + k^2 G(\mathbf{r}) = -\delta(\mathbf{r}), \tag{19}$$

where wavenumber k is given by

$$k^2 = \begin{cases} \omega^2/c^2 \text{ (acoustic wave equation)}, \\ i\omega\mu\sigma \text{ (electromagnetic diffusion equation)}. \end{cases} \tag{20}$$

In this study, we assume that the magnetic permeability μ is that of free space and that acoustic wave velocity c and electric conductivity σ are real, which implies that wavenumber k is real for the wave equation and complex for the diffusion equation. The 3D Green function for the Helmholtz equation is given as (Morse & Feshbach1953)

$$G(\mathbf{r}) = \frac{1}{4\pi r} e^{ikr}, \tag{21}$$

where $r = |\mathbf{r}|$.

We denote wavenumbers of the reference and perturbed media as k_0 and k, respectively. From equation (3), the perturbation is defined as

$$P = k^2 - k_0^2, \tag{22}$$

and wavenumber of the perturbed medium is expressed as

$$k = k_0 \sqrt{1 + \frac{P}{k_0^2}}. \tag{23}$$

The scattered field $S(\mathbf{r})$ is the difference between the Green functions of the perturbed and reference media:

$$S(\mathbf{r}) = \frac{1}{4\pi r} \left[\exp\left(ik_0 r \sqrt{1 + \frac{P}{k_0^2}} \right) - \exp(ik_0 r) \right], \tag{24}$$

and the forward scattering series expresses the scattered field $S(\mathbf{r})$ as a series in order of the perturbation P. Note that a function of a complex variable z, $f(z) = \sqrt{1+z}$, has a singular point (branch point) at $z = -1$, and the radius of convergence of the Taylor series expansion around $z = 0$ extends up to the singular point. The series for the exponential is absolutely convergent. Therefore, equation (24) shows that the forward scattering series converges only for small perturbations compared to the reference medium properties such that

$$\left| \frac{P}{k_0^2} \right| < 1. \tag{25}$$

The above requirement of convergence implies the following convergence criteria:

$$\begin{cases} c > c_0/\sqrt{2} \text{ (acoustic wave equation)}, \\ \sigma < 2\,\sigma_0 \quad \text{(electromagnetic diffusion equation)}. \end{cases} \tag{26}$$

Taylor series expansion on equation (24) shows that the nth order term in the forward series is expressed as

$$S_n(\mathbf{r}) = G_0(\mathbf{r})\, \alpha_n(ik_0 r) \left[\frac{P}{k_0^2} \right]^n, \tag{27}$$

where $\alpha_n(ik_0 r)$ is nth order power series of $ik_0 r$ such that

$$\alpha_n(ik_0 r) = \frac{1}{2^n\, n!} \sum_{m=1}^{n} \beta_{n,m}\, (ik_0 r)^{n-m+1}, \tag{28}$$

and

$$\beta_{n,m} = \begin{cases} 1 & (m = 1), \\ -\dfrac{\beta_{n,m-1}}{m-1} \displaystyle\sum_{l=m-1}^{n-1} l & (m = 2, 3, 4, \cdots, n). \end{cases} \tag{29}$$

The convergence rate is, therefore,

$$R_n^F(\mathbf{r}) = \left| \frac{S_{n+1}(\mathbf{r})}{S_n(\mathbf{r})} \right| = \left| \frac{\alpha_{n+1}(ik_0 r)}{\alpha_n(ik_0 r)} \right| \left| \frac{P}{k_0^2} \right|. \tag{30}$$

The above equation shows that R_n^F is proportional to $|P/k_0^2|$, and the forward scattering series converges fast for weak perturbation. To appreciate the contribution of α_{n+1}/α_n on the convergence rate, we consider an acoustic wave problem where the frequency f is 50 Hz, wave velocity c is 3,000 m/s, and wavenumber k_0 is about 0.1 m^{-1}. Figure 4 shows the variation of $|\alpha_{n+1}/\alpha_n|$ at two spatial locations: one is 3 wavelengths apart from the source ($k_0 r = 6\pi$) and the other is 6 wavelengths ($k_0 r = 12\pi$). The figure shows that $|\alpha_{n+1}/\alpha_n|$ is larger for $k_0 r = 12\pi$ than for $k_0 r = 6\pi$ and implies that as the source-receiver offset increases, more series terms are necessary to reach convergence.

The formal expression of convergence rate given in equation (30) is valid for both the wave and diffusion equations. The wavenumber of the diffusion problem (equation (20)) has real and imaginary parts, and the

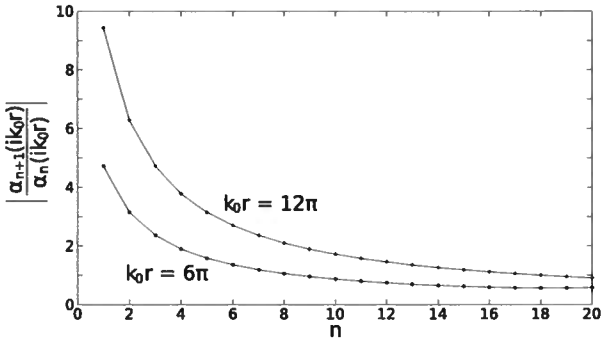

Figure 4. Convergence rate of forward scattering series. The ratio $|\alpha_{n+1}/\alpha_n|$ in equation (30) for increasing number of n is compared at two spatial locations: one is 3 wavelengths apart from the source ($k_0r = 6\pi$) and the other is 6 wavelengths ($k_0r = 12\pi$).

Green function for the diffusion equation generally exhibits faster spatial decay than that for the wave equation, which has real wavenumber. However, equation (30) indicates that there is no fundamental difference in the convergence rate between the forward scattering series for the diffusion equation and the series for the wave equation. In fact, fast spatial decay of the diffusive field does not necessarily mean fast convergence of the scattering series for the diffusion equation. This counterintuitive behavior of the convergence rate can be comprehended by considering the following three functions: e^x, e^{-x}, and e^{ix}. The three functions exhibit different variations as a function of x, but their Taylor series expansions in the variable x show the same convergence rate. This property of the convergence rate implies that the comparison of the convergence speed between wave propagation and diffusion depends on the specific parameters that we incorporate instead of the difference in the behavior of the physical fields. In the following, we choose representative parameters that reflect the hydrocarbon exploration situations and compare the convergence of the forward scattering series for the acoustic wave equation with that for the electromagnetic diffusion equation. The details of the parameters are introduced in the next section.

While the forward scattering series expresses the scattered field $S(\mathbf{r})$ as a power series in order of the perturbation P, the inverse series expresses the perturbation as a power series in order of the scattered field. Rewriting equation (24), the perturbation is expressed as a function of the scattered field:

$$P(\mathbf{r}) = -\frac{2ik_0}{r}\ln\left(1+\frac{S(\mathbf{r})}{G_0(\mathbf{r})}\right) - \frac{1}{r^2}\left[\ln\left(1+\frac{S(\mathbf{r})}{G_0(\mathbf{r})}\right)\right]^2. \quad (31)$$

Note that the function $f(z) = \ln(1+z)$ is singular at $z = -1$, and the radius of convergence of the Taylor series expansion centered at $z = 0$ extends up to the singular point. Equation (31) therefore shows that the inverse scattering series converges only for weak scattered fields that satisfy

$$\left|\frac{S(\mathbf{r})}{G_0(\mathbf{r})}\right| = \left|\frac{G(\mathbf{r})}{G_0(\mathbf{r})} - 1\right| = \left|e^{i(k-k_0)r} - 1\right| < 1. \quad (32)$$

By performing a Taylor series expansion of equation (31), it can be shown that the nth order term in the inverse series is given by

$$P_n(\mathbf{r}) = 2\left[\gamma_n(k_0, r) + \zeta_n(r)\right]\left[\frac{S(\mathbf{r})}{G_0(\mathbf{r})}\right]^n, \quad (33)$$

where

$$\gamma_n(k_0, r) = (-1)^n \frac{ik_0}{nr}, \quad (34)$$

$$\zeta_n(r) = \frac{\eta_n}{n!\, r^2}, \quad (35)$$

and

$$\eta_n = \begin{cases} 0 & (n = 1), \\ -(n-1)\eta_{n-1} + (-1)^{n-1}(n-2)! & (n = 2, 3, 4, \cdots). \end{cases} \quad (36)$$

The above formal expression of the inverse scattering series is valid for both the wave and diffusion equations. Figure 5 shows the absolute values of γ_n and ζ_n in equation (33). When the wavenumber of the reference medium is $k_0 = 0.1$ m^{-1}, $|\zeta_n|$ is much smaller than $|\gamma_n|$ at $r = 100$ m. The coefficient $|\gamma_n|$ is proportional to k_0/r and $|\zeta_n|$ is to $1/r^2$. Therefore, compared to ζ_n, γ_n is significant at a large source-receiver offset and for a large wavenumber of the reference medium. Ignoring ζ_n, the convergence rate of the inverse scattering series is approximated as

$$R_n^I = \left|\frac{P_{n+1}(\mathbf{r})}{P_n(\mathbf{r})}\right| \simeq \left|\frac{\gamma_{n+1}}{\gamma_n}\frac{S(\mathbf{r})}{G_0(\mathbf{r})}\right| = \left|\frac{n}{n+1}\frac{S(\mathbf{r})}{G_0(\mathbf{r})}\right|. \quad (37)$$

The above equation shows that as the scattering becomes stronger, the convergence speed of the inverse scattering series becomes slower.

4 MODEL TESTS OF SCATTERING SERIES SOLUTIONS

As noted in the previous section, a comparison of the convergence rates between wave propagation and diffusion depends on the specific parameters that we incorporate. We therefore choose parameters that are widely applied for exploring hydrocarbon reservoirs. For the application of the scattering series expressions (given by equations (27) and (33)) to the acoustic wave and electromagnetic diffusion problems, we adopt the parameters summarized in Table 1. Note we assume a velocity perturbation of 10% for the acoustic wave problem and a perturbation with a factor 10 ($\sigma_0/\sigma = 10$) for the electromagnetic diffusion problem. We also assume that magnetic permeability of the medium is the same as that of free space ($\mu = 4\pi \times 10^{-7}$ N/A^2).

Table 1. Summary of physical parameters adopted for model tests, where c and σ represent acoustic wave velocity and electric conductivity, respectively. Wavenumber k is derived from equation (20). The perturbation is real for the acoustic wave problem and imaginary for the electromagnetic diffusion problem.

Acoustic wave problem		Electromagnetic diffusion problem	
f	50 Hz	f	10 Hz
c_0	3.0×10^3 m/s	σ_0	1.0×10^{-1} S/m
c	3.3×10^3 m/s	σ	1.0×10^{-2} S/m
k_0^2	1.10×10^{-2} m^{-2}	$\lvert k_0^2 \rvert$	7.90×10^{-6} m^{-2}
k^2	0.91×10^{-2} m^{-2}	$\lvert k^2 \rvert$	0.79×10^{-6} m^{-2}
$P = k^2 - k_0^2$	-0.19×10^{-2} m^{-2}	$\lvert P \rvert = \lvert k^2 - k_0^2 \rvert$	7.11×10^{-6} m^{-2}

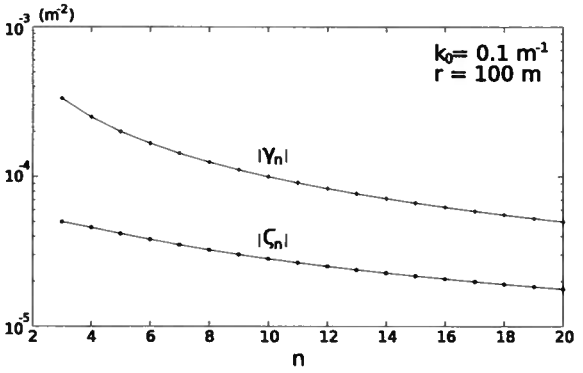

Figure 5. Comparison of the absolute values of γ_n and ζ_n in equation (33). For $k_0 = 0.1$ m^{-1} and $r = 100$ m, $|\zeta_n|$ is much smaller than $|\gamma_n|$. The two terms are dependent on k_0/r and $1/r^2$, respectively, which implies γ_n is significant at a large source-receiver offset and for a large wavenumber of the reference medium.

Figures 6 and 7 show the spatial variation of the forward scattering series for the acoustic wave and electromagnetic diffusion equations, respectively. The solutions derived from the forward series (solid curve) are compared with the analytic solution of the scattered field (dotted curve), which is expressed as

$$S(\mathbf{r}) = \frac{e^{ikr} - e^{ik_0 r}}{4\pi r}. \tag{38}$$

The scattered field of the acoustic wave equation (dotted curve in Figure 6) exhibits spatial oscillations, amplitude modulation, and geometric spreading. The scattered field of the electromagnetic diffusion equation (dotted curve in Figure 7) shows exponential amplitude decay and monotonous phase change. From equation (27), the first order term in the forward series is

$$S_1(\mathbf{r}) = \frac{iP}{8\pi k_0} e^{ik_0 r} \tag{39}$$

and near the source, exhibits better agreement with the analytic solution than at the far receiver location. As we include higher order terms, the partial sum of the forward series approaches the analytical solution of the scattered field. Note that except for short source-receiver offset, the forward scattering series for the electromagnetic diffusion equation ($N = 5$ in the middle panel of Figure 7) requires fewer terms to achieve good agreement with the analytic solution than the series for the acoustic wave equation ($N = 15$ in the middle panel of Figure 6). We therefore conclude that for the employed parameters (Table 1) which are representative of hydrocarbon exploration, the forward scattering series for the electromagnetic diffusion equation converges

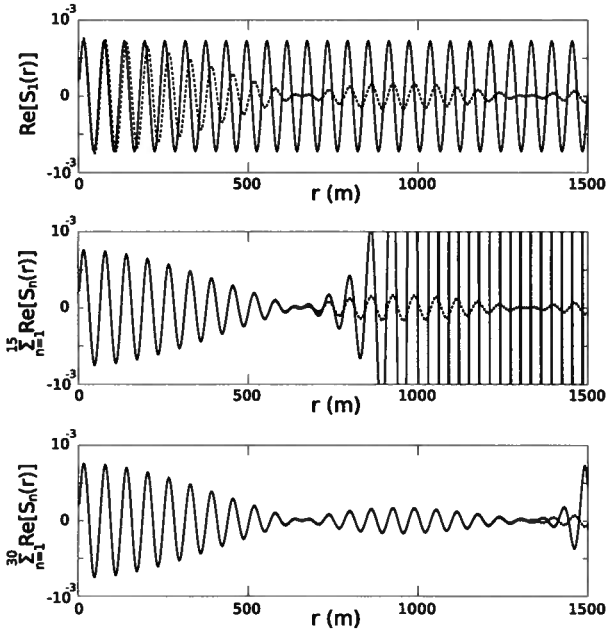

Figure 6. Spatial variation of forward scattering series for the acoustic wave equation (real part only). The employed parameters are summarized in Table 1. The solutions derived from the forward series (solid curve) are compared with the analytic solution of the scattered field (dotted curve). The top, middle, and bottom panels show the partial sum $\sum_{n=1}^{N} S_n(\mathbf{r})$ for $N = 1$, $N = 15$, and $N = 30$, respectively. As we include higher order terms in the forward series, the partial sum of the forward series approaches the analytic solution of the scattered field at an increasing range of r.

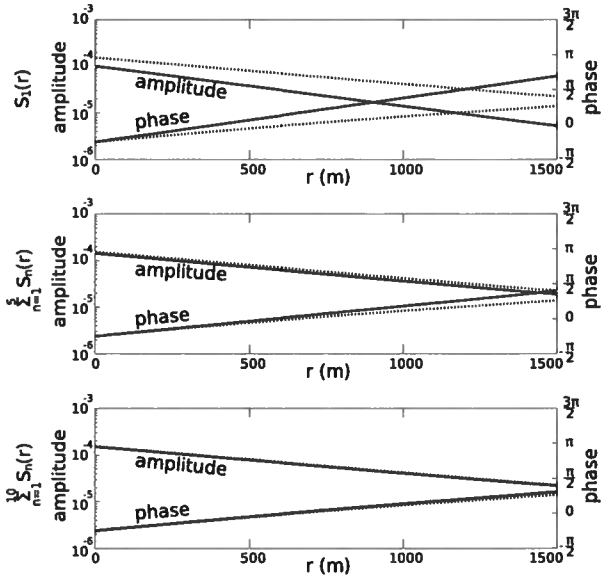

Figure 7. Spatial variation of the forward scattering series for the electromagnetic diffusion equation. The employed parameters are summarized in Table 1. The solutions derived from the forward series (solid curve) are compared with the analytic solution of the scattered field (dotted curve). The top, middle, and bottom panels show the partial sum $\sum_{n=1}^{N} S_n(\mathbf{r})$ for $N = 1$, $N = 5$, and $N = 10$, respectively. As we include higher order terms in the forward series, the partial sum of the forward series approaches the analytic solution of the scattered field at an increasing range of r.

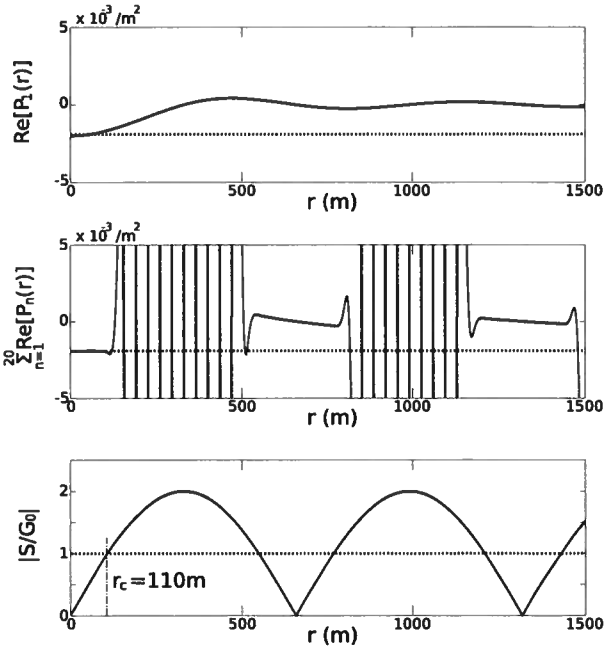

Figure 8. Spatial variation of the inverse scattering series for the acoustic wave equation (real part only). The employed parameters are summarized in Table 1. In the top and middle panels, the solutions derived from the inverse series (solid curve) are compared with the exact value of the perturbation $\omega^2(1/c^2 - 1/c_0^2)$ (dotted line) which is real. The first term in the inverse series (the top panel) exhibits significant discrepancy from the exact value. The partial sum up to the 20th order term in the inverse series (the middle panel) converges to the exact value within a limited range where $r < r_c$ and diverges elsewhere. The bottom panel shows the spatial variation of $|S(\mathbf{r})/G_0(\mathbf{r})|$.

faster and requires fewer series terms than does the series for the acoustic wave equation.

Figures 8 and 9 show the spatial variation of the inverse scattering series for the acoustic wave and electromagnetic diffusion equations, respectively. The solutions derived from the inverse series (solid curve) are compared with the exact value of the perturbation (dotted line) which is real for the wave equation and imaginary for the diffusion equation. In these figures, r_c describes the maximum distance for which the inverse scattering series converges as described below. Considering the convergence criterion given in equation (32), the variation of $|S/G_0|$ (solid curve) is also compared with the threshold value for convergence (dotted line). The first order term in the inverse series exhibits significant deviation from the exact value. The partial sum of the inverse series up to the 20th order term converges to the exact value within the range that extends from $r = 0$ to the location where the convergence criterion is satisfied. However, the partial sum of the inverse series diverges for $r > r_c$. Compared to the inverse series for the acoustic wave equation (Figure 8), the series for the electromagnetic diffusion equation (Figure 9) converges to the exact value of the perturbation in a wider spatial range. This convergence pattern suggests that for the employed parameters, the inverse scattering series for the electromagnetic diffusion equation converges faster than does the series for the acoustic wave equation. The above observations also reveal that the convergence criterion given in equation (32) plays a crucial role in the reconstruction of the perturbation. We therefore perform more detailed analysis on the convergence criterion.

As noted before, wavenumber k is real for the acoustic wave equation. Denoting the spatial radius of convergence for the inverse series of the wave equation as r_c, we derive the following relation from equation (32):

$$\left| e^{i(k-k_0)r_c} - 1 \right| = 1. \tag{40}$$

The spatial radius of convergence is, therefore, given as

$$r_c = \frac{\pi}{3\,|k - k_0|}. \tag{41}$$

In case of the electromagnetic diffusion problem, the wavenumber is derived from $k^2 = i\omega\mu\sigma$, and we denote the wavenumber as

$$k = \frac{1+i}{\sqrt{2}}|k|. \tag{42}$$

The convergence criterion given in equation (32) is

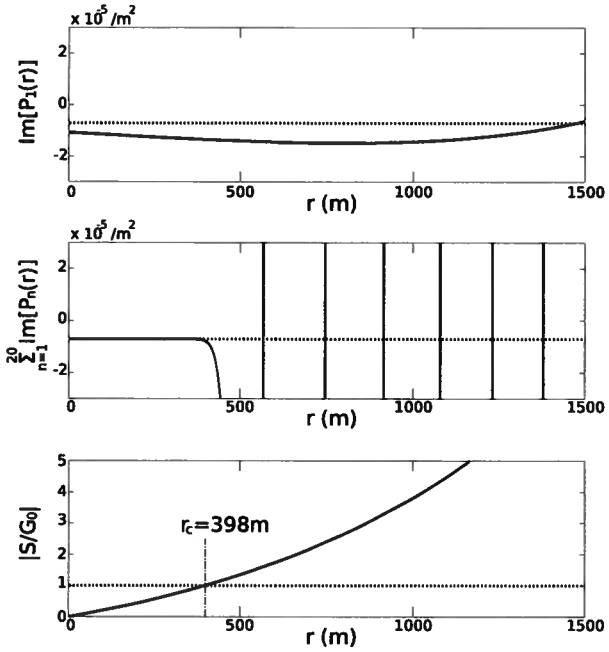

Figure 9. Spatial variation of the inverse scattering series for the electromagnetic diffusion equation (imaginary part only). The employed parameters are summarized in Table 1. In the top and middle panels, the solutions derived from the inverse series (solid curve) are compared with the exact value of the perturbation $i\omega\mu(\sigma - \sigma_0)$ (dotted line) which is imaginary. The first term in the inverse series (the top panel) exhibits significant discrepancy from the exact value. The partial sum up to the 20th order term in the inverse series (the middle panel) converges to the exact value within a limited range where $r < r_c$ and diverges elsewhere. The bottom panel shows the spatial variation of $|S(\mathbf{r})/G_0(\mathbf{r})|$.

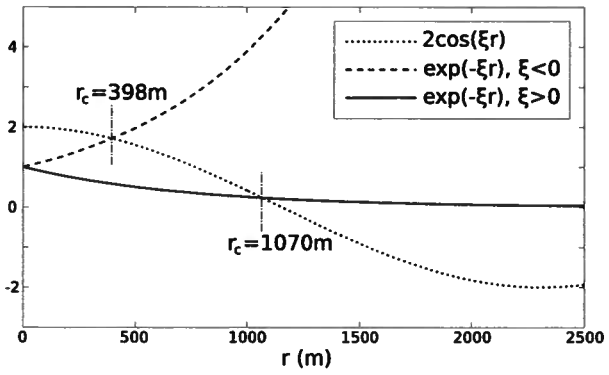

Figure 10. Derivation of the spatial radius of convergence r_c for the electromagnetic diffusion problem. The dashed and solid curves show the left-hand side of equation (45) for $\xi < 0$ and $\xi > 0$, respectively, while the dotted curve shows the right-hand side of equation (45). Applying the parameters summarized in Table 1, r_c is derived as 398 m. On the other hand, by switching the two conductivity values in Table 1 ($\sigma \leftrightarrow \sigma_0$), r_c is derived as 1070 m.

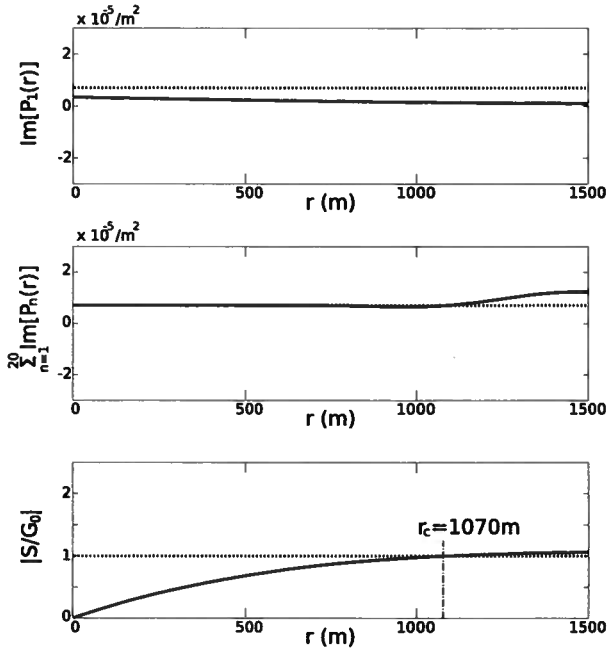

Figure 11. Spatial variation of the inverse scattering series for the electromagnetic diffusion equation (imaginary part only). The medium properties of the perturbed and reference media are switched from the previous case shown in Figure 9 and Table 1. Note that the spatial range where $|S(\mathbf{r})/G_0(\mathbf{r})| < 1$ is wider than the case shown in Figure 9.

rewritten as follows:

$$\left|\frac{S(\mathbf{r})}{G_0(\mathbf{r})}\right| = \left|e^{-\frac{|k|-|k_0|}{\sqrt{2}}r} e^{i\frac{|k|-|k_0|}{\sqrt{2}}r} - 1\right| < 1. \qquad (43)$$

Denoting $\xi = (|k| - |k_0|)/\sqrt{2}$, we establish the following relation at $r = r_c$ (the spatial radius of convergence for the inverse series of the diffusion equation):

$$\left|e^{-\xi r} e^{i\xi r} - 1\right| = 1, \qquad (44)$$

which can be simplified as

$$e^{-\xi r} = 2\cos\xi r. \qquad (45)$$

Equation (45) is a transcendental equation for the spatial radius of convergence r_c that is analyzed graphically in Figure 10. The dotted curve shows the right-hand side of equation (45) while the dashed and solid curves show the left-hand side for $\xi < 0$ and $\xi > 0$, respectively. The distance r_c for which the inverse scattering series converges is larger for positive value of ξ ($\sigma > \sigma_0$) than for negative value of ξ ($\sigma < \sigma_0$). This means that the spatial radius of convergence is larger when choosing a reference model with a small electric conductivity.

Equation (43) shows that as r increases, the ratio $|S/G_0|$ exhibits exponential variation with distance: there is exponential decrease when $|k| > |k_0|$ ($\sigma > \sigma_0$) and exponential growth when $|k| < |k_0|$ ($\sigma < \sigma_0$). The inverse scattering problem aims to recover the unknown

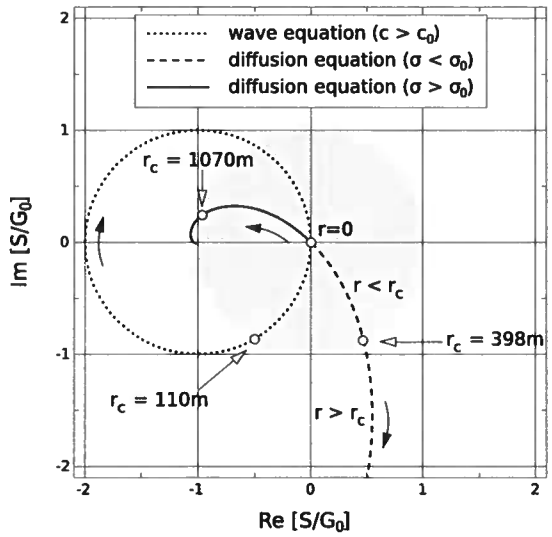

Figure 12. The variation of S/G_0 in the complex plane for different values of r. The origin of the complex plane indicate $r = 0$, and the arrows denote the directions of increasing r. Three different cases shown in Figures 8, 9, and 11 are compared. The shaded region denotes the area where the inverse series converges.

perturbation from the measured field and a reference model, and we have freedom of choosing a reference model. Therefore, the exponential variation of the ratio $|S/G_0|$ in equation (43) illustrates that given the actual medium, we can accelerate the convergence of the inverse series for the electromagnetic diffusion equation by choosing a reference medium that is less conductive (smaller wavenumber) than the actual medium. On the other hand, the acoustic wave equation has a real wavenumber, and the sign of $k - k_0$ is irrelevant to the convergence criterion (equation (41)). Figure 11 shows the spatial variation of the inverse scattering series for the electromagnetic diffusion equation when the perturbed and reference media switch roles ($\sigma \leftrightarrow \sigma_0$) from the previous case shown in Figure 9. Compared to the case when the reference medium is more conductive than the actual medium (Figure 9), the spatial range of the convergence shown in Figure 11 is wider.

Figure 12 shows the path of S/G_0 in the complex plane as the source-receiver offset r increases for three different cases: the inverse scattering series for the acoustic wave equation (dotted curve), the series for the electromagnetic diffusion equation that corresponds to Figure 9 (dashed curve), and the series for the electromagnetic diffusion equation with the reversed medium properties (solid curve). As the source-receiver distance increases, the value of S/G_0 moves away from the origin. In the case of acoustic wave propagation, the path forms a closed circle, and the sign of $c - c_0$ determines the direction of the movement as r increases (clockwise direction when $c > c_0$ and counterclockwise direction when $c < c_0$). On the other hand, the path of S/G_0 does not form a closed circle for the electromagnetic diffusion problem. Depending on the sign of $\sigma - \sigma_0$, the ratio S/G_0 moves out of the convergence area ($\sigma < \sigma_0$) or converges to the point where $S/G_0 = -1$ ($\sigma > \sigma_0$). This shows that the convergence of the inverse series for the electromagnetic diffusion equation can be facilitated by choosing a reference medium that is less conductive than the actual medium. The different paths represented by the dashed curve ($\sigma < \sigma_0$) and solid curve ($\sigma > \sigma_0$) demonstrates the significance of the choice of the reference medium for the convergence of the inverse scattering series for the electromagnetic diffusion problem.

5 CONCLUSIONS

We analyzed the difference between applying the scattering series method to the acoustic wave and electromagnetic diffusion equations for an infinite 3D medium. Analysis of the formal expressions of the scattering series solutions shows that there is no fundamental difference in the convergence rate between the forward scattering series for the acoustic wave equation and the series for the electromagnetic diffusion equation; the analysis also illustrates that rapid spatial decay of the diffusive field does not necessarily mean fast convergence of the scattering series for the diffusion equation. The model tests suggest, however, that for parameters representing geophysical experiments, the convergence speed of the scattering series solutions for the electromagnetic diffusion equation is faster than that for the acoustic wave equation. The model tests also show that for the electromagnetic diffusion equation, we can facilitate the convergence of the inverse scattering series by designing a reference medium that is less conductive than the actual medium. In this study, we considered homogeneous media where the electromagnetic signal diffuses away from the source, and there is no signal that diffuses back from any perturbed structure, which we eventually aim to reconstruct. It requires further research to identify how much we can generalize the above conclusions to the inverse scattering series problems of a 2D or 3D model reconstruction.

6 ACKNOWLEDGEMENTS

This work was supported by the Consortium Project on Seismic Inverse Methods for Complex Structures at Center for Wave Phenomena (CWP). We acknowledge Arthur Weglein (University of Houston), Evert Slob (Delft University of Technology) and Yuanzhong Fan for helpful information, discussions, and suggestions. We are also grateful to colleagues of CWP for valuable discussions and technical help.

REFERENCES

Chave, A., and Cox, C. S., 1982, Controlled electromagnetic sources for measuring electrical conductivity beneath the oceans 1. forward problem and model study: Journal of Geophysical Research, **87**, no. B7, 5327 – 5338.

Colton, D., and Kress, R., 1998, Inverse acoustic and electromagnetic scattering theory: , Springer, 2nd edition.

Constable, S., and Srnka, L., 2007, An introduction to marine controlled-source electromagnetic methods for hydrocarbon exploration: Geophysics, **72**, no. 2, WA3 – WA12.

Cox, C. S., Constable, S. C., Chave, A. D., and Webb, S. C., 1986, Controlled-source electromagnetic sounding of the oceanic lithosphere: Nature, **320**, no. 6057, 52 – 54.

Gel'fand, I. M., and Levitan, B. M., 1951, On the determination of a differential equation from its spectral function: Izvestiya Akademii Nauk SSSR Seriya Matematicheskaya, **15**, no. 4, 309 – 360.

Hoversten, G. M., Cassassuce, F., Gasperikova, E., Newman, G. A., Chen, J., Rubin, Y., Hou, Z., and Vasco, D., 2006, Direct reservoir parameter estimation using joint inversion of marine seismic AVA and CSEM data: Geophysics, **71**, no. 3, C1 – C13.

Jackson, J. D., 1999, Classical electrodynamics: , John Wiley & Sons, 3rd edition.

Jost, R., and Kohn, W., 1952, Construction of a potential from a phase shift: Physical Review, **87**, no. 6, 977 – 992.

Mavko, G., Mukerji, T., and Dvorkin, J., 1998, The rock physics handbook - tools for seismic analysis in porous media: , Cambridge University Press.

Morse, P. M., and Feshbach, H., 1953, Methods of theoretical physics: , McGraw Hill Company.

Moses, H. E., 1956, Calculation of the scattering potential from reflection coefficients: Physical Review, **102**, no. 2, 559 – 567.

Palacky, G. J., 1987, Resistivity characteristics of geologic targets: Resistivity characteristics of geologic targets:, 53 – 129.

Prosser, R. T., 1969, Formal solutions of inverse scattering problems: Journal of Mathematical Physics, **10**, no. 10, 1819 – 1822.

Ramirez, A. C., and Weglein, A. B., 2009, Green's theorem as a comprehensive framework for data reconstruction, regularization, wavefield separation, seismic interferometry and wavelet estimation: A tutorial: Geophysics, **74**, no. 6, W35 – W62.

Snieder, R., 1990a, A perturbative analysis of non-linear inversion: Geophysical Journal International, **101**, no. 3, 545 – 556.

——— 1990b, The role of the born approximation in nonlinear inversion: Inverse Problems, **6**, no. 2, 247 – 266.

Taylor, J. R., 1972, Scattering theory - the quantum theory of nonrelativistic collisions: , Wiley.

Weglein, A. B., Boyse, W. E., and Anderson, J. E., 1981, Obtaining three-dimensional velocity information directly from reflection seismic data: An inverse scattering formalism: Geophysics, **46**, no. 8, 1116 – 1120.

Weglein, A. B., Gasparotto, F. A., Carvalho, P. M., and Stolt, R. H., 1997, An inverse-scattering series method for attenuating multiples in seismic reflection data: Geophysics, **62**, no. 6, 1975 – 1989.

Weglein, A. B., Araujo, F. V., Carvalho, P. M., Stolt, R. H., Matson, K. H., Coates, R. T., Corrigan, D., Foster, D. J., Shaw, S. A., and Zhang, H., 2003, Inverse scattering series and seismic exploration: Inverse Problems, **19**, no. 6, R27 – R83.

Weglein, A. B., Zhang, H., Ramirez, A. C., Liu, F., and Lira, J. E. M., 2009, Clarifying the underlying and fundamental meaning of the approximate linear inversion of seismic data: Geophysics, **74**, no. 6, WCD1 – WCD13.

Zhang, H., and Weglein, A. B., 2009a, Direct non-linear inversion of multi-parameter 1D elastic media using the inverse scattering series: Geophysics, **74**, no. 6, WCD15 – WCD27.

——— 2009b, Direct nonlinear inversion of 1D acoustic media using inverse scattering subseries: Geophysics, **74**, no. 6, WCD29 – WCD39.

Extracting the Green's function for static problems from dynamic fields

Roel Snieder[1], Evert Slob[1,2] & Kees Wapenaar[2]
[1] *Center for Wave Phenomena, Colorado School of Mines, Golden CO 80401,*
[2] *Dept. of Geotechnology, Delft University of Technology, P.O. Box 5048, 2600 GA Delft, The Netherlands*

ABSTRACT
The theory of Green's function extraction from field fluctuations has originally been derived in geoscience applications for wave propagation problems. Although current application of this technique is not restricted to wave propagation, there was no theory for Green's function extraction of static fields. We present the theory of Green's function extraction of static fields and illustrate the theory with a numerical example. The theory presented here is applicable to potential fields and to DC resistivity problems. The ability to extract static fields from field fluctuations makes it possible, in principle, to extract static fields from passive measurements of field fluctuations. This can be particularly relevant for continuous monitoring of the subsurface with electrical fields.

Key words: Green's function extraction, potential fields, static fields

1 INTRODUCTION

Extraction the Green's function from field fluctuations is a rapidly growing field in science and engineering (Curtis *et al.*, 2006; Larose *et al.*, 2006; Wapenaar *et al.*, 2008). In seismological applications this technique is usually referred to as *seismic interferometry*. The principle of Green's function extraction has up to this point been applied to time-dependent problems. This may have been caused by the fact the underlying theory was originally related to time-reversal, e.g. (Derode *et al.*, 2003). The current theory has mostly been applied to problems involving wave propagation, such problems are inherently time-dependent.

In this work we show that the principle of Green's function extraction can be applied to static fields. The theory presented here is a simplified version of the more general formulation of *Lagrangian Green's function extraction* (Snieder *et al.*, 2010), and we restrict ourselves to the Green's function extraction for a potential field problem. It may appear to be a paradox that one can extract the Green's function of static fields from dynamic field fluctuations. The underlying principle is, however, not complicated. As an example, we show numerical simulations where random dipoles are present in an electrostatic system. At every moment in time, different dipoles generate the field, which at any moment in time depends only on the instantaneous dipole distribution. (This is actually the definition of the quasi-static response.) We show theoretically and numerically that by averaging over all dipole distributions one can extract the electrostatic response. Since the response is quasi-static, it does not matter whether the fields are generated by time-dependent electrical dipoles, or by an ensemble of dipoles; in the end this gives the same response. In the following section we derive the theory, which we illustrate with a numerical example in the subsequent section.

2 GREEN'S FUNCTION EXTRACTION IN ELECTROSTATICS

In linear dielectric media, the electric displacement $\mathbf{D}$ is related to the electric field $\mathbf{E}$ by the relation $\mathbf{D} = \varepsilon\mathbf{E}$, with $\varepsilon(\mathbf{r})$ the electrical permittivity (Jackson, 1975). Using the field equation $(\nabla \cdot \mathbf{D}) = q$, with $q(\mathbf{r})$ the charge density, and the relation $\mathbf{E} = -\nabla u$, with $u(\mathbf{r})$ the electric potential, the following field equation results

$$0 = \nabla \cdot (\varepsilon(\mathbf{r})\nabla u(\mathbf{r})) + q(\mathbf{r}) \; . \tag{1}$$

If instead of the electrostatic problem we consider direct currents in a conducting medium, then the charge density $q(\mathbf{r})$ is replaced by a volume density of charge injection or extraction rate $-\dot{q}(\mathbf{r})$ (the minus sign comes from the historical convention that the loss of charge from the source region constitutes a positive electric current), and the electric permittivity $\varepsilon(\mathbf{r})$ is replaced by the conductivity $\sigma(\mathbf{r})$. This leaves equation (1) intact with different symbols (Stratton, 1941). This results in a formulation for the extraction of the resistivity tensor in conducting media from field fluctuations (Slob *et al.*, 2010).

The derivation of the Green's function extraction is based on representation theorems, but is actually simpler than earlier derivation for Green's function extraction for acoustic waves (Derode *et al.*, 2003; Wapenaar *et al.*, 2005) because the static fields considered here are real. We consider two states, labeled A and B, and take the field equation (1) for state A, multiply it with the field of state B and integrate over a volume V to give

$$\int_V u_B(\mathbf{r})q_A(\mathbf{r})dV = -\int_V u_B(\mathbf{r})\nabla\cdot(\varepsilon(\mathbf{r})\nabla u_A(\mathbf{r}))\,dV\,. \quad (2)$$

Using the identity $u_B\nabla\cdot(\varepsilon\nabla u_A) = \nabla\cdot(\varepsilon u_B\nabla u_A) - \varepsilon(\nabla u_A\cdot\nabla u_B)$ and applying Gauss' theorem gives

$$\begin{aligned}\textstyle\int_V u_B(\mathbf{r})q_A(\mathbf{r})dV &= -\oint_{\partial V}\varepsilon(\mathbf{r})u_B(\mathbf{r})\frac{\partial u_A(\mathbf{r})}{\partial n}dS \\ &\quad + \textstyle\int\varepsilon(\mathbf{r})\left(\nabla u_A(\mathbf{r})\cdot\nabla u_B(\mathbf{r})\right)dV\,,\end{aligned} \quad (3)$$

where ∂V denotes the boundary of the volume V. When the potential u_B or the normal component of the electric field $\partial u_A/\partial n$ vanishes on the boundary, the first integral on the right hand side vanishes, and

$$\int_V u_B(\mathbf{r})q_A(\mathbf{r})dV = \int\varepsilon(\mathbf{r})\left(\nabla u_A(\mathbf{r})\cdot\nabla u_B(\mathbf{r})\right)dV\,. \quad (4)$$

The fields decay sufficiently rapid with distance that the surface integral also vanishes when the surface is take at infinity. We next take use a point source for the two states ($q_A(\mathbf{r}) = \delta(\mathbf{r}-\mathbf{r}_A)$ and $q_B(\mathbf{r}) = \delta(\mathbf{r}-\mathbf{r}_B)$), the corresponding fields are, by definition, given by the Green's functions $G(\mathbf{r},\mathbf{r}_A)$ and $G(\mathbf{r},\mathbf{r}_B)$, respectively. Inserting this in expression (4) gives

$$G(\mathbf{r}_A,\mathbf{r}_B) = \int_V\varepsilon(\mathbf{r})\left(\nabla G(\mathbf{r},\mathbf{r}_A)\cdot\nabla G(\mathbf{r},\mathbf{r}_B)\right)dV\,. \quad (5)$$

In order to establish the connection of this equation with the Green's function extraction from field fluctuations we use the field generated by an electric dipole distribution $\mathbf{p}(\mathbf{r})$ (Jackson, 1975)

$$u(\mathbf{r}_0) = \int_V\left(\nabla G(\mathbf{r}_0,\mathbf{r})\right)\cdot\mathbf{p}(\mathbf{r})dV\,. \quad (6)$$

We next consider random dipole sources that are spatially and directionally uncorrelated and satisfy

$$\langle p_i(\mathbf{r}_1)p_j(\mathbf{r}_2)\rangle = |S|^2\varepsilon(\mathbf{r}_1)\delta(\mathbf{r}_1-\mathbf{r}_2)\delta_{ij}\,, \quad (7)$$

where $|S|^2$ measures the strength of the dipole sources. For the moment we consider an ensemble of identical electrostatic systems, each with their own excitation by dipoles, and $\langle\cdots\rangle$ denotes an ensemble average. Multiplying expression (5) with $|S|^2$, using the fact that for this problem G is real, and using the summation convention, gives

$$\begin{aligned}G(\mathbf{r}_A,\mathbf{r}_B)|S|^2 &= |S|^2\textstyle\int_V\varepsilon(\mathbf{r})\partial_i G(\mathbf{r},\mathbf{r}_A)\partial_i G^*(\mathbf{r},\mathbf{r}_B)dV \\ &= \textstyle\int_V\int_V|S|^2\varepsilon(\mathbf{r}_1)\delta(\mathbf{r}_1-\mathbf{r}_2)\delta_{ij} \\ &\quad\times\partial_i G(\mathbf{r}_1,\mathbf{r}_A)\partial_j G^*(\mathbf{r}_2,\mathbf{r}_B)dV_1dV_2 \\ &= \langle\textstyle\int_V\partial_i G(\mathbf{r}_1,\mathbf{r}_A)p_i(\mathbf{r}_1)dV_1\int_V\partial_j G^*(\mathbf{r}_2,\mathbf{r}_B)p_j(\mathbf{r}_2)dV_2\rangle \\ &= \langle u(\mathbf{r}_A)u^*(\mathbf{r}_B)\rangle\,,\end{aligned} \quad (8)$$

where the identity $\int f_i(\mathbf{r})g_i(\mathbf{r})dV = \int\int f_i(\mathbf{r}_1)\delta(\mathbf{r}_1-\mathbf{r}_2)\delta_{ij}g_j(\mathbf{r}_2)dV_1dV_2$ has been used in the second identity, expression (7) in the third equality, and expression (6) in the last identity. This means that the electrostatic Green's function $G(\mathbf{r}_A,\mathbf{r}_B)$ follows from the ensemble average of the correlation of field fluctuations recorded at $\mathbf{r}_A$ and $\mathbf{r}_B$ that are excited by uncorrelated dipole sources.

In reality one may not have an ensemble of identical electrostatic systems, but one may have a system where random sources fluctuate with time. When the characteristic time of the temporal variations in these dipole sources is large compared to the time it takes for light to propagate through the system, the response of the system is quasi-static. In that case the ensemble average can be replaced by a temporal average over the field fluctuations. In fact, the approach to replace an ensemble average by an average over time is common in seismology where averaging over multiple non-overlapping time windows is used to extract the dynamic Green's function (Larose *et al.*, 2006; Sabra *et al.*, 2005; Shapiro *et al.*, 2005). By applying the same principle to quasi-static field fluctuations one can extract the electrostatic Green's function from temporal field fluctuations.

3 NUMERICAL SIMULATION OF GREEN'S FUNCTION RETRIEVAL IN ELECTROSTATICS

In this example we illustrate the theory for the Green's function extraction for the electrostatic potential by cross-correlating the fields generated by random electric dipoles within a conducting spherical shell with radius R at which the potential vanishes. Using the method of images, one can show that the potential generated by a dipole $\mathbf{p}$ at location $\mathbf{r}$ inside the shell vanishes at the shell $r = R$ when one adds the fields generated by a monopole $q' = (R/r^2)(\mathbf{p}\cdot\hat{\mathbf{r}})$ and a dipole $\mathbf{p}' = -(R/r)^3\left(\mathbf{p}-2(\mathbf{p}\cdot\hat{\mathbf{r}})\hat{\mathbf{r}}\right)$, both at location $\mathbf{r}' = (R/r)^2\mathbf{r}$ outside the shell (Snieder *et al.*, 2010). We

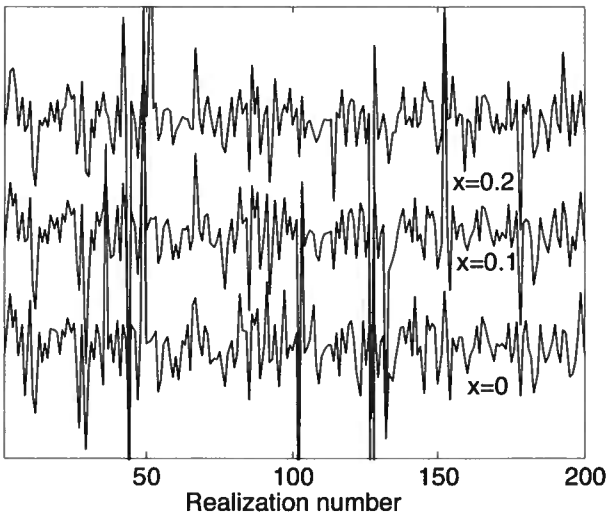

Figure 1. Two hundred realizations of the potential at the x-axis at $x = 0$, $x = 0.1$, and $x = 0.2$, respectively.

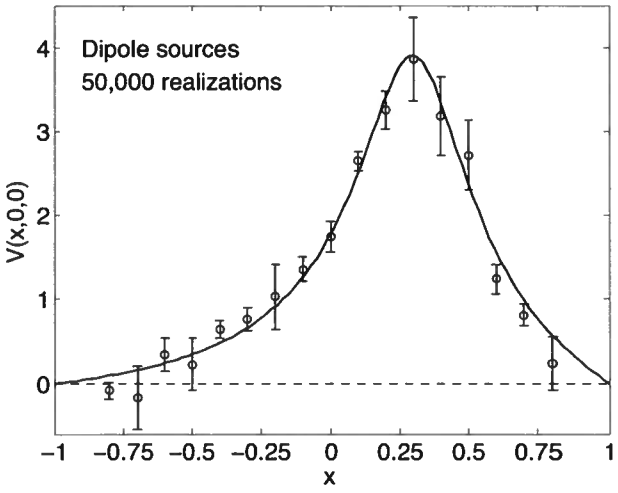

Figure 2. Open symbols: the potential and its standard deviation reconstructed from 50,000 realizations of random dipoles. Solid line: the true potential for a monopole at $(0.3, 0.2, 0)$.

use a system of units scaled in such a way that $4\pi\varepsilon_0$ and R are both equal to 1.

The Green's function extraction is applied to equation (8). In each realization the field $u(\mathbf{r})$ is generated by ten random dipoles at locations that are drawn from a uniform distribution within the sphere. Each component from each dipole is drawn from a uniform distribution between -1 and +1. In equation (8) we use $\mathbf{r}_B = (0.3, 0.2, 0)$ and choose $\mathbf{r}_A$ along the x-axis of a coordinate system that has its origin at the center of the sphere. Figure 1 shows the potential in 200 realizations at three points along the x-axis. The potential at each point has the character of white noise, which is not surprising because the dipoles in every realization are uncorrelated and have zero mean. The potential at the different locations is, however, correlated. It is these correlations in the fields generated by random sources that contains the information that ultimately leads to the extraction of the Green's function. Note that it does not matter whether one considers figure 1 to show different realizations, or whether it shows a time series of the quasi-static electric response of a system that exhibits quasi-random electric dipoles as a function of time.

Figure 2 shows the cross correlation of 50,000 realizations of the field fluctuations recorded at location $\mathbf{r}_B = (0.3, 0.2, 0)$ and various locations along the x-axis. In all examples shown, the realizations are divided in 10 bins that each contains 5,000 realizations that are drawn from the same statistical distribution. The cross-correlation of field fluctuations in the different bins is used to compute the mean of the cross-correlation of field fluctuations and the variance in this mean (Hogg & Craig, 1978). The variance of the mean is shown with the error bars on figure 2. The mean and error thus computed do not depend much on the number of bins chosen, which means that the averaging over the bins has the same statistical effect as the averaging over realizations within each bin. The solid line in figure 2 shows the potential due to a unit point charge at location $\mathbf{r}_B$, which is the desired Green's function. The cross-correlations of field fluctuations, and their errors, are multiplied with a common scale factor that minimizes the difference of the cross-correlation and the Green's function. This scale factor accounts for the term $|S|^2$ in equation (8). Note that the potential estimated from the cross-correlation of field fluctuations generated by random dipole sources agrees with the true Green's function within the shown standard deviations. This confirms that the Green's function for this static example can indeed by extracted from the cross-correlation of field fluctuations.

The Green's function in the example of figure 2 was extracted from the cross-correlation of field fluctuations excited by random dipoles. In each realization, the field was generated by the simultaneous action of 10 dipoles. In order to investigate what happens when the dipoles do not have a random orientation, we repeated the numerical experiment of figure 2, but now used the fixed dipole $\mathbf{p} = (1, 1, 1)$ in every realization. Ten of these dipoles were placed randomly within the spherical shell in every realization. The estimate of the Green's function estimated from the cross-correlations of the associated field fluctuations is shown in figure 3. In this case cross-correlation of field fluctuations does not lead to an acceptable estimate of the Green's function. The reason for this discrepancy is that according to equation (7) the orientation of different dipole vec-

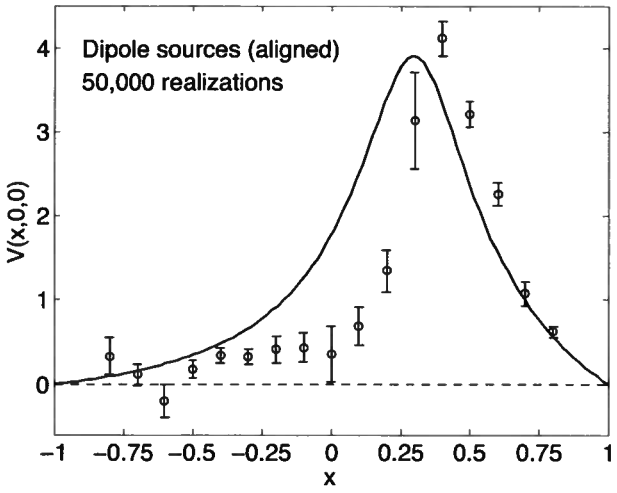

Figure 3. Open symbols: the potential and its standard deviation reconstructed from 50,000 realizations of aligned dipoles with dipole moment $\mathbf{p} = (1, 1, 1)$. Solid line: the true potential for a monopole at $(0.3, 0.2, 0)$.

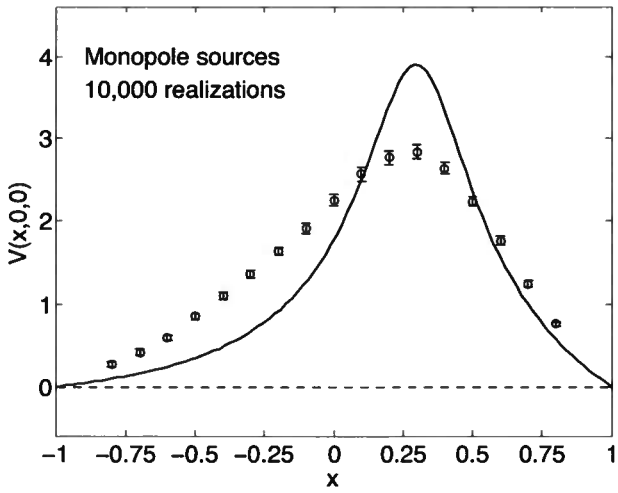

Figure 4. Open symbols: the potential and its standard deviation reconstructed from 10,000 realizations of random monopoles. Solid line: the true potential for a monopole at $(0.3, 0.2, 0)$.

tors must be uncorrelated. This assumption is violated when a constant dipole vector is used for every dipole.

One might think that it does not really matter whether field fluctuations are generated by dipoles or by monopoles (point charges). We show in figure 4 the field extracted from cross-correlation of 10,000 realizations of field fluctuations generated by monopoles. In each realization ten point charges are placed at random positions within the shell. Each point charge is drawn from a uniform distribution between -1 and 1. Note that the standard deviation in figure 4 is much smaller than that in figure 2, despite the fact that five time less realizations are used. There are two reasons for this. First, for random dipole orientations, one carries out an implicit averaging over the direction of the dipole vectors, such averaging is not needed for monopole sources. Second, the dipole fields vary more rapidly with space than the monopole field do, hence the dipole fields must be sampled more finely by point charges to mimic the volume integrals in expression (8). Note that the cross-correlation of field fluctuations caused by random monopoles does not lead to an acceptable extraction of the Green's function.

The examples of the figures 2 and 4 illustrate the paradox that one needs field fluctuations excited by random dipoles to extract the monopole field. This is fortunate; natural field fluctuations cannot be caused by monopoles because the random occurrence of monopoles is not consistent with charge conservation. Charges are neither created nor destroyed in a source-free region. This means that only dipoles or higher order multipoles can excite field fluctuations. For the expected localized fluctuations, where the local charge separation is orders of magnitude smaller than that of the measurement scale, the contribution of the dipole moments dominates the potential field, and the electric potential is given by equation (6). The occurrence of dipole moments in a material can have four basic causes: electronic, ionic, dipolar and space charge polarization (Khesin *et al.*, 1996). Relaxation times of the first three processes are usually smaller than 1 μs, while for the last process the relaxation time can be as large as 1 s. These time scales are extremely long compared to the propagation time of light through system of the size of a laboratory experiment or geophysical field experiments. Field fluctuations can be generated, for example in natural rocks by electromagnetic radiation in fracturing rocks or in stressed rocks before fracturing. During fracturing, bonds are broken. The larger the number of cut bonds, the larger is the number of excited atoms, and hence the greater becomes the electromagnetic radiation amplitude. These electromagnetic oscillations behave like surface vibrational optical waves, where positive charges move together in a diametrically opposite phase to the negative ones and decay exponentially into the material like Rayleigh waves. The resulting oscillating electric dipole is the source of the electromagnetic radiation. The pulse amplitude decays due to an interaction with bulk phonons and the life time of the measurable electric field varies between several to 100 μs (Bahat *et al.*, 2005). Random field fluctuations caused by charge separation have been observed in water-saturated porous media that were drained (Haas & Revil, 2009). Each charge separation in that system is thought to be caused by the burst of a meniscus in the pore space, the so-called *Haines jump*. The appli-

cation to direct current resistivity problems and the connection with the fluctuation-dissipation theorem is discussed elsewhere in more detail (Slob *et al.*, 2010).

4 CONCLUSION

The theory and numerical examples presented here show that the principle of Green's function extraction from field fluctuations can be applied to static problems. We illustrate this with an example from electrostatics, but we have shown elsewhere that the electrical conductivity tensor can be extracted from field fluctuations in a DC current problem (Slob *et al.*, 2010). Extending the theory for Green's function extraction from dynamic problems creates the possibility to extract the Green's function for potential fields and DC currents from field fluctuations. This makes it possible, in principle, to interrogate the properties of static fields in the subsurface without active sources. This is useful when active sources can not de deployed. Furthermore, extracting static fields from field fluctuations could make it possible to monitor the static fields in the subsurface in a continuous fashion. This can be a valuable tool for continuous monitoring. The spectacular examples of continuous monitoring from seismic noise (Wegler & Sens-Schönfelder, 2007; Brenguier *et al.*, 2008) offer hope that the principle of Green's function extraction can also be applied for continuous monitoring of quasi-static fields.

Acknowledgments. This research was financed by the NSF (grant EAS-0609595) and by the sponsors of the Consortium for Seismic Inverse Methods for Complex Structures at the Center for Wave Phenomena.

REFERENCES

Bahat, D., Rabinovitch, A., & Frid, V. 2005. *Tensile Fracturing in Rocks.* Berlin: Springer-Verlag.

Brenguier, F., Campillo, M., Hadziioannou, C., Shapiro, N.., & Larose, E. 2008. Postseismic relaxation along the San Andreas Fault at Parkfield from continuous seismological observations. *Science*, **321**, 1478–1481.

Curtis, A., Gerstoft, P., Sato, H., Snieder, R., & Wapenaar, K. 2006. Seismic interferometry – turning noise into signal. *The Leading Edge*, **25**, 1082–1092.

Derode, A., Larose, E., Tanter, M., de Rosny, J., Tourin, A., Campillo, M., & Fink, M. 2003. Recovering the Green's function from far-field correlations in an open scattering medium. *J. Acoust. Soc. Am.*, **113**, 2973–2976.

Haas, A., & Revil, A. 2009. Electrical burst signature of pore-scale displacements. *Water Resources Res.*, **45**, W10202.

Hogg, R.V., & Craig, T. 1978. *Introduction to mathematical statistics.* Fourth edn. New York: Macmillan.

Jackson, J.D. 1975. *Classical electrodynamics.* 2nd edn. New York: John Wiley.

Khesin, B., Alexeyev, V., & Eppelbaum, L. 1996. *Interpretation of geophysical fields in complicated environments.* London: Kluwer Academic Publishers.

Larose, E., Margerin, L., Derode, A., van Tiggelen, B., Campillo, M., Shapiro, N., Paul, A., Stehly, L., & Tanter, M. 2006. Correlation of random wavefields: an interdisciplinary review. *Geophysics*, **71**, SI11–SI21.

Sabra, K.G., Gerstoft, P., Roux, P., Kuperman, W.A., & Fehler, M.C. 2005. Surface wave tomography from microseisms in Southern California. *Geophys. Res. Lett.*, **32**, L14311.

Shapiro, N.M., Campillo, M., Stehly, L., & Ritzwoller, M.H. 2005. High-resolution surface-wave tomography from ambient seismic noise. *Science*, **307**, 1615–1618.

Slob, E., Snieder, R., & Revil, A. 2010. Retrieving electric resistivity data from self-potential measurements by cross-correlation. *Geophys. Res. Lett.*, **37**, L04308.

Snieder, R., E., Slob., & Wapenaar, K. 2010. Lagrangian Green's function extraction, with applications to potential fields, diffusion, and acoustic waves. *New J. Phys., in press.*

Stratton, Julius. A. 1941. *Electromagnetic theory.* New York: McGraw-Hill Book Company Inc.

Wapenaar, K., Fokkema, J., & Snieder, R. 2005. Retrieving the Green's function by cross-correlation: a comparison of approaches. *J. Acoust. Soc. Am.*, **118**, 2783–2786.

Wapenaar, K., Draganov, D., & Robertsson, J.O.A. (eds). 2008. *Seismic Interferometry: History and Present Status.* SEG Geophysics Reprints Series, vol. 26. Tulsa, OK: Society of Exploration Geophysics.

Wegler, U., & Sens-Schönfelder, C. 2007. Fault zone monitoring with passive image interferometry. *Geophys. J. Int.*, **168**, 1029–1033.

Seismic anisotropy in exploration and reservoir characterization: An overview

I. Tsvankin[1], J. Gaiser[2], V. Grechka[3], M. van der Baan[4], & L. Thomsen[5]

[1] *Colorado School of Mines, Department of Geophysics, Center for Wave Phenomena, Golden, CO, USA.*
[2] *Geokinetics, Denver, CO, USA.*
[3] *Shell Exploration & Production Company, Houston, TX, USA.*
[4] *University of Alberta, Department of Physics, CEB, 11322-89 Ave., Edmonton, Alberta, T6G 2G7, Canada.*
[5] *Delta Geophysics, Houston, TX, USA.*

ABSTRACT

Recent advances in parameter estimation and seismic processing have allowed incorporation of anisotropic models into a wide range of seismic methods. In particular, vertical and tilted transverse isotropy are currently treated as an integral part of velocity fields employed in prestack depth migration algorithms, especially those based on the wave equation. Here, we briefly review the state of the art in modeling, processing, and inversion of seismic data for anisotropic media. Topics include optimal parameterization, body-wave modeling methods, P-wave velocity analysis and imaging, processing in the τ–p domain, anisotropy estimation from vertical seismic profiling (VSP) surveys, moveout inversion of wide-azimuth data, amplitude-variation-with-offset (AVO) analysis, processing and applications of shear and mode-converted waves, and fracture characterization. When outlining future trends in anisotropy studies, we emphasize that continued progress in data-acquisition technology is likely to spur transition from transverse isotropy to lower anisotropic symmetries (e.g., orthorhombic). Further development of inversion and processing methods for such realistic anisotropic models should facilitate effective application of anisotropy parameters in lithology discrimination, fracture detection, and time-lapse seismology.

Key words: Seismic anisotropy, velocity analysis, prestack migration, parameter estimation, transverse isotropy, AVO analysis, multicomponent data, mode-converted waves, shear-wave splitting, fracture characterization, vertical seismic profiling

1 INTRODUCTION

The area of applied seismic anisotropy is undergoing rapid transformation and expansion. Whereas the theoretical foundation for describing anisotropic wave propagation had been developed a long time ago, the multiparameter nature of anisotropic models had precluded their widespread application in seismic exploration and reservoir monitoring. The role of anisotropy has dramatically increased over the past two decades due to advances in parameter estimation, the transition from poststack imaging to prestack depth migration, the wider offset and azimuthal coverage of 3D surveys, and acquisition of high-quality multicomponent data. Currently, many seismic processing and inversion methods operate with anisotropic models, and there is little doubt that in the near future anisotropy will be treated as an inherent part of velocity fields.

A detailed historical analysis of developments in seismic anisotropy can be found in Helbig and Thomsen (2005), so here we mention just several milestones. The work of Crampin (1981, 1985), Lynn and Thomsen (1986), Willis et al. (1986), Martin and Davis (1987), and others convincingly demonstrated that anisotropy has a first-order influence on shear and mode-converted PS-waves, which split into the fast and slow modes with orthogonal polarizations. Shear-wave processing

based on Alford (1986) rotation and its modifications has helped document ubiquitous azimuthal anisotropy in the upper crust typically caused by near-vertical systems of aligned fractures and microcracks. Acquisition and processing of high-quality multicomponent offshore surveys starting in the mid-1990's clearly showed that PP- and PS-wave sections could not be tied in depth without making the velocity model anisotropic.

In contrast, anisotropy-induced distortions in P-wave imaging (the focus of the majority of exploration surveys) are less dramatic, especially for poststack processing of narrow-azimuth, moderate-spread data. Also, incorporating anisotropy into velocity analysis requires estimation of several independent, spatially variable parameters, which may not be constrained by P-wave reflection traveltimes. Hence, the progress in P-wave processing can be largely attributed to breakthroughs in parameterization of transversely isotropic (TI) models, most notably the introduction of Thomsen (1986) notation and the discovery of the P-wave time-processing parameter η (Alkhalifah and Tsvankin, 1995). The exploding interest in anisotropy and the importance of the parameterization issue have made Thomsen's classical '86 article the top-cited paper ever published in the journal *Geophysics*.

More recently, the inadequacy of isotropic velocity models was exposed by the advent of prestack depth migration, which is highly sensitive to the accuracy of the velocity field. As a result, TI models with a vertical (VTI) and tilted (TTI) axis of symmetry have become practically standard in prestack imaging projects all over the world. For instance, anisotropic algorithms produce markedly improved images of subsalt exploration targets in the Gulf of Mexico, which has long been considered as a region with relatively "mild" anisotropy.

The goal of this paper is to give a brief description of the state of the art in anisotropic modeling, processing, and inversion and outline the main future trends. It is impossible to give a complete picture of the field in a journal article, and the selection of the material inevitably reflects the personal research experience and preferences of the authors. For in-depth discussion of theoretical and applied aspects of seismic anisotropy, we refer the reader to the books by Helbig (1994), Thomsen (2002), Tsvankin (2005), and Grechka (2009).

2 NOTATION FOR ANISOTROPIC MEDIA

One of the most critical issues in seismic data analysis for anisotropic media is a proper design of model parameterization. Whereas the stiffness coefficients (c_{ij}) are convenient to use in forward-modeling algorithms, they are not well-suited for application in seismic processing and inversion. An alternative notation for transverse isotropy was introduced by Thomsen (1986), who suggested to describe the medium by the symmetry-direction velocities of P- and S-waves (V_{P0} and V_{S0}, respectively) and three dimensionless parameters (ϵ, δ, and γ), which characterize the magnitude of anisotropy. The parameter ϵ is close to the fractional difference between the P-wave velocities in the directions perpendicular and parallel to the symmetry axis, so it defines what is often simplistically called the "P-wave anisotropy." Likewise, γ represents the same measure for SH-waves. While the definition of δ seems less transparent, this parameter also has a clear meaning – it governs the P-wave velocity variation away from the symmetry axis and also influences the SV-wave velocity.

Although Thomsen originally used the assumption of weak anisotropy (i.e., $|\epsilon| \ll 1$, $|\delta| \ll 1$, and $|\gamma| \ll 1$), his notation has since emerged as the best choice in seismic processing for TI media with *any* magnitude of velocity variations. Indeed, Thomsen parameters capture the combinations of the stiffness coefficients constrained by seismic signatures (for details, see Tsvankin, 2005). In particular, P-wave kinematics for TI media with a given symmetry-axis orientation depend on just three Thomsen parameters (V_{P0}, ϵ, and δ; the contribution of V_{S0} is negligible), rather than four stiffness coefficients (c_{11}, c_{33}, c_{13}, and c_{55}). Thomsen notation is especially convenient for reflection data processing because it greatly simplifies expressions for normal-moveout (NMO) velocity, quartic moveout coefficient, amplitude-variation-with-offset (AVO) response, and geometric spreading. Linearization of exact equations in ϵ, δ, and γ provides valuable insight into the influence of transverse isotropy on seismic wavefields and helps guide inversion and processing algorithms.

Moreover, the contribution of anisotropy to time-domain processing of P-wave reflection data for VTI media is absorbed by the single "anellipticity" parameter η close to the difference between ϵ and δ

$$[\eta \equiv (\epsilon - \delta)/(1 + 2\delta)] \, .$$

The interval values of η and the NMO velocity for horizontal reflectors [$V_{\rm nmo}(0)$] are sufficient to perform normal-moveout and dip-moveout corrections, prestack and poststack time migration for VTI models with a laterally homogeneous overburden (Alkhalifah and Tsvankin, 1995). Most importantly, the time-processing parameters $V_{\rm nmo}(0)$ and η can be estimated just from P-wave reflection traveltimes using NMO velocity of dipping events or nonhyperbolic moveout.

The parameters required for P-wave imaging and AVO analysis in VTI media are listed in Table 1. Whereas ϵ usually quantifies the magnitude of P-wave velocity variations, the parameters of more importance in seismic processing are δ and η. Laboratory measurements of the anisotropy parameters for sedimentary rocks from different regions are summarized by Wang (2002). Both rock-physics and seismic data indicate that vertical and tilted transverse isotropy in sedimentary basins are mostly associated with the intrinsic anisotropy of shales caused by aligned plate-shaped clay

Full set	Depth imaging	Time imaging	AVO (intercept, gradient)
V_{P0}	V_{P0}	$V_{\rm nmo}(0)$	V_{P0}
ϵ or η	ϵ or η	η	–
δ	δ	–	δ
V_{S0}	–	–	V_{S0}

Table 1. P-wave parameters for imaging and AVO analysis in VTI media. The parameter $V_{\rm nmo}(0) = V_{P0}\sqrt{1+2\delta}$ is the NMO velocity for horizontal reflectors.

particles. Many sedimentary formations including sands and carbonates, however, contain vertical or steeply dipping fracture sets and should be described by effective symmetries lower than TI, such as orthorhombic (see below). The effective anisotropy parameters are also influenced by fine layering on a scale small compared to seismic wavelength (Backus, 1962).

The principle of Thomsen notation has been extended to orthorhombic (Tsvankin, 1997; 2005), monoclinic (Grechka et al., 2000) and even the most general, triclinic (Mensch and Rasolofosaon, 1997) models. For instance, Tsvankin's notation for orthorhombic media preserves the attractive features of Thomsen parameters in describing the symmetry-plane velocities, traveltimes, and plane-wave reflection coefficients of P-, S_1-, and S_2-waves. It also reduces the number of parameters responsible for P-wave kinematics and provides a unified framework for treating orthorhombic and TI models in parameter-estimation methods operating with wide-azimuth, multicomponent data (Grechka et al., 2005).

Estimation of anisotropy from P-wave vertical seismic profiling (VSP) data acquired under a structurally complex overburden involves expressing the vertical slowness component in terms of the polarization direction. This problem, discussed in more detail below, leads to the definition of Thomsen-style anisotropy parameters specifically tailored to VSP applications (Grechka and Mateeva, 2007; Grechka et al., 2007).

Furthermore, Thomsen notation has been generalized for *attenuative* TI and orthorhombic media in order to facilitate analytic description and inversion of body-wave attenuation coefficients (Zhu and Tsvankin, 2006, 2007). For a model with VTI symmetry of both the real and imaginary parts of the stiffness matrix, this notation (in addition to Thomsen's velocity-anisotropy parameters) includes the vertical attenuation coefficients of P- and S-waves ($\mathcal{A}_{P0}$ and $\mathcal{A}_{S0}$) and three dimensionless parameters (ϵ_Q, δ_Q, and γ_Q) responsible for attenuation anisotropy. Linearization of the P-wave phase attenuation coefficient in the anisotropy parameters yields an expression that has exactly the same form as Thomsen's (1986) weak-anisotropy approximation for P-wave phase velocity.

Whereas the optimal choice of notation is a prerequisite for successful anisotropic parameter estimation and processing, it is also important in forward modeling, which is discussed next.

3 FORWARD MODELING OF BODY WAVES

The ability to compute synthetic seismograms has always been a high priority in geophysics since accurate forward modeling can be a valuable aid in seismic interpretation and inversion. Unfortunately, a fully anisotropic (triclinic) Earth is characterized by 21 stiffness coefficients (or Thomsen-style parameters) and density, all of which may vary in space.

Full-waveform modeling can be implemented by solving the wave equation for a general 3D (an)elastic medium using numerical techniques such as finite-difference, finite-element, pseudospectral and spectral-element methods (Kosloff and Baysal, 1982; Virieux, 1986; Komatitsch and Tromp, 1999). Although originally many of these approaches were developed for isotropic media, most have been extended to handle anisotropic, anelastic media (Carcione et al., 1988; Komatitsch et al., 2000); for a recent review, see Carcione et al. (2002).

Despite the constantly increasing computational power, full anisotropic (i.e., with 21 stiffnesses) modeling using the above techniques is still rarely attempted due to the scale of the problem and staggering number of possible models. In practice three avenues are commonly explored to facilitate interpretation and reduce computation demands: (i) simplifications to theory; (ii) reduction of information content in the acquired data; and (iii) limitations to considered structures, anisotropic symmetries, and/or medium types. For instance, seismic waves are often represented through rays, thereby invoking a high-frequency approximation (simplifications to theory). Also, one can choose to analyze traveltimes and/or amplitudes only (reduction in information content), treat only specific types of anisotropy, assume that wave motion can be described by P-wave propagation in acoustic media, and/or impose lateral continuity and consider only vertically heterogeneous struc-

tures (constraints on media and/or structures). Obviously, several approaches can be combined to develop an appropriate interpretation strategy.

The earliest efforts to compute body-wave synthetics in anisotropic media focused on either simulation of full waveforms for simple models with at most one interface (Buchwald, 1959; Lighthill, 1960) or traveltime calculations by means of geometric ray theory (Vlaar, 1968; Červený, 1972). The former efforts were motivated by the development of ultrasonic techniques for the measurement of dynamic elastic constants of pure crystals and metals (Musgrave, 1970; Auld, 1973). The latter approach was largely directed at explaining and understanding anomalous body-wave properties observed in refraction experiments and seismic arrays (Hess, 1964).

The ray method is a far-field, high-frequency, asymptotic approximation, which can handle laterally and vertically heterogeneous anisotropic media under the assumption that the medium parameters vary smoothly on the scale of wavelength. In addition to being much less computationally intensive than finite-difference schemes and similar numerical methods, ray theory makes it possible to model individual wave types rather than the whole wavefield. Ray tracing can be used to generate both traveltimes and amplitudes; yet serious difficulties arise (especially for amplitude computations) near singular areas, such as caustics, cusps and conical points on the wavefronts, shadow zones, and propagation directions for which the velocities of the split S-waves are close (Gajewski and Pšenčík, 1987). Some of these problems are related to wavefront folding when many rays pass through a common focal point or focal line – a phenomenon that complicates the evaluation of geometric spreading. Geometric ray theory also excludes head waves. Despite its limitations, ray theory is still at the heart of many migration algorithms that employ ray tracing for efficient generation of traveltime tables. A more detailed discussion of ray theory can be found in the paper by Carcione et al. (2002) and monographs by Červený (2001) and Chapman (2004).

The reflectivity method takes an alternative avenue to compute full-waveform synthetics in laterally homogeneous media (Kennett, 1983). The technique is based on plane-wave decomposition of point-source radiation combined with the solution of the plane-wave reflection/transmission problem for layered media obtained using so-called "propagator matrices" (Haskell, 1953; Gilbert and Backus, 1966). It can model both kinematic and dynamic properties of recorded wavefields including all primary and multiple reflections, conversions and head waves, as long as the 1D assumption (i.e., the elastic properties vary only with depth) is satisfied (Fuchs and Müller, 1971; Kennett, 1972). The anisotropic reflectivity method, originally developed for VTI models and symmetry-plane wave propagation (Keith and Crampin, 1977; Booth and Crampin, 1983), has been extended to azimuthally anisotropic media (Fryer and Frazer, 1984; Tsvankin and Chesnokov, 1990).

Despite its 1D model assumption, the reflectivity method has proved to be a valuable tool for understanding and interpreting wave-propagation phenomena in both VSP and surface-seismic acquisition geometries. For instance, Mallick and Frazer (1991) employ this technique to study P-wave amplitude variations with offset and azimuth in a medium containing vertical fractures and demonstrate how azimuthal amplitude anomalies can help reveal fracture orientation.

4 P-WAVE VELOCITY ANALYSIS AND IMAGING

Most isotropic time- and depth-migration algorithms [Kirchhoff, Stolt, phase-shift, phase-shift-plus-interpolation (PSPI), Gaussian beam, finite-difference, etc.] have been generalized for VTI and, in many cases, TTI media (e.g., Sena and Toksöz, 1993; Anderson et al., 1996; Alkhalifah, 1997; Ren et al., 2005; Zhu et al., 2007a). The key issue in anisotropic processing, however, is reliable estimation of the velocity model from reflection data combined with borehole and other information. The parameter η responsible for time processing in VTI media can be obtained by inverting either dip-dependent NMO velocity or nonhyperbolic (long-spread) reflection moveout (Alkhalifah and Tsvankin, 1995; Alkhalifah, 1997; Toldi et al., 1999; Fomel, 2004; Tsvankin, 2005; Ursin and Stovas, 2006). Then the η-field can be refined in the migrated domain using migration velocity analysis (Sarkar and Tsvankin, 2004) or reflection tomography (Woodward et al., 2008).

Building VTI velocity models in the depth domain typically requires *a priori* constraints because the vertical velocity V_{P0} and the parameters ϵ and δ can seldom be determined from P-wave reflection moveout alone. In many cases, V_{P0} is found from check shots or well logs at borehole locations and used in combination with the stacking (NMO) velocity to compute the parameter δ. Note that ignoring the contribution of δ to NMO velocity in isotropic processing leads to misties in time-to-depth conversion. Then the velocity field can be constructed by interpolating the parameters V_{P0} and δ between the boreholes and estimating η (and, therefore, ϵ) from reflection data. Integration of seismic and borehole data can be facilitated by applying geologic constraints in the process of interpretive model updating (Bear et al., 2005) or rec asting the generation of a dense anisotropic velocity field as an optimization problem. An efficient tool for building heterogeneous VTI models is postmigration grid tomography based on iterative minimization of residual moveout after prestack depth migration (Woodward et al., 2008).

Anisotropic migration with the estimated Thomsen parameters typically produces sections with better focusing and positioning of reflectors for a wide range

of dips including steep interfaces, such as flanks of salt domes. The 2D line in Figure 1 is used by Alkhalifah et al. (1996) to illustrate the improvements achieved by anisotropic time processing in offshore West Africa where thick TI shale formations cause serious imaging problems (Ball, 1995). For example, VTI dip-moveout and poststack migration algorithms succeeded in imaging the fault plane at midpoint 7.5 km and depth 3 km (the right arrow in Figure 1b), which is absent on the isotropic section (Figure 1a). Also, the major fault plane between the midpoints at 2 km and 8 km (it stretches up and down from the middle arrow in Figures 1a,b) and gently dipping reflectors throughout the section appear more crisp and continuous. Accurate fault imaging beneath the shales plays a major role in prospect identification in the area.

It is even more critical to properly account for anisotropy in prestack depth migration because the results of prestack imaging are highly sensitive to the quality of the velocity model. The section in Figure 2b was produced by applying VTI migration velocity analysis (MVA) and Kirchhoff prestack depth migration to the line from Figure 1 (Sarkar and Tsvankin, 2006). MVA was carried out by dividing the section into factorized VTI blocks, in which the parameters ϵ and δ are constant, while the velocity V_{P0} is a linear function of the spatial coordinates. Factorized VTI is the simplest model that allows for both anisotropy and heterogeneity and requires minimal *a priori* information to constrain the relevant parameters (Sarkar and Tsvankin, 2004). In the absence of pronounced velocity jumps across layer boundaries, knowledge of the vertical velocity at the top of a piecewise-factorized VTI medium is sufficient to estimate the parameters V_{P0}, ϵ, and δ along with the velocity gradients throughout the section using only P-wave data (Figures 3a,c,d).

The velocity analysis revealed significant lateral velocity gradients in some of the layers (Figure 3a), which could not be handled by time-domain techniques. As a result, the depth-domain parameter estimation produced a more reliable, laterally varying η-field (Figure 3b). The depth imaging facilitated structural interpretation of the deeper part of the section by removing the false dips seen in Figure 2a. Also, most antithetic faults that look fuzzy on the time section are well focused, and subhorizontal reflectors within the anisotropic layers are better positioned and stacked. This and many other published case studies demonstrate that a major advantage of anisotropic depth imaging is in providing accurate well ties without sacrificing image quality.

In tectonically active areas or in the presence of dipping fracture sets the symmetry axis of TI formations can be tilted, and the VTI model becomes inadequate. Tilted transverse isotropy is common in the Canadian Foothills, where shale layers are often bent and may have steep, variable dips (e.g., Vestrum et al., 1999).

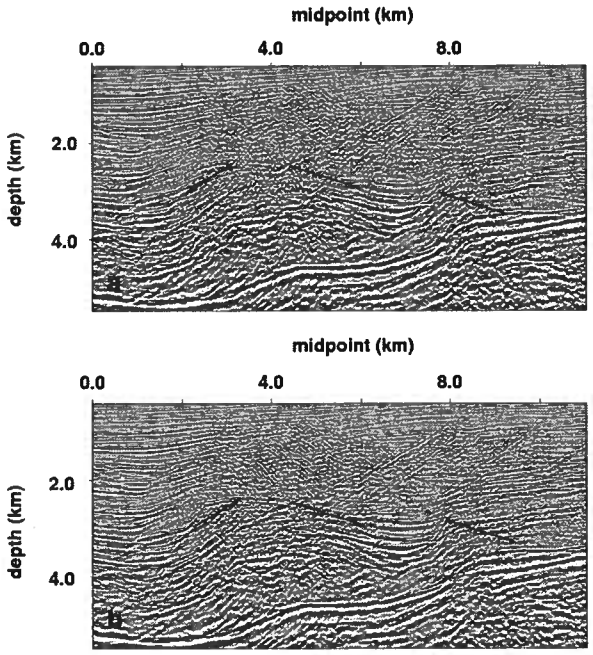

Figure 1. Comparison between isotropic and VTI time imaging (after Alkhalifah et al., 1996, and Sarkar and Tsvankin, 2006). A 2D line from West Africa after (a) isotropic and (b) anisotropic time imaging. The processing sequence included NMO and DMO corrections and poststack phase-shift time migration. Both time sections are stretched to depth. The arrows point to the main improvements achieved by taking anisotropy into account.

Also, uptilted shale layers near salt domes may cause serious difficulties in imaging steeply dipping segments of the salt flanks (Tsvankin, 2005). A detailed description of distortions caused by applying VTI algorithms to data from typical TTI media can be found in Behera and Tsvankin (2009), who extend MVA to TI models with the symmetry axis orthogonal to reflectors. In their case studies from the Gulf of Mexico, Huang et al. (2009) and Neal et al. (2009) demonstrate that accounting for the tilt of the symmetry axis produces significant improvements in imaging of steep dips, fault resolution, and spatial positioning of reflectors. The inadequacy of VTI models for many subsalt plays in the Gulf of Mexico has become especially apparent with acquisition of wide-azimuth surveys. In complicated structural environments, the full benefits of TI imaging can be realized with reverse time migration (RTM) based on solving the two-way wave equation (Huang et al., 2009). RTM with TTI or VTI velocity models is already widely used in GoM subsalt imaging projects.

Despite the recent successes, parameter estimation for heterogeneous TTI media remains a highly challenging problem, even with the common assumption that the symmetry axis is orthogonal to reflectors. Methods currently under development combine TI ray-based reflection tomography with check shots and walkaway VSP

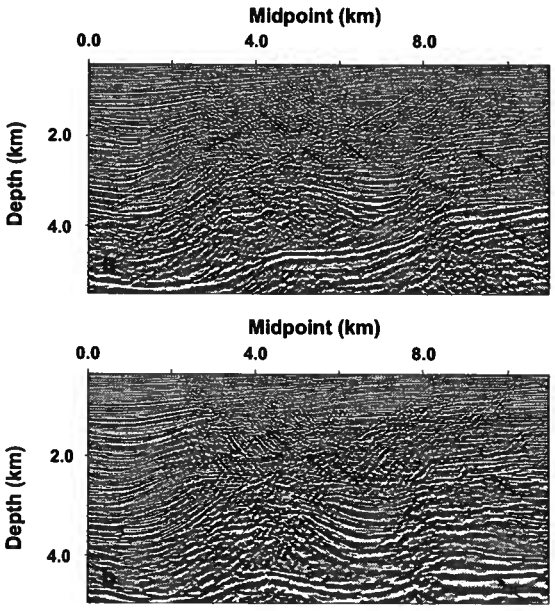

Figure 2. Comparison between VTI time and depth imaging (after Sarkar and Tsvankin, 2006). The line from Figure 1 after (a) anisotropic time processing (same as Figure 1b) and (b) anisotropic MVA and prestack depth migration. The arrows point to the main differences between the two sections.

surveys (e.g., Bakulin et al., 2009). It is likely that processing of high-quality wide-azimuth surveys in some a reas will require employing more complicated (but more realistic), orthorhombic velocity models. A promising direction for high-resolution anisotropic velocity analysis is full-waveform inversion, which so far has been developed mostly for acoustic models.

5 SLOWNESS-BASED PROCESSING AND INVERSION

Processing and inversion of surface seismic data is mostly done in the time-offset domain; yet other domains may offer advantages in terms of noise suppression and/or inversion for anisotropy parameters. It is especially beneficial to transform seismic data into the slowness domain, with applications as diverse as common-conversion-point sorting, anisotropy estimation, geometric-spreading correction, and amplitude and full-waveform inversion.

Snell's law states that the horizontal slowness p does not change along a ray in 1D models. This fact helps identify correlated pure-mode (PP) and converted (PS) reflections from the same interface that have common downgoing P-wave ray segments (and, therefore, the same horizontal slownesses). Identification of common ray segments leads to a straightforward common-conversion-point sorting scheme in both the time-offset and intercept time - horizontal slowness (τ-p) domains

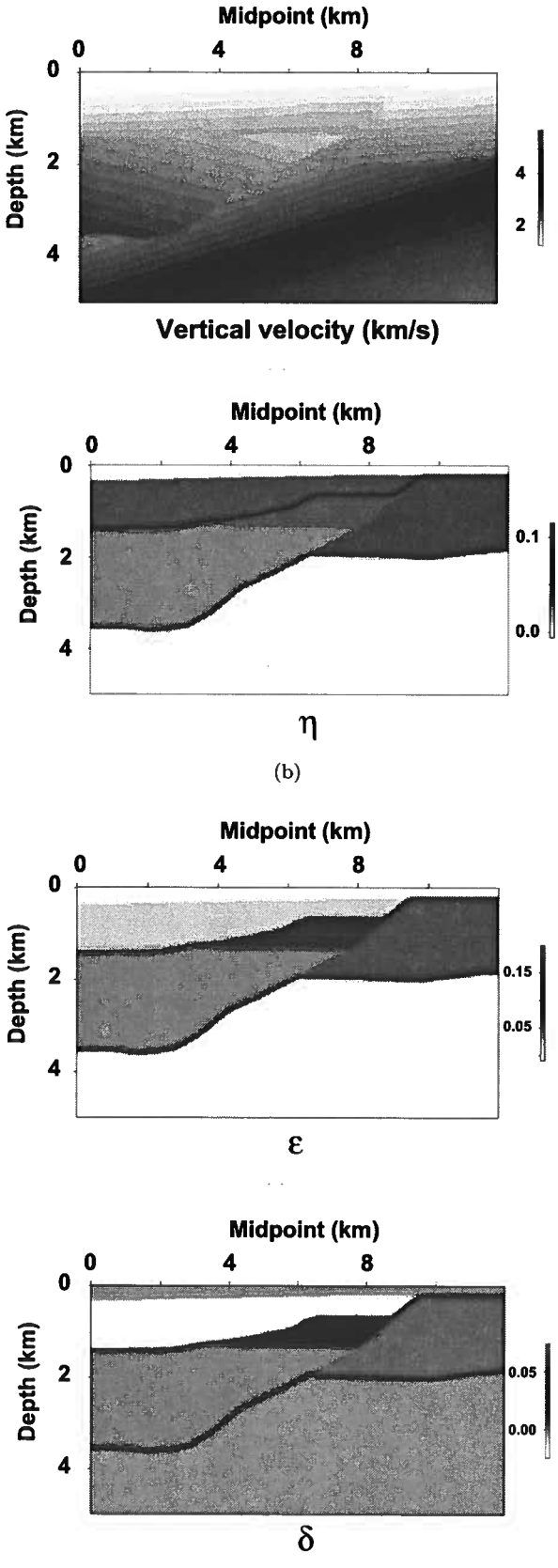

Figure 3. Estimated parameters (a) V_{P0}; (b) η; (c) ϵ; and (d) δ used to generate the depth-migrated section in Figure 2b (after Sarkar and Tsvankin, 2006).

(Van der Baan, 2005). In the presence of lateral and vertical velocity variations one can still identify PP and PS reflections with the same takeoff angles (i.e., the same horizontal slownesses) at the source by matching their time slopes in common-receiver gathers. This more general scheme called "PP+PS=SS" (discussed in more detail below) is designed to construct the traveltimes of pure-mode SS reflections solely from acquired PP- and PS-waves (Grechka and Tsvankin, 2002).

Slowness-based traveltime inversion can also increase the accuracy of interval parameter estimation. Anisotropic traveltime inversion is often based on moveout approximations that become unnecessary if seismic data are processed by means of a plane-wave decomposition, such as the τ-p transform. Indeed, plane-wave propagation is directly governed by phase rather than group velocities because the interval $\tau(p)$ curves represent rescaled versions of the slowness functions (Hake, 1986). Note that phase velocities generally are less complex mathematically compared to group velocities.

A τ-p domain approach has been applied by Gaiser (1990) to analysis of VSP data, by Hake (1986) and Van der Baan and Kendall (2002, 2003) to inversion of reflections traveltimes, and by Mah and Schmitt (2003) to processing of ultrasonic measurements. Similar gains in accuracy can be obtained by formulating slowness-based inversion algorithms directly in the time-offset domain (Douma and Van der Baan, 2008; Fowler et al., 2008; Dewangan and Tsvankin, 2006a; Wang and Tsvankin, 2009). It should be mentioned that the velocity-independent layer-stripping method of Dewangan and Tsvankin (2006a) is valid for an arbitrarily heterogeneous target horizon. An important feature of slowness-based algorithms is that they replace Dix-type differentiation of moveout parameters with traveltime stripping (Figure 4), which increases the accuracy and stability of interval parameter estimates.

Plane-wave decomposition also represents a convenient tool for geometric-spreading correction in horizontally layered media. Indeed, plane waves in 1D models are not subject to geometric spreading (in contrast to spherical waves); this is implicitly used in the reflectivity method discussed above (Fuchs and Müller, 1971; Kennett, 1983; Fryer and Frazer, 1984). Wang and McCowan (1989), Dunne and Beresford (1998) and Van der Baan (2004) explicitly employ plane-wave decomposition to remove the geometric-spreading factor from the amplitudes of all primary and multiple reflections (including mode conversions) simultaneously. Subsequent moveout correction and stacking in the τ-p domain (Stoffa et al., 1981, 1982) generates higher-quality stacked sections compared to those produced by the standard time-offset stacking process (Figure 5). Interestingly, stacking in the slowness domain preserves head waves suppressed by conventional processing (Van der Baan, 2004).

Finally, plane-wave decomposition may facilitate amplitude analysis at far offsets near and beyond the critical angle, where the wavefield in the time-offset domain cannot be described by plane-wave reflection coefficients (Van der Baan, 2004; Van der Baan and Smit, 2006; Tsvankin, 1995a). Thus, slowness-based processing and inversion has many advantages for data from anisotropic media. Indeed, it has been suggested in the literature that seismic inversion techniques should be applied to slant-stacked data obtained after a plane-wave decomposition (Müller, 1971; Fryer, 1980; Treitel et al., 1982). This approach is also suitable for full-waveform inversion in stratified media (Kormendi and Dietrich, 1991; Martinez and McMechan, 1991; Ji and Singh, 2005) and separation of interfering PP and PS waves (Van der Baan, 2006).

6 ANISOTROPY ESTIMATION FROM VSP DATA

The concept of operating with slowness measurements is also essential in processing of vertical seismic profiling surveys. Although anisotropic velocity models have to be built based on surface reflection data for most applications in seismic exploration, VSP can often provide useful complementary anisotropy estimates. Because those estimates are made at seismic frequencies, they have an important advantage over well-log anisotropy measurements, which pertain to the frequency range of $10^3 - 10^4$ Hz and require upscaling for use in seismic processing. The anisotropy parameters constrained by VSP data strongly depend on both the acquisition design and the magnitude of lateral heterogeneity of the overburden.

The simplest VSP experiment involves a single geophone placed in a well. First-break P-wave times picked from such VSP data reflect the influence of effective anisotropy between the earth's surface, where the seismic sources are located, and the geophone's depth. Because this depth is known, P-wave walkaway VSP data (or the combination of surface reflection data and check shots) for laterally homogeneous VTI media yield the effective Thomsen parameter δ. Whether or not it is possible to estimate another anisotropy parameter (η or ϵ) governing P-wave kinematics depends on the presence of sufficiently large offsets in the data. While the usefulness of such low-resolution anisotropy estimates might be questioned, P-wave traveltimes recorded in any VSP geometry help build an exact depth-migration operator suitable for constructing a subsurface image near the geophone.

The opposite "end member" is a wide-azimuth, multicomponent VSP survey recorded by a string of geophones placed beneath a laterally homogeneous overburden. Such VSP data make it possible to obtain a complete (triclinic) local stiffness tensor near the borehole. This is demonstrated by Dewangan and Grechka (2003) who apply the so-called slowness-polarization

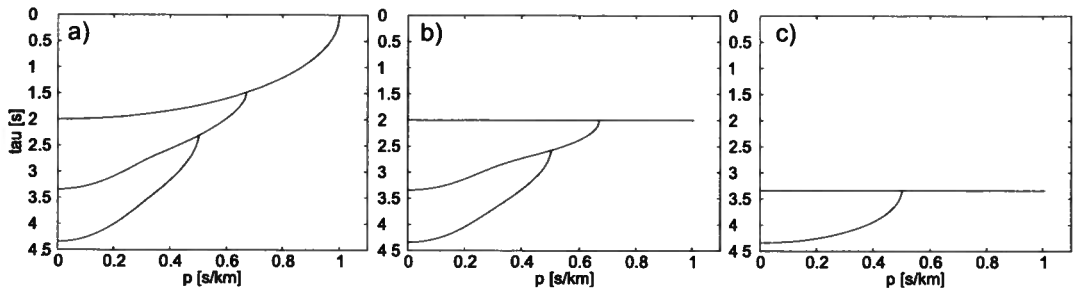

Figure 4. Layer stripping in the τ-p domain (after Van der Baan and Kendall, 2002). A hyperbolic moveout curve in the time-offset domain maps onto an ellipse in the τ-p domain, and nonhyperbolic moveout manifests itself by a deviation from the ellipse. (a) Moveout curves in the τ-p domain are created by summing the contributions of the individual layers. Removing the influence of (b) the top layer or (c) the two top layers yields the moveout in the corresponding interval. The first and third layers are isotropic, whereas the second layer is anisotropic, as evidenced by the strong deviation of its interval moveout from an ellipse on plot (b).

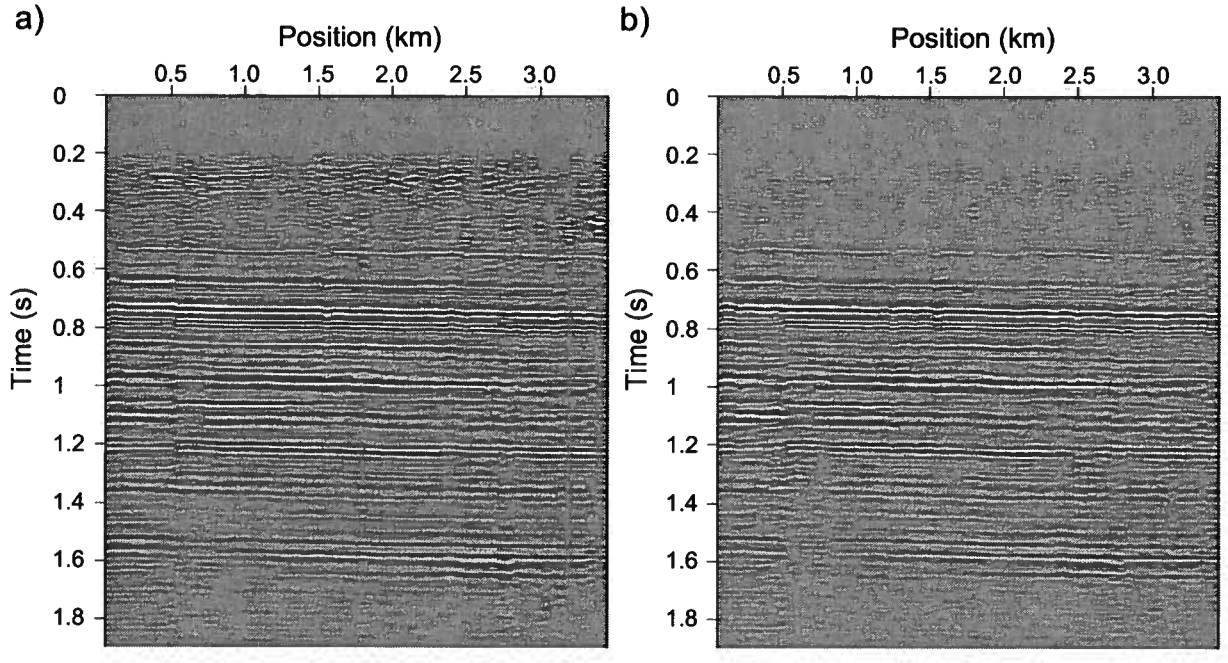

Figure 5. Comparison of stacking techniques on field data (after Van der Baan, 2004). (a) A conventional t-x stacked section after the geometric-spreading correction. (b) The same section obtained by stacking in the τ-p domain after applying plane-wave decomposition to remove geometric spreading. The two sections are structurally similar but τ-p processing produced a higher signal-to-noise ratio at small traveltimes and somewhat different reflector amplitudes between 1.3 s and 1.6 s.

method (White et al., 1983; de Parscau, 1991; Hsu et al., 1991; Horne and Leaney, 2000) to estimate anisotropy from the traveltimes and polarization directions of P-, S_1-, and S_2-waves recorded at Vacuum Field (New Mexico, USA). They conclude that the VSP measurements can be well-described by an orthorhombic model with a near-horizontal symmetry plane. Unfortunately, the slowness-polarization method can be successfully implemented only when lateral heterogeneity of the overburden is negligible. Then the horizontal slowness components, which are measured on common-receiver gathers and pertain to seismic sources at the earth's surface, can be used to reconstruct the slowness surface at geophone locations (Gaiser, 1990; Miller and Spencer, 1994; Jílek et al., 2003).

Strong lateral heterogeneity (for instance, due to the presence of salt in the overburden) renders reconstruction of the slowness surfaces inaccurate and often makes shear-wave arrivals too noisy for anisotropic inversion. Consequently, anisotropy has to be inferred from P-waves only, which leads to the introduction of Thomsen-style parameters for P-wave VSP inversion.

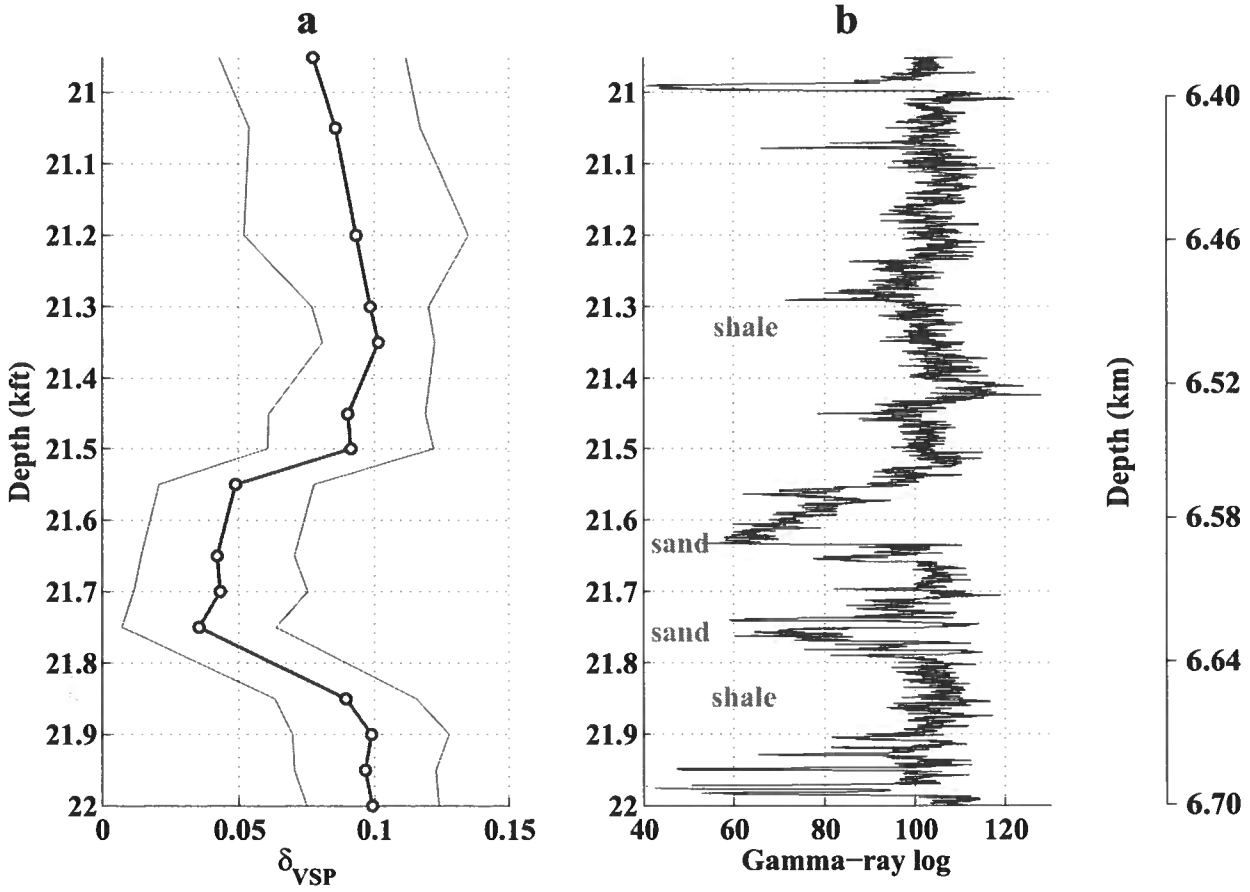

Figure 6. Comparison of (a) the anisotropy parameter δ_{VSP} (bold line) estimated from VSP for subsalt sediments in the Gulf of Mexico with (b) a gamma-ray log (after Grechka and Mateeva, 2007). The thin lines on plot (a) mark the standard deviation of δ_{VSP}.

The measured quantities include the P-wave vertical slowness component, q, expressed as a function of the polar (ψ) and azimuthal (φ) angles of the polarization vector. The values of q, ψ, and φ do not depend on the structural complexity of the overburden and correspond to the vicinity (with the spatial extent approximately equal to the wavelength) of downhole geophones. If the medium around the borehole is VTI, the vertical slowness q is independent of the polarization azimuth φ, and the weak-anisotropy approximation for $q(\psi)$ takes the form (Grechka and Mateeva, 2007)

$$q(\psi) = \frac{\cos\psi}{V_{P0}}\left(1 + \delta_{VSP}\sin^2\psi + \eta_{VSP}\sin^4\psi\right), \qquad (1)$$

where

$$\delta_{VSP} = \frac{\delta}{(V_{P0}/V_{S0})^2 - 1} \quad \text{and}$$

$$\eta_{VSP} = \eta\frac{(V_{P0}/V_{S0})^2 + 1}{(V_{P0}/V_{S0})^2 - 1} \qquad (2)$$

are the anisotropy parameters responsible for the P-wave slowness-of-polarization dependence.

The pairs $\{\delta_{VSP}, \eta_{VSP}\}$ and $\{\delta, \eta\}$ play comparable roles for processing of P-wave VSPs acquired along vertical boreholes and of P-wave surface reflection data, respectively, in VTI media. Indeed, equation 1 reveals that δ_{VSP} is responsible for the near-vertical variation of $q(\psi)$, while η_{VSP} governs the vertical slowness at larger polarization angles. Importantly, δ_{VSP} and η_{VSP} absorb the shear-wave velocity V_{S0}, rendering its value unnecessary for fitting the P-wave slowness-of-polarization functions. Grechka and Mateeva (2007) illustrate this point and present estimates of δ_{VSP} and η_{VSP} in a salt body and subsalt sediments in the deepwater Gulf of Mexico. Wheras the salt proved to be nearly isotropic, δ_{VSP} in the subsalt sediments exhibits a clear correlation with lithology (Figure 6). As is usually the case for the parameter δ, the value of δ_{VSP} is larger in shales than in a predominantly sandy interval.

This technique of anisotropy estimation from P-

wave VSP surveys has been extended to azimuthal anisotropy. For example, Grechka et al. (2007) invert wide-azimuth VSP data acquired at tight-gas Rulison Field (Colorado, USA) for Tsvankin's (1997) parameters of orthorhombic media and show that the estimated anisotropic model is consistent with the presence of gas-filled vertical fractures in a VTI host rock.

7 AZIMUTHAL MOVEOUT ANALYSIS

Azimuthal variation of traveltimes, amplitudes, and attenuation coefficients of reflected waves can provide valuable information about anisotropy associated with natural fracture systems, nonhydrostatic stresses, or dipping TI layers (e.g., Lynn et al., 1999; Rüger, 2002). Wide-azimuth P-wave data are often acquired on land for purposes of fracture characterization via azimuthal moveout and AVO analysis. The rapid advent of wide-azimuth offshore technology, designed primarily for better imaging of subsalt exploration targets, is expected to further stimulate development of processing algorithms for azimuthally anisotropic models.

Moveout analysis of wide-azimuth, conventional-spread data is based on the concept of the NMO ellipse and on the generalized Dix-type averaging equations (Grechka and Tsvankin, 1998; Grechka et al., 1999). The normal-moveout velocity of pure (non-converted) reflected waves expressed as a function of the azimuth α of the CMP line is given by the following quadratic form:

$$V_{\rm nmo}^{-2}(\alpha) = W_{11}\cos^2\alpha + 2\,W_{12}\sin\alpha\cos\alpha + W_{22}\sin^2\alpha, \qquad (3)$$

where $\mathbf{W}$ is a symmetric 2×2 matrix determined by the medium properties around the zero-offset ray. If the traveltime increases with offset in all azimuthal directions (i.e., in the absence of reverse move out), $V_{\rm nmo}(\alpha)$ traces out an *ellipse* even for arbitrarily anisotropic, heterogeneous media. Furthermore, equation 3 can be applied to mode-converted waves, if their moveout in CMP geometry is symmetric with respect to zero offset (this is the case for horizontally layered models with a horizontal symmetry plane).

The equation of the NMO ellipse provides a simple way to correct for the azimuthal variation in stacking velocity often ignored in conventional processing. Even more importantly, the semiaxes and orientation of the NMO ellipse can be used in anisotropic parameter estimation and fracture characterization. A critical issue in moveout analysis of wide-azimuth data is separation of the influence of anisotropy and lateral heterogeneity (in the form of velocity gradients, dipping interfaces, velocity lenses, etc.) on reflection traveltimes (e.g., Jenner, 2009).

A data-driven correction of the NMO ellipse for lateral velocity variation in horizontally layered media is suggested by Grechka and Tsvankin (1999), who present a complete processing sequence for azimuthal moveout inversion that also includes 3D "global" semblance analysis and generalized Dix differentiation of effective NMO ellipses. They show that the orientation of the P-wave interval NMO ellipses produced by this methodology in the Powder River Basin (Wyoming, USA) is well-correlated with the depth-varying fracture trends in the field.

P-wave azimuthal moveout analysis has proved to be effective in predicting the dominant fracture orientation in many other exploration regions (e.g., Corrigan et al., 1996; Lynn et al., 1999; Tod et al., 2007). Jenner (2001), who has developed a trace-correlation approach for estimating the NMO ellipse, shows that the fast NMO-velocity direction at Weyburn field in Canada is aligned with the dominant fracture strike and the polarization vector of the fast S-wave; this implies that the medium symmetry is HTI or orthorhombic. Still, in some cases the NMO ellipse is rotated with respect to the shear-wave polarization directions, which may indicate the presence of lower symmetries.

Since the P-wave NMO ellipse constrains only three combinations of the medium parameters, its inversion for the physical properties of fractures (e.g., fracture compliances) suffers from ambiguity, which can be reduced by using the NMO ellipses of the split S-waves, nonhyperbolic moveout, or other (amplitude, borehole) information. For instance, joint inversion of the NMO ellipses of P- and S-waves with *a priori* constraints helps build even orthorhombic and monoclinic velocity models (Grechka et al., 2000; Vasconcelos and Grechka, 2007); more details are given in the section on fracture characterization.

Among the first to recognize the benefits of employing nonhyperbolic (long-spread) reflection moveout in anisotropic parameter estimation was Sena (1991), whose analytic traveltime expressions for multilayered, weakly anisotropic media are based upon the "skewed" hyperbolic moveout formulation of Byun et al. (1989). Long-spread, wide-azimuth P-wave traveltime in azimuthally anisotropic media can be accurately described by generalizing the nonhyperbolic moveout equations of Tsvankin and Thomsen (1994) and Alkhalifah and Tsvankin (1995) originally designed for VTI media. Vasconcelos and Tsvankin (2006) develop a moveout-inversion algorithm for horizontally layered orthorhombic media based on the extended Alkhalifah-Tsvankin equation:

$$t^2(x,\alpha) = t_0^2 + \frac{x^2}{V_{\rm nmo}^2(\alpha)} - \frac{2\eta(\alpha)\,x^4}{V_{\rm nmo}^2(\alpha)\left[t_0^2\,V_{\rm nmo}^2(\alpha) + (1+2\eta(\alpha))\,x^2\right]}, \qquad (4)$$

where t_0 is the zero-offset time, $V_{\rm nmo}(\alpha)$ is the NMO ellipse (equation 3), and $\eta(\alpha)$ is the azimuthally varying anellipticity parameter. Equation 5 can be combined

with the velocity-independent layer-stripping method (Dewangan and Tsvankin, 2006a) to compute the interval traveltime in the target layer and estimate the interval NMO ellipse and anellipticity parameters $\eta^{(1)}$, $\eta^{(2)}$, and $\eta^{(3)}$ (Wang and Tsvankin, 2009). Nonhyperbolic moveout inversion of wide-azimuth data not only represents a promising fracture-characterization technique (see the case study in Vasconcelos and Tsvankin, 2006), but also provides the input parameters for P-wave time imaging and geometric-spreading correction in layered orthorhombic media.

8 PRESTACK AMPLITUDE ANALYSIS

Angle-dependent reflection and transmission coefficients contain valuable information about the local medium properties on both sides of an interface. Therefore, analysis of amplitude variations with incidence angle (usually called AVO – amplitude variation with offset) and/or azimuth is often used in reservoir characterization. Because reflection coefficients are determined by the elastic properties averaged on the scale of seismic wavelength, AVO analysis can achieve a much higher vertical resolution than traveltime methods.

Exact equations for plane-wave reflection coefficients are cumbersome even for isotropy and, therefore, rarely used in processing. Whereas exact reflection coefficients for VTI media and symmetry planes of orthorhombic media can still be obtained in closed form (Daley and Hron, 1977; Rüger, 2002), for lower symmetries it is necessary to apply computational schemes (e.g., Fryer and Frazer, 1984; Jílek, 2002a,b). Important insight into anisotropic reflectivity is provided by linearized weak-contrast, weak-anisotropy approximations, which have a much simpler form and often reduce the number of free parameters. The approximate P-wave reflection coefficient for VTI media depends on the contrasts in the vertical P- and S-wave velocities (V_{P0} and V_{S0}), density, and the parameters δ and ϵ (Banik, 1987; Thomsen, 1993; Rüger, 1997). Although the contribution of δ distorts the AVO gradient, the P-wave AVO signatures in isotropic and VTI media are generally similar, which complicates amplitude inversion for the five independent parameters. Indeed, as shown by de Nicolao et al. (1993), only two parameters can be resolved from the isotropic reflection coefficient.

Analysis of azimuthal amplitude variations shows considerably more promise, in particular for estimation of dominant fracture directions in naturally fractured (e.g., tight-gas and tight-oil) reservoirs (Mallick and Frazer, 1991; Gray et al., 2002). Linearized P-wave reflection coefficients were derived for HTI media and symmetry planes of orthorhombic media by Rüger (1997, 1998) and for arbitrary anisotropy by Vavryčuk and Pšenčík (1998); for details, see Rüger's (2002) comprehensive monograph. Application of these analytic expressions in quantitative AVO inversion, however, is hindered by nonuniqueness in parameter estimation. Instead, it is more common to reconstruct the azimuthal variation (which is close to elliptical) of the magnitude of the AVO gradient (Gray et al., 2002; Hall and Kendall, 2003). For HTI and orthorhombic media, the extrema of the AVO gradient lie in the orthogonal vertical symmetry planes of the model.

If azimuthal anisotropy is caused by one set of vertical fractures, the maximum AVO gradient may be either parallel or perpendicular to the fractures, which generally leads to a 90°-uncertainty in the fracture azimuth. Despite this ambiguity, the azimuthally varying P-wave AVO response has been successfully used for estimating the dominant fracture orientation and, in some cases, mapping "sweet spots" of intense fracturing (e.g., Gray et al., 2002; Gray and Todorovic-Marinic, 2004; Xu and Tsvankin, 2007). For instance, Hall and Kendall (2003) demonstrate that the direction of the minimum AVO gradient at Valhall field is well-aligned with faults inferred from coherency analysis (Figure 7).

For HTI and orthorhombic media with a single fracture set, the difference between the symmetry-plane AVO gradients is proportional to the fracture density (which is close to the shear-wave splitting parameter) and also depends on the fracture infill (Rüger, 2002). Therefore, even for such simple models the inversion of the P-wave AVO gradient for the fracture properties is generally nonunique. In principle, fracture density and saturation can be constrained by combining the P-wave AVO response and NMO ellipse, but this approach is applicable only to relatively thick, weakly heterogeneous reservoirs (e.g., Xu and Tsvankin, 2007). Additional complications may be caused by multiple fracture sets (which lower the symmetry to at least orthorhombic) and the presence of fractures on both sides of the target reflector. For such realistic fractured reservoirs, it is highly beneficial to employ multicomponent data in azimuthal AVO analysis (Bakulin et al., 2000; Jílek, 2002a,b; DeVault et al., 2002). In particular, Jílek (2002b) presents a methodology for joint nonlinear AVO inversion of wide-azimuth PP and PS reflections for TI and orthorhombic media.

Another interesting possibility is to combine azimuthal AVO and attenuation analysis, which helps remove the uncertainty in estimating the fracture orientation for HTI media (Clark et al., 2009). Furthermore, body-wave attenuation coefficents are highly sensitive to anisotropy and fracturing and may potentially provide powerful fracture-characterization attributes (Chapman, 2003; Zhu et al., 2007b; Chichinina et al., 2009; Maultzsch et al., 2009). On the other hand, in some cases azimuthally varying attenuation (if unaccounted for) may distort the AVO signature. Efficient velocity-independent techniques for estimating interval offset- and azimuth-dependent attenuation from frequency-domain reflection amplitudes are suggested by Behura and Tsvankin (2009) and Reine et al. (2009).

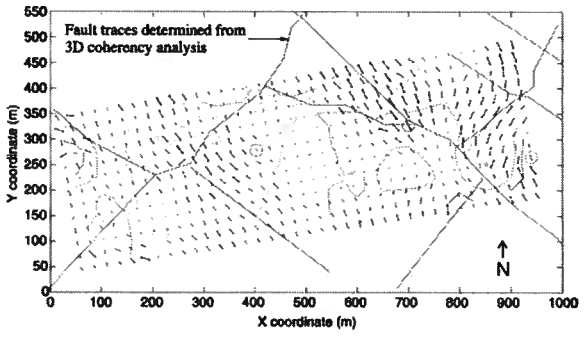

Figure 7. Application of P-wave azimuthal AVO analysis to fracture detection at Valhall field (after Hall and Kendall, 2003). The fracture azimuths (ticks) estimated from the azimuthally varying AVO gradient for the top-chalk horizon are compared with interpreted fault traces. Note the general alignment of fractures with large-scale faulting, especially near the faults trending from northwest to southeast. In the southeast corner, fractures also appear to be perpendicular to the surface curvature defined by the time contours (the contours are plotted at 20-ms intervals, with the red color indicating deeper areas).

AVO analysis is designed to operate with the plane-wave reflection coefficient at the target interface. The recorded amplitude of reflected waves, however, also depends on the source/receiver directivity and such propagation factors as geometric spreading, transmission coefficients, and attenuation (Martinez, 1993; Maultzsch et al., 2003). Anisotropic layers in the overburden focus or defocus seismic energy like an optical lens, thus distorting the amplitude distribution along the wavefront and causing pronounced angle variations of geometric spreading (Tsvankin, 1995b, 2005; Stovas and Ursin, 2009). In that case, robust reconstruction of the angle-dependent reflection coefficient requires an anisotropic geometric-spreading correction.

Geometric spreading in the time-offset domain is related to the convergence or divergence of ray beams (Gajewski and Pšenčík, 1987) and, therefore, can be computed directly from the spatial derivatives of traveltime (Vanelle and Gajewski, 2003). This ray-theory result is exploited in the moveout-based geometric-spreading correction devised for horizontally layered VTI models by Ursin and Hokstad (2003) and extended to wide-azimuth, long-spread PP and PS data from azimuthally anisotropic media by Xu and Tsvankin (2006, 2008). In particular, this correction has proved to be essential in azimuthal AVO analysis of reflections from the bottom of relatively thick fractured reservoirs (Xu and Tsvankin, 2007).

On the whole, recent developments have laid the groundwork for transforming anisotropic AVO analysis into a valuable reservoir-characterization tool.

9 PROCESSING AND APPLICATIONS OF MULTICOMPONENT DATA

Early applications of shear-wave seismology had to cope with erratic and unpredictable data quality and misties between SS-wave reflections at the intersection of 2D acquisition lines (Lynn and Thomsen, 1986; Willis et al., 1986). This caused serious difficulties in generating interpretable shear-wave sections and using multicomponent data in lithology discrimination and fracture characterization. Alford (1986) suggested that these problems are related to shear-wave splitting due to azimuthal anisotropy and proposed simple rotation operators to transform SS data into two principal sections containing the fast and slow modes. Likewise, Martin and Davis (1987) discuss the need to rotate converted PS-waves acquired for fracture-characterization purposes at Silo Field (Colorado, USA).

Shear waves in anisotropic media exhibit birefringence (shear-wave splitting) and travel as two separate modes with different velocities and orthogonal (for the same phase direction) polarizations. If the medium is HTI or orthorhombic with a horizontal symmetry plane, the vertically traveling split S-waves are polarized in the symmetry planes of the model. The magnitude of shear-wave splitting at vertical incidence is described by the parameter $\gamma^{(S)}$, which is close to the fractional difference between the velocities of the fast (S_1) and slow (S_2) modes and can be estimated as $\gamma^{(S)} \approx (t_s - t_f)/t_f$, where t_s and t_f are the traveltimes of the waves S_2 and S_1, respectively. After separating the split shear waves on prestack data, it may be possible to evaluate their NMO ellipses and AVO signatures.

9.1 Pure-mode SS-waves

Processing surface shear-wave data for azimuthal anisotropy analysis has primarily involved 1D compensation for splitting at near-vertical propagation directions. Alford's (1986) rotation algorithm operates on four-component, stacked (supposed to be equivalent to zero-offset) data excited by two orthogonal sources and recorded by two orthogonal receivers. Data can be acquired on a 2D line, with sources and receivers oriented parallel (inline) and perpendicular (crossline) to the acquisition azimuth. The four recorded S-wave displacement components can be represented in the form of the following 2×2 matrix:

$$\mathbf{D} = \begin{pmatrix} D_{XX} & D_{XY} \\ D_{YX} & D_{YY} \end{pmatrix}, \tag{5}$$

where X denotes inline and Y crossline; the first letter in the subscript refers to the source orientation, and the second letter to the receiver orientation. Prestack shear-wave data depend on the anisotropic velocity field and have polarization properties controlled by the azimuth of the line with respect to the symmetry planes. However, stacking or performing AVO inversion of 4C data

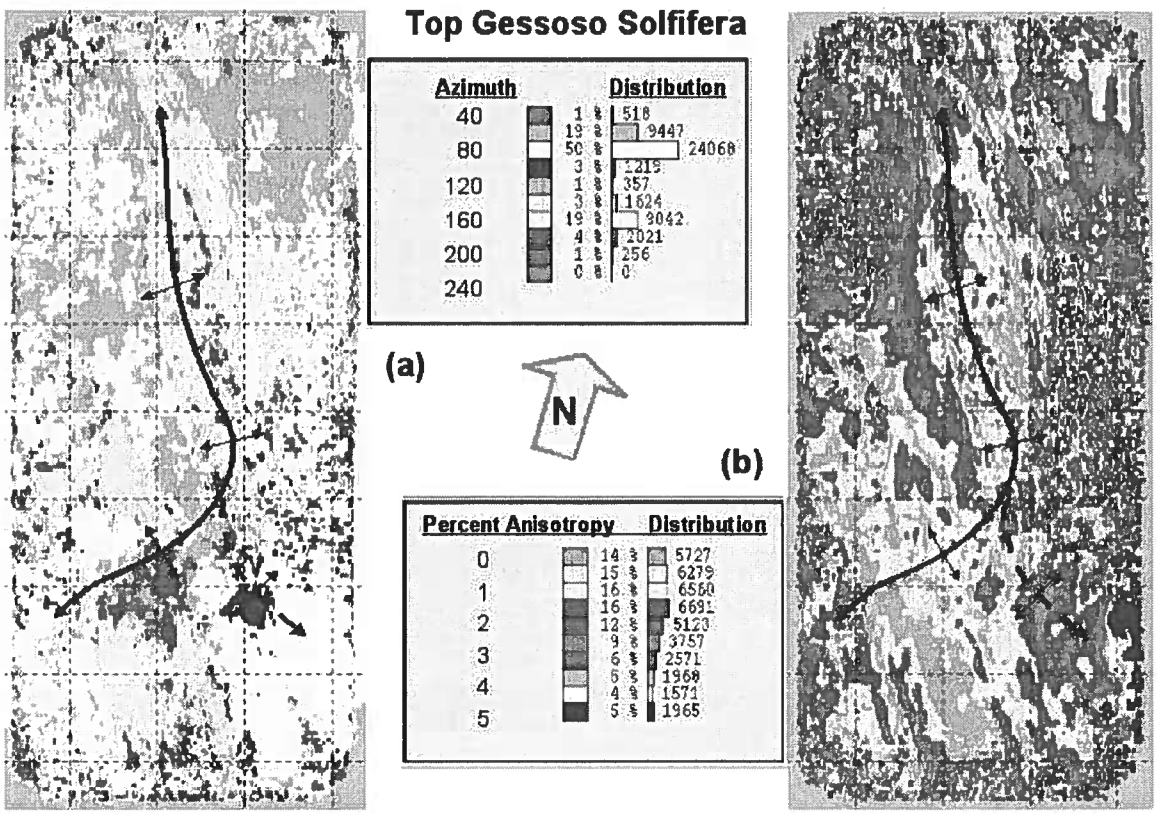

Figure 8. (a) Polarization azimuth of the PS_1-wave and (b) the shear-wave splitting coefficient (in percent) above the Gessoso Solfifera formation at Emilio Field (after Gaiser et al., 2002). The north direction is rotated about 15° clockwise.

can provide an estimate of the difference between the normal-incidence reflection coefficients (i.e., AVO intercepts) of the split S-waves, which is governed by the parameter $\gamma^{(S)}$ regardless of the original propagation azimuth.

Thus, even for 2D acquisition geometry, pure shear modes can yield information about azimuthal anisotropy. When the acquisition line is parallel to a vertical symmetry plane and the medium is laterally homogeneous, no reflection energy should be present on the off-diagonal components in equation 5. Out-of-plane (obliquely oriented) lines, however, may contain significant coherent energy on D_{XY} and D_{YX}. Alford's (1986) 4C operator simultaneously rotates the sources and receivers in order to estimate the symmetry-plane azimuths and traveltime difference between the fast and slow S-waves:

$$\mathbf{D}' = \mathbf{R}_S \, \mathbf{D} \, \mathbf{R}_R^T, \qquad (6)$$

where $\mathbf{R}$ is a 2×2 matrix of rotation around the vertical axis for sources ($\mathbf{R}_S$) and receivers ($\mathbf{R}_R$), and T denotes transpose. Rotation is applied to each CDP consisting of a 4C group of traces. For a certain rotation angle that corresponds to the minimum energy on the off-diagonal components D'_{XY} and D'_{YX}, the data appear as if they were acquired in one of the symmetry planes. This means that the diagonal components, D'_{XX} and D'_{YY}, correspond to the fast and slow shear waves and can be processed to estimate the splitting coefficient.

The 4C rotation dramatically improves the quality of shear-wave reflection data and makes them suitable for lithology discrimination (Alford, 1986). By combining Alford rotation of VSP data with layer stripping, Winterstein and Meadows (1991) evaluate S-wave splitting related to in-situ stress and fractures at Cymric and Railroad Gap oil fields (California, USA). Whereas Alford's method assumes the principal anisotropy directions (i.e., the azimuths of the symmetry planes) to be invariant with depth, Winterstein and Meadows (1991) identify well-resolved, abrupt changes in the splitting coefficient at several depth levels that could be important for reservoir characterization. Thomsen et al. (1999) extend the layer-stripping technique to reflected S-waves and discuss the analytic basis for separating the split shear modes on both 4C and 2C (single-source) data.

There have been numerous successful applications of shear-wave splitting for purposes of fracture characterization (e.g., Mueller, 1990; Crampin, 2003; Vasconcelos and Grechka, 2007). Traveltime and amplitude dif-

ferences between the fast and slow shear waves, as well as their NMO ellipses, can help estimate fracture orientation, density and, in some cases, make inferences about fluid saturation. Also, Angerer et al. (2000) show that shear-wave splitting is a more sensitive time-lapse (4D) indicator of pressure changes in response to CO_2 injection than P-wave velocities. Their synthetic seismograms based on the anisotropic poroelastic theory of Zatsepin and Crampin (1997) match stacked data before and after injection. Terrell et al. (2002) arrive at similar conclusions in their time-lapse study of CO_2 flood at Weyburn Field in Canada. There is little doubt that moveout and amplitude inversion of multicomponent, multiazimuth data offers the best hope of estimating the anisotropy parameters of subsurface formations.

9.2 Mode-converted PS-waves

The majority of multicomponent surveys is acquired without shear-wave sources, so the reflected wavefield is largely composed of compressional waves and mode-converted PS-waves. The most prominent P-to-S conversion typically happens at the reflector; such PS events are sometimes called "C-waves" (Thomsen, 1999). For horizontally layered, azimuthally isotropic media converted PS-waves are polarized in the incidence (sagittal) plane (i.e., they result from P-to-SV conversion). However, if the incident P-wave propagates outside vertical symmetry planes of azimuthally anisotropic media, the reflected PS-wave splits into the fast (PS_1) and slow (PS_2) modes, neither of which is generally polarized in the sagittal plane (e.g., Jílek, 2002a).

An important processing step for mode conversions in the presence of azimuthal anisotropy is rotation of receiver directions from an acquisition coordinate system to a source-centered, radial and transverse coordinate system (Gaiser, 1999). This procedure reveals azimuthal traveltime variations of PS_1- and PS_2-waves on the stacked radial components, as well as polarity reversals in the principal anisotropy directions on the stacked transverse components (Li and MacBeth, 1999).

Similar to pure-mode SS reflections, the fast and slow PS-waves have to be separated for further processing. The feasibility of PS-wave splitting analysis is demonstrated by Garotta and Granger (1988) who analyze the amplitude ratios of the transverse and radial components and apply 2C rotation and layer stripping. Gaiser (1997) shows that Alford rotation and layer stripping (a method similar to that of Winterstein and Meadows, 1991), are applicable to PS-waves in reverse VSP geometry. His technique operates with 4C data from equation 5 where the two rows correspond to source-receiver azimuths 90° apart. The principle of Alford rotation is extended to wide-azimuth PS-wave surveys by Dellinger et al. (2002) who replace stacking of PS_1 and PS_2 reflections with an appropriately designed tensor migration. Their results from Valhall Field are mixed, which suggests that azimuthal and lateral velocity variations may seriously complicate PS-wave processing. Recently there has been renewed interest in developing a more formal inversion approach to the PS-wave layer-stripping problem where the objective function is formulated in terms of the PS_1-wave polarization azimuth and the traveltime difference between the split PS-waves (e.g., Bale et al., 2009; Haacke et al., 2009; Simmons, 2009).

In addition to such well-documented applications as imaging beneath gas clouds and lithology discrimination, mode-converted data provide valuable attributes for fracture/stress characterization (Gaiser, 2000). After performing layer stripping of 3D ocean-bottom-cable (OBC) PS-wave data over Valhall Field, Olofsson et al. (2002) describe a dramatic "ring of anisotropy" in the overburden where the PS_1-wave is polarized transversely around the production platform. The correlation of this anisotropy pattern with sea-floor subsidence caused by the reservoir collapse after years of production suggests that shear waves are highly sensitive to local, deformation-induced stresses. Sensitivity of the polarization direction of the PS_1-wave to local stresses over anticlines has also been observed at Emilio Field in the Adriatic Sea (Gaiser et al., 2002), and at Pinedale Field in Wyoming, USA (Gaiser and Van Dok, 2005). As illustrated by Figure 8, the PS_1-wave at Emilio Field is polarized parallel to the crest of a doubly plunging anticline (thick black arrows), where anisotropy is generally higher.

Finally, it is important to note that the moveout asymmetry of PS-waves (i.e., their traveltime generally does not stay the same when the source and receiver are interchanged) helps constrain the parameters of tilted TI media (Dewangan and Tsvankin, 2006b) and characterize dipping (non-vertical) fracture sets (Angerer et al., 2002).

9.3 Joint processing of PP and PS data

Conventional isotropic processing of high-quality multicomponent offshore OBC surveys routinely produces depth misties between PP and PS sections, in large part due to the strong influence of anisotropy on PS-wave moveout. The high sensitivity of mode conversions to anisotropy represents an asset for joint anisotropic inversion of PP and PS data (e.g., Grechka et al., 2002a; Foss et al., 2005). For example, the parameters V_{P0}, ϵ, and δ influence the kinematics of both P- and SV-waves in TI media, which underscores the importance of multicomponent data in anisotropic velocity analysis.

Widespread use of converted waves, however, is hindered not just by the higher acquisition cost of multicomponent surveys, but also by difficulties in PS-wave processing. Such properties of mode conversions as moveout asymmetry, reflection point dispersal, and polarity reversals present significant challenges

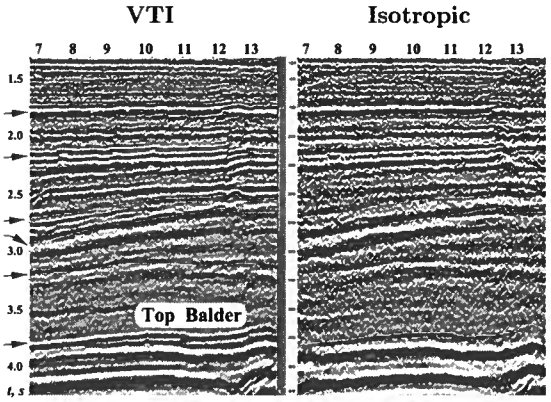

Figure 9. Common-conversion-point stacks of PSV-waves for a 2D line above the Siri reservoir in the North Sea (after Grechka et al., 2002b). Acquired PP- and PSV-waves were processed using the PP+PS=SS method to compute the traveltimes of the corresponding SS (SVSV) reflections. The section on the left was computed with a VTI velocity model obtained from stacking-velocity tomography of the recorded PP-waves and constructed SS-waves. The section on the right was produced without taking anisotropy into account.

for velocity-analysis and imaging algorithms. These problems motivated the development of the so-called "PP+PS=SS" method designed to construct primary SS (in general, both S_1 and S_2) reflections with the correct kinematics from PP and PS data (Grechka and Tsvankin, 2002). The key idea of the method, which operates on PP and PS reflections acquired in split-spread geometry, is to match the time slopes (horizontal slownesses) of PP- and PS-waves on common-receiver gathers. This procedure helps identify PP and PS events reflected at the same (albeit unknown) subsurface points, and the SS-wave traveltime can be obtained as a simple linear combination of the PP and PS times. To avoid time picking, Grechka and Dewangan (2003) devised the full-waveform (interferometric) version of the PP+PS=SS method based on a specially designed convolution of PP and PS traces.

Although the PP+PS=SS method should be preceded by PP-PS event registration, it does not require information about the velocity field and is valid for arbitrarily anisotropic, heterogeneous media. The moveouts of the recorded PP-waves and computed SS-waves can be combined in anisotropic velocity analysis using, for example, 3D stacking-velocity tomography (Grechka et al., 2002a). The case study from the North Sea in Figure 9 demonstrates that this methodology greatly improves the quality of PS-wave stacked sections (Grechka et al., 2002b). Application of the PP+PS=SS method followed by VTI processing provided a much better image of the reservoir top (top Balder, the deepest arrow on the left) and a crisp picture of faulting in the shallow layers. Accounting for anisotropy also boosted higher frequencies in the stack and, therefore, increased temporal resolution.

10 FRACTURE CHARACTERIZATION

By some estimates, fractured reservoirs contain about one-third of the world's hydrocarbon reserves. Since aligned fractures create velocity and attenuation anisotropy on the scale of seismic wavelength, seismic fracture characterization is largely based on the anisotropic processing/inversion methods discussed above.

In the past few years, significant progress has been achieved both in effective media theories and seismic characterization of multiple fracture sets. The theoretical advances are mainly attributed to increased computing power, which made it possible to construct so-called digital rocks and examine how such realistic features as crack intersections, shape irregularities, microcorrugation, and partial contacts of the fracture faces influence the effective elastic properties. It has been shown that multiple sets of irregular, possibly intersecting fractures that have random shape irregularities are well approximated by isolated, penny-shaped cracks (Grechka and Kachanov, 2006, and references therein).

Another important result, known from theoretical studies of Kachanov (1980, 1993) and confirmed numerically by Grechka et al. (2006), is that multiple, arbitrarily oriented sets of fractures embedded in an otherwise isotropic host rock yield an effective medium of approximately orthorhombic symmetry. This statement is valid for both dry and liquid-filled fractures. The former are close to so-called scalar cracks (in terminology of Schoenberg and Sayers, 1995), which always yield effective orthotropy (i.e., orthorhombic symmetry) in the non-interaction approximation. The latter contribute mainly to shear-wave anisotropy (i.e., to parameters analogous to the splitting coefficient $\gamma^{(S)}$) and also do not produce any substantial deviations from orthorhombic symmetry.

The closeness of the effective elasticity of cracked solids to orthotropy implies that multiple systems of fractures appear to long (compared to the fracture sizes) seismic waves as three orthogonal or principal sets. For instance, N sets of dry fractures that have the individual crack densities $e^{(k)}$ and the normals $\boldsymbol{n}^{(k)}$ $(k = 1, \ldots, N)$ to the fracture faces are equivalent to three "principal" sets, whose densities and orientations are found as the eigenvalues and eigenvectors of the crack-density tensor (Kachanov, 1980, 1993):

$$\alpha_{ij} = \sum_{k=1}^{N} e^{(k)} n_i^{(k)} n_j^{(k)}, \quad (i, j = 1, 2, 3). \tag{7}$$

Vasconcelos and Grechka (2007) employ this theory to characterize multiple vertical fracture sets from wide-azimuth, multicomponent seismic reflection data

recorded at Rulison Field. The fracture orientations obtained from seismic data are consistent with the FMI (Formation MicroImager) log acquired in the study area. In addition, Vasconcelos and Grechka (2007) construct an orthorhombic velocity model of the Rulison reservoir by jointly inverting P- and S-wave NMO ellipses. This inversion is possible primarily because crack-induced orthotropy is governed by fewer independent parameters than general orthorhombic media, making estimation of these parameters better posed and ea sier to implement. Still, comparison of the spatially varying crack densities with the estimated ultimate recovery (EUR) of the available wells shows little correlation. This problem, typical for a number of other tight-gas fields in North America, should motivate further development of robust seismic technologies capable of detecting accumulations of hydrocarbons in fractured formations.

11 THE ROAD AHEAD

Progress in geophysics is usually driven by data; whenever we acquire a new type of data, we can expect to discover unexpected features that cannot be handled by existing methodologies. In hindsight, these surprises should have been foreseen (and maybe were foreseen by a few savants), but they always do surprise most of us.

Today, the industry routinely acquires high-quality wide-azimuth 3D marine data with the goal of better illuminating subsalt targets. When processing such data, we are discovering that azimuthally variable seismic velocity is often required to flatten the wide-azimuth image gathers. This will surely lead us to further develop methods dealing with azimuthal anisotropy, which have been applied primarily to land data sets. Also, it is already clear that horizontal transverse isotropy (HTI) is not an appropriate model for most formations with vertical cracks, and TTI is probably an oversimplified symmetry for dipping beds. Future developments will include extension of velocity-analysis and migration algorithms to more realistic orthorhombic models. Although a solid foundation for parameter estimation and imaging in orthorhombic media has already been built, finding robust and cost-effective processing solutions is a serious challenge, especially for tilted orthotropy. Also, it would not be practical to operate with a parameter set that is not constrained by available seismic data. Another direction of future research with a high potential payoff in velocity analysis is anisotropic full-waveform inversion of reflection data, which should become feasible with continuing increase in computing power.

An interesting feature of anisotropy is that, although usually it is weak (i.e., the dimensionless anisotropy parameters typically are much smaller than unity), in many contexts it has a strong influence on seismic data. In particular, the contribution of anisotropy to reflection coefficients is comparable to the isotropic "fluid" and "lithology" factors, which is particularly noticeable in the azimuthally varying P-wave AVO response. Anisotropy in the overburden also causes pronounced distortions in the geometric-spreading factor for reflected waves. Hence, it is easy to predict that more emphasis will be placed on understanding and utilizing amplitude signatures in anisotropic media, likely including attenuation measurements. Experimental data indicate that attenuation anisotropy, especially that produced by fluid-saturated fractures, may be orders of magnitude higher than velocity anisotropy. Therefore, azimuthally varying (and, possibly, frequency-dependent) attenuation coefficients may provide sensitive reservoir-characterization attributes.

Anisotropic phenomena are especially noticeable in shear and mode-converted wavefields; it is usually impossible to deal with shear data without considering anisotropy. In so doing, completely new concepts (unknown in isotropy) arise, such as shear-wave splitting. For example, acquisition of high-quality PS-wave data in recent years revealed strong conversion of energy (P-to-S) at near-normal incidence, which is prohibited by the standard model of plane-wave reflection from a planar boundary between isotropic or VTI halfspaces. Some of candidate explanations of these anomalous PS arrivals involve anisotropy (e.g., tilted TI on either side of the reflector). Whatever the eventual solution to this problem, it will likely entail a revision of conventional AVO models and algorithms for both PP- and PS-waves. Also, wide-azimuth, multicomponent data will play a major role in robust parameter estimation for realistic orthorhombic and, in some cases, lower-symmetry media. Note that the split shear-wave primary reflections (S_1 and S_2) with the correct kinematics can be generated from wide-azimuth PP and PS data using the 3D version of the PP+PS=SS method.

Whereas anisotropic P-wave imaging essentially amounts to looking "past" anisotropy at exploration targets, progress in processing/inversion techniques is putting more emphasis on employing anisotropy parameters as attributes in reservoir characterization and lithology discrimination. One of interesting emerging applications of anisotropic attributes is in time-lapse seismic for compacting reservoirs because the shear-wave splitting coefficient, traveltime shifts and other compaction-related signatures are strongly influenced by stress-induced anisotropy. Physical characterization of the subsurface in terms of lithology, fluids, fractures, pore pressure, and permeability will require improved rock-physics and geomechanics methods operating with anisotropic models.

12 ACKNOWLEDGMENTS

We are grateful to our numerous colleagues for their contributions discussed in the paper and for fruitful discussions that improved our understanding of the subject.

We appreciate the reviews by K. Helbig, A. Rüger and A. Stovas, who made a number of helpful suggestions. I.T. acknowledges the support of the Center for Wave Phenomena at Colorado School of Mines.

REFERENCES

Alford, R. M., 1986, Shear data in the presence of azimuthal anisotropy: 56th Annual International Meeting, SEG, Expanded Abstracts, 476–479.

Alkhalifah, T., 1997, Seismic data processing in vertically inhomogeneous TI media: Geophysics, **62**, 662–675.

Alkhalifah, T., and I. Tsvankin, 1995, Velocity analysis for transversely isotropic media: Geophysics, **60**, 1550–1566.

Alkhalifah, T., I. Tsvankin, K. Larner, and J. Toldi, 1996, Velocity analysis and imaging in transversely isotropic media: Methodology and a case study: The Leading Edge, **15**, 371–378.

Anderson, J. E., T. Alkhalifah, and I. Tsvankin, 1996, Fowler DMO and time migration for transversely isotropic media: Geophysics, **61**, 835–844.

Angerer, E., S. Crampin, X-Y. Li, and T. L. Davis, 2000, Time-lapse seismic changes in a CO_2 injection process in a fractured reservoir: 70th Annual International Meeting, SEG, Expanded Abstracts, 1532–1535.

Angerer, E., S. A. Horne, J. E. Gaiser, R. Walters, S. Bagala, and L. Vetri, 2002, Characterization of dipping fractures using PS mode-converted data: 72nd Annual International Meeting, SEG, Expanded Abstracts, 1010–1013.

Auld, B. A., 1973, Acoustic fields and waves in solids: J. Wiley and Sons.

Backus, G. E., 1962, Long-wave elastic anisotropy produced by horizontal layering: Journal of Geophysical Research, **67**, 4427–4440.

Bakulin, A., V. Grechka, and I. Tsvankin, 2000, Estimation of fracture parameters from reflection seismic data – Parts I, II, and III: Geophysics, **65**, 1788–1830.

Bakulin, A., M. Woodward, D. Nichols, K. Osypov, and O. Zdraveva, 2009, Building TTI depth models using anisotropic tomography with well information: 79th Annual International Meeting, SEG, Expanded Abstracts, Paper TOM 2.6.

Bale, R., B. Gratakos, B. Mattocks, S. Roche, K. Poplavskii, and X. Li, 2009, Shear wave splitting applications for fracture analysis and improved imaging: Some onshore examples: First Break, **27**, 73–83.

Ball, G., 1995, Estimation of anisotropy and anisotropic 3-D prestack migration, offshore Zaire: Geophysics, **60**, 1495–1513.

Banik, N. C., 1987, An effective parameter in transversely isotropic media: Geophysics, **52**, 1654–1664.

Bear, L. K., T. A. Dickens, J. R. Krebs, J. Liu, and P. Traynin, 2005, Integrated velocity model estimation for improved positioning with anisotropic PSDM: The Leading Edge, **24**, 622–626.

Behera, L., and I. Tsvankin, 2009, Migration velocity analysis for tilted transversely isotropic media: Geophysical Prospecting, **57**, 13–26.

Behura, J., and I. Tsvankin, 2009, Estimation of interval anisotropic attenuation from reflection data: Geophysics, **74**, no. 6, A69–A74.

Booth, D. C., and S. Crampin, 1983, The anisotropic reflectivity method: Theory: Geohysical Journal of the Royal Astronomical Society, **72**, 755–766.

Buchwald, V., 1959, Elastic waves in anisotropic media: Proceedings of the Royal Society of London A, **235**, 563–580.

Byun, B. S., D. Corrigan, and J. E. Gaiser, 1989, Anisotropic velocity analysis for lithology discrimination: Geophysics, **54**, 1564–1574.

Carcione, J., D. Kosloff, and R. Kosloff, 1988, Wave-propagation simulation in anelastic anisotropic (transversely isotropic) solid: Mech. Appl. Math., **41**, 319–345.

Carcione, J., G. C. Herman, and A. P. E. ten Kroode, 2002, Seismic modeling: Geophysics, **67**, 1304–1325.

Červený, V., 1972, Seismic rays and ray intensities in inhomogeneous anisotropic media: Geophysical Journal of the Royal Astronomical Society, **29**, 1–13.

———, 2001, Seismic ray theory: Cambridge University Press.

Chapman, C. H., 2004, Fundamentals of seismic wave propagation: Cambridge University Press.

Chapman, M., 2003, Frequency-dependent anisotropy due to mesoscale fractures in the presence of equant porosity: Geophysical Prospecting, **51**, 369–379.

Chichinina, T., I. Obolentseva, L. Gik, B. Bobrov, and G. Ronquillo-Jarillo, 2009: Attenuation anisotropy in the linear-slip model: Interpretation of physical modeling data: Geophysics, **74**, no. 5, WB165–WB176.

Clark, R. A., P. M. Benson, A. J. Carter, and C. A. Guerrero Moreno, 2009, Anisotropic P-wave attenuation measured from a multi-azimuth surface seismic reflection survey: Geophysical Prospecting, **57**, 835–845.

Corrigan, D., R. Withers, J. Darnall, and T. Skopinski, 1996, Fracture mapping from azimuthal velocity analysis using 3-D surface seismic data: 66th Annual International Meeting, SEG, Expanded Abstracts, 1834–1837.

Crampin, S., 1981, A review of wave motion in anisotropic and cracked elastic media: Wave Motion, **3**, 343–391.

Crampin, S., 1985, Evaluation of anisotropy by shear-wave splitting: Geophysics, **50**, 142–152.

Crampin, S., 2003, The New Geophysics: Shear-wave splitting provides a window into the crack-critical rock mass: The Leading Edge, **22**, 536–549.

Daley, P., and F. Hron, 1977, Reflection and transmission coefficients for transversely isotropic media: Bulletin of the Seismological Society of America, **67**, 661–675.

Dellinger, J., S. Brandsberg-Dahl, R. Clarke, and L. Thomsen, 2002, Alford rotation after tensor migration: 72nd Annual International Meeting, SEG, Expanded Abstracts, 982–985.

de Nicolao, A., G. Drufuca, and F. Rocca, 1993, Eigenvectors and eigenvalues of linearized elastic inversion: Geophysics, **58**, 670–679.

de Parscau, J., 1991, P- and SV-wave transversely isotropic phase velocity analysis from VSP data: Geophysical Journal International, **107**, 629–638.

DeVault, B., T. L. Davis, I. Tsvankin, R. Verm, and F. Hilterman, 2002, Multicomponent AVO analysis, Vacuum field, New Mexico: Geophysics, **67**, 701–710.

Dewangan, P., and V. Grechka, 2003, Inversion of multicomponent, multiazimuth, walkaway VSP data for the stiffness tensor: Geophysics, **68**, 1022–1031.

Dewangan, P., and I. Tsvankin, 2006a, Velocity-independent layer stripping of PP and PS reflection traveltimes: Geophysics, **71**, no. 4, U59–U65.

———, 2006b, Modeling and inversion of PS-wave moveout asymmetry for tilted TI media: Part 1 – Horizontal TTI layer: Geophysics, **71**, no. 4, D107–D122.

Douma, H., and M. Van der Baan, 2008, Rational interpolation of qP-traveltimes for semblance-based anisotropy estimation in layered vti media: Geophysics, **73(4)**, D53–D62.

Dunne, J., and G. Beresford, 1998, Improving seismic data quality in the Gippsland Basin (Australia): Geophysics, **63**, 1496–1506.

Fomel, S., 2004, On anelliptic approximations for qP velocities in VTI media: Geophysical Prospecting, **52**, 247–259.

Foss, S.-K., B. Ursin, and M. V. de Hoop, 2005, Depth-consistent reflection tomography using PP and PS seismic data: Geophysics, **70**, U51–U65.

Fowler, P. J., A. Jackson, J. Gaffney, and D. Boreham, 2008, Direct nonlinear traveltime inversion in layered VTI media: 78th Annual International Meeting, SEG, Expanded Abstracts, 3028–3032.

Fryer, G. J., 1980, A slowness approach to the reflectivity method for seismogram synthesis: Geophysical Journal of the Royal Astronomical Society, **63**, 747–758.

Fryer, G. J., and L. N. Frazer, 1984, Seismic waves in stratified anisotropic media: Geophysical Journal of the Royal Astronomical Society, **78**, 691–710.

Fuchs, K. and G. Müller, 1971, Computation of synthetic seismograms with the reflectivity method and comparison with observations: Geophysical Journal of the Royal Astronomical Society, **23**, 417–433.

Gaiser, J. E., 1990, Transversely isotropic phase velocity analysis from slowness estimates: Journal of Geophysical Research, **95**, 241–254.

———, 1997, 3-D converted shear wave rotation with layer stripping: U.S. Patent 5,610,875.

———, 1999, Enhanced PS-wave images and attributes using prestack azimuth processing: 69th Annual International Meeting, SEG, Expanded Abstracts, 699–702.

———, 2000, Advantages of 3-D PS-wave data to unravel S-wave birefringence for fracture detection: 70th Annual International Meeting, SEG, Expanded Abstracts, 1201–1204.

Gaiser, J. E., and R. Van Dok, 2005, Borehole calibration of PS-waves for fracture characterization: Pinedale field, Wyoming: 75th Annual International meeting, SEG, Expanded Abstracts, 873–876.

Gaiser, J. E., E. Loinger, H. Lynn, and L. Vetri, 2002, Birefringence analysis at Emilio field for fracture characterization: First Break, **20**, 505–514.

Gajewski, D., and I. Pšenčík, 1987, Computation of high-frequency seismic wavefields in 3-D laterally inhomogeneous anisotropic media: Geophysical Journal of the Royal Astronomical Society, **91**, 383–411.

Garotta, R., and P. Y. Granger, 1988, Acquisition and processing of 3C×3D data using converted waves: 58th Annual International Meeting, SEG, Expanded Abstracts, 995–998.

Gilbert, F., and G. E. Backus, 1966, Propagator matrices in elastic wave and vibration theory: Geophysics, **31**, 326–332.

Gray, F. D., and D. Todorovic-Marinic, 2004, Fracture detection using 3D azimuthal AVO: CSEG Recorder, **29**, 5–8.

Gray, F. D., G. Roberts, and K. J. Head, 2002, Recent advances in determination of fracture strike and crack density from P-wave seismic data: The Leading Edge, **21**, 280–285.

Grechka, V., 2009, Applications of seismic anisotropy in the oil and gas industry: European Association of Geoscientists and Engineers.

Grechka, V., and P. Dewangan, 2003, Generation and processing of pseudo shear-wave data: Theory and case study: Geophysics, **68**, 1807–1816.

Grechka, V., and M. Kachanov, 2006, Effective elasticity of fractured rocks: A snapshot of the work in progress: Geophysics, **71**, W45–W58.

Grechka, V., and A. Mateeva, 2007, Inversion of P-wave VSP data for local anisotropy: Theory and a case study: Geophysics, **72**, D69–D79.

Grechka, V., and Tsvankin, I., 1998, 3-D description of normal moveout in anisotropic inhomogeneous media: Geophysics, 63, 1079–1092.

———, 1999, 3-D moveout inversion in azimuthally anisotropic media with lateral velocity variation: Theory and a case study: Geophysics, **64**, 1202–1218.

———, 2002, PP+PS=SS: Geophysics, **67**, 1961–1971.

Grechka, V., P. Contreras, and I. Tsvankin, 2000, Inversion of normal moveout for monoclinic media: Geophysical Prospecting, **48**, 577–602.

Grechka, V., A. Pech, and I. Tsvankin, 2002a, Multicomponent stacking-velocity tomography for transversely isotropic media: Geophysics, **67**, 1564–1574.

———, 2005, Parameter estimation in orthorhombic

media using multicomponent wide-azimuth reflection data: Geophysics, **70**, no. 2, D1–D8.

Grechka, V., I. Tsvankin, and J. K. Cohen, 1999, Generalized Dix equation and analytic treatment of normal-moveout velocity for anisotropic media: Geophysical Prospecting, **47**, 117–148.

Grechka, V., I. Vasconcelos, and M. Kachanov, 2006, The influence of crack shape on the effective elasticity of fractured rocks: Geophysics, **71**, D153–D160.

Grechka, V., I. Tsvankin, A. Bakulin, C. Signer, and J. O. Hansen, 2002b, Anisotropic inversion and imaging of PP and PS reflection data in the North Sea: The Leading Edge, **21**, No. 1, 90–97.

Grechka, V., A. Mateeva, G. Franco, C. Gentry, P. Jorgensen, and J. Lopez, 2007, Estimation of seismic anisotropy from P-wave VSP data: The Leading Edge, **26**, No. 6, 756–759.

Haacke, R. R., G. K. Westbrook, and S. Peacock, 2009, Layer stripping of shear-wave splitting in marine PS-waves: Geophysical Journal International, **176**, 782–804.

Hake, H., 1986, Slant stacking and its significance for anisotropy: Geophysical Prospecting, **34**, 595–608.

Hall, S., and J. M. Kendall, 2003, Fracture characterization at Valhall: Application of P-wave amplitude variation with offset and azimuth (AVOA) analysis to a 3-D ocean-bottom data set: Geophysics, **68**, 1150–1160.

Haskell, N. A., 1953, The dispersion of surface waves on multilayer media: Bulletin of the Seismological Society of America, **43**, 17–34.

Helbig, K., 1994, Foundations of elastic anisotropy for exploration seismics: Pergamon Press.

Helbig, K., and L. Thomsen, 2005, 75+ years of anisotropy in exploration and reservoir seismics: A historical review of concepts and methods: Geophysics, **70**, 9ND–23ND.

Hess, H. H., 1964, Seismic anisotropy of the uppermost mantle under oceans: Nature, **203**, 629–631.

Horne, S., and S. Leaney, 2000, Short note: Polarization and slowness component inversion for TI anisotropy: Geophysical Prospecting, **48**, 779–788.

Hsu, K., M. Schoenberg, and J. Walsh, 1991, Anisotropy from polarization and moveout: 61st Annual International Meeting, SEG, Expanded Abstracts, 1526–1529.

Huang, T., Y. Zhang, H. Zhang, and J. Young, 2009, Subsalt imaging using TTI reverse time migration: The Leading Edge, **28**, No. 4, 448–452.

Jenner, E., 2001, Azimuthal anisotropy of 3-D compressional wave seismic data, Weyburn field, Saskatchewan, Canada: Ph.D. thesis, Colorado School of Mines.

———, 2009, Data example and modelling study of P-wave azimuthal anisotropy potentially caused by isotropic velocity heterogeneity: First Break, **27**, 45–50.

Ji, Y., and S. C. Singh, 2005, Anisotropy from full waveform inversion of multicomponent seismic data using a hydrid optimization method: Geophysical Prospecting, **53**, 435–445.

Jílek, P., 2002a, Converted PS-wave reflection coefficients in weakly anisotropic media: Pure and Applied Geophysics, **159**, 1527–1562.

———, 2002b, Modeling and inversion of converted-wave reflection coefficients in anisotropic media: A tool for quantitative AVO analysis: Ph.D. thesis, Colorado School of Mines.

Jílek, P., B. Hornby, and A. Ray, 2003, Inversion of 3D VSP P-wave data for local anisotropy: A case study: 73rd Annual Meeting, Society of Exploration Geophysics, Expanded Abstracts, 1322–1325.

Kachanov, M., 1980, Continuum model of medium with cracks: Journal of the Engineering Mechanics Division, ASCE, **106** (EM5), 1039–1051.

———, 1993, Elastic solids with many cracks and related problems: in Hutchinson, J. W. and Wu, T. (editors), Advances in Applied Mechanics, **30**, 259–445.

Keith, C. M. and S. Crampin, 1977, Seismic body waves in anisotropic media: Synthetic seismograms: Geohysical Journal of the Royal Astronomical Society, **49**, 225–243.

Kennett, B. L. N., 1972, Reflections, rays, and reverberations: Bulletin of the Seismological Society of America, **64**, 1685–1696.

———, 1983, Seismic wave propagation in stratified media: Cambridge University Press.

Komatitsch, D., and J. Tromp, 1999, Introduction to the spectral-element method for 3-D seismic wave propagation: Geophysical Journal International, **139**, 806–822.

Komatitsch, D., C. Barnes, and J. Tromp, 2000, Simulation of anisotropic wave propagation based upon a spectral element method: Geophysics, **65**, 1251–1260.

Kormendi, F., and M. Dietrich, 1991, Nonlinear waveform inversion of plane-wave seismograms in stratified elastic media: Geophysics, **56**, 664–674.

Kosloff, D., and E. Baysal, 1982, Forward modeling by the Fourier method: Geophysics, **47**, 1402–1412.

Li, X.-Y., and C. MacBeth, 1999, Fracture detection with marine P-S mode conversion: Proceedings of the Offshore Technology Conference, Houston, TX, Paper no. 10941-MS.

Lighthill, M. J., 1960, Study of magneto-hydrodynamic waves and other anisotropic wave motions: Philosophical Transactions of the Royal Society of London, A, **252**, 397–430.

Lynn, H. B., and L. Thomsen, 1986, Shear wave exploration along the principal axis: 56th Annual International Meeting, SEG, Expanded Abstracts, 474–476.

Lynn, H. B., D. Campagna, K. M. Simon, and W. E. Beckham, 1999, Relationship of P-wave seismic attributes, azimuthal anisotropy, and commercial gas pay in 3-D P-wave multiazimuth data, Rulison Field, Piceance Basin, Colorado: Geophysics, **64**, 1293–1311.

Mah, M., and D. R. Schmitt, 2003, Determination of

complete elastic stiffnesses from ultrasonic phase velocity measurements: Journal of Geohysical Research, **108 (B1)**, 2016.

Mallick, S., and L. N. Frazer, 1991, Reflection/transmission coefficients and azimuthal anisotropy in marine seismic studies: Geophysical Journal International, **105**, 241–252.

Martin, M. A., and T. L. Davis, 1987, Shear-wave birefringence: A new tool for evaluating fractured reservoirs: The Leading Edge, **6**, 22–28.

Martinez, R. D., 1993, Wave propagation effects on amplitude variation with offset measurements: A modeling study: Geophysics, **58**, 534–543.

Martinez, R. D., and G. A. McMechan, 1991, τ-p seismic for viscoelastic media – Part 2: Linearized inversion: Geohysical Prospecting, **39**, 157–181.

Maultzsch, S., M. Chapman, E. Liu, and X.-Y. Li, 2009, Anisotropic attenuation in VSP data: Journal of Seismic Exploration, **16**, 145–158.

Maultzsch, S., S. Horne, S. Archer, and H. Burkhardt, 2003, Effects of an anisotropic overburden on azimuthal amplitude analysis in horizontal transversely isotropic media: Geophysical Prospecting, **51**, 61–74.

Mensch, T., and P. Rasolofosaon, 1997, Elastic-wave velocities in anisotropic media of arbitrary symmetry – generalization of Thomsen's parameters ϵ, δ, and γ: Geophysical Journal International, **128**, 43–64.

Miller, D. E., and C. Spencer, 1994, An exact inversion for anisotropic moduli from phase slowness data: Journal of Geophysical Research, **99**, 651–657.

Mueller, M. C., 1990, Prediction of lateral variability in fracture intensity using multicomponent shear-wave surface seismic as a precursor to horizontal drilling in the Austin Chalk: Geophysical Journal International, **107**, 409–416.

Müller, G., 1971, Direct inversion of seismic observations: Journal of Geophysics, **37**, 225–235.

Musgrave, M. J. P., 1970, Crystal acoustics: Introduction to the study of elastic waves and vibrations in crystals: Holden-Day.

Neal, S., N. R. Hill, and Y. Wang, 2009, Anisotropic velocity modeling and prestack Gaussian-beam depth migration with applications in the deepwater Gulf of Mexico: The Leading Edge, **28**, No. 9, 1110–1119.

Olofsson, B., J. Kommedal, O. Barkved, R. Alexandre, J. E. Brunelliere, and E. Muyzert, 2002, Continuous progress in processing multicomponent data - A case study: 64th Annual EAGE meeting, Extended Abstracts, F-22.

Reine, C. A., R. A. Clark, and M. van der Baan, 2009, Interval-Q measurements from surface seismic data using a robust prestack inversion algorithm: 71st Annual Meeting, EAGE, Extended Abstracts, S041.

Ren, J., C. Gerrard, J.McClean, and M. Orlovich, 2005, Prestack wave-equation depth migration in VTI media: The Leading Edge, **24**, 618–620.

Rüger, A., 1997, P-wave reflection coefficients for transversely isotropic models with vertical and horizontal axis of symmetry: Geophysics, **62**, 713–722.

———, 1998, Variation of P-wave reflectivity with offset and azimuth in anisotropic media: Geophysics, **63**, 935–947.

———, 2002, Reflection coefficients and azimuthal AVO analysis in anisotropic media: Society of Exploration Geophysicists.

Sarkar, D., and I. Tsvankin, 2004, Migration velocity analysis in factorized VTI media: Geophysics, **69**, 708–718.

———, 2006, Anisotropic migration velocity analysis: Application to a data set from West Africa: Geophysical Prospecting, **54**, 575–587.

Schoenberg, M., and C. Sayers, 1995, Seismic anisotropy of fractured rock: Geophysics, **60**, 204–211.

Sena, A. G., 1991, Seismic traveltime equations for azimuthally anisotropic and isotropic media: Estimation of interval elastic properties: Geophysics, **56**, 2090–2101.

Sena, A. G., and M. N. Toksöz, 1993, Kirchhoff migration and velocity analysis for converted and nonconverted waves in anisotropic media: Geophysics, **58**, 265–276.

Simmons, J. L., 2009, Converted-wave splitting estimation and compensation: Geophysics, **74**, no. 1, D37–D48.

Stoffa, P. L., J. B. Diebold, and P. Buhl, 1981, Inversion of seismic data in the τ–p domain: Geophysical Research Letters, **8**, 869–872.

———, 1982, Velocity analysis of wide aperture seismic data: Geophysical Prospecting, **30**, 25–57.

Stovas, A., and B. Ursin, 2009, Improved geometric-spreading approximation in layered transversely isotropic media: Geophysics, **74**, no. 5, D85–D95.

Terrell, M. J., T. L. Davis, L. T. Brown, and R. F. Fuck, 2002, Seismic monitoring of a CO2 flood at Weyburn field, Saskatchewan: Demonstrating the robustness of time-lapse seismology: 72nd Annual International Meeting, SEG, Expanded Abstracts, 1673–1676.

Thomsen, L., 1986, Weak elastic anisotropy: Geophysics, **51**, 1954–1966.

———, 1993, Weak anisotropic reflections, *in* Castagna, J. and M. Backus, eds., Offset dependent reflectivity, 103–114, SEG.

———, 1999, Converted-wave reflection seismology over inhomogeneous, anisotropic media: Geophysics, **64**, 678–690.

———, 2002, Understanding seismic anisotropy in exploration and exploitation: European Association of Geoscientists and Engineers.

Thomsen, L., I. Tsvankin, and M. C. Mueller, 1999, Coarse-layer stripping of vertically variable azimuthal anisotropy from shear-wave data: Geophysics, **64**, 1126–1138.

Tod, S., B. Taylor, R. Johnston, and T. Allen, 2007,

Fracture prediction from wide-azimuth land data in SE Algeria: The Leading Edge, **26**, 1154–1160.

Toldi, J., T. Alkhalifah, P. Berthet, J. Arnaud, P. Williamson, and B. Conche, 1999, Case study of estimation of anisotropy: The Leading Edge, **18**, 588–594.

Treitel, S., P. R. Gutowski, and D. E. Wagner, 1982, Plane-wave decomposition of seismograms: Geophysics, **47**, 1375–1401.

Tsvankin, I., 1995a, Seismic wavefields in layered isotropic media: Samizdat Press, Colorado School of Mines.

———, 1995b, Body-wave radiation patterns and AVO in transversely isotropic media: Geophysics, **60**, 1409–1425.

———, 1997, Anisotropic parameters and P-wave velocity for orthorhombic media: Geophysics, **62**, 1292–1309.

———, 2005, Seismic signatures and analysis of reflection data in anisotropic media, 2nd ed.: Elsevier Science Publ. Co., Inc.

Tsvankin, I., and E. M. Chesnokov, 1990, Synthesis of body-wave seismograms from point sources in anisotropic media: Journal of Geophysical Research, **95 (B7)**, 11317–11331.

Tsvankin, I., and L. Thomsen, 1994, Nonhyperbolic reflection moveout in anisotropic media: Geophysics, **59**, 1290–1304.

Ursin, B., and K. Hokstad, 2003, Geometrical spreading in a layered transversely isotropic medium with vertical symmetry axis: Geophysics, **68**, 2082–2091.

Ursin B., and A. Stovas, 2006, Traveltime approximations for a layered transversely isotropic medium: Geophysics, **71**, D23–D33.

Van der Baan, M., 2004, Processing of anisotropic data in the τ-p domain: I—Geometric spreading and moveout corrections: Geophysics, **69**, 719–730.

———, 2005, Processing of anisotropic data in the τ-p domain: II—Common-conversion-point sorting: Geophysics, **70 (4)**, D29–D36.

———, 2006, PP/PS Wavefield separation by independent component analysis: Geophysical Journal International, **166**, 339–348.

Van der Baan, M., and J.-M. Kendall, 2002, Estimating anisotropy parameters and traveltimes in the τ-p domain: Geophysics, **67**, 1076–1086.

———, 2003, Traveltime and conversion-point computations and parameter estimation in layered, anisotropic media by τ-p transform: Geophysics, **68**, 210–224.

Van der Baan, M., and D. Smit, 2006, Amplitude analysis of isotropic P-wave reflections: Geophysics, **71 (6)**, C93–C103.

Vanelle, C., and D. Gajewski, 2003, Determination of geometrical spreading from traveltimes: Journal of Applied Geophysics, **54**, 391–400.

Vasconcelos, I., and V. Grechka, 2007, Seismic characterization of multiple fracture sets at Rulison Field, Colorado: Geophysics, **72**, B19–B30.

Vasconcelos, I., and I. Tsvankin, 2006, Nonhyperbolic moveout inversion of wide-azimuth P-wave data for orthorhombic media: Geophysical Prospecting, **54**, 535–552.

Vavryčuk, V. and I. Pšenčík, 1998, PP-wave reflection coefficients in weakly anisotropic elastic media: Geophysics, **63**, 2129–2141.

Vestrum, R. W., D. C. Lawton, and R. Schmid, 1999, Imaging structures below dipping TI media: Geophysics, **64**, 1239–1246.

Virieux, J., 1986, P-SV propagation in heterogeneous media – Velocity-stress finite-difference method: Geophysics, **51**, 889–901.

Vlaar, N. J., 1968, Ray theory for an anisotropic inhomogeneous elastic medium: Bulletin of the Seismological Society of America, **58**, 2053–2072.

Wang, D. Y., and D. W. McCowan, 1989, Spherical divergence correction for seismic reflection data using slant stacks: Geophysics, **54**, 563–569.

Wang, X., and I. Tsvankin, 2009, Estimation of interval anisotropy parameters using velocity-independent layer stripping: Geophysics, **74**, no. 5, WB117–WB127.

Wang, Z., 2002, Seismic anisotropy in sedimentary rocks, part 2: Laboratory data: Geophysics, **67**, 1423–1440.

White, J. E., L. Martineau-Nicoletis, and C. Monash, 1983, Measured anisotropy in Pierre shale: Geophysical Prospecting, **31**, 709–725.

Willis, H., G. Rethford, and E. Bielanski, 1986, Azimuthal anisotropy: The occurence and effect on shear wave data quality: 56th Annual International Meeting, SEG, Expanded Abstracts, 479–481.

Winterstein, D. F., and M. A. Meadows, 1991, Changes in shear-wave polarization azimuth with depth in Cymric and Railroad Gap oil fields: Geophysics, **56**, 1349–1364.

Woodward, M. J., D. Nichols, O. Zdraveva, P. Whitfield, and T. Johns, 2008, A decade of tomography: Geophysics, **73**, no. 5, VE5–VE11.

Xu, X., and I. Tsvankin, 2006, Anisotropic geometrical-spreading correction for wide-azimuth P-wave reflections: Geophysics, **71**, no. 5, D161–D170.

———, 2007, A case study of azimuthal AVO analysis with anisotropic spreading correction: The Leading Edge, **26**, no. 12, 1552–1561.

———, 2008, Moveout-based geometrical-spreading correction for PS-waves in layered anisotropic media: Journal of Geophysics and Engineering, **5**, 195–202.

Zatsepin, S. V., and S. Crampin, 1997, Modelling the compliance of crustal rock: I - Response of shear-wave splitting to differential stress: Geophysical Journal International, **129**, 477–494.

Zhu, T., S. H. Gray, and D. Wang, 2007a, Prestack Gaussian-beam depth migration in anisotropic media: Geophysics, **72**, no. 3, S133–S138.

Zhu, Y., and Tsvankin, I., 2006, Plane-wave propa-

gation in attenuative transversely isotropic media: Geophysics, **71**, no. 2, T17–T30.

———, 2007, Plane-wave attenuation anisotropy in orthorhombic media: Geophysics, **72**, no. 1, D9–D19.

Zhu, Y., I. Tsvankin, P. Dewangan, and K. van Wijk, 2007b, Physical modeling and analysis of P-wave attenuation anisotropy in transversely isotropic media: Geophysics, **72**, no. 1, D1–D7.

Moveout inversion of wide-azimuth P-wave data for tilted TI media

Xiaoxiang Wang & Ilya Tsvankin
Center for Wave Phenomena, Geophysics Department, Colorado School of Mines, Golden, Colorado 80401

ABSTRACT

TTI (transversely isotropic with a tilted symmetry axis) models have been widely used for velocity analysis and imaging in many exploration areas, such as the Canadian Foothills and the Gulf of Mexico. In a previous publication, we discussed 2D stacking-velocity inversion for the interval parameters of TTI media composed of homogeneous layers separated by plane interfaces. Here, this 2D algorithm is extended to 3D wide-azimuth data by including P-wave NMO ellipses and two horizontal slowness components (time slopes) in the objective function. If the symmetry axis is perpendicular to the bottom of each layer, it is possible to estimate the interval symmetry-direction velocity V_{P0}, anisotropy parameter δ, and the reflector orientation using only one borehole constraint – the reflector depth. The algorithm can tolerate small (1/10 of the dip) deviation of the symmetry axis from the reflector normal. However, as is the case for the 2D problem, the parameter ϵ can seldom be constrained without using nonhyperbolic moveout inversion. If the symmetry axis deviates from the reflector normal but is confined to the dip plane, stable parameter estimation requires a relationship between the tilt and dip in each layer. When the tilt represents a free parameter, the input data have to be supplemented by wide-azimuth VSP traveltimes with the offset reaching at least 1/4 of the maximum reflector depth. Moreover, the additional angle coverage provided by VSP data may help resolve the parameter ϵ in the upper part of the model.

Key words: transverse isotropy, tilted symmetry axis, TTI, P-wave, wide-azimuth, azimuthal anisotropy, NMO ellipse, borehole, VSP

1 INTRODUCTION

Transversely isotropic media with a tilted symmetry axis (TTI) provide marked improvements in prestack imaging of P-wave data (Charles *et al.*, 2008; Huang *et al.*, 2008; Neal *et al.*, 2009). Allowing for the symmetry-axis tilt results in more plausible velocity models for sedimentary formations in complex geological settings (Vestrum *et al.*, 1999; Behera & Tsvankin, 2009; Bakulin *et al.*, 2009).

P-wave velocities and traveltimes in TTI media can be expressed through the symmetry-direction velocity V_{P0} and Thomsen (1986) anisotropy parameters ϵ and δ defined with respect to the symmetry axis. The symmetry-axis orientation is defined by the tilt angle ν with the vertical and the azimuth β. Although many migration algorithms have been extended to TTI media, accurate estimation of the interval anisotropy parameters and the symmetry-axis orientation remains a difficult problem.

For example, Grechka *et al.* (2001) discuss 2D inversion of P-wave normal-moveout (NMO) velocities and zero-offset traveltimes for the parameters of a dipping TTI layer with the symmetry axis perpendicular to the bedding. Their algorithm is based on several *a priori* assumptions about the model and requires reflection data from a horizontal interface beneath the TTI layer.

A review of several other parameter-estimation algorithms for TTI media (e.g., Grechka *et al.*, 2002a) can be found in our previous publication (Wang & Tsvankin, 2010, hereafter referred to as Paper I), where we develop a 2D inversion methodology for a stack of homogeneous

TTI layers separated by plane dipping interfaces. P-wave NMO velocities, reflection slopes, and zero-offset traveltimes are supplemented with reflector depths measured in a borehole, as well as with check-shot and near-offset VSP traveltimes. Even for a single TTI layer, the medium parameters cannot be resolved without constraining the tilt of the symmetry axis. Therefore, in Paper I the symmetry axis is assumed to be orthogonal to the layer's bottom, which is typical for dipping shale layers (Isaac & Lawton, 1999; Vestrum *et al.*, 1999; Charles *et al.*, 2008). As a result, the 2D algorithm produces stable estimates of the interval parameters V_{P0} and δ provided the range of dips does not exceed 30°.

Here, we present a 3D extension of the inversion algorithm from Paper I by including the NMO ellipses and two horizontal slownesses (reflection time slopes) in the objective function. Wide-azimuth data provide additional information for estimating the interval Thomsen parameters, which helps relax the constraints on model geometry and increase the stability of the inversion. First, we discuss parameter estimation for models with the symmetry axis orthogonal to reflectors. Then we extend the method to models with arbitrary tilt and show that stable inversion requires the addition of VSP data. Synthetic tests on noise-contaminated data help evaluate the accuracy and stability of estimating the interval TTI parameters for different types of input data.

2 3D INPUT DATA VECTOR

As in Paper I, we consider a stack of homogeneous TTI layers separated by plane, dipping, non-intersecting boundaries (Figure 1). However, the dip planes of model interfaces no longer have to be aligned. From 3D multi-azimuth P-wave data recorded at a common midpoint (CMP) with the coordinates $\mathbf{Y} = [Y_1, Y_2]$, we obtain the zero-offset reflection traveltimes $t_0(\mathbf{Y}, n)$ for all reflectors, the corresponding NMO velocities $V_{\rm nmo}(\alpha)$ (α is the azimuth), and the time slopes $\mathbf{p}(\mathbf{Y}, n) = [p_1(\mathbf{Y}, n), p_2(\mathbf{Y}, n)]$, where p_1 and p_2 are the horizontal slowness components of the zero-offset ray. The azimuthally-dependent NMO velocity is described by an elliptical function in the horizontal plane (Grechka & Tsvankin, 1998):

$$V_{\rm nmo}^{-2}(\alpha) = W_{11}\cos^2\alpha + 2W_{12}\sin\alpha\cos\alpha + W_{22}\sin^2\alpha\,, \quad (1)$$

where $\mathbf{W}$ is a symmetric matrix,

$$W_{ij} = \tau_0 \frac{\partial^2 \tau}{\partial x_i \partial x_j}\bigg|_{\mathbf{x}=\mathbf{Y}}, \quad (i,j=1,2)\,. \quad (2)$$

Here $\tau(x_1, x_2)$ is the one-way traveltime from the zero-offset reflection point to the location $\mathbf{x}\{x_1, x_2\}$ at the surface and τ_0 is the one-way zero-offset traveltime. The matrices $\mathbf{W}(\mathbf{Y}, n)$ can be obtained from azimuthal velocity analysis of reflection data based on the hyperbolic moveout equation parameterized by the NMO ellipse (Grechka & Tsvankin, 1999).

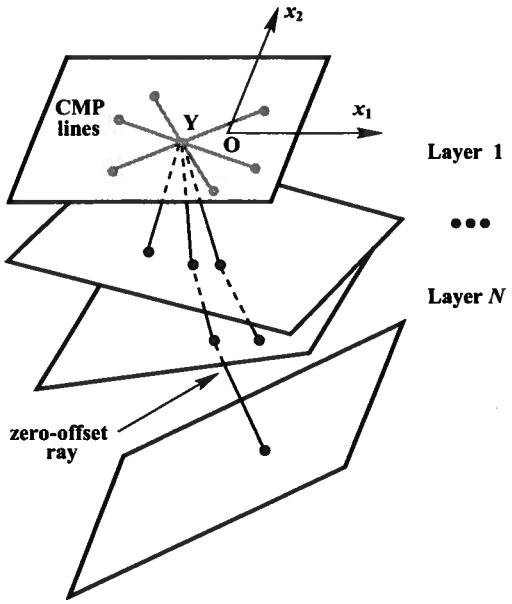

Figure 1. Zero-offset rays and a multiazimuth CMP gather for a model composed of a stack of TTI layers separated by plane dipping interfaces (after Grechka *et al.*, 2002b).

Grechka & Tsvankin (2002) devise a Dix-type averaging procedure to model the effective NMO ellipse for heterogeneous anisotropic media. They show that the exact NMO ellipse can be obtained by averaging the intersections of the interval NMO-velocity surfaces with the layer boundaries. All information for computing the NMO ellipse of a given reflection event is contained in the results of tracing just one (zero-offset) ray.

Because each layer is homogeneous with plane boundaries (Figure 1), it is sufficient to acquire the input data in a single multiazimuth CMP gather (Grechka *et al.*, 2002b). The reflector depths $z_{\rm b}(n)$ are assumed to be measured in a borehole, which may be placed away from the CMP location (the subscript "b" denotes borehole data). Therefore, the vector of input data for 3D inversion is as follows:

$$\mathbf{d} = \{t_0(n), p_1(n), p_2(n), W_{11}(n), W_{12}(n), W_{22}(n), z_{\rm b}(n)\} \quad (n = 1, 2, \ldots, N)\,, \quad (3)$$

where all components are the effective quantities for the n-th reflector.

3 SYMMETRY AXIS ORTHOGONAL TO THE REFLECTOR

It is common to put constraints on the symmetry-axis orientation using *a priori* information (Charles *et al.*, 2008; Huang *et al.*, 2008; Bakulin *et al.*, 2009). If TI layers were rotated by tectonic processes after sedimen-

tation, the symmetry axis typically remains perpendicular to the layering, which means that its tilt ν and azimuth β coincide with the dip ϕ and azimuth ψ of the reflector, respectively. The relative simplicity of this model significantly improves the stability of parameter estimation.

3.1 Inversion for a single TTI layer

First, we consider a homogeneous TTI layer with the symmetry axis orthogonal to its bottom. The dip plane of the reflector represents a vertical symmetry plane for the whole model, and therefore, includes one of the axes of the NMO ellipse. Thus, the orientation of the NMO ellipse yields the reflector azimuth ψ which coincides with the symmetry-axis azimuth β.

The semiaxis of the NMO ellipse in the dip plane is obtained from the isotropic cosine-of-dip relationship (Tsvankin, 2005):

$$V_{\rm nmo}^{(1)}(\phi) = \frac{V_{\rm nmo}(0)}{\cos\phi}, \tag{4}$$

where $V_{\rm nmo}(0) = V_{P0}\sqrt{1+2\delta}$ is the NMO velocity from a horizontal interface beneath a VTI medium (i.e., the symmetry axis is rotated along with the reflector). Alternatively, the dip component of the NMO velocity can be represented using the ray parameter $p = \sqrt{p_1^2 + p_2^2}$:

$$V_{\rm nmo}^{(1)}(p) = \frac{V_{\rm nmo}(0)}{\sqrt{1 - p^2 V_{P0}^2}}, \tag{5}$$

where $p = \sin\phi / V_{P0}$ because the phase-velocity vector of the zero-offset ray (and the ray itself) is parallel to the symmetry axis. The strike component $V_{\rm nmo}^{(2)}$ of the NMO velocity is given by (Grechka & Tsvankin, 2000):

$$V_{\rm nmo}^{(2)} = V_{\rm nmo}(0) = V_{P0}\sqrt{1+2\delta}. \tag{6}$$

Therefore, by combining the two semiaxes of the NMO ellipse (equations 5 and 6) and using the measured time slope p, we can find the symmetry-direction velocity V_{P0}. Then the dip $\phi = \nu$ is obtained from equation 4, and the anisotropy parameter δ from equation 6. Depth information for a single layer is not needed because the reflector depth z below the CMP location can be computed from the zero-offset traveltime t_0:

$$z = \frac{V_{P0}\, t_0}{2\cos\phi}. \tag{7}$$

However, P-wave hyperbolic moveout in this model is independent from the anisotropy parameter ϵ. In summary, the geometry and the parameters V_{P0} and δ of a single TTI layer can be resolved without using any borehole information.

3.2 Inversion for layered TTI media

Here, we present a 3D extension of the 2D stacking-velocity inversion algorithm from Paper I ("stacking-velocity tomography") to layered TTI media. If the symmetry axis in each layer is perpendicular to its bottom ($\nu^{(n)} = \phi^{(n)}$ and $\beta^{(n)} = \psi^{(n)}$), the model vector is

$$\mathbf{m} = \{V_{P0}^{(n)}, \epsilon^{(n)}, \delta^{(n)}, \phi^{(n)}, \psi^{(n)}\}, \quad (n = 1, 2, \ldots, N). \tag{8}$$

First, we assume the depths $z_{\rm b}(n)$ to be known from borehole measurements; later on, we discuss the inversion without using the depth constraint.

3.2.1 Inversion methodology

As in Paper I, we specify the trial set $\mathbf{m}$ of the interval parameters (equation 8) and trace zero-offset rays through the model with the geometry partially fixed by the known reflector depths. The ray-tracing results yield the zero-offset traveltimes $t_0^{\rm calc}(n)$, the horizontal slowness components $p_1^{\rm calc}(n)$ and $p_2^{\rm calc}(n)$, and the Dix-type averaging procedure produces the effective NMO ellipses $\mathbf{W}^{\rm calc}(n)$. The NMO velocity $V_{\rm nmo}^{\rm calc}(n,\alpha)$ for any azimuth α can be computed from equation 1.

The vector $\mathbf{m}$ (equation 8) is estimated by minimizing the following objective function (based on L^2-norm) for all N reflectors simultaneously:

$$\mathcal{F}(\mathbf{m}) \equiv \sum_{n=1}^{N} \left\{ \frac{\left\|p_1^{\rm calc}(n) - p_1(n)\right\|^2}{\sigma^2[p_1(n)]} + \frac{\left\|p_2^{\rm calc}(n) - p_2(n)\right\|^2}{\sigma^2[p_2(n)]} + \frac{\left\|t_0^{\rm calc}(n) - t_0(n)\right\|^2}{\sigma^2[t_0(n)]} + \frac{\left\|V_{\rm nmo}^{\rm calc}(n,\alpha) - V_{\rm nmo}(n,\alpha)\right\|^2}{\sigma^2[V_{\rm nmo}(n,\alpha)]} \right\}, \tag{9}$$

where σ^2 represents the variance of each measurement, and the azimuth α varies from 0° to 180°. For 2D models, the objective function also includes check-shot traveltimes, and reflector dips are assumed to be known. Here, wide-azimuth data provide additional information that replaces those borehole constraints.

In a single TTI layer, the parameter ϵ cannot be found from conventional-spread P-wave moveout. However, as discussed in Paper I, $\mathbf{p}(n)$, $t_0(n)$, and $\mathbf{W}(n)$ for layered TTI models are influenced by the values of $\epsilon^{(n)}$ in the overburden (except for models with parallel interfaces). Therefore, the interval parameter ϵ is estimated along with the other unknowns, although it is not expected to be well-constrained.

3.2.2 Synthetic examples

As in Paper I, the algorithm was tested for a suite of layered TTI models ($0 \le \epsilon \le 0.5$ and $-0.2 \le \delta \le 0.3$) with reflector dips ranging from 0° to 60°. Table 2 shows the inversion results for a three-layer medium with relatively close azimuths of the interfaces (Table 1 and Figure 2). The results of a test for another three-layer medium with a wide range of interface azimuths but identical dips (Table 1 and Figure 3) are listed in Table 3. The inversion is performed for 200 realizations of

	Layer 1	Layer 2	Layer 3
V_{P0} (km/s)	1.5	2.0	2.5
ϵ	0.10	0.20	0.25
δ	-0.10	0.10	0.12

Table 1. Interval parameters of a three-layer TTI model.

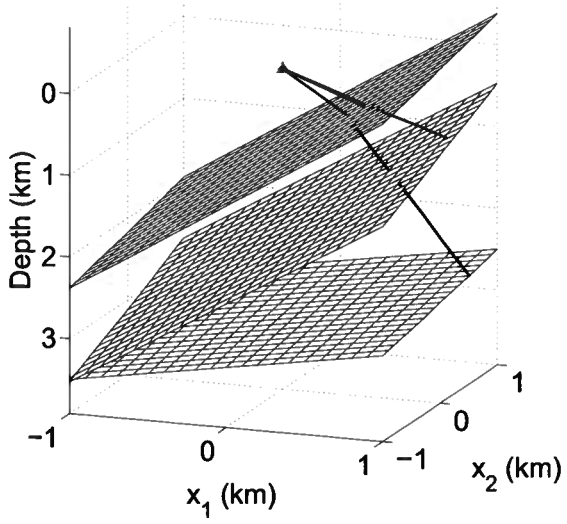

Figure 2. Zero-offset P-wave rays in a three-layer TTI model with the interval parameters listed in Table 1. The input data are computed by anisotropic ray tracing. The symmetry axis in each layer is perpendicular to its bottom. The dips and azimuths are $\phi^{(1)} = \phi^{(2)} = 50°$, $\phi^{(3)} = 20°$, $\psi^{(1)} = 10°$, $\psi^{(2)} = 20°$, and $\psi^{(3)} = 30°$. The reflector depths below the CMP (located at the origin of the coordinate system) are $z_b(1) = 1$ km, $z_b(2) = 2$ km, and $z_b(3) = 3$ km.

noise-contaminated input data using the measurement values as the variances σ^2 in equation 9.

For both models, the interval parameters V_{P0} and δ and the reflector dips and azimuths are recovered with sufficiently high accuracy. As expected, the standard deviations are higher in the third (deepest) layer (about 5% for V_{P0} and 0.06 for δ), primarily due to the smaller contribution of the deeper layers to the effective reflection traveltimes. However, in contrast to layer-stripping techniques, our tomography-style algorithm possesses the advantage of mitigating error accumulation with depth. An important factor that influences the inversion accuracy is the layer thickness; the thickness-to-depth ratio below the CMP location should reach at least 0.25 to ensure stable interval estimates. As expected, the standard deviations of the parameter ϵ are much larger than those of δ, although ϵ-estimates are not substantially biased.

For plausible ranges of ϵ and δ ($|\epsilon| \leq 0.5$; $|\delta| \leq 0.3$), the errors in the interval parameters V_{P0}, δ, ϕ, and ψ remain small if the symmetry axis deviates from the reflector normal in the dip plane by less than one tenth of the dip value ($\phi/10$; i.e., $\beta = \psi$, but $\nu \neq \phi$). For example, we used the tilts $\nu^{(n)} = 9\,\phi^{(n)}/10$ ($n = 1, 2, 3$) for the second model (Table 1 and Figure 3) to generate the input data and applied our algorithm assuming that $\nu^{(n)} = \phi^{(n)}$ (Table 4). The slight deviation of the symmetry axis from the reflector normal causes a mild bias in the estimates, but the standard deviations are mostly controlled by the noise level, which is the same as in the previous tests.

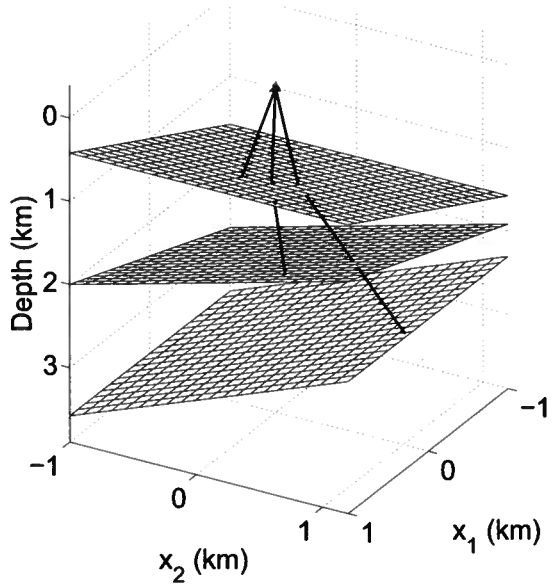

Figure 3. Zero-offset P-wave rays in a three-layer TTI model with the interval parameters listed in Table 1. The symmetry axis in each layer is perpendicular to its bottom. The dips and azimuths are $\phi^{(1)} = \phi^{(2)} = \phi^{(3)} = 30°$, $\psi^{(1)} = 0°$, $\psi^{(2)} = 45°$, and $\psi^{(3)} = 90°$. The reflector depths below the CMP are $z_b(1) = 1$ km, $z_b(2) = 2$ km, and $z_b(3) = 3$ km.

If the reflector depths are also unknown, the trade-off between $z(n)$ and other parameters increases errors in the inversion results. For example, we performed the inversion for the previous model (Table 1 and Figure 3) without using depth information for the same level of noise in the input data. The standard deviations of V_{P0} and δ in the third layer increase to 7% and 0.09, respectively. The mean values of V_{P0} (2.61 km/s) and δ (0.08) are also strongly biased. The mean value of $z(3)$ (actual quantity is 3 km) is 3.04 km with the standard deviation 0.12 km.

4 SYMMETRY AXIS DEVIATING FROM REFLECTOR NORMAL

The assumption of the symmetry axis being perpendicular to the reflector is too restrictive when tectonic processes and sedimentation occur together (Bakulin *et al.*, 2009). Also, for stress-induced anisotropy in sediments

	V_{P0} (km/s)		δ		ϵ		ϕ (°)		ψ (°)	
	mean	sd (%)	mean	sd	mean	sd	mean	sd	mean	sd
Layer 1	1.50	1	-0.10	0.01	0.21	0.22	50.0	0.2	10.0	0.1
Layer 2	2.00	3	0.10	0.03	0.25	0.11	50.0	0.4	19.9	0.3
Layer 3	2.49	5	0.12	0.06	0.25	0.23	20.2	2.2	30.1	1.9

Table 2. Inversion results for the three-layer TTI model from Table 1 and Figure 2. The input data are distorted by Gaussian noise with the standard deviations equal to 1% for $p_1(n)$, $p_2(n)$, and $t_0(n)$, and 2% for the NMO velocities. The mean values and standard deviations of the inverted parameters are denoted by "mean" and "sd," respectively.

	V_{P0} (km/s)		δ		ϵ		ϕ (°)		ψ (°)	
	mean	sd (%)	mean	sd	mean	sd	mean	sd	mean	sd
Layer 1	1.50	1	-0.10	0.01	0.10	0.04	30.0	0.3	0.0	0.1
Layer 2	2.00	2	0.10	0.03	0.20	0.07	30.0	0.3	45.1	1.4
Layer 3	2.51	5	0.12	0.06	0.26	0.23	30.0	0.5	90.1	2.0

Table 3. Inversion results for the three-layer TTI model from Table 1 and Figure 3. The noise level in the input data is the same as in Table 2.

near salt bodies, the symmetry is largely controlled by the principal stress direction which is not necessarily aligned with the normal to the bedding (Bakulin *et al.*, 2009).

To account for the deviation of the symmetry axis from the reflector normal, the tilt ν can be expressed as a function of the dip ϕ using geologic data. For example, the simultaneous influence of tectonic forces and sedimentation typically makes ν smaller than ϕ (e.g., $\nu = \phi/2$ or $\nu = 3\phi/4$). In the next test, we use the three-layer model with the interval parameters listed in Table 1 and the model geometry shown in Figure 2, but with $\nu \neq \phi$. The symmetry axis in each layer is confined to the dip plane (i.e., $\beta^{(n)} = \psi^{(n)}$, $n = 1, 2, 3$) with the tilt $\nu^{(n)} = \phi^{(n)}/2$. The known relationship between ν and ϕ is sufficient for the algorithm to produce stable estimates of the interval parameters V_{P0} and δ and the reflector orientation (Table 5).

4.1 Tilt as an unknown parameter

Here, we relax the assumption that the tilt ν represents a known function of the dip ϕ. It is still assumed that the symmetry-axis azimuth β in each layer coincides with the dip-plane azimuth ψ, but the parameter ν has to be found from the inversion. Thus, the model vector includes one more unknown:

$$\mathbf{m} = \{V_{P0}^{(n)}, \epsilon^{(n)}, \delta^{(n)}, \nu^{(n)}, \phi^{(n)}, \psi^{(n)}\}, \quad (n = 1, 2, \ldots, N). \tag{10}$$

Making ν a free parameter significantly increases the nonuniqueness of the inversion. For 2D models, simultaneous estimation of V_{P0}, ϵ, δ, and ν proves to be ambiguous, even if the reflector depths and dips are measured in a borehole. Our tests indicate that 3D wide-azimuth data supplemented by the known reflector depths still cannot be used to resolve the tilt along with the other TTI parameters. Therefore, we propose to add wide-azimuth walkaway VSP (vertical seismic profiling) traveltimes $t_{\rm VSP}$ to the input data:

$$\mathbf{d} = \{t_0(n), p_1(n), p_2(n), W_{11}(n), W_{12}(n), W_{22}(n), z_{\rm b}(n), t_{\rm VSP}\}. \tag{11}$$

We employ an array of sources at the surface and one VSP receiver per layer located close to the layer's bottom. Similar to the zero-offset reflected rays, we trace VSP rays in a trial model and compute the difference between the modeled and observed traveltimes. Then, the objective function takes the form

$$\mathcal{F}(\mathbf{m}) \equiv \sum_{n=1}^{N} \left\{ \frac{\left\|p_1^{\rm calc}(n) - p_1(n)\right\|^2}{\sigma^2[p_1(n)]} + \frac{\left\|p_2^{\rm calc}(n) - p_2(n)\right\|^2}{\sigma^2[p_2(n)]} + \frac{\left\|t_0^{\rm calc}(n) - t_0(n)\right\|^2}{\sigma^2[t_0(n)]} + \frac{\left\|t_{\rm VSP}^{\rm calc} - t_{\rm VSP}\right\|^2}{\sigma^2[t_{\rm VSP}]} + \frac{\left\|V_{\rm nmo}^{\rm calc}(n,\alpha) - V_{\rm nmo}(n,\alpha)\right\|^2}{\sigma^2[V_{\rm nmo}(n,\alpha)]} \right\}. \tag{12}$$

4.1.1 Synthetic examples

Numerical testing shows that it is sufficient to add one check-shot source and several VSP sources located around the borehole with the offset exceeding 1/4 of the largest reflector depth. To achieve full azimuthal coverage, eight VSP sources are placed along a circle with a

	V_{P0} (km/s)		δ		ϕ (°)		ψ (°)	
	mean	sd (%)	mean	sd	mean	sd	mean	sd
Layer 1	1.50	1	-0.10	0.01	29.8	0.3	0.0	0.0
Layer 2	1.99	2	0.09	0.03	30.3	0.3	44.3	1.4
Layer 3	2.50	5	0.10	0.06	30.1	0.5	89.5	2.0

Table 4. Inversion results for the three-layer TTI model from Table 1 with the model geometry shown in Figure 3. The symmetry axis in each layer is confined in the dip plane, but is no longer perpendicular to the reflector ($\nu^{(1)} = \nu^{(2)} = \nu^{(3)} = 27°$). The noise level is the same as in the previous tests.

	V_{P0} (km/s)		δ		ν (°)		ψ (°)	
	mean	sd (%)	mean	sd	mean	sd	mean	sd
Layer 1	1.50	1	-0.10	0.01	25.0	0.2	10.0	0.0
Layer 2	2.01	4	0.10	0.06	25.0	0.4	20.0	0.5
Layer 3	2.50	4	0.12	0.04	10.0	0.6	30.0	0.8

Table 5. Inversion results for the three-layer TTI model from Table 1 with the model geometry shown in Figure 2. The tilt of the symmetry axis in each layer is equal to one-half of the reflector dip. The noise level is the same as in the previous tests.

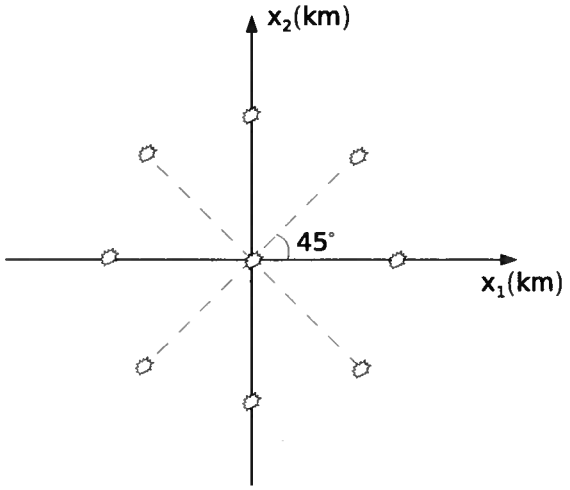

Figure 4. Distribution of VSP sources at the surface. The check-shot source is located close to the borehole ($x_1 = 0.01$, $x_2 = 0$). The VSP lines are separated by 45°, and the offset of each VSP source is 1 km.

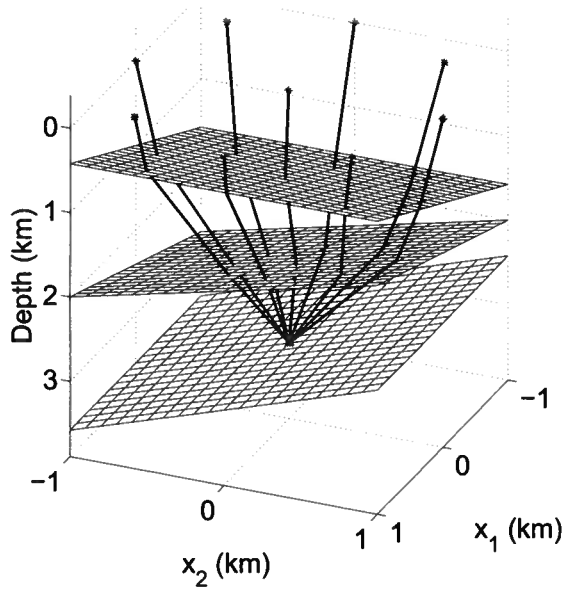

Figure 5. VSP rays for the receiver located at the bottom of a three-layer TTI model with the interval parameters listed in Table 1. The symmetry axis in each layer is confined in the dip plane. The tilts, dips, and azimuths are $\nu^{(1)} = \nu^{(2)} = \nu^{(3)} = 20°$, $\phi^{(1)} = \phi^{(2)} = \phi^{(3)} = 30°$, $\psi^{(1)} = 0°$, $\psi^{(2)} = 45°$, and $\psi^{(3)} = 90°$. The vertical borehole is below the coordinate origin, and the reflector depths at the borehole location are $z_b(1) = 1$ km, $z_b(2) = 2$ km, and $z_b(3) = 3$ km.

45° increment in azimuth (Figure 4). With this distribution of the VSP sources, we compute the input data for a three-layer model (Table 1 and Figure 5) using anisotropic ray tracing. The inversion results for 100 realizations of noise-contaminated data are listed in Table 6. We also test another model with larger tilt angles $\nu^{(1)} = \nu^{(2)} = \nu^{(3)} = 40°$ (Table 7).

Despite the additional constraints provided by VSP data, the standard deviations in the tilt increase rapidly with depth because the inversion for ν is still ill-conditioned. However, the interval parameters V_{P0} and δ and the reflector orientation can be recovered with sufficient accuracy. Also, the VSP data help constrain the parameter ϵ in the top two layers, while estimation of ϵ in the bottom layer is ambiguous because of the reduced

	V_{P0} (km/s)		δ		ϵ		ν (°)		ϕ (°)		ψ (°)	
	mean	sd (%)	mean	sd	mean	sd	mean	sd	mean	sd	mean	sd
Layer 1	1.50	1	-0.10	0.01	0.10	0.02	20.9	2.8	30.0	0.5	0.0	0.4
Layer 2	2.00	1	0.09	0.03	0.21	0.06	20.3	5.0	30.0	0.6	45.3	1.0
Layer 3	2.48	2	0.13	0.06	0.24	0.12	23.9	10.1	30.1	0.8	90.0	1.1

Table 6. Inversion results for the three-layer TTI model from Table 1 using reflection and VSP data (Figure 5). The positions of the check-shot and VSP sources are shown in Figure 4. The tilts are $\nu^{(1)} = \nu^{(2)} = \nu^{(3)} = 20°$. The input data are distorted by Gaussian noise with the standard deviations equal to 1% for $p_1(n)$, $p_2(n)$, $t_0(n)$, and $t_{\rm VSP}^{\rm calc}$, and 2% for the NMO velocities.

	V_{P0} (km/s)		δ		ϵ		ν (°)		ϕ (°)		ψ (°)	
	mean	sd (%)	mean	sd	mean	sd	mean	sd	mean	sd	mean	sd
Layer 1	1.50	1	-0.10	0.01	0.10	0.01	40.0	0.9	30.0	0.5	0.1	0.5
Layer 2	2.00	1	0.10	0.03	0.21	0.05	40.4	6.5	30.0	0.6	45.1	0.8
Layer 3	2.50	3	0.12	0.06	0.31	0.11	39.0	12.5	29.9	0.8	90.0	1.1

Table 7. Inversion results for the three-layer TTI model from Table 1 using reflection and VSP data (Figure 5). The positions of the check-shot and VSP sources are shown in Figure 4. The tilts are $\nu^{(1)} = \nu^{(2)} = \nu^{(3)} = 40°$. The noise level is the same as in Table 6.

angle coverage of the VSP rays at depth. To resolve the parameter ϵ in piecewise homogeneous TTI models, it is necessary to use long-offset VSP or reflection data.

It should be mentioned that the deviation of the symmetry axis from the reflector normal reduces the stability of parameter estimation. When the difference between ν and ϕ is large, small errors in the input data are significantly amplified by the inversion algorithm. Therefore, the tilt should be confined to the range $\phi/2 \le \nu \le 3\phi/2$, which is typical for most TTI formations.

5 DISCUSSION AND CONCLUSIONS

The tilt of the symmetry axis in TI media makes the medium azimuthally anisotropic, and wide-azimuth P-wave data provide valuable constraints on the TTI parameters. If the symmetry axis is perpendicular to the reflector, the P-wave NMO ellipse is sufficient for estimating the parameters V_{P0} and δ of a single dipping TTI layer. Conventional-spread P-wave data also yield the depth and orientation of the reflector, but the parameter ϵ remains unconstrained without using long-offset moveout.

For homogeneous TTI layers separated by plane dipping interfaces, the input data include the effective NMO ellipses, zero-offset traveltimes, and reflection slopes supplemented by the reflector depths measured in a borehole. The interval parameters are estimated by a 3D tomography-style algorithm that represents an extension of the 2D method introduced in Paper I. As long as the symmetry axis in each layer is kept orthogonal to its bottom, the interval parameters V_{P0} and δ and the reflector dips ϕ and azimuths ψ are well-resolved. If the magnitude of anisotropy is not uncommonly large ($|\epsilon| \le 0.5$; $|\delta| \le 0.3$), small deviations of the symmetry axis from the reflector normal ($\pm\phi/10$) do not distort the inversion results. Inversion without depth information produces parameter estimates with larger bias and standard deviation.

If the symmetry axis is not perpendicular to the reflector but the tilt represents a known function of the reflector dip ϕ, the 3D inversion algorithm can still resolve V_{P0}, δ, and the reflector orientation. We also examined the possibility of estimating the tilt from the data under the assumption that the symmetry axis is confined to the dip plane of the reflector. Numerical testing demonstrates that stable inversion requires additional input data, such as check-shot and walkaway VSP traveltimes. VSP data should have full azimuthal coverage and the distance between the VSP sources and the borehole has to reach 1/4 of the largest reflector depth. Another essential requirement is for the tilt to fall into the range $\phi/2 \le \nu \le 3\phi/2$. Depending on the offset range of VSP data, it may be possible to constrain the parameter ϵ in the shallow part of the section.

Velocity variations on the scale of conventional spread-length may cause errors in the estimated parameters. Our aim, however, is to design an efficient algorithm for building an initial TTI model using wide-azimuth P-wave data at several borehole locations. An accurate initial model may help ensure the convergence of velocity-analysis algorithms that operate in the migrated domain (e.g., reflection tomography).

6 ACKNOWLEDGMENTS

We are grateful to Vladimir Grechka (Shell) and Andres Pech (IPN, Mexico) for making available their codes. We also thank Andrey Bakulin (WesternGeco), Paul Fowler (WesternGeco), and Ken Larner (CWP) for numerous helpful suggestions. This work was supported by the Consortium Project on Seismic Inverse Methods for Complex Structures at CWP.

References

Bakulin, A., Woodward, M., Nichols, D., Osypov, K., & Zdraveva, O. 2009. Building TTI depth models using anisotropic tomography with well information. *79th Annual International Meeting, SEG, Expanded Abstracts*, 4029–4033.

Behera, L., & Tsvankin, I. 2009. Migration velocity analysis for tilted TI media. *Geophysical Prospecting*, **57**, 13–26.

Charles, S., Mitchell, D. R., Holt, R. A., Lin, J., & Mathewson, J. 2008. Data-driven tomographic velocity analysis in tilted transversely isotropic media: A 3D case history from the Canadian Foothills. *Geophysics*, **73**, VE261–VE268.

Grechka, V., & Tsvankin, I. 1998. 3D description of normal moveout in anisotropic inhomogeneous media. *Geophysics*, **63**, 1079–1092.

Grechka, V., & Tsvankin, I. 1999. 3D moveout inversion in azimuthally anisotropic media with lateral velocity variation: theory and a case study. *Geophysics*, **64**, 1202–1218.

Grechka, V., & Tsvankin, I. 2000. Inversion of azimuthally dependent NMO velocity in transversely isotropic media with a tilted axis of symmetry. *Geophysics*, **65**, 232–246.

Grechka, V., & Tsvankin, I. 2002. NMO-velocity surfaces and Dix-type formulas in anisotropic heterogeneous media. *Geophysics*, **67**, 939–951.

Grechka, V., Pech, A., Tsvankin, I., & Han, B. 2001. Velocity analysis for tilted transversely isotropic media: A physical-modeling example. *Geophysics*, **66**, 904–910.

Grechka, V., Pech, A., & Tsvankin, I. 2002a. Multicomponent stacking-velocity tomography for transversely isotropic media. *Geophysics*, **67**, 1564–1574.

Grechka, V., Pech, A., & Tsvankin, I. 2002b. P-wave stacking-velocity tomography for VTI media. *Geophysical Prospecting*, **50**, 151–168.

Huang, T., Xu, S., Wang, J., Ionescu, G., & Richardson, M. 2008. The benefit of TTI tomography for dual azimuth data in Gulf of Mexico. *78th Annual International Meeting, SEG, Expanded Abstracts*, 222–226.

Isaac, J. H., & Lawton, D. C. 1999. Image mispositioning due to dipping TI media: A physical seismic modeling study. *Geophysics*, **64**, 1230–1238.

Neal, Scott L., Hill, N. Ross, & Wang, Yue. 2009. Anisotropic velocity modeling and prestack Gaussian-beam depth migration with applications in the deepwater Gulf of Mexico. *The Leading Edge*, **28**, 1110–1119.

Thomsen, L. 1986. Weak elastic anisotropy. *Geophysics*, **51**, 1954–1966.

Tsvankin, I. 2005. *Seismic signatures and analysis of reflection data in anisotropic media, 2nd edition.* Elsevier Science Publ. Co., Inc.

Vestrum, R. W., Lawton, D. C., & Schmid, R. 1999. Imaging structures below dipping TI media. *Geophysics*, **64**, 1239–1246.

Wang, X., & Tsvankin, I. 2010. Stacking-velocity inversion with borehole constraints for tilted TI media. *Geophysics (accepted for publication).*

Correction for the influence of velocity lenses on nonhyperbolic moveout inversion for VTI media

Mamoru Takanashi[1,2] & Ilya Tsvankin[1]

[1] *Center for Wave Phenomena, Geophysics Department, Colorado School of Mines, Golden, Colorado 80401*
[2] *Japan Oil, Gas and Metals National Corporation, Chiba, Japan*

ABSTRACT

Nonhyperbolic moveout analysis plays an increasingly important role in velocity model building because it provides valuable information for anisotropic parameter estimation. However, lateral heterogeneity associated with stratigraphic lenses such as channels and reefs can significantly distort the moveout parameters, even when the structure is relatively simple.

Here, we discuss nonhyperbolic moveout inversion for 2D models that include a low-velocity isotropic lens embedded in a VTI (transversely isotropic with a vertical symmetry axis) medium. Synthetic tests demonstrate that a lens can cause substantial, laterally varying errors in the normal-moveout velocity ($V_{\rm nmo}$) and the anellipticity parameter η. The area influenced by the lens can be identified using the residual moveout after the nonhyperbolic moveout correction and the dependence of errors in $V_{\rm nmo}$ and η on spreadlength.

To remove lens-induced traveltime distortions from prestack data, we propose an algorithm that involves estimation of the incidence angle of the ray passing through the lens for each recorded trace. Using the velocity-independent layer-stripping method of Dewangan and Tsvankin, we compute the lens-induced traveltime shift from the zero-offset time distortion (i.e., from "pull-up" or "push-down" anomalies).

Synthetic tests demonstrate that this algorithm substantially reduces the errors in the effective and interval parameters $V_{\rm nmo}$ and η. The corrected traces and reconstructed "background" values of $V_{\rm nmo}$ and η are suitable for anisotropic time imaging and producing a high-quality stack.

Key words: P-waves, anisotropy, transverse isotropy, velocity analysis, lateral heterogeneity, velocity lenses, nonhyperbolic moveout inversion, traveltime shifts

1 INTRODUCTION

Kinematics of P-wave propagation in VTI (transversely isotropic with a vertical symmetry axis) media are governed by the vertical velocity V_0 and the Thomsen parameters ϵ and δ (Tsvankin & Thomsen, 1994). P-wave reflection traveltime in laterally homogeneous VTI media above a horizontal or dipping reflector depends only on the normal moveout velocity $V_{\rm nmo}$ and the anellipticity parameter η (Alkhalifah & Tsvankin, 1995; Tsvankin, 2005):

$$V_{\rm nmo} = V_0\sqrt{1+2\delta}\,, \tag{1}$$

$$\eta = \frac{\epsilon-\delta}{1+2\delta}\,. \tag{2}$$

The parameters $V_{\rm nmo}$ and η, which control all P-wave time-processing steps, can be obtained from nonhyperbolic moveout or dip-dependent NMO velocity. In particular, the nonhyperbolic moveout equation introduced by Alkhalifah & Tsvankin (1995) and its extension for layered media (Alkhalifah, 1997; Grechka & Tsvankin, 1998; Tsvankin, 2005) have been widely used for estimating $V_{\rm nmo}$ and η and building anisotropic velocity models.

Nonhyperbolic moveout analysis is performed under the assumption that the overburden is laterally homogeneous on the scale of spreadlength. However, even

gentle structures often contain small-thickness lenses (such as channels and carbonate reefs), whose width is smaller than the spreadlength (Armstrong et al., 2001; Fujimoto et al., 2007; Takanashi et al., 2008; Jenner, 2009; see Figure 1). For isotropic media, lateral heterogeneity of this type has been recognized as one of the sources of the difference between the moveout and true medium velocities (Al-Chalabi, 1979; Lynn & Claerbout, 1982; Toldi, 1989; Blias, 2009). Such lens-induced errors in $V_{\rm nmo}$ lead to misties between seismic and well data (Fujimoto *et al.*, 2007).

Although the moveout parameters (especially η) were shown to be sensitive to correlated traveltime errors (Grechka & Tsvankin, 1998), overburden heterogeneity is seldom taken into account in nonhyperbolic moveout inversion. Grechka (1998) shows analytically that a constant lateral velocity gradient does not distort the estimates of $V_{\rm nmo}$ and η, if anisotropy and lateral heterogeneity are weak. The second and fourth horizontal velocity derivatives, however, can cause errors in $V_{\rm nmo}$ and η. Still, Grechka's (1998) results are limited to a single horizontal layer and cannot be directly applied to models with thin lenses.

Recently, isotropic traveltime tomography has been used to estimate the velocity inside the lens and remove the lens-induced velocity errors (Fujimoto *et al.*, 2007; Fruehn *et al.*, 2008). These case studies show the importance of integrating seismic and geologic information and understanding the relationship between the overburden heterogeneity and velocity errors. In principle, laterally varying anisotropy parameters can be estimated from anisotropic reflection tomography (e.g. Woodward *et al.*, 2008). However, if the lens location is unknown, lens-induced traveltimes shifts can hinder accurate parameter estimation on the scale of spreadlength.

Here, we study the influence of velocity lenses on nonhyperbolic moveout inversion for 2D VTI models. To analyze lens-induced distortions of reflection data, we perform finite-difference modeling and apply moveout inversion using the Alkhalifah-Tsvankin (1995) nonhyperbolic equation. We show that even a relatively thin velocity lens may cause pronounced errors in the moveout parameters $V_{\rm nmo}$ and η and describe several criteria that can help identify range of common-midpoint (CMP) locations, for which reflected rays cross the lens. To remove lens-induced traveltime shifts, we propose a correction algorithm designed for gently dipping anisotropic layers. Synthetic tests demonstrate that this algorithm suppresses lens-related distortions on the stacked section and substantially reduces errors in the effective and interval parameters $V_{\rm nmo}$ and η.

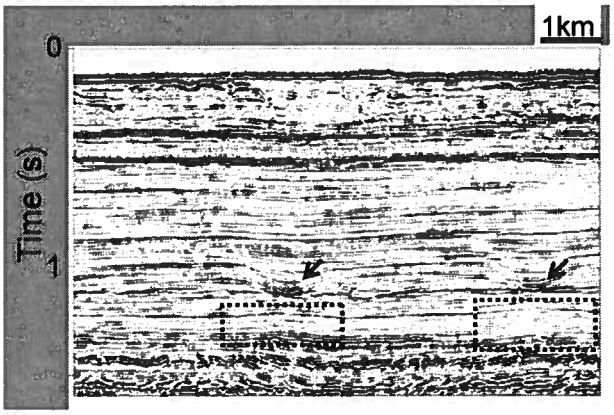

Figure 1. Time-migrated section from the central North Sea (after Armstrong *et al.*, 2001). Amplitude anomalies at the bottom of the channel-like structures (arrows) and pull-up anomalies below the structures (inside the rectangles) indicate the presence of lateral heterogeneity associated with the channel fills. Pull-up and push-down anomalies caused by high and low velocities, respectively, in channels or carbonate reefs are also observed in other hydrocarbon-producing regions, such as the Middle East and Northwest Australia.

2 DISTORTIONS CAUSED BY VELOCITY LENSES

To generate synthetic data, we perform finite-difference simulations (using Seismic Unix code *suea2df*; Juhlin, 1995) and ray tracing for 2D models that include a low-velocity isotropic lens inside a VTI layer. The parameters $V_{\rm nmo}$ and η are estimated from nonhyperbolic moveout inversion based on the Alkhalifah-Tsvankin (1995) equation:

$$t^2 = t_0^2 + \frac{x^2}{V_{\rm nmo}^2} - \frac{2\eta x^4}{V_{\rm nmo}^2[t_0^2 V_{\rm nmo}^2 + (1+2\eta)x^2]}, \qquad (3)$$

where t is the P-wave traveltime as a function of the offset x and t_0 is the zero-offset time. Equation 3 can be applied to layered VTI media with the effective parameters given by (Tsvankin, 2005):

$$V_{\rm nmo}^2(N) = \frac{1}{t_0(N)} \sum_{i=1}^{N} (V_{\rm nmo}^{(i)})^2 t_0^{(i)}, \qquad (4)$$

$$\eta(N) = \frac{1}{8}\left\{ \frac{1}{V_{\rm nmo}^4(N)\, t_0(N)} \left[\sum_{i=1}^{N} (V_{\rm nmo}^{(i)})^4 (1+8\eta^{(i)})\, t_0^{(i)} \right] - 1 \right\}, \qquad (5)$$

where $t_0^{(i)}$, $V_{\rm nmo}^{(i)}$, and $\eta^{(i)}$ are the interval values, and N is the number of layers.

Although the Alkhalifah-Tsvankin equation provides a good approximation for P-wave moveout in VTI media, the estimates of η are sensitive to correlated traveltime errors because of the tradeoff between η and $V_{\rm nmo}$

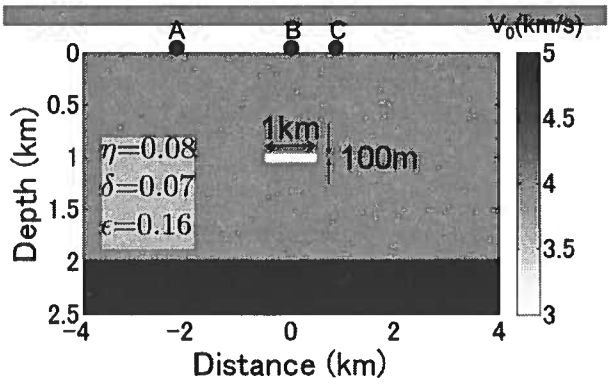

Figure 2. Single VTI layer with an isotropic lens. The lens velocity is 3 km/s; the background parameters are $V_0 = 4$ km/s, $\delta = 0.07$ and $\epsilon = 0.16$. Points A, B and C correspond to CMP locations discussed in the text. The test is performed for a spreadlength of 4 km; the target depth is 2 km.

(Grechka & Tsvankin, 1998). In our model, such errors are caused by an isotropic velocity lens in the overburden.

2.1 Single-layer model

First, we consider a rectangular lens embedded in a homogeneous VTI layer (Figure 2). The section in Figure 3 is computed by a finite-difference algorithm for common-midpoint (CMP) gathers outside the lens (location A) and at the center of the lens (location B). Whereas the lens does not distort traveltimes at location A, it causes a near-offset time delay of 17 ms and waveform distortions (related to the influence of the side and edges of the lens) in the mid-offset range at location B.

Using equation 3, we find the best-fit $V_{\rm nmo}$ and η for the target reflector from a 2D semblance scan; for comparison, we also perform conventional hyperbolic moveout inversion (Figure 4). The NMO velocity estimated from the nonhyperbolic equation at location A is close to the analytic value. At location B, however, $V_{\rm nmo}$ is about 10% greater, although the exact effective NMO velocity should decrease by 2% due to the low velocity inside the lens. At a CMP location near the edge of the lens (location C), $V_{\rm nmo}$ is 7% smaller than the exact value. Interestingly, nonhyperbolic moveout inversion produces an error in $V_{\rm nmo}$, which is two times larger than that obtained from hyperbolic moveout analysis.

The reason for the lens-induced distortion in $V_{\rm nmo}$ is described in Al-Chalabi (1979) and Biondi (2006) (Figures 5a,b). Near-offset rays at location B pass twice through the lens, while far-offset rays miss the lens completely. Since the lens has a lower velocity, this leads to a smaller traveltime difference between the near- and far-offset traces and, therefore, a higher NMO velocity. In contrast, for location C, the lens is missed by near-offset

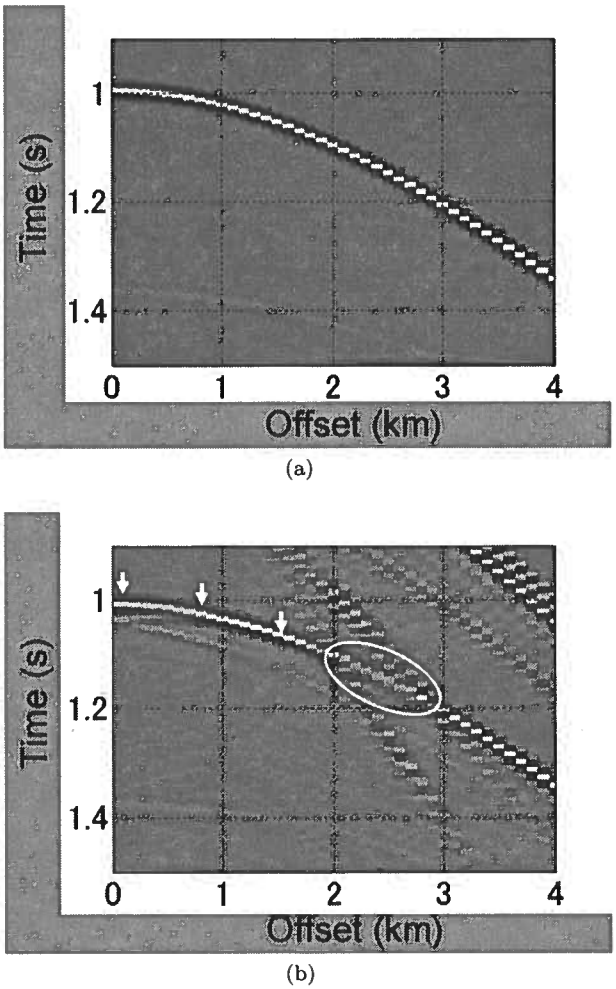

Figure 3. Comparison of CMP gathers for the model from Figure 2 computed (a) outside the lens (location A) and (b) above the center of the lens (location B) with a finite-difference algorithm. The traveltime shifts at near offsets (arrows) at location B cause significant errors in the parameters $V_{\rm nmo}$ and η. The lens-related waveform distortion at location B is contoured by the ellipse.

rays and the traveltime difference between the near and far offsets becomes larger, which reduces $V_{\rm nmo}$ (Figure 5b).

The nonhyperbolic inversion gives a closer approximation to the actual traveltime due to the contribution of the additional parameter η. Hence, the best-fit nonhyperbolic moveout curve at location B reproduces the increase in the near-offset traveltime, which causes a pronounced deviation of the estimated $V_{\rm nmo}$ from the exact value (Figure 5c). Note that the hyperbolic correction distorts the velocity $V_{\rm nmo}$ outside the lens due to the influence of nonhyperbolic moveout.

The laterally varying η-curve resembles the reversed version of the $V_{\rm nmo}$-curve. While in the absence

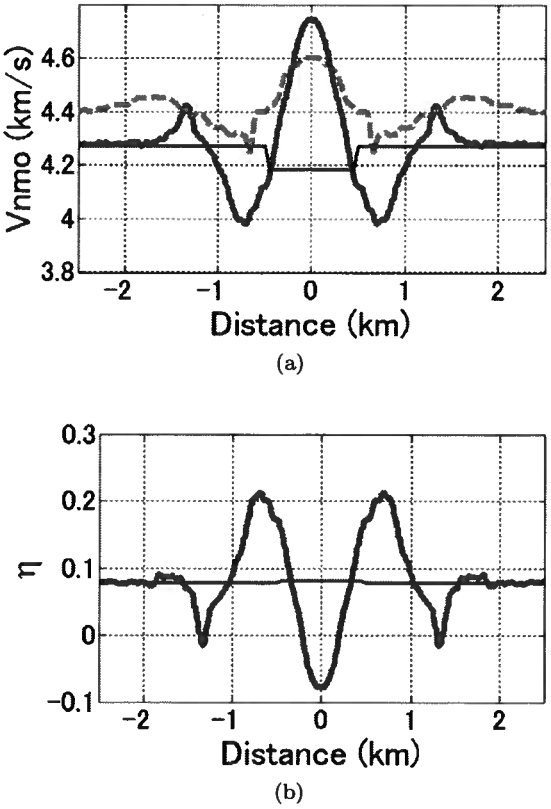

Figure 4. Lateral variation of the inverted (a) V_{nmo} and (b) η (bold solid lines) along the line using a spreadlength of 4 km (the spreadlength-to-depth ratio $X/D = 2$). The dashed line on plot (a) is the NMO velocity obtained from hyperbolic moveout analysis for the same spreadlength. The exact effective V_{nmo} (equation 4) and η (equation 5) are marked by thin solid lines.

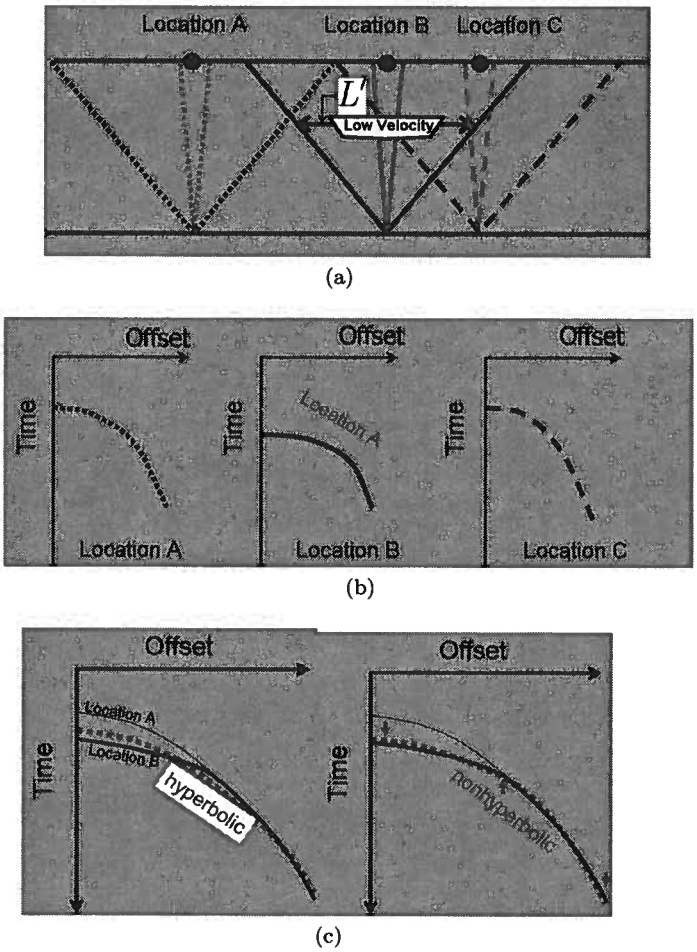

Figure 5. (a) Schematic picture of near- and far-offset raypaths from a horizontal reflector beneath a low-velocity lens at three CMP locations (modified from Biondi, 2006). (b) The influence of the lens on the moveout curves. The raypaths and moveout curves at locations A, B and C are shown by dotted, solid and dashed lines, respectively. (c) Schematic estimated moveout curves (dotted lines) obtained from hyperbolic (left) and nonhyperbolic (right) inversion at location B. The actual moveouts at locations A and B are shown by thin and bold solid lines, respectively.

of the lens the effective η at location B should almost coincide with the background $\eta = 0.08$, the estimated $\eta = -0.07$ is much smaller. The understated value of η is explained by the need to compensate for the overstated estimate of V_{nmo} in reproducing traveltimes at moderate and large offsets (Grechka & Tsvankin, 1998; Tsvankin, 2005). The magnitude of the variation (the difference between the largest and smallest values) in η along the line is close to 0.3.

2.2 Dependence of distortions on the lens parameters

Using ray-traced synthetic data, we investigate the dependence of the inverted moveout parameters on the velocity, width, and depth of the lens. The replacement of finite differences with ray tracing does not significantly change the inversion results.

As expected, the magnitude of the errors in V_{nmo} and η is proportional to the velocity contrast between the lens and the background (Figure 6a). When the spreadlength is fixed, the time distortions depend on the ratio W/L', where W is the width of the lens and L' is the maximum horizontal distance between the incident and reflected rays at the lens depth (Figure 5a). Note that L' decreases with increasing lens depth. For the model used in the test, the distortions in V_{nmo} and η are largest when the width of the lens is 0.5 km (or $W/L' = 0.25$) (Figure 6b). On the other hand, the error in V_{nmo} estimated from hyperbolic moveout inversion has a flat maximum for the width ranging from 0.5 km to 1.5 km.

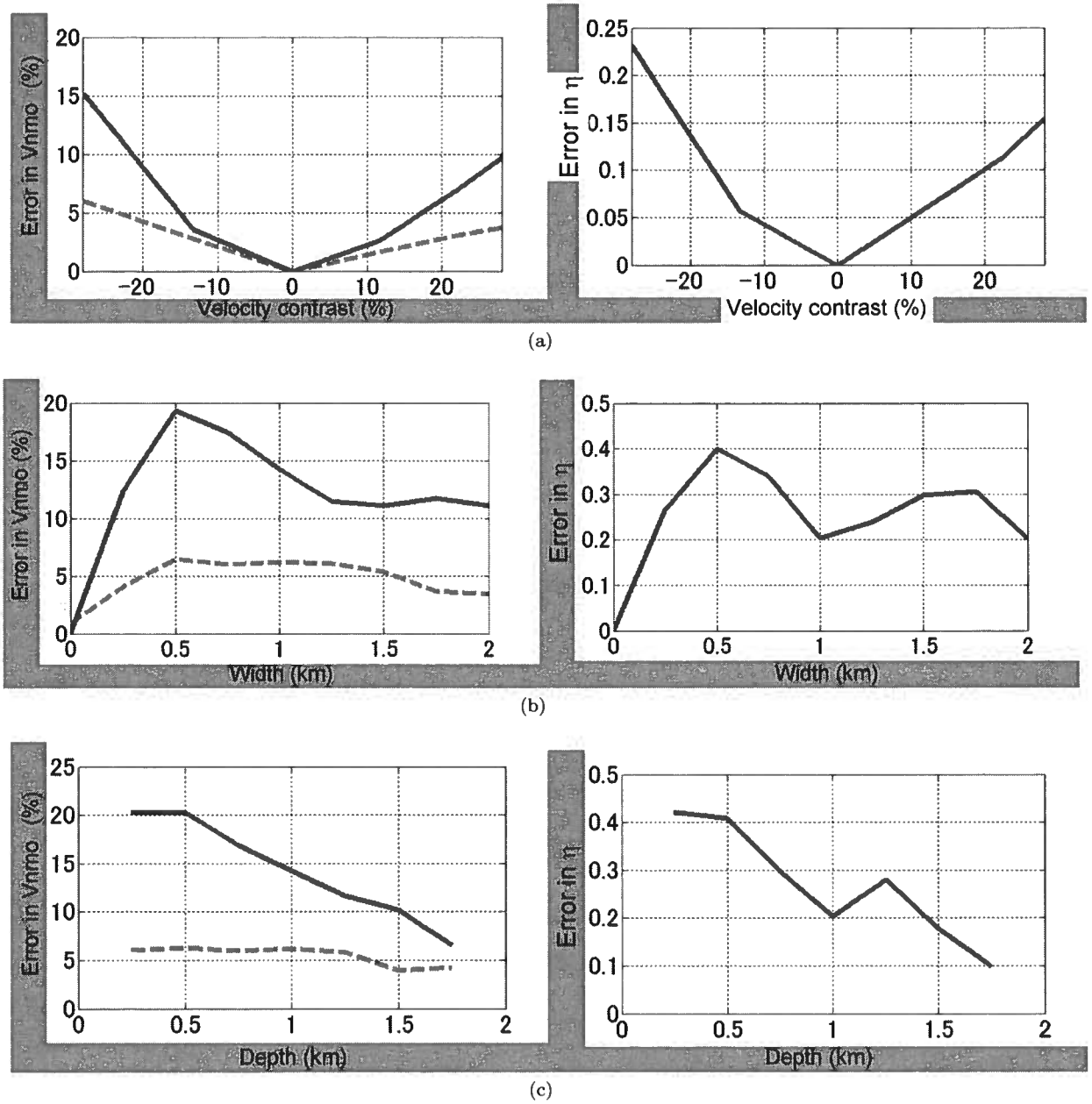

Figure 6. Dependence of the magnitude of the variation in V_{nmo} (left) and η (right) on (a) the velocity contrast defined as $(V_{\text{lens}} - V_{\text{back}})/V_{\text{back}}$, where V_{lens} is the lens velocity and V_{back} is the background velocity, (b) the width and (c) the depth of the lens. V_{nmo} is obtained from nonhyperbolic (solid lines) and hyperbolic (dashed lines) moveout inversion. The spreadlength is 4 km (offset-to-depth ratio $X/D = 2$).

Since W/L' at the surface is 0.25 ($W = 1$ km, spreadlength is 4 km) in this model, a shallower lens causes larger errors in V_{nmo} and η (Figure 6c). For a depth of 0.25 km ($W/L' = 0.29$), the errors are close to the largest distortions for the test in Figure 6b.

2.3 Identifying lens-induced distortions

Identifying the range of CMP locations influenced by the lens is critical for avoiding the use of distorted parameters. It is clear from the above results that large variations of V_{nmo} and η on the scale of spreadlength are strong indications of the lens. Using the single-layer lens model, we suggest two additional indicators of the

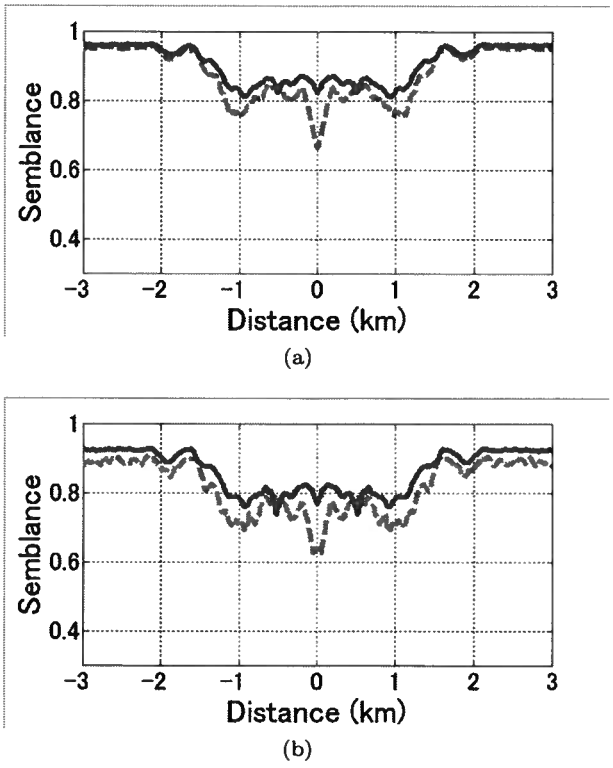

Figure 7. Semblance value for moveout-corrected gathers before (dashed line) and after (solid line) applying trim statics. The data were contaminated by random noise with the signal-to-noise ratio equal to (a) 10 and (b) 5.

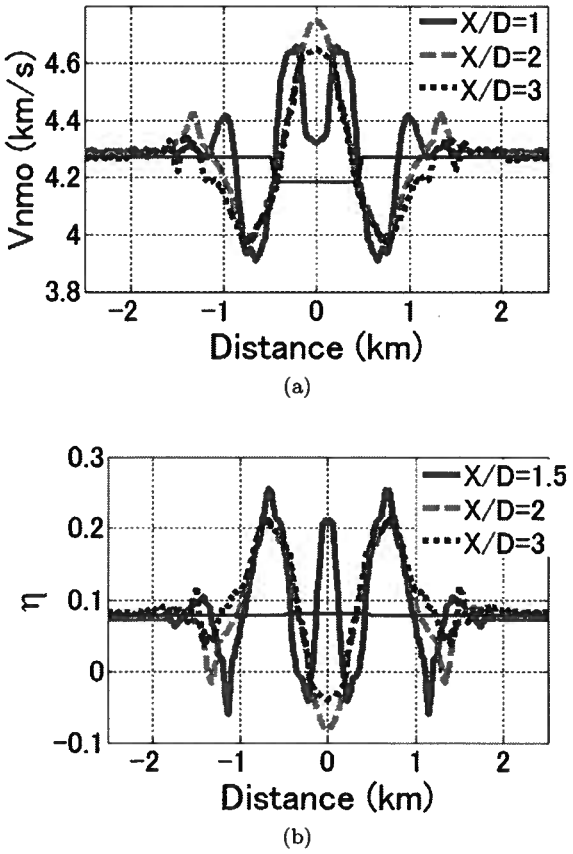

Figure 8. Dependence of (a) V_{nmo} and (b) η on the spreadlength-to-depth ratio (X/D).

lens – residual moveout after application of nonhyperbolic moveout correction and the dependence of V_{nmo} and η on spreadlength.

The moveout curve distorted by the lens cannot be completely flattened by the nonhyperbolic moveout equation. To estimate the magnitude of the residual moveout, one can use so-called trim statics (Ursenbach & Bancroft, 2001). Trim statics involves cross-correlation between a near-offset trace and all offset traces, which helps evaluate the statics shifts needed to eliminate the residual moveout. Due to the presence of residual moveout in the area influenced by the lens, application of trim statics increases the semblance (Figure 7). Still, the semblance value after trim statics at location B is lower than that at location A because of the lens-induced waveform distortions.

Trim statics, however, may not perform well when the data contain random or coherent noise (Ursenbach & Bancroft, 2001). If the signal-to-noise (S/N) ratio is less than five, trim statics increases the semblance by aligning noise components in the statics-corrected gather (Figure 7). Thus, trim statics can be used to delineate the area influenced by the lens only for relatively high S/N ratios.

Another possible lens indicator is the variation of the moveout parameters with spreadlength. As shown in Figure 8, the shape of the V_{nmo}- and η- curves is highly sensitive to the spreadlength-to-depth ratio (X/D). In contrast, the estimated moveout parameters at location A outside the lens are weakly dependent on spreadlength.

2.4 Layered model

The conclusions drawn above remain valid for a more realistic, layered model containing a parabola-shaped lens, which causes a maximum time distortion (or push-down anomaly) of 18 ms (Figure 9). We generate synthetic data with finite-differences and apply nonhyperbolic moveout inversion for the two interfaces (A and B) below the lens (Figure 10).

For a spreadlength of 4 km, the maximum distortion (the maximum deviation from the exact value) in V_{nmo} reaches approximately 9% for interface A and 11% for interface B (Figure 10), while the distortion in η

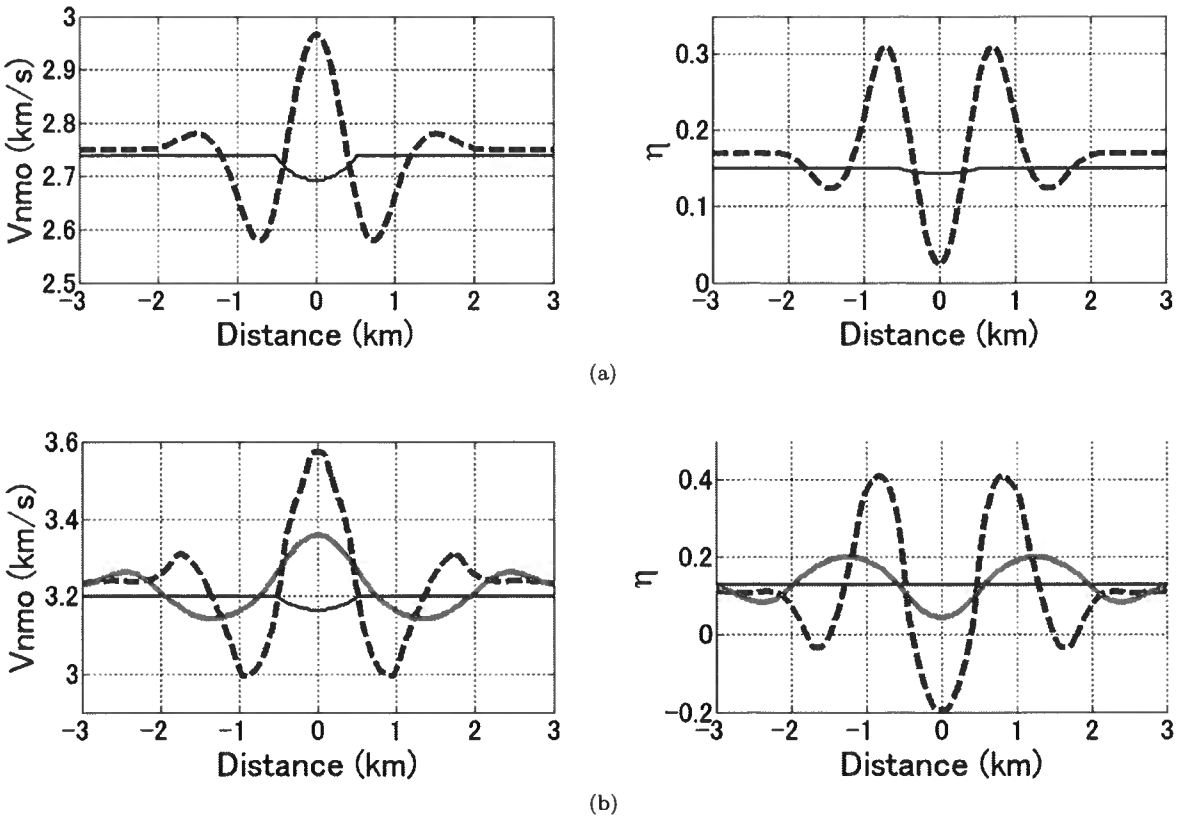

Figure 10. Lateral variation of estimated V_{nmo} (left) and η (right) for the model from Figure 9 for (a) interface A and (b) interface B. The dashed lines correspond to a spreadlength of 4 km, solid lines [only on plot (b)] to a spreadlength 6 km. The thin solid lines mark the exact parameters.

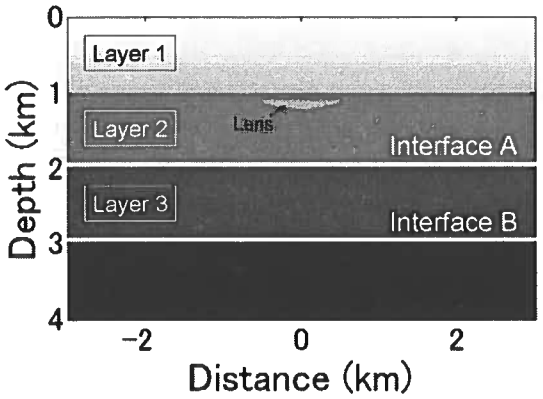

Figure 9. Layered model with a parabola-shaped lens. The first layer is isotropic and vertically heterogeneous; V_0 changes from 1.5 km/s at the surface to 2.5 km/s at the 1 km depth. The second layer is homogeneous VTI with $V_0 = 3.5$ km/s, $\delta = 0.07$ and $\epsilon = 0.16$ and contains an isotropic lens with $V_0 = 2.7$ km/s. The maximum thickness of the lens is 100 m. The third layer is homogeneous VTI with $V_0 = 4.2$ km/s, $\delta = 0.05$ and $\epsilon = 0.1$.

reaches 0.15 and 0.33, respectively. The larger errors for interface B are related to its lower ratio X/D.

When we use a spreadlength of 6 km ($X/D = 2$), the distortions in V_{nmo} and η for interface B decrease to 5% and 0.08, respectively. As is the case for a homogeneous background medium, the moveout-corrected gather exhibits residual moveout in the area influenced by the lens (Figure 11). Thus, the presence of residual moveout and the dependence of the moveout parameters on the spreadlength can serve as lens indicators for layered media as well.

3 CORRECTION ALGORITHM

It is clear from the modeling results that even a thin lens can cause significant errors in the parameters V_{nmo} and η. Another serious lens-induced distortion is the push-down anomaly on the stacked time section (Figure 12a). Although the time anomaly becomes smaller if the stack is produced using the background moveout parameters estimated away from the lens, the stacked event then has a smaller power because of a larger residual moveout

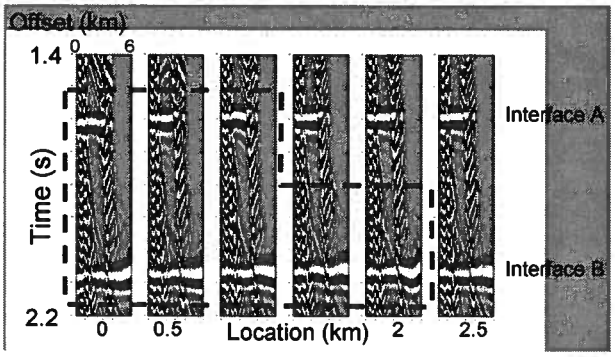

Figure 11. Moveout-corrected gathers computed using the best-fit parameters $V_{\rm nmo}$ and η. Residual moveout is observed inside the area marked by the dashed line.

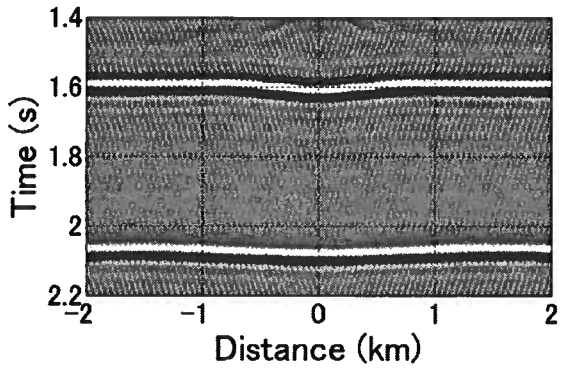

(a)

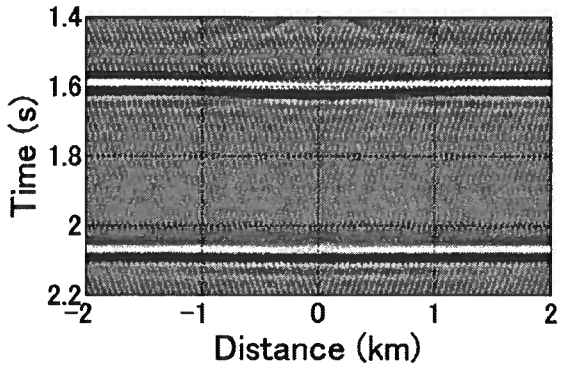

(b)

Figure 12. Stacked section generated using (a) the best-fit moveout parameters and (b) the background parameters.

(Figure 12b). Clearly, it is desirable to produce an accurate stacked section without reducing the stack power. Here, we introduce two methods for correcting P-wave data from layered VTI media for the influence of the lens. One of them is designed to mitigate the distortions on the stacked section using trim statics. The other method makes it possible to remove the traveltime distortions from each recorded trace and, therefore, obtain both accurate moveout parameters and a high-quality stack.

3.1 Trim statics

By eliminating residual moveout, trim statics makes all traces kinematically equivalent to the zero-offset trace (Figure 13a). Thus, trim statics increases stack power and generates a stack that kinematically reproduces the zero-offset section (compare Figure 13b with Figure 12a).

To remove the zero-offset time distortion, we assume that the zero-offset raypath is not influenced by the lens and remains vertical for all horizontal interfaces. Then the distortion of t_0 should be the same at interfaces A and B. This assumption allows us to use the estimated push-down at interface A for correcting the time distortions for both interfaces. The resulting stacked section is kinematically correct and has a high stack power (Figure 13c). However, as discussed above, trim statics works only for high S/N ratios and cannot be used to estimate the background values of $V_{\rm nmo}$ and η.

3.2 Prestack traveltime shifts

3.2.1 Method

The correction algorithm discussed here is designed for a horizontally layered overburden containing the lens, but the target reflector can be dipping or curved. Unlike the statics correction, this technique involves computation of traveltime shifts as functions of offset and target depth (Figure 14a). As the input data we use the zero-offset time shifts ("pull-up" or "push-down" anomalies, Δt_0) for the horizontal reflector immediately below the lens. The lens-related perturbation of the raypath is assumed to be negligible, so that the ray in the layer containing the lens can be considered straight. Then the ray crossing the lens can be reconstructed using the velocity-independent layer-stripping method (VILS) of Dewangan & Tsvankin (2006).

VILS builds the interval traveltime-offset function by performing kinematic downward continuation of the wavefield without knowledge of the velocity model. Each layer in the overburden is supposed to be laterally homogeneous with a horizontal symmetry plane, so that the raypath of any reflection event is symmetric with respect to the reflection point. The bottom of the target layer, however, can be curved and the layer itself can be heterogeneous. Wang & Tsvankin (2009) show that VILS provides more robust estimates of the interval moveout parameters in VTI and orthorhombic models than Dix-type equations.

VILS can be applied to our model under the as-

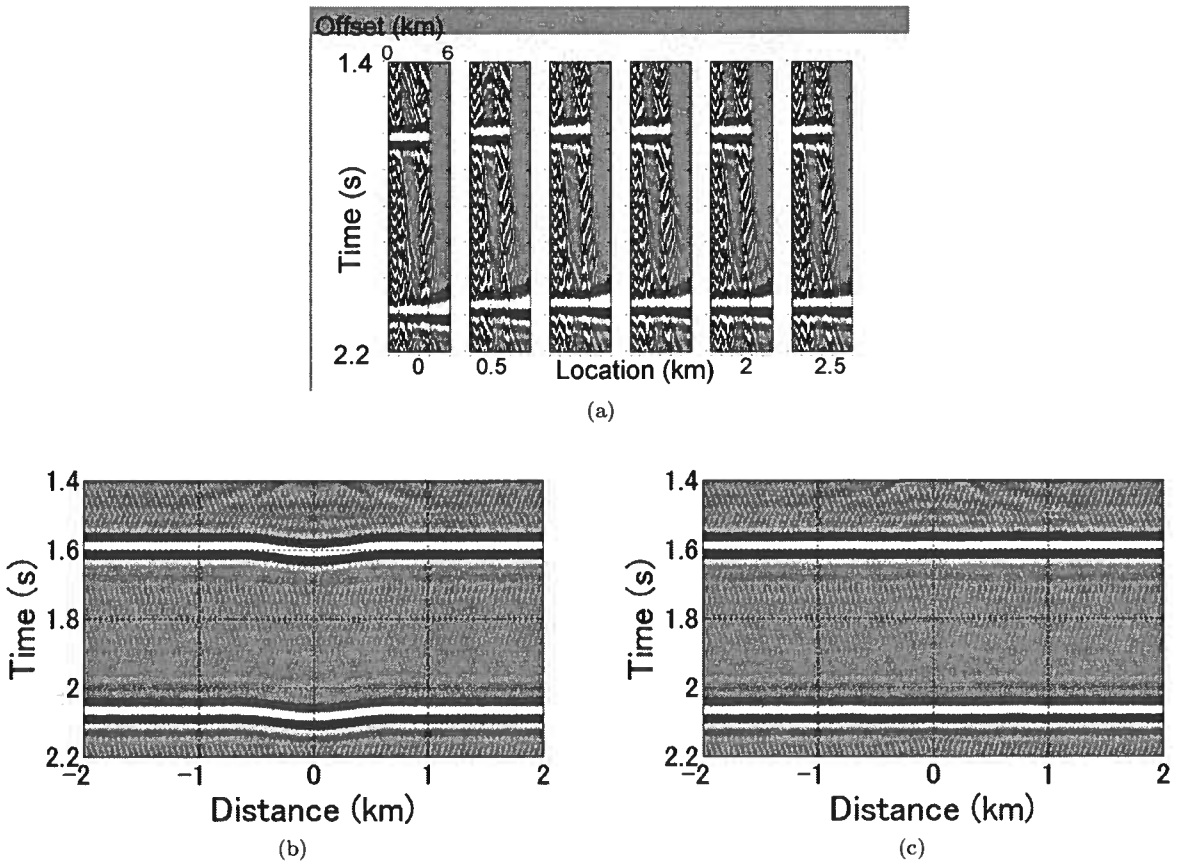

Figure 13. (a) Moveout-corrected gather after application of trim statics; (b) the stacked section after trim statics, and (c) the stacked section from plot (b) after removing the push-down anomaly at interface A.

sumption that the raypath in the overburden is not distorted by the lens. The idea of VILS is to identify reflections from the top and bottom of a certain layer that share the same upgoing and downgoing ray segments. This is accomplished by matching time slopes on common-receiver and common-source gathers. Application of VILS to the reflections from the target and top of the layer containing the lens yields the horizontal coordinates x_{T1} and x_{R1} (Figure 14a). Likewise, the coordinates x_{R2} and x_{T2} are estimated by combining the target event with the reflection from the bottom of the layer containing the lens.

Under the straight-ray assumption, we find the horizontal coordinates of the crossing points and the ray angles (Figures 14a,b):

$$x_{TL} = x_{T1} + \frac{z'_{TL}(x_{T2} - x_{T1})}{z}, \tag{6}$$

$$x_{RL} = x_{R1} - \frac{z'_{RL}(x_{R1} - x_{R2})}{z}, \tag{7}$$

$$\cos\theta_{TL} = \frac{z}{\sqrt{(x_{T2} - x_{T1})^2 + z^2}}, \tag{8}$$

$$\cos\theta_{RL} = \frac{z}{\sqrt{(x_{R1} - x_{R2})^2 + z^2}}, \tag{9}$$

where z is the thickness of the layer with the lens, and z'_{TL} and z'_{RL} are the distances from the lens to the top of the layer at locations x_{TL} and x_{RL}, respectively.

If the lens produces a sufficiently strong reflection and the layer is vertically homogeneous, the ratio z'/z can be estimated from the corresponding zero-offset traveltimes (t'/t). In the layered model, we can clearly identify the lens reflection at t = 1.15 s on the stacked section (Figure 15a). This indicates that the horizontal coordinates and the ray angles can be estimated without complete information about the velocity and anisotropy parameters. Then the total lens-related traveltime shift for the target event (Δt_{ta}) can be computed as

$$\Delta t_{\mathrm{ta}} = \frac{1}{2}\left(\frac{\Delta t_0(x_{TL}, 0)}{\cos\theta_{TL}} + \frac{\Delta t_0(x_{RL}, 0)}{\cos\theta_{RL}}\right), \tag{10}$$

where $\Delta t_0(x_{TL}, 0)$ and $\Delta t_0(x_{RL}, 0)$ are the zero-offset time distortions below the lens at locations x_{TL} and

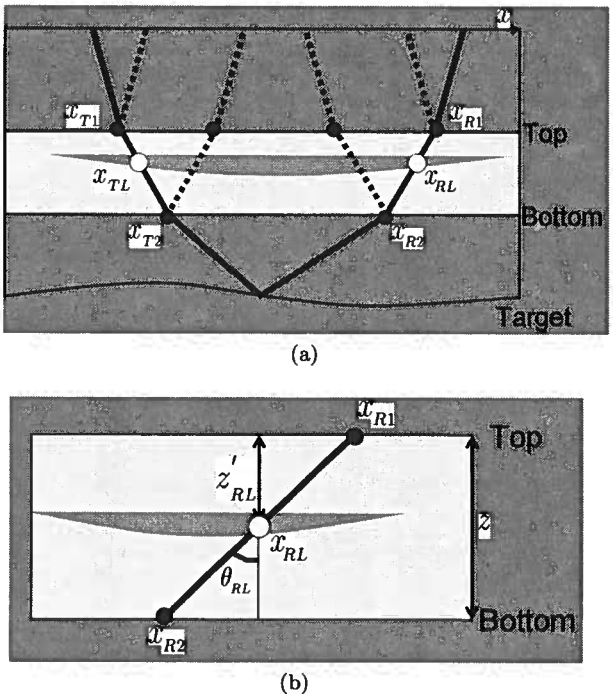

Figure 14. (a) Ray diagram of the correction algorithm. The horizontal coordinates x_{T1}, x_{T2} and x_{R1}, x_{R2} are determined from the velocity-independent layer-stripping method. (b) Upgoing ray segment crossing the lens. Using the values of z'_{RL} and z, we can compute the horizontal location of the crossing point (x_{RL}) and the ray angle (θ_{RL}).

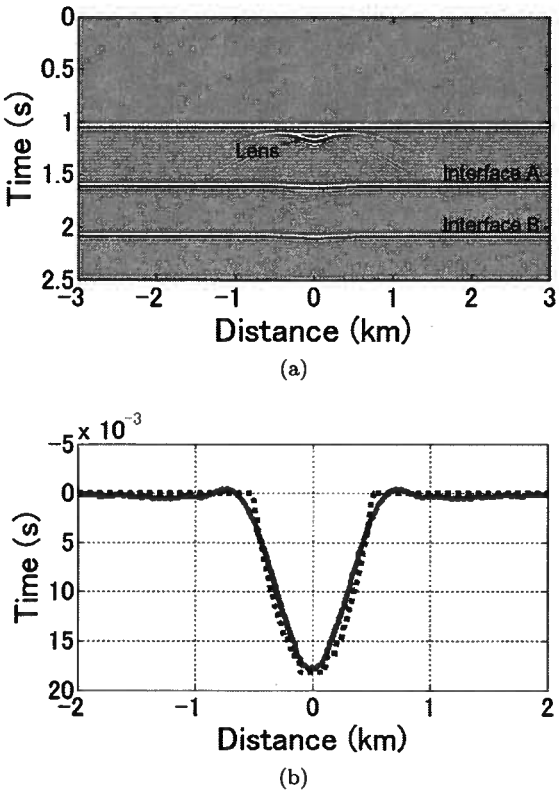

Figure 15. (a) Near-offset stacked section obtained for the offset range from 0 to 200 m, and (b) the magnitude of the push-down anomaly (solid line) estimated by picking the maximum amplitude along interface A. The dotted line in (b) is the exact Δt_0.

x_{RL}, respectively. Both $\Delta t_0(x_{TL},0)$ and $\Delta t_0(x_{RL},0)$ can be estimated from the near-offset stack. The ray angles θ_{TL} and θ_{RL} do not have to be the same, which makes the algorithm suitable for dipping or curved target reflectors.

After the correction, the kinematics of the prestack data should be close to the reflection traveltime described by the background values of $V_{\rm nmo}$ and η. The interval parameters $V_{\rm nmo}^{(i)}$ and $\eta^{(i)}$ can be computed using the layer-stripped data corrected for the lens-induced time shifts. The removal of the time distortions also helps generate an accurate stacked section.

3.2.2 Synthetic test

The prestack correction algorithm is tested here on the layered model from Figure 9. First, we need to estimate the three required input quantities: Δt_0, the ratio z'/z, and the thickness z of the layer containing the lens. The values of Δt_0 (Figure 15b) and z'/z (t'/t) are obtained from the near-offset stacked section (Figure 15a). For purposes of this test, the thickness of the layer containing the lens is assumed to be known.

Application of traveltime shifts computed from equation 10 eliminates the time-varying push-down anomaly and increased the S/N ratio of the stacked section (Figure 16a). Also, the correction significantly reduces the residual moveout in the moveout-corrected gathers (Figure 16b) and the errors in the effective parameters $V_{\rm nmo}$ and η (Figure 17a). For interface B, the distortion in $V_{\rm nmo}$ decreases from 5% to less than 1%, and in η from 0.08 to 0.02. Figure 17b shows that the correction algorithm also produces much more accurate interval parameters $V_{\rm nmo}$ and η estimated from the layer-stripped data. The remaining errors are largely caused by the straight-ray assumption for the layer containing the lens.

It is important to evaluate the sensitivity of the parameter estimation to errors in the input data. Extensive testing shows that when the error in Δt_0 is smaller than 25%, the moveout-corrected gather is almost flat. To test the sensitivity to the ratio z'/z, we move the lens down by 100 m and 200 m, which corresponds to 10% and 20% errors in z'/z. Although distortions in the moveout-corrected gather become noticeable when the error reaches 20%, the magnitude of the residual moveout is still much smaller than that before the correction.

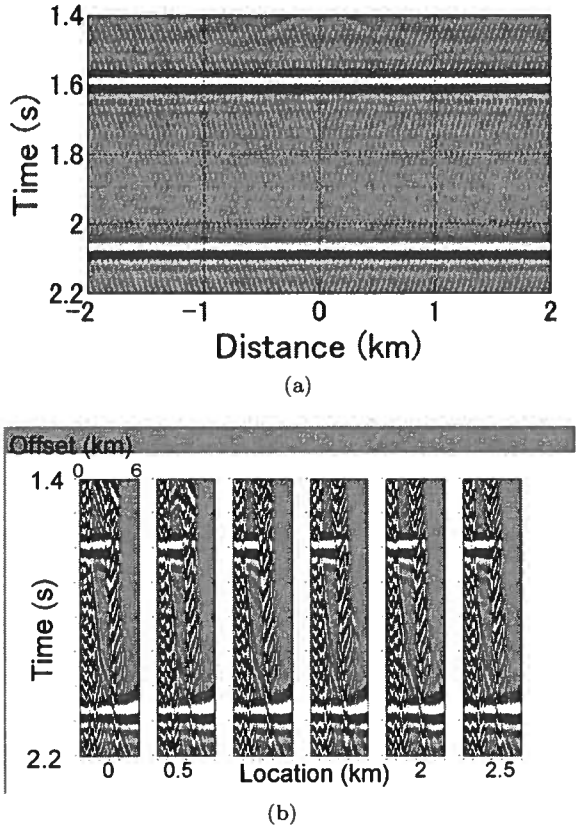

Figure 16. (a) Stacked section and (b) moveout-corrected gathers obtained after applying prestack traveltime shifts that compensate for the influence of the lens.

Finally, a thickness error up to 20% proves to have little impact on the output of the correction algorithm. An accurate stacked section can be generated even for somewhat larger errors in these input quantities.

4 DISCUSSION

The correction algorithm requires knowledge of the zero-offset time anomaly Δt_0, the ratio z'/z and the thickness z of the lens-containing layer. In the synthetic test, Δt_0 was accurately estimated from the push-down anomaly on the near-offset stacked section, and the ratio z'/z was obtained from the corresponding time ratio t'/t using the reflection from the lens (Figure 15). Since depth uncertainty seldom exceeds 20% in practice, errors in z are not expected to have a significant impact on the correction results.

The suggested approach should be applicable to many field data sets. For example, the time section from the central North Sea in Figure 1 contains channel-like structures and pull-up anomalies (marked area in Figure 1), which indicate the presence of high-velocity channel fills (Armstrong *et al.*, 2001). The lens reflections are sufficiently strong for estimating the ratio t'/t (and, therefore, z'/z), and the pull-up time anomaly can be accurately measured as well.

Our algorithm can also be applied to layered media with multiple lenses, if it is possible to estimate the values of Δt_0 and z'/z for each lens separately. Then the total traveltime shifts are obtained by summing the individual lens-induced time distortions. However, the algorithm will produce distorted time shifts when a layer contains multiple lenses or the lens reflections cannot be identified. Also, the algorithm assumes a laterally homogeneous overburden and straight rays in the layers containing the lenses. Therefore, the correction may become inaccurate when the overburden includes dipping interfaces or has a strong velocity contrast between the lens and the background.

5 CONCLUSIONS

We demonstrated that a relatively thin velocity lens may cause significant, laterally varying distortions in the moveout parameters V_{nmo} and η estimated from nonhyperbolic moveout analysis. The magnitude of the distortion depends on the width and depth of the lens and is proportional to the velocity contrast between the lens and the background. The error in V_{nmo} is larger after nonhyperbolic moveout inversion compared with the conventional hyperbolic algorithm applied for the same spreadlength, particularly when the lens is narrow or is located in a shallow layer. Hence, although nonhyperbolic moveout analysis produces smaller residual moveout and higher stacking power than the hyperbolic equation, it does not guarantee a more accurate estimation of NMO velocity in the presence of lateral heterogeneity.

Identifying the area influenced by the lens is critical for avoiding use of distorted moveout parameters. We showed that the residual moveout can serve as a lens indicator because the lens-induced distortion cannot be completely removed by nonhyperbolic moveout inversion. The presence of residual moveout can be identified from the increase in semblance after application of trim statics, provided the signal-to-noise ratio is sufficiently high. A lens also manifests itself by making the moveout parameters strongly dependent on spreadlength and the lateral coordinate.

To correct for lens-induced traveltime shifts on prestack data, we developed an algorithm based on velocity-independent layer stripping (VILS). Synthetic tests confirmed that the algorithm successfully removes lens-induced distortions on the stacked section and substantially reduces the errors in the effective and interval parameters V_{nmo} and η. The correction requires estimates of the zero-offset time distortion Δt_0, the thickness z of the layer containing the lens and the ratio z'/z, where z' is the distance between the lens and the top of

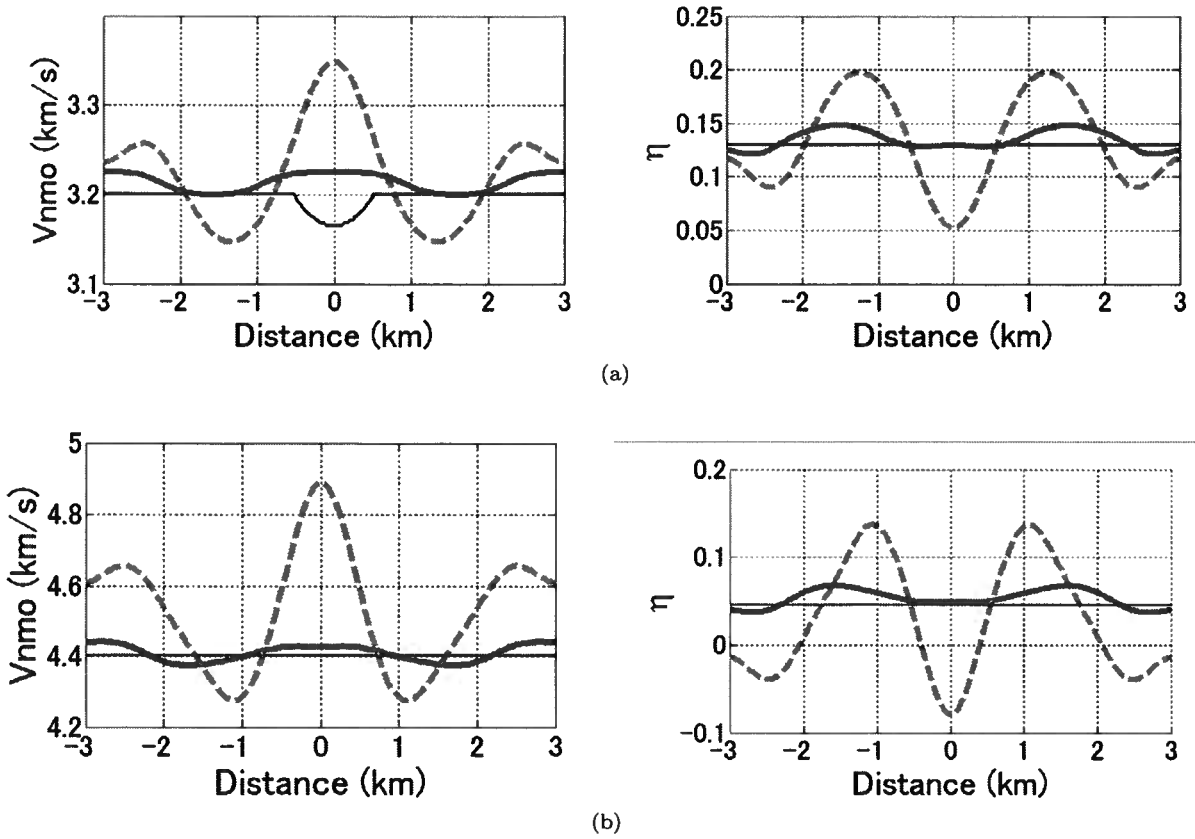

Figure 17. (a) Inverted effective parameters V_{nmo} (left) and η (right) for interface B before (dashed line) and after (thick solid line) applying the correction algorithm ($X/D = 2$). (b) The interval parameters V_{nmo} and η in the third layer (2-3 km) estimated before (dashed line) and after (thick solid line) applying the correction algorithm. The spreadlength (before applying VILS) is 6 km. Thin solid lines mark the exact parameters.

the lens-containing layer. The parameters Δt_0 and z'/z can be obtained from reflection data, while z cannot be found without additional (e.g., borehole) information. However, errors up to 20% in the Δt_0 and z, as well as a 10% error in the ratio z'/z, do not significantly hamper the performance of the algorithm.

Although we presented the correction method for a 2D model that contains a single lens, it can be extended to wide-azimuth data from layered media with well-separated multiple lenses. Potentially, the 3D version of the algorithm can be used to correct for the influence of small-scale lateral heterogeneities on azimuthal moveout inversion.

6 ACKNOWLEDGMENTS

We are grateful to members of the A(nisotropy)-Team of the Center for Wave Phenomena (CWP), Colorado School of Mines (CSM), for helpful discussions. This work was supported by Japan Oil, Gas and Metals National Corporation (JOGMEC) and the Consortium Project on Seismic Inverse Methods for Complex Structures at CWP.

REFERENCES

Al-Chalabi, 1979, Velocity determination from seismic reflection data , Applied Science Publishers.

Alkhalifah, T., and Tsvankin, I., 1995, Velocity analysis for transversely isotropic media: Geophysics, **60**, 1550–1566.

Alkhalifah, T., 1997, Velocity analysis using nonhyperbolic moveout in transversely isotropic media: Geophysics, **62**, 1839–1854.

Armstrong, T., McAteer, J., and Connolly, P., 2001, Removal of overburden velocity anomaly effects for depth conversion: Geophysical Prospecting, **49**, 79–99.

Biondi, B. L., 2006, 3D seismic imaging , Society of Exploration Geophysicists.

Blias, E., 2009, Stacking velocities in the presence of

overburden velocity anomalies: Geophysical Prospecting, **57**, 323–341.

Dewangan, P., and Tsvankin, I., 2006, Velocity-independent layer stripping of PP and PS reflection traveltimes: Geophysics, **71**, no. 4, U59–U65.

Fruehn, J., Jones, I. F., Valler, V., Sangvai, P., Biswal, A., and Mathur, M., 2008, Resolving near-seabed velocity anomalies: Deep water offshore eastern India: Geophysics, **73**, no. 5, VE235–VE241.

Fujimoto, M., Takanashi, M., Szczepaniak, M., and Yoshida, T., 2007, Application of prestack depth migration across the Ichthys field, Browse basin: ASEG Annual Meeting, Expanded Abstracts.

Grechka, V., and Tsvankin, I., 1998, Feasibility of nonhyperbolic moveout inversion in transversely isotropic media: Geophysics, **63**, 957–969.

Grechka, V., 1998, Transverse isotropy versus lateral heterogeneity in the inversion of P-wave reflection traveltimes: Geophysics, **63**, 204–212.

Jenner, E., 2009, Data example and modelling study of P-wave azimuthal anisotropy potentially caused by isotropic velocity heterogeneity: First Break, **27**, 45–50.

Juhlin, C., 1995, Finite-difference elastic wave propagation in 2D heterogeneous transversely isotropic media: Geophysical Prospecting, **43**, 843–858.

Lynn, W. S., and Claerbout, J. F., 1982, Velocity estimation in laterally varying media: Geophysics, **47**, 884–897.

Takanashi, M., Kaneko, M., Monzawa, N., Imahori, S., Ishibashi, T., and Sakai, A., 2008, Removal of overburden channel effects through channel velocity modeling and prestack depth migration for an oil field offshore Abu-Dhabi: Abu Dhabi International Petroleum Exhibition and Conference, SPE 117982.

Toldi, J., 1989, Velocity analysis without picking: Geophysics, **54**, 191–199.

Tsvankin, I., and Thomsen, L., 1994, Nonhyperbolic reflection moveout in anisotropic media: Geophysics, **59**, 1290–1304.

Tsvankin, I., 2005, Seismic signatures and analysis of reflection data in anisotropic media , 2nd ed, Elsevier Science Publishing Company, Inc.

Ursenbach, C. P., and Bancroft, J. C., 2001, Playing with fire: Noise alignment in trim and residual statics: 71th Annual Internatinal Meeting, SEG, Expanded Abstracts, 1973-1976.

Wang, X., and Tsvankin, I., 2009, Estimation of interval anisotropy parameters using velocity-independent layer stripping: Geophysics, **74**, no. 5, WB117–WB127.

Woodward, M. J., Nichols, D., Zdraveva, O., Whitfield, P., and Johns, T., 2008, A decade of tomography: Geophysics, **73**, no. 5, VE5–VE11.

Estimation of interval shear-wave attenuation from mode-converted data

Bharath Shekar & Ilya Tsvankin

ABSTRACT

Interval attenuation measurements provide valuable information for reservoir characterization and lithology discrimination. Here, we extend the attenuation layer-stripping method of Behura and Tsvankin to mode-converted (PS) waves with the goal of estimating the interval S-wave attenuation coefficient. By identifying PP and PS events with shared ray segments and applying the PP+PS=SS method, we first perform kinematic construction of pure shear (SS) events in the target layer and overburden. Then, the modified spectral-ratio method is used to compute the effective shear-wave attenuation coefficient for the target reflection. Finally, application of the dynamic version of velocity-independent layer stripping to the constructed SS reflections yields the interval S-wave attenuation coefficient in the target layer. The attenuation coefficient estimated for a range of source-receiver offsets can be inverted for the interval attenuation-anisotropy parameters. The method is tested on a multicomponent synthetic data set from layered VTI (transversely isotropic with a vertical symmetry axis) media generated with the anisotropic reflectivity method.

Key words: attenuation, anisotropy, multicomponent data, shear waves

Introduction

Attenuation analysis provides seismic attributes sensitive to the physical properties of the subsurface. Reliable attenuation measurements have become feasible with acquisition of high-quality reflection and borehole data. Attenuation is often found to be anisotropic (directionally dependent) due to a variety of factors such as the intrinsic anisotropy of the material, the presence of aligned fluid-fractures (Batzle et al., 2005), or interbedding of thin layers with different properties (Zhu et al., 2007). The magnitude of attenuation anisotropy can be much higher than that of velocity anisotropy, and the symmetry of the attenuation coefficient can be different than that of the velocity function (Liu et al., 2007).

The quality factors Q_P and Q_S are widely used as measures of P- and S-wave intrinsic attenuation, respectively (Zhu, 2006). Dvorkin and Mavko (2006) observe that the ratio Q_S^{-1}/Q_P^{-1} can serve as an indicator of hydrocarbons because the values of Q_P and Q_S in fluid-saturated rocks are close, while in dry or gas-saturated rocks $Q_P \gg Q_S$. Adam (2008) suggests that time-lapse studies of attenuation are useful in monitoring reservoir fluids. Chichinina et al. (2009) conduct ultrasonic laboratory experiments for models with VTI symmetry. Their results show that the symmetry-axis attenuation of P-waves is much greater than that of S-waves in dry samples, while for oil-saturated models, the two models have comparable attenuation. Shear-wave attenuation in heavy oils is closely linked to temperature, and hence could be useful in seismic monitoring of thermal recovery processes (Behura et al., 2007).

De et al. (1994) report measurements of the shear-wave quality factor from vertical seismic profiling (VSP) surveys and sonic logs. It is more difficult to study S-wave attenuation using reflection data due to such problems as the high level of noise and statics problems for shear waves. Behura and Tsvankin (2009) combine the velocity-independent layer stripping (VILS) method of Dewangan and Tsvankin (2006) with the spectral-ratio method to estimate the interval attenuation of pure PP or SS reflected waves. They identify the overburden and target events that share ray segments in the overburden to compute the interval traveltime and then the interval attenuation coefficient in the target layer. Their algo-

rithm is data-driven and does not require information about the velocity or attenuation in the overburden.

Shear waves, however, cannot be excited offshore, and shear-wave sources are seldom used on land. Therefore, here we extend the technique of Behura and Tsvankin (2009) to mode-converted data by supplementing it with the PP+PS=SS method of Grechka and Tsvankin (2002). First, we discuss how the PP+PS=SS method can be combined with VILS to construct SS-wave moveout in the target layer and overburden from PP and PS data. Then the interval S-wave attenuation coefficient is obtained by extending the kimenatic construction procedure to frequency-domain amplitudes processed using the spectral-ratio method. Finally, we apply the algorithm to synthetic data generated for a layered VTI medium and investigate the accuracy of the inversion for the SV-wave attenuation-anisotropy parameters.

Methodology

For simplicity, the method is described for 2D models, but it can be extended to 3D wide-azimuth data. We operate with pure-mode (PP) and mode-converted (PS) reflections for a medium with an arbitrarily anisotropic, heterogeneous target layer overlaid by a laterally homogeneous overburden with a horizontal symmetry plane in each layer. In the 2D version of the method the vertical incidence plane is supposed to be a plane of mirror symmetry for the whole model. Therefore, both rays and the corresponding phase-velocity vectors are confined to the incidence plane, and converted waves represent in-plane polarized PSV modes. The P-to-S conversion is assumed to occur only at the reflector. We begin with a description of the algorithm designed to compute the interval shear-wave traveltimes and then discuss estimation of the interval shear-wave attenuation coefficient in the target layer.

Kinematic layer stripping for interval shear-wave traveltimes

To estimate the interval shear-wave traveltimes in the target layer, we combine the PP+PS=SS method with velocity-independent layer stripping (VILS) developed by Dewangan and Tsvankin (2006). Suppose P-wave sources and receivers of both P- and S-waves are continuously distributed along the acquisition line. As discussed by Grechka and Tsvankin (2002), matching time slopes on common-receiver gathers at the source location A allows us to identify the PP (ARB) and PS (ARC) target events that share the downgoing segment AR and the reflection point R at the bottom of the target layer (Figure 1). Likewise, for a P-wave source at B, we find PP (BRA) and PS (BRD) target events that share the downgoing segment BR. This procedure

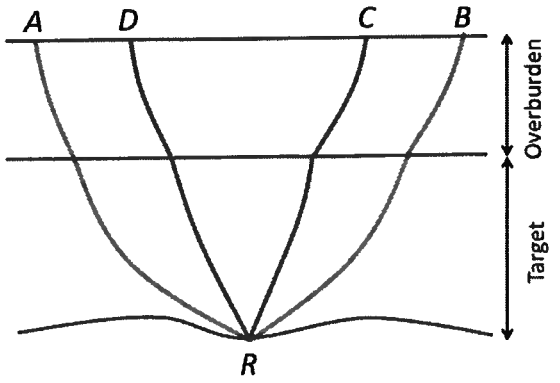

Figure 1. 2D ray diagram illustrating the PP+PS=SS method for PP and PS reflections from the bottom of the target layer. The wavefield is excited in split-spread geometry by P-wave sources located at points A and B. Target PP (ARB) and PS (ARC) events share the downgoing segment AR and, therefore the reflection point R at the bottom of the target layer. Another pair of PP (BRA) and PS (BRD) target events share the downgoing segment BR. The constructed SS target event corresponds to DRC.

makes it possible to construct the SS event DRC, where C and D are the coordinates of S-wave receivers. For brevity, we denote the PP (ARB) and PS (ARC and BRD) events by $\mathrm{PP_E}$, $\mathrm{PS_{E1}}$, and $\mathrm{PS_{E2}}$ (respectively) and the constructed SS event DRC by $\mathrm{SS_E}$ ("E" refers to effective events reflected from the bottom of the target layer). The exact shear-wave traveltime for the reflection $\mathrm{SS_E}$ is (Grechka and Tsvankin, 2002)

$$t_{SS_E} = t_{PS_{E1}} + t_{PS_{E2}} - t_{PP_E}. \qquad (1)$$

The constructed event $\mathrm{SS_E}$ can be treated (in a kinematic sense) as a pure reflection mode excited by a shear-wave source.

Next, we find the interval shear-wave traveltime in the target layer, which requires knowledge of the traveltime in the overburden. Since the data are assumed to be generated with a P-wave source, it is necessary to apply the PP+PS=SS method repeatedly to construct SS reflections in the overburden (Figure 2). To layer-strip the segment DR of the SS-wave, we need to obtain the coordinate of point I and the traveltime along the overburden segment ID. Note that the horizontal slowness along any ray in the laterally homogeneous overburden should be preserved.

First, we form a common-receiver gather of the PS-wave at location D and identify the point (E) where the time slope (horizontal slowness) coincides with that at D. The obtained overburden PS event EID shares the segment ID with the target SS event CRD (Figure 2b). Then we form a common-source PP gather at location E to find the point F where the time slope (horizontal slowness) coincides with that at E, which means that

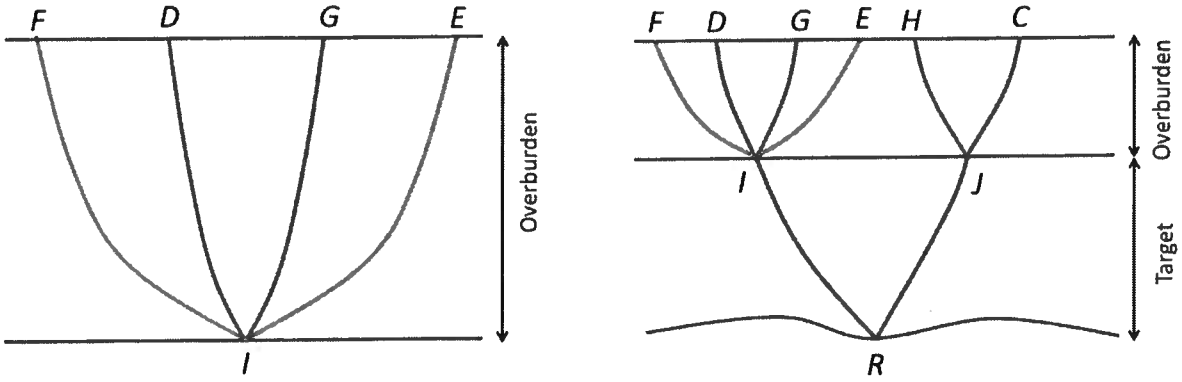

Figure 2. Layer stripping of the constructed SS events. (a) Application of the PP+PS=SS method is applied to kinematically construct pure SS-waves in the overburden. PP (EIF) and PS (EID) events share the downgoing segment EI and the reflection point I at the bottom of the overburden. Another pair of PP (FIE) and PS (FIG) overburden events share the downgoing segment FI. (b) The constructed overburden SS event DIG shares the segment ID with the target SS reflection.

the overburden PP event EIF shares the downgoing segment EI with the PS event EID (Figure 2a).

The moveout functions of the overburden PP, PS, and SS events are symmetric with respect to zero offset. Therefore, the receiver coordinate of the overburden PS event FIG can be found from

$$x_G = x_E + x_F - x_D. \tag{2}$$

The constructed event DIG (denoted by $\mathrm{SS}_{\mathrm{O1}}$, where "O" refers to the overburden and "1" to the left segment of the target SS event in Figure 2b) shares the segment ID with the target SS event DRC (Figure 2b). The PP event EIF will be denoted by $\mathrm{PP}_{\mathrm{O1}}$ and the PS events EID and FIG by $\mathrm{PS}_{\mathrm{O1}}$. The exact traveltime of the event $\mathrm{SS}_{\mathrm{O1}}$ is then given by

$$t_{SS_{O1}} = 2t_{PS_{O1}} - t_{PP_{O1}}, \tag{3}$$

and the lateral coordinate of location I is

$$x_I = \frac{x_D + x_G}{2}. \tag{4}$$

Likewise, we can apply the PP+PS=SS method to construct the overburden SS event HJC ($\mathrm{SS}_{\mathrm{O2}}$) that shares the segment JC with the target event SS_{E} (Figure 3). The corresponding traveltime $t_{SS_{O2}}$ and the lateral coordinate of point J are obtained using the algorithm discussed above. The interval shear-wave traveltime in the target layer is given by

$$t_{SS_T} = t_{SS_E} - \frac{1}{2}\left(t_{SS_{O1}} + t_{SS_{O2}}\right). \tag{5}$$

The interval traveltime t_{SS_T} corresponds to the raypath IRJ of the target event SS_{T}.

If the target is horizontal and laterally homogeneous, the raypaths of the downgoing and upgoing overburden events correspond to the same ray parameter and, therefore, are symmetric with respect to the vertical. Then $t_{SS_{O1}} = t_{SS_{O2}}$, and it is sufficient to apply the PP+PS=SS method just to one of the overburden segments of the target event SS_{E}.

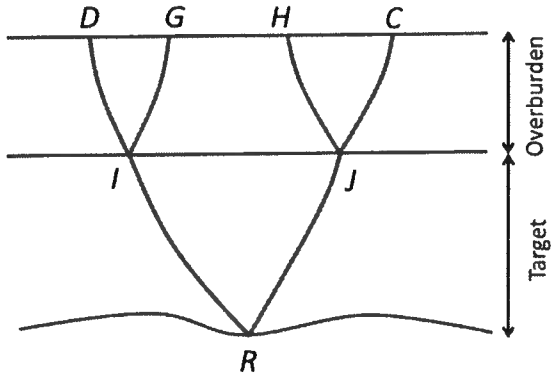

Figure 3. Raypaths of the constructed SS events. The target SS event DRC shares the segments ID and JC with the overburden events DIG and HJC, respectively. The method produces the interval traveltime along the raypath IRJ.

Layer stripping for interval shear-wave attenuation

Behura and Tsvankin (2009) combine VILS with the spectral-ratio method and apply their attenuation layer-stripping algorithm to frequency-domain amplitudes of pure-mode reflections. This technique can be extended to the combination of PP- and PS-waves analyzed

above. The ray-theoretic frequency-domain amplitudes of the waves PP_E, PS_{E1} and PS_{E2} (Figure 1) can be written as

$$|U_{PP_E}| = S(\omega)\,\mathcal{G}_{PP_E}\, e^{-k^I_{P,AR}\,l_{AR} - k^I_{P,RB}\,l_{RB}}, \quad (6)$$

$$|U_{PS_{E1}}| = S(\omega)\,\mathcal{G}_{PS_{E1}}\, e^{-k^I_{P,AR}\,l_{AR}}\, e^{-k^I_{S,RC}\,l_{RC}}, \quad (7)$$

$$|U_{PS_{E2}}| = S(\omega)\,\mathcal{G}_{PS_{E2}}\, e^{-k^I_{P,BR}\,l_{BR}}\, e^{-k^I_{S,RD}\,l_{RD}}, \quad (8)$$

where $S(\omega)$ is the spectrum of the source wavelet. The coefficients $k^I_{P,XY}$ and $k^I_{S,XY}$ are the average P- and S-wave group attenuation coefficients along the raypath XY, the length of the raypath XY is denoted by l_{XY}. The coefficients $\mathcal{G}_{PP_E}$, $\mathcal{G}_{PS_{E1}}$ and $\mathcal{G}_{PS_{E2}}$ include the source/receiver directivity, reflection/transmission coefficients along the raypath, and the geometrical spreading of the corresponding events. Equations 6, 7, and 8 can be combined to compute the attenuation coefficient of the reflection SS_E constructed by the PP+PS=SS method:

$$\begin{aligned} |U_{SS_E}| &= \frac{|U_{PS_{E1}}|\,|U_{PS_{E2}}|}{|U_{PP_E}|} \\ &= \mathcal{G}_E\, S(\omega)\, e^{-k^I_{S,DR}\,l_{DR} - k^I_{S,RC}\,l_{RC}}, \end{aligned} \quad (9)$$

where the ratio $\mathcal{G}_E = \mathcal{G}_{PS1_E}\,\mathcal{G}_{PS2_E}/\mathcal{G}_{PP_E}$ is assumed to be independent of frequency. It should be noted that $|U_{SS_E}|$ in equation 9 does not represent the actual amplitude of the primary SS reflection. While the PP+PS=SS method reproduces the kinematics of shear-wave primaries, it cannot yield the true amplitudes without knowledge of the velocity model (Grechka and Tsvankin, 2002; Grechka and Dewangan, 2003). Although equation 9 can be used to obtain the effective S-wave attenuation coefficient by evaluating the slope of $\ln|U_{SS_E}|$, its application is hampered by the need to evaluate the source spectrum $S(\omega)$, which is often difficult to do in practice.

However, as shown below, $S(\omega)$ is eliminated in the estimation of the interval S-wave attenuation coefficient. The ray-theoretic frequency-domain amplitudes of the waves PP_{O1} and PS_{O1} (Figure 2) can be written as

$$\begin{aligned} |U_{PP_{O1}}| &= S(\omega)\,\mathcal{G}_{PP_{O1}}\, e^{-k^I_{P,O1}\,(l_{EI}+l_{IF})} \\ &= S(\omega)\,\mathcal{G}_{PP_{O1}}\, e^{-2\,k^I_{P,O1}\,l_{EI}}, \end{aligned} \quad (10)$$

$$|U_{PS_{O1}}| = S(\omega)\,\mathcal{G}_{PS_{O1}}\, e^{-k^I_{P,O1}\,l_{EI}}\, e^{-k^I_{S,O1}\,l_{ID}}, \quad (11)$$

where $k^I_{P,O1}$ and $k^I_{S,O1}$ are the average P-wave and S-wave group attenuation coefficients along the raypaths PP_{O1} and PS_{O1}, respectively. Equations 10 and 11 can be combined to compute the attenuation of the constructed shear-wave SS_{O1} in the overburden:

$$|U_{SS_{O1}}| = \frac{|U_{PS_{O1}}|^2}{|U_{PP_{O1}}|} = \mathcal{G}_{O1}\, S(\omega)\, e^{-2\,k^I_{S,O1}\,l_{ID}}, \quad (12)$$

where $\mathcal{G}_{O1} = \mathcal{G}^2_{PS_{O1}}/\mathcal{G}_{PP_{O1}}$. Likewise, the attenuation coefficient for the overburden event SS_{O2} can be found from

$$|U_{SS_{O2}}| = \frac{|U_{PS_{O2}}|^2}{|U_{PP_{O2}}|} = \mathcal{G}_{O2}\, S(\omega)\, e^{-2\,k^I_{S,O2}\,l_{JC}}, \quad (13)$$

The problem is now reduced to the attenuation analysis of pure modes considered by Behura and Tsvankin (2009). Equations 9, 12 and 13 can be combined to compute the interval shear-wave attenuation in the target layer as follows:

$$\begin{aligned} |U_{SS_T}| &= \frac{|U_{SS_E}|^2}{|U_{SS_{O1}}|\,|U_{SS_{O2}}|} \\ &= \mathcal{G}_T\, e^{-2(\,k^I_{S,DR}\,l_{DR} + k^I_{S,RC}\,l_{RC})} \\ &\quad e^{2\,(k^I_{S,O1}\,l_{ID} + k^I_{S,O2}\,l_{JC})}, \end{aligned} \quad (14)$$

where $\mathcal{G}_T = \mathcal{G}^2_E/(\mathcal{G}_{O1}\,\mathcal{G}_{O2})$. Taking the logarithm of equation 14 yields:

$$\begin{aligned} \ln|U_{SS_T}| &= \ln\mathcal{G}_T - 2(\,k^I_{S,DR}\,l_{DR} + k^I_{S,RC}\,l_{RC}) \\ &\quad + 2\,(k^I_{S,O1}\,l_{ID} + k^I_{S,O2}\,l_{JC}). \end{aligned} \quad (15)$$

Since $k^I_{S,DR}\,l_{DR} = k^I_{S,IR}\,l_{IR} + k^I_{S,O1}\,l_{ID}$ and $k^I_{S,RC}\,l_{RC} = k^I_{S,RJ}\,l_{RJ} + k^I_{S,O2}\,l_{JC}$, equation 15 can be rewritten as

$$\begin{aligned} \ln|U_{SS_T}| &= \ln\mathcal{G}_T - 2\,k^I_{S,IR}\,l_{IR} - 2\,k^I_{S,RJ}\,l_{RJ} \\ &= \ln\mathcal{G}_T - 2\,k^I_{S,T}\,(l_{IR} + l_{RJ}), \end{aligned} \quad (16)$$

where the coefficient $k^I_{S,T}$ represents the average group attenuation coefficient along the shear-wave raypath in the target layer.

Interval phase attenuation coefficient for a homogeneous target layer

If the target layer is heterogeneous, equation 16 provides only the offset-dependent average interval attenuation coefficient. Interpretation of attenuation measurements can be significantly simplified for horizontal, homogeneous layers with a horizontal symmetry plane. Then the length of the raypath in the target layer is given by $l_{IR} + l_{RJ} = V_g\,t_{SS_T}$, where V_g is the shear-wave group velocity along the ray IR (Figure 3), and t_{SS_T} is the interval shear-wave traveltime in the target layer. As a result, equation 16 reduces to

$$\ln|U_{SS_T}| = \ln\mathcal{G}_T - 2\,k^I_{S,T}\,V_g\,t_{SS_T}. \quad (17)$$

Behura and Tsvankin (2009) show that equation 17 can be used to obtain the interval *phase* attenuation coefficient of P- or S-waves. According to their results, equation 17 can be rewritten as

$$\ln|U_{SS_T}| = \ln\mathcal{G}_T - 2\,\omega\,\mathcal{A}_S\,t_{SS_T}, \quad (18)$$

where ω is the angular frequency and $\mathcal{A}_S = k^{I,Ph}/k^{R,Ph}$ is the S-wave phase attenuation coefficient (Zhu, 2006) for a zero inhomogeneity angle (the angle between the real and imaginary parts of the wave vector); $k^{I,Ph}$ and

$k^{R,Ph}$ are the magnitudes of the imaginary and real parts of the wave vector, respectively, for S-waves.

The shear-wave interval traveltime in the target layer (t_{SS_T}) is computed from equation 5 using the kinematic layer stripping. Hence, the slope of the logarithmic spectral ratio in equation 18 yields the phase attenuation coefficient for the phase angle corresponding to a given group direction (e.g., to the raypath IR in Figure 3). If the slope is constant, $\mathcal{A}_S$ and the quality factor $Q_S \approx 1/(2\mathcal{A}_S)$ are independent of frequency. If the slope varies with frequency, $\mathcal{A}_S$ has to be computed from the instantaneous slope, which yields a frequency-dependent attenuation coefficient and quality factor.

For VTI and orthorhombic media, the S-wave phase attenuation coefficient can be inverted for the attenuation-anisotropy parameters introduced by Zhu and Tsvankin (2006, 2007). The SV-wave phase attenuation coefficient in VTI media is approximately given by (Zhu and Tsvankin, 2006):

$$\mathcal{A}_{SV}(\theta) = \mathcal{A}_{S0}\,(1 + \sigma_Q \sin^2\theta \cos^2\theta), \qquad (19)$$

where $\mathcal{A}_{S0} \approx 1/(2Q_{S0})$ is the symmetry-direction SV attenuation coefficient and Q_{S0} is the vertical quality factor. The parameter σ_Q determines the variation of $\mathcal{A}_{SV}$ away from the symmetry direction and depends on the attenuation-anisotropy parameters ϵ_Q and δ_Q, as well as on the vertical velocities and quality factors P- and S-waves.

Whereas the phase attenuation coefficient is expressed as a function of the phase angle, our method computes $\mathcal{A}_{SV}$ for a certain source-receiver offset at the top of the target layer. Estimating the phase angle for a given source-receiver pair generally requires knowledge of the anisotropic velocity field in the interval of interest.

Synthetic example

The method was tested on synthetic multicomponent data from a horizontally stratified VTI model (Figure 4). The sources were placed on the top of the model, while the receivers were on the bottom of the water layer. Our method is applicable to this source-receiver geometry because it utilizes events with shared ray segments in the overburden.

Synthetic reflection data were generated using an anisotropic reflectivity code (Schmidt and Tango, 1986). PP and PS events from the top and bottom of the target were identified on the vertical and radial displacement components of the shot gather (Figure 5). Kinematic layer stripping of the shear-wave traveltimes produced the interval moveout in the third (target) layer shown in Figure 6. The layer-stripped interval traveltimes practically coincide with the exact values computed by ray tracing. It should be noted that the maximum offset for the constructed shear-wave in the target layer is limited

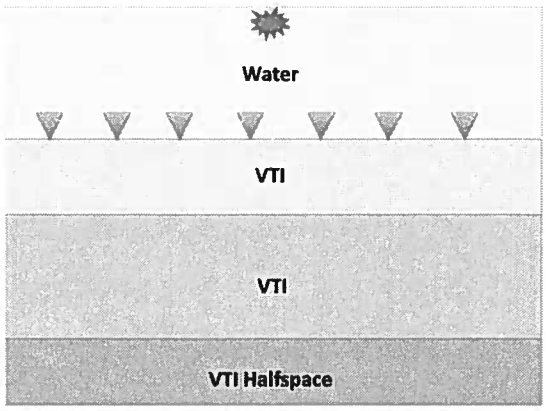

Figure 4. Synthetic model used to test the algorithm. The source is placed on the top of the model and the receivers are on the water bottom. The water is purely isotropic and elastic with the P-wave velocity $V_P = 1500$ m/s and thickness $d = 2000$ m. The other three layers have VTI symmetry for both velocity and attenuation. For the second layer, the vertical P- and S-wave velocities are $V_{P0} = 1600$ m/s and $V_{S0} = 800$ m/s, thickness $d = 600$ m, and velocity-anisotropy parameters are $\epsilon = 0.30$, and $\delta = 0.10$; the attenuation parameters are $Q_{P0} = 20$, $Q_{S0} = 50$, $\epsilon_Q = 0.30$, and $\delta_Q = 0.20$. In the third layer, $V_{P0} = 1700$ m/s, $V_{S0} = 900$ m/s, $d = 1000$ m, $\epsilon = 0.25$, $\delta = 0.10$, $Q_{P0} = 100$, $Q_{S0} = 20$, $\epsilon_Q = 0.20$, and $\delta_Q = 0.10$. The parameters of the bottom halfspace are $V_{P0} = 2500$ m/s, $V_{S0} = 1400$ m/s , $\epsilon = 0.30$, $\delta = 0.10$, $Q_{P0} = 50$, $Q_{S0} = 50$, $\epsilon_Q = 0.40$, and $\delta_Q = 0.30$.

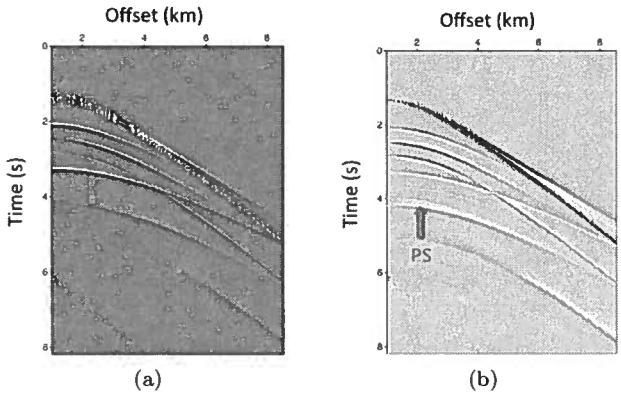

Figure 5. Vertical (a) and horizontal (b) displacement components of a shot gather for the model from Figure 4. The target PP and PS events are marked by the red arrows in (a) and (b), respectively.

by the critical angle for SP mode conversions, which is equal to 32°.

The input amplitudes were obtained by computing the vector sum of the radial and vertical displacement components. Frequency-domain amplitudes were found by windowing the arrivals and applying the Fourier transform. The target layer is horizontal, homogeneous,

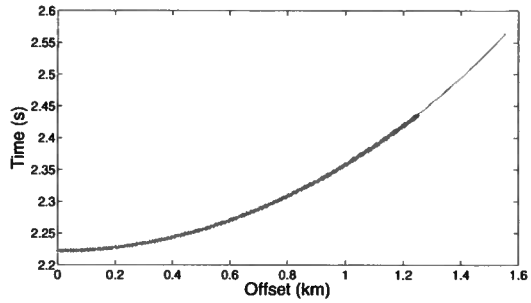

Figure 6. Interval shear-wave traveltime in the third layer (red stars) computed using the PP+PS=SS method and velocity-independent layer-stripping. The gray curve marks the exact traveltime.

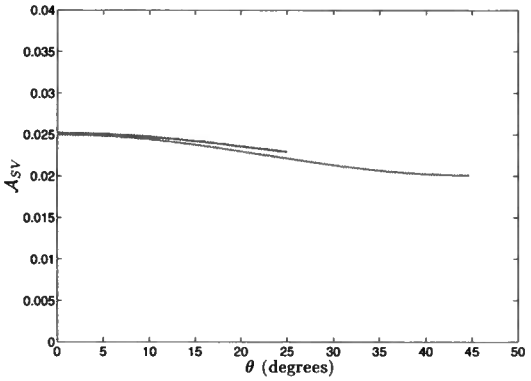

Figure 7. Estimated S-wave interval phase attenuation coefficient $\mathcal{A}_{SV}$ for the third layer (red line) as a function of the phase angle θ. The gray line marks the exact coefficient $\mathcal{A}_{SV}$.

and has a horizontal plane of symmetry (it is VTI). Therefore, the interval shear-wave phase attenuation coefficient in the target layer was computed from equation 18 using the algorithm discussed above. The SV-wave phase angles were obtained from the corresponding group angles using the known velocity function in the target layer. The parameters $\mathcal{A}_{S0} = 0.025$ and $\sigma_Q = -0.61$ were found by least-squares fitting of equation 19 to the estimated values of shear-wave phase attenuation coefficient $\mathcal{A}_{SV}$. The obtained parameter $\mathcal{A}_{S0}$ is close to its actual value (0.025), but there is a significant error in the parameter σ_Q (the actual value is -0.78) due to the limited range of phase angles for the reflected S-leg of the PS-wave. The exact and best-fit curves of the shear-wave phase attenuation coefficient $\mathcal{A}_{SV}$ are displayed in Figure 7.

Discussion

Despite the generally successful test results, the proposed method has several limitations. First, the range of phase angles for the constructed SS-wave is restricted due to two factors: the small amplitudes of PS-waves at near offsets and the critical angle for converted waves. Typical values for the critical angle are about 30°, which causes instability in the inversion for the attenuation-anisotropy parameter σ_Q. Estimation of σ_Q may be more accurate for hard rocks with a high V_S/V_P ratio, for which the critical angle for SP mode conversions is higher. However, the algorithm should provide tight constraints on the symmetry-direction coefficient $\mathcal{A}_{S0}$. Second, because the data are generated by a P-wave source, it is necessary to repeatedly apply the PP+PS=SS method to construct SS events, which could lead to error accumulation in the attenuation analysis. Third, the algorithm is supposed to operate with isolated reflection events. Amplitude distortions due to interference (e.g. with multiples) may hinder S-wave attenuation estimates.

To express $\mathcal{A}_{SV}$ as a function of the phase angle (equation 19), it is necessary to know the velocity function. However, as discussed by Behura and Tsvankin (2009), the difference between the phase and group angles for moderately anisotropic models does not substantially distort attenuation coefficients. It should be mentioned, however, that even computation of the group angle for a given source-receiver pair requires velocity information.

Conclusions

We extended the algorithm of Behura and Tsvankin (2009), originally introduced for pure modes, to the combination of PP- and PS-waves with the goal of estimating the shear-wave interval attenuation coefficient. Our technique involves repeated application of the PP+PS=SS method followed by velocity-independent layer stripping (VILS), for both traveltime and frequency-domain amplitudes. In the 2D implementation of the method discussed here, the vertical incidence plane has to be a plane of mirror symmetry in all layers including the target. VILS is designed for a laterally homogeneous (although possibly vertically heterogeneous) overburden with a horizontal symmetry plane in each layer. If this assumption is satisfied, our method does not require knowledge of the overburden velocity and attenuation parameters.

For heterogeneous target layers, the algorithm estimates the average S-wave interval group attenuation coefficient for a range of source-receiver offsets. If the target is horizontal, homogeneous, and has a horizontal symmetry plane, it is possible to obtain the interval phase attenuation coefficient for the constructed SS events.

Synthetic modeling for layered VTI media confirmed the accuracy of the method in estimating the interval SV-wave phase attenuation coefficient $\mathcal{A}_{SV}$. The range of phase angles for the constructed SS reflection is limited by the small amplitudes of PS-waves at near offsets and the critical angle for the reflected S-leg. The coefficient $\mathcal{A}_{SV}$ can be inverted for the symmetry-direction coefficient $\mathcal{A}_{S0}$ and, under favorable circumstances, for the attenuation-anisotropy parameter σ_Q.

The combination of the shear-wave attenuation coefficient with P-wave attenuation measurements can help detect the presence of fluids in a reservoir. The 3D version of our method can be applied to wide-azimuth data to evaluate the azimuthal variation of shear-wave attenuation, which is sensitive to fluid-filled natural fracture sets.

Acknowledgments

We are grateful to the members of the A(nisotropy)-Team of the Center for Wave Phenomena (CWP), Colorado School of Mines, for fruitful discussions. Support for this work was provided by the Consortium Project on Seismic Inverse Methods for Complex Structures at CWP and by the Research Partnership to Secure Energy for America (RPSEA).

References

Adam, L., 2008, Elastic and visco-elastic laboratory properties in carbonates: PhD thesis, Colorado School of Mines.

Batzle, M., R. Hofmann, and M. Prasad, 2005, Seismic attenuation: Observations and mechanisms: 75th Annual International Meeting, SEG, Expanded Abstracts, 1565–1568.

Behura, J., M. Batzle, R. Hofmann, and J. Dorgan, 2007, Heavy oils: Their shear story: Geophysics, **72**, no.5, E175–E183.

Behura, J. and I. Tsvankin, 2009, Estimation of interval anisotropic attenuation from reflection data: Geophysics, **74**, no.6, A69–74.

Chichinina, T., I. Obolentseva, L. Gilk, B. Bobrov, and G. Ronquillo-Jarillo, 2009, Attenuation anisotropy in the linear-slip model: Interpretation of physical modeling data: Geophysics, **74**, no.5, WB165–WB176.

De, G. S., D. F. Winterstein, and M. A. Meadows, 1994, Comparision of P- and S-wave velocities and Q's from VSP and sonic log data: Geophysics, **59**, 1512–1529.

Dewangan, P. and I. Tsvankin, 2006, Velocity-independent layer stripping of PP and PS reflection traveltimes: Geophysics, **71**, no.4, U59–U65.

Dvorkin, J. P. and G. Mavko, 2006, Modeling attenuation in reservoir and nonreservoir rock: The Leading Edge, **25**, 194–197.

Grechka, V. and P. Dewangan, 2003, Generation and processing of pseudo-shear-wave data: Theory and case study: Geophysics, **68**, 1807–1816.

Grechka, V. and I. Tsvankin, 2002, PP + PS = SS: Geophysics, **67**, 1961–1971.

Liu, E., M. Chapman, I. Varela, X. Li, J. H. Queen, and H. Lynn, 2007, Velocity and attenuation anisotropy: Implication of seismic fracture charecterizations: The Leading Edge, **26**, 1170–1174.

Schmidt, H. and G. Tango, 1986, Efficient global matrix approach to the computation of synthetic seismograms: Geophysical Journal of the Royal Astronomical Society, **84**, 331–359.

Zhu, Y., 2006, Seismic wave propagation in attenuative anisotropic media: PhD thesis, Colorado School of Mines.

Zhu, Y. and I. Tsvankin, 2006, Plane-wave propagation in attenuative transversely isotropic media: Geophysics, **71**, no.2, T17–T30.

———, 2007, Plane-wave attenuation anisotropy in orthorhombic media: Geophysics, **72**, no.1, D9–D19.

Zhu, Y., I. Tsvankin, and I. Vasconcelos, 2007, Effective attenuation anisotropy of thin-layered media: Geophysics, **72**, no.5, D93–D106.

Coupled geomechanical and seismic modeling of compaction-induced traveltime shifts for multicomponent data

Steven Smith & Ilya Tsvankin
Colorado School of Mines, Center for Wave Phenomena, Golden Colorado

ABSTRACT

Time-lapse seismic methods have proven successful in evaluating changes in reservoirs caused by production. Accurate modeling of compaction-related time shifts requires combining geomechanics with full-waveform simulation of seismic data. Here, we study the influence of compaction-induced stress and strain around a reservoir on compressional (P), mode-converted (PS), and shear (S) waves. Geomechanical reservoir models are used to generate stress-related stiffness coefficients, which serve as input to 2D anisotropic finite-difference modeling. Reflectors are placed at multiple depths to evaluate time-lapse anomalies for different source locations and a wide range of reservoir pressure. The baseline and monitor shot records are processed by windowed cross-correlation analysis to compute "visualization surfaces" of time shifts with respect to the baseline survey. Our modeling results show that the spatial pattern of time shifts for PS- and S-waves is generally similar to that for P-waves. However, while P-wave traveltimes above the reservoir increase after compaction, PS- and S-wave traveltimes there are slightly reduced. The traveltimes of all modes decrease for reflectors below the stressed reservoir. Almost constant time shifts of PS- and S-waves for a range of offsets and source locations indicate that the contribution of stress-induced velocity anisotropy to shear-wave signatures is weak, because the symmetry is close to elliptical. The developed methodology not only helps understand the behavior of traveltime shifts for PS- and S-waves, but can be used in the inversion for the stress field.

Key words: geomechanics, seismic modeling, stress-induced anisotropy, converted waves, shear waves, time-lapse, compacting reservoir, transverse isotropy, VTI

Introduction

General Overview

Time-lapse (4D) monitoring of oil and gas reservoirs is based on estimating the differences between seismic signatures measured for baseline and monitor surveys (Calvert, 2005). Pore-pressure reduction inside a reservoir causes stress, strain, and impedance changes throughout the section. The type, magnitude, and spatial distribution of differences between time-lapse data sets allow production engineers and interpreters to map oil drainage patterns and reservoir block connectivity. This information is helpful in enhanced recovery operations, such as fracturing and flooding.

Production-induced stress fields depend on both volumetric and shear strains associated with changes in pore fluid pressure and bulk modulus of the reservoir. In addition to pressure drop and impedance variations within the reservoir, the surrounding rock undergoes stress and strain redistribution. Compaction-induced stress and strain in the overburden can create or reactivate normal and reverse faults, resulting in small to moderate earthquakes in close proximity to the reservoir (Zoback, 2007). Concentrated regions

of high subsurface stress (Bachrach et al., 2007) may cause shearing of wells, which must then be abandoned, repaired, or side-tracked to resume production. An example of widespread stress/compaction damage is found in Wilmington Field, Long Beach, California. This field experienced approximately 30 feet of subsidence from 1931-1952, with significant damage to over 200 production wells, associated infrastructure, bridges, and wharfs of the Terminal Island area in Long Beach (McCann and Wilts, 1951; Strehle, 1987).

Time-lapse seismic data are often migrated to generate images reflecting changes in the reservoir. Signatures measured in time-lapse surveys also have potential for estimating subsurface stress. Synthetic modeling of pore-pressure-dependent time shifts for multiple horizons above and below the reservoir can be used to study the influence of spatially varying stresses on the kinematics of reflected waves. Traveltime shifts, coupled with well-pressure histories, can serve as input to inversion algorithms designed to reconstruct reservoir pressure at locations distant from existing wells. Time-shift measurements for reflectors and events most sensitive to changes in reservoir pressure and stress may be exploited to devise a flexible monitoring program that reduces repetition of full-scale monitoring surveys.

In this paper, we describe a method for semi-coupled geomechanical and full-waveform seismic modeling of multicomponent data acquired above compacting reservoirs. First, we review recent advances in the field of uniaxial/vertical stress compaction and time-lapse processes in the reservoir. We also discuss the work of Fuck et al. (2009, 2010), who studied the influence of compaction-induced stress and strain on the velocity field and P-wave time shifts using the nonlinear theory of elasticity. Then we introduce our semi-coupled geomechanical/seismic modeling methodology and describe the time shifts of P-, PS-, and S-waves for a simple model of a rectangular reservoir embedded in a homogeneous host rock.

Compaction-Induced Velocity Perturbations

Compaction and Stress

A number of recent publications discuss seismic time shifts associated with compaction, subsidence and related subsurface stress perturbations. These approaches typically involve some form of "semi-coupled" geomechanical and seismic modeling. Semi-coupled models cyclically solve systems of equations for interrelated processes, but the partial differential equations (PDEs) and their solvers remain separate; for example, wave-propagation PDEs are not directly coupled to Navier stress/strain PDEs (Olden et al., 2001; Minkoff et al., 2004; Sen and Settari, 2005). Most existing studies have been limited to evaluation of vertical stress/strain and analysis of time shifts on stacked/zero-offset data (Hatchell and Bourne, 2005; Roste, 2007; Landrø and Stammeijer, 2004). Zero-offset time shifts can help estimate the change in the reservoir thickness, allowing improved monitoring of reservoir volume (i.e., barrels-in-place). Traveltime perturbations obtained from uniaxial compaction models are particularly significant for soft reservoir rock. However, more general stress-based formulations (including triaxial stress) help constrain the deviatoric stress tensor responsible for stress-induced anisotropy (Fuck et al., 2009). Heterogeneous, anisotropic velocity fields caused by reservoir compaction result in perturbations of shear-wave splitting and azimuthally varying moveout velocity (Olofsson et al., 2003; Herwanger and Horne, 2009).

P-wave Time Shifts

It has been shown that reservoir compaction induces stress changes resulting in spatially varying, anisotropic velocity fields inside and outside the reservoir (Herwanger and Horne, 2005; Herwanger et al., 2007; Fuck et al., 2009). For 2D reservoir models, the stress-induced symmetry is transversely isotropic, with a nearly vertical symmetry axis (VTI); the symmetry axis noticeably deviates from the vertical only near the reservoir corners (Fuck et al., 2009). Fuck and Tsvankin (2009), Prioul et al. (2004), and Shapiro and Kaselow (2005) show that stress-induced anisotropy is close to elliptical, with approximately equal values of the anisotropy parameters ϵ and δ.

Fuck et al. (2009) analyze stress-induced anisotropy caused by a pore pressure drop in a rectangular reservoir embedded in originally homogeneous host rock (Figure 1). They derive an approximate expression for traveltime changes by using the nonlinear theory of elasticity and evaluating traveltime perturbations along reference rays traced through an unstressed background. Fuck et al. (2009) also model compaction-induced P-wave time shifts using anisotropic ray tracing for the reservoir model in Figure 1. They demonstrate that traveltime shifts are controlled by the combination of volumetric and deviatoric strains. The volumetric strain, given by

$$\Delta e_{kk} = \frac{1}{3}\left(\Delta\epsilon_{11} + \Delta\epsilon_{22} + \Delta\epsilon_{33}\right). \quad (1)$$

is significant only inside the reservoir ($\Delta\epsilon_{ii}$ is the dilatation component along the i^{th} axis). Therefore, traveltime shifts for reflections above the reservoir are generated by deviatoric stress and strains. The most significant time shifts, however, occur for reflectors beneath the reservoir. Raypaths for these events are influenced by the deviatoric stress around of the reservoir, but also pass through the reservoir itself, which experiences the bulk of compaction-induced volumetric strain (Δe_{kk}). Fuck et al. (2009) demonstrate that offset variations of time shifts for reflections both above and below the reservoir are largely controlled by the deviatoric strains responsible for velocity anisotropy. Figure

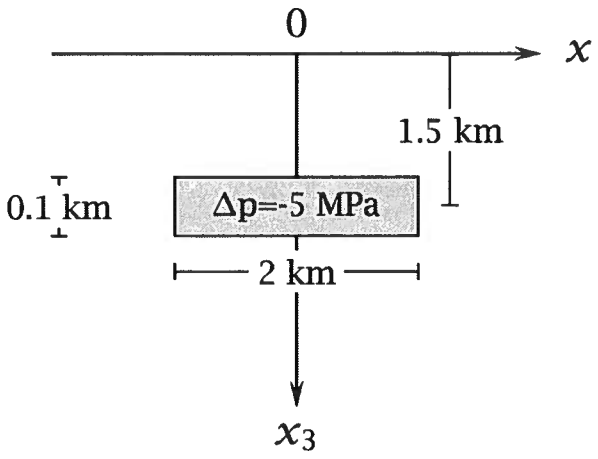

Figure 1. Reservoir geometry used by Fuck (2009) and Fuck et al. (2009). Pore-pressure (P_p) reduction occurs only within the reservoir, resulting in an anisotropic velocity field due to the excess stress and strain. For geomechanical modeling, the reservoir is located in a model-space measuring 20,000 x 10,000 m. The model dimensions are sufficient for obtaining stress, strain, and displacement which are close to those for an infinite medium. The reservoir is comprised of and embedded in homogeneous Berea sandstone (ρ = 2140 kg/m^3, V_P = 2300 m/s, V_S = 1456 m/s) with the following, density-normalized third-order stiffness coefficients: $C_{111}/\rho = -13,904$ GPa, $C_{112}/\rho = 533$ GPa, and $C_{155}/\rho = 481$ GPa (Prioul et al., 2004). The Biot coefficient is set to 0.85. Velocities in the model are reduced by 10% from the laboratory values to account for the difference between static and dynamic stiffnesses in low-porosity rocks (Yale and Jamieson, 1994). Here, we analyze PS- and S-wave time shifts for this model for 5 MPa and 20 MPa pore-pressure drops.

2 shows both the magnitude and spatial distribution of P-wave traveltime perturbations obtained by ray tracing around the rectangular reservoir in Figure 1. If the unstressed medium is not homogeneous, the contrast in the rigidity modulus μ between the reservoir and surrounding rock influences the stress/strain perturbation inside and near the reservoir (Fuck et al., 2010).

Seismic velocities change when the local stiffnesses of the rock are altered due to compression or shearing. This change for linearly elastic materials can be described using Hooke's law:

$$s_{ij} = c_{ijkl}\,\epsilon_{kl}, \tag{2}$$

where **s** is the stress tensor (denoted by **s** to avoid confusion with the anisotropy parameter σ), and ϵ is the strain tensor. Equation 2 implicitly assumes that the stiffness coefficients relating stress to strain remain constant. The stiffnesses, however, change as a function of strain (Prioul et al., 2004; Fuck et al., 2009):

$$c_{ijkl} = c^o_{ijkl} + \frac{\partial c_{ijkl}}{\epsilon_{mn}}\,\Delta\epsilon_{mn} = c^o_{ijkl} + c_{ijklmn}\,\Delta\epsilon_{mn}. \tag{3}$$

In the Voigt matrix notation, equation 3 can be written as

$$C_{\alpha\beta} = C^o_{\alpha\beta} + C_{\alpha\beta\gamma}\,\Delta\epsilon_\gamma. \tag{4}$$

The third-order stiffness coefficients c_{ijklmn} are derived from higher-order terms of the strain-energy function (Hearmon, 1953; Sarkar et al., 2003; Prioul et al., 2004). The strain-induced changes in stiffness described by equations 3 and 4 result in spatially varying stiffness/velocity perturbations around a compacting reservoir. The Voigt matrix notation is convenient because it simplifies the summation in equation 3 and analysis of the symmetry of the strain-induced velocity field (Fuck and Tsvankin, 2009).

Fuck et al. (2009) express the P-wave traveltime in a stressed medium as the sum of the isotropic background traveltime and a perturbation that depends on the stress-induced stiffness changes. Application of equations 3 and 4 yields compaction-related time shifts as a function of two independent third-order coefficients – C_{111} and C_{112}.

Experimentally obtained $C_{\alpha\beta}$ values (Prioul et al., 2004) make it possible to model changes in the stiffness coefficients caused by stress/strain applied to an isotropic medium. Triaxial compaction-related stress causes a combination of volumetric and deviatoric strain perturbations resulting in orthorhombic symmetry. In two dimensions the symmetry is transversely isotropic, as discussed above.

The spatial distribution of the compaction-induced stress/strain may be complex, depending on the background properties and the structural geology/petrology of the reservoir (Fuck, 2009; Fuck et al., 2010). Additional complexity is caused by pronounced reservoir heterogeneity An example would be a tilted reservoir with multiple aggregate bulk moduli caused by the natural separation of brine and liquid/gas hydrocarbons (Johnston, 2010).

Methodology

We devised a modeling methodology and software package to study time-lapse multicomponent wavefields for compacting reservoirs. 2D, semi-coupled geomechanical and full-waveform modeling was implemented employing an approach similar to that of Minkoff et al. (2004), Herwanger and Horne (2005), Herwanger and Horne (2009) and Fuck (2009). The methodology can handle multi-compartment reservoirs of various shapes, depths, tilts, and independent pressure histories.

Compaction-induced displacement, strain, and stresses for our geomechanical reservoir models are computed using COMSOL PDE software (COMSOL AB, 2008). Geomechanical physics for a subsurface inclusion such as a reservoir are described by Zoback (2007). The fluid within the reservoir is under pore pressure (P_p) that counteracts overburden stress. Another pressure

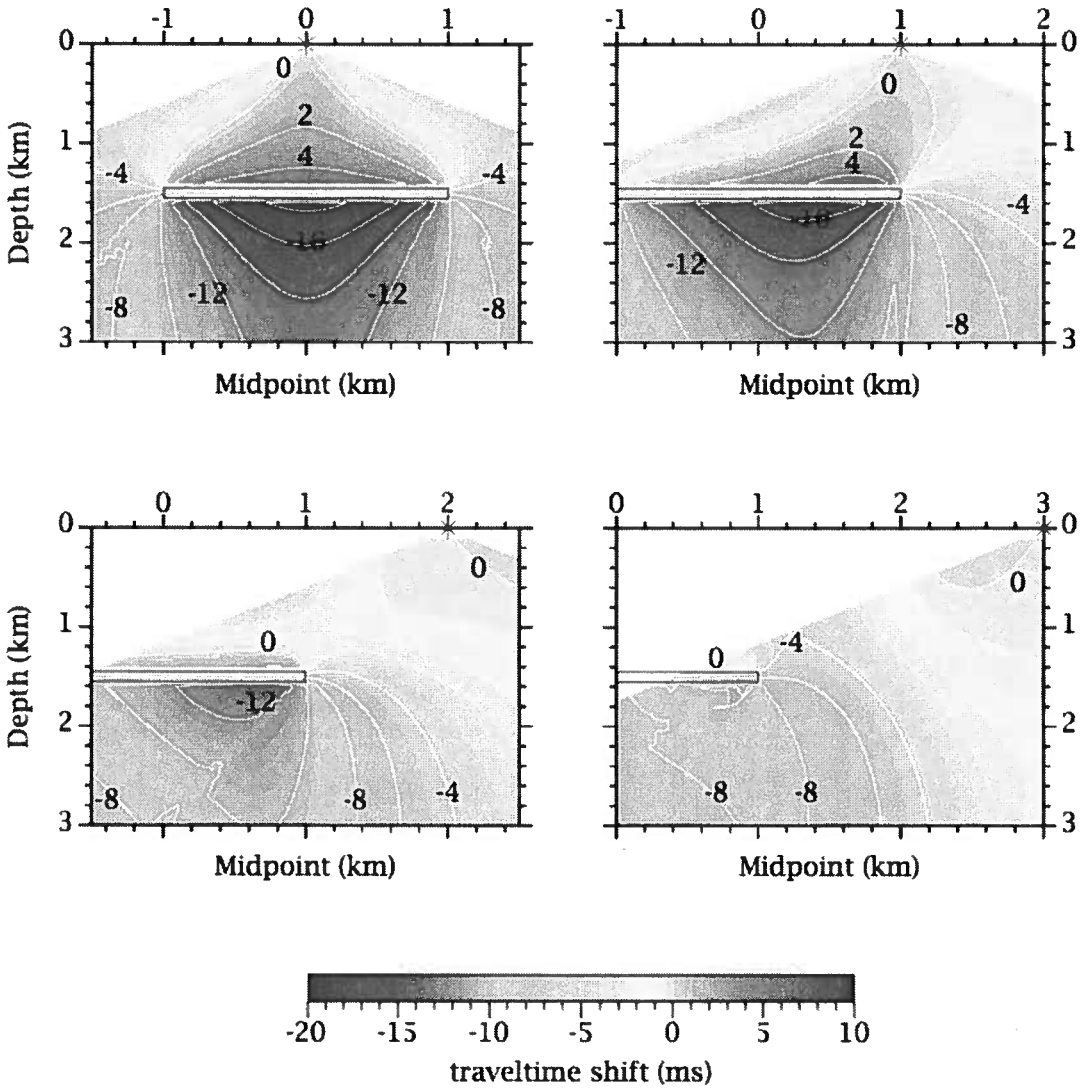

Figure 2. P-wave traveltime shifts computed by ray tracing for the model from Figure 1 (after Fuck et al. (2009)). The asterisk marks the source location at the surface. The time shift (ms) shown at each (X,Z) point corresponds to the reflection form a horizontal interface at depth Z recorded at the source-receiver offset $2(X - X_0)$, where X_0 is the source coordinate.

component is provided by grain-to-grain contact in the matrix via the viscoelastic Biot coefficient α:

$$P_{\text{bulk}} \simeq P_{\text{p}} + P_{\text{matrix}} \simeq \alpha P, \tag{5}$$

with

$$\alpha = 1 - \frac{K_{\text{a}}}{K_{\text{g}}}, \tag{6}$$

where K_{a} is the aggregate bulk modulus of the rock frame and fluids, and K_{g} is the bulk modulus of the grain material (Mavko et al., 2003). Initially, the system is assumed to be in hydrostatic equilibrium such that the reservoir pressure balances that of the overburden column:

$$P_{\text{res}} = P_{\text{over}}, \tag{7}$$

$$\alpha P_{\text{p}} = \left(1 - \frac{K_{\text{a}}}{K_{\text{g}}}\right) P_{\text{p}} = \rho_{\text{over}} * g * z_{\text{res}}. \tag{8}$$

Changes in reservoir pressure are due just to changes in the pore fluid pressure P_{p}. These pressure changes are linear, and are used as the force function for the Navier equation $[-\nabla \cdot (c\nabla \mathbf{u}) = \mathbf{F}]$ governing the system's stress state (COMSOL AB, 2008). Due to the presence of the Biot coefficient, the pore pressure needed

to maintain equilibrium results in an overpressured reservoir volume, which is typical for a freshly tapped reservoir. As verified by Fuck et al. (2009), the resulting numerical stress/strain fields for a rectangular inclusion are close to analytic solutions obtained by Hu (1989).

The resulting stress/strain fields are processed with an algorithm based on the nonlinear theory of elasticity to calculate the stiffness coefficients (Fuck et al., 2009). These stiffnesses serve as input to the SFEWE 2D anisotropic finite-difference modeling code (Sava and Godwin, 2010), which generates multicomponent seismic data. The SFEWE software excites both P- and S-waves by applying directional forces oriented along the X and Z axes. The source signal is a Ricker wavelet with a center frequency of 44 Hz and an effective bandwidth of approximately 110 Hz. Time shifts for P, PSV, and SV waves are measured from the modeled wavefields by computing cross-correlations of windowed arrivals in the baseline and monitor surveys; the windowing is performed along the best-fit moveout curves.

Synthetic Test

We test our software package on the reservoir model of Fuck et al. (2009) in Figure 1. Use of homogeneous material in the geomechanical modeling is justified for two reasons. First, Kosloff et al. (1980a) advocate the use of homogeneous media at basin scales because depositional formations outside the reservoir are typically composed of uniform source sediments. Second, we aim to observe only the influence of stress-induced anisotropy in the reservoir and overburden. Further, Fuck et al. (2010) show that the impact of background heterogeneity around the reservoir is generally insignificant. Reservoir geometry simulates a simplest case scenario, such as a fault-bound, relay-ramp block trap in a rift system like the North Sea, similar to Heidrun field (Whitley, 1992). The pore pressure reductions of 5 MPa and 20 MPa typically correspond to small to moderate reservoir pressure changes (Zoback, 2007). The use of anisotropic finite-different seismic modeling is important because it generates both kinematic and amplitude information. Furthermore, the output of the modeling code requires processing techniques that could be used on actual field data.

To evaluate depth-dependent time shifts for the reservoir located at 1500 m, a 10-m thin reflecting layer is moved downward through the model. This reflector has a high density of 3000 kg/m^3 in order to generate sufficiently large reflection amplitudes. The reflector is so thin that it is not expected to perturb the overall structure of the heterogeneous stress, strain, and stiffness changes. Baseline and monitor wavefields are computed separately for each reflector to eliminate interference with multiple reflections. For the 2D (X-Z plane) geometry used in the experiment, changes occur only in the stiffness coefficients $C_{11}, C_{13}, C_{33}, C_{55}, C_{15}$, and C_{35}, resulting in a tilted transversely isotropic (TTI) medium with a small tilt of the symmetry axis (as discussed above).

Throughout the process, the reservoir is assumed to have sufficiently large dimensions in the out-of-plane direction to allow the use of 2D modeling. We also assume that host rock with nonlinear compaction behavior may be modeled using Hooke's law with a strain-dependent set of stiffness coefficients. Compaction-induced density changes in the overburden are neglected because our software is unable to model density or porosity changes at this time.

Typical time-lapse common-shot gathers for a receiver array spanning -3000 to +3000 meters are shown in Figure 3. Here, the 10 m thin reflector is located 50 m above the top of the reservoir. The gather for the unstressed medium includes only the P-, PS-, and S-wave events from the reflector. The impedance change due to the pressure drop in the reservoir (Figure 3(b)) generates reflections from the reservoir boundaries with amplitudes comparable to those of the reflection events in Figure 3(a).

Our resulting stresses, strains, displacements, and P-wave time shifts are close to those of Fuck et al. (2009). The time shifts for the reflections from the top of the reservoir (Figure 4(a)) are close to those obtained by Fuck (2009) with ray tracing (Figure 2). Directly at the top of the reservoir the P-wave time shifts are on the order of 7-8 ms. Secondary geomechanical validation is provided by comparing our stress/strain fields to those constructed by Kosloff et al. (1980a) for the Wilmington field, with both generating surface subsidence of similar magnitude.

Analysis of Results

Our primary goal is to study the time shifts of PS- and S-waves. The SV-wave velocity in TI media (in our case, anisotropy is induced by stress) is primarily controlled by the parameter σ (Tsvankin, 2005):

$$\sigma = \left(\frac{V_{P0}}{V_{S0}}\right)^2 (\epsilon - \delta), \tag{9}$$

where V_{P0} and V_{S0} are the vertical P- and S-wave velocities. The linearized SV-wave velocity as a function of the phase angle with the symmetry axis (θ) can be written as

$$V_{SV}(\theta) = V_{S0}\left(1 + \sigma \sin^2\theta \ \cos^2\theta\right). \tag{10}$$

For elliptical anisotropy ($\epsilon = \delta$) $\sigma = 0$, $V_{SV} \approx V_{S0}$, and the velocity is independent of angle (isotropic). For example, at the center of the reservoir, computed values of σ are -0.08 for the 5 MPa pressure drop, and -0.15 for the 20 MPa pressure drop. Therefore, compaction-induced changes in the shear-wave vertical velocity have the greatest impact on PS- and S- wave time shifts

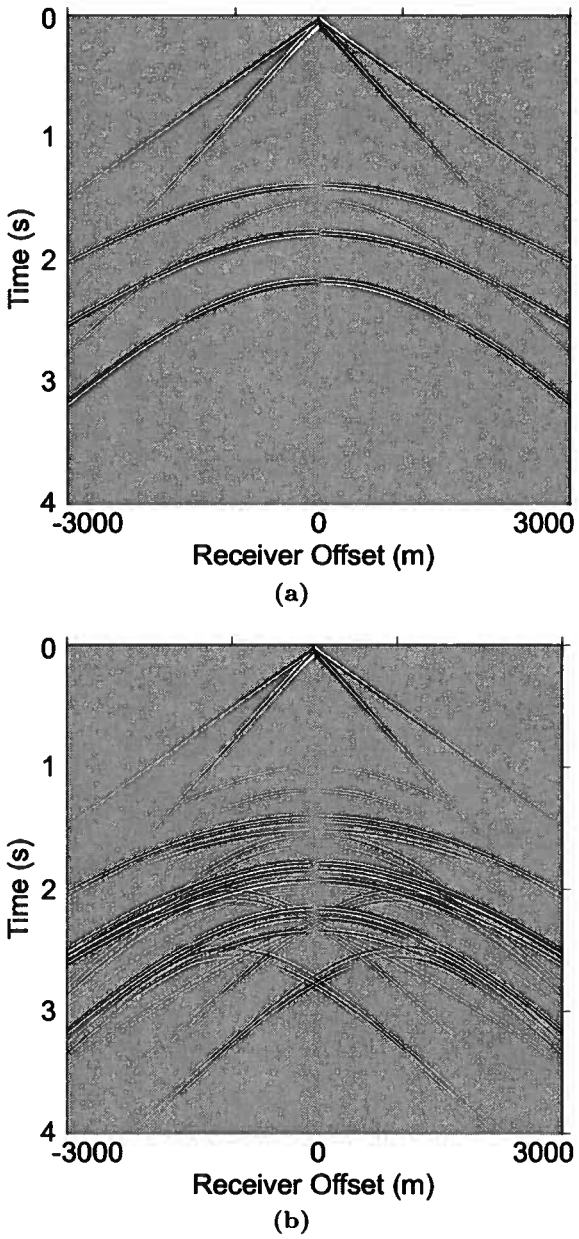

Figure 3. Common-shot gathers of the horizontal displacement for an isotropic, unstressed reservoir model (a) and for the model with the pressure drop $\Delta P_p = 20$ MPa inside the reservoir (b) (see Figure 1). For both cases a thin, high-density reflector is positioned immediately above the reservoir at 1400 m depth (the reservoir is between 1450 m and 1550 m). The isotropic case shows clear P-, PS-, and S-wave reflections. In addition to stress-induced anisotropy, pore-pressure decrease in the reservoir alters its impedance, generating reflections and diffraction tails.

near and beneath the reservoir. Compaction-induced increases to V_{S0} inside the reservoir are approximately 270 m/s for the 5 MPa pressure drop, and 500 m/s for the 20 MPa pressure drop.

Figures 4, 5, and 6 show time shifts due to pressure drops of 5 MPa (left column) and 20 MPa (right column). Each surface is comprised of "hull curves" of time shifts computed by cross-correlation of arrivals from the set of thin reflectors placed in the stressed and unstressed models. These hull curves span the entire model from left to right at 14 depths between 200 and

3000 meters, with two reflectors positioned close to the upper and lower reservoir boundaries.

Complete time-shift plots, generated by interpolating between the hull curves, show lead/lag behavior similar to that obtained by Fuck (2009) using ray tracing (Figure 2). For all types of arrivals, time shifts above the reservoir are relatively small, with PS- and S-waves showing a traveltime decrease (or time lead), due to an increase in V_{S0} inside the reservoir. For P-waves the shifts are positive, indicating a time lag. At the top of the reservoir, Figure 4(a) shows a 5 ms P-wave lag, which is close to the 4 ms lag computed by Fuck et al. (2009) (see Figure 2 for the source coordinate $X_0 = 0$).

For all wave modes, the traveltimes for reflectors beneath the reservoir decrease after compaction because of increased velocity within the reservoir and near its edges. Time "leads" from beneath the reservoir for PS- and S-waves are approximately 2-3 times those for P-waves. When $\Delta P_p = 20$ MPa, the time shifts of PS- and S-waves are up to two times larger than those for a drop of 5 MPa.

The reservoir and small regions at its edges experience the largest velocity changes that confine the most significant time shifts of PS- and S-waves to reflections from interfaces beneath the reservoir. The zone of largest time shifts moves laterally to the opposite side of the reservoir from the source location with increasing X-coordinate of the source. The maximum time shifts below the reservoir occur along a line connecting the source with the far edge of the reservoir because waves propagating in that direction spend the longest time in the region of the most pronounced velocity change. The small variation of S-wave time shifts with offset confirms that compaction-induced anisotropy is close to elliptical and, therefore, has weak influence on shear waves (equation 10). Time shifts for pure S-waves are controlled by the compaction-induced velocity V_{S0}. However, PS-wave offset time-shifts are slightly higher, indicating that their P-wave branch experiences increased time shifts with offset due to the stress-induced anisotropy.

Limitations

Although the general behavior of the delay surfaces correctly describes expected time shifts, there are anomalies indicative of processing artifacts. For example, an unusually large time-lead occurs on the SV data at approximately 1000-1400 m depth, and $\pm$1800 m offset. Similarly implausible time shifts are observed at a depth close to 2000-2500 m and extreme left-hand offsets of the PS data. These anomalies are caused by diffraction tails from the edges of the reservoir interfering with returns from the thin reflector (for example, see Figure 3(b)). This issue becomes more serious when the impedance contrast between the reservoir and host rock increases for larger pressure drops ΔP_p. We fit the cross-correlation timeshift curves with a user-adjustable low-pass filter and produce smoothed time-delay measurements that follow the general trend of actual time shifts. However, the combination of diffraction-tail interference or cross-correlation jitter with the current smoothing filter can cause noticeable anomalies. Post-processing improvements can overcome this issue. Despite the limited number of anomalies related to cross-correlation difficulties, the modeling package reveals correct general trends in the data.

Conclusions

Using semi-coupled geomechanical and finite-difference seismic modeling, we have developed a methodology for simulating the influence of reservoir compaction on P-, PS-, and S-wave reflections. Our process combines geomechanical computation of stresses, strains and strain-induced stiffnesses perturbations with 2D full-waveform (finite-difference) modeling for heterogeneous, anisotropic media. Velocity perturbations generated by compaction-related stress and strain are sampled by a thin reflector moved at regular depth intervals through the model. Measurements of time shifts between stressed and unstressed reservoir models are computed using windowed cross-correlations of the baseline and monitor surveys.

Numerical results for a homogeneous model with a rectangular reservoir showed that time shifts of PS- and S-waves above the reservoir are smaller in magnitude and opposite in sign from P-wave shifts. For reflectors below reservoir, however, the PS- and S-wave time shifts are approximately two to three times the P-wave time shifts. A four-fold increase in the pressure drop from 5 MPa to 20 MPa makes the time shifts up to two times larger. Time shifts for both PS- and S-waves have a similar spatial distribution as for P-waves but with a less significant dependence on the distance of the source from the center of the reservoir ($X_0 = 0$ m). The offset variation of S-wave time shifts is weak because stress-induced anisotropy is close to elliptical, and the SV-wave velocity is almost independent of angle.

Our processing generates full-waveform, multicomponent time-lapse seismic data and time shifts that can potentially be used to invert for the subsurface stress field. Finite-difference modeling also helps compute accurate amplitudes suitable for evaluating the AVO (amplitude variation with offset) response. The software is capable of handling tilted and multi-compartment reservoirs embedded in a heterogeneous background.

Future work will include stress-dependent rock modeling using the method of Shapiro (2003) and derivation of analytic equations for describing time shifts of PS- and S-waves. Sensitivity kernel analysis of the overburden after Liu and Tromp (2006) will be employed to identify stress-sensitive acquisition geometries and wave modes suitable for "reduced-footprint" seismic

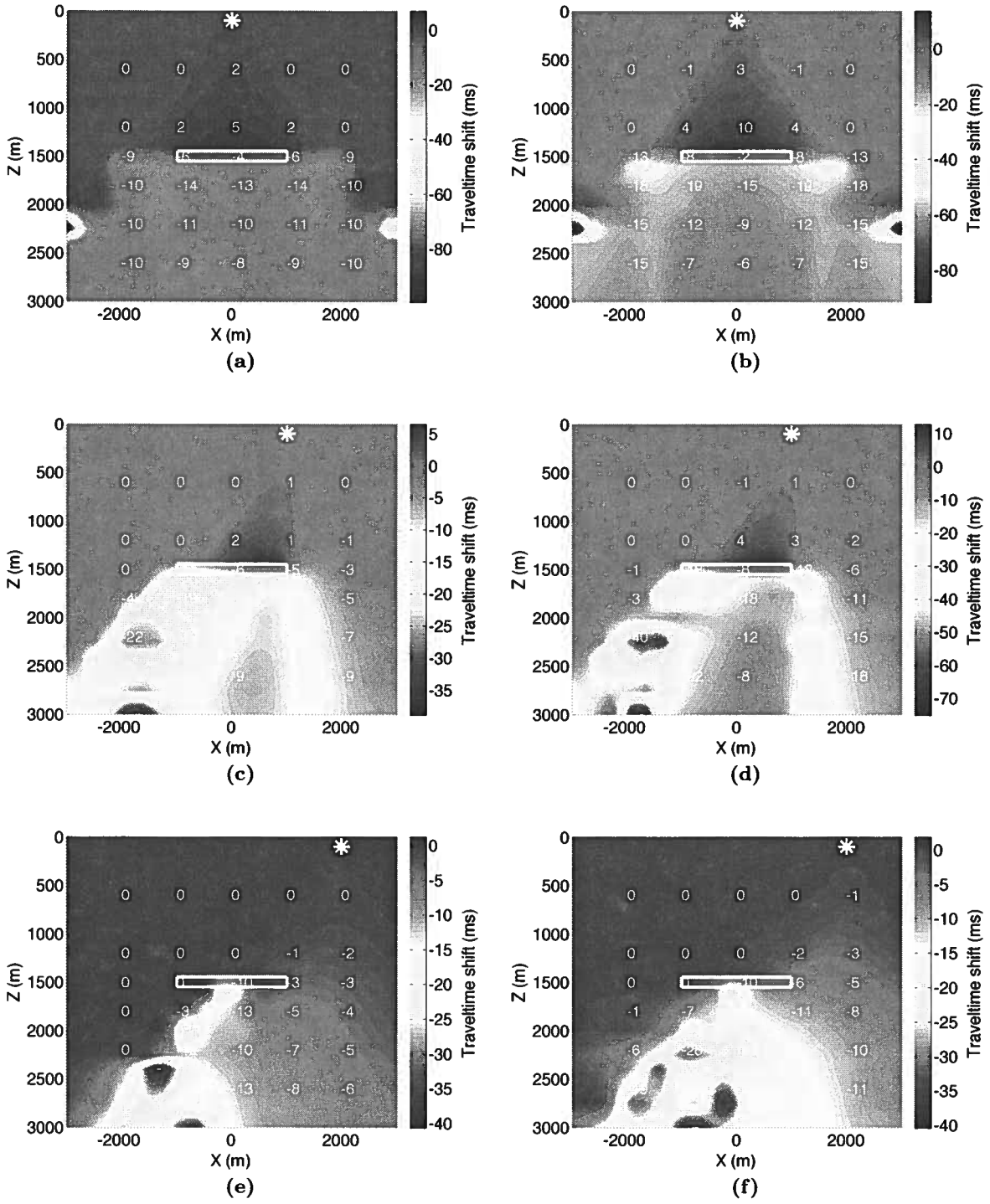

Figure 4. P-wave time shifts for the model in Figure 1 (same display as in Figure 2) produced by our modeling package for shot locations of X=0 m (a and b), X=1000 m (c and d), and X=2000 m (e and f). Pore-pressure drops are 5 MPa for the left column, and 20 MPa for the right column. The white rectangle marks the reservoir, while the white asterisk marks the shot location.

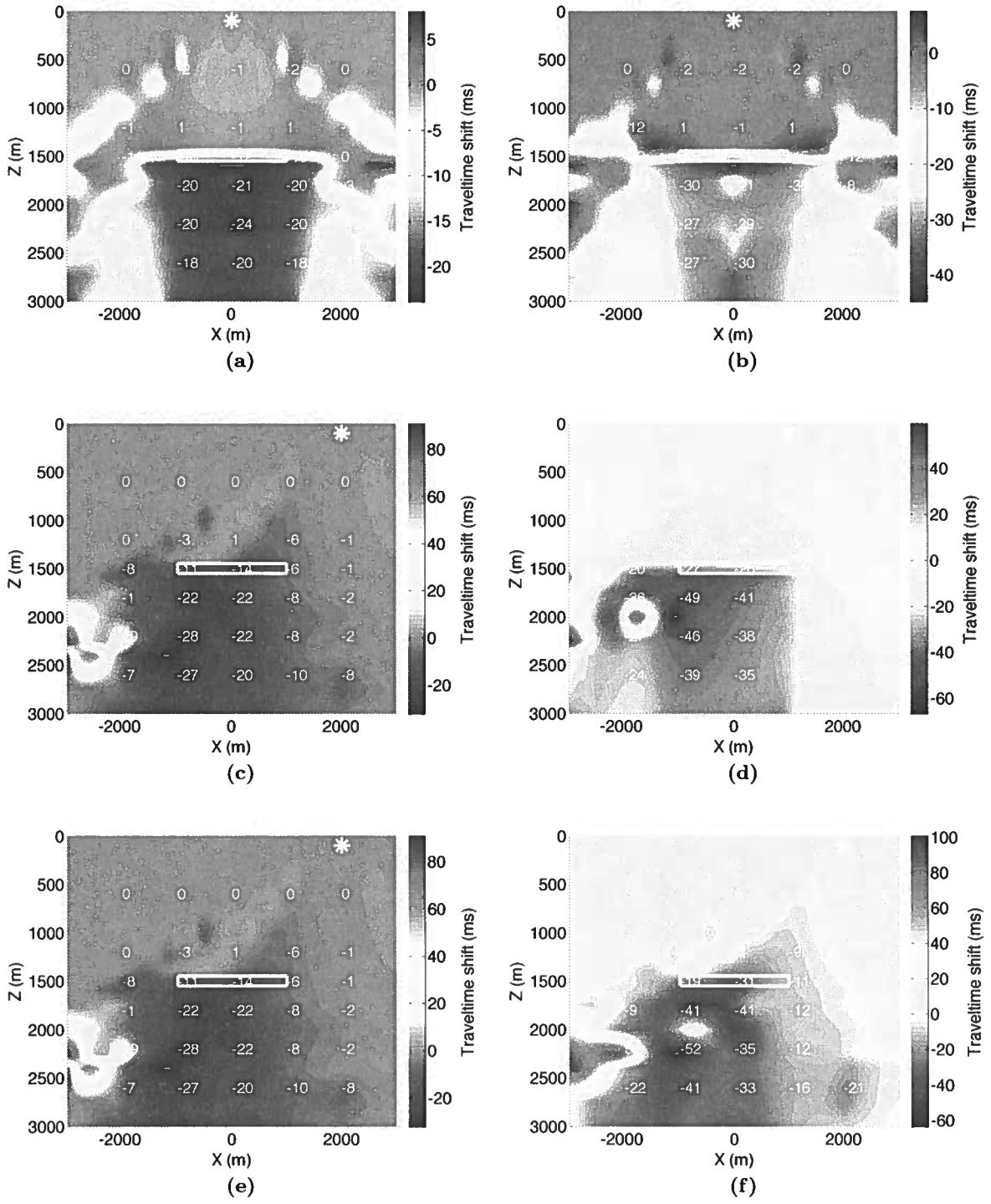

Figure 5. PS-wave time shifts for the model in Figure 1 (same display as in Figure 4) produced by our modeling package for shot locations of X=0 m (a and b), X=1000 m (c and d), and X=2000 m (e and f). Pore-pressure drops are 5 MPa for the left column, and 20 MPa for the right column.

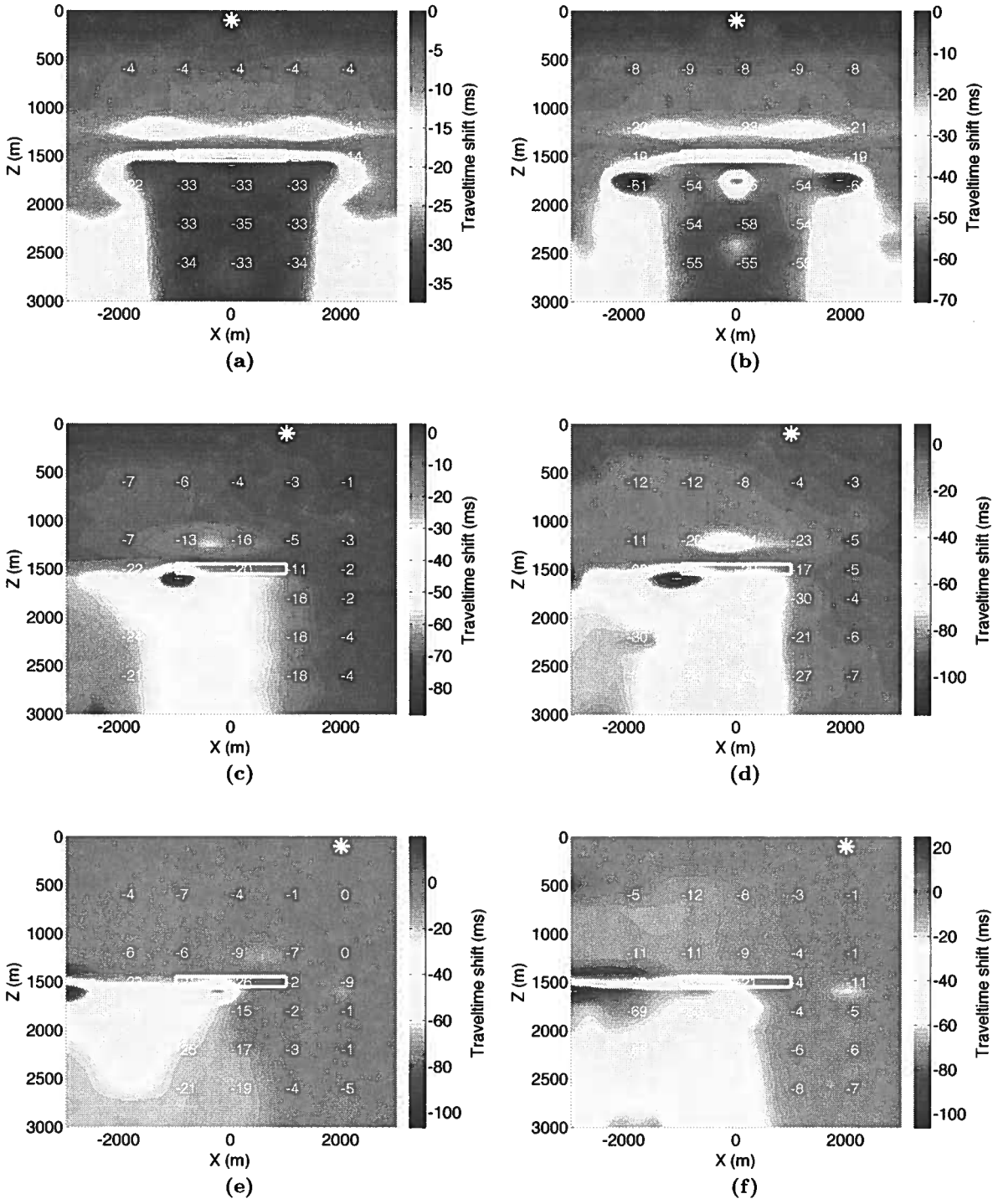

Figure 6. S-wave time shifts for the model in Figure 1 (same display as in Figure 4) produced by our modeling package for shot locations of X=0 m (a and b), X=1000 m (c and d), and X=2000 m (e and f). Pore-pressure drops are 5 MPa for the left column, and 20 MPa for the right column.

reservoir monitoring. These developments should aid in drilling and asset management for producing fields.

Acknowledgments

We wish to thank R. Fuck (Schlumberger, Cambridge), M. Batzle (CSM/CRA), A. Bakulin and J. Herwanger (WesternGeco, Houston), D. Gajewski (U. Hamburg), D. Johnston (ExxonMobil), and I. Vasconcelos (IonGeo) for discussions, comments, and suggestions, J. Godwin, T. Cullison, J. Yan (CSM/CWP), and G. M. Silva (MIT, EAPS) for assistance with Madagascar/Scons, and John Stockwell (CSM/CWP) for technical help. This work was supported by the Consortium Project on Seismic Methods for Complex Structures at CWP.

References

Bachrach, R., S. Noeth, N. Banik, M. Sengupta, G. Bunge, B. Flack, R. Utech, C. Sayers, P. Hooyman, L. de Boer, L. Leu, B. Troyer, and J. Moore, 2007, From pore-pressure prediction to reservoir characterization: A combined geomechanics-seismic inversion workflow using trend-kriging techniques in a deepwater basin: The Leading Edge, **26**, 590.

Calvert, R., 2005, Insights and methods for 4D reservoir monitoring and characterization. Distinguished Instructor Short Course, No. 8: Society of Exploration Geophysicists.

COMSOL AB, 2008, COMSOL Multiphysics. COMSOL AB, http://www.comsol.com/.

Fuck, R. F., 2009, Modeling of seismic signatures for reservoir characterization: Applications involving fracture- and stress-induced seismic velocity anisotropy: PhD thesis, Colorado School of Mines.

Fuck, R. F., A. Bakulin, and I. Tsvankin, 2009, Theory of traveltime shifts around compacting reservoirs: 3D solutions for heterogeneous anisotropic media: Geophysics, **74**, no. 1, D25–D36.

Fuck, R. F. and I. Tsvankin, 2009, Analysis of the symmetry of a stressed medium using nonlinear elasticity: Geophysics, **74**, no. 5, WB79–WB87.

Fuck, R. F., I. Tsvankin, and A. Bakulin, 2010, Influence of background heterogeneity on traveltime shifts for compacting reservoirs: submitted to Geophysics.

Hatchell, P. and S. Bourne, 2005, Rocks under strain: Strain-induced time-lapse time shifts are observed for depleting reservoirs: The Leading Edge, **24**, 1222–1225.

Hearmon, R., 1953, 'Third-Order' elastic coefficients: Acta Crystalographia, **6**, 331–340.

Herwanger, J. and S. Horne, 2005, Linking geomechanics and seismics: Stress effects on time-lapse multicomponent seismic data: 67^{th} Annual International Meeting, EAGE, Expanded Abstracts.

Herwanger, J., E. Palmer, and C. R. Schiøtt, 2007, Anisotropic velocity changes in seismic time-lapse data: 77^{th} International Meeting, SEG,Expanded Abstracts, **26**, 2883–2887.

Herwanger, J. V. and S. A. Horne, 2009, Linking reservoir geomechanics and time-lapse seismics: Predicting anisotropic velocity changes and seismic attributes: Geophysics, **74**, no. 4, W13–W33.

Hu, S. M., 1989, Stress from a parallelepipedic thermal inclusion in a semispace: Journal of Applied Physics, **66**, 2741–2743.

Johnston, D., 2010, Personal communication. ExxonMobil.

Kosloff, D., R. F. Scott, and J. Scranton, 1980a, Finite element simulation of Wilmington oil field subsidence : I. linear modelling: Tectonophysics, **65**, 339–368.

———, 1980b, Finite element simulation of Wilmington oil field subsidence: II. nonlinear modelling: Tectonophysics, **70**, 159–183.

Landrø, M. and J. Stammeijer, 2004, Quantitative estimation of compaction and velocity changes using 4D impedance and traveltime changes: Geophysics, **69**, 949.

Liu, Q. and J. Tromp, 2006, Finite-frequency kernels based on adjoint methods: Bulletin of the Seismological Society of America, **96**, 2383–2397.

Mavko, G., T. Mukerji, and J. Dvorkin, 2003, The rock physics handbook: Tools for seismic analysis in porous media: Cambridge University Press.

McCann, G. D. and C. H. Wilts, 1951, A mathematical analysis of the subsidence in the Long Beach-San Pedro area: Technical report, Caltech.

Minkoff, S. E., C. M. Stone, S. Bryant, and M. Peszynska, 2004, Coupled geomechanics and flow simulation for time-lapse seismic modeling: Geophysics, **69**, 200–211.

Olden, P., P. Corbett, R. Westerman, J. Somerville, B. Smart, and N. Koutsabeloulis, 2001, Modeling combined fluid and stress change effects in the seismic response of a producing hydrocarbon reservoir: The Leading Edge.

Olofsson, B., T. Probert, J. H. Kommedal, and O. I. Barkved, 2003, Azimuthal anisotropy from the valhall 4C 3D survey: The Leading Edge, **22**, 1228.

Prioul, R., A. Bakulin, and V. Bakulin, 2004, Nonlinear rock physics model for estimation of 3D subsurface stress in anisotropic formations: Theory and laboratory verification: Geophysics, **69**, 415.

Roste, T., 2007, Monitoring overburden and reservoir changes from prestack time-lapse seismic data - applicaitons to chalk fields: PhD thesis, Norwegian University of Science and Technology.

Sarkar, D., A. Bakulin, and R. L. Kranz, 2003, Anisotropic inversion of seismic data for stressed media: Theory and a physical modeling study on berea sandstone: Geophysics, **68**, 690.

Sava, P. and J. Godwin, 2010, SFEWE elastic fi-

nite difference wave-propagation development code for the Madagascar seismic software collection. http://www.reproducability.org.

Sen, V. and A. T. Settari, 2005, Coupled geomechanical and flow modeling of compacting reservoirs: The Leading Edge, **24**, 1284–1286.

Shapiro, S. A., 2003, Elastic piezosensitivity of porous and fractured rocks: Geophysics, **68**, 482–486.

Shapiro, S. A. and A. Kaselow, 2005, Porosity and elastic anisotropy of rocks under tectonic stress and pore-pressure changes: Geophysics, **70**, no. 5, N27–N38.

Strehle, R., 1987, Subsidence in long beach: Presented at the AAPG Pacific Section - Oil Producing Areas in Long Beach.

Tsvankin, I., 2005, Seismic signatures and analysis of reflection data in anisotropic media, volume 29. Handbook of Geophysical Exploration, Seismic Exploration: Elsevier Science.

Whitley, P. K., 1992, The geology of heidrun: A giant oil and gas field on the mid-norwegian shelf, chapter 24, 383–406. A. A. P. G, giant oil and gas fields of the decade 1978-1988 ed.

Yale and Jamieson, 1994, Static and dynamic mechanical properties of carbonates: Proceedings of the 1st Proceedings of the 1st North American Rock Mechanics Symposium, 463–471.

Zoback, M. D., 2007, Reservoir geomechanics: Cambridge University Press.